K. K. Pant
Sanjay Kumar Gupta
Ejaz Ahmad   *Editors*

Catalysis for Clean Energy and Environmental Sustainability

Petrochemicals and Refining Processes -
Volume 2

Springer

Catalysis for Clean Energy and Environmental Sustainability

K. K. Pant • Sanjay Kumar Gupta • Ejaz Ahmad
Editors

Catalysis for Clean Energy and Environmental Sustainability

Petrochemicals and Refining Processes - Volume 2

Editors
K. K. Pant
Department of Chemical Engineering
Indian Institute of Technology Delhi
New Delhi, Delhi, India

Sanjay Kumar Gupta
Department of Civil Engineering
Indian Institute of Technology Delhi
New Delhi, Delhi, India

Ejaz Ahmad
Department of Chemical Engineering
Indian Institute of Technology
(ISM) Dhanbad
Dhanbad, Jharkhand, India

To Our Parents, Families & Prof. K.K. Pant's Late Father Shri Pitamber Pant Ji

Preface

Considering the need for clean energy and environmental sustainability, significant progress has been made in catalyst synthesis processes using green chemistry principles and their applications in petrochemicals and refining processes. However, most of the books published on petrochemicals and refining processes have discussed primarily conventional catalysts which are in use for decades. As a result, there are not many books published which exclusively discuss green chemistry principles applied in the development of catalytic materials for petrochemicals and refining applications. Thus, volume II of the book covers current industrial catalytic processes that employ green chemistry principles and conventional catalytic processes. Several chapters have been written by scientists and researchers working in India's largest oil and gas industries for publication in volume II of the book, which includes the practical problems faced by the refiners and a real-life understanding of the catalytic processes. Also, chapters highlighting fundamental aspects of the catalytic processes in refining, petrochemicals and allied areas have been contributed by prominent academicians from different parts of the world.

Volume II contains 22 chapters covering different aspects of refining and petrochemicals that include insights into the nature of active phase, support, additives, catalyst synthesis, activation, deactivation and regeneration for hydrotreating, and hydrodesulfurization process, recent developments in catalysis for fluid catalytic cracking processes, alkylation processes, and C_3-based petrochemicals production. The discussions have been further extended to the selective hydrogenation of 1,3-Butadiene, natural gas conversion to petrochemicals, C-H bond activation, and flue gas treatment via dry reforming of methane, followed by a discussion on catalysts deactivation and challenges in refining and petrochemicals. Eventually, non-conventional catalytic materials for petrochemicals and refining have been introduced and discussed. Further chapters in the book cover technologies related to handing and conversion of refining industries by-products conversion such as pet-coke gasification and steam reforming followed by a discussion on technologies for syngas conversion to via Fischer-Tropsch reaction. A detailed discussion on micro-channel microreactors, catalyst synthesis, reaction kinetics and effect of CO_2 in syngas has been presented. Eventually, further discussions have been directed towards

tackling one of the most prominent problems of the twenty-first century, i.e. CO_2 capture and conversion. In this regard, several state-of-the-art CO_2 conversion processes to dimethyl ether, methanol and chemicals using catalyst materials have been discussed. Besides, CO_2 capture technologies using ionic liquids and deep eutectic solvents have been elaborated. Besides, catalytic materials for olefins polymerization and stability and destabilization of water-in-crude oil emulsion have been discussed. We understand that volume II will serve as reference materials for academicians working on materials synthesis and scientists and engineers working in the refining and petrochemical industries. Moreover, volume II will also serve as a ready to refer valuable resource for early career researchers and established researchers from chemical engineering, chemistry, biochemistry, biotechnology, mechanical engineering and interdisciplinary areas of research.

The overall flow and content is the outcome of several rounds of discussion, reviews and revisions. Therefore, the editors are highly indebted to all the reviewers for their precious time, thoughtful comments and valuable suggestions without which it would not have been possible to reach this stage. The editors would also like to thank all the authors for their patience during several rounds of revisions and timely responses. The editors would also like to sincerely thank Springer Nature for timely publication of the book and highly indebted to the Springer Nature team members especially Mr. Dinesh Vinayagam (Production Editor), Mr. Aaron Schiller, Mr. Joseph Quatela, and Ms. Amelie von Zumbusch for their constant support throughout the process starting from proposal stage to final book publication. The editors would like to thank and acknowledge the support of their lab members Dr. Shireen Quereshi and Mr. Prashant Ram Jadhao for their backend work, follow up with contributors, maintaining the record of all the documents and assistance in chapters review from the time of proposal to the publication of both the books. The editors are also highly indebted and obliged to their family members for their patience, care and unconditional support to complete both the volumes of the book.

New Delhi, Delhi, India   K. K. Pant
New Delhi, Delhi, India   Sanjay Kumar Gupta
Dhanbad, Jharkhand, India   Ejaz Ahmad

Contents

Recent Advances in Hydrotreating/Hydrodesulfurization Catalysts: Part I: Nature of Active Phase and Support

G. Valavarasu and B. Ramachandrarao

Abstract Hydrotreating/hydrodesulfurization is one of the important refining processes to improve the quality of petroleum fractions such as naphtha, aviation fuels, diesel, vacuum gas oils, and residue in terms of lower sulfur content and improved combustion performance. Over the years, the importance of this process increased multifold due to stringent environmental regulations imposed by several countries worldwide. Catalysts form the core of hydrotreating reactions in order to increase the rate of hydrodesulfurization reactions and enhance the active sites for removal of refractory sulfur species from petroleum fractions. In view of the importance of catalysts in carrying out hydroprocessing reactions, the present chapter (Part I) reviews the recent advances in hydrotreating/hydrodesulfurization in terms of the nature of active phase and support materials. It is imperative to understand these latest developments to design a suitable hydrotreating catalyst with required activity, selectivity, and long-term stability in order to produce ultralow sulfur/low aromatic fuels and lubricating oils.

1 Introduction

Hydroprocessing is broadly classified as a catalytic refining process carried out in the presence of hydrogen at higher temperatures and hydrogen partial pressures either to improve the quality of fuels/lubricating oils (hydrotreating) or convert the low-value vacuum gas oil (VGO) and residue into high-value fuels/lubricating oils (hydrocracking). Hydrodesulfurization (HDS) refers to the specific application of hydrotreating (HDT) for the removal of sulfur compounds from petroleum fractions

G. Valavarasu (✉) · B. Ramachandrarao
HP Green R&D Center, Hindustan Petroleum Corporation Limited,
Bengaluru, Karnataka, India
e-mail: valavarasu@hpcl.in

such as naphtha, kerosene, diesel, VGO, and residue. Catalysts form the heart of the process because all of the hydroprocessing reactions occur over the surface of the catalyst. The field of hydroprocessing catalysis is continuously evolving due to the growing demand for clean middle distillates and increasingly stringent specifications for automotive fuels such as gasoline and diesel. Also, lower demand for heavy fuel oils has been driving the refining industry more toward residue hydroprocessing, and in recent times, catalytic hydroprocessing has taken center-stage among residue upgradation processes. Researchers are continuously developing new-generation high-activity catalysts and novel process configurations to cater to the needs of changing refining market demands and product quality requirements.

The performance of hydroprocessing operations, both hydrotreating and hydrocracking, depends largely on the following aspects for any given feedstock characteristics:

- Type of reactor system.
- Type of the catalyst system.
- Process parameters.

For a particular type of reactor system, the type of catalyst can be tailored to meet the requirements of specific product slate and product quality for a given feedstock. Catalysts also play an important role in the selection of process parameters for a particular hydroprocessing application.

Hydroprocessing catalysts that are widely employed in commercial applications are metals of group VI A (Mo and W) with promoter metals of group VIII A (Co and Ni) or noble metals (Pt and Pd) supported on a suitable support material. The common support materials include alumina, silica-alumina, and zeolites. The active sites of the metal promote hydrogenation/dehydrogenation reactions, and the acid sites of the support promote hydrocracking reactions. The catalyst should also possess good mechanical strength to withstand the severe process conditions such as high pressure and high temperature employed during hydroprocessing along with appropriate physical properties such as surface area, pore volume, pore diameter, and pore size distribution for better activity and molecular diffusion.

Feedstock properties have a significant effect on the performance of hydroprocessing catalysts and thus play an essential role during the design of hydroprocessing catalysts for a particular service. Parameters such as the concentration of heteroatoms (mostly sulfur and nitrogen) and molecular weight distribution of the feedstock need to be considered for the design of distillate hydroprocessing catalysts, while the concentration of metals and asphaltenes are the major factors in the case of catalyst design for heavy oil hydroprocessing. Several factors need to be considered while designing a catalyst for a particular hydroprocessing application such as the type of active metals, choice of support, promoters, mechanical and physical properties, feedstock characteristics, extent of conversion, required product slate, etc. Since catalyst design is of paramount importance for the success of hydroprocessing applications, it is essential to delve into the advances in the area of hydroprocessing catalysis and the factors influencing the performance and operation of these catalysts. The present chapter focuses mainly on the catalytic

advancements in the area of hydrotreating/hydrodesulfurization of petroleum fractions with respect to the nature of active phase and support material.

2   Chemistry of Deep Hydrotreating/Hydrodesulfurization

The chemistry of petroleum hydroprocessing has been extensively studied and reported in the literature. Hydroprocessing involves a combination of hydrotreating and hydrocracking reactions. During the hydrotreating process, predominant reactions are removal of heteroatoms and saturation of unsaturated hydrocarbons (olefins and aromatics) with minimal hydrocracking of the feedstock. During the hydrocracking process, cracking reactions occur predominantly in addition to hydrotreating reactions resulting in significant conversion of the feedstock into high-quality lighter fractions. Catalysts play an important role during hydrotreating of petroleum fractions in controlling the rate of certain chemical reactions. The chemical reactions involved in the hydrotreating process are of two types: desirable and undesirable reactions (Table 1). Desirable reactions are those that help the main purpose of the hydrotreating process, while undesirable reactions are those that result in the loss of valuable components of feed or decrease of catalyst activity.

Hydrodesulfurization refers to the removal of organic sulfur from various hydrocarbon fractions. There are a wide variety of organic sulfur compounds present in various petroleum fractions, which include mercaptans, sulfides, disulfides, and thiophene derivatives. Mercaptans, sulfides, and disulfides are aliphatic sulfur compounds. Other thiophenic sulfur compounds can be broadly grouped into the following three categories:

1. Thiophenes.
2. Benzothiophenes.
3. Dibenzothiophenes.

It is easier to remove sulfur from compounds such as mercaptans, sulfides, and disulfides. However, it is increasingly difficult to remove sulfur from aromatic sulfur compounds such as thiophenes, benzothiophenes, dibenzothiophenes, and substituted dibenzothiophenes during the hydrotreating process. Thiophenes are the easiest to desulfurize compared to benzothiophenes and dibenzothiophenes. It is

Table 1   Desirable and undesirable reactions during hydrotreating of petroleum fractions

Desirable reactions	Undesirable reactions
Hydrodesulfurization	Hydrocracking
Hydrodenitrogenation (HDN)	Coking
Hydrodeoxygenation	
Saturation of olefinic compounds	
Hydrogenation of aromatic compounds	
Hydrodemetallization (HDM)	

difficult still to desulfurize substituted dibenzothiophenes such as 4,6-dimethyl dibenzothiophene (4,6 DMDBT) due to the refractory nature of these substituted compounds. Lower HDS reactivity of 4,6 DMDBT is ascribed to the steric hindrance of the substituent groups for accessing the active sites by sulfur species. Although sulfur present in the crude oil is distributed among the various distillation fractions, most of the sulfur tends to concentrate in the higher boiling fractions. During hydrotreating, HDS reactions take place concurrently along with other reactions such as hydrodenitrogenation, saturation of aromatics/olefins, hydrodeoxygenation, etc. As the specification of sulfur becomes tougher in fuels and desulfurization requirements change continuously, it is of paramount importance to remove sulfur from refractory species such as benzothiophenes, dibenzothiophenes, and substituted dibenzothiophenes. Sulfur removal from such refractory compounds usually requires saturation of adjacent aromatic ring to obtain catalytic access of the sulfur molecule with the consumption of hydrogen. The type of hydrotreating catalyst plays an important role in achieving such deep desulfurization in order to produce ultralow sulfur fuels such as gasoline and diesel.

Hydrodesulfurization reaction occurs mainly through the following two pathways:

- Direct desulfurization (DDS) pathway.
- Hydrogenation (HYD) pathway.

In the direct desulfurization pathway, the sulfur compound is removed directly from the hydrocarbon molecule by hydrogenolysis reaction, and in the hydrogenation pathway, hydrogenation reaction occurs as the first step followed by hydrogenolysis. Cobalt molybdenum-type catalysts mostly desulfurize hydrocarbons through the DDS pathway, while nickel molybdenum catalysts desulfurize through the hydrogenation pathway. The actual reaction pathway for desulfurization of a particular sulfur compound depends mainly on the type of catalyst and process conditions, especially hydrogen partial pressure employed during the reactions. Hydrodesulfurization through the DDS pathway consumes less hydrogen compared to the HYD pathway since the latter requires prior hydrogenation of one of the aromatic rings before the actual HDS reaction. The structure or shape of the sulfur-containing molecule also plays a role in determining the HDS reaction pathway. The reaction network for the HDS of 4,6-DMDBT over NiMo catalysts supported on meso-microporous Y zeolites through different reaction pathways such as direct desulfurization, hydrogenation, and isomerization is presented in Fig. 1 [1].

Hydrodesulfurization reactions are inhibited by certain compounds such as hydrogen sulfide (H_2S), nitrogen compounds, and polynuclear aromatics. Each of the reaction pathways is being inhibited by specific compounds. Hydrodesulfurization by the DDS pathway is inhibited by H_2S and basic nitrogen compounds. The HYD pathway is inhibited by all types of nitrogen compounds and polynuclear aromatics.

Tao et al. [2] studied the inhibiting effects of nitrogen compounds such as quinolone and indole on the HDS of thiophenic sulfur compounds in straight-run gas oil over a NiW/Al_2O_3 catalyst and showed that quinolone has a stronger inhibiting effect on HDS than indole has. The nitrogen inhibiting effects on the thiophenic
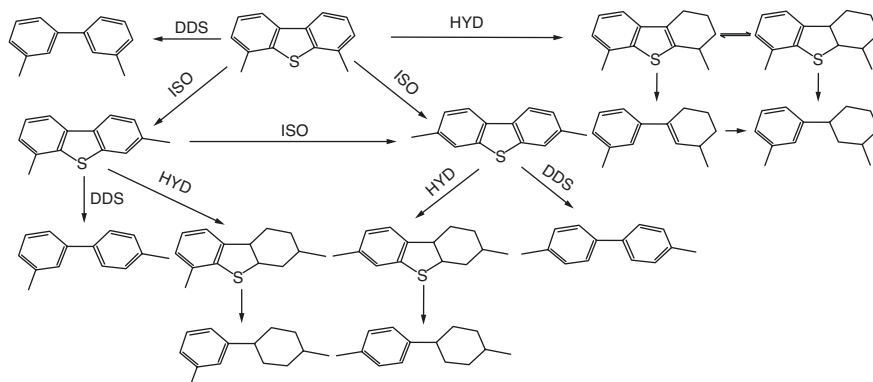
Fig. 1 HDS reaction of 4,6-DMDBT over NiMo/MY catalysts [1] (Reprinted from Applied Catalysis B: Environmental, 238, Wenwu Zhou, Qiang Wei, Yasong Zhou, Meifang Liu, Sijia Ding, Qi Yang, Hydrodesulfurization of 4,6-dimethyldibenzothiophene over NiMo sulfide catalysts supported on meso- microporous Y zeolite with different mesopore sizes, 212–224, 2018, with permission from Elsevier)

sulfur compounds decreased in the order: 4,6-DMDBT > 4-MDBT > C1DBT > DBT > C2-C3DBT in their study. Stanislaus et al. [3] described in detail the deep HDS chemistry and kinetics in their comprehensive review of the recent advances in the science and technology of ultralow sulfur diesel (ULSD) production.

3 Process Description

The process flow diagram of a typical diesel hydrotreater unit is shown in Fig. 2. The fresh diesel feedstock (usually a mixture of straight-run diesel and cracked gas oils) is initially heated in a feed-effluent exchanger and mixed with hydrogen gas streams (make up and recycle hydrogen). The combined feed is heated in a charge heater to the reactor inlet temperature. The furnace outlet stream is then sent to the top of the reactor. The reactor usually has multiple catalyst beds with different types and quantity of catalysts. In most of the cases, multiple reactors (usually two) are used along with a number of catalyst beds. Cold recycle hydrogen is used as a quench gas to control the exothermic temperature increase in the reactors. The amount of interbed quench gas depends on the type of diesel feedstock processed in the unit. Diesel hydrotreater units processing higher volumes of cracked stocks such as FCC light cycle oil (LCO) and light coker gas oil (LCGO) require more quench gas due to the highly exothermic nature of olefin and aromatic saturation reactions. The reactor effluent after exchanging heat with the incoming feed is sent to a high-pressure separator to separate the gas and liquid stream. The hydrogen-rich gas stream is separated and recycled to the reactor after removal of acid gases in the amine scrubber unit. Wash water is added upstream of the air cooler to dissolve
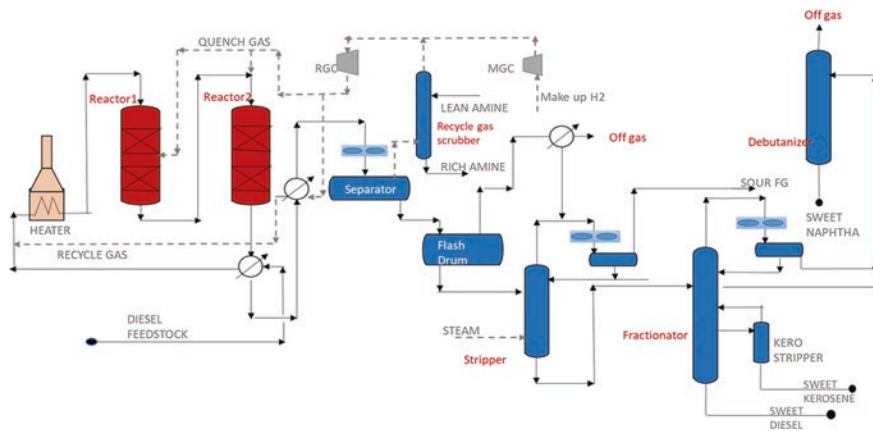
Fig. 2 Typical flow diagram of diesel hydrotreater unit

ammonium bisulfide, which otherwise causes corrosion in the downstream equipment. The liquid from the separator and flash drum is sent to a stripper to strip off hydrogen sulfide from the liquid. The stripper bottom product is routed to a fractionator in which naphtha, kerosene, and diesel streams are separated.

The process flow of most of the diesel hydrotreaters is similar to the one discussed above, with minor differences in the separation system and number of reactors. In the case of two-stage hydrotreaters, H_2S is removed from the first-stage product using mostly hydrogen as stripping medium, and the sulfur-free diesel is processed in the second stage over sulfur-sensitive noble metal-based hydrogenation catalysts to carry out deep aromatic saturation for cetane improvement. The process flow of other feed hydrotreaters such as naphtha, kerosene, vacuum gas oil, lube oils, and residue are also almost similar to that of diesel hydrotreating.

4 Physicochemical Properties

4.1 Chemical Composition of Catalysts

Hydrotreating catalysts comprise mainly two components, namely, active metals and support. The metal components that promote hydrogenolysis and hydrogenation functions are usually supported on suitable inert material such as alumina. These are basically supported metallic catalysts using either single metal or combination of two or more metals, but common catalysts contain two metals with one metal as the active component and another as a promoter. Most of the hydrotreating catalysts are made of sulfides of Group VI A metals (Mo, W) promoted by sulfides of Ni or Co and supported on high surface area carriers such as alumina, silica-alumina, and zeolites. γ-Alumina is the most commonly used support material in

Table 2 Typical physicochemical properties of CoMo/Al$_2$O$_3$ and NiMo/Al$_2$O$_3$ HDT catalysts

Property	CoMo/Al$_2$O$_3$	NiMo/Al$_2$O$_3$
Physical properties		
Shape	Extrudate trilobe or quadralobe	Extrudate trilobe or quadralobe
Diameter, mm	1.4–2.5	1.4–2.5
Length, mm	5–6	5–6
Surface area, m^2/g	125–200	125–200
Pore volume, ml/g	0.3–0.5	0.3–0.5
Bulk density, kg/m^3	650–850	650–850
Chemical properties		
MoO$_3$, wt%	15–25	15–25
NiO, wt%	2–4	3–5
P, wt%	1–5	1–4

HDT catalysts. In some special HDT applications, Group VIII noble metals such as Pt and/or Pd are also used on suitable supports. These noble metal-based HDT catalysts are used predominantly in the clean second stage of distillate hydrotreating units, especially to promote hydrogenation reactions and improve the cetane number of gas oils. The various combinations of metal sulfides (active components and promoters) do not have similar activity for promoting various hydrotreating reactions. The combinations of sulfide pairs are carefully chosen based on the type of feed and desired conversion.

Most common catalysts employed in refineries for various HDT applications are sulfided Co-Mo or Ni-Mo oxides supported on alumina. Co-Mo catalysts are the preferred choice when HDS is the desired reaction, and Ni-Mo catalysts are preferred when HDN and hydrogenation are the desired reactions. Hydrotreating catalysts typically contain about 2–6 wt% of promoter Co or Ni and 8–20 wt% of Mo active component or 10–25 wt% W active component. Catalyst composition, especially the chemical composition of active components, plays a major role in determining the overall activity of the hydrotreating catalysts. Typical physicochemical properties of industrial hydrotreating catalysts are listed in Table 2.

4.2 Structure of Support

The choice of support material and its characteristics influence the catalyst activity and selectivity profiles for various HDT applications. γ-Alumina is the most commonly used support material for HDT catalysts due to the following advantages:

- Provides high surface area.
- Assists in better dispersion of active metals.
- Provides high porosity.
- Provides good mechanical strength to the catalyst.
- Is highly stable.

- Is easy to form into desired shapes.
- Is relatively cheap.

Recently, other supports such as mixed oxides and zeolites have also been reported for hydrotreating applications. HDT catalysts usually do not require highly acidic supports in order to suppress the cracking activity and increase product yields unlike hydrocracking catalysts. The surface area of the support material is normally in the range of 100–350 m²/g. The structure of the support plays an important role in influencing the catalytic activity. Commonly used hydrotreating catalyst support such as γ-alumina with similar chemical composition but varied structure was found to exhibit different conversions during cracking of n-heptane due to the differences in the support structure [5].

4.3 Acidity

Acidity is provided by acid sites present in the hydrotreating catalyst support. The proper balance of acid strength and acid site distribution is essential for optimum activity and selectivity of HDT catalysts. Acidity does not play a major role in HDT/HDS catalysts since most of the reactions occur over metallic sites and acidic activity is not much desirable due to the formation of lighter ends and resultant loss of valuable product yield due to hydrocracking reaction. In contrast, support acidity plays a crucial role in the case of hydrocracking catalysts to impart the cracking activity and product conversion. Weak acidity with strong hydrogenation activity is the primary requirement for any hydrotreating catalyst.

4.4 Textural Properties

Textural properties of hydrotreating catalysts such as geometric structure and morphology from the macro- to the microlevel influence the performance of HDT catalysts in a significant manner. These textural properties are listed in Table 3.

Microlevel catalyst properties such as pore size and pore size distribution greatly influence the hydrotreating activity. HDT catalysts have different mesopore/

Table 3 Textural properties of hydrotreating catalysts

Textural properties	
Macrolevel properties	Microlevel properties
Size of the catalyst particle	Surface area
Shape of the catalyst particle (e.g., pellets, rings, extrudates, lobes)	Pore structure
	Pore size
	Pore size distribution

macropore size distribution depending upon the application and usually possess bimodal pore size distribution. Distillate HDS catalysts are designed with small pores (about 7–10 nm pore size distribution), while residue HDS catalysts have mesopores in the range of 10–20 nm. HDM catalysts are designed with large mesopores in the 10–50 nm range. Support macroporosity is also a desirable property with regard to increasing the access of reactants to the active catalyst surface and minimizing diffusional limitations. The total porosity of HDT catalysts is typically in the range of 0.5–0.6 or less in order to maintain catalyst pellet strength. Porosity is related to pellet strength, and catalyst pellet strength usually decreases with increasing porosity. There is an optimum combination of surface area and pore diameter, which gives the highest catalyst activity. For a given catalyst of similar chemical composition but differing pore size, feed properties also play an important role in the catalyst activity [6]. High HDS activity could be obtained with the small pore catalyst of high surface area for light gas oil feed due to less diffusion limitations of small molecules to the interior of the catalyst in comparison with heavy feeds such as VGO and residue.

Macrolevel properties such as size and shape of the catalyst particles also influence the hydroprocessing catalyst performance in terms of activity and pressure drop. Hydroprocessing catalysts are manufactured with different shapes and sizes depending on the type of application. The size of the fixed bed hydroprocessing catalysts generally ranges from about 1.5 to 10 mm in diameter with length-to-diameter ratios of about 1 for pellets and about 3 or 4 for extrudates [7]. Large catalyst particles offer diffusion resistance, decrease the rate of reaction, and thus reduce the catalyst activity per unit mass. In order to overcome the diffusion limitations, large catalyst particles are manufactured with holes or various shapes in order to increase the surface-to-volume ratio [8]. Although small particles do not pose diffusion issues, they are prone to higher pressure drop in fixed bed reactors. Shaped catalysts such as trilobes and quadralobes are widely employed in hydrotreating due to their advantages in terms of high external surface area and better accessibility to the interior of the catalyst compared to extrudates.

Bambrick [9] showed the influence of particle size on the relative weight activity for the same catalyst with different shapes such as cylinder and trilobes. It was observed in general that the surface area is the principal factor for catalyst activity while the size and shape of the catalyst particle will have influence on the pressure drop in fixed beds. For a given equivalent particle diameter, catalyst shapes were ranked according to the relative pressure drops as follows:

Rings < Beads < Pellet < Extrudates < Crushed particles

5   Characterization and Testing of HDT Catalysts

Characterization and testing of HDT catalysts are crucial for both refiners and catalyst manufacturers to understand the interaction between the composition, physicochemical properties, and catalyst performance. Since industrial HDT catalysts are

Table 4 Classification of catalyst characterization and testing [10]

S. no.	Classification	Referred properties
1	Evaluation of chemical composition and chemical structure	• Elemental composition, surface composition • Composition, structure, and properties of individual crystallographic phases • Nature and properties of functional groups present on the catalyst surface
2	Evaluation of texture and mechanical properties	• Size and shape of catalyst particles • Surface area • Pore size, pore size distribution • Attrition resistance • Crushing strength
3	Evaluation of catalyst performance	• Catalyst activity • Catalyst selectivity • Catalyst stability measured in terms of life

complex mixtures comprising multiple metals along with one or more additives/promoters, it is very important to understand the complexity of the catalytic system for the following reasons:

- Design and development of a new catalyst system (Catalyst manufacturer).
- Monitor the quality of manufactured catalysts (Catalyst manufacturer).
- Selection of a better catalyst system for existing units (Refiner).

There is continuous and enormous progress being made in the development and application of highly sophisticated catalyst characterization tools that revolutionized the field of heterogeneous catalysis. Since the refining catalysis is mostly based on heterogeneous catalyst systems, researchers quickly made use of sophisticated characterization equipment to synthesize highly active, selective, and stable catalysts by tailoring the composition, structure, and other properties. Catalyst characterization and testing can be broadly classified into three distinct but interrelated groups as presented in Table 4.

Chemical composition refers to the concentration of various catalytic materials/functional groups present on the surface of the hydrotreating catalyst. The texture of the catalyst includes both geometric structure and morphology, ranging from macroscale down to microscale. Mechanical properties such as abrasion/attrition resistance, crushing strength, and thermal shock resistance are also very important during industrial operations. Evaluation of catalyst performance involves the characterization of the catalyst in terms of activity, product selectivity, and catalyst life.

6   Advances in Hydrotreating Catalysts

Catalysts play a pivotal role during hydrotreating of different petroleum fractions, either to produce clean fuels or pretreat the feeds prior to further processing. Catalysts usually enhance the rate of different hydrotreating reactions such as HDS,

HDN, and hydrogenation of unsaturated hydrocarbons. Industrial HDT catalysts usually consist of molybdenum supported on γ-alumina and promoted with either cobalt or nickel. Although CoMo- and NiMo-based hydrotreating catalysts had been the mainstay in the commercial units, there was a need to improve the activity of these catalysts due to the introduction of stringent fuel quality regulations, especially with respect to sulfur during the 1990s spearheaded by the USA and Europe. Refiners were forced to comply with the specifications of ultralow sulfur fuels such as diesel and gasoline (sulfur: 10–15 ppmw) in several countries following the mandate in developed countries such as the USA and Europe.

The activity of traditional hydrotreating catalysts was not sufficient to meet the new specifications, and severe process conditions such as high reactor temperatures, low space velocity, and high hydrogen partial pressure were required in the hydrotreaters to meet the stringent specifications. The use of low-activity catalysts under severe process conditions resulted in higher catalyst deactivation rates with shorter cycle lengths and lower unit throughput. Catalyst suppliers and researchers were continuously striving to develop highly active and stable catalysts for reducing sulfur content to ultralow levels from hydrocarbon streams such as diesel and gasoline. Improved understanding of the important aspects of hydrotreating catalysts such as nature of the active phase and their structure, support effects, and the textural characteristics of the supports paved the way in developing high-activity catalysts with improved performance.

Better catalyst characterization tools helped in unraveling the mystery shrouded with hydrotreating catalysts, and a scientific basis was explained for the performance of new-generation catalysts in terms of their activity, selectivity, and long-term stability. Catalyst scientists used some of the advanced catalyst characterization methods such as high-resolution transmission electron microscopy (HR-TEM), Mössbauer emission spectroscopy (MES), and extended X-ray absorption fine structure (EXAFS) along with molecular modeling tools to comprehend the nature of active phase present in sulfided hydrotreating catalysts [11]. A comprehensive review of the hydrotreating catalyst developments for deep hydrodesulfurization of diesel was written focusing on the nature of active sites, effect of support and additives, improvements in catalyst preparation techniques, etc. by Stanislaus et al. [4].

6.1 Nature of Active Phase in HDT/HDS Catalysts

Different models have been proposed in the literature to explain the nature of active sites in the unpromoted and promoted molybdenum oxide-based HDT catalysts. Some of the features of the proposed models are listed below:

- Coordinately unsaturated (CUS) sites or exposed Mo ions with sulfur vacancies located at the edges and corners of MoS_2 structures were found to be active for promoting HDT reactions in the case of unpromoted MoS_2 catalysts.
- Basal planes are usually not active in the adsorption of molecules and do not usually contribute to catalytic activity.

- Widely accepted model proposes Co-Mo-S or Ni-Mo-S as the active phase for promoting hydrogenation and hydrogenolysis reactions in the case of promoted Co-Mo- or Ni-Mo-based HDT catalysts [12–14]. In this Co-Mo-S or Ni-Mo-S model, MoS_2 nanocrystals are reported to be the basic building blocks of the catalytic structure with the promoter atoms (Co or Ni) located at the edges of the MoS_2 layers in the same plane as that of Mo atoms. The active catalytic sites are considered to be the edge sites of the MoS_2 nanocrystallites with the promoter atoms such as Co or Ni located in the same plane forming Co-Mo-S or Ni-Mo-S active sites.

There are two distinct types of active sites (Co (Ni)–Mo-S) reported in the literature for promoting HDT reactions depending upon the intrinsic activity of the individual catalytic sites, Type I and Type II sites. Out of these active sites, Type II catalytic sites were reported to possess higher intrinsic activity for HDT reactions compared to Type I sites. Strong interaction between metal ions and support will result in the formation of less active Type I Co-Mo-S structures with remaining Mo-O-Al linkages, which are characterized by incomplete sulfiding [15–17]. Some of the features of the catalytic active sites are listed in Table 5.

Some of the important factors that can be tuned and controlled to form Type II active structures in order to increase the intrinsic activity of HDT catalysts are listed below:

- Nature and properties of support.
- Catalyst preparation parameters.
- Sulfiding method.

The synergy between the promoter (Co or Ni) atoms and active catalytic material (Mo) plays an important role in enhancing the HDS activity. In the past, several theories were proposed to elucidate the synergy between Co and Mo in the Co-Mo-S phase in enhancing the hydrodesulfurization reaction in terms of electronic properties of the catalytic materials [18–20]. The rate of HDS was correlated with the number of active sites or sulfur vacancies at the catalyst surface, and this number in turn is inversely proportional to the metal-sulfur bond strength. In this manner,

Table 5 Features of HDT catalytic active sites

| Feature	Type I	Type II
Activity	Comparatively low intrinsic activity	High intrinsic activity
Metal–support interaction (MSI)	Strong interaction	Weaker interaction
Dispersion	High dispersion of single slabs of MoS_2	Highly coordinated sites with less disperse MoS_2
Slab structure	Single slabs of MoS_2 (monolayer type structure)	MoS_2 mainly arranged in stacks (multilayered structure)
Nature of sulfiding	Incomplete sulfiding with residual Mo-O-Al linkages to the support	Almost complete sulfiding due to higher sulfur coordination of Mo and co or Ni

higher HDS activity is attributed to the weaker metal-sulfur bond strength. In Co-promoted MoS₂-based HDS catalysts, the decrease in Mo-S bond strength and improved HDS activity is attributed to the electron donation from promoter Co to Mo atom. The promotion effect of Co in HDS catalysts by weakening the metal-sulfur bond strength is well understood and confirmed using both theoretical estimations and experiments. Morphology of the sulfide phase can be tuned by increasing the metal content and addition of organic additives [21]. Increased metal loading results in a progressive increase in MoS₂ slab length with little effect on stacking, while introduction of organic additives such as ethylene glycol and citric acid resulted in the reduction of MoS₂ slab length and enhancement in the stacking due to variation in metal–support interaction.

Topsoe et al. [22] used advanced catalyst characterization tools such as scanning tunneling microscopy (STM) to identify a special type of Mo electronic edge sites termed as "brim sites" in hydrotreating catalysts, which are altogether different from Type I and Type II active sites. These brim sites tend to bind the sulfur-containing hydrocarbon molecules due to their metallic character and react with hydrogen available at neighboring edge sites. Brim sites are not co-coordinately unsaturated sites and usually exhibit higher hydrogenation activity compared to the conventional type of active sites. It was proposed that brim sites promote hydrogenation reactions and both the edges are responsible for direct sulfur removal. The hydrogenation mechanism involving brim sites is used to explain several catalytic phenomena such as inhibitions, steric hindrance of alkyl substituents, and poisoning effects in a better way compared to the vacancy model.

Tuxen et al. [23] investigated the effect of carbon incorporation as carbide into MoS₂ nanocluster during sulfidation with organic sulfur compounds such as dimethyl disulfide (DMDS) or dimethyl sulfide (DMS) using STM, XPS, and density functional theory (DFT) calculations. Their studies showed the strong influence of the choice of sulfiding agent on the morphology and dispersion of the sulfided phase and ultimately on the catalytic activity of the freshly sulfided phase. The presence of carbon in the form of carbides was not observed at the edge sites of MoS₂ under HDS conditions due to unfavorable thermodynamics. There was no evidence for the existence of surface or bulk carbide phases in HDS catalysts, and substitution of sulfur in MoS₂ nanoclusters incorporated with carbon was not energetically favorable and stable.

Chen et al. [21] studied the morphology and selectivity of the sulfide phase of CoMo catalyst in the HDS of 4,6-DMDBT and hydrodearomatization (HDA) of 1-methylnaphthalene (1-MN) by increasing the metal content and incorporation of organic additives such as ethylene glycol and citric acid. The change in morphology of the sulfide phase resulted in modifications in the DDS, HYD, and HDA activities of the catalyst along with hydrogen consumption. Based on XPS and HR TEM analysis of the corner and edge sites of sulfide slabs of CoMoS sites, it was revealed that the corner and edge sites of the sulfide phase are responsible for the DDS and HYD routes for the HDS of 4,6-DMDBT, respectively. Figure 3 shows the relationship between the ratio of corner and edge sites of the CoMoS phase and rate constants of DDS and HYD reactions on various catalysts, and the linear relationship

Fig. 3 Relationship between $C(CoMoS_C)/C(CoMoS_E)$ and k_{DDS}/k_{HYD} on various CoMo catalysts [21] (Reprinted from Catalysis Today, 292, W. Chen, X. Long, M. Li, H. Nie, D. Li, Influence of active phase structure of CoMo/Al_2O_3 catalyst on the selectivity of hydrodesulfurization and hydrodearomatization 97–109, 2017, with permission from Elsevier)
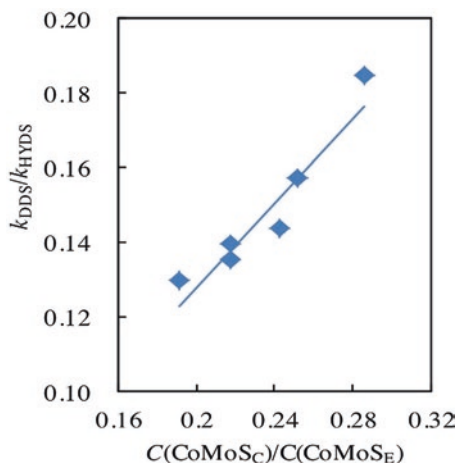
confirms their conclusion on the responsible sites for DDS (corner) and HYD (edge) reactions. Both hydrogenation of 4,6-DMDBT and HDA of 1-MN were found to occur on the edge sites of the MoS_2 slabs. As the stacking of the slabs increases, hydrogenation of 4,6-DMDBT was more promoted than the HDA of 1-MN.

Liu et al. [24] used PVP-assisted synthesis of NiMo oxide catalysts (NiMo-x) with varied PVP contents (referred to as x) to prepare and study the influence of various NiMo phases on the HDS reactions of DBT. Based on XRD analysis, α- and β-NiMoO$_4$ and ammonium nickel molybdate were observed on the NiMo precursors, while MoS_2 and Ni_3S_2 phases were observed in sulfided NiMo catalysts (Fig. 4). Sulfided NiMo catalysts derived from β-NiMoO$_4$ were found to be more active for HDS of dibenzothiophene (DBT) compared to those from α-NiMoO$_4$ due to facile reduction of nickel oxide and molybdate resulting in the formation of active NiMoS phase.

The structure and stability of the active phase play a pivotal role in HDT catalyst performance, which primarily depends on the extent of metal–support interaction. Proper design of the active phase structure is essential for improved catalyst performance, which can be attained through optimization of catalyst preparation and sulfidation conditions as shown in Fig. 5 for the HDS of 4,6-DMDBT [25]. Catalyst preparation parameters such as support properties and metal precursors in the impregnating solution and sulfidation conditions such as pressure, temperature, and gas composition play an important role in catalyst performance. As the severity of hydrotreating increases for various feeds due to stringent HDS, HDN, and HDM requirements, highly active and stable catalytic active phase is needed for better activity. SINOPEC claims to apply the knowledge of reaction chemistry for the design of active phase structure in HDT catalysts to achieve desirable activity, selectivity, and stability. Nie et al. [25] reported higher catalytic activity in various HDT catalysts through the following modifications in preparation methods:
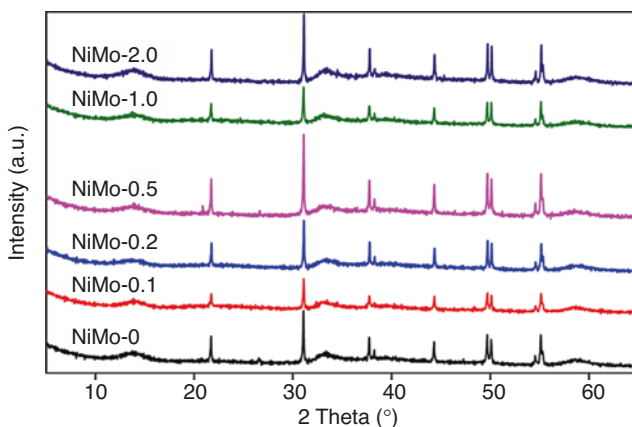
Fig. 4 XRD patterns of the unsupported sulfided NiMo catalysts [24] (Reprinted from Catalysis Today, 282, Huan Liu, Changlong Yin, Xuehui Li, Yongming Chai, Yanpeng Li, Chenguang Liu, Effect of NiMo phases on the hydrodesulfurization activities of dibenzothiophene, 222–229, 2017, with permission from Elsevier)
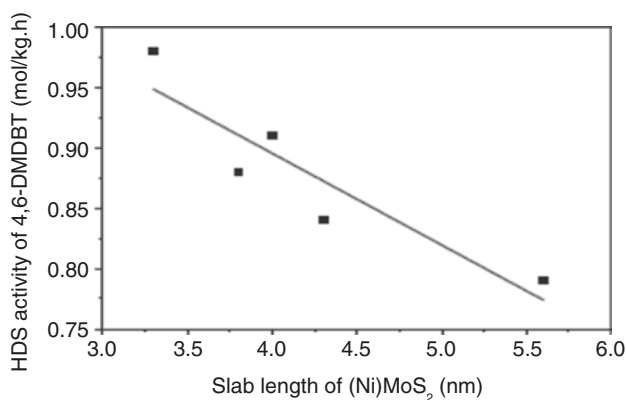
Fig. 5 Effect of catalyst active phase design in terms of $(Ni)MoS_2$ slab length on HDS activity of 4,6-DMDBT [25] (Reprinted from Catalysis Today, 316, Hong Nie, Huifeng Li, Qinghe Yang, Dadong Li, Effect of structure and stability of active phase on catalytic performance of hydrotreating catalysts, 13–20, 2018, with permission from Elsevier)

- Posttreatment of the active phase structure in the case of gasoline HDS to increase selectivity.
- CoMo- and NiMo-based HDT catalysts for diesel containing well-dispersed active phase slabs with moderate MSI.
- Highly active and stable NiMo-based resid HDS catalysts through strong MSI.

In general, unsupported noble metal sulfide catalysts possess high catalytic activity compared to MoS_2-based catalysts. However, Ni or Co promotion in MoS_2 and dispersion on high surface area alumina makes it highly effective for HDT

application in the refining industry. Studies have been performed to investigate the promotion effect of noble metals such as Pt, Pd, Ru, Rh, and Ir with MoS_2-based catalysts supported on alumina using decomposition and impregnation of bimetallic molecular clusters on the HDS, HDN, and HYD activities of a feedstock containing DBT, indole, and naphthalene [26]. The hydrotreating activities followed the order: $Mo_3Ir > Mo_3Rh > Mo_3Ru > Mo_3Pt > Mo_3Pd$. Although Mo_3Ir- and Mo_3Rh-based catalysts were found to have strong synergy and higher HDT activity, their performance is inferior compared to the Mo_3Ni catalyst.

The effect of the nature of catalytic active phases on the extent of HDS and olefin saturation reactions will be helpful in the development of highly selective FCC gasoline HDS catalysts that require selective removal of sulfur compounds with minimum octane loss. Huang et al. [27] investigated the nature of CoMoS and MoS_2 active phases co-existing on sulfided $CoMo/Al_2O_3$ catalysts for the selective HDS of gasoline. They prepared two series of catalysts: $CoMo/Al_2O_3$ catalysts with different EDTA/Co molar ratios and EDTA containing $CoMo/Al_2O_3$ catalysts with different Co contents. HDS activity of the sulfided $CoMo/Al_2O_3$ catalysts was primarily enhanced by the high concentration of CoMoS phases, while olefin hydrogenation activity was improved by high concentration of MoS_2 active phases.

Grønborg et al. [28] used advanced characterization tools such as STM to study the cluster shapes and edge transformations in MoS_2 structure and promoted CoMoS-type HDS catalysts under reducing conditions both through experimental observations and DFT predictions. It was shown that the reduced catalyst clusters were terminated with a fractional coverage of sulfur, representing the catalyst in its active state. The presence of catalytically active S-H groups was found on the Co-promoted edge sites by adsorption of a proton-accepting molecular marker.

There is a new trend in using DFT simulations for the identification of active sites and complex reaction pathways in the hydrotreating catalysis due to its industrial importance. DFT studies will be useful to get new insights into the nature of active sites, and this knowledge could be used in the design of efficient HDT catalysts for the production of ULSD. Li et al. [29] utilized DFT calculations using a dispersion correction method to construct a novel corner site model of MoS_2 and investigate the DDS and HYD pathways. Based on mechanistic and energetic analysis, it was found that the C-S bond cleavage had the highest energy barrier for both reaction DDS and HYD pathways and DDS is more favorable on corner sites of MoS_2 compared to HYD pathway. They also compared the activation energies of both reaction pathways on four different active sites (Mo edge, S edge, CoMoS edge, and corner) for the HDS of thiophene and concluded that corner sites play a major role in the HDS of thiophenic sulfur compounds through mostly DDS pathway.

6.2   Supports or Carriers

Support material with optimized physicochemical characteristics is the prime prerequisite for the preparation of good HDT catalysts with high activity and long-term stability. Supports provide the required surface area for dispersion of metals. The

active metals are supported on a carrier in HDT catalysts, and the most commonly used support or carrier material is γ-Al$_2$O$_3$ due to its favorable characteristics in terms of textural/mechanical properties and relatively low cost. γ-Al$_2$O$_3$ carrier usually provides high surface area for maximum dispersion of active phases and good mechanical strength to the catalyst. Alumina does not act as an inert carrier material in hydrotreating catalysts but plays a significant role in the catalyst performance through interaction with the active metals [30]. Interaction of support and active metals plays an important role in enhancing the activity of hydrotreating catalysts. For example, silica-supported Ni-Mo or Co-Mo hydrotreating catalysts exhibit relatively lower activity compared to alumina-supported catalysts due to weak interactions between the silica support and active metals [10]. Support–metal interaction affects the catalytic activity by strongly influencing the formation and dispersion of active catalytic phases such as Co-Mo-S and Ni-Mo-S on the surface of the catalyst.

Although γ-alumina has favorable characteristics in terms of mechanical strength resulting in longer catalyst life and high surface area and pore volume, it was reported to have strong interaction with transition metal oxides leading to incomplete sulfidation and lower HDS performance of the final catalyst. This fact resulted in the search for the development of better supports to overcome the limitations of traditional alumina support. Some of the support materials investigated by researchers for their suitability in HDT/HDS applications include carbon, TiO$_2$, ZrO$_2$, zeolites (e.g., USY), MgO, clays, silica, zirconia, titania, and mesoporous materials (e.g., MCM-41).

Acidic supports such as zeolites and amorphous silica-alumina were also considered for HDS catalysts, and studies were performed for their effectiveness using CoMo, NiMo, or Mo metallic phases. The acidic zeolites and amorphous silica-alumina-based catalysts were found to improve the HDS of recalcitrant sulfur species such as 4,6-DMDBT due to enhanced isomerization of the alkyl groups resulting in the suppression of the steric hindrance effect. Among the acidic components, Y zeolite has been found to be effective for the removal of refractory sulfur species from diesel due to its favorable physical properties, acid strength, acidity, and hydrogen transfer activity. Incorporation of supports with high acidity in HDT/HDS catalysts could enhance the rate of HDS of refractory sulfur compounds by promoting reactions such as isomerization and dealkylation, which may favorably remove the steric hindrance of these molecules [31–36]. Isoda et al. [31, 35, 36] studied deep HDS pathways for 4,6-DMDBT with the addition of 5 wt% Y-zeolite in CoMo/Al$_2$O$_3$ catalyst and found favorable HDS activity through modification of the molecular structure of the refractory species through isomerization and demethylation of methyl groups. Pawelec et al. [37], Tanga et al. [38], and Sun et al. [39] studied bifunctional HDS catalysts with incorporation of different acidic components such as β zeolite, ZSM-5, and Y zeolites in the support material. The Brønsted acidity of these catalysts was responsible for the isomerization activity, which enabled removal of steric hindrance for sulfur removal [33].

As already discussed, metal–support interactions play a key role in the formation of Type I and Type II catalytic active sites and result in differences in the catalyst activity. In addition to this, support interactions are also found to affect the degree

of stacking of MoS_2 and Co-Mo-S structures. Modification of γ-Al_2O_3 support through incorporation of zeolites and some metal oxides was also attempted to promote the desulfurization of sterically hindered sulfur species such as alkyl DBTs through isomerization and dealkylation. Some of these mixed oxide supports tested for HDS applications include Al_2O_3-SiO_2, Al_2O_3-TiO_2, Al_2O_3-ZrO_2, and Al_2O_3-P_2O_5. Other mixed supports include Al_2O_3-HY and Al_2O_3-F.

Hydrodesulfurization of model compounds (DBT and its derivatives) and straight-run gas oils over mixed metal oxide TiO_2-Al_2O_3 showed much higher activity for desulfurization compared to supported alumina-based HDT catalysts [14, 40–42]. Incorporation of Ti in the different support materials such as alumina, SBA-15, and MCM-41 was found to show higher HDS performance for metal sulfide catalysts compared to Ti-free supports due to weak Mo-S interaction and creation of more sulfur vacancies due to reduction of Ti species to Ti3+ species under HDS reaction conditions and subsequent transfer of spare electrons into the Mo3d conduction band [43–47].

Fujikawa et al. [48] prepared CoMo HDS catalyst for the production of ULSD using phosphorous and citric acid as additives on HY-Al_2O_3 support and showed three times higher HDS activity compared to conventional CoMoP/Al_2O_3 catalyst for the HDS of straight-run light gas oil feedstocks under industrial HDT conditions. Ding et al. [49] studied hydrotreating of LCO using NiW catalysts containing Y zeolite and found that these catalysts were suitable for deep HDS due to their stability and suitable pore size distribution for the diffusion and reaction of large sulfur compounds such as alkyl substituted dibenzothiophenes.

Nakano et al. [50] investigated the effect of surface modification of USY zeolite with alumina on the HDS and cracking activity of the Ni-Mo/Al_2O_3 catalysts. Various catalysts were prepared by coating of alumina over USY zeolite in different proportions, and the performance of these catalysts was compared with physically mixed alumina and USY zeolite-based catalysts. High HDS activity along with significant hydrocracking activity was observed using the catalyst prepared by physical mixing of alumina and USY zeolite. In the case of alumina-coated USY zeolite catalysts, an optimum amount of alumina coating, neither too low nor too high, was required to obtain a better balance between HDS and hydrocracking activity.

Wang et al. [51] prepared bifunctional highly loaded NiMoW catalysts with different amounts of USY zeolites incorporated during synthesis of precursor using the hydrothermal method and used them for the HDS of 4,6-DMDBT. HR TEM images of the sulfided catalysts (with 0% and 10% USY zeolite in precursor) showed a decrease in the average stacking number and average slab length in 10% USY zeolite resulting in more accessible active sites for the HDS reactions (Fig. 6). The product distribution during hydrogenation of 4,6-DMDBT over NiMoW–USY catalysts with different wt% of USY zeolite in the precursor showed that loading of 10 wt% USY zeolite is optimal in order to obtain better HDS activity through favorable textural and morphological properties.

Han et al. [51] showed the effect of support Brønsted acidity of NiMo and alumina-based HDS catalysts on the improved HDS and HDN activity of model compounds through the electronic effect of the support Brønsted acid sites on the
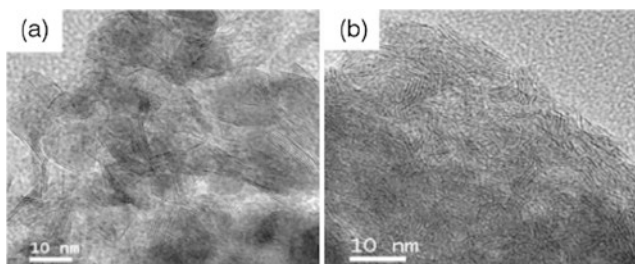
Fig. 6 HR TEM images of sulfided NiMoW catalysts with 0% and 10% USY zeolite in the precursor [51]. (**a**) Catalyst with 0% USY in precursor (**b**) Catalyst with 10% USY in precursor (Reprinted from Catalysis Communications, 88, Yiyan Wang, Changlong Yin, Xuepin Zhao, Chenguang Liu, Synthesis of bifunctional highly-loaded NiMoW catalysts and their catalytic performance of 4,6-DMDBT HDS, 13–17, 2017, with permission from Elsevier)

edge sites of adjacent MoS_2 nanoslabs. The electronic effect facilitates the formation of CUS and enhances the acidity of -SH species and also exhibits high isomerization activity in addition to promoting HDS and HDN activity of the catalyst.

Although Y zeolite has been reported to be an effective support for carrying out HDS reactions, the strong acid strength and acid site density of Y zeolite may result in hydrocarbon yield loss. Modification of Y zeolites using different metals assumed significance to moderate and adjust the acidic properties and improve the pore structure. Zhou et al. [52] modified USY zeolites with gallium, phosphorous, and a combination of gallium and phosphorous and used them as support for the preparation of NiMo-based HDS catalysts for application in the HDS of FCC diesel. Ga- and P-modified USY zeolite catalysts showed higher HDS and HDN efficiencies compared to conventional NiMo-based catalysts.

Zhang et al. [51] synthesized CoMo-based HDS catalysts using crystalline zeolite nanorods modified with Ti as support material and showed higher activity and stability for the HDS of 4,6-DMDBT than CoMo catalysts supported on Ti-free mesoporous ZSM-5 and pure silicon silicalite-1 zeolites, SiO_2–TiO_2 and γ-Al_2O_3.

Sun et al. [54] studied the effect of divalent tin on the molecular sieve SnSAPO-5 and its modulation to alumina support through formulation of efficient NiW-based deep HDS catalysts using 4,6-DMDBT as a model compound. Substitution of trivalent aluminum by divalent tin in the framework of SnSAPO-5 resulted in an increased number of Lewis and Brönsted sites and higher HDS rates compared to other catalysts synthesized with the same active metal content. The higher HDS performance and TOF in the case of tin-modified SAPO-5-Al_2O_3 composite catalyst was attributed to suitable catalyst acidity, higher sulfidation degree, and increased stacking of WS_2 slabs, which are essential for the development of ultra-deep desulfurization of petroleum fractions such as diesel to meet the increasingly stringent sulfur specifications.

Meng et al. [55] prepared a highly active trimetallic NiMoW-based HDS catalyst using Zr modified mesoporous KIT-5 material as support and showed highest activities for the HDS of DBT and 4,6-DMDBT due to enhanced catalyst acidity and better active metal distribution.

Studies using other support materials such as nanoporous alumino-silicate, e.g., MCM-41, Al-MCM-41, and SBA-15, and carbon supports were also reported in the literature for CoMo- and NiMo-based HDS catalysts [56–60]. Nanoporous alumino-silica-based HDS catalysts are found to possess certain advantages such as high surface area, high metal loading, high dispersion of active phase, and better feed accessibility resulting in higher activity compared to conventional alumina-based catalysts. Catalysts based on carbon support have been found to show high HDS activity with decreased coke deactivation but have disadvantages due to rapid sintering of the active phase under reaction conditions and nonregenerability after deactivation. Although HDS catalysts using these new and novel supports were found to perform better compared to conventional alumina-supported catalysts in laboratory studies in terms of activity and selectivity, their application in industrial HDS/HDT units requires extensive data generation and validation on their deactivation and regeneration characteristics, economics of the formulations, etc.

Han et al. [61] synthesized γ-alumina with interconnected pore structure with the presence of highly ordered mesopores within the walls of the macropore cages using a sol-gel process using a mesoporous structure-directing agent. A CoMo-based HDS catalyst was prepared using the interconnected meso-microporous alumina support and tested for the catalytic performance for HDS of DBT. The CoMo-based catalyst supported on the interconnected γ-Al_2O_3 exhibited higher HDS activity compared to the catalyst prepared using conventional mesoporous-based commercial support due to better accessibility of the reactants to the active sites. HDT catalysts prepared using mesoporous aluminas have found to be highly active compared to conventional γ-alumina-based catalysts due to their better textural properties (surface area and pore volume), week acidity, improved metal dispersion, and lower Mo reduction tempertures. Badoga et al. [62] synthesized NiMo-based catalysts using mesoporous alumina support and studied the performance for the HDT of heavy gas oil. Mesoporous alumina was synthesized using pluronic P-123 as a structure-directing agent and aluminum isopropoxide as a precursor for aluminum with varied HNO_3/H_2O ratios ranging from 0 to 2. There are changes in the textural properties and the structure of the NiMo catalysts prepared using mesoporous aluminas with an increase in water content. NiMo catalysts prepared using synthesized mesoporous alumina with HNO_3/H_2O ratio of 0.6 showed the highest HDS and HDN activity.

Li et al. [63] showed high HDS activity for 4,6-DMDBT for the NiMo catalyst supported on tailored γ-Al_2O_3. The support was synthesized by hydrothermal treatment of pseudoboehmite. The high catalytic activity was attributed to their favorable crystal structure, better dispersion of Ni-Mo-S active phases, decrease in the amount of hydroxyl groups, and tetrahedral cation vacancies.

Dong et al. [64] prepared mesoporous alumina microspheres comprising an assembly of highly crystallized alumina nanorods using a template-free hydrothermal method with hierarchical pore structure and high specific surface area. Later, bimetallic macro–mesoporous MoNi/Al_2O_3 catalysts were prepared using the hierarchical alumina with better dispersion of the active Mo and Ni metals and higher HDS and HDM activity compared to single pore catalysts.

Peng et al. [65] deposited cobalt and molybdenum nanoparticles on the mesoporous γ-Al_2O_3 with the addition of an organic compound and found that the catalyst was easily reduced with the organic compound resulting in better sulfidation degree and enhanced HDS activity. This catalyst was commercially tested for diesel HDS application to produce ULSD and also reported to be highly stable.

Tang et al. [66] prepared CoMo-based HDS catalysts using mesoporous mordenite nanofibers with bundle structure as a support material. The mesoporous catalyst showed very high HDS activity for HDS of 4,6-DMDBT (99.1%) compared to a conventional γ-alumina-supported CoMo catalyst (61.5%). The high activity was ascribed to the migration of spillover hydrogen from micropores to CoMo active sites present in the mesopores.

Dugulan et al. [67] investigated the sulfiding behavior and hydrotreating performance of CoMo- and NiMo-based HDT catalysts supported on carbon. Although structural evolution and active phase transition are similar for CoMo/C and CoMo/Al_2O_3 catalysts, some sintering was observed for carbon-supported catalysts. In the case of the NiMo/C catalyst, strong adsorption of dibenzthiophene, quinoline, and polyaromatics in comparison with NiMo/alumina resulted in significantly high HDS and HDN activity for DBT and quinolone, respectively. However, the NiMo/C catalyst showed poor activity for the HDT of heavy gas oil due to competitive adsorption of polyaromatics along with sulfur and nitrogen compounds on the catalytic active sites.

AL-Hammadi et al. [68] prepared a novel carbon-nanofiber-doped alumina as a support material for the CoMo (AlCNFMoCo)-based catalyst and compared its HDS activity with the alumina-supported CoMo (AlMoCo) catalyst for the HDS of DBT in a batch reactor. They showed that the HDS activity of carbon-nanofiber-doped alumina catalysts is better than conventional catalysts due to high mesoporous surface area, better dispersion of active metals on the support, and good textural properties. Also, they proposed DDS as the predominant reaction mechanism for the carbon-nanofiber-doped alumina catalyst compared to the HYD pathway based on GC-MS analysis of reaction products. However, long-term stability of these catalysts and performance using actual feedstock need to be assessed.

HDT catalysts prepared using silica-modified alumina supports were also investigated through different synthesis methods to enhance the activity for the removal of refractory sulfur compounds through incorporation of moderate acidity to the catalyst. Silica incorporated in alumina structure modifies the catalyst properties and performance depending upon the method of incorporation. Rayo et al. [69] prepared NiMo-based HDT catalysts using 5 wt% Si in alumina by two different methods, one by incorporation of Si into boehmite (NiMo/Si-Al), followed by drying and calcination. In another method, Si was incorporated into the surface of already calcined alumina (NiMo/Si/Al), which resulted in different surface structures of the Si oxide layer. The performance of these two catalysts was different for the HDS of partially hydrotreated Maya crude oil and cumene hydrocracking applications. The highest activity for HDT of refractory sulfur compounds present in the hydrotreated Maya crude oil/diesel blend feedstock was achieved using the catalyst
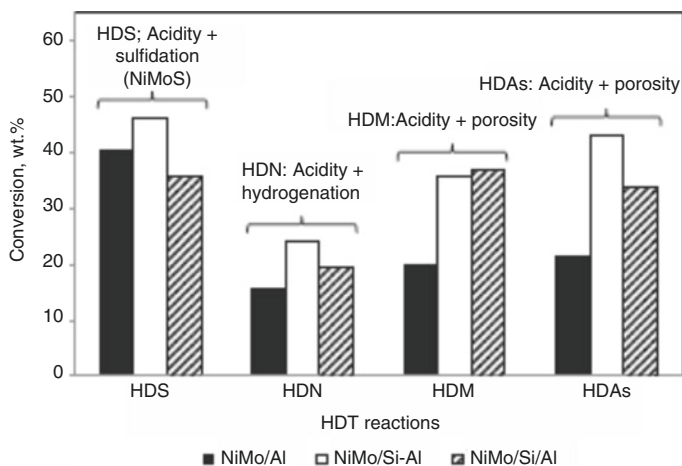
Fig. 7 Activity of NiMo/Al and silica incorporated alumina catalysts [69] (Reprinted from Fuel, 239, Patricia Rayo, Pablo Torres-Mancera, Guillermo Centeno, Fernando Alonso, Jose Antonio D. Munoz, Jorge Ancheyta, Effect of silicon incorporation method in the supports of NiMo catalysts for hydrotreating reactions, 1293–1303, 2019, with permission from Elsevier)

prepared with incorporation of Si into boehmite, which was ascribed to better dispersion of active phase combined with favorable porosity and acidity (Fig. 7).

Hybrid supports such as zeolites modified with the incorporation of activated carbon were also used as support materials for CoMo-based catalysts. Optimal loading of carbon on zeolite could achieve better metal dispersion, moderate acidity, and uniform mesoporous structure resulting in higher HDS activity [70].

Zhou et al. [1] synthesized NiMo catalysts supported on meso-microporous Y zeolites with different mesoporous diameters (0, 4, 6, and 8 nm) and tested the catalytic performance for the HDS of 4,6-DMDBT (Table 6). The higher HDS performance for the mesopore catalysts is due to decrease in MSI, higher MoS_2 stacking numbers, lower slab lengths, and better dispersion/sulfidation of Mo favoring the formation of highly active edge and corner sites. Optimal pore size is required for the HDS of 4,6-DMDBT due to its steric hindrance and pore diffusion effects. These effects dominate for catalysts with lower pore diameters of less than 4 nm. Catalysts with 6 nm pore diameter exhibited higher HDS performance due to reduced pore diffusion and steric hindrance effects. They also correlated the HDS selectivity with mesopore size. There is a linear correlation of HYD and DDS activities with the number of Mo atoms located either at the edge or corner sites of the MoS_2, respectively.

Liu et al. [71] synthesized a novel, bimodal mesoporous nanorod-Al_2O_3 via the hydrothermal method in the presence of polyethylene glycol (PEG) to enable the formation of favorable nanostructure in alumina with relatively higher crystallinity through proper control of the pore structure, crystal parameters, and morphology of the support. The CoMo-based catalysts prepared using the support showed higher activity for the HDS of 4,6-DMDBT than the catalyst with mono-modal alumina

Table 6 Activation energies and rate constants for the HDS of 4,6-DMDBT over NiMo catalysts supported on micro-mesoporous Y zeolite catalysts at 290 °C with mesopore sizes of 0, 4, 6, and 8 nm (DMDBT conversion of 50 ± 0.4%) [1, 2]

Catalysts	Ea (kJmol^{-1})	TOF (h^{-1})	k_{HDS}, μmol h^{-1} g^{-1}	k_{DDS}, μmol h^{-1} g^{-1}	k_{HYD}, μmol h^{-1} g^{-1}	k_{ISO}, μmol h^{-1} g^{-1}	HYD/ DDS[a]
NiMo/ HMY-0	81.5	1.8	307	138	98	178	0.71 (1.47)
NiMo/ HMY-4	108.0	2.9	617	259	173	426	0.63 (2.44)
NiMo/ HMY-6	121.2	3.5	783	337	196	572	0.58 (2.86)
NiMo/ HMY-8	121.8	3.4	761	327	190	571	0.58 (3.18)

Reprinted from Applied Catalysis B: Environmental, 238, Wenwu Zhou, Qiang Wei, Yasong Zhou, Meifang Liu, Sijia Ding, Qi Yang, Hydrodesulfurization of 4,6-dimethyldibenzothiophene over NiMo sulfide catalysts supported on meso- microporous Y zeolite with different mesopore sizes, 212–224, 2018, with permission from Elsevier
[a]Values in the brackets are the HYD/DDS ratios without counting the isomerized products

Table 7 Properties of different bimodal mesoporous aluminas (BMA-x) and CoMo-based HDS catalysts [71]

Sample	BET surface area (m²/g)	Pore volume (cm³/g)	Pore size (nm)
BMA-1	284.1	0.66	4.0, 15.4
BMA-2	333.6	0.95	3.4, 15.3
BMA-3	334.8	0.97	3.0, 11.2
BMA-4	494.7	1.02	2.7, 11.1
CoMo-BMA-1	204.2	0.38	3.9, 15.4
CoMo-BMA-2	280.8	0.74	3.3, 15.4
CoMo-BMA-3	283.1	0.75	2.9, 11.2
CoMo-BMA-4	400.3	0.81	2.6, 11.1
CoMo-CA	219.7	0.45	5.0

Reprinted from Applied Catalysis B: Environmental, 121, Xinmei Liu, Xiang Li, Zifeng Yan, Facile route to prepare bimodal mesoporous γ-Al2O3 as support for highly active CoMo-based hydrodesulfurization catalyst, 50–56, 2012, with permission from Elsevier
BMA-x bimodal mesoporous aluminas synthesized with varying PEG contents, *CoMo-BMA-x* CoMo-based catalysts prepared using respective aluminas, *CoMo-CA* reference catalyst prepared using commercial pseudoboehmite as a support

structure due to lower metal–support interaction, lower reduction temperature of molybdenum oxide, more active sites, high crystal phase dispersion, shorter crystal length, higher degree of stacking, and lower pore diffusion effect. In this study, HYD was found to be the dominant reaction pathway for the HDS of 4,6-DMDBT compared to DDS due to the steric hindrance effect of the molecule. The characteristics of different bimodal mesoporous aluminas and supported catalysts are presented in Table 7.

Zhang et al. [72] prepared NiMo HDS catalysts with different crystal forms of alumina using $AlCl_3 \cdot 6H_2O$ and Al $(NO_3) \cdot 9H_2O$ as alumina sources and studied their catalytic performance for FCC diesel hydrodesulfurization. They reported the HDS efficiencies to be of the order: NiMo/δ-Al_2O_3 > NiMo/γ-Al_2O_3 > NiMo/θ-Al_2O_3. The higher HDS and HDN activities for FCC diesel in the case of NiMo/δ-Al_2O_3 were attributed to the concentrated pore size distribution, moderate MSI, and the highest sulfidation degree.

Gao et al. [73] synthesized γ-alumina-supported MoS_3 nanoparticles (MoS_3/ Al_2O_3) by a chemical deposition method and later prepared pre-sulfided bimetallic HDS catalysts through Ni promotion. Use of MoS_3 as a precursor enabled better nickel promoter decoration onto the edges of MoS_2 nanoslabs forming Type II sites and higher sulfidation degree that resulted in higher HDS activity.

CoMoS catalysts supported on mesostructured titania were studied for HDS of 4,6-DMDBT by Naboulsi et al. [74], and results were compared with conventional alumina-supported catalysts. The mesostructured titania-supported catalyst was found to favor the DDS pathway, which was attributed to the intrinsic acidic properties (both Lewis and Brönsted acidities) of the supports retained even after the impregnation of Co and Mo, arising from the coexistence of both phases.

Asadi et al. [75] reported a novel method for synthesis of nano pseudoboehmite powders with varying textural properties based on CO_2-assisted neutralization of $NaAlO_2$ aqueous solution in a semi-batch membrane microreactor. Later, the nanopowders were utilized to prepare a number of nano γ-Al_2O_3 supports as well as supported NiMo catalysts with varied average pore sizes and investigated the effect of catalyst pore size on HDS performance using straight-run gas oil and its blend with cracked gas oil. The highest HDS was obtained using catalysts with the average pore size of 8.0 (5.9) and 9.1 (7.2) nm, respectively, for both feedstocks. The study highlighted the significance of the pore size on the HDS activity of the catalyst and the novel synthesis of mesoporous γ-Al_2O_3 supports with a controlled average pore size of up to 20 nm.

Xie et al. [76] reported the synthesis of novel composites made from monodispersed porous Al-glycolate spheres (NiMo/Al-SP) through alcoholysis or hydrolysis treatments as HDT catalysts and tested their performance for HDS of DBT and HYD of naphthalene. The novel catalyst showed 71.22% DBT and 88.28% naphthalene conversion at 270 °C temperature, 5 MPa initial H_2 pressure, and 10 h reaction time.

Valles et al. [77] reported iridium-based catalysts as alternatives for conventional CoMo/Al_2O_3 or NiMo/Al_2O_3 catalysts for HDT application. They studied the HDS, HDN, and hydrogenation activities of iridium catalysts supported on different zirconium-modified SBA-15 supports using model compounds. The sol-gel method was used to synthesize zirconium-modified SBA-15 supports using two sources of zirconium, zirconyl chloride, and zirconium (IV) propoxide with lactic acid as the coordinating ligand. Zirconium is mainly present as tetrahedral Zr4+ species and provides better dispersion and reducibility of iridium active species apart from providing higher acidity to the catalyst. The catalyst synthesized using zirconium propoxide and lactic acid was found to be the most active catalyst for HYD of tetralin,

HDN of indole and quinoline, and HDS of DBT and 4,6-DMDBT due to moderate acidity and other favorable structural and morphological characteristics.

Zheng et al. [78] prepared novel composite support β-SBA-16 using both β zeolite and SBA-16 and showed higher hydrodesulfurization activity for the NiMo/β--SBA-16 catalyst compared to Al-modified SBA-16 and the traditional Al_2O_3-supported catalysts due to higher acidity and better synergy between Brønsted and Lewis acid sites. They also confirmed the high activity based on DFT calculations. Wang et al. [79] prepared mesoporous Al-SBA-16 as support for NiMo-based catalysts and showed higher isomerization activity for the HDS of DBT and 4.6-DMDBT.

Asadi et al. [80] prepared NiMo catalysts with composite USY/γ-Al_2O_3 supports and studied the effect of active phase and compositions of support on the activity. The most active composite catalyst contained 10 wt% USY zeolite, loaded with 18 wt% Ni and Mo oxides with Ni/(Ni + Mo) and EDTA/Ni molar ratios of 0.417 and 2, respectively, and the HDS results were validated using model and experiments.

Although the mixed oxide-based bifunctional catalysts possess advantages in terms of high surface area and good acid–base properties for promoting HDS of sterically hindered sulfur compounds, they are prone to rapid deactivation at the acid sites due to coking and poisoning by basic nitrogen compounds. Although acidic supports were reported to be effective for HDS of refractory sulfur compounds, they have certain issues such as (a) difficulty in the impregnation and dispersion of active phases on the support surface and (b) pore size limitations, which may restrict the accessibility of bulky reactant molecules such as 4,6-DMDBT. Also, the acidic supports may promote hydrocracking reactions that will result in loss of valuable hydrocarbon yields. Strong acid site density and Brönsted acidity of zeolite containing catalysts could cause rapid deactivation by formation of coke [81] apart from the formation of lighter products resulting in yield loss.
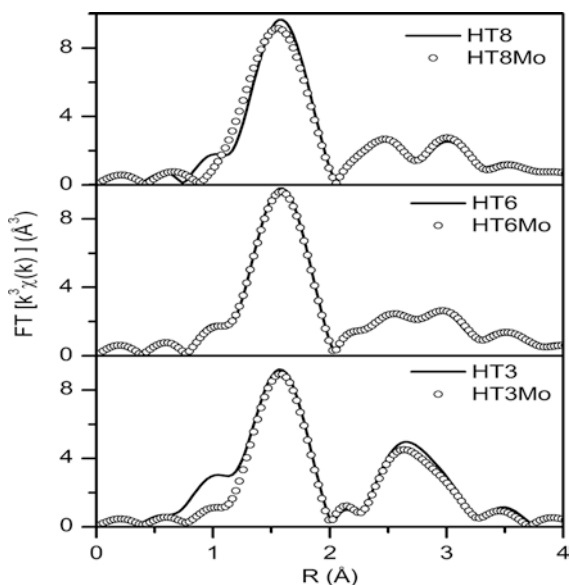
6.3   Unsupported Catalysts

Unsupported transition metal-based catalysts such as sulfides, carbides, and nitrides of cobalt, molybdenum, and tungsten and also metal phosphides were studied in the literature as promising catalysts for HDT/HDS reactions. Unsupported mixed sulfides prepared using the same family of metals as that of supported catalysts were reported to exhibit high activity for HDS, HDN, and HDA compared to the supported catalysts [82]. Hermann et al. [83] studied the unsupported RuS_2, Rh_2S_3, and NbS_3 for their HDS performance and found that these catalysts possessed higher desulfurization activity compared to Co-Ni and No-W metal sulfides. Unsupported trimetallic catalysts such as Ni-Mo-W sulfide were found to exhibit about three times higher activity for HDS compared to Al_2O_3-supported NiMo and CoMo catalysts [84–86]. Such unsupported trimetallic catalysts were successfully used in commercial hydrotreaters for deep HDS of diesel fraction by Albamarle using the trade name NEBULA. Although other forms of unsupported catalysts such as metal

carbides, nitrides, and phosphides were also studied by many researchers for their HDS activity, most of these studies are limited in their scope, and further extensive research work is needed to study the catalytic performance in terms of their activity, selectivity, and stability before utilizing them for commercial applications.

Santiago Arias et al. [87] prepared unsupported NiMoAl hydrotreating catalysts using layered double hydrooxides (LDHs) or hydrotalcite-type materials as precursors. NiAl-terephthalate LDHs were prepared with different Al/(Al + Ni) ratios in the range of 0.3–0.8 by ion exchange and calcination with ammonium heptamolybdate. The mixed oxides contained about 33–43 wt% Mo and Ni/Mo ratios in the range of 0.5–1.4. Molybdenum is mostly incorporated as intercalated heptamolybdate anions (Fig. 8). Calcined mixed oxides with surface areas in the range of 26–122 m^2/g were sulfided in situ and tested simultaneously for HDS of DBT and hydrogenation of tetralin at a high pressure of 70 bar and temperature of 613 K in a batch reactor. The HDS and hydrogenation activities of NiMoAl catalysts prepared from LDHs were found to be higher than conventional NiMo/Al$_2$O$_3$ catalysts and similar to Al-free unsupported NiMo catalysts, but with a higher preference for hydrogenation route.

Eijsbouts et al. [88] reviewed the technical and economic impacts of replacing conventional promoters (Co and Ni) in HDT catalysts due to the classification of several Ni and some soluble Co compounds as carcinogenic and toxic. Catalysts based on noble metals are highly expensive, and other inexpensive catalyst compositions do not possess sufficient activity for ULSD and VGO FCC pretreatment applications. Their review covered the history of conventional HDT catalysts and alternate catalyst compositions (single transition metal sulfides, promotion with other transition metal sulfides, Fe-based catalysts, metal carbides, metal nitrides,

Fig. 8 Fourier-transformed Ni K-edge EXAFS spectra for the NiAl-terephthalate LDHs [87] (Reprinted from Catalysis Today, 213, Santiago Arias, Yordy E. Licea, Luz Amparo Palacio, Arnaldo C. Faro Jr., Unsupported NiMoAl hydrotreating catalysts prepared from NiAl-terephthalate hydrotalcites exchanged with heptamolybdate, 198–205, 2013, with permission from Elsevier)

and metal phosphides). They also compared the RVA of HDN and HDS reactions for mixed first-row transition metals with W supported on Al_2O_3 versus Ni-Mo reference catalysts with RVA of 100 in VGO hydrotreating application. Based on their study, the authors concluded that it would be difficult to replace the conventional Co-Mo, Ni-Mo, and Ni-W catalysts for HDS/HDN applications based on the activity, selectivity, stability, and economics, and the status quo would continue for the near future.

Song et al. [89] used a new and simple method to prepare bulk and supported nickel phosphide (Ni_2P) using thermal treatment of a solid mixture containing $Na(H_2PO_3)_2$ and $NiCl_2.6H_2O$ in certain molar ratio as precursors. In this method, bulk Ni_2P was formed by heating the physical mixture of the precursors at 200–300 °C for 1 h in a nitrogen atmosphere. Nickel phosphide was formed by decomposition of NaH_2PO_3 to release phosphine and subsequent reduction of nickel ions. The activity of supported Ni_2P/SiO_2 catalysts for HDS of DBT was found to be good at different temperatures.

Varakin et al. [90] synthesized unsupported molybdenum disulfide catalysts (MoS_2/Al_2O_3 and $MoS_2/C/Al_2O_3$) and compared their HDS performance for DBT with the catalysts prepared from ammonium tetrathiomolybdate with and without structural agents. Bulk MoS_2 catalysts prepared by etching of the MoS_2/Al_2O_3 showed higher selectivity for the HDS of DBT, and sulfur was predominantly removed through the hydrogenation pathway. The high HYD/DDS activity of the bulk catalysts was attributed to the high ratio of HYD sites on spatial angles relative to centers on the rim and edges due to the low slab length and minimal average number of MoS_2 layers.

Li et al. [91] studied gasoline HDS with minimum olefin saturation using an unsupported Co-Mo catalyst and compared the performance with the CoMo/γ--Al_2O_3 catalyst. The HDS activity of the unsupported catalyst was reported to be fourfold compared to the supported catalyst for model compounds and full range FCC gasoline due to differences in MoS_2 slab morphologies such as curvature, slab length, and stacking number. Curved MoS_2 structure was found to promote olefin isomerization reaction without saturation resulting in improved octane rating. Alhough increased slab length and higher stacking number of MoS_2 in the unsupported catalyst resulted in higher desulfurization selectivity, the effect of slab length was predominant in influencing the HDS selectivity compared to the stacking number.

Xie et al. [93] showed improved activities for MoS_2-Co_3S_4 hollow polyhedrons for the hydrogen evolution reaction and HDS compared to the pure MoS_2, Co_3S_4 and MoS_2-Co_3S_4 nanoparticles prepared by conventional coprecipitation methods due to the better morphology and synergy between Co_3S_4 and MoS_2. Synthesis of MoS_2-Co_3S_4 hollow polyhedrons was reported by the vulcanization of Mo-doped ZIF-67. Li et al. [92] synthesized Co-Mo sulfide with a hollow structure using a combination of co-precipitation and low-temperature sulfurization in ethanol solution. Formation of porous Co-Mo sub-microtubes was reported with high specific surface area, more active sites, and active component exposure in order to obtain a higher degree of HDS for DBT.

CoMgMoAl-layered double hydroxides with varied Co and Mo contents were also studied for the selective HDS of model compound thiophene in the presence of cyclohexene as an olefinic compound and n-heptane. The LDHs showed higher selectivity for HDS in comparison with industrial catalysts. Co-Mo catalysts prepared using Zn-Al-layered double hydroxides were also reported for the selective HDS of FCC gasoline [94]. Coelho et al. [95] prepared unsupported heptamolybdate-CoMgAl hydrotalcites from terephthalate precursors and reported higher HDS selectivity compared to conventional CoMo/Al$_2$O$_3$ catalysts.

7 Conclusions

Research in hydrotreating/hydrodesulfurization catalysis has advanced multifold after the introduction of stringent fuel specifications, especially with respect to sulfur content in both gasoline and diesel. Catalysis scientists have overcome the challenges and are able to come up with highly active catalysts for producing ultralow sulfur diesel due to advancements in catalyst characterization techniques, preparation strategies, active phase dispersion methods, tuning the support structure, and understanding the micro- and macrolevel happenings on the catalyst. Catalyst advancements along with simultaneous process improvements helped the refiners to achieve their environmental targets in meeting the fuel specifications. Catalysis science in hydrotreating is still advancing in terms of new mixed supports, novel preparation methods for better dispersion of active components, use of unsupported catalysts, additives for reducing MSI, etc. All the recent research advances are aimed at improving the activity of the current generation catalysts while also simultaneously enhancing the selectivity for removal of sulfur from refractory aromatic sulfur species and stability of the catalyst. It is of paramount importance to increase the yields of desired hydrocarbons by tuning the catalyst acidity. There is interdependence of different catalytic functions, which needs to be considered in order to reduce sulfur content and increase hydrocarbon yields. There is a balance in activity that is needed for any successful catalyst. The present chapter discussed the current advancements in the nature of active phase and catalyst support, specifically aimed to achieve ultralow sulfur content in petroleum fuels.

References

1. Zhou W, Wei Q, Zhou Y, Liu M, Ding S, Yang Q (2018a) Hydrodesulfurization of 4,6-dimethyldibenzothiophene over NiMo sulfide catalysts supported on meso-microporous Y zeolite with different mesopore sizes. Appl Catal B Environ 238:212–224

2. Tao X, Zhou Y, Wei Q, Ding S, Zhou W, Liu T, Li X (2017) Inhibiting effects of nitrogen compounds on deep hydrodesulfurization of straight-run gas oil over a NiW/Al$_2$O$_3$ catalyst. Fuel 188:401–407

3. Stanislaus A, Marafi A, Rana MS (2010) Recent advances in the science and technology of ultra low sulfur diesel production. Catal Today 153:1–68

4. Zhou W, Zhang Q, Zhou Y, Wei Q, Lin D, Ding S, Jiang S, Zhang Y (2018b) Effects of Ga- and P-modified USY-based NiMoS catalysts on ultra-deep hydrodesulfurization for FCC diesels. Catal Today 305:171–181

5. Plumail JC, Marseu R, Martino G, Toulhoa H (1988) Proceedings of the symposium on recent developments, Hydrot. Catal., 6–10 June 1988, Toronto

6. Moyse BM, Cooper BH, Alberg A (1984) NPRA annual meeting paper AM-84-59, Mar 1984, San Antonio TX

7. Satterfield CN (1991) Heterogeneous catalysis in industrial practice. McGraw-Hill, New York, NY, p 87

8. Scherzer J, Gruia AJ (1996) Hydrocracking science and technology. Marcel Dekker, Inc., New York, NY, p 44

9. Bambrick WE (1987) U.S. Patent 4 673 664 16 Jun 1987

10. Santra M, Pulikottil AC (2000). Verma RP, Bhatnagar AK (ed) Hydroprocessing in petroleum refining industry – a compendium. Lovraj Kumar memorial trust, Indian oil Institute of Petroleum Management, Gurgaon, India, 21–22 Jan 2000

11. Xavier KO, Pulikottil AC, Santra M, Verma RP (2005) Hydrodesulfurization catalysts: evolution and future challenges, presented in a compendium on 'catalysts in hydrocarbon processing & fertilizer industry'. In: 8th National workshop, vol 25–26, Nov 2005. Lovraj Kumar Memorial Trust, New Delhi

12. Topsoe H, Clausen BS, Topsoe NY, Zeuthen P (1990) Progress in the design of hydrotreating catalysts based on fundamental molecular insight. Stud Surf Sci Catal 53:77–102

13. Topsoe H, Clausen BS, Massoth FE (1996) In: Anderson JR, Boudart M (eds) Hydrotreating catalysis – science and technology, vol 11. Berlin, Springer

14. Topsoe H (2007) The role of co-Mo-S type structures in hydrotreating catalysts. Appl Catal A Gen 322:3–8

15. Lehveld RG, van Dillen AJ, Geus JW, Komgsberger DC (1997) A Mo-K edge XAFS study of the metal sulfide-support interaction in (co) Mo supported alumina and titania catalysts. J Catal 165:184–196

16. Vissenberg MJ, van der Meer Y, Hensen EJM, de Beer VRJ, van der Kraan AM, van Santen RA, van Veen JAR (2001) The effect of support interaction on the sulfidability of Al$_2$O$_3$ and TiO$_2$ supported CoW and NiW hydrodesulfurization catalysts. J Catal 198:151–163

17. Shen B, Li H, Zhang W, Zhao Y, Zhang Z, Wang X, Shen S (2005) A novel composite support for hydrotreating catalyst aimed at ultra-clean fuels. Catal Today 106:206–210

18. Pecoraro TA, Chianelli RR (1981) Hydrodesulfurization catalysis by transition metal sulfides. J Catal 67:430–445

19. Harris S, Chianelli RR (1986) Catalysis by transition metal sulfides: a theoretical and experimental study of the relation between the synergic systems and the binary transition metal sulfides. J Catal 98:17–31

20. Norskov JK, Clausen BS (1992) Understanding the trends in the hydrodesulfurization activity of the transition metal sulfides. H Topsoe Catal Lett 13:1–8

21. Chen W, Long X, Li M, Nie H, Li D (2017) Influence of active phase structure of CoMo/Al$_2$O$_3$ catalyst on the selectivity of hydrodesulfurization and hydrodearomatization. Catal Today 292:97–109

22. Topsoe H, Hinnemann B, Norksov JK, Lauritsen JP, Besenbacher F, Hansen PL, Hytoft G, Egeberg RG, Knudsen KG (2005) The role of reaction pathways and support interactions in the development of high activity hydrotreating catalysts. Catal Today 12:107–108

23. Tuxen A, Gøbel H, Hinnemann B, Li Z, Knudsen KG, Topsøe H, Lauritsen JV, Besenbacher F (2011) An atomic-scale investigation of carbon in MoS$_2$ hydrotreating catalysts sulfided by organosulfur compounds. J Catal 281:345–351

24. Liu H, Yin C, Li X, Chai Y, Li Y, Liu C (2017) Effect of NiMo phases on the hydrodesulfuriza-tion activities of dibenzothiophene. Catal Today 282:222–229
25. Nie H, Li H, Yang Q, Li D (2018) Effect of structure and stability of active phase on catalytic performance of hydrotreating catalysts. Catal Today 316:13–20
26. Herbst K, Brorson M, Carlsson A (2010) Hydrotreating activities of alumina-supported bime-tallic catalysts derived from noble metal containing molecular sulfide clusters Mo_3S_4M' (M' = Ru, Rh, Ir, Pd, Pt). J Mol Catal A Chem 325:1–7
27. Huang T, Xu J, Yu F (2018) Effects of concentration and microstructure of active phases on the selective hydrodesulfurization performance of sulfided $CoMo/Al_2O_3$ catalysts. Appl Catal B Environ 220:42–56
28. Grønborg SS, Salazar N, Bruix A, Rodríguez-Fernández J, Thomsen SD, Hammer B, Lauritsen JV (2018) Visualizing hydrogen-induced reshaping and edge activation in MoS_2 and co-promoted MoS_2 catalyst clusters. Nat Commun 9. https://doi.org/10.1038/s41467-018-04615-9
29. Li S, Liu Y, Feng X, Chen X, Yang C (2019) Insights into the reaction pathway of thiophene hydrodesulfurization over corner site of MoS_2 catalyst: a density functional theory study. Mol Catal 463:45–53
30. Oyama ST (1992) Preparation and catalytic properties of transition metal carbides and nitrides. Catal Today 15:179–200
31. Isoda T, Nagao S, Korai Y, Mochida I (1996a) HDS reactivity of alkldibenzothiophenes in gas oil. 1. Acid assisted desulfurization of 4,6-dimethyldibenzothiophene through isomerization and cracking. ACS Div Petrol Chem 41:559–562
32. Bataille F, Lemberton JL, Pérot G, Leyrit P, Cseri T, Marchal N, Kasztelan S (2001) Sulfided Mo and CoMo supported on zeolite as hydrodesulfurization catalysts: transformation of diben-zothiophene and 4,6-dimethyldibenzothiophene. Appl Catal A Gen 220:191–205
33. Pérot G (2003) Hydrotreating catalysts containing zeolites and related materials-mechanistic aspects related to deep desulfurization. Catal Today 86(1–4):111–128
34. Ramirez J, Sanchez-Minero F (2008) Support effects in the hydrotreatment of model mol-ecules. Catal Today 130:267–271
35. Isoda T, Nagao S, Korai Y, Mochida I (1996b) HDS reactivity of alkldibenzothiophenes in gas oil. 2. HDS activity of 4,6-dimethyldibenzothiophene and its reaction pathway over Ni loaded Y-Zeolite and $CoMo/Al_2O_3$. ACS Div Petrol Chem 41:563–573
36. Isoda T, Nagao S, Ma X, Yozo Korai A, Mochida I (1996c) Hydrodesulfurization pathway of 4,6-dimethyldibenzothiophene through isomerization over Y-zeolite containing CoMo/Al2O3 catalyst. Energy Fuel 10(5):1078–1082
37. Pawelec B, Mariscal R, Navarro RM, Bokhorst SV, Rojas S, Fierro JLG (2002) Hydrogenation of aromatics over supported Pt-Pd catalysts. Appl Catal A Gen 225(1–2):223–237
38. Tanga T, Yina C, Wanga L, Jia Y, Xiao FS (2008) Good sulfur tolerance of a mesoporous beta zeolite-supported palladium catalyst in the deep hydrogenation of aromatics. J Catalogue 257(1):125–133
39. Sun Y, Wang H, Prins R (2010) Hydrodesulfurization with classic co–MoS2 and Ni–MoS2/γ--Al2O3 and new Pt–Pd on mesoporous zeolite catalysts. Catal Today 150(3–4):213–217
40. Ramirez J, Ruiz-Ramirez L, Cedeno L, Harle V, Vrinat M, Breysse M (1993) Titania-alumina mixed oxides as supports for molybdenum hydrotreating catalysts. Appl Catal A Gen 93:163–180
41. Breysse M, Afanasiev P, Geantet C, Vrinat M (2003) Overview of support effects in hydrotreat-ing catalysts. Catal Today 86:5–16
42. Muralidhar G, Srinivas BN, Rana MS, Kumar M, Maity SK (2003) Mixed oxide supported hydrodesulfurization catalysts – a review. Catal Today 86:45–60
43. Ramírez J, Cedeño L, Busca G (1999) The role of titania support in Mo-based hydrodesulfur-ization catalysts. J Catal 184:59–67
44. Silva-Rodrigo R, Calderón-Salas C, Melo-Banda JA, Domínguez JM, Vázquez-Rodríguez A (2004) Synthesis, characterization and comparison of catalytic properties of NiMo- and NiW/Ti-MCM-41 catalysts for HDS of thiophene and HVGO. Catal Today 98:123–129

45. Ramírez J, Macías G, Cedeño L, Gutiérrez-Alejandre A, Cuevas R, Castillo P (2004) The role of titania in supported Mo, CoMo, NiMo, and NiW hydrodesulfurization catalysts: analysis of past and new evidences. Catal Today 98:19–30

46. Castillo-Villalón P, Ramírez J, Cuevas R, Vázquez P, Castañeda R (2016) Influence of the support on the catalytic performance of Mo, CoMo, and NiMo catalysts supported on Al_2O_3 and TiO_2 during the HDS of thiophene, dibenzothiophene, or 4,6-dimethyldibenzothiophene. Catal Today 259:140–149

47. Ganiyu SA, Alhooshani K, Ali SA (2017) Single-pot synthesis of Ti-SBA-15-NiMo hydrodesulfurization catalysts: role of calcination temperature on dispersion and activity. Appl Catal B Environ 203:428–441

48. Fujikawa T, Kimura H, Kiriyama K, Hagiwara K (2006) Development of ultra-deep HDS catalyst for production of clean diesel fuels. Catal Today 111(3–4):188–193

49. Ding L, Zheng Y, Zhang Z, Chen J (2007) Hydrotreating of light cycle oil using WNi catalysts containing hydrothermally and chemically treated zeolite Y. Catal Today 125:229–238

50. Nakano K, Ali SA, Kimd H-J, Kim T, Alhooshani K, Park J-I, Mochida I (2013) Deep desulfurization of gas oil over NiMoS catalysts supported on alumina coated USY-zeolite. Fuel Process Technol 116:44–51

51. Wang Y, Yin C, Zhao X, Liu C (2017) Synthesis of bifunctional highly-loaded NiMoW catalysts and their catalytic performance of 4,6-DMDBT HDS. Catal Commun 88:13–17

52. Han W, Nie H, Long X, Li M, Yang Q, Li D (2017) Effects of the support Brønsted acidity on the hydrodesulfurization and hydrodenitrogenation activity of sulfided NiMo/Al_2O_3 catalysts. Catal Today 292:58–66

53. Zhang L, Dai Q, Wenqian F, Tang T, Dong P, He M, Chen Q (2018) CoMo catalyst on zeolite TS-1 nanorod assemblies with high activity in the hydrodesulfurization of 4,6-dimethyldibenzothiophene. J Catal 359:130–142

54. Sun H, Sun H, Zhang X, Yu Q, Zeng P, Guo Q, Wang D, Wen G, Zhang W, He S, Shen B (2019) Effect of divalent tin on the SnSAPO-5 molecular sieve and its modulation to alumina support to form a highly efficient NiW catalyst for deep desulfurization of 4,6-Dimethyldibenzothiophene. ACS Catal 9:6613–6623

55. Meng Q, Peng D, Duan A, Zhao Z, Liu J, Shang D, Wang B, Jia Y, Liu C, Hu D (2020) Trimetallic catalyst supported zirconium modified Threedimensional mesoporous silica material and its Hydrodesulfurization performance of dibenzothiophene and 4,6-dimethydibenzothiophene. Ind Eng Chem Res 59(2):654–667

56. Klimova T, Ramirez J, Calderon M, Dominguez JM (1998) New Mo and NiMo catalysts supported on MCM-41/alumina for thiophene hydrodesulfurization. Stud Surf Sci Catal 117:493–500

57. Song C, Reddy KM (1999) Mesoporous molecular sieve MCM-41 supported co-Mo catalyst for hydrodesulfurization of dibenzothiophene in distillate fuels. Appl Catal A Gen 176:1–10

58. Klimova T, Calderon M, Ramirez J (2003) Ni and Mo interaction with Al-containing MCM-41 support and its effect on the catalytic behavior in DBT hydrodesulfurization. Appl Catal A Gen 240:29–40

59. Kouzu M, Kuriki Y, Hamdy F, Sakanishi K, Sugimoto Y, Saito I (2004) Catalytic potential of carbon-supported NiMo-sulfide for ultra-deep hydrodesulfurization of diesel fuel. Appl. Catal A Gen 265:61–67

60. Gutierrez OY, Perez F, Fuentes GA, Bokhimi X, Klimova T (2008) Deep HDS over NiMo/Zr-SBA-15 catalysts with varying MoO_3 loading. Catal Today 130:292–301

61. Han D, Li X, Zhang L, Wang Y, Yan Z, Liu S (2012) Hierarchically ordered meso/macroporous γ-alumina for enhanced hydrodesulfurization performance. Microporous Mesoporous Mater 158:1–6

62. Badoga S, Sharma RV, Dalai AK, Adjaye J (2015) Synthesis and characterization of mesoporous aluminas with different pore sizes: application in NiMo supported catalyst for hydrotreating of heavy gas oil. Appl Catal A Gen 489:86–97

63. Li H, Li M, Nie H (2014) Tailoring the surface characteristic of alumina for preparation of highly active NiMo/Al$_2$O$_3$ hydrodesulfurization catalyst. Microporous Mesoporous Mater 188:30–36
64. Dong Y, Xu Y, Zhang Y, Lian X, Yi X, Zhou Y, Fang W (2018) Synthesis of hierarchically structured alumina support with adjustable nanocrystalline aggregation towards efficient hydrodesulfurization. Appl Catal A Gen 559:30–39
65. Peng C, Guo R, Feng X, Fang X (2019) Tailoring the structure of Co-Mo/mesoporous γ-Al$_2$O$_3$ catalysts by adding multi-hydroxyl compound: a 3000 kt/a industrial-scale diesel ultra-deep hydrodesulfurization study. Chem Eng J 377:119706
66. Tang T, Zhang L, Wenqian F, Ma Y, Xu J, Jiang J, Fang G, Xiao F-S (2013) Design and synthesis of metal sulfide catalysts supported on zeolite nanofiber bundles with unprecedented hydrodesulfurization activities. J Am Chem Soc 135(31):11437–11440
67. Dugulan AI, van Veen JAR, Hensen EJM (2013) On the structure and hydrotreating performance of carbon-supported CoMo- and NiMo-sulfides. Appl Catal B Environ 142–143:178–186
68. AL-Hammadi SA, Al-Amer AM, Saleh TA (2018) Alumina-carbon nanofiber composite as a support for MoCo catalysts in hydrodesulfurization reactions. Chem Eng J 345:242–251
69. Rayo P, Torres-Mancera P, Centeno G, Alonso F, Munoz JAD, Ancheyta J (2019) Effect of silicon incorporation method in the supports of NiMo catalysts for hydrotreating reactions. Fuel 239:1293–1303
70. Saleh TA, Sulaiman KO, AL-Hammadi SA (2020) Effect of carbon on the hydrodesulfurization activity of MoCo catalysts supported on zeolite/ active carbon hybrid supports. Appl Catal B Environ 263:117661. https://doi.org/10.1016/j.apcatb.2019.04.062
71. Liu X, Li X, Yan Z (2012) Facile route to prepare bimodal mesoporous γ-Al$_2$O$_3$ as support for highly active CoMo-based hydrodesulfurization catalyst. Appl Catal B Environ 121–122:50–56
72. Zhang M-h, Fan J-y, Chi K, Duan A-j, Zhao Z, Meng X-l, Zhang H-l (2017) Synthesis, characterization, and catalytic performance of NiMo catalysts supported on different crystal alumina materials in the hydrodesulfurization of diesel. Fuel Process Technol 156:446–453
73. Gao Y, Han W, Long X, Nie H, Li D (2018) Preparation of hydrodesulfurization catalysts using MoS$_3$ nanoparticles as a precursor. Appl Catal B Environ 224:330–340
74. Naboulsi I, Lebeau B, Linares CF, Aponte SB, Mallet M, Michelin L, Bonne M, Carteret C, Blin J-L (2018) Selective direct desulfurization way (DDS) with CoMoS supported over meso-structured titania for the deep hydrodesulfurization of 4,6- dimethydibenzothiophene. Appl Catal A Gen 563:91–97
75. Asadi AA, Alavi SM, Royaee SJ, Bazmi M (2018) Ultra-deep hydrodesulfurization of feedstock containing cracked gasoil through NiMo/γ-Al$_2$O$_3$ catalyst pore size optimization. Energy Fuel 32(2):2203–2212
76. Xie K, Fang Y, Liu B, Li C (2018) Enhanced catalytic activity of monodispersed porous Al$_2$O$_3$ colloidal spheres with NiMo for simultaneous hydrodesulfurization and hydrogenation. RSC Adv 8:18059
77. Valles VA, Sa-ngasaeng Y, Martínez ML, Jongpatiwut S, Beltramone AR (2019) HDT of the model diesel feed over Ir-modified Zr-SBA-15 catalysts. Fuel 240:138–152
78. Zheng P, Hu D, Meng Q, Liu C, Wang X, Fan J, Duan A, Xu C (2019) Influence of support acidity on the HDS performance over β-SBA-16 and Al-SBA-16 substrates: a combined experimental and theoretical study. Energy Fuel 33:1479–1488
79. Wang X, Mei J, Zhao Z, Chen Z, Zheng P, Jianye F, Li H, Fan J, Duan A, Xu C (2018) Controllable synthesis of spherical Al-SBA-16 mesoporous materials with different crystal sizes and its high isomerization performance for hydrodesulfurization of dibenzothiophene and 4,6-dimethyldibenzothiophene. Ind Eng Chem Res 57(7):2498–2507
80. Asadi AA, Royaee SJ, Mahdi S, Bazmi M (2019) Ultra-deep hydrodesulfurization of cracked and atmospheric gasoil blend: direct and interactive impacts of support composition, chelating agent, metal and promoter loadings. Fuel Process Technol 187:36–51

81. Solis D, Agudo AL, Ramirez J, Klimova T (2006) Hydrodesulfurization of hindered dibenzothiophenes on bifunctional NiMo catalysts supported on zeolite-alumina composites. Catal Today 116(4):469–477

82. Eijsbouts S, Mayo SW, Fujita K (2007) Unsupported transition metal sulfide catalysts: from fundamentals to industrial application. Appl Catal A Gen 322:58–66

83. Hermann N, Brorson M, Topsoe H (2000) Activities of unsupported second transition series metal sulfides for hydrodesulfurization of sterically hindered 4,6-dimethyldibenzothiophene and of unsubstituted dibenzothiophene. Catal Lett 65:169–174

84. Soled SL, Miseo S, Krycak R, Vroman H, Ho TC, Riley K (2000) Nickel molybdenum tungstate hydrotreating catalysts, US Patent 6,299,760

85. Plantenga FL, Cefortain R, Eijsbouts S, van Houtert F, Soled SL, Miseo S, Krycak R, Anderson G, Fujita K (2003) NEBULA: a hydroprocessing catalyst with breakthrough activity. Stud Surf Sci Catal 145:407–410

86. Soled SL, Miseo S, Zhiguo H (2005) Bulk Ni-Mo-W catalysts made from precursors containing an organic agent, US Patent 7544632

87. Arias S, Licea YE, Palacio LA, Faro AC (2013) Unsupported NiMoAl hydrotreating catalysts prepared from NiAl-terephthalate hydrotalcites exchanged with heptamolybdate. Catal Today 213:198–205

88. Eijsbouts S, Anderson GH, Bergwerff JA, Jacobi S (2013) Economic and technical impacts of replacing co and Ni promotion in hydrotreating catalysts. Appl Catal A Gen 458:169–182

89. Song L, Zhang S, Wei Q (2011) A new route for synthesizing nickel phosphide catalysts with high hydrodesulfurization activity based on sodium dihydrogenphosphite. Catal Commun 12:1157–1160

90. Varakin AN, Mozhaev AV, Pimerzin AA, Nikulshin PA (2018) New highly active unsupported carbon-containing MoS_2 hydrodesulfurization catalysts prepared by support leaching. Appl Catal B Environ 2018:238

91. Li P, Chen Y, Zhang C, Huang B, Liu X, Liu T, Jiang Z, Li C (2017a) Highly selective hydrodesulfurization of gasoline on unsupported co-Mosulfide catalysts: effect of MoS_2 morphology. Appl Catal A Gen 533:99–108

92. Li G, Yue L, Fan R, Liu D, Li X (2017b) Synthesis of a co–Mo sulfide catalyst with a hollow structure for highly efficient hydrodesulfurization of dibenzothiophene. Cat Sci Technol 7:5505

93. Xie Y, Chen L, Jin Q, Yun J, Liang X (2019) MoS_2-Co_3S_4 hollow polyhedrons derived from ZIF-67 towards hydrogen evolution reaction and hydrodesulfurization. Int J Hydrog Energy 44:24246–24255

94. Wang T, Yu F, Wang X, Chou L, Lin H (2015) Selectivity enhancement of CoMoS catalysts supported on tri-modal porous Al_2O_3 for the hydrodesulfurization of fluid catalytic cracking gasoline. Fuel 157:171–176

95. Coelho TL, Licea YE, Palacio LA, Faro AC (2015) Heptamolybdate-intercalated CoMgAl hydrotalcites as precursors for HDS-selective hydrotreating catalysts. Catal Today 250:38–46

Recent Advances in Hydrotreating/ Hydrodesulfurization Catalysts: Part II— Catalyst Additives, Preparation Methods, Activation, Deactivation, and Regeneration

G. Valavarasu and B. Ramachandrarao

Abstract Additives play a key role in enhancing the activity of hydrotreating catalysts by means of influencing metal–support interactions, improving dispersion of active metals on the support, enhancing the sulfidation degree, increasing stacking of metal sulfide slabs on the support, etc. Additives are also reported to enhance the stability of the catalysts apart from modifying their activity. Another aspect of hydrotreating catalyst manufacture is the method of preparation of these catalysts, which will influence the metal dispersion, support interactions, and ultimately the performance. The present chapter (Part II) reviews the recent advances in hydrotreating/hydesulfurization catalysts in terms of additives/modifiers and various preparation methods. Other aspects of catalysts such as activation, deactivation, and regeneration are also being discussed upon. Apart from this, catalyst requirements for different hydrotreating feedstocks have also been covered, considering the importance of feedstock type and characteristics on the selection of suitable catalysts.

Keywords Hydrotreating · Hydrodesulfurization · Hydrocracking · Catalyst deactivation · Catalyst regeneration · Refining

1 Introduction

Catalysts play an important role in increasing the rate of hydrotreating reactions. As discussed in Part 1 of the article, hydrotreating uses either metals of group VI A (Mo and W) along with promoter metals of group VIII A (Co and Ni) or noble metals (Pt and Pd) supported on alumina, silica-alumina, and/or zeolites as catalysts. HDT catalysts should possess high activity, selectivity, and stability in order to produce stringent product specifications such as sulfur, nitrogen, and aromatics. Apart from

G. Valavarasu (✉) · B. Ramachandrarao
HP Green R&D Center, Hindustan Petroleum Corporation Limited,
Bengaluru, Karnataka, India
e-mail: valavarasu@hpcl.in

the choice of active metals and support material, additives also play a significant role in modifying the catalyst and enhancing its performance. Proper catalyst preparation method needs to be considered while designing a hydrotreating catalyst in order to obtain the required composition and properties. Since the choice of additives and preparation methods is of paramount importance for the design of successful hydrotreating catalysts, it is essential to delve into the advances in these areas. It is also essential to understand the activation/sulfidation, deactivation, and regeneration of HDT/HDS catalysts in order to obtain a complete understanding of hydrotreating catalysts. The present chapter focuses mainly on the catalytic advancements in the area of hydrotreating/hydrodesulfurization of petroleum fractions in terms of additives, catalyst preparation methods, catalyst activation, deactivation and regeneration, and catalyst selection for different feedstocks.

2 Preparation of Hydrotreating Catalysts

Hydrotreating catalysts are usually prepared by a variety of manufacturing methods. A complex relationship exists between catalyst formulation, preparation method, and catalyst properties in the case of hydrotreating catalysts. Chemical composition also plays a major role in determining the performance of industrial hydrotreating catalysts such as content of active metals and concentration of promoters and additives. Nevertheless, physical and mechanical properties of the catalysts are also important to overcome the diffusional limitations of hydrocarbon molecules, particle attrition due to poor mechanical strength, and pressure drop issues. Preparation of supported metal catalysts used in industrial hydrotreating and hydrocracking units usually involves the following steps [1]:

– Precipitation.
– Filtration (decantation, centrifugation).
– Washing.
– Drying.
– Forming.
– Calcining.
– Impregnation of active metals.
– Activation/sulfidation.

Some of the additional steps such as kneading, mulling, grinding, and sieving may also be used along with the above methods depending upon the specific requirement. Scherzer and Gruia [1] provide a detailed account of catalyst preparation and manufacturing methods for hydroprocessing catalysts.

3   Advances in Hydrotreating Catalysts

There are several advances in hydrotreating catalysts in terms of activity, selectivity, and stability due to better characterization tools and improved understanding of the nature of active sites, support material, and the interaction between the active metals and support. Use of additives or modifiers is found to enhance the catalytic activity through altering the metal–support interactions, increasing the number of active sites, etc. This is also supported by the choice of preparation methods. Stanislaus et al. [2] have provided a comprehensive review of the effect of additives and improvements in catalyst preparation techniques in HDT/HDS catalysts.

3.1   *Additives/Modifiers and Their Effects*

Additives or modifiers are certain elements/metals incorporated to the alumina support, especially to enhance the HDT/HDS catalyst performance through modification of the acidic and basic characteristics of the support material. Additives play an important role in the modern HDT/HDS catalysts by means of the following:

- Influence metal–support interactions.
- Improve dispersion and distribution of active phases in the support.
- Enhance reducibility and sulfidability of the metals (Co, Ni, and Mo).
- Enhance the catalytic activity for HDS due to improved acidity characteristics.
- Decrease coking tendency of the catalyst.
- Improve thermal stability of the Al_2O_3 support.
- Increase MoS_2 stacking and result in the formation of larger MoS_2 slabs.

Some of the additives that have been utilized in the HDT catalysts include phosphorous, boron, fluoride, silica, lanthanum, zinc, vanadium, and magnesium. Out of these, phosphorous is the most important modifier used in commercial catalysts to improve the hydrodenitrogenation (HDN) activity of NiMo-Al_2O_3 catalysts [3]. Modification of support by addition of phosphorous was found to have beneficial effects in HDT/HDS catalysts through better dispersion of active metal sulfide phase, lower interaction between metal and support, higher Type II Ni (Co)-Mo-S sites, lower coking, and increased MoS_2 stacking [4]. Fluoride and boron addition was found to be effective in the formation of more active Type II Co-Mo-S or Ni-Mo-S phases in the catalyst in order to improve the activity of the conventional catalysts for the HDS of refractory sulfur species [5–7].

There is an optimal loading of additives during the preparation of hydrotreating catalysts, which provides higher HDS and HDN activity. DeCanio and Weissman [8] studied boron-modified commercial Ni-Mo/Al_2O_3 hydrotreating catalysts using FT-IR analysis of adsorbed NO and pyridine and using gas-oil HDS and HDN activities. Figure 1 shows the first-order rates of sulfur and nitrogen removal (Ks and Kn) as a function of boron loading for a gas-oil feedstock. Although both reaction rates
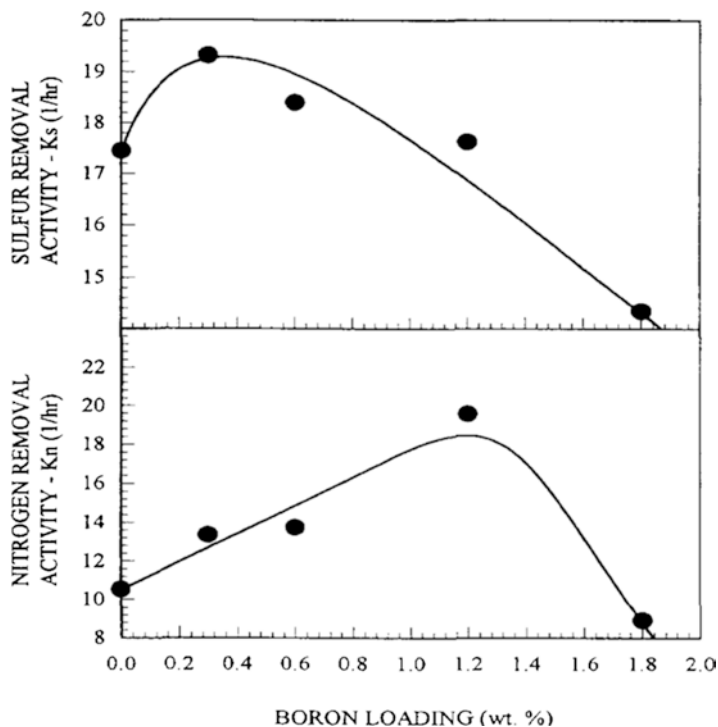
Fig. 1 Effect of boron loading on the sulfur and nitrogen removal activities of boron-modified commercial Ni-Mo/Al$_2$O$_3$ HDT catalysts for a gas-oil feedstock [8] (Reprinted from Colloids and Surfaces A: Physicochemical and Engineering Aspects, 105, Elaine C. DeCanio, Jeffrey G. Weissman, FT-IR analysis of borate-promoted Ni-Mo/Al$_2$O$_3$ hydrotreating catalysts, 123–132, 1995, with permission from Elsevier)

increased with boron loading, the maximum rate for sulfur removal occurred at 0.3 wt% boron loading while the maximum attained at 1.2 wt% boron content for nitrogen removal. The lower catalytic performance at higher boron loadings was attributed to the presence of bulk borate phases and decreasing surface acidity in the catalyst.

Incorporation of phosphorous through phosphoric acid was found to increase the activity of CoMo/Al$_2$O$_3$-based HDS catalysts but decrease the activity of Mo/Al$_2$O$_3$ catalysts based on the study carried out by van Haandel et al. [9]. The increased activity of CoMo/Al$_2$O$_3$ is attributed to reduced formation of Co$_9$S$_8$ and enhanced promotion effect by Co due to treatment with phosphoric acid. Zepeda et al. [10] synthesized NiMo catalysts supported on Al- and P-modified HMS mesoporous substrate and tested their HDS performance using thiophene and 4,6-DMDBT model compounds with an objective to evaluate the effect of Al and P additives on the catalyst activity. The NiMo/Al-HMS-P catalyst containing 1.0 wt% of P showed the highest HDS activity due to the proper balance between the active phase dispersion and the highest hydrogenation activity.

Zhou et al. [11] studied the HDS and HDN of FCC diesel using NiMo/USY zeolite catalysts modified with gallium, phosphorous, and a combination of gallium and phosphorous. Ga- and P-modified USY zeolite catalysts showed higher HDS and HDN efficiencies compared to conventional NiMo-based catalysts. Higher HDS activity of gallium- and phosphorous-modified USY catalysts, especially for the removal of refractory organosulfur compounds present in FCC diesel, was attributed to the modulation of acidity of USY zeolite, weak metal–support interactions leading to higher degree of sulfidation and better dispersion of Mo species (Table 1). Gallium-modified catalysts were prepared using 2 wt% of Ga_2O_3 in HUSY (ultra-stable HY) zeolite, and phosphorous-modified catalysts were prepared using 3 wt% P_2O_5 in HUSY zeolite using an incipient wetness impregnation method.

Rashidi et al. [12] prepared various CoMo-based nanoalumina-supported HDS catalysts containing additives such as phosphorous, boron, and citric acid (CA) and studied their HDS activity using straight-run light gas-oil feedstock with a sulfur content of 13,500 ppm. The mesoporous nanoalumina had high surface area, pore size and pore volume, surface defects, and acidic surface compared to conventional microalumina resulting in higher dispersion of active metals to enable the formation of CoMoS Type II sites on the final catalyst. Nanostructured mesoporous alumina was found to be a promising support to produce ULSD catalysts with favorable physicochemical and textural properties. Addition of phosphorus and boron was found to modify the catalyst acidity, reduce MSI, increase promotion effect, and improve dispersion of the active phase in order to achieve better HDS activity. Addition of citric acid formed Co-CA complexes and thus reduced the cobalt and alumina interactions and improved metal dispersion, sulfidation degree, etc., resulting in better catalytic performance. Also, the catalyst deactivation through coke deposition in nanoalumina-based catalysts was lower compared to conventional microalumina-based catalysts.

Nadeina et al. [13] studied the effect of incorporation of boric and phosphoric acids to impregnating solutions on the structure and properties of NiMo catalysts for VGO HDT application. The NiMo–citrate complex was initially formed in the solution followed by the introduction of boric and phosphoric acids and final calcination done at high temperatures of 900 °C in order to ensure mixed γ- and δ-Al_2O_3 phases

Table 1 Results of Ni 2p XPS characterization of the sulfided NiMo-based USY catalysts with various promoters [11]

Catalysts	Cat-1	Cat-2	Cat-3	Cat-4
$Ni_{sulfidation}$ (%)	92	94	95	95
Ni2+ (%)	8	6	5	5
NiSx (%)	38	21	43	9
NiMoS (%)	54	73	52	86

Reprinted from Catalysis Today, 305, Wenwu Zhou, Qing Zhang, Yasong Zhou, Qiang Wei, Lin Du, Sijia Ding, Shujiao Jiang, Yanan Zhang, Effects of Ga- and P-modified USY-based NiMoS catalysts on ultra-deep hydrodesulfurization for FCC diesels, 171–181, 2018, with permission from Elsevier

Cat-1 NiMo/USY, *Cat-2* NiMo//GaUSY, *Cat-3* NiMo/PUSY, *Cat-4* NiMo/PGaUSY

in the support. Based on the testing of prepared catalysts for VGO HDT application, it was observed that B introduction into the impregnation solution decreased the activity due to the formation of bulk BO_3 particles and small decline in the amount of Mo on the catalyst surface in the form of Mo4+ while the addition of phosphorous increased the catalytic activity. Simultaneous introduction of both phosphoric and boric acids into the impregnating solution increased the catalyst activity through an increase in the number of MoS_2 layers in the slab.

Li et al. [14] showed higher HDS and HYD activity for NiMo-Al$_2$O$_3$ catalysts prepared using citric acid due to an increase in active NiMoS phase and morphology control of MoS_2 phase. Higher catalytic activity was observed when Ni was complexed with CA preferentially before Mo in the impregnation solution. Also, CA has not shown any promotional effect within the monometallic Mo/Al$_2$O$_3$ catalyst.

Xia et al. [15] prepared CoMo/γ-Al$_2$O$_3$ catalysts with different loadings of additives (Ce and/or P) to investigate the effect of Ce and P modifications on the catalyst for the HDS of FCC gasoline. Phosphorous addition could slightly increase the stacking number of MoS_2 by reducing MSI. Addition of cerium to the small amount of 1.75 wt% could increase average slab length and stacking number apart from providing Brønsted acidity to the support with the net effect of increasing the catalytic activity for HDS of thiophene and isomerization of olefins. They showed the highest thiophene HDS and olefin isomerization conversions of 98.58% and 19.51%, respectively, for the catalyst modified with both cerium and phosphorus exhibiting the synergistic effect of Ce and P for the HDS of FCC gasoline with minimum octane loss. The octane loss is minimized due to high olefin isomerization activity of the catalyst, which is beneficial for removal of sulfur from FCC gasoline by retaining the octane number.

Saleh et al. [16] investigated the effect of boron addition on the HDS activity of CoMo/γ-Al$_2$O$_3$ catalyst with varied boron contents and reported optimum boron concentration of about 5 wt% for higher activity for the HDS of DBT.

Mendoza-Nieto et al. [17] studied the effect of CA addition on trimetallic NiMoW catalysts prepared using different supports such as conventional γ-Al$_2$O$_3$ and mesoporous SBA-15 for the HDS of DBT and 4,6-DMDBT. Their study showed higher dispersion of active metals and better HDS activity using CA for SBA-15-based trimetallic catalysts compared to conventional alumina-based catalysts, highlighting the dependence of support on the additive effect of CA during the preparation of trimetallic hydrotreating catalysts. The citric acid effect is less when the metal–support interaction is strong as in the case of γ-Al$_2$O$_3$-based NiMoW catalysts, while the improved catalytic performance was obtained for the SBA-15-based catalyst due to lower MSI.

Vatutina et al. [18] studied different ways of addition of P to the CoMo-based HDT catalyst during the synthesis and found that the addition of the precursor of P into the impregnation solution resulted in an increase in HDS activity of DBT compared to other methods of P addition due to change in the active phase structure, increase in the stacking number of active species, and decrease in MSI. Other methods of P addition such as the addition of P into the kneading paste or by

impregnating of a support had a negative influence on catalytic activity due to the formation of $CoAl_2O_4$ compounds and reduced content of promoter cobalt in the active phase.

Fan et al. [19] proposed a hydrothermal deposition method assisted by cetyltrimethylammonium bromide and fluorine for modulating the morphology of supported metal nanoparticles in $NiWF/Al_2O_3$ HDS catalysts. This catalyst synthesis approach was found to promote the dispersion of W by bridging and anchoring the metal nanoparticles on the surface of fluorinated alumina support and also lowered subsequent agglomeration of W during calcination. This method was reported to provide higher HDS activity compared to the conventional impregnation method due to improved metal dispersion, higher promotion effects, and more accessible Ni-W-S active sites.

3.2 Catalyst Preparation Methods

Hydrotreating catalysts are prepared by impregnation of active metals (Mo and Co or Ni) on the surface of the support material such as alumina. The metal components are used in the form of aqueous solutions to form respective metal ions that will be subsequently deposited on the surface of the support using different impregnation techniques. The following are the widely used impregnation techniques for the preparation of hydrotreating catalysts:

- Incipient wetness impregnation.
- Equilibrium adsorption.

In the first method, the support is contacted with a solution containing the metal precursor salts in a predetermined volume of water sufficient to fill the pores. In the second method, molybdenum from an aqueous solution of ammonium heptamolybdate is adsorbed on the support over an extended period of time till equilibrium is reached and followed by the filtration of the leftover liquid [2]. Modified impregnating methods through the addition of chelating agents or complexing agents to the impregnating solution were found to be advantageous in improving the activity of HDS catalysts through the following:

- Formation of a maximum number of Type II Co-Mo-S and Ni-Mo-S active phases with very high selectivity.
- Enhanced reducibility of molybdenum.
- Reducing the strong interaction between support and metal.
- Improved dispersion of metals over the support.
- Higher promotion effect resulting in a strong synergy between Co(Ni) and Mo sulfides.

Chelating or complexing agents are beneficial in delaying the sulfidation temperature of promoter metals (Co or Ni), which otherwise start sulfiding at lower temperatures compared to Mo resulting in poor sulfidation of the catalyst with

problems in the formation of highly active Type II Co-Mo-S and Ni-Mo-S structures. Chelating agents strongly interact with the promoter ions (Co or Ni), leading to higher sulfidation temperature of promoter metals compared to Mo, which results in the formation of sulfided cobalt atoms at the edges of already formed molybdenum sulfide slabs creating highly active Type II sites. Studies by Kubota et al. [20] and Okamoto et al. [21] illustrate the beneficial effects of chelating agents on the improvement of HDT/HDS catalyst activity. Chelating agents were also found to increase the Type II active structures in the catalyst by preventing the strong interactions between metals and support [5]. Some of the chelating agents used in the preparation of HDT/HDS catalysts along with impregnating solution to improve the catalytic activity include citric acid, glycol, urea, nitriloacetic acid, and ethylenediaminetetraacetic acid. The activity and selectivity of HDS catalysts are also influenced by the calcination and sulfidation temperatures, and the effects of these parameters vary for different reaction systems [22].

In one of the studies by van Haandel et al. [9], the effect of organic additives on catalyst activity was found to be more pronounced in promoted catalysts than in unpromoted ones by means of enhancing the Co-Mo interaction through better sulfidation of Mo and Co by forming weak complexes. They used α-hydroxycarboxylic acids (citric acid, tartaric acid, and gluconic acid) and aminopolycarboxylic acids (NTA, EDTA) as organic additives during preparation of HDS catalysts and found that the α-hydroxycarboxylic acids are more effective as organic additives compared to the latter in order to improve catalyst activity as shown in Table 2 for the HDS of dibenzothiophene with and without additives. The higher activity and promotion effect in the case of weak chelating agents such as α-hydroxycarboxylic acids are due to the formation of weak complexes with cobalt that decompose

Table 2 Dispersion (f_{Mo}) and DBT turnover frequency (TOF) of CoMo/Al$_2$O$_3$ catalysts [9]

Sample	f_{Mo}	TOF$_{DBT}$ (s^{-1})
CoMo^{dr}	0.265	0.014
CoMo^{cal}	0.271	0.018
CoMo-PA^{dr}	0.268	0.015
CoMo-PA^{cal}	0.269	0.022
CoMo-PA-PEG	0.261	0.025
CoMo-CA	0.263	0.028
CoMo-NTA	0.254	0.025

Reprinted from Journal of Catalysis, 351, L. van Haandel, G.M. Bremmer, E.J.M. Hensen, Th. Weber, The effect of organic additives and phosphoric acid on sulfidation and activity of (Co) Mo/Al$_2$O$_3$ hydrodesulfurization catalysts, 95–106, 2017, with permission from Elsevier

f_{Mo} fraction of accessible Mo edge atoms, *PA* phosphoric acid, *PEG* polyethyleneglycol, *CA* citric acid, *NTA* nitrilotriacetic acid, *EDTA* ethylenediaminetetraacetic acid, [dr] dried only; [cal] calcined

readily, resulting in fast sulfidation at 20 bar H_2/H_2S pressure at 350 °C. The intrinsic activity of the catalysts measured in terms of turnover frequency for catalysts prepared using additives was substantially higher than prepared without using additives, as shown by the highest TOF value of 0.028 s^{-1} for CoMo-CA.

Chen et al. [23] showed that modification of HDS catalysts using organic additives (ethylene glycol and CA) resulted in the reduction of MoS_2 slab length and increased stacking due to change in MSI. Temperature is one of the key factors in the preparation of unsupported MoS_2 nanocatalysts, which affects the hydrotreating activity. Initial temperature and synthesis temperature both are found to play an important role in tuning the morphology, crystalline nature, and catalyst properties and eventually in the catalytic activity. Zhang et al. [24] synthesized unsupported MoS_2 catalysts using the hydrothermal method at different initial and synthesis temperatures and tested for their HDS and HDN activities using light cycle oil as feedstock. Higher synthesis temperature and initial temperature favored higher HDS and HDN activities due to curved/shortened MoS_2 slabs and enhanced crystallinity. In the CAT-20-200, the initial temperature is mentioned as 20 °C and the synthesis temperature is 200 °C.

Being one of the catalyst preparation methods, chemical vapor deposition (CVD) was found to improve the formation of highly active Co-Mo-S active phases in a selective manner resulting in substantially high catalytic activity compared to CoMo catalysts prepared using the impregnation method [25, 26].

Although literature is replete with the use of several new catalyst preparation techniques such as CVD and incorporation of other modifiers/additives into the hydrotreating catalysts for obtaining highly active catalytic sites, most of these methods/materials are not commercially proven yet, and these are still in the development stage in the laboratory. Further research work is needed to validate the findings in terms of activity, selectivity, and stability characteristics and utilize these novel methods and materials in the preparation of economically viable catalysts for HDS/HDT application.

Liu et al. [27] prepared highly active HDS catalysts using PVP-assisted synthesis of both supported and unsupported NiMo oxide catalysts with varying PVP contents and showed high activity for the HDS of DBT due to the formation of favorable active phases such as MoS_2 and Ni_3S_2 nanoparticles on the sulfided catalyst.

Wang et al. [28] synthesized mesoporous γ-Al_2O_3 support material with different textural properties and acidities using $AlCl_3 \cdot 6H_2O$ as an aluminum source and polyethylene glycol as a mesostructure-directing agent by tuning the hydrothermal aging temperature. Two-step incipient wetness impregnation method was subsequently used to prepare NiMo/γ-Al_2O_3 catalysts and studied for their HDS performance using model compounds. Catalyst synthesized at an aging temperature of 363 K showed the highest HDS activity due to favorable textural properties, acidity, and MSI apart from optimal metal dispersion, sulfidation, and MoS_2 stacking. Also, this catalyst resulted in the highest HYD/DDS ratio for the HDS of 4,6-DMDBT, indicating the predominance of the hydrogenation pathway over DDS for the HDS reaction. Wang et al. [29] synthesized mesoporous alumina with different crystal forms from the boehmite sol and used them as supports for bimetallic sulfided NiMo

HDS catalysts. The NiMo/δ-Al$_2$O$_3$ catalyst was found to exhibit higher HDS activity for model compounds compared to the NiMo/γ-Al$_2$O$_3$ catalyst prepared using the same mesoporous material. Also, the NiMo/δ-Al$_2$O$_3$ catalyst showed higher hydrogenation activity and removed sulfur predominantly by the HYD route. Higher HDS activity and selectivity of the NiMo/δ-Al$_2$O$_3$ catalyst prepared using mesoporous alumina were attributed to the balanced acidity, MSI, and suitable dispersion/stacking of the active phases along with its favorable textural characteristics.

Braggio et al. [30] prepared two NiMo catalysts with different methods, co-impregnation and post-treatment using citric acid as a chelating agent to study the effect of catalyst preparation method on the HDS and hydrogenation of DBT. In the post-treatment method, impregnation of citric acid was done on the calcined CoMo catalyst. HDS reactions were carried out in a three-phase reactor with and without quinolone to understand the inhibition effects. DDS was found to be the favored route for the HDS of the DBT molecule. The catalyst prepared using the post-treatment method was more effective for hydrotreating compared to the co-impregnation catalyst due to higher density of active sites on the catalyst and better sulfidation behavior. The inhibition effect of quinolone was more for the catalyst prepared by post-treatment, but this was offset by the higher activity of the catalyst than that of the co-impregnation catalyst.

Singh et al. [31] reported the preparation of ultrasmall bimetallic NiMo oxidic nanoclusters supported on alumina to carry out HDS reactions. Colloidal synthesis was used to prepare the metal oxide nanoclusters with oleic acid and oleylamine as ligands, and subsequently the nanoclusters were incorporated into the pores of alumina support. The ligands were removed later through calcination of the supported catalysts followed by sulfidation. HDS activity of the nanocolloidal-based catalyst was found to be better compared to the catalyst prepared using the conventional wet impregnation method with DBT and diesel as feedstocks due to ultrasmall size of the metal oxide nanoclusters on the support and better dispersion (Fig. 2).

Liu et al. [32] synthesized hexagonal, ordered, and highly dispersed mesoporous NiMo-Al$_2$O$_3$ catalysts with 20 wt% MoO$_3$ and varying NiO contents using a one-pot evaporation-induced self-assembly (EISA) method with P123 as a structure-directing agent and anhydrous ethanol as a solvent. High activity was observed using the catalyst prepared with Ni/Mo molar ratio of 1:1 for the HDS of DBT due to the formation of an easily reducible form of molybdate in the octahedral site and better dispersion of MoS$_2$ nanoparticles. Also, the ordered mesoporous NiMo-Al$_2$O$_3$ catalysts removed sulfur predominantly through the DDS route, as shown by the formation of biphenyl in the product.

Dong et al. [33] synthesized hierarchically structured alumina hollow microspheres with high specific surface area and favorable pore volume and acidity via a citric-acid-modulated hydrothermal method and prepared highly active NiMo-based catalysts and tested for HDS of DBT.

Cheche et al. [34] utilized waste rubber tires to make activated carbon for subsequent preparation of NiMo-based bimetallic HDS catalysts through the wetness co-impregnation method subjecting to various calcination temperatures. The highest activity for HDS of DBT was observed for the catalyst calcined at 300 °C due to
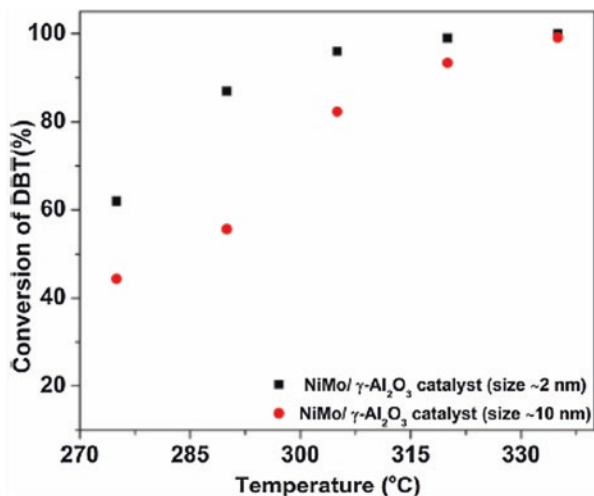
Fig. 2 Comparison of HDS activity of NiMo nanoparticles (size 2 nm and 10 nm) supported on γ-Al2O3 [32] (Reprinted from Applied Catalysis B: Environmental, 185, Rupesh Singh, Deepak Kunzru, Sri Sivakumar, Monodispersed ultrasmall NiMo metal oxide nanoclusters as hydrodesulfurization catalyst, 163–173, 2016, with permission from Elsevier)

high surface area, favorable pore size, and acidity characteristics. Xu et al. [35] prepared NiMo/SiO$_2$-Al$_2$O$_3$-based ULSD catalysts using a novel gemini surfactant-assisted synthesis of Mo precursor and reported higher catalytic activity for the HDS of 4,6-DMDBT and FCC diesel compared to the conventional catalysts synthesized by a hydrothermal method due to better active phase dispersion, improved stacking, and formation of a large extent of accessible Ni-Mo-S phases after Ni incorporation.

Huang et al. [36] proposed a hydrothermal deposition method for the preparation of a Co$_4$Mo$_{12}$/Al$_2$O$_3$-based HDS catalyst through deposition of heteropoly compounds on Al$_2$O$_3$ and showed higher activity for the HDS of DBT compared to the catalysts prepared using an incipient wetness impregnation method. The reasons attributed to the high catalytic activity are weak MSI, higher MoS$_2$ stacking, and high concentration of CoMoS phases due to high Co/Mo ratios.

Cabello et al. [37] prepared Co$_2$Mo$_{10}$- and CoMo$_6$-based hetropoly compounds and showed higher activity for the HDS of thiophene and hydrogenation of cyclohexane compared to conventional Co-Mo-based catalysts. The higher activity was attributed to the good adsorptive interaction of heteropolyoxometalates with the support and uniform distribution of active sites on the catalyst surface.

Hensen et al. [38] studied various supported Mo sulfide catalysts and showed that the HDS and HYD selectivities can be fine-tuned by the morphology of MoS$_2$ phase and the choice of support. The choice of support material was found to dictate the morphology and dispersion of active phases. MoS$_2$ slab structures with a multi-layered morphology were reported in the case of Mo/SiO$_2$ and Mo/ASA catalysts. Mo/C had the highest MoS$_2$ dispersion. Carbon support exhibited high HYD

activity for thiophene and toluene due to the large fraction of corner sites, whereas Mo/ASA exhibited low intrinsic HDS activities, which was compensated by very high hydrogenation activity.

The patent literature also describes the making of high-activity HDS catalysts using various methods and applications [39–41].

4　Catalyst Activation/Sulfidation

Hydrotreating catalysts need to be activated before starting the reactions either through sulfiding or reduction step depending on the type of catalyst to make them catalytically active. HDT catalysts are usually supplied in the oxide form of metals (Ni, Co, Mo, W oxides, or Pt/Pd oxides). The oxide form is not the active form to carry out HDT/HDS reactions; this has to be converted into the sulfide form of metals before carrying out HDT/HDS reactions in the case of nonnoble metal or base metal catalysts. Thus, fresh hydrotreating catalysts or regenerated catalysts need to be activated through catalyst sulfiding or presulfiding before processing with actual feed. The fresh or regenerated catalyst should not be exposed to hydrogen while in an oxidized state above 200 °C because hydrogen could reduce the catalyst metal oxides into metals and render the catalyst useless for the HDT reactions. Also, the reduction reaction is highly exothermic and occurs at a faster rate due to which there are chances of catalyst damage. There are two approaches employed by refiners for sulfiding/activation of the HDT catalysts: in situ sulfiding and ex situ sulfiding.

In situ sulfiding is the most commonly used sulfiding method in refineries and performed in either vapor or liquid phase. Liquid phase sulfiding is carried out with or without the aid of a sulfiding agent. Sulfiding is accomplished with the help of a sulfiding feed, which may be a straight-run distillate such as diesel or kerosene with at least 1.0–2.0 wt% sulfur or straight-run distillate spiked with a sulfiding agent such as dimethyldisulfide (CH_3-S-S-CH_3) (DMDS), dimethyl sulfide (CH_3-S-CH_3), etc. Many refiners prefer liquid phase sulfiding using spiking agents such as DMDS along with straight-run distillates compared to either vapor phase or liquid phase sulfiding without spiking agents due to the advantages in terms of less sulfidation and start-up time. Sulfiding is normally carried out in the presence of hydrogen gas. Cracked feeds with the content of unsaturated olefinic hydrocarbons are not preferable for sulfidation of HDT/HDS catalysts since they are prone to coking and polymerization and interfere with proper sulfiding of the catalysts. DMDS is the widely used sulfiding agent for the presulfiding of hydrotreating catalysts due to some of their advantages compared to other sulfiding agents in terms of its higher sulfur content and lower sulfidation/start-up period. Another advantage of using DMDS is the better control of exothermic sulfiding reactions due to two-step decomposition and sulfiding, which reduces the chance of reactor exotherms. The sulfiding agent such as DMDS initially breaks down into hydrogen sulfide and then initiates the sulfiding process. Complete sulfiding of Co-Mo- and Ni-Mo-type HDS catalysts require about 10 wt% sulfur on the catalyst. Vapor phase sulfiding is

carried out using a mixture of about 2–5 vol.% of H_2S in hydrogen, and this is not being commonly practiced in refineries.

Although DMDS is the most common sulfiding agent used for catalyst sulfiding application, use of tertiary-butyl polysulfide (TBPS) is also gaining significance in recent times [42]. However, sulfur content of TBPS (54%) is lower than that of DMDS (68%). TBPS is preferred in certain sulfiding applications where a lower decomposition temperature and lower methane make is desirable. Some of the other sulfiding agents are dimethyl sulfide (DMS) and dimethyl sulfoxide (DMSO).

van Haandel et al. [43] studied the activation of $CoMo/Al_2O_3$ catalysts prepared with phosphoric acid (PA) and citric acid as additives in both gas phase (using H_2/H_2S at 1 or 20 bar pressure) and liquid phase activation (using a mixture of DMDS/n-hexadecane at 20 bar H_2 pressure) methods. Gas-phase sulfiding with H_2/H_2S was found to occur gradually from room temperature to 350 °C. Activation at elevated pressure (20 bar) was beneficial in terms of increased sulfidation rate and higher degree of Mo sulfidation without affecting the particle size. Citric acid increased the gas-phase sulfidation rate at higher pressure due to reduced metal–support interaction (MSI) and enhanced Mo reducibility. Sulfidation in the liquid phase predominantly formed single layers of MoS_2 in contrast to the multilayer stacks formed after gas phase activation, emphasizing the importance of activation conditions on the formation of MoS_2 stacks. Catalysts prepared with PA were reported to be most stable and active for gas-oil HDS compared to those prepared using CA. During ex situ presulfiding process, sulfiding conditions play an important role in the morphology and performance of $CoMoS/\gamma\text{-}Al_2O_3$ catalysts [44]. Some companies such as Eurocat and Porocel offer patented ex situ sulfiding and activation services for hydroprocessing catalysts.

5   Catalyst Deactivation

Hydrotreating catalysts gradually lose their catalytic activity during the course of operation, and this deactivation phenomenon hampers the catalyst's ability with respect to the extent of sulfur removal in the case of HDT/HDS operations. Catalyst activity usually depends on the number of active sites available on the catalyst for the desirable reactions. The main cause of deactivation is due to the loss of active sites of the catalyst. Catalyst activity is measured in terms of relative rates of HDS reaction for HDT/HDS type of operation. In Industrial applications, catalyst activity is measured in terms of the temperature required for obtaining specific HDS levels.

Hydrotreating catalysts undergo gradual deactivation over the cycle life due to the following reasons:

- Metal deposition on the catalyst surface.
- Coke laydown on the surface.
- Poisoning of the active sites by strongly adsorbed species.
- Change in the catalyst structure (metal sintering/agglomeration).
- Pore mouth plugging by metals or coke.

In commercial hydrotreating units, reactor temperature needs to be gradually increased to maintain constant catalytic activity in order to obtain required desulfurization levels. The degree of deactivation is usually measured in terms of the profile of temperature rise as a function of time during the operations. Normally, catalyst deactivation rates are dependent on the feed source and process conditions. Heavier feedstock such as residue will deactivate at a faster rate compared to lighter feeds. Generally, heavier feeds contain higher amounts of contaminants, and thus they need to be operated at higher process severity (high temperature, hydrogen partial pressure, etc.), resulting in shorter catalyst life. Also, rates of deactivation are not the same for different hydroprocessing reactions such as hydrodesulfurization, hydrodenitrogenation, hydrodearomatization, etc. for different feeds and process conditions.

Deactivation rates commonly encountered during hydroprocessing of petroleum fractions vary from <1 to 4–5 °C/month depending upon the type and nature of feedstock. Lighter hydrocarbon fractions such as straight-run naphtha deactivate at a slower rate of <1 °C/month, while cracked naphtha deactivates at the rate of 2-4 °C/month during hydrotreating. Straight-run and light hydrocarbon feeds deactivate at a slower rate compared to cracked stock and heavy hydrocarbons. Furimsky and Massoth [45] presented a detailed review of the deactivation of hydroprocessing catalysts covering all aspects of deactivation.

5.1 Deactivation Due to Coke

Coke is usually a mixture of carbon (90 wt%) and hydrogen (10 wt%). It is deposited gradually on the surface of the hydrotreating catalyst due to polymerization and condensation reactions of polycyclic aromatic species and other unsaturated intermediates formed by the hydrotreating and hydrocracking reactions. Coke reduces the activity of the catalyst, and thus reactor temperature needs to be increased over time to obtain the same HDS conversions. The higher temperatures will further aggravate the coke formation through enhanced coking reactions.

Deactivation due to coke formation occurs at a rapid rate during the initial stages of operation, resulting in a rapid build-up of coke on the catalyst surface. After this initial stage of rapid coke deposition, the rate of coke laydown becomes gradual and attains a steady state. Again, the coke builds up faster with the mostly deactivated catalyst, especially due to severe processing conditions such as higher reactor temperatures employed near the end-of-run conditions. During this period, the catalyst needs to be unloaded and regenerated for reuse.

Aromatic compounds, especially polycyclic aromatics and asphaltenes, are the primary precursors responsible for coke formation during hydroprocessing through polycondensation/polymerization reactions. As the amount of coke increases on the catalyst, the pore diameter and pore volume both decrease, resulting in the shift of

pore size distribution toward smaller pores. The extent of coke and metal deposition on the catalyst is dependent on the properties of the feed and process conditions. Coke is not a permanent poison, and regeneration of the spent catalyst by burning off the coke in the presence of air/oxygen usually restores the catalyst activity near to fresh catalyst conditions.

5.2 Deactivation Due to Metals

Deactivation due to poisoning by metals occurs simultaneously with that of coke deactivation and depends on the feedstock properties and process conditions. Nickel and vanadium are the predominant metals present in petroleum, shale oil fractions, and heavy oils. Table 3 provides the list of contaminant metal poisons for hydroprocessing catalysts that are present in petroleum fractions. Feedstocks derived from coal will contain metals such as Fe, Ti, Ca, Mg, etc.

Metals commonly enter into the reactor system through the following:

- Metals present in the feedstock as organometallic compounds (mostly Ni and V). Since crude oil contains metals, they are distributed in various fractions.
- Feedstock contaminants (Fe, As, Na, Ca, Mg, P, etc.).
- Additives or chemicals used in certain processes (anti-foaming additives used in coker units contain silicon compounds).

Unlike coke deposition, metals are usually deposited on the catalyst at a steady rate, more or less in a linear pattern with respect to time-on-stream. Metal deposition on hydrotreating catalysts leads to the loss of surface area and pore volume and can affect the metal function sites or the acid function sites or both. The effect and extent of poisoning vary with different metals. For example, Ni and V deposit at the inlet of the pores or near the outer catalyst surface resulting in deactivation of the catalyst through pore blockage, which restricts the accessibility of the reactants to the active interior surface area. Sodium and silicon result in reduced regenerability of the catalyst, while arsenic, lead, and sodium lead to poisoning of active sites. Metal deposition on the catalyst depends on the position of the catalyst particle in the reactor and process conditions. Most of the metal and sulfur deposition occurs

Table 3 Metal poisons for hydroprocessing catalysts

Common metal poisons	Other less common metal poisons
Nickel (Ni)	Calcium (ca)
Vanadium (V)	Potassium (K)
Sodium (Na)	Phosphorous (P)
Iron (Fe)	Mercury (hg)
Silicon (Si)	Lead (Pb)
Arsenic (as)	

at the inlet of the reactor catalyst bed, while most of the carbon deposits at the outlet of the reactor bed.

Properties of the catalyst such as surface area, pore volume, and mean pore diameter are also important factors that determine the metal tolerance of the hydrotreating catalysts. Metal poisoning or deactivation is irreversible and thus affects the overall catalyst life. Catalyst regeneration also cannot reverse the effects of metal deactivation. Incorporation of a guard bed containing a demetallization catalyst ahead of the main HDT catalyst bed will protect the high activity hydrotreating catalyst from metal poisoning.

5.3 Deactivation by Poisoning of Active Sites

Catalyst poisons are substances that are strongly chemisorbed on the active sites and decrease the number of such sites available for the desired reaction resulting in lower catalyst activity. Also, these poisons can compete with the reactant molecules for adsorption in the same type of active site. In most of the cases, this kind of poisoning is reversible, and removal of the poisoning compound from the system will gradually restore the catalyst activity by reversing the poisoning effect. Some of the reversible poisons that hamper the activity of hydroprocessing catalysts are basic nitrogen compounds, hydrogen sulfide, and carbon monoxide. The catalyst activity loss due to the effect of temporary poisons is compensated in some cases by operating the unit at higher reactor temperatures for enhancing the rate of reaction. However, this will result in a higher rate of catalyst deactivation through an enhanced rate of coke formation.

5.4 Change in the Structure of the Catalyst (Metal Sintering/ Agglomeration)

High temperatures encountered during hydrotreating operations affect gradual changes in the structure of the catalyst active phase resulting in slow and irreversible loss in the catalyst activity and stability. Deactivation caused by high temperatures is primarily due to the following reasons with respect to changes in the catalyst active phase:

- Sintering and segregation of active phase through diffusion of active metals into support.
- Recrystallization of the active material into a different form.
- Interaction of the metals present in the feed with catalyst metals resulting in the changes in the active sites.

Sintering and segregation of active metals could result in the growth in the size of MoS_2 slabs and decreased metal dispersion, which can cause reduced catalytic activity due to less number of active metallic sites. Sintering also depletes MoS_2 slabs of promoters (Co or Ni) affecting the catalyst activity due to reduced promotional effect since the active phase for the HDT reactions is the CoMoS or NiMoS phase. Metals (arsenic, sodium, iron, etc.) present in the feedstock can interact with the catalyst metals (Co, Mo, W) and form compounds such as $AsMo_4$, $Co_3As_2O_8$, Na_2MoO_4, Na_2WO_4, $FeMoO_4$, $CoFe_2O_4$, etc. that will alter the nature of catalytic active sites and cause deactivation of the catalyst.

Zhang et al. [46] studied the deactivation of HDS catalysts and mechanism with unsupported nano MoS_2 and supported catalysts using LCO as feedstock under extreme process conditions. Spent nano MoS_2 was found to exhibit lower deactivation through coke deposition compared to the supported catalyst and also resulted in the formation of soft coke in the absence of acidic supports. The decomposition of the active phase played an insignificant role in the deactivation of nano MoS_2 unlike supported catalysts. Marafi et al. [47] studied the deactivation of Mo/Al_2O_3, $Ni-Mo/Al_2O_3$, and $Ni-MoP/Al_2O_3$ catalysts in atmospheric residue HDS and found that coking tendency of the reactions was of the following order: HDS ← HDM ← HDS/HDN. Initial coke build-up was very rapid during hydrotreating of residue with carbon deposition up to 20 wt% reached within 120 h in their study. There are two types of coke reported such as soft coke and refractory surface coke on the spent catalyst with the deposition mainly through adsorption at the catalyst support without affecting the metal sulfide phase. The nature of coke deposition depends on the type of catalyst as the HDM and HDS catalysts contained more aromatic and condensed type of coke with less alkyl substituents, while the HDS/HDN catalyst contained coke with low aromaticity due to its high hydrogenation activity. The study showed the strong influence of physicochemical properties (SA, PV, metal content) on catalyst deactivation by both coke and metals.

6 Catalyst Regeneration

Hydrotreating catalysts gradually get deactivated during the operation and need to be regenerated to restore the lost activity and reuse it for another cycle. Regeneration gains significance due to high cost of fresh HDT catalysts and the stringent environmental regulations for spent catalyst disposal. It is not possible to restore the catalyst activity to the levels of a fresh catalyst after regeneration, and in general, the HDT catalyst loses 5–15% of original activity with each regeneration. Usually, the catalyst can be used with 2–3 regenerations beyond which it has to be dumped and the fresh catalyst has to be replaced in the reactors. The extent of recovery of catalytic activity after regeneration depends on the amount of metals deposited on the catalyst and the severity of the process. Catalyst regeneration is performed to burn off the coke deposited on the catalyst in a controlled manner by oxidation with air or diluted oxygen. Along with air or oxygen, steam or nitrogen is also used as a

diluent. Catalyst regeneration is an exothermic reaction. It usually restores the catalyst activity lost due to the gradual accumulation of coke on the catalyst, but it does not recover the loss in activity due to poisoning by metals such as nickel, vanadium, iron, etc.

There are two modes of catalyst regeneration: in situ and ex situ regeneration. Ex situ regeneration is also called off-site regeneration. In the in situ mode, regeneration is carried out within the reactor itself and the coke is burned off using air, steam/air, or nitrogen/air mixtures. In the ex situ regeneration, the catalyst is removed from the reactor and the regeneration is carried out off-site. In the past, in situ regeneration was commonly practiced in refineries using a lengthy procedure involving unit downtime and production loss. Also, better control of regeneration could not be achieved during in situ regeneration resulting in fines generation and increased pressure drop. Poor in situ regeneration usually results in poor catalyst performance with reduced unit throughputs and/or lower severity operation and ultimately ends up in premature or prescheduled replacement of the catalyst.

Ex situ regeneration involves regeneration by any third-party on a chargeable basis. Since the refiner is ready with a fresh catalyst charge, the fresh catalyst is loaded in the reactor and the spent catalyst is sent to any of the service providers. At present, most of the refiners prefer ex situ regeneration in place of in situ regeneration due to the following advantages:

- Better control of regeneration operation such as exothermicity, oxygen diffusion, formation of water and SO_2, etc.
- Better recovery of catalyst activity.
- Less unit downtime and better economics.
- Minimization of environmental and safety hazards.

Regeneration of hydroprocessing catalysts burns off the coke, but this will not ensure proper re-dispersion of the active metals on the catalyst surface. For re-dispersion of active metals, a wet process called "rejuvenation" is performed immediately after the regeneration step. More than 90% of the original catalyst activity is usually restored in the ex situ regeneration process utilizing the combination of both regeneration and rejuvenation processes. Kallinikos et al. [50] studied HDS catalyst deactivation in a laboratory reactor through a hybrid neural network model and compared the results with the deactivation of industrial hydrotreater catalysts. They found that the deactivation of the industrial reactor is more or less uniform without significant variation at different locations. Also, faster deactivation was observed for hydrogen consuming reactions than the HDS reactions, which indicates lower hydrogen consumption with time on stream for specified product sulfur content.

Pimerzin et al. [51] studied reactivation of the spent industrial $CoMo/Al_2O_3$ HDT catalyst using a combination of oxidative regeneration and rejuvenation methods. The spent catalyst was obtained from an industrial, low-pressure gas-oil HDT unit (4.5 MPa) after 2 years and 2 months of operation in ULSD service. The MoO_3 and CoO content of the industrial catalyst was about 16.2% and 4.6%, respectively. Rejuvenation of the catalyst was performed using different organic acids such as citric and thioglycolic acids, glycols such as ethylene and triethylene glycols, and

dimethylsulfoxide. Textural properties and pore volume distributions could be restored upon oxidative regeneration and rejuvenation with organic compounds. Figure 3 shows the pore volume distribution of fresh, spent, and oxidatively regenerated catalysts. The spent catalyst showed bimodal pore size distribution with the formation of micropores due to carbon deposits on the original pore, which disappeared upon combustion of coke restoring the original pore size distribution for the regenerated catalyst. Rejuvenation of the regenerated catalyst could retain the PSD, but there had been a significant decrease in SA and PV of the catalysts, which were regained after sulfidation of the rejuvenated catalyst.

In the study of Pimerzin et al. [51], although oxidative regeneration could restore about 70–85% of activity compared to the fresh catalyst for the hydrodesulfurization of DBT and hydrogenation of naphthalene, rejuvenation achieved the almost complete restoration of both HDS and hydrogenation activities through improved dispersion of active phase and increased $(Co/Mo)_{slab}$ and $(Co/Mo)_{edge}$ ratios and formation of new highly active CoMoS phases.

Bui et al. [52] studied the role of the addition of organic additives during the regeneration of the used industrial $Co(Ni)Mo/Al_2O_3$-based HDS catalyst to restore the catalytic activity. The effect of maleic acid was studied for the activation of the regenerated catalyst at different steps of the preparation, and finally, HDS activity
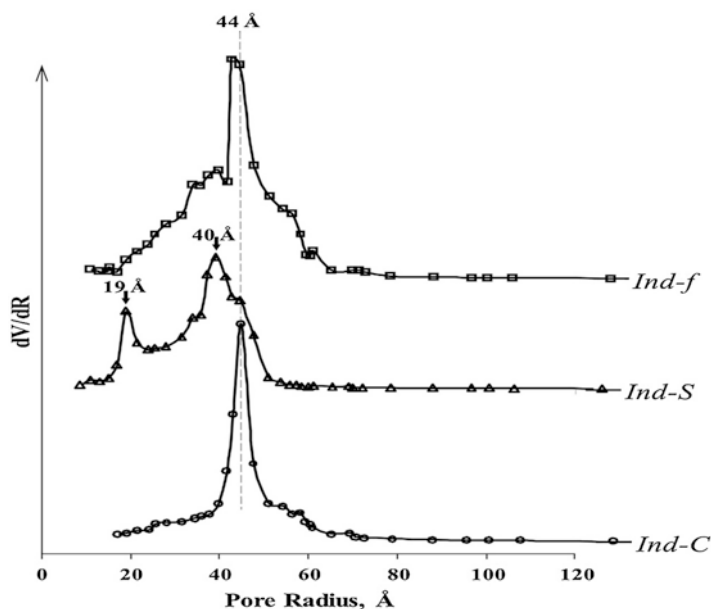
Fig. 3 Pore volume distribution of fresh, spent, and oxidatively regenerated catalysts [51]. *Ind-f* fresh catalyst, *Ind-S* spent catalyst, *Ind-C* oxidatively regenerated catalyst at 500 °C for 2 h in laboratory furnace (Reprinted from Fuel Processing Technology, 173, Aleksey Pimerzin, Andrey Roganov, Alexander Mozhaev, Konstantin Maslakov, Pavel Nikulshin, Andrey Pimerzin, Active phase transformation in industrial $CoMo/Al_2O_3$ hydrotreating catalyst during its deactivation and rejuvenation with organic chemicals treatment, 56–65, 2018, with permission from Elsevier)

evaluation was performed using 4,6-DMDBT and a straight-run gas oil feedstock. Maleic acid was found to extract Co from the $CoMoO_4$ species forming a cobalt maleate complex. The addition of maleic acid resulted in more rapid sulfidation of Mo without releasing Co significantly from the cobalt maleate complex before reaching 300 °C, which resulted in the formation of higher proportion of Co-promoted MoS_2 phase and enhanced HDS catalytic performance. Santolalla-Vargas et al. [53] studied in situ reactivation of spent HDS catalysts with molybdenum acetylacetonate previously washed with xylene and 2,6-bis-(1-hydroxy-1,1-diphenyl-methyl)pyridine and further investigated for the HDS of straight-run gas oil. Aromatic carbons and coke with larger crystallite size were removed from the spent catalyst by washing chemicals. In situ reactivation with molybdenum acetylacetonate could help in the deposition of Mo on the catalyst and increase its surface content, which otherwise could decrease during the leaching process. This novel method of regeneration/rejuvenation was claimed to enhance the MoS_2 species, lower the carbon concentration, and shorten the coke crystallite size resulting in a higher gas-oil HDS activity.

Regeneration and reuse of residue hydroprocessing catalysts gain significance due to generation of a large volume of these catalysts in refineries due to their high deactivation rates. However, regeneration of residue HDS catalysts is more difficult compared to distillate/naphtha HDS catalysts due to the presence of high concentrations of metals such as vanadium and also the requirement of severe regeneration conditions. Iwamoto [54] reviewed the regeneration of residue HDS catalysts and showed the effects of the presence of vanadium on the regeneration activity. Vanadium was found to increase the regeneration temperature due to its oxidative properties apart from reducing the capacity for activity recovery and decreasing catalyst strength.

7   Catalysts for Different Hydrotreating Feedstocks

Proper selection of the catalyst plays an important role in getting the most out of their performance in terms of activity, selectivity, and stability. Some aspects that need to be considered for selection of catalysts with regard to particular hydrotreating application are feedstock type and properties, process conditions, and required product yields and properties. Due to the differences in the properties of different feeds such as naphtha, distillates, vacuum gas oils, and heavy residues, the catalyst design and selection criteria vary significantly among them. Apart from molecular weight distribution between these feedstocks, there are significant variations in the properties such as asphaltenes, metals, and heteroatoms. Due to these differences, the catalysts used for hydrotreating of residues are not the same as those used for distillates or naphtha.

Activity, selectivity, and stability are the three important characteristics that are considered for catalyst selection for any particular HDT application. Activity is defined as the ability of the catalyst to increase the rate of specific reaction such as

HDS, HDN, hydrocracking, HDM, etc. Catalyst activity is usually measured in terms of the reaction temperature at which it produces products meeting the required specifications for a given feed while all other process parameters are unchanged. For a specific feedstock, a catalyst that gives the required product quality or conversions at lower operating temperature is the best ones in terms of activity. Selectivity expresses the ability of the catalyst to favor the desired chemical transformations in comparison with other reactions to produce selected products with specified properties. For example, FCC naphtha HDS requires a catalyst that needs to perform selective HDS with minimum saturation of olefins in order to retain octane number. The stability of the catalyst is defined as a change in the activity or performance of the catalyst with time-on-stream when the feedstock and process conditions are stable. The catalyst stability is measured in terms of the cycle length. Catalyst stability or life is affected by several factors such as the following:

- Presence of poisons in the feedstock such as metals.
- Inactivation by one or more of the products.
- Loss of a volatile agent from the catalyst.
- Loss of activity due to a change in the crystal phase.

Selection of hydrotreating catalysts is mostly based on the comparison between required start-of-run (SOR) temperatures to achieve certain product quality in terms of product sulfur or yields. Apart from catalyst activity and selectivity, catalyst stability is also an important factor to be considered during catalyst selection. A catalyst that performs well under SOR conditions may have poor stability and deactivate faster than other catalysts that performed slightly less under those conditions. Based on the initial activity, selectivity, and overall life, economic comparison needs to be performed incorporating product value based on specific conversion and yields, energy cost, cost of catalyst, etc., and a suitable catalyst needs to be selected using economic considerations for those catalysts that meet the conversion or product quality or product yield requirements.

7.1 Selection of Hydrotreating Catalysts for Gasoline and Gas Oils

The choice of the catalyst depends on the specific process requirement such as hydrodesulfurization, hydrodenitrogenation, aromatics hydrogenation, olefin saturation, and hydrocracking. Table 4 presents the selection of common catalysts for different hydrotreating applications. In general, the Co-Mo catalyst is the best choice for hydrodesulfurization of straight-run feedstock such as virgin naphtha, kerosene, and gas oils. Although it is true that Co-Mo catalysts are well suited for HDS of straight-run feeds, high-activity Ni-Mo catalysts also exhibit substantially high activity for the HDS of petroleum fractions, but with higher hydrogen

Table 4 Selection of common catalysts for hydrotreating applications

Catalyst type	Applications
Co-Mo/Al$_2$O$_3$	HDS of straight-run feeds
Ni-Mo/Al$_2$O$_3$	Hydrodenitrogenation Hydrogenation of aromatics/olefins HDS of cracked feeds
Ni-W	Aromatic saturation
Pt or Pd	Aromatic saturation in a pure sulfur-free environment

consumption due to the difference in the reaction mechanism at which both these catalysts operate.

The Ni-Mo catalyst is best suited for hydrodenitrogenation and hydrogenation of unsaturated hydrocarbon molecules such as olefins and aromatics due to its high hydrogenation activity compared to Co-Mo catalysts. Although Ni-Mo-type catalysts are well suited for nitrogen removal, Co-Mo catalysts also exhibit reasonably good hydrodenitrogenation activity for lighter feedstock. However, Co-Mo catalysts are not a good choice when the feed nitrogen content is substantially high even for light feeds due to catalyst poisoning. For high nitrogen-containing feeds, Ni-Mo is the best choice. Also, Ni-Mo catalysts are frequently chosen when processing feedstocks containing more than 20% of cracked stock due to their high hydrogenation activity. In some applications, Ni-W based catalysts are used where there is a requirement of high activity for the saturation of aromatics. In two-stage hydrotreating processes, noble metal (Pt or Pd)-based hydrogenation catalysts are used for aromatic saturation applications in sulfur-free, pure second-stage environment, especially to improve cetane number of diesel fuel. Since noble metal catalysts possess high activity for hydrogenation of aromatics, they can be operated at lower reactor temperatures compared to Co-Mo- or Ni-Mo-based catalysts in a clean reaction environment.

Ni-Mo hydrotreating catalysts are usually preferred for vacuum gas-oil HDT/HDS, FCC feed pretreatment, and hydrocracker pretreat applications, which mainly use light and heavy vacuum gas-oil feedstocks. VGO hydrotreating application requires catalysts with high hydrogenation activity such as Ni-Mo/Al$_2$O$_3$ due to the following reasons:

- Deep sulfur removal from predominantly refractory sulfur species such as alkylated dibenzothiophenes.
- Deep HDN for higher FCC and hydrocracker conversions.
- Aromatic saturation for improved FCC conversions.

Klimov et al. [55] studied the use of trimetallic Co-Ni-Mo/Al$_2$O$_3$ catalysts with varying Co and Ni contents for deep HDT of VGO and showed that the catalyst containing 1.8% Co and 1.2% Ni being the highly active ones compared to other compositions. The higher activity of these trimetallic catalysts was ascribed to the presence of mixed Ni-Co-Mo-S active phases. They proposed the formation of

mixed active phase by the location of Co on vacant positions of MoS_2, followed by the incorporation of Ni on the available sites.

Guo et al. [56] investigated the hydrogenation activity (alkylation, HDS, and HDN) of CoMo and NiMo catalysts possessing high Brönsted acid sites for the hydroprocessing of diesel feedstocks with an objective to achieve optimal HDS through proper choice of catalysts and stacking systems. For feedstocks with high sulfur and low nitrogen and aromatic contents, CoMo-type catalysts showed the highest HDS activity. NiMo-type catalysts showed the highest HDS and HDN activity for feedstocks with high nitrogen and aromatic contents. Stacking of CoMo and NiMo catalysts was reported as the optimal combination to obtain the highest HDS activity for processing diesel feedstocks with moderate nitrogen and aromatic contents due to their synergistic effects.

Zhang et al. [48] synthesized various alumina supports by rehydration–dehydration of the γ-Al_2O_3 under varied hydrothermal temperatures and further prepared CoMo/Al_2O_3 catalysts to study the HDS of model FCC naphtha. The improved HDS selectivity of the catalyst was ascribed to the weak MSI, as well as lower dispersion of MoS_2 that resulted in large edge-to-corner ratios of CoMoS slabs. Apart from the improved catalyst, the authors proposed a two-step process scheme involving selective HDS and mercaptan removing catalysts to achieve ultralow sulfur gasoline with minimum octane loss.

Sharifi et al. [57] synthesized W/HZSM-5 catalysts with different SiO_2/Al_2O_3 ratios for simultaneous HDS and octane improvement for heavy naphtha through aromatization. Optimized catalyst formulations in combination with process improvements such as HDS and aromatization will result in the restoration of the lost octane number during HDS. The importance of the role of Co in the MoS_2 HDS catalyst was investigated by Bin et al. [59] for the selective HDS of FCC gasoline. Cobalt was found to make a significant difference in catalytic properties by affecting the microstructure and composition of the active phase. The presence of Co improved HDS activity with only a slight effect on olefin hydrogenation.

Coupling aromatization and HDS reactions for heavy naphtha feed were studied by Sharifi et al. [58] using the Ni/HZSM-5 catalyst with different SiO_2/Al_2O_3 ratios. Higher HDS activity with total sulfur reduction of 88% was observed with a SiO_2/Al_2O_3 ratio of 60, and the RON increase from 52 to 94 was achieved at the ratio of 40 due to the synergistic effect of Brönsted and Lewis surface acid sites of the catalyst.

Liu et al. [28] studied the synergy of the Co promoter on the performance of the MoS_2 phase in selective FCC gasoline HDS by tuning the catalyst preparation steps. The preparation steps of cobalt and molybdenum species were regulated to adjust the proportion of Co-Mo-S, Co_9S_8, and MoS_2 phases. Initial impregnation of Co on the support was found to show better HDS activity and selectivity due to weak interaction between Co and MoS_2 phases and decreased cobalt decoration on the MoS_2 phase resulting in the formation of more Co_9S_8 phase. Hydrogen spillover effects caused by the Co_9S_8 phase improved HDS activity and selectivity through creation of more CUS and SH groups.

The role of support is very important in the activity and selectivity of HDS catalysts since the supports can change the morphology of the active phase. Change in support may result in the modulation of MSI. León et al. [70] studied NiW over Al_2O_3-TiO_2 and ZrO_2-TiO_2 mixed supports and showed their high catalytic activity for light hydrocarbons. Li et al. [60] prepared $Co/MoS_2 \pm x$ catalysts with rich defects and high stacking layers and studied for their HDS activity and hydrogenation selectivity for model gasoline. HDS selectivity was found to improve through proper control of the crystal size of CoMo sulfide crystallites.

Xu et al. [61] studied the HDS activity of nickel yttrium-based catalysts supported on single-walled carbon nanotubes and reported better HDS activity for FCC gasoline compared to monometallic catalysts owing to the small size of metal particles. Wang et al. [62] prepared $CoMoS/Al_2O_3$ catalysts with different support pore sizes and tested their performance for the hydrodesulfurization of FCC gasoline. $CoMoS/Al_2O_3$ catalysts prepared using micro- or mesoporous Al_2O_3 showed higher HDS activity and lower selectivity. Catalysts prepared using macroporous Al_2O_3 showed higher selectivity due to tuning of the MoS_2 slabs and the weakening of the internal diffusion resistance. The $CoMoS/Al_2O_3$ catalyst prepared using the support alumina with trimodal pore structure showed balanced HDS activity and selectivity compared to the reference catalyst prepared using K- and P-modified Al_2O_3.

7.2 Selection of Hydrotreating Catalysts for Heavy Feedstocks Such as Residue

Heavy feeds such as atmospheric and vacuum residue are characterized by increased contents of heteroatoms (sulfur, nitrogen, and oxygen), metals (Ni and V), and asphaltenes, and thus hydrotreating/hydrocracking of such residues require multiple catalyst systems with different functionalities used in series. HDM catalysts are used ahead of the hydrotreating/hydrocracking catalysts to remove the metals from the feed and carry out disaggregation of asphaltenes and resins. The residue hydrotreating catalysts are almost similar to those used for lighter fractions such as diesel and VGO in terms of their chemical composition. In general, heavy feedstock hydrotreating catalysts require very good hydrogenation activity to ensure better decarbonization and improved catalyst life cycle by delaying coke formation. Ni-Mo-based catalysts fare better due to their high hydrogenation activity for heavy feedstock hydrotreating. Noble metal-based hydrotreating catalysts are not used for heavy residue due to their high sulfur contents.

The physical properties (surface area, pore volume, pore size, pore size distribution) and shape of the catalysts play a crucial role in the hydrotreating of heavy residue due to the complex structure and composition of heavy molecules. The physical properties of the hydrotreating catalysts vary between light and heavy feeds. Heavy feed catalysts use smaller particles to ensure less diffusional path for the feed molecules to access the interior of the catalyst pores in order to ensure effective

utilization of the active surface. To overcome the limitations of high-pressure drop due to the utilization of smaller particles, ring-shaped or polylobe particles are used in residue HDT units to provide high surface and improved accessibility of feed molecules into the interior of the catalyst with reduced pressure drop. A chestnut-bur-type catalyst with a specific pore structure design was reported to be beneficial to increase the accessibility of feed molecules to the catalyst interiors [63].

The HDS and HDM reactivity of molecules and diffusion limitations depend on the size of the resid molecules [64]. Ancheyta et al. [65] explained various aspects of heavy petroleum feed hydroprocessing, including catalysts, in a brief tutorial. Takahashi et al. [66] prepared a HDM catalyst with low activity and used a combination of HDM and HDS catalysts with medium-pore Al_2O_3 as a support material for the HDT of atmospheric residue under deep HDS conditions to study the influence of chemical composition on the life of the HDM catalyst. Their study suggested that use of low temperature in the guard bed reactor resulted in lower coke deposition and improved catalyst life.

For residue hydroprocessing, especially for HDM, large-pore supports such as alumina are required due to the large molecules present in the residue. Stanislaus et al. [67] prepared a large-pore HDM catalyst using Al_2O_3 as a support and studied the pore enlargement mechanism through changes in the alumina phase during hydrothermal treatment of γ-alumina with and without additives. They used different additives such as phosphorous, fluorine, phenol, and acetic acid. The reason for pore enlargement was attributed to the formation and growth of boehmite into large crystallites due to rehydration of γ- Al_2O_3. Evaluation of a wide-pore NiMo/γ-Al_2O_3 catalyst showed higher activity for HDM and asphaltenes conversion during vacuum residue hydrotreating. Also, the use of wide-pore catalysts resulted in the uniform distribution of the deposited metals within the catalyst pellet compared to that of a conventional HDM catalyst. Kressmann et al. [68] and Rana et al. [69] reviewed the advances in heavy oil upgradation processes and catalysts.

8 Commercial HDT/HDS Catalysts

There are several commercial catalysts available in the market for the HDT/HDS of petroleum fractions, starting from naphtha to heavy residue. However, the catalyst market is predominantly captured by selective major catalyst manufacturing companies with a proven track record. Improved catalysts are being continuously developed and deployed by these companies based on improvements in catalyst preparation methods, addition of modifiers, improvements in supports, etc. Most of the new-generation commercial hydrotreating catalysts are made of CoMo or NiMo type supported on alumina with application for deep HDS and aromatic hydrogenation of petroleum fractions. Some catalyst suppliers also provide trimetallic catalysts of NiCoMo or NiMoW type either supported on alumina or as an unsupported bulk metal catalyst (e.g., Nebula catalyst supplied by Albemarle). In certain applications where high aromatic hydrogenation activity is required in a clean sulfur-free

environment, precious metal-type catalysts (e.g., Pt or Pd) are also used as the second-stage catalyst, especially in diesel HDT units for improvement of cetane number. Some of the catalyst suppliers who offer HDT/HDS catalysts include Haldor Topsoe, Axens (IFP), Criterion, Albemarle, Advanced Refining Technologies (ART), UOP, etc. Most of the new-generation catalysts possess very high activity for hydrodesulfurization/hydrotreating with almost 2–4 times more activity compared to earlier generation catalysts. These catalysts are manufactured using novel and proprietary methods to maximize Type II active sites to product ultralow sulfur diesel and gasoline.

9 Conclusions

Hydrotreating/hydrodesulfurization of petroleum fractions is the mainstay in the refining industry in order to produce environmentally benign fuels and lubricating oils as mandated by several countries. Improvements in the catalyst activity occurred severalfold during the last 2–3 decades due to several factors such as advanced catalyst characterization tools, improved preparation methods to increase the metal dispersion, and use of additives/modifiers during catalyst preparation in order to tune the metal–support interactions. Some of these tools and methods helped the scientists to overcome the limitations on catalyst activity and improve the stability simultaneously. Much work has also been done in understanding the other aspects of catalysis such as catalyst activation, deactivation, and regeneration/rejuvenation in order to obtain the maximum activity out of HDT/HDS catalysts. Also, it is preferable to use a proper choice of a catalyst system for a particular hydrocarbon feedstock in order to achieve optimum levels of desulfurization, denitrification, and aromatic saturation.

References

1. Scherzer J, Gruia AJ (1996) Hydrocracking science and technology. Marcel Dekker, Inc., New York, NY, p 44
2. Stanislaus A, Marafi A, Rana MS (2010) Recent advances in the science and technology of ultra low sulfur diesel (ULSD) production. Catal Today 153:1–68
3. Topsoe H, Clausen BS, Massoth FE (1996) In: Anderson JR, Boudart M (eds) Hydrotreating catalysis – science and technology, vol 11. Berlin, Springer
4. Tong-na ZHOU, Hai-liang YIN, Shu-na HAN, Yong-ming CHAI, Yun-qi LIU, Chen-guang LIU (2009) Influences of different phosphorus contents on NiMoP/Al$_2$O$_3$ hydrotreating catalysts. J Fuel Chem Technol 37(3):330–334
5. Sun M, Nicosia D, Prins R (2003) The effect of fluorine, phosphate and chelating agents on hydrotreating catalysts and catalysis. Catal Today 86:173–189

6. Ding L, Zhang Z, Zheng Y, Ring Z, Chen J (2006) Effect of fluorine and boron modification on the HDS, HDN and HDA activity of hydrotreating catalysts. Appl Catal A Gen 301:241–250

7. Saih Y, Segawa K (2009) Catalytic activity of CoMo catalysts supported on boron-modified alumina for the hydrodesulfurization of dibenzothiophene and 4,6-dimethyldibenzothiophene. Appl Catal A Gen 353:258–265

8. DeCanio EC, Weissman JG (1995) FT-IR analysis of borate- promoted Ni-Mo/Al$_2$O$_3$ hydrotreating catalysts. Colloids Surf A Physicochem Eng Asp 105:123–132

9. van Haandel L, Bremmer GM, Hensen EJM, Weber T (2017) The effect of organic additives and phosphoric acid on sulfidation and activity of (co) Mo/Al$_2$O$_3$ hydrodesulfurization catalysts. J Catal 351:95–106

10. Zepeda TA, Infantes-Molina A, Díaz de León JN, Fuentes S, Alonso-Núñez G, Torres-Otañez G, Pawelec B (2014) Hydrodesulfurization enhancement of heavy and light S-hydrocarbons on NiMo/HMS catalysts modified with Al and P. Appl Catal A Gen 484:108–121

11. Zhou W, Zhang Q, Zhou Y, Wei Q, Lin D, Ding S, Jiang S, Zhang Y (2018) Effects of Ga- and P-modified USY-based NiMoS catalysts on ultra-deep hydrodesulfurization for FCC diesels. Catal Today 305:171–181

12. Rashidi F, Sasaki T, Rashidi AM, Kharat AN, Jozani KJ (2013) Ultradeep hydrodesulfurization of diesel fuels using highly efficient nanoalumina-supported catalysts: impact of support, phosphorus, and/or boron on the structure and catalytic activity. J Catal 299:321–335

13. Nadeina KA, Kazakov MO, Danilova IG, Kovalskaya AA, Stolyarova EA, Dik PP, Gerasimov EY, Prosvirin IP, Chesalov YA, Klimov OV, Noskov AS (2019) The influence of B and P in the impregnating solution on the properties of NiMo/γ-δ-Al$_2$O$_3$ catalysts for VGO hydrotreating. Catal Today 329:2–12

14. Li Y, Zhang T, Liu D, Liu B, Lu Y, Chai Y-M, Liu C (2019) Study of the promotion effect of citric acid on the active NiMoS phase in NiMo/Al$_2$O$_3$ catalysts. Ind Eng Chem Res 58(37):17195–17206

15. Xia B, Cao L, Luo K, Liang Z, Wang X, Gao J, Xu C (2019) Effects of the active phase of CoMo/γ-Al$_2$O$_3$ catalysts modified using cerium and phosphorus on the HDS performance for FCC gasoline. Energy Fuel 33(5):4462–4473

16. Saleh TA, AL-Hammadi SA, Al-Amer AM (2019) Effect of boron on the efficiency of MoCo catalysts supported on alumina for the hydrodesulfurization of liquid fuels. Process Saf Environ Prot 121:165–174

17. Arturo Mendoza-Nieto J, Robles-Mendez F, Klimova TE (2015) Support effect on the catalytic performance of trimetallic NiMoW catalysts prepared with citric acid in HDS of dibenzothiophenes. Catal Today 250:47–59

18. Vatutina YV, Klimov OV, Stolyarova EA, Nadeina KA, Danilova IG, Chesalov YA, Gerasimov EY, Prosvirin IP, Noskov AS (2019) Influence of the phosphorus addition ways on properties of CoMo-catalysts of hydrotreating. Catal Today 329:13–23

19. Fan Y, Xiao H, Shi G, Liu H, Bao X (2011) A novel approach for modulating the morphology of supported metal nanoparticles in hydrodesulfurization catalysts. Energy Environ Sci 4:572

20. Kubota T, Hosomi N, Bando KK, Matsui T, Okamoto Y (2003) In situ fluorescence XAFS study for hydrodesulfurization catalysts. Phys Chem Chem Phys 5:4510–1515

21. Okamoto Y, Ishihara S, Kawano M, Satoh M, Kubota T (2003) Preparation of co-Mo/Al$_2$O$_3$ model sulfide catalysts for hydrodesulfurization and their application to the study of the effects of catalyst preparation. J Catal 217:12–22

22. Reinhoudt HR, Troost R, van Langeveld AD, van Veen JAR, Sie ST, Moulijn JA (2001) The nature of the active phase in sulfided NiW/γ-Al$_2$O$_3$ in relation to its catalytic performance in hydrodesulfurization reactions. J Catal 203:509–515

23. Chen W, Long X, Li M, Nie H, Li D (2017) Influence of active phase structure of CoMo/Al$_2$O$_3$ catalyst on the selectivity of hydrodesulfurization and hydrodearomatization. Catal Today 292:97–109

24. Zhang H, Lin H, Zheng Y, Hu Y, MacLenna A (2015) Understanding of the effect of synthesis temperature on the crystallization and activity of nano-MoS$_2$ catalyst. Appl Catal B Environ 165:537–546

25. Okamoto Y (2008) A novel preparation-characterization technique of hydrodesulfurization catalysts for cleaner fuels. Catal Today 132:9–17

26. Kubota T, Rinaldi N, Okumura K, Honma T, Hirayama S, Okamoto Y (2010) In situ XAFS study of the sulfidation of Co-Mo/B$_2$O$_3$/Al$_2$O$_3$ hydrodesulfurization catalysts prepared by using citric acid as a chelating agent. Appl Catal A Gen 373:214–221

27. Liu H, Yin C, Li X, Chai Y, Li Y, Liu C (2017) Effect of NiMo phases on the hydrodesulfuriza-tion activities of dibenzothiophene. Catal Today 282:222–229

28. Liu B, Liu L, Wang Z, Chai Y, Liu H, Yin C, Liu C (2017) Effect of hydrogen spillover in selec-tive hydrodesulfurization of FCC gasoline over the CoMo catalyst. Catal Today 282:214–221

29. Wang X-l, Zhao Z, Chen Z-t, Li J-m, Duan A-j, Xu C-m, Gao D-w, Cao Z-k, Zheng P, Fan J-y (2017) Effect of synthesis temperature on structure-activity-relationship over NiMo/γ--Al$_2$O$_3$ catalysts for the hydrodesulfurization of DBT and 4,6-DMDBT. Fuel Process Technol 161:52–61

30. Wang X, Zhao Z, Zheng P, Chen Z, Duan A, Xu C, Jiao J, Zhang H, Cao Z, Ge B (2016) Synthesis of NiMo catalysts supported on mesoporous Al$_2$O$_3$ with different crystal forms and superior catalytic performance for the hydrodesulfurization of dibenzothiophene and 4,6-dimethyldibenzothiophene. J Catal 344:680–691

31. Braggio FA, de Mello MD, Magalhaes BC, Zotin JL, Silva MAP (2019) Effects of citric acid addition method on the activity of NiMo/γ-Al$_2$O$_3$ catalysts in simultaneous hydrodesulfuriza-tion and hydrodenitrogenation reactions. Energy Fuel 33:1450–1457

32. Singh R, Kunzru D, Sivakumar S (2016) Monodispersed ultrasmall NiMo metal oxide nano-clusters as hydrodesulfurization catalyst. Appl Catal B Environ 185:163–173

33. Liu H, Li Y, Yin C, Wu Y, Chai Y, Dong D, Li X, Liu C (2016) One-pot synthesis of ordered mesoporous NiMo-Al$_2$O$_3$ catalysts for dibenzothiophene hydrodesulfurization. Appl Catal B Environ 198:493–507

34. Dong Y, Yu X, Zhou Y, Xu Y, Lian X, Yi X, Fang W (2018) Towards active macro–mesoporous hydrotreating catalysts: synthesis and assembly of mesoporous alumina microspheres. Cat Sci Technol 8:1892

35. Cheche UA, Alhooshani KR, Adamu S, Thagfi JA, Saleh TA (2019) The effect of calcination temperature on the activity of hydrodesulphurization catalysts supported on mesoporous acti-vated carbon. J Clean Prod 211:1567–1575

36. Xu J, Huang T, Yu F (2017) Highly efficient NiMo/SiO$_2$-Al$_2$O$_3$ hydrodesulfurization catalyst prepared from gemini surfactant-dispersed Mo precursor. Appl Catal B Environ 203:839–850

37. Huang T, He S, Chang J, Xu J, Yu F (2019) Preparation of a superior Co$_4$Mo$_{12}$/Al$_2$O$_3$ hydrode-sulfurization catalyst by the hydrothermal deposition of heteropoly compounds on Al$_2$O$_3$. Catal Commun 122:68–72

38. Cabello CI, Cabrerizo FM, Alvarez A, Thomas HJ (2002) Decamolybdodicobaltate(III) het-eropolyanion: structural, spectroscopical, thermal and hydrotreating catalytic properties. J Mol Catal A Chem 186:89–100

39. Hensen EJM, Kooyman PJ, van der Meer Y, van der Kraan AM, de Beer VHJ, van Veen JAR, van Santen RA (2001) The relation between morphology and hydrotreating activity for sup-ported MoS$_2$ particles. J Catal 199:224–235

40. Bhan OK (2006) High activity hydrodesulfurization catalyst, a method of making a high activ-ity hydrodesulfurization catalyst, and a process for manufacturing an ultra-low sulfur distillate product, US Patent No. 20060060510A1

41. Wu J, Ellis ES, Sokolovskii V, Lowe DM, Volpe Jr. AF (2015) Selective catalysts having high temperature alumina supports for naphtha hydrodesulfurization, US Patent No.: US 9,175,232 B2

42. Soled SL, Miseo S, Baumgartner JE, Nistor I, Nandi P, Guzman J, Levin D, Wilson S, Bergweff JA, Huiberts RJ, Van Loevezijn A (2018) Hydroprocessing catalysts and their production, Patent No. US 10,022,712 B2
43. Roberts CD (2008) Improve sulfiding of hydroprocessing catalysts. Hydrocarb Process 2008:133–135
44. van Haandel L, Bremmer GM, Hensen EJM, Weber T (2016) Influence of sulfiding agent and pressure on structure and performance of CoMo/Al$_2$O$_3$ hydrodesulfurization catalysts. J Catal 342:27–39
45. Liu B, Liu L, Chai Y, Zhao J, Li Y, Liu D, Liu Y, Liu C (2018) Effect of sulfiding conditions on the hydrodesulfurization performance of the ex-situ presulfided CoMoS/γ-Al$_2$O$_3$ catalysts. Fuel 234:1144–1153
46. Furimsky E, Massoth FE (1999) Deactivation of hydroprocessing catalysts. Catal Today 52(4):381–495
47. Zhang H, Lin H, Zheng Y (2019) Deactivation mechanism study of unsupported nano MoS$_2$ catalyst. Carbon Resour Convers:3, 60. https://doi.org/10.1016/j.crcon.2019.09.003
48. Zhang C, Liu X, Liu T, Jiang Z, Li C (2019) Optimizing both the CoMo/Al$_2$O$_3$ catalyst and the technology for selectivity enhancement in the hydrodesulfurization of FCC gasoline. Appl Catal A Gen 575:187–197
49. Marafi M, Al-Omani S, Al-Sheeha H, Stanislaus A (2007) Utilization of metal-fouled spent residue hydroprocessing catalyst in the preparation of an active HDM catalyst. Ind Eng Chem Res 46:1968–1974
50. Kallinikos LE, Bellos GD, Papayannakos NG (2008) Study of the catalyst deactivation in an industrial gasoil HDS reactor using a mini-scale laboratory reactor. Fuel 87:2444–2449
51. Pimerzin A, Roganov A, Mozhaev A, Maslakov K, Nikulshin P, Pimerzin A (2018) Active phase transformation in industrial CoMo/Al$_2$O$_3$ hydrotreating catalyst during its deactivation and rejuvenation with organic chemicals treatment. Fuel Process Technol 173:56–65
52. Bui N-Q, Geantet C, Berhault G (2015) Maleic acid, an efficient additive for the activation of regenerated CoMo/Al$_2$O$_3$ hydrotreating catalysts. J Catal 330:374–386
53. Santolalla-Vargas CE, Santes V, Sanchez-Minero F, Issis R-I, Goiz O, Lartundo-Rojas L, Diaz L, Luna-Ramirez R, Vald'es OU, de los Reyes JA, G'omez E (2019) In situ reactivation of spent NiMoP/γ-Al$_2$O$_3$ catalyst for hydrodesulfurization of straight-run gas oil. Catal Today 329:44–52
54. Iwamoto R (2013) Regeneration of residue hydrodesulfurization catalyst. J Jpn Petrol Inst 56(3):109–121
55. Klimov OV, Nadeina KA, Dik PP, Koryakina GI, Pereyma VY, Kazakov MO, Budukva SV, Gerasimov EY, Prosvirin IP, Kochubey DI, Noskov AS (2016) CoNiMo/Al$_2$O$_3$ catalysts for deep hydrotreatment of vacuum gasoil. Catal Today 271:56–63
56. Guo R, Cao Z, Fang X (2018) The development of catalysts and their stacking technology for diesel ultra-deep hydrosulfurization. Catal Today 316:21–25
57. Sharifi K, Halladj R, Royaee SJ, Nasr MRJ (2018) Synthesis of W/HZSM-5 catalyst for simultaneous octane enhancement desulfurization process of gasoline production. Powder Technol 338:638–644
58. Sharifi K, Halladj R, Royaee SJ, Nasr MRJ (2018) A new approach for gasoline upgrading: coupling octane enhancement and desulfurization of heavy straight-run naphtha over Ni/HZSM-5 catalyst. Catal Commun 115:31–35
59. Bin L, Lei L, Yong-ming C, Jin-chong Z, Chen-guang L (2018) Essential role of promoter co on the MoS2 catalyst in selective hydrodesulfurization of FCC gasoline. J Fuel Chem Technol 46(4):441–450
60. Li P, Liu X, Zhang C, Chen Y, Huang B, Liu T, Jiang Z, Li C (2016) Selective hydrodesulfurization of gasoline on co/MoS$_{2 \pm x}$ catalyst: effect of sulfur defects in MoS$_{2 \pm x}$. Appl Catal A Gen 524:66–76

61. Xu K, Li Y, Xu X, Zhou C, Liu Z, Yang F, Zhang L, Wang G, Gao J, Xu C (2015) Single-walled carbon nanotubes supported Ni–Y as catalyst for ultra-deep hydrodesulfurization of gasoline and diesel. Fuel 160:291–296
62. Wang T, Li J, Yi S, Wang C, Gao Y, Chou L, Yao W (2015) The tuning of pore structures and acidity for Zn/Al layered double hydroxides: the application on selective hydrodesulfurization for FCC gasoline. J Energy Chem 24:432–440
63. Le Page JF, Chatila SG, Davidson M (1992) Resid and heavy oil processing. Editions Technip, Paris
64. Ferreira C, Tayakout-Fayolle M, Guibard I, Lemos F, Toulhoat H, Ramôa Ribeiro F (2012) Hydrodesulfurization and hydrodemetallization of different origin vacuum residues: characterization and reactivity. Fuel 98:218–228
65. Ancheyta J, Rana MS, Furimsky E (2005) Hydroprocessing of heavy petroleum feeds: tutorial. Catal Today 109 (1–4:3–15
66. Takahashi T, Higashi H, Kai T (2005) Development of a new hydrodemetallization catalyst for deep desulfurization of atmospheric residue and the effect of reaction temperature on catalyst deactivation. Catal Today 104(1):76–85
67. Stanislaus A, Al-Dolama K, Absi-Halabi M (2002) Preparation of a large pore alumina-based HDM catalyst by hydrothermal treatment and studies on pore enlargement mechanism. J Mol Catal A Chem 181:33–39
68. Kressmann S, Morel F, Harle V, Kasztelan S (1998) Recent developments in fixed-bed catalytic residue upgrading. Catal Today 43:203–215
69. Rana MS, Sámano V, Jorge A, Diaz JAI (2007) A review of recent advances on process technologies for upgrading of heavy oils and residua. Fuel 86:1216–1231
70. Díaz de León JN, Zavala-Sánchez LA, Suárez-Toriello VA, Alonso-Núñez G, Zepeda TA, Yocupicio RI, de los Reyes JA, Fuentes S (2017) Support effects of NiW catalysts for highly selective sulfur removal from light hydrocarbons. Appl Catal B Environ 213:167–176

Recent Developments in FCC Process and Catalysts

Ajay R. Khande, Prabha K. Dasila, Supriyo Majumder, Pintu Maity, and Chiranjeevi Thota

Abstract Fluid catalytic cracking (FCC) is the major conversion process used in oil refineries to produce valuable hydrocarbons from crude oil fractions. The demand for oil-based products is ever increasing, and research has been ongoing to improve the performance of FCC catalysts, which are complex mixtures of zeolite, matrix, clay, and binder materials. In this chapter, an overview of the basic understanding of the FCC process, catalysts, and the latest developments in this research area is given. Developments discussed also include approaches for processing very heavy or very light crude oil fractions. Furthermore, these developments enable refiners to process complex feedstocks and increase yields of propylene, olefins, and gasoline/diesel-range fuels. The current chapter also contains a brief history of FCC as well as details of the process, chemical reactions involved, catalyst materials, and recent developments in FCC catalysis research.

Keywords Fluid catalytic cracking · Zeolite · Crude oil · Catalytic materials

1 Introduction

The fluid catalytic cracker (FCC) is one of the most integral conversion processes in a modern petroleum refinery. Colloquially known as the workhorse of the refinery, it converts low-value vacuum distillates into high octane gasoline and LPG by cracking heavier hydrocarbon molecules in the presence of a fluidized bed of particulate catalyst. Other conversion processes include the hydrocracker, which is usually intended for diesel maximization and delayed coker units, which convert residue to valuable products. The total installed capacity for FCC units worldwide was around 14.4 million barrels per day [1]. It processes about a third of the total refinery's throughput and contributes the majority of the world's gasoline demand [2]. Out of the total 700 refineries

A. R. Khande · P. K. Dasila · S. Majumder · P. Maity · C. Thota (✉)
Corporate R&D Centre, Bharat Petroleum Corporation Ltd,
Greater Noida, Uttar Pradesh, India
e-mail: ajayrajukhande@bharatpetroleum.in; prabhakiran@bharatpetroleum.in;
supriyomajumder@bharatpetroleum.in; pmaity@bharatpetroleum.in; chiranjeevit@
bharatpetroleum.in

worldwide, around 500 of them have FCC units commissioned in their setup [3]. Some of the major licensors of FCC technology are Kellogg Brown & Root, CB&I Lummus, ExxonMobil Research and Engineering, Shell Global Solutions International, Stone & Webster Engineering Corporation, Institut Francais du Petrole (IFP), and Universal Oil Products [4–10]. All these licensors have their unique configurations and advantages, but the core principle remains the same. The yield of gasoline is heavily dependent on the morphology of the FCC catalyst. Refiners maximize their margins by optimizing the FCC unit's operating parameters and work in conjunction with catalyst manufacturers to optimize catalyst formulations. The FCC units are flexible in terms of hydrocarbon feed, required yields of gasoline or LPG, and compliance with environmental regulations.

Although the FCC technology is over 79 years old, new and upcoming refining trends keep the field engaging for academia and industries around the world. New sources of hydrocarbon feeds like shale oil and tight oil, novel and customizable catalysts, mining of heavier crude oil yielding more residue, alternate energy, and shift of product demand toward petrochemicals are some trends that keep FCC technology front and center when it comes to innovation in conversion technologies. The demand for automotive gasoline is predicted to decline in the next 30 years due to the rise of more sustainable energy sources. However, the demand for petrochemicals and polymers, in particular, continues to skyrocket as there is a continuous gap in the market for the supply of light olefinic hydrocarbons, which are required to synthesize these petrochemicals [11]. Steam cracking of light hydrocarbon streams has traditionally been the main source of such light olefins [12]. However, the existing capacity worldwide is unable to satisfy the increasing demand. FCC units are now being designed to work at higher severity to maximize yields of light olefins and work in conjunction as a petrochemical complex in an attempt to placate the demand for petrochemical feedstock and still keep oil refinery's margins viable in a possible scenario when automotive fuels have been completely substituted by superior and sustainable sources of energy [13].

2   Fluid Catalytic Cracker

Fluid catalytic cracking (FCC) is one of the most flexible and profitable secondary processes in an oil refinery. FCC converts low-value distillates and residues into cleaner and premium hydrocarbon products such as liquefied petroleum gas (LPG), gasoline. The yields of these sought-after products strongly depend upon the source of feedstock, operating conditions of the unit, and, most importantly, the type of catalyst. FCC technology is very complex due to intricate hydrodynamics, heat transfer and mass transfer effects, and complex cracking kinetics, which are still not understood perfectly. These complex interactions coupled with the economic importance of the unit have motivated many research efforts on catalyst development, additive development, modeling, and optimization of FCC processes.

FCC units operate at elevated temperatures and near atmospheric pressure. The catalyst is a finely divided silica/alumina-based particulate mixture. This catalyst, when fluidized with steam, flows similar to a fluid inside the unit. Any FCC can be

broadly divided into three sections on the basis of operation: the riser–reactor, the regenerator, and the fractionator. The cracking and separation of catalyst and product occur in the riser–reactor section. Carbon generated during cracking reactions gets deposited on the catalyst surface, and cracking activity progressively decreases. At the exit of the reactor, the catalyst is separated from the reaction mass by cyclones, and the spent catalyst is sent to the regenerator. In the regenerator, the catalyst is continuously regenerated by burning off the coke using air. In the fractionator, the cracked gasses are fractionated into liquid and gaseous product streams. Other auxiliary units such as feed preheater, air, and flue gas systems are required for control and optimal operation of this unit for regenerating the catalyst.

3   History of the FCC Process

Internal combustion engines provide outstanding reliability and durability, with more than 250 million highway vehicles in the country relying on it. Along with gasoline or diesel, they can also utilize renewable or alternative fuels (e.g., natural gas, propane, biodiesel, or ethanol) [14]. Initially, the motor gasoline used in these primitive automobiles was mostly derived from straight-run products of crude distillation at atmospheric pressure. The typical yield of gasoline from such distillation was around 20 vol.%. The increasing demand and low yield of gasoline by conventional distillation paved the way for the advent of thermal cracking. William Burton of Standard Oil Company Indiana commercialized the first thermal cracking process in 1913 [15, 16]. This process involved destructive distillation of crude under pressure. Subsequently, many other competitive designs were developed. The Dubbs process [17] licensed by Universal Oil Products Co. (UOP) was one of the most popular ones. It was also founded by T.Ogden Armour in the same year. In this process, a light crude was continuously cracked in furnace tubes along with simultaneous removal of residue from the system. The gasoline yield placated the rapidly increasing demand for gasoline; however, this gasoline was of relatively poorer quality. It caused premature combustion or "knocking," which would damage the cylinders of the automobile engines. Additives like tetra ethyl lead were discovered in 1920 that would improve the ignition quality of the gasoline. However, high olefinicity led to stability issues and gum deposits [26]. During this period, the invention of octane engine created a direct correlation between gasoline composition and its performance.

The inherent limitations of thermal cracking and a French engineer named Eugene Houdry's long-standing fascination with racing cars led to the discovery of catalytic cracking, now known as the Houdry process (Fig. 1), [18, 19] which he developed in association with the Socony-Vacuum Oil Co (now Mobil). This process made use of a fixed bed reactor with two large motor-operated valves that switched between vessels. The first commercialized Houdry process went on stream in 1937 at Sun Oil's refinery. Initially, the catalyst used was activated clay, which was subsequently replaced by synthetic silica–alumina. This process developed
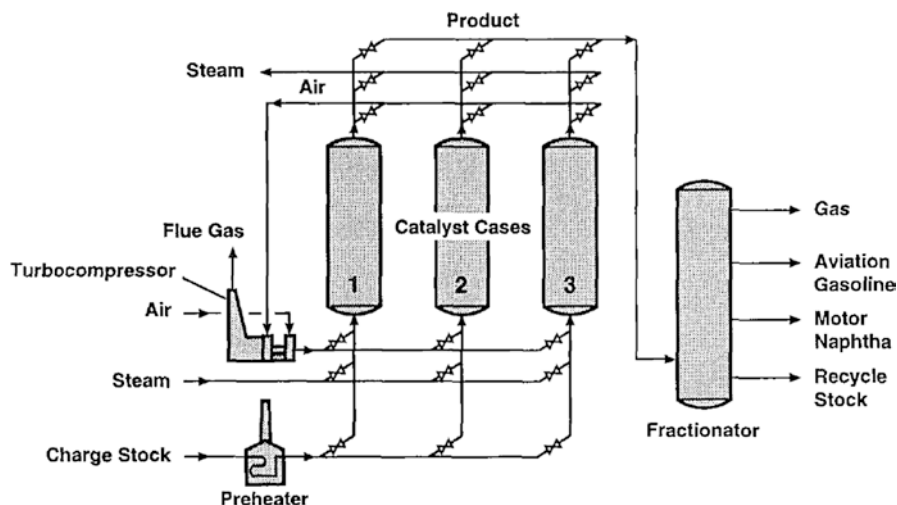
Fig. 1 Houdry's catalytic cracking process [26]

high-quality aviation fuel during the Second World War. Since the process utilized a fixed bed reactor, the catalyst gradually deactivated and the gasoline yields would continuously drop before regeneration of catalyst would be carried out.

This meant the process operated in a semicontinuous cyclic operation. A step toward a truly continuous process was replacing the old valve switching mechanism that alternated feed and combustion air for regeneration with a bucket lift mechanism to move the catalyst itself from the reaction to regeneration zones (Fig. 2). As the catalyst's particle size was further reduced by the development of synthetic beads, the bucket system was soon replaced by an air-lift system. This process was called the thermofor catalytic cracking (TCC) process [20].

This process was replaced by the FCC process because of the higher catalyst to oil ratio and higher achievable regenerator temperatures. Due to licensing disputes with Houdry, Standard Oil (Jersey) formed a consortium of eight companies dubbed the Catalytic Research Associates (CRA: Jersey), M.W. Kellogg Co., Royal Dutch Shell, the Standard Oil Co. of Indiana, Anglo-Iranian Oil Co. (now known as BP), Universal Oil Products Co. (now known as UOP), the Texas Corp. (which became Texaco), and IG Farben, which would develop a process that would design a process different from Houdry's patent. Work in fluidization and pneumatic transfer of solids in Massachusetts Institute of Technology (MIT) coupled with CRA's efforts led to commissioning of a pilot plant PECLA-1 (Powdered Experimental catalyst Louisiana). A year later in 1942, the system (now called PCLA1, Fig. 3) was scaled up to commercial scale and started up [21, 22]. It was an up-flow reactor–regenerator setup, which used a clay-based catalyst. It was based on the principle that a dense bed of particles can be suspended at a low gas velocity in a manner to lift it up to behave similar to a liquid [23]. Better diffusion characteristics, the higher
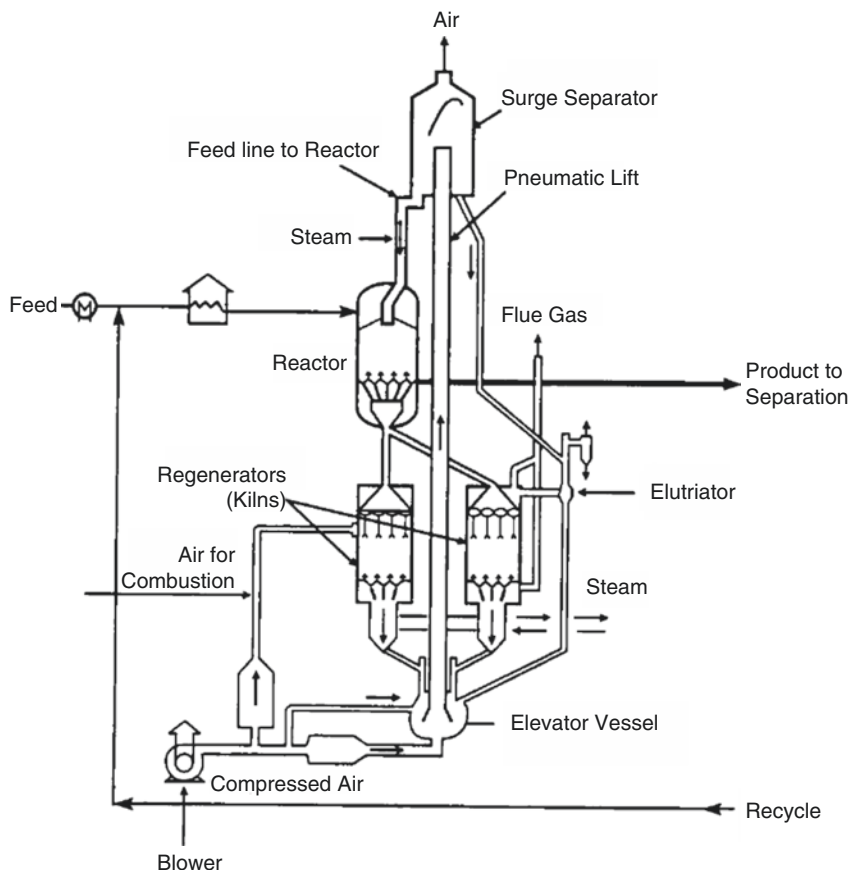
Fig. 2 Thermofor catalytic cracking (TCC) process [26]

catalyst to oil ratio, higher regeneration temperature, heat balance, and continuous operation are a few of the many features of this plant.

Post the successful start-up of PCLA [14], there was rapid development in FCC unit designs. The new designs differed in reactor–regenerator configurations, number and placement of cyclones, number and placement of feed nozzles, parallel operation, recycle, catalyst coolers, etc.

The primitive catalytic cracking processes utilized activated clay-based catalysts. This was followed by the use of synthetic amorphous silica–alumina- or silica–magnesia-based combinations during the 1940s. These catalysts showed better selectivity toward gasoline compared to coke and gas [27]. The next major milestone during the 1960s was the development of synthetic crystalline microporous aluminosilicates called zeolites (roughly translates to boiling stone) at Union Carbide and Mobil Oil Co. The zeolite relevant to the FCC process was synthetic faujasite or zeolite Y developed by Breck [24] at Union Carbide. Zeolite Y has high
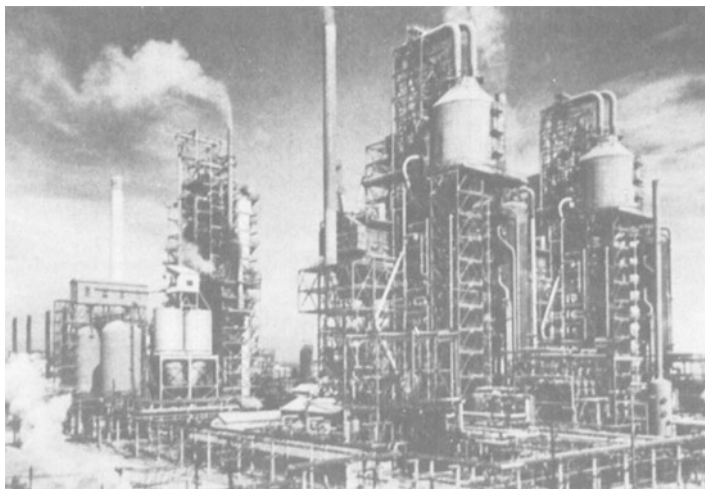
Fig. 3 PCLA-1 (left) and PCLA-2 (middle and right) [26]. Photo credit: Roskam Esso

surface area, pore volume, and acidity to selectively crack heavier hydrocarbons into gasoline range molecules. Zeolite catalyst was first commercially manufactured by Grace Davison and Filtrol. Zeolite structure inherently is not stable in the high steam partial pressure environment of an FCC unit [28]. Its stability was improved by dealuminating the zeolite by consecutive steaming, washing, and leaching cycles. This dealuminated zeolite was called ultra-stable Y or simply US-Y. Another widely practiced method studied in the 1980s is to improve the zeolite's stability by ion exchange of aluminum counter-ions with rare-earth ions. Such ion-exchanged zeolites are called RE-Y (Fig. 4). These stabilized zeolites, however, reduced gasoline octane by catalyzing bimolecular hydrogen transfer reactions [29].

This new generation of catalysts led to fundamental alterations to the design and operation of FCC units. Since they had high selectivity and activity, it was observed that at the existing contact time in FCC reactors, a copious amount of coke was formed, which caused lower yield and heat balance issues. This led to the conclusion that much shorter residence time was required to maintain the selectivity toward desired products. Hence, fluidized bed cracking was substituted by riser cracking. Any and all configurations post-1964 incorporated the riser cracking design (Fig. 5).

Further developments in this field were motivated by either a desire to upgrade resid feed in the FCC or to maximize propylene yield for petrochemical manufacture. Design improvements on the conventional FCC design were made to incorporate the high coke yielding resid feed, the higher catalyst to oil ratio required, higher capacity of the wet gas compressor, better metallurgy, efficient cyclones, better feed nozzles, catalyst cooling, etc. Technologies such as deep catalytic cracking (DCC), petro FCC, resid FCC, etc. emerged. A catalyst that can withstand the high concentration of metal impurities in resid feed was developed. A new zeolite with
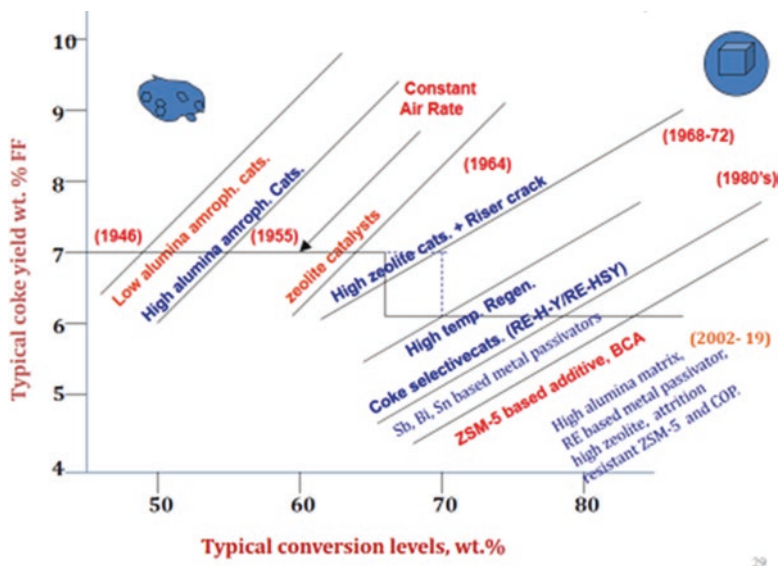
Fig. 4 Evolution of modern FCC catalyst [89]
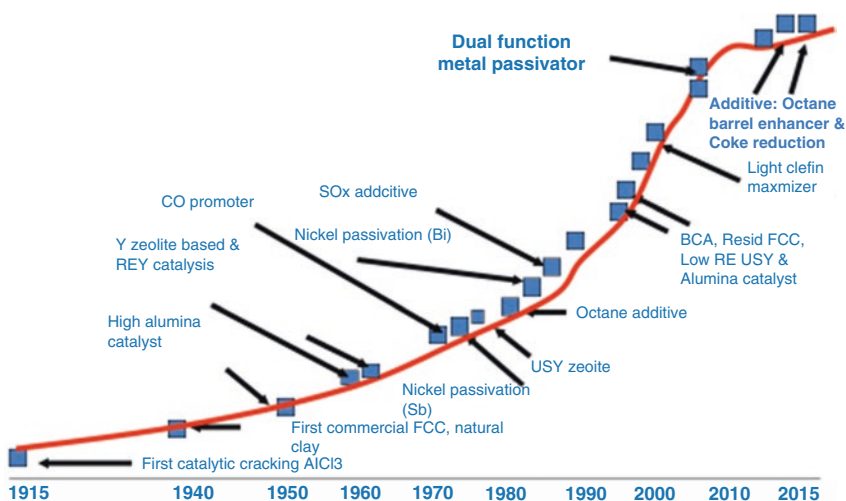
Fig. 5 Evolution of FCC catalyst additives [90]

widespread applications was developed by Argauer and Landolt [25] at Mobil Oil Co. called ZSM-5. It was a microporous zeolite that selectively crack heavier ole-finic hydrocarbons to increase the yield of propylene for petrochemical manufacture purposes and alkylate yield to improve gasoline octane. ZSM-5 is widely used by refiners to offset the LPG yield loss and octane loss caused by using US-Y or RE-Y.

4 The FCC Process

Fluid catalytic cracking (FCC) is a secondary refining process for conversion of heavy gas oils into valuable hydrocarbon products such as LPG, gasoline, and distillate fuel oil. The FCC process is divided into four sections, as shown in Fig. 6. In the reactor section, feed is injected into the riser where cracking reactions occur in the presence of a hot catalyst. The separation of hydrocarbons from the spent catalyst occurs in the reactor, which acts as a disengaging vessel. In the regenerator section, controlled combustion is used to remove the coke formed on the catalyst. FCC units operate at high temperature and moderate pressure with a finely divided silica/alumina-based catalyst. After separation of the catalyst, the hydrocarbons are separated into the desired products in the main fractionator. The heat liberated during the combustion of coke supplies the heat required to vaporize the atomized and preheated feedstock and also the heat of reaction. The heat energy possessed by the flue gas escaping the regenerator is utilized in the power recovery section. FCC gasoline historically has been the principal blend component for motor spirit pool. Light cycle oil (LCO) is a diesel boiling range material and can be used as a diesel blend component after hydrotreating. Heavier cuts such as heavy cycle oil (HCO) and clarified oils (CLO) are either recycled or used as fuel oil blend components and are excellent cutter stock for vacuum resid. The olefinic LPG produced in the FCC process can be used in downstream alkylation and polymerization processes to yield more gasoline.

A standout feature of FCC is the free flow of catalyst within the system along with the reaction mixture in the vapor phase. Due to this fluidization, there is efficient contact between the catalyst and hydrocarbons, leading to better selectivity and reduced thermal cracking.
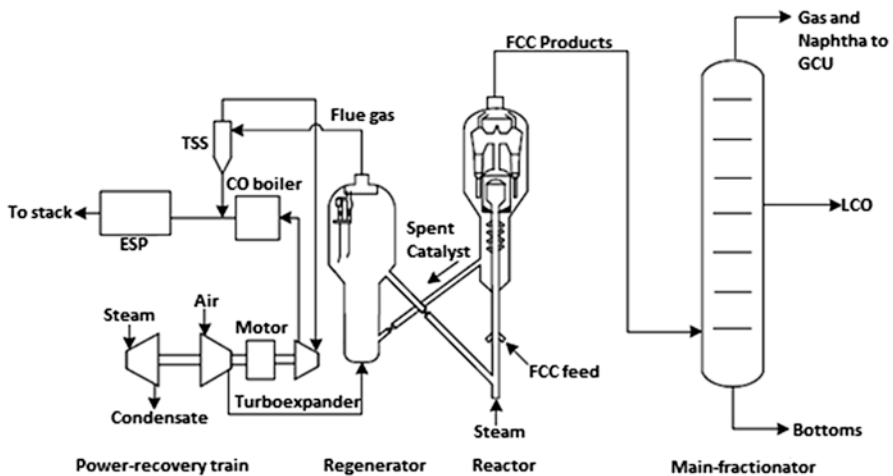
Fig. 6 Diagram of a conventional FCC unit [34]
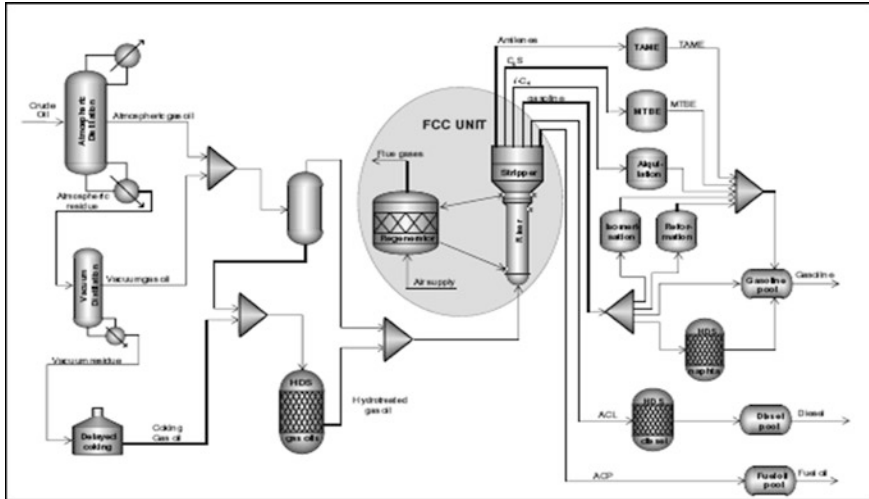
Fig. 7 Location of the FCC unit in the refinery [33]

FCC unit is the heart of a refinery (Fig. 7) because of its physical position, size, and economic impact, and the most important is its flexibility for a different mode of operations. FCC units are preceded by basic separation processes such as atmospheric and vacuum distillation units; catalytic reacting processes such as hydrotreatment; and minor additional units, pumps, stabilization towers, and so on. Downstream, FCC units supply products mainly to the gasoline pool, but also to other units that require light hydrocarbons. Finally, when there is a high level of sulfur in the gasoline, FCC units supply feedstock for hydrodesulphurization processes.

FCC process can operate in three modes of operations [33]. The first mode is primarily to make gasoline, in a second mode primarily making diesel, and in a third mode to make primarily LPG/propylene. Table 1 shows the general operating conditions and yields from a different mode of operations. Gasoline, diesel, and LPG are produced in all three modes, but each mode maximizes the primary product intended.

The FCC process involves a number of steps to get the final product starting from feed selection and pretreatment to product purification. All these are discussed in subsequent paragraphs.

4.1 Feed Selection and Pretreatment

Since the 1970s, the primary feedstock for catalytic cracking has been vacuum distillate known as gas oil (VGO). Most refineries can produce enough VGO for their FCC units. Depending on the market demands for fuel oils, visbreaking or coker distillate, as well as deasphalted oil, can also be used to supplement the feed. In

Table 1 Different modes of FCC units

Operating conditions	LPG mode	Gasoline model	Distillate mode
Riser top temp., °C	550–570	500–527	490–500
Riser contact time, s	2	4	2
Catalyst MAT activity	75	75	60
Cat/oil ratio	10–15	6–7	4.5
Dense temp., °C	770–700	728	642
CRC, wt%	0.05	0.05	0.5
Product yields, wt%			
Dry gas	6.5	4	2
LPG	40	18	10
Gasoline (C_5–150 °C)	25	41	30
TCO (150–370 °C)	10	26	44
CLO (370 °C+)	4	6	10
Coke	6.5	5	4
216 °C—conversion	90	81	50

some cases, a portion of the straight-run gas oil was included in the catalytic cracker feed [30].

The hydrocarbons injected into the FCC as feedstock come from a vacuum distillation tower and boil in the gas oil range of 350–550 °C+. FCC is flexible enough to process gas oils from other secondary units such as delayed coker and hydrocracker. The feed is preheated to 260–370 °C. The FCC products drawn off from a fractionator are generally used to heat this [31]. The degree of preheat can influence the reactor temperature and catalyst circulation, thereby affecting product yields to some extent.

The main feedstocks for FCC units are as follows:

- Straight-run feedstocks.

    – Flashed distillate (~370–580 °C) from high vacuum units.
    – Short residue from high vacuum units.
    – Light long residue (~370+) from crude distillation units.

- Hydrogenated feedstocks.

    – Hydrotreated flashed distillate.
    – Hydrowax from hydrocracker bottom.
    – Hydrogenated cycle oils.

- Miscellaneous.

    – Heavy gas oil.
    – Coker gas oil.

Besides the above-mentioned sources of hydrocarbon feedstock, refiners often recycle some portion of the streams from the fractionator. These streams like heavy cycle oil (HCO) and clarified oil (CLO) are heavy and aromatic rich mixtures,

Table 2 Properties of different VGOs derived from variety of crudes [34]

FCC feeds	Bakken	Eagle Ford	Maya Blend	WTI
API gravity, ⁰API	24.5	31.9	21.0	26.3
Sulfur, wt%	0.27	0.18	2.05	0.46
Nitrogen, wt%	0.11	0.01	0.18	0.13
Acidity, mg KOH/g	0.053	0.049	0.085	0.095
Refractive index, 67 °C	1.4824	1.4588	1.4980	1.4759
Nickel, ppm	0.47	0.09	0.64	0
Vanadium, ppm	0.14	0.08	4.48	0
CCR, wt%	0.68	0.03	0.47	0.01

which can be further cracked in the FCC. The remaining portion is blended and sold as fuel oil.

FCC can process hydrocarbons having a wide tolerance of density, volatility, and contaminants. Properties of a feed crackable in FCC are shown in Table 2. Contaminants such as mercaptans, sulfides, basic and neutral nitrogen, and trace metals, such as nickel, vanadium, sodium, iron, and calcium, affect the product yield and its specification. The catalyst consumption of the unit also increases due to permanent poisoning. Most of the lighter crackable feed sulfur ends up in the gasoline and LPG. Nitrogen compounds temporarily affect the acidity of the catalyst, resulting in lower conversion levels and NO_x emissions. However, metallic impurities cause the most problems. Their effects on the cracking catalyst are quite detrimental. Nickel increases the coke and gas yield, while vanadium destroys the zeolite microstructure.

4.2 Reactor–Stripper–Regenerator Section

Post the advent of riser cracking, in modern FCC units, virtually all the reactions occur within 1.5–3.0 s over the catalyst's surface [31], and the products are separated in the reactor in which the catalyst and vapors are disengaged using cyclones. The preheated atomized feed enters the riser near the base through multiple nozzles, where it mixes with the hot regenerated catalyst (Fig. 8). The catalyst to oil weight ratio is typically in the range of 4:1–9:1. The heat absorbed by the catalyst in the regenerator provides the heat required to vaporize the atomized feed and the necessary energy for the endothermic reactions. The typical regenerated catalyst temperature is in the range of 677–732 °C [31].

As the heavy hydrocarbon molecules of the feed crack into several smaller hydrocarbon molecules, the volume of the catalyst–vapour mixture expands and moves up the riser. Efficient vaporization of feed in the entry zone of the riser/reactor heavily affects the cracking performance of the feed. The rate of cracking and yield of products are controlled by the riser temperature and amount of catalyst. The
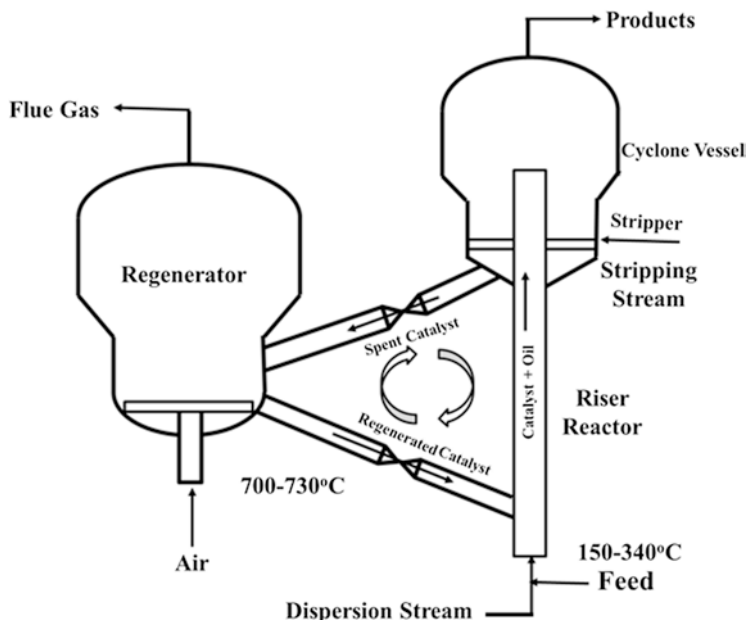
Fig. 8 Schematic of riser–reactor–regenerator [34]

cracking process gradually retards along the riser due to the reduction in activity caused by the inevitable deposition of coke on the catalyst surface.

The spent catalyst falls down the cyclone diplegs into the stripper. In the stripper, high-pressure steam displaces the remaining hydrocarbons adsorbed on the catalyst's surface. An efficient catalyst stripper design provides intimate contact between the catalyst and steam. It is important to minimize the amount of hydrocarbon vapors carried over to the regenerator, but not all the hydrocarbon vapors can be displaced from the catalyst pores in the stripper. A fraction of them is carried with the spent catalyst into the regenerator. Improper stripping can cause high regenerator temperatures and high hydrogen content on coke. The stripped catalyst enters the regenerator through the spent catalyst standpipe (SCSP). The flow of the catalyst to the regenerator is controlled by the spent catalyst slide valve (SCSV). The opening of the valve depends upon the level of the catalyst in the stripper.

The catalyst entering the regenerator contains 0.5–1.5 wt% coke. This coke blocks the pores and active sites on the catalyst. In the regenerator, heated air is used to fluidize the catalyst and burn off this coke and regenerate the catalyst. The combustion of coke provides the heat energy required to crack heavy hydrocarbons in the riser. This combustion can be partial or complete, i.e., excess air supplied. There are cyclones to separate the catalyst from the resulting flue gasses; the catalyst trickles down the diplegs into the regenerated catalyst standpipe (RCSP), whereas the flue gas escapes from the top of the regenerator. The flow of the catalyst in the RCSP

is controlled by the regenerated catalyst slide valve (RCSV), and the opening of this valve is dependent on the reactor temperature.

4.3 Catalyst Separation

The catalyst along with the gaseous product stream after exiting the riser enters into the reactor vessel. In modern FCC operations, the reactor serves as a housing for the cyclones. In the early application of FCC, the reactor vessel provided further bed cracking, as well as being a device used for additional catalyst separation. There are cyclones in the regenerator as well. These schemes separate approximately 75–99% of the catalyst from product vapors [31]. Most cyclone systems operate in two stages. The combined separation efficiency observed is about 99%. The primary cyclone doubles as a riser termination device and the primary separator, which separates up to 97% of the catalyst. The dipleg of this cyclone is generally immersed in the catalyst bed. The secondary cyclone separates the remaining catalyst, and the hydrocarbon vapors escape to the plenum chamber (Fig. 9).

4.4 Main Fractionation of Products and Gas Recovery

The product vapor exiting the riser is de-superheated and separated in the main fractionator. The vapors enter the fractionator from the bottom in which they are condensed and vaporized to achieve the required separation. The reactor vapor is de-superheated and cooled by several pump around streams. The cooled pump
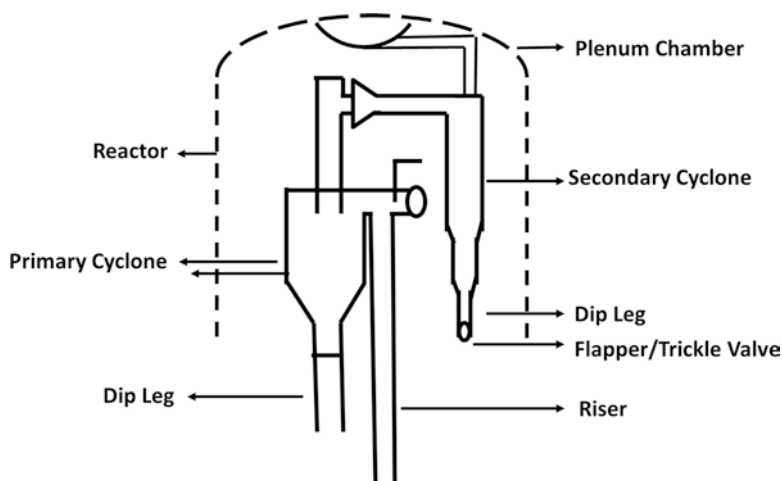
Fig. 9 Two-stage cyclones [34]

around the stream also serves as a scrubbing medium to wash down catalyst fines entrained in the vapors.

The bottom product of the fractionation is called slurry oil or clarified oil (CLO) or decant oil (DO). This product was used as a cutter stock to make fuel oil, but that is being discontinued. CLO contains the entrained catalyst particles (expressed as ash content wt%), which had escaped the reactor. Hence, CLO is stored in a settler, and a slip stream is recycled back to the riser. The HCO is a product obtained from a side draw above the CLO. Heavy cycle oil (HCO) is generally used as a pump around for the main fractionator or recycled to the riser. Light cycle oil (LCO) is a side draw, which is actually used as a product. It is added to the diesel pool post hydrotreatment or can be used as a pump around the stream. The heavy naphtha side draw is used as an extraction medium in the gas concentration section or blended into the gasoline pool. The top gaseous product is processed in the gas concentration unit after it being pressurized in a wet gas compressor. In the gas concentration unit, the gaseous product is separated into dry gas, C3, C4, and light stabilized naphtha (Fig. 10). The C3 hydrocarbons can be later separated to obtain olefins, and C4 hydrocarbons can be separated to obtain isobutene [33].

The most important product from the conventional FCC unit is gasoline, whose yield ranges between 46 and 51 wt% for standard feedstock and can increase to about 60 wt% for hydrotreated feedstock. The second commercial product is LPG. LPG yield is about 12–15 wt%. Other yields dry gas (~5 wt%), LCO (~15 wt%), and HCO (~8 wt%) are not subjected to quality standards, but it is felt that the lower the aromatic content in liquid products, the better the quality. About 4–6 wt% of the original feedstock converts to coke, which deposits on the catalyst surface, blocking the pores and, consequently, decreasing catalyst activity. All these yields are subject to change, depending on the type of feedstock (from heavy to hydrotreated) and the production objectives of the catalyst [32, 33].

4.5   *Modified Catalytic Cracking Processes*

Different high-severity FCC units are developed for a variety of feedstocks, starting from C4 hydrocarbons to all the way up to residue. A few common features of the above processes are similar, except that some of them have a downer in place of a riser or double risers [35]. Table 3 summarizes all the processes.

Importantly, all of them require very high reaction severity, e.g., riser temperature of 550–675 °C, the catalyst to oil ratio of 15–30, reactor pressure of 0.5 kg/cm^2 (g) to 1.5 kg/cm^2 (g), and using mixed catalyst composition consisting of USY zeolite-based FCC catalyst and ZSM-5 zeolite-based additive in different ratios [35]. The innovative features of all the processes are mainly (1) hardware configuration and (2) catalyst formulation depending upon feedstock chosen for processing. All of the above processes, except ACO and Superflex, are employed for the conversion of mainly hydrotreated VGO, or heavy feedstock.
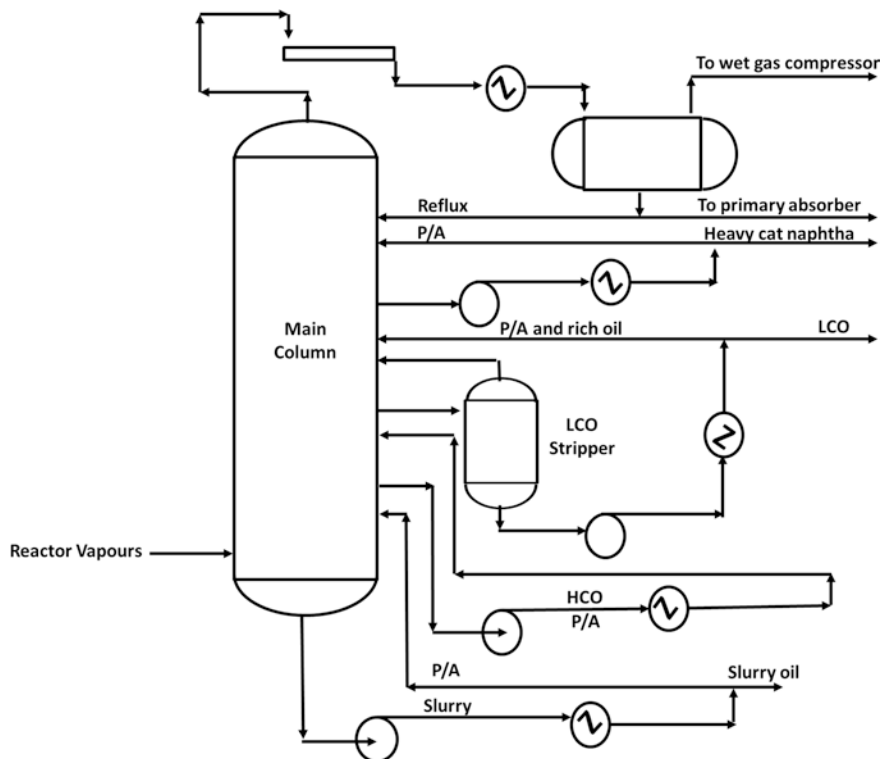
Fig. 10 Main fractionator [31]

However, processes like Superflex, ACO, etc., are developed to convert low-value naphtha feedstock to light olefins by employing ZSM-5 zeolite-based catalyst at very high reaction severity. Since these light feedstocks make very less catalytic coke, these processes require external heat supply to satisfy the heat demand for the endothermic cracking reaction in the riser [47].

4.6 Catalyst Deactivation and Coke Formation

There are two mechanisms by which a particulate catalyst deactivates: physical and chemical. Physical phenomena are sintering at high temperature, malocclusion, and loss of surface area due to attrition [36].

The chemical mechanisms are more prevalent and can be subdivided into three categories:

- Loss of acidity of the catalyst due to reactions with alkaline metals or basic nitrogenous entities.

Table 3 Propylene mode FCC technologies [35]

Process	Developer/ licensor	Propylene yield, wt%	Ethylene yield, wt%	Remarks
Deep catalytic cracking (DCC-I and DCC-II)	RIPP-Sinopec/ stone Webster	14.6–28.8	4–6	Commercialized, several plants in and outside China
Catalytic pyrolysis Process (CPP)	RIPP-Sinopec/ stone Webster	24.6	20	VGO and heavy feeds, commercial trials in China
High-severity FCC (HS–FCC)	Nippon/ KFUPM/ JCCP/Saudi Aramco	17–25	3.8–4.7	Downer, high severity (temperature, C/O), 500 BPD cold flow model
Indmax	IndianOil co./ ABB Lummus	17–25	3.70	Upgrades heavy cuts at high C/O 15–25
Maxofin	ExxonMobil and KBR	18	4.3	Variations with Superflex to increase propylene
NEXCC	Fortum	16.1	3.4	High C/O, short contact time, multi-port cyclones
PetroFCC	UOP	22	6.0	Additional reaction, severity along with RxCat design
Selective component Cracking (SCC)	ABB Lummus	24	NA	High-severity operation (temperature, C/O)
High-olefins FCC	Petrobras	20–25	NA	Downer, high temperature, C/O
Ultraselective cracking	IFP/stone Webster/Total	NA	NA	200 BPD downer demo unit
Advance catalytic olefins(ACO)	KBR & SK Corp.	24–30	28–35	Naphtha feed with very high recycle and very high temperature
MILOS	Shell global solutions	15–23	3.1	Dual riser design
RFCC PetroRiser^{SM}	Axens	10–12	NA	Incorporates a second riser, resid feed
SUPERFLEX™	KBR	38–48	20	C_4-C_8 olefinic feed, commercial (Sasol-12/2006)
MCC (multizone catalytic cracking)	Reliance industries limited	25–34	16–19	• Sequential processing of different feedstock in multizone catalytic cracking in single riser depending on cracking behavior of hydrocarbon • Also process high coke-making feedstock like residue, slurry oil, etc. at the upper end of the riser and then burn off the coke, thus produced in separate regenerator to satisfy the heat balance requirement

- Chemisorption of metallic impurities in the pores of the catalyst. Such pore blockage, contrary to conventional coking, is irreversible.
- Fouling or excess coking due to the presence of resinous or asphaltic hydrocarbons in the feed [36].

Modern catalysts are manufactured to be sufficiently stable to withstand these above mechanisms in the usual range of operations. They can preserve their activity for several weeks while cracking heavily contaminated feeds. Fresh catalyst needs to be added periodically to make up for the lost catalyst activity. Coke gets deposited on the catalyst due to undesired side reactions taking place in FCC and affects the intrinsic activity by covering sites and blocking pores. This loss of activity due to coke deposition is very fast but is reversible, and the catalyst can be regenerated easily by burning off the coke deposited on the catalyst surface. Due to the cyclic nature of the process, the catalyst particles may undergo attrition, producing fines that will result in particulate emissions and loss of catalyst as fines. The age distribution of catalyst particles also affects the activity of the catalyst in cracking reactions [37, 38]. At any instant of time, the catalyst in the reactor is composed of a mixture of new low metal concentration, high-activity and old high metal concentration, low-activity catalyst particles. This mixture of new and old catalysts from an industrial FCC unit is collectively called equilibrium catalyst [46][39].

5   The FCC Catalyst

The FCC catalyst is a fine mixture of four main components: zeolite, matrix, binder, and clay having an average particle size (APS) of 75 μm [72] (Fig. 11).

Artificially crystallized zeolites are commercially synthesized by digesting a mixture of sodium silicate, sodium aluminate, and caustic for several hours. Crystallization is a slow process; hence, some seeds are added so that the process takes about 10 h at 100 °C. Manufacturing a quality zeolite having the intended textural properties requires fine control over temperature, pH of solution, and retention time. The crystalline powder obtained is termed NaY, and it contains approximately 13 wt% Na_2O. Such a high amount of Na_2O is the reason for the inherent stability issues faced by zeolites in the regenerator. To improve its hydrothermal stability, its sodium content is reduced by the de-alumination process (discussed earlier) to obtain ultra-stable Y-zeolite (US-Y) or by ion exchange with ammonium or rare-earth ions (La or Ce) followed by calcination to obtain (RE-Y).

To manufacture FCC catalyst, zeolite, clay, alumina, and binders are mixed into a slurry. The slurry is then spray dried into fine microspheres using atomizers and hot air. The textural properties of the final product catalyst depend heavily on the spray-drying conditions and the constituents of the slurry.
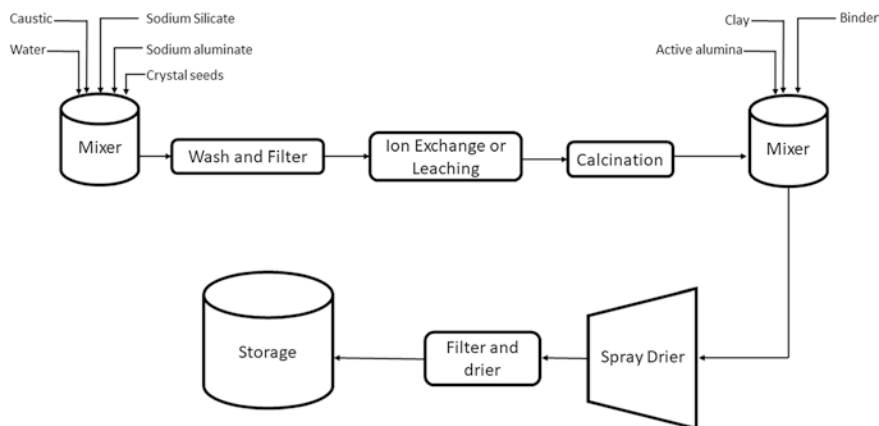
Fig. 11 FCC catalyst manufacture [72]

5.1 Zeolite

Zeolites are synthetic microporous aluminosilicates. It is the key ingredient of the FCC catalyst, which contributes to motor gasoline selectivity. Zeolites make up about 10–50% of the catalyst's volume. To understand the cracking that occurs within the zeolite, it is essential to be familiar with the morphology of the zeolite itself (Fig. 12).

Zeolites have a fixed lattice structure made up of repeating tetrahedrons. Each tetrahedron has either silica or an aluminum atom at its center and oxygen atoms at the corners. These lattices form very small pores of approximately 8 Å diameter. Such small pores contribute to the high selectivity toward gasoline and LPG olefins since large hydrocarbon molecules cannot diffuse into these pores. Hence, zeolites are also called molecular sieves. Zeolites tend to get de-aluminated in the extreme hydrothermal conditions in the regenerator. This causes the collapse of the lattice structure and formation of extra framework alumina. This reduces the acid site density of the zeolite. To counter this effect, rare earths are added to zeolites to modify selectivity and activity and increase hydrothermal stability. Its concentrations vary up to 16 wt% (Figs. 13 and 14).

5.2 Matrix

Matrix refers to the active mesoporous, amorphous alumina in the FCC catalyst. Sometimes, the alumina in the matrix can be of crystalline nature as well. It makes up about 5–25% of the catalyst volume. It provides the primary cracking sites for heavier hydrocarbons. It has a pore size suitable for the diffusion of larger hydrocarbons. These hydrocarbons are pre-cracked on the acid sites of the matrix. The

Fig. 12 Silicon/
aluminum-oxygen
tetrahedron [66]
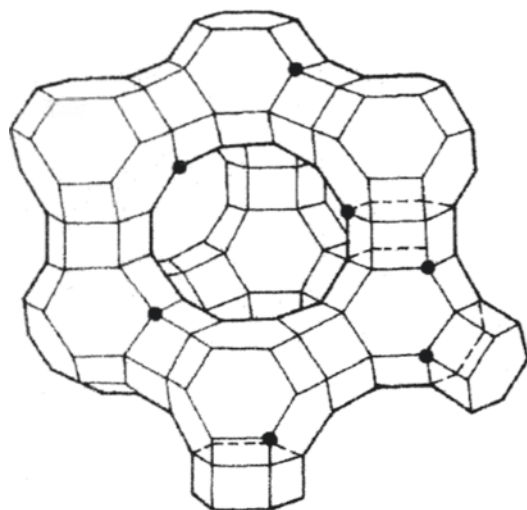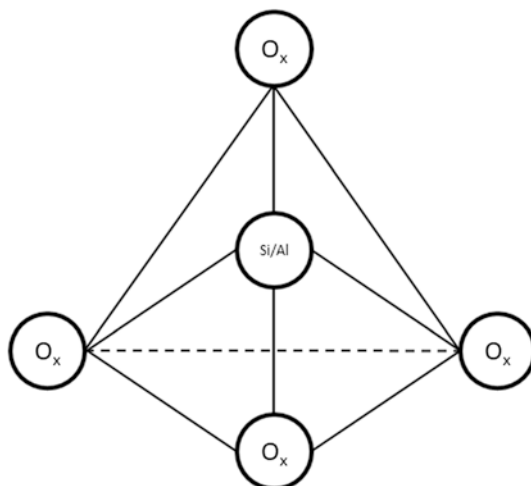
Aluminium atoms	7
UCS	24.25 Å
Silica-Alumina ratio	54

Fig. 13 Geometry of USY zeolite [66]

hydrocarbons cracked on the matrix sites can then easily diffuse into the zeolite pores for further cracking and isomerization, thereby increasing yields of gasoline and LPG. The acid sites of the matrix lack the selectivity of zeolites; however, they are responsible for the bottom-cracking characteristics and coke selectivity of the FCC catalyst. The matrix and zeolite both contribute to the activity of the FCC catalyst. The matrix sites also serve as traps for vanadium, nickel impurities, and basic nitrogen. Matrix manufactured to perform as metal traps contains an active vanadium trapping alumina and rare earth to neutralize the detrimental effects of the
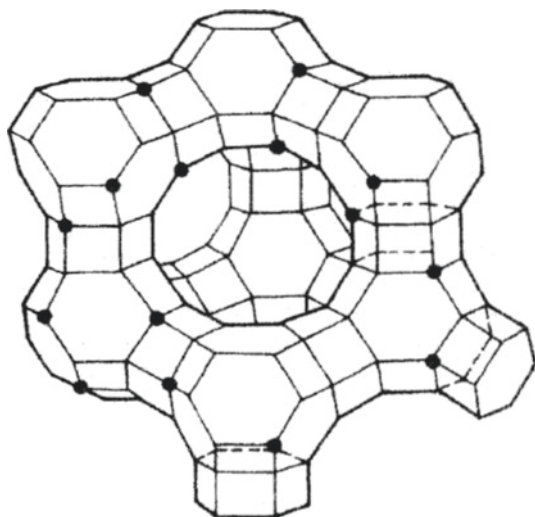
Aluminium atoms	23
UCS	24.39 Å
Silica-Alumina ratio	15

Fig. 14 Geometry of RE-Y zeolite [66]

metals in the hydrocarbon feed. Because of this, the zeolite is prevented from getting deactivated, and hence catalyst life is increased.

5.3 Binder and Filler

The binder serves to hold the catalyst particle together. It may or may not contribute to the catalyst's activity. The filler is mainly used to dilute the activity of the catalyst. Both binder and filler are some forms of macroporous silica and alumina clays (e.g., kaolin clay). They serve to provide mechanical strength, pore accessibility, attrition resistance, and a heat transfer medium to the FCC catalyst. If the pore accessibility of the FCC catalyst is poor, the stripping of the catalyst gets affected, leading to higher hydrogen and dry gas yields. Low mechanical strength and attrition resistance cause loss of catalyst in the form of fines that escape from the top of the regenerator. Furthermore, the reaction of binder's aluminum ions with zeolite produces new acidic sites, which can modify the surface acidity of the zeolite and alter the activity of the catalyst.

5.4 FCC Catalyst Additives

A modern FCC unit in its lifetime may face hydrocarbon feeds that drastically vary from one another. For maximum refinery margins, various production and environmental constraints are laid down on the unit's operation. FCC additives are added in

small amounts to satisfy these constraints by improving a specific yield (gasoline, LCO, propylene), reducing emissions (SO_x, NO_x, H_2S) and producing cleaner products. These additives become a part of the unit's catalyst inventory, increase the FCC unit's operating window, and make it more flexible to process heavier, contaminated, and hence cheaper hydrocarbon feeds and thereby increasing the profitability and flexibility of the FCC unit.

5.4.1 CO Combustion Promoter

While cracking hydrocarbons, coke gets deposited onto the catalyst pores in the reactor section after which the catalyst enters the regenerator. In the regenerator, the coke deposits are burned off using heated air along with some additional oxygen added optionally. Based on this coke combustion process, the FCC units can be categorized as partial combustion or full combustion mode of operation. In full combustion mode of operation, excess hot air is supplied to the regenerator to completely convert some amount of the deposited coke into carbon dioxide. Since coke has a complex molecular structure, the mechanism of its combustion is quite complicated. However, all of the carbon atoms participating in the combustion are converted to carbon dioxide. In partial combustion as the name suggests, limited air is provided for combustion of deposited coke. Hence, some of the carbon atoms participating in the combustion remain as coke and carbon monoxide. The partial combustion units are accompanied by a CO boiler, which converts the carbon monoxide in the flue gas coming from the regenerator into carbon dioxide. The heat from this reaction is utilized in steam generation. Partial combustion units accompanied with a catalyst cooler are very flexible in terms of maintaining the desired severity of operation.

The heat associated with CO combustion is quite high (10,100 kJ/kg std) [48]. For high-severity operations, it was deemed profitable to be incorporated this heat into the dense phase of the regenerator [51]. However, in the case of incomplete combustion, some CO combustion can occur in the dilute phase where it may affect the metallurgy of the regenerator. This phenomenon is called afterburning.

CO combustion promoters are additives that restrict the combustion of coke in the dense phase of the regenerator only. This helps in optimizing yields by a flexible switch of operation between partial and full combustion modes. The key components of any CO promoter are transition metals that catalyze the CO combustion but at the same time remain stable in the hydrothermal conditions of the regenerator [49, 50]. The metals in the CO combustion promoter should not add to the existing metal contamination of the base catalyst.

The initial CO promoters were chromium-based and used in TCC units, and they showed satisfactory combustion promotion but affected overall activity. Around 1972, it was first proposed to use minute quantities of platinum (1–10 ppm) to manufacture CO promoter additive. The first CO promoter was prepared in early 1973 by R. C. Wilson, Jr. by impregnating Re-Y zeolite with H_2PtCl_6. During trials, the regeneration gas contained only CO_2, no CO; cracking yields were acceptable.

Different routes are explored for making the promoted catalyst. The most successful and simplest route involved the exchange of either the calcined zeolite or, preferably, the almost finished spray-dried catalyst with an exchangeable form of Pt (300–800 ppm), such as the $Pt(NH_3)_4^{2+}$ cation [52]. The first actual commercial demonstration was done in a TCC unit at Husky Oil in Salt Lake City in 1974 [53]. The test was successful, complete CO combustion was observed, and 4 wt% increase in conversion was obtained due to higher reaction temperature. After this trial, W. R. Grace's Davison division began manufacturing Pt-promoted catalysts under agreement with Mobil and several other refiners utilized the CO combustion promoter.

It has been observed that the use of platinum-based CO promoters encourage the formation of NO_x gasses in some FCC regenerators. This led to the development of nonplatinum CO promoters. In cases where platinum-based promoters were observed to cause increased NOx emissions in flue gasses, the use of nonplatinum CO promoters with comparable levels of CO oxidation was preferred.

By 1979, the use of CO combustion promoters became quite common. Addition of CO combustion promoter can be at regular intervals (two times a day 1–2 kg additive per ton) or as and when required. The catalyst additive practice paved the way to new development in catalyst addition systems, and several new technologies and additives were explored.

5.4.2 NO_x Reduction Additives

Nitrogen oxides (NO, N_2O, NO_2) are photochemically active gasses, which contribute to the greenhouse effect and acid rains. They are also pungent in odor and cause chronic respiratory illnesses. Generally, NO_x is a pollutant related to transport; however, flue gasses from FCC units processing heavily contaminated (non-hydrotreated) feeds also contain a significant amount of NO_x. In a complete combustion regenerator, around 5% of the organic nitrogen content of the hydrocarbon feed, ends up as NO_x. With more stringent environmental regulations, it is in the best interest of refiners to monitor the flue gas compositions and rectify any deviation to the laiddown regulations caused by pollutants, especially SO_x and NO_x.

It is relatively easier for refiners to use NO_x reduction additives compared to modifying their existing flue gas treatment facilities. Addition of NO_x reduction additives to the catalyst inventory requires no changes or modifications and is quite flexible in terms of the amount required for the degree of NO_x reduction (Fig. 15).

The basic principle behind NO_x reduction is selectively reducing nitrogen oxides to nitrogen. The catalyst is modified by a copper, zinc, or a rare-earth element with oxygen trapping capabilities. The reduction of NO by CO in the presence of oxygen using additive with iridium supported on Ce-promoted alumina showed up to 40% oxygen excess in the feed (e.g., 0.7% vol. in the feed in the conditions they used); the activity in NO reduction and at the same time CO oxidation are quite high but decrease, increasing oxygen excess to 100% [55].
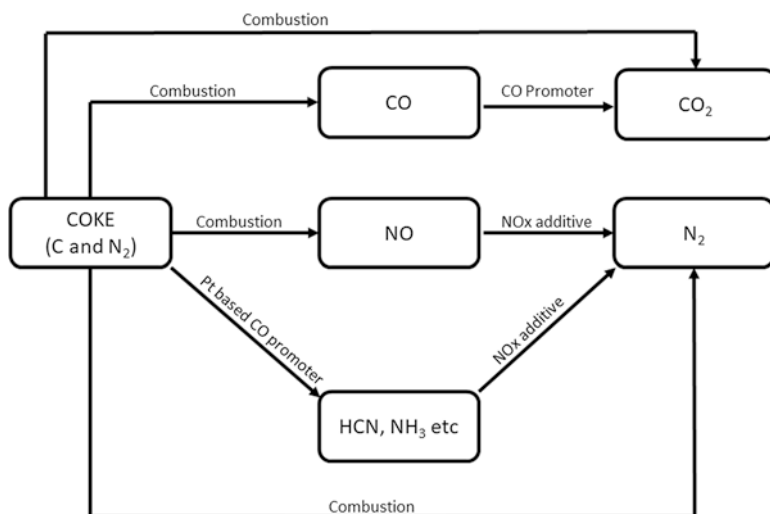
Fig. 15 NO_x reduction mechanism [54]

Excessive use of Pt-based CO combustion promoters reduces carbon monoxide in the regenerator but increases the nitrogen oxide level. Carbon monoxide reduces nitrogen dioxide to nitrogen [54]. Platinum-based CO combustion promoters catalyze the reaction between HCN and NO. Nonplatinum-based CO combustion promoters convert HCN to nitrogen and hence achieve both CO combustion and NO_x reduction.

5.4.3 SO_x-Reduction Additives

The FCC unit contributes to the majority of the SO_x (SO_2, SO_3) present in the refinery's emissions. Hence, it comes under special legislature when it comes to environmental regulations [8]. SO_x emissions are strictly monitored since they contribute to acid rain and PM10 particulate formation and causes respiratory issues to surrounding areas and settlements, especially in areas dense with industrial complexes [56].

SO_x is produced when an FCC unit processes hydrocarbon feed containing sulfur impurities, which end up adsorbed on the catalyst as part of coke. When this coke-laden catalyst is regenerated in hydrothermal conditions of the regenerator, the sulfur present in the coke oxidizes to SO_x and exits the regenerator as part of flue gas.

Various alternatives for SO_x reduction include reducing the sulfur content of the incoming hydrocarbon feed using hydrotreating technologies and reducing the sulfur content of flue gas using a flue gas scrubber. Utilizing SO_x-reduction additives is an alternative that requires the minimum capital and process modifications.

A SO_x-reduction additive must have three primary components. The first step in the mechanism of SO_x transfer additives is the oxidation of SO_2. Under FCC regenerator conditions, SO_2 is favored over SO_3. Thus, SO_x transfer additives contain catalytic ingredients that promote the oxidation of SO_2 and a metal oxide component, which chemisorb the SO_3 in the regenerator. In the reactor, the magnesium sulfate is reduced by hydrogen to form magnesium sulfide. The magnesium in the alumina spinel is less basic than free magnesium oxide, thereby making the sulfate easier to reduce. The magnesium sulfide is then hydrolyzed to a magnesium oxide in the stripper, which returns to the regenerator to complete the catalytic cycle. The sulfur gets released from the reactor gas product in the form of hydrogen sulfide (Fig. 16). This is then recovered as elemental sulfur using the sulfur recovery facilities available with the refiners [73].

The first-generation SO_x additives were commercialized during the 1980s. Research and development work conducted at Arco and then at Katalistiks [54] resulted in the commercialization of additive based on the $MgAl_2O_4$ spinel structure. The performance of this additive depended on the unit's mode of operation (full or partial combustion) and the MgO content of the additive. The spinel structure was hence limited by its MgO content and superseded by new hydrothermally stable hydrotalcite-based SO_x-reduction additive. The significance of the hydrotalcite structure is that it allows for the incorporation of far more MgO into the additive's structure, which results in significantly higher SO_x-reduction activity and efficiency. Further refinements led the way to the current generation of SO_x-reduction additives [55, 57, 58].

Most of the modern commercial additives contain MgO, Al_2O_3, and rare-earth elements, in particular Ce [45]. MgO and Al_2O_3 have the function of taking up SO_3, Al_2O_3 has the function of dispersing and equilibrating the alkalinity of MgO, and Ce has the function of promoting oxidation and reduction reactions of S compounds.
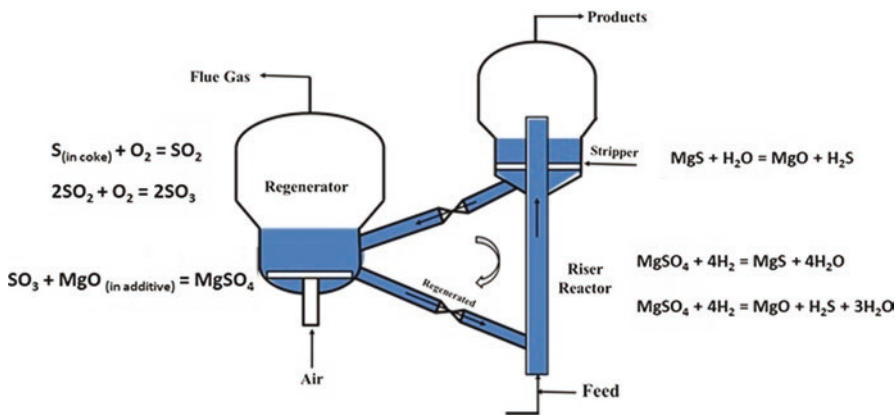
Fig. 16 Mechanism of SO_x-reduction additive [73]

5.4.4 Metal Passivators

The various mechanisms by which the FCC catalyst loses its activity were discussed earlier. Deactivation of FCC catalyst over a period of time during operation affects the overall activity and selectivity toward the desired products. Deactivation of FCC catalysts can be classified as reversible and irreversible. Reversible deactivation is contributed by the organic nitrogen compounds in the hydrocarbon feed, which reduce the acidity of the catalyst and, also because of heavy polycyclic aromatic compounds, get adsorbed on the catalyst and are unable to escape the lattice and eventually end up as coke [59, 60]. Irreversible deactivation is caused by three mechanisms. The turbulent hydrothermal conditions of the FCC regenerator contribute to attrition of the catalyst causing loss of material in the form of fines, which escapes the unit as part of flue gas. In addition to this, the loss of porosity and surface area due to steam also affect the catalyst activity. Zeolites, in particular, are the most susceptible to such hydrothermal deactivation.

Metallic compounds (particularly Ni and V) better known as catalyst poisons present in the feed get adsorbed on to the FCC catalyst's pores as nonstrippable and nonregenerable complexes. Vanadium contaminants destroy the zeolite structure of the catalyst, and both nickel and vanadium contaminants promote the undesirable hydrogenation reactions in the FCC unit, which increases the yield of dry gas. In the oxygen-rich environment of the FCC regenerator, the vanadium compounds adsorbed on the catalyst (typically in an oxidation state of +3) get oxidized. This oxidizes vanadium to +5 state and reacts to form vanadic acid (H_3VO_4); at this state, vanadium has high intraparticle mobility and can easily penetrate the catalyst particle and destroy the zeolite structures. This leads to a permanent reduction of surface area and pore clogging of the catalyst. A fixed amount of fresh catalyst addition rate is maintained continuously or at intervals to account for this loss of activity coupled with off-loading a portion of equilibrium catalyst. Unfortunately, the metal level on FCC catalysts is seldom in equilibrium, and catalyst deactivation by vanadium does not take place in isolation, but combined with and influenced by hydrothermal deactivation [61–64]. The vanadium species at its elevated oxidation state hence cannot be completely phased out without the use of dedicated metal passivators [65].

The incorporation of metal passivators in the feed has become the norm due to trends such as high regenerator temperature and low API hydrocarbon feed of resid nature [66]. Phillips Petroleum Company discovered and developed the antimony metal passivation process in the early 1970s and successfully applied the process at its Borger, Texas heavy oil cracker (HOC) in 1976 [67]. Hydrogen and coke yields were significantly lower, and gasoline yield increased. FCC units with limited gas handling capacity (wet gas compressor and main air blower) will benefit immensely due to the reduction in gas formation and less coking. Other benefits include higher conversion and throughput, as well as improved resid upgradation (Fig. 17).

Incorporation of metal passivators in any FCC unit is unique and tailor-made with respect to hydrocarbon feed and operating parameters. Models and laboratory testing are often used to predict yields that are often used to optimize passivation

Fig. 17 Effect of antimony addition on yields [67]
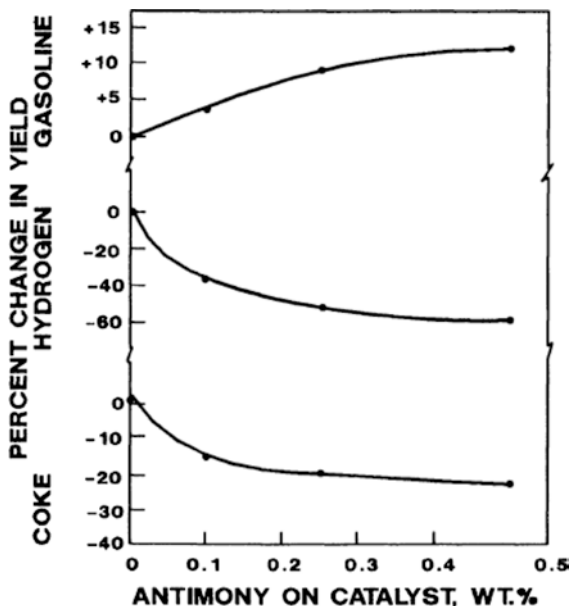
performance. Antimony forms an alloy with nickel compounds and gets deposited on the equilibrium catalyst. This alloy has low hydrogenation activity and also interferes with the hydrogenation reactions catalyzed by vanadium.

Metal passivators containing antimony are known to cause partial passivation of CO combustion promoter [68]. Innovations were made to overcome this reduction in the activity of the CO combustion promoters. Passivation of metals with antimony, however, does not affect the performance of the SO_x-reduction catalysts [69].

5.4.5 ZSM-5

A new zeolite with widespread applications was developed by Argauer and Landolt [70] at Mobil Oil Co. called Zeolite Socony Mobil-5 (ZSM-5). It is a microporous zeolite that selectively cracks heavier olefinic hydrocarbons to increase the yield of propylene for petrochemicals and alkylate yield to improve gasoline octane. It has low rare-earth content and a high silica to alumina ratio. Hence, it has low acid site density, which discourages hydrogen transfer and isomerization reactions.

At the same time, it has high acidity and low pore size (0.5 nm) compared to Y-zeolite (0.74 nm), which enables the cracking of heavy olefins (C5-C7) and restricts entry of branched and cyclic hydrocarbons. These heavy olefins are cracked at their center, which predominantly produces propylene and a small quantity of ethylene and butylene. Since cyclic hydrocarbons have restricted entry to the active sites, excess coke formation is also avoided (Fig. 18).
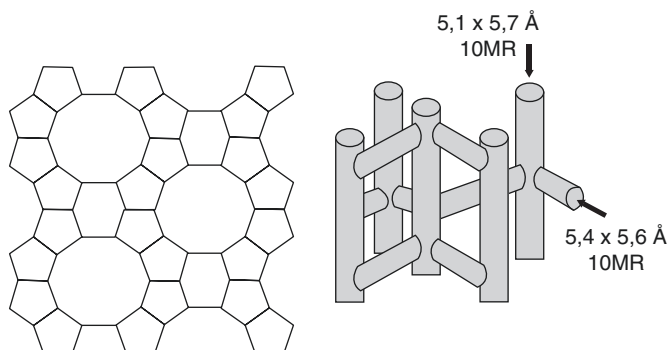
Fig. 18 Tunnel pore structure of ZSM-5 [71]

Since it has a tunnel-shaped, zigzag 3D pore structure, it does not get deactivated significantly by coke deposition and also has high hydrothermal stability [71].

The effect of adding ZSM-5 to the FCC unit can be observed instantly in terms of propylene yield. This makes ZSM-5 very flexible to add to the catalyst inventory as and when required. The utility of ZSM-5 can be further improved when used with a suitable Y-zeolite. It can be customized to maximize the generation of C5–C7 olefins by cracking heavier hydrocarbon feed and at the same time limit hydrogen transfer and isomerization reactions. Dealuminated zeolite with low rare-earth content and low acid site density is suitable for this purpose.

Similar to Y-zeolites, ZSM-5 is also susceptible to hydrothermal deactivation in the high-temperature and high-pressure conditions of the regenerator. Repeated contact in such an environment causes de-alumination of the framework and lattice destruction. The increased pore size due to the destroyed lattice allows bimolecular cracking and isomerization, which reduces the propylene yield. The stability of ZSM-5 is prolonged by treating the zeolite with phosphorus. The phosphate species react with the active sites to form an adduct in which the phosphate ions force the aluminum ion into an octahedral lattice formed by hydroxyl bridges. This process is reversible prior to heat treatment and calcination of the zeolite. Post calcination, some loss in crystallinity and formation of extra framework aluminum are observed. The porosity and accessibility are decreased when the ZSM-5 is fresh in the unit and the extra framework aluminum catalyzes the cracking. However, in subsequent cycles of operation, net olefin formation is greater and coke formation is lower than untreated ZSM-5 [74].

5.4.6 Gasoline Sulfur Reduction Additive

Worldwide legislative drive for better air quality requires modifications in fuel quality, especially in transportation fuel like gasoline and diesel. The FCC process contributes significantly to the total sulfur content in the refinery gasoline pool. This sparked the interest in making attempts to reduce the sulfur content if FCC gasoline

uses catalyst additives. Moreover, catalyst additive-based sulfur reduction in FCC gasoline is economically efficient and does not require much capital expenditure.

Typical full-range FCC gasoline contains sulfur in the form of mercaptans, sulfides, disulfides, thiophenes, and benzothiophenes. Mercaptans, sulfides, and disulfides are present in the lighter fraction of gasoline pool and can easily be cracked in the presence of a catalyst to liberate sulfur as H_2S. The middle fraction of gasoline mostly contains tetrahydrothiophene, thiophenes, and alkyl thiophenes. Although tetrahydrothiophene gets cracked in the presence of Lewis acidic catalyst, reduction levels for thiophenes typically vary from 30% to 40%. The most difficult species to remove are the benzothiophenes found in the heaviest portion of the gasoline [75].

Gasoline sulfur reduction (GSR) additive can be added separately from the host FCC catalyst via a second hopper, and their effects are observed fairly quickly. Fluid catalytic cracking additives reduce sulfur in gasoline by the selective cracking of sulfur compounds into H_2S in situ in the FCC riser. Grace Davison, Albermarle, and Interact have FCC catalyst additive technologies specifically developed to catalytically reduce sulfur-containing compounds in the gasoline boiling range [79].

Grace Davison's sulfur reduction additives, GSR-1 and D-Prism, commercialized in 1995 and 2001, respectively, are most effective in reducing sulfur species in light naphtha, and a typical sulfur reduction of 15–25% is achieved in the presence of 10 wt% of the additive. Patents assigned to Grace on FCC additives disclosed Lewis acid component (Ni, Cu, Zn, Ag, Cd, In, Sn, Hg, Ti) supported on alumina. Zhao et al. [78] reported a composition containing vanadium oxalate supported on alumina for gasoline sulfur reduction and sulfur in gasoline (without benzothiophene) dropped by 55–65% as compared to the base FCC catalyst. Most of the patents assigned to Grace and ExxonMobil are mostly about additives with metal components containing V and Zn [80–82].

Albemarle reported 26% reduction in light naphtha sulfur on the commercial performance of GSR additive, Resolve 750 at 20% of overall catalyst inventory. Myrstad et al. [79] described a composition for reducing sulfur content in hydrocarbons, wherein the additive comprised a hydrotalcite material that had been impregnated with a Lewis acid preferably Zn, Cu, Ni, Co, Fe, and Mn. In 1999, Andersson [81] investigated several groups of additives with different compositions to reduce sulfur in gasoline by depositing various metals and metal oxides on different supports. The sulphur reduction ability of different compositions follows Zn/hydrotalcite > ZrO/alumina > Zn/titania > Mn/alumina. Shan et al. [81] showed that an additive comprising USY/ZnO/alumina has an excellent sulfur removal effect, and ~50% reduction in gasoline sulfur was achieved with 30% of the additive with only a little change in product distribution. In a very recent commercial use at BPCL Mumbai Refinery, GSR catalyst developed by BPCL showed ~33% reduction in gasoline sulfur in the presence of 10% of overall catalyst inventory. The catalyst composition reuses the FCC equilibrium catalyst for the novel GSR additive preparation. Various metal oxides on FCC equilibrium catalyst were found to be effective catalysts in reducing sulfur from fuel streams [76, 77].

5.4.7 Bottom-Cracking Additives

In recent years, the crude oils available to refineries are becoming heavier. Meanwhile, the demand for high-value products such as gasoline and middle distillates is increasing. Therefore, designing of FCC catalyst for processing heavy crudes is the key challenge to a catalyst developer for achieving these targets.

The addition of a non-zeolitic active matrix material to the catalyst formulation is an accepted method to improve catalyst performance when processing heavier hydrocarbons. As different hydrocarbon feeds contain varying amounts of heavier components, independent balancing of zeolite and matrix material is required for optimized product yields. Bottom-cracking additives are separately formulated mesoporous catalyst particles characterized by high active matrix surface area. Adding them to the catalyst inventory will improve product selectivity and reduce bottom yields [83]. Designing catalyst pore structure for efficient diffusion is an important consideration in all catalytic cracking applications, especially when processing heavier feedstocks. Molecular simulations have shown that molecules boiling in the 700–1000 °F range are about 10–30 Å in diameter [84]. Configurational diffusion models indicate that the catalyst pore size must be 10–20 times larger than the size of the molecules to avoid significant diffusional limitations [85]. Thus, if these two results are considered together, we conclude that an FCC catalyst must have pore diameters of 100–600 Å to allow for the effective diffusion of larger molecules. This is consistent with both laboratory observation (Fig. 19) [85] and commercial experience and emphasizes the importance of the proper design of the catalyst pore structure (Fig. 20).

Research work by Grace Davison has focused on bottom-cracking mechanisms, which have been classified into three different reaction types:

- Type I: precracking and feed vaporization.
- Type II: dealkylation of alkyl aromatics.
- Type III: conversion of naphthenoaromatics.
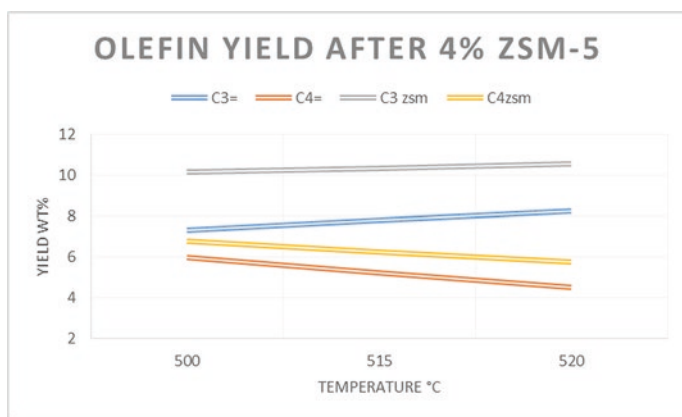
Fig. 19 Effect of ZSM-5 addition on olefin yield [88]

Type I reactions are driven by matrix design and FCC hardware design. As described above, mesopores in the 100–600 Å range are needed for effective bottom cracking. Increasing the catalyst pore volume in this range will enhance bottom cracking. The second type of bottom-cracking reaction is the conversion of alkyl-aromatics in which zeolite activity is much more effective than matrix for this deal-kylation reaction. Increasing the zeolite activity resulted in increased conversion and reduced bottom yield. The third type of bottom-cracking reaction is the conversion of naphthenoaromatic compounds. Conversion of polynuclear aromatics (PNA) is known to be very difficult. However, it is possible to selectively crack saturated naphthenic rings attached to the aromatic cores of these PNAs with an appropriately designed catalyst. Since typical naphthenoaromatic molecules are too large to fit into the zeolite pores, it is expected that cracking of the naphthenic rings will take place on matrix sites or the external surface of the zeolite [85].

6   Chemistry

There are a multitude of reactions that occur when hydrocarbon feed is introduced to a hot regenerated catalyst. As we previously discussed, the unit cell of the FCC catalyst is a tetrahedron with either silicon or aluminum atoms at its center. These silicon ions are at a +4 and aluminium ions are in a +3 oxidation state. Hence, an extra charge of −1 is required to establish neutrality. These sites are of acidic nature since they donate proton or cations. The catalyst's acid sites are of both Bronsted (proton donor) and Lewis (electron pair acceptor) type.
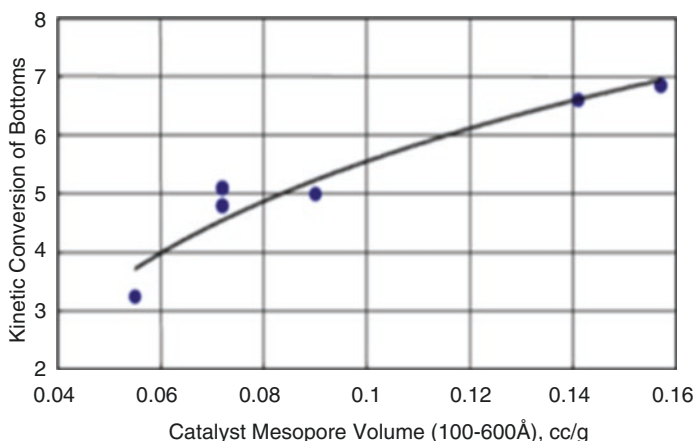
Fig. 20 Improvement in bottom cracking with mesopore volume [85]

Catalytic cracking is based on carbocation chemistry. A carbocation is a positively charged ion consisting of carbon functionality. Carbocations can be classified as carbonium ions (CH_5^+) or carbenium ions (R-CH_2^+).

A carbonium ion is formed when a proton donated by a catalyst's Bronsted site attacks a paraffin molecule in the hydrocarbon feed.

$$CH4 + H^+ \rightarrow \overset{+}{C}H_5$$
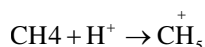
A carbenium ion is formed by adding a positive charge from a Bronsted site to an olefin molecule in the hydrocarbon feed or removing a hydride by a Lewis site from paraffin.

$$CH_4 \rightarrow \overset{+}{C}H3 + H^-$$

$$C_2H_4 + H^+ \rightarrow \overset{+}{C}_2 H_5$$
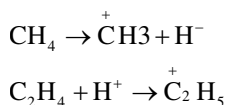
Olefins in the hydrocarbon feed are generally the result of free radical cracking at high temperature. These carbocations tend to rearrange themselves to form tertiary ions since they have higher stability. This causes the final products to have a higher quantity of branched chains compared to thermal cracking and hence a higher octane number.

Primary   Secondary   Tertiary
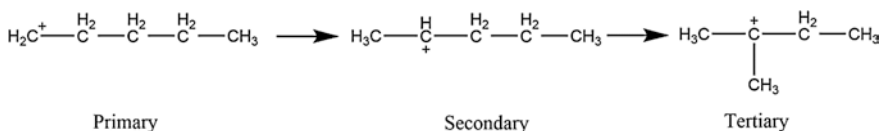
6.1 Cracking Reactions

The cracking reactions proceed through three steps:

- Initiation.
- Propagation.
- Termination.

The initiation involves the generation of carbocations at the acid sites of the catalyst (discussed above). In the propagation step, the carbonium ions attack long-chain paraffinic hydrocarbons to produce a smaller alkane and a carbenium ion.
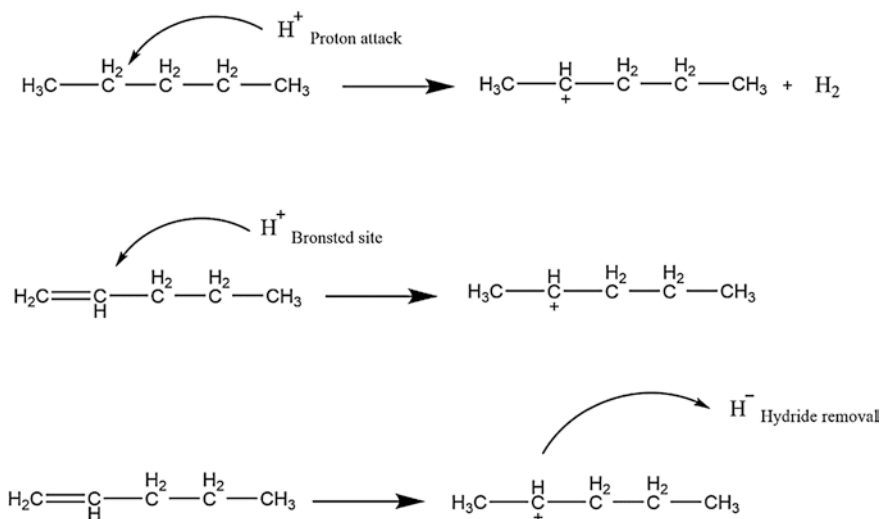
The carbenium ions formed on the Lewis and Bronsted sites undergo β-scission (breakage of the C-C bond, two carbons away from the location of positive charge) to produce an olefin and a smaller carbenium ion.
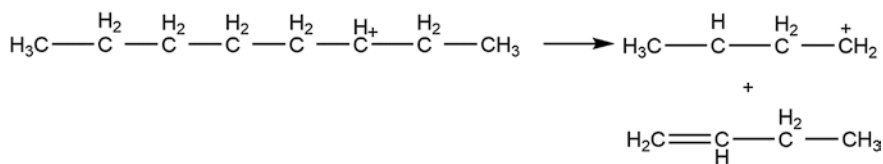
These newly formed carbenium ions can then continue a series of chain reactions. The smaller carbenium ions made up of four or five carbon atoms do not crack easily; instead, they pass on their positive charge to larger hydrocarbons with longer chains to further propagate the cracking reactions.
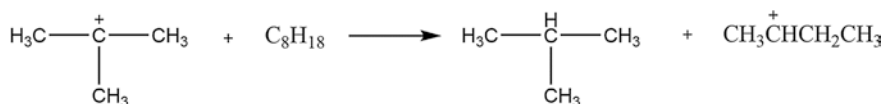
Finally, in termination steps, carbenium ions donate a proton to restore a Bronsted acid site and produce an olefin as the final product, or they abstract a hydride ion to restore a Lewis acid site producing an i-alkane product, and the ionic chain reaction continues.

$$CH_3\overset{+}{C}HCH3CH4 \longrightarrow H_2C{=\!\!=\!\!=}CHCH_2CH_3 \quad + \quad \overset{+}{H}$$

$$CH_3\overset{+}{C}HCH_2CH_3 \longrightarrow H_3C-\underset{\underset{CH_3}{|}}{\overset{\overset{H}{|}}{C}}-CH_3 \quad + \quad H^-$$
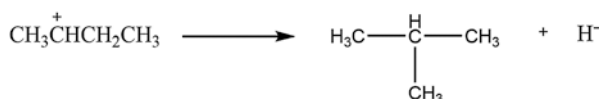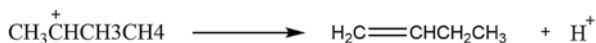
6.2 Isomerization Reactions

The carbenium ions formed tend to rearrange themselves to a tertiary ion since it has a higher life than a primary or secondary ion. When these tertiary ions crack long-chained hydrocarbons via β-scission, they produce branched product molecules.

$$H_3C-\overset{H_2}{C}-\overset{\overset{H}{|}}{\underset{+}{C}}-\overset{H_2}{C}-CH_3 \longrightarrow H_2\overset{+}{C}-\underset{\underset{CH_3}{|}}{\overset{\overset{H}{|}}{C}}-\overset{H_2}{C}-CH_3$$

$$H_3C-\overset{H_2}{C}-\overset{\overset{H}{|}}{\underset{+}{C}}-\overset{H_2}{C}-CH_3 \longrightarrow H_3C-\underset{+}{\overset{\overset{H}{|}}{C}}-\underset{\underset{CH_3}{|}}{\overset{\overset{H}{|}}{C}}-CH_3$$
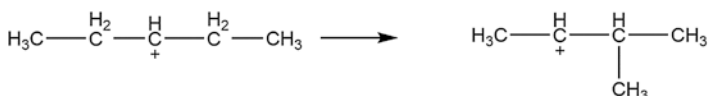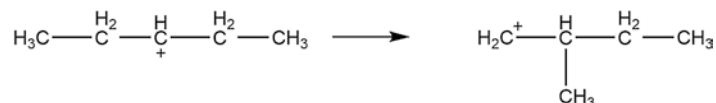
Since such hydrocarbons perform better in the octane test, isomerization reactions are favorable to the final product quality. High octane olefins like i-butylene are also formed, which contribute to the alkylate stream or used in the production of methyl tertiary butyl ether (MTBE) or tertiary amyl methyl ether (TAME). These products can be blended in the gasoline pool to significantly improve the octane number. Branched hydrocarbon products also have a lower pour point and cloud point, which is a desirable trait in diesel-range products [41–43].

6.3 Coke Formation

Catalytic cracking of hydrocarbons forms deposits of coke on the catalyst. The burning of this coke in the regenerator is the source of heat for all the endothermic cracking reactions. However, the chemistry of coke formation is very complex and not yet understood. Different types of coke have different effects on the cracking activity, e.g., depending on the feedstock characteristics; catalytic coke may have a

greater influence on catalyst activity than additive coke. There are five main types of coke identified in catalytic cracking [86]:

- Catalytic coke—from condensation and dehydrogenation.
- Catalyst-to-oil coke—hydrocarbons entrained in the small pores and not removed by the stripper.
- Thermal coke—formed by a free radical mechanism; it is important at high reaction temperatures and also yields hydrogen. It is less important than catalytic coke due to the low extent of thermal cracking at typical FCC conditions.
- Additive coke (or Conradson coke)—from heavy molecules already present in the feed. Its amount correlates directly with the Conradson carbon residue (residue remaining after the fuel has been pyrolyzed by raising the temperature to 800 °C).
- Contaminant coke—from dehydrogenation catalyzed by Ni, Fe, and V (Fig. 21).

$$4C_6H_{12} \longrightarrow 3C_6H_{14} + C_6H_6$$
$$\text{olefins} \qquad \text{paraffins} \quad \text{aromatics}$$

$$3C_4H_8 + C_6H_{12} \longrightarrow 3C_4H_{10} + C_6H_6$$
$$\text{olefins} \quad \text{naphthene} \qquad \text{paraffins} \quad \text{aromatics}$$
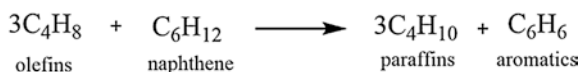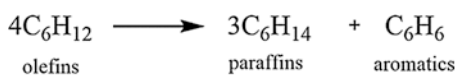
It is generally accepted that the unsaturated molecules formed by carbenium ion cracking as well as aromatics formed by the isomerization and cyclization are the main precursors to coke. These precursors polymerize to form complex polycyclic hydrocarbons that deposit in the pores of the catalyst due to diffusional restrictions. Coke-selective catalysts focus on these precursors and crack them so that they can escape the lattice cage structure before getting trapped as coke. Coke yield is directly linked to the riser operating temperature. At higher temperature, a greater amount of
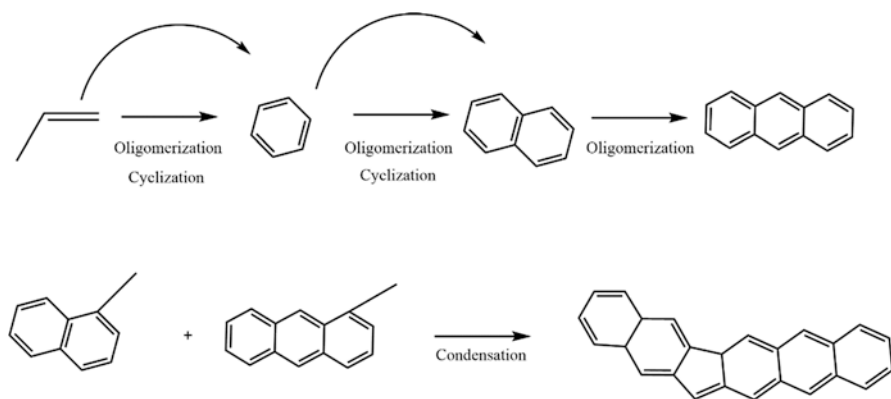
Fig. 21 Catalytic coke formation [37]

olefin polymerization yields a higher amount of coke. Coke is also related to hydrocarbon feed. A feed with higher asphaltenes yields more coke than lighter cleaner feedstock with high API [44, 87].

6.4 Hydrogen Transfer Reactions

Hydrogen transfer is a bimolecular reaction in which two olefins adsorb on adjacent acid sites. One of the olefins saturates while the other forms a naphthene. The naphthene forms an aromatic compound by hydrogen transfer with another olefin.

$$\underset{\text{Olefins}}{4C_6H_{12}} \rightarrow \underset{\text{Paraffins}}{3C_6H_{14}} + \underset{\text{Aromatics}}{C_6H_6}$$

$$\underset{\text{Olefins}}{3C_4H_8} + \underset{\text{Naphthene}}{C_6H_{12}} \rightarrow \underset{\text{Paraffins}}{3C_4H_{10}} + \underset{\text{Aromatics}}{C_6H_6}$$
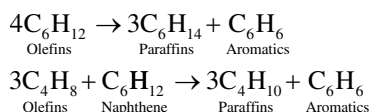
The final products are paraffins and aromatics since aromatics are difficult to crack the reaction terminates.

Hydrogen transfer reactions occur more frequently on rare-earth exchanged catalysts. Since rare earths form bridges between adjacent acid sites to stabilize the zeolite structure, hydrogen transfer happens easily.

These reactions increase the gasoline yield and reduce light olefin yield. The gasoline has more stability and lower octane number. The octane loss due to olefin saturation outweighs the higher aromatic concentration; hence, the octane number reduces drastically.

6.5 Undesirable Reactions

The reactions that affect the yield of desired end products (gasoline, LPG) in a negative way are undesired reactions.

Hydrogen transfer reactions occur to some degree in all FCC processes, but on a larger scale, they severely affect the octane rating of the gasoline product. Over-cracking of lighter olefins is also another undesirable reaction, which is detrimental to the LPG yield and increases coke and dry gas yield. De-alkylation of branched hydrocarbons is also undesirable since it reduces octane rating of product gasoline and the dealkylated part contributes to the dry gas yield.

The reactions most detrimental to the overall conversion is due to the metal contaminants (Ni and V) present in the hydrocarbon feedstock. These metal contaminants catalyze the dehydrogenation reactions, which produce light olefins that contribute to the dry gas yield and also polymerize to increase the coke make. Hence, hydrotreating of FCC feedstock is generally practiced. In addition to this, additives in the form of metal traps are also used. These metal traps are basic metal

oxides, which react with acidic metal complexes and precipitate them in the form of stable silicates or sulfates [40].

7 Propylene Maximization

The world's automotive fuel demand has been experiencing a slow decline along the recent years. With the emergence of efficient engines, sustainable alternate energy sources, and migration to electric power and fuel cells, it is predicted that the automotive fuel market will decline sharply in the coming years. At the same time, the consumption of oil for petrochemical manufacture will soon overtake that of automotive fuels according to a study by IEA [11]. By 2030, petrochemicals will contribute to more than a third in the world's oil demand. The key driver behind this is the ever-increasing demand for plastics and fertilizer, which has overtaken the requirement of other bulk materials like steel, aluminum, and cement. Hence, refiners are gradually shifting their priorities toward manufacturing raw materials for petrochemical synthesis.

C2/C3 olefins are the most significant contributors to petrochemical synthesis, and their demand has increased in the recent 10 years [12]. Steam or naphtha cracking is still the major provider of ethylene and propylene, contributing more than 70% of the world's supply. The FCC unit produces an average 5 wt% propylene on a fresh feed basis, but efforts are being made to increase this quantity and propylene recovery units are installed to obtain propylene of high purity for polymer manufacture. Existing FCC units can be optimized to obtain a higher propylene yield (15 wt %), or a dedicated cracking unit developed on the principles of the FCC unit can be commissioned to obtain high amounts of propylene (20 wt%) [13].

7.1 Operational Modifications for Propylene Manufacture

In an FCC unit, hydrocarbon feeds (VGO), when subjected to cracking conditions for a long residence time, end up as dry gas or coke. Propylene is an intermediate compound, which is formed during carbenium ion cracking of gasoline range olefins as discussed earlier. However, among the secondary reactions such as hydrogen transfer, isomerization, oligomerization, and aromatization reactions, hydrogen transfer, in particular, depletes most of the light olefins formed by cracking. The degree of hydrogen transfer can be tracked using hydrogen transfer index (HTI) (Figs. 22 and 23) [27].

$$HTI = i - C4 \, yield \, / \, total \, C4 \, in \, LPG.$$

GASOLINE YIELD V/S TEMP
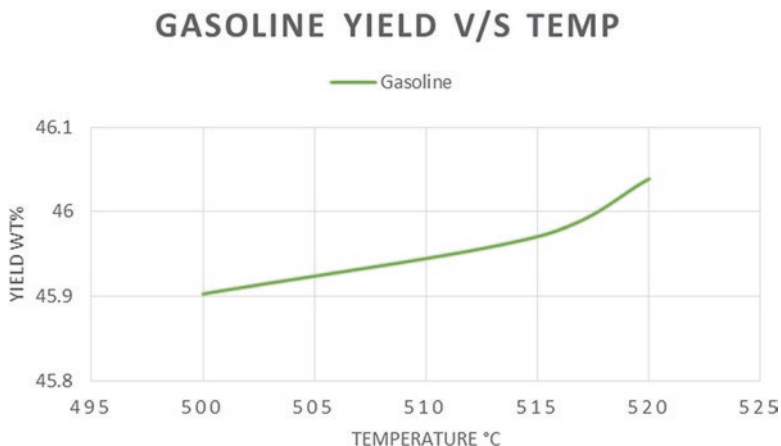
— Gasoline

Fig. 22 Changes in gasoline yield with temperature [88]

LPG YIELD V/S TEMP

— LPG
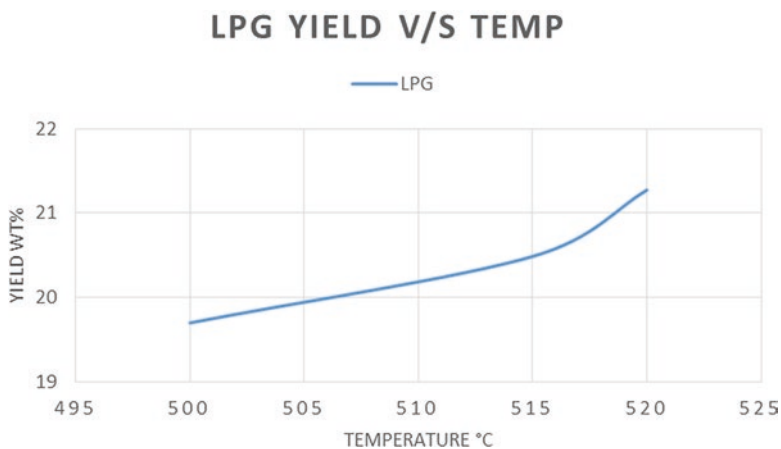
Fig. 23 Changes in LPG yield with temperature [88]

Increasing the cracking temperature increases the catalyst circulation rate. This increases the LPG yield, thereby increasing the yield of propylene. Higher temperature with shorter residence time promotes the endothermic cracking reactions and limits the exothermic hydrogen transfer reactions [5]. This increases the selectivity toward propylene (Figs. 24 and 25).

Higher temperatures also favor thermal cracking reactions, which increase the coke and dry gas yields; hence, a catalyst with good coke selectivity is applicable. An increase in reaction temperature by 10 °C increases propylene yield by 0.9 wt% [26]. The increase in reaction temperature is limited by the wet gas compressor or the main air blower's capacity as well as the coke make and metallurgy of the unit. Higher catalyst circulation means higher catalyst to oil ratio; this results in the unit

OLEFIN YIELD V/S TEMP
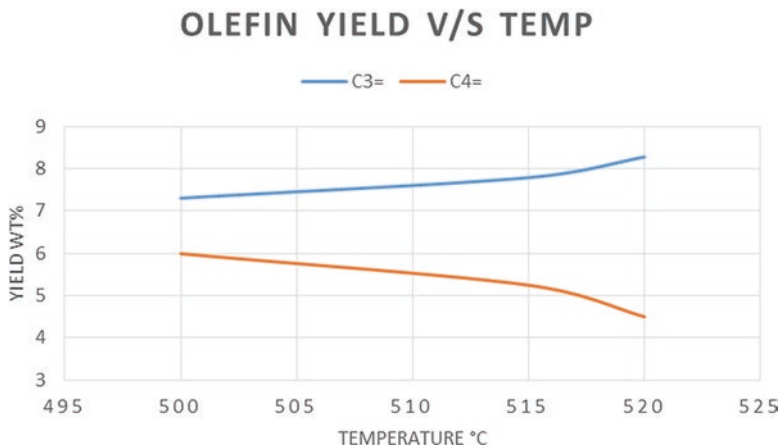
Fig. 24 Changes in light olefin yield with temperature [88]

PROPYLENE VS HTI
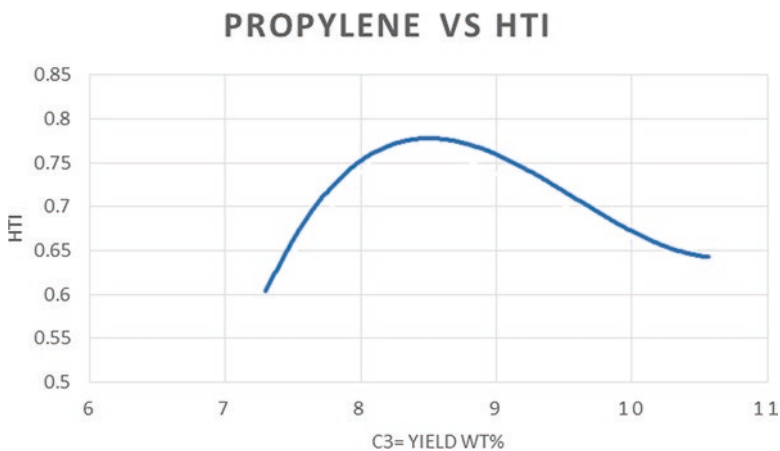
Fig. 25 Changes in propylene yield with HTI [88]

running on high severity. Hence, a higher yield of coke and gas is also observed; however, it is offset by increased margins due to high propylene yield.

Since hydrogen transfer is a bimolecular reaction, reducing the hydrocarbon partial pressure will shift the reaction's equilibrium toward olefins [25]. Hence, optimizing reactor–regenerator pressure balance and/or addition of high amount of diluents (steam) to the riser is advisable if propylene maximization is intended. Modern high-severity FCC units (PFCC, HSFCC, DCC, etc.), which are designed for high propylene yield, consume high amounts of steam for this purpose.

Feed characteristics also affect propylene yield. Feeds having a high hydrogen to carbon ratio and a lower amount of contaminants generally favor the yield of light

olefins. Commercial data presented by Axens indicate an increase in propylene yield by 1.5–2.0 wt% for every 0.5 wt% increase in feed hydrogen content [8].

7.2 ZSM-5 Addition

ZSM-5 is a shape-selective zeolite, which is specially developed for producing high octane motor gasoline. However, since the late 1990s, its application has focussed on maximizing yields of light olefins. It has low rare-earth content and a high silica to alumina ratio. Hence, it has low acid site density, which discourages hydrogen transfer and isomerization reactions. At the same time, it has high acidity and low pore size (0.5 nm) compared to Y-zeolite (0.74 nm), which enables the cracking of heavy olefins (C5–C7) and restricts entry of branched and cyclic hydrocarbons. These heavy olefins are cracked at their center, which predominantly produces propylene and a small quantity of ethylene and butylene. Since cyclic hydrocarbons are restricted entry to the active sites, excess coke formation is also avoided (Fig. 26).

Since it has a tunnel-shaped, zigzag 3D pore structure, it does not get deactivated significantly by coke deposition and also has high hydrothermal stability (Fig. 27) [29].

The effect of adding ZSM-5 to the FCC unit can be observed instantly in terms of propylene yield. This makes ZSM-5 very flexible to add to the catalyst inventory as and when required. The utility of ZSM-5 can be further improved when used with a suitable Y-zeolite. It can be customized to maximize the generation of C5–C7 olefins by cracking heavier hydrocarbon feed and, at the same time, limit hydrogen transfer and isomerization reactions. De-aluminated zeolite with low rare-earth content and low acid site density is suitable for this purpose.

Similar to Y-zeolites, ZSM-5 is also susceptible to hydrothermal deactivation in the high-temperature and high-pressure conditions of the regenerator. Repeated contact in such an environment causes de-alumination of the framework and lattice destruction. The increased pore size due to the destroyed lattice allows bimolecular

Fig. 26 Tunnel pore structure of ZSM-5 [71]

OLEFIN YIELD AFTER 4% ZSM-5
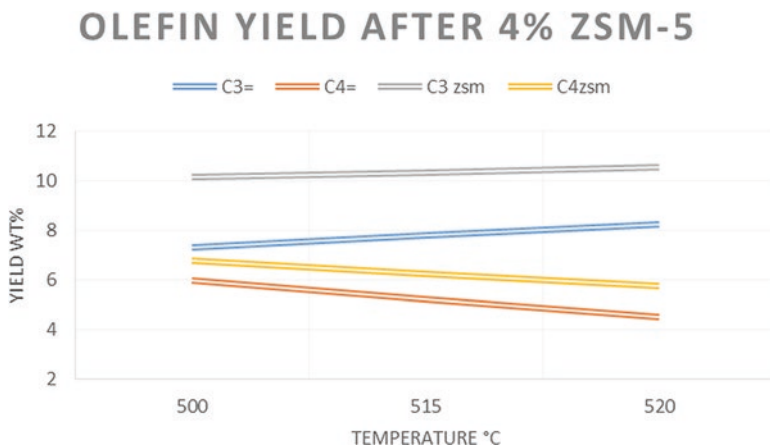
Fig. 27 Effect of ZSM-5 addition on olefin yield [88]

cracking and isomerization, which reduces the propylene yield. The stability of ZSM-5 is prolonged by treating the zeolite with phosphorus. The phosphate species react with the active sites to form an adduct in which the phosphate ions force the aluminum ion into an octahedral lattice formed by hydroxyl bridges. This process is reversible prior to heat treatment and calcination of the zeolite. Post calcination, some loss in crystallinity and formation of extra framework aluminum are observed. The porosity and accessibility are decreased when the ZSM-5 is fresh in the unit and the extra framework aluminum catalyzes the bimolecular cracking. However, in subsequent cycles of operation, net olefin formation is greater and coke formation is lower than untreated ZSM-5.

8 Resid Processing

The source of hydrocarbon feed for the FCC unit, i.e., the crude oil, has been observed to be getting heavier in terms of API and contaminated with asphaltenes and metal complexes. This results in a lower yield of gas oil and greater volume of resid during distillation. Hence, the volume of vacuum gas oil obtained per barrel of crude is steadily reducing, and the amount of resid hydrocarbons is on the rise. Resid processing facilities (hydrocracker, delayed coker, etc.) are limited by their capacities, whereas the FCC units worldwide are running underutilized. New emerging FCC unit designs featuring superior metallurgy, higher capacity of gas concentration facilities, and flexible coke burning are able to co-process this excess resid along with vacuum gas oil.

To upgrade resid hydrocarbons, the proper design of the FCC catalyst is a critical part of the overall process optimization. Minimizing diffusional limitations of the catalyst pores coupled with higher acid site density so that large molecules found in

resid can be cracked is an important consideration in the design of resid catalysts, among others. Resid feeds are generally characterized by their high amount of contaminant metals and high carbon to hydrogen ratio, which yields copious amount of coke and dry gas when processed. Hydrotreating the feed before processing helps but requires significant capital and operation cost. Polyaromatic compounds in the feed, which remain unsaturated in the hydrotreating process, oligomerize to form refractory compounds, which end up as coke. Vanadium and nickel contaminants catalyze hydrogenation reactions, which increase the dry gas yield. Hence, catalyst coke selectivity is another important catalyst performance characteristic. Higher coke yield translates to higher dense bed temperature in the regenerator, which further lowers cat/oil ratio and conversion and can damage the catalyst or even the unit's metallurgy itself. Resid processing units are hence normally equipped with catalyst coolers and multiple stages of regeneration. Catalyst stability at high temperatures and metal trapping characteristics are ensured by rare-earth stabilization of zeolite and rare-earth-based vanadium traps. Feedstock properties along with the dominant bottom-cracking mechanisms characteristic of the feed must also be considered when designing zeolite and matrix activity. Resistance to less common catalyst poisons such as iron is more critical for resid processing. Iron contaminants alter the average bulk density of catalyst, thereby affecting fluidization, and also adsorb onto the catalyst's surface forming nodules. These nodules intensify the attrition between catalyst particles and generate plenty of fines, which severely influence units' smooth running. A dense layer formed on the catalyst's surface after iron contamination, and the dense layer stops reactants to diffuse to inner structures of the catalyst.

9 Summary

Fluid catalytic cracking (FCC) is a versatile process that can process a wide variety of feeds at a wide range of operating conditions to obtain the required yield and maximize the refinery's profit. The profitability of any FCC unit relies largely on the properties of the catalyst. Any and all limitations in the unit's design can be supplemented by using the appropriate catalyst additives. There have been numerous developments in the field of process design, operation, separation, catalyst design, and synthesis; however, research has not come to a standstill. With the gradual shift of the energy market toward alternate energy, the relevance of FCC has been shifted from a refinery to the petrochemical complex. FCC can greatly contribute to the ongoing integration of refineries to petrochemical complexes and help to maintain the relevance of oil refining companies in the years to come.

References

1. Avidan, (2018) Oil Gas J: pp 52–59
2. Harris J (2019) Emily Sandys. Refinery capacity report, EIA
3. Dharmakirti Joshi, Prasad Koparkar (2019), CRISIL report, pp 1–9
4. Phillip K. Niccum (2006), FCC process for converting C3/C4 feeds to olefins and aromatics KBR LLC, US7611622B2
5. Stephen J. Stanley, Francis D. Mccarthy Charles Sumner Gary (1997), Olefin plant recovery system employing catalytic distillation, CB&I Tech, CA2281850C
6. Albert Yuan-Hsin Hu (1997), Controlled FCC catalyst regeneration using a distributed air system, ExxonMobil Oil Corp, CA2201764A1
7. Othman A, Taha M, Rashid K (2012), Automation and control of energy efficient fluid catalytic cracking processes for maximizing value added products, Saudi Arabian Oil Co. US9765262B2
8. Johnson AR, Ross JL, Saraf AV (1993), Process for catalytically cracking paraffin rich feedstocks comprising high and low concarbon components, Stone and Webster Engg Corp, AU663399B2
9. Chatron-Michaud P, Majcher P, Morel F (2014), Process for the production of carbon black from at least one FCC slurry cut, comprising a specific hydrotreatment, IFPEN, US9512319B2
10. Milestones in UOP FCC Technology, internal UOP document
11. IEA (2018) The future of petrochemicals. IEA, Paris
12. Chauvel A, Lefebvre G (1989) Petrochemical processes. Editions Technip, IFP Publications, Paris
13. Wiwel P, Hinnemann B, Hidalgo-Vivas A, Zeuthen P, Petersen BO, Duus JØ (2010) Ind Eng Chem Res 49:3184–3193
14. Houdry EJ (1948) Houdry process for catalytic cracking. Chem Eng News 26:45
15. Wang Z (2010), Comprehensive organic name reactions and reagents, WILEY-VCH Verlag GmbH: pp 1501–1503
16. Thayer AM (2013) The catalysis chronicles. Chem Eng News : pp 64–68
17. Avidan, Edwards M, Owen H (1990), Oil Gas J, pp 33–38
18. Vassiliou M, Lanham S (2009) The A to Z of the petroleum industry. Scarecrow Press UK, pp 240–241
19. Zecchina A, Califano S (2017) The development of catalysis a history of key processes and personas in catalytic science and technology. Wiley, Hoboken, NJ, pp 83–84
20. Wrench R, Wilson J, Logwinuk KH (1986) Fifty years of catalytic cracking. M.W. Kellogg Co. publication, London
21. Reichle AD (1992) Oil Gas J:41–48
22. Reichle AD (1992) Proceedings 1992 NPRA national meeting, New Orleans, pp. 92–93
23. American Chemical Society (1998) The fluid bed reactor – a national historic chemical landmark. https://www.acs.org/content/dam/acsorg/education/whatischemistry/landmarks/fluid-bedreactor/fluid-bed-reactor-commemorativebooklet.pdf. Accessed Dec 2019
24. Breck DW, Togayyaada NY (1964) Crystalline Zeolite Y Union Carbide Corporation, US3130007
25. Argauer RJ, Landolt (1969), Crystalline zeolite ZSM-5 and method of preparing the same, ExxonMobil Oil Corp, US3702886
26. Avidan (1993) Studies in surface science and catalysis, vol 76. Elsevier B.V, pp 12–15
27. Venuto P, Habib (1979) Fluid catalytic cracking with zeolite catalysts. Marcel Dekker, Inc., New York, NY, p 30
28. Xue N, Olindo R, Lercher (2010) Impact of forming and modification with phosphoric acid on the acid sites of HZSM-5. J Phys Chem C 114:15763–15770
29. Moscou L, Lakeman M (1970) Acid sites in rare-earth exchanged Y-zeolites. J Catal 16:173–180
30. Raseev S (2003) Catalytic processes in petroleum refining. Marcel Dekker Inc., New York

31. Sadeghbeigi R (2000). Fluid catalytic cracking handbook: Design, Operation and Troubleshooting, 2nd edn Butterworth Heinemann: pp 28–37
32. Surinder P (2003) Refining processes handbook. Gulf Professional Publishing, Oxford, p 114
33. Ancheyta JJ (2016), Deactivation of Heavy Oil Hydroprocessing Catalysts: Fundamentals and Modelling, 1st edn. Wiley, Hoboken, NJ: pp 207–302
34. Worldwide refinery processing review, (2014) fourth quarter. Hydrocarbon Publishing: pp 2–9
35. Oil & Natural Gas of a multi volume (10 volumes) book, Chapter: Energy Science and Technology of Volume-3 , Publisher: Studium Press, 2014
36. Froment GF (2001) Modelling of catalyst deactivation. Appl Catal A Gen 117:212
37. Stockwell DM, Wieland WS (2000) Proceedings of the second international symposium on deactivation and testing of catalysts, 219th ACS National Meeting, Preprints, pp 310–316
38. Bayerlein RA, Tamborski GA, Marshall CL (1990) Proceedings of the symposium on advances in FCC technology II, ACS Meeting, pp 694–702
39. Cerqueira HS, Caeiro G, Costa L, Ribeiro FR (2008) Deactivation of FCC catalysts. J Mol Catal A Chem 292:1–13
40. Alsabei R, Nagy ZK, Nassehi V (2008, Prague) Process simulators based control design for a fluid catalytic cracking unit. 18th International congress of chemical and process engineering (CHISA)
41. Van Landeghem F, Nevicato D, Pitault I, Forissier M, Turlier P, Derouin C, Bernard JR (1996) Fluid catalytic cracking: modelling of an industrial riser. Appl Catal 138:381–405
42. Weekman VW Jr, Nace DM (1970) Kinetics of catalytic cracking selectivity in fixed, moving and fluid bed reactors. AICHE J 16(3):397–404
43. Pitault I, Nevicato D, Forissier M, Bernard JR (1994) Kinetic model on a molecular description for catalytic cracking of vacuum gas oil. Chem Eng Sci 49:4249–4262
44. YingXim S (1991) Deactivation by coke in residuum catalytic cracking. In: Bartholomew CH, Butt JB (eds) Catalysts deactivation. Elsevier, Amsterdam, pp 327–331
45. Voorhies A (1945) Carbon formation in catalytic cracking. Ind Eng Chem 37:318–322
46. Cerqueira HS, Caeiro G, Costa L, Ribeiro FR (2008) Deactivation of FCC catalysts. J Mol Catal A Chem 292(1–2):1–13
47. Speight JG (2019) Natural gas: a basic handbook, 2nd edn. Gulf Professional Publishing, pp 219–276
48. Kassel LS (1943), Prevention of afterburning in fluidized catalytic cracking processes, Universal Oil Products Co, US2436927
49. Plank CJH, Hansford RC (1949), Process for continuous hydrocarbon conversion with a silica-aluminachromium oxide catalyst, ExxonMobil Oil Corp, US2647860
50. Horecky Fahrig CJ, Shields RJ, McKinney CO, Fluid catalytic cracking process with substantially complete combustion of carbon monoxide during regeneration of catalyst Standard Oil Co. US3909392
51. Schwartz AB (1979), Cracking catalyst ExxonMobil Oil Corp. US4251395
52. Chester AW, Schwartz AB, Stover WA, McWilliams JP (1981) CO combustion promoters: past and present. ChemTech 11:50–58
53. Yaluris G, Peters AW, Zhao X (1999) Proceedings of the 212th ACS national meeting, Orlando, FL 41(3): pp 901
54. Dishman KL, Doolin PK, Tullock LD (1998) NOx emissions in fluid catalytic cracking catalyst regeneration. Ind Eng Chem Res 37:4631
55. Wen B, He M, Costello C (2002) Simultaneous catalytic removal of NOx, SOx, and CO from FCC regenerator. Energy Fuel 16:1048
56. Davey SW (1999) Proceedings of the European refining technology conference, Paris
57. Yoo JS, Bhattacharyya AA, Radlowski CA, Karch JA (1988) Catalytic SOx abatement: the role of magnesium aluminate spinel in the removal of SOx from fluid catalytic cracking (FCC) flue gas. Ind Eng Chem Res 31:1252
58. Yoo JS, Bhattacharyya AA, Radlowski CA, Karch JA (1993) Proc 10th Int Congr Catal Hungary: pp 1391
59. Fu C, Schaffer AM (1985) Effect of nitrogen compounds on cracking catalysts. Ind Eng Chem Prod Res Dev 24:68–75

60. Leuenberger EL (1985) Oil and Gas J, pp. 125
61. Rawlence DJ, Gosling K (1991) Irreversible deactivation of FCC catalysts. Catal Today 11:47–59
62. Keyworth DA, Turner WJ, Reid TA (1988), Oil and Gas J, pp. 65
63. Beyerlein RA, Tamborski GA, Marshall CL, Meyers BL, Hall JB, Higgins BJ (1991) In: Occelli ML (ed) ACS symposium series 452, chapter 8. ACS, Washington, DC, p 109
64. O'Connor P, Gevers AW, Humphries A, Gerritsen LA, Desai PH (1991) In: Occelli ML (ed) ACS symposium series 452, Chapter 8. ACS, Washington, DC, p 318
65. Stokes OM (1988) Grace Davison Catalagram no. 77
66. Dale GH, McKay DL (Sept. 1977) Passivate Metals in FCC Feeds. Hydrocarb Process 56(9):97–102
67. Zhao X, Peters AW, Weatherbee GW (1997) Nitrogen chemistry and NOx control in a fluid catalytic cracking regenerator. Ind Eng Chem Res 36:4535–4542
68. Pettersen FA, Blanton WA (1986) Paper 37e. AICHE, summer national meeting, Boston, MA
69. Ono Y, Yashima K (2000) Science and engineering of zeolite. Kodansha Sci 7:11
70. Sadeghbeigi R (2000) Fluid catalytic cracking handbook, 2nd edn. Gulf Professional Publishing, Houston, TX, pp 95–97
71. Rheaume L, Ritter RE (1988) ACS symposium series 375 Ocelli MO, 9 edn, pp 146–161
72. Siddiqui MAB, Aitani AM (2007) FCC gasoline sulfur reduction by additives: a review. Pet Sci Technol 25:299–313
73. Alkemade U, Dougan T (1996) New catalytic technology for FCC gasoline reduction without yield penalty. Stud Surf Sci Catal 100:303–311
74. Alkemade U, Dougan T (1996) New catalytic technology for FCC gasoline reduction without yield penalty. In: Absi-Halabi M (ed) Catalysts in petroleum refining and petrochemical industries. Elsevier, Amsterdam, pp 303–315
75. Purnell S, Hunt D, Leach D (2002) Catalytic reduction of sulfur and olefins in the FCCU. Presented at the NPRA annual meeting, San Antonio, TX
76. Wormsbecher R, Kim G (1994), Sulfur reduction in FCC gasoline, WR Grace and Co Conn, US5376608
77. Wormsbecher R, Kim G (1996), Sulfur reduction in FCC gasoline, WR Grace and Co Conn, US5525210
78. Zhao X, Bhore N, Cheng W, Kumar R, Roberie T, Ziebarth M (2001), Gasoline sulfur reduction in fluid catalytic cracking, WO0121732
79. Myrstad T, Boe B, Rytter E, Engan H, Corma A, Rey F (1999), Reduction of sulphur content in FCC-naphtha US6497811
80. Andersson P, Pirjamali M, Jaras S, Kizling M (1999) Cracking catalyst additives for sulfur removal from FCC gasoline. Catal Today 53:565–573
81. Shan H, Li C, Yuan M, Yang H (2002) Preprints 47:55–57
82. Gokak DT, Thota C, Rai P, Jose N, Viswanathan PS (2017). Sulphur reduction catalyst additive composition in fluid catalytic cracking and method of preparation thereof, US9533928
83. Zhao X, Cheng WC, Rudesill JA (2002) AM-02-53 presented at the NPRA annual meeting, San Antonio, TX
84. Pumell S (2003) A comprehensive approach to catalyst design for residue applications. Annual meeting, 23–25 Mar, San Antonio, TX
85. Gates BC, Katzer JR, Schuit GG (1979) Chemistry of catalytic processes. McGraw-Hill, New York, NY
86. Venuto PB, Habib ET (1979) Fluid catalytic cracking with zeolite catalysts. Marcel Dekker, Inc., New York, NY
87. Koermer G, Deeba M (1991) The chemistry of FCC coke formation. Catal Rep 7(2)
88. Ajay K, Prabha D, Supriyo M, Pintu M, Chiranjeevi T (2020) Propylene maximization studies. Unpublished data
89. Mohan Prabhu K (2019) Catalysis basics & designing of FCC catalysts and additives, invited talk at BPCL
90. Alex C (2019) Pulikottil, Recent developments in FCC catalysts, invited talk at National Catalysis work shop held at IIT Delhi

Emerging Trends in Solid Acid Catalyst Alkylation Processes

Shivanand M. Pai, Raj Kumar Das, S. A. Kishore Kumar, Lalit Kumar, Ashvin L. Karemore, and Bharat L. Newalkar

Abstract The development of green catalytic processes is receiving more focus during recent times due to ever-increasing environmental concerns. As a result of this, numerous attempts are being made to develop eco-friendly catalyst systems. This has resulted in the emergence of novel zeolite-based solid acid catalyst systems, which now offer a platform for the development of environmentally benign catalytic processes. Considering this aspect, the present chapter reviews evolution of zeolite-based catalytic system for (a) C4-alkylation to meet EURO/BS-VI gasoline RON specifications, (b) valorization of benzene through alkylation route, and (c) toluene alkylation for styrene production and brings out their current commercial practice and future outlook in industrial processes. Since these processes are mostly useful in industrial production of bulk chemical or monomers, the focus of the chapter lies in the development of novel catalytic systems in line with their evolvement of commercial/industrial processes.

Keywords Alkylation · Hydroalkylation · Dehydrogenation · Styrene · BS-VI gasoline · Research octane number

Abbreviations

ABS	Acrylonitrile-butadiene-styrene plastic
atm	Atmospheres (unit for pressure)
BF3	Boron trifluoride
BS-VI	Bharat Stage 6 fuel specifications
Bz	Benzene
C	Carbon/coke
CCR	Continuous catalytic reforming
CH	Cyclohexane
CHB	Cyclohexylbenzene
CO	Carbon monoxide

S. M. Pai · R. K. Das · S. A. K. Kumar · L. Kumar · A. L. Karemore · B. L. Newalkar (✉)
Corporate R&D Centre, Bharat Petroleum Corporation Limited,
Uttar Pradesh, Greater Noida, India
e-mail: newalkarbl@bharatpetroleum.in

Conv.	Conversion
DCHB	Dicyclohexylbenzene
DMHs	Dimethyl hexanes
EB	Ethylbenzene
EPS	Expanded polystyrene foam
GRM	Gross refinery margin
H_2SO_4	Sulfuric acid
HF	Hydrofluoric acid
Ho	Hammett acidity
IL	Ionic liquid
LDH	Layered double hydroxides
micro-meso zeolite	Zeolites containing both micropores and mesopores
MS	Motor spirit
MTBE	Methyl tertiary-butyl ether
Nafion	Sulfonated tetrafluoroethylene-based fluoropolymer copolymer
n_B/n_L	Ratio of Brönsted to Lewis acid sites
–OH	Hydroxyl
RON	Research octane number
RVP	Reid vapor pressure
SAN	Styrene-acrylonitrile plastic
SAR	Silica to alumina ratio
SbF5	Antimony pentafluoride
SBR	Styrene-butadiene rubber
Si/Al ratio	Silicon to aluminum ratio
SM	Styrene monomer
SMPO process	Styrene monomer-propylene oxide process
T	Temperature
t	Time
TMPs	Trimethyl pentanes
UoM	Unit of measurement
USY zeolite	Ultrastable Y zeolite
v/v	Volume/volume
wt%	Weight percentage

1   Introduction

Today, the implementation of stringent emission norms worldwide has added impetus to regulate transportation fuel specifications mainly with regard to SOx, NOx, and particulate matter emissions. Consequently, Euro VI transportation fuel specifications are being implemented, causing substantial reduction in the allowable concentration of aromatics, olefins, and sulfur content in gasoline (Table 1).

Table 1 Major changes in regular MS specifications under different grades

Specifications	UoM	Euro III		Euro IV		Euro V/VI	
		Regular	Premium	Regular	Premium	Regular	Premium
Sulphur	Max, ppm	150	150	50	50	10	10
RON, min	No.	91	95	91	95	91	95
Bz (max)	Vol%	1	1	1	1	1	1
Aromatics (max)	Vol%	42	42	35	35	35	35
Alkenes (max)	Vol%	21	18	21	18	21	18

Table 2 Octane ratings of alkylate and other oxygenates in the gasoline pool

Stream/component	RON
Alkylate	97
Ethanol	109
MTBE	117
Toluene	120.1
o-Xylene	120.0
m-Xylene	145.0
p-Xylene	146.0
Ethyl benzene	107.4

The concentration of aromatics has been reduced from 42 v/v% to 35 v/v%, while olefins have been restricted to 21 v/v% [1].

Such reduction is substantial as it impacts Euro VI gasoline composition in terms of research octane number (RON). Table 2 shows the RON values of typical gasoline components [2]. This is mainly because aromatics and olefins are a high-octane component of gasoline. Therefore, reduction in their concentration has to be supplemented by other high-octane streams. To mitigate this issue, there is a need to blend aromatic and olefin-free high RON stream. In this context, the reformate stream from the naphtha reforming unit has limitations in terms of aromatic content, which imposes limitations on its blending to meet aromatic content of Euro VI specifications.

On the other hand, oxygenate-based blend stocks, namely methyl tertiary-butyl ether (MTBE) and ethanol, have been evaluated. However, enhancement in their concentration for meeting RON specifications is found to have major limitations with regard to environmental concern for using MTBE and meeting Reid vapor pressure (RVP) parameter of gasoline while using ethanol as blendstock. This is mainly due to the fact that MTBE is found to cause drinking water contamination even at ppb concentrations. Hence, it will be phased out in several countries [3]. Therefore, to meet RON specification of Euro VI gasoline, alkylate stream is preferred. Typically, the alkylate stream is produced by the alkylation of isobutane with C3-C5 alkenes in the presence of strong acids. Alkylate has a high-octane number and low RVP, and it is free of sulfur, aromatics, and alkenes.

Furthermore, with increasing use of alkylate as the blendstock for transportation fuels, refiners are facing problems in handling aromatics in the MS pool. As a result,

aromatics, especially benzene, are saturated to cyclic hydrocarbons to produce MS pool blendstock. However, keeping in view the ever-increasing pressure on gross refinery margin (GRM) improvement and high hydrogen production cost, it is of utmost importance to valorize the aromatics stream, especially benzene, with the process having an ease of integration with existing refinery operation. Acid-catalyzed aromatic alkylation is such a route that could fetch several valuable petro-chemicals or chemical intermediates. Ethyl benzene, styrene, cumene, and xylene are such valuable monomers/intermediates that come through benzene alkylation. Thus, the integration of refinery units with petrochemical units with a suitable choice of advanced catalyst bed has become popular among oil refiners. Accordingly, several processes and catalyst formulations have been developed and licensed by technology providers. Today, considering the future outlook of aromatic/benzene consumption for obtaining valorized products, benzene to cyclohexylbenzene (CHB) and toluene to styrene are gaining major focus by researchers and technology developers. Benzene and toluene conversion to CHB and styrene, respectively, would offer a platform for valorization of gasoline-range aromatics.

In view of the above, the present chapter deals with the issues related to the current processes for production of alkylate, cyclohexylbenzene, and styrene and brings out the advances made in improving these processes in terms of development of green catalytic processes.

1.1 C$_4$-Alkylation

Alkylates were first produced during World War II in the late 1930s and early 1940s by the collaborative effort of companies in America to produce high-quality and high-octane gasoline to be used in the warplanes. Since then, various catalysts and processes have been improved upon as alkylation is becoming an essential unit for refiners to produce Euro-VI gasoline. Alkylation of isobutane with C$_3$-C$_5$ olefins in the presence of catalyst results in the production of high RON stream for the gasoline pool [4]. Currently, the contribution of the alkylate to the gasoline pool is approximately 15%, and research octane numbers (RONs) of about 93–97 are obtained for the products [5].

Conventionally, alkylation is carried out by employing conventional mineral acid catalysts; however, such processes are now being avoided due to corrosion issues related to catalyst nature, toxicity, environmental damage due to production of high amounts of effluents, and the complexities involved in the process. Thus, environmentally friendly solid acid-catalyzed processes are now being considered, and research efforts are being carried out in this area. The use of heterogeneous catalysts serves as a platform to overcome the environmental concerns by reducing the capital and operational expenditures. The desired catalyst systems are being developed based on the alkylation mechanism as given below.

1.1.1 C4-Alkylation Fundamentals

Alkylation is a bimolecular nucleophilic substitution reaction wherein the olefin molecule reacts with an iso-paraffin such as isobutane to form branched paraffins in the presence of strong Bronsted or Lewis acid catalyst [6]. The acid catalyst helps in forming carbocation intermediate, which undergoes rearrangement to form the carbocation that is most stable and then the stabilized electron-deficient cation reacts with electron-rich olefin to form large alkyl cation. Such a large cation eventually abstracts tertiary proton from isobutene and generates isoalkane/alkylates as a product along with isobutane cation. Isobutane cation helps in propagating the reaction further by reacting with another olefin molecule. The schematic diagram of the detailed catalytic mechanism is given below using hydrofluoric acid (HF) as an acid catalyst (Fig. 1). In the case of HF, fluoride acts as a stable anion and it donates proton as a Bronsted acid source to form cation intermediate. However, for Lewis acid-catalyzed alkylation, the metal complex-based cation coordinates with olefin to generate carbocation intermediates, and thus the rest of the mechanism for forming alkylates remains the same.

1.1.2 Current/Conventional Alkylation Processes: Mineral Acids

Today, conventional alkylation processes use strong mineral acids such as sulfuric (H_2SO_4) and hydrofluoric acids as alkylation catalysts in refineries, of which 45% of the world's installed capacity is based on H_2SO_4 and 55% is based on HF [7–13]. Since the reaction proceeds via carbocation intermediates, it can undergo several side reactions by rearranging to various stable forms and results in the formation of a complex product mixture (about 75–150 compounds) having a wide boiling range. The reaction of isobutane with 1-butene and 2-butene leads to the formation of trimethyl pentanes (TMPs) in the presence of sulfuric and hydrofluoric acids with the product having an octane number in the range of 90–98 (Table 3) [14]. However, this requires the proper selection of feedstock, catalysts, and operating conditions.

The HF-based processes are more severe as compared to H_2SO_4-based processes with respect to the reaction conditions. For achieving high-octane number with lower acid consumption, it is required to maintain high surface area at the interface of the catalyst and hydrocarbon along with continuous acid emulsion and an acid to hydrocarbon ratio of 45:65 (v/v) [15]. The quantity and quality of products are governed by factors such as concentration of alkane, space velocity of olefin, temperature, concentration of catalyst, and mixing. Even though there are significant technological advancements over the years for the production of alkylates using mineral acid catalyst, the environmental concern still remains a major challenge while using such strong liquid acids.

Stept-1: Formation of cation
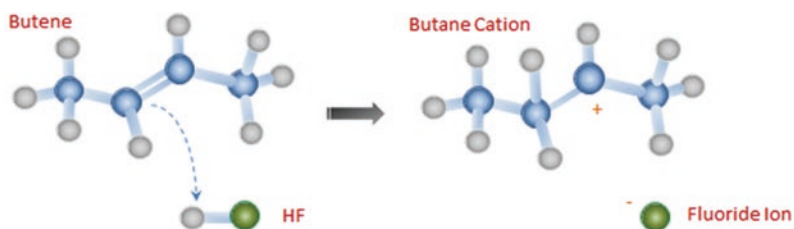
Step-2: Cation rearrangement

Step-3: Reaction with olefin
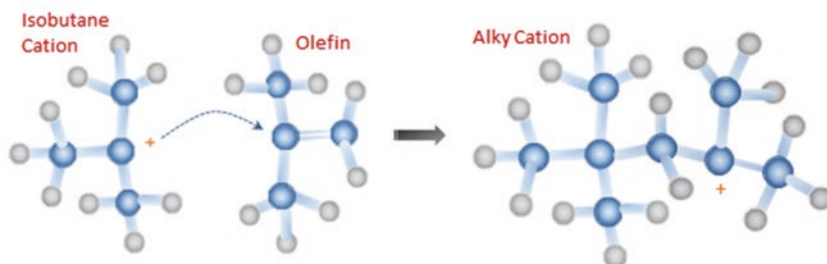
Step-4: Chain termination and isobutane cation generation
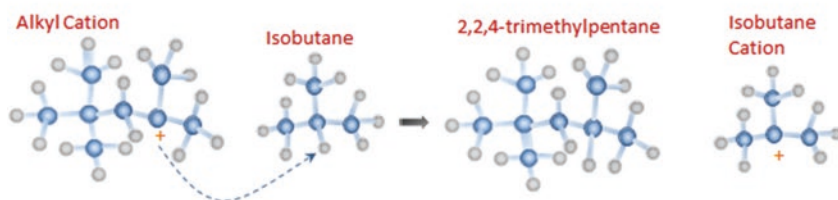
Step-5: Recovery of the catalyst
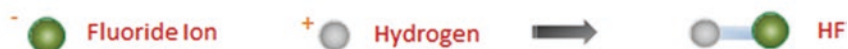
Fig. 1 Mechanism of the alkylation process

Table 3 Conventional catalysts used in the alkylation reaction and octane numbers achieved by them

	HF	H_2SO_4
	RON	RON
Propylene	89–92	91–93
1-Butene	97–98	90–91
2-Butene	97–98	96–97
Isobutene	90–91	94–95
Amylenes	90–92	90–92

1.1.3 Development of Environmentally Friendly Solid Catalysts for Alkylation Processes

The use of heterogeneous catalysts can overcome environmental and corrosion problems with reduced capital and revenue costs. The solid acid catalyst system can be based on Bronsted or Lewis acids. Aluminum chloride ($AlCl_3$)-based catalyst in the presence of hydrochloric acid was the first Lewis acid catalyst used in this reaction. The salts of hydrofluoric acid such as antimony pentafluoride (SbF_5) and boron trifluoride (BF_3) have also been exploited for C_4 alkylation reactions [16]. Other solid acid catalysts like zeolites, sulfated zirconia, mixed oxides and heteropolyacids, and acid resins have also been explored by researchers for alkylation reactions [17–46].

Sulfated zirconia and sulfated alumina are good catalysts for this reaction. Sulfated zirconia is highly active due to higher strength of acid sites equivalent to Hammett acidity (Ho) of ≤ -16.04, while sulfated alumina, due to its low acidity (Ho ≤ -14.5), possesses low activity [47–52]. However, sulfated alumina is widely available, heat resistant, cost effective, and thermally stable due to which it is considered superior to sulfated zirconia. The activity of sulfated oxides depends on the amount of the sulfate content, and only the monolayer coverage of the substrate is required, after which there is a decrease in the catalytic activity and faster deactivation due to accumulation of the sulfate ions. The accumulation of the sulfate ions leads to reduction in pore size distribution and pore diameter of the catalyst support due to the transformation of mesopores to micropores. The catalytic activity initiates when the content of the sulfate ion reaches more than half of the monolayer coverage [53]. The properties of the catalysts depend on the type of sulfate precursor used. The use of sulfuric acid as a precursor initially leads to the dissolution of the support and subsequent deposition of sulfate species at the time of drying. When ammonium sulfate is used as the precursor, the interaction with the support occurs during the calcination stage. The active sites are mainly monosulfate or polysulfate species bonded to the oxide surface in the case of sulfate-promoted oxides [48, 54–56].

The synthetic polymer Nafion (sulfonated tetrafluoroethylene-based fluoropolymer copolymer) can also be used for C_4 alkylation [57–60]. Even though Nafion possesses strong acidity due to the presence of electron-withdrawing perfluorocarbon groups, its low surface area is the cause of poor catalytic activity. The use of

high surface area support results in an increase in the surface area of the Nafion moiety [45, 61–64]. When Nafion resin was supported on mesostructured SBA-15 modified by –OH capping, a high surface area of 400 m² g⁻¹ was obtained with narrow pore size distribution. The capping of surface –OH leads to a decrease in the density of surface silanol groups, thus providing a hydrophobic environment for the isobutane/1-butene reaction [65]. Its thermal stability ranges between 453 and 473 K [66].

Zeolites, especially large pore, are also found to be effective for alkylation of butenes with isobutane, due to their large pore size and excellent hydrothermal stability [67–69]. Although zeolite catalyzes hydride transfer, which is a rate determining step, in C_4 alkylation they undergo fast deactivation [70–73]. In this context, Faujasites (Zeolite-X and Y), beta, mordenite, and MCM-22 [20, 26, 27, 74–98] have been studied. Lanthanum- or cerium-modified zeolite catalysts prepared via ion exchange route offer preference for the formation of high RON hydrocarbons 2,3,3- and 2,3,4-TMPs (RON 106.1 and 102.7) as compared to 2,2,4-TMP (RON-100) [26, 99]. The effect of zeolite pore diameter can be observed from the difference in TMP distribution obtained while using zeolites vis-à-vis mineral acids (H_2SO_4/HF) [7]. Likewise, alkyl chloride-doped C4 alkylation over metal-exchanged Y-zeolite is reported to have significantly slower deactivation with the TMPs being produced at higher concentration in the product as compared to the H-form of the zeolite [100]. This is because of the formation of a metal halide and framework-bonded alkoxide in the presence of an alkyl halide and the Lewis acidity of the metal site present on the metal-exchanged zeolite. The alkoxide so formed acts as a carbocation to participate in the reaction as shown in Fig. 2 [7, 70, 71].

However, rapid deactivation of zeolite-based catalysts poses a challenge for the development of the commercial alkylation process. The limitations of zeolite-based catalysts are given in the following section.

1.1.4 Challenges of Zeolite-Based Catalysts: Deactivation

Based on the literature data, the formation of trimethyl pentanes (TMPs) over zeolite-based catalysts is often reported to decrease with an increase in the time of the reaction. This decrease in the formation of TMPs may be attributed to many factors such as the concentration of olefins in feed, feed rate, and reaction temperature. Moreover, it is also limited due to the framework acidity of zeolite. The lower
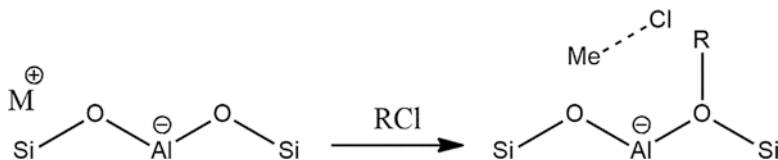
Fig. 2 Formation of framework alkoxide on metal-exchanged zeolites in the presence of an alkyl chloride

framework acidity of zeolite limits hydride transfer step; therefore, it is essential to tune the SAR ratio of the zeolite framework to maintain hydride transfer rate during reaction [70, 71, 101–103]. Such a feature is imparted to the zeolite catalyst by lowering the Si/Al ratio to an optimum level (Table 4). It is a well-known fact that zeolite catalysts undergo rapid deactivation due to coke formation [17, 36, 85] owing to the presence of olefinic precursors in constraint pore geometry. The deactivation rate is influenced by the temperature of the reaction as it affects the oligomerization, sorption property, and diffusion phenomena, which are major factors for the formation of trimethyl pentanes (TMPs) in zeolite framework [7, 84, 104].

Reaction at low temperature favors the adsorption and oligomerization while coke formation occurs at higher temperature [21, 37, 105]. All the aforementioned side reactions occur along with alkylation and are unavoidable. Therefore, the acidity and the pore structure of the catalyst are important to increase the extent of alkylation reactions and minimize side reactions over the zeolite catalyst [68, 106]. Therefore, the stability of the zeolite-based catalysts is a major hurdle toward the successful implementation of such processes. The regeneration of the catalyst can be done to overcome the loss due to catalyst deactivation. The literature suggests that for solid catalysts to be competitive with existing processes based on H_2SO_4 and HF, the catalyst must survive multiple regeneration (as many as several hundred) cycles [181]. To achieve this objective, the concept of wide pore and micro-meso zeolites have been effectively used in developing zeolite-based catalysts.

Thus, research on zeolites with extra-large pores and/or with shorter diffusion pathway is being carried out extensively. Frameworks like VPI-5, UTD-1, and ECR-34 containing rings of 18, as well as 14 T-atoms, have been synthesized [107–109]. However, these systems offer lower acidity, less thermal stability, and

Table 4 Comparison of product selectivities of Y zeolites with different silica to alumina ratios [17]

Catalyst	Y-1	Y-2	Y-3	Y-4
Si/Al	5.4	13.6	35.3	62.2
$C_{5+}(wt\%)$				
C_5-C_7	24	19.2	10.5	13.3
C_8	59.5	54.4	49.3	39.6
C_{9+}	16.5	26.4	39.8	47.1
$C_8(wt\%)$				
TMP	70.0	63.0	11.9	18.2
DMH	23.1	30.6	55.3	55.2
Olefins	6.9	6.4	32.8	26.6
TMP/DMH ratio	3.03	2.06	0.22	0.22
TMPs (wt%)				
2,2,4-TMP	34.2	32.9	22.6	26.3
2,2,3-TMP	7.4	6.3	18.1	15.3
2,3,4-TMP	28.3	31.6	36.8	36.2
2,3,3-TMP	30.1	29.2	22.5	22.2
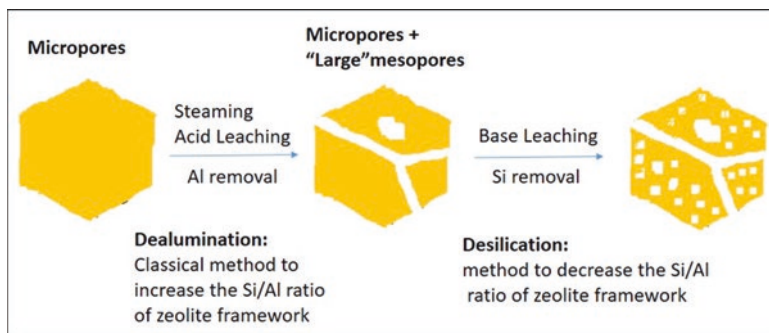
Fig. 3 Top-down approach to hierarchical zeolite

unidirectional pore systems. Furthermore, unsuccessful attempts have been made to reduce the inter-crystalline diffusion path by tailoring morphology and crystal size of the zeolite.

The development of hierarchical zeolite systems might help to overcome the above synthetic limitations and to reduce the inter-crystalline diffusion path in zeolite micropores [110–112]. Hierarchical zeolites couple within them the catalytic features provided by the micropores and the higher diffusivity provided by the large mesopores. However, the connectivity between the various levels of pores is vital to maximize the benefits of interconnected hierarchy, which refers to the voids network generated within the crystal space by fragmentation of the microporous crystal. Typically, hierarchical zeolite systems, also known as micro-meso zeolites, are extensively prepared by top-down and bottom-up approaches. The top-down approaches are based on postsynthetic treatments and easy to scale up and experimentally simple [113, 114], as shown in Fig. 3. The concept of micro-meso zeolites is being investigated for the development of improved catalysts for the C_4 alkylation process.

Based on the aforementioned solid acid catalysts developed/being developed, commercial processes are evolved. The details for the same are given in the following section.

1.1.5 Zeolite-Based Commercial C_4 Alkylation Processes: Key Feature Requirement

Owing to rapid deactivation due to coking, it is imperative to state that methodology for catalyst regeneration holds the key to the commercial success of the process. Commercial processes are being developed depending on three key regeneration methods, which are described below.

1. *Cyclic regeneration*: The concept of fluid catalytic cracking has been exploited to carry out regeneration of zeolite-based catalysts. This requires zeolite with excellent thermal stability, which is usually demonstrated by ultrastable zeolite

Y. However, it offers a challenge in its adoption for alkylation process development due to the exothermic nature of the reaction, which in turn demands rapid cooling of regenerated catalyst to meet desired low to moderate temperature in the reaction zone.

2. *Solvent extraction*: This concept employs solvent to extract hydrocarbon deposits from the spent catalyst but has limitations in extracting coke. In the alkylation process, solvents like isobutane and supercritical solvents have been tested for their effectiveness, but they all lead to only partial restoration of the activity.

3. *In situ regeneration in the presence of hydrogen*: Hydrogen is also widely used in the regeneration of solid acid catalysts. The treatment is carried out at reaction as well as elevated temperatures. The catalyst is typically loaded with a hydrogenation function, for example, a nobel metal. The regeneration takes place through two mechanisms depending on the temperatures used. Hydrogenation of highly unsaturated species, which block the acid sites and not the pores, takes place at temperatures below 373 K. At higher temperatures, hydrocracking of the bulky long-chain alkanes, which block the pores, occurs, resulting in the regeneration of the catalyst.

Considering these facts, solid acid alkylation processes are developed as per details given below:

CB&I, Albemarle Corp., and Neste Corp. AlkyClean™ Process

The world's first commercial-scale, solid acid catalyst-based alkylation unit with a capacity of 2700 barrels per day of alkylate production (100,000 tpy), based on the AlkyClean technology jointly developed by CB&I, Albemarle Corp., and Neste Corp., has been put on stream in 2015 at Zibo Haiyi Fine Chemical Co. Ltd., China [115]. The AlkyClean technology uses Pt/US-Y, a fixed-bed zeolite developed by Albemarle with the trade name of AlkyStar. The temperature of the operation is 323–363 K, and the isobutane/alkene feed ratio is kept between 8 and 10 [116]. There are no stringent requirements for feed treatment as the catalyst is robust and insensitive to feed impurities. A high-quality alkylate product is produced by the AlkyClean process using the novel reactor scheme of CB&I, without the use of conventional liquid acid catalysts typical of conventional alkylation technologies, thus making the process inherently safer and cost effective. With the elimination of downstream treatment of waste streams such as acid soluble oils, the AlkyClean process is an efficient technology for the production of alkylate compared to mineral acid-based process. The process utilizes a series of reactors with distributed injection of olefin feed to achieve high isobutane/alkene ratios internally. It is claimed that the reactor configuration reduces the alkene gradients across the reactor by achieving a high degree of mixing. Thus, the process operates with multiple reactors, which alternate between reaction and regeneration mode of operations. The regeneration is performed at reaction temperature and at an elevated temperature of 523 K. In both cases, the regeneration is carried out in the hydrogen

atmosphere, and the catalyst is partially regenerated at low temperature and fully regenerated at high temperatures.

LURGI EUROFUEL® Process

A zeolite Y-catalyzed alkylation process termed as LURGI EUROFUEL® has been jointly developed by LURGI and Süd-Chemie AG. The reactor is based on the concept of tray distillation towers. The catalyst is mixed with isobutane and fed at the top of the tower, and the alkene-isobutane mixture is introduced in stages (Fig. 4). The evaporation of the reaction mixture helps in the dissipation of the heat evolved during the reaction. Thus, overall pressure and the composition of the liquid control the process temperature. The agitation of the catalyst reactant mixture is achieved by the boiling mixture of alkylate and isobutane. The separation of the catalyst takes place at the bottom of the column, and most of the alkylate/isobutane mixture is taken to the separation section. The separated isobutane is recycled and taken to the top of the reaction column by mixing with the catalyst. The catalyst is intermittently exposed to high hydrogen levels in order to reduce the pile-up of unsaturated compounds on the catalyst surface.

The zeolite Y-based catalyst employed in the process is tuned to achieve high concentration of Brønsted acid sites and lower concentration of Lewis acid sites along with hydrogenation function. The operating temperature of the process is in the range of 323–373 K with the ratio of i-butane/alkene maintained between 6 and 12, and the space velocity of the alkene is higher than in the liquid acid-based processes [117].
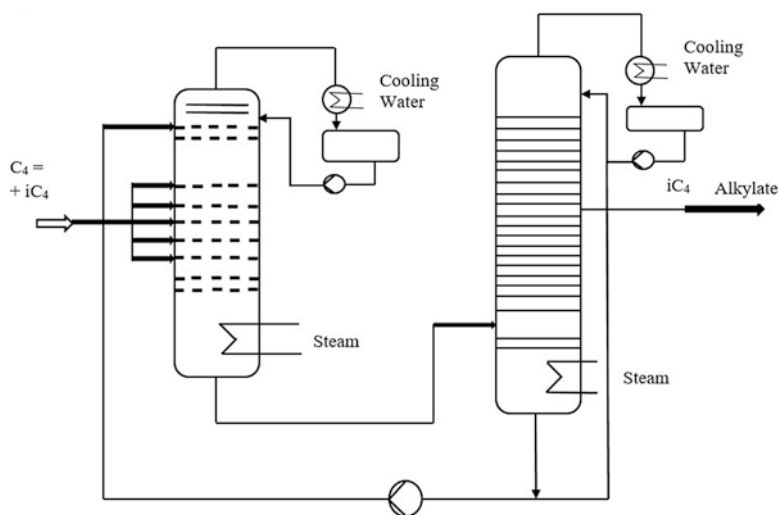
Fig. 4 Lurgi Eurofuel® solid acid-based alkylation process. (Adapted from [117])

KBR K-SAAT™ Process

The K-SAAT next-generation solid acid alkylation technology is developed jointly by M/s KBR and Exelus. The key component of the K-SAAT technology is a highly engineered zeolite Y-based ExSact catalyst, which provides superior alkylation performance by overcoming the occurrence of rapid deactivation in solid acid catalysts. This highly engineered catalyst with regard to pore architecture and framework acidity allows optimized reactions in the form of reduced mass transfer to prevent pore blockage while promoting alkylation over polymerization and favors the formation of 2-butene from 1-butene and highly selective toward 2,2,3 and 2,3,4-trimethylpentane. It is characterized by higher activity, 24 h of cycle time, 5 years of catalyst life, high alkylate RON, and simplified process design. This K-SAAT process is a highly efficient, cost-effective, environmentally benign, and safe technology for production of higher quality alkylate as compared to the conventional liquid acid catalysts or other solid acid catalysts (Table 5).

In view of the above, advances in solid acid catalysts have enabled the development of robust and commercially viable catalyst systems, which now offer as an alternative for the traditional mineral acid-based alkylation process. The summary of developed alternative processes is given below in Table 6.

1.2 Aromatic Alkylation: Industrial Importance

Introduction of an alkyl group into the organic compound, through aromatic proton substitution, is often referred to as alkylation. Acidic catalyst plays a vital role in the alkylation reaction. In the case of acid-catalyzed alkylation, the alkyl group generally forms a stable carbocation intermediate, which is then inserted through pi-electron cloud of an electron-rich aromatic core by substituting a hydrogen atom. As an example, toluene alkylation with ethanol is given in Fig. 5.

Sometimes, the side chain attached to the aromatic core, for example, methyl group in toluene, can undergo deprotonation in the presence of basic catalysts and imparts electron-rich anionic centre to react with alkyl carbocation to form

Table 5 Comparison of K-SAAT with mineral acid-based processes

| | K-SAAT | Mineral acid-based process | |
		H_2SO_4	HF
Alkylate RON	99+	98	95–96
Alkylate yield (vol/vol olefin)	1.88	1.77	1.78
Acid soluble oil formation	0%	1–1.5%	0.5%
CAPEX	1.0	1.2[a]	–
OPEX (including maintainence)	1.0	1.4	1.6
Special metallurgy	No	Yes	Yes

[a]Excludes the acid regeneration facility

Table 6 Summary of commercial alkylation technologies

Process	Licensor	Catalyst	Reactor type	Operating conditions
AlkyClean	Akzo Nobel/ CBI	Pt/USY catalyst	Multiple fixed-bed reactors in parallel for continuous regeneration	Temperature = 323–363K
Alkylene	UOP	Proprietary catalyst	FCC-like reactor for continuous regeneration	Temperature = 283–313K P/O = 6–15
EUROFUEL	Lurgi	FAU-based catalyst	Reactive distillation	Temperature = 323–373K P/O = 6–12
Fixed-bed alkylation (FBA)	Haldor Topsøe	Triflic acid supported on porous material	Fixed bed	Temperature = 273–293K
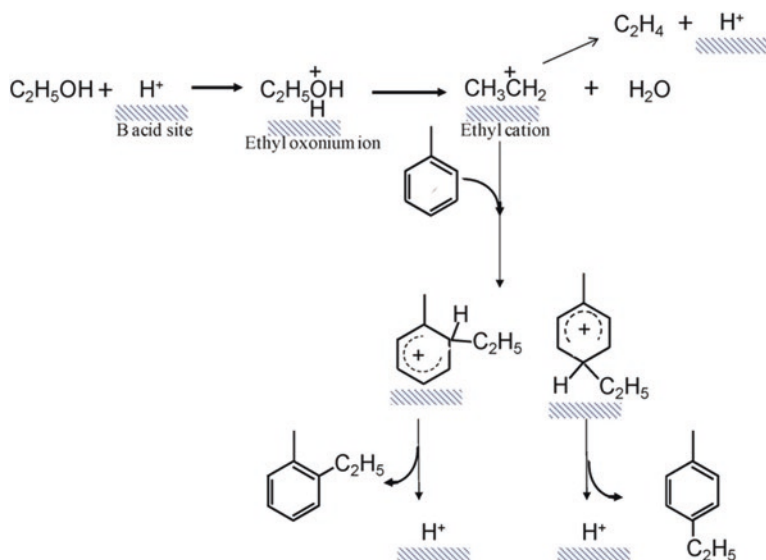
Fig. 5 Ring alkylation on aromatic compounds

side-chain alkylation product. Thus, aromatic alkylation requires (a) alkylating agent, (b) acidic catalyst for ring alkylation, and (c) basic catalyst for side-chain alkylation. Refiners use benzene, toluene, and xylene as aromatic sources and methanol, ethanol, ethylene, isopropanol, propylene, cyclohexene, etc. as alkylating agents. Depending on the source of aromatics and alkylating agents, several aromatic alkylation products such as xylene, ethylbenzene, cumene, and liner alkyl benzene are commercially available and are widely being used as vital petrochemical intermediates (Fig. 6).

In recent times, benzene alkylation with cyclohexene, which is produced in situ via partial hydrogenation of benzene's double bonds, is bringing major attraction to researchers and technology developers. Such alkylation produces cyclohexyl
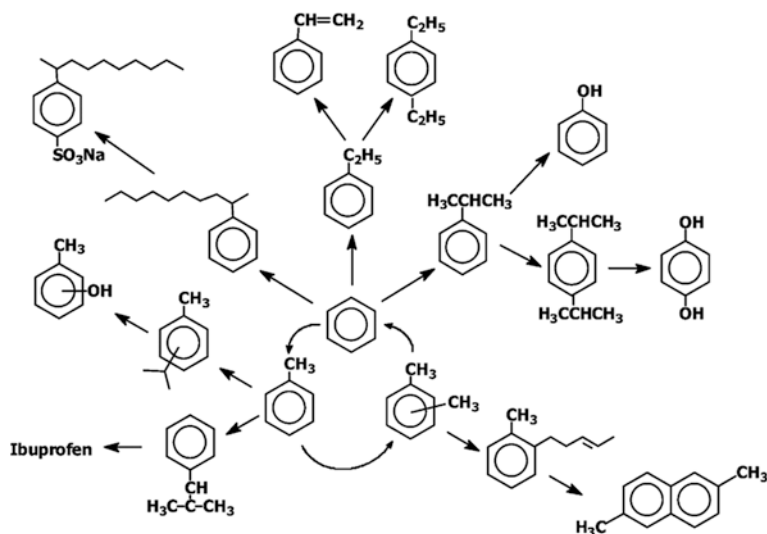
Fig. 6 Petrochemicals' value chain

benzene (CHB) as a valuable product. CHB can be the potential replacement of cumene for the phenol production process.

Typically, Brönsted acids such as HF, H_2SO_4, and H_3PO_4 and Lewis acids such as $AlCl_3$, $AlMe_3$, and BF_3 are the common acids for such alkylation. However, these acids are very strong in nature, and thus carbocations undergo various associations and dissociation reaction resulting in several byproducts. Furthermore, these acids are corrosive in nature and pose challenges in process operation and handling process effluent. Therefore, solid acid catalysts have gained significant importance in developing eco-friendly alkylation processes. In this context, zeolites have gained significant attention owing to their nature, framework structure, and pore architecture, which provide better product selectivity in comparison with conventional acid catalysts. Thus, zeolite-based catalysts are becoming one of the sustainable alternatives for alkylation process development.

This section entails (a) benzene alkylation to CHB, a promising alternative to conventional cumene-based phenol production process and (b) toluene side-chain alkylation to styrene, a less energy consuming process than conventional styrene production through dehydrogenation route. Furthermore, it deals with the sustainable zeolite catalyst development on said alkylation processes with their emerging trend, commercial processes, and future prospect in commercial realization.

1.2.1 Hydroalkylation of Benzene to Cyclohexylbenzene (CHB)

CHB has a wide range of applications from solvents and plasticizer in plastics to the areas of coatings and adhesive [118]. In lithium-ion batteries, it is used as an over charge protecting agent, also as a starting material for synthesis of LCD derivatives.

Biphenyl, which is produced by dehydrogenation of CHB, is mainly used in heat transfer applications and as a dye carrier in the textile industry [119]. The CHB value chain is depicted in Fig. 7.

CHB can also be used as an intermediate for the synthesis of phenol. Phenol is used in the synthesis of several industrially important products like bisphenol A, alkylphenols, phenolic resins, and caprolactam [120]. Currently, the Hock process is the most widely used technology for phenol production globally. This process is based on alkylation of benzene in the presence of propylene to produce cumene and subsequently its oxidation to cumene hydroperoxide and its further cleavage to phenol and side product acetone [120, 121]. This process is economical when the demand for both phenol and acetone is proportionate to their production rate of 1:1 molar ratio for phenol and acetone. However, the global phenol demand is increasing at a much rapid rate than for acetone, making the Hock process less viable [120–122]. Therefore, there is a need to look for an alternative process for phenol production.

One of the potential attractive routes for phenol could be the synthesis of benzylic hydroperoxide by oxidation of cyclohexylbenzene and splitting of the hydroperoxide to produce phenol and cyclohexanone, as shown in Fig. 8. Furthermore, the cyclohexanone co-produced in this alternate route is more valuable and is useful for the production of adipic acid, caprolactam, and nylon [123, 124]. This process does not utilize costly propylene as a raw material [120–122]. However, the
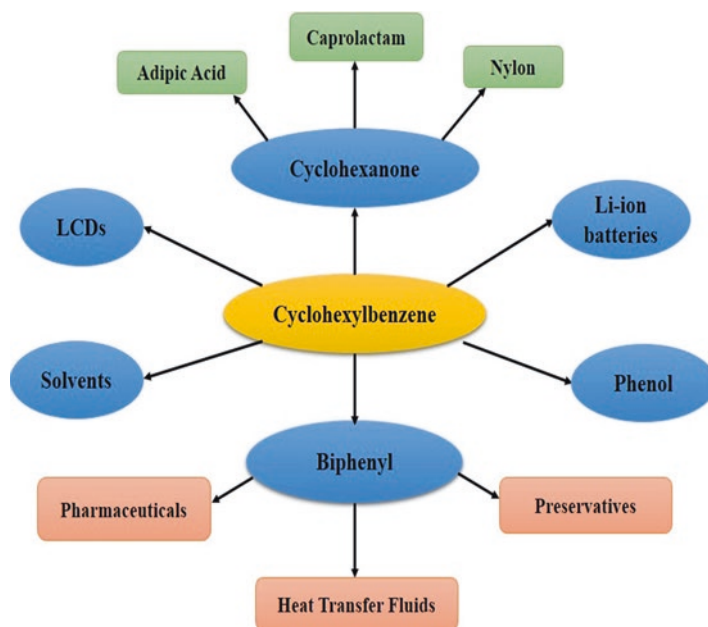
Fig. 7 The CHB value chain
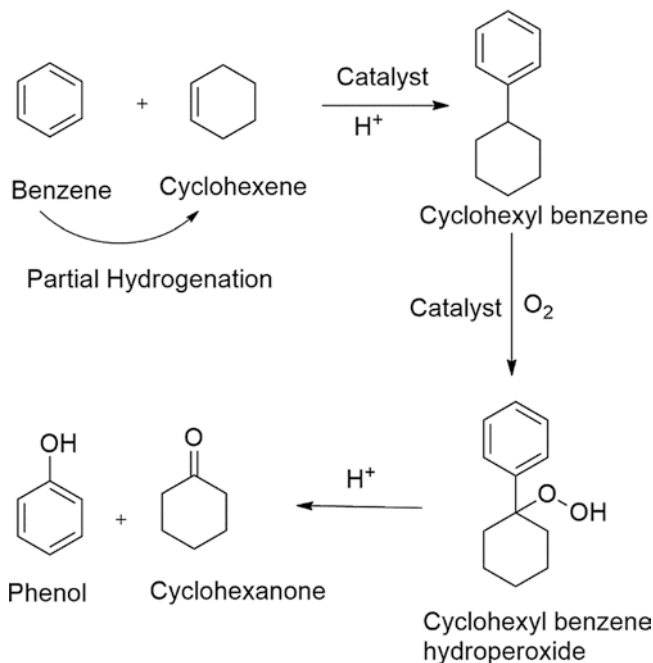
Fig. 8 Synthesis of phenol from CHB

commercial production of CHB will depend on the development of efficient catalysts and economical process.

1.2.2 Conventional Process for Synthesis of CHB

The conventional route for production of CHB is direct alkylation of benzene with cyclohexene in the presence of aluminum chloride or sulfuric acid as catalysts. This route not only offers low selectivity (around 44%) for CHB but also uses catalysts that are hazardous in nature [125, 126]. Hence, it is essential to look for alternate environmentally benign routes to overcome the hazards associated with the conventional route.

1.2.3 Alternative Route for Hydroalkylation of Benzene

Hydroalkylation of benzene involving partial hydrogenation of benzene followed by alkylation of benzene is a potential alternative route for CHB synthesis [123, 127]. Bifunctional catalysts are required for hydroalkylation reaction where cyclohexene is produced by partial hydrogenation of benzene on metal sites and
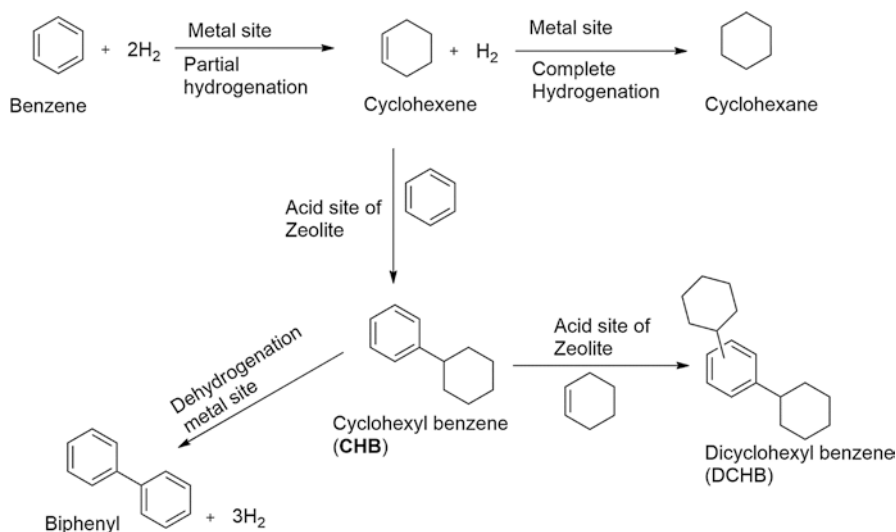
Fig. 9 Benzene hydroalkylation pathway for CHB

alkylation of benzene with cyclohexene takes place on the acid site to produce CHB, as shown in Fig. 9.

During the reaction, side products like cyclohexane, dicyclohexylbenzene (DCHB), and methyl cyclopentane are reported to form, which affect the selectivity of CHB. It is further reported that formation of bicyclohexyl also takes place by hydrogenation of CHB under severe operating conditions [123, 127]. The literature reports the use of several bifunctional catalyst recipes based on metals like Ni, Co, Zn, Pd, Pt, Ru, Rh, Re, and Sn supported on SiO_2, Al_2O_3, and zeolites like MOR, Beta, 13X, and MCM-22 for benzene hydroalkylation [120–122, 128, 129]. The production of CHB as a side product was first reported during the hydrogenation of benzene using nickel catalyst in the presence of phosphoric anhydride [130]. Subsequently, production of CHB was reported on solid catalysts through hydrogenation of benzene using alkali metal supported on Al_2O_3 as a catalyst and group VIII metal deposited on acid function like SiO_2-Al_2O_3, $AlCl_3$, and BF_3 [126, 131]. Since then, several research articles and patent by prominent industrial companies like Shell, Phillips Petroleum, Universal Oil, Texaco, Total, and Exxon Mobil have been published/filed for the production of CHB [132–135].

The effect of catalyst pretreatment and operating conditions on the catalyst activity were studied for hydroalkylation of benzene on a series of nickel-supported silica-alumina catalysts in batch reactor [136]. This study reported that selectivity of CHB is proportional to the quantity of acid sites, and silica-alumina with 42 wt% of alumina was the best support for the hydroalkylation reaction due to higher acidity of the support . The author also studied the effect of catalyst metal content on the hydroalkylation selectivity and activity. The activity of the catalyst increased with nickel content; however, CHB selectivity decreased due to higher hydrogenation

activity with increased metal loading. Furthermore, an increase in reduction temperature of the catalyst leads to an increase in the activity of the catalyst without affecting product selectivities. Nickel content of 3–5 wt%, catalyst reduction temperature of 723–773 K, catalyst calcination temperature of 973–1073 K, and reaction temperature of 473 K are found to be optimal. The best catalyst was 5 wt%Ni loaded on silica-alumina wherein selectivity of 64% was obtained for CHB at 35% conversion of benzene.

A four-component catalyst system consisting of zeolite 13X loaded with platinum, nickel, and rare-earth ions has been reported for benzene hydroalkylation [127]. The study reported the effect of Ni, Pt, and rare-earth metal content on the performance of the catalyst in terms of its activity and selectivity for benzene hydroalkylation. It has been reported that only Ni/13X favors the formation of cyclohexane during benzene hydroalkylation whereas by modification of the Ni/13X with rare-earth metals favors the formation of CHB by hydroalkylation route. This improvement in selectivity for rare-earth-modified Ni/13X is due to the reduction in adsorption strength of benzene by alteration in the electron transfer to the metal, which favors hydroalkylation over hydrogenation, thus improving the selectivity for CHB [127]. This study also claims that hydroalkylation is favored at lower temperatures by addition of small quantity of platinum, which facilitates a better reduction of nickel. With the addition of 0.1 wt% platinum, the temperature required to achieve similar benzene conversion was reduced from 670 to 450 K. A selectivity of 70% was obtained for CHB on the best catalyst, 5 wt%Ni/10 wt%Re/0.1 wt%Pt loaded on 13X zeolite at a benzene conversion of 20% [127].

Benzene hydroalkylation activity was also studied on palladium-supported beta zeolite in a batch process [128]. This study reported the effect of parameters like metal loading, type of metal, and zeolite silica to alumina ratio (25–200), on the performance of the catalyst. Zeolite beta with a low Si/Al ratio showed higher selectivity for alkylation due to the presence of higher Brønsted acid sites. The nickel-loaded catalyst showed very low activity, whereas ruthenium and rhodium showed high activity with a benzene conversion of around 100%; however, the selectivity for CHB was very low (around 2%). On the other hand, the palladium-modified catalyst gave a selectivity of 67% at a benzene conversion of 28%. 0.2 wt% palladium was reported to be optimal for achieving respectable CHB selectivity. With an increase in Pd loading beyond 0.2wt%, the activity of the catalyst increased, leading to higher benzene conversion. However, the CHB selectivity is reported to decrease due to increased hydrogenation activity leading to complete hydrogenation of the intermediate cyclohexene. This study also reported the effect of reaction conditions like temperature, pressure, and reaction time on the activity and selectivity of the catalyst. With an increase in reaction temperature, benzene conversion increased linearly; however, the selectivity of CHB decreased due to an increase in the selectivity for cyclohexane and DCHB. A similar trend was seen with an increase in hydrogen pressure and reaction time. Based on the obtained results, it was concluded that zeolite beta with a silica to alumina ratio of 25 and loaded with 0.2% Pd having an optimum ratio of metal active sites and acidic sites is a potential catalyst for benzene hydroalkylation and is the key for selectivity to CHB. This study also

investigated the effect of zeolite acidity, nature of metal, and metal wt% to derive optimum catalyst composition for hydroalkylation of benzene.

Hydroalkylation activity of mordenite and beta zeolites modified with 0.2 wt% of ruthenium has been performed in a batch reactor with cyclohexane as a solvent [137]. The study demonstrated that beta zeolite with 0.2 wt% Ru possessed higher activity than mordenite loaded with 0.2 wt% Ru due to easy access of acid sites for hydroalkylation, leading to the selectivities of 60–40% for CHB and DCHB cumulatively at a benzene conversion of 30 and 80%, respectively. Comparing the results at the same benzene conversion showed higher CHB selectivity using beta zeolite with 0.2 wt% Ru as compared to mordenite loaded with 0.2 wt% Ru.

More recently, hydroalkylation of benzene using more complex Pd/HBeta core–shell catalyst with extra acid sites produced by coating Si-Al framework outside the conventional Pd/HBeta has been reported [138]. Thus, prepared zeolites were modified with Palladium metal 0.1–4.0 wt%) and evaluated for hydroalkylation of benzene using a batch reactor. By employing the above approach, the Lewis and Bronsted acid sites of Pd/HBeta increased by 19 and 58%, respectively, as compared to Pd/HBeta. Furthermore, Pd@HBeta showed 44% CHB selectivity at 85% conversion of benzene as compared to 25% CHB selectivity using Pd/HBeta at similar benzene conversion. The enhanced activity and CHB selectivity in the case of Pd@HBeta as compared to Pd/HBeta were attributed to the presence of higher Bronsted acidity in the case of Pd@HBeta. Additionally, increased Pd metal loading on Pd@HBeta and Pd/HBeta increased benzene conversion; however, CHB selectivity decreased, thus confirming the fact that higher metal sites favor hydrogenation instead of hydroalkylation. Hydroalkylation performance of different metal-modified HBeta catalyst were also evaluated under similar operating conditions. Beta zeolite modified with 0.2 wt% Rh and Ru yielded benzene conversion of 85% followed by Pd with 56% benzene conversion. On the other hand, Ni-modified beta showed very low benzene conversion (1.3%) without any CHB yield. Among all the metal tested, CHB selectivity was the highest for Pd (25.1%), followed by Rh (18.3%) and Ru (15.8%) at the same benzene conversions of 85%. Similarly, the effect of support acidity on hydroalkylation performance was studied using different catalyst supports (HY, HMCM-41, γ-Al_2O_3, and SiO_2). Among all the catalysts tested, Pd/ SiO_2 showed the least activity for benzene conversion as there are no acid sites present on the catalyst support followed by Pd/MCM-41, Pd/HY, and Pd/γ-Al_2O_3. However, on catalysts Pd/ SiO_2, Pd/MCM-41 and Pd/γ-Al_2O_3 selectivity for CHB was insignificant, thus confirming the fact that Brönsted acid sites are vital for the hydroalkylation reaction. In addition to this, the effect of the ratio of Brönsted acid sites and Lewis acid (n_B/n_L) and Brönsted acid/metal sites (n_B/n_m) were also studied. As per obtained results, higher ratio of n_B/n_L is found to favor hydroalkylation. Furthermore, the effect of metal particle size has been investigated. The obtained results showed that catalysts with smaller metal particles showed marginally higher benzene conversion with higher selectivity for cyclohexane, whereas catalysts with higher metal particle size favored hydroalkylation.

Summary of suitable features for the literature-reported bi-functional hydroalkylation catalysts is listed in Table 7. Several bifunctional catalyst recipes

Table 7 Summary of suitable features of reported bi-functional hydroalkylation catalyst

Features	Purpose	Details from literature	Reference
Metal type	Hydrogenation of benzene to cyclohexene requires metal function	Pt, Pd, Ru, Rh, and Ni	[128, 139]
Metal content	Metal site density affects the activity of the catalyst	0.2–5 wt%	[136, 139, 140]
Promoters	Helps in desorption of cyclohexene from the catalyst surface. Upon desorption, cyclohexene alkylates with benzene to form CHB	Ca, Sn, Ni, and rare-earth metals	[127]
Promoters content	Important for increasing the hydroalkylation selectivity	0.1–10 wt%	[127]
Zeolites type	Provides the acid function for the catalyst and the acid function is required for the alkylation reaction	MOR, Beta, 13X, Y, MCM-22	[137, 138]
Si/Al ratio of zeolites	Density of acid sites is critical for the catalyst performance in terms of activity and selectivity	1–100	[128, 141]
Acid to metal site molar ratio	The ratio of acid to metal site density of the catalyst influences the hydrogenation and alkylation reaction to happen in tandem, leading to higher selectivity for hydralkylation	20–120	[142, 143]

comprising zeolites like MOR, beta, 13X, Y, and MCM-22 with metals like Pd, Ru, Ni, Pt, and Rh supported on them have been studied for hydroalkylation of benzene. There are several critical properties like metal type, metal content, zeolite type, acid site density, and acid to metal site molar ratio that affect the activity of the catalyst and selectivity of CHB during the hydroalkylation of benzene. Summary of preferable operating conditions from literature reports for the hydroalkylation of benzene is reported in Table 8. An increase in the reaction temperature leads to an increase in the benzene conversion due to an increase in reaction rates at higher temperatures; however, higher temperature leads to more side reactions leading to a drop in hydroalkylation selectivity. Furthermore, too much high temperature favors dehydrogenation reactions leading to a drop in hydrogenation activity as well. Similarly, hydrogen pressure has a positive influence on benzene conversions due to an increase in hydrogen availability on the catalyst surface at higher pressure. However, high pressure favors hydrogenation reactions leading to lower hydroalkylation selectivity. The same is the case with hydrogen to benzene ratio with higher hydrogen to benzene ratio favoring benzene conversion, and very high values of hydrogen to benzene ratio leads to lower CHB selectivity. In view of the above, there are optimum values for all these parameters where benzene conversion and CHB selectivity are at commercially feasible values. The performance of benzene hydroalkylation catalysts mentioned in the literature is summarized in Table 8. A list of several catalyst formulations reported in the literature is described in Table 9, out of which catalysts 5, 6, and 8 have shown superior catalytic performance in hydroalkylation of benzene at reasonably higher benzene conversions and exhibited good selectivity for CHB [144].

Table 8 Summary of suitable features of reported bi-functional hydroalkylation catalyst

Operating condition	Benzene conversion	CHB selectivity
Temperature	Favorable	Nonfavorable
Pressure	Favorable	Nonfavorable
Contact time	Favorable	Nonfavorable
Benzene to H_2 mole ratio	Favorable	Nonfavorable

1.3 Toluene Alkylation with Methanol to Styrene

Styrene is the most important part of the value chain of the modern petrochemical industry, and its market is continuously growing at a rate of 4% per year. Its demand has grown from around 20,000 kilotons in 2000 to around 28,000 kilotons in 2010 [145]. The demand for synthetic styrene-butadiene rubber (SBR) increased during World War II, and this prompted the rapid development of technology and the expansion of its capacity. The process for styrene was first developed by Dow Chemical in the 1930s in the USA and BASF company in Germany, and this effort consummated in the commissioning of several large-scale production facilities and styrene became an important raw material in the chemical industry. Today, polystyrene is the most important polymer synthesized from polystyrene. Styrene is also the building block for several other polymers and co-polymers like styrene-butadiene rubber (SBR), styrene-acrylonitrile (SAN) plastic, acrylonitrile-butadiene-styrene (ABS) plastic, expanded polystyrene foam (EPS), and unsaturated polyester resins. A number of products are produced across a wide range of industries by using the aforementioned materials as there is no direct end use for styrene. Many of these products can be recycled and offer very good insulation qualities. These products can be used in packaging, electronics for consumer applications, construction, transportation, and medical applications. The conventional processes for styrene production are given below.

1.3.1 Conventional Process for Production of Styrene

Currently, styrene is produced on an industrial scale by employing two major processes: (1) Dehydrogenation of ethylbenzene (EB) in an adiabatic system developed by ABBLummus/UOP, which is also known as the Classic SM™ process, and (2) SMPO process developed by SHELL.

The other processes for production of styrene are, e.g., STEX process by Toray in which styrene is extracted from pyrolysis gasoline and the isothermal dehydrogenation of ethyl benzene (EB) by Lurgi [146]. EB required for the dehydrogenation is produced by alkylation of benzene with ethylene in the liquid phase. Some of the EB producing processes are the EBMax™ by Mobil–Raytheon and EBOne™ by UOP (Fig. 10).

Table 9 Performance of different hydroalkylation catalysts described in the literature

Sr. no.	Catalyst	Operating conditions	Conversion of benzene (%)	Selectivity (%)	Ref. no	Remarks
1	5 wt%Ni/ SiO$_2$-Al$_2$O$_3$	473 K, 58 bar, 0.6 h	35%	64% CHB	[136]	Batch process
2	Pt/Ni/Re-13X	443 K, pressure = 35 bar, H$_2$/HC = 1:1 LHSV(h^{-1}) = 16	20%	CH 20% CHB 75% Others 5%	[127]	Low benzene conversion with tri-metallic/bifunctional catalyst and 50% drop in activity in 500 min of operation
3	0.2%Pd/Hβ25	473 K, pressure = 50 bar, H$_2$/HC = 1:1	28.1%	CH 24.9% CHB 67.2% DCHB 7.9%	[126]	Low benzene conversion under batch conditions
4	0.2%Ru/Hβ25	443 K, pressure = 10 bar	28%	CH 50% CHB 40% DCHB 10%	[137]	Low benzene conversion under batch conditions
5	0.3%Ru/0.3% Sn/MCM-22	393 K, Pressure = 8 bar, H$_2$/HC = 1:1, WHSV(h^{-1}) = 1	43.9%	CH 12.8% CHB 71.4% DCHB15.2% Others 0.6%	[119]	Bimetallic-functional catalyst comprising proprietary zeolite
6	0.3%Pd/MCM-22	423 K, pressure = 10 bar, WHSV(h^{-1}) = 2, H$_2$/HC = 1:1	48.6%	CH 10.5% CHB 70.3% DCHB 17.5% Others 1.7%	[144]	Catalyst comprising patented zeolite
7	1.63%Ni/0.79%F/ 7.3%W/Al$_2$O$_3$-SiO$_2$	423 K, pressure = 55 bar, 0.09 L of H$_2$/cc of benzene	26.1%	CH 15.44% CHB 62.6% DCHB 18.3% Others 3.6%	[132]	Multi metal/functional catalyst with batch process
8	0.3%Pd/MCM-49	423 K, pressure = 10 bar, WHSV(h^{-1}) = 0.52, H$_2$/HC = 0.64	33.6%	CH 4.2% CHB 75.8% DCHB 15.5% Others 4.5%	[144]	Catalyst comprising patented zeolite
9	0.3%Pd/HBeta	1 g cat, 3.6 mg of benzene, 40 bar, T = 473 K t = 180 min	64.1%	CH 69.2% CHB 24.3% Others 6.5%	[138]	Batch process with powder catalyst
10	0.2%Pd/HY	1 g cat, 3.6 mg of benzene, 40 bar, T = 473 K t = 180 min	83.7%	CH 71.8% CHB 21.4% Others 6.7%	[138]	Batch process with powder catalyst
11	0.2%Rh/HBeta	1 g cat, 3.6 mg of benzene, 40 bar, T = 473 K t = 180 min	86.3%	CH 59.6% CHB 18.3% Others 21.9%	[138]	Batch process with powder catalyst
12	0.2%Pd@HBeta	1 g cat, 3.6 mg of benzene, 40 bar, T = 473 K t = 180 min	85.6%	CH 49.8% CHB 44% Others 6.2%	[138]	Batch process with powder catalyst employing zeolite prepared by complex procedure of coating silica-alumina framework outside the conventional Pd/HBeta
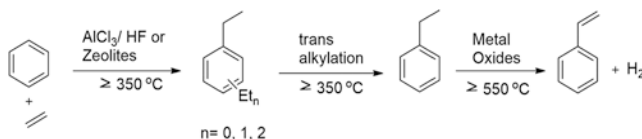
Fig. 10 Conventional scheme for styrene production

Dehydrogenation of Ethylbenzene Under Adiabatic Conditions

Styrene is commercially produced by the catalytic dehydrogenation of ethylbenzene under adiabatic conditions. Globally, 75% of the styrene plants operate using this process. IG Farbe first discovered and developed this process in 1931. The technology for this process was further modified, and commercialization of the improved technology was done by an American styrene-producing company, ABBLummus/UOP under the name of Classic SM™ process. The catalyst for this reaction is the iron oxide promoted with potassium wherein the potassium-ferrite phase, $KFeO_2$, is reported to be the active phase for the ethylbenzene dehydrogenation [147, 148]. The average life of the catalyst is approximately 1–2 years [149]. Formation of coke takes place by the polymerization of the product styrene, which is promoted by the presence of Brönsted basic sites during the course of the reaction, which subsequently decomposes to graphite-like structures via dehydrogenation on the catalyst surface [150]. The catalyst is regenerated in the presence of steam wherein the gasification process of carbonaceous deposits is reported to take place in the presence of potassium. Carbon deposited on the catalyst surface forms carbon monoxide (CO) and carbon dioxide (CO_2) in the presence of steam ($C + H_2O \rightarrow CO + H_2$ followed by $CO + H_2O \rightarrow CO_2 + H_2$).

The flow scheme of a typical adiabatic EB dehydrogenation plant as used by, e.g., ABB Lummus/UOP is shown in Fig. 11 and contains the following process steps and units [151]: (1) a superheater up to a maximum temperature of ≈993 K for the generation of steam to achieve a temperature of 913 K required for the reaction. (2) Two adiabatic, fixed-bed, radial flow reactors, which comprise the dehydrogenation unit, and the outlet stream of the first reactor is reheated before passing through the second reactor as there is a drop in the process temperature under adiabatic reaction conditions. Steam is also used for dilution of the vaporized feed, which is a mixture of fresh ethylbenzene in combination with the recycled ethylbenzene from the distillation tower. The optimum styrene yield is achieved at the minimum cost of the utility by adjusting the feed ratio of steam to ethylbenzene. With this, the conversion of ethylbenzene in the first reactor is about 35 and 65% overall.

As low pressures favor the reaction, the reactors are operated under a vacuum of 0.5–0.8 atm. (3) An efficient heat recovery system is used to recover the heat from the reactor effluent to minimize the energy consumption. (4) The effluent from the reactor is condensed and (5) separated into vent (off) gas and (6) a stream of steam condensate. The off-gas stream (5) consisting mainly of hydrogen and carbon dioxide is used as fuel for generation of steam in the superheater or as a feed stream for generation of chemical hydrogen after compression and recovery of the aromatics
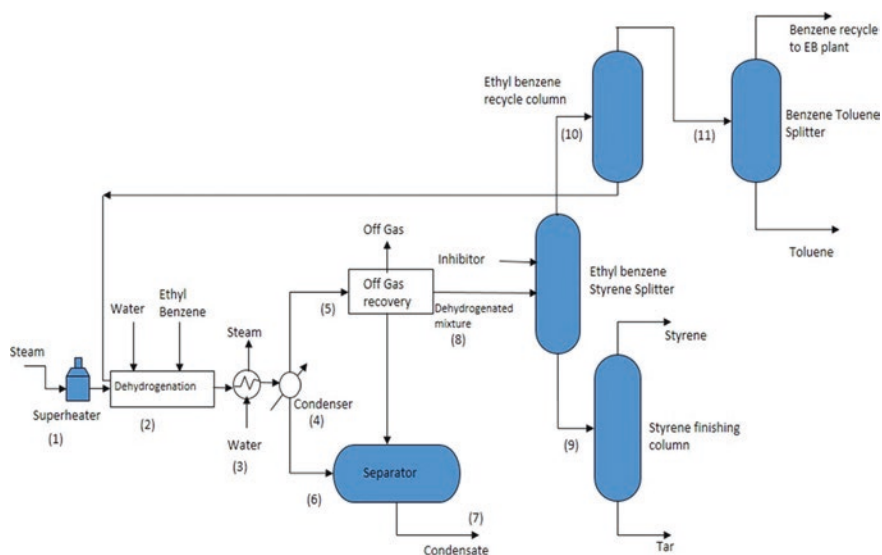
Fig. 11 The process flow of a typical adiabatic ethylbenzene dehydrogenation plant. (Adapted from [151])

by passing through the off-gas recovery section. The steam condensate (6) is reused after steam-stripping and treatment. The separator (7) separates the hydrocarbon and water phases from the condenser (4) and off-gas recovery section (5). The styrene monomer product (9), recycle ethylbenzene (10), and other aromatic byproducts like benzene, toluene, and α-methylstyrene (11) are recovered from the fractionator (8). Competing reactions that take place are the thermal dealkylation of ethylbenzene to benzene and the catalytic conversion of styrene to toluene [152]. The polymerization of styrene in the process equipment is prevented by addition of inhibitors like free radical scavengers. Typically, at 69% EB conversion, over 97 mol% selectivity to styrene is obtained along with 99.85 wt% purity of styrene monomer for this process. There are however several drawbacks in this process. The overall reaction of dehydrogenation of ethylbenzene is thermodynamically limited and endothermic in nature with $\Delta H = 124.9$ kJ mol^{-1} at 873 K. The process requires steam to be generated at high temperatures and supplied to the adiabatic reactors for the reaction temperatures of above 873 K [148, 153]. However, the use of high quantity of steam acts as a feed diluent to shift the reaction to higher equilibrium conversions [148, 153] and also prevents catalyst deactivation by reducing coke formation. Further deactivation of the catalyst also takes place by other processes like (1) physical degradation, (2) change in oxidation state of the Fe_2O_3 due to metastable Fe-carbide formation, and (3) loss and/or redistribution of potassium promoters [153].

The plant producing styrene also has other disadvantages such as the reactor operating under low pressure/vacuum, the four-column separation unit, the requirements of superheated steam for the reaction, and the interstage reheater that is costly. Some of these disadvantages have been overcome with the development of

the SMART SM™ process based on the Classic SM™ by ABBLummus/UOP [146]. In this process, ethylbenzene is dehydrogenated in the presence of molecular oxygen resulting in the formation of water and styrene. The heat required for the dehydrogenation reaction is supplied by the oxidative dehydrogenation reaction. This modification results in the reduction of the superheated steam requirements and eliminates the need for the costly interstage reheater and also results in EB conversion of higher than 80% with 99.85 wt% purity of styrene monomer.

Auto-oxidation of Ethylbenzene, Followed by Dehydration (SMPO Process)

The process developed and used by Royal Dutch SHELL is another major styrene production route and accounts for 15% of the styrene produced globally. It is an altogether different approach to styrene [151]. Propylene epoxide is coproduced along with styrene, starting from ethylbenzene [154]. The process comprises auto-oxidation of ethylbenzene to ethylbenzene hydroperoxide (90% selectivity) in the presence of air over a catalyst mixture consisting of zinc and copper oxides. The conversion of EB (13%) is kept low to minimize the formation of byproducts. The oxygen transfer between the ethylbenzene hydroperoxide and propene then leads to the formation of the corresponding 1-phenylethanol with >70% selectivity and propene-epoxide with 70–85% selectivity in the presence of a metallic catalyst along with acetophenone (5–7% selectivity). The metallic catalysts used are molybdenum in liquid-phase (ARCO) [147] or heterogeneous titanium catalyst (SHELL) [155]. The acetophenone co-produced in the oxygen transfer process is also hydrogenated in the liquid phase to 1-phenylethanol to improve the yields. A selectivity of 92% for 1-phenylethanol is obtained at acetophenone conversion of 90%. Subsequently, styrene is formed by gas-phase dehydration of 1-phenylethanol over highly selective titania/silica catalyst at 573 K, after which styrene monomer purity of 99.7 wt% is typically obtained in the process. The ratio of styrene to propylene epoxide produced in this process is approximately 2–2.5. The description of the flow scheme of a typical ethylbenzene auto-oxidation plant containing the following process steps and units is given below [155], and the flow scheme is given in Fig. 12.

The plant consists of the auto-oxidation reactor, where the EB oxidation takes place in the presence of air or oxygen to produce ethylbenzene hydroperoxide, and the second reactor, an epoxidation reactor, where the transfer of oxygen from the obtained hydroperoxide to propene takes place to produce 1-phenyl ethanol and propylene oxide. Both reactors are maintained at a temperature of 373–403 K and pressure in the range of 20–50 bar. The effluent of the second reactor is sent to the first distillation column where the unreacted propylene is separated from the propylene epoxide/1-phenylethanol mixture, and this effluent from the first distillation column is subsequently fed to the second distillation column for the recovery of propylene epoxide. The last step is the conversion of 1-phenylethanol to styrene in the dehydration reactor. The SMPO is a "cleaner" and much less energy-intensive process as compared to the conventional dehydrogenation route (less by-products). However, the serious drawback of this combined reaction is that capacity of styrene
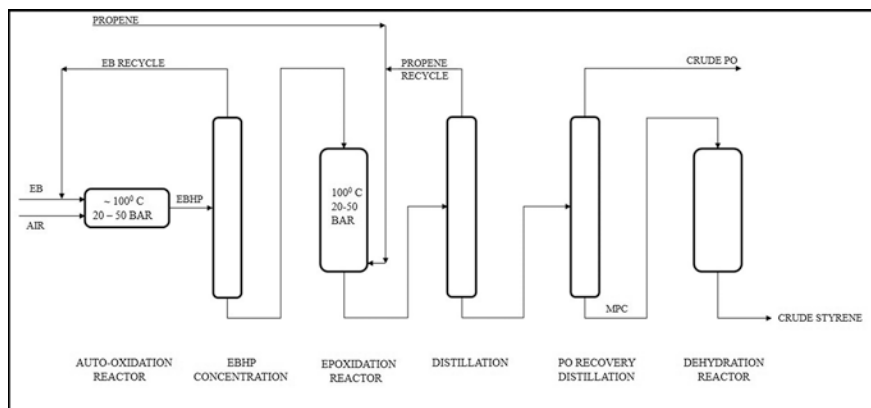
Fig. 12 Simplified flow diagram of the SMPO process. (Adapted from [154])

production is controlled by the demand for propylene epoxide required for the production of propylene glycols and polyurethanes. Therefore, attempts are being made to carry out direct epoxidation of propene to propylene epoxide on catalysts based on silver and gold in the presence of propene, hydrogen, and oxygen [149]. SHELL is currently exploring another source of oxygen, cumene hydroperoxide from phenol plants [149]. Another drawback in the SMPO production plant is the use of high-pressure reactors (20–50 bar). Hence, there is a need to develop energy-efficient and cost-effective process for styrene production, considering the aforementioned limitations of currently practiced commercial processes.

1.3.2   Development of Alternate Process for Styrene Production

Toluene and methanol can be alkylated for the production of styrene as an alternative route based on the single-step side-chain alkylation to produce styrene directly with the formation of hydrogen and water as co-products. A great deal of research has been done in the last four to five decades in this area; however, the development of the catalyst to match the yields and selectivity of the commercial processes has been difficult. The advantages of this process are the use of cost-effective raw materials. In any process, about 90% of the operating cost comprises the raw materials used for production, and lower cost feedstocks can impact the economics of the process to a large extent. The raw material savings are obtained by replacing toluene and methanol with benzene and ethylene. The new process completely eliminates the highly energy-intensive EB dehydrogenation step and is one of the primary drivers for research in this area. This step is a part of the conventional process that uses large amounts of superheated steam to provide the endothermic heat of reaction and is a significant addition to the operating cost of the plant. The endotherm is about half as large for the side-chain alkylation reaction, and this, combined with the

reduced number of processing steps, leads to a substantial reduction in the cost of capital investment as compared to the existing technology.

1.3.3 Chemistry of Side-Chain Methylation of Toluene with Methanol

In the base-catalyzed alkylation of toluene with methanol, the addition of the methyl group takes place on the side chain attached to the ring, and hence the process is called side-chain alkylation of toluene. The main reaction products are ethyl benzene and styrene, as shown in Fig. 13. The side-chain reaction of toluene with methanol has received worldwide attention since it has the potential for a new novel route to styrene production. Conceptually, this reaction occurs in two parts: the formation of formaldehyde by endothermic dehydrogenation of methanol and the exothermic addition of formaldehyde to toluene to produce styrene and ethyl benzene. Both processes, when properly balanced, make the entire process of side-chain toluene methylation nearly thermodynamically zero [156].

This reaction was first reported over low Si/Al ratio X zeolites with moderate basicity wherein high selectivity of styrene and ethylbenzene was obtained in the toluene methylation [157]. After this work, many catalysts have been reported based on modified X, Y, and other zeolites. Styrene and ethylbenzene were the main products over Na-, K-, Rb-, and Cs-modified X and Y zeolites, while xylene was observed over Li-X and Li-Y zeolites during toluene alkylation with methanol [158]. Side-chain alkylation was favored over Cs- and B-modified zeolite 13X deposited with Cu and Ag in the presence of hydrogen as a carrier gas [152]. Binary zeolites prepared using KX, KY, KM, and KZSM-5 showed higher activity as compared to the individual zeolites. The binary zeolites, when further modified with KOH and boric acid, showed improved selectivity to styrene, which implies that the optimum level of acid–base sites is essential for the reaction [159]. Further studies reinforced that the selectivity to side-chain alkylation improved with the addition of phosphoric and H_3BO_3 to ion exchange solution. High selectivity of >50% for styrene (SM) and EB calculated on the basis of methanol was observed on Cs-X zeolite modified with borate. The high selectivity for styrene over Cs-X could be explained on the basis of the adsorption of toluene among two or more large cations present in the X-zeolite super-cage with large number of cations in such a way that (1) the toluene molecule was at higher electrostatic potential than expected and (2) the methyl group only was easily accessible for alkylation (3) because of the strong interaction of cations with aromatic molecules. Also, incorporation of the borate in the super-cage slowed down the decomposition of the real alkylating agent, formaldehyde [160].
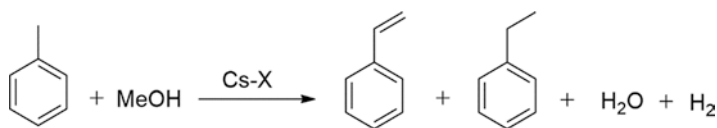
Fig. 13 Side-chain alkylation of toluene with methanol

The Cs-X zeolite shows higher alkylation activity as compared to boron-impregnated Cs^+ exchanged X, and this may be due to the increase in acidity of the boron-impregnated catalyst [161–164]. On the other hand, boron-impregnated catalyst exhibited higher selectivity to toluene alkylation and activity compared to Cs-X zeolites impregnated with CsO since it increased the dehydrogenation activity for methanol [165]. This was because the incorporation of boron results in a lowering of the overall basic strength of the CsO cluster by producing $B_2Cs_2O_4$ species inside the zeolite channels.

The primary aim of the addition of boron to Cs-X was to poison the higher strength basic sites in order to reduce the decomposition of formaldehyde to carbon monoxide during the side-chain toluene methylation without inhibiting the active sites required for alkylation [166]. In another study, it was reported that alkali-exchanged X and Y zeolites with high basicity were active for toluene alkylation but also caused decomposition of methanol to CO to a higher extent. However, the Cs-exchanged L and beta zeolites exhibited low formic acid decomposition to CO but required higher temperatures to attain similar aromatic yields during the side-chain alkylation compared to X and Y zeolites [167].

Theoretical studies involving quantum chemical calculation have suggested that the requirement of basic sites for side-chain alkylation is indispensable. However, specific combinations of acidic and basic sites promote side-chain alkylation to achieve better selectivity [168]. Rb-X promoted with a small amount of Li^+ ions was more active as compared to Rb-X for *p*-xylene side-chain alkylation [169, 170] due to the presence of slightly stronger acid sites in Li-Rb-X. The decomposition of formic acid intermediate was suppressed due to the incorporation of Li^+ ions.

It is reported that in toluene alkylation process, the ability to dehydrogenate methanol and the selectivity to side-chain methylation of toluene are directly proportional to the basicity imposed by the alkali metal cation-exchanged zeolites. The topology of the zeolite and the Si/Al ratio are responsible for the proximity of acid–base sites and the zeolite basicity. The introduction of metal oxide clusters into the zeolite pores imparts high basicity to the zeolite and can promote side-chain toluene alkylation with methanol [165, 171, 172]. However, large amounts of CO are formed from methanol decomposition over such strongly basic material.

It was reported that Fe-Mo dual catalyst oxide deposited over Cs^+-exchanged zeolites leads to enhancement in the styrene/ethylbenzene ratio by a factor of 4.5. The Fe-Mo promoted zeolites were found to be active at 598 K [163] as against the requirement of temperatures higher than 648 K for the unpromoted single Cs^+-exchanged catalysts. This may be due to the concerted interaction of toluene with Cs^+-exchanged zeolite and Fe-Mo oxide.

The use of layered double hydroxides (LDH) for side-chain toluene alkylation is also reported [173]. As shown in Table 10, Mg-Al-LDH was selective for toluene side-chain alkylation with methanol by mainly producing styrene and EB, while the other LDHs synthesized using Co, Ni, Cu, and Zn gave a mixture of side chain as well as ring-alkylated products, viz., xylene and mesitylene. The selectivity of styrene was found to be higher over Mg-Al-LDHs with low Al content. Higher ethyl benzene formation was observed at 673 K.

Table 10 The toluene side-chain alkylation on calcined LDHs: effect on conversion and product [173]

Catalysts	Toluene conversion (wt%)	Product yield (mol%)			
		Ethylbenzene	Styrene	Xylene	Mesitylene
Mg-Al (3.0)	36.4	22.3	9.6	3.0	
Mg-Al (4.0)	34.7	19.2	12.0	2.1	
Mg-Al (5.0)	28.1	14.6	11.3	1.2	
Mg-Al (7.0)	21.0	10.2	9.1		
Mg-Al (10.0)	17.6	7.0	8.9		
Co-Al (3.0)	26.0	15.8	–	8.7	
Ni-Al (3.0)	31.5	14.2	–	15.4	1.1
Cu-Al (3.0)	34.8	16.3	–	13.6	
Zn-Al (3.0)	22.7	16.8	–	5.7	–
MgO	10.6	7.9	2.1	–	–

The effect of ZnO and other additives like Cs2O and ZrB2O5 on the side-chain methylation of toluene has been reported to substantially increase both toluene conversion and styrene selectivity by promoting the formation of formaldehyde from methanol, which in turn increases styrene formation and reduces the transfer hydrogenation of styrene to ethylbenzene [174]. High toluene conversion of 4.6% and styrene selectivity of 76.1% were obtained over ZnO/Cs-X and ZrB2O5/Cs-X, respectively.

1.3.4 Industrial Process for Toluene Alkylation with Methanol to Styrene: Exelus Process

The researchers at Exelus have developed a new process named ExSyM for producing styrene monomer from toluene and methanol. This has been accomplished by integrating principles of process design and reaction engineering with advances in zeolite catalyst science and has been instrumental in achieving significantly higher selectivities (>80%) for EB/SM at 698 K and 1 atm. pressure by reduction in methanol decomposition rates and enhanced conversions. The flow scheme is shown in Fig. 14. Hence, the catalyst designed for the new ExSyM process system is much superior as compared to other catalyst systems designed for the side-chain alkylation reaction in terms of its performance. The developed catalyst is currently being tested for its long-term stability.

1.4   Future Prospective

The following section gives a way forward and proposes certain future directions for the process discussed in the aforementioned sections.
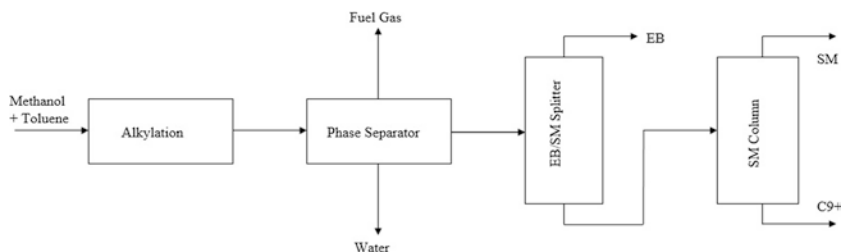
Fig. 14 Toluene alkylation with methanol to styrene: Exelus process

1.4.1 C$_4$ Alkylation

The commercialization of solid acid-based catalysts for C$_4$ alkylation has revolutionized the process for alkylate production. It has altogether eliminated the safety and environmental concerns associated with the conventional mineral acid-based processes. However, another technology that is coming up as a greener alternative is the ionic liquid (IL)-based C$_4$alkylation. Recently, mega oil firms M/s Chevron and M/s UOP-Honeywell have collaborated and replaced one of their existing alkylation plants using HF as the catalyst with ionic liquid-based catalysts. This is the best example of retrofitting the new technology with the conventional one. Therefore, it can be said that the ionic liquid-based technology can be best suited for retrofitting with the conventional C$_4$ alkylation technologies and easily adapted by companies who want to shift to greener alternatives with minimal capital expenditure. However, the issues associated with the use of ionic liquids are their cost, recyclability, and handling problems as the most active ionic liquids are moisture sensitive, which leads to the formation of HCl and finally the deactivation of the ionic liquids. Unless these issues are addressed, the use of ionic liquid-based technology will lead to high operating costs. Nevertheless, one way for use of the IL-based technology is retrofitting with the existing HF/H$_2$SO$_4$-based plants while incurring minimal capital expenditure. On the other hand, the solid acid-based C4 alkylation technologies can be adapted by companies which are proposing to set up new plants for the production of alkylate. The solid acid catalyst-based C$_4$ alkylation processes are economically feasible with lower operations cost as compared to the conventional mineral acid and the new ionic liquid-based processes due to the excellent recyclability of the solid acid catalyst. In future, we can see both the solid acid and the ionic liquid-based C$_4$ alkylation technology being adapted by companies, which eventually will lead to the phasing out of the conventional mineral acid-based technologies.

1.4.2 Hydroalkylation of Benzene

In future, there are high chances of this process getting commercialized keeping in view of the applicative potential of CHB. The effluent stream of the hydroalkylation process can be separated into three fractions: (a) C6 stream consisting of benzene and cyclohexane, (b) cyclohexylbenzene, and (c) C18 stream consisting of dicyclohexylbenzene (DCHB). As the raw material benzene is a stream from the refinery, the proposed process can be integrated with commonly practiced continuous catalytic reforming (CCR) operation for naphtha up-gradation in refinery operation to produce high RON gasoline blendstock. The flow scheme of the process for such integration is shown below in Fig. 15.

The proposed scheme utilizes benzene from the BTX product stream of the CCR unit, which is subjected to hydroalkylation in the presence of hydrogen to produce CHB. After the separation of CHB, the fraction containing C_6 hydrocarbons can be used as motor gasoline blendstock or can be recycled to the hydroalkylation reactor with the removal of purge stream to eliminate cyclohexane buildup in the C_6 recycle streams or alternatively fraction containing C_6 hydrocarbons can be blended with refinery CCR feedstock. In the CCR reactor, cyclohexane in the C_6 fraction is converted to benzene by dehydrogenation reaction, which can be recycled. The fraction containing dicyclohexylbenzene can be transalkylated using additional benzene to enhance the CHB yields using zeolite-based catalysts such as beta and Y-zeolites [175].
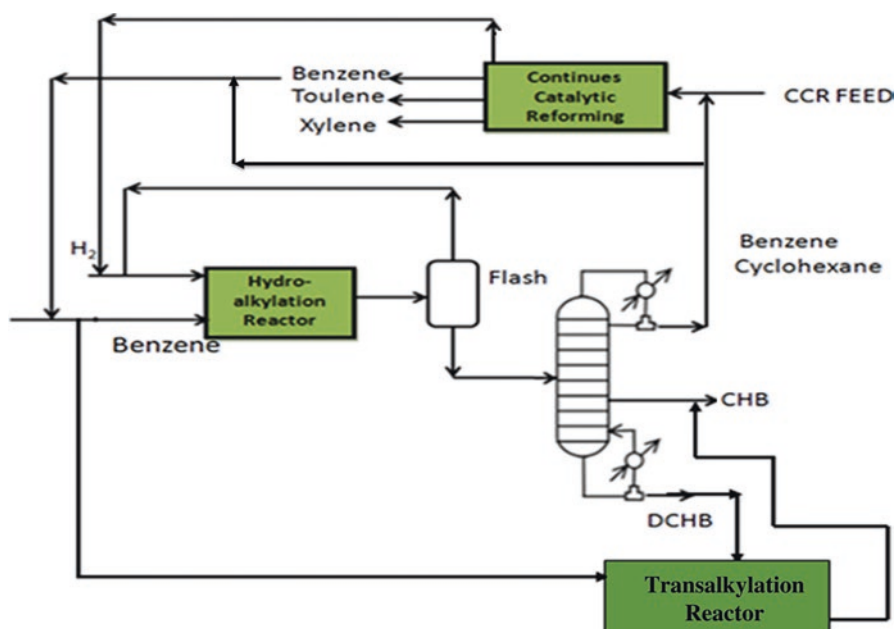
Fig. 15 Process scheme for integration of the CHBproduction with the existing refinery

1.4.3 Toluene Alkylation with Methanol to Styrene

The novel route for producing styrene via side-chain toluene alkylation with methanol appears to be a promising alternative technology. The main focus in the past decades has been on developing suitable catalysts for this reaction. To date, the model catalyst for the toluene side-chain alkylation has been the Cs-modified zeolite X and has shown good catalytic performance. However, more intense research is required to develop highly active catalysts for styrene production by toluene side-chain alkylation. The catalytic conversion of toluene achieved until now is still unsatisfactory due to the difficulty in the activation of the C–H on the toluene side chain. In future, to achieve the activation of the C-H bond, low valent transition metal catalysts such as Pd, Rh, and Ru, which are used extensively in the formation of C–C bond via C–H activation, should be tested for toluene side-chain alkylation reaction [176–178]. Meanwhile, the work done on composite catalysts for dehydrogenation of MeOH can shed some light on catalyst design and aid in coupling of the EB dehydrogenation and toluene side-chain alkylation to improve the selectivity to styrene [179, 180]. Additionally, the use of alternative reactants like formaldehyde and syngas (CO + H$_2$) can be investigated instead of methanol. Specifically, formaldehyde looks promising as it is an intermediate of methanol dehydrogenation and could be a potential reactant for enhancing the conversion of toluene and selectivity to styrene.

References

1. Technical background on India BS VI fuel specifications by International Council on Clean Transportation
2. www.enggcyclopedia.com
3. Hilman IM, Muraza O (2016) Conversion of Isobutylene to Octane-Booster Compounds after Methyl tert-Butyl Ether Phase out: The Role of Heterogeneous Catalysis. Ind Eng Chem Res 55: 11193–11210
4. Albright LF (2003) Alkylations Industrial, Encyclopedia of Catalysis; Edited by : Howath, I. T, John Wiley and Sons, New York, Vol. 1, pp 226-281
5. Pryor P (2001). In: Leawood KS (ed) Personal communication. Stratco, Leawood
6. http://www.refinerlink.com/blog/Liquid_Gold_Black_Box/
7. Corma A, Martínez A (1993) Chemistry, catalysts, and processes for isoparaffin-olefin alkylation: actual situation and future trends. Catal Rev Sci Eng 35(4):483–570
8. Boronat M, Viruela P, Corma A (1999) Theoretical study of bimolecular reactions between carbenium ions and paraffins: the proposal of a common intermediate for hydride transfer, disproportionation, dehydrogenation, and alkylation. J Phys Chem B 103(37):7809–7821
9. Branzaru J (2001) Introduction to sulfuric acid alkylation unit process design. Stratco, Leawood
10. Hommeltoft SI (2001) Isobutane alkylation—Recent developments and future perspectives. Applied Catalysis A: General 221, 421–428

11. Albright LF (2003) Alkylation of isobutane with C3-C5 olefins to produce high-quality gaso-lines: physicochemical sequence of events. Ind Eng Chem Res 42(19):4283–4289
12. Scott B (1992) Hydrocarbon Process 71:77
13. Hoffman HL (1991) Hydrocarbon Processing, 37
14. Singhal S, Agarwal S, Arora S, Singhal N, Kumar A (2017) Solid acids: potential catalysts for alkene–isoalkane alkylation. Catal Sci Technol 7:5810–5819
15. Kranz K (2003) Alkylation chemistry: mechanisms, operating variables and olefin interac-tions. Stratco, Leawood
16. Hommeltoft SI, Ekelund O, Zavilla J (1997) Role of ester intermediates in isobutane alkylation and its consequence for the choice of catalyst system. Ind Eng Chem Res 36(9):3491–3497
17. Corma A, Martínez A, Martínez C (1994) Isobutane/2-butene alkylation on ultrastable Y zeo-lites: influence of zeolite unit cell size. J Catal 146(1):185–192
18. Corma A, Juan-Rajadell MI, López-Nieto JM, Martinez A, Martínez C (1994) A compara-tive study of O_4^{2-}/ZrO$_2$ and zeolite beta as catalysts for the isomerization of n-butane and the alkylation of isobutane with 2-butene. Appl Catal A Gen 111(2):175–189
19. Unverricht S, Ernst S, Weitkamp J (1994) In: Weitkamp J, Karge HG, Pfeifer H, Hölderich W (eds) Zeolites and related microporous materials: state of the art. Elsevier, Amsterdam, p 1693
20. Cardona F, Gnep NS, Guisnet M, Szabo G, Nascimento P (1995) Reactions involved in the alkylation of isobutane with 2-butene and with propene on a USHY zeolite. Appl Catal A Gen 128(2):243–257
21. Chu YF, Chester AW (1986) Reactions of isobutane with butene over zeolite catalysts. Zeolites 6(3):195–200
22. Corma A, Martínez A, Arroyo PA, Monteiro JLF, Sousa-Aguiar EF (1996) Isobutane/2-butene alkylation on zeolite beta: influence of post-synthesis treatments. Appl Catal A Gen 142(1):139–150
23. Nivarthy GS, He Y, Seshan K, Lercher JA (1998) Elementary mechanistic steps and the influ-ence of process variables in isobutane alkylation over H-BEA. J Catal 176(1):192–203
24. Loenders R, Jacobs PA, Martens JA (1998) Alkylation of isobutane with 1-butene on zeolite beta. J Catal 176(2):545–551
25. Mukhergee M, Nehlsen J (2007) Reduce alkylate costs with solid-acid catalysts. Hydrocarbon Process 86:110–114
26. Stöcker M, Mostad H, Rørvik T (1994) Isobutane/2-butene alkylation on faujasite-type zeo-lites (H EMT and H FAU). Catal Lett 28(2–4):203–209
27. Feller A, Guzman A, Zuazo I, Lercher JA (2004) On the mechanism of catalyzed isobutane/butene alkylation by zeolites. J Catal 224(1):80–93
28. Albright LF (2009) Present and future alkylation processes in refineries. Ind Eng Chem Res 48(3):1409–1413
29. Weitkamp J, Jacobs PA (1993) "Isobutane/1-Butene Alkylation on Pentasil-Type Zeolite Catalysts" Studies in Surface Science and Catalysis; Volume 75; pp 1735-1738, New fron-tiers in catalysis. Edited by: Guczi L, Solymosi F, Tetenyi P, Proceedings of the 10th interna-tional congress on catalysis. Elsevier, Amsterdam,
30. Khadzhiev SN, Gerzeliev IM. In: Am. Chem. Soc., New York City Meeting, 25–30 August 1991, p 799
31. Gardos G, Redey A, Kovacs M, Kristof J (1983) Activity change of the H(NH$_4$), LA-FAU, Y zeolite with the time in the alkylating reaction of isobutane. Hung J Ind Chem 11:403–407
32. Huss A Jr, Kirker GW, Keviller KM, Thomson RT (1991) Isoparaffin-olefin alkylation pro-cess. US Patent 4992615
33. Chu CT, Hussain A, Huss A Jr, Kresge CT, Roth WJ (1993) Isoparaffin-olefin alkylation process with zeolite MCM-36. US Patent 5258569
34. Huang TJ (1983) Heterogeneous isoparaffin/olefin alkylation. US Patent 4384161
35. Guo C, Liao S, Qian Z, Tanabe K (1994) Alkylation of isobutane with butenes over solid acid catalysts. Appl Catal A Gen 107(2):239–248
36. Corma A, Gómez V, Martínez A (1994) Zeolite beta as a catalyst for alkylation of isobutane with 2-butene. Influence of synthesis conditions and process variables. Appl Catal A Gen 119(1):83–96

37. Corma A, Martínez A, Martínez C (1994) Influence of process variables on the continuous alkylation of isobutane with 2-butene on superacid sulfated zirconia catalysts. J Catal 149:52–60
38. Chellappa AS, Miller RC, Thomson WJ (2001) Supercritical alkylation and butene dimerization over sulfated zirconia and iron-manganese promoted sulfated zirconia catalysts. Appl Catal A Gen 209(1–2):359–374
39. Krylov OV (2004) Heterogeneous catalysis. Akademkniga, Moscow
40. Sarsani VR, Wang Y, Subramaniam B (2005) Toward stable solid acid catalysts for 1-butene + isobutane alkylation: investigations of heteropolyacids in dense CO_2 media. Ind Eng Chem Res 44(16):6491–6495
41. Okuhara T, Yamashita M, Na K, Misono M (1994) Alkylation of isobutane with butenes catalyzed by a cesium hydrogen salt of 12-tungstophosphric acid. Chem Lett 23(8):1451–1454
42. Essayem N, Kieger S, Coudurier G, Védrine JC (1996) Comparison of the reactivities of $H_3PW_{12}O_{40}$ and $H_4SiW_{12}O_{40}$ and their K^+, NH_4^+ and Cs^+ salts in liquid phase isobutane/butene alkylation. Stud Surf Sci Catal 101(A):591–600
43. Gayraud PY, Stewart IH, Derouane-Abd Hamid SB, Essayem N, Derouane EG, Védrine JC (2000) Performance of potassium 12-tungstophosphoric salts as catalysts for isobutane/butene alkylation in subcritical and supercritical phases. Catal Today 63(2–4):223–228
44. Blasco T, Corma A, Martínez A, Martínez-Escolano P (1998) Supported heteropolyacid (HPW) catalysts for the continuous alkylation of isobutane with 2-butene: the benefit of using MCM-41 with larger pore diameters. J Catal 177(2):306–313
45. Botella P, Corma A, López-Nieto JM (1999) The influence of textural and compositional characteristics of Nafion/silica composites on isobutane/2-butene alkylation. J Catal 185(2):371–377
46. Lyon C, Subramaniam B, Pereira C (2001) Enhanced isooctane yields for 1-butene/isobutane alkylation on SiO2-supported Nafion® in supercritical carbon dioxide. Stud Surf Sci Catal 139:221–228
47. Davis BH, Keogh RA, Srinivasan R (1994) Sulfated zirconia as a hydrocarbon conversion catalyst. Catal Today 20(2):219–256
48. Song X, Sayari A (1996) Sulfated zirconia-based strong solid-acid catalysts: recent progress. Catal Rev Sci Eng 38:329–412
49. Arata K (1996) Preparation of superacids by metal oxides for reactions of butanes and pentanes. Appl Catal A Gen 146(1):3–32
50. Arata K, Matsuhashi H, Hino M, Nakamura H (2003) Synthesis of solid superacids and their activities for reactions of alkanes. Catal Today 81(1):17–30
51. Satoh K, Matsuhashi H, Arata K (1999) Alkylation to form trimethylpentanes from isobutane and 1-butene catalyzed by solid superacids of sulfated metal oxides. Appl Catal A Gen 189(1):35–43
52. Arata K, Hino M (1990) Solid catalyst treated with anion. XVIII. Benzoylation of toluene with benzoyl chloride and benzoic anhydride catalysed by solid superacid of sulfate-supported alumina. Appl Catal 59(1):197–204
53. Smirnova MY, Urguntsev GA, Ayupov AB, Vedyagin AA, Echevsky GV (2008) Isobutane/butene alkylation on sulfated alumina: influence of sulfation condition on textural, structural and catalytic properties. Appl Catal A Gen 344(1–2):107–113
54. Ferreira ML, Rueda EH (2002) Theoretical characterization of alumina and sulfated-alumina catalysts for n-butene isomerization. J Mol Catal A Chem 178(1–2):147–160
55. Yang J, Zhang M, Deng F, Luo Q, Yi D, Ye C (2003) Solid state NMR study of acid sites formed by adsorption of SO_3 onto γ-Al_2O_3. Chem Commun 3(7):884–885
56. Hino M, Kurashige M, Matsuhashi H, Arata K (2006) The surface structure of sulfated zirconia: studies of XPS and thermal analysis. Thermochim Acta 441(1):35–41
57. Prakash GKS, Olah GA (1990) Acid-Case Catalysis, Proceedings of the international symposium on Acid base catalysis, p 59
58. Rajadhyaksha RA, Chaudhari DD (1988) Alkylation of phenol by C9 and C12 olefins. Bull Chem Soc Japan 61:1379–1381

59. Olah GA, Kaspi J, Bukala J (1977) Heterogeneous catalysis by solid superacids. 3. Alkylation of benzene and transalkylation of alkylbenzenes over graphite-intercalated Lewis acid halide and perfluorinated resin-sulfonic acid (Nafion-H) catalysts. J Org Chem 42(26):4187–4191

60. Hasegawa H, Higashimura T (1980) Selective alkylation of aromatic hydrocarbons with styrene by solid polymeric oxo acids. Polym J 12(6):407–409

61. Harmer MA, Farneth WE, Sun Q (1998) Towards the sulfuric acid of solids. Adv Mater 10(15):1255–1257

62. Arata K, Matsuhashi H (1990) Solid superacids. Adv Catal 37:165–211

63. Shen W, Dubé D, Kaliaguine S (2008) Alkylation of isobutane/1-butene over periodic mesoporous organosilica functionalized with perfluoroalkylsulfonic acid group. Catal Commun 10(3):291–294

64. Heidekum A, Harmer MA, Hoelderich WF (1998) Highly selective Fries rearrangement over zeolites and Nafion in silica composite catalysts: a comparison. J Catal 176(1):260–263

65. Shen W, Gu Y, Xu H, Dubé D, Kaliaguine S (2010) Alkylation of isobutane/1-butene on methyl-modified Nafion/SBA-15 materials. Appl Catal A Gen 377(1–2):1–8

66. Misono M, Okuhara T (1993) Chemtech 23(11):23

67. Weitkamp J, Traa Y (1997), Handbook of heterogeneous catalysis. Edited by: Ertl G, Knözinger H, Weitkamp J, VCH, Weinheim, pp 2039–2069

68. Dalla Costa BO, Querini CA (2010) Isobutane alkylation with butenes in gas phase. Chem Eng J 162(2):829–835

69. Yoo K, Burckle EC, Smirniotis PG (2001) Comparison of protonated zeolites with various dimensionalities for the liquid phase alkylation of i-butane with 2-butene. Catal Lett 74(1–2):85–90

70. Corma A, Faraldos M, Mifsud A (1989) Influence of the level of dealumination on the selective adsorption of olefins and paraffins and its implication on hydrogen transfer reactions during catalytic cracking on USY zeolites. Appl Catal 47(1):125–133

71. Corma A, Faraldos M, Martínez A, Mifsud A (1990) Hydrogen transfer on USY zeolites during gas oil cracking: influence of the adsorption characteristics of the zeolite catalysts. J Catal 122(2):230–239

72. Zheng L, Xiaojin T, Lifeng H, Shuandi H (2016) Modeling of isobutane/butene alkylation using solid acid catalysts in a fixed bed reactor. China Pet Process Petrochem Technol 18(2):63–69

73. Klingmann R, Josl R, Traa Y, Gläser R, Weitkamp J (2005) Hydrogenative regeneration of a Pt/La-Y zeolite catalyst deactivated in the isobutane/n-butene alkylation. Appl Catal A Gen 281(1–2):215–223

74. Feller A, Lercher JA (2004) Chemistry and technology of isobutane/alkene alkylation catalyzed by liquid and solid acids. Adv Catal 48:229–295

75. Kirsch FW, Potts JD, Barmby DS (1968) Prepr Am Chem Soc Div Pet Chem 13(1):153–164

76. Garwood WE, Venuto PB (1968) Paraffin-olefin alkylation over a crystalline aluminosilicate. J Catal 11(2):175–177

77. Kirsch FW, Potts JD, Barmby DS (1972) Isoparaffin-olefin alkylations with crystalline aluminosilicates. I. Early studies-C4-olefins. J Catal 27(1):142–150

78. Minachev KM, Mortikov ES, Zen'kovskii SM, Mostovoi NV, Kononov NF (1977) Prepr Am Chem Soc Div Pet Chem 22:1020–1024

79. Weitkamp J (1980). In: Rees LVC (ed) Proceedings of the 5th international on zeolite conference, Heyden, London, Philadelphia, Rheine, p 858

80. Juguin B, Raatz F, Marcilly C (1988) French Patent 2631956

81. Salgado H, CT&F, Cienc (2016) Tecnol Futuro 3(6):91–104

82. Flego C, Galasso L, Kiricsi I, Clerici MG (1994) In: Delmon B, Delmon B, Froment G (eds) Catalyst deactivation. Elsevier, Amsterdam, p 585

83. Flego C, Kiricsi I, Parker WO, Clerici MG (1995) Spectroscopic studies of LaHY-FAU catalyst deactivation in the alkylation of isobutane with 1-butene. Appl Catal A Gen 124(1):107–119

84. Weitkamp J (1980) "Catalysis by zeolites", Studies in Surface Science and Catalysis; Volume 5, p 65–75; In: Imelik B, Naccache C, Ben Taarit Y, Vedrine J.C, Coudurier G, Praliaud H (eds) Elsevier, Amsterdam

85. Corma A, Martinez A, Martinez C (1996) The role of extra framework aluminum species in USY catalysts during isobutane/2-butene alkylation. Appl Catal A Gen 134(1):169–182

86. Simpson M, Wei J, Sundaresan S (1996) In: Anastas P, Williamson T (eds) ACS symposium series 626. American Chemical Society, p 105

87. Rørvik T, Mostad H, Ellestad OH, Stöcker M (1996) Isobutane/2-butene alkylation over faujasite type zeolites in a slurry reactor. Effect of operating conditions and catalyst regeneration. Appl Catal A Gen 137(2):235–253

88. De Jong KP, Mesters CMAM, Peferoen DGR, Van Brugge PTM, De Groot C (1996) Paraffin alkylation using zeolite catalysts in a slurry reactor: chemical engineering principles to extend catalyst lifetime. Chem Eng Sci 51(10):2053–2060

89. Sekine Y, Tajima Y, Ichikawa Y, Matsukata M, Kikucki E (2012) J Jpn Pet Inst 55(5):308–318

90. Querini CA, Roa E (1997) Deactivation of solid acid catalysts during isobutane alkylation with C4 olefins. Appl Catal A Gen 163(1–2):199–215

91. Zhuang Y, Ng FTT (2000) Isobutane/1-butene alkylation on LaNaY catalysts modified by alkali and alkaline-earth cations. Appl Catal A Gen 190(1–2):137–147

92. Yoo KS, Smirniotis PG (2005) Zeolites-catalyzed alkylation of isobutane with 2-butene: influence of acidic properties. Catal Lett 103(3–4):249–255

93. Pater J, Cardona F, Canaff C, Gnep NS, Szabo G, Guisnet M (1999) Alkylation of isobutane with 2-butene over a HFAU zeolite. Composition of coke and deactivating effect. Ind Eng Chem Res 38(10):3822–3829

94. Ginosar DM, Thompson DN, Burch KC (2004) Recovery of alkylation activity in deactivated USY catalyst using supercritical fluids: a comparison of light hydrocarbons. Appl Catal A Gen 262(2):223–231

95. Josl R, Klingmann R, Traa Y, Gläser R, Weitkamp J (2004) Regeneration of zeolite catalysts deactivated in isobutane/butene alkylation: an in situ FTIR investigation at elevated H2 pressure. Catal Commun 5(5):239–241

96. Sievers C, Zuazo I, Guzman A, Olindo R, Syska H, Lercher JA (2007) Stages of aging and deactivation of zeolite LaX in isobutane/2-butene alkylation. J Catal 246(2):315–324

97. Guzman A, Zuazo I, Feller A, Olindo R, Sievers C, Lercher JA (2006) Influence of the activation temperature on the physicochemical properties and catalytic activity of La-X zeolites for isobutane/cis-2-butene alkylation. Microporous Mesoporous Mater 97(1–3):49–57

98. Sievers C, Liebert JS, Stratmann MM, Olindo R, Lercher JA (2008) Comparison of zeolites LaX and LaY as catalysts for isobutane/2-butene alkylation. Appl Catal A Gen 336(1–2):89–100

99. Rørvik T, Dahl IM, Mostad HB, Ellestad OH (1995) Nafion-H as catalyst for isobutane/2-butene alkylation compared with a cerium exchanged Y zeolite. Catal Lett 33(1–2):127–134

100. Rosenbach N, Mota CJA (2005) Isobutane/2-butene alkylation with zeolite Y without Brønsted acidity. J Braz Chem Soc 16(4):691–694

101. Pine LA, Maher PJ, Wachter WA (1984) Prediction of cracking catalyst behavior by a zeolite unit cell size model. J Catal 85(2):466–476

102. Lovink HJ, Pine LA (eds) (1990) The hydrocarbon chemistry of FCC Naphtha formation. Technip, Paris, p 1

103. Dwyer J, Karim K, Ojo AF (1991) Bimolecular hydrogen transfer over zeolites and SAPOs having the faujasite structure. J Chem Soc Faraday Trans 87(5):783–786

104. Feller A, Guzman A, Zuazo I, Lercher JA (2003) A novel process for solid acid catalyzed isobutane/butene alkylation. Stud Surf Sci Catal. 145:67–72

105. Yoo K, Smirniotis PG (2002) The influence of Si/Al ratios of synthesized beta zeolites for the alkylation of isobutane with 2-butene. Appl Catal A Gen 227(1–2):171–179

106. Weitkamp J, Traa Y (1999) Isobutane/butene alkylation on solid catalysts. Where do we stand? Catal Today 49(1–3):193–199

107. Freyhardt CC, Tsapatsis M, Lobo RF, Balkus KJ, Davis ME Jr (1996) A high-silica zeolite with a 14-tetrahedral-atom pore opening. Nature 381:295–298

108. Davis ME, Saldarriaga C, Montes C, Garces J, Crowder C (1988) A molecular sieve with eighteen-membered rings. Nature 331:698–699

109. Strohmaier KG, Vaughan DEW (2003) Structure of the first silicate molecular sieve with 18-ring pore openings, ECR-34. J Am Chem Soc 125:16035–16039

110. Verboekend D, Pérez-Ramírez J (2011) Design of hierarchical zeolite catalysts by desilication. Catal Sci Technol 1(6):879–890

111. Verboekend D, Thomas K, Milina M, Mitchell S, Pérez-Ramírez J, Gilson JP (2011) Towards more efficient monodimensional zeolite catalysts: N-alkane hydro-isomerisation on hierarchical ZSM-22. Catal Sci Technol 1(8):1331–1335

112. Chen LH, Li XY, Rooke JC, Zhang YH, Yang XY, Tang Y et al (2012) Hierarchically structured zeolites: synthesis, mass transport properties and applications. J Mater Chem 22(34):17381–17403

113. de Jong KP, Zecevic J, Friedrich H, de Jongh PE, Bulut M, van Donk S, Kenmogne R, Finiels A, Hulea V, Fajula F (2010) Zeolite Y crystals with trimodal porosity as ideal hydrocracking catalysts. Angew Chem 122(52):10272–10276

114. de Jong KP, Zecevic J, Friedrich H, de Jongh PE, Bulut M, van Donk S, Kenmogne R, Finiels A, Hulea V, Fajula F (2010) Zeolite Y crystals with trimodal porosity as ideal hydrocracking catalysts. Angew Chem Int Ed 49(52):10074–10078

115. Rosalie Starling (2015) Hydrocarbon engineering energy global. https://www.energy-global.com

116. Van Broekhoven EH, Mas Cabre FR, Bogaard P, Klaver G, Vonhof M (1999) Process for alkylating hydrocarbons. US Patent 5986158

117. Buchold H, Dropsch H, Eberhardt J (2002) Proceedings of the world petroleum congress 2002, Rio de Janeiro

118. Shuang H, Lian-hai L (2006) Highly regioselective hydrogenation of biphenyl to phenylcyclohexane. In: The proceedings of the 3rd international conference on functional molecules

119. Chang CD, Cheng JC, Helton TE, Steckel MA, Stevenson SA (2000) Hydroalkylation of aromatic hydrocarbons. US Patent 6037513

120. Chen T, Cheng JC, Helton TE, Buchanan JS (2011) Process for the production cyclohexylbenzene. US Patent 7910779

121. Chen T, Cheng JC, Benitez FM, Helton TE, Stanat JE (2012) Process for the production cyclohexylbenzene. US Patent 8106243

122. Cheng J. C, Chen T, Ghosh P (2012) Process for production cyclohexylbenzene, US Patent 8178728

123. Jun Q, Komura K, Kubota Y, Sugi Y (2007) Synthesis of cyclohexylbenzene by hydroalkylation of benzene over Pd/Hβ binary catalyst. Chin J Catal 28:246–250

124. Chen TJ, Benitez FM, Cheng JC, Stanat JE, Buchanan JS (2011) Process for the production of cyclohexylbenzene. US Patent 7906685

125. Corson BB, Ipatieff VN (1937) Influence of cyclohexene concentration in the alkylation of benzene by cyclohexene. Dealkylation of cyclohexylbenzenes. J Am Chem Soc 59(4):645–647

126. Slaugh LH (1968) Hydrogenation of benzene to phenylcyclohexane with supported alkali metal catalysts. Tetrahedron 24:4523–4533

127. Fahy J, Trimm DL, Cookson DJ (2001) Four component catalysis for the hydroalkylation of benzene to cyclohexyl benzene. Appl Catal A Gen 11:259–268

128. Kumar SAK, John M, Pai SM, Ghosh S, Newalkar BL, Pant KK (2017) Selective hydroalkylation of benzene over palladium supported Y-zeolite: effect of metal acid balance. J Mol Catal 442:27–38

129. Becker CL, Nair H, Lattner JR, Kuechler KH (2016) Process for producing cyclohexylbenzene. US Patent 9458067B2

130. Truffault R (1934) Bull Soc Chim 1:391

131. Louvar JJ, Francoy A (1970) Hydroalkylation of aromatic compounds. J Catal 16:62–68
132. Slaugh LH, Leonard JA (1967) Phenylcyclohexane process. US Patent 3412165
133. Suggitt RM, Falls W, Crone JM Jr, Arkell A (1972) Hydroalkylation of mononuclear aromatic hydrocarbons. US Patent 3784617
134. Makkee M (1991) Reductive alkylation process. US Patent 5053571
135. Reed LE (1992) Hydroalkylation of aromatic hydrocarbons. US Patent 5146024
136. Yamazaki Y, Masuda A, Kawai T, Kimura S (1976) Hydroalkylation of benzene and methyl-benzenes. Bull Jpn Petrol Inst 18:25–31
137. Kralik M, Vallusova Z, Laluch J, Mikulec J, Macho V (2008) Comparison of ruthenium catalysts supported on beta and mordenite in the hydrocycloalkylation of benzene. Petrol Coal 50:44–51
138. Li Z, Fu X, Gao C, Huang J, Li B, Yang Y, Gao J, Shen Y, Peng Z, Yang J, Liu Z (2020) Enhancing the matching of acid/metal balance by engineering an extra Si-Al framework outside Pd/HBeta catalyst towards benzene hydroalkylation. Catal Sci Technol 10:1467–1476
139. Borodina IB, Ponomareva OA, Yuschenko VV, Ivanova II (2009) Hydroalkylation of benzene and ethylbenzene over metal-containing zeolite catalysts. Petrol Chem 49:66–73
140. Borodina IB, Ponomareva OA, Fajula F, Bousquet J, Ivanova II (2007) Hydroalkylation of benzene and ethylbenzene over metal containing zeolite catalysts. Microporous Mesoporous Mater 105:181–188
141. Ivanova II, Borodina IB, Ponomareva OA, Yuschenko VV, Fajula F, Bousquet J (2007) Hydroalkylation of benzene and ethylbenzene over Ru- and Ni-containing zeolite catalysts—novel catalytic route for ethylcyclohexylbenzene synthesis. In: 40th international zeolite conference, pp 1228–1235
142. Anaya F, Zhang L, Tan Q, Resasco DE (2015) Tuning the acid–metal balance in Pd/ and Pt/ zeolite catalysts for the hydroalkylation of m-cresol. J Catal 328:173–185
143. Zhao C, Song W, Lercher JA (2012) Aqueous phase hydroalkylation and hydro-deoxygenation of phenol by dual functional catalysts comprised of Pd/C and H/La-BEA. ACS Catal 2:2714–2723
144. Dakka JM, DeCaul LC, Xu T (2009) Process for making cyclohexylbenzene. US Patent 7579511
145. http://www.styreneforum.org
146. Weissermel K, Arpe HJ (1997) Industrial organic chemistry. Third completely revised edition. VCH Verlagsgesellschaft mbH, Weinheim, pp 335–342
147. Lee EH (1973) Catal Rev 8:285
148. Meima GR, Menon PG (2001) Catalyst deactivation phenomena in styrene production. Appl Catal A Gen 212:239
149. Hesselink W (2001) Shell chemicals magazine, second quarter
150. Kuhrs C, Arita Y, Weiss W, Ranke W, Schlögl R (2001) Understanding heterogenous catalysis on an atomic scale: a combined surface science and reactivity investigation for the dehydrogenation of ethylbenzene over iron oxide catalysts. Top Catal 14:111
151. James DH, Castor WM (2001) In: Ullmann's encyclopedia of industrial chemistry, 6th ed (Electronic). Wiley-VCH Verlag GmbH, Weinheim
152. Lacroix C, Deluzarche A, Kinnemann A, Boyer A (1984) Promotion role of some metals (Cu, Ag) in the side chain alkylation of toluene by methanol. Zeolites 4:109
153. Mimura N, Tuatara I, Saito M, Hattori T, Ohkuma K, Ando M (1998) Dehydrogenation of ethylbenzene over iron oxide-based catalyst in the presence of carbon dioxide. Catal Today 45:61
154. Lange JP, Mesters CMAM (2001) Mass transport limitations in zeolite catalysts: the dehydration of 1-phenyl-ethanol to styrene. Appl Catal A Gen 210:247–255
155. Kieboom APG, Moulijn JA, Sheldon RA, Van Leeuwen PWMN (1999) Catalytic Processes in Industry, Studies in Surface Science and Catalysis 123: pp 29–80; Catalysis: An Integrated Approach; Van Santen RA, Van Leeuwen PWMN, Moulijn JA, Averill BA (eds), Elsevier, Amsterdam

156. Shreiber EH, Rhodes MD, Roberts GW (1999) Methanol dehydrogenation with Raney copper in a slurry reactor. Appl Catal B Environ 23(1):9–24
157. Sidorenko YN, Galich PN, Gutyrya VS, Il'in VG, Neimark IE (1967) Condensation of toluene and methanol upon synthetic ceolites containing-exchange cations of alkali metals. Dokl Akad Nauk SSSR 173:132
158. Yashima T, Sato K, Hayasaka T, Hara N (1972) J Catal 26:303
159. Wang X, Wang G, Shen D, Fu C, Wei M (1991) Zeolites 11:254
160. Uniland ML, Baker GE (1981) In: Moser WR (ed) Catalysis in organic reactions. Marcel Dekker, New York
161. Guo WG, Zhang ZW, Liang J, Cai GY, Chen GQ (1991) In: Proceedings of the international conference on petroleum refinery and petrochemical process, vol 3, pp 1459–1465
162. Guo WG, Zhang ZW, Liang J, Cai GY, Chen GQ (1993) Chin Chem Lett 4:873
163. Das NK, Pramanik K (1997) Side-chain alkylation of toluene with methanol over single zeolite catalysts. J Indian Chem Soc 74:701–705
164. Das NK, Pramanik K (1997) Side-chain alkylation of toluene with methanol over dual catalysts comprising X-zeolites and Fe-Mo oxide. J Indian Chem Soc 74:705–708
165. Archier D, Coudurier G, Naccache C (1992) In: Von Ballmoos R, Higgins JB, Treacy MMJ (eds) Proceedings of the 9th international zeolite conference, Montreal, vol 2. Butterworth-Heinemann, Boston, pp 525–533
166. Wieland WS, Davis RJ, Garces JM (1996) Solid base catalysts for side-chain alkylation of toluene with methanol. Catal Today 28:443
167. Wieland WS, Davis RJ, Garces JM (1998) J Catal 173:490
168. Itoh H, Miyamoto A, Murakami Y (1980) J Catal 64:284
169. Itoh H, Hattori T, Suzuki K, Miyamoto A, Mirakami Y (1981) J Catal 72:170
170. Itoh H, Hattori T, Suzuki K, Mirakami Y (1983) Role of acid and base sites in the side-chain alkylation of alkylbenzenes with methanol on two-ion-exchanged zeolites. J Catal 79:21–33
171. Hathaway PE, Davis ME (1989) J Catal 119:479
172. Usachev NY, Lapidus AL, Usacheva ON, Savel'yev MM, Krasnova LL, Minachev KM (1993) Petrol Chem 33:291
173. Manivannan R, Pandurangan A (2009) Formation of ethyl benzene and styrene by side chain methylation of toluene over calcined LDHs. Appl Clay Sci 44:137–143
174. Hattori H, Amusa AA, Jermy RB, Aitani AM, Al-khattaf SS (2016) Zinc oxide as efficient additive to cesium ion-exchanged zeolite X catalyst for side-chain alkylation of toluene with methanol. J Mol Catal A Chem 424:98–105
175. Wang K, Chen JC, Helton TE (2012) Transalkylation of polycyclohexylbenzenes. US Patent Appl. No. 2012/0046499 A1
176. Garces JM, Stone FC, Bates SI, Curnutt JL, Scheldt FH (1988) Deactivation and regeneration of zeolite CsNaX catalyst used for the side chain alkylation of toluene with methanol. Stud Surf Sci Catal 37:505–511
177. Li JH, Xiang H, Liu M, Wang QL, Zhu ZR, Hu ZH (2014) The deactivation mechanism of two typical shape-selective HZSM-5 catalysts for alkylation of toluene with methanol. Catal Sci Technol 4:2639–2649
178. Korwar S, Burkholder M, Gilliland SE, Brinkley K, Gupton BF, Ellis KC (2017) Chelation-directed C–H activation/C–C bond forming reactions catalyzed by Pd(II) nanoparticles supported on multiwalled carbon nanotubes. Chem Commun 53:7022–7025
179. Ritleng V, Sirlin C, Pfeffer M (2002) Ru-, Rh-, and Pd-catalyzed C-C bond formation involving C-H activation and addition on unsaturated substrates: reactions and mechanistic aspects. Chem Rev 102:1731–1769
180. Luo CZ, Gandeepan P, Cheng CH (2013) A convenient synthesis of quinolizinium salts through Rh(III) or Ru(II)-catalyzed C-H bond activation of 2-alkenylpyridines. Chem Commun 49:8528–8530
181. van Broekhoven EH, Mas Cabre FR, Bogaard P, Klaver G, Vonhof M (1999) US Patent 5986158

C3-Based Petrochemicals: Recent Advances in Processes and Catalysts

Chanchal Samanta and Raj Kumar Das

Abstract The petrochemical and chemical industries are key enablers of modern societies. Transportation, construction, packaging, food processing, textile, water distribution, medical equipment, and in various other sectors petrochemicals and chemicals are used in making products for improving the quality of our modern living. Among the major five types of feedstocks (as listed below), light olefins are the most important chemical building blocks for the production of the various downstream petrochemicals.

- Light olefins: ethylene and propylene
- C_4 hydrocarbons: Butanes, butenes, butadiene
- Aromatics: Benzene, toluene, and xylenes (BTX)
- Long-chain *n*-paraffin: Kerosene-derived C_9-C_{17} paraffins
- Syngas: a mixture of carbon monoxide and hydrogen

Ethylene and propylene are two major light olefins, used as key petrochemical building blocks. Ethylene is used in the production of polyethylene, ethylene chloride, ethylene oxide, etc. These products are used in the construction and packaging, plastic processing, and textile industries, to name just a few examples. Similarly, propylene, the simplest C_3 olefin, is used in making a number of useful derivatives such as polypropylene, propylene oxide, acrylonitrile, acrylic acid, cumene, isopropanol, etc. The global propylene demand was around 100 MMTA (million metric tons per annum) in 2015 which is expected to increase at a 3.6% CAGR (compound annual growth rate) to more than 140 MMTA by 2025 due to wider applications of the propylene derivatives in the consumer market. For instance, polypropylene, a key derivative of propylene, is one of the best-selling plastics, extensively used in automobiles and in the manufacturing of packaging films. Acrylonitrile, another propylene derivative, is used in making acrylic fibers and coatings. Similarly, propylene oxide is used extensively for the manufacturing of polyurethanes and other chemicals, acrylic acid and oxo alcohols are employed in PVC plasticizers and coatings-based applications, cumene is used to make epoxy resins and polycarbonate, and isopropyl alcohol is used as solvent, and so on. Not only plastic processing,

C. Samanta (✉) · R. K. Das
Corporate R&D Centre, Bharat Petroleum Corporation Limited,
Greater Noida, Uttar Pradesh, India
e-mail: chanchalsamanta@bharatpetroleum.in; rajkumardas001@bharatpetroleum.in

but also the packaging industry, the furnishing sector as well as the automotive industries are the major consumers of propylene derivatives.

Propylene is a highly activated synthetic molecule and thus it needs to be converted selectively to its derivatives for their cost-effective production. Both propylene production and its selective conversion processes for the production of other chemicals have gone through important improvement in recent times. Thus, it is being felt that it would be interesting to capture the most recent advances in the processes and catalysts associated with propylene production and subsequent conversion of propylene to important C3 chemicals to global readers. The main aim of this book chapter is to bring important aspects of various commercial processes and catalysts involved in the production of propylene and propylene-derived chemicals namely, propylene oxide, acrylonitrile, isopropanol, and acrylic acid. About two-thirds of global propylene is consumed to make polypropylene (PP), which is one of the most versatile plastic materials with good mechanical and chemical properties. However, information related to polypropylene production technologies and associated catalysts is beyond the scope of this chapter.

Keywords Heterogeneous catalysts · Selective hydrogenation · Palladium catalysts · 1,3-Butadiene · 1-Butene · Density functional theory

Abbreviations

2-EHA	2-Ethyl hexyl acrylate
3-HP	3-Hydroxy propionic acid
ABS	Acrylonitrile-butadiene styrene
ACN	Acrylonitrile
atm.	Atmospheres (unit for pressure)
CAGR	Compound annual growth rate
CARENA	Catalytic reactors based on new materials
Conv.	Conversion
DCC	Deep catalytic cracking
DIPE	Diisopropyl ether
DME	Dimethyl ether
DTP	Dominant technology for propylene production
EBHP	Ethylbenzene hydroperoxide process
ECH	Epichlorohydrin
EPS	Expanded polystyrene foam
FCC	Fluid catalytic cracking
GTO	Gas to oil
HPPO	Hydrogen peroxide-to-propylene-oxide
IPA	Isopropyl alcohol
LPG	Liquefied petroleum gas
MMTPA	Million metric ton per annum

MTO	Methanol to olefin
MTP	Methanol to propylene
OCP	Olefin cracking process
OCT	Olefin conversion technology
PDH	Propane dehydrogenation
PEM	Proton exchange membrane
PO	Propylene oxide
POC	Propylene oxide cumene only
R2P	Residue to propylene
R2R	Reactor-2-regenerators
RFCC	Resid fluid catalytic cracking
SAN	Styrene-acrylonitrile resin
SAP	Super absorbent polymer
SOEC	Solid oxide electrolyzer cell
T	Temperature
t	Time
TBHP	Tertiary butyl hydroperoxide
TSC	Thermal steam cracking
USY zeolite	Ultra stable Y zeolite
wt%	Weight percentage

1 Introduction

1.1 Natural Sources of C3 Molecule: Current Scenario

The simplest C3 molecule is propane. It is found in petroleum and natural gas deposits and is extracted as a by-product during the processing of natural gas. Although propane is widely available, until recently, it has limited applications in the production of C3-based chemicals. Propane is a thermodynamically stable molecule ($\Delta_f H°$ gas = −104.7 kJ/mol) and primarily being used as a heating source. On the other hand, its olefin counterpart propylene is a highly active molecule ($\Delta_f H°$ gas = 20.26 kJ/mol), is widely used as the feedstock for C3-based petrochemicals. Propylene derivative especially polypropylene offers superior performance than polyethylene with regard to the mechanical and chemical properties. Propylene consumption has increased significantly over the last two decades because of the tremendous growth in the polypropylene uses. In 2015, around 65–70% of global propylene was consumed in the manufacturing of polypropylene [1]. Approximately 7% of the propylene was consumed for the production of propylene oxide. The remaining propylene was used in the production of cumene, acrylonitrile, isopropyl alcohol, and acrylic acid.

In comparison to ethylene-derived chemicals, propylene-derived chemicals offer superior performance, which is driving demand for propylene in developed

countries. However, propylene demand has outpaced its supply from the conventional sources because of the two major reasons: (a) steam cracker route mostly produce ethylene as a major product and (b) due to shift in the lighter feedstock in steam cracker after the advent of shale gas. Ethane has become an inexpensive source of steam cracker unit which limits the production of propylene [2]. Most of the recent crackers commissioned and some are under construction in the North America and Western Europe are using and expected to use ethane predominantly or exclusively. The changing scenarios of feedstock and the growing demand for propylene have forced petrochemicals manufacturers to build on-purpose plant and search for alternative options wherein crude can be processed directly for light olefins production, such as crude to chemicals process.

Traditionally, two major sources of propylene supply come as by-product [3]. First one is the steam cracking of hydrocarbon feedstock (such as naphtha or butane) and the second one is fluid catalytic cracking (FCC) unit in refineries. Reminders of propylene supply comes from the on-purpose propylene production processes (Fig. 1).

Depending on the purity of propylene, propylene goes to downstream polymer and chemicals production. For example, polymer-grade propylene (≥99.5% purity) is extensively used in the production of polyolefins, acrylates, methacrylates, and acrylonitrile. On the other hand, chemical-grade propylene (93–94% purity) is used for the production of commodity chemicals such as oxo alcohols, propylene oxide, and phenol. The refinery grade propylene (60–70% purity) needs to be upgraded for the production of propylene-derived chemicals [5]. Because of this, on-purpose production routes are taking center stage to make chemical/polymer grade propylene to supplement the deficit as well as to cater the need of growing demand for chemical and polymer-grade propylene.
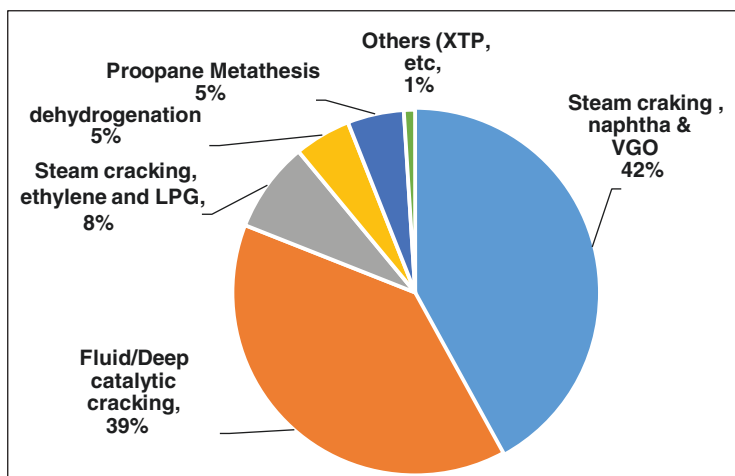
Fig. 1 Global propylene production by processes from hydrocarbon feedstock [4]

2 Propylene Production

2.1 *Traditional Sources*

As per market research firm IHS Markit, in 2013, around 55% of propylene production was based on the steam cracking process, 34% was from combined refinery processes such as FCC, RFCC, and DCC and the remaining 11% production was from on-purpose routes. This scenario is changing rapidly because of the growing demand for propylene and advancement in the catalytic technologies for on-purpose propylene production routes. It is estimated that by 2025, the contribution from on-purpose routes will rise significantly to 25–30%, while the steam cracking process will contribute 40–45% and combined refinery processes will contribute 30–35%. A schematic diagram of propylene value chain is provided in Fig. 2.

2.1.1 Non-catalytic Route: Thermal Steam Cracking (TSC) Process

The thermal steam cracking (TSC) process, designed to make ethylene as a major product, is one of the major sources of propylene where propylene is produced as a by-product. The reactions occuring in the thermal cracking are complex in nature and propagate via free radical. Essentially, two types of reactions occur in the TSC process:
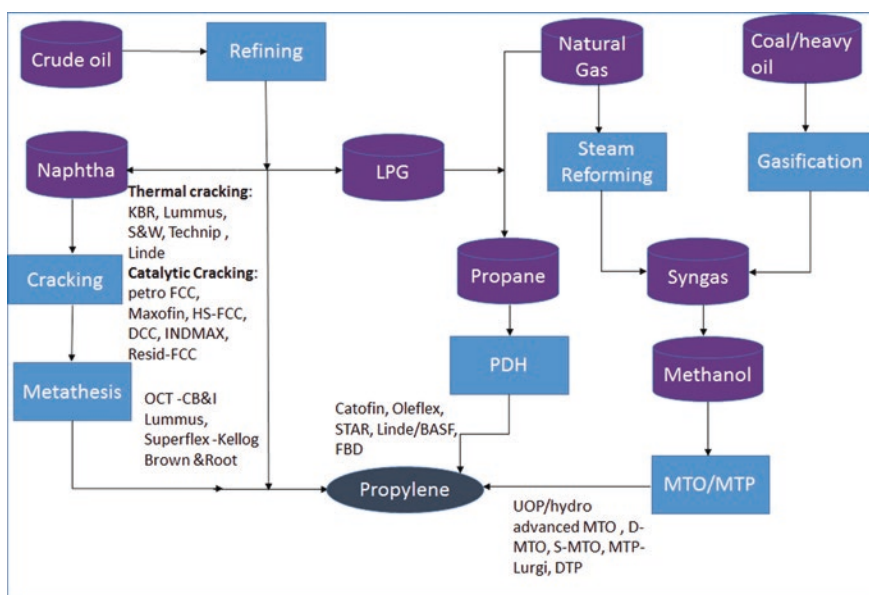
Fig. 2 Propylene value chain through various processes [6]

- Primary cracking: paraffin and olefins are formed initially.
- Secondary cracking: light products are formed that are rich in olefins.

Thermal steam cracking (TSC) process needs high energy; around 3.050 kcal/kg of energy is consumed for per kg of produced olefin [7]. In steam cracking, a liquid hydrocarbon (such as naphtha or gas oil) or a gaseous feedstock such as ethane, propane, or butane is mixed with steam and then introduced into a heated furnace at 790–850 °C in the absence of oxygen [8]. The products composition depends on the properties of hydrocarbon feedstock, hydrocarbon to steam ratio, cracking temperature, and furnace residence time. In the modern cracking furnaces, the residence time is precisely controlled to improve the yield of desired products [9]. Steam cracking leads to the formation of small paraffin molecules through C–C bond breaking and alkenes through C–H bond breaking by radical mechanism. Alkene at high temperature undergoes side reactions and thus coke is also formed after cyclo-dehydrogenation. Propylene to ethylene ratio can be altered by changing feedstock and cracking severity [10]. Light hydrocarbon feedstocks (such as ethane, LPG, or light naphtha) predominantly produce ethylene, propylene, and butadiene. On the other hand, heavier feedstocks (such as heavy naphtha or gas oil) produce lighter olefins such as ethylene, propylene, butadiene as well as aromatic-rich hydrocarbon fractions suitable for gasoline blend or as fuel oil [9]. The higher cracking severity favors the production of ethylene and benzene, whereas lower severity favors relatively higher amounts of propylene, C_4-hydrocarbons, and liquid products. The decision of steam cracker configuration depends on the feedstock availability such as liquid feedstock is used predominately in the Europe and Asia but less so in the Middle East and North America [11]. Most of the recent gas crackers have been constructed and under construction are located in the North America and the Middle East because of the availability of shale gas and natural gas. A number of technology licensors such as KBR, ABB Lummus, Technip, Linde AG, Stone & Webster offer steam cracking technology [12].

2.1.2 Catalytic Routes

The second-largest source of propylene is the refinery fluid catalytic cracking (FCC) unit. FCC is a major secondary refinery process and traditionally it has been operated either in gasoline or distillate mode. As the refining sector is facing various new challenges such as surplus refining capacity, competitive refinery margins, and lower demand of transportation fuels, refiners are paying more attention for the integration of petrochemicals production with refineries. As a result, refiners are focusing on improvement of the propylene yield in the traditional FCC and setting up Resid FCC (RFCC) units. RFCC process is a modified version of traditional FCC process and was conceptualized in the early 1980s [13]. Technip and Stone & Webster Process Technology formed an Alliance with Total, IFP, and Axens to develop a Resid FCC process which is known as R2R™ (Reactor-2-Regenerator). Since then, this Alliance has been the leader in the refining industry for RFCC
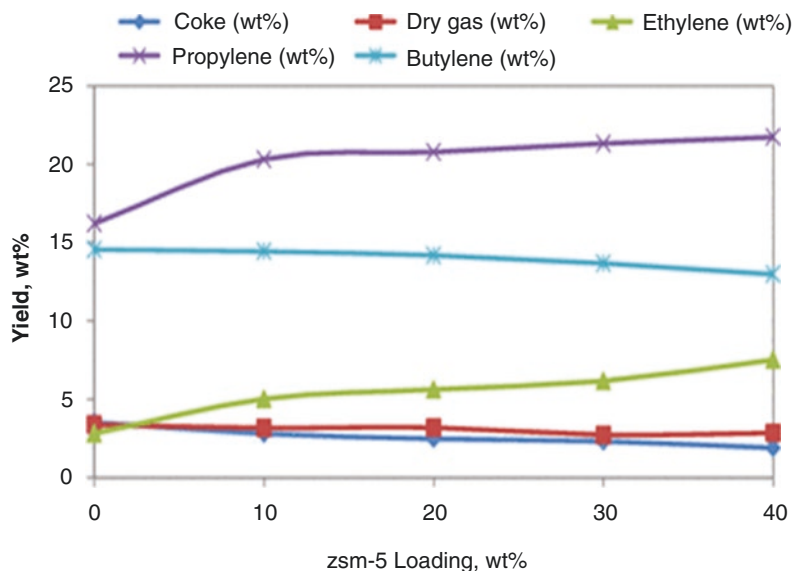
Fig. 3 ZSM-5 loading and its impact in propylene yield [19]

technology with more licensed units than all other licensors combined [13]. The Alliance is also a leader in the Resid-to-Propylene (R2P™) technology [14]. These technologies are based on modifying FCC technologies. Similarly, several FCC-based technologies have been developed and licensed by modifying catalyst's formulation—specifically the pore architecture of zeolite, changing hardware configuration, and finally by optimizing reaction parameters—by changing operational severity. For instance, ZSM-5 zeolite can be used along with conventional ultra-stable Y (USY) zeolite-based FCC catalyst in FCC units without changing much of the unit configuration for propylene yield maximization [15–17]. INDMAX–FCC process developed by Indian Oil/Lummus is one of such FCC technologies which does not require much change in hardware in FCC units. Deep catalytic cracking (DCC) technology developed by SINOPEC uses entirely ZSM-5-based catalyst system for propylene maximization with high severity condition [18]. By changing ZSM-5 content in the FCC catalyst system from 0 to 20% (Fig. 3), propylene production yield can be maximized [20]. A comparison of various FCC-based technologies is provided in Table 1.

Other renowned technologies for propylene maximization are UOP's petro FCC, KBR's Maxofin process [22], and Axen/S&W's HS-FCC process [23]. These technologies involve modification in the hardware of the reactor system along with proprietary catalyst to increase the propylene selectivity. By employing, all these technologies, refinery streams comprising recoverable fractions of propylene are combined into a mixed C3 stream and then the mixture is subjected for propylene separation. Such a mixed stream is to be distilled out to obtain propylene (b.p.—47.7 °C) as the overhead product and as the bottom fraction propane

Table 1 Typical operating conditions and product yields for usual FCC and modified FCC-based process [21]

Parameters	FCC	DCC	PetroFCC	HS-FCC
Reaction temperature (°C)	530	580	550	600
Contact time (s)	2–5	10	2–5	0.5–1.0
Cat/oil ratio	5	15	10	25
Product yield (wt%)				
Ethylene	1.5	5.4	6	2.3
Propylene	4.8	14.3	22	15.9
Mixed butanes	6.9	14.7	14	17.4
Gasoline	51.5	39	28	37.8
Heavy and light oils	21	15.6	14.5	9.9
Coke	4.5	4.3	5.5	6.5
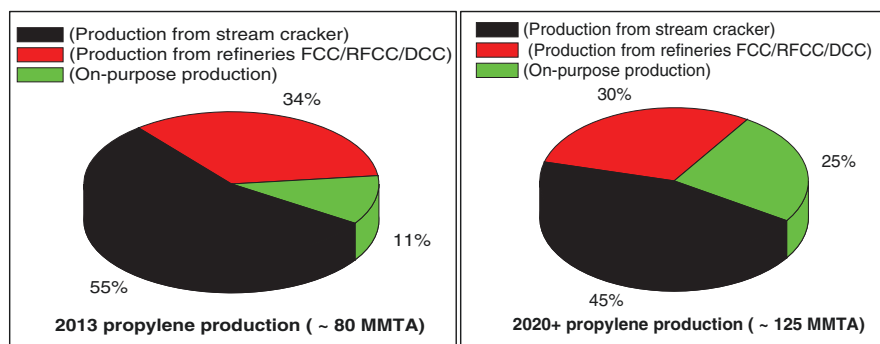
Fig. 4 Contribution of different technologies for global propylene production in the past and future. (Source: IHS Markit report 2013)

(b.p.—42.1 °C) along with traces of other heavier products [24]. However, propylene derived from such refinery processes needs to be purified/upgraded for the downstream production of propylene-based chemicals and polymers.

2.2 Alternative Sources/Processes: On-Purpose Propylene Production

On-purpose propylene production route is increasingly being relevant to fill the gap of growing demand for propylene (Fig. 4). The two major drivers behind the on-purpose routes are (a) higher demand for propylene than ethylene; and (b) construction of more new ethane crackers (which produces less propylene) than naphtha crackers. On-purpose production routes such as propane dehydrogenation (PDH), methanol-to-olefins (MTO), methanol-to-propylene (MTP), and olefin metathesis are gaining attention to fulfill the growing demand for propylene.

2.2.1 Propane Dehydrogenation (PDH)

Gradually, PDH has become a preferred route for the on-purpose production of chemical grade propylene. Propane, the feedstock for PDH process, comes as by-product while processing of natural gas or from refinery liquefied petroleum gas (LPG). The recent discovery of shale gas in the North America and the vast reserve of natural gas in the Middle East have boosted the commercial prospect of PDH technology [25]. There are five major proven PDH technologies available in a commercial scale, these include: (a) CATOFIN process by ABB Lummus Global, (b) OLEFLEX process by UOP (c) steam active reforming (STAR) by Krupp Udhe, (d) PDH by Linde-BASF-Statoil, and (e) fluidized bed dehydrogenation (FBD) by Snamprogetti. Each technology has its own merits and demerits. Major difference among all the PDH technologies comes from reactor technology, catalyst type, operating conditions, and performance of the catalyst (Table 2).

STAR process is based on fixed-bed reactor and Pt-Sn catalyst supported on zinc-aluminate and with calcium/magnesium aluminate as binder is used. The reaction is operated at 500–600 °C at 5–6 bar pressure. Steam is co-fed with feed/propane for coke reduction and thus it is called steam-activated reforming (STAR) [27, 28]. Snamprogetti and Yarsintez commercialized fluidized bed dehydrogenation

Table 2 Commercial process for propane dehydrogenation (PDH) and process conditions [26]

S. no.	Technology Licensor	Type of reactor	Catalyst formulation	Process condition	Performance of the catalyst
1	CB&I Lummus (Catofin)	Multiple parallel fixed-bed reactors	18–20 wt% CrO_x on Al_2O_3 support, promoted by Na or K (1–2 wt%)	575 °C, 0.2–0.5 bar	Conversion >15%, C3 = selectivity: 98%
2	UOP (Honeywell) Oleflex	Fluidized catalytic reactor	<1 wt% Pt and 1–2 wt% Sn on Al_2O_3 support, promoted by Na or K (0–1 wt%)	525–705 °C, 0.2–0.5 bar	Conversion >20%, C3 = selectivity: 98%
3	Uhde (STAR: steam-activated reforming)	Fixed-bed reactor	Pt-Sn on zinc−aluminate support and calcium/magnesium−aluminate binder	500–600 °C, 5–9 bar	Conversion >20%, C3 = selectivity: 98%
4	Linde/BASF	Fixed-bed reactor (similar like STAR process)	Pt-Sn supported on ZrO_2	590 °C, 5–9 bar	Conversion >20%, C3 = selectivity: 98%
5	Snamrogetti/ Yarsintez (FBD: fluidized bed dehydrogenation)	Fluidized catalytic reactor	CrO_x/Al_2O_3 catalyst, with alkali metal promoter	550–600 °C, 1.1–1.5 bar	Conversion >15%, C3 = selectivity: 98%

(FBD) process [29]. The reactor system is similar like cracking reactor. Alkane/propane is fed to the reactor at 550–600 °C and at 1.1–1.5 bar with catalyst system of CrO_x/Al_2O_3 with added alkaline metal-based promoter. Linde-BASF process [27, 28] is mostly similar to STAR process with little different in catalyst system and operating condition. Pt-Sn-based catalyst with ZrO_2 support is used for co-processing of feed/propane and steam (at 590 °C) for dehydrogenation reaction.

PDH technology is proven and reasonably well established. However, the main drawbacks of this route are relatively high capital costs due to multiple reactor system, rapid deactivation of catalyst due to coke deposition, and importantly it needs for the long-term supply of low-cost propane which becomes region-specific such as propane is available in the Middle East. The advantage of the PDH process is that selectivity and yield of propylene can reach up to 95% and 90%, respectively. Among the five PDH technologies mentioned above, Catofin and Oleflex are the two major commercially proven PDH technologies and several plants are operational based on these technologies. Both technologies have a similar operating temperature, pressure and offer propylene selectivity of ~90%. The per pass conversion of propane to propylene in the Catofin and Oleflex processes are 45–50% and 35–40%, respectively (Table 3).

Catofin PDH process [33] uses multiple parallel adiabatic fixed-bed reactors and goes through multiple steps: dehydrogenation of propane to propylene, compression of reactor effluent, recovery, and purification of propylene product. Supported

Table 3 Comparison of Catofin and Oleflex PDH processes [30–32]

Parameters	Catofin PDH process	Oleflex PDH process
Process type	Semi-continuous	Continuous
Reactor system	Horizontal, fixed bed in parallel	Vertical, catalyst moving bed in series
Catalyst type	Cr-based	Pt-based
Catalyst life	2–3 years	5–7 years
Type catalyst regeneration Regeneration cycle time	In situ, cyclic regeneration 10–20 min	Continuous catalyst regeneration (CCR) 7 days
Reactor inlet temperature	600–610 °C	630–650 °C
Reactor pressure	0.3–1.0 bar	1.2–2.0 bar
Conversion per pass	45–50%	35–40%
Propylene selectivity	80–90%	80–90%
CO_2 emissions	High	Low
Advantages	• Lower C3 consumption • Lower catalyst cost • No H_2 recycle gas • No separate CCR facility required	• Safe and reliability in operation • Longer catalyst life • High on-stream operation
Disadvantages	• Frequent reactor change by cycle operation (12 min) • Cr-based catalyst	• Complicated rector internals design • Higher capex and opex

chromium-alumina catalyst (Cr_2O_3/Al_2O_3; with 18–20 wt% of Cr) is used for the PDH reaction. Efficient reactor system to drive selective dehydrogenation of propane to propylene and regeneration of the catalyst are the most critical parameters in designing Catofin PDH plants. Since the dehydrogenation reaction is endothermic, a high temperature is required to drive the reaction which leads to the coke deposition on the catalyst. Thus, dehydrogenation and catalyst regeneration steps are carried out in short intervals of every 10–12 min with short periods of purging and evacuation operations in-between. Coke deposition results in loss of catalyst activity and decrease bed temperature. Regeneration of the catalyst is achieved by burning deposited coke on the catalyst by blowing hot air on the catalyst bed which simultaneously recovers the bed temperature under oxidizing conditions. The average lifetime of the catalyst is 2–3 years in industrial operation and the catalyst activity gradually decreases over the time due to the loss of active metal and sintering of the active metal particles.

Another key feature of Catofin PDH technology is the use of heat generating material (HGM) [34] developed by Clariant. HGM is a proprietary metal-oxide material suitable to produce heat and drive the endothermic dehydrogenation reaction to increase yields. HGM also reduces energy requirement and emissions. As a result, HGM enhances the performance advantages of Catofin technology and catalysts. A number of (>10 Nos) Catofin PDH plants are operational in the world and INEOS, Europe's largest petrochemicals company, is constructing one of the largest Catofin PDH plants (having capacity of 750,000 tons/year) at Antwerp, Belgium which is expected to come on stream in 2023 [35].

Oleflex ™ PDH process developed by UOP is a continuous catalytic dehydrogenation process. In Oleflex process, a fluidized bed reactor along with catalyst regeneration unit is used. Propane dehydrogenation is performed over Pt-Sn-based catalyst at the temperature range of 630–650 °C and 1–3 bar pressure. The catalyst is regenerated by burning coke and re-dispersing Pt by chlorine-air mixture. The life of the catalyst is 1–3 years. UOP has continuously improved catalyst performance for the Oleflex process since the arrival of the first-generation catalyst (DeH-6) in 1990 followed by second Generation catalyst (DeH-8, in 1992), third Gen (DeH-10 in 1993), fourth Gen (DeH-12 in 1996), fifth Gen (DeH-14 in 2001), sixth Gen (DeH-16 in 2007), seventh Gen (DeH-18 in 2014), and further improvement to DeH-24 and DeH-26 [36]. The new generation DeH catalyst is based on alkaline metal-doped Pt/Al_2O_3 catalyst with 0.3–0.5 wt% Pt loading promoted with a second metal such as Sn, Zn, or Cu. The continuous improvement in the next generation catalyst performance indicates there is tremendous scope in improving the activity and stability of a catalyst system by optimizing metal loading, modifying synthesis parameters, and introducing a second metal to optimize the cost as well as the performance of the catalyst. The new generation DeH catalyst provides 30% higher coking stability and has much higher attrition resistant while offering superior activity and selectivity. The superior performance and improved attrition resistance have helped UOP to design >1000 KTA PDH plant. The main advantages of the Oleflex process are the ability to continuously regenerate catalysts without interrupting propylene production and low energy consumption. Because of this, Oleflex process

has outsmarted other PDH technologies and 18 Oleflex units out of the 28 operating PDH units are currently running with world's largest propylene Oleflex plant having production capacity of 750,000 tons/year [36].

2.2.2 Olefin Inter-conversion and Metathesis

Propylene production through olefin inter-conversion/metathesis techniques is a proven and emerging on-purpose propylene production process. It is obvious that the typical steam cracker which produced ethylene as a major product stream is not able to supply the necessary propylene demand. To some extent, propylene demand can be met through on-purpose and standalone propylene production facilities. Catalytic olefin inter-conversion and olefin metathesis technologies can provide a flexible option to the refiners to integrate existing cracker unit for augmenting net propylene production. CB&I Lummus developed olefin conversion technology (OCT) [37] which converts ethylene to propylene by employing two-step catalytic process which consists of bi-functional catalytic system (Fig. 5). Mixed feed stream of ethylene and 2-butene is used for the OCT reaction at 260 °C and 30–35 bar pressure. Two catalysts are used in the reactor (a) WO_3/SiO_2-based catalyst to carry out cross metathesis reaction [39] and (b) followed by MgO-based catalyst to drive isomerization reaction [40, 41] from 1-butene to 2-butene which is then used during metathesis reaction. The OCT technology can be integrated with ethane cracker unit for propylene production from less expensive and more available ethylene feed. Such an integrated process was first developed by Lyondell Petrochemical Co. in Texas to produce 136,000 tons/year of propylene. The OCT technology was also integrated with ethane cracker unit through two-step transformation process in Abu Dhabi. At first, ethylene from ethane cracker is dimerized to obtain
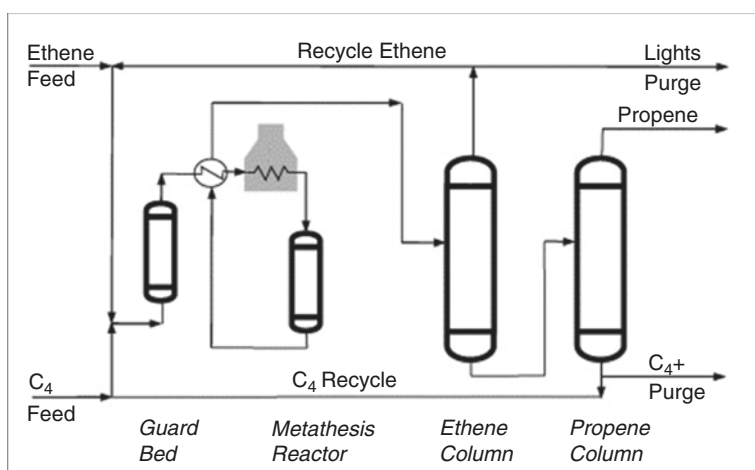
Fig. 5 Process flow diagram of propylene production through OCT process [38]
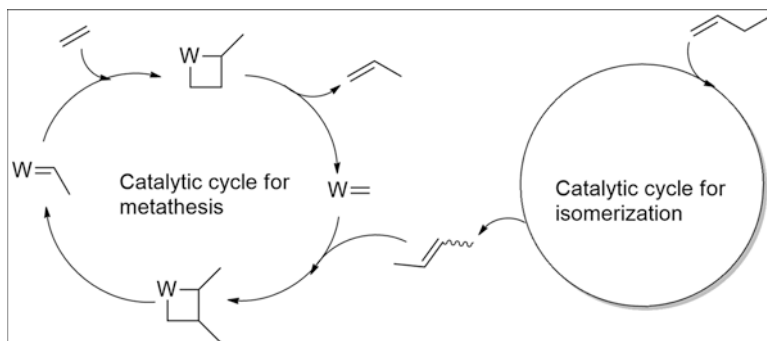
Scheme 1 Mechanism of propylene production through OCT process (metathesis coupled with isomerization) [42]

2-butene-dominated feed (90% 2-butene) in presence of Phillip's nickel-based homogenous catalyst and then the 2-butene-rich feed is underwent metathesis reaction in presence of Lummus's WO_3/SiO_2 catalyst to produce propylene (Scheme 1). However, these units need access to large C4 streams that need to be free of isobutylene and butadiene.

Superflex process, licensed by Kellogg Brown & Root, and developed by Arco chemical, is one of such olefin interconversion processes that converts light hydrocarbons (in the range of C4 to C8) into a propylene-rich stream. However, the major problem with such units is the requirement of abundant supply of C4 stream which should not contain isobutylene and butadiene fractions. Another olefin interconversion technology developed by Exxon Mobil uses ZSM-5-based catalyst that converts C_4 light pygas and light naphtha to propylene and ethylene stream [3].

2.2.3 Methanol to Olefins (MTO)/Methanol-to-Propylene (MTP) Process

On-purpose propylene production through MTO and MTP processes are currently being pursued in few countries where coal and natural gas source are abundant. Such processes are alternatively known as coal-to-olefins (CTO) and gas-to-olefins (GTO) processes. Both these routes go through the common route of syngas production followed by the conversion of syngas to methanol and then methanol is used to produce propylene using commercial technologies known as MTO and MTP process [43]. Four major methanol to olefin conversion technologies are commercially available [44] such as (a) S-MTO, (b) D-MTO/D-MTO-II, (c) UOP/Norsk Hydro's MTO, and (d) Lurgi's MTP [45, 46]. S-MTO process [47, 48] developed by Sinopec and is now one of the major licensing technologies in the MTO process in China. D-MTO/D-MTO-II technology was developed by Dalian Institute of Chemical Physics (DICP) and was commercialized by Sinopec. Currently, D-MTO/D-MTO-II technology has occupied 70% market share for MTO process in China. D-MTO-II technology [49] comprises three major sections: (a) fluidized reactor with catalyst
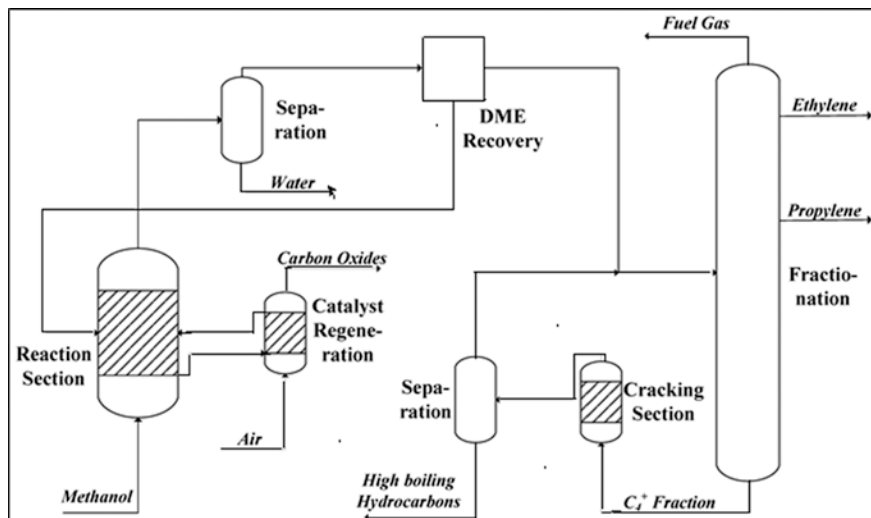
Fig. 6 Schematic process flow diagram of MTO process [6]

system, (b) catalyst regeneration section, and (c) production separation section for separating propylene from ethylene and heavier hydrocarbon (C4 or above). Catalyst in fluidized reactor undergoes an acid-catalyzed reaction at 400–500 °C and 0.1–0.3 MPa pressure and the reaction is exothermic in nature. Both S-MTO and D-MTO/D-MTO-II technology uses SAPO-34-based zeolite catalyst system and the major difference in the technological front is that S-MTO process uses novel type of SAPO-34 which can maximize propylene over ethylene production by modifying the zeolite's pore. About 43% of propylene yield can be achieved through S-MTO process. In UOP/Norsk Hydro MTO process [50–52], methanol is preheated to its vapor phase before putting into the reactor (Fig. 6) for the conversion of methanol to dimethyl ether (DME). The vapor-phase reaction is carried out at 350–540 °C and 0.1–0.3 MPa. Propylene is recovered in the product recovery section and heavier hydrocarbon is cracked into C3 and C4 olefins.

In Lurgi's MTP process [53] methanol is first passed through a pre-heating system at 260 °C and then the vaporized feed is passed through a DME reactor in the presence of an acidic dehydration catalyst. In the DME reactor, about 75% of methanol is converted to DME and then mixed feed (75% of DME and 25% of methanol) is passed through the MTP reactor (Fig. 7) where reaction occurs at 470 °C over a catalyst in the presence of steam (0.75–2 kmol steam/kmol reaction mixture). The conversion of DME/methanol to propylene in the first MTP reactor is around 90%. A series of MTP reactors are used for propylene yield maximization and catalyst regeneration in sequence. MTO process can handle crude methanol and more suitable for ethylene production; however, the flexibility in the process allows propylene production up to 45% of total output. UOP in association with total S.A [54] has further improved the MTO process to boost propylene output by integrating with an
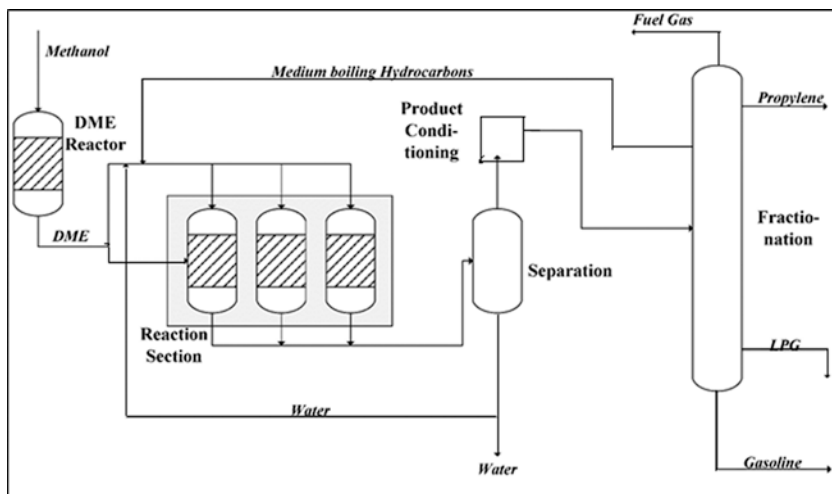
Fig. 7 Schematic process flow diagram of MTP process [6]

Table 4 MTO/MTP-based commercial process and their operating conditions [55]

S. no.	Technology Licensor	Reactor type	Catalyst	Process condition
1	UOP/hydro advanced MTO/OCT (Total S.A)	Fluidized	SAPO-34 ()	T: 400–550 °C, P: 1–4 atm.
2	D-MTO (Dalian Institute of Chemical Physics	Fluidized	SAPO-34	T: 400–550 °C, P: 4–5 atm.
3	S-MTO (Sinopec MTO)	Fluidized	SAPO-34	T: 400–550 °C, P: 1–5 atm.
4	MTP (Lurgi)	Fixed bed	Modified ZSM-5	P: 1.3 bar, T: 480 °C

olefin cracking process (OCP). OCP process takes the heavier olefins from the MTO unit and converts them into lighter olefins, particularly to propylene. UOP-Total has started licensing integrated MTO/OCP process. Various features of commercial MTO/MTP process, their operating conditions, reactor system, and catalyst system used are given in Table 4 [55]. MTP process has advantage of producing polymer grade propylene independent of feedstock, the process also allows in situ regeneration of catalyst and thereby offers continuous operation and minimum downtime. MTP process generates valuable by-products such as ethylene, LPG, and gasoline. This process consumes around 3.5 tons of methanol for per ton of propylene production.

DTP® process, jointly developed by JGC and Mitsubishi Chemical, is another on-purpose propylene technology, which offers high yield of propylene [56]. The process uses dimethyl ether (DME) or methanol as a feed. In addition, olefins by-products from naphtha cracker can also be used as feed in the process. DTP process involves zeolite-based catalyst and a fixed-bed adiabatic reactor and offers high yield of

propylene with hydrocarbon recycling. DTP® technology has been demonstrated at Mitsubishi Chemical's Mizushima Plant. Various features of commercial MTO/MTP processes [57–59] and their operating condition are summarized in Table 4.

3   Commercial Propylene Production with Feed Suitability

In summary, all the propylene production processes have its own merits and demerits for producing propylene in commercial scale. Since the on-purpose production route is taking frontline to reduce the gap between the world propylene demand and its supply, various feedstocks such as naphtha, light olefins (ethylene and butene), propane, and methanol (oxygenates) are being valorized based on the availability of the feedstocks by various selective processes for high purity propylene production. Different feedstocks and associated suitable process technologies used in the production of propylene are summarized in Table 5 [60, 61].

Table 5 Various parameters for selection of suitable process for commercial propylene production based on feedstock [60, 61]

Feedstock	Process	Merits (a) and demerits (b)	Operating condition	Final yield of propylene
Paraffin/ naphtha	Steam cracking	(a) Mature technology (b) Propylene obtained as a by-product recovery, the process is energy-intensive, and economical only at large-scale production	750–900 °C, 2–3 atm.	13–16%
Ethane	Route-1: Steam cracking, ethylene dimerization, metathesis	(a) Technology is well-established and provides polymer grade propylene (b) Requires high purity olefin (ethylene and 2-butene) feedstock for metathesis	For olefin meta thesis 20–50 °C (re-alumina catalyst), 300–375 °C (WO_3-silica) and at 5–15 atm.	Ethane cracking: ~80–85% dimerization and metathesis: 90–95%
Propane	Propane dehydrogenation (PDH)	(a) Proven technology, less process steps, chemical grade propylene (b) Endothermic reaction, catalyst shows deactivation tendency	540–700 °C, 0.1–4 atm.	80–85%

<div align="right">(continued)</div>

Table 5 (continued)

Feedstock	Process	Merits (a) and demerits (b)	Operating condition	Final yield of propylene
Ethylene and butene	Metathesis	(a) Suitable where ethylene is abundant severe condition (b) Feedstock specific, yields depend on feedstock purity	20–50 °C (re-alumina catalyst), 300–375 °C	90–95%
C4 to C10 olefins	Olefins interconversion using proprietary ZSM-5-based catalyst	(a) Operating and investment cost is low (b) Yield is low	400–550 °C, 1–2 atm.	40–50%
Gas oil	Route-1: FCC unit (FCCU) with conventional operating condition	(a) Operational flexibility, propylene yield can be tuned using different catalyst (b) Catalyst deactivation, large CO_2 emission, low grade propylene, investment cost is very high	500–600 °C, 1.7–2.4 atm.	For conventional FCC: 4–7%, FCC + ZSM-5: 7–10%
	Route-2: FCCU with high severity operating condition in presence of proprietary ZSM-5 zeolite additive	(a) Yield improved over conventional FCC (b) High operation cost and still propylene purity remains concern	>600 °C, 1.7 atm.	15–25%
Coal	Route-1: Gasification of coal to syngas, syngas to methanol and MTP	(a) Matured technology, chemical grade propylene, feedstock flexibility (b) Multiple steps, endothermic SMR and gasification for syngas production	For MTO/MTP process: 350–500 °C, 0.1–4 atm. For OCP: 400–550 °C, 1–2 atm.	MTO for propylene: 80–85%
	Route-2: Gasification of coal to syngas, syngas to methanol, MTO couple with olefin cracking process (OCP)			
Natural gas	Reforming to syngas, methanol synthesis, MTO with OCP			

4 Propylene Derivatives

Numerous propylene derivatives are produced based on the market demands. Among all the derivatives, a substantial increase in the consumption of polypropylene-based materials over the last two decades has been the key driver for the growing demand of propylene. As per IHS report, more than 65% of propylene was consumed worldwide in 2015 for the production of polypropylene [1]. Approximately, 7% of the propylene was employed in the production of propylene oxide, which is a key intermediate for the synthesis of propylene glycol and polyols. The rest of the propylene was utilized in the manufacture of cumene, and other important C3-based chemicals. Since this book chapter is intended not to cover polymerization chemistry, apart from polypropylene other valuable C3 chemicals derived from propylene such as propylene oxide, isopropyl alcohol, acrylonitrile, and acrylic acid have been covered with the relevant information entailing their recent advances in the commercial as well as emerging processes and associated catalyst developments.

4.1 *Propylene Oxide (PO)*

Propylene oxide (PO) is one of the fastest-growing consumers of propylene and around ten million tons of PO production in the world justifies its impact in the chemical industry. PO is used in the production of various valuable products (Fig. 8) such as polyols, propylene glycol, propylene glycol ethers, and polyurethane. Polyol is one of the most important PO derivatives and its consumption is rising nearly 4% per year and is expected to continue the similar growth in the coming decade. Polyol is widely used in the production of polyurethane foams, by reactions with isocyanates, like methylene diphenyl diisocyanate (MDI) or toluene di-isocyanate (TDI). Polyurethanes are versatile material and used in making flexible foams, which are used in furniture, mattresses, and cushions for automobiles or rigid foams, which are mainly used for insulation for housing and construction. Other applications of PO include solvents and miscellaneous chemicals used in oil field drillings, flame retardants, synthetic lubricants, etc. Consequently, demand for PO is continuously increasing with a rate of 8% per annum especially in the Asia-Pacific region as the automobile industry is growing substantially.

4.1.1 Propylene Oxide (PO) Production: Commercial Processes

At present, there are five major industrial processes for the production of PO [63]. These are (a) chlorohydrin (CL) process, (b) *tert*-butyl hydroperoxide (TBHP) or PO/TBA (propylene oxide-*tert*-butyl alcohol) process, (c) ethyl benzyl hydroperoxide (EBHP) or PO/SM (propylene oxide-styrene monomer) process, (d) HPPO (hydrogen peroxide to propylene oxide) process, and (e) cumene hydroperoxide

Fig. 8 Applications of propylene oxide [62]
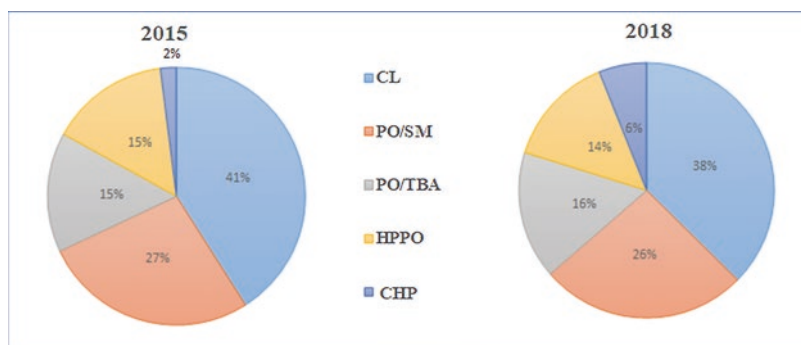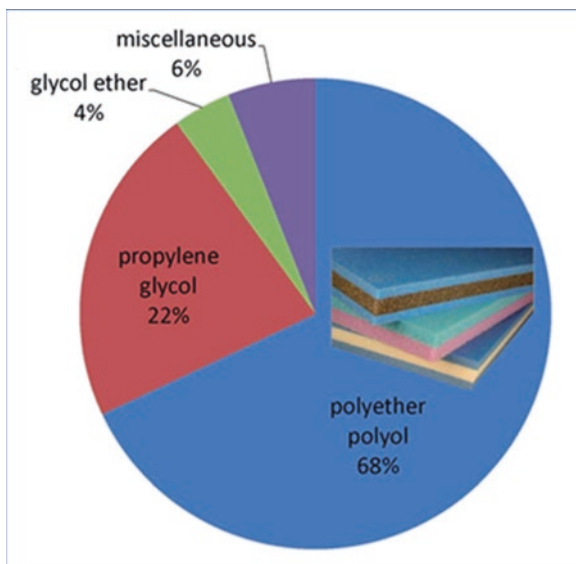
Fig. 9 Changing scenarios of global PO production by processes [63, 64]

(CHP) process. The global contribution of PO production by these processes is shown in Fig. 9.

Currently, cholorohydrin, EBHP, and TBHP have a combined PO production share of about 80%. However, this scenario is shifting toward more environmentally friendly and economical technology based on the CHP and HPPO processes. The drawbacks of cholorohydrin, EBHP, and TBHP processes are the generation of additional co-products. For instance, in the case of chlorohydin process [65–67], for each ton of PO production approximately 2.0 tons of $CaCl_2$ is generated as by-product and the process consumes 1.4 ton of chlorine and 1.0 ton of calcium hydroxide (Table 6). Additionally, the process consumes large volume of water which in turn generates $CaCl_2$ or NaCl (NaOH is as neutralizing medium) containing

Table 6 Industrial journey of commercial propylene oxidation processes [65]

Process	1st Gen (1910–)	2nd Gen (1960–)		3rd Gen (2003–)	4th Gen (2008–)	5th Gen
		SM/PO	PO/TBA			
Feedstock	Propylene	Ethylbenzene and propylene	Isobutane and propylene	Cumene and propylene	Propylene	Propylene or propane
Oxidation source	Cl$_2$ and H$_2$O	Air	Air	Air	H$_2$O$_2$	Air or O$_2$
Byproduct (t/t-PO)	CaCl$_2$ (2.0)	Styrene (2.5)	TBA (2.1)	–	H$_2$O	–
Propylene selectivity	Low	Medium	Medium	High	High	–
Sustainability index	Low	Medium	Medium	Medium	High	High

First generation (1910–): chlorohydrin process
Second generation (1960–): (a) PO/SM co-production, (b) PO/TBA process
Third generation (2003–): Sumitomo PO only production
Fourth generation ((2008–): HPPO process
Fifth generation (under development): direct oxidation of propylene/propane to PO

wastewater. Because of this chlorohydrin route is disfavored for new plant start-ups in most locations [68]. The environmental viability of a modern chlorohydrin plant depends on its scale of production, wherein large-scale plants can be fully integrated with chlorine/caustic plants.

In the PO/SM process (also known as EBHP process) [69–71] ethylbenzene is used as a feedstock which is oxidized in the presence of air to produce ethylbenzene hydroperoxide. Epoxidation of propylene with ethylbenzene hydroperoxide leads to the formation of propylene oxide and 1-phenyl ethanol as a co-product (Scheme 2). In the subsequent step, 1-phenyl ethanol is further dehydrated to form styrene using titania or alumina catalyst [72]. LyondellBasell and Shell are the two major global players for this process technology [66, 73].

In the EBHP process, every ton of PO production leads to approximately 2.5 tons of styrene co-production [74]. Co-produced styrene is a useful chemical and is employed as a valuable monomer in the production of a number of homopolymers such as polystyrene (PS), expandable polystyrene (EPS), and various copolymers such as acrylonitrile-butadiene-styrene (ABS) resins, styrene-acrylonitrile (SAN) resin, acrylonitrile-styrene-acrylate (ASA), styrene-butadiene (SB) latexes, styrene-butadiene rubber (SBR), and unsaturated polyester resins. These products have versatile applications in packaging, construction, domestic appliances, home furnishings, and so on. Because of this, EBHP process continues to support the PO production.

In TBHP process [75–77] isobutane is used as a feedstock and tert-butyl alcohol (TBA) is generated as a co-product along with propylene oxide (Scheme 3).

By employing this process, approximately 2.1 tons of TBA is produced as by-product for each ton of PO [63]. TBA can be used in the production of two ether-based oxyfuels, methyl tertiary butyl ether (MTBE) and ethyl tertiary butyl ether
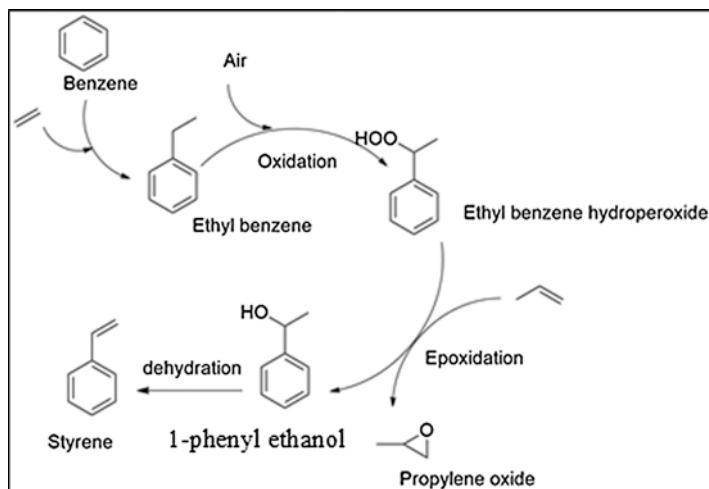
Scheme 2 Reactions associated with the EBHP process
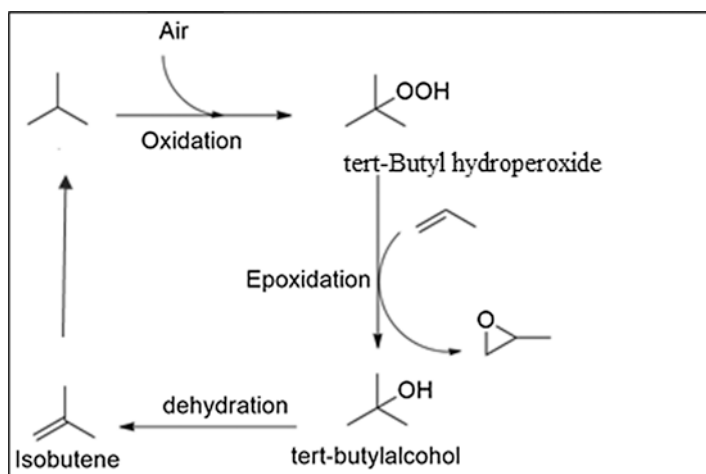
Scheme 3 Reactions associated with the TBHP process

(ETBE). These ethers are used as octane-booster in gasoline that help gasoline burn cleaner and reduce emission from automobiles. MTBE has a number of advantages over other octane boosters such as lower content of benzene, formaldehyde, and volatile organic compounds. MTBE is used as gasoline octane booster additive in many parts of the world especially in India and China; however, its use in the USA and Europe has been banned by laws. MTBE has a negative health effect if contaminated with groundwater due to spillage at gasoline stations and transportation.

The choice between EBHP and TBHP process largely depends on the utilization of co-product in the existing refinery complex and demand of the co-product, especially in the domestic market. If the refinery is intregated with downstream petrochemicals complex, EBHP is a preferred choice, while TBHP process is suitable for integrating with refineries since MTBE can be produced and utilized as gasoline octane booster additive. Interestingly, both EBHP and TBHP processes are attractive in China and India since there are high demand for both styrene and MTBE. However, cost of styrene and TBA are severely affected by market conditions. Thus, PO production economics through THBP or EBHP process is not the optimal one and therefore companies have strategically shifted toward better alternatives.

An improved hydroperoxide process based on using cumene as a feedstock instead of ethylbenzene has been invented and commercialized by Sumitomo Chemical, Japan. This process is called as "Cumene PO-only" process and is fundamentally similar to EBHP and TBHP processes, but avoids the formation of by-products since the co-product is recycled back as feedstock (Scheme 4).

Three different types of reactions are involved in the overall cumene-PO only process [78]: (a) oxidation; (b) epoxidation; and (c) hydrogenation. Sumitomo Chemical has developed novel mesoporous titanium silicalite (TS-1)-based zeolite having pore diameter of 1–20 nm as compared to the classical microporous TS-1 zeolite having pore size of 0.5–0.6 nm [78]. Sumitomo's mesoporous TS-1 has higher surface area and superior performance in the epoxidation reaction.

Sumitomo Chemical commercialized the first PO-only (200,000 tons/year) plant in Japan in 2003. The second plant was built at Petro Rabigh, Saudi Arabia, and started production in 2009. The technology is also licensed to S-OIL Corp. of South Korea with a capacity of 300,000 tons/year, came on stream in 2018. Two more
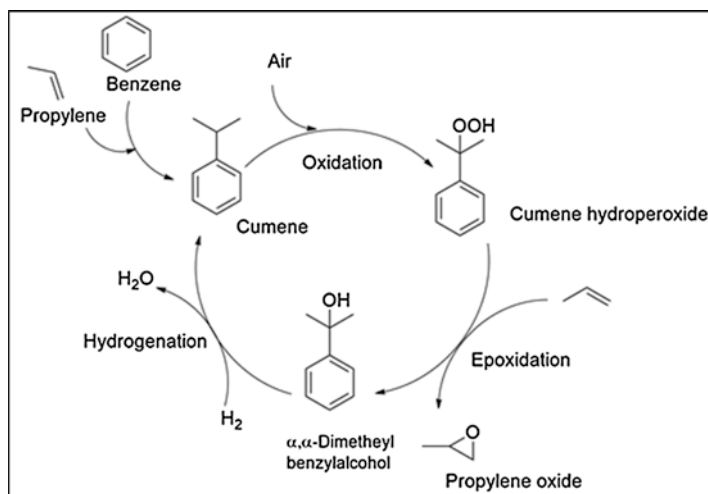
Scheme 4 Reactions associated with the Cumene "PO-only" process

plants will be constucted: a subsidiary of PTT Global Chemical Public Company Limited of Thailand is constructing a plant of 200,000 tons/year and is due to be completed in 2020. Bharat Petroleum Corporation Limited, India has entered into an agreement with Sumitomo Chemical to set up a 300,000 tons/year PO plant which is expected to come stream in 2022–2023 [79]. The new PO only cumene process offers higher yield of PO with only producing small amounts of by-products as well as environmentally superior than the conventional hydroperoxide processes [80].

Fourth-generation PO-only process uses hydrogen peroxide as an oxidant. BASF-Dow and Evonik-Udhe both have developed their proprietary HPPO technology [81]. This method produces only water as co-product and therefore has highest environmental footprints. The HPPO process [82] is revolutionizing the practical implementation of the sustainable catalytic oxidation using H_2O_2 as an oxidant. A number of HPPO plants have been commissioned in the last few years to cater the growing demand for PO [83]. The largest HPPO plant (390,000 tons/year) owned and operated by SCG-Dow is located in Map Ta Phut, Thailand, and producing PO since 2011. Two other HPPO plants are: (a) located at Antwerp, Belgium operated jointly by BASF-Dow (since 2008) with a capacity of 300,000 tons/year [84] and (b) operated by SKC (since 2008) with a capacity of 300,000 tons/year at Ulsan, South Korea and technology licensed by Evonik-Uhde [85]. In the BASF-Dow process [86], PO production is performed in a fixed-bed reactor over a TS-1 catalyst [87–91]. Evonik-Uhde technology also uses a Ti-silicalite catalyst. In all the above-mentioned HPPO plants, H_2O_2 is produced from the classical anthraquinone oxidation (AO) process for PO production. It is claimed by the companies that PO production based on the HPPO process is more economical compared to other PO production processes as HPPO plants require 25% less capital to build [92].

HPPO process produces water as only by-product along with PO as a major product. Apart from water, unlike other traditional processes, there is no other by-product formation and thus the process has the highest environmental footprints (Scheme 5). Traditional process generates styrene monomers and propylene dichloride as by-products which can be avoided in the HPPO process. In general, the HPPO process is environmentally superior in comparison to other conventional PO processes.

The other environmental benefits of the HPPO plant when compared to traditional PO production technologies include reduction in wastewater by about 80%, decrease in energy consumption by about 35%, and fewer requirements for physical footprint and infrastructure, and simpler raw material integration. Owing to such breakthrough process technology, BASF and Dow received together the Presidential Green Chemistry Challenge Award in 2010 from the US Environmental Protection Agency (EPA) [93]. This award is a great recognition and validates the greener environmental footprints of the HPPO technology.
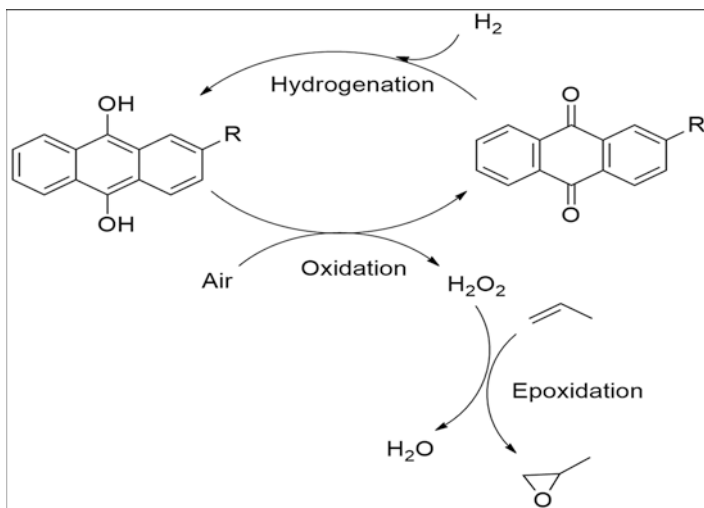
Scheme 5 Hydrogen peroxide propylene oxide (HPPO) process coupled with AO process

4.1.2 Future Outlook of PO Production

The most obvious choice for PO production would be based on the direct selective oxidation of propylene or propane using air or oxygen as an oxidizing agent [94]. The selective propylene oxidation using molecular oxygen for PO synthesis is often considered as the Holy Grail in catalysis research. A number of chemical companies and academic institutes have been working to develop this route for several years. However, because of the unsymmetrical nature of the propylene molecule, its selective oxidation to PO is severely limited by thermodynamics [95, 96]. Oxidation using molecular oxygen required high energy of 498 kJ/mol for dissociating O–O double bond. Once O–O bond is dissociated, oxygen tends to accumulate negative charge (O–), and thus preferentially attacks the weakly bound allylic hydrogen atoms (–CH$_3$) of propylene resulting in the production of acrolein (Scheme 6).

On the other hand, overoxidation of propylene leads to thermodynamically favored CO$_2$ and H$_2$O molecules. Thus, to obtain industrially relevant selectivity for PO, the rate of side reactions has to be minimized with the help of highly selective oxidation catalyst.

AIST-Nippon Shokubai has made significant progress on the development of selective oxidation of propylene to PO by the reaction of propylene, O$_2$ and H$_2$ using nano gold catalyst in the same reactor [97]. As silver-based catalyst is used in the commercial ethylene oxide production, the silver catalyst had been also explored in the epoxidation of propylene. PO selectivity of 50–80% was achieved, while further improvement in terms of the catalytic performances for PO production was achieved using gold nanoparticles (NPs, 2.0–5.0 nm) [98] deposited on anatase TiO$_2$ or mesoporous titanium-silicate catalyst [99–101] owing to which the reductive activation of O$_2$ with H$_2$ is obtained at milder condition.
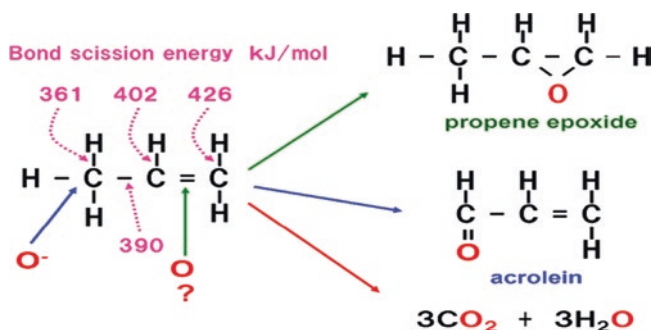
Scheme 6 Various pathways for oxidation of propylene

4.2 Acrylonitrile (ACN)

Acrylonitrile (ACN) is a versatile chemical intermediate and annually more than 14 billion pounds of ACN is produced worldwide. ACN has a unique chemical structure (CH_2=CH–C≡N) containing nitrile (–C≡N) as well as C–C double bond in conjugation. Nitrile group can undergo hydrolysis to give acrylic acid and followed by acrylates by esterification with alcohol. The double bond in ACN can take part in various reactions such as Diels-Alder reaction, hydrogenation, cyanoethylation, hydroisomerization, and hydroformylation reactions. Thus various useful chemicals can be produced employing ACN as an intermediate (Fig. 10).

The primary end uses of acetonitrile are acrylonitrile-butadiene-styrene (ABS), styrene-acrylonitrile (SAN) resin, acrylic fiber, and acrylamide. As per IHS Markit data, the acrylonitrile market is expected to grow at a CAGR of over 3% during 2019–2024. One of the major factors for this growth is the increasing demand for ABS which is a durable thermoplastic used in automotive components, telephone and computer casings, and sports equipment. Another material nitrile rubber is used in the manufacture of hoses for pumping fuel. Acrylonitrile is also used in the production of plastic resins, paints, adhesives, and coatings. Owing to its protective property, high chemical strength, and resistance to bases, acids, and other corrosive compounds, acrylonitrile products are highly preferred for packaging in the electronic appliance and the food and beverage industries.

4.2.1 Acrylonitrile Production: Commercial Advancement

Acetylene Route

Charles Moureu, a French organic chemist, first synthesized acrylonitrile in 1893. However, it did not see commercial importance till the 1930s, when new applications of acrylic fibers started in textiles and synthetic rubber industries [103]. The early commercial production was based on the acetylene route (Scheme 7) and some of the major producers of acrylonitrile using this route were BASF, American
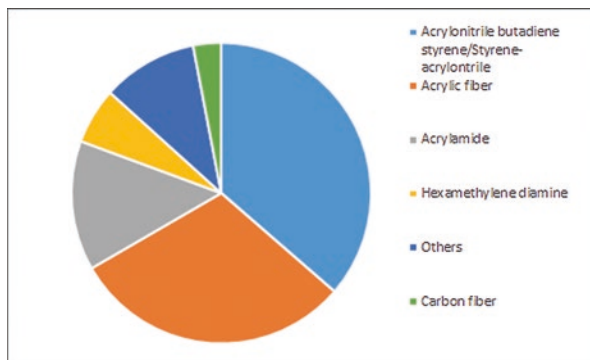
Fig. 10 Various applications of acrylonitrile and its derivatives [102]

$$\text{Acetylene} + HCN \rightarrow CH_2=CH-C\equiv N + \quad H^0{}_{298} = -175 \text{ kJ/mol}$$
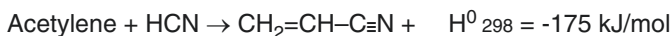
Scheme 7 Hydrocyanation of acetylene

Cyanamid, Dupont, Union Carbide, and Monsanto. The process was the main route of ACN production before the arrival of ammoxidation process in the 1970s [104].

The reaction was performed in dilute hydrochloric acid at 80–90 °C and in the presence of cuprous chloride and ammonium chloride as catalysts. High molar yield of ACN (90%) was obtained with acetaldehyde, vinyl acetylene, divinylacetylene, vinyl chloride, cyano butane, lacto nitrile, and methyl vinyl ketone as minor by-products. Availability and high cost of acetylene, along with involvement of multiple steps for separation of catalysts as well as by-products were the major drawbacks of the acetylene-based process. During 1960s, annual production of ACN was around 260 million pounds (125 KTA), and it was treated as a low-volume speciality chemical. However, a discovery of numerous applications of ACN derivatives propel its demand and thus, it was imperative to explore alternative routes based on cheaper feedstocks to make ACN production economically attractive. Methods such as addition of hydrocyanic acid to ethylene oxide (Scheme 8), addition of hydrocyanic acid to acetaldehyde (Scheme 9), nitrosation of propylene (Scheme 10), and dehydrogenation of propionitrile (Scheme 11) were explored [105]. Later, ammoxidation of propylene (Scheme 12) also known as SOHIO process, displaced all the processes [7, 8].

ACN can be obtained from reactions of ethylene oxide with aqueous hydrocyanic acid at 60 °C and subsequent dehydration of ethylene cyanohydrin in the liquid phase at 200 °C. Ethylene cyanohydrin process was first produced acrylonitrile in Germany and on industrial-scale production in America.

Another process for ACN synthesis was based on the reaction of acetaldehyde with hydrocyanic acid (Scheme 9). However, such process did not reach the industrial scale.

Nitrosation of propylene (Scheme 10) was another process exploited for acrylonitrile synthesis, however the process never achieved commercial success.

Dehydrogenation of propionitrile (Scheme 11) is also reported in the literature for ACN synthesis. However, the method did not see commercial reality.

$$C_2H_2O + HCN \rightarrow HO\text{-}CH_2\text{-}CH_2\text{-}CN \rightarrow CH_2\text{=}CH\text{-}CN + H_2O$$
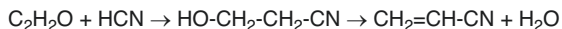
Scheme 8 Hydrocyanation of acetaldehyde followed by dehydration

$$CH_3CHO + HCN \rightarrow CH_3\text{-}CHOH\text{-}CN \rightarrow CH_3CHCN + H_2O$$

Scheme 9 Dehydrogenation of propionitrile

$$CH_2\text{=}CH\text{-}CH_3 + NO \rightarrow CH_2\text{=}CH\text{-}CN + H_2$$
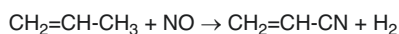
Scheme 10 Nitrasation of propylene

$$CH_3\text{-}CH_2\text{-}CN \rightarrow CH_2\text{=}CH\text{–}C\text{≡}N + H_2$$
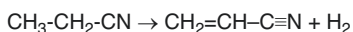
Scheme 11 Dehydrogenation of propionitrile

The arrival of SOHIO process in 1960s dramatically changed the scenario of the ACN production and annual worldwide production of acrylonitrile rapidly increased from 260 million pounds in 1960 to more than 11.4 billion pounds in 2005 [103].

Ammoxidation Route

Currently, the SOHIO process accounts for more than 95% of the world's ACN production. SOHIO process was initially developed in 1957 by Standard Oil Company, or SOHIO which was later acquired by British Petroleum (BP) in 1978. Currently, the acrylonitrile technology licensing and catalyst businesses are part of INEOS. SOHIO process uses propylene, ammonia, and air (O_2) as feeds. At present, the SOHIO process makes around 7 billion kg/year of acrylonitrile worldwide [106], which is equivalent to 1 kg/year per person on planet earth. The SOHIO process entails the production of acrylonitrile through the direct gas-phase oxidation of propylene in the presence of a heterogeneous bismuth-phosphomolybdate-based catalyst with ammonia and oxygen (from air) as feed gases (Scheme 12).

As a result lower acrylonitrile yield is obtained in the SOHIO process if the catalyst used is not highly selective. A schematic process flow diagram of commercial SOHIO process is shown in Fig. 11. The commercial SOHIO process uses fluid bed reactors (10–12 m dia) and with a large amount of catalyst (75,000 kg of catalyst/reactor) and the particle size of the catalysts ranges between 40 and 100 μm for effective fluidization [104]. The reactors are operated in the temperature range of 420–450 °C and 1.5–3 bar pressure. The residence time is kept low of 5–8 s and a superficial linear gas velocity between 0.2 and 0.5 m/s is used for effective operation. With this innovation, in 1960s, a plant having production capacity of 47.5 million pounds/year was set up by Sohio Oil. The new process reduced the cost of the acrylonitrile production by half as compared to the acetylene-based production process. Therefore, acetylene-based acrylonitrile production plant was gradually replaced by novel propylene ammoxidation process and most of the acrylonitrile

Main reaction

$H_2C=CH-CH_3 + 3/2O_2 + 3/2NH_3 \rightarrow 3/2CH_3-CN + 3H_2O$ --   (i)

The reactions (ii to vii in Scheme 12) among propylene, ammonia and oxygen can lead to the formation of a number of by-products as follows:

Side Reactions

$H_2C=CH-CH_3 + 9/2\ O_2 \rightarrow 3CO_2 + 3H_2O$ (ii)

$H_2C=CH-CH_3 + 3\ O_2 \rightarrow 3CO + 3H_2O$ (iii)

$H_2C=CH-CH_3 + O_2 \rightarrow CH_2-CH-CHO + 3H_2O$ (iv)

$H_2C=CH-CH_3 + 3O_2 + 3NH_3 \rightarrow 3H-CN + 6H_2O$ (v)

$H_2C=CH-CH_3 + 3/2O_2 + 3/2NH_3 \rightarrow 3/2CH_3-CN + 3H_2O$ (vi)

$NH_3 + 3/4O_2 \rightarrow 1/2N_2 + 3/2H_2O$ (vii)
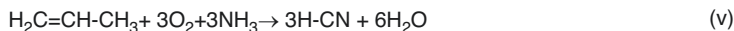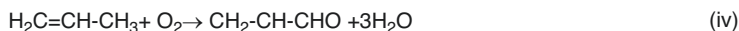
Scheme 12 Non-selective partial and complete oxidation of propylene and ammonia to by-products
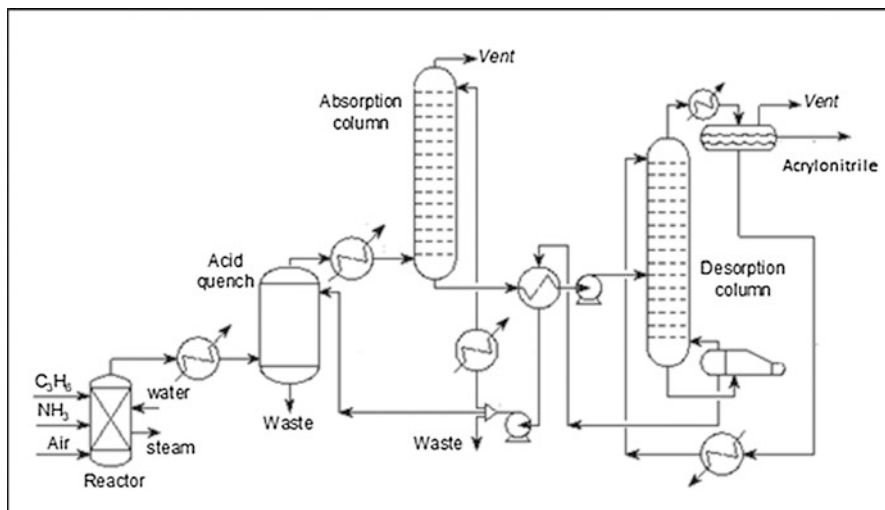
Fig. 11 Schematic process flow diagram of the commercial propylene ammoxidation process [107]

Table 7 Various molybdate-based commercial catalysts and their performance in acrylonitrile production

Improvement of catalyst's version	Catalyst formulation	Acrylonitrile yield (%)
1st generation (1960–1963)	$Bi_9PMo_{12}O_{52}$ (50% support)	55
2nd generation (1963–1965)	$Fe_{4.5}Bi_{4.5}PMo_{12}O_{52}$-$SiO_2$ (50% support)	65
Advanced multicomponent catalyst:		
1. 1969–1970	1. $K_{0.1}(Ni, Co)_9Fe_3BiPMo_{12}O_3$-$SiO_2$ (50% support)	75
2. 1975–1991	2. $(K, Cs)_{0.15}(Ni, Co, Mn)_8(Fe, Cr)_{2.5}BiMo_{13.2}O_x$-$SiO_2$ (50% support)	78–80
3. 1992–1995	3. $(K, Cs)_{0.15}(Ni, Mg, Mn)_{7.5}(Fe, Cr)_{2.3}Bi_{0.5}Mo_{12}O_x$-$SiO_2$ (50% support)	>80

Table 8 Various antimonate-based commercial catalyst and the yield of acrylonitrile

Improvement of catalyst's version	Catalyst formulation	Acrylonitrile yield (%)
Early catalyst	$Fe_{4.5}Sb_{8.6}O_x$-supported with 40% SiO_2	65
	$USb_{4.6}O_x$-supported with 40% SiO_2	70
Advanced multicomponent catalyst	$Na_{0.3}(Cu, Mg, Zn, Ni)_{0-4}(v, W)_{0.5-1}Mo_{0.5-2.5}Te_{0.2-5}Fe_{10}Sb_{13-20}O_x$ supported with 40% SiO_2	75

plant was licensed by SOHIO process. From then, BP chemical developed several catalyst formulations for propylene ammoxidation (Fig. 11) with acrylonitrile yield improvement and few of them were commercialized (given in Tables 7 and 8). Till date, the most effective commercial ammoxidation catalyst is based on bismuth-molybdates which promote selective ammoxidation reaction through catalytic cycle as shown in Fig. 12.

4.2.2 Recent Advances in Ammoxidation Catalyst

The first-generation commercial ammoxidation catalyst which was discovered in the late 1950s by SOHIO after about 2 years of exploratory research was a $Bi_9PMo_{12}O_{52}$ which offered 55% of acrylonitrile yield [104]. Although the catalyst life was about 2 years, it was sufficient to initiate commercial production of acrylonitrile because of its high market demand. Since the SOHIO process is based on the fluidized bed reactor, attrition resistant catalyst was a prerequisite in the commercial operation. To impart attrition resistant catalyst, silica was mixed with metal oxides for offering mechanical strength while spherical particles were made through spray drying route. Since then, several catalyst formulations were developed by SOHIO
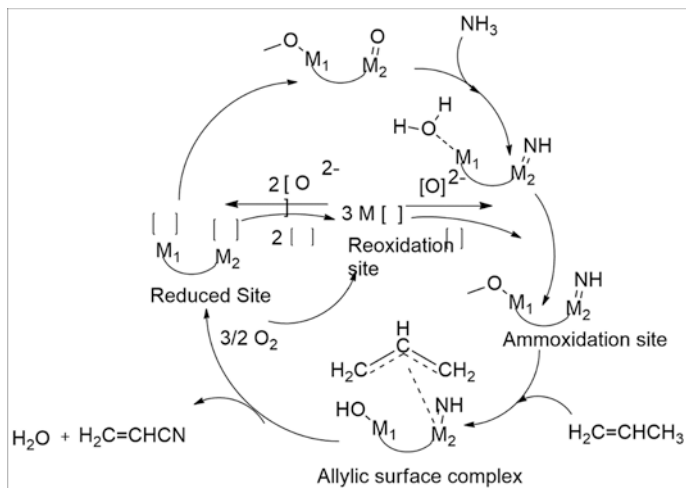
Fig. 12 Mechanism of selective ammoxidation of propylene over molybdate catalyst [108–111]

during 1960–1995 for improving the catalyst stability and ACN yield ranging from 55% to 82%. In second-generation catalyst [112, 113], ACN yield was improved from 55% to 65% by introducing redox element Fe into the bi-phosphomolybdates (first-generation catalyst). Though ammoxidation yield improvement was significant in second-generation catalyst, at high O_2 partial pressure, $Fe_2Mo_3O_{12}$ was produced from the catalyst system which promoted overoxidation of propylene (complete combustion to CO_x). To circumvent such an issue, redox chemistry was re-thought and divalent element such as Ni, Co, and alkali metal such as K was incorporated into the structure to prepare first multiphase catalyst system for ammoxidation reaction. The yield was improved significantly to 75–79% (commercial yield 75%). Fe(II) is stabilized in presence of divalent Ni(II) and Co(II) at oxidizing condition. From stabilized iron-molybdate, oxygen is dissociated, incorporated, and transmitted in lattice site for effective ammoxidation reaction. Alkali is incorporated to kill the surface acidity and thereby acrylonitrile selectivity improvement is achieved. Accordingly, several multicomponent mixed oxide catalyst developed by SOHIO from 1969 to 1995 and acrylonitrile yield reached to >80% [114–117]. Interestingly, the seventh and subsequent generation of catalysts are still based on $Bi_2O_3 \cdot MoO_3$, but the catalyst system is much more complex than the first generation and are based on multicomponent, multiphase catalytic system, e.g., (K,Cs)(Ni,Co,Mg,Mn)(Fe,Cr)BiMoO. The advanced catalysts can give about 83% acrylonitrile yield and with catalyst life of about 10 years. It is interesting to mention that although the current catalyst can offer 83% yield of acrylonitrile, there is still room for further improvement since the thermodynamic limit can yield 100% acrylonitrile [104].

Notably, most of the commercial catalyst comprises bi-phosphomolybdates as an active component. Without bismuth, catalytic activity was not obtained. Montedison

Corporation developed Te-molybdate-based catalyst [118–120]. However, the volatility of Te made the catalyst system commercially less important [104].

Apart from molybdate, there is few commercial success with antimonite-based catalyst for propylene ammoxidation. Non-radioactive uranium-based antimonate catalyst system [121–124] was also developed by SOHIO in late 1960 and ACN yield was higher than firsst- and second-generation catalyst. However, the catalyst was phased out later in 1970 due to the residual radioactivity and heavy uranium contamination. Fe-based antimonate [125] is also somewhat successful commercially; however, loss of antimony from the catalyst is the reason for the low popularity. Another multicomponent antimonate-based ammoxidation catalyst [126] is used in commercial unit by Nitto Corporation. However, for SOHIO process (now BP), so far bi-phosphomolybdates remain the dominant ammoxidation catalyst. Even with the most sophisticated multicomponent Bi-Mo-O_x catalysts (SOHIO Catalyst-49 and C-49-C) the acrylonitrile yields lie between 80% and 82%, because of the unavoidable high number of by-products generated from the undesired reactions at the complete conversion of propylene.

4.2.3 Emerging Alternatives: Propane Ammoxidation and Its Catalyst

Since propane is a readily available and inexpensive feedstock than propylene, the obvious choice for ACN production would be based on propane. However, propane is a thermodynamically stable molecule than propylene and requires improved catalyst or higher operating temperature for its activation. Several companies such as Asahi, Mitsubishi, and BP chemicals have been developing the propane ammoxidation process as a replacement to propylene ammoxidation process. Two routes can be employed for technological development for propane ammoxidation: (a) propane dehydrogenation followed by traditional ACN production through SOHIO process: integration of two-step process, (b) direct ammoxidation of propane. However, propane dehydrogenation is expensive and thus integration of dehydrogenation and ammoxidation is a major bottleneck to the solution. Naturally direct ammoxidation of propane is more attractive choice to the researcher across the globe.

BP commissioned a demonstration plant in 1997 for making acrylonitrile using propane as feedstock and as per the company's estimation, it could reduce the production cost further by at least 20% in comparison to propylene-based ammoxidation [127]. The major limiting step for this process is to activate propane for ammoxidation reaction. Propane adsorption into the catalyst system is approximately ten times lower than its propylene counterpart.

$$\text{Propane ammoxidation}: CH_3 - CH_2 - CH_3 + NH_3 + 2O_2$$
$$\rightarrow CH_2 = CH - C \equiv N + 4H_2O$$

$$\text{Propylene ammoxidation}: CH_3 - CH = CH_2 + NH_3 + 3/2O_2$$
$$\rightarrow CH_2 = CH - C \equiv N + 3H_2O$$
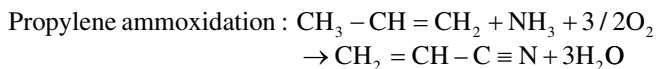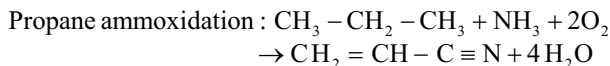
In the last several years, tremendous efforts have been made for developing propane ammoxidation catalyst system and various multicomponent catalyst systems [128–130] have been explored. Mitsubishi/Asahi catalyst system based on MoV(Nb,Ta)(Te,Sb)O can give about 65% acrylonitrile yield. The catalytic system contains two distinct phases, M1- the paraffin-activating phase and M2- the propylene mop-up phase which acts synergistically. The active sites are isolated from each other by Nb- or Ta-containing pentagonal bipyramids and different elements offer unique catalytic functions to synergistically promote selectivity for desired product. The olefin- and paraffin-based ammoxidation reactions although relatively mature still present challenges to the physical, inorganic, and synthetic chemist, to further explore the development of new materials. It is also of scientific curiosity to investigate the nature of the catalytic active sites capable of the complex molecular transformations required for the ammoxidation process. It would be also interesting to discover new and still more effective compositions for making acetonitrile production with 100% yield as per the maximum theoretical thermodynamic limit [104]. Fe-Bi/SiO$_2$-based catalyst system is examined at 500 °C for propane ammoxidation reaction which showed 49% yield of acrylonitrile at 36% propane conversion [131]. However, such acrylonitrile yield is not sufficient to replace propylene ammoxidation method as far as techno-commercial feasibility is concerned.

Very recently, a novel method of acrylonitrile production from renewable feedstock such as 3-hydroxypropanoate (ethyl 3-HP), which can be made from 3-hydroxypropionic acid (3-HP), has been established [132]. 3-HP can be produced from sugars catalyzed by the selective microbes. The process is based on two steps first being the dehydration of ethyl 3-HP (at 260 °C) over TiO$_2$ catalyst to ethyl acrylate followed by nitrilation with ammonia to ACN over TiO$_2$ catalyst at 315 °C. Another promising renewable route is based on glycerol dehydration to propylene followed by ammoxidation of propylene to ACN. Thrust for renewable acrylonitrile from bio-based alternative sources will increase to avoid petroleum-based propylene price volatility and also for reducing the carbon footprint of the existing ACN process.

4.3 Acrylic Acid

4.3.1 Chemical and Technical Aspects of Acrylic Acid

Acrylic acid (CH$_2$=CHCOOH) is one of the simplest unsaturated carboxylic acids. It has a unique chemical structure comprising of a vinyl group connected to a carboxylic acid. Due to the presence of C=C and C=O bond conjugation, acrylic acid can undergo both electrophilic addition and nucleophilic substitution reactions. Such a conjugated C–C double bond can stabilize free radical and thus undergo free radical polymerization reactions in presence of a suitable initiator. The carboxyl group later can allow nucleophilic displacement reactions as well as esterification reactions to incorporate the desired functional group into the polymer moiety. Crude

acrylic acid, obtained from plant, is later upgraded to two different grades of acrylic acids. Technical Grade or ester grade acrylic acid (94% purity and the remaining 6% comprises mainly maleic anhydride, propionic acid, acetic acid, and furfural) and glacial and polymer grade acrylic acid (98–99.7% purity) [133]. About 55% of the crude acrylic acid is used as ester grade acrylic acid. The remaining 45% is further purified to make glacial acrylic acid. Commodity acrylic esters are produced from ester or technical grade acrylic acid. Commodity acrylic esters are widely used for the production of surface coatings materials, sealants and adhesives, textiles, plastic additives, and paper treatments. Polyacrylic acid, polyacrylic acid copolymers, and anionic polyelectrolytes-based polymers are produced using highly purified acrylic acid, i.e., glacial acrylic acid. Polyacrylic acids are further modified to produce superabsorbent polymers (SAPs). Some other applications of homo and co-polymers of polyacrylic acid and acrylates are dispersants/antiscalants, anionic polyelectrolytes for water treatment, and rheology modifiers. The increasing area of applications for acrylic acid is superabsorbent polymers (SAPs) and detergent polymers. SAPs are cross-linked polyacrylates that have the ability to absorb more than 100–200 times liquid of their own weight. Detergent polymers made from combination of homopolymer polyacrylates and copolymers of polyacrylic acid with maleic anhydride and then the combination are used both in zeolites and phosphates-based washing powder formulations. Increasing middle-class population, extending lifespan and health awareness increasing demand, consumption, and growth for the acrylic acid (AA)-based superabsorbent polymer market [134].

4.3.2 Global Acrylic Acid Market Overview

Global acrylic acid market is expected to reach USD 22.6 billion by 2022. According to a new study by Grand View Research, Inc., the key driver for expecting market growth is the increasing demand of glacial acrylic acid in superabsorbent polymers (SAP) production. Versatile applications of SAP in niche segments such as water treatment chemicals and radiation-cured coatings in emerging markets of Asia Pacific and Central & South America are expected to contribute important role in high demand acrylic acid growth projection. Consumption of acrylate esters took an estimated 50% of demand share till 2014. Growing application of various acrylate derivatives such as ethyl acrylate, butyl acrylate, and 2-EHA for usage in paints, coatings, and textiles industry is expected to contribute to the product's growth further. As per the current glacial acrylic acid consumption, it is expected to witness the highest CAGR projection of 5.7% from 2015 to 2022 as per Fig. 13.

There are several key manufacturers of acrylic acid and acrylic-based derivatives for consumers products. Companies like Arkema (France), Evonik Industries (Germany), The Dow Chemical Company (U.S.), Hexion Inc. (U.S.), BASF SE (Germany), Nippon Shokubai Co. Ltd. (Japan), Mitsubishi Chemical Holdings Corporation (Japan), Holding (Russia), PJSC Sibur LG Chem Ltd., and Sasol Limited (South Africa) are leading the market shares.
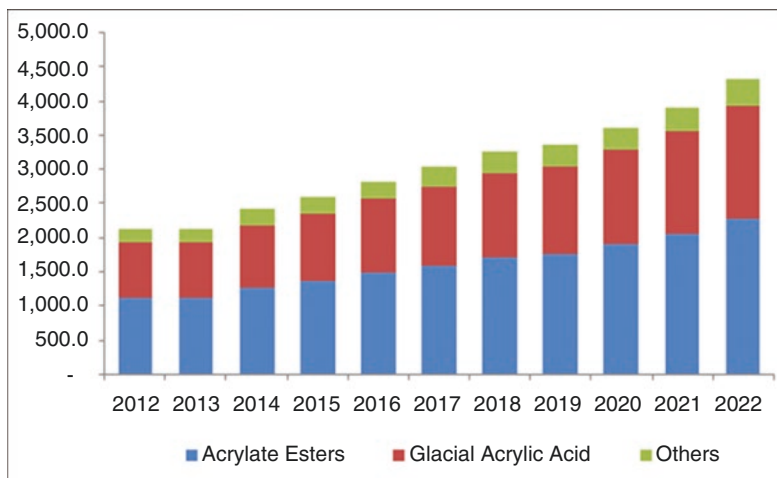
Fig. 13 Growth projection of acrylic acids, acrylates, and others [135]

4.3.3 Acrylic Acid Production: Recent Trend vs. Conventional Production

Conventionally acrylic acid is produced using propylene. However, several other bio-based acrylic acid production is underway especially for polyacrylic acid polymer production for disposable diaper application. Arkema has developed two-step process for acrylic acid production from glycerin which is the by-product of biodiesel manufacturing process. The first step is acrolein production, followed by acrolein oxidation to acrylic acid [136]. Though glycerin-based acrylic acid production is ready for commercial production by Arkema, cost competitiveness with conventional propylene-based acrylic acid process is holding back for commercialization. OPXBio, Cargill, Novozymes, and BASF are developing 3-hydroxypropionic acid (3-HP)-based process for acrylic acid production. Requisite R&D activities have been completed and it is now ready for commercial production. In similar line, Myriant has developed lactic acid-based acrylic acid production process in collaboration with an academic institute such as MIT and Pennsylvania State University (especially for catalyst development for dehydration of lactic acid to acrylic acid at 80% conversion and 90% selectivity) [137]. Various routes for acrylic acid production are given in Fig. 14.

However, bio-based acrylic acid production is facing serious challenges in terms of cost competitiveness due to the advent of shale gas resource which makes propane as low cost and abundant material, and consequently energy companies are putting several on-purpose propane dehydrogenation plants for low-cost propylene and related chemical production at lower price. Also, on-purpose production of propylene based on methanol has increased significantly.

The prices of acrylic acid highly depends on the cost of propylene. With the continuous increase in the capacity of propylene production, some countries take advantage of being low-cost manufacturer of acrylic acid. For example, China is
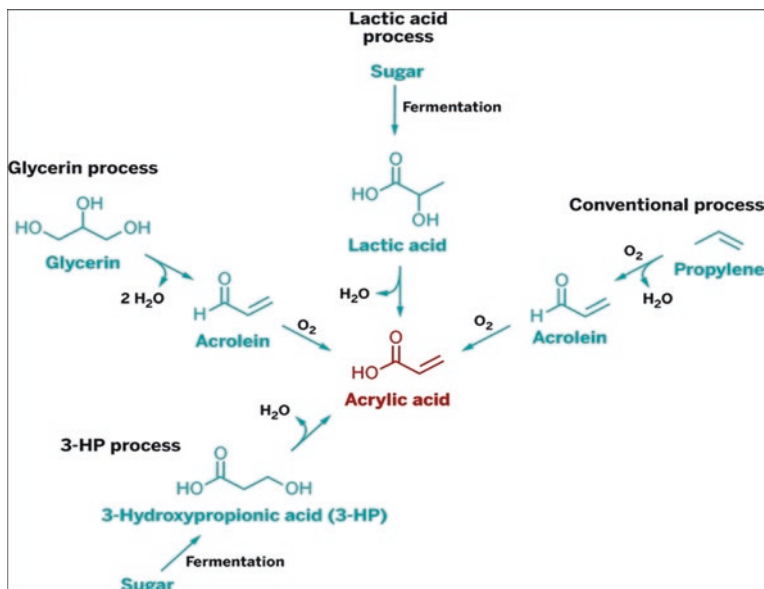
Fig. 14 Various pathway for acrylic acid production [137]

producing large quantities of propylene from steam crackers and coal-based MTO/MTP process and has increased production of acrylic acid for SAP production. BASF-YPC (a 50:50 joint venture of BASF and Sinopec) has constructed a new super-absorbent polymer (SAP) plant with a capacity of 60,000 mtpa [138].

4.3.4 Processes for the Production of Acrylic Acid: Commercial Perspective

The oxidation of acrolein is the earliest synthesis of acrylic acid and it was occurred in 1843. Since 1927, several commercial processes have come up for producing acrylic acid that include ethylene cyanohydrins process, the Reppe process, the β-propiolactone process, and the acrylonitrile hydrolysis. In recent time, the research effort has been put to develop microbe for producing 3-hydroxypropionic acid by fermentation. 3-Hydroxypropionic acid then underwent dehydration reaction to form acrylic acid.

Acrylic Acid Production from Propylene by Catalyzed Oxidation

Currently, the majority of acrylic acid is produced through two-step selective partial oxidation of propylene in presence of suitable catalytic system [139]. Two reactions happen in tubular fixed-bed reactor system connecting in series. Following two reactions occur in two reactors (Scheme 13).

Step-1

$H_2C=CH–CH_3+ O_2 \rightarrow H_2C=CH–CHO + H_2O$ $\Delta H = -340.8$ kJ/mol -----(i)
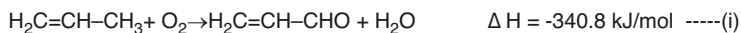
Propylene   Acrolein

Step-2

$H_2C=CH–CHO +0.5O_2 \rightarrow H_2C=CH–COOH$ $\Delta H = -254.1$ kJ/mol ------(ii)

Acrolein   Acrylic acid

Scheme 13 Two steps process for conversion of propylene to acrylic acid via acrolein

The first oxidation step employs highly active and very selective heterogeneous catalysts consisting of V- and Mo-based mixed metal system for oxidizing propylene to acrolein. In the second step, acrolein further undergoes selective oxidation to acrylic acid in presence of Co-Mo-based oxides at reaction temperatures of 200–300 °C with short contact times (~2 s) [140]. The current process offers acrylic acid yields of around 80–90% considering water absorption in the first step of reaction. Both the reactions are highly exothermic in nature and thus efficient heat removal from the reactors is necessary as per as operational point of view is concerned. The heat liberated from the reaction is exploited to produce steam and also molten heat transfer salt is circulated through the reactors to maintain safe and desired reactor temperature. After the reaction, gaseous product from the reactor is then sent to a quench tower, where the majority of the acrylic acid is recovered. Thereafter, acrylic acid solution from quench tower is routed to an extractor. Small portion of acrylic acid is recovered from uncondensed gases in an offgas treater. Part of the residual gas obtained by the top of the quench tower is incinerated, with the balance being recycled to the first-step reactor. The aqueous solution is sent to downstream units for product recovery. A schematic diagram with process description for commercial acrylic acid production plant is given in Fig. 15.

In the next step, liquid-liquid extraction is employed to separate out water and the resulting crude acrylic acids is passed further into two columns to remove the solvent and acetic acid. Finally, the crude acrylic acid is purified to an ester grade acrylic acid through a column bed for obtaining an extremely pure acrylic acid. Since acrylic acid is prone to polymerize, an inhibitor has to be added at critical points in the plants. One-step acrylic acid production by propylene production is also one of the alternative options. However, one-step process offers significantly low acrylic acid yield in comparison to the two steps acrylic acid production process [139]. The required temperature for the first step for the two-step process is in the range of 320–330 °C and for the second step is 210–225 °C. It is clear from the temperature data that higher activation energy is required to convert propylene than acrolein for the oxidation reaction. As one-step acrylic acid production process requires higher temperature around 325–350 °C [142], control of selectivity by avoiding the formation of undesired side products is one of the key challenges in the direct process. Various mixed oxide-based commercial catalyst formulation and
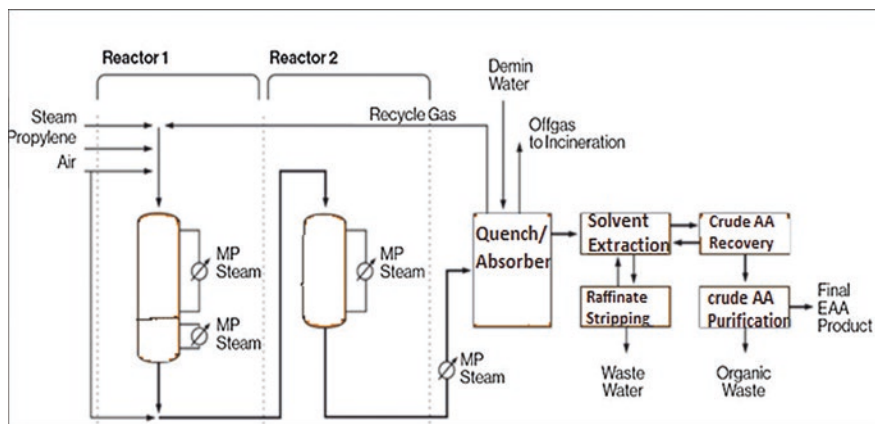
Fig. 15 Schematic diagram for the production process of acrylic acid from propylene [141]

their performance in acrylic production for both one-step and two-step processes are given in Tables 9, 10 and 11.

It is evident from Table 11 that single-step propylene conversion to acrylic acid has a much lower yield as compared to two-step conversion process (Scheme 14).

Acrylic Acid from Propane

Since propylene is a synthetic molecule, the obvious economic choice for making acrylic acid would be from naturally occurring propane than propylene. However, propane ($\Delta_f H°_{gas}$ = −104.7 kJ/mol) is thermodynamically much stable molecule than propylene ($\Delta_f H°_{gas}$ = 20.41 kJ/mol) and thus it has very low reactivity under various reaction condition. It has very high C–H bond strength at the terminal methyl position causing difficult to activate terminal position. The terminal C–H bond is even stronger than C–C bond and thus there is quite a high chance to obtain undesired side product while conducting partial propane oxidation to meaningful products. However, technical challenges are needed to overcome considering low-cost propane availability and for utilizing this abundant source for high-value chemical production (Scheme 15).

Even though tremendous research effort has been put for the development of one-step oxidation process for propane to acrylic acid production, the process is yet to see commercial success. Several catalyst systems such as vanadium phosphate [142], VPO/TiO$_2$-SiO$_2$, heteropolyacid compounds [175], and multicomponent metal oxides [176] have been explored for the single-step conversion of propane to acrylic acid. Among various catalyst systems, Mo-V-Te-Nb-O catalyst exhibits promising activity, wherein 70–80% of propane conversion with 50–60% of acrylic acid selectivity have been obtained.

Table 9 First stage catalysts of two-stage process and their performances

Company	Catalyst composition	Operating condition (feed propylene and air)			Results				
		C_3H_6 (%)	Air (%)	Temp (°C)	Conv. (%)	ACR (%)	AA (%)	ACR yield (%)	Total yield (%)
SOHIO [143]	Mo-Bi/SiO$_2$	9.5	53.3	454	56.9	71.8		40.9	
Knapsack [144]	Mo-Bi-Fe-P	9.7	4.1	400	70	84		58.8	
Nippon Kayaku [145, 146]	$Mo_{12}Bi_1Fe_1Ni_{4.5}Co_4P_{0.08}$	5.9	58.8	310	95.5	82.8	6	79.1	84.8
	$Mo_{12}Bi_1Fe_2Ni_1Co_3P_2K_{0.2}$	6.2	62.5	305	96	92	3	88	91
Nippon Shokubai [147, 148]	$Mo_{10}Bi_1Fe_1W_2Co_4K_{0.06}Si_{1.35}$	4	51	320	97	93	6.2	90.2	96.2
Sumitomo-Chemical [149]	$Mo_{12}Bi_1Fe_{5.1}Ni_6Tl_{0.3}P_{0.1}Mg_3$	6.7	46.7	375	96.3	86.6	7.1	83.6	90.4
Mitsubishi Petrochemical [150, 151]	$Mo_{12}Bi_1Fe_{0.4}Ni_{4.5}Co_4B_{0.1}Na_{0.05}Si_{6.3}$	4.5	53	350	99.4	81.4	13.6	80.9	94.4
Ube Industries [152]	$Mo_{10}Bi_{0.9}Fe_2Co_8V_{0.05}K_{0.05}$	6.7	67.6	330	98.8	91.4	2.4	90.3	92.7

ACR% acrolein selectivity, *AA%* acrylic acid selectivity

Table 10 Second-stage catalyst of two-stage process and their performances

| Company | Catalyst composition | Operating condition (feed: acrolein, air and H_2O) | | | | Results | | |
		ACR (%)	Air (%)	H_2O (%)	Temp (°C)	Conv. (%)	AA (%)	AA yield (%)
TOSOH [153]	Mo-V/SiO_2 (Mo/V = 2–8)	8	44	48	300	92	82	75.4
Rikagaku Res. Labs. [154]	$Mo_{100}V_{10}A_{13}Cu_{10}$/Al sponge	4	30	40	320	98.4	97.6	96
Toagosei Chemical [155]	$Mo_{17.7}V_{0.3}As_{1.43}$/$SiO_2$	5.1	38.5	51.7	320	96.5	91	87.8
Nippon Kayaku [156]	$Mo_{12}V_2W_{0.5}$/SiO_2	5.9	58.8	35.3	220	97.8	89	87
Nippon Kayaku [157]	$Mo_{12}V_3Cu_{2.5}Fe_{1.25}Mn_{0.1}Mg_{0.1}P_{0.1}$	2.8	24.2	73	210	99	98.5	97.5
Celanese [158]	$Mo_{12}V_3W_{1.2}Mn_3$	4.4	28.5	50	300	99	93	92
BASF [159]	$Mo_{12}V_2W_2Fe_3$	3.1	27.5	43	230	99	91.9	91
Nippon Shokubai [160]	$Mo_{12}V_{4.8}W_{2.4}Cu_{2.2}Sr_{0.5}$/$Al_2O_3$	4	51	45	255	100	97.5	97.5
SOHIO [161]	$Mo_{12}V_5W_{1.2}Ce_3$/SiO_2	5.9	58.8	35.3	288	100	96.1	96.1
Sumitomo Chemical [162]	$Mo_{12}V_3Cu_3Zn_1$/SiO_2	5	40	55	260	98.4	96.1	94.6
Mitsubishi Petrochem [163]	$Mo_{100}V_{20}Cu_2$	4	50	46	290	99.5	95.3	94.8

AA% acrylic acid selectivity

$$H_2C\ CH–CH_3 + 2O_2 \rightarrow H_2C = CH–COOH + H_2O;\ \Delta H = -254\ \text{kJ/mol}$$
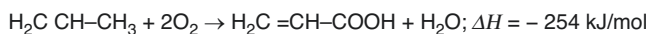
Scheme 14 One-step propylene oxidation to acrylic acid

$$C_3H_8 + 2O_2 \rightarrow CH_2=CH–COOH + 2H_2O\ \Delta H = -715\ \text{kJ/mol (at catalytic reaction condition)}.$$
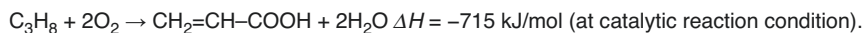
Scheme 15 One-step propane oxidation to acrylic acid

Table 11 One-step oxidation of propylene to acrylic acid

Company	Composition of catalyst	Temperature (°C)	Conversion (%)	Acrylic acid yield (%)	Acrolein yield (%)
Nippon Shokubai [164, 165]	Mo-W-Te-Sn-Co	350	92.7	65	–
	Nb-W-Co-Ni-Bi--Fe-Mn-Si-Z	325	99.6	73	11
Nippon Kayaku [166]	Ni-Co-Fe-Bi-As-Mo	350	99.6	60	–
Mitsubishi Rayon [167, 168]	Mo-Bi-Te-P-Co, Sb	390	85	53	–
	Mo-Ni-Co-Bi-Pd	355	72	50	–
Montecatini Edison [169]	Mo-V-Fe	400	84	61	–
BASF [170]	Mo-W-Te-Fe-Mn	340	89	38	–
Mitsibishi Petrochemical [171]	Mo-Sn-Te-P-Fe-Si	425	97	46	37
Asahi Glass [172]	Mo-Co-Te-Si, Ge, Ti, Zr	400	99	49	24
TOSOH [173]	Mo-Te-Co-Fe-P	370	87	34	35
Goodrich [174]	Mo-Te-Th-P	345	90	36	24

Recently, a published article in futuristic research about acrylic acid production described about the activation of inert propane CARENA (*CA*talytic membrane *Re*actors-based on *N*ew m*A*terials for C1-C4 valorization). It was an EU funded project carried out between 2011 and 2015 (Fig. 16). In this process, Mo/Bi-based mixed metal oxide was prepared by a sol-gel method which was employed for selective oxidation of propylene in a mixed propane feed with an increased catalytic performance over the standard catalytic system. Additionally, a Pd-loaded zeolite membrane catalyst was developed on the surface of 1 mm beads of γ-Al$_2$O$_3$ support for selective oxidation of CO in a propane-rich mixture.

By using this catalyst, a mild oxidation condition is achieved wherein selective CO oxidation temperature is around 65 °C. Propylene oxidation was carried out with pure oxygen in the presence of catalytic system in a pilot-scale unit (at a scale of about 1–3 kg h^{-1}) wherein 95% of propylene conversion and 85% of acrylic acid yield were achieved.

Several other promising catalysts have been developed by inventors that provide reasonably good propane or propylene conversion and selectivity to acrylic acid (Table 12). Some of the catalyst system and its process technology are in commercial practice.
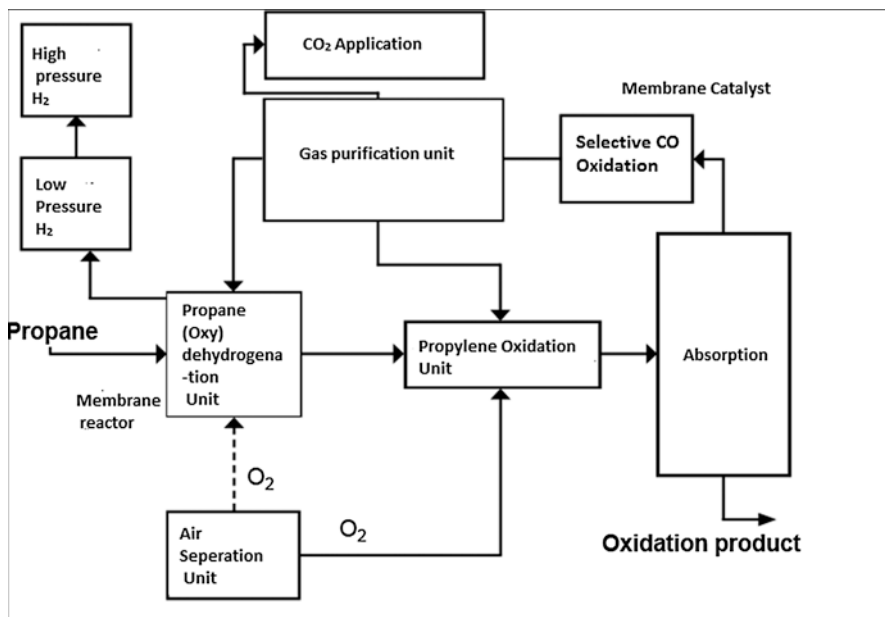
Fig. 16 Propane oxidation using membrane-oxidation catalyst in presence of CO [177]

4.4 Isopropyl Alcohol (IPA) and Its Industrial Importance

Isopropyl alcohol (IPA), which is often called as the first modern synthetic petrochemical, is one of the important lower alcohols—ranked third in commercial production behind methanol and ethanol [181]. IPA is widely used in hand sanitizer formulations and sold as rubbing alcohol in supermarkets and drugstores. IPA has similar physical characteristics with those of short-chains alcohols and mixes well with water. The major application of IPA is as solvent and used in various sectors such as paints, printing inks, in drug synthesis, and in the cosmetic and personal care products (Fig. 17). IPA is also used as a chemical intermediate in the production of acetone and base chemicals used in the cosmetics and pesticide formulations. Besides, IPA is also one of the most readily saleable chemicals and exempted from most of the government regulations and no special taxes are levied like ethanol selling [184].

Based on the end applications, several grades of IPA are produced and available in the market such as industrial/technical, cosmetic, pharmaceutical (USP), reagent, and electronic [182, 183]. End uses of various grades of IPA are given in Table 13.

Industrial-grade IPA is mostly consumed in the USA, Western Europe, China, Japan, and India as direct solvent applications. As per IHS Markit data, the global demand of IPA was around 2.60 million metric tons in 2018 and expected to grow at a CAGR of 2.6% to 2022 [185].

Table 12 Catalyst and process for propane/propylene oxidation to acrylic acid

Inventors	Year/U.S Patent No.	Technology/process	Catalyst	Operating condition	Performance indicator
ExxonMobil Research/Wang Kun et al. [178]	2011/7,910,772	Gas-phase two-step propylene oxidation (a) Propylene to acrolein over mixed metal oxide (b) Acrolein to acrylic acid The catalyst was produced in two phases: M1 (orthorhombic about 60–90%) and M2 (pseudo-hexagonal) Sol-gel technique used for catalyst preparation	$Mo_1V_{0.01-1}Te_{0.01-1}Sb_{0.01-1}O_{0.01-1}$	Reactor: Fixed bed/or fluidized bed Feed composition in mole ratio: $C_3:O_2:N_2:H_2O$ 5:9:67:17 Reaction temp: 380 °C Pressure: 1 atm. and GHSV = 2672 h^{-1} Pre-conditioning of catalyst carried out at 200 °C in N_2 150 mL/min	50% acrylic acid yield
BASF SE/Dieterle et al. [179]	2010/7,795,470	Gas-phase propane oxidation to acrylic acid. Mixed metal oxide catalyst was used for propane oxidation Crystalization is used for acrylic acid removal form water-acrylic acid solution	$Mo_1V_{0.33}Te_{0.15-1}Nb_{0.11}O_x$	Reactor: Fixed bed tubular Feed composition in mole ratio: $C_3:O_2:CO:H_2O$ 3.3:10:5:41.7 Temp: 350 °C, pressure: 2 bar Catalyst was pre-conditioned at 200 °C	Propane conversion: 27 mol% Acrylic acid selectivity: 60 mol%
Rohm and Haas Company/Gaffney et al. [180]	2010/7,718,568	Gas-phase oxidation of propane/mixture of propane and propylene Catalyst was prepared by hydrothermal technique	$Mo_{0.1}V_{0.3}Te_{0.23}Nb_{0.11}O_x$	Reactor: Fluidized bed Feed composition in mole ratio: $C_3:O_2:Steam$ 1:96:3 Temp: 300–400 °C Pressure: 1 atm. GHSV: 300–2000 h^{-1}	Propane conversion: 75% Acrylic acid yield: 52%
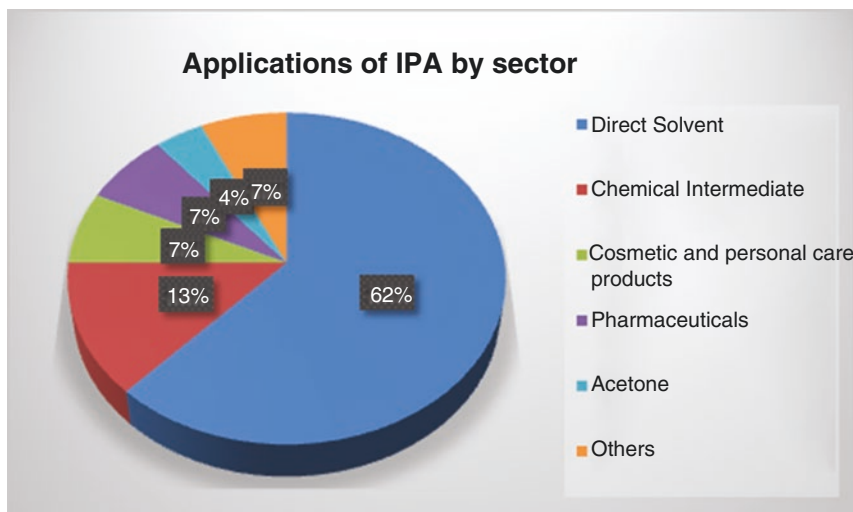
Fig. 17 Applications of IPA by sectors [182, 183]

4.4.1 Industrial Journey of IPA Production Processes

Indirect Hydration of Propylene

The indirect hydration of propylene was the only process for IPA production until the first commercial direct-hydration process introduced in 1951 [186]. The indirect hydration process consists of two steps (Schemes 16 and 17). The first step is the reaction between propylene and sulfuric acid to produce monoisopropyl and diisopropyl sulfates followed by the reaction with water that hydrolyzes these intermediates into isopropyl alcohol. The first step involves the absorption of propylene-rich gases into 85% sulfuric acid at 20–25 °C to form isopropyl hydrogen sulfate via the addition of the acid across the double bond (Scheme 16).

In the indirect process, both reaction temperature and concentration of the acid play an important role for the selective production of IPA. Higher concentration of acid favors olefin absorption and higher temperature promote higher conversion. In the subsequent step, hydrolysis of the intermediate monoester with water gives isopropanol and diluted sulfuric acid (Scheme 17). The second step is carried out in a lead-lined vessel to counter corrosive nature of sulfuric acid.

The indirect hydration process has a serious operational and environmental impact. Almost all units of the plant are subjected to the highly corrosive sulfuric

$$CH_3-CH=CH_2 + H_2SO_4 \cdot H_2O \rightarrow CH_3C(H)(SO_3H)CH_3$$
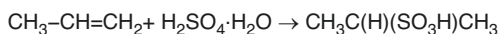
Scheme 16 Sulphonation of propylene

$$CH_3C(H)O(SO_3H)CH_3 + H_2O(\text{excess}) \rightarrow CH_3CHOHCH_3 + H_2SO_4(\text{dil.})$$
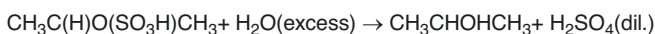
Scheme 17 Hydrolysis of sulphonated adduct of propylene

Table 13 Applications of various grades of IPA

Sr no.	Grade of IPA	Applications
1	Technical grade	Solvent for the extraction and purification of natural products such as vegetable oil and animal fats, as coolant in beer production, as polymerization modifier, as de-icing agent, as a preservative
2.	Cosmetic grade	Used in toiletries and rubbing alcohol
3.	Pharmaceutical grade	Used in pharmaceutical products such as medicinal tablets, as disinfectants, sterilizers, and skin creams
4.	Electronic grade	As a cleaner for printed circuit boards (PCBs), flat panel displays, and other electronic devices
5.	Industrial grade	Production of important chemicals such as methyl isobutyl carbinol (MIBC), methyl isobutyl ketone (MIBK), isopropyl acetate, isoproylamine, diisopropyl ether, and *tert*-butyl isopropyl ether

acid and the process suffers from low selectivity, i.e., the use of sulfuric acid as a catalyst leads to the formation of large amounts of secondary dialkyl ethers and oligomers. Moreover, with increasing temperature, olefin undergoes polymerization reaction which can seriously affect downstream operation. The other major limitation of the process is the dilution of sulfuric acid with water which makes the recovery of sulfuric acid from the diluted solution difficult and energy-intensive. Although the indirect process has several limitations, utilization of low alkene containing raffinate streams seems to be the only advantageous as compared to the direct hydration process which requires propylene rich steam [187].

Direct Hydration of Propylene

The acid-catalyzed direct hydration of propylene (Scheme 18) to IPA is an exothermic and equilibrium limited reaction. The equilibrium can be controlled to favor the desired product IPA at high pressures and low temperatures. However, at lower temperature reaction kinetics is not favored and the advantage of low temperature is difficult to utilize. On the other hand, high temperature favors subsequent etherification reaction of IPA (Scheme 19) to diisopropylether (DIPE) which can lead to decreasing yield of IPA. Thus, most known catalysts require optimum temperature to be effective and productive.

The first small-scale direct hydration plant was built by ICI in 1951. The process used a WO_3–ZnO supported on SiO_2. The reactor was operated at 230–290 °C and 20.3–25.3 MPa. Likewise, in the Veba-Chemie process, operational since 1966, a vaporized stream of propylene and water is passed through an acidic catalyst bed (H_3PO_4 supported on SiO_2) at 180–260 °C and 2.5–2.6 MPa.

The first large-scale plant based on the direct hydration process was started in 1972 by Deutsche Texaco AG in Meerbeck, Germany. The molar feed ratio of water

$$CH_3CH{=}CH_2 + H_2O \leftrightarrow (CH_3)_2CHOH \quad \Delta H = -50 \text{ kJ/mol}$$
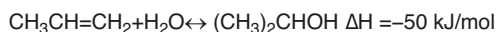
Scheme 18 Direct hydration of propylene

to propylene was about 12.5:1 to 15:1 and the conversion of propylene was at least 75% per pass. An acidic ion exchange resin was used to catalyze the process. Due to lower concentration of propylene in the feed, there is a complete conversion of organic phase, i.e., propylene. As a result, IPA is formed in a dilute aqueous phase (approx. 5–7 mol% of isopropyl alcohol). The diluted IPA containing aqueous phase needs to be concentrated to the near of the alcohol-water azeotrope by conventional distillation followed by an azeotropic distillation to recover dry isopropyl alcohol. Few limitations of Deutsche Texaco process were further improved in the Tokuyama Soda process. The disadvantages of the gas-phase processes are largely avoided by employing a weakly acidic aqueous catalyst solution of a silicotungstate (Table 14). In the Tokuyama process, catalyst is recycled and requires little replenishment as compared to other processes. Moreover, corrosion and environmental-related problems get minimized because of the use of less corrosive acid and completely closed reactor system. Additionally, on account of the low gas recycle ratio, regular commercial propylene of 95% purity can be used as feedstock. The Tokuyama Soda process offers 60–70% per pass propylene conversion and 98–99 mol% selectivity for IPA based on converted propylene. Diisopropyl ether (DIPE) is the principal by-product in the acid-catalyzed direct hydration of propylene in the production of IPA.

The principal difference between the direct and indirect processes is that much higher pressure is required for the direct hydration process. The slate and

Etherification: $2\ (CH_3)_2CHOH \leftrightarrow H_2O + (CH_3)_2CHO\text{-}CH(CH_3)_2 (Diisopropylether\text{-}DIPE)$
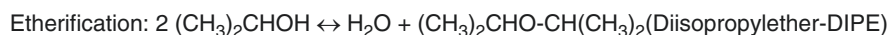
Scheme 19 Etherification of isopropyl alcohol

Table 14 Comparison of various direct propylene hydration processes

Process type	Fixed bed vapor-phase	Mixed vapor liquid-phase	Liquid phase
Manufacturer (production since)	Veba Chemie (1966)	Deutsche Texaco (1972)	Tokuyama Soda (1973)
Catalyst	WO_3-ZnO/H_3PO_4	Ion-exchange resin	Aqueous silocotungstate
Propylene feed stream (wt%)	99	92	95
Operating pressure (MPa)	2.5–2.6	6–10	15–20
Operating temperature (°C)	180–260	130–150	240–270
Feed ratio (water/propylene)	1:4–10	12.5–15:1	
Propylene recycle/feed mole ratio	94–95%	25%	30–40%
Water recycle/feed-mole ratio	40–80%	94–95%	
Per pass propylene conversion	5–6%	75%	60–70%
IPA selectivity	96%	93%	98–99%
Reference	[188]	[189]	[190, 191]

distribution of products and by-products from each process are similar, and systems for refining IPA are essentially the same. Depends on the intended applications, IPA is upgraded through isotopic distillation. Other post purification steps such as aqueous extractive distillation or treatment by a fixed bed adsorption process using activated carbon or molecular sieves are employed to improve further quality of IPA for medical purposes.

Emerging Alternative: IPA from Acetone

Acetone hydrogenation is an emerging alternative route which is gaining popularity in recent times for IPA production [192]. This route accounted for only 2% of total global IPA production in 2000, which jumped to nearly 25% by 2018. This increase is attributed to the oversupply of acetone from the phenol production process. In the Hock phenol process (Scheme 20), 1 mol of acetone is produced per mole of phenol. However, the demand for phenol is very different from that of acetone, which creates unfavorable demand/supply scenario for acetone. For example, in the synthesis of bisphenol A, phenol and acetone are consumed in a molar ratio of 2:1, which leads to oversupply of acetone [193].

Mitsui Chemicals, Japan is a major producer of phenol using Hock phenol process. Acetone is a cheaper chemical and its market price varies based on supply/demand. Thus, depending on the market conditions, Mitsui converts co-product acetone to isopropanol [194], which can further be converted to propylene for use in the cumene production. Since 2010, Novapex, a subsidiary of Novacap Group (now Seqens) has been producing IPA (40,000 tons/year) from the plant located at Roussillon, France based on the Mitisui's acetone hydrogenation technology [195]. Other companies have also been working on the development of the acetone to IPA process (Table 15).

Recently, a process based on high-temperature metal-supported "semi" heterogeneous catalysts for hydrogenation of acetone to IPA at 250 °C has been reported. A number of different catalyst systems such as Pd/silica, Au and Pt/Al$_2$O$_3$, Pt/ SiO$_2$, Pt supported on TiO$_2$ microspheres, and kaiselgur-supported Cu, Pt, Pd, and Rh were used in the process [200]. Another catalyst system based on semi-hollow porous nano-palladium grown on ITO substrate is reported to effectively hydrogenate acetone to isopropanol with a yield as high as 99.8% [201]. The semi-hollow and spongy structure with high porosity along with highly surface defect are reasons behind responsible key factors for the high performance of the nano catalyst in the hydrogenation reaction.
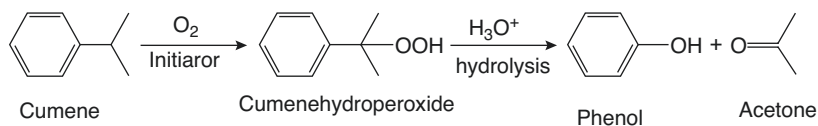
Scheme 20 Cumene peroxidation and hydrolysis of cumenehydroperoxide

Table 15 Various catalysts system explored for acetone hydrogenation to IPA

Assignee	Air Products and Chemicals, Inc.	Mitsui Petrochemical Industries	Arco Chemical Technology	Phenolchemie GmbH & Co. KG
Catalyst	Ni-Cr, Co-Cr	Ni/Al alloy	Supported Ru	Ni, Cu, Cr, Ru, α-Al_2O_3, TiO_2, ZrO_2, Muttilte
Process type	Liquid phase	Fixed bed	Fixed	Two stages: First stage: Circulator Second stage: Tube reactor
Temperature (°C)	60–200	100	75–180	60–140
Pressure, bar	7–138	19.6	1–5	20–50
H_2/acetone molar ratio		2.44	1–5	1–5
Acetone conversion, %	98.7	99.9	90	99.5
IPA selectivity %	99.0	99.6	90	99.9
Reference	[196]	[197]	[198]	[199]

Upcoming Trend with Respect to Current Research

As production of renewable electricity is increasing drastically because of worldwide adoption of solar and wind energy to drive decarbonization of chemical, transportation, and energy sectors, cost of electricity is coming down steadily. As a result, electrochemical processes are becoming popular and several big plants are coming up for the production of green hydrogen using renewable electricity. In this regard, electrochemical hydrogenation (ECH) of acetone is also being explored to produce isopropanol [202]. This route provides an alternative way of upgrading biofuels with less energy consumption and chemical waste as compared to conventional methods. Polymer electrolyte membrane fuel cell (PEMFC) hardware was used as an electrochemical reactor to hydrogenate acetone to produce isopropanol. The process produces diisopropyl ether (DIPE) as a by-product. It is reported that when ECH was carried out at 65 °C and atmospheric pressure, selectivity (>90%) was achieved at a current efficiency of 59.7%.

5 Concluding Remarks and Industrial Outlook

Worldwide demand for propylene and propylene-derived chemicals is increasing to support economic development. This book chapter presents an overview of important commercial technologies and catalysts used in the production of propylene in traditional and various emerging on-purpose production routes. The industrial

journey of commercial technologies of four important propylene-derived chemicals viz. propylene oxide, acrylonitrile, acrylic acid, and isopropanol, and recent advancement in regard to the processes and catalysts used in the production of these chemicals have been reviewed and presented. As chemical industries are looking for improving environmental footprints of the existing chemical production processes, a lot of thrust is now being given on the development of greener production routes for improving sustainability in the chemical industry. As demand for by-product free production routes is need of the hour, the chemical industry is putting greater efforts on the development of energy-efficient and environment-friendly processes. Stringent environment regulations and the need for reducing dependency on petroleum-based feedstock will drive use of alternative feedstock, chemicals, and new catalytic materials. The use of traditional refinery feedstock will see decline in the production of petrochemicals while gas and renewable hydrogen-based economy will take center stage at twenty-first century.

In the near future, a significant amount of propylene production will come from on-purpose routes using locally available sources such as natural gas and coal. Methanol produced from syngas through gasification of municipal solid waste and biomass, and its further conversion to propylene holds promise to partly reduce the carbon footprint of the propylene production. High severity FCC process will be used increasingly to produce more propylene as feedstock in the integrated petrochemicals complex as demand for liquid transportation fuel is expected to decline due to the advent of CNG, hybrid, and EVs. Also, lighter feedstocks such as propane, butane will be used for production of olefins in the short to medium term. In medium to long term, a significant amount of propylene production will come from methanol derived from biomass or hydrogenation of recycling CO_2 when these technology mature. As the cost of renewable electricity is decreasing significantly, it will find greater applications in the production of renewable hydrogen through alkaline water electrolysis, PEM (proton exchange membrane), and high temperature SOEC (solid oxide electrolyzer cell)-based processes, which in turn will be used in the chemicals production. Hydrogenation of CO and CO_2 using renewable hydrogen is expected to play an important role in the production of various chemicals via syngas and methanol intermediates. The use of new types of feedstocks will demand new types of catalytic material with robust performance toward activity, selectivity, and stability.

By-product free processes with simpler process steps will attract more interest in the production of chemicals. The use of hydrogen peroxide and molecular oxygen as an environmental-friendly oxidant will find greater roles in the production of propylene oxide and other oxygenated chemicals. Research and developmental efforts toward the development of acrolein and acrylic acid production from bio-based renewable sources will attract more interest to counter the propylene price volatility and reduce environmental and carbon footprints. Two renewable feedstocks, glycerol and 3-hydroxyl propionic acid, hold promise for acrolein and acrylic acid production. The most efficient route for glycerol to acrylic acid would be based on one-step catalytic oxydehydration. The development of efficient and selective bi-functional catalyst containing both active acid and redox sites is

expected to drastically reduce the cost of acrylic acid production while improving the environmental footprint of the process in the future. However, the challenges associated with the catalyst deactivation and control of the selectivity are important factors that need to be solved for any successful implementation of single-step process and use of the renewable feedstocks.

Circular and low carbon economy will drive the chemical and petrochemical industries of twenty-first century that will demand development of advanced materials, intensified reactor technology, and distributed production based on small-scale modular and energy-efficient plants. In future, important C3-based chemicals have to be produced utilizing cheaper and alternative feedstocks such as propane, acetone, renewable methanol, and bio-based sources with the continued advances in the catalytic technology.

References

1. Chemicals prices, news and analysis, chemicals market intelligence (2011) http://www.icis.com/v2/chemicals/9076455/propylene/uses.html. Accessed 16 Aug 2011
2. Corma A, Corresa E, Mathieu Y, Sauvanaud L, Al-Bogami S, Al-Ghrami MS, Bourane A (2017) Crude oil to chemicals: light olefins from crude oil. Cat Sci Technol 7:12–46
3. Propylene Production and Manufacturing Process I. C. I. S (Independent Commodity Intelligence Services) (2007) https://www.icis.com/explore/resources/news/2007/11/06/9076456/propylene-production-and-manufacturing-process
4. Bender M (2014) An overview of industrial processes for the production of olefins—C4 hydrocarbons. Chem Bio Eng Rev 1:136–147
5. Peter E, Richard K (2012) Propene. Ullmann's encyclopedia of industrial chemistry. Wiley-VCH, Weinheim
6. Jasper S, El-Halwagi MM (2015) A techno-economic comparison between two methanol-to-propylene processes. Processes 3:684–698
7. Marcello DF (2017) New catalytic process for production of olefins, oil & gas portal. http://www.oil-gasportal.com/new-catalytic-process-for-production-of-olefins/?print=print
8. Ante J (2013) Production of olefins—steam cracking of hydrocarbons, petroleum refining and petrochemical processes, natural gas composition, classification, processing. https://pdfs.semanticscholar.org/c70b/5a3ae45c4e1750ffdc3a7ec21ddbfa12a390.pdf?_ga=2.187285610.354597134.1582640836-121132309.1582640836
9. Werner P (2011) Polyolefins. Applied plastics engineering handbook, processing and materials, plastic design library. Elsevier, Amsterdam, pp 23–48
10. Leon B (2011) Optimizing FCC operations in a high rare earth cost (market: part I). RefineryOperations.com, vol 2, pp 1–7
11. Eren C, Nathan L, Theo JS, Jeremy W (2018) Petrochemicals 2030: reinventing the way to win in a changing industry. https://www.mckinsey.com/industries/chemicals/our-insights/petrochemicals-2030-reinventing-the-way-to-win-in-a-changing-industry
12. Advance in Naphtha Steam Cracking (Process Economics Program Report, 248A) IHS Markit report. https://ihsmarkit.com/pdf/RP248A_toc_173653110917062932.pdf. Accessed Dec 2005
13. Resid RFCC, Axens solutions. https://www.axens.net/product/process-licensing/10071/r2r.html
14. Resid to propylene, axenes solutions, website: https://www.axens.net/product/process-licensing/20043/r2p-resid-to-propylene.html

15. Knight J, Mehlberg R (2011) Maximize propylene from your FCC unit: innovative use of catalyst and operating conditions increases on-purpose olefin production: refining developments. Hydrocarb Process 90:91–95

16. Degnan TF, Hitnis GKC, Schipper PH (2000) History of ZSM-5 fluid catalytic cracking additive development at mobil. Microporous Mesoporous Mater 35:245–252

17. Biswas J, Maxwell IE (1990) Recent process- and catalyst-related development in fluid catalytic cracking. Appl Catal 63:1–18

18. Li Z, Shi W, Wang X, Jiang F (1994) Deep catalytic cracking process for light-olefins production. ACS Symp Ser 571:33–42

19. Akah A, Al-Ghrami M (2015) Maximizing propylene production via FCC technology. Appl Petrochem Res 5:377–392

20. Soni D, Rao MR, Saidulu G, Bhattacharyya D, Satheesh VK (2009) Catalytic cracking process enhances production of olefins. Petrol Technol Q Q4:95–100

21. Aitani A (2006) Propylene production, encyclopedia of chemical processing. Taylor & Francis, New York

22. Eng CN, Miller RB. Dual riser FCC reactor process with light and mixed light/heavy feeds. US Patent 7491315

23. Parthasarathi RS, Alabduljabbar SS (2014) HS-FCC high-severity fluidized catalytic cracking: a newcomer to the FCC family. Appl Petrochem Res 4:441–444

24. Martin BH (2005) Handbook of chemical technology and pollution control, 3rd edn. Academic, New York

25. Henning G (2013) U.S. shale boom to boost LPG exports, bring down prices, Business News, Reuters. https://www.reuters.com/article/us-energy-lpg/u-s-shale-boom-to-boost-lpg-exports-bring-down-prices-idUSBRE9A30G820131104

26. Nawaz Z (2015) Light alkane dehydrogenation to light olefin technologies: a comprehensive review. Rev Chem Eng 31:1–24

27. Caspary KJ, Gehrke H, Heinritz-Adrian M, Schwefer M (2008) In: Ertl G, Knozinger H, Weitkamp J (eds) Handbook of heterogeneous catalysis. Wiley-VHC Verlag GmbH, Weinheim, pp 3206–3229

28. The Uhde STAR process: oxydehydrogenation of light paraffins to olefins. http://www.thyssenkruppuhde.de/fileadmin/documents/brochures/uhde_brochures_pdf_en_12.df

29. Sanfilippo D, Miracca I (2005) Oxidation and functionalization: classical and alternative routes and sources. In: Ernst S, Gallei E, Lercher JA, Rossini S, Santacesaria E (eds) Proceedings of the DGMK conference, German Society for Petroleum and Coal Science and Technology (DGMK), Hamburg

30. GS Engineering/Construction (ed) (2008) Propylene technology by PDH & Metathesis

31. Lummus-Technology-CB&I-Company (2009) Chicago. CATOFIN dehydrogenation, vol 31, pp 1–2

32. Hisham A, Maddah A (2018) Comparative study between propane dehydrogenation (PDH) technologies and plants in Saudi Arabia. Am Sci Res J Eng, Technol Sci 45:49–63

33. CATOFIN dehydrogenation (2013) http://www.com/images/uploads/tech_sheets/CatofinDehyrogenation-12.pdf. Accessed 23 Oct 2013

34. New clariant CATOFIN propane dehydrogenation catalysts delivers significant savings (2013) http://newsroom.clariant.com/newclariant-catofin-propane-dehydrogenation-catalyst-delivers significant savings/. Accessed 23 Oct 2013

35. INEOS selects site for €3-billion European petrochemical complex (2019) Oil Gas J. https://www.ogj.com/refiningprocessing/refining/capacities/article/17278908/ineos-selects-site-for-3billion-european-petrochemical-complex. Accessed 15 Jan 2019

36. Michael M, Jeffrey W (2019) On-purpose propylene production. PTQ Q1: 1–5. https://www.digitalrefining.com/article/1002264,On_purpose_propylene_production.html#.XlVKs6Yh3IU

37. Metathesis (2005) Kirk-Othmer encyclopedia of chemical technology, vol 20, 5th edn. Wiley, New York, pp 1–29

38. Mol JC (2004) Industrial application of olefin metathesis. Mol Catal A Chem 213:39–45
39. Gartside RJ, Greene M. Catalyst and process for the metathesis of ethylene and butene to produce propylene. World Patent 2006052688
40. Gartside RJ, Greene MI, Kaleem H (2006) Maximize butene-1 yields. Hydrocarbon Process Int Ed 85(57–58):60–61
41. Gartside RJ, Greene MI, Quincy JJ. Process for producing propylene and hexene from C4 olefin streams. US Patent 6777582B2
42. Popoff N, Mazoyer E, Pelletier J, Gauvin RM, Taoufik M (2013) Expanding the scope of metathesis: a survey of polyfunctional, single-site supported tungsten systems for hydrocarbon valorization. Chem Soc Rev 42:9035–9054
43. Banach M (2017) Take the profitable path to olefins using UOP technologies. In: Honeywell oil & gas technologies symposium, Cairo, Egypt
44. Gogate MR (2019) Methanol-to-olefins process technology: current status and future prospects. Petrol Sci Technol 37:559–565
45. Koempel H, Liebner W (2007) Lurgi's methanol to propylene (MTP) report on a successful commercialisation. In: Proceedings of the 8th natural gas conversion symposium, Natal, Brazil, 27–31 May 2007, pp 261–281
46. Koempel H, Liebner W, Wagner M (2005) Lurgi's gas to chemicals (GTC): advanced technologies for natural gas monetization. In: Proceedings of the Gastech 2005, Bilbao, Spain, 14–17 March 2005
47. Hongxing L, Zaiku X, Guoliang Z (2013)The progress of SINOPEC methanol-to-olefins (S-MTO) technology. In: New technologies and alternative feedstocks in petrochemistry and refining, DGMK conference October 9-11 Dresden, Germany
48. S-MTO methanol to olefins technology (2018) Sinopec. http://oil.vcdcenter.com/wp-content/uploads/2018/12/SMTO.pdf. Accessed Dec 2018
49. Liu Z, Ye M (2016) DMTO and beyond: DICP's sustainable innovations in technologies for on-purpose production of light olefins from methanol. In: 16 AIChE, spring meeting, Houston, TX
50. Hurd D, Park S, Kan J (2014) FITT research: China's coal-to-olefins industry. AG, Hong Kong: Deutsche Bank. Accessed 2 Jul 2014
51. Vora B, Marker TL, Nilsen HR (1998) Process for producing light olefins from crude methanol. US Patent 5714662
52. Funk GA, Myers D, Vora B (2004) A different game plan. Hydro Eng 12:25–28
53. Lurgi (2008) Methanol to propylene—MTP®. Lurgi AG, Frankfurt am Main, Germany. http://www.lurgi.com/website/fileadmin/user_upload/pdfs/19_Methan-Propylen-E_rev060707.pdf
54. Olah GA, Goeppert A, Surya Prakash GK (2009) Beyond oil and gas: the methanol economy. Wiley-VCH, Weinheim. ISBN: 9783527324224
55. Gogate MR (2019) Methanol-to-olefins process technology: current status and future prospects. Petrol Sci Technol 37:1–7. https://doi.org/10.1080/10916466.2018.1555589
56. Okita A, Honda K (2012) Selective propylene production process using methanol/dimethyl-ether and olefin as raw materials. Petrotech 35:581
57. Eng CN, Arnold EC, Vora B (1998) Integration of the UOP/HYDRO MTO process into ethylene plants. In: AIChE spring national meeting, session 16, fundamental topics in ethylene production, New Orleans, LA, USA, 8–12 March 1998; Paper 16g
58. Barger P (2002) Methanol to olefins (MTO) and beyond. Catal Sci Ser 3:239–260
59. Koempel H, Liebner W (2007) Lurgi's methanol to propylene (MTP). Report on a successful commercialization. In: Proceedings of the 8th natural gas conversion symposium, Natal, Brazil, 27–31 May 2007, pp 261–281
60. Farshi A, Shaiyegh F, Burogerdi SH, Dehgan A (2011) FCC process role in propylene demands. Petrol Sci Technol 29:875–885
61. Zacharopoulou V, Lemonidou A (2017) Olefins from biomass intermediates: a review. Catalysts 8:2–19. https://doi.org/10.3390/catal8010002

62. Manz TA, Yang B (2014) Selective oxidation passing through η3-ozone intermediates: applications to direct propene epoxidation using molecular oxygen oxidant. RSC Adv 4:27755–27774. https://doi.org/10.1039/c4ra03729d

63. Kawabata T, Koike H, Yamamoto J, Yoshida S (2019) Trends and views in the development of technologies for propylene oxide production. Sumitomo Kagaku (English edition). Report 1, pp 1–9. https://www.sumitomo-chem.co.jp/english/rd/report/files/docs/2019E_1.pdf

64. IHS markit (2015) Propylene oxide PEP consolidated report CR003

65. Shang S-Y, Mei L, Fu P (2016) Progress in producing technology of propylene oxide. Advanced materials, technology application. World Scientific, Singapore, pp 62–71. https://doi.org/10.1142/9789813200470_0008

66. Goyal R, Singh O, Agrawal A, Samanta C, Sarkar B (2020): Advantages and limitations of catalytic oxidation with hydrogen peroxide: from bulk chemicals to lab scale process, Catalysis Reviews, https://doi.org/10.1080/01614940.2020.1796190

67. Dittmeyer R, Keim W, Kreysa G, Oberholz A (eds) (2005) Winnacker-Küchler: Chemische Technik, 5th edn. Wiley-VCH, Weinheim

68. Japan External Trade Organization (2018) Chuugoku ni okeru Kankyou Kisei to Shijou Kibo no Saishin Doukou Chousa 2018-nen 1-gatsu. (Survey on Latest Trends in Environmental Regulations and Market Scale in China, January 2018). https://www5.jetro.go.jp/newsletter/shanghai/2018/180126/doukou.pdf

69. Pell M, Korchak EI (1969) Epoxidation using ethylbenzene hydroperoxide with alkali or adsorbent treatment recycle ethylbenzene. US Patent 3439001

70. Dubner WS, Cochran RN (1993) Propylene oxide-styrene monomer process. US Patent 5210354

71. Van Der Sluis JJ (2003) Process for the preparation of styrene and propylene oxide. US Patent 6504038

72. Oyama ST (2011) Mechanisms in homogeneous and heterogeneous epoxidation catalysis. Elsevier, Amsterdam

73. Cavani F, Teles JH (2009) Sustainability in Catalytic Oxidation: An Alternative Approach or a Structural Evolution? ChemSusChem, 2 (6), 508–534. https://doi.org/10.1002/cssc.200900020

74. Hibi T, Iwanaga K, Ito S, Koike H, Oku N (2009) Development of a new Acetophenone hydrogenation process for propylene oxide production. Sumitomo Kagaku, II, Osaka, pp 1–7

75. Ghanta M, Fahey DR, Busch DH, Subramaniam B (2013) Comparative economic and environmental assessments of H₂O₂-based and tertiary butyl hydroperoxide-based propylene oxide technologies. ACS Sust Chem Eng 1:268–277. https://doi.org/10.1021/sc300121j

76. Kollar J (1967) Epoxidation process. US Patent 3351635

77. Marquis ET, Keating KP, Knifton JF, Smith WA, Sanderson JR, Lustri J (1990) Epoxidation of olefins in a polar medium. US Patent 4891437

78. Weissermel K, Arpe H-J (2004) Industrial organic chemistry, 5th ed, translated by T. Mukaiyama, Tokyo Kagaku Dozin, p 289

79. https://www.sumitomo-chem.co.jp/english/news/detail/20190819e.html

80. https://www.sumitomo-chem.co.jp/english/rd/report/files/docs/20060100_ely.pdf

81. Schmidt F, Bernhard M, Morell H, Pascaly M, Oggi C (2014) Chem Today 32:31–35

82. Russo V, Tesser R, Santacesaria E, Di Serio M (2013) Chemical and technical aspects of propene oxide production via hydrogen peroxide (HPPO process). Ind Eng Chem Res 52:1168–1178. https://doi.org/10.1021/ie3023862

83. Lin M, Xia C, Zhu B, Li H, Shu X (2016) Green and efficient epoxidation of propylene with hydrogen peroxide (HPPO process) catalyzed by hollow TS-1 zeolite: a 1.0 kt/a pilot-scale study. Chem Eng J 295:370–375. https://doi.org/10.1016/j.cej.2016.02.072

84. http://www.chemicals-technology.com/projects/basf-hppo/. Accessed Jan 2013

85. http://www.knak.jp/big/evonik-hppo.htm. Accessed Jan 2013

86. Grosch GH, Mller U, Walch A, Rieber N, Fischer M, Quaiser S, Harder W, Eller K, Bassler P, Wenzel A, Kaibel G, Stammer A, Henkelmann J, Battcher A, Teles JH, Schulz M, Treiber G (2003) Method for oxidizing an organic compound containing at least one C-C double bond. US Patent 6518441

87. Yap N, Andres RP, Delgass WN (2004) Reactivity and stability of Au in and on TS-1 for epoxidation of propylene with H_2 and O_2. J Catal 226:156

88. Nijhuis TA, Huizinga BJ, Makkee M, Moulijn JA (1999) Direct epoxidation of propene using gold dispersed on TS-1 and other titanium-containing supports. Ind Eng Chem Res 38:884

89. Zheng X, Zhang Q, Guo Y, Zhan W, Guo Y, Wang Y, Lu G (2012) Epoxidation of propylene by molecular oxygen over supported Ag−Cu bimetallic catalysts with low Ag loading. J Mol Catal A Chem 357:106–111

90. Tatsumi T, Nakamura M, Yuasa K, Tominaga H (1991) Shape selectivity as a function of pore size in epoxidation of alkenes with supported titanium catalysts. Catal Lett 10:259–262

91. Perego C, Carati A, Ingallina P, Mantegaza MA, Bellussi G (2001) Production of titanium containing molecular sieves and their application in catalysis. Appl Catal A Gen 221:63–72

92. Short PL (2009) BASF, Dow Open. Novel propylene oxide plant. Chem Eng News 87:21

93. https://www.epa.gov/greenchemistry/presidential-green-chemistry-challenge-2010-greener-synthetic-pathways-award

94. Khatib SJ, Oyama ST (2015) Direct oxidation of propylene to propylene oxide with molecular oxygen: a review. Catal Rev 57:306–344. https://doi.org/10.1080/01614940.2015.1041849

95. Vaughan O, Kyriakou G, Macleod N, Tikhov M, Lambert R (2005) Copper as a selective catalyst for the epoxidation of propene. J Catal 236:401–404. https://doi.org/10.1016/j.jcat.2005.10.019

96. Ghosh S, Acharyya SS, Tiwari R, Sarkar B, Singha RK, Pendem C, Bal R (2014) Selective oxidation of propylene to propylene oxide over silver-supported tungsten oxide nanostructure with molecular oxygen. ACS Catal 4:2169–2174. https://doi.org/10.1021/cs5004454

97. Kalavachev YK, Hayashi T, Tshbota S, Haruta M (1997) 3rd world congress on oxidation catalysis. Elsevier, Amsterdam

98. Haruta M (1997) Size- and support-dependency in the catalysis of gold. Catal Today 36:153

99. Nijhuis TA, Visser T, Weckhuysen BM (2005) Mechanistic study into the direct epoxidation of propene over gold/titania catalysts. J Phys Chem B 109:19309

100. Nijhuis TA, Chen J, Kriescher SMA, Schouten JC (2010) The direct epoxidation of propene in the explosive regime in a microreactor: a study into the reaction kinetics. Ind Eng Chem Res 49:10479

101. Chen J, Halin SJA, Schouten JC, Nijhuis TA (2011) Kinetic study of propylene epoxidation with H_2 and O_2 over Au/Ti−SiO_2 in the explosive regime. Faraday Discuss 152:321

102. Nexant markets and profitability (2018) Market analytics: acrylonitrile. https://www.nexanteca.com/reports/market-analytics-acrylonitrile-2018

103. The SOHIO acrylonitrile process (2007) Americian Chemical Society. Accessed 14 Nov 2007

104. Grasselli RK (2011) In: Hess C, Schlögl R (eds) Ammoxidation of propylene and propane to acrylonitrile nanostructured catalysts: selective oxidations. Royal Society of Chemistry, London

105. Brazdil JF (2012) Acrylonitrile. Ullmann's encyclopedia of industrial chemistry. Wiley, Hoboken. https://doi.org/10.1002/14356007.a01_177.pub3

106. Grasselli RK, Ferruccion T (2016) Acrylonitrile from biomass: still far from being a sustainable process. Top Catal 59:1651–1658

107. Bastião DS (2019) Study of the eco-efficiency of acrylonitrile production processes. http://www.revistasg.uff.br/index.php/sg/article/view/1455/html_1

108. Grasselli RK (2002) Fundamental principles of selective heterogeneous oxidation in catalysis. Top Catal 21:79–88

109. Grasselli RK (1999) Advances and future trends in selective oxidation and ammoxidation catalysis. Catal Today 14:49

110. Callahan JL, Milberg EC (1966) Process for preparing olefinically, unsaturated nitriles. US Patent 3230246

111. Grasselli RK (1997) Handbook of heterogeneous catalysis. In: Ertl G, Knoezinger H, Weitkamp J (eds) 4.6.6. Ammoxidation. Wiley-VCH, Weinheim, p 2302

112. Grasselli RK (1983) In: Bonnelle JP, Delmon B, Derouane EG (eds) Surface properties and catalysis by non-metals. D. Riedel, Dordrecht, pp 273–289
113. Kurt S, Wilhelm V, Joachim K, Rolf S, Gunter S. Process for preparing unsaturated nitriles. US Patent No. 3226422
114. Grasselli RK, Hardman HF (1972) Process for the manufacture of isoprene from isoamylenes and methyl butanols and catalyst therefore. US Patent 3642930
115. Grasselli RK, Miller AF, Hardman HF. Process for the manufacture of acrylonitrile and methacrylonitrile. US Patent 4503001
116. Grasselli RK, Suresh DD, Hardman HF. Production of unsaturated nitriles. US Patent 4139552
117. Suresh DD, Maria S, Michael F, Seely J. Catalyst for the manufacture of acrylonitrile and methacrylonitrile. US Patent 5212137
118. Caporali G, Ferlazzo N, Giordano N. Process for the continuous production of olefinically unsaturated nitriles. US Patent 3691224
119. Bart JCJ, Giordano N (1980) Structure and activity of tellurium-molybdenum oxide acrylonitrile catalysts. J Catal 64:356–370
120. Bart JCJ, Giordano N (1984) Structure of the cerium-molybdenum-tellurium oxide acrylonitrile catalyst. Ind Eng Chem Prod Res Dev 23:56
121. Grasselli RK, Callahan JL (1969) Structure-catalytic efficiency relationships in U Sb oxide acrylonitrile synthesis catalysts. J catal 14:93–103
122. Grasselli RK, Suresh DD, Knox K (1970) Crystalline structures of USb3O10 and USbO5 in acrylonitrile catalysts. J Catal 18:356–358
123. Grasselli RK, Suresh DD, Knox K (1972) Aspects of structure and activity in U Sb oxide acrylonitrile catalysts. J Catal 25:273–291
124. Callahan J L, Berthold G. Mixed antimony oxide-uranium oxide oxidation catalyst. US Patent 3198750
125. Sasaki Y, Utsumi H, Miyaki K. Iron antimony-containing metal oxide catalyst composition and process for producing the same. Jap Patent 3142549
126. Sasaki Y, Nakamura T, Nakamura Y, Moriya K, Utsumi H, Saito S (1983) Process for production of acrylonitrile. US Patent 4370279
127. Krieger J (1996) Propane route to acrylonitrile holds promise of savings. Chem Eng News 74(39):18–19
128. Ushikubo T, Oshima K, Kayou A, Hatano M (1997) Ammoxidation of propane over Mo-V-Nb-Te mixed oxide catalysts. Spillover and migration of surface species on catalysts. In: Proceedings of the 4th international conference on spillover, pp 473–480. https://doi.org/10.1016/s0167-2991(97)80871-3
129. Hinago H, Komada S (2000) Ammoxidation catalyst for use in producing acrylonitrile or methacrylonitrile from propane or isobutane by ammoxidation. US Patent 6063728
130. Ushikubo T (2000) Recent topics of research and development of catalysis by niobium and tantalum oxides. Catal Today 57:331–338
131. Adams RD, Elpitiya G, Khivantsev K, Blom D, Alexeev OS, Amiridis MD (2015) Ammoxidation of propane to acrylonitrile over silica-supported Fe-bi nanocatalyst. App Catal A: Gen 501:10–16
132. Karp et al (2017) Science 358:1307–1310
133. Nexant (2010) Acrylic acid, process evaluation/research planning (PERP) 08/09. www.chemsys.com
134. IHS Markit report (2016) CEH Superabsorbent polymers report. https://ihsmarkit.com/Info/0319/acrylates-sap-client-webinar.html
135. Grand view Research Inc (2017) grandviewresearchinc.weebly.com/blog/acrylic-acid-market-is-expected-to-show-a-momentous-role-in-demand-development
136. Tullo AH (2013) Hunting for biobased acrylic acid. Chem Eng News 19:18–19
137. Nova Institute for ecology and Innovation (2015) Bio-based building blocks and polymers in the world. http://www.bio-based.eu/market_study/media/files/15-05-13_Bio-based_Polymers_and_Building_Blocks_in_the_World-nova_Booklet.pdf
138. World of Chemical (2014) BASF, Sinopec JV to build acrylic acid. SAP plant in Nanjing, China. https://www.chemicals-technology.com/projects/basf/

139. Nojiri N, Sakai Y, Watanabe Y (1995) Two catalytic technologies of much influence on progress in chemical process development in Japan. Catal Rev 37:145–178. https://doi.org/10.1080/01614949508007093
140. Ohara T, Sato T, Shimizu N, Schwind GPH, Weiberg O, Marten K, Greim H (2003) Acrylic acid and derivatives. Ullmann's encyclopedia of industrial chemistry. Wiley-VCH, Weinheim, pp 1–19
141. https://www.engineering-airliquide.com/acrylic-acid-lurgi-nippon-kayaku-technology
142. Lin MM (2001) Selective oxidation of propane to acrylic acid with molecular oxygen. Appl Catal A Gen 207:1–16
143. Callahan JL, Foreman B W (1960) Process for the oxidation of olefins. US Patent 2941007
144. Sennerwalt K, Gehrmann K, Vogt W, Schafer S (1960) Process for the manufacture of unsaturated aldehydes or ketones. US Patent 3171859
145. Takenaka S, Yamaguchi G (1969) Acrolein by propylene oxidation. JP 44006245
146. Takenaka S, Kido Y, Shimabara T, Ogawa M (1971) Catalysts for the oxidation of propylene to acrolein. DE 2038749
147. Nagai I, Yanagisawa I, Ninomiya M, Oohara T (1976) Oxidation of propylene. JP 51004113
148. Takata M, Aoki R, Sato T (1983) Catalyst for oxidation of propylene. DE 3300044
149. Shiraishi T, Kishiwada S, Shimizu S, Hommaru S, Atsumi A, Ichihashi H, Nagaoka Y (1973) JP Patent 4849710A
150. Koshikawa T (1974) Acrolein and acrylic acid from propylene. JP 49030308
151. Watanabe Y, Sugihara T, Takagi K, Imanari M, Nojiri N (1972) JP Patent 4741329B
152. Umemura Y, Oodan K, Suzuki K, Bandou Y, Hisayuki T. (1980) Acrolein. JP Patent 55157529
153. Izawa S, Ono I, Iikuni T (1965) JP Patent 411775B
154. Yanagida M , Kitahara M (1969) JP Patent 4426287B
155. Suzuki S, Itoh H, Inoue H (1970) JP Patent 4516090B
156. Takenaka S, Yamaguchi K (1969) JP Patent 4412129B
157. Ogawa M (1987) JP Patent 6234742B
158. Allen GC (1969) Oxidation of unsaturated aldehydes to the corresponding acids. US Patent 3644509
159. Krabetz R, Engelbach H (1970) Production of acrylic acid by oxidation of acrolein. US Patent 3845120
160. Wada M, Ninomiya M, Yanagisawa I, Ohara T (1978). JP Patent 536127B
161. Dolhyj SR, Milberger EC (1975) Ger Patent 2448804
162. Shiraishi T, Ichihashi H, Kikuzono Y, Nagaoka Y (1982) JP Patent 57298B
163. Kadowaki K, Koshikawa T (1974) JP Patent 44169B
164. Kurata N, Matsumoto T, Ohara T, Oda K (1967) JP Patent 42-9805B
165. Nagai I, Yanagisawa I, Ninomiya M, Ohara T (1983) JP Patent 5817172B
166. Takenaka S, Yamaguchi G (1970) JP Patent 454970A
167. Takayama Y, Nakayama Y, Asao S, Tokumichi Y, Mizukami S (1967) JP Patent 4212243
168. Kita T, Ishii H (1972) JP Patent 476606B
169. Croci M, Cavaterra E (1969) Process for the preparation of unsaturated acids. US Patent 3736355
170. Krabetz R, Engelbach H (1967) Production of acrylic acid. US Patent 3527797
171. Komuro I, Kadowaki K, Koshikawa T (1972) JP Patent 4722813B
172. Ukihashi H, Oda Y, Kojima G (1971) JP Patent 469134B
173. Ono I, Iikuni T, Mizoguchi J (1972). JP Patent 4714204B
174. Eden JS (1967, 1969) Catalytic process for preparing unsaturated acids and aldehydes. US Patent 3520923 (1967) and US Patent 3585152
175. Mizuno N, Tateishi M, Iwamoto M (1995) Pronounced catalytic activity of Fe0.08Cs2.5H1.26PVMo11O40 for direct oxidation of propane into acrylic acid. Appl Catal A Gen 128:L165–L170
176. Luo L, Labinger J, Davis M (2000) Catalysis and surface science. In: Poster, 219th ACS meeting, March 2000. The catalyst was provided by BP Amoco

177. Velazco MR, McDonnell W, Smith AWJ (2017) Molybdenum/bismuth based mixed metal oxide catalysts for selective propylene oxidation and zeolite membrane protected palladium/alumina catalysts for selective carbon monoxide oxidation and application in a process loop using a propane feed. Johnson Matthey Technol Rev 61:5–15

178. Wang K, Vartuli JC, Mortier WJ, Dakka JM, Lemon RC, Mixed metal oxide catalysts and processes for their preparation and use. US Patent 7910772

179. Dieterle M, Heilek J, Mueller-Engel KJ. Method for the heterogeneously catalyzed partial direct oxidation of n-propane to acrylic acid. US Patent 7795470

180. Gaffney AM, Song R. Hydrothermally synthesized Mo-V-M-Nb-X oxide catalysts for the selective oxidation of hydrocarbons. US Patent 7718568

181. Hancock EG (1973) Propylene and its industrial derivatives. E. Benn, London

182. Persistent Market Search (2020) Isopropanol market: global industry analysis and forecast 2016–2026. https://www.persistencemarketresearch.com/market-research/isopropanol-market.asp

183. IHS Markit (2018) Isopropyl alcohol (IPA); chemical economics handbook. https://ihsmarkit.com/products/isopropyl-alcohol-ipa-chemical-economics-handbook.html

184. Xu Y, Chuang KT, Sanger AR (2002) Design of a process for production of isopropyl alcohol by hydration of propylene in a catalytic distillation column. J Trans IChemE 80(Part A):686–694

185. Beroe Advantage Procurement (2018) Global market outlook on isopropanol. Isopropanol Market Intelligence. https://www.beroeinc.com/commodity/ipa-market/

186. Kroschwitz JI (1991) Kirk–Othmer encyclopedia of chemical technology, vol 20, 4th edn. Wiley, New York, pp 216–240

187. Roy A (2018) The text book of industrial chemistry. Technology & Engineering (Lulu.com). ISBN-13: 978-0359095896

188. Ester W (1970) Process for production of alcohols by catalytic hydration of olefins. GB Patent 1201181

189. Neier W, Woellner J (1972) Use cation catalyst for IPA. Hydrocarb Process 51:113–116

190. Onoue Y, Mitzutani Y, Akiyama S, Izumi Y (1978) Hydration with water. ChemTech 8:432–435

191. Izumi Y, Kawasaki Y, Tani M (1973) Process for the preparation of alcohols. US Patent 3758615

192. Lin YP (2012) Asian Chemical profile: isopropanol, ICIS (Independent Commodity Intelligence Service). https://www.icis.com/explore/resources/news/2012/12/16/9624355/asian-chemical-profile-isopropanol/

193. Kosaka Y, Sinclair KB (1982) Bisphenol A: from phenol and acetone with an ion exchange resin catalyst, Union Carbide Technology, Process Economics Reviews, PEP'82-1. https://ihsmarkit.com/pdf/RW82-1-1_220283110917062932.pdf

194. Mitsui Chemicals Inc (2011) New facilities to produce acetone-based isopropyl alcohol at Osaka works. https://jp.mitsuichemicals.com/en/release/2011/pdf/110829e.pdf

195. Ovrebekk H (2008) Novapex to build 40,000 t/year France IPA plant, ICIS (Independent Commodity Intelligence Services) https://www.icis.com/explore/resources/news/2008/07/18/9141257/novapex-to-build-40-000-t-yr-france-ipa-plant/

196. Hayes KS, Mitchell JW, Niak A, Turcotte MG. Hydrogenation of acetone. US Patent 7041857

197. Fukuhara H, Matsunaga F, Shibuta Y, Tachi T. Preparation of Isopropanol. US Patent 5081321

198. Rueter MA. Acetone hydrogenation using a supported ruthenium catalyst. US Patent 5495055

199. Pompetzki W, Schuler J, Maschmeyer D. Process for the hydrogenation of acetone. US Patent 6930213

200. Balouch A, Ali Umar A, Shah AA, Mat Salleh M, Oyama M (2013) Efficient heterogeneous catalytic hydrogenation of acetone to isopropanol on semihollow and porous palladium nanocatalyst. ACS Appl Mater Interfaces 5:9843–9849. https://doi.org/10.1021/am403087m

201. Rahman A (2010) Catalytic hydrogenation of acetone to isopropanol: an environmental benign approach. Chem React Eng Catal 5:113–126

202. Li C, Sallee AM, Zhang X, Kumar S (2018) Electrochemical hydrogenation of acetone to produce isopropanol using a polymer electrolyte membrane reactor. Energies 11:2691

Selective Hydrogenation of 1,3-Butadiene to 1-Butene: Review on Catalysts, Selectivity, Kinetics and Reaction Mechanism

P. R. Selvakannan, Long Hoang, V. Vijay Kumar, Deepa Dumbre, Deshetti Jampaiah, Jagannath Das, and Suresh K. Bhargava

Abstract Catalytic hydrogenation of 1,3-butadiene to produce selectively 1-butene has considerable importance in the hydrocarbon industry and presents a significant challenge in tuning the catalyst selectivity towards 1-butene, understanding the reaction and kinetic mechanism. Selective hydrogenation over metal oxide-supported palladium catalysts is considered as a standard process; however, selectivity towards 1-butene is achieved by alloying palladium with other metals that facilitate the desorption of adsorbed alkene intermediate and limit further hydrogenation to form butane. In this book chapter, we summarize the current state of the art and perception of various factors that control the catalyst activity, adsorption of intermediates on the active sites and eventually the selectivity. In particular, we present a concise description of active metal dispersion, structure sensitivity, influence of support, promoter and their role in governing the selectivity of 1-butene from 1,3-butadiene hydrogenation. Then, this chapter highlights the detailed analysis of reaction kinetics and reaction mechanisms that are proposed clearly. Finally, a brief overview of the theoretical investigations for 1,3-butadiene hydrogenation using density functional theory (DFT) calculations has also been discussed for a variety of catalysts and followed discussion about summary and future outlook.

Keywords Heterogeneous catalysts · Selective hydrogenation · Palladium catalysts · 1,3-Butadiene · 1-Butene

P. R. Selvakannan (✉) · L. Hoang · V. V. Kumar · D. Dumbre · D. Jampaiah · J. Das
S. K. Bhargava (✉)
Centre for Advanced Materials and Industrial Chemistry, School of Science, RMIT University, Melbourne, VIC, Australia
e-mail: selvakannan.periasamy@rmit.edu.au; suresh.bhargava@rmit.edu.au

1   Introduction

Hydrogenation processes of poly-unsaturated hydrocarbons to selectively produce alkenes have attracted significant interest since 1990s, due to the high demand of alkenes from the petrochemical and polymer industries. Initial work on the catalytic hydrogenation was developed considerably during early 1960s, particularly with the boom of olefin production by steam cracking. Majority of the catalytic hydrogenation processes are used in refining and petrochemical sector, specifically the downstream units of the mother plant, the cracker, e.g. selective hydrogenations of acetylenes, methyl acetylenes, propadienes, 1,3-butadienes, selective hydrogenations of C5 unsaturates, etc. All of these molecules are produced in large scale due to their use as fuels, fuel precursors, polymerization precursors, etc. In particular, C4-rich streams consisting of 1-butene are currently used as precursors for the production of polybutene and co-monomer of low-density polyethylene. However, the presence of 1,3-butadiene in the C4 stream blocks the active sites of the polymerization catalyst, which inhibit the polymerization kinetics. Thus, there is a wide scope for understanding and developing newer and improved active, selective and stable catalysts of industrial importance, which can convert 1,3-butadiene into 1-butene selectively. In addition, this specific hydrogenation reaction is considered as a model reaction to investigate the catalytic, structural and electronic properties of the catalyst. Due to these advantages, a continued research activity on hydrogenation of 1,3-butadiene is significant from both fundamental and applied aspects, to achieve a better insight in the catalyst, process, and mechanism—key factors which control the catalyst performance as well as selectivity. Owing to the practical and theoretical importance, it is very important to collate the different aspects of this process from the existing literature to understand the reaction mechanism of hydrogenation reaction. Thus, this book chapter provides a detailed information of the selective catalytic hydrogenation of 1,3-butadiene, and summarizes the knowledge, significance and future scope of this heterogeneous catalytic process. Specifically, product selectivity and kinetics of this reaction, which were correlated to factors such as the effect of the support, the structure sensitivity, size of the active sites, metal dispersion, promoters and additives, are discussed in detail.

1.1   Significance and Background

To realize the potential of a model reaction to probe the catalyst structure, it is important to understand the hydrogenation reaction of 1,3-butadiene, physical properties of both 1,3-butadiene as well as the expected hydrogenated products from 1,3-butadiene (Table 1). Their chemical structures including the reactants and the products in this reaction sequence are also presented in Fig. 1, which clearly shows how the reaction kinetics on different catalyst can affect the product selectivity. From the data listed, the density of butane (2.480 g/cm^3) is higher than

Table 1 Comparison of physical properties of reactants and products

Compound/ property	Formula	Molar mass (g/ mol)	Density (g/ cm^3)	Melting point (°C)	Boiling point (°C)
1,3-Butadiene	C_4H_6	54.09	0.614	−108.9	−4.4
1-Butene	C_4H_8	56.11	0.620	−185.3	−6.4
Cis-2-butene	C_4H_8	56.11	0.641	−138.9	3.7
Trans-2-butene	C_4H_8	56.11	0.641	−138.9	3.7
Butane	C_4H_{10}	58.12	2.480	−140.0	−1.0
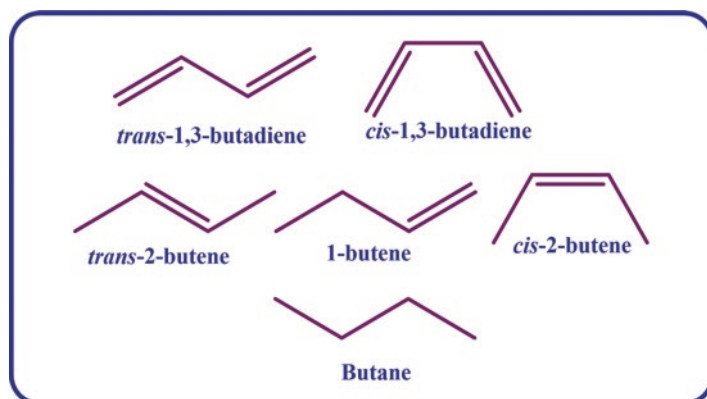
Fig. 1 Chemical structures of reactant and products in 1,3-butadiene hydrogenation

that of other products and 1,3-butadiene. No other significant differences in physical properties can be observed between the 1,3-butadiene and its products after hydrogenation.

As mentioned in the introduction, the 1-butene-rich cut, also known as C4 alkenes cut, was available after butadiene and isobutene extraction at the downstream operation of cracker unit in any petrochemical industries and refineries [1, 2]. Further, the process of the selective hydrogenation of 1,3-butadiene in C4 alkenes cut could produce a linear low-density polyethylene (LLDPE) polymer [3]. 1-Butene was mainly used as a co-monomer and a trace quantity of 1,3-butadiene present in the feed, can adversely affect the polymerization (olefin) as well as durability of catalysts and this process can reduce the rate of total polymer production. In addition, 1-butene with 99 wt% purity and 1,3-butadiene residue (<10 ppm) are required for an LLDPE co-monomer [4].

Therefore, selective conversion of 1,3-butadiene into 1-butene is a key issue during this hydrogenation process and this high selectivity is prominent for polymer quality [5]. The high selectivity can be achieved if the process overcomes the reaction steps of 1-butene isomerization (to form 2-butenes) and/or its subsequent hydrogenation (to form n-butane). Moreover, selective butadiene hydrogenation is an attractive model reaction, which permits investigation on both activity and
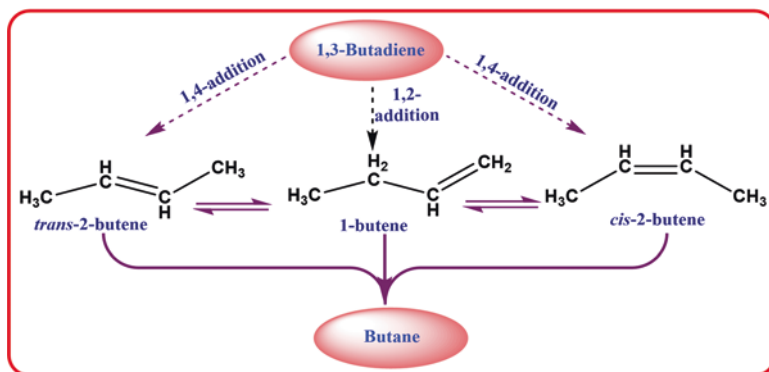
Scheme 1 Isomerization route of double bonds in butenes and subsequent hydrogenation step of butene to butane

selectivity aspects on various catalysts, because there are four probable reaction products (1-butene, butane, *cis*- and *trans*-butene) [6].

In the case of 1,3-butadiene hydrogenation, selectivity can take mainly in the forms of regio-selectivity, where the reduction of one C=C bond is favoured over that of another in different surroundings (terminal C=C undergo faster reduction compared to the internal one). Regio-selective hydrogenation of a 1,3-butadiene is basically controlled by the same factors, which control the reactivity of alkenes, when a competitive hydrogenation occurs in binary mixtures. Compared to other substituted double bonds, a terminal C=C bond is preferentially hydrogenated on the active site of the catalyst. However, another kind of selectivity can be observed due to the competition between unreacted diene and intermediately formed monoene for the same active site. Moreover, the other intermediate (*trans*-2-butene) can be formed due to the isomerization of 1-butene (Scheme 1).

2   Selective Hydrogenation of 1,3-Butadiene: Key Factors in Catalysts Design

To gain a deeper insight into the design of catalysts for selective hydrogenation of 1,3-butadiene, a detailed survey of the literature was carried out and the following key factors were identified. Supported metal catalysts are the main family of catalysts that were tested for their reaction; therefore, their, size, morphology, dispersion, interaction with the support were studied and correlated with the activity of the catalyst and product selectivity. Kinetic study and reaction pathway, order of the reaction, adsorption on metallic surfaces, effect of support, structure sensitive and the effect of metal dispersion and the use of additives, ad-species, and promoters were the key parameters, which were identified as important parameters in controlling the catalyst activity and product selectivity. In the following sections, each of

these parameters is discussed in detail; however, it should be noted that all these factors affect the reaction synergistically to control the activity and selectivity. Detailed analysis from the reported literature presented in this chapter is organized as follows.

2.1   Kinetic Study and Reaction Pathway

The selectivity of this hydrogenation reaction is an important parameter, therefore studying the reaction kinetics of this reaction on various catalysts and establishes a probable mechanism that can provide the bridge between the experimental results and theoretical prediction. In this specific heterogeneous catalytic hydrogenation process, reactants and protects are geometrical isomers, therefore the reaction kinetics also provide an insight into stereo/regio-selectivity. The adsorption kinetics of these isomers on the active sites of the catalysts was found to vary with isomer to isomer, therefore studying the kinetics can provide the information about stereo/regio-selectivity on each catalyst. Over many years, the stereochemistry of different heterogeneous catalysts in selective hydrogenation reactions has been a substantially interesting subject [1, 7–17]. The kinetic investigations reported in the open literature are usually carried out in the gas phase or liquid phase (usually under industrial processing conditions: atmospheric pressures and low temperatures). The alkenes hydrogenation over the heterogeneous catalysts has been investigated for almost 80 years. In 1934, Horiuti and Polanyi [16] explained the hydrogenation of 1,3-butadiene reaction mechanism, in which 1,2 and 1,4-addition of two conjugated C=C double bonds produced 1-butene and 2-butene, respectively. In addition, due to the existence of *cis* or *trans* isomers of 1,3-butadiene, the hydrogenation reaction can produce either *cis*- or *trans*-2-butene. Further hydrogenation of the *cis* or *trans* isomer products obviously produces butane [18, 19]. Well et al. investigated initially the 1,3-butadiene hydrogenation reaction over different metals (Ru, Ir, Fe, Pt, Co, Rh, Pd, Cu, Os, and Ni) supported by alumina (Al_2O_3) [18, 20–22]. It was proposed that the reaction mechanism exhibit two types of selective behaviours namely 1,2 and 1,4 addition over alumina-supported metal catalysts (Scheme 1).

As shown, the formation of 1-butene was mainly responsible for 1,2 hydrogenation pathway. Interestingly, 2-butene formation occurred on Pd through a 1,4-addition pathway. Moreover, the relative yields of *cis*- and *trans*-2-butene were dependent on the conformational characteristics of adsorbed precursors. On the other hand, Boitiaux et al. reported that 1-butene was formed through syn or anti-adsorbed 1,3-butadiene on Pd, Pt and Rh metals, in which *trans*-butene and *cis*-butene were formed through anti- and *cis*-configurations [8–10]. Among active metals, the behaviour of Pt and Rh for the purpose of 1,3-budadiene hydrogenation was found to be quite similar, and each of them nearly resembles to that of Pd, the only difference being in the initial butane formation. 1-Butene can undergo several other consecutive or parallel transformations to generate *cis*-2-butene, *trans*-2-butene and butane. Butane formation occurs through a semi-hydrogenated species,

generated from a syn-adsorbed 1,3-butadiene, from which *cis*-2-butenes are formed. Addition of hydrogen occurs mostly/largely in the 1,2 positions, and to some extent at the 1,4 position. Further hydrogenation of 1-butene starts only after a high conversion of butadiene. Pradier et al. [23] reported the hydrogenation of 1,3-butadiene over Pt(110) and Pt(100) and it was found that the process to re-adsorb 1-butene at >50% conversion level, when desorption of a fraction of butadiene occurs, is likely to occur than the process of second hydrogenation of 1-butene in the adsorbate state before it leaves the surface. The proposed pathway was found to be similar to the earlier observation that 1-butene is more strongly bonded to transition metals as compared to that for 2-butenes. Butane formation by the readsorption of 2-butene on the metal site was not considered significant enough to be considered in the kinetics. Further, Boitiaux et al. [24, 25] proposed a mechanism of carbene formation (Scheme 2) on different metal sites, which can explain the selective formation of butane when the ratio of *trans*/*cis*-2-butene ratio was found to be low. Pt and Rh show entirely different results to that are obtained over the Pd due to the negligible selectivity towards butane and high ratio of *trans*/*cis* butenes over the Pd; the first two yield butane and a small *trans*/*cis* ratio. From these studies, it was concluded that the metal site, which would not facilitate carbene formation would not produce butane selectively. To find out the specificity of the hydrogenation process in detail, isotopic labelling studies were conducted, wherein deuterated 1,3-butadiene was used as a reaction. This reaction was investigated over the Al_2O_3-supported Ni, Cu, Pt, Pd, Rh and Co catalysts [18, 22, 26, 27]. The detailed compositional analysis of the products was studied as a function of different conversion [21] while keeping
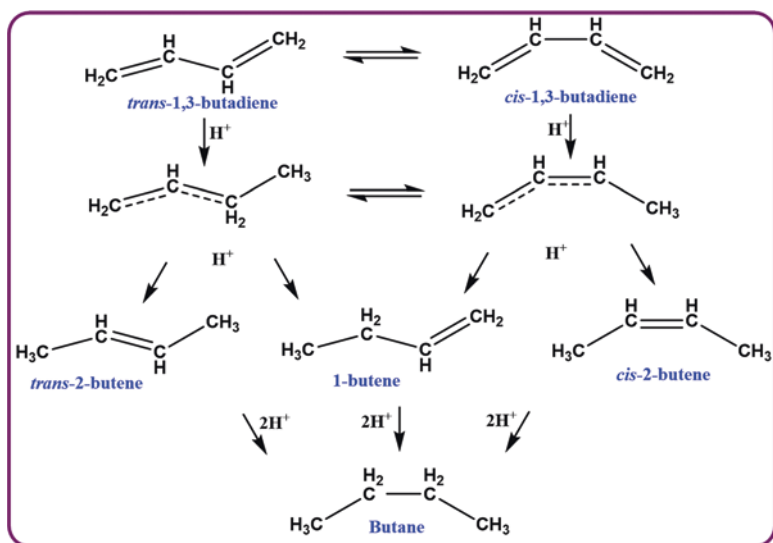
Scheme 2 Mechanism of 1,3-butadiene hydrogenation process via carbene formation mechanism. (Adapted from [24, 25], Applied Catalysis J.P. Boitiaux et al. Copyright (1989) with permission from Elsevier)

pressure and temperature constant. Earlier studies have demonstrated that these two variables including pressure and temperature have shown similar results for all the metal catalysts. These studies have shown that the deuterium distributions in the butenes were approximately the same. This could happen only when each of the butenes was an initial product, and not the result of the isomerization of any other as well as the absence of both the 1,2- and 1,4-addition processes. Another major conclusion drawn from this study was that there was limited but adjustable exchange of the hydrogen atoms of the reactant. Appearance of small amounts of hydrogen in the deuterated reactants and products shows that the concentration of atoms on the surface was small under prevailing experimental conditions [18, 21].

2.2   Reaction Order of Reactants: 1.3-Butadiene, Hydrogen, 1-Butene

As the reactants and few products of this reaction have the tendency to competitively adsorb on the catalytic sites, the reaction order was found to be different on different catalysts, therefore understanding the reaction order with respect to the reactants and products can provide valuable information about the product selectivity. The main parameters which characterize the hydrogenation process are (a) the sum of all three butenes (i.e. total butenes) selectivity and (b) individual butene isomer selectivity, i.e. the fraction of butenes that each isomer constitutes (*trans*, *cis*-2-butene and 1-butene). Over many of the metal catalysts from Groups 8 to 10, the selectivity to the sum of all three butenes was close to unity and the composition was unaffected until the complete consumption of reactant 1,3-butadiene; therefore, it was more strongly adsorbed than the products. Kinetics studies on hydrogenation of 1,3-butadiene in gas phase or liquid phase have shown that the intrinsic reaction rate was zero order with respect to the butadiene and approximately first order with respect to hydrogen [7–15, 17, 28–31]. Strong and preferential adsorption of 1,3-butadiene over 1-butene were indicated from the measurements of reaction orders and activation energies. Moreover, each unsaturated compound has different adsorption strength and always selectivity for the hydrogenation reaction depends on these adsorption energies. Compared to *n*-butenes, 1,3-butadiene has high propensity to be hydrogenated. Only, when the concentration of 1,3-butadiene was lower in the mixture, *n*-butene was found to be hydrogenated preferentially to *n*-butane. Oudar et al. [32, 33] observed two kinetic regimes for the 1,3-butadiene hydrogenation and H_2-D_2 exchange over the Pt(110) surface and pressure conditions used for this reaction are 200–400 Torr. Reaction orders with respect to the hydrogen and butadiene were found to be 1 and 0, respectively at >130 Torr of hydrogen pressures. It was also observed that the selectivity was independent of the hydrogen pressure applied, and every two Pt atoms of the catalyst surface was covered by one butadiene molecule. Below critical hydrogen pressure (~125 Torr); the reaction order was 2 and 0 with respect to hydrogen and 1,3-butadiene, respectively. Another

important observation was the butane selectivity decreases with the hydrogen pressure. Yoon et al. [31] studied the isomerization and hydrogenation reactions of *cis*-2-butene and 1-butene on Pt foil and Pt(111), Pt(100), Pt(755) single-crystal surfaces and reported that the reaction selectivity was independent of reactant mixture but changes slightly with reaction temperature.

2.3 DFT Studies on Catalytic Hydrogenation of Butadiene

Catalytic hydrogenation of 1,3-butadiene is considered as a model catalytic process for olefin/diene hydrogenation in refining/petrochemical industry and adsorption studies of these unsaturated hydrocarbons on metallic surfaces are of basic and practical interest. Therefore, the majority of studies [19, 29, 34–41] have focused on the use of DFT calculations in comparison with experimental data to investigate the interaction of 1,3-butadiene, 2-*cis/trans*-butenes and 1-butene on various metal surfaces. Valcárcel et al. first studied the interaction of different hydrocarbons (1,3-butadiene, 1-butene and 2-*cis/trans*-butenes) over various Pd(111) and Pt (111) surfaces using DFT calculations [41, 42].

Two different modes of 1,3-butadiene adsorption on these surfaces were suggested [36, 37]. They are 1,2,3,4-tetra-σ adsorption and 1,4-metallacycle-type adsorption during the process as shown in Fig. 2, in which the first type adsorption was stable. This structure was consistent with the qualitative molecular orbital calculations[43] as well as the results from the electron energy loss spectroscopy (EELS) and thermal desorption spectroscopy (TDS) [44]. Among different pathways as discussed in Fig. 2, the di-σ-mode was the most stable adsorption structure for the formation of butene isomers [40], as suggested by NEXAFS, UPS, TDS and EELS results [44–46]. The experimental observations clearly evidenced the formation of butene over Pd surface with high selectivity. On the other hand, in case
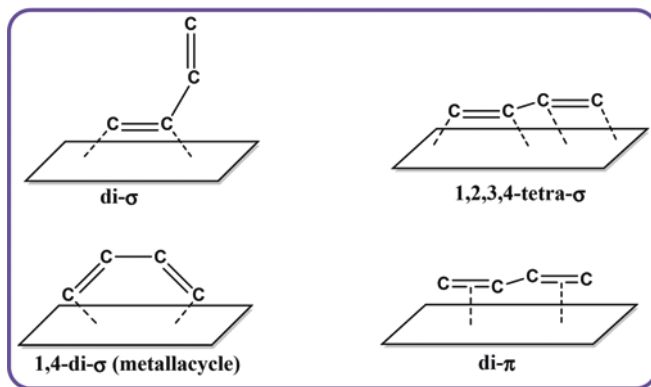
Fig. 2 Adsorption structures proposed for 1,3-butadiene. *(Adapted with permission from [48]. Copyright 1989 American Chemical Society)*

of Pt surfaces, the dehydrogenation radical species formation was competitive with the butene, which obviously prefers low selectivity towards butene formation; thereby the butanes will be the primary products. Among the reaction pathways, di-σ mode of the interaction was further strongly supported by additional experimental [47] and theoretical [48] works (Fig. 2). Experimental results from other studies have also reported that 100% formation of 1-butene alone was occurred on Pd(111) surface, whereas 60% of formation was only observed on Pt(111) surface [23, 47, 49, 50]. This variation between the reaction on the Pd and Pt surfaces was mainly attributed to the differences in 1,3-butadiene and butenes adsorption strengths towards these two metal surfaces (Fig. 3). It was considered that the strong adsorption nature of 1,3-butadiene can easily replace the weakly adsorbed butene on Pd(111) surface, thereby higher selectivity obtained. However, in case of Pt(111) surface, equivalent strength of both 1,3-butadiene and butene, a lower selectivity was observed. This hypothesis was supported by extended Huckel theory calculations [48] and experimental studies [51].

However, Mittendorfer et al. [40] found that almost there were no significant differences between Pt and Pd with respect to the relative adsorption energies of butadiene versus butene. These authors suggested that the higher activity over Pd most likely due to the ease of butene desorption from Pd(111) surface as compared with Pt(111) surface. Belelli [34] studied the adsorption of three butene isomers (*cis/trans*-2-butene and 1-butene) on a stepped Pd(422) surface using a DFT and compared with those found for a free defect surface as Pd(111). The 1-butene was predicted to be more stable on free defect surface when compared with the Pd(422) surface in contrast to the preference of *cis/trans*-2-butene to be adsorbed on the stepped surface. Yang et al. [19] performed both theoretical calculations and catalytic experiments for the selectivity towards 1,3-butadiene hydrogenation in presence of Au nanoparticles.

Nano Au surfaces preferably produced the *cis*-form of 2-butene instead of *trans*-form. It was found that the Au nanoparticle size strongly influenced the *cis-/trans* ratio. Sheng Chen et al. [52] proposed adsorption configurations of different form of reactants and products over Au(211) surface. As shown in Fig. 4, the adsorption energies of *cis/trans*-2-butene, and 1-butene were similar, however weaker than those of *cis/trans* 1,3-butadiene. Due to these differences, the H atom and butadiene
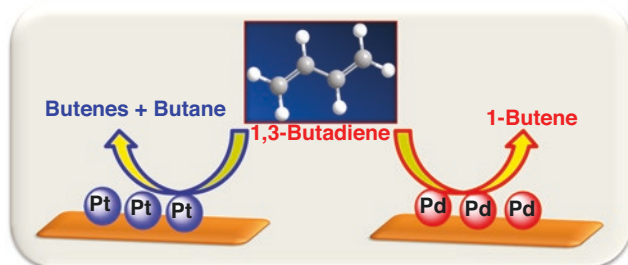
Fig. 3 Product selectivity of 1,3-butadiene hydrogenation over Pd and Pt surfaces
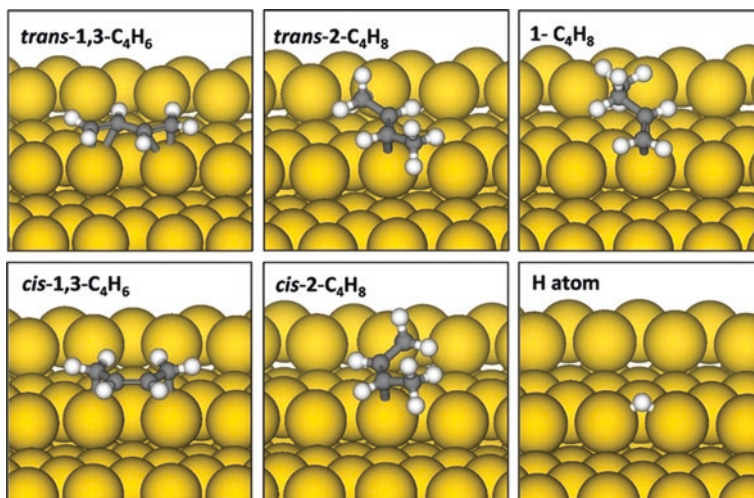
Fig. 4 Adsorption configurations of *trans-/cis-*1,3-butadiene, *trans-/cis-*2-butene, 1-butene and H atoms on Au(211). The yellow, grey and white balls denote the gold, carbon and hydrogen atoms, respectively [52]. *(Reprinted from [52], Catalysis Today Sheng Chen* et al. *Copyright (2018) with permission from Elsevier)*

adsorbs at the bridge site along the step edges of Au(211) surface, and all the butenes produced adsorb at the step edges with a π-bonded configuration. Similar trend was also observed for Cu and Ag model nanoclusters, when they use theoretical calculations. Another interesting point observed for the case of Pt surfaces, butane formation was predominant from the beginning of the reaction [8–10]. Butane was formed in much higher proportion as compared to butenes and becomes the primary product. This different behaviour was not ascribed to a very low desorption rate of the intermediate olefin but to the nature of the partially hydrogenated species. Additionally, the reactivity of metallacyclic intermediates that could play a vital role in hydrogenation-dehydrogenation reactions has been reported in several reports [53–55]. Very recently, DFT calculations carried out by Hou et al. [38] and Gomez et al. [36, 37] found that the Pd-terminated bimetallic surface is more reactive and selective to form 1-butene, which was also further supported by TPD experiments. On the Pd_1Ni_3(111) and PdNiPd(111) surface, a very low binding energy (BE) was seen for 1-butene, which was confirmed that it can readily desorb from the surface to form 1-butene rather than butane. This clearly showed that 1,3-butadiene can be converted to 1-butene avoiding further hydrogenation to form butane. In summary, the structure and adsorption state of unsaturated hydrocarbons on metal surfaces strongly influenced the hydrogenation reactions. It was proved that the reaction of 1,3-butadiene on Pd surfaces selective towards butenes whereas on Pt surfaces it can be hydrogenated to butane along with butenes. The differences between Pd and Pt surfaces were assigned to the difference in adsorption state via the C=C double bonds present in butadiene. Furthermore, it was believed that the catalytic reaction was also influenced by the adsorption structure of the reactant

[39]. It can be concluded that the key to the butene selectivity depended on the relative stability of radical intermediates over metal surfaces. This could explain why Pt surfaces always show poor selectivity for the formation of butene rather than it always exhibited high selectivity towards butanes.

2.4   Influence of the Support on Hydrogenation of 1,3-Butadiene

The different metal surfaces clearly showed various mechanisms and selectivities; further, the presence of support can influence the reaction pathway and selectivity towards butenes. There have been a number of studies carried out at investigating the support effects [56–61]. Primet et al. [60] investigated various supported platinum catalysts with low metal loading (<1 wt%) for the hydrogenation of 1,3-butadiene. It was found that the acidic sites presented on the support can cause an electron shift through the interface between meta-support interfaces. Consequently, the bond strength between unsaturated hydrocarbons and the metal active sites can be altered, thus changing the selectivity and reaction rate. In addition, the catalyst deactivation can also be affected by the other properties such as acidity of the support and the pore diffusion. Recent work by Pattamakomsan et al. [62] also revealed that the Pd/Al_2O_3 catalytic performance was improved when the mixed Al_2O_3 structure support consists of 80% θ- and 20% α-Al_2O_3 rather than pure Al_2O_3. The relatively high acidity and BET surface area of Al_2O_3 yielded higher dispersion of Pd and significantly enhanced rate of hydrogenation. Moreover, the bimodal pore distribution of the mixed-phase θ/α Al_2O_3 promoted butene desorption products to obtain a much lower formation of butane when compared to the pure θ-Al_2O_3 that had only small pores. It can be concluded that Al_2O_3 support with different phase compositions effected the selectivity towards 2-butene. Moreover, Hou et al. [63] investigated the influence of various supports such as Al_2O_3, SiO_2, CeO_2, ZrO_2, and TiO_2 on Pd-Ni surfaces for the selectivity butadiene hydrogenation towards different products. As discussed in Fig. 5, each support favoured different selectivity for the butenes. Among the expected products (1-butene, *cis*-2-butene, and *trans*-2-butene), alumina support showed highest selectivity towards 1-butene. The following is the order of selectivity towards 1-butene: $Al_2O_3 > SiO_2 > CeO_2 \sim ZrO_2 > TiO_2$. It can be concluded that the strong metal-support interaction between Pd-Ni and alumina played a key role on 1-butene selectivity over other supports. Furthermore, Cukic et al. [56] used high-throughput experimentation for Pd/Al_2O_3 catalyst with different variables such as stirring rate, calcination temperature, the solution pH, and the time taken for impregnation, and heating rate. It was found that these parameters influenced the conversion of 1,3-butadiene significantly. For example, during the impregnation process, the use of excess solution caused a decrease in activity when compared to the incipient wetness impregnation. On the other hand, the ramping rate for drying, and the holding time for (both drying and calcination) did not show
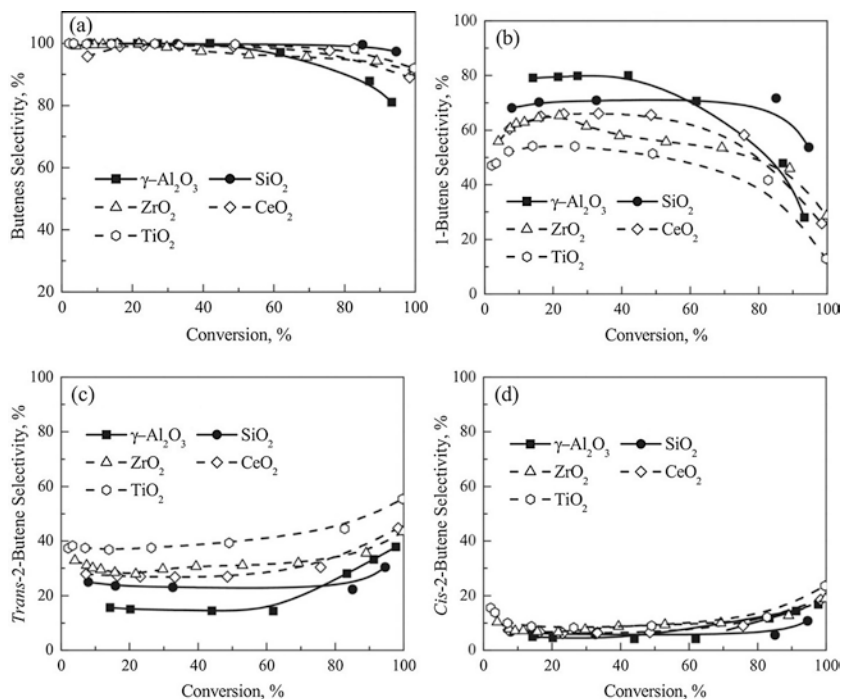
Fig. 5 Selectivities to (**a**) butenes, (**b**) 1-butene, (**c**) *trans*-2-butene and (**d**) *cis*-2-butene over Pd–Ni bimetallic catalysts on different supports [63] (*Reprinted from [63], Applied Catalysis A Hou, R et al. Copyright (2015) with permission from Elsevier*)

any significant changes in the activity. Several studies also claim that using porous active site can influence the 1,3-butadiene hydrogenation process. It was explained that the hydrogen porous membrane catalyst can provide an independent control of the surface concentrations of hydrogen and other substances which can be readily hydrogenated. That means the membrane can be Pd itself or it may act as support material for the active species. Liu et al. [4] reported the use of mono- and bimetallic hollow-fibre catalytic reactor for the purification of 1-butene. Interestingly, the isomerization of 1-butene was significantly controlled due to the synergistic interaction between bimetals. Moreover, Ciebien et al. [64] reported that Pd nanoclusters membrane catalyst synthesized within microphase-separated di-block copolymer films are active and selective catalysts for the selective hydrogenation of 1,3-butadiene, although the clusters were completely surrounded by a bulk polymer matrix. It was observed that the selectivity was enhanced in case of Pd membranes while compared to non-membranes. The increase in selectivity can be due to the lower hydrogen pressure, which allowed steady-state concentration reactants away from equilibrium and consequently suppressed the side-reactions over the working catalyst. In summary, the above survey appraisal of variables makes evident that there were many important variables involved in the preparation of catalysts for the

1,3-butadiene hydrogenation reaction. Particularly, acidic properties of the support, heating rate of calcination, stirring speed, impregnation time, pH of the solution, drying and calcination temperature were shown to play vital role in promoting the selective hydrogenation of butadiene into butene.

It was worthwhile to emphasize that the selective 1,3-butadiene hydrogenation can be significantly improved with palladium membrane.

2.5   Structure Sensitive and the Effect of Metal Dispersion

As discussed above, the 1,3-butadiene hydrogenation usually leads to the formation of many different products and the desired product selectivity relied on these molecules adsorption preferences towards metal sites. This structure sensitive reaction was first confirmed by Silvestre-Albero et al. [65–67]. They found through the kinetic measurements on Pd(110) and Pd(111) for their conversion and selectivity that the selective 1,3-butadiene hydrogenation on Pd catalysts was a structure-sensitive reaction (Fig. 6). The strong structure sensitivity was understood by evoking the unusual electronic structural properties of Pd nanoparticles. Due to the presence of unique electron-deficient Pd clusters, the electron-rich diene molecules can be chemisorbed, which lead to self-poisoning as compared to larger size nanoparticles [32, 33, 68, 69]. The catalytic properties of supported metal catalysts can also be influenced by the particle size, therefore the influence of particle size was studied systematically to understand their role on the activity and the product selectivity. Both activity (turnover frequency; TOF) and selectivity can be affected by the change in dispersion/particle size of the metal which are mostly due to geometric and electronic effects [70, 71]. When metal atoms replaced by other metal atoms through doping approach, the chemisorption nature of catalyst can be altered. This effect can also be called electronic or "ligand effect".

The activity correlation with the Pd catalysts and its dispersion in the hydrogenation of dienes was more straightforward, in which a strong conflicting behaviour is usually found [12, 13, 15, 72–75]. In many cases, the specific reactivity of Pd is
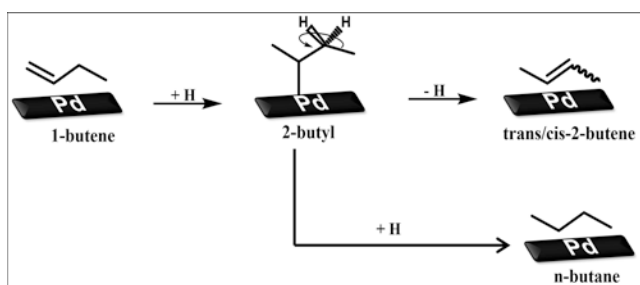
Fig. 6 Proposed reaction schemes for the 1-butene isomerization and hydrogenation [65–67]. (*Reprinted from [65], Silvestre-Albero, J.* et al. *Copyright (2005) with permission from Elsevier*)

unchanged until the dispersion amount is 20–35%; however, this might be different, when different supports used [72, 76]. However, the catalytic activity was decreased as the amount of Pd dispersion increased. Furthermore, as the number of active metal particles decreases, the electronic properties of metal particles were influenced. Perfect explanation can be provided through the chemisorption of highly electron–rich diene molecules. If less number of active metal particles available, the selectivity towards 1,3-butadiene hydrogenation for the butene will be decreased. It was also observed that the metal atoms with high coordination number were characteristic of larger particles and whilst small particles possess crystals with atoms of low co-ordination number. Furthermore, the active nanoparticle size can also play a significant role in heterogeneous catalysis due to the unique properties at nanoscale. The utilization of transition metals with a 1–20 nm nanoparticles size in catalysis is vital as they mimic the activation of metal surface which lead to high selectivity and efficacy to the desired reaction. These small-sized nanoparticles can also be called as the clusters derived from metal atoms, and are usually stabilized by ligands, surfactants, and polymers/dendrimers protecting their surfaces with varying sizes (ranging from 10 to 100 nm). However, the most active nanoclusters are only few hundreds of atoms with one or a few nanometres in diameter. It is reported that the sizes of the noble-metal structures and specific crystal facets, such as Pd, Pt, Au and Ni [19, 62, 66–68, 73–75, 77–85] significantly influence on their chemisorption properties and hence, catalytic performance. Hence, special nanostructures with well-defined shapes and uniform sizes are highly needed to control their performance for the hydrogenation reaction. According to Piccolo et al. [86], the conversion rates of butadiene-to-butenes on the fresh model catalysts can be related as follows: Au(111) < Pd-Au(111) < Pd-Au(110) < Pd(111). Unlike on Pd(111), the butane production rate was very low and the butenes selectivity reached ~100% on Pd-Au(111). It should also be noted that the diffusion of hydrogen toward bulk of the Pd-based single-crystals seems to play a key role and the surface hybrid formation accounts for the Pd-Au surface activation. Michalak et al. [39] reported that the catalysts having ensembles of 1.8 and 0.9 nm in size of Pt enhanced 20 and 30% of total hydrogenation of 1,3-butadiene to *n*-butane when compared to 6.7 and 4.6 nm size of Pt. It can be concluded that the small-sized nanoparticles effected conversion rate. As shown in Fig. 7, the larger size (4.6 and 6.7 nm) Pt nanoparticles favour insertion of H-atom at the terminal site of carbon atom, which is similar to those observed for bulk Pt materials. In case of smaller sized (0.9 and 1.8 nm) Pt nanoparticles, the insertion H-atom occurred at two places, which includes at low coordination sites as well as at terminal carbon site. Moreover, Lucci et al. reported that isolated Pt atoms were responsible for the deactivation of catalyst, thereby less selectivity towards butene formation. This was due to the preferential hydrogen activation and unable to break the C-C bond [87]. In contrast, other researchers reported that the 1,3-butadiene hydrogenation reaction is in fact independent of the metal particle size [66, 67]. In particular, a study was focused on demonstrating the hydrogenation of 1,3-butadiene was independent on particle size (in spite of being structure sensitive) for the case of Pd/Al$_2$O$_3$ catalyst. The catalytic activity of different-sized Pd nanoparticles was correlated with the Pd(110) and Pd(111)
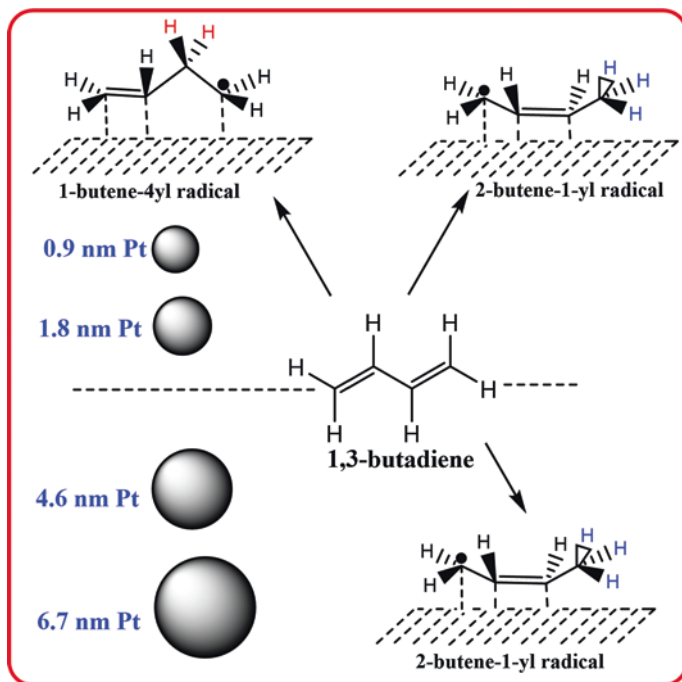
Fig. 7 Proposed reaction pathways for Pt nanoparticles with different sizes. (*Reprinted with permission from [39]. Copyright 2013 American Chemical Society*)

surfaces under similar reaction conditions. It was found that the 4 nm-sized Pd nanoparticles showed similar activity while compared to the larger size of Pd nanoparticles.

It was suggested that the author bridges the "materials gap" between the surface science studies on single crystals and heterogeneous catalysis on metal NPs. Besides using Pt and Pd as active sites, 1,3-butadiene hydrogenation reaction catalysed by gold has also received a significant attention due to its potential to catalyse the preferential oxidation and selectivity [88]. Bulk Au is chemically inert (as Au is one of the noble metals), and has seldom rarely been considered to be an effective catalyst. However, small-size gold nanoparticles have been reported to be remarkably selective towards partially hydrogenated product during hydrogenation of alkadienes [58, 75, 86, 88–90]. In contrast, the Au catalysts display low activity than that of the group VIII metals and is attributed to its limited capability to dissociate H_2 [91]. The dissociation capacity of Au depends strongly on the amount of available low coordination sites on the Au nanoparticles and is thus facilitated with decrease in particle size. In summary, the smaller size metal nanoparticle and metal clusters that are having dynamic surface reorganization played a key role in adsorption and catalytic properties. In fact, Pd nanoparticles showed lateral flexibility, which was benefited for the breaking of olefinic bond in 1,3-butadiene and facilitated hydrogenation reaction for the formation of butene. This was proved from the

preferential reaction to the unsaturated coordinated sites (corners and edges) of butadiene, which results in a local Pd lattice expansion and channels formation for barriers less hydrogen diffusion into the pore volume of Pd nanoparticles. Due to lower reaction barrier for H diffusion on Pd surface, the hydrogenation of C=C bond is easily shattered, which facilitated the hydrogenation reaction.

2.6 The Use of Additives, Adspecies and Promoters

Several authors have suggested adding alkali additives on catalyst surface could play a significant role in selective hydrogenation [28, 92]. Massardier [49] investigated the effect of K and Na on Pt single crystals to modify the metal electronic properties. It was found that the improved properties increased the selectivity towards 1,3-butadiene hydrogenation (Table 2). Alkali additives, up to an alkali coverage of 0.4, improved the activity and selectivity towards the 1,3-butadiene hydrogenation. Till this value (0.4), it acted as an electron donor and altered the relative energies of metal orbitals and adsorbate. The enhancement in catalytic activity noticed both on the more open structures and on K-promoted Pt, possibly be related to a weakening of bond strength of the hydrocarbon adsorption and (or) an increase in the H-metal bond strength. It was further proved by Song (2001) [93] that the K addition influenced the electron density around Ni, which increased the 1-butene selectivity.

Fewer studies also have investigated the additive's influence on competitive hydrogenation of alkenes and dienes and the factors influencing intrinsic selectivity. Pd is the major active metal which features in most of the industrial applications and many promoters have been tested with few being successful. Nitrogen or sulphur-containing organic molecules act as selective poisons, being more strongly held than alkenes but less strongly adsorbed than dienes. Boitiaux et al. investigated the effect of additives in the selective hydrogenation of dienes and alkynes [24, 25]. These work reported that the addition of a donor ligand (e.g., piperidine) and

Table 2 Catalytic behaviour of low-index faces of Pt (*Reprinted from[49], Journal of Catalysis Massardier, J.* et al. *Copyright (1988) with permission from Elsevier*)

Catalysts	N at 298 K[a] (s^{-1})	S_1		S_2
		b	c	
Pt(100)	4	0.54	0.50	0.55
Pt(110)	7	0.64	0.60	0.55
Pt(111)	2	0.58	0.55	0.50
Pt(100) + K[d]	4	0.60	0.54	0.80

N turn over number; $S_1 = \Sigma$ butenes/Σ conversion; $S_2 = $ 1-butene/Σ butenes
[a]$pH_2 \simeq 755$ Torr, $pC_4H_6 \simeq 5$ Torr
[b]Up to 50% conversion
[c]At 80% conversion
[d]K Coverage $(\Theta_K) \leq 0.43$

electron-attracting additives (e.g., phosphorus, oxygen, sulphur and chlorine) over Pt and Rh catalysts influenced the activity and selectivity. Piperidine modified metal site showed a decrease in the rate of hydrogenation of 1-butene and 1,3-butadiene over the pure Pt/Rh catalysts. Selectivity for olefin formation from 1,3-butadiene was increased on Pt surface, whereas selectivity change was negligible in case of Rh surface. In case of electron attracting additives, for example, nitrogen compounds increase the hydrogenation rate of 1,3-butadiene on an Rh catalyst. In case of Pt, an increase in the selectivity for l-butene was observed and the direct formation of butane is drastically reduced due to specific preference of 1,2-addition. In contrast with pure geometric effects, no correlation was obtained with the electronic properties of the additive. Sárkány (1995–1997) [69, 94, 95], in a series of 4 papers, investigated the hydrogenation of 1,3-butadiene on catalysts prepared from the different methods in the effects of various poisonings or adspecies. The presence and formation of polyenes in the vicinity of metallic sites was due to the unusual hydrogenation character of the $Pd_2Ni_{50}Nb_{48}$ ribbon. It was further confirmed by Alves [28] that in the case of liquid-phase hydrogenation of 1,3-butadiene, 1-butene in the presence of isoprene on a commercial Pd/Al_2O_3 catalyst, concentration of 1-butene practically remains unchanged even when the liquid was almost depleted from 1,3-butadiene. It was proven that the isoprene adsorption strength was higher than that of 1-butene and lower than that of 1,3-butadiene. Hence, it was clear that isoprene was a good option to use as an additive to improve the 1-butene selectivity in 1-butene purification processes. Adspecies formed from *n*-butylamine on Cu/SiO_2 seem to influence the competition between diene and *n*-butenes. The electronic effect of the adspecies can be emphasized by the variation in the intrinsic hydrogenation selectivity towards diene in presence of methanol. Preadsorption of methanol on Cu/SiO_2 caused electronic modification of Cu sites (through decomposition of methoxy species), and this increased the *cis* 2-butene. Formation of 1-butene prevails on the sample reduced at 753 K, and this points to the facile 1,2-addition of hydrogen atoms to adsorbed diene. Improved 2-butene formation rate over the Cu sites perturbed by alcohol appears to show that 1,4 addition mechanism is preferred. These finding points to the formation of π-allyl or π, σ bonded C_4H_7 species rather than 1-butene isomerization in the gas phase or adsorbed phase. Firmly held adspecies generated from butylamine or diene favour the formation of alkene by the adsorption of *n*-butene. The presence of carbonaceous or hydrocarbonaceous deposited on Pd/Ag catalyst increases the formation of butane. Several authors [68, 69, 96] have proposed that carbonaceous overlayers present on the catalyst surface play a key role in hydrogenation. Hydrocarbonaceous deposits affect the competition between diene and *n*-butenes and therefore increases the 1-butene selectivity in the hydrogenation of 1,3-butadiene. Wu et al. [96] studied the selectivity in the hydrogenation of 1,3-butadiene on using molybdenum nitride catalyst and the observed high selectivity towards 1-butene is most likely due to the weak interaction between 1,3-butadiene and nitrogen atoms present in the molybdenum nitride catalyst surface. Silvestre-Albero and co-workers [65] reported that small quantities of CO addition dramatically altered the selectivity over the Pd(110) surface, i.e. the hydrogenation to *n*-butane was totally suppressed; however,

the butenes hydrogenation and isomerization (to *cis*- and *trans*-2-butene) were hardly affected. In addition, the presence of CO reduces the surface concentration of hydrogen which is also still adequate for hydrogenation (of 1,3-butadiene) and isomerization (of 1-butene) and is insufficient for butene hydrogenation. Further, Yardimci et al. [97] reported that the selectivity of *n*-butene goes up when the Rh is selectively poisoned with CO ligands (Scheme 3). The poisoning effect is more evident if the support act as the electron-donor (e.g. MgO) and the Rh is in the form of approximated dimer clusters. The selective Rh/MgO carbonyl dimers limits the activity for dissociation of H_2 and thus avoid the formation of butane for controls the butane forming catalytic routes the catalytic routes that yield butane, limiting the activity for dissociation of hydrogen to avoid the formation of butane via primary reactions. This also favours the bonding of 1,3-butadiene over butenes to control secondary reactions giving butane. The selectivity to *n*-butene of >99% was obtained with 97% of 1,3-butadiene conversion over this catalyst. The catalytic performance of supported metal was influenced by the particle size as well as their interactions with the support material and any other active components (second metal and/or promoter). The promoter and/or the second metal can (a) influence the first metal through electronic interactions and (b) get involved in the reaction by directly bonding to reactants or intermediates. Sometimes, the interactions present between the metals are complex and mostly unidentified/mysterious. Consequently, there are many options to prepare bimetallic catalysts with different properties. One of the major themes of basic and fundamental research having a practical application has been the use of selective bimetallic catalysts for better selectivity as well as minimizing the undesirable side-reactions, i.e. isomerization and hydrogenation of the alkene. Many reported observations discussed the bimetallic catalysts, in which addition of other metal to Pd could selectively hydrogenate butadiene, and explained the high selectivity [6, 38, 58, 68, 79, 80, 82, 90, 98, 99]. Several reports were published, in which for Pd-Ag/Al_2O_3, Pd-Ag/SiO_2, Pd-Au/SiO_2 and Pd-Cu/Al_2O_3, it was found that 99% selectivity was observed without any isomerization of butene
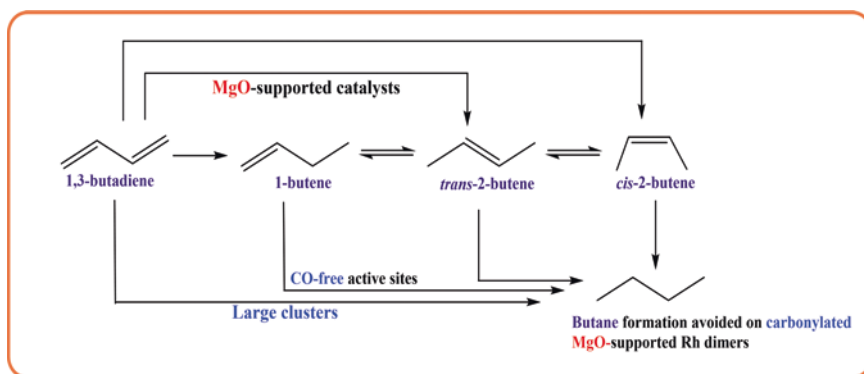
Scheme 3 Reaction pathways for 1,3-butadiene hydrogenation proposed by Yardimci, et al. (*Reprinted with permission from [97]. Copyright 2012 American Chemical Society*)

[58,100–102]. It can be concluded that the bimetallic catalysts showed highest selectivity when compared to monometallic catalyst; however, Pd-Au and Pd-Ag supported on SiO_2 showed less selectivity when compared to Al_2O_3 support.

To summarize, for the selective hydrogenation reaction on metal surfaces, the selectivity towards 1-butene is tremendously dependent on the electronegativity-supported metal catalyst system, and hence, can be regulated either by modulating the properties of supported metal (by another metal/or promoter species?). Moreover, carbonaceous deposits formed on the surface of a catalyst during the reaction/ process under prevailing reaction/operation conditions (ratio of reactants, temperature, etc.) alter the catalyst surface characteristics, e.g. dispersion of metal(s), Promoters further modify the surface and disturb the electronic properties of Pd or metals. Additives affect the adsorption of reactants and formation of surface residues, as well. This knowledge facilitates one to have a better expertise of the overall process to improve the selectivity, by appropriately selected combination of catalysts, additives/promoters and fine tuning the reaction conditions.

3 Summary and Future Outlook

The major findings from the detailed literature review on 1,3-butadiene selective hydrogenation with heterogeneous catalysts are: (a) selectivity in this reaction relies upon the different adsorption strengths of the unsaturated reactants and products. Butadiene tends to be preferentially adsorbed on all active sites blocking the access of *n*-butenes, when it was present in excess. 1-Butene hydrogenation to butane and its isomerization to *cis*-butene was found to occur only, when butadiene concentration becomes low during the course of the reaction; (b) the acidity of the support plays a critical role in mediating electron transfer through the metal-support interface, that ultimately changes the bond strength between unsaturated hydrocarbons and the metal active sites which results in changing the selectivity and reaction rate; (c) changing the dispersion and the metal particle size may affect both activity and selectivity. Their role in tuning the activity and selectivity are attributed to their geometric and electronic effects; (d) hydrogenation of butadiene over metal catalysts, the selectivity for 1-butene formation is governed by the electronegativity of the catalyst. Hence, selectivity may be affected either by changing the supported metal and/or by the additive species; (e) the use of bimetallic catalysts has been proved that it is right approach for improved selectivity as well as minimizing the undesirable side-reactions of full isomerization and hydrogenation of the desired alkene. These observations foster the interest to develop bimetallic nanoparticles with well-defined geometric shapes and dimensions and are still continuing with the desire to regulate their performance for selective hydrogenation of 1,3-butadiene. The role of second metal in bimetallic catalysts, various additives and acidity of the supports in controlling the selectivity needs to be studied to gain further insight into the underlying mechanism.

References

1. Alves JA et al (2012) Kinetic study of the selective catalytic hydrogenation of 1,3-butadiene in a mixture of n-butenes. J Ind Eng Chem 18(4):1353–1365
2. Pérez D et al (2015) Study of the selective hydrogenation of 1,3-butadiene in three types of industrial reactors. Fuel 149:34–45
3. Méndez FJ et al (2017) Selective hydrogenation of 1,3-butadiene in the presence of 1-butene under liquid phase conditions using structured catalysts. Catal Today 289:151–161
4. Liu D et al (2018) Theoretical investigation of selective hydrogenation of 1,3-butadiene on Pt doping Cu nanoparticles. Appl Surf Sci 456:59–68
5. Aguilar-Tapia A et al (2016) Selective hydrogenation of 1,3-butadiene over bimetallic Au-Ni/TiO2 catalysts prepared by deposition-precipitation with urea. J Catal 344:515–523
6. Lozano L et al (2013) Influence of toluene on the catalytic activity of NiPdCe catalyst for selective hydrogenation of 1,3-butadiene. Fuel 110:76–82
7. Ardiaca NO et al (2001) Experimental procedure for kinetic studies on egg-shell catalysts. The case of liquid-phase hydrogenation of 1,3-butadiene and n-butenes on commercial Pd catalysts. Catal Today 64(3–4):205–215
8. Boitiaux JP et al (1987) Hydrogenation of unsaturated hydrocarbons in liquid phase on palladium, platinum and rhodium catalysts. III. Quantitative selectivity ranking of platinum, palladium and rhodium in the hydrogenation of 1-butene, 1,3-butadiene and 1-butyne using a single reaction scheme. Appl Catal 35(2):193–209
9. Boitiaux JP et al (1987) Liquid phase hydrogenation of unsaturated hydrocarbons on palladium, platinum and rhodium catalysts. Part I: kinetic study of 1-butene, 1,3-butadiene and 1-butyne hydrogenation on platinum. Appl Catal 32:145–168
10. Boitiaux JP et al (1987) Liquid phase hydrogenation of unsaturated hydrocarbons on palladium, platinum and rhodium catalysts. Part II: kinetic study of 1-butene, 1,3-butadiene and 1-butyne hydrogenation on rhodium; comparison with platinum and palladium. Appl Catal 32:169–183
11. Gaube J, Klein HF (2014) Kinetics and mechanism of butene isomerization/hydrogenation and of 1,3-butadiene hydrogenation on palladium. Appl Catal A Gen 470:361–368
12. Goetz J et al (1996) Kinetic aspects of selectivity and stereoselectivity for the hydrogenation of buta-1,3-diene over a palladium catalyst. Ind Eng Chem Res 35(3):703–711
13. Goetz J et al (1996) Kinetics of buta-1,3-diene hydrogenation over palladium catalysts. Chem Eng Sci 51(11):2879–2884
14. Goetz J et al (1997) Kinetics of buta-1,3-diene hydrogenation over 0.5% Pd/γ-Al2O3 catalyst. Chem Eng Technol 20(2):138–143
15. Goetz J et al (1996) Low-loaded Pd/α-Al2O3 catalysts: influence of metal particle morphology on hydrogenation of buta-1,3-diene and hydrogenation and isomerization of but-1-ene. J Catal 164(2):369–377
16. Horiuti I, Polanyi M (1934) Exchange reactions of hydrogen on metallic catalysts. Trans Faraday Soc 30:1164–1172
17. Santiso EE et al (2008) Isomerization kinetics of small hydrocarbons in confinement. Adsorption 14(2–3):181–188
18. Bates AJ et al (1970) The hydrogenation of akladienes. Part IV. The reaction of buta-1,3-diene with deuterium catalysed by rhodium, palladium, and platinum. J Chem Soc AInorgan Phys Theor:2435–2441

19. Yang XF et al (2010) Unusual selectivity of gold catalysts for hydrogenation of 1, 3-butadiene toward cis-2-butene: a joint experimental and theoretical investigation. J Phys Chem C 114(7):3131–3139
20. Bond GC et al (1965) 587. The hydrogenation of alkadienes. Part I. the hydrogenation of buta-1,3-diene catalysed by the noble group VIII metals. J Chem Soc:3218–3227
21. Phillipson JJ et al (1969) The hydrogenation of alkadienes. Part III. The hydrogenation of buta-1,3-diene catalysed by iron, cobalt, nickel, and copper. J Chem Soc A Inorg Phys Theor:1351–1363
22. Wells PB, Bates AJ (1968) The hydrogenation of alkadienes, part II. The hydrogenation of buta-1,3-diene catalysed by rhodium, palladium, iridium, and platinum wires. J Chem Soc A Inorg Phys Theor:3064–3069
23. Pradier CM et al (1988) Hydrogenation of 1,3-butadiene on Pt(111). Comparison with results on Pt(110) and Pt(100). Appl Catal 43(1):177–192
24. Boitiaux JP et al (1989) Additive effects in the selective hydrogenation of unsaturated hydrocarbons on platinum and rhodium catalysts. II. Influence of various compounds containing phosphorus, oxygen, sulphur and chlorine on the catalytic performance of platinum catalyst. Appl Catal 49(2):235–246
25. Boitiaux JP et al (1989) Additive effects in the selective hydrogenation of unsaturated hydrocarbons on platinum and rhodium catalysts: I: influence of nitrogen-containing compounds. Appl Catal 49(2):219–234
26. Meyer EF, Burwell RL (1963) The reaction between deuterium and 1-butyne, 1,2-butadiene, and 1,3-butadiene on palladium-on-alumina catalyst. J Am Chem Soc 85(19):2881–2887
27. Nudel JN et al (1984) Selective hydrogenation of 1,3-butadiene over LaCoO3 perovskite. J Catal 89(2):362–370
28. Alves JA et al (2004) Selective hydrogenation of 1,3-butadiene: improvement of selectivity by using additives. Chem Eng J 99(1):45–51
29. Chizallet C et al (2011) Thermodynamic stability of buta-1,3-diene and but-1-ene on Pd(111) and (100) surfaces under H 2 pressure: a DFT study. J Phys Chem C 115(24):12135–12149
30. Wuchter N et al (2006) Comparison of selective gas phase- and liquid phase hydrogenation of (cyclo-)alkadienes towards cycloalkenes on Pd/alumina egg-shell catalysts. Chem Eng Technol 29(12):1487–1495
31. Yoon C et al (1997) Hydrogenation of 1,3-butadiene on platinum surfaces of different structures. Catal Lett 46(1–2):37–41
32. Oudar J et al (1987) 1,3-Butadiene hydrogenation on single crystals of platinum: I. mechanism and carbon deactivation on Pt(110). J Catal 107(2):434–444
33. Oudar J et al (1987) 1,3-Butadiene hydrogenation on single crystals of platinum: II. Sulfur poisoning of Pt(110). J Catal 107(2):445–450
34. Belelli PG et al (2010) Unsaturated hydrocarbons adsorbed on low coordinated Pd surface: a periodic DFT study. Surf Sci 604(3–4):386–395
35. Feixas F et al (2011) Understanding conjugation and hyperconjugation from electronic delocalization measures. J Phys Chem A 115(45):13104–13113
36. Gómez G et al (2010) The adsorption of 1,3-butadiene on Pd/Ni multilayers: the interplay between spin polarization and chemisorption strength. J Solid State Chem 183(12):3086–3092
37. Gómez G et al (2014) Evaluating Pd–Ni layered catalysts for selective hydrogenation of 1,3-butadiene: a theoretical perspective. J Mol Catal A Chem 394:151–161
38. Hou R et al (2014) Selective hydrogenation of 1,3-butadiene on PdNi bimetallic catalyst: from model surfaces to supported catalysts. J Catal 316:1–10
39. Michalak WD et al (2013) Structure sensitivity in Pt nanoparticle catalysts for hydrogenation of 1,3-butadiene: in situ study of reaction intermediates using SFG vibrational spectroscopy. J Phys Chem C 117(4):1809–1817
40. Mittendorfer F et al (2003) Adsorption of unsaturated hydrocarbons on Pd(111) and Pt(111): a DFT study. J Phys Chem B 107(44):12287–12295

41. Valcárcel A et al (2004) Comparative DFT study of the adsorption of 1,3-butadiene, 1-butene and 2-cis/trans-butenes on the Pt(1 1 1) and Pd(1 1 1) surfaces. Surf Sci 549(2):121–133
42. Valcárcel A et al (2005) Selectivity control for the catalytic 1,3-butadiene hydrogenation on Pt(111) and Pd(111) surfaces: radical versus closed-shell intermediates. J Phys Chem B 109(29):14175–14182
43. Baetzold RC (1987) Properties of chemisorbed ethylene and butadiene. Langmuir 3(2):189–197
44. Avery NR, Sheppard N (1986) The use of thermal desorption and electron energy loss spectroscopy for the determination of the structures of unsaturated hydrocarbons chemisorbed on metal single-crystal surfaces. II. Cis- and trans-but-2-ene, but-2-yne and buta-1,3-diene on Pt(111). Proc R Soc Lond A Math Phys Sci 405(1828):27–39
45. Cassuto A, Tourillon G (1994) The adsorption of butene-1, isobutene, cis-2-butene and trans-2-butene on Pt(111) at 95 K: NEXAFS and UPS results. Surf Sci 307–309(Part A):65–69
46. Tsai Y-L, Koel BE (1997) Temperature-programmed desorption investigation of the adsorption and reaction of butene isomers on Pt(111) and ordered Pt−Sn surface alloys. J Phys Chem B 101(15):2895–2906
47. Tourillon G et al (1996) Buta-1,3-diene and but-1-ene chemisorption on Pt(111), Pd(111), Pd(110) and Pd50Cu50(111) as studied by UPS, NEXAFS and HREELS in relation to catalysis. J Chem Soc Faraday Trans 92(23):4835–4841
48. Maurice V, Minot C (1989) A theoretical investigation of the adsorption modes of ethene, 1,3-butadiene, 1-butene, and cis- and trans-2-butenes on the unreconstructed (110) surface of platinum. Langmuir 5(3):734–741
49. Massardier J et al (1988) Platinum single crystals: the effect of surface structure and the influence of K and Na on the activity and the selectivity for 1,3-butadiene hydrogenation. J Catal 112(1):21–33
50. Ouchaib T et al (1989) Competitive hydrogenation of butadiene and butene on palladium and platinum catalysts. J Catal 119(2):517–520
51. Bertolini JC et al (1996) A comparative study of 1,3-butadiene and 1-butene chemisorbed on Pt(111), and Pd(111). Surf Sci 349(1):88–96
52. Chen S, Yang B (2020) Theoretical understandings on the unusual selectivity of 1,3-butadiene hydrogenation to butenes over gold catalysts. Catal Today 347:134–141
53. Bent BE et al (1991) Thermal decomposition of alkyl halides on aluminum. 2. The formation and thermal decomposition of surface metallacycles derived from the dissociative chemisorption of dihaloalkanes. J Am Chem Soc 113(4):1143–1148
54. Chrysostomou D et al (2001) Thermal chemistry of C3 metallacycles on Pt(111) surfaces. J Phys Chem B 105(25):5968–5978
55. Scoggins TB, White JM (1997) Thermal chemistry of allyl bromide adsorbed on Pt(111). J Phys Chem B 101(40):7958–7967
56. Cukic T et al (2007) The influence of preparation variables on the performance of Pd/Al2O3 catalyst in the hydrogenation of 1,3-butadiene: building a basis for reproducible catalyst synthesis. Appl Catal A Gen 323:25–37
57. Hugon A et al (2009) Influence of the reactant concentration in selective hydrogenation of 1,3-butadiene over supported gold catalysts under alkene rich conditions: a consideration of reaction mechanism. Gold Bull 42(4):310–320
58. Kolli NE et al (2013) Bimetallic Au-Pd catalysts for selective hydrogenation of butadiene: influence of the preparation method on catalytic properties. J Catal 297:79–92
59. Liu C et al (2015) Hydrogenation of 1,3-butadiene over Au and Pt/SiO2-N catalysts at low temperature. Catal Commun 67:72–77
60. Primet M et al (1990) Influence of the support towards platinum catalysed 1,3-butadiene hydrogenation. Appl Catal 58(1):241–253
61. Sarkany A et al (1995) Participation of support sites in hydrogenation of 1,3-butadiene over Pt/Al2O3 catalysts. Appl Catal A Gen 127(1–2):77–92

62. Pattamakomsan K et al (2010) Effect of mixed Al2O3 structure between θ- and α-Al2O3 on the properties of Pd/Al2O3 in the selective hydrogenation of 1,3-butadiene. Catal Commun 11(5):311–316

63. Hou R et al (2015) Effect of oxide supports on Pd–Ni bimetallic catalysts for 1,3-butadiene hydrogenation. Appl Catal A Gen 490:17–23

64. Ciebien JF et al (1999) Membrane catalysts for partial hydrogenation of 1,3-butadiene: catalytic properties of palladium nanoclusters synthesized within diblock copolymer films. Mater Sci Eng C 7(1):45–50

65. Silvestre-Albero J et al (2005) Atmospheric pressure studies of selective 1,3-butadiene hydrogenation on Pd single crystals: effect of CO addition. J Catal 235(1):52–59

66. Silvestre-Albero J et al (2006) From Pd nanoparticles to single crystals: 1,3-butadiene hydrogenation on well-defined model catalysts. Chem Commun (1):80–82

67. Silvestre-Albero J et al (2006) Atmospheric pressure studies of selective 1,3-butadiene hydrogenation on well-defined Pd/Al2O3/NiAl(110) model catalysts: effect of Pd particle size. J Catal 240(1):58–65

68. Cooper A et al (2014) Design of surface sites for the selective hydrogenation of 1,3-butadiene on Pd nanoparticles: Cu bimetallic formation and sulfur poisoning. Catal Sci Technol 4(5):1446–1455

69. Sárkány A et al (1995) Hydrogenation of 1,3-butadiene over catalysts prepared from amorphous Pd2Ni50Nb48 ribbon: effect of self-poisoning on competitive adsorption. Appl Catal A Gen 124(2):L181–L187

70. Ponec V (1983) Catalysis by alloys in hydrocarbon reactions. In: Eley HPDD, Paul BW (eds) Advances in catalysis, vol 32. Academic, New York, pp 149–214

71. van Santen RA (1982) Chemical-bonding aspects of heterogeneous catalysis. I. Chemisorption by metals and alloys. Recueil des Travaux Chimiques des Pays-Bas 101(4):121–136

72. Boitiaux JP et al (1983) Preparation and characterisation of highly dispersed palladium catalysts on low surface alumina, their notable effects in hydrogenation. In: Poncelet PGG, Jacobs PA (eds) Studies in surface science and catalysis, vol 16. Elsevier, Amsterdam, pp 123–134

73. Schimpf S et al (2002) Supported gold nanoparticles: in-depth catalyst characterization and application in hydrogenation and oxidation reactions. Catal Today 72(1–2):63–78

74. Umpierre AP et al (2005) Selective hydrogenation of 1,3-butadiene to 1-butene by Pd(0) nanoparticles embedded in imidazolium ionic liquids. Adv Synth Catal 347(10):1404–1412

75. Zhang X, Xu BQ (2005) Size effect of zirconia nanoparticles in Au/ZrO2 catalysts for 1,3-butadiene hydrogenation. Chem J Chin Univ 26(1):106–110

76. Tardy B et al (1991) Catalytic hydrogenation of 1,3-butadiene on Pd particles evaporated on carbonaceous supports: particle size effect. J Catal 129(1):1–11

77. Berhault G et al (2007) Preparation of nanostructured Pd particles using a seeding synthesis approach-application to the selective hydrogenation of buta-1,3-diene. Appl Catal A Gen 327(1):32–43

78. Dal Santo V et al (2012) Selective butadiene hydrogenation by Pd nanoparticles deposed onto nano-sized oxide supports by CVD of Pd-hexafluoroacetylacetonate. Inorg Chim Acta 380(1):216–222

79. Delannoy L et al (2014) Selective hydrogenation of butadiene over TiO2 supported copper, gold and gold-copper catalysts prepared by deposition-precipitation. Phys Chem Chem Phys 16(48):26514–26527

80. Lu F et al (2014) Plant-mediated synthesis of Ag-Pd alloy nanoparticles and their application as catalyst toward selective hydrogenation. ACS Sustain Chem Eng 2(5):1212–1218

81. Luza L et al (2014) The partial hydrogenation of 1,3-dienes catalysed by soluble transition-metal nanoparticles. ChemCatChem 6(3):702–710

82. Massard R et al (2007) Strained Pd overlayers on Ni nanoparticles supported on alumina and catalytic activity for buta-1,3-diene selective hydrogenation. J Catal 245(1):133–143

83. Piccolo L et al (2008) Tuning the shape of nanoparticles to control their catalytic properties: selective hydrogenation of 1,3-butadiene on Pd/Al2O3. Phys Chem Chem Phys 10(36):5504–5506
84. Zhang W, Wang D, Yan R (2011) Supported Nanoparticles and Selective Catalysis: A Surface Science Approach. In Selective Nanocatalysts and Nanoscience (eds A. Zecchina, S. Bordiga and E. Groppo).
85. Zhang ZC et al (2012) Pd cluster nanowires as highly efficient catalysts for selective hydrogenation reactions. Chem Eur J 18(9):2639–2645
86. Piccolo L et al (2005) Pd-Au single-crystal surfaces: segregation properties and catalytic activity in the selective hydrogenation of 1,3-butadiene. Surf Sci 592(1–3):169–181
87. Lucci FR et al (2015) Selective hydrogenation of 1,3-butadiene on platinum–copper alloys at the single-atom limit. Nat Commun 6:8550
88. Zhang X et al (2007) Comparative study of Au/ZrO2 catalysts in CO oxidation and 1,3-butadiene hydrogenation. Catal Today 122(3–4):330–337
89. Okumura M et al (2002) Hydrogenation of 1,3-butadiene and of crotonaldehyde over highly dispersed Au catalysts. Catal Today 74(3–4):265–269
90. Redjala T et al (2006) Bimetallic Au-Pd and Ag-Pd clusters synthesised by γ or electron beam radiolysis and study of the reactivity/structure relationships in the selective hydrogenation of buta-1,3-diene. Oil Gas Sci Technol 61(6):789–797
91. Stobiński L et al (1999) Molecular hydrogen interactions with discontinuous and continuous thin gold films. Appl Surf Sci 141(3–4):319–325
92. Yi H et al (2017) Coating Pd/Al2O3 catalysts with FeOx enhances both activity and selectivity in 1,3-butadiene hydrogenation. Chin J Catal 38(9):1581–1587
93. Song MW et al (2001) The enhancement of 1-butene selectivity in the hydrogenation of 1,3-butadiene over K-Ni catalysts. J Chem Eng Japan 34(11):1407–1414
94. Sarkany A (1997) Semi-hydrogenation of 1,3-butadiene on adspecies modified Pd-Ni, Co and Cu catalysts. Appl Catal A Gen 149(1):207–223
95. Sarkany A (1997) Semi-hydrogenation of 1,3-butadiene over Pd-Ag/α-Al2O3 poisoned by hydrocarbonaceous deposits. Appl Catal A Gen 165(1–2):87–101
96. Wu Z et al (2000) IR study on selective hydrogenation of 1,3-butadiene on transition metal nitrides: 1,3-butadiene and 1-butene adsorption on Mo2N/γ-Al2O3 catalyst. J Phys Chem B 104(51):12275–12281
97. Yardimci D et al (2012) Tuning catalytic selectivity: zeolite- and magnesium oxide-supported molecular rhodium catalysts for hydrogenation of 1,3-butadiene. ACS Catal 2(10):2100–2113
98. Pattamakomsan K et al (2011) Selective hydrogenation of 1,3-butadiene over Pd and Pd-Sn catalysts supported on different phases of alumina. Catal Today 164(1):28–33
99. Wang T et al (2013) Selection of oxide supports to anchor desirable bimetallic structures for ethanol reforming and 1,3-butadiene hydrogenation. Chin J Catal 34(11):2009–2017
100. Furlong BK et al (1994) 1,3-butadiene selective hydrogenation over Pd/alumina and CuPd/alumina catalysts. Appl Catal A Gen 117(1):41–51
101. Miura H et al (1993) Preparation of egg-shell type Pd-Ag and Pd-Au catalysts by selective deposition and hydrogenation of 1,3-butadiene. Stud Surf Sci Catal 75:2379–2382
102. Liu C et al (1998) Mono- and bimetallic catalytic hollow-fiber reactors for the selective hydrogenation of butadiene in 1-butene. Appl Catal A Gen 172(1):23–29

Thermocatalytic Conversion of Natural Gas to Petrochemical Feedstocks Via Non-oxidative Methods: Theoretical and Experimental Approaches

Sourabh Mishra, Tuhin Suvra Khan, M. Ali Haider, and K. K. Pant

Abstract Requirement of efficient technologies to convert natural gas (methane) into value-added products such as ethylene, aromatics (BTX), methanol and DME is prompted due to recent discovery of large reserves of shale and natural gas. To date, different direct and indirect processes have been explored involving all oxidative/non-oxidative routes. Direct conversion of methane into liquid aromatic hydrocarbons under oxygen-free environment (non-oxidative routes) is one of the promising approaches for natural gas upgradation. Direct methane to aromatic conversion which is also known as methane dehydroaromatization (MDA) reaction is performed at a temperature above 600 °C and atmospheric pressure producing benzene as major product and hydrogen as by-product. Lower thermodynamic equilibrium conversion and fast catalyst deactivation are the major challenges with the reaction which restricts its commercialization. Mo/HZSM-5 and Mo/HMCM-22 are the well-known catalysts used for this reaction showing >90% benzene selectivity with 11% methane conversion at 700 °C. Fast catalyst coking due to carbonaceous deposits results in a lower yield of aromatic products. This can be controlled via different experimental treatments such as tuning in catalytic constituents, cofeeding with H_2 and oxygenates (CO_2, CO, steam) and reactor design including

S. Mishra
Catalytic Reaction Engineering Lab, Department of Chemical Engineering, Indian Institute of Technology Delhi, New Delhi, India

Renewable Energy and Chemicals Lab, Department of Chemical Engineering, Indian Institute of Technology Delhi, New Delhi, India

T. S. Khan
Light Stock Processing Division, CSIR-Indian Institute of Petroleum, Dehradun, India

M. A. Haider
Renewable Energy and Chemicals Lab, Department of Chemical Engineering, Indian Institute of Technology Delhi, New Delhi, India

K. K. Pant (✉)
Department of Chemical Engineering, Indian Institute of Technology Delhi, New Delhi, Delhi, India
e-mail: kkpant@chemical.iitd.ac.in

catalyst regeneration protocol. Mechanistic studies of MDA reaction also provide insights to control coke content by identifying active sites. With this purpose, here we intend to deliver insights on MDA reaction catalysed by zeolite-supported molybdenum catalyst and investigations on catalyst stability controlling coke deposition by providing an overview of combined theoretical and experimental studies. In this book chapter, different ways to control the catalytic activity and stability have been discussed based on catalytic parameters and reactor configurations.

Keywords Natural gas · Methane dehydroaromatization · Molybdenum carbide · Mo/zeolite · Carburization

1   Introduction

Large reserves of natural gas, shale gas and methane hydrates worldwide are attracting attention of industrial and academic community as a potential source of clean energy and feedstock for value-added chemicals. However, most of these reserves of methane are located in remote areas which impart gas transportation challenges over long distances to populated areas and hence economically not feasible. This emphasizes the development of technologies for onsite methane (major source of natural/shale gas) conversion into transportable liquid and other high-value chemicals such as olefins, paraffins, aromatics and hydrogen. Methane, which is the major content of natural gas, is a thermodynamically stable molecule emerging challenges to the chemical community for its activation and direct conversion into useful chemicals. Schematic pathways, currently known, for methane utilization producing value-added chemicals are depicted in Fig. 1. From decades, routes for methane upgradation are explored which involves indirect pathway where methane is first reformed into a mixture of CO and H_2 (synthesis gas), using steam or partial oxidative reforming [1, 2]. From syn-gas (CO + H_2), methanol, dimethyl ether (DME) and other high-value chemicals such as paraffins, olefins, gasoline and diesel can be produced using Fischer Tropsch (FT) process [3, 4]. Methane utilization via syn-gas route has been successfully commercialized and different plants are currently in operation [5]. However, reactions involving syn-gas route require severe high temperature and high pressure conditions and hence the production of syn-gas and its compression typically accounts high capital costing and is energy-intensive for operating the plants [5]. Investigating other direct alternative routes to reduce economy and energy consumption relative to indirect syn-gas processing, it is expected that direct methane conversion route producing value-added chemicals also require high temperatures due to high chemical inertness of methane molecule. Direct methane conversion into chemicals without going through the intermediate step of syn-gas production involves oxidative or non-oxidative treatment. In direct routes of
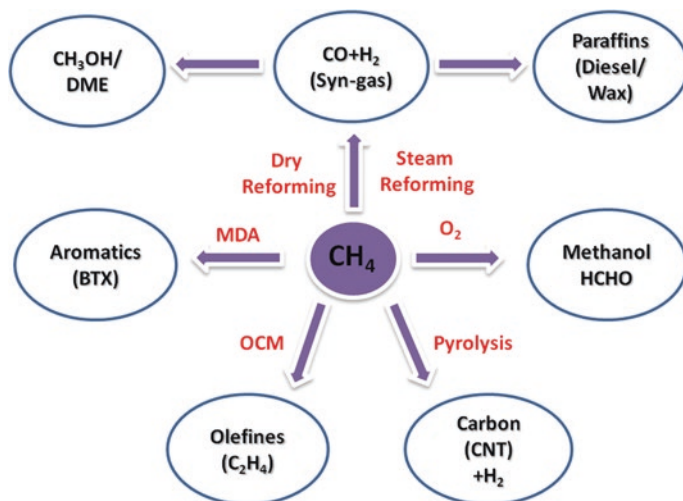
Fig. 1 Different routes of methane conversion producing value-added chemicals

methane conversion, processes such as partial oxidation of methane into methanol/ formaldehyde, oxidative coupling of methane-producing ethylene and MDA-producing aromatic compounds have been explored. Thermodynamically, direct conversion of methane into other commodity chemicals is favourable in presence of oxidants and hence methane oxidation has been widely studied in direct methane utilization. In this reference, methane oxidation to methanol, formaldehyde and other oxygenates constitutes an important thrust in the research area of petrochemical industries [6]. However, lower methane conversion with poor methanol yield is the major limitation which does not make this process successful in comparison to syn-gas route.

Another prominent route using methane oxidation was claimed by Lunsford in 1985 reporting that methane could be converted into ethane/ethylene via oxidative coupling using magnesium oxide catalyst at 600 °C [7]. To date, oxidative coupling of methane (OCM) has been broadly studied and a maximum methane conversion up to 25% with 80% of C_2 selectivity has been reported [8]. A major drawback with OCM observed is further oxidation of C_2 hydrocarbons in the presence of oxygen-producing carbon dioxide, carbon monooxide and water which results in lower ethylene selectivity at high conversion. These limitations restrict for OCM commercialization. In the pursuit to conduct direct methane upgradation, another route involves methane transformation into liquid aromatic hydrocarbons under non-oxidative conditions. Wang et al. in 1993 firstly investigated methane to aromatic reaction on ZSM-5-supported molybdenum catalyst producing mainly benzene with hydrogen as by-product under oxygen-free environment [9]. As the process (later known as MDA) marks higher selectivity towards aromatic compounds (mainly benzene) using direct methane activation, several investigations have been carried out on MDA reaction up to date [10]. Common challenges and

observations resulted from previous studies in MDA reaction are fast catalyst deactivation, lower per pas methane conversion, dependency on catalytic constituents and reactor configuration [10]. A variety of catalysts based on different 3*d*, 4*d* transition metal anchored inside microchannels of zeolite have been studied [5]. In the investigation, it has been observed that HZSM-5/HMCM-22-supported molybdenum is the most selective catalyst for MDA reaction resulting in higher methane conversion and benzene yield at 700 °C [11]. Fast catalyst deactivation in MDA reaction is supposed to be due to severe coke deposits in the form of poly-aromatic-hydrocarbons (PAH) and/or graphitic carbon during the course of reaction [12]. This is the major limitation which restricts its commercialization. Nevertheless, research community working in the area of MDA process has incorporated remarkable modifications in the process upgrading catalytic constituents, reactant feeding (oxygenates with methane) and reactor configurations, which significantly controls methane conversion, benzene yield and catalyst stability. This chapter discusses the current scenario in the development of the MDA process by providing molecular insights of catalytic constituents (Mo/Zeolite) which controls the key steps such as methane activation, aromatization and coking of MDA reaction. Simultaneously, reaction parameters and reactor configurations which direct the kinetics of the reaction are also covered in this chapter.

1.1 Thermodynamics of MDA

Methane hydrocarbon is a stable molecule and exhibits high C–H bond dissociation energy (439 kJ/mol) [13]. In MDA reaction, methane conversion into benzene is thermodynamically unfavourable at lower temperatures. In addition, pyrolysis of methane at highly endothermic conditions (MDA reaction condition) results in coke formation which is a major side reaction, simultaneously occurring at MDA reaction conditions [14]. Despite this, a considerable amount of benzene is formed between the temperature range 700–900 °C at atmospheric pressure. As per Z. R. Ismagilov and J. J. Spivey reports in 2008 and 2014 respectively [14, 15], thermodynamics of MDA process along with side reaction is mentioned by Eqs. (1)–(3) as shown below;

$$6CH_4(g) \rightarrow C_6H_6(g) + 9H_2(g) \tag{1}$$
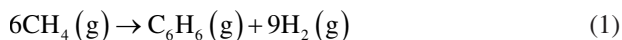
$$\Delta_r G^\circ = +433 \text{kJ/mol}, \quad \Delta_r H^\circ = +531 \text{kJ/mol}$$

$$2CH_4(g) \rightarrow C_2H_6(g) + H_2(g) \tag{2}$$
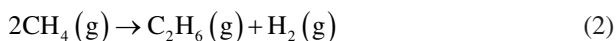
$$\Delta_r G^\circ = +72 \text{kJ/mol}, \quad \Delta_r H^\circ = +73 \text{kJ/mol}$$

$$2CH_4(g) \rightarrow C_2H_4(g) + 2H_2(g) \tag{3}$$
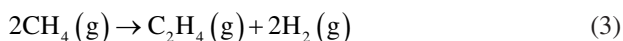
$$\Delta_r G^\circ = +81 \text{kJ/mol}, \quad \Delta_r H^\circ = +216 \text{kJ/mol}$$

Table 1 Equilibrium composition of basic MDA products (benzene, ethane and ethylene) [14]

T/K	CH$_4$ conversion (%)	Equilibrium composition (wt%)				
		CH$_4$	H$_2$	C$_2$H$_6$	C$_2$H$_4$	C$_6$H$_6$
$6CH_4 = C_6H_6 + 9H_2$						
800	2.5	97.5	0.5			2.0
1000	13.8	86.2	2.6			11.2
1200	40	60.0	7.4			32.6
$2CH_4 = C_2H_6 + H_2$						
800	1.0	99.0	0.1	0.9		
1000	3.0	97.0	0.2	2.8		
1200	5.0	95.0	0.3	4.7		
$2CH_4 = C_2H_4 + 2H_2$						
800	1.0	99.0	0.1		0.9	
1000	5.0	95.0	0.6		4.3	
1200	20.0	80.0	2.5		17.5	

In addition, equilibrium concentrations of the common products in MDA process have also been analysed in the temperature range of 800–1200 K based on thermodynamic studies and are shown in Table 1 as per previous reports [14]. MDA reaction is thermodynamically favourable than other side reactions such as methane to ethane and ethylene at 1000 K and results in 13.8% equilibrium conversion of methane into benzene (Table 1).

1.1.1 Effect of Co-feeding Agents

Addition of oxygenates, hydrogen and/or other light hydrocarbons as co-feed with methane drives the thermodynamic equilibrium and upgrades the methane conversion in MDA reaction. Several experimental studies have been performed using different co-feeding agents with methane in view of advancing the MDA process. Catalyst deactivation due to severe coke formation is the major challenge with MDA reaction. To control the coke formation, oxygenates such as CO, CO_2 and CH_3OH have been used as co-feeding agent with methane [16]. Hydrogen has been also reported as co-feeding agent with methane controlling coke formation. As per P. M. Bijani report in 2012, increase in H_2/CH_4 ratio enhances the selectivity of light hydrocarbons but reduces coke selectivity [17]. Benzene selectivity has been observed maximum at 0.26 ratio of H_2/CH_4. Thermodynamics favours MDA reaction in presence of oxygen ($\Delta_r G° = -1624$ kJ/mol, Eq. (4)) and other hydrocarbons ($\Delta_r G^{973K} = -36.2$ kJ/mol, Eq. (5)) as per J. J. Spivey reports in 2014 [15]. Although the presence of oxygen (or other oxidants) favours the MDA thermodynamics, aromatic selectivity decreases due to further oxidation or decomposition of BTX products into carbonaceous deposits. Thermodynamic calculations on alkanes/alkenes as co-feeding agent with methane supports the experimental evidences as reported earlier; however, it limits in quantification with respect to methane conversion [15].

$$6CH_4\left(g\right)+9/2O_2\left(g\right) \rightarrow C_6H_6\left(g\right)+9H_2O\left(g\right) \qquad (4)$$
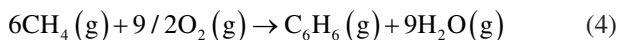
$$\Delta_rG^\circ = -1624\,kJ/mol, \qquad \Delta_rH^\circ = -1846\,kJ/mol$$

$$2CH_4\left(g\right)+n-C_4H_{10}\left(g\right) \rightarrow C_6H_6\left(g\right)+6H_2\left(g\right) \qquad (5)$$
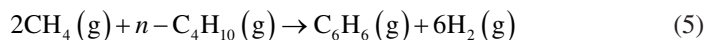
$$\Delta_rG^{973K} = -36.2\,kJ/mol, \qquad \Delta_rH^{973K} = +396\,kJ/mol$$

1.1.2 Effect of Hydrogen Removal in MDA

In attempts of equilibrium shift of methane to benzene conversion in MDA reaction, in situ removal of hydrogen (H_2) from the reaction mixture is an effective step to adjust thermodynamic conversion of methane. Hydrogen is the major by-product along with carbonaceous species at 973 K and atmosphere pressure in MDA reaction. Increase in temperature does not affect the equilibrium constant of MDA reaction which shows that MDA reaction is strongly limited by thermodynamics. Selective removal of H_2 from the MDA reaction mixture shifts the chemical equilibrium towards the desired products as per previous reports [18, 19]. According to thermodynamic calculations, methane conversion in the MDA reaction towards C_6H_6 and H_2 increases with the removal of H_2 as marked by filled circles in Fig. 2 [5]. Thus, thermodynamic study directs that H_2 removal from reaction mixture significantly upgrades the equilibrium methane conversion which can be experimentally achieved with modified reactor configuration, e.g. membrane-type reactors can absorb or remove the in situ generated H_2 and enhance the desired product selectivity.
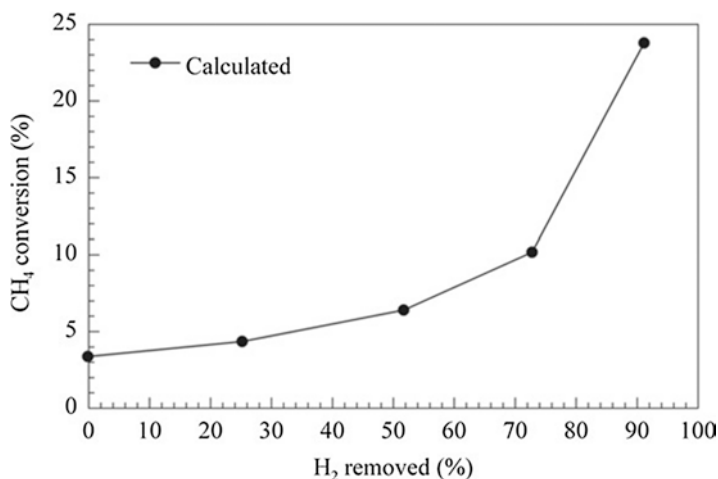
Fig. 2 Equilibrium methane conversion with respect to H_2 removal (%) during MDA reaction at 883 K and 0.5 MPa. (Reproduced with permission from Journal of Energy Chemistry 22 (2013) 1–20 [5])

In summary, thermodynamic analysis corroborates that methane conversion into benzene and hydrogen in MDA process is thermodynamically favourable only at limited conditions, and is expected to be kinetically driven to undesired solid carbonaceous species. Addition of other oxygenates (O_2, CO, CO_2 and CH_3OH) and light hydrocarbons with methane also controls thermodynamics and experimentally have been shown to drive the MDA reaction with certain limitations.

1.2 Catalysts for MDA Reaction

Basically, molybdenum-supported ZSM-5 is the well-known catalyst for methane dehydroaromatization reaction as firstly reported by Wang et al. in 1993 [9]. Being an important reaction, MDA was widely investigated for long time and different metals besides molybdenum (Mo) were tested with ZSM-5. Cr, W, Mn, Fe, Ni, Zn, Cu, Re, V and various other transition metals were analysed for MDA reaction and it was concluded that Mo supported over zeolite is the most active metal for methane aromatization reaction [5]. However transition metals such as Re, W and Cu supported over ZSM-5 have been reported with 7, 5.7 and 2.4 methane conversion having higher benzene selectivity (48% for Re, 94% for W and 70% for Cu) respectively [10]. Zeolite support also controls the activity of Mo/Zeolite catalyst as it imparts bi-functionality for methane to aromatic reaction. Microporous and mesoporous zeolites with unique framework structure, shape selectivity and strong acidity tune the metal interaction and dispersion and thus affect the activity. Different types of zeolites along with molybdenum have been investigated showing activity towards MDA reaction [20]. ZSM-5 contains two-dimensional pore structures with 10-membered rings and effective pore diameter (0.6 nm) equivalent to the kinetic diameter of benzene molecule which provides shape selectivity to aromatized products. Due to these characteristics and high thermal stability of ZSM-5, it has been frequently used for MDA reaction along with molybdenum to date [21]. In addition to ZSM-5, other zeolite supports such as HMCM-22, ZSM-11, H-β, H-Y, ZSM-8, HMCM-41, HMCM-36 and ITQ type zeolites have also been tested for MDA reaction as per previous reports [5, 22]. Different outcomes and suggestions were made with these supports in reference to MDA activity and it was concluded that HMCM-22 and HMCM-49 besides ZSM-5 are also effective supports for the synthesis of molybdenum-based catalyst for MDA activity. Basically, Mo/HZSM-5 and Mo/HMCM-22 are known as well-established catalysts showing similar MDA activity. However, reports for higher stability of Mo/HMCM-22 with high benzene selectivity in comparison to Mo/HZSM-5 are also claimed [23]. HMCM-22 has unique framework structure as compared to HZSM-5 zeolite support, due to which a better tolerance of coke deposits occurs in this zeolite and results in higher benzene selectivity. HMCM-22 possesses a unique pore structural design with two independent pore systems: two-dimensional 10-ring sinusoidal pore system (4.1 × 5.1 Å), and a larger, three-dimensional 12-ring super-cage system interconnected via 10-ring windows (4.0 × 5.5 Å). This type of pore structure and presence

of supercages are supposed to be responsible for high coke accumulation ability of HMCM-22 zeolite, while retaining shape selectivity is the necessity for aromatic formation. This combination promotes the selectivity of aromatic compounds and stabilizes the Mo/HMCM-22 catalyst under MDA reaction conditions [24]. Due to unique framework characteristics, zeolite support known as TNU-9 has been also used for Mo-based catalyst in MDA reaction and results in higher activity than conventional ZSM-5 support [25]. In view of catalytic constituents of Mo/Zeolite catalyst, both molybdenum and zeolite supports have their own characteristics in the MDA activity. In MDA reaction, methane C–H bond activation and C–C coupling occur at metallic (Mo) sites which provides ethylene intermediate. Ethylene is further aromatized at acidic sites of zeolite support of the catalyst. Acidity of the catalyst is tuned by varying Si/Al ratio zeolite support. Thus molybdenum concentration and zeolite acidity of the catalyst must be in trade off for effective MDA activity.

1.2.1 Effect of Mo Dispersion

Molybdenum loading over zeolite (HZSM-5/HMCM-22) support significantly affects the Mo dispersion which controls the MDA activity as studied in detail in the previous reports [26, 27]. In the earlier work, 2–6 wt% molybdenum loading has been optimized for MDA activity and it is found that higher Mo loading (>6 wt%) is not effective and results in lower benzene yield [28]. Lower Mo loading maintains the integrity of zeolite framework such as crystallinity and porosity and also prevents extraction of framework Al species which results in $Al_2(MoO_4)_3$ species [29]. Higher Mo loading shows large clusters of in situ generated molybdenum carbide (the active site for C–H activation and C–C coupling) which retards the catalytic activity as nano-cluster of molybdenum carbide have been reported as highly active centres [10]. In addition, Mo species interacts with the zeolite framework via its acidic sites, thus exchange of acidic protons with molybdenum occurs which reduces the acidity of zeolite support and hence reduces the total acidity of MDA catalyst. Reduction in acidity also affects the yield and conversion. Thus a trade off between molybdenum concentration and zeolite acidity must be maintained to achieve higher activity.

1.2.2 Effect of Zeolite Acidity

As per zeolite chemistry, negative charge at aluminium atoms in the framework is compensated by cations which are further exchanged with other required cations. The proton cation is incorporated via well-known ion exchange with NH_4^+ ions followed by calcinations at higher temperatures (450–550 °C) and provides Brønsted acid sites (BAS) [30]. This directs that Brønsted acid sites directly depend on Al concentration of zeolite framework and hence variation in Al content would change the Brønsted acidity over the framework. As per the mechanism of MDA reaction, firstly initial MoO_x species grafted over zeolite framework is converted into active

Mo_xC_y (Mo_2C) at which methane dehydrogenation and coupling to ethylene occurs. In the second step, ethylene intermediate oligomerizes to benzene at the Brønsted acid sites (BAS) of the zeolites and hence the concentration of BAS plays a crucial role in MDA catalyst. In the previous reports, several studies on acidity effect by varying SiO_2/Al_2O_3 (SAR) ratio of zeolite framework has been performed for MDA catalyst activity [31]. Lower SAR results in higher BAS concentration over the framework and has been reported most effective for MDA activity as compared to higher SAR value [32]. Different techniques such as NH_3-TPD and pyridine FT-IR are the basic tools to analyse the acidity concentration and strength. In MDA reaction, HZSM-5 and HMCM-22 with $SiO_2/Al_2O_3 = 30$ (Si/Al = 15) have been widely studied showing high activity along with molybdenum [32, 33]. Besides acidity incorporation to the Mo/Zeolite catalyst, BAS controls MoO_x diffusion and its anchoring inside the zeolite channels which affect the catalytic activity. According to Gao et al. reports in 2015, anchoring sites for MoO_x species inside HZSM-5 zeolite channels strongly depends on Si/Al ratio of HZSM-5 [34]. On varying the Si/Al ratio (from 15 to 140), MoO_x anchoring site inside the zeolite framework is observed to change from double Al atom site to single Al atom sites and at higher Si/Al ratio (~140), it shifts to double Si atom sites at the outer surface of the zeolite framework as depicted in Fig. 3. This directs that at higher Si/Al ratio, most of the molybdenum oxide species interacts with Si atoms at the outer surface of zeolite framework due to lower Brønsted acid sites and results in lower activity of Mo/HZSM-5 catalyst. In a recent study of S. Mishra et al., (2020), it has been claimed that maximum transformation of initial molybdenum oxide species into active molybdenum carbide/oxycarbide occurs at lower Si/Al ratio (HMCM-22) during induction period/carburization which results in higher activity of Mo/HMCM-22 catalyst with low carbonaceous deposits [35]. Thus Si/Al ratio also controls the molybdenum carbide content which is related to initial MoO_x anchoring inside the zeolite channels. The Si/Al ratio of zeolite sample can be tuned via initial synthetic routes or post-treatments such as dealumination/desilication in the thought of improving MDA catalyst activity [36].

Low Si/Al ⟶ High Si/Al
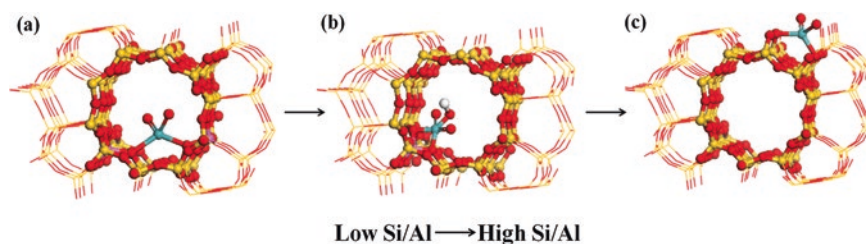
Fig. 3 Anchoring of initial MoO_x species over zeolite framework with respect to different Si/Al: (**a**) double Al atom site at lower Si/Al, (**b**) single Al atom site at moderate Si/Al, and (**c**) single Si atom site at high Si/Al

1.2.3 Promoter Effect over MDA Catalyst

Besides controlling Mo concentration and Brønsted acidity of MDA catalyst (Mo/Zeolite), attempts of promoter metal addition to Mo/Zeolite catalyst have also been performed in view of improving activity. In these attempts, different metals such as Ga, Zn, Cr, Cu, Ni, W, Pd, Pt, etc. have been studied as promoters for MDA catalyst and results in the positive effect on activity and stability [5, 37, 38]. Nevertheless, different observations have been seen in previous studies showing inconsistencies in results of metal-promoted Mo/Zeolite catalysts. As negative effect of promoter metals over Mo/Zeolite catalyst have also been claimed in previous reports [39]. This may be due to the different treatments used for catalyst preparation and different reaction conditions. In addition, due to complex insights of MDA catalyst activity, mechanistic understanding of various promoters' effect over Mo/Zeolite catalyst has not been clearly stated. Promoter metals such as Ru improves the stability of Mo/HZSM-5 catalyst [40], Ni and Co have also been reported for improving the stability of Mo/HZSM-5 catalyst via preventing aggregation of Mo species as per recent studies of Sridhar et al. (2020) [41]. Ahmed K. Aboul-Gheit et al. in 2011 have reported Zn as promoter over Mo/HZSM-5 for its lower carbon deposition which is advantageous in MDA reaction [42]. Victor Abdelsayed and co-workers in 2015 have claimed increased benzene formation rate for Fe-Mo/ZSM-5 catalysts as compared to unpromoted Mo/ZSM-5 catalyst [43]. Cr incorporation over Mo/ZSM-5 catalyst tunes the acidity which promotes the catalytic activity as per previous reports [38]; however, it remains contradictory whether Cr and Mo species simultaneously interact with acid sites or separately. Thus additive metals along with molybdenum significantly control the catalytic activity and stability; however, their interaction and incorporation over Mo/Zeolite catalyst is still debatable and thus needs more scientific investigations to study the bimetallic MDA catalyst.

1.2.4 Induction Effect: Carburization

In MDA reaction, Mo/Zeolite catalyst is firstly reduced or carburized to achieve its active phase for reaction progress. After calcination, oxide form of catalyst MoO_3/Zeolite is generally converted into its carbide or oxycarbide form (Mo_2C/Zeolite) which is the active site for methane activation and C–C coupling reactions in MDA process [35]. During the transformation of MoO_3/Zeolite to Mo_2C/Zeolite phase, formation of oxygenates such as CO, CO_2 and H_2O occurs in the initial period which is known as induction or carburization period before aromatization reaction. Molybdenum carbide species (Mo_2C) generated in the induction period has been confirmed using different techniques (XPS, XNASE) [44]. A mixture of H_2 and CH_4 (3:1 or 4:1) or pure methane is used for carburization/reduction of MoO_3/Zeolite which results in carbide or oxycarbide form of molybdenum [45]. As per reports of Lee et al. in 2000, during the transformation of MoO_3 into Mo_2C, mainly two steps occur in which the first is the reduction of initial MoO_3 to MoO_2 whereas the second step is the carburization of MoO_2 resulting into molybdenum carbide (Mo_2C) [33].

In 1997, Wang et al. have claimed that during the induction period complete transformation of MoO_x into Mo_2C does not occur and some oxide or oxycarbide forms of molybdenum remain over the catalyst which shows that nature of molybdenum species during the induction may be different [46]. In addition, different forms of molybdenum carbide such as β-Mo_2C and α-MoC_{1-x} have been also claimed in the induction period in which α-MoC_{1-x} form is reported effective for higher activity and stability for MDA catalyst [47, 48]. Duration of induction period also affect the carburization depending on the carburizing agent (CO, light hydrocarbons) but is observed independent of temperature [49]. Catalytic constituent such as Mo loading and Si/Al ratio of Mo/Zeolite catalyst significantly affect the carburization process. Higher molybdenum loading results in higher reducibility due to formation of agglomerated MoO_x species over zeolite surface. Variation in Si/Al ratio of zeolite not only tunes the acidity of Mo/Zeolite catalyst but also control the anchoring of initial MoO_x species over zeolite framework as discussed in Sect. 1.2.2. Change in anchoring mode of MoO_x species via Si/Al ratio variation controls the MoO_x and zeolite interaction and thus affects the reducibility of MoO_x species as also confirmed by recent studies of Zhao et al. [50].

1.3 Mechanistic Insights of MDA Reaction

Methane dehydroaromatization reaction occurs over bifunctional Mo/Zeolite catalyst at which methane C–H activation and C–C coupling takes place on molybdenum site whereas aromatization of intermediates occurs at Brønsted acid sites of the zeolite. Thus basically methane activation, ethylene formation via C–C coupling and aromatization by acidic sites control the methane conversion and benzene yield. Aromatization of intermediates is significantly controlled by zeolite shape selectivity and its acidity as discussed in Sect. 1.2.

In MDA reaction, methane C–H activation and C–C coupling are key steps and occurs over active phase of molybdenum species. Initial MoO_x species are reduced or carburized to form molybdenum oxycarbide or carbide in the induction period as discussed in Sect. 1.2.4. Lunsford et al. in 1996 have firstly reported the induction period required in MDA reaction for Mo/HZSM-5 catalyst and claimed transformation of MoO_x species into molybdenum carbide in the induction period using characterization tools such as XPS and XRD [51]. In the induction period, no hydrocarbon with negligible coke deposits is formed except CO and water vapours (H_2O) as major products. The active phase of molybdenum is rigorously debated in previous reports and is considered to be a carbidic or oxycarbidic [52]. As per experimental investigations of Weckhuysen et al. in 2016, methane activation starts over the oxycarbide phase of molybdenum [53]. Nevertheless, benzene formation starts only when MoO_x is completely carburized/reduced into molybdenum carbide (Mo_xC_y) species. Identification of molybdenum carbide structure has been a debatable discussion in reported theoretical and experimental studies. Experimentally, Mo_2C clusters have been characterized as molybdenum carbide structure by XANES/

EXAFS as per previous studies [53]. Gao et al. in 2015 have claimed Mo_4C_2 as the most stable Mo carbide nanocluster formed at MDA reaction conditions and reports theoretical calculations showing methane C–H activation barrier of 112 kJ/mol at Mo_4C_2 cluster grafter over ZSM-5 channels [34]. Other forms of molybdenum carbide phase have also been reported using genetic algorithms (GA) such as MoC_3 (Mo_2C_6) [54]. Pant and co-workers in 2018 have reported detailed theoretical calculations on Mo_4C_2 and Mo_2C_6 clusters showing results for C–H activation and C–C coupling reactions providing ethylene intermediate as depicted form Figs. 4, 5, 6, and 7 [55]. In Fig. 4a, Mo_4C_2cluster has been shown in which two types of Mo sites [$Mo^{(1)}$ and $Mo^{(2)}$] coordinated with carbons are available for methane activation. In the study, C–H activation barrier has been reported to be lower at $Mo^{(1)}$ type sites (116 kJ/mol) as compared to that at $Mo^{(2)}$ type sites (151 kJ/mol) which directs that the first C–H activation of methane molecule is likely to occur on the $Mo^{(1)}$ type sites of Mo_4C_2 clusters. Geometries of reactant (a′), transition state (CH_3–H^{TS}), and product (b′) have been shown in Fig. 4b with bond length measurements in Å.

After performing calculations for second methane molecule activation at different Mo sites, $Mo^{(1)}$ sites at which first methane activation was occurred are considered suitable site for second methane molecule activation and subsequent C–C coupling as depicted in reaction diagram shown in Fig. 5a, b. The second methane molecule has been activated at the same $Mo^{(1)}$ atom with an activation barrier of 117 kJ/mol almost similar to first C–H activation barrier. After that different key elementary steps have been performed over Mo_4C_2 cluster to achieve the ethylene intermediate as per reports. Complete potential energy diagram for C–H activation
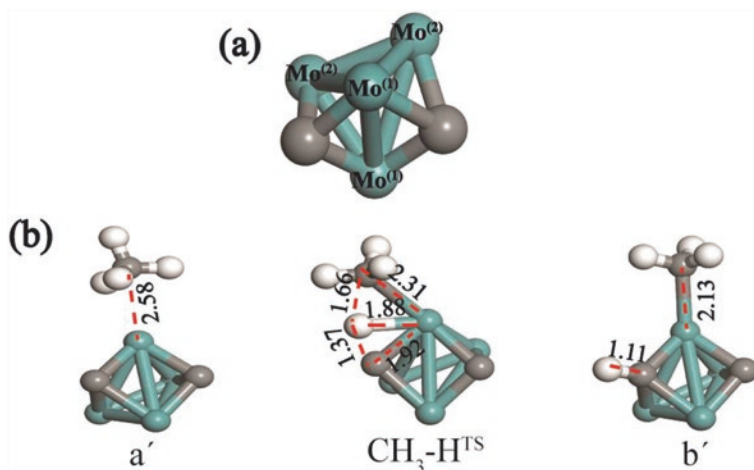
Fig. 4 Geometry of (**a**) Mo_4C_2nanocluster and (**b**) reactant, transition and product states showing first C–H activation of methane over the $Mo^{(1)}$ site (bond lengths in Å). (Reproduced with permission from *J. Phys. Chem. C* 2018, 122, 11754–11764 [55]. *Copyright (2018) American Chemical Society*)
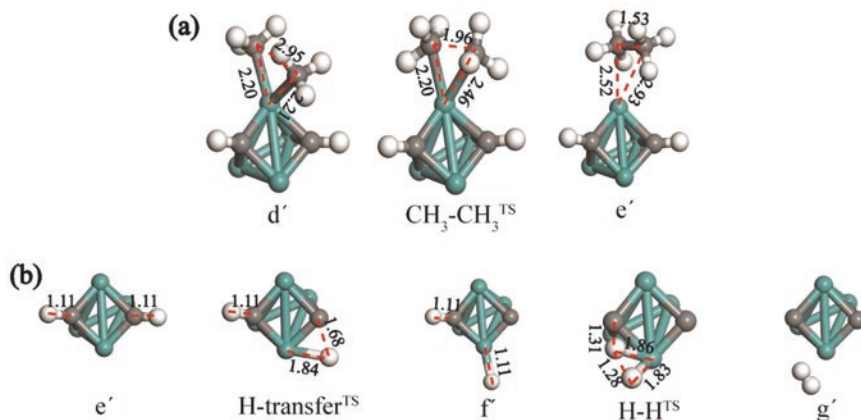
Fig. 5 Geometry of the reactant, TS and product states for (**a**) CH_3–CH_3 coupling reaction and (**b**) H_2 formation and desorption reaction steps over Mo_4C_2 nanocluster (bond lengths in Å). (Reproduced with permission from *J. Phys. Chem. C* 2018, 122, 11754–11764 [55]. *Copyright (2018) American Chemical Society*)
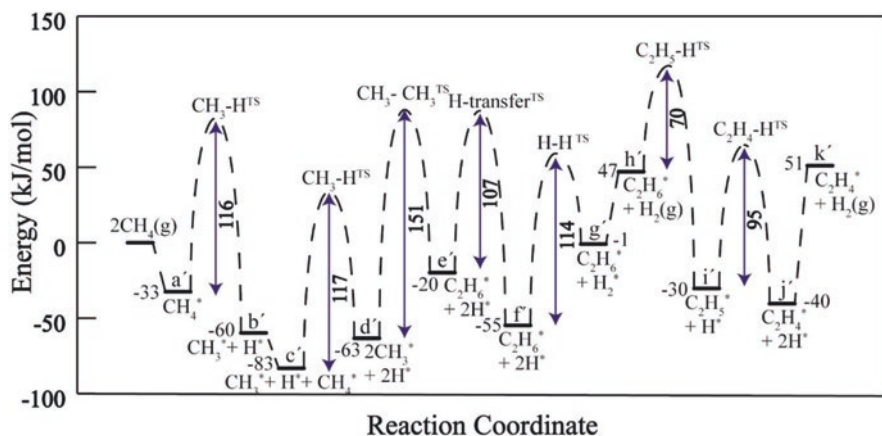
Fig. 6 Potential energy diagram for C–H activation and C–C coupling reaction steps to form ethylene over Mo_4C_2 nanocluster. (Reproduced with permission from *J. Phys. Chem. C* 2018, 122, 11754–11764 [55]. *Copyright (2018) American Chemical Society*)

and C–C coupling steps forming ethylene over Mo_4C_2 cluster has been shown in Fig. 6.

In addition, apart from Mo_4C_2 cluster, another Mo_2C_6 cluster (Fig. 7a) has also been studied for all the C–H activation and C–C coupling reaction steps. A 119 kJ/mol of first methane activation barrier (slightly higher than that on Mo_4C_2) has been calculated over the $Mo^{(1)}$ site of Mo_2C_6 cluster. Reactant (a″), TS (CH_3–H^{TS}) and product (b″) geometries showing C–H activation over $Mo^{(1)}$-C_{Mo} site have been depicted in Fig. 7b. In results, it has been observed that of the two clusters, Mo_2C_6
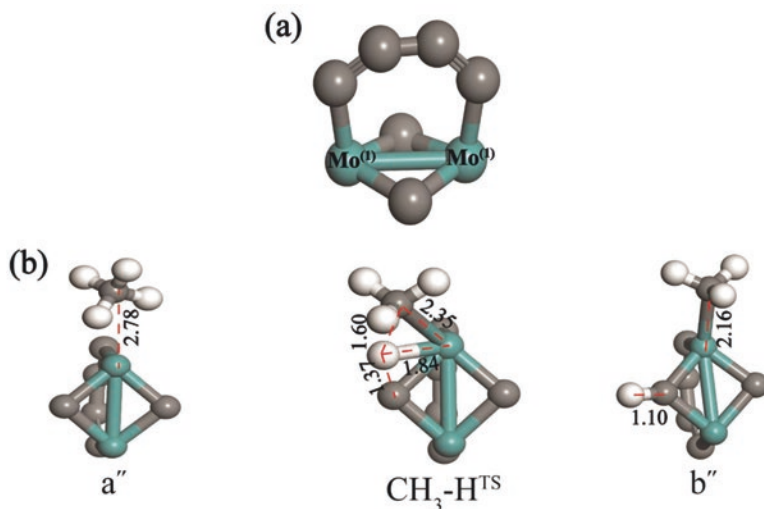
Fig. 7 Geometry of (**a**) Mo_2C_6 nanocluster and (**b**) reactant, transition and product states showing first C–H activation of methane over $Mo^{(1)}$ site (bond lengths in Å). (Adapted with permission from *J. Phys. Chem. C* 2018, 122, 11754–11764 [55]. *Copyright (2018) American Chemical Society*)

results in significantly lower activation barriers for C–C coupling reaction step which directs that whereas methane may be activated on both Mo_4C_2 and Mo_2C_6 clusters, the C–C coupling and subsequent higher coupling reactions to form aromatic product are likely to occur over Mo_2C_6 clusters anchored inside the zeolite channels. In the study, residual charge effect over the clusters which significantly affects the elementary reaction energy barriers confirms that the reducibility of the molybdenum carbide/oxycarbide is a key factor and controls the Mo/Zeolite activity [55]. A linear correlation has been obtained between cluster residual charge and first C–H activation barrier which directs that the lesser residual charge on Mo_xC_y cluster results in lowering of methane dehydrogenation barrier as depicted in Fig. 8. Thus the overall mechanistic study correlates the effect of Mo_xC_y clusters with charge to activity which may help in improving the MDA catalyst activity and stability via controlling the Mo_xC_y structure.

In recent studies of Gao et al. (2019), a comparative mechanistic studies on oxycarbide and carbide form of molybdenum have been reported in which oxycarbide form is taken into account for effective MDA catalyst stability [56]. Generally, molybdenum carbide species agglomerate during the progress of reaction and accumulate coke deposits which lead to deactivation. However, catalyst regeneration by oxygen pulsing treatments can recover these active species. The agglomeration of molybdenum species leading to coke formation can also be avoided by co-feeding with oxygenates ($O_2/CO/CO_2$) that partially transforms coked-Mo_2C species into an oxycarbide form of molybdenum during the course of reaction and controls agglomeration and coking. Thus it will be desirable to control the molybdenum structure in an oxycarbide form instead of fully carbide structure of Mo which promotes
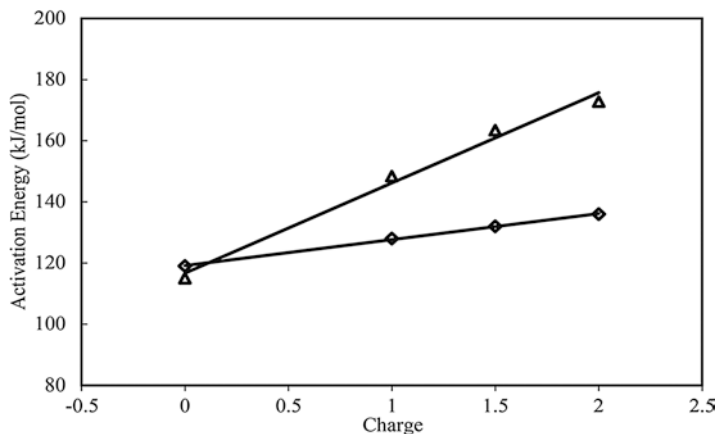
Fig. 8 Effect of cluster residual charge on first C–H activation energies over Mo_4C_2 (triangle) and Mo_2C_6 clusters (diamond). (Reproduced with permission from *J. Phys. Chem. C* 2018, 122, 11754–11764 [55]. *Copyright (2018) American Chemical Society*)
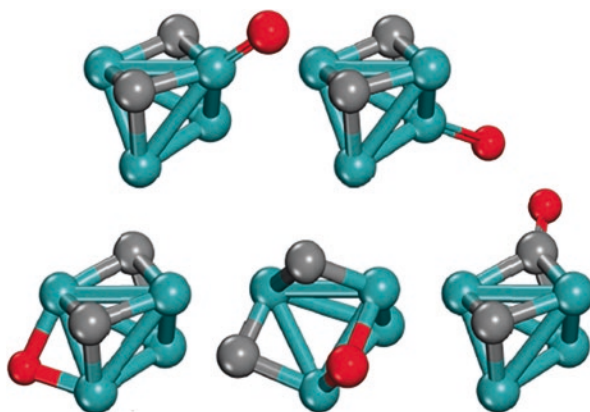
Fig. 9 Structure of Mo_4C_2O oxycarbide nanocluster identified with the genetic algorithm. (Reproduced with permission from *J. Phys. Chem. C* 2019, 123, 22281–22292 [56]. *Copyright (2019) American Chemical Society*)

carbidic coke [56]. Different Mo_4C_2O (oxycarbide) clusters identified via genetic algorithm have been shown in Fig. 9. Theoretical calculations have been performed for oxycarbide clusters (Mo_4C_2O) grafted over ZSM-5 channels comparing with carbide clusters (Mo_4C_2) and it has been reported that presence of oxygen does not affect the activation energy and hence does not alter the rate of methane activation. In conclusion, it is suggested to maintain oxycarbide phase of molybdenum nanocluster as it controls undesirable coking and agglomeration without affecting the rate of methane activation. This can be achieved by co-feeding with oxygen containing molecules such as CO_2 or CH_3OH.

After methane activation and C–C coupling reactions over active molybdenum carbide or oxycarbide nanoclusters producing ethylene intermediate, in the second step of the MDA reaction, ethylene oligomerization occurs at BAS of zeolite support which results in final aromatic products (BTX). This is controlled by Si/Al ratio of zeolite support in Mo/Zeolite catalyst as discussed in Sect. 1.2.2. Major challenge with the reaction is to control over-aromatization of benzene and toluene products. Further aromatization leads to coke formation in the form of poly-aromatic-hydrocarbons (PAH) as per previous reports [15]. However, other forms of coke such as CH_x type or molybdenum-associated carbide coke are also responsible for catalyst deactivation which can be controlled via optimizing the composition and size of active molybdenum carbide or oxycarbide nanocluster [15]. Contrary to this, there are various contradictions in mechanistic insights of chain elongation reactions producing aromatic product and coke formation after C–C coupling reactions at Mo sites. Polyaromatic hydrocarbons can be controlled by optimizing Si/Al ratio and BAS strength inside the zeolite channels which triggers the oligomerization reaction.

1.4 Reaction Parameters

1.4.1 Effect of Temperature

Methane dehydroaromatization is highly endothermic reaction limited by thermodynamic equilibrium (Eq. (1)) as discussed in Sect. 1.1. It requires high temperatures (973 K) to achieve remarkable methane conversion into aromatic hydrocarbons performed in a fixed-bed type reactor [57, 58]. As per previous reports, the methane conversion rate in MDA reaction is a function of temperature as supported by thermodynamics calculations which approve the need of high temperature in this case. However, high-temperature range causes fast catalyst deactivation by severe coke deposition and promote agglomeration of metallic particles reducing the active phases of MDA catalyst [58]. Different observations have been made in the previous experimental reports on optimization of temperature for MDA reaction and it has been concluded that 973–1073 K temperature range is the optimum range for methane conversion into aromatic hydrocarbons. Above these range of temperatures, decrease in benzene yield has been reported probably due to loss in the active phase of Mo/HZSM-5 catalyst resulting in severe coke formation. In addition, lower temperatures range has also been claimed for MDA reaction as an alternative aspect of lower energy requirement which directly relates to the economy of the process [59, 60].

1.4.2 Effect of Pressure

Thermodynamically, it has been shown that a decrease in pressure favours the conversion rate; however, selectivity towards benzene is observed with a slight decrease in MDA reaction as per previous reports [17]. According to previous experimental report, at lower pressure range below 1 bar, the benzene formation rate rapidly decreases with time on stream, whereas at higher pressure (above 1 bar), the rate of benzene formation is observed to increase with time on stream achieving higher stability [61]. Generally, moderate pressure range (1–3 bar) applied to MDA reaction results in higher stability and activity to the Mo/Zeolite catalyst [61]. In recent studies of Hensen et al. (2019), the advantageous effect of high pressure (up to 15 bar) has been claimed for Mo/ZSM-5 catalyst in MDA reaction [12]. Fast coke hydrogenation at higher pressure results in lower coke selectivity and retains active catalyst surface for further reaction. Thus modification in pressure range can improve benzene yield with lower coke deposition and can take the MDA process at the commercial level.

1.4.3 Effect of Space Velocity

Generally, increase in space velocity leads to decrease in conversion rate as per reaction engineering. Different experimental reports have been claimed on space velocity effect for the reaction and it has been observed that decrease in the space velocity increases the methane conversion to aromatic hydrocarbons at 873–998 K [27, 62] with increased duration of the induction period. In the product distribution, an increase in the space velocity results in higher ethylene selectivity whereas lower selectivity towards benzene [63]. Lower space velocity favours the catalyst deactivation due to high residence time as also experimentally observed in earlier reports. Thus a rigorous optimization controlling temperature, pressure and space velocity can upgrade the MDA process.

1.5 Reactor Configuration

Reactor design is another major aspect in the MDA process which significantly controls methane conversion and product yield. Fixed-bed reactor is the most widely used setup for MDA reaction. For the industrial and academic community, MDA process is being a challenge for commercialization due to its thermodynamic and kinetic limitations. However, MDA process is upgraded via increase in temperature or decrease in pressure, but these parameters cannot take the process at the industrial level. Reactor configuration considering different factors such as multiple pas conversion instead of single pas conversion, catalyst regeneration via in situ coke removal, in situ H_2 removal from the reaction mixture, etc. can actually improve the technology for commercial purposes. Circulating fluidized-bed reactor setup and

membrane reactor units are the effective configuration for MDA process upgradation. Multiple fixed-bed reactors in parallel series can be another configuration in which some zones can be used for catalyst regeneration under the flow of oxygenates/H_2.

1.5.1 Circulating Fluidized-Bed Reactor Setup

In terms of heat dissipation, catalyst regeneration, uniform temperature, etc., fluidized bed unit is advantageous in comparison to fixed-bed unit. Due to these positive factors, MDA reaction can be studied using bubbling and circulating fluidized bed reactors. In 2009, a comparative study of fixed and fluidized bed reactor for MDA reaction has been performed using Mo/HZSM-5 catalyst and higher yield of benzene is claimed with fluidized bed unit having severe coke deposition [64]. Quartz fluidized bed reactor has been reported for methane conversion into aromatic hydrocarbons under non-oxidative conditions by Wei and co-workers [65]. Similar results as observed in fixed-bed reactor have been claimed in the experimental studies highlighting the role of temperature, space velocity and partial pressure. Concept of circulating fluidized bed reactor for continuous periodic operation in case where high catalyst deactivation rate occurs has been proposed in previous reports [66]. This provides effective design for continuous periodic operations with proper heat transfer management resolving hot spot limitations as observed in fixed-bed unit. The schematic of two-bed type of circulating fluidized bed reactor has been shown in Fig. 10.

Figure 10 depicts the schematic design of circulating fluidized bed reactor unit in which methane to aromatic conversion reaction occurs in reactor unit having fresh Mo/Zeolite catalyst whereas regeneration unit is used to remove coke deposits over spent Mo/Zeolite catalyst using oxidants such as O_2 and H_2. Simultaneously, regenerated catalyst is circulated from regeneration unit to reactor unit for continuous operation and high catalytic activity. This reactor configuration can be effective for methane dehydroaromatization process at the industrial level.

In another configuration of reactor design, Menndez et al. in 2010 have proposed a two-zone fluidized bed reactor in view of resolving the fast catalyst deactivation issues [67]. In the reactor design, two different zones of reaction and catalyst regeneration are created making fluid bed by feeding reactant methane at an intermediate stage and oxidant inlets from the bottom of the reactor respectively. Authors have achieved 8% methane conversion with more than 90% aromatic selectivity at 700 °C using 6%Mo/HZSM-5 catalyst and 1% CO_2 regenerating oxidant.

1.5.2 Membrane Reactor

As per thermodynamic studies (Sect. 1.1.2), in situ removal of hydrogen from the MDA reaction mixture shifts the chemical equilibrium towards the desired benzene product. This can be achieved with a suitable membrane-type reactor that has a

Fig. 10 Schematic of circulating fluidized bed reactor unit
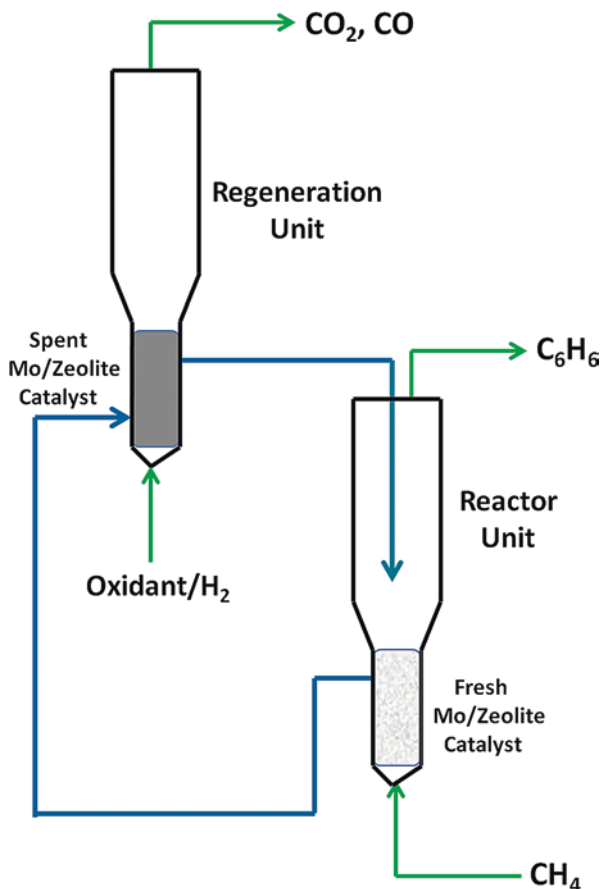
comparable H_2 penetration rate to its formation rate in MDA process. For this membrane type configuration, different reports are available performing MDA reaction. Ichikawa and co-workers [19] in 2003 have claimed that formation rates of desired aromatics products in MDA reaction with 3%Mo/ZSM-5 catalyst are improved 2–10 times by removal of hydrogen by-product using a Pd membrane reactor. In overall 100 h of MDA reaction time, >60% of total H_2 produced has been selectively removed by Pd membrane unit. Similarly, Grandjean et al. in 2003 have reported Pd–Ag membrane type reactor for H_2 consumption in MDA reaction using 0.5%Ru–3%Mo/HZSM-5 catalyst at 873 K [49]. Maximum of 8% methane conversion was claimed which was observed to increase up to 17% at 973 K temperature due to higher formation rate of hydrogen. In 2002, Iglesia et al. have claimed a dense SrCe0.95Yb0.05O$_3$, a thin film (ca. 2 µm) as membrane unit to remove H_2 during the non-oxidative methane conversion into aromatic range of hydrocarbons over Mo/HZSM-5 catalyst [68]. It was observed that at 950 K, only 7% of hydrogen was consumed showing similar results of methane conversion and product

selectivity as observed in fixed-bed unit. On increasing temperature, higher amount of H_2 was released (16%) showing an improvement in conversion and benzene selectivity.

1.6   Summary

Non-oxidative methane conversion into higher hydrocarbons is of huge potential curiosity as emerging high-value aromatic compounds with pure hydrogen as side product direct from natural gas in one-step reaction. However, thermodynamic and kinetic based limitations in methane dehydroaromatization restrict its commercialization. Besides aromatic compounds (benzene, toluene and xylene) and hydrogen in MDA reaction, carbonaceous species is another major product which is thermodynamically favoured at MDA conditions and thus imparts fast catalytic deactivation which is a major challenge in the MDA process. To overcome these limitations, different experimental approaches such as the addition of oxygenates (CO_2, CO, H_2O and CH_3OH) and light hydrocarbons (C_2–C_4) to methane feed, in situ H_2 removal using modified reactor configuration, incorporation of catalyst regeneration protocol, etc. have been implemented by chemical community to control the thermodynamic and kinetic inertness of MDA reaction. High chemical inertness of methane molecule imparts certain limitations for its activation and coupling to higher hydrocarbons and thus requires high energy for the MDA process. Combined theoretical and experimental studies can control these kinds of limitations. Mo/ZSM-5 is the best catalyst studied for the MDA reaction and results in higher methane conversion with remarkable benzene yield. Major constituents of MDA catalyst are active molybdenum carbide/oxycarbide (Mo_xC_y) species and Brønsted acid sites of zeolite which controls the anchoring of active Mo_xC_y species inside the zeolite channels. Theoretically, different molybdenum carbide/oxycarbide structure has been optimized and identified for MDA reaction analysis which directs that stable Mo_xC_y nanocluster anchored at suitable site (Al site) inside the channel of zeolite framework significantly controls the overall activity of MDA catalyst. Thus, understanding the mechanistic insights of MDA reaction and modifications in reactor configuration can significantly upgrade the MDA process at industrial level.

References

1. Ashcroft AT, Cheetham AK, Green MLH, Vernon PDF (1991) Partial oxidation of methane to synthesis gas using carbon dioxide. Nature 352:225–226. nature.com/articles/352225a0
2. Wang S, Lu (Max) GQ, Millar GJ (1996) Carbon dioxide reforming of methane to produce synthesis gas over metal-supported catalysts: state of the art. Energy Fuels 10:896–904. https://doi.org/10.1021/ef950227t

3. Stiles AB, Chen F, Harrison JB, Hu X, Storm DA, Yang HX (1991) Catalytic conversion of synthesis gas to methanol and other oxygenated products. Ind Eng Chem Res 30:811–821. https://doi.org/10.1021/ie00053a002

4. Ma T, Imai H, Shige T, Sugio T, Li X (2015) Synthesis of hydrocarbons from H_2-deficient syngas in Fischer-Tropsch synthesis over Co-based catalyst coupled with Fe-based catalyst as water-gas shift reaction. J Nano 2015:268121. https://doi.org/10.1155/2015/268121

5. Ma S, Guo X, Zhao L, Scott S, Bao X (2013) Recent progress in methane dehydroaromatization: from laboratory curiosities to promising technology. J Energy Chem 22:1–20. https://doi.org/10.1016/S2095-4956(13)60001-7

6. Xi Y, Heyden A (2019) Direct oxidation of methane to methanol enabled by electronic atomic monolayer-metal support interaction. ACS Catal 9(7):6073–6079. https://doi.org/10.1021/acscatal.9b01619

7. Ito T, Lunsford JH (1985) Synthesis of ethylene and ethane by partial oxidation of methane over lithium-doped magnesium oxide. Nature 314:721–722. nature.com/articles/314721b0

8. Lu YA, Xu ZS, Tian ZJ, Zhang T, Lin LW (1999) Methane aromatization in the absence of an added oxidant and the bench scale reaction test. Catal Lett 62:215–220. https://doi.org/10.1023/A:1019063425801

9. Wang LS, Tao LX, XieM S, Xu GF, Huang JS, Xu YD (1993) Dehydrogenation and aromatization of methane under non-oxidizing conditions. Catal Lett 21:35–41. https://doi.org/10.1007/BF00767368

10. Majhi S, Mohanty P, Wang H, Pant KK (2013) Direct conversion of natural gas to higher hydrocarbons: a review. J Energy Chem 22:543–554. https://doi.org/10.1016/S2095-4956(13)60071-6

11. Liu S, Wang L, Ohnishi R, Ichikawa M (1999) Bifunctional catalysis of Mo/HZSM-5 in the dehydroaromatization of methane to benzene and naphthalene XAFS/TG/DTA/MASS/FTIR characterization and supporting effects. J Catal 181:175–188. https://doi.org/10.1006/jcat.1998.2310

12. Kosinov N, Uslamin EA, Meng L, Parastaev A, Liu A, Hensen EJM (2019) Reversible nature of coke formation on Mo/ZSM-5 methane dehydroaromatization catalysts. Angew Chem Int Ed 58:7068–7072. https://doi.org/10.1002/anie.201902730

13. Schwach P, Pan X, Bao X (2017) Direct conversion of methane to value-added chemicals over heterogeneous catalysts: challenges and prospects. Chem Rev 117:8497–8520. https://doi.org/10.1021/acs.chemrev.6b00715

14. Ismagilov ZR, Matus EV, Tsikoza LT (2008) Direct conversion of methane on Mo/ZSM-5 catalysts to produce benzene and hydrogen: achievements and perspectives. Energy Environ Sci 1:526–541. https://doi.org/10.1039/B810981H

15. Spivey JJ, Hutchings G (2014) Catalytic aromatization of methane. Chem Soc Rev 43:792–803. https://doi.org/10.1039/C3CS60259A

16. Majhi S, Pant KK (2013) Direct conversion of methane with methanol toward higher hydrocarbon over Ga modified Mo/H-ZSM-5 catalyst. J Ind Eng Chem 20:2364–2369. https://doi.org/10.1016/j.jiec.2013.10.014

17. Bijani PM, Sohrabi M, Sahebdelfar S (2012) Thermodynamic analysis of nonoxidative dehydroaromatization of methane. Chem Eng Tech 35:1–9. https://doi.org/10.1002/ceat.201100436

18. Yaws CL (1999) Chemical properties handbook: physical, thermodynamic, environmental, transport, safety, and health related properties for organic and inorganic chemicals. McGraw-Hill, New York. accessengineeringlibrary.com/content/book/9780070734012

19. Kinage AK, Ohnishi R, Ichikawa M (2003) Marked enhancement of the methane dehydro-condensation toward benzene using effective Pd catalytic membrane reactor with Mo/ZSM-5. Catal Lett 88:199–202. springer.com/article/10.1023/A:1024022124804

20. Wong ST, Xu Y, Liu W, Wang L, Guo X (1996) Methane activation without using oxidants over supported Mo catalysts. Appl Catal A Gen 136:7–17. https://doi.org/10.1016/0926-860X(95)00260-Xm

21. Balyan S, Haider MA, Khan TS, Pant KK (2020) Boric acid treated HZSM-5 for improved catalyst activity in non-oxidative methane dehydroaromatization. Cat Sci Technol 10:3857–3867. https://doi.org/10.1039/D0CY00286K

22. Shu Y, Ohnishi R, Ichikawa M (2002) Stable and selective dehydrocondensation of methane towards benzene on modified Mo/HMCM-22 catalyst by the dealumination treatment. Catal Lett 81:9–17. https://doi.org/10.1023/A:1016016307893

23. Bai J, Liu S, Xie S, Xu L, Lin L (2004) Comparison of 6Mo/MCM-22 and 6Mo/ZSM-5 in the MDA process. React Kinet Catal Lett 82:279–286. https://doi.org/10.1023/B:REAC.0000034838.13695.b0

24. Lim TH, Nam K, Song IK, Lee KY, Kim DH (2018) Effect of Si/Al2 ratios in Mo/H-MCM-22 on methane dehydroaromatization. Appl Catal A Gen 552:11–20. https://doi.org/10.1016/j.apcata.2017.12.021

25. Liu H, Yang S, Wu S, Shang F, Yu X, Xu C, Guan J, Kan Q (2011) Synthesis of Mo/TNU-9 (TNU-9 Taejon National University no. 9) catalyst and its catalytic performance in methane non-oxidative aromatization. Energy 36:1582–1589. https://doi.org/10.1016/j.energy.2010.12.073

26. Aboul-Gheit AK, Awadallah AE (2009) Effect of combining the metals of group VI supported on H-ZSM-5 zeolite as catalysts for non-oxidative conversion of natural gas to petrochemicals. J Nat Gas Chem 18:71–77. https://doi.org/10.1016/S1003-9953(08)60080-8

27. Chen LY, Lin LW, Xu ZS, Li XS, Zhang T (1995) Dehydro-oligomerization of methane to ethylene and aromatics over molybdenum/HZSM-5 catalyst. J Catal 157:190–200. https://doi.org/10.1006/jcat.1995.1279

28. Sarioglan A, Senatalar AE, Savasci OT, Taarit YB (2004) The effect of CaC$_2$ on the activity of MFI-supported molybdenum catalysts for the aromatization of methane. J Catal 228:114–120. https://doi.org/10.1016/j.jcat.2004.08.033

29. Liu W, Xu Y, Wong ST, Wang L, Qiu J, Yang N (1997) Methane dehydrogenation and aromatization in the absence of oxygen on MoHZSM-5: a study on the interaction between Mo species and HZSM-5 by using ^{27}Al and ^{29}Si MAS NMR. J Mol Catal A 120:257–265. https://doi.org/10.1016/S1381-1169(96)00427-X

30. Thomas JM, Thomas WJ (1996) Principles and practice of heterogeneous catalysis. Wiley-VCH, Berlin

31. Ha VTT, Tiep LV, Meriaudeau P, Naccache C (2002) Aromatization of methane over zeolite supported molybdenum: active sites and reaction mechanism. J Mol Catal A 181:283–290. https://doi.org/10.1016/S1381-1169(01)00373-9

32. Liu L, Ma D, Chen H, Zheng H, Cheng M, Xu Y, Bao X (2006) Methane dehydroaromatization on Mo/HMCM-22 catalysts: effect of SiO$_2$/Al$_2$O$_3$ ratio of HMCM-22 zeolite supports. Catal Lett 108:25–30. https://doi.org/10.1007/s10562-006-0023-0

33. Ma D, Shu Y, Cheng M, Xu Y, Bao X (2000) On the induction period of methane aromatization over Mo-based catalysts. J Catal 194:105–114. https://doi.org/10.1006/jcat.2000.2908

34. Gao J, Zheng Y, Jehng JM, Tang Y, Wachs IE, Podkolzin SG (2015) Identification of molybdenum oxide nanostructures on zeolites for natural gas conversion. Science 348:686–690. https://doi.org/10.1126/science.aaa7048

35. Mishra S, Haider MA, Pant KK (2020) Controlling the evolution of active molybdenum carbide by moderating the acidity of Mo/HMCM-22 catalyst in methane dehydroaromatization. Catal Lett 150:3653. https://doi.org/10.1007/s10562-020-03269-x

36. Wang H, Su L, Zhuang J, Tan D, Xu Y, Bao X (2003) Post-steam-treatment of Mo/HZSM-5 catalysts: an alternative and effective approach for enhancing their catalytic performances of methane dehydroaromatization. J Phys Chem B 107:12964–12972. https://doi.org/10.1021/jp0225931

37. Liu BS, Jiang L, Sun H, Au CT (2007) XPS, XAES, and TG/DTA characterization of deposited carbon in methane dehydroaromatization over Ga-Mo/ZSM-5 catalyst. Appl Surf Sci 253:5092–5100. https://doi.org/10.1016/j.apsusc.2006.11.031

38. Zhang Y, Wang D, Fei J, Zheng X (2002) Effect of Cr addition on the methane aromatization performance of the Mo/HZSM-5 catalyst. Aust J Chem 55:531–534. https://doi.org/10.1071/CH01170

39. Kubota T, Oshima N, Nakahara Y, Yanagimoto M, Okamoto Y (2006) XAFS characterization of Mo/ZSM-5 catalysts for methane conversion to benzene: effect of additives. J Jpn Petrol Inst 49:127. https://doi.org/10.1627/jpi.49.127

40. Shu Y, Xu Y, Wong S-T, Wang L, Guo X (1997) Promotional effect of Ru on the dehydrogenation and aromatization of methane in the absence of oxygen over Mo/HZSM-5 catalysts. J Catal 170:11–19. https://doi.org/10.1006/jcat.1997.1726

41. Sridhar A, Rahman M, Molina AI, Wylie BJ, Borcik CG, Khatib SJ (2020) Bimetallic Mo-Co/ZSM-5 and Mo-Ni/ZSM-5 catalysts for methane dehydroaromatization: a study of the effect of pretreatment and metal loadings on the catalytic behaviour. Appl Catal A Gen 589:117247. https://doi.org/10.1016/j.apcata.2019.117247

42. Aboul-Gheit AK, Awadallah AE, Aboul-Enein AA, Mahmoud A-LH (2011) Molybdenum substitution by copper or zinc in H-ZSM-5 zeolite for catalyzing the direct conversion of natural gas to petrochemicals under non-oxidative conditions. Fuel 90:3040–3046. https://doi.org/10.1016/j.fuel.2011.05.010

43. Abdelsayed V, Shekhawat D, Smith MW (2015) Effect of Fe and Zn promoters on Mo/HZSM-5 catalyst for methane dehydroaromatization. Fuel 139:401–410. https://doi.org/10.1016/j.fuel.2014.08.064

44. Wang D, Lunsford JH, Rosynek MP (1997) Characterization of a Mo/ZSM-5 catalyst for the conversion of methane to benzene. J Catal 169:347–358. https://doi.org/10.1006/jcat.1997.1712

45. Mishra S, Balyan S, Pant KK, Haider MA (2017) Non-oxidative conversion of methane into higher hydrocarbons over Mo/MCM-22 catalyst. J Chem Sci 129:1705–1711. https://doi.org/10.1007/s12039-017-1374-3

46. Wang L, Xu Y, Wong S-T, Cui W, Guo X (1997) Activity and stability enhancement of MoHZSM-5-based catalysts for methane non-oxidative transformation to aromatics and C_2 hydrocarbons: effect of additives and pretreatment conditions. Appl Catal A 152:173–182. https://doi.org/10.1016/S0926-860X(96)00366-3

47. Chu N, Yang J, Wang J, Yu S, Lu J, Zhang Y, Yin D (2010) A feasible way to enhance effectively the catalytic performance of methane dehydroaromatization. Catal Commun 11:513–517. https://doi.org/10.1016/j.catcom.2009.12.004

48. Bouchy C, Schmidt I, Anderson JR, Jacobsen CJH, Derouane EG, Hamid SBDA (2000) Metastable fcc α-MoC$_{1-x}$ supported on HZSM5: preparation and catalytic performance for the non-oxidative conversion of methane to aromatic compounds. J Mol Catal A 163:283–296. https://doi.org/10.1016/S1381-1169(00)00392-7

49. Iliuta MC, Iliuta I, Grandjean BPA, Larachi F (2003) Kinetics of methane nonoxidative aromatization over Ru-Mo/HZSM-5 catalyst. Ind Eng Chem Res 42:3203–3209. https://doi.org/10.1021/ie030044r

50. Zhao K, Jia L, Wang J, Hou B, Li D (2019) The influence of the Si/Al ratio of Mo/HZSM-5 on methane non-oxidative dehydroaromatization. New J Chem 43:4130–4136. https://doi.org/10.1039/C9NJ00114J

51. Wang D, Lunsford JH, Rosynek MP (1996) Catalytic conversion of methane to benzene over Mo/ZSM-5. Top Catal 3:289–297. https://doi.org/10.1007/BF02113855.pdf

52. Zheng H, Ma D, Bao X, Hu JZ, Kwak JH, Wang Y, Peden CHF (2008) Direct observation of the active center for methane dehydroaromatization using an ultrahigh field ^{95}Mo NMR spectroscopy. J Am Chem Soc 130:3722–3723. https://doi.org/10.1021/ja7110916

53. González IL, Oord R, Rovezzi M, Glatzel P, Botchway SW, Weckhuysen BM, Beale AM (2016) Molybdenum speciation and its impact on catalytic activity during methane dehydroaromatization in zeolite ZSM-5 as revealed by operando X-ray methods. Angew Chemie Int Ed 55:5215–5219. https://doi.org/10.1002/ange.201601357

54. Gao J, Zheng Y, Fitzgerald GB, Joannis JD, Tang Y, Wachs IE, Podkolzin SG (2014) Structure of Mo_2C_x and Mo_4C_x molybdenum carbide nanoparticles and their anchoring sites on ZSM-5 zeolites. J Phys Chem C 118:4670–4679. https://doi.org/10.1021/jp4106053

55. Khan TS, Balyan S, Mishra S, Pant KK, Haider MA (2018) Mechanistic insights into the activity of Mo-carbide clusters for methane dehydrogenation and carbon–carbon coupling reactions to form ethylene in methane dehydroaromatization. J Phys Chem C 122:11754–11764. https://doi.org/10.1021/acs.jpcc.7b09275

56. Zheng Y, Tang Y, Gallagher JR, Gao J, Miller JT, Wachs IE, Podkolzin SG (2019) Molybdenum oxide, oxycarbide, and carbide: controlling the dynamic composition, size, and catalytic activity of zeolite-supported nanostructures. J Phys Chem C 123:22281–22292. https://doi.org/10.1021/acs.jpcc.9b05449

57. Iliuta MC, Larachi F, Grandjean BPA, Iliuta I, Sayari A (2002) Methane nonoxidative aromatization over Ru-Mo/HZSM-5 in a membrane catalytic reactor. Ind Eng Chem Res 41:2371–2378. https://doi.org/10.1021/ie010977s

58. Zhang W, Smirniotis PG (1999) On the exceptional time-on-stream stability of HZSM-12 zeolite: relation between zeolite pore structure and activity. Catal Lett 60:223–228. https://doi.org/10.1023/A:1019079612655

59. Xu Y, Wang J, Suzuki Y, Zhang ZG (2011) Effect of transition metal additives on the catalytic stability of Mo/HZSM-5 in the methane dehydroaromatization under periodic CH_4-H_2 switch operation at 1073 K. Appl Catal A 409-410:181–193. https://doi.org/10.1016/j.apcata.2011.10.003

60. Cui Y, Xu YB, Suzuki Y, Zhang ZG (2011) Experimental evidence for three rate-controlling regions of the non-oxidative methane dehydroaromatization over Mo/HZSM-5 catalyst at 1073 K. Cat Sci Technol 1:823–829. https://doi.org/10.1039/C1CY00083G

61. Shu Y, Ohnishi R, Ichikawa M (2002) Pressurized dehydrocondensation of methane toward benzene and naphthalene on Mo/HZSM-5 catalyst: optimization of reaction parameters and promotion by CO_2 addition. J Catal 206:134–142. https://doi.org/10.1006/jcat.2001.3481

62. Rival O, Grandjean BPA, Guy C, Sayari A, Larachi F (2001) Oxygen-free methane aromatization in a catalytic membrane reactor. Ind Eng Chem Res 40:2212–2219. https://doi.org/10.1021/ie001089k

63. Solymosi F, Szoke A, Cserenyi J (1996) Conversion of methane to benzene over Mo_2C and Mo_2C/ZSM-5 catalysts. Catal Lett 39:157–161. https://doi.org/10.1007/BF00805576

64. Cook B, Mousko D, Hoelderich W, Zennaro R (2009) Conversion of methane to aromatics over Mo_2C/ZSM-5 catalyst in different reactor types. Appl Catal A Gen 365:34–41. https://doi.org/10.1016/j.apcata.2009.05.037

65. Huang H, Qian W, Wei T, Li Y, Wei F (2006) Methane aromatization in fluidized bed reactor. Chin J Chem Ind Eng 57:1918–1922

66. Xu Y, Lu J, Wang J, Suzuki Y, Zhang Z-G (2011) The catalytic stability of Mo/HZSM-5 in methane dehydroaromatization at severe and periodic CH_4-H_2 switch operating conditions. Chem Eng J 168:390–402. https://doi.org/10.1016/j.cej.2011.01.047

67. Gimeno MP, Soler J, Herguido J, Menendez M (2010) Counteracting catalyst deactivation in methane aromatization with a two zone fluidized bed reactor. Ind Eng Chem Res 49:996–1000. https://doi.org/10.1021/ie900682y

68. Liu Z, Li L, Iglesia E (2002) Catalytic pyrolysis of methane on Mo/H-ZSM5 with continuous hydrogen removal by permeation through dense oxide films. Catal Lett 82:175. https://doi.org/10.1023/A:1020510810548

Insights into Sustainable C–H Bond Activation

Dewal S. Deshmukh, Vaishali S. Shende, and Bhalchandra M. Bhanage

Abstract Over the recent past, the straight functionalization of inert C–H bond has already been identified as an advanced technique for the synthesis of organic molecules. It has provided a step-, pot- and atom-economic synthetic approach to attain structurally challenging organic scaffolds using simpler, pre-functionalized substrates by single operation and thereby arisen as a sustainable substitution to traditional organic transformations. Regardless of the clear evolution and improvements in metal-catalysed C–H functionalization reactions, these kinds of conversions quiet face considerable restrictions with respect to green chemistry regarding the catalyst reusability, media, time efficiency, energy efficiency, byproducts, requirement of additives as well as oxidants. Encouraged with the necessity for green and sustainable chemistry, researchers attempt further effective routes in this area for the construction of organic scaffolds. Recently, distinguished achievements were attained with the expansion of sustainable methodologies in C–H activation reactions. The attention of the book section is to summarize the progress of greener methodologies for C–H functionalization reactions which incorporate applications of greener solvents, microwave irradiation, photocatalysis, homogeneous recyclable catalytic systems, heterogeneous catalysts, oxidizing directing groups, electrochemical methods, etc., during the past few years. The book chapter emphasizes selected fascinating and encouraging examples of greener methodologies in C–H activation approaches.

Keywords C–H activation · Green-chemistry · Catalysis

D. S. Deshmukh
Department of Chemistry, Shri Shivaji Arts, Commerce and Science College, Akola, India

V. S. Shende · B. M. Bhanage (✉)
Department of Chemistry, Institute of Chemical Technology, Mumbai, India
e-mail: bm.bhanage@ictmumbai.edu.in

1 Introduction

Various environmental threats as well as undesired, destructive side effects are being caused by the development of chemical processes [1]. Natural deposits that comprise massive quantities of non-renewables drive the existing economy [2] and economically expended material goes back to the environment by opposite flow [3]. This economy–ecosphere resources flow controls the chemical sustainability issues [4]. Recently, innovative dimensions were observed in the analysis of resources for energy and materials. The requirement to change these resources was intensified by the climate change and impact of carbon dioxide. A definite quantity of fossil resources will extinct after a certain period of time, suggested by the set theory. In this regard, the advancement of the technological aspect of a sustainable development has become indispensable [5]. In order to conserve fossil resources and to control its increasing price, the scientific community has desire to expand the employment of renewables in the chemical and other fields. Also, methodologies that favour the synthesis of target-related end-products using simple and easily accessible precursors in a quick and cost-effective manner are willingly appealed by modern organic synthesis [6–8].

In chemical field, numerous environmental sensible terminologies were brought in during 1980s and 1990s, e.g. green chemistry, sustainable chemistry, environmental chemistry, clean chemistry and benign chemistry. However, these terminologies are topic of argument for scientists as these are not well explicated [9, 10]. The expansion of the perceptions of the concept 'green chemistry' [11] has developed from the ambition of chemists to diminish synthetic steps and the quantity of harmful waste generated, also, additionally, to discover benign and more selective conversions. Green chemistry, as the name implies, delivers the plan and advancement of consecutive methods that follows a set of assumptions that exclude or minimize harmful constituents within production, outline as well as employment of chemical products. It turns out profoundly efficient access for the inhibition of pollution and hence being one of the central themes of modern organic chemistry [12, 13]. Some significant green chemistry characteristics comprise (a) lessening the usage of harmful substances, (b) evolution of harmless reagents and solvents, (c) enhanced energy efficiency and atom economy of reactions, (d) investigating new multi-component reactions to reduce the reaction steps in a synthesis procedure, (e) lessening harmful waste generation, and (f) evolution of recyclable reagents and catalysts.

Following the green chemistry principles, synthetic chemists are taking efforts for the advancement of milder and selective reagents that necessitate ambient conditions. One of the major considerations associated with them is the exclusion of harmful solvents. Curtailing the usage of such solvents as well as energy utilization is one of the most crucial barriers in evolving greener methodologies. Organic synthesis with metal scavengers, solid-supported reagents, catalysts, microwave-strategy, electrochemical synthesis, reusable catalytic systems, oxidant-free conditions, and green solvents efficiently fulfils several above principles of green

chemistry. In this context, transition metal-catalysed C–H activation reactions further have been arisen as a potent green chemistry approach recently. This is because such conversions offer several advantages like it avoids the necessity of prior efforts for activation of the starting substrates.

1.1 C–H Activation: A Green and Economical Synthetic Protocol

Depletable resources namely crude oil and natural gas are the source of most of organic molecules and materials [14, 15]. Utilization of such feedstocks to convert into another useful chemicals is the great opportunity as well as challenge for the chemists. This involves cleavage and construction of another C–C bonds and converting C–H bonds into desired functional groups. This objective has been achieved by using most traditional pathways like initial C–H bond functionalization such as radical functionalization [16, 17] or partial aerobic oxidations [18]. Such functionalization is then succeeded by an alterable order of steps to provide anticipated functional groups or C–C bonds in order to synthesize the targeted frameworks. This widely significant approach is referred as functional group interconversion strategy [19, 20].

Although functional group interconversion strategy has been established as a vital tool in organic transformations, it generally leads to highly wasteful methodologies as it requires multiple steps from unfunctionalized starting substrates to functionalized products, hence suffer from limitations. In this fashion, serious environmental restrictions are being faced by fine chemical and pharmaceutical industries and hence they are attempting to diminish or exclude waste, and also harmful and tedious methods. In this regard, a modern chemistry has paid considerable attention towards the advancement of ideal synthetic methodologies which are potential, cost-effective and ecologically benign in order to synthesize complex moieties.

From the viewpoint of green chemistry, highly efficient and step economic metal-catalysed straight activation of C–H bonds has potential to replace traditional organic transformations in order to synthesize complex organic scaffolds. In contrast to conventional methodologies for such kind of bond construction, activation of C–H bond avoids the initial functionalization (for instance, halogenation or borylation) of the target molecules that drops number of steps. Ideally, multiple step synthesis could thus be modulated into single-step synthesis permitting straight approach to anticipated frameworks, thereby decreasing the quantity of unwanted refuse of multistep transformations. Accordingly, through the enhanced step and atom economy, synthetic 'shortcuts' could be attained [21, 22]. Therefore, transition metal-catalysed C–H bond activation claims to be an ideal and influential approach to construct bonds and establish functional groups in a straight manner. This is frequently believed as a 'Holy Grail' in organic synthesis and has been widely studied over the past decades, leading to substantial progress in the area [23, 24].

1.2   Challenges in C–H Activation Reactions

However, two major challenges must be conquered in order to develop transition metal-catalysed C–H activation as a practical tool in organic synthesis. C–H bond is inert by thermodynamic consideration, so challenging to break, particularly in the existence of some active functional groups which are higher in reactivity. Taking into consideration the substantial energies that are essential in regard to direct activation of C–H bonds, one can understand the magnitude of the challenge for these kinds of transformations. C–H bonds of modest hydrocarbons are most challenging to activate as they have bond dissociation energies (BDEs) within 96 and 105 kcal/mol. On the other hand, the BDEs for Me–Cl and Me–Br are 83.7 and 72.1 kcal/mol, respectively and hence possible to functionalize easily. Besides that, C–H bond functionalization is also kinetically difficult as compared to other C–X bond-breaking reactions as it does not contain suitable lone pairs for the coordination with transition metal catalyst [25]. Thus, inertness of C–H bonds become the first challenge. The second challenge is monitoring the site-selectivity. Out of several adjacent C–H bonds with comparable reactivity, functionalizing a specific C–H bond has long stood as a highly desirable goal.

In order to address the first challenge, various transition metals have been tested for the reaction with the C–H bonds to establish more labile C–M bonds which could be further converted into other desired functional groups. Whereas, developing various strategies like the utility of intrinsic electronic nature of substrates [26, 27] and directing groups could be the solution for the second challenge [28, 29]. The catalytic systems for C–H bond functionalization, to be effective by synthesis point of view, furthermore would have to be (a) stabilized in the existence of the necessary oxidizing agents, (b) not disabled after coordination of another functional groups in the target product or solvent, (c) restrictive for a particular kind of C–H bond in a molecule, and (d) decelerate to catalyse the unnecessary reaction (over-oxidation) of the products. The development of novel efficient approaches for organic synthesis providing a consolidate solution for all these critical challenges applying mild/green methods is a valuable objective for organic chemistry researchers. On the other hand, the existing worldwide ecological and resource problems are inspiring for additional investigation and advancement of sustainable methodologies.

2   C–H Activations Using Heterogeneous Catalysis

Exploiting stoichiometric amount of reagents for organic transformations is now considered as an old-fashioned strategy. Nowadays, enhanced catalytic systems can boost the yield of product and reduce the energy and wealth expenditures that add to raised chemical costs. The last few decades have witnessed the advancement in the field of catalysis as several highly competent and selective catalysts have been

evolved. Today, the ideal catalytic systems should have characteristic common requirements like it should be highly active, selective, durable, recyclable, compatible with practical reaction conditions, broadly applicable as well as cost, safety and environmentally benign. Conventionally, the phrase catalysis is generally divided into two divisions, i.e. homogeneous and heterogeneous catalysis which are just similar to a pair of twins with dissimilar features [30–32]. Among these, homogeneous catalysts, largely organometallics, possessed a substantial development and were utilized with varied reactive reagents to generate a huge amount of fine chemicals. In these systems, the starting reactant and active centres of catalysts exist in the identical phase and because of clear availability of active centres to the reactant, high activity performance is obtained. Whereas, the active centres of catalysts and the reactants are in a distinct phase in case of heterogeneous catalysis.

The active site is recognized in homogeneous catalytic systems, and much that is appearing in catalysis is detectable and alterable. As a result of this, extensively used classical homogeneous catalysis has become an indispensable part of modern organic chemistry [33]. For instance, the development of C–C, C–N, C–O bonds using homogeneous catalysts with transition metals having extensive industrial utilization which is creating interest to chemists [34, 35], due to its capability to accomplish the reaction under gentle conditions with improved selectivity as well as yields [36–39]. In this way, homogeneous catalytic systems have been extensively recognized as further efficient, selective as well as effortless for analysis and prediction as compared to heterogeneous systems.

Though the huge number of homogeneous catalysts are extensively utilized in industries, the stability, cost, and availability of the catalysts (ligands and metal) are the key considerations restricting its utilization on the commercial scale [40, 41]. For example, rhodium catalysts have extensive application in organic chemistry [42–44], while a recent study exposes a severe hike in the market cost of rhodium so that it becomes the costliest transition metal [45]. Similarly, palladium has wide application as a catalyst in numerous C–C bond formations [46], which also exists as an endangered and expensive element. In this view, considerable recognition has been given for the advancement of methods for approximately quantitative recycle as well as reuse of these precious metals. Additionally, the serious resistance in the application of homogeneous catalytic systems exhibited by distinct disadvantages such as complications in isolation as well as the separation of the ultimate product from reaction media and reutilization of exhaustible valuable organometallic catalysts or costly ligands. In many cases the overall product gets contaminated with a minute quantity of the metal catalyst (at ppm or at ppb level), so the total regaining of the metal catalysts from the reaction mixture becomes a challenging task. In the drug as well as pharmaceutical manufacturing, it is essential to eliminate the trace metal catalyst from ultimate pure product entirely as it can be responsible for crucial metal adulteration problem thus degrading the human health. According to guidelines by the European Medicines Agency, the acceptable oral exposure to such metals in a medicinal constituent is supposed to be usually not more than 10 ppm per day [47].

Issue of isolation of catalyst and final products from the reaction medium makes the catalytic system non-reusable as well as the complete procedure difficult, which become the considerable threat in the progress of novel ambitious synthesis and methodologies. Genuinely, the generation of waste and accordingly a disadvantage in terms of chemical and ecological expenses is correlated with this process. In order to develop reusable catalytic systems for organic synthesis from both academic and industrial viewpoints, resource conservancy and ecological preservation are absolutely significant commercial and environmental motives. In this view, the advancement of an effective, eco-friendly, recyclable and reusable catalytic system has become indispensable for the tenable development of a chemical business [48, 49]. Nevertheless, recycling of metals can be challenging which demands for scientific investigation so that greater can be attained with a lesser amount of metals.

In this perception, heterogeneous catalysis can conquer the above shortcomings as it offers the vision for simplicity of separation and recycling of the metal-catalyst accompanied by easy product purification as well as possibly continuous or numerous treatments of final products [50, 51], which signifies the primary advantage over homogeneous catalysis. Also, it possesses the similar reaction mechanisms with their homogeneous counterparts, accompanied by even considerable turnover numbers (TONs) and/or turnover frequencies (TOFs) [52, 53]. An additional fascinating feature is the feasibility to utilize heterogeneous catalytic systems to attain a precise selectivity in sites, or a shift in selectivity, and perhaps an enhancement in the catalytic activity. This could in assumption be achieved by the development of hybrid molecular frameworks. Heterogeneous catalysis has become a key aspect in the progress of tenable procedures in fuel and fine chemical production, where chemical productivity has to be linked with financial and ecological requirements. Some of these procedures, for example, catalytic hydrogenations are one of the most primitive reactions in this direction which are nowadays usually introduced as green chemistry [54]. Indeed, it has become one of the greenest sectors of the chemical manufacturing in the past decades. So, the progress of reusable heterogeneous catalytic systems is immensely fascinating not only as such systems permit for an easy separation by filtration and therefore possible to recycle [50, 55], but also for designing innovative chemical procedures.

Considering the above preferences and in order to promote more reasonable straight C–H activation reactions, the application of heterogeneous catalytic systems is notably appealing, even though the inactivity of the C–H bond has turned this auspicious execution somewhat challenging [56, 57]. In this section, we have provided certain instances of the expeditious current advancement in selective C–H activations using heterogeneous catalytic systems.

2.1 C–H Arylation

In 2014, Parsharamulu et al. designed a three-dimensional mesoporous silica in combination with a highly diffused palladium nanoparticle composite catalyst (PS-3). The large surface area innovative heterogeneous PS-3 catalyst was employed
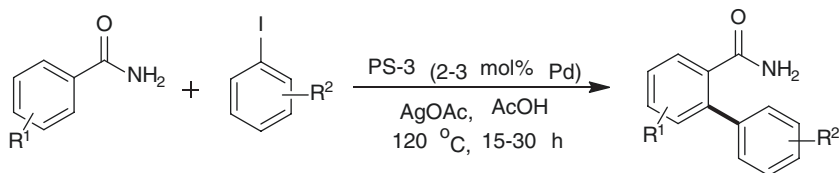
Scheme 1 Heterogeneous Pd-catalysed *ortho* arylation of amides
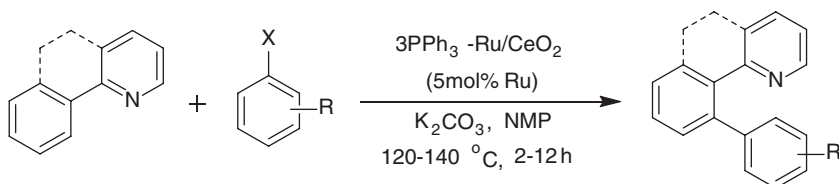
Scheme 2 Arylation of aromatic substrates using heterogeneous PPh$_3$-modified Ru/CeO$_2$catalyst

initially as a potential and recyclable catalyst for the construction of biphenyl-2-carboxamides using the ligand-free environment (Scheme 1) [58]. This protocol involves ortho sp^2 C–H bond activation of benzamides accompanied by arylation using aryl iodides employing the straightforward CONH$_2$ in the form of directing group. The methodology has additional advantages of outstanding site-selectivity, tolerance for various functional groups, predominance for the generation of mono-arylated products, convenience to operate, recyclability for five successive runs without substantial loss in activity as well as selectivity, and stability of catalyst within the reaction standards.

Miura et al. developed a heterogeneous PPh$_3$-modified Ru/CeO$_2$catalyst which exhibited outstanding catalytic activity for the arylation of aromatic substrates using aryl halides in order to synthesize the arylated products with good selectivity as well as yields (Scheme 2) [59]. However, both mono- and diarylated products could be observed on performing the reaction with non-fused aromatic rings like 2-phenylpyridine or 1-phenyl-2-pyrazol. The recycling study of the catalyst was performed and it was observed that this catalytic system found to be reusable with negligible substantial decrease in activity.

2.2 Addition of C–H Bond to Vinylsilanes

The similar catalytic system, ruthenium immobilized on CeO$_2$ was then employed effectively by Wada and co-workers in order to add a C–H bond of various aromatic ketones to vinylsilanes (Scheme 3) [60]. For this, the main substrate was triethoxy(vinyl) silane, despite ethoxydimethyl(vinyl)silane has also been described. This transformation could be carried out on a large amount under solvent less conditions to attain an improved turnover number. Efforts for the complete recyclability of this catalytic
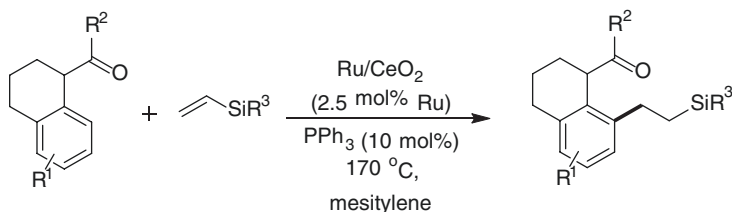
Scheme 3 Ru/CeO$_2$ catalytic system for the addition of a C–H bond

system were ineffective; however, the PPh$_3$-modified Ru/CeO$_2$catalyst exhibited fascinating catalytic activity excluding any substantial leaching into the reaction mixture.

2.3 C–H Acylation

In the year 2013, Venugopal with co-workers employed the heterogeneous palladium(II)/magnesium–lanthanum mixed oxide (Pd(II)/Mg–La) as a potential catalytic system in favour of the oxidative straightforward acylation of sp^2 C–H bonds of arene with alcohols (Scheme 4) [61]. For this, TBHP acts as an oxidant for the in situ generation of aldehydes from alcohols which is then followed by acylation with 2-aryl pyridines in order to generate aryl ketones. The catalyst could be easily recycled up to four runs successively with persistent activity as well as selectivity.

2.4 C–H Cyanation

The same research team later applied this reusable catalytic system also for the cyanation of aromatic C–H bonds as well as tandem Suzuki–cyanation reactions (Scheme 5) [62]. NH$_4$HCO$_3$ and DMSO were used combinedly as the cyanation source and Cu(NO$_3$)$_2$·3H$_2$O as an oxidant for the C–H bond cyanation in order to provide aromatic nitriles with an exceptional regioselectivity and moderate to good product yields. They have also designed a tandem methodology concerning Suzuki coupling reaction accompanied by a cyanation utilizing the similar heterogeneous catalytic system for the access of aromatic nitriles from simple 2-halopyridines. The catalyst reusability was verified, exhibiting almost persistent activity and selectivity with successive reaction runs.

2.5 C–H Oxygenation

In 2015, Cohen with co-worker designed a palladium-containing heterogeneous MOF UiO-66-PdTCAT and applied it efficiently in order to activate sp^2 C–H bond regioselectively (Scheme 6) [63]. This metalated MOF could easily oxidize
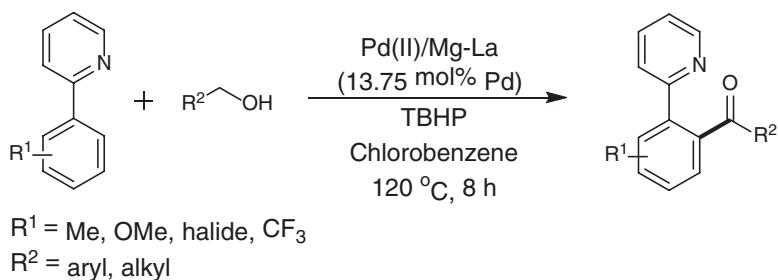
Scheme 4 Pd(II)/Mg–La system in favour of oxidative acylation of arene with alcohols

Scheme 5 Pd(II)/Mg–La system for the cyanation reactions
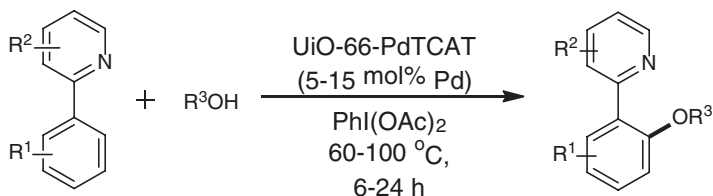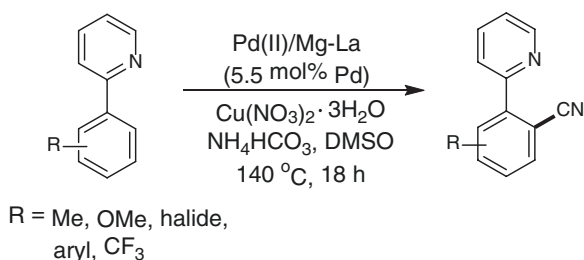
Scheme 6 sp^2 C–H bond oxygenation using palladium-containing heterogeneous MOF

aromatic compounds to convert sp^2 C–H bonds to ethers and aryl halides. In this methodology, simple alcohols and (diacetoxyiodo) benzene were used as the oxidizing agents for the alkoxylation reaction.

2.6 C–H Nitrogenation

Bai et al. prepared heterogeneous Co-based catalyst (Co$_9$(BTC)$_6$(TPT)$_2$(H$_2$O)$_{15}$) by simply pyrolysing cobalt comprising MOF to acquire well-dispersed cobalt nanoparticles surrounded by carbonized organic ligands. The designed catalyst has a great potential in terms of oxidative C(sp^2)–H bond amidation of a large number of aldehydes using formamides with the aim to synthesize benzamides with good to excellent yields and benign reaction conditions (Scheme 7) [64]. A broad array of aromatic and some aliphatic aldehydes were undergone amidation reaction with
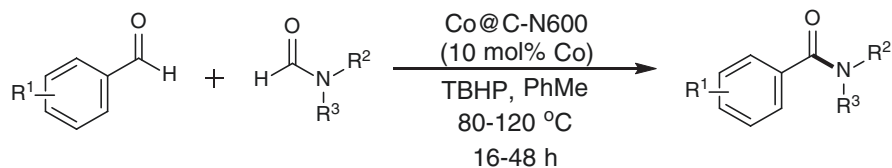
Scheme 7 Heterogeneous Co-based catalyst for the oxidative C(sp^2)–H bond amidation

formamides with the help of TBHP as an oxidizing agent. Furthermore, the developed catalyst perhaps readily reutilized repeatedly with merely a slight decrease in the product yield.

2.7 C–H Halogenation

Pascanu et al. employed a heterogeneous Pd-containing Fe-based MOF [Pd@MIL-88B-NH$_2$(Fe)] and a Pd-containing Cr-based MOF [Pd@MIL-101-NH$_2$(Cr)] catalysts to carry out the directed C–H activation followed by halogenation of an extensive array of aromatic substrates (Scheme 8) [65]. Pd@MOF nanocomposites were capable of controlling the selectivity among monoiodination or diiodination of the product 2-arylpyridines by regulating the reaction conditions. The MOFs exhibit fascinating efficiency with benign reaction conditions and shorter duration, also could be recycled for minimum five successive runs, preserving the activity.

2.8 Fujiwara–Moritani Reaction

In 2011, Ying group formulated an effective heterogeneous palladium-polyoxometalate nanomaterial Pd-PV$_3$Mo$_9$/C catalyst and applied it for carbon–carbon bond development through C–H activation and oxidative amination followed by C–N bond construction with the utilization of molecular oxygen in terms of terminal oxidant (Scheme 9) [66]. The protocol explains the oxidative olefination of anilides with acrylates using comparatively benign reaction conditions with minimum waste generation and catalyst recyclability.

2.9 Miscellaneous Reaction

Chen et al. proposed the Pd/CeO$_2$-catalysed oxidative C–H functionalization protocol in order to synthesize indoles from anilines and internal alkynes (Scheme 10) [67]. The methodology necessitates just a catalytic quantity of copper(II) salt as
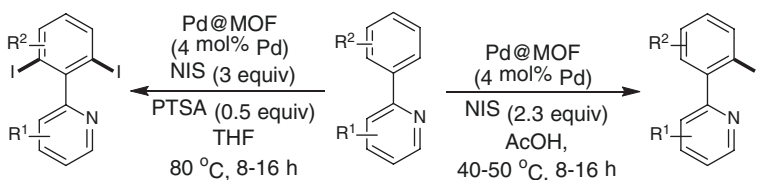
Scheme 8 Heterogeneous Pd-containing Fe-based MOF for the directed C–H halogenation
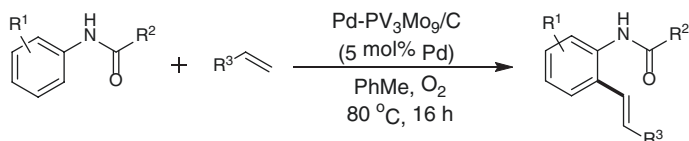
Scheme 9 Olefination of anilides with acrylates using heterogeneous palladium-polyoxometalate nanomaterial

R^1 = Me, OMe, MeS, Ar, halide,
 COMe, CO_2Me, OCF_3
R^2, R^3 = aryl, alkyl
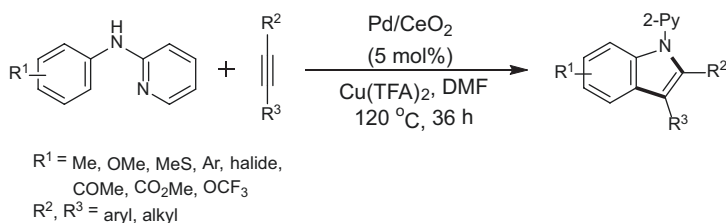
Scheme 10 Pd/CeO$_2$-catalysed oxidative C–H functionalization to synthesize indoles

co-catalyst plus atmospheric oxygen as the terminal oxidizing agent; however, the catalyst was unable to recycle completely.

3 Homogeneous Reusable Media for C–H Functionalization Reactions

Homogeneous catalysis is extensively recognized because it is more efficient and selective. It has benefits such as the viability of predicting chemical conversions using spectroscopic techniques in order to acquire a knowledge of the real active species, transition states and mechanistic information. On the other hand, notably, the reactivity and selectivity of the heterogeneous catalysts are lesser than the homogeneous ones since the active sites in heterogeneous catalytic systems are difficult to access as compared to homogeneous systems. These are assumed as the result of steric of support template and mass transport impacts, resulting from the deep stash of active sites within these templates, thus restricting the approach of

reactants [68]. However, owing to the advantage of recyclability, few workers described the heterogeneous reusable catalytic systems in order to carry out C–H bond activation reactions [50, 51, 69]. Nevertheless, a critical obstacle in the application of heterogeneous catalytic systems is the possible leaching of the catalyst into the reaction mixture, resulting into limitation of its employment. On the other hand, homogeneous catalysts possess additional improvements of significant turnover number (TON) and turnover frequency (TOF). In such systems, it is possible to achieve the anticipated chemo-, regio- and enantioselectivity of the final molecules by merely transforming the catalytic active centre. On account of the great reactivity and selectivity, the homogeneous catalysts are mostly preferable compared to the corresponding heterogeneous catalysts and established ample employment in the chemical enterprise [70].

Considering the recyclability issue of homogeneous catalysis, until now an extensive conclusion is yet to be attained that depicts a chief obstruction for its large-scale employment. Reusing the homogeneous catalytic systems decreases the total expense of the procedure and prevents the wastage production of the method and hence it performs a notably crucial function in the direction of the viable and massive manufacturing of fine chemicals. In this view, a replacement for catalyst recycling competitive with conventional homogeneous catalysis and heterogeneous catalysis is immensely anticipated. Thus, exhaustive investigation in the area of development of diverse approaches to merge the characteristics of homogeneous and heterogeneous catalysts is under progress. The key purpose is to develop the catalyst that is extremely reactive, principally reusable type, absolutely product selective and need to be persistent within specified reaction conditions. Designing of the catalytic system possessing such characteristics and fruitful employment at the laboratory as well as manufacturing scale will decrease the total expenditure of the reaction system.

Economic competence and reasonable metal contamination standards by chemical enterprises have an impact on a direction for the progress of recyclable, homogeneous catalysis to furnish better synthetically modifiable and feasible catalysts in order to optimize comfort in segregation from valuable end products [71]. Heterogenization of homogeneous catalysts belongs to the efficient techniques to resolve the trouble of separating and isolating the valuable homogeneous metal catalysts and generating a novel catalytic system [72–74]. This can be attained by the aggregation or immobilization of active molecules on the exterior of solid or inside the pores of the solid substance [75]. Although immobilizing strategy promotes the reuse of catalyst, it eventually lowers down the performance of catalyst and/or selectiveness in reactions. On the other hand, such approach moreover increases the preliminary expenditure of the catalytic system and additionally several similar anchored catalytic systems might be protected by patent protocol which would have its particular juridical and economic challenges for their financial exploitation.

Alternative strategies emphasized on the advancement of novel protocols that would enable the isolation of the catalysts from the reaction medium [76, 77]. Furthermore, the substantial attempt has been paid for the progress of catalytic

systems for biphasic reactions [78, 79]; regardless of that, rare commercially feasible instances have come to the forefront [80]. Moreover, easier and potential methodologies, e.g. employment of supercritical carbon dioxide (CO_2) [81, 82] and ionic liquids [83, 84] as solvents were suggested. Despite these approaches deliver distinguished significances, among them, supercritical CO_2 operates under high pressure with discharge of CO_2 gas. In contrast, ionic liquids are usually expensive, procedures for their preparation are arduous, and their toxic nature and ecological stress are yet unidentified, particularly the first generation of ionic liquids are crucial with respect to their toxic nature [85, 86]. This perhaps turns out to be an obstacle in its evolution as a solvent for green synthesis. Also, different organic solvents are broadly employed in organic conversions and have been a reason for a major issue owing to their corresponding environmental threats. Thus, a visionary preference of the reaction medium performs a crucial function in the establishment of an area of growing viable organic transformations [87, 88] and considerable focus has been dedicated for the progress of the effective and reusable catalytic systems for C–H functionalizations.

In this view, conventional solvents in organic chemistry can be replaced by polyethylene glycols (PEGs). On account of the characteristics such as lower vapour pressure, economical, thermal persistency, biodegradability, stability in both acidic and basic conditions, easily recoverable, and less toxic, these act as a suitable solvent for ecologically favourable and harmless organic conversions [89–91]. Moreover, having certain characteristics, PEGs were served for catalyst immobilization [92], nanoparticle stabilization [93], ligand stabilization [94] and as phase transfer catalysts [95].

In the light of the superiority shown by PEG, a green and sustainable solvent system, it has been fruitfully employed as a medium for the metal-catalysed cross-coupling transformations like Heck reaction [96], Suzuki reaction [97, 98], the homocoupling and cross-coupling of aryl halides [99], the straightforward arylation of 1,2,3-triazoles [100], carbonylative Suzuki [101], and carbonylative Sonogashira couplings [89], hydrosilylation of terminal alkynes [102] and C−H functionalization [103] with easy reusability of solvents as well as precious metals. Illustrative examples and innovative features of the recycling approaches in C–H activation reactions considering sustainable chemistry, cost-effectiveness, technical usefulness and toxicity viewpoint have been concisely discussed here.

In 2015, Cai and co-workers proposed recyclable [$RuCl_2(p$-cymene)]$_2$/Cu(OAc)$_2$/ PEG-400/H_2O catalytic system for the efficient and green synthesis of phthalide derivatives (Scheme 11) [104]. The stated catalytic system demonstrated a higher efficiency to achieve the cascaded intermolecular oxidative C–H bond alkenylation/ oxa-Michael addition of benzoic acids with alkenes in order to attain desired products. The proposed catalytic system potentially reused up to sixth time with negligible decrease in catalytic activity.

Encouraged by the work done by Cai group, Bhanage research group extensively explored the recyclability of Ru(II)/PEG-400 catalytic systems for C–H functionalization reactions [103]. First, highly efficient Ru(II)/PEG-400 catalytic system has been employed for the annulation reaction of *N*-methoxybenzamides, benzoic acids
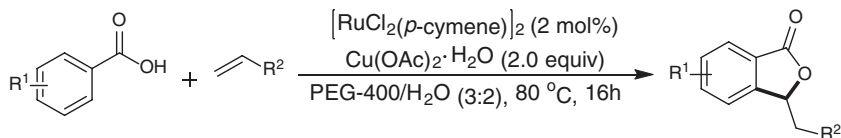
Scheme 11 Ru catalysed oxidative alkenylation

X = NHOMe/NMeOMe/OH   Y = NH/NMe/O
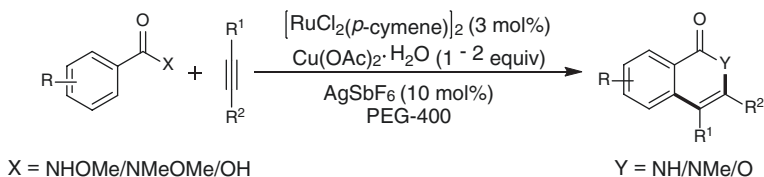
Scheme 12 Ruthenium-catalysed annulations of *N*-methoxybenzamides, benzoic acids, *N*-methoxy-*N*-methylbenzamides with alkyne
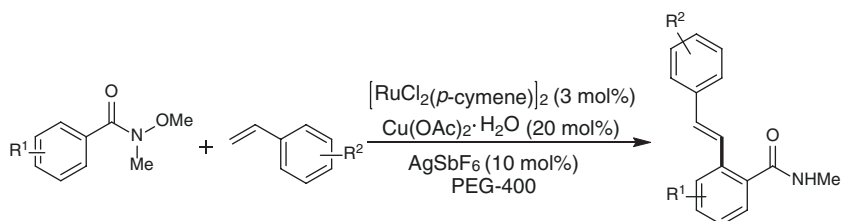
Scheme 13 Ruthenium-catalysed oxidative olefination

and *N*-methoxy-*N*-methylbenzamides with alkynes for the synthesis of isoquinolinones, isocoumarins and *N*-methyl isoquinolinones respectively (Scheme 12).

The same report suggests the application of similar catalyst on account of the olefination of Weinreb amides to get the respective products (Scheme 13). The proposed protocol is competent for the regioselective and stereoselective development of C–C, C–O and C–N bonds by the single operation breaking of C–H, N–H, O–H and N–O bonds. Also, the methodology is recyclable, cost-effective, scalable, atom economic, and works under moderate reaction conditions with easy extraction procedure, thus environmentally benign.

In the next work, isocoumarin has been synthesized directly from *N*-methoxyaromatic amide by one-pot synthesis strategy employing *tert*-butyl nitrite in the form of an origin for oxygen [105]. The similar catalytic system, Ru(II)/PEG-400 was used in order to activate the ortho C−H bond of amides followed by annulation reaction with alkynes. This method also had advantages of recyclability, non-hazardous side products and scale up to gram level.

Later, the same researchers identified a sustainable methodology in order to construct isoquinolines with the help of Ru(II)/PEG-400, a reusable catalytic system [106]. Annulation reaction of *N*-tosylhydrazone with alkynes could be feasible

through C–H/N–N functionalization. The developed methodology is more cost-effective and greener due to reusability of catalytic system, easy extraction process, shorter reaction duration, biodegradable solvent, and adaptivity up to the gram scale.

Further, this catalytic system has been explored in order to activate ortho C–H bond of ketazines using microwave approach in favour of rapid, atom economic and sustainable synthesis of isoquinolines (Scheme 14) [107]. In the same report, the methodology has been extended successfully with the purpose of construction of isoquinolinones by ortho C–H functionalization of dibenzoylhydrazine. The protocol is highly atom economic as both the nitrogen atoms of directing groups could be incorporated to the anticipated products by annulation with alkynes through C–H/N–N bond functionalization. In addition, the method is environmentally benign due to considerably reduced duration with easy extraction process, catalyst reusability, external oxidant and silver or antimony salt-free conditions, gram-scale synthesis and employment of biodegradable solvent.

Besides the extensive exploration of $[RuCl_2(p\text{-cymene})]_2$ as homogeneous recyclable catalyst for C–H activation reactions, in 2017, Jian et al. employed the facile and reusable catalytic system for the straightforward arylation of heteroarenes by C–H bond activation utilizing reasonable aryl chlorides by means of electrophilic reagents (Scheme 15) [108]. A moderately economical catalyst $RuCl_3 \cdot xH_2O$ and environmentally benign solvent PEG-400 have been utilized in presence of air excluding any additive or ligand. The protocol enables the control of proportion of mono- to diarylated products easily by modifying the reaction circumstances. Moreover, the catalyst could be recycled for six times and the methodology could be effortlessly scaled up to the gram level using 0.3 mol% Ru catalyst.

In 2019, Ackermann group applied the extensively appropriate oxidative palladium-catalyst for the formulation of an effective protocol for the aerobic
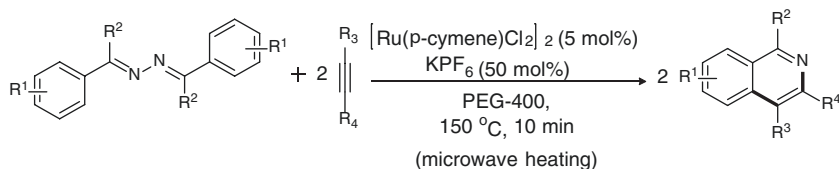
Scheme 14 Ru catalysed rapid annulation of ketazines
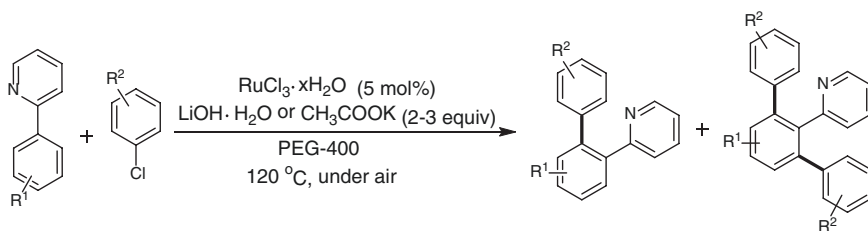
Scheme 15 Ru-catalysed direct arylation of heteroarenes
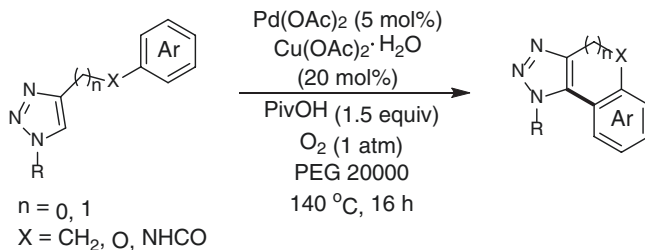
Scheme 16 Oxidative palladium catalyst for construction of cyclodehydrogenative biheteroaryl
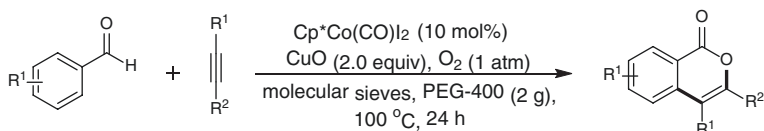
Scheme 17 Synthesis of isocoumarins by Cp*Co(III)-catalysed oxidative annulation of aromatic aldehydes

dehydrogenative C–H/C–H arylations of 1,2,3-triazoles (Scheme 16) [109]. A catalyst consisting Pd(OAc)$_2$ in PEG provided the exclusive construction of cyclodehydrogenative biheteroaryl, comprising the step-economical formation of bio-active derivatives in an aerobic manner. Moreover, the practicability of the aerobic C–H arylation was evidenced as the palladium in the PEG system perhaps reused up to the fourth cycle without substantial reduction in catalytic activity. Also, this recyclable system eliminates the employment of volatile and unsafe organic solvents as the reaction medium.

Recently, Tao et al. explored the recyclability of cost-effective first-row transition metal catalyst [110]. They have proposed environmentally mild and cost-effective Co/Cu/PEG-400 catalytic system for the oxidative cyclization of aromatic aldehydes in the combination of internal alkynes in favour of the access of isocoumarins (Scheme 17). This could be accomplished by ortho C−H bond activation of aromatic aldehydes using Cp*Co(III) catalyst and PEG-400. The catalytic system could be reused up to the third cycle with constant high effectiveness.

4 Oxidizing Directing Groups for C–H Functionalizations

The fascination of chemists to reduce steps of synthesis as well as the quantity of noxious waste generated, and, additionally, to discover benign and higher selective conversions have resulted in the expansion of the perceptions of green chemistry [11]. In this context, transition metal-catalysed cross-coupling transformations using C–H bond functionalizations have come up in the last decade as these conversions avoid the necessity for initial steps to activate the substrate. One of the most

prominent approach in order to realize the selectivity and controllability in C–H functionalization is the insertion of a heteroatom-containing neighbouring directing group (DG) into the substrate. Directing groups not only act as a Lewis base for coordinating the transition metal [111, 112] but also can lead the metal catalyst to a desired and precise reactive position out of many available sites and therefore enhance the selectivity to a great extent [26, 113]. Nevertheless, the application of DGs still possesses certain shortcomings [114], for instance (1) at the C–H activation step, only directing role is played by the DGs and fragment of it leftovers in the target molecule, (2) the installation and elimination of the directing group adds to the total count of operations for the synthesis, and (3) additional modification of the directing group is ever problematic as well as unreasonable, that mostly restricts the framework diversification of the desired molecule.

Accordingly, employment of inventive DGs possessing enhanced directing potentials and so characterizing convenient functional groups that are tuneable and exhibit higher standards of reactivity and selectivity should be favourable. On the other hand, regarding the catalytic cycle, it mostly comprises a high-oxidation-state transition-metals in the form of endorser and produces the anticipated products along with low-oxidation-state metal species generated by reductive elimination. Thus, the catalysts need to be regenerated in their active oxidation state. As a consequence of this, a general drawback in most of the transition metal-catalysed C–H functionalizations is the necessity of an equivalent or excessive amount of external oxidizing agents. These are mostly toxic metal salts like copper or silver salts, benzoquinone or potassium persulphate which are used for the turnover of the expensive transition-metal catalysts and to sustain the catalytic cycle. For instance, although conventional cross-coupling/cyclization reactions involving oxidation were extensively implemented for the formation of numerous heterocyclic compounds, in particular indoles [115], pyrroles [116], pyridines [117], isoquinolines [118] and isoquinolines [119], the DG performs only a directing function, and an equivalent quantity of external oxidizing agents is necessary in order to regenerate the catalysts. This creates an equivalent quantity of unwanted side products and off-cycle side reactions which obviously provides lower atom economy and reduces the total 'greenness' of the procedure. In the oxidative ruthenium-catalysed C–H annulation methodologies, air or molecular oxygen has even utilized as the oxidizing agent in the last few years [120, 121]. Thus, in the interest of conquering the shortcomings established by the external oxidizing agents, it would be superlative to endorse a technique for synthesis consisting ease, security, and environmental benignity along with superior selectivity as well as variety. The advancement of multiple role DGs could be among the best solutions to tackle this problem.

In order to regenerate the active transition-metal catalyst, a novel strategy was pioneered effectively by the researchers like Hartwig [122], Yu [123], Glorius [124], Guimond and Fagnou [125, 126] and Ackermann [127] individually. The employment of systems that serve together by means of DG as well as (internal) oxidizing agent simultaneously is an evolving tactic in the area of C–H functionalization chemistry [128]. This leads to enhanced levels of reactivity and additionally possesses obvious strengths of selectivity, yield and substrate scope. It also avoids the

necessity for an external oxidizing agent, furthermore developing the total 'greenness' of the method.

Directing group as an internal oxidant usually comprises a covalent bond, that is capable for oxidation of the metal with lower valency to sustain the turnover of the catalyst (for instance, via an oxidative addition), but is discrete from the C–H activated and functionalized position. The preliminary models of the internal oxidant applied an N–O bond of *N*-oxide, *N*-pivaloyloxy and *N*-methoxy functionality considering demanding shaft for C–N bond construction as well as catalyst turnover also. With the advancement of the internal oxidant approach, N–N, N–S, S–Cl and Si–H bonds were also recognized for this purpose. An initial emphasize by Patureau and Glorius [128] set attention for examining the merits proposed by redox-neutral tactic as compared to the analogous conversions which utilize external oxidants. The nitrogen-oxygen, nitrogen-nitrogen and oxygen-oxygen bonds are increasingly prevailing in the class of the established oxidative directing groups with the release of a small molecule like water, alcohol, carboxylic acid, and amide, that were employed for the turnover of Rh, Pd, Ru catalysts in redox-neutral coupling reactions [129–136]. However, other covalent bonds comprising heteroatoms are less efficient in the redox-neutral C–H functionalization reactions [137]. In comparison with the application of external oxidants, this technique can induce enhanced standards of reactivity and selectivity in addition to a wider scope. The approach is expanding within the field of C–H activation and it is successfully recognized for benign conditions and higher selectivity, thus, being of great synthetic value. In this view, this segment of the book chapter emphasises on the progress of this modern approach with some established protocols.

4.1   N–O Bond as an Internal Oxidant

A novel conceptual protocol has been provided by Tan et al. in 2010 for the palladium-catalysed straight amination of aromatic C–H bonds utilizing oxime esters as a directing group following redox-neutral strategy (Scheme 18) [122]. Using this methodology, indoles were synthesized effectively preventing disadvantages of the common approaches involving an external oxidizing agent [138, 139] or a strongly reactive nitrene as nitrogen source [140, 141].

Next, Chiba and co-workers established a methodology with moderate reaction conditions for the development of pyridine derivatives using easily accessible α,β-unsaturated ketoximes and internal alkynes (Scheme 19) [142]. The α,β-unsaturated
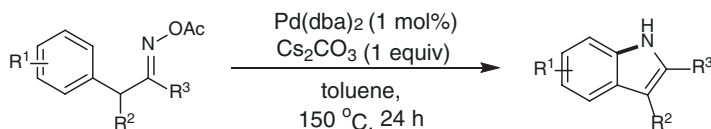
Scheme 18 External oxidant-free Pd(0)-catalysed indole synthesis
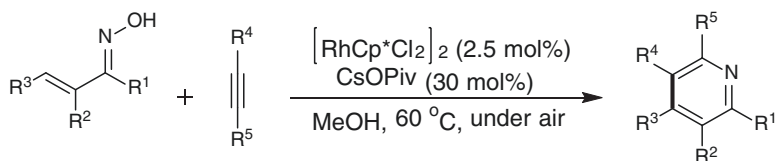
Scheme 19 Oxime as an internal oxidant for the access of pyridines

ketoximes undergo annulation reaction by activating vinylic C–H bond and developing C–N bond under redox-neutral conditions catalysed by [Cp*RhCl$_2$]$_2$–CsOPiv catalyst, in which the N–O bond of oximes is able to act as an internal oxidant.

Later, *N*-methoxybenzamides were explored in the form of an oxidizing directing group in favour of Rh(III)-catalysed olefination reaction via C–H bond functionalization in order to achieve moderate, rational, selective, and efficient development of tetrahydroisoquinolinone derivatives (Scheme 20) [124]. Moreover, the selectivity of the anticipated target molecules could be attained by modifying the substituent of the directing group.

Then ortho-alkenylated tertiary anilines were prepared by significantly selective ortho C–H olefination of smoothly accessible tertiary aniline *N*-oxides as a novel oxidizing directing group (Scheme 21) [133]. N–O bond acts as an internal oxidant in the given Rh(III)-catalysed C–H functionalization protocol.

Zhang et al. in 2014 documented a rhodium(III)-catalysed access of substituted acetophenones by combination of quinoline *N*-oxide and internal alkynes (Scheme 22) [143]. The process enabled the employment of the N–O bond as a directing group in order to activate C–H bond as well as acts as a source of an oxygen atom.

4.2 O−O Bond as an Internal Oxidant

Subsequently, the peresters have been also revealed itself effective in favour of the redox-neutral type of C–H activation reactions. In 2015, Cui with his colleagues established a moderate and effective Rh(III)-catalysed redox-neutral C–H functionalization of peresters for the access of different isocoumarins by annulation with alkynes (Scheme 23) [130]. This methodology, for the first time, reports the splitting of an oxidizing O−O bond as an internal oxidant.

4.3 N–N Bond as an Internal Oxidant

The N–N bond has been also proved to have excellent potential for the redox-neutral kind of reactions. In 2013, Wang et al. achieved annulation of *N*-substituted *N*-phenylnitrous amides with internal alkynes for the construction of *N*-alkyl indoles using Rh(III) catalyst excluding the use of any external oxidant or additive (Scheme 24)
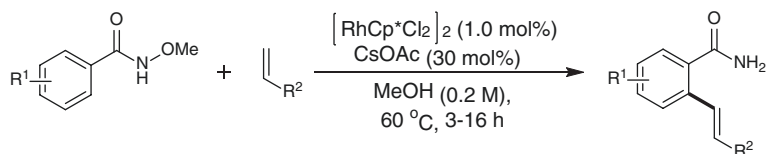
Scheme 20 Rh(III)-catalysed olefination using *N*-methoxybenzamides directing group
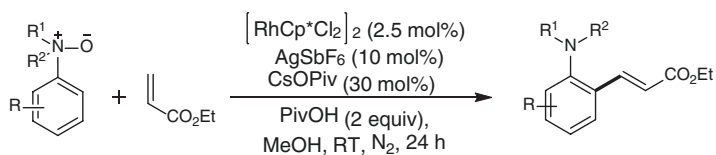
Scheme 21 *N*-oxides assisted C–H olefination reaction
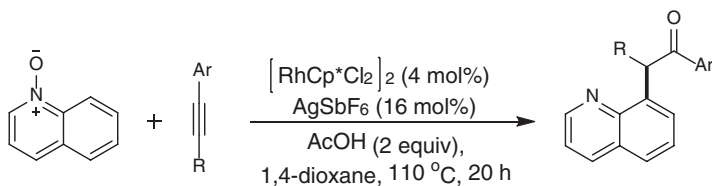
Scheme 22 N–O bond as an internal oxidant for Rh(III)-catalysed access of substituted acetophenones
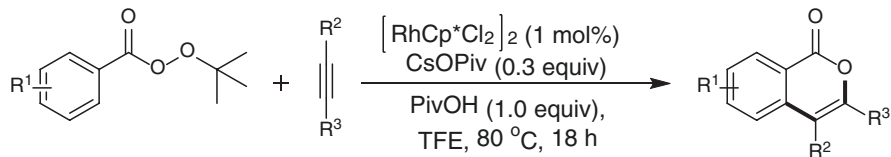
Scheme 23 Peresters as an oxidizing directing group for the redox-neutral access of isocoumarins
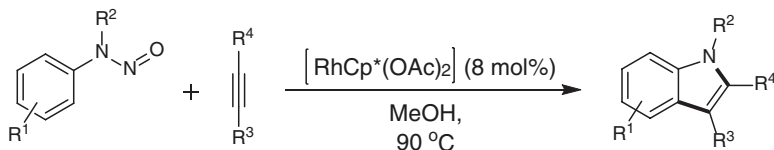
Scheme 24 Rh(III)-catalysed synthesis of indoles using N–N bond as an internal oxidizing agent
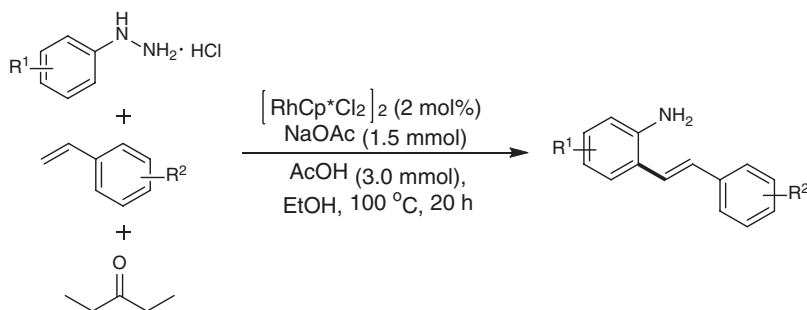
Scheme 25 Access to 2-vinylanilines by rhodium(III)-catalysed olefination of hydrazones
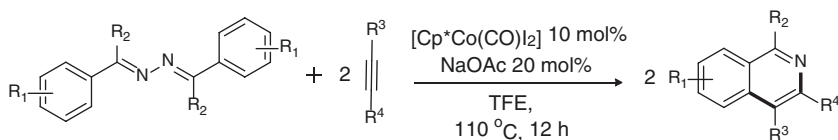
Scheme 26 Cp*Co(III)-catalysed C–H/N–N functionalization in order to synthesize isoquinolines

[144]. The novel nitroso directing group acts as an internal oxidant for the redox-neutral type C–H functionalization reactions by cleaving N–N bond. The protocol highlighted a facilitating catalytic system and operational process with improved regioselectivity.

Later, Muralirajan et al. generated hydrazones in situ from arylhydrazine and ketone for its Rh(III)-catalysed olefination by activating ortho C–H bond [145]. The methodology provides an external oxidant-free and easy access to unprotected 2-vinylanilines by the application of ketazines as a directing group along with internal oxidant for catalyst turnover in C–H functionalization reaction (Scheme 25).

Further, symmetrical ketazines were explored in the form of an oxidizing directing group by Deshmukh et al. in order to access isoquinolines by C–H/N–N bond functionalization/annulation reaction (Scheme 26) [146]. The proposed methodology works efficiently using air-stable Cp*Co(III), a first-row transition metal catalyst having additional superiority of cost-effectiveness, atom economy and gram-scale synthesis.

4.4 N–S Bond as an Internal Oxidant

The N−S bond also proved to have application as an internal oxidant for redox-neutral reactions and this was claimed for the first time by Dong and co-workers in 2014 (Scheme 27) [147].
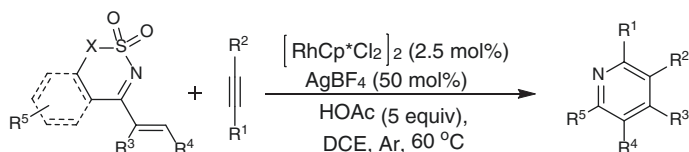
Scheme 27 N–S bond as an internal oxidant for synthesis of pyridines

They have reported the first example of N–S bond of *N*-sulphonyl ketimines working as a discrete internal oxidizing agent in order to access highly functionalized pyridines by reaction with internal alkynes via rhodium(III)-catalysed C–H bond functionalization. This methodology comprises desulphonylation and C–C/C–N bond development within moderate reaction circumstances.

4.5 N–C Bond as an Internal Oxidant

The application of N–C bond as an internal oxidant has been mentioned by Gogoi and co-workers. They constructed 8-amido isocoumarins using easily accessible isatins as the oxidizing directing group (Scheme 28) [148]. The Ru(II)-catalysed protocol follows the redox-neutral type annulation reaction with alkynes via C–H bond functionalization in which the C–N amide bond of isatins acts as an internal oxidant.

4.6 S–Cl Bond as an Internal Oxidant

The example of the S–Cl bond as an internal oxidant was explained by Wu and co-workers for the chemo- and regioselective development of sulphonylated quinoline *N*-oxides (Scheme 29) [149]. A convenient strategy was given for inexpensive copper(I)-catalysed direct C2-sulphonylation of quinoline *N*-oxides using commercially accessible and cost-effective sulphonylation reagents by activating the C–H bond utilizing the sulphur–chlorine bond as an internal oxidant.

4.7 Si–H Bond as an Internal Oxidant

Ureshino et al. in 2010 proposed rhodium-catalysed dual activation of Si–H and C–H bonds of biarylhydrosilanes in order to synthesize silafluorenes through dehydrogenation (Scheme 30) [150]. The methodology occurs by a fascinating internal oxidant approach in which the Si–H bond plays function of internal oxidant avoiding the requirement of any external oxidant.
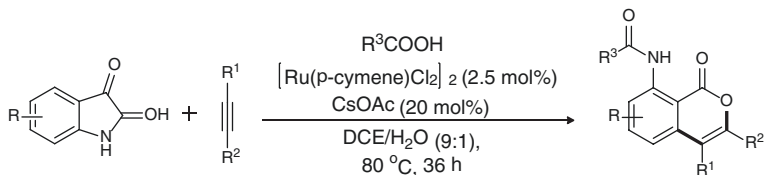
Scheme 28 N–C bond as an internal oxidant for synthesis of isatins
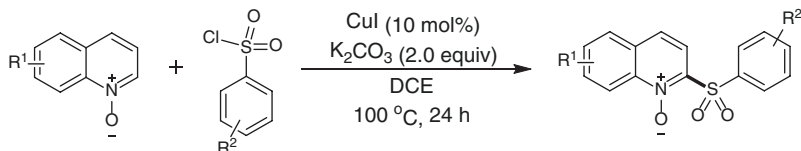
Scheme 29 S–Cl bond as an internal oxidant for synthesis of sulphonylated quinoline *N*-oxides
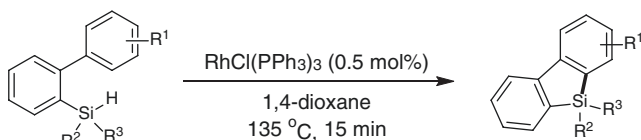
Scheme 30 Rh(I)-catalysed synthesis of silafluorenes
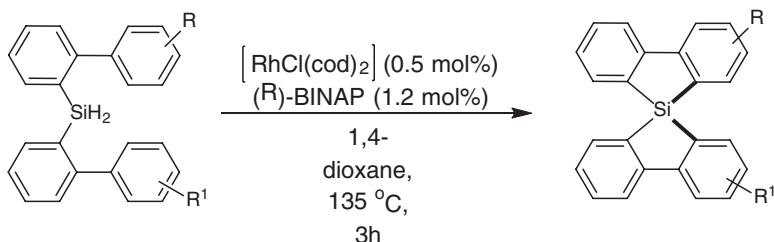
Scheme 31 Rh(I)-catalysed double dehydrogenative cyclization of bis(biphenyl)silanes

Afterwards, Takai research group again revealed the role of Si–H bond as an internal oxidant in the report of asymmetric access to chiral spirosilabifluorenes from bis(biphenyl)silanes catalysed by rhodium(I) metal along with a chiral phosphine ligand (Scheme 31) [151]. The protocol proceeds through double dehydrogenative cyclization of bis(biphenyl)silanes and provides chiral products with improved yields as well as enantioselectivities.
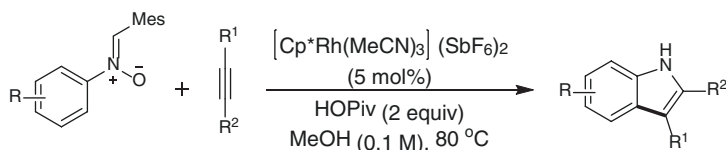
Scheme 32 Nitrones as the oxidizing directing group for the C–H annulation reaction

4.8 Other Internal Oxidizing Directing Groups

In addition to the above-mentioned bonds, some other functional groups are also known to possess the role of the internal oxidant (Scheme 32) [152]. For instance, nitrones were applied in the form of the oxidizing directing group for the rhodium(III)-catalysed activation of C–H bond succeeded by annulation with alkynes in order to synthesize indoles. The redox neutral tactic eliminates the necessity of an external oxidizing agent as well as it also exhibits enhanced functional group toleration.

5 Synthesis in Green Solvents Using C–H Activation

C–H activation by transition metal catalysis has evolved as a significant methodology in syntheses and developed as an alternative to the conventional way for cross-coupling methods. Given these significant achievements, the reaction solvents used for C−H activation reactions are a serious issue of concern from the environmental point of view. The most commonly used solvents viz. acetic acid (AcOH), toluene, trifluoroethanol (TFE), trifluoroacetic acid (TFA), dimethylacetamide (DMA), dichloromethane (DCM), tetrahydrofuran (THF), 1,4-dioxane, dichloroethane (DCE), methanol (MeOH), dimethylformamide (DMF), and *N*-methyl-2-pyrrolidone (NMP) are utilized for C–H activation processes possess toxic, volatile, explosive, and flammable nature. To overcome this issue, the green solvent concept has been evolved to build the sustainable approach towards C–H activation [153–155]. Variety of solvents with bio-based, non-toxic and sustainability nature have been developed to minimize the organic pollution occurred as a result of chemical synthesis. Solvents derived from biomass sources are utilized for transition metal-assisted C–H activation processes and a brief overview of these solvents is discussed in this section. Several review articles have presented an overview of reactions of C–H activations in green solvents [153–155].

In recent years, a major emphasis has been on further enhancing the sustainability of the C–H activation strategy. Organic pollution is mainly founded by organic solvents used in the chemical reactions; hence, a variety of renewable, bio-based and non-hazardous solvents have been developed and used as subsidiary solvents in place of organic solvents. Bio-based solvents are commercially available and shows varied properties with high viscosity, solubility, melting point, low toxicity,

non-volatility and good biodegradability. The safe, readily available, cost-effective and non-flammable nature of bio-based solvent makes them as eco-friendly solvents in organic reactions. Herein, in this section, we have summarized representative illustrations of C–H activation of the well-known green solvents like water and bio-based solvents such as polyethylene glycols (PEG), gamma-valerolactone (GVL) or 2-methyltetrahydrofuran (2-MeTHF).

5.1 Water

Many of the alternative solvents [156, 157] have demonstrated the purpose of green solvents for various organic transformations and to meet the green chemistry principle of limiting the use of organic solvents to reduce chemical waste, but none of them are as green as water. Water acts as green solvent due to its various properties such as abundance, cost-efficiency, environment compatibility, non-toxicity and non-flammability.

Variety of examples of C–H activation using water as solvent have been reviewed in recent review articles [154, 158, 159]. Ackermann et al. established the ruthenium-catalysed C–H bond alkenylation of aromatic sulphonic acids, sulphonamides and sulphonyl chlorides in water as solvent (Scheme 33) [160]. The reaction proceeded without the addition of additive but addition of $AgSbF_6$ led to a significant boost of reaction efficiency.

Upadhyay et al. developed a process for isoquinolines synthesis via C–H activation reaction of benzamides catalysed by Rh using water as solvent and air as a solitary oxidant (Scheme 34) [161]. The developed protocol showed maximum yield of product and precipitation of product after completion of the reaction with the use of water as solvent and displayed different regioselectivities with substituted alkynes and meta-selectivity with meta-alkynes.
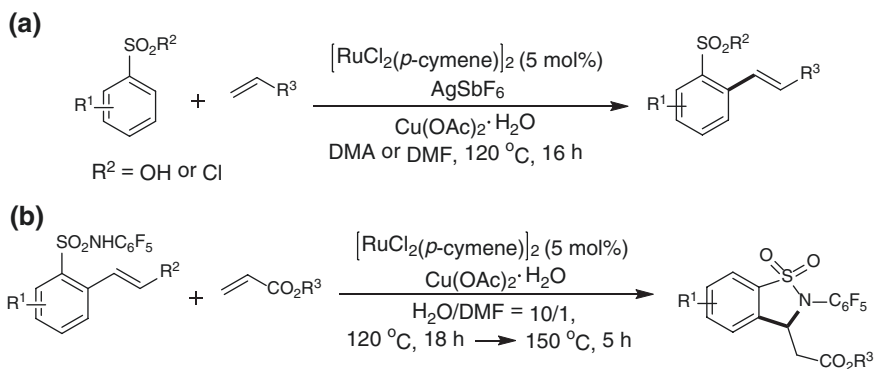
Scheme 33 Ru-catalysed (**a**) C–H bond alkenylation of aromatic sulphonic acids and/sulphonyl chlorides and (**b**) C–H bond alkenylation of sulphonamides
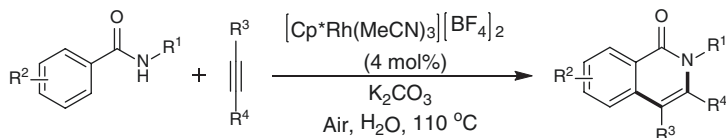
Scheme 34 Rh-catalysed C–H activation of substituted benzamides
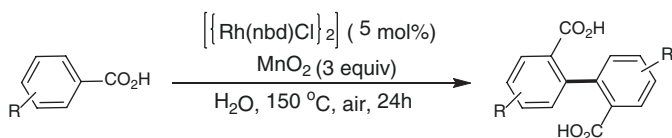
Scheme 35 Rhodium(I)-catalysed oxidative dimerization reaction of aromatic acids

Li et al. for the first-time developed rhodium(I)-catalysed oxidative dimerization reaction of aromatic acids to obtain 2,2′-diaryl acids by two direct C–H bond activations in water (Scheme 35) [162]. Practical application of the developed procedure has demonstrated for the construction of the antitumor natural product ellagic acid in an effective and regiospecific manner.

Hu et al. developed Pd-catalysed β-C–H arylation reaction of ketones and arylboronic acids in water with very mild reaction conditions. Arylboronic acids used as nucleophilic aryl sources and *o*-iodoxybenzoic acid as the oxidant have been used in this direct β-C–H arylation reaction (Scheme 36) [163]. This method offers a succinct pathway for the production of β-arylated ketones and direct asymmetric β-C–H arylation reaction of ketones could be performed.

Pu et al. explored the C–H alkylation reaction of maleimides and aromatic acids in water and reaction showed varying chemoselectivity with substituted benzoic acid (Scheme 37) [164]. In this reaction, the carboxyl group played an important role of a classical or traceless directing group and thereby generated two different products, i.e. 2-alkyl substituted benzoic acids and alkyl-substituted benzenes.

Recently in 2019, studies for Pd(II)-catalysed C(sp^2)–H arylation and methylation of methyl, aryl, heteroaryl iodides, and sp^2 carbons both at β- and γ-positions were performed by Mitra et al. (Scheme 38) [165]. Synthesis of pyridine and arylated acid synthons was carried out with the use of 3-amino-1-methyl-1*H*-pyridin-2-one as bidentate *N,O*-directing group (DG) in the aqueous medium.

Maji et al. for the first-time developed synthesis of chromones by means of Ir-catalysed C–H functionalization and annulation of salicylaldehyde and diazoketones (Scheme 39) [166]. This protocol afforded the C-3 substituted chromones in good yield by one-pot decarboxylation and employing *tert*-butyl diazoester.
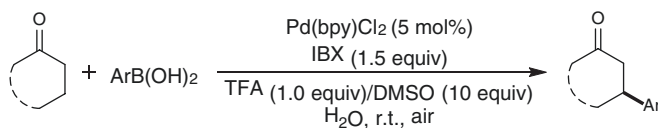
Scheme 36 Pd-catalysed direct β-C–H arylation reaction of arylboronic acids and ketones
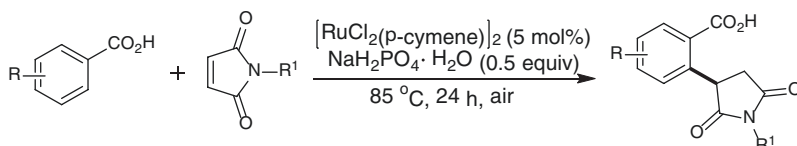
Scheme 37 Ru-catalysed C–H alkylation reaction of aromatic acids with maleimides

R = H, F, Me; n = 0,1
R^1 = Me, benzyl
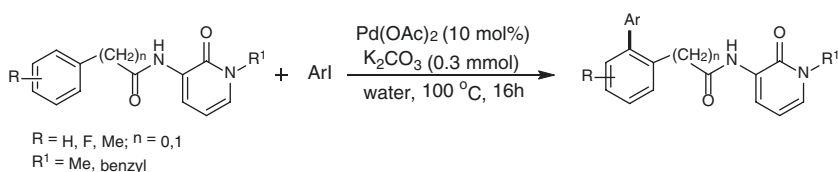
Scheme 38 Pd-catalysed C(sp^2)–H arylation and methylation in water
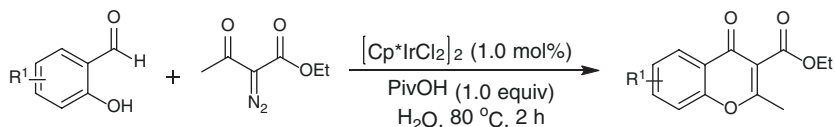
Scheme 39 Ir-catalysed C–H functionalization and annulation reaction of salicylaldehyde and diazo-ketones

5.2 Polyethylene Glycols (PEGs)

With various important properties of polyethylene glycols (PEGs) such as non-corrosive and non-flammable nature and ready availability, and its easy availability in the varied array of molecular weights in the range of 300 to 10,000,000 g/mol, makes PEG as a green reaction media for various organic transformations [91, 167, 168]. Results for this part of the work has been mentioned in the homogeneous reusable media for C–H activation reactions (please refer Sect. 3 of this chapter). Several review articles in the past years have reviewed the C–H activation research work performed in PEG solvent [168]. Ruthenium-catalysed isoquinolines synthesis were performed using PEG solvent [169, 170]. Ruthenium-catalysed synthesis of isobenzofuranones [120] was also developed in combination with Cu catalyst in PEG-400/water (3:2) solvent system (Scheme 40) and afforded good yield with wide substrate scope for substituted benzoic acid and electron deficient alkenes [104].
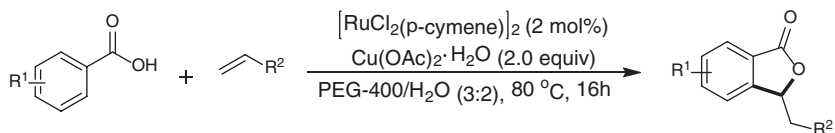
Scheme 40 Ruthenium-catalysed synthesis of phthalides via C−H alkenylation in PEG-400/H_2O
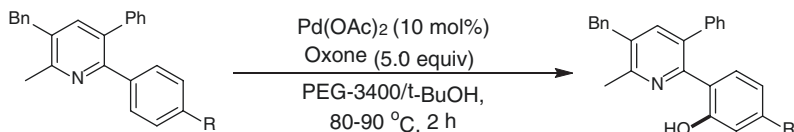
Scheme 41 Pd-catalysed C−H hydroxylation of 2-arylpyridines in PEG-3400/t-BuOH
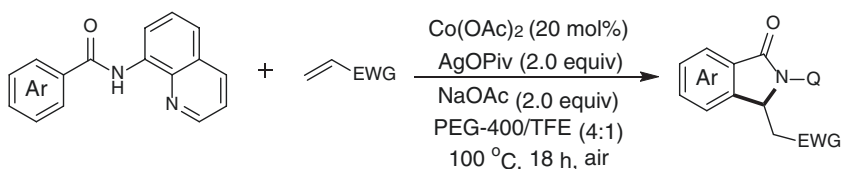
Scheme 42 Co-catalysed isoindolinone synthesis in PEG-400/TFE

Palladium-catalysed hydroxylation of 2-arylpyridines to monohydroxylated products (Scheme 41) were obtained in a combination of PEG-3400/t-BuOH by Kim et al. [171]. The Ackermann group explored the study of cobalt-catalysed C–H activation in PEG solvent for construction of isoindolinones from alkenes and aromatic amides [172] and later used this protocol along with AgOPiv and Co(OAc)₂ playing the role of an oxidant and the catalyst respectively (Scheme 42).

Cui and co-workers later on demonstrated the cobalt-catalysed C–H/N–N activation reaction to synthesize isoquinoline derivatives from alkynes and benzylamides in PEG-400 solvent (Scheme 43) [173]. This protocol led to the development of desired isoquinolines with successful participation of both internal and terminal alkynes in the activation reaction.

5.3   2-Methyltetrahydrofuran (2-MeTHF)

A cost-effective and readily available solvent, 2-methyltetrahydrofuran (2-MeTHF) is synthesized using sustainable sources of levulinic acid and furfural [174–178]. McMullin et al. detailed the *ortho*-C–H-alkenylation of *N*-aryloxazolidinones with the use of [RuCl₂(*p*-cymene)]₂, Cu (OAc)₂ · H_2O and AgSbF₆, in 2-MeTHF as green solvent (Scheme 44a). Studies performed by Frost et al. also demonstrated that Ruthenium catalysts were very effective in 2-MeTHF for structurally related *N*-aryl
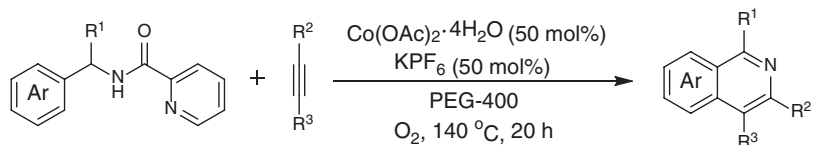
Scheme 43 Cobalt-catalysed C–H/N–N activation reaction for isoquinolines synthesis in PEG-400

(a) oxazolidionone DG
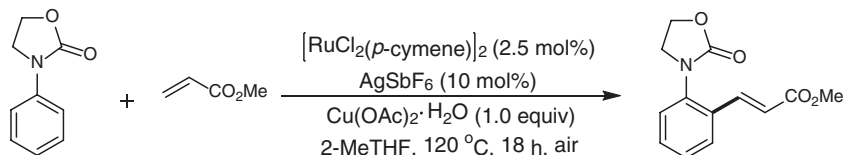
(b) hydantoin DG
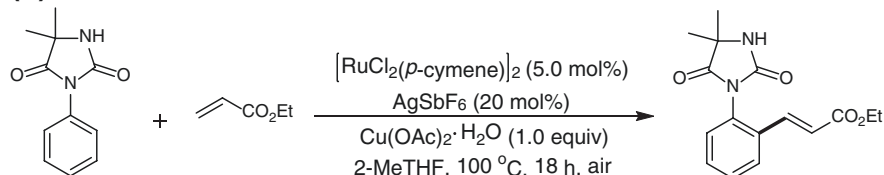
(c) succinimide DG
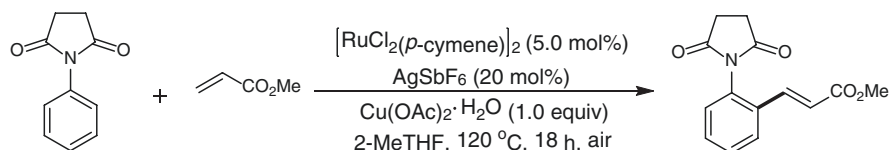
(d)
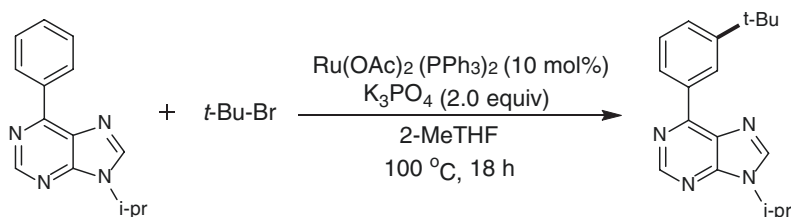
Scheme 44 2-MeTHF as a green solvent for Ru-catalyzed (**a**) alkenylation of oxazolidinones, (**b**) alkenylation of hydantoin, (**c**) alkenylation of succinimide, (**d**) alkylation of purines

hydantoins and *N*-aryl succinimides (Scheme 44b, c). On the other hand, [Ru(OAc)$_2$(PPh$_3$)$_2$] as the catalyst was utilized for meta-selective C–H alkylation of purines by Ackermann et al. (Scheme 44d) [178].

(a)

(b)
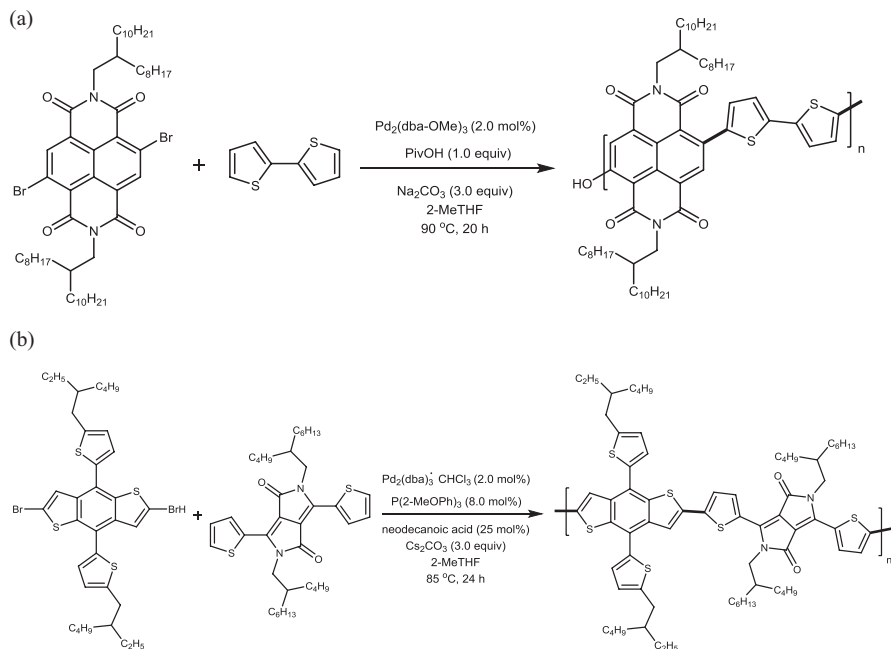
Scheme 45 2-MeTHF as a green solvent for Pd-catalyzed synthesis of (**a**) PNDIT2 and (**b**) benzodithiopene-alt-diketopyrrolopyrrole

Synthesis of novel bioactive compounds is achieved with direct C−H arylation polymerization using palladium catalysts. Sommer et al. demonstrated the palladium-catalysed synthesis of PNDIT$_2$ (n-type copolymer) in 2-MeTHF from unsubstituted bithiophene and 2,6-dibromonapthalene diimide (NDIBr$_2$) and achieved 98% yield of PNDIT$_2$ under optimized conditions (Scheme 45a) [179]. Recent work by Marks et al. presented the palladium-catalysed DAP reaction in 2-MeTHF for the synthesis of benzodithiopene-alt-diketopyrrolopyrrole (Scheme 45b) [180].

Cook et al. explored the iron-catalysed ortho-alkylation reaction of aromatic amides in 2-MeTHF [181, 182] and used 8-aminoquinolines as bidentate chelating aid with Fe(acac)$_3$ as iron precursor catalyst and 1,2-dis(diphenylphosphino)ethane (dppe) as the ligand (Scheme 46a, b).

5.4 γ-Valerolactone (GVL)

γ-Valerolactone (GVL) is a completely degradable, bio-based aprotic solvent obtained from lignocellulosic biomass and carbohydrates [183–186]. Recently, Ackermann/Vaccaro reviewed the use of GVL as a green and eco-friendly reaction solvent for transition metal-assisted organic transformations [187, 188].

a) primary alkylation
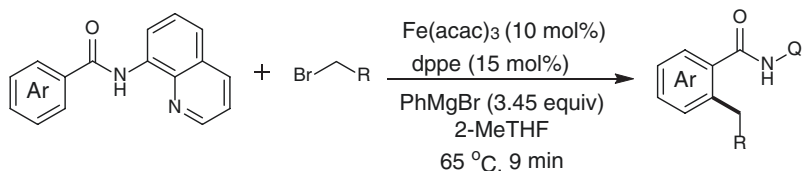
b) secondary alkylation
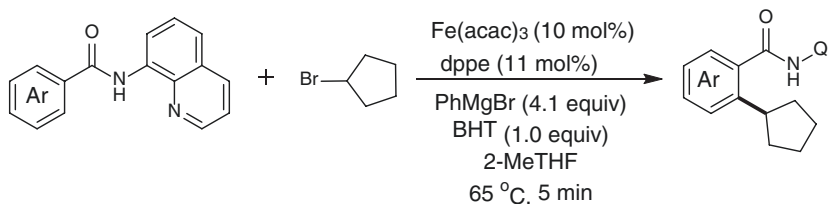
Scheme 46 2-MeTHF as a green solvent for iron catalyzed (**a**) primary alkylation and (**b**) secondary alkylation of aromatic amides

Various palladium-catalysed C–H activation reactions using GVL as a green solvent has been reported in the literature [185]. Few representative examples are mentioned here. In 2016, Ackermann and Vaccaro demonstrated the utilization of GVL as a green solvent for palladium-catalysed Catellani reaction and effectiveness of GVL was observed over other classical solvents like DMF, NMP and MeCN [189]. Use of two palladium sources viz. Pd EnCat 30 and Pd/Al$_2$O$_3$ was demonstrated for reaction (Scheme 47a) and the later found to be very robust in nature due to low leaching (~2 ppm) and recyclability of the catalyst. Direct arylation reaction of 1,2,3-triazoles and aryl bromides was represented by the same groups using Pd/C catalyst and GVL as solvent (Scheme 47b) [190] and found to be effective for wide functional group tolerance and excellent position selectivity with high yields. Moreover, Ackermann and Vaccaro et al. explored the continuous flow C−H functionalization of 1,2,3-triazoles with the use of Pd/C catalyst and organic base and GVL as a solvent (Scheme 47c) [191]. This demonstrated continuous flow strategy led to the great durability, efficient recovery and recyclability of the catalyst.

Very few examples of the Ruthenium-catalysed C–H functionalization methods using GVL as a reaction medium has been developed by Ackerman group (Scheme 48) [183–188]. Ruthenium-catalysed oxidative alkenylation reaction to synthesize phthalide derivatives from alkenes and aryl carboxylic acids is reported using molecular oxygen playing a role of an oxidant and GVL as a reaction media (Scheme 48a) [192]. Alkenylation of arylacetamide was performed in the GVL solvent by Ackerman's group (Scheme 48b) [193].

GVL solvent found to be beneficial for cobalt-catalysed Himaya type C–H functionalization involving arylation of interesting C(sp^3)–H bond (Scheme 48c) [194].

a)

b)

c)
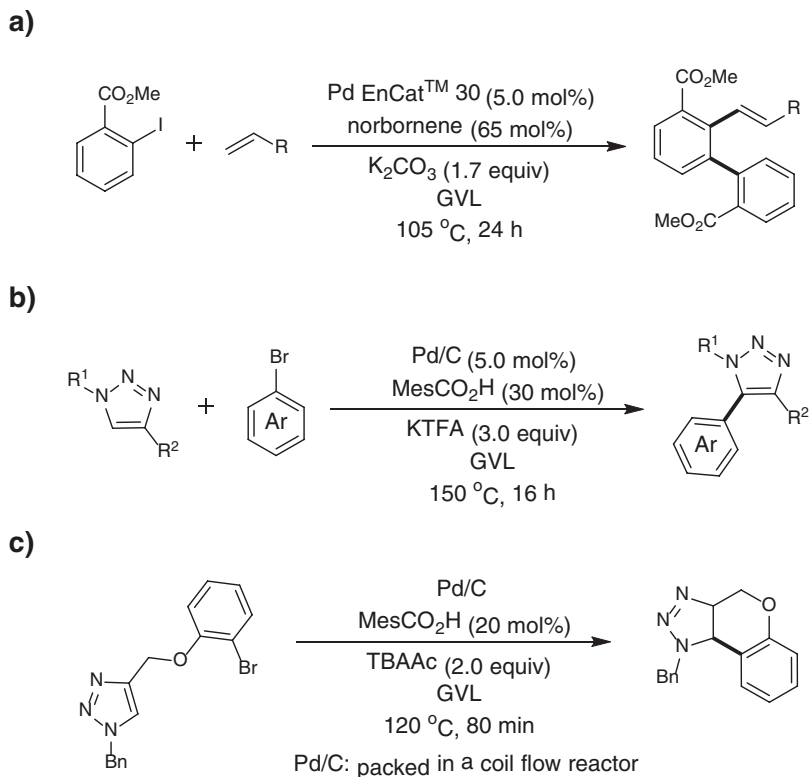
Scheme 47 GVL as green reaction medium for palladium catalyzed (**a**) Catellani reaction, (**b**) direct arylation reaction of 1,2,3-triazoles and aryl bromides and (**c**) continuous flow approach for the C–H functionalization of 1,2,3-triazoles

6 Photocatalytic C–H Bond Activations

Heterocyclic compounds involving a variety of natural compounds and synthesized pharmaceutical moieties occur in a broad scope of biologically active molecules. In the course of the past decade, synthesis of heterocyclic compounds through C–H activation reaction has attracted increasing attention from organic chemists [23, 153, 195–198]. Due to its eco-friendly and energy-conversant features, visible-light-mediated photoredoxcatalysis has experienced quick improvement over the previous decade. As of late, the utilization C–H functionalization by visible light-mediated photocatalysis [199–201] for the development of heterocyclic frameworks has risen as developing area in the organic synthesis [195–202]. Functionalization of different classes of organic compounds comprising ethers, alcohols, aldehydes, ketones, amides, esters, nitriles, alkyl aromatics, and alkanes could be performed by photocatalysed C–H functionalization [203–205]. This section of the book chapter gives an overview of the representative examples of C–H activations with the aid of photocatalysis.

a)

b)

c)
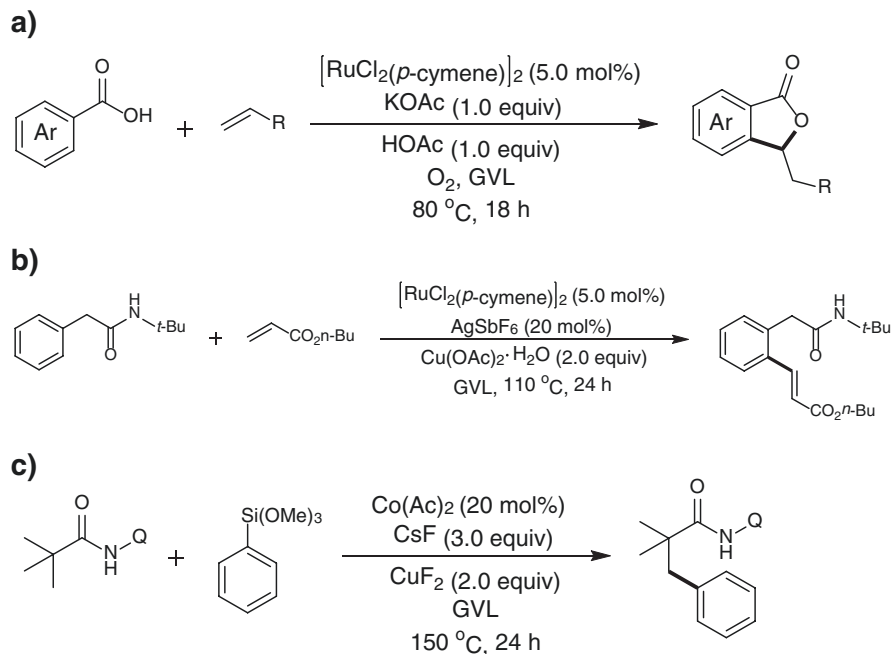
Scheme 48 GVL as a green solvent for (**a**) Ruthenium catalyzed oxidative alkenylation reaction to synthesize phthalide derivatives, (**b**) Ruthenium catalyzed alkenylation of arylacetamide and (**c**) cobalt-catalyzed Himaya type C–H functionalization involving arylation
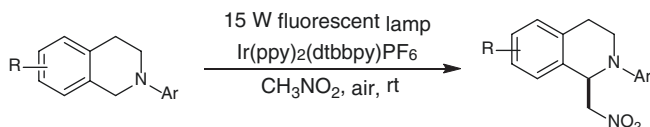
Scheme 49 Visible-light-induced Aza-Henry reaction of nitroalkanes and tertiary *N*-arylamines

Stephenson's group in 2010 demonstrated the visible-light-mediated α-amino C–H bond functionalization of tetrahydroisoquinoline using nitroalkanes along with tertiary *N*-arylamines through an oxidative approach of aza-Henry reaction (Scheme 49) [206]. This simple methodology afforded high chemical yield with very low catalytic amount 1 mol% Ir(III) catalyst with no usage of outside oxidant. Xiao's group has demonstrated major contributions in the area of photocatalytic C(sp^3)–H activation for the construction of heterocycles [207–211].

In 2011, Xiao et al. explored a photocatalytic strategy to synthesize pyrrolo[2,1-*a*] isoquinolines by visible-light-mediated oxidation reaction with [3 + 2] cycloaddition reaction followed by aromatization with oxidative approach (Scheme 50) [207]. This novel strategy provided rapid access to different derivatives of pyrrolo[2,1-*a*] isoquinolines in a significant yield.
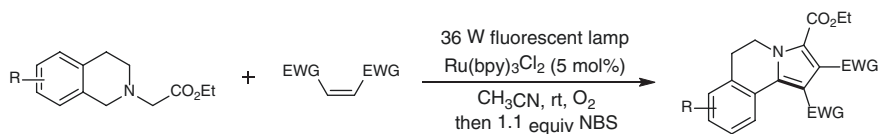
Scheme 50 Visible-light-mediated C–H bond functionalization for the synthesis of pyrrolo[2,1-*a*] isoquinolines
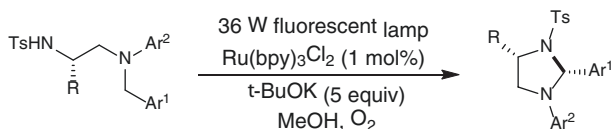
Scheme 51 Ruthenium-catalysed visible-light-induced intramolecular cyclization of diamines

The same group discovered a methodology to develop diastereoselective tetrahydroimidazoles by cyclization of diamines via visiblelight-assisted C–H bond activation (Scheme 51) [211]. The developed strategy results in the production of diastereoselective products with good yields.

Rueping et al. in the same year demonstrated the construction of *N*-heterocycles through visible-light-assisted azomethine ylide formation using Ru catalyst (Scheme 52) [212]. Cycloaddition reaction along with photoredox cycle has been merged for the first time to attain the simultaneous formation of two C–C bond in a diastereoselective manner.

Visible light photoredox-assisted C–H activation of tertiary amines for the construction of tetrahydroquinoline derivatives (Scheme 53) has been developed by Rueping et al. [213]. In this inter- and intramolecular way of C–H activation reaction, oxygen served the purpose of chemical shift to generate two different products from the similar starting material but with different pathways.

In 2014, Zhou et al. [214] demonstrated the iridium-catalysed visible-light-induced synthesis of 3-acylindoles by oxidative cyclization reaction of *o*-alkynylated *N,N*-dialkylamines in good yields (Scheme 54). This particular strategy of an intramolecular oxidation allowed simultaneous construction of C–O and C–C bonds.

Different results have been published in the past for the photocatalytic sp^2 C–H activation reactions for the reductive dehalogenation of activated carbon–halogen bond [215], formation of 2-substituted benzothiazole from thioamide [216], 2,3-disubstituted indoles [217], formation of carbazole [218], synthesis of indole derivatives [211, 219], and good yield of product has been obtained with the photoredox catalysis by avoiding harsh conditions, high temperatures and catalyst loadings.

Wu et al. in 2015 demonstrated visible-light-assisted C–H bond activation of amino acid (Scheme 55) using Ru(bpy)$_3$(PF$_6$)$_2$ as a photosensitizing agent and Co(dmgH)$_2$pyCl as a catalyst [220]. Various indole moieties, β-keto esters and glycine esters or indole derivatives were transformed to the expected products of cross-coupling reaction with great yields under visible light irradiation.
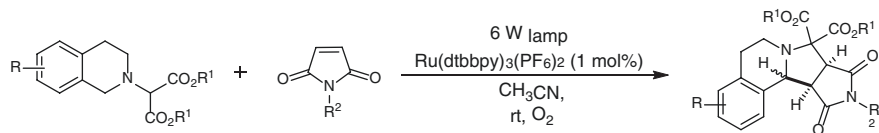
Scheme 52 Visible-light-assisted synthesis of *N*-heterocycles via ylide development and cycloaddition reaction
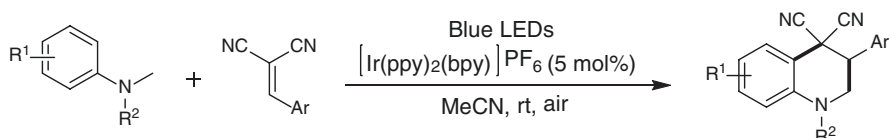
Scheme 53 Visible-light-catalysed C–H activation reaction of tertiary amine
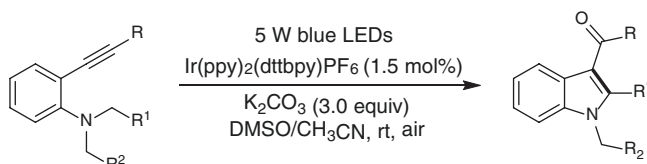
Scheme 54 Visible-light photoredox synthesis of 3-acylindoles from amines
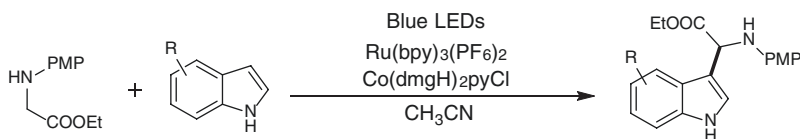
Scheme 55 Visible light-mediated C−H bond activation of amino acid for construction of indoles and H$_2$evolution
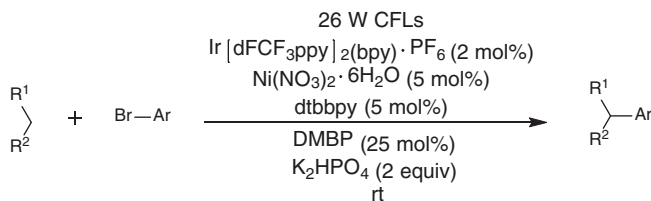
Scheme 56 Photochemical Ni-catalysed C−H arylation of (hetero)aryl bromides

Nickel-catalysed photochemical C–H arylation for coupling of benzylic C(sp^3)−H bonds with (hetero)aryl bromides using Ir photocatalyst (Scheme 56) has been demonstrated by Heitz et al. [221]. Mechanistic investigation performed suggested that excitation of nickel and generation of bromine radical are facilitated by energy transfer in triplet−triplet mode using iridium photocatalyst.
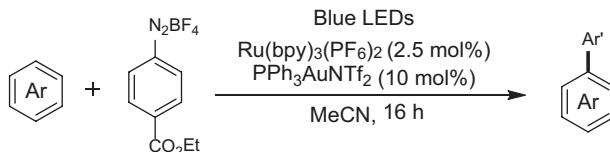
Scheme 57 Gold-catalysed photoredox C–H activation of arenes

Lee et al. in 2017 established the first protocol for cross-coupling of arene moiety through gold catalysed C–H activation by merging gold and photoredox dual catalysts (Scheme 57) [222]. Major limitation encountered with the earlier gold-catalysed C–H activation owe to the usage of stoichiometric oxidants and generated waste [223].

This drawback is overcome via dual catalyst approach and also offered good regioselectivity with simple reaction protocol. By using conjugated *N,O*-bidentate copper (II) complexes as a novel photoinitiators, free radicals were generated by UV treatment and these free radicals were used for intramolecular imine C–H bond activation to construct cyclized products (Scheme 58) [224].

Combination of photocatalysis and organocatalysis carried out a selective C–H alkylation of alcohols to construct lactone derivatives (Scheme 59) by a group of Kokotos [225]. In this strategy, phenylglyoxylic acid was used as photocatalyst and household bulbs are utilized as a light source. Using this simple method, C–H activation-alkylation/lactonization of alcohols were performed with α, β-unsaturated esters to obtain γ-lactones in excellent yields.

Effective use of uranyl nitrate hexahydrate as a photocatalyst was performed under blue light irradiation for direct conversion of C–H bond to C–C bond via hydrogen atom transfer (HAT) [226].

This protocol offered smooth functionalization of unactivated (cyclo)alkanes with electrophilic olefins (Scheme 60).

Moreover, $C(sp^3)$–H activation of allylic and benzylic hydrocarbons is a challenging task but this is achieved by Gong's group [227] using a combined approach of a hydrogen atom transfer (HAT) organophotocatalyst and a chiral bisoxazoline (BOX) catalyst of a non-precious transition metal (Scheme 61). Rapid and low-cost strategy enabled to activate benzylic, allylic hydrocarbons unactivated alkanes moiety with excellent regioselectivity (up to >50:1 r.r.) and stereoselectivity (up to 99.5% e.e.) in the products.

Another breakthrough achievement was established by Greaney et al. in visible light-induced C–H activation of arenes using dual-function ruthenium catalysis [228]. Developed reaction protocol operates at room temperature and provides a wide substrate range for a variety of heteroarenes when coupled with aliphatic halides affording C–C coupling products in good yield (Scheme 62).

On the other side, alkyl aminative defunctionalization of non-activated alkenes via radical pathways is still limited and performed with intramolecular versions [229–231]. However, the report by Li et al. demonstrated the aminative difunctionalization reaction of non-activated alkenes using copper-catalyst with *N*-halodialkylamines as the terminal dialkylamino source (Scheme 63) [232]. With
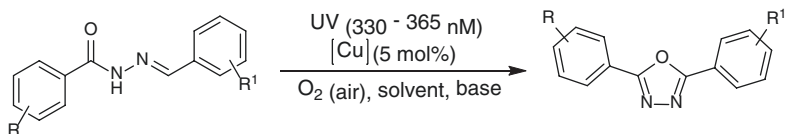
Scheme 58 Intramolecular imine C–H bond activation
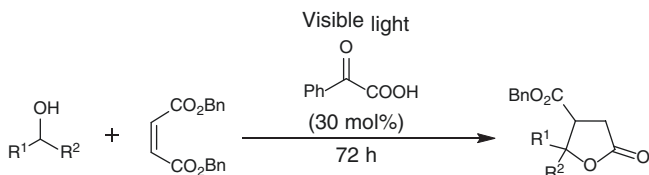
Scheme 59 C–H alkylation/lactonization of alcohols to γ-lactones
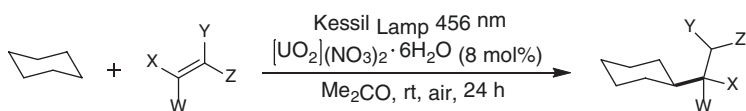
Scheme 60 Uranyl-photocatalysed C−H to C−C bond conversion
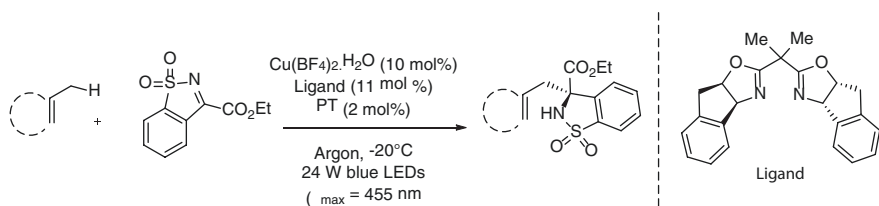
Scheme 61 C(sp3)–H activation of allylic and benzylic hydrocarbons
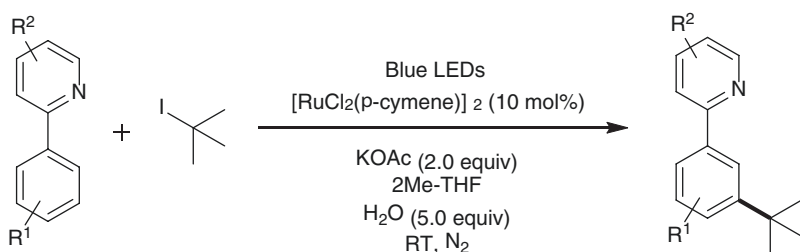
Scheme 62 Ruthenium-catalysed C–H activation reaction of arenes with aliphatic halides
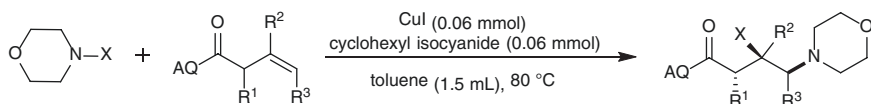
X = Cl or Br

Scheme 63 Copper-catalysed aminative difunctionalization of non-activated alkenes

the use of this reaction protocol, intramolecular amoniohalogenation and a three-component aminoazidation reaction were conducted in a very efficient way with remarkable regioselectivity and stereoselectivity in the products.

Various recent articles in the literature presented the major significant contributions in C–H functionalization including radical addition to *N*-tosylimines using decatungstate photocatalyst [233], α-C–H alkynylation of ethers and alkynyl bromides [234], metal-free alkylheteroarylation of unactivated olefins [235], difunctionalizations of alkenes to synthesize fluoroalkyl ketones [236], nickel-catalysed photoredox $C(sp^3)$–H activation of amides with thioethers [237] and for $C(sp^3)$–H functionalization of glycine moieties to construct 1,3-oxazolidines [238].

Over the past few years, continuous flow microreactor technology has gained significant impact and has been recognized as permitting technology to avoid mass transfer issues occurred in various reactions. Continuous flow microreactor technology is providing means to scale operationally complex transformations including photochemical reactions [239, 240]. Developments of C–H activation in the area of continuous flow microreactor has been carried out very recently for benzylic C–H oxidation [241], $C(sp^3)$–H aerobic oxidation [242] and for C–H functionalization of heteroarenes [243]. These photochemical transformations in continuous flow microreactor offered several advantages of low-cost operational simplicity, easy product separation and good yield of products.

7 Microwave-Assisted C–H Activation Reactions

Organic synthesis by microwave-assisted reactions has been emerged as a more straightforward and substantial platform in modern organic chemistry [244–246]. C–H activation reactions are often performed with high temperature and long reaction times; the use of microwave irradiation offers several advantages as it productively attains the need of the high temperatures necessary to accomplish C–H activation. Hence microwave-assisted C–H activation is gaining popularity in laboratory-scale medicinal chemistry due to its rewarding advantages such as reproducibility, operational simplicity, safety and simple scale up procedure [247–250]. Many microwave-assisted C–H activation reactions permit an efficient path to bi(hetero)aryl compounds having applications in medicinal chemistry and organic materials [251]. This section of book chapter gives an overview of some of the important accomplishments in the microwave-assisted C–H activation reactions.

When compared with other transition metal catalysis, palladium catalysts represented enormous applications in microwave-assisted C–H activation reactions. With this background, Baber et al. demonstrated the synthesis of chiral complexes of palladium with bis(phosphite) PCP-pincer ligands via C–H activation of ligands by thermal heating and observed enormous enhancement in the reaction rate under microwave irradiation (Scheme 64) [252].

These complexes were utilized for allylation of aldehydes and offered promising enantioselectivity in resulting products. Microwave-mediated palladium-catalysed

Reagents and conditions: (i) $\left[PdCl_2(NCPh)_2\right]$, DCE, reflux, 6d, 77%
(ii) $\left[PdCl_2(NCMe)_2\right]$, μv, 300 W, 150 °C, 1 h, 92%
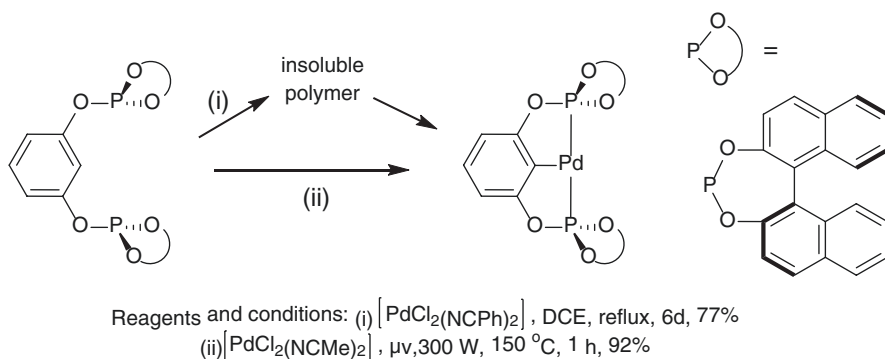
Scheme 64 C–H activation of bis(phosphite) PCP-pincer ligands for synthesis of chiral Pd-bis(phosphite) PCP-pincer complexes
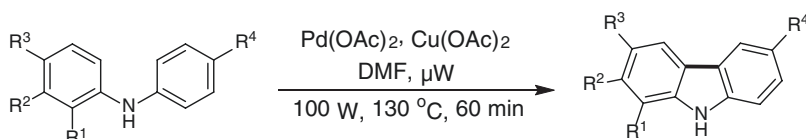
Scheme 65 Palladium-catalysed microwave-assisted C–H activation of arylamines

intramolecular C–H bond activation of arylamines was performed to construct carbazole and carbazolequinone derivatives (Scheme 65) and this study reports the broad scope of oxidative biaryl coupling reactions with good yield of products [253].

Additionally, Jain et al. described the C5-H arylation of L-histidine in a regioselective manner by using aryl iodides as coupling partners (Scheme 66) and reported good yield of *N*-benzylated imidazole while sustaining chirality [254]. Owing to the broad range of biological significance of arylated amino acids embedded in peptides, arylation of amino acid was important.

Another accomplishment in the area of palladium-catalysed microwave-assisted polycondensation was achieved by Kanbara et al. by arylation reaction between 3,4-ethylenedioxythiophene and 9,9-dioctyl-2,7-dibromofluorene (Scheme 67) [255]. This effective protocol is found to be significant to construct π-conjugated polymers having optoelectronic properties under microwave irradiation with short reaction time and low Pd loading.

Microwave-assisted Pd-catalysed orthogonal regioselective C–H arylation reactions of thiazole derivatives were carried out by Wünsch and Itami [256]. These thiazole derivatives act as potentially better σ1 receptor ligands. Regioselective arylation of thiazole derivatives was enhanced under microwave irradiation and resulted in arylated product showed improved σ1 receptor affinity (Scheme 68).

Alkenylation of C2–H bond of the 3H-imidazo[4,5-*b*]pyridine via microwave heating was first time established by Piguel et al. [257]. This reaction protocol used combination of Pd and Cu catalysis and led to the construction of numerous
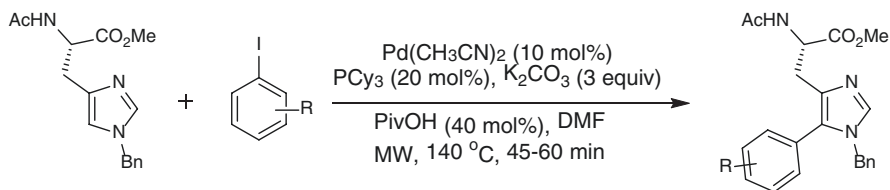
Scheme 66 Regioselective synthesis of benzylated imidazole via C5–H arylation reaction of protected L-histidine
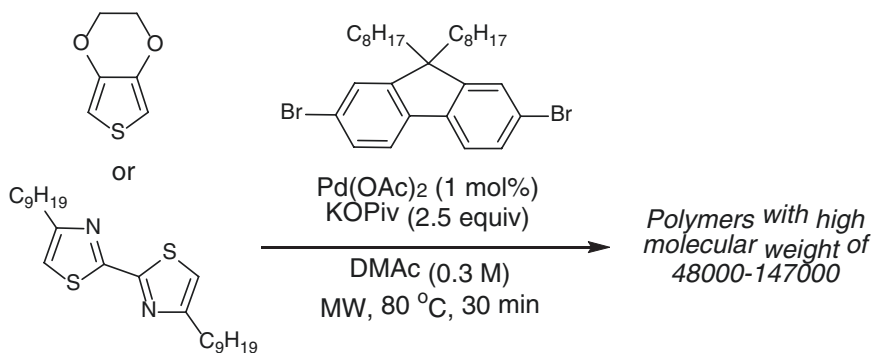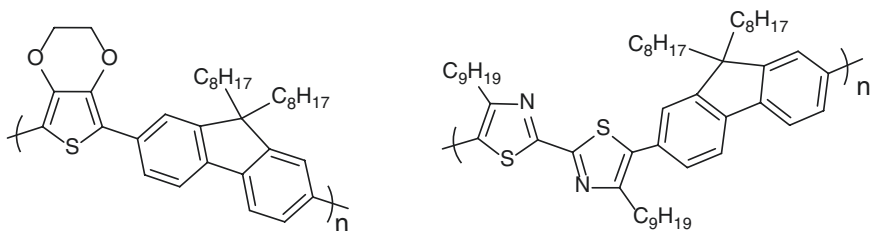
Scheme 67 Microwave-assisted direct arylation condensation reaction of 3,4-(ethylenedioxy) thiophene and 9,9-dioctyl-2,7-dibromofluorene for synthesis of polymers
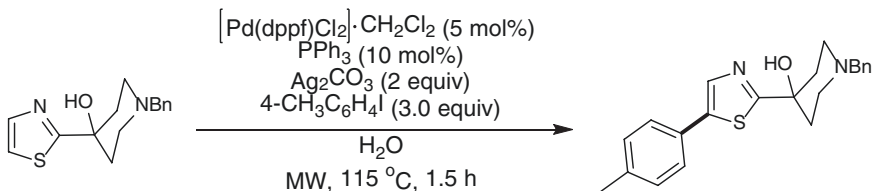
Scheme 68 Microwave-assisted Pd-catalysed C5–H arylation of thiazoles
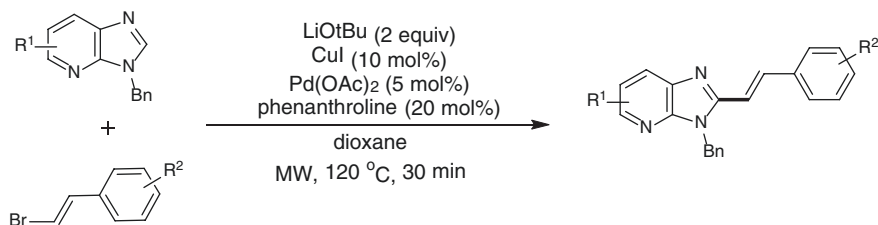
Scheme 69 Pd-Cu-catalysed C2–H alkenylation reaction of imidazo[4,5-*b*]pyridines and bromostyrenes

2-vinyl-3*H*-imidazo[4,5-*b*]pyridine derivatives in high yields with formation of single *E*-stereoisomer (Scheme 69).

Pd-catalysed arylation of quinazolinones and pyrido-pyrimidinones with aryl halides were developed by Besson and Fruit et al. via sequential C–H arylation [258]. Presented methodology reported regioselective C2 and C7 arylation to obtain diarylated compounds of high significance in drug discovery (Scheme 70).

Another study conducted by Besson et al. using combined Cu/Pd catalysis reports the C2–H arylation of *N*-3 substituted quinazolin-4(3*H*)-ones and (hetero) aryl chlorides (Scheme 71) [259]. Introduction of pyridine, diazines and thiophenes derivatives, at the 2-position of quinazolin-4(3*H*)-ones was performed very effectively using this method with good yields in less reaction time. Hu et al. demonstrated the palladium-catalysed and silver-assisted direct C-5–H arylation of 1,2,4-oxadiazoles with aryl iodides under microwave irradiation (Scheme 72) [260]. This protocol reported the construction of 3,5-diaryl-1,2,4-oxadiazole moieties in good yields and practical demonstration of concise syntheses of a novel and potent RET inhibitor.

Effectiveness of microwave-assisted C–H activation reactions were also established for the synthesis of platinum (II) and platinum (IV) complexes with diimidazolylidene ligands [261]. Additionally, microwave-assisted cross-coupling via C–H arylation was also conducted under catalyst-free system via S_NAr of pentafluorobenzene compounds along with indole or azole derivatives [262]. Pd-catalysed site-specific C-8 arylation/reduction of quinoline *N*-oxides with aryl halides were reported by Larionov et al. via microwave irradiation [263]. Pd(OAc)$_2$ in combination with Ag$_3$PO$_4$ salt and additive showed best C-8 selectivity (Scheme 73).

Arylation of quinoline via tandem approach (*N*-oxidation/C8–H arylation/reduction) by microwave heating was developed first [264] and later the same methodology was successfully adopted to construct C-8-arylated compounds from quinaldic acid *N*-oxide in good yield (Scheme 74) [265]. Thus, microwave-assisted C–H arylation has contributed for the development of very important scaffolds in medicinal chemistry.

Another noteworthy achievement in the microwave-assisted C–H alkylation of azoles involving three components was established by Van der Eycken et al. by performing very demanding synthesis of amine tethered azole compounds [266]. Cu-catalysed C–H alkylation of azoles has been explored via three components
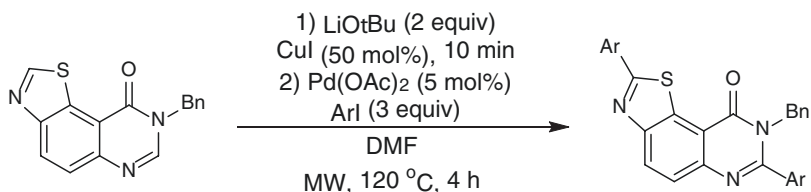
Scheme 70 Microwave-assisted C–H arylation reaction of thiazolo[5,4-*f*]quinazolin-9(8*h*)-one and aryl iodides
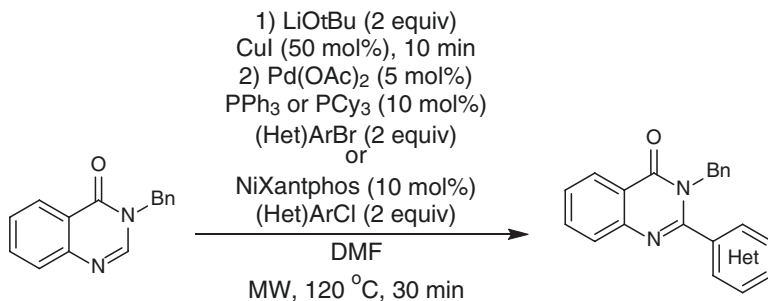
Scheme 71 C2–H arylation reaction of *N*-3-substituted quinazolin-4(3*H*)-ones and (hetero)aryl chlorides
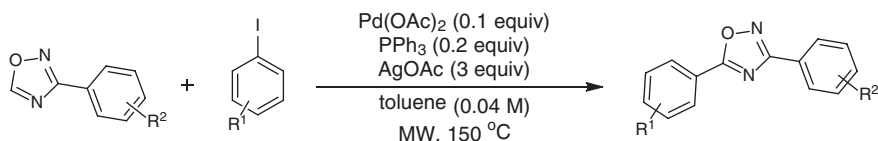
Scheme 72 Palladium-catalysed direct C-5–H arylation of 1,2,4-oxadiazoles with aryl iodides
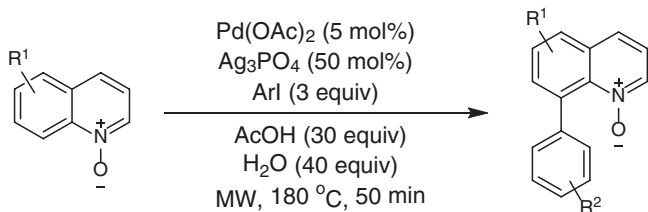
Scheme 73 Pd-catalysed site-specific C-8 arylation/reduction of quinoline *N*-oxides with aryl halides

coupling reaction involving heteroarene–amine–aldehyde/ketone (Scheme 75). The synthesized amine tethered azole derivatives bearing alkylamine chain at C2 position are considered as privileged substructure found in natural products possessing antibiotic action.
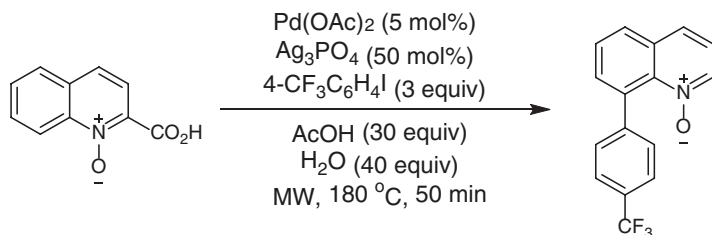
Scheme 74 Synthesis of C-8-arylated quinoline oxides via sequential C8–H arylation and C2-decarboxylation reaction
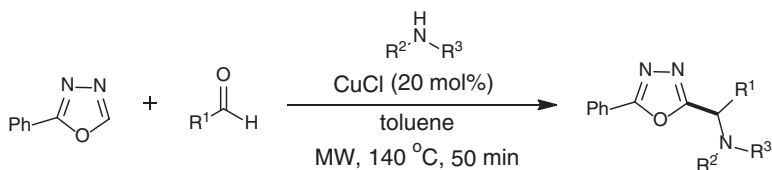
Scheme 75 Three-component C–H coupling reaction of 5-phenyloxadiazole with aldehydes and amines
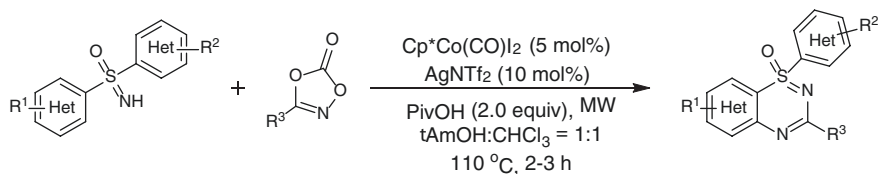
Scheme 76 Microwave-assisted direct C–H activation and C–N bond formation reaction

Chen et al. also reported microwave-mediated Cp*Co(III)-catalysed C–H activation and C–N bond development to obtain thiadiazine 1-oxide derivatives (Scheme 76) [267]. The reaction system is effective for broad substrate category without external oxidant and leads to the synthesis of medicinally significant thiadiazine 1-oxides in excellent yield.

Though microwave-assisted C–H functionalization was mostly performed with Pd and Cu catalysts but few noteworthy results of ruthenium-catalysed microwave aided C–H functionalization are also demonstrated in the literature. Van der Eycken et al. reported the microwave-assisted Ru-catalysed C–H activation of N-substituted α-amino ester molecules [268]. This microwave-assisted strategy presented an effective synthesis of isoquinolines with broad variety of N-benzoyl α-amino ester derivatives in moderate to outstanding yields (Scheme 77).

Tan et al. established significant and operationally easy cyclization method utilizing C–H bond activation to rapidly access heterocyclic products (Scheme 78) that are currently difficult to obtain with alternative methods [269]. The procedure is
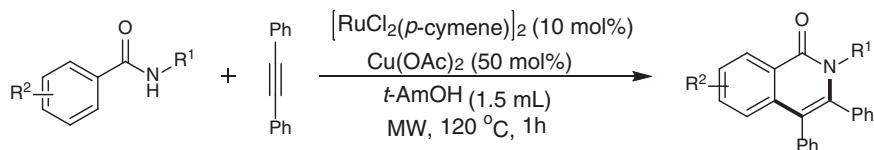
Scheme 77 Ru-catalyzed ortho-C–H activation for synthesis of substituted isoquinolines
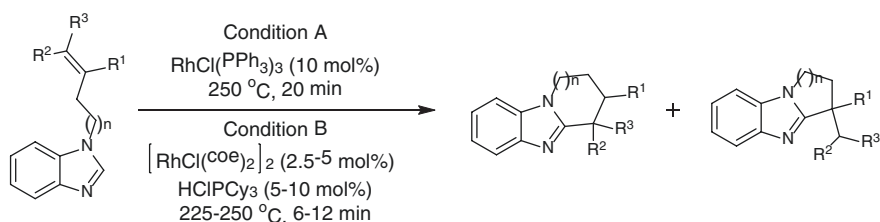
Scheme 78 Rh-catalysed intramolecular coupling of a benzimidazole C–H bond
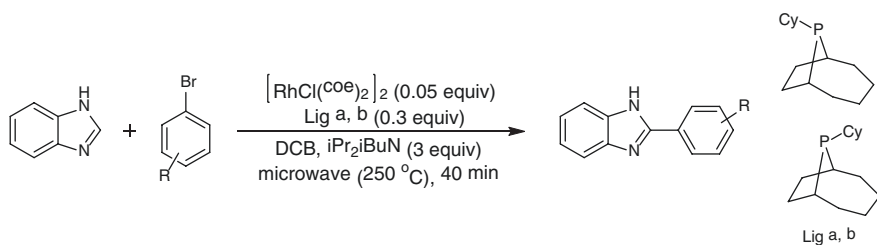
Scheme 79 Rh-catalysed C–H arylation of azoles and aryl halides

well applicable for the rapid synthesis of various heterocycles under optimized reaction conditions. Ellman et al. demonstrated the rhodium-catalysed arylation of azoles and aryl halides through C–H bond activation under microwave irradiation (Scheme 79) [270]. This method reported the tolerance of wide substrate scope and application of microwave radiation in this reaction led to the reduced reaction time.

Jun et al. reported the microwave-assisted Rh-catalysed N-annulation of ketones and alkynes (Scheme 80) [271]. This method afforded the quick synthesis of a wide array of isoquinoline and pyridine compounds in high yields under microwave irradiation. Four-component N-annulation reactions of alkyne with cycloalkanones was also presented to construct tetrahydroquinoline moiety. Recently, Van der Eycken et al. reported the microwave-assisted rhodium(III)-catalysed intramolecular annulation to develop the synthesis of the indolizinone and quinolizinone moieties (Scheme 81) [272]. Microwave-assisted annulation via C(sp^2)–H activation combined with Ugi reaction demonstrated as the rapid approach for diversification of peptidomimetics and oligopeptides.
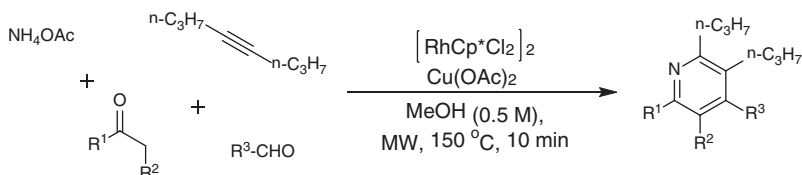
Scheme 80 Microwave-assisted Rh(III)-catalysed, four-component N-annulation reaction
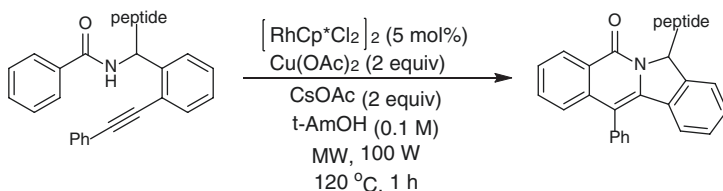
Scheme 81 Rhodium(III)-catalysed annulation of oligopeptides

Some of the noteworthy results of microwave-assisted Rh-catalysed C–H activation also reported for the Heck-type and [4 + 1] annulation coupling reaction [273] and synthesis of pyrazolo[1,5-*a*]pyrimidines derivatives [274] and presented the significant yield of products. Compilation of transition metal catalysis and microwave radiation led to the significant advancements in the organic synthesis in the greener way. Taking into account the advantages offered by the microwave irradiation technology, different potential medicinal and bioactive molecules could be produced in very short reaction time and in high yield.

8 Electrochemical C–H Functionalization

C–H bond functionalization has arisen as an innovative tool in organic synthesis for the synthesis of C–C bonds. Recently, oxidative C–H activation has largely employed stoichiometric amount of costly and harmful metal oxidants, bargaining the general economical nature of C–H activation science. On the other hand, electrochemical C–H actuation is distinguished as a progressively effective system that uses storable electrical power. In this presentation, the significance of electrocatalytic C–H activation highlighting the recent developments will be discussed. Various review articles summarized the electrocatalytic C–H activations [275–277] in past decades and it was observed that this tool has gained significant achievements in C–H activation area. This section of the chapter will present an overview about the current progresses occurred in the electrocatalytic C–H activation.

Li et al. in 2015 demonstrated the first example of Friedel−Crafts alkylation via aryl C–H bond activation of *N*-vinylamides by electrochemical in situ generation of tris(*p*-bromophenyl)aminium (TBPA) radical cation [278]. The heterocyclic
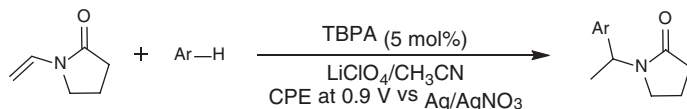
Scheme 82 Friedel−Crafts alkylation reaction with vinylpyrrolidin-2-one mediated by electrochemically preprepared TBPA

products were obtained in an excellent yield of good yield (Scheme 82). This work represents an excellent example of combination of electrochemically generated TBPA radical cation and an easily recyclable polymeric ionic liquid−carbon black (PIL−CB) as a supporting electrolyte for catalytic electrosynthesis.

Further in 2017, Ma et al. established the first illustration of palladium-catalysed C–H activation reactions via anodic oxidation [279]. Decarboxylative couplings of various oxime ethers with $MeBF_3K$ and phenyl glyoxylic acid were performed differently and observed that acylation took place very efficiently with good yields of products (Scheme 83). The use of electrochemical process represents an effective alternative for the conventional processes having the limitation of using harsh chemical oxidants.

Another significant achievement in the arena of electrocatalytic C–H functionalization was discovered by Ackermann et al. by performing Co-catalysed C–H oxygenation reaction with very mild reaction setup via electrochemical reaction (Scheme 84) [280]. Valued functional groups including ester, nitrile, thioether, tertiary amines, ketone and halide substituents tested for Co-catalysed electrochemical C–H activation regime and resulted in an excellent yield of products.

Later in 2018, Zeng et al. demonstrated the dehydrogenative lactonization of C–H bond via electrochemical pathway to obtain different lactone and coumarin derivatives [281]. Another study conducted by Zeng et al. reported the oxidative α-C–H thiocyanation reaction of ketones and sulphenylation of ketones by electrochemical approach using redox catalyst NaI and proton catalyst Amberlyst-15(H)® [or A-15(H)] of heterogeneous salt structure (Scheme 85) [282]. Under constant current conditions, the electrochemistry was performed in a simple complete cell prepared with simple graphite plate electrodes.

First study of rhodium-catalysed electrooxidative twofold C–H/C–H alkenylation was conducted by Ackermann et al. with benzamides and benzoic acids as coupling partners and electricity as the terminal oxidant (Scheme 86) and afforded products in reasonably good yields [283].

Also, the first study of nickel-catalysed electrooxidative C–H amination reaction was conducted by Ackermann et al. (Scheme 87) [284]. Variety of substrates along with electron-deficient arenes were efficiently tolerated for C–H nitrogenation reactions with very high chemo- and position-selectivity using the developed nickel electro-regime. The same group explored the first report of the Ir-catalysed C–H activation via electrooxidative approach along with redox-catalyst (Scheme 88) [285]. This synergistic iridium electrocatalysis strategy is applicable for wide substrate scope and produced products C–H annulation products with great chemoselectivity and excellent yields.
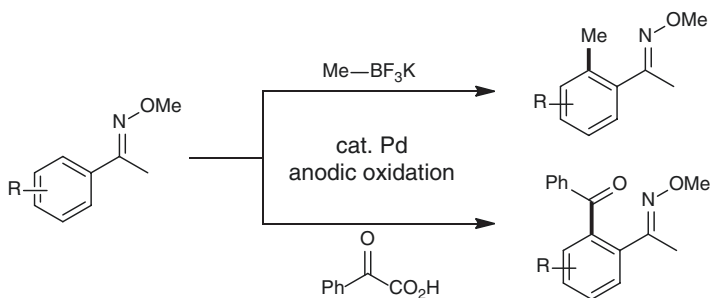
Scheme 83 C(sp²)–H couplings via anodic oxidation
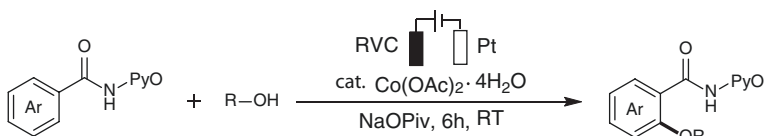
Scheme 84 Electrochemical C−H oxygenation
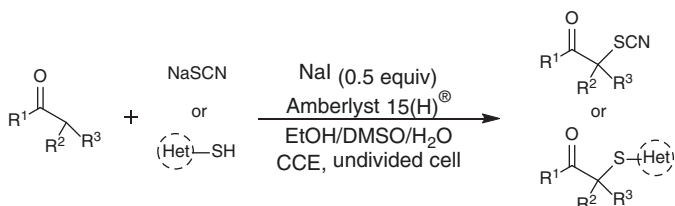
Scheme 85 Electrochemical oxidative α-thiocyanation of different ketones
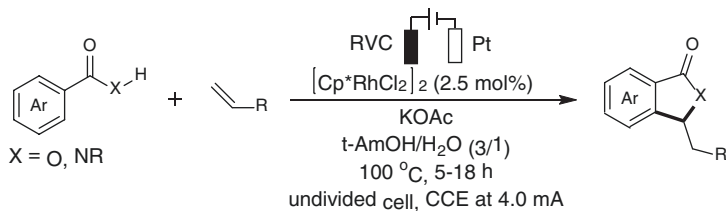
Scheme 86 Rhodium-catalysed electrooxidative twofold C–H/C–H alkenylation
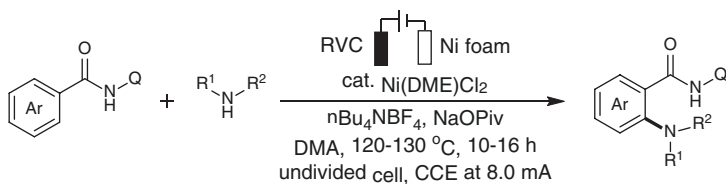
Scheme 87 Ni-catalysed electrooxidative C–H amination reaction with amines
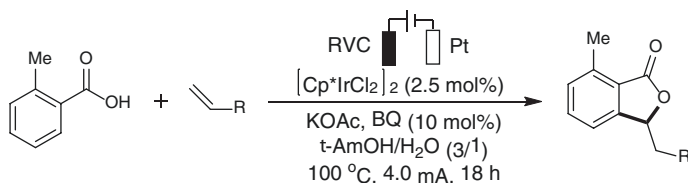
Scheme 88 Iridium-catalysed electrochemical C–H alkenylation
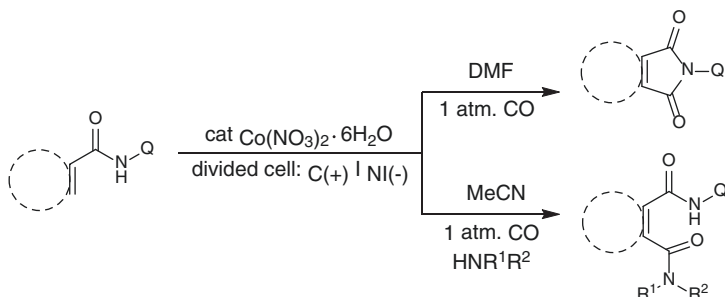
Scheme 89 Electrochemical intra- and intermolecular carbonylation

Transition-metal-catalysed oxidative C(X)–H and C–H carbonylation using carbon monoxide stands as one of the most used methods to develop carbonyl compounds. However, the drawbacks associated with this method such as expensive nature of method, unwanted generation of chemical waste renders it be a less effective method and thus the scope for most effective method to avoid these drawbacks is encouraged. Lei et al. developed an electrochemical strategy to overcome these issues and reported C–H/N–H carbonylation reaction with H_2 generation via anodic oxidation (Scheme 89) [286]. With this strategy, different amide products with intra- and intermolecular carbonylation were constructed having good functional group scope in 31–99% yields.

Zhao et al. developed C–H activation reaction of biaryl ketoximes via electrocatalysis for the synthesis of polycyclic *N*-heteroaromatic compounds and their corresponding *N*-oxides [287]. Dehydrogenative cyclization of oximes was performed using Pt cathode to construct a wide range in chemo- and regioselective formation of *N*-heteroaromatic *N*-oxides in excellent yield (Scheme 90).

Ackermann et al. reported the study of Ru-catalysed annulation of alkyne by C–H/N–H and C–H/O–H activation of phenols or aryl carbamates via electrochemical process (Scheme 91) [288]. This highly sustainable Ru(II)-electrocatalytic method was conducted in a protic solvent such as alcohol/H_2O and afforded outstanding regio-, chemo-, and position-selectivity in the formed products.

In a similar manner, C−H/N−H activations by electrochemical oxidative approach were performed using cobalt catalyst for internal alkyne annulation [289]. First, example of electrochemical induced allene annulations with Co-catalysed C–H activation was discovered by Ackermann group (Scheme 92) [290]. The
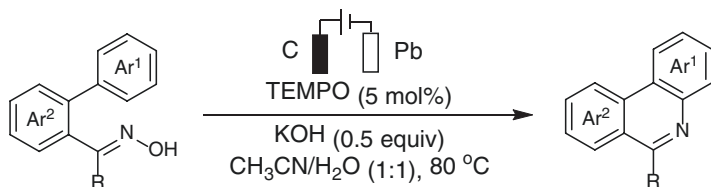
Scheme 90 Electrochemical dehydrogenative cyclization of oximes
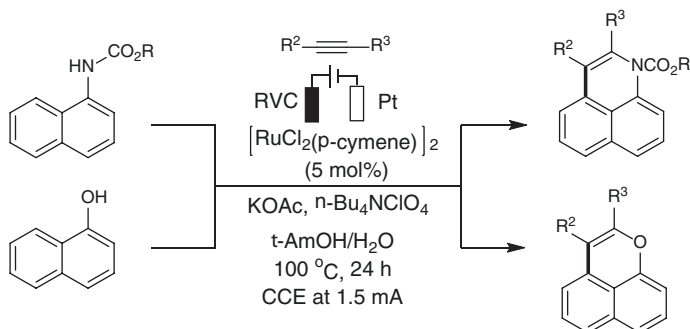
Scheme 91 Electrochemical C–H activation of phenols/carbamates with alkynes
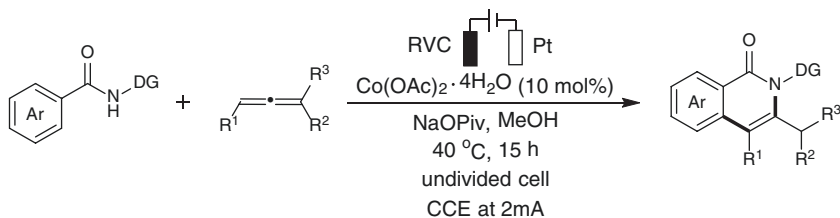
Scheme 92 Electrochemical allene annulation
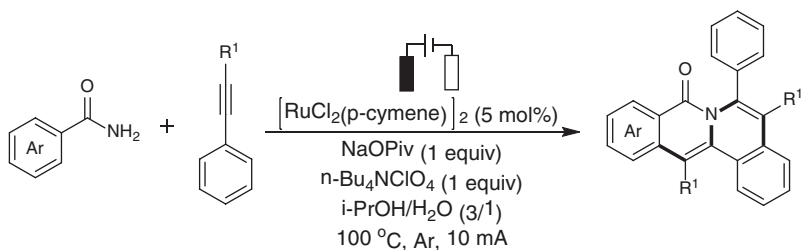
Scheme 93 Electrochemically enabled dual C–H activation of amides

sturdiness and flexibility of the designed electrochemical C–H annulation strategy were reproduced for different allene moieties in significant yields. Similarly, C−H/ N−H functionalization with allenes was demonstrated by the same group using
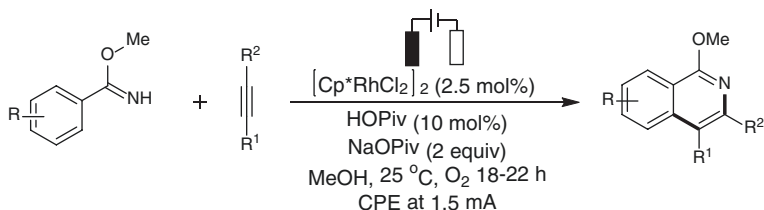
Scheme 94 Flow-rhodaelectro-enabled C–H bond activation of imidates and alkynes
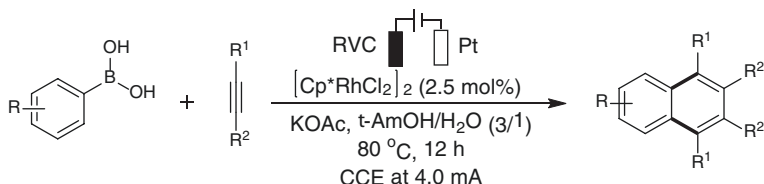
Scheme 95 C−H activation of boronic acids and alkynes via rhodaelectro catalysis

cobalt-catalysed electrooxidative annulation with hydrazide as a directing group [291].

Recently, Tang et al. accomplished the first illustration of electrochemical double C–H functionalization of amides and alkynes by dehydrogenative annulation to develop polycyclic isoquinolinones (Scheme 93) [292]. This strategy without any oxidant delivered the products with improved chemo and regioselectivity and was found to be very competent as compared to other traditional methods using strong oxidant conditions. Ackermann et al. in 2019 demonstrated the first report of rhodaelectro-catalysed C–H activation of imidate and unsymmetrical alkyne in electrochemical flow reactor (Scheme 94) [293]. This electrochemical-flow annulation reaction was recognized to be operative for both intra- and intermolecular annulation with a variety of substrates and led to the synthesis of isoquinoline products with excellent chemoselectivity. The concept of rhodaelectro-catalysed C–H bond activation was again combined with [2 + 2 + 2] alkyne annulation of boronic acids and cyclodehydrogenation to construct the varyingly substituted polycyclic aromatic hydrocarbons (PAHs) (Scheme 95) [294]. This concept offers several advantages of being green and sustainable over conventional chemical oxidants with the use of electricity as a green oxidant, wide substrate scope and easy operational set up.

Huang et al. demonstrated mild and oxidant-free electrochemical protocol for C–H phosphorylation of secondary amine with diethyl phosphate (Scheme 96) [295]. This approach was effective to tolerate wide functionality of a series of cyclic and chain secondary amines and produced products with satisfactory yields.

Fine chemicals with nitrile group incorporated in it is of specific interest using C–H activation of alkyl nitriles as it offers high economy. Noteworthy achievement in the extent of electrochemical C–H bond functionalization was accomplished recently by He et al. [296] to synthesize sulphur-comprising β-enaminonitrile molecules in a stereoselective manner via Csp³–H oxidative activation of acetonitrile by
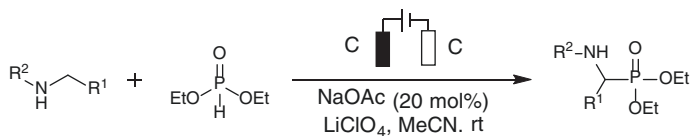
Scheme 96 Directed C−H phosphorylation of amine
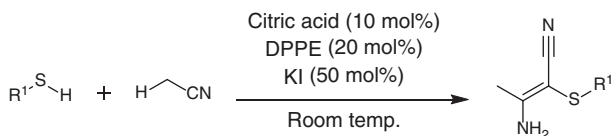
Scheme 97 Electrooxidative Csp³–H bond activation of acetonitrile
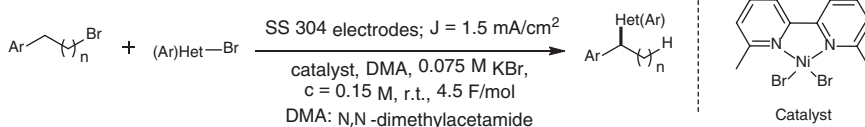
Scheme 98 Electro-reductive cross-coupling of aryl and alkyl bromides

electrochemical process (Scheme 97). This strategy involved the radical-induced $C(sp^3)$–H oxidative activation of acetonitrile via KI-mediated anodic oxidation. Different sulphur-containing β-enaminonitrile products with various functional groups were formed with (Z)-tetrasubstituated olefins in good stereoselectivity.

Rueping et al. developed the first electrocatalytic approach for Ni-catalysed cross-coupling of electrophiles for the construction of 1,1-diarylalkane derivatives from aryl and alkyl halides (Scheme 98) [297]. The protocol was applicable for wide substrate group tolerance of various alkyl halides and achieved excellent regioselectivities of products under mild reaction conditions.

Biomass-derived renewable solvents are alternative resources of energies and it can be used in molecular catalysis and organic synthesis reactions. In this area, Ackermann et al. achieved the C–H activation of benzamides with alkynes through cobalt-electrocatalysis in biomass-derived glycerol by utilizing renewable wind and solar energy [298].

Electrochemistry serving as operationally easy platform for performing organic reactions wherein electron being the only reagents and helping to reduce the energy consumption by minimizing the reagent waste. Hence, electrochemical organic synthesis is gaining massive impact in the modern organic chemistry. The strategies discussed herein give access to the challenging and weakly coordinating functionalities in high yields through electrochemical C–H activation with the advantages of electricity as green oxidant, mild reaction conditions and user-friendly set up. Considering these unique features of electrochemical C–H activations, it is believed that this will be a great reliable and adaptable platform for the various bond construction to the upcoming era of the scientific community in organic chemistry.

9 Conclusions

The development of greener methodologies for the access of organic scaffolds has been considerably focused by the modern organic chemistry over the last decades. Also, C–H functionalization technique has been considered as a sustainable approach with the potential to replace traditional organic conversions for the access of complex organic scaffolds. In this context, protocols combining the advantages of greener methodologies and C–H activation strategy appear very attractive, as these approaches offer more sustainable alternatives to conventional organic transformations. This chapter demonstrated the development of greener methodologies for C–H activation reactions which include use of greener solvents, microwave irradiation, photocatalysis, homogeneous recyclable catalytic systems, heterogeneous catalysts, oxidizing directing groups, electrochemical methods, etc. during the past few years. The book chapter highlighted selective most fascinating and inspiriting examples of greener methodologies in C–H functionalization protocols. These methodologies attempted to resolve the issues of catalyst reusability, reaction media, time efficiency, energy efficiency, byproducts, requirement of additives as well as oxidants. The target products are extensively significant in various sectors with higher commercial value. Respective development of these chemical products is greatly favourable both economically and ecologically. Moreover, most of the highlighted systems lay the foundation for the initiation of novel viewpoints in the advancement of methodologies which leads the 'green chemistry' principles.

References

1. Clark JH, Luque R, Matharu AS (2012) Green chemistry, biofuels, and biorefinery. Annu Rev Chem Biomol Eng 3:183
2. Linthorst JA (2010) An overview: origins and development of green chemistry. Found Chem 12(1):55
3. Baron M (2012) Towards a Greener Pharmacy by More Eco Design. Waste and Biomass Valorization 3:395
4. Richard KH, Concepción JG, Constable DJC, Sarah RA, Graham GAI, Gail F, James S, Steve PB, Alan DC (2011) Expanding GSK s solvent selection guide—embedding sustainability into solvent selection starting at medicinal chemistry. Green Chem 13:854
5. Kumar A, Gupta G, Srivastava S (2011) Functional ionic liquid mediated synthesis (FILMS) of dihydrothiophenes and tacrine derivatives. Green Chem 13:2459
6. Wender PA, Handy ST, Wright DL (1997) Towards the Ideal Synthesis. Chem Ind 19:765
7. Hudlicky T, Natchus MG (1993) In: Hudlicky T (ed) Organic synthesis: theory and applications. Jai Press, Greenwich
8. Wender PA (1996) Introduction: Frontiers in Organic Synthesis. Chem Rev 96:1
9. Eissen M, Metzger JO (2002) Environmental Performance Metrics for Daily Use in Synthetic Chemistry. Chem Eur J 8(16):3580
10. Centi G, Perathoner S (2003) Catalysis and sustainable (green) chemistry. Catal Today 77(4):287
11. Anastas P, Eghbali N (2010) Green Chemistry: Principles and Practice. Chem. Soc. Rev. 39:301

12. Kumar A, Tripathi VD, Kumar P (2011) β-Cyclodextrin catalysed synthesis of tryptanthrin in water. Green Chem 13:51
13. Biermann U, Bornscheuer U, Meier MAR, Metzger JO, Schäfer HJ (2011) Oils and fats as renewable raw materials in chemistry. Angew Chem Int 50:3854
14. Hess J, Bednarz D, Bae J, Pierce J (2011) Petroleum and Health Care: Evaluating and Managing Health Care's Vulnerability to Petroleum Supply Shifts. Am. J. Public Health 101:1568
15. Schwartz BS, Parker CL, Hess J, Frumkin H (2011) Public Health and Medicine in an Age of Energy Scarcity: The Case of Petroleum. Am. J. Public Health 101:1560
16. Walling C, Jacknow BB (1960) Positive Halogen Compounds. I. The Radical Chain Halogenation of Hydrocarbons by t-Butyl Hypochlorite1. J. Am. Chem. Soc. 82:6108
17. Recupero F, Punta C (2007) Free Radical Functionalization of Organic Compounds Catalyzed by N-Hydroxyphthalimide. Chem. Rev. 107:3800
18. Brühne F, Wright E (2011) Benzaldehyde. In: Ullmann's encyclopedia of industrial chemistry. Wiley-VCH, Weinheim
19. Davies HML, Du Bois J, Yu J-Q (2011) C–H Functionalization in organic synthesis. Chem. Soc. Rev. 40:1855
20. Das P, Dutta A, Bhaumik A, Mukhopadhyay C (2014) Heterogeneous ditopic ZnFe2O4 catalyzed synthesis of 4H-pyrans: further conversion to 1,4-DHPs and report of functional group interconversion from amide to ester. Green Chem. 16:1426
21. Gutekunst WR, Baran PS (2011) C–H functionalization logic in total synthesis. Chem. Soc. Rev. 40:1976
22. Yamaguchi J, Yamaguchi AD, Itami K (2012) C-H bond functionalization: emerging synthetic tools for natural products and pharmaceuticals. Angew. Chem. Int. Ed. 51: 8960
23. Ackermann L (2011) Carboxylate-assisted transition-metal-catalyzed C-H bond functionalizations: mechanism and scope. Chem. Rev. 111:1315
24. Song G, Wang F, Li X (2012) C–C, C–O and C–N bond formation via rhodium(iii)-catalyzed oxidative C–H activation. Chem. Soc. Rev. 41:3651
25. Blanksby SJ, Ellison GB (2003) Bond Dissociation Energies of Organic Molecules. Acc. Chem. Res. 36:255
26. Kuhl N, Hopkinson MN, Wencel-Delord J, Glorius F (2012) Beyond Directing Groups: Transition-Metal-Catalyzed C–H Activation of Simple Arenes. Angew. Chem. Int. Ed. 51:10236
27. Rossi R, Bellina F, Lessi M, Manzini C (2014) Cross-Coupling of Heteroarenes by C–H Functionalization: Recent Progress towards Direct Arylation and Heteroarylation Reactions Involving Heteroarenes Containing One Heteroatom. Adv. Synth. Catal. 356:17
28. Lyons TW, Sanford MS (2010) Palladium-catalyzed ligand-directed C-H functionalization reactions. Chem. Rev. 110:1147
29. Zhang F, Spring DR (2014) Arene C–H functionalisation using a removable/modifiable or a traceless directing group strategy. Chem. Soc. Rev. 43:6906
30. de Vries JG, Jackson SD (2012) Homogeneous and heterogeneous catalysis in industry. Catal. Sci. Technol. 2:2009
31. Luz I, Llabres i Xamena FX, Corma A (2012) Bridging homogeneous and heterogeneous catalysis with MOFs: Cu-MOFs as solid catalysts for three-component coupling and cyclization reactions for the synthesis of propargylamines, indoles and imidazopyridines. J. Catal. 285:285
32. Somorjai GA (2008) in The 13th International Symposium on Relations Between Homogeneous and Heterogeneous Catalysis - An Introduction. Top. Catal. 48:1
33. Leeuwen v, WNM P (2005) Homogeneous Catalysis. Springer-Verlag, Berlin Heidelberg
34. de Meijere A, Diederich F, Eds. (2004) in Metal-Catalyzed Cross-Coupling Reactions, Vol. 2, Wiley-VCH: Weinheim
35. Beller M, Bolm C (2004) Transition metals for organic synthesis, 2nd edn. Wiley-VCH, Weinheim

36. Martin R, Buchwald SL (2008) Palladium-Catalyzed Suzuki−Miyaura Cross-Coupling Reactions Employing Dialkylbiaryl Phosphine Ligands. Acc. Chem. Res. 41:1461

37. Saito B, Fu GC (2007) Alkyl−Alkyl Suzuki Cross-Couplings of Unactivated Secondary Alkyl Halides at Room Temperature. J. Amer. Chem. Soc. 129:9602

38. Diebolt O, Braunstein P, Nolan SP, Cazin CS (2008) Room-temperature activation of aryl chlorides in Suzuki–Miyaura coupling using a [Pd(μ-Cl)Cl(NHC)]2 complex (NHC = N-heterocyclic carbene). Chem. Commun. 27:3190

39. Billingsley KL, Buchwald SL (2008) A general and efficient method for the Suzuki-Miyaura coupling of 2-pyridyl nucleophiles. Angew. Chem. Int. Ed., 47:4695

40. Garrett CE, Prasad K (2004) The Art of Meeting Palladium Specifications in Active Pharmaceutical Ingredients Produced by Pd-Catalyzed Reactions. Adv. Synth. Catal. 346:889

41. Welch CJ, Albaneze-Walker J, Leonard WR, Biba M, DaSilva J, Henderson D, Laing B, Mathre DJ, Spencer S, Bu X, Wang T (2005) Adsorbent Screening for Metal Impurity Removal in Pharmaceutical Process Research. Org. Process Res. Dev. 9:198

42. Kuriyama M, Nagai K, Yamada K-i, Miwa Y, Taga T, Tomioka K (2002) Hemilabile Amidomonophosphine Ligand−Rhodium(I) Complex-Catalyzed Asymmetric 1,4-Addition of Arylboronic Acids to Cycloalkenones. J. Am. Chem. Soc. 124:8932

43. Lautenes M, Dockendorff C, Fagnou K, Malicki A (2002) Rhodium-Catalyzed Asymmetric Ring Opening of Oxabicyclic Alkenes with Organoboronic Acids. Org. lett. 4:1311

44. Jang H-Y, Krische MJ (2004) Catalytic C−C Bond Formation via Capture of Hydrogenation Intermediates. Acc. Chem. Res. 37:653

45. Enthaler S, Junge K, Beller M (2008) Sustainable Metal Catalysis with Iron: From Rust to a Rising Star? Angew. Chem., Int. Ed. 47:3317

46. Piontek A, Bisz E, Szostak M (2018) Iron-Catalyzed Cross-Couplings in the Synthesis of Pharmaceuticals: In Pursuit of Sustainability. Angew. Chem. Int. Ed. 57:11116

47. Guideline on the specification limits for residues of metal catalysts or metal reagents, European Medicines Agency, London, 21-02-2008. Document reference EMEA/CHMP/SWP/4446/2000

48. Cole-Hamilton DJ, Tooze RP (eds) (2006) Homogeneous catalysis advantages, problems in catalyst separation, recovery, recycling. Springer, Dordrecht

49. Baker RT, Tumas W (1999) Toward Greener Chemistry. Science 284:1477

50. Reay AJ, Fairlamb IJS (2015) Catalytic C–H bond functionalisation chemistry: the case for quasi-heterogeneous catalysis. Chem. Commun. 51:16289

51. Santoro S, Kozhushkov SI, Ackermann L, Vaccaro L (2016) Heterogeneous catalytic approaches in C–H activation reactions. Green Chem. 18:3471

52. Mizuno N, Misono M (1998) Heterogeneous Catalysis. Chem. Rev. 98:199

53. Yoon M, Srirambalaji R, Kim K (2012) Homochiral Metal–Organic Frameworks for Asymmetric Heterogeneous Catalysis. Chem. Rev. 112:1196

54. Warner JC, Anastas (1998) Green Chemistry, Oxford Univeristy Press, New York

55. Cano R, Schmidt AF, McGlacken GP (2015) Direct arylation and heterogeneous catalysis; ever the twain shall meet. Chem. Sci. 6:5338

56. Ranu BC, Bhadra S, Saha D (2011) Green recyclable supported catalyst for useful organic transformations. Curr. Org. Synth. 8:146

57. Molnár Á (2011) Efficient, Selective, and Recyclable Palladium Catalysts in Carbon−Carbon Coupling Reactions. Chem. Rev. 111:2251

58. Parsharamulu T, Venkanna D, Kantam ML, Bhargava SK, Srinivasu P (2014) The First Example of ortho-Arylation of Benzamides over Pd/Mesoporous Silica: A Novel Approach for Direct sp2 C–H Bond Activation. Ind. Eng. Chem. Res. 53:20075

59. Miura H, Wada K, Hosokawa S, Inoue M (2010) Recyclable Solid Ruthenium Catalysts for the Direct Arylation of Aromatic C–H Bonds. Chem. –Eur. J. 16:4186

60. Miura H, Wada K, Hosokawa S, Inoue M. (2010) Catalytic Addition of Aromatic C–H Bonds to Vinylsilanes in the Presence of Ru/CeO2. Chem-CatChem 2:1223

61. Kishore R, Kantam ML, Yadav J, Sudhakar M, Laha S, Venugopal A (2013) Pd/Mg–La mixed oxide catalyzed oxidative sp2 Csingle bondH bond acylation with alcohols. J. Mol. Catal. A: Chem. 379:213

62. Kishore R, Yadav J, Venu B, Venugopal A, Kantam ML (2015) A Pd(ii)/Mg–La mixed oxide catalyst for cyanation of aryl C–H bonds and tandem Suzuki–cyanation reactions. New J. Chem. 39:5259

63. Fei H, Cohen SM (2015) Metalation of a Thiocatechol-Functionalized Zr(IV)-Based Metal–Organic Framework for Selective C–H Functionalization. J. Am. Chem. Soc. 137:2191

64. Bai C, Yao X, Li Y (2015) Easy Access to Amides through Aldehydic C–H Bond Functionalization Catalyzed by Heterogeneous Co-Based Catalysts. ACS Catal. 5:884

65. Pascanu V, Carson F, Solano MV, Su J, Zou X, Johansson MJ, Martín-Matute B (2016) Selective Heterogeneous C–H Activation/Halogenation Reactions Catalyzed by Pd@MOF Nanocomposites. Chem. – Eur. J. 22:3729

66. Chng LL, Zhang J, Yang J, Amoura M, Ying JY (2011) C–C Bond Formation via C–H Activation and C–N Bond Formation via Oxidative Amination Catalyzed by Palladium-Polyoxometalate Nanomaterials Using Dioxygen as the Terminal Oxidant. Adv. Synth. Catal. 353:2988

67. Chen J, He L, Natte K, Neuman H, Beller M, Wu X-F (2014) Palladium@Cerium(IV) Oxide-Catalyzed Oxidative Synthesis of N-(2-Pyridyl)indoles via C–H Activation Reaction. Adv. Synth. Catal. 356:2955

68. Zahmakiran M, Özkar S (2011) Metal nanoparticles in liquid phase catalysis; from recent advances to future goals. Nanoscale 3:3462

69. Guo Z, Liu B, Zhang Q, Deng W, Wang Y, Yang Y (2014) Recent advances in heterogeneous selective oxidation catalysis for sustainable chemistry. Chem. Soc. Rev. 43:3480

70. Bhaduri S, Mukesh D (2014) Homogeneous Catalysis: Mechanisms, Industrial Applications, 2nd Edition, Wiley

71. Blaser H-U (2003) Enantioselective catalysis in fine chemicals production. Chem Commun: 293

72. Benaglia M (2009) Recoverable, Recyclable Catalysts; John Wiley & Sons: Chichester

73. Wittmann S, Schatz A, Grass R, Stark W, Reiser O (2010) A Recyclable Nanoparticle-Supported Palladium Catalyst for the Hydroxycarbonylation of Aryl Halides in Water. Angew. Chem. Int. Ed. 49:1867

74. Basset J-M, Copéret C, Soulivong D, Taoufik M, Thivolle-Cazat (2010) Metathesis of Alkanes and Related Reactions. J. Acc. Chem. Res. 43:323

75. Collis AEC, Horvath IT (2011) Heterogenization of homogeneous catalytic systems. Catal. Sci. Technol. 1:912Collis AEC, Horvath IT (2011) Heterogenization of homogeneous catalytic systems. Catal. Sci. Technol. 1:912

76. Cole-Hamilton DJ (2003) Homogeneous Catalysis--New Approaches to Catalyst Separation, Recovery, and Recycling. Science 299:1702

77. Carmichael AJ, Earle MJ, Holbrey JD, McCormac PB, Seddon KR (1999) The Heck Reaction in Ionic Liquids: A Multiphasic Catalyst System. Org. Lett. 1:997

78. Pozzi G, Shepperson I (2003) Fluorous chiral ligands for novel catalytic systems. Coord Chem Rev 242:115

79. Herrmann WA, Kohlpainter CW (1993) Water-Soluble Ligands, Metal Complexes, and Catalysts: Synergism of Homogeneous and Heterogeneous Catalysis. Angew Chem Int Ed Engl 32:1524

80. De Vos DE, Vankelecom IFJ, Jacobs PA (eds) (2005) Chiral catalyst immobilization and recycling. Wiley-VCH, Weinheim

81. Olmos A, Asensio G, Pérez PJ (2016) Homogeneous Metal-Based Catalysis in Supercritical Carbon Dioxide as Reaction Medium. ACS Catal. 6:4265

82. Gava R, Olmos A, Noverges B, Varea T, Funes-Ardoiz I, Belderrain TR, Caballero A, Maseras F, Asensio G, Pérez PJ (2015) Functionalization of CnH2n+2 Alkanes: Supercritical

Carbon Dioxide Enhances the Reactivity towards Primary Carbon–Hydrogen Bonds. ChemCatChem 7:3254

83. Hu YL, Wu YP, Lu M (2018) Co (II)-C12 alkyl carbon chain multi-functional ionic liquid immobilized on nano-SiO2 nano-SiO2@CoCl3-C12IL as an efficient cooperative catalyst for C–H activation by direct acylation of aryl halides with aldehydes. Appl. Organomet. Chem. 32:e4096

84. Cotugno P, Monopoli A, Ciminale F, Milella A, Nacci A (2014) Palladium-Catalyzed Cross-Coupling of Styrenes with Aryl Methyl Ketones in Ionic Liquids: Direct Access to Cyclopropanes. Angew. Chem. Int. Ed. 53:13563

85. Ruokonen S-K, Sanwald C, Sundvik M, Polnick S, Vyavaharkar K, Duša F, Holding AJ, King AWT, Kilpeläinen I, Lämmerhofer M, Panula P, Wiedmer SK (2016) Effect of Ionic Liquids on Zebrafish (Danio rerio) Viability, Behavior, and Histology; Correlation between Toxicity and Ionic Liquid Aggregation. Environ. Sci. Technol. 50:7116

86. Kumar M, Trivedi N, Reddy CRK, Jha B (2011) Toxic Effects of Imidazolium Ionic Liquids on the Green Seaweed Ulva lactuca: Oxidative Stress and DNA Damage. Chem. Res. Toxicol. 24:1882

87. Stefanidis G, Stankiewicz A (eds) (2016) Alternative Energy Sources for Green Chemistry, The Royal Society of Chemistry, Cambridge

88. Tundo P, Perosa A, Zecchini F (eds) (2007) Methods and Reagents for Green Chemistry: An Introduction, John Wiley & Sons, Hoboken

89. Zhao H, Cheng M, Zhang J, Cai M (2014) Recyclable and reusable PdCl2(PPh3)2/PEG-2000/ H2O system for the carbonylative Sonogashira coupling reaction of aryl iodides with alkynes. Green Chem. 16:2515

90. Cecchini MM, Charnay C, De Angelis F, Lamaty F, Martinez J, Colacino E (2014) Poly(ethylene glycol)-Based Ionic Liquids: Properties and Uses as Alternative Solvents in Organic Synthesis and Catalysis. ChemSusChem 7:45

91. Vafaeezadeh M, Hashemi MM (2015) Polyethylene glycol (PEG) as a green solvent for carbon–carbon bond formation reactions. J. Mol. Liq. 207:73

92. Bergbreiter DE (2002) Using Soluble Polymers To Recover Catalysts and Ligands. Chem. Rev. 102:3345

93. Han W, Liu C, Jin Z (2008) Aerobic Ligand-Free Suzuki Coupling Reaction of Aryl Chlorides Catalyzed by In Situ Generated Palladium Nanoparticles at Room Temperature. Adv. Synth. Catal. 350:501

94. Burley GA, Davies DL, Griffith GA, Lee M, Singh K (2010) Cu-Catalyzed N-Alkynylation of Imidazoles, Benzimidazoles, Indazoles, and Pyrazoles Using PEG as Solvent Medium. J. Org. Chem. 75:980

95. Chandrasekhar S, Narsihmulu C, Sultana SS, Reddy NR (2002) Poly(ethylene glycol) (PEG) as a Reusable Solvent Medium for Organic Synthesis. Application in the Heck Reaction. Org. Lett. 4:4399

96. Declerck V, Colacino E, Bantreil X, Martinez J, Lamaty F. (2012) Poly(ethylene glycol) as reaction medium for mild Mizoroki–Heck reaction in a ball-mill. Chem. Commun. 48:11778

97. Li J-H, Liu W-J, Xie Y-X (2005) Recyclable and Reusable Pd(OAc)2/DABCO/PEG-400 System for Suzuki−Miyaura Cross-Coupling Reaction. J. Org.Chem. 70:5409

98. Liu L, Zhang Y, Wang Y (2005) Phosphine-Free Palladium Acetate Catalyzed Suzuki Reaction in Water. J. Org. Chem. 70:6122

99. Wang L, Zhang Y, Liu L, Wang Y (2006) Palladium-Catalyzed Homocoupling and Cross-Coupling Reactions of Aryl Halides in Poly(ethylene glycol). J. Org. Chem. 71:1284

100. Ackermann L, Vicente R (2009) Catalytic Direct Arylations in Polyethylene Glycol (PEG): Recyclable Palladium(0) Catalyst for C−H Bond Cleavages in the Presence of Air. Org. Lett. 11:4922

101. Zhou Q, Wei S, Han W (2014) In Situ Generation of Palladium Nanoparticles: Ligand-Free Palladium Catalyzed Pivalic Acid Assisted Carbonylative Suzuki Reactions at Ambient Conditions. J. Org. Chem. 79:1454

102. Xu C, Huang B, Yan T, Cai M (2018) A recyclable and reusable K2PtCl4/Xphos-SO3Na/ PEG-400/H2O system for highly regio- and stereoselective hydrosilylation of terminal alkynes. Green Chem. 20:391

103. Yedage SL, Bhanage BM (2016) Ru(ii)/PEG-400 as a highly efficient and recyclable catalytic media for annulation and olefination reactions via C–H bond activation. Green Chem. 18:5635

104. Zhao H, Zhang T, Yan T, Cai M (2015) Recyclable and Reusable [RuCl2(p-cymene)]2/ Cu(OAc)2/PEG-400/H2O System for Oxidative C–H Bond Alkenylations: Green Synthesis of Phthalides. J. Org. Chem. 80:8849

105. Yedage SL, Bhanage BM (2017) tert-Butyl Nitrite-Mediated Synthesis of N-Nitrosoamides, Carboxylic Acids, Benzocoumarins, and Isocoumarins from Amides. J. Org. Chem. 82:5769

106. Deshmukh DS, Bhanage BM (2018) N-Tosylhydrazone directed annulation via C–H/N–N bond activation in Ru(ii)/PEG-400 as homogeneous recyclable catalytic system: a green synthesis of isoquinolines. Org. Biomol. Chem. 16:4864

107. Deshmukh DS, Gangwar N, Bhanage BM (2019) Rapid and Atom Economic Synthesis of Isoquinolines and Isoquinolinones by C–H/N–N Activation Using a Homogeneous Recyclable Ruthenium Catalyst in PEG Media. Eur Journal of Organic Chemistry 2019:2919

108. Jian L, He H-Y, Huang J, Wu Q-H, Yuan M-L, Fu H-Y, Zheng X-L, Chen H, Li R-X (2017) Combination of RuCl3·xH2O with PEG – a simple and recyclable catalytic system for direct arylation of heteroarenes via C–H bond activation. RSC Adv. 7:23515

109. Ferlin F, Reddy Yetra S, Warratz S, Vaccaro L, Ackermann L (2019) Reusable Pd@PEG Catalyst for Aerobic Dehydrogenative C−H/C−H Arylations of 1,2,3-Triazoles. Chemistry A European journal 25:11427

110. Tao L-M, Li C-H, Chen J, Liu H (2019) Cobalt(III)-Catalyzed Oxidative Annulation of Benzaldehydes with Internal Alkynes via C-H Functionalization in Poly(ethylene glycol). J. Org. Chem. 84:6807

111. Chen Z, Wang B, Zhang J, Yu W, Liu Z, Zhang Y (2015) Transition metal-catalyzed C–H bond functionalizations by the use of diverse directing groups. Org. Chem. Front. 2:1107

112. Sun H, Guimond N, Huang Y (2016) Advances in the development of catalytic tethering directing groups for C–H functionalization reactions. Org. Biomol. Chem. 14: 8389

113. Rousseau G, Breit B (2011) Removable directing groups in organic synthesis and catalysis. Angew. Chem. Int. Ed. 50:2450

114. Murai S, Kakiuchi F, Sekine S, Tanaka Y, Kamatani A, Sonoda M, Chatani N (1993) Efficient catalytic addition of aromatic carbon-hydrogen bonds to olefins. Nature 366:529

115. Stuart DR, Bertrand-Laperle M, Burgess KMN, Fagnou K (2008) Indole Synthesis via Rhodium Catalyzed Oxidative Coupling of Acetanilides and Internal Alkynes. J. Am. Chem. Soc. 130:16474

116. Rakshit S, Patureau FW, Glorius F (2010) Pyrrole Synthesis via Allylic sp3 C−H Activation of Enamines Followed by Intermolecular Coupling with Unactivated Alkynes. J. Am. Chem. Soc. 132:9585

117. Song G, Chen D, Pan C-L, Crabtree RH, Li X (2010) Rh-Catalyzed Oxidative Coupling between Primary and Secondary Benzamides and Alkynes: Synthesis of Polycyclic Amides. J. Org. Chem. 75:7487

118. Guimond N, Fagnou K (2009) Isoquinoline Synthesis via Rhodium-Catalyzed Oxidative Cross-Coupling/Cyclization of Aryl Aldimines and Alkynes. J. Am. Chem. Soc. 131:12050

119. Hyster TK, Rovis T (2010) Rhodium-Catalyzed Oxidative Cycloaddition of Benzamides and Alkynes via C−H/N−H Activation. J. Am. Chem. Soc. 132:10565

120. Warratz S, Kornhaaß C, Cajaraville A, NiepötteWarratz S, Kornhaaß C, Cajaraville A, Niepötter B, Stalke D, Ackermann L (2015) Ruthenium(II)-catalyzed C-H activation/alkyne annulation by weak coordination with O2 as the sole oxidant. Angew. Chem. Int. Ed. 54:5513r B, Stalke D, Ackermann L (2015) Angew Chem Int Ed 54:5513

121. Bechtoldt A, Tirler C, Raghuvanshi K, Warratz S, Kornhaaß C, Ackermann L (2016) Ruthenium Oxidase Catalysis for Site-Selective C-H Alkenylations with Ambient O2 as the Sole Oxidant. Angew. Chem. Int. Ed. 55:264

122. Tan Y, Hartwig JFJ (2010) Palladium-Catalyzed Amination of Aromatic C−H Bonds with Oxime Esters. Am. Chem. Soc. 132:3676

123. Ng K-H, Chan ASC, Yu W-Y (2010) Pd-Catalyzed Intermolecular ortho-C−H Amidation of Anilides by N-Nosyloxycarbamate. J. Am. Chem. Soc. 132:12862

124. Rakshit S, Grohmann C, Besset T, Glorius F (2011) Rh(III)-Catalyzed Directed C−H Olefination Using an Oxidizing Directing Group: Mild, Efficient, and Versatile. J. Am. Chem. Soc. 133:2350

125. Guimond N, Gouliaras C, Fagnou K (2010) Rhodium(III)-Catalyzed Isoquinolone Synthesis: The N−O Bond as a Handle for C−N Bond Formation and Catalyst Turnover. J. Am. Chem. Soc. 132:6908

126. Guimond N, Gorelsky SI, Fagnou K (2011) Rhodium(III)-Catalyzed Heterocycle Synthesis Using an Internal Oxidant: Improved Reactivity and Mechanistic Studies. J. Am. Chem. Soc. 133:6449

127. Ackermann L, Fenner S (2011) Ruthenium-Catalyzed C–H/N–O Bond Functionalization: Green Isoquinolone Syntheses in Water. Org. Lett. 13:6548

128. Patureau FW, Glorius F (2011) Oxidizing directing groups enable efficient and innovative C-H activation reactions. Angew. Chem. Int. Ed. 50:1977

129. Chinnagolla RK, Pimparkar S, Jeganmohan M (2012) Ruthenium-Catalyzed Highly Regioselective Cyclization of Ketoximes with Alkynes by C–H Bond Activation: A Practical Route to Synthesize Substituted Isoquinolines. Org. Lett. 14:3032

130. Mo J, Wang L, Cui X (2015) Rhodium(III)-Catalyzed C–H Activation/Alkyne Annulation by Weak Coordination of Peresters with O–O Bond as an Internal Oxidant. Org. Lett. 17:4960

131. Liu G, Shen Y, Zhou Z, Lu X (2013) Rhodium(III)-catalyzed redox-neutral coupling of N-phenoxyacetamides and alkynes with tunable selectivity. Angew. Chem. Int. Ed. 52:6033

132. Hyster TK, Ruhl KE, Rovis T (2013) A Coupling of Benzamides and Donor/Acceptor Diazo Compounds To Form γ-Lactams via Rh(III)-Catalyzed C–H Activation. J. Am. Chem. Soc. 135:5364

133. Huang X, Huang J, Du C, Zhang X, Song F, You J (2013) N-Oxide as a Traceless Oxidizing Directing Group: Mild Rhodium(III) –Catalyzed C–H Olefination for the Synthesis of ortho–Alkenylated Tertiary Anilines. Angew. Chem. Int. Ed. 52:12970

134. Wang H, Grohmann C, Nimphius C, Glorius F (2012) Mild Rh(III)-Catalyzed C–H Activation and Annulation with Alkyne MIDA Boronates: Short, Efficient Synthesis of Heterocyclic Boronic Acid Derivatives. J. Am. Chem. Soc. 134:19592

135. Kornhaaß C, Kuper C, Ackermann L (2014) Ferrocenylalkynes for Ruthenium–Catalyzed Isohypsic C–H/N–O Bond Functionalizations. Adv. Synth. Catal. 356:1619

136. Yang F, Ackermann L (2014) Dehydrative C–H/N–OH Functionalizations in H2O by Ruthenium(II) Catalysis: Subtle Effect of Carboxylate Ligands and Mechanistic Insight. J. Org. Chem. 79:12070

137. Yu S, Liu S, Lan Y, Wan B, Li X (2015) Rhodium-Catalyzed C–H Activation of Phenacyl Ammonium Salts Assisted by an Oxidizing C–N Bond: A Combination of Experimental and Theoretical Studies. J. Am. Chem. Soc. 137:1623

138. Brasche G, Buchwald SL (2008) C-H functionalization/C-N bond formation: copper-catalyzed synthesis of benzimidazoles from amidines. Angew. Chem. Int. Ed. 47:1932

139. Mei T-S, Wang X, Yu J-Q (2009) Pd(II)-Catalyzed Amination of C−H Bonds Using Single-Electron or Two-electron Oxidants. J. Am. Chem. Soc. 131:10806

140. Stokes BJ, Dong H, Leslie BE, Pumphrey AL, Driver TG (2007) Intramolecular C−H Amination Reactions: Exploitation of the Rh2(II)-Catalyzed Decomposition of Azidoacrylates. J. Am. Chem. Soc. 129:7500

141. Chiba S, Hattori G, Narasaka K (2007) Rh(II)-catalyzed Isomerization of 2-Aryl-2H-azirines to 2,3-Disubstituted Indoles. Chem. Lett. 36:52

142. Too PC, Noji T, Lim YJ, Li X, Chiba S (2011) Rhodium(III)-Catalyzed Synthesis of Pyridines from α,β-Unsaturated Ketoximes and Internal Alkynes. Synlett 19:2789
143. Zhang X, Qi Z, Li X (2014) Rhodium(III) –Catalyzed C–C and C–O Coupling of Quinoline N-Oxides with Alkynes: Combination of C–H Activation with O–Atom Transfer. Angew. Chem. Int. Ed. 126:10970
144. Wang C, Huang Y (2013) Traceless Directing Strategy: Efficient Synthesis of N-Alkyl Indoles via Redox-Neutral C–H Activation. Org. Lett. 15:5294
145. Muralirajan K, Haridharan R, Prakash S, Cheng C-H (2015) Rhodium(III) –Catalyzed in situ Oxidizing Directing Group–Assisted C–H Bond Activation and Olefination: A Route to 2-Vinylanilines. Adv. Syn. Cat. 357:761
146. Deshmukh DS, Yadav PA, Bhanage BM (2019) Cp*Co(iii)-catalyzed annulation of azines by C–H/N–N bond activation for the synthesis of isoquinolines. Org. Biomol. Chem. 17:3489
147. Zhang Q-R, Huang J-R, Zhang W, Dong L (2014) Highly Functionalized Pyridines Synthesis from N-Sulfonyl Ketimines and Alkynes Using the N–S Bond as an Internal Oxidant. Org. Lett. 16:1684
148. Kaishap PP, Sarma B, Gogoi S (2016) The amide C–N bond of isatins as the directing group and the internal oxidant in Ru-catalyzed C–H activation and annulation reactions: access to 8-amido isocoumarins. Chem. Commun. 52:9809
149. Wu Z, Song H, Cui X, Pi C, Du W, Wu Y (2013) Sulfonylation of Quinoline N-Oxides with Aryl Sulfonyl Chlorides via Copper-Catalyzed C–H Bonds Activation. Org. Lett. 15:1270
150. Ureshino T, Yoshida T, Kuninobu Y, Takai K (2010) Rhodium-Catalyzed Synthesis of Silafluorene Derivatives via Cleavage of Silicon−Hydrogen and Carbon−Hydrogen Bonds. J. Am. Chem. Soc. 132:14324
151. Kuninobu Y, Yamauchi K, Tamura N, Seiki T, Takai K (2013) Rhodium-Catalyzed Asymmetric Synthesis of Spirosilabifluorene Derivatives. Angew. Chem. Int. Ed. 52:1520
152. Zhou Z, Liu G, Chen Y, Lu X (2015) Rhodium(III)-Catalyzed Redox-Neutral C–H Annulation of Arylnitrones and Alkynes for the Synthesis of Indole Derivatives. Adv. Synth. Catal. 357:2944
153. Li B, Pierre H, Dixneuf (2013) sp2 C–H bond activation in water and catalytic cross-coupling reactions. Chem Soc Rev 42:5744
154. Yang J, Fu T, Long Y, Zhou X (2017) Bifunctional Ion Pair Catalysts from Chiral α-Amino Acids. Chin J Org Chem 37:1111
155. Gandeepan P, Kaplaneris N, Santoro S, Vaccaro L, Ackermann L (2019) Biomass-Derived Solvents for Sustainable Transition Metal-Catalyzed C–H Activation. ACS Sustainable Chem Eng 7:8023
156. Lipshutz BH, Gallou F, Handa S (2016) Evolution of Solvents in Organic Chemistry. ACS Sustainable Chem Eng. 4: 5838
157. Sheldon R (2005) Green solvents for sustainable organic synthesis: state of the art. Green Chem. 7:267
158. Nie R, Lai R, Lv S, Xu Y, Guo L, Wang Q, Wu Y (2019) Water-mediated C–H activation of arenes with secure carbene precursors: the reaction and its application. Chem Commun 55:11418
159. Herrerías CI, Yao X, Li Z, Li C-J (2007) Reactions of C−H Bonds in Water. Chem Rev 107:2546
160. Ma W, Mei R, Tenti G, Ackermann L (2014) Ruthenium(II)-Catalyzed Oxidative C–H Alkenylations of Sulfonic Acids, Sulfonyl Chlorides and Sulfonamides. Chem Eur J 20:15248
161. Upadhyay N, Thorat V H, Sato R, Annamalai P, Chuang S-C, Cheng C-H (2017) Synthesis of isoquinolones via Rh-catalyzed C–H activation of substituted benzamides using air as the sole oxidant in water. Green Chem 19:3219
162. Gong H, Zeng H, Zhou F, Li C (2015) Rhodium(I)-catalyzed regiospecific dimerization of aromatic acids: two direct C-H bond activations in water. Angew Chem Int Ed 54:5718
163. Hu X, Yang X, Dai X-J, Li C-J (2017) Palladium-Catalyzed Direct β-C−H Arylation of Ketones with Arylboronic Acids in Water. Adv Syn Catal 359:2402

164. Pu F, Liu Z-W, Zhang L-Y, Fan J, Shi X-Y (2019) Switchable C−H Alkylation of Aromatic Acids with Maleimides in Water: Carboxyl as a Diverse Directing Group. ChemCatChem 11: 4116

165. Mitra T, Kundu M, Roy B (2020) Additive-Free, Pd-Catalyzed 3-Amino-1-methyl-1 H-pyridin-2-one-Directed C(sp 2)-H Arylation and Methylation in Water. J Org Chem 85:345

166. Debabarma S, Md Raja S, Modak B, Maji MS (2019) On-Water Cp*Ir(III)-Catalyzed C-H Functionalization for the Synthesis of Chromones through Annulation of Salicylaldehydes with Diazo-Ketones. J Org Chem 84:6207

167. Chen J, Spear SK, Huddleston JG, Rogers RD (2005) Polyethylene glycol and solutions of polyethylene glycol as green reaction media. Green Chem 7:64

168. Colacino E, Martinez J, Lamaty F, Patrikeeva LS, Khemchyan LL, Ananikov VP, Beletskaya IP (2012) PEG as an alternative reaction medium in metal-mediated transformations. Coord Chem Rev 256:2893

169. Li J, Tang M, Zang L, Zhang X, Zhang, Z, Ackermann L (2016) Amidines for Versatile Cobalt(III)-Catalyzed Synthesis of Isoquinolines through C–H Functionalization with Diazo Compounds. Org Lett 18:2742

170. Wang H, Koeller J, Liu W, Ackermann L (2015) Cobalt(III) −Catalyzed C−H/N−O Functionalizations: Isohypsic Access to Isoquinolines. Chem Eur J 21:15525

171. Kim SH, Lee HS, Kim SH, Kim JN (2008) Regioselective ortho-hydroxylation of aryl moiety of 2-arylpyridines using Pd(OAc)2/Oxone in PEG-3400/tert-BuOH. Tetrahedron Lett 49:5863

172. Ma W, Ackermann L (2015) Cobalt(II)-Catalyzed Oxidative C–H Alkenylations: Regio- and Site-Selective Access to Isoindolin-1-one. ACS Catal 5:2822

173. Kuai C, Wang L, Li B, Yang Z, Cui X (2017) Cobalt-Catalyzed Selective Synthesis of Isoquinolines Using Picolinamide as a Traceless Directing Group. Org Lett 19:2102

174. Cai CM, Zhang T, Kumar R, Wyman CE (2014) Integrated furfural production as a renewable fuel and chemical platform from lignocellulosic biomass. J Chem Technol Biotechnol 89:2

175. Mariscal R, Maireles-Torres P, Ojeda M, Sádaba I, López Granados M (2016) Furfural: a renewable and versatile platform molecule for the synthesis of chemicals and fuels. Energy Environ Sci 9:1144

176. Bozell JJ, Moens L, Elliott DC, Wang Y, Neuenscwander GG, Fitzpatrick SW, Bilski RJ, Jarnefeld JL (2000) Production of levulinic acid and use as a platform chemical for derived products. Resour Conserv Recycl 28:227

177. Khoo HH, Wong LL, Tan J, Isoni V, Sharratt P (2015) Synthesis of 2-methyl tetrahydrofuran from various lignocellulosic feedstocks: Sustainability assessment via LCA. Resour Conserv Recycl 95:174

178. Warratz S, Burns DJ, Zhu C, Korvorapun K, Rogge T, Scholz J, Jooss C, Gelman D, (2017) meta-C-H Bromination on Purine Bases by Heterogeneous Ruthenium Catalysis. Angew Chem Int Ed 56:1557

179. Matsidik R, Luzio A, Hameury S, Komber H, McNeill C R, Caironi M, Sommer M (2016) Effects of PNDIT2 end groups on aggregation, thin film structure, alignment and electron transport in field-effect transistors. J Mater Chem C 4:10371

180. Aldrich TJ, Dudnik AS, Eastham ND, Manley EF, Chen LX, Chang RPH, Melkonyan FS, Facchetti A, Marks TJ (2018) Suppressing Defect Formation Pathways in the Direct C–H Arylation Polymerization of Photovoltaic Copolymers. Macromolecules 51:9140

181. Monks BM, Fruchey ER, Cook SP (2014) Iron–Catalyzed C(sp2)–H Alkylation of Carboxamides with Primary Electrophiles. Angew Chem Int Ed 53:11065

182. Fruchey ER, Monks BM, Cook SP (2014) A Unified Strategy for Iron-Catalyzed ortho-Alkylation of Carboxamides. J Am Chem Soc 136:13130

183. Alonso DM, Wettstein SG, Dumesic JA (2013) Gamma-valerolactone, a sustainable platform molecule derived from lignocellulosic biomass. Green Chem 15:584

184. Zhang Z (2016) Synthesis of γ-Valerolactone from Carbohydrates and its Applications. ChemSusChem 9:156

185. Farrán A, Cai C, Sandoval M, Xu Y, Liu J, Hernáiz MJ, Linhardt RJ (2015) Green Solvents in Carbohydrate Chemistry: From Raw Materials to Fine Chemicals. Chem Rev 115:6811
186. Liguori F, Moreno-Marrodan C, Barbaro P (2015) Environmentally Friendly Synthesis of γ-Valerolactone by Direct Catalytic Conversion of Renewable Sources. ACS Catal 5:1882
187. Santoro S, Ferlin F, Luciani L, Ackermann L, Vaccaro L (2017) Biomass-derived solvents as effective media for cross-coupling reactions and C–H functionalization processes. Green Chem 19:1601
188. Santoro S, Marrocchi A, Lanari D, Ackermann L, Vaccaro L (2018) Towards Sustainable C−H Functionalization Reactions: The Emerging Role of Bio-Based Reaction Media. Chem Eur J 24:13383
189. Rasina D, Kahler-Quesada A, Ziarelli S, Warratz S, Cao H, Santoro S, Ackermann L, Vaccaro L (2016) Heterogeneous palladium-catalysed Catellani reaction in biomass-derived γ-valerolactone. Green Chem 18:5025
190. Ackermann L, Vicente R, Born R (2008) Palladium-Catalyzed Direct Arylations of 1,2,3-Triazoles with Aryl Chlorides using Conventional Heating. Adv Synth Catal 350:741
191. Ferlin F, Luciani L, Santoro S, Marrocchi A, Lanari D, Bechtoldt A, Ackermann L, Vaccaro L (2018) A continuous flow approach for the C–H functionalization of 1,2,3-triazoles in γ-valerolactone as a biomass-derived medium. Green Chem 20:2888
192. Bechtoldt A, Baumert ME, Vaccaro L, Ackermann L (2018) Ruthenium(ii) oxidase catalysis for C–H alkenylations in biomass-derived γ-valerolactone. Green Chem 20:398
193. Bu Q, Rogge T, Kotek V, Ackermann L (2018) Distal Weak Coordination of Acetamides in Ruthenium(II)-Catalyzed C−H Activation Processes. Angew Chem Int Ed 57:765
194. Bu Q, Gońka E, Kuciński K, Ackermann L (2018) Cobalt-Catalyzed Hiyama-Type C−H Activation with Arylsiloxanes: Versatile Access to Highly ortho-Decorated Biaryls. Chem Eur J 25:2213
195. Li BJ, Yang SD, Shi ZJ (2008) Recent Advances in Direct Arylation via Palladium-Catalyzed Aromatic C-H Activation. Synlett 949
196. Ackermann L, Vicente R, Kapdi AR (2009) Transition-metal-catalyzed direct arylation of (hetero)arenes by C-H bond cleavage. Angew Chem Int Ed 48: 9792
197. Tsai AS, Wilson RM, Harada H, Bergman RG, Ellman JA (2009) Rhodium catalyzed enantioselective cyclization of substituted imidazoles via C–H bond activation. Chem Commun:3910
198. Fischmeister C, Doucet H (2011) Greener solvents for ruthenium and palladium-catalysed aromatic C–H bond functionalisation. Green Chem 13:741
199. Crabtree RH (1993) Photocatalysis in C-H Activation. Springer, Netherlands
200. Chen J-R, Hu X-Q, Lu L-Q, Xiao W-J (2016) Exploration of Visible-Light Photocatalysis in Heterocycle Synthesis and Functionalization: Reaction Design and Beyond. Acc Chem Res 49:1911
201. Capaldo L, Ravelli D (2017) Hydrogen Atom Transfer (HAT): A Versatile Strategy for Substrate Activation in Photocatalyzed Organic Synthesis. Eur J Org Chem 15:2056
202. Protti S, Fagnoni M, Ravelli D (2015) Photocatalytic C–H Activation by Hydrogen-Atom Transfer in Synthesis. ChemCatChem, 10:1516
203. Fagnoni M, Dondi D, Ravelli D, Albini A (2007) Photocatalysis for the Formation of the C−C Bond. Chem Rev 107:2725
204. Ravelli D, Dondi D, Fagnoni M, Albini A (2009) Photocatalysis. A multi-faceted concept for green chemistry. Chem Soc Rev 38:1999
205. Tzirakis MD, Lykakis IN, Orfanopoulos M (2009) Decatungstate as an efficient photocatalyst in organic chemistry. Chem Soc Rev 38:2609
206. Condie AG, Gonzalez-Gomez JC, Stephenson CRJ (2010) Visible-Light Photoredox Catalysis: Aza-Henry Reactions via C−H Functionalization. J Am Chem Soc 132:1464
207. Zou Y-Q, Lu L-Q, Fu L, Chang N-J, Chen J-R, Xiao W-J (2011) Visible-light-induced oxidation/[3+2] cycloaddition/oxidative aromatization sequence: a photocatalytic strategy to construct pyrrolo[2,1-a]isoquinolines. Angew Chem Int Ed 50:7171

208. Xuan J, Cheng Y, An J, Lu LQ, Zhang XX, Xiao W-J (2011) Visible light-induced intramolecular cyclization reactions of diamines: a new strategy to construct tetrahydroimidazoles. Chem Commun 47:8337

209. Xuan J, Feng Z-J, Duan S-W, Xiao W-J RSC (2012) Room temperature synthesis of isoquino[2,1-a][3,1]oxazine and isoquino[2,1-a]pyrimidine derivatives via visible light photoredox catalysis. Adv 2:4065

210. Deng Q-H, Zou Y-Q, Lu L-Q, Tang Z-L, Chen J-R, Xiao W-J (2014) De novo synthesis of imidazoles by visible-light-induced photocatalytic aerobic oxidation/[3+2] cycloaddition/aromatization cascade. Chem Asian J 9:2432

211. Xia X-D, Xuan J, Wang Q, Lu L-Q, Chen J-R, Xiao W-J (2014) Synthesis of 2-Substituted Indoles through Visible Light-Induced Photocatalytic Cyclizations of Styryl Azides. Adv Synth Catal 356:2807

212. Rueping M, Leonori D, Poisson T (2011) Visible light mediated azomethine ylide formation—photoredox catalyzed [3+2] cycloadditions. Chem Commun 47:9615

213. Zhu S, Das A, Bui L, Zhou H, Curran DP, Rueping M (2013) Oxygen Switch in Visible-Light Photoredox Catalysis: Radical Additions and Cyclizations and Unexpected C–C-Bond Cleavage Reactions. J Am Chem Soc 135:1823

214. Zhang P, Xiao T, Xiong S, Dong X, Zhou L (2014) Synthesis of 3-Acylindoles by Visible-Light Induced Intramolecular Oxidative Cyclization of o-Alkynylated N,N-Dialkylamines. Org Lett 16:3264

215. Tucker JW, Narayanam JM, Krabbe SW, Stephenson CRJ (2010) Electron transfer photoredox catalysis: intramolecular radical addition to indoles and pyrroles. Org Lett12:368

216. Cheng Y, Yang J, Qu Y, Li P (2012) Aerobic Visible-Light Photoredox Radical C–H Functionalization: Catalytic Synthesis of 2-Substituted Benzothiazoles. Org Lett 14:98

217. Maity S, Zheng N (2012) A Visible-Light-Mediated Oxidative C–N Bond Formation/Aromatization Cascade: Photocatalytic Preparation of N-Arylindoles. Angew Chem Int Ed 51: 9562

218. Hernandez-Perez AC, Collins SK (2013) A Visible-Light-Mediated Synthesis of Carbazoles. Angew Chem Int Ed 52:12696

219. Farney EP, Yoon TP (2014) Visible-Light Sensitization of Vinyl Azides by Transition-Metal Photocatalysis. Angew Chem Int Ed 53:793

220. Gao X-W, Meng Q-Y, Li J-X, Zhong J-J, Lei T, Li X-B, Tung C-H, Wu L-Z (2015) Visible Light Catalysis Assisted Site-Specific Functionalization of Amino Acid Derivatives by C–H Bond Activation without Oxidant: Cross-Coupling Hydrogen Evolution Reaction. ACS Catal 5:2391

221. Heitz DR, Tellis JC, Molander GA (2016) Photochemical Nickel-Catalyzed C–H Arylation: Synthetic Scope and Mechanistic Investigations. J Am Chem Soc 138:12715

222. Gauchot V, Sutherland DR, Lee A-L (2017) Dual gold and photoredox catalysed C–H activation of arenes for aryl–aryl cross couplings. Chem Sci 8:2885

223. Boorman TC, Larrosa I (2011) Gold-mediated C–H bond functionalisation. Chem Soc Rev 40:1910

224. Ren X, Wang Q, Yu W, Zhan X, Yao Y, Qin B, Dong M, He X (2017) Photoredox catalytic intramolecular imine C–H bond functionalization using ligand free Cu(ii) salts. Org Chem Front 4:2022

225. Kaplaneris N, Bisticha A, Papadopoulos GN, Limnios D, Kokotos CG (2017) Photoorganocatalytic synthesis of lactones via a selective C–H activation–alkylation of alcohols. Green Chem 19:4451

226. Capaldo L, Merli D, Fagnoni M, Ravelli D (2019) Visible Light Uranyl Photocatalysis: Direct C–H to C–C Bond Conversion. ACS Catalysis 9:3054

227. Li Y, Lei M, Gong L (2019) Photocatalytic regio- and stereoselective C(sp3)–H functionalization of benzylic and allylic hydrocarbons as well as unactivated alkanes. Nat Catal 2:1016

228. Sagadevan A, Greaney MF (2019) meta-Selective C−H Activation of Arenes at Room Temperature Using Visible Light: Dual-Function Ruthenium Catalysis. Angew Chem Int Ed 58:9826
229. Noack M, Göttlich R (2020) Copper (I) catalysed cyclisation of unsaturated N-benzoyloxyamines: an aminohydroxylation via radicals . Chem Commun 38:536
230. Banwell MG, Lupton DW (2006) Tandem Radical Cyclization Reactions, Initiated at Nitrogen, as an Approach to the CDE-Tricyclic Cores of Certain Post-secodine Alkaloids. Heterocycles 68:71
231. Sirinimal HS, Hebert SP, Samala G, Chen H, Rosenhauer GJ, Schlegel HB, Stockdill JL (2018) A Synthetic and Computational Study of Tin-Free Reductive Tandem Cyclizations of Neutral Aminyl Radicals. Org Lett 20:6340
232. Li Y, Liang Y, Dong J, Deng Y, Zhao C, Su Z, Guan W, Bi X, Liu Q, Fu J (2019) Directed Copper-Catalyzed Intermolecular Aminative Difunctionalization of Unactivated Alkenes. J Am Chem Soc 141:18475
233. Supranovich VI, Levin VV, Dilman AD (2019) Radical Addition to N-Tosylimines via C–H Activation Induced by Decatungstate Photocatalyst. Org Lett 21:4271
234. Xie X, Liu J, Wang L, Wang M (2019) Visible-Light-Induced Alkynylation of α-C–H Bonds of Ethers with Alkynyl Bromides without External Photocatalyst. Eur J Org Chem 2020:1534
235. Fang J, Dong W-L, Xu G-Q, Xu P-F (2019) Photocatalyzed Metal-Free Alkylheteroarylation of Unactivated Olefins via Direct Acidic C(sp3)–H Bond Activation. Org Lett 21:4480
236. Li L, Luo H, Zhao Z, Li Y, Zhou Q, Xu J, Li J, Ma Y-N (2019) Photoredox-Catalyzed Remote Difunctionalizations of Alkenes To Synthesize Fluoroalkyl Ketones with Dimethyl Sulfoxide as the Oxidant. Org Lett 21:9228
237. Si X, Zhang L, Hashmi ASK (2019) Benzaldehyde- and Nickel-Catalyzed Photoredox C(sp3)–H Alkylation/Arylation with Amides and Thioethers. Org Lett 21:6329
238. Yang X, Zhu Y, Xie Z, Li Y, Zhang Y (2020) Visible-Light-Induced Charge Transfer Enables Csp3–H Functionalization of Glycine Derivatives: Access to 1,3-Oxazolidines. Org Lett 22:1638
239. T Noel (2017) Photochemical Processes in Continuous-Flow Reactors, World Scientific Singapore
240. Cambie D, Bottecchia C, Straathof NJW, Hessel V, Noel T (2016) Applications of Continuous-Flow Photochemistry in Organic Synthesis, Material Science, and Water Treatment. Chem Rev 116:10276
241. Lesieur M, Genicot C, Pasau P (2018) Development of a Flow Photochemical Aerobic Oxidation of Benzylic C–H Bonds. Org Lett 20:1987
242. Laudadio G, Govaerts S, Wang Y, Ravelli D, Koolman HF, Fagnoni M, Djuric SW, Noel T (2018) Selective C(sp 3)-H Aerobic Oxidation Enabled by Decatungstate Photocatalysis in Flow. Angew Chem Int Ed 57:4078
243. Bottecchia C, Martín R, Abdiaj I, Crovini E, Alcazar J, Orduna J, Blesa MJ, Carrillo JR, Prieto P, Noël T (2019) De novo Design of Organic Photocatalysts: Bithiophene Derivatives for the Visible-light Induced C−H Functionalization of Heteroarenes. Adv Synth Catal 361:945
244. Larhed M, Moberg C, Hallberg A (2020) Microwave-accelerated homogeneous catalysis in organic chemistry. Acc Chem Res 35:717
245. Wathey B, Tierney J, Lidstrom P, Westman J (2002) The impact of microwave-assisted organic chemistry on drug discovery. Drug DiscoVery Today 7:373
246. Lew A, Krutzik PO, Hart ME, Chamberlin AR (2002) Increasing Rates of Reaction: Microwave-Assisted Organic Synthesis for Combinatorial Chemistry. J Comb Chem 4:95
247. Baghbanzadeh M, Pilger C, Kappe CO (2011) Palladium-Catalyzed Direct Arylation of Heteroaromatic Compounds: Improved Conditions Utilizing Controlled Microwave Heating. J Org Chem 76:8138
248. Mehta VP, Van der Eycken E (2011) Microwave-assisted C–C bond forming cross-coupling reactions: an overview. Chem Soc Rev 40:4925

249. Sharma A, Vacchani D, Van der Eycken E (2013) Developments in Direct C–H Arylation of (Hetero)Arenes under Microwave Irradiation. Chem Eur J 19:1158

250. Gupta AK, Singh N, Singh KN (2013) Microwave Assisted Organic Synthesis: Cross Coupling and Multicomponent Reactions. Curr Org Chem 17:474

251. Besson T, Fruit C (2016) Recent Developments in Microwave-Assisted Metal-Catalyzed C–H Functionalization of Heteroarenes for Medicinal Chemistry and Material Applications. Synthesis 48:3879

252. Baber RA, Bedford RB, Betham M, Blake ME, Coles SJ, Haddow MF, Hursthouse MB, Orpen AG, Pilarski LT, Pringle PG, Wingad RL, (2006) Chiral palladium bis(phosphite) PCP-pincer complexes via ligand C-H activation. Chem Commun 37:3880

253. Sridharan V, Martín MA, Menéndez JC (2009) Acid-Free Synthesis of Carbazoles and Carbazolequinones by Intramolecular Pd-Catalyzed, Microwave-Assisted Oxidative Biaryl Coupling Reactions - Efficient Syntheses of Murrayafoline A, 2-Methoxy-3-methylcarbazole, and Glycozolidine. Eur J Org Chem 27:4614

254. Mahindra A, Bagra N, Jain R (2013) Palladium-Catalyzed Regioselective C-5 Arylation of Protected l-Histidine: Microwave-Assisted C–H Activation Adjacent to Donor Arm. J Org Chem 78:10954

255. Choi S J, Kuwabara J, Kanbara T (2013) Microwave-Assisted Polycondensation via Direct Arylation of 3,4-Ethylenedioxythiophene with 9,9-Dioctyl-2,7-dibromofluorene. ACS Sustainable Chem Eng 1:878

256. Kokornaczyk A, Schepmann D, Yamaguchi J, Itamib K, Wünsch B (2016) Microwave-assisted regioselective direct C–H arylation of thiazole derivatives leading to increased σ1 receptor affinity. Med Chem Commun 7:327

257. Baladi T, Granzhan A, Piguel S (2016) Microwave-Assisted C-2 Direct Alkenylation of Imidazo[4,5-b]pyridines: Access to Fluorescent Purine Isosteres with Remarkably Large Stokes Shifts. Eur J Org Chem 2016:2421

258. Harari M, Couly F, Fruit C, Besson T (2016) Pd-Catalyzed and Copper Assisted Regioselective Sequential C2 and C7 Arylation of Thiazolo[5,4-f]quinazolin-9(8H)-one with Aryl Halides. Org Lett 18:3282

259. Godeau J, Harari M, Laclef S, Deau E, Fruit C, Besson T (2015) Cu/Pd-Catalyzed C-2–H Arylation of Quinazolin-4(3H)-ones with (Hetero)aryl Halides. Eur J Org Chem 35: 7705

260. Li S, Wan P, Ai J, Sheng R, Hu Y, Hu Y (2017) Palladium-Catalyzed, Silver-Assisted Direct C-5-H Arylation of 3-Substituted 1,2,4-Oxadiazoles under Microwave Irradiation. Adv Synth Catal 359:772

261. Khlebnikov V, Heckenroth M, Müller-Bunz H, Albrecht M (2013) Platinum(ii) and platinum(iv) complexes stabilized by abnormal/mesoionic C4-bound dicarbenes. Dalton Trans 42:4197

262. Diness F, Begtrup M (2014) Sequential Direct SNAr Reactions of Pentafluorobenzenes with Azole or Indole Derivatives. Org Lett 16:3130

263. Mfuh AM, Larionov OV (2015) Heterocyclic N-Oxides - An Emerging Class of Therapeutic Agents. Curr Med Chem 22:2819

264. Stephens DE, Lakey-Beita J, Atesin AC, Ateşin TA, Chavez G, Arman HD, Larionov OV (2015) Palladium-Catalyzed C8-Selective C–H Arylation of Quinoline N-Oxides: Insights into the Electronic, Steric, and Solvation Effects on the Site Selectivity by Mechanistic and DFT Computational Studies. ACS Catal 5:167

265. Stephens DE, Lakey-Beita J, Chavez G, Ilie C, Arman HD, Larionov OV (2015) Experimental and mechanistic analysis of the palladium-catalyzed oxidative C8-selective C-H homocoupling of quinoline N-oxides. Chem Commun 51:9507

266. Vachhani DD, Sharma A, Van der Eycken E (2013) Copper-catalyzed direct secondary and tertiary C-H alkylation of azoles through a heteroarene-amine-aldehyde/ketone coupling reaction. Angew Chem Int Ed 52:2547

267. Huang J, Huang Y, Wang T, Huang Q, Wang Z, Chen Z (2017) Microwave-Assisted Cp*CoIII-Catalyzed C–H Activation/Double C–N Bond Formation Reactions to Thiadiazine 1-Oxides. Org Lett 19:1128

268. Sharma N, Bahadur V, Sharma UK, Saha D, Li Z, Kumar Y, Colaers J, Singh BK, Van der Eycken EV (2018) Microwave-Assisted Ruthenium-Catalysed ortho-C−H Functionalization of N-Benzoyl α-Amino Ester Derivatives. Adv Syn Catal 360:3083

269. Tan KL, Vasudevan A, Bergman RG, Ellman JA, Souers AJ (2003) Microwave-Assisted C−H Bond Activation: A Rapid Entry into Functionalized Heterocycles. Org Lett 5:2131

270. Lewis JC, Wu JY, Bergman RG, Ellman JA (2006) Microwave-Promoted Rhodium-Catalyzed Arylation of Heterocycles through C–H Bond Activation. Angew Chem Int Ed 45:1589

271. Lee H, Sim Y-K, Park J-W, Jun C-H (2014) Microwave-Assisted, Rhodium(III)-Catalyzed N-Annulation Reactions of Aryl and α,β-Unsaturated Ketones with Alkynes. Chem Eur J 20:323

272. Song L, Tian G, Blanpain A, Van Meervelt L, Van der Eycken EV (2019) Diversification of Peptidomimetics and Oligopeptides through Microwave-Assisted Rhodium(III)-Catalyzed Intramolecular Annulation. Adv Syn Catal 361:4442

273. Sherikar MS, Prabhu KR (2019) Weak Coordinating Carboxylate Directed Rhodium(III)-Catalyzed C–H Activation: Switchable Decarboxylative Heck-Type and [4 + 1] Annulation Reactions with Maleimides. Org Lett 21:4525

274. Hoang GL, Streit AD, Ellman JA (2018) Three-Component Coupling of Aldehydes, Aminopyrazoles, and Sulfoxonium Ylides via Rhodium(III)-Catalyzed Imidoyl C–H Activation: Synthesis of Pyrazolo[1,5-a]pyrimidines. J Org Chem 83:15347

275. Ackermann L (2020) Metalla-electrocatalyzed C–H Activation by Earth-Abundant 3d Metals and Beyond. Acc Chem Res 53:84

276. Jiao K-J, Xing Y-K, Yang Q-L, Qiu H, Mei T-S (2020) Site-Selective C–H Functionalization via Synergistic Use of Electrochemistry and Transition Metal Catalysis. Acc Chem Res 53:300

277. Kärkäs MD (2018) Electrochemical strategies for C–H functionalization and C–N bond formation. Chem Soc Rev 47:5786

278. Li L-J, Jiang Y-Y, Lam CM, Zeng C-C, Hu L-M, Little RD (2015) Aromatic C–H Bond Functionalization Induced by Electrochemically in Situ Generated Tris(p-bromophenyl) aminium Radical Cation: Cationic Chain Reactions of Electron-Rich Aromatics with Enamides. J Org Chem 80:11021

279. Ma C, Zhao C-Q, Li Y-Q, Zhang L-P, Xu X-T, Zhang K, Mei TS (2017) Palladium-catalyzed C–H activation/C–C cross-coupling reactions via electrochemistry. Chem Commun 53:12189

280. Sauermann N, Meyer T, Tian C, Ackermann L (2017) Electrochemical Cobalt-Catalyzed C–H Oxygenation at Room Temperature. J Am Chem Soc 139:18452

281. Zhang S, Li L, Wang H, Li Q, Liu W, Xu K, Zeng C (2018) Scalable Electrochemical Dehydrogenative Lactonization of C(sp2/sp3)–H Bonds. Org Lett 20:252

282. Liang S, Zeng C-C, Tian H-Y, Sun B-G, Luo X-G, Ren F (2018) Redox Active Sodium Iodide/Recyclable Heterogeneous Solid Acid: An Efficient Dual Catalytic System for Electrochemically Oxidative α-C−H Thiocyanation and Sulfenylation of Ketones. Adv Syn Catal 360:1444

283. Qiu Y, Kong W-J, Struwe J, Sauermann N, Rogge T, Scheremetjew A, Ackermann L (2018) Electrooxidative Rhodium-Catalyzed C-H/C-H Activation: Electricity as Oxidant for Cross-Dehydrogenative Alkenylation. Angew Chem Int Ed 57:5828

284. Zhang S-K, Samanta RC, Sauermann N, Ackermann L (2018) Nickel-Catalyzed Electrooxidative C−H Amination: Support for Nickel(IV). Chem Eur J 24:19166

285. Qiu Y, Stangier M, Meyer TH, Oliveira JC, Ackermann L (2018) Iridium-Catalyzed Electrooxidative C-H Activation by Chemoselective Redox-Catalyst Cooperation. Angew Chem Int Ed 57:14179

286. Zeng L, Li H, Tang S, Gao X, Deng Y, Zhang G, Pao C-W, Chen J-L, Lee J-F, Lei A (2018) Cobalt-Catalyzed Electrochemical Oxidative C–H/N–H Carbonylation with Hydrogen Evolution. ACS Catal 8:5448

287. Zhao H-B, Xu P, Song J, Xu H-C (2018) Cathode Material Determines Product Selectivity for Electrochemical C-H Functionalization of Biaryl Ketoximes. Angew Chem Int Ed 57:15153

288. Mei R, Koeller J, Ackermann L (2018) Electrochemical ruthenium-catalyzed alkyne annulations by C–H/Het–H activation of aryl carbamates or phenols in protic media. Chem Commun, 54:12879

289. Mei R, Sauermann N, Oliveira JCA, Ackermann L (2018) Electroremovable Traceless Hydrazides for Cobalt-Catalyzed Electro-Oxidative C–H/N–H Activation with Internal Alkynes. J Am Chem Soc 140:7913

290. Meyer TH, Oliveira JCA, Sau SC, Ang NWJ, Ackermann L (2018) Electrooxidative Allene Annulations by Mild Cobalt-Catalyzed C–H Activation. ACS Catalysis 8:9140

291. Mei R, Fang X, He L, Sun J, Zou L, Mab W, Ackermann L (2020) Cobaltaelectro-catalyzed oxidative allene annulation by electro-removable hydrazides. Chem Commun 56:1393

292. Wang Z-Q, Hou C, Zhong Y-F, Lu Y-X, Mo Z-Y, Pan Y-M, Tang H-T (2019) Electrochemically Enabled Double C–H Activation of Amides: Chemoselective Synthesis of Polycyclic Isoquinolinones. Org Lett 21:9841

293. Kong W-J, Finger LH, Messinis AM, Kuniyil R, Oliveira JCA, Ackermann L (2019) Flow Rhodaelectro-Catalyzed Alkyne Annulations by Versatile C–H Activation: Mechanistic Support for Rhodium(III/IV). J Am Chem Soc 141:17198

294. Kong W-J, Finger LH, Oliveira JCA, Ackermann L (2019) Rhodaelectrocatalysis for Annulative C-H Activation: Polycyclic Aromatic Hydrocarbons through Versatile Double Electrocatalysis. Angew Chem Int Ed 58:6342

295. Huang M, Dai J, Cheng X, Ding M (2019) Electrochemical Approach for Direct C–H Phosphonylation of Unprotected Secondary Amine. Org Lett 21:7759

296. He T-J, Ye Z, Ke Z, Huang J-M (2019) Stereoselective synthesis of sulfur-containing β-enaminonitrile derivatives through electrochemical Csp3–H bond oxidative functionalization of acetonitrile. Nature Commun 10:1

297. Kumar GS, Peshkov A, Brzozowska A, Nikolaienko P, Zhu C, Rueping M (2020) Nickel-Catalyzed Chain-Walking Cross-Electrophile Coupling of Alkyl and Aryl Halides and Olefin Hydroarylation Enabled by Electrochemical Reduction. Angew Chem 132:6513

298. Meyer TH, Chesnokov GA, Ackermann L (2020) Cobalta-Electrocatalyzed C−H Activation in Biomass-Derived Glycerol: Powered by Renewable Wind and Solar Energy. ChemSusChem 13:668

Flue Gas Treatment via Dry Reforming of Methane

Satyam Gupta, Neeraj Koshta, Raghvendra Singh, and Goutam Deo

Abstract Flue gas emission from coal-fired power plants is a major pollutant having constituents, which have a significant role in global warming. Currently, processes to sequester carbon dioxide from flue gas are not cost-effective. Thus, there is a need to develop an alternative process where we can utilize CO_2 in flue gas, producing useful energy-containing or petrochemical products. Dry reforming of methane is one such process in which carbon dioxide can be used. Carbon dioxide serves as an oxidizer of methane, producing a mixture of hydrogen and carbon monoxide. Water is also a product. However, at present, this process has several challenges. The challenges include improving the H_2/CO ratio and decreasing catalyst coking. This is especially true for low-cost catalysts. Coking and H_2/CO ratios in the product are thermodynamically inter-related thus bringing kinetics and aspects of catalyst design into the equation to achieve economically desirable H_2/CO ratios, while not having forbidden rates of carbon deposition. Here, we discuss the thermodynamic and kinetic aspect of this reaction to achieve a low rate of carbon deposition. Further, we discuss various aspects of catalyst design and process changes to achieve low carbon deposition. We also discuss current kinetic models of this reaction and compare them since the kinetics will have an effect on reactor design. Finally, we conclude this chapter by discussing various constraints currently faced towards the industrial use of dry reforming of methane using flue gas and suggest remedial steps.

Keywords Dry reforming · Tri reforming · Alleviate coking · Eley-Rideal model · Bradford mechanism · Tsipouriari mechanism

S. Gupta · N. Koshta · R. Singh (✉) · G. Deo (✉)
Department of Chemical Engineering, Indian Institute of Technology Kanpur, Kanpur, India
e-mail: goutam@iitk.ac.in; raghvend@iitk.ac.in

1 Introduction

Flue gases are produced from the exhaust of combustion units, which include those from coal-fired and natural gas-fired burners. The main constituents of flue gas are N_2, CO_2, H_2O and O_2, with a trace amount of SO_2 and NO_x. Typical compositions of flue gas from coal-fired and natural gas-fired burners are given in Table 1.

The flue gas composition in mol percentage based on the typical composition of Indian coal and an air to fuel ratio of 1.3 is $CO_2 = 12.840$, $O_2 = 4.527$, $H_2O = 7.5576$ and $N_2 = 75.032$. The CO_2 emitted from these burners is a greenhouse gas (GHG), which has been linked to global warming [2]. The CO_2 emitted by India is about 1.6 tonnes of CO_2 per capita, which is well below the global average of 4.4 tonnes [2]. However, the population of India plays a big role and the global share of CO_2emissions by India is about 6.4%.

Considering that the energy requirement of India is increasing, it is expected that the amount of CO_2 emitted by India will further increase. The government has initiated several alternatives that do not involve coal, natural gas and other fossil fuels to decrease the amount of CO_2 emitted. Despite these considerations, it is expected that the CO_2 amount in the atmosphere will continue to be a concern.

One of the alternatives being recently examined is to use the flue gas from the burners to produce chemicals. For example, the flue gas composition is a potent source of chemicals once methane (CH_4), another GHG, is added. It has been proposed that the mixture of CO_2, O_2 and H_2O, with N_2 as a diluent, can be reacted with CH_4 to produce syngas. Syngas is a mixture of CO and H_2, which can be used to produce several C_1-chemicals, which include methanol, aldehydes and others [3]. Flue gas also has small amounts of impurities present, such as oxides of sulphur and nitrogen. It is likely that these impurities need to be separated before the flue gas can be processed. Thus, instead of separating CO_2 from flue gas, the flue gas itself can be used as the raw material along with CH_4 for syngas production.

Due to the combined presence of CO_2, O_2 and H_2O, the combined conversion of flue gas with CH_4 is commonly referred to as the tri-reforming of methane. The "tri" refers to the combination of steam reforming of methane (SRM), dry reforming of methane (DRM) and partial oxidation of methane (POX). Other combinations of reactions have also been proposed. Also important during the tri-reforming reaction is the water gas shift reaction (WGS), or its reverse (RWGS). The WGS or RWGS

Table 1 Typical composition of flue gas [1]

Gas	Natural gas-fired burners	Coal-fired burners
	mol (%)	
CO_2	9.0	13.0
O_2	2.5	4.0
H_2O	19.0	9.0
N_2	69.5	74.0

Table 2 Stoichiometry of the four main reactions involved in tri-reforming of methane

Process	Reaction	Reaction number
SRM	$H_2O + CH_4 \rightarrow 3H_2 + CO$	1
DRM	$CO_2 + CH_4 \rightarrow 2H_2 + 2CO$	2
POX	$O_2 + 2CH_4 \rightarrow 2CO + 4H_2$	3
WGS	$CO + H_2O \rightarrow CO_2 + H_2$	4

reactions have been proposed to be at equilibrium under normal operating conditions [4]. These four reactions are stoichiometrically represented in Table 2.

To effectively carry out these reactions so that syngas is produced, a suitable catalyst is required.

In what follows, we have first investigated the thermodynamics of the DRM reaction in terms of equilibrium conversions and product yields. The DRM reaction is then extended to include the effect of O_2 and H_2O on the conversions and H_2/CO ratio at different temperatures. Critical in this analysis is to consider the formation of carbon as a product. Following the thermodynamic analysis, we present, as an example, some of our results on the effect of O_2 addition on the conversions, H_2/CO ratio, and carbon deposition at two reaction temperatures. Since operating conditions and catalyst design are some of the degrees of freedom to achieve the desired composition of the syngas, we have taken up catalyst improvement strategies to alleviate coking next. Then, we have discussed kinetics of DRM reaction, wherein, various mechanisms have been discussed and compared. Finally, analysis of a proposed process of the tri-reforming reaction has been carried out in the process modelling section, and a review of catalyst improvement strategies for tri-reforming is presented.

2 Thermodynamics Equilibrium Aspects of the DRM Reaction

Operating conditions, such as temperature and feed composition, have an effect on the CH_4 and CO_2 conversions, H_2/CO ratio and carbon formation. These effects need to be analysed using thermodynamics so that the limits of the process can be recognized, and it is possible to identify regions of high conversion and H_2/CO ratio, and low carbon formation. Thermodynamic or equilibrium calculations can be conveniently carried out by minimizing the Gibbs free energy of the process instead of having to limit ourselves to the minimum number of reactions involved. Gibbs free energy minimization routines are readily available on standard software, such as ASPEN PLUS™, and have been used by a number of investigations [5–7].

2.1 Temperature Has an Effect on Methane Conversion at Equilibrium

Using the Gibbs free energy minimization routine and considering CO, H_2, H_2O and solid-carbon as the products, we found that as the temperature increases from 0 °C the equilibrium conversion of methane decreases, and reaches a minimum at approximately 340 °C. A further increase in temperature increases the conversion of methane. A similar trend is observed for CO_2 conversion, except that the lowest conversion is achieved at around 550 °C. The H_2/CO ratio, on the other hand, decreases monotonically as the temperature increases, and asymptotically approaches a value of unity as the temperature reaches about 900 °C (Fig. 1). Usually, low temperature studies are avoided due to the small rates and often high-temperature studies, greater than 500 °C, are examined.

2.2 Temperature Also Has an Effect on Product Yield at Equilibrium

Assuming CO, H_2, H_2O and solid-carbon as the only products, the equilibrium amount of H_2 and CO formed follows a sigmoidal curve, asymptotically reaching the highest value at temperatures more than 1000 °C, where complete conversion of
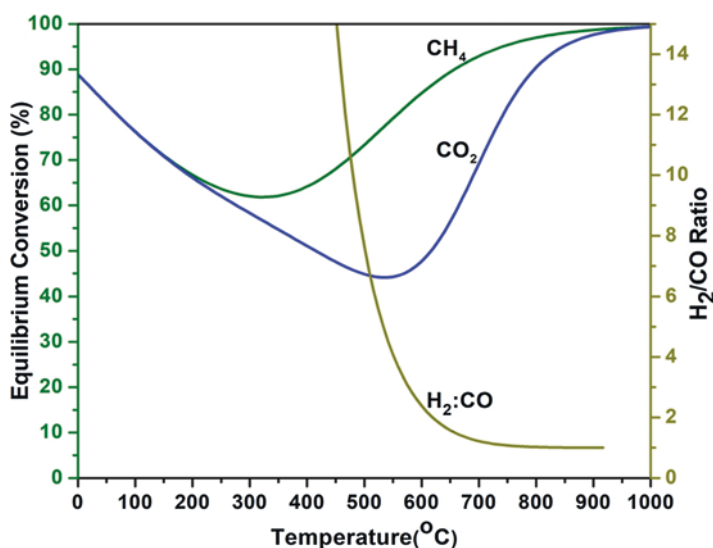
Fig. 1 Effect of temperature on equilibrium conversion of CH_4, CO_2 and H_2/CO ratio. The DRM and carbon formation reactions have been modelled in ASPEN PLUS™. Inlet moles: F_{CH4} = 1 mol/h and F_{CO4} = 1 mol/h

the reactants takes place. At temperatures of 1000 °C and above the stoichiometric formation of H_2 and CO by the DRM reaction, given by reaction number 2 in Table 2, is achieved. In contrast, the undesirable carbon yield decreases with increase in temperature and so does the yield of water (Fig. 2). To explain the variations of H_2, CO, H_2O and solid-carbon with temperature, at temperatures lower than 1000 °C, we need to consider at least three independent reactions, which may include the DRM reaction, a reaction involving H_2O (e.g. WGS or RWGS) and one involving solid-carbon (e.g. methane cracking). Our results shown in Figs. 1 and 2 are in agreement with those of Pakhare and Spivey [8].

Though coke is produced in significant amounts at temperatures less than 1000 °C, it is possible to decrease its presence by considering different reactor set-ups. For example, coke formation and its removal can be stoichiometrically represented by reactions 5 and 6 below (Table 3).

Thus, for lower coking rate, reactions 5 and 6 should proceed, such that the net rate of coke formation is very small or negligible. This suggests that reaction 5 should proceed at a rate equal to reaction 6. Interestingly, experimental results validate this prediction. Ginsburg et al. studied dry reforming of methane in a CREC riser over 20 wt% Ni/USY-zeolite catalyst and found that as CH_4/CO_2 ratio increases, the moles of coke formed per mole of methane converted increases [9]. An increase in the CH_4/CO_2 reaction is expected to increase reaction 5 relative to 6.

One possibility to overcome carbon deposition is to carry out the reaction in a recycle reactor with low per pass conversion to lower coke formation. In the recycle
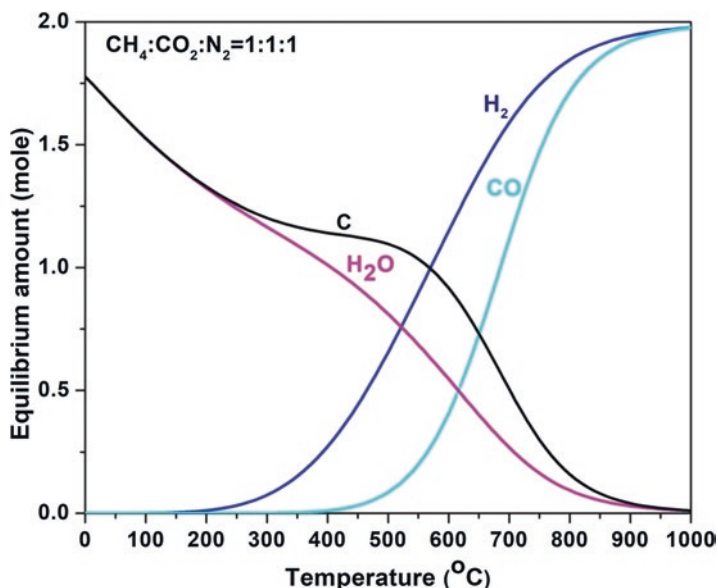
Fig. 2 Effect of temperature on product distribution of DRM at thermodynamics equilibrium condition. The DRM and carbon formation reactions have been modelled in ASPEN PLUS™. Inlet moles: $F_{CH4} = 1$ mol/h and $F_{CO4} = 1$ mol/h

Table 3 Reactions showing carbon formation and removal during DRM

Process	Reaction	Reaction number
Coke formation	$CH_4 \rightarrow C + 2H_2$	5
Coke removal	$CO_2 + C \rightarrow 2CO$	6
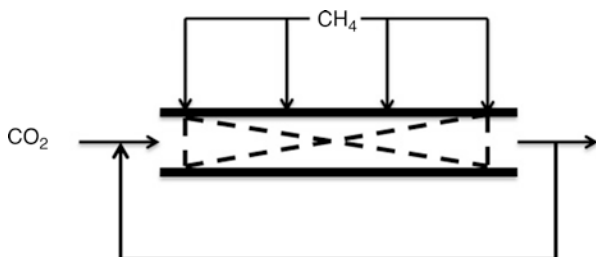
Fig. 3 Schematic of a reactor system for the DRM reaction

reactor, excess of CO_2 may be used. The unused CO_2 should be separated and recycled to achieve high overall conversions of methane. An alternative reactor system shown in Fig. 3 may be one that introduces multiple side-streams of CH_4 with excess CO_2, which is also recycled.

Higher H_2/CO ratio in the product may be required for different final products in the petrochemical industry in which H_2 and CO are provided by DRM. Equilibrium analysis of the DRM reaction showed that as the CH_4/CO_2 ratio in feed increases, the H_2/CO ratio in the product increases for a fixed operating temperature [10]. In contrast, for a fixed CH_4/CO_2 ratio as the operating temperature decreases, the H_2/CO ratio increases and reaches a limiting value of the fixed H_2/CO ratio as given in the feed. Consequently, a high CH_4/CO_2 ratio and lower operating temperature should be preferred for a high H_2/CO ratio in the product. However, these two requirements also cause higher coke formation. Thus, there exists an optimum operating temperature and feed ratio that minimizes coke formation while satisfying the requirement of H_2/CO ratio in the product stream of that DRM reaction, which can then be used as a feed for a specific petrochemical product.

In this section on thermodynamic analysis, we observed that as the temperature increases the methane conversion increases while H_2/CO ratio and carbon formation decrease. In the next section, we present our experimental data examining the effect of temperature on the conversions, H_2/CO ratio and carbon formation. We also add oxygen, another component of flue gas, to the reactants and show its effect on the three output parameters of the product.

3 Effect of Changing Operating Conditions of the Reactor on Conversions, H_2/CO Ratio and Carbon Deposition from Experimental Observations Using a Ni/$MgAl_2O_4$ Catalyst

A 10% Ni/$MgAl_2O_4$ catalyst (surface area = 62 m²/g) was synthesized using an incipient wetness impregnations technique [11]. The catalyst was calcined at 850 °C and then reduced in hydrogen at 752 °C. Using H_2-chemisorption and temperature-programmed reduction, the effective dispersion of this Ni/$MgAl_2O_4$ catalyst was determined to be 5.3%. This catalyst was then tested for the variation of operating conditions of a DRM reaction carried out in a down-flow fixed-bed reactor.

3.1 Increasing Reactor Temperature Increases Conversion

Temperature increases the conversions, provided the conversions are below the equilibrium conversions at that particular temperature. For the Ni/$MgAl_2O_4$ catalysts synthesized above, increasing the reaction temperature from 600 to 750 °C increases the CH_4 and CO_2 conversions of the DRM reaction, as shown in Figs. 4 and 5. The choice of these two temperatures is such that we operate the reactor at a temperature where carbon deposition is favoured (600 °C) and where the carbon amount is lowered (750 °C) as per the equilibrium values shown in Fig. 2. Based on the
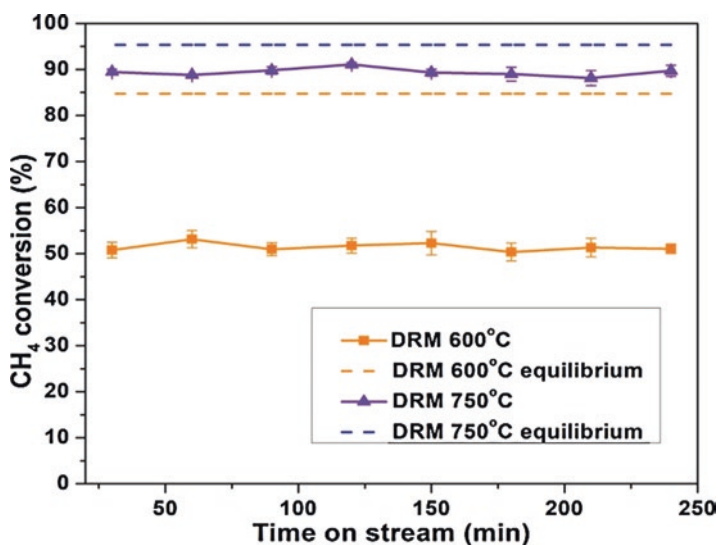
Fig. 4 Variation of % CH_4 during 4 h TOS for DRM (CH_4:CO_2:N_2 = 1:1:1) at 1 atm. over 10% Ni/$MgAl_2O_4$ at 600 and 750 °C
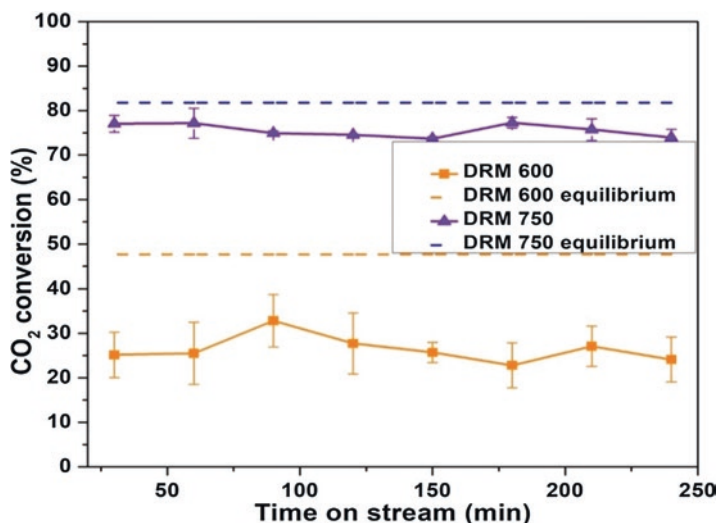
Fig. 5 Variation of %CO_2 conversion during 4 h time on stream for DRM (CH_4:CO_2:N_2 = 1:1:1) at 1 atm. over 10%Ni/MgAl$_2$O$_4$ at 600 and 750 °C

equilibrium data the conversions at 600 °C are significantly lower than the equilibrium conversion values, whereas the conversions are closer to equilibrium at 750 °C (Figs. 4 and 5). Since the conversions are not much affected by the time-on-stream (TOS) up to 4 hr., the catalyst does not get significantly deactivated during this limited time period. Furthermore, the conversions of CH_4 are larger than those observed for CO_2, which is consistent with high contact time data used in the present study. At high contact time, the conversions are expected to approach equilibrium. At low contact times, the CH_4 conversions have been reported to be lower than CO_2 conversions due to the presence of the RWGS reaction, which consumes additional CO_2 [12].

3.2 Increasing Reactor Temperature Marginally Increases the H$_2$/CO Ratio

Attaining higher H$_2$/CO ratio is desirable for further processing of products of the DRM reaction. Although equilibrium H$_2$/CO ratios decrease significantly as the temperature of the reactor increases, we found a small increase in actual H$_2$/CO ratio from 0.64 to 0.73 as the reactor temperature was increased (Fig. 6). An increase in H$_2$/CO ratio indicates that the reactor was operating under the kinetic regime.
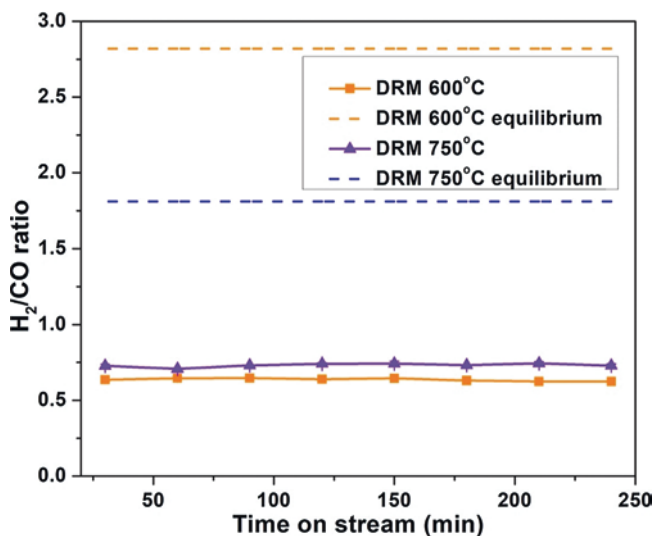
Fig. 6 Variation of H_2/CO ratio during 4 h time on stream for DRM ($CH_4:CO_2:N_2 = 1:1:1$) at 1 atm. over 10% $Ni/MgAl_2O_4$ at 600 and 750 °C

3.3 More Carbon Formed on Catalyst at Low Temperature

Solid-carbon is often detected on Ni-based catalysts [12]. To qualitatively analyse the carbon formed, the FESEM image of the fresh and spent catalysts after 4 h of TOS were obtained. Images show a significantly higher amount of carbon formation at 600 °C than at 750 °C (Fig. 7). Furthermore, the solid-carbon formed was whisker type. Quantitative TGA and CHN/O analysis of the spent catalyst (Table 4) also confirms that higher amounts of carbon were formed at lower temperatures for 4 h TOS.

3.4 Adding O_2 Reduces CO_2 Conversion Without Affecting CH_4 Conversion Significantly

Another strategy to decrease the amount of solid-carbon deposited on the catalyst is the use of oxygen as a co-feed along with the reactants (CH_4 and CO_2). Such an operation is referred to as oxidative dry reforming of methane (ODRM). Oxygen and carbon dioxide can both oxidize methane by two different reactions. It is desirable that oxygen preferably oxidizes the solid-carbon so that the solid-carbon formed would decrease. Adding O_2 slightly increases the methane conversion, and this conversion continues to increase as the oxygen amount in the feed increases though the initial increase is insignificant (Figs. 8 and 9). In contrast, the CO_2 conversion decreases since it appears that the presence of oxygen facilitates methane complete combustion instead of partial oxidation (Figs. 10 and 11). However, the oxidation of solid-carbon would also give rise to a decrease in CO_2 conversion and is discussed below.
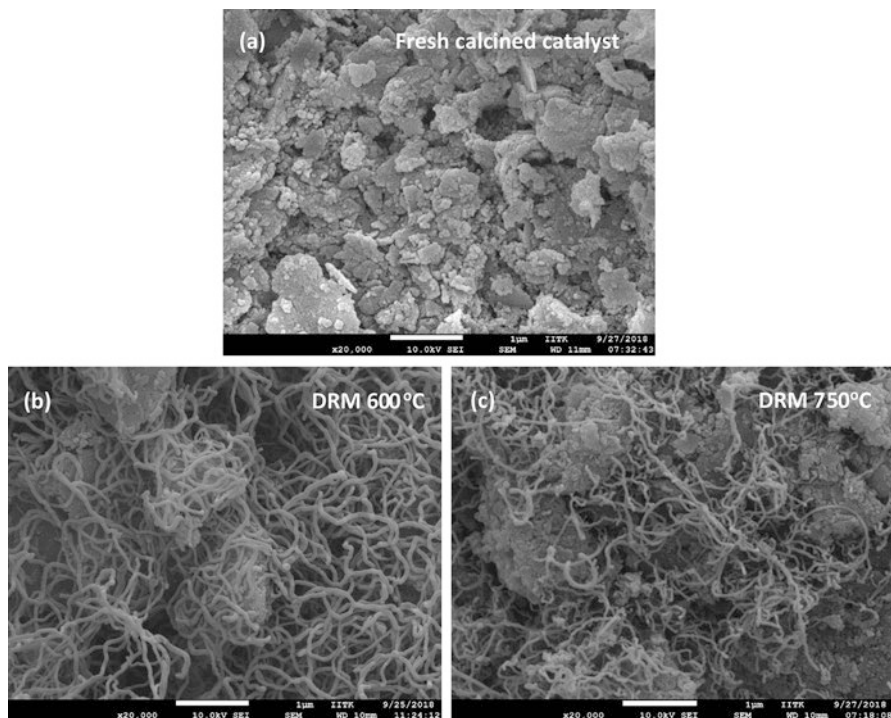
Fig. 7 FESEM images of the spent catalyst for DRM reaction over Ni/MgAl$_2$O$_4$ after 4 h of reaction in (**a**) fresh calcined catalyst, (**b**) DRM at 600 °C, and (**c**) DRM at 750 °C

Table 4 CHN/O and TGA analysis for elemental carbon on 10% Ni/MgAl$_2$O$_4$ during DRM at 600 and 750 °C after 4 h TOS

Reaction temperature (°C)	% Carbon deposited on the spent catalyst by CHN/O	TGA analysis (total % weight loss)
600	53.28	58.30
750	2.43	13.18
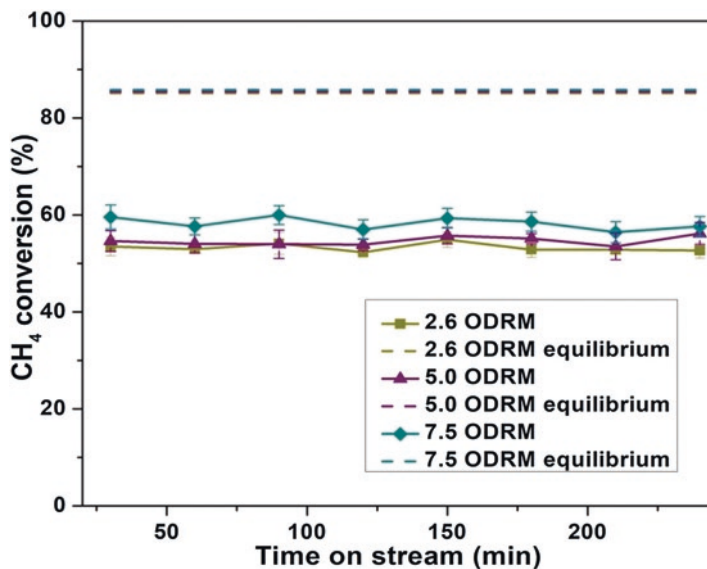
Fig. 8 Variation of % CH$_4$ conversion for (2.6, 5.0 and 7.5) ODRM during 4 h TOS over 10% Ni/MgAl$_2$O$_4$ catalyst at 600 °C
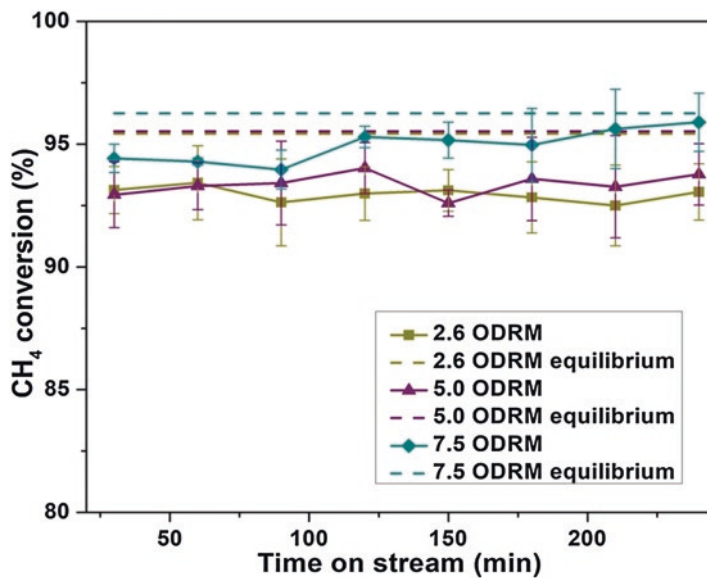
Fig. 9 Variation of % CH$_4$ conversion for (2.6, 5.0 and 7.5) ODRM during 4 h TOS over 10% Ni/MgAl$_2$O$_4$ catalyst at 750 °C
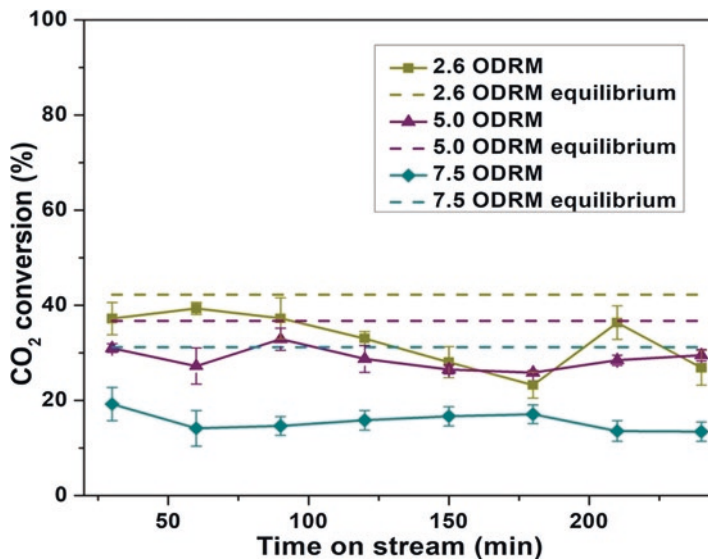
Fig. 10 Variation of % CO_2conversion for (2.6, 5.0 and 7.5) ODRM during 4 h TOS over 10% Ni/ MgAl$_2$O$_4$ catalyst at 600 °C
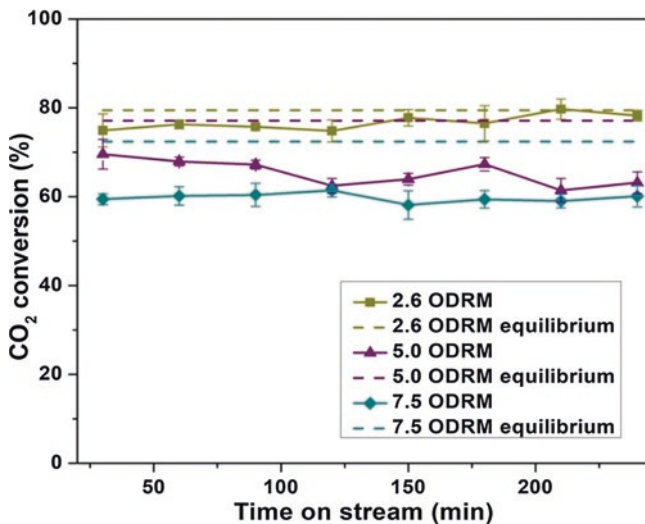
Fig. 11 Variation of % CO_2conversion for (2.6, 5.0 and 7.5) ODRM during 4 h TOS over 10% Ni/ MgAl$_2$O$_4$ catalyst at 750 °C
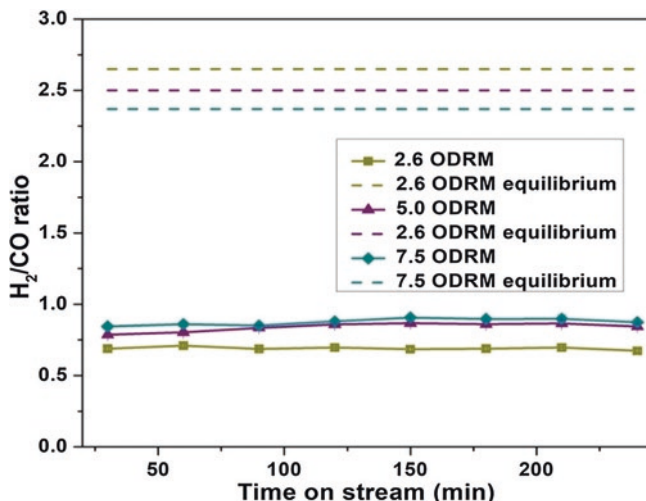
Fig. 12 Variation of H_2/CO ratio for (2.6, 5.0 and 7.5) ODRM during 4 h TOS over 10% Ni/ $MgAl_2O_4$ catalyst at 600 °C
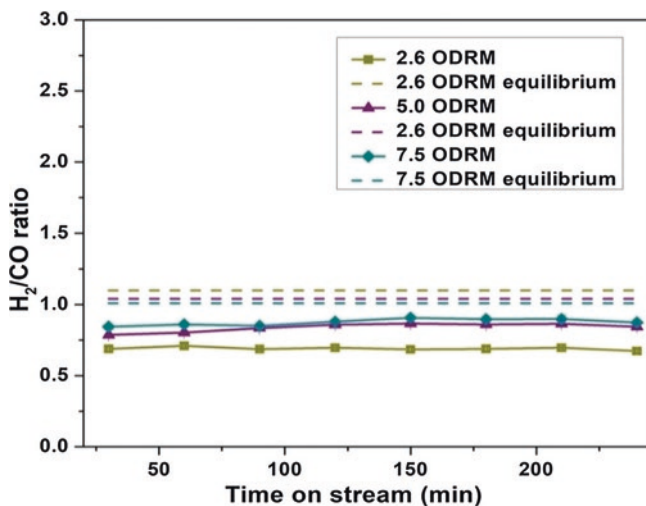
Fig. 13 Variation of H_2/CO ratio for (2.6, 5.0 and 7.5) ODRM during 4 h TOS over 10% Ni/ $MgAl_2O_4$ catalyst at 750 °C

3.5 H_2/CO Ratio Marginally Increases with Increase in O_2 Concentration

The H_2/CO ratio at equilibrium decreases with increase in O_2 concentration. However, in the fixed-bed reactor studies, the H_2/CO ratio increases slightly with increase in O_2 concentration at both reaction temperatures (Figs. 12 and 13). It appears that the effect of O_2 has a similar trend as the effect of temperature on H_2/CO ratio (Fig. 6).

3.6 O₂ Reduces Carbon Deposition on the Catalyst

Similar to the effect of temperature, adding O_2 also reduces the carbon deposited on the catalyst (Fig. 14 and Table 5). However, a significant amount of solid-carbon is still present on the catalyst at a reaction temperature of 600 °C. The decrease in
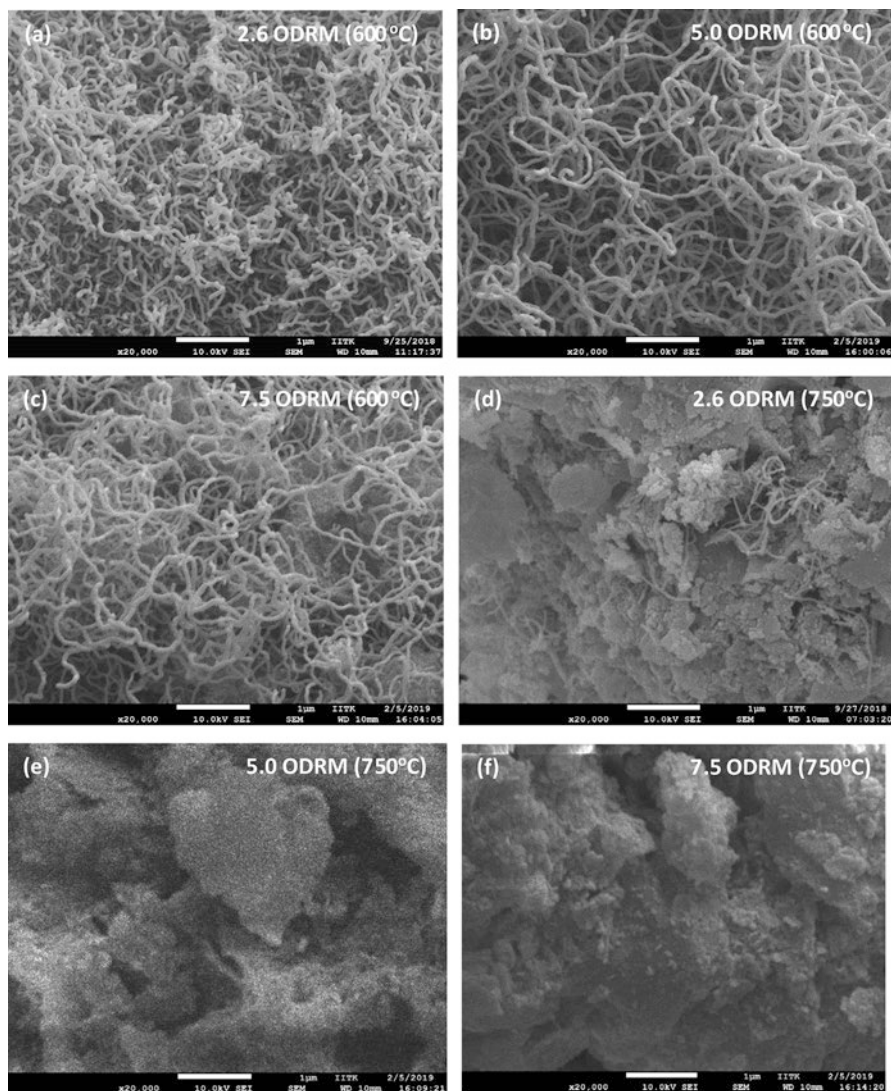
Fig. 14 FESEM images of the spent Ni/MgAl$_2$O$_4$ catalyst for ODRM reactions after 4 h of TOS for: (**a**) 2.6 ODRM at 600 °C, (**b**) 5.0 ODRM at 600 °C, (**c**) 7.5 ODRM at 600 °C, (**d**) 2.6 ODRM at 750 °C, (**e**) 5.0 ODRM at 750 °C, and (**f**) 7.5 ODRM at 750 °C

Table 5 CHN/O and TGA analysis for elemental carbon on 10% $Ni/MgAl_2O_4$ during ODRM at 600 and 750 °C after 4 h TOS

Reaction condition	Reaction temperature (°C)	% Carbon deposited on the spent catalyst by CHN/O	TGA analysis (total % weight loss)
2.6ODRM	600	51.2	57.4
5.0ODRM		49.3	Not determined
7.5ODRM		29.4	Not determined
2.6ODRM	750	1.4	10.1
5.0ODRM		0.6	Not determined
7.5ODRM		0.6	Not determined

solid-carbon in the spent catalyst may also contribute partially to the decrease in CO_2 conversion as observed above.

3.7 XPS Analysis of the Spent Catalyst

Different types of carbon have been detected during the DRM reaction over supported nickel catalysts [11, 13, 14]. These carbonaceous species are classified as carbidic carbon, graphitic carbon and carbon associated with oxygenated species. Furthermore, these carbonaceous species are identified by the binding energy of C_{1s} in the XPS as shown in Fig. 15. The presence of the different type of carbonaceous species appears to depend on the temperature and presence of oxygen. With increasing temperature and with oxygen present in the feed, the carbon associated with oxygenated species, such as alcohol or ether groups, significantly decrease. This is evident when one compares Fig. 15a with c, or Fig. 15a with b, or Fig. 15c with d. Thus, operating conditions such as a temperature of 750 °C rather than 600 °C and addition of oxygen help reduce carbon formation.

4 Catalyst Improvement Strategies to Alleviate Coking

The catalyst composition itself can be tuned to attain coking resistance. In what follows, we present observations on the design of catalyst to reduce carbon deposition on it.

4.1 Adding Basic Component to Ni Catalyst System May Reduce Coke Deposition

Structure and composition of catalyst play an important role in determining the amount of carbon formed on the catalysts during DRM and associated reactions. An ultrasound-assisted co-precipitation method showed that increasing Ni content in
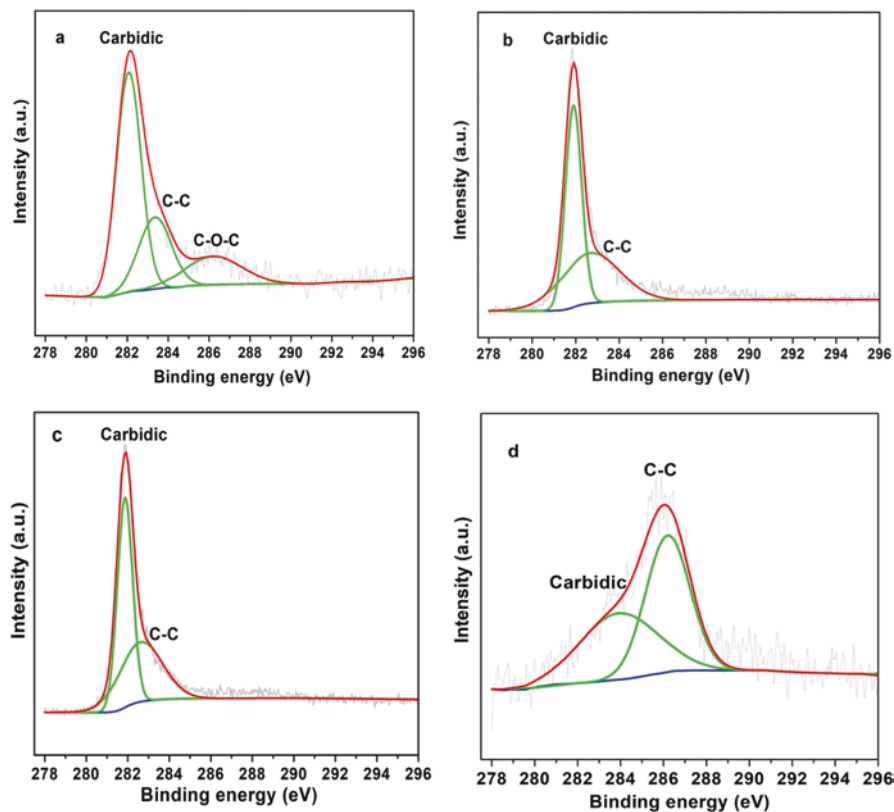
Fig. 15 XPS spectra in the C1s region for the spent $Ni/MgAl_2O_4$ catalyst after 4 h of TOS for the: (**a**) DRM reaction, (**b**) 2.6ODRM reaction, (**c**) DRM reaction, and (**d**) 2.6ODRM reaction. Reaction conditions: pressure = 1 bar, temperature = 600 °C for (**a**) and (**b**) and 750 °C for (**c**) and (**d**)

the mesoporous structure increases catalytic activity and carbon deposition [15]. While Ni loading increases carbon deposition, the addition of hydroxyapatite and fluoroapatite stabilized the catalyst. This is likely due to their basic property and ability to chemisorb CO_2 [16]. Adding Mg and Co to over alumina-supported Ni catalyst increased both the activity and coke resistance in comparison to supported Ni alone or Ni/Co [17]. In addition, variation in support has also shown an effect on carbon deposition. For example, MgO-γ-Al_2O_3 and $MgAl_2O_4$ supports compared to alumina alone have shown better coke resistance and sintering resistance due to better interaction between Ni and Mg, which gave rise to highly dispersed Ni active metal [18]. Since hydroxyapatite, fluoroapatite, and magnesium oxide are bases, it can be concluded that adding a basic component to the catalyst may enhance its coke resistance property. However, several properties of catalyst are coupled. For example, a base may have an effect on the: (i) the electronic property of Ni, (ii) interaction of the catalyst with CO_2, (iii) the dispersion of Ni, or (iv) interaction of carbon with Ni and the support. It is also possible that the base may have an effect

on several of these properties simultaneously, resulting in changes in both conversion and coke deposition. For example, we have seen that alumina-supported nickel catalysts possessing strong metal support interactions showed better carbon resistance compared to $MgAl_2O_4$-supported nickel at comparable conversions [11]. Thus, more carefully controlled experiments are required to quantify the effect of base addition and to clearly delineate the mechanism of carbon deposition on catalyst.

4.2 Potassium Aluminate Shown to Enhance Coke Resistance Property of NiAl₂O₄

Formation of nickel aluminate has been shown to increase coke resistance characteristics of Ni/Al_2O_3 catalyst [19]. Nickel aluminate, $NiAl_2O_4$, is usually formed by calcining the Ni/Al_2O_3 catalyst at high temperature. The formation of nickel aluminate is readily detected using UV–Vis spectroscopy as shown in Fig. 16. In Fig. 16, an elbow at 550 nm and peaks at 596 and 632 nm correspond to nickel aluminate [12]. In contrast, similar peaks in $Ni/MgAl_2O_4$ preparation are largely absent likely due to better stability of magnesium aluminate over nickel aluminate as shown in Fig. 17. Among aluminates, Ni aluminate has been shown to have several fold higher activity and significantly less coke formation in comparison to Ni-Co aluminates together [20]. The increase in activity of Ni aluminate was attributed to better interaction between active Ni and nickel aluminate, while a decrease in coking was
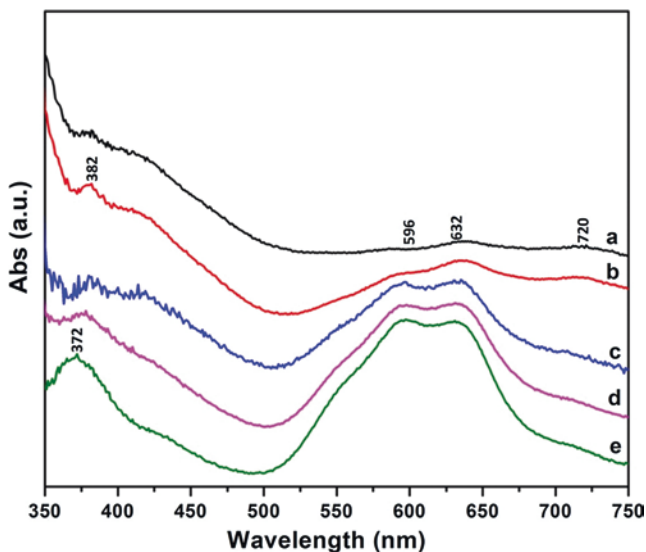
Fig. 16 UV–Vis spectra obtained under ambient conditions of 10%Ni/Al_2O_3 calcined at: (**a**) 500 °C, (**b**) 600 °C, (**c**) 650 °C, (**d**) 700 °C, and (**e**) 800 °C
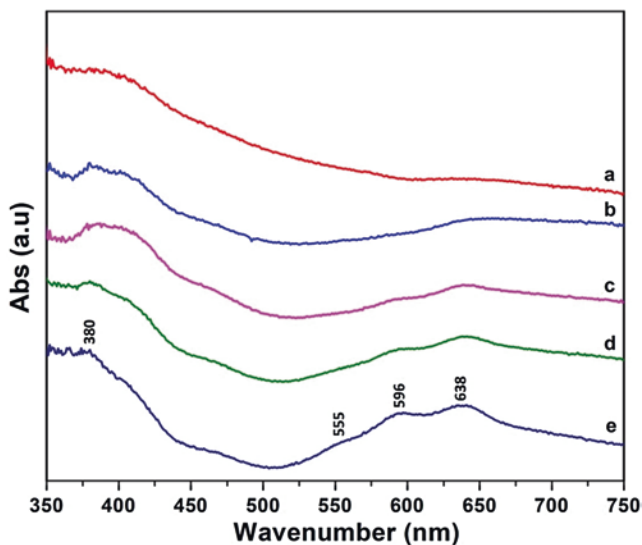
Fig. 17 UV–Vis spectra obtained under ambient conditions of 10% Ni/MgAl$_2$O$_4$calcined at: (**a**) 600 °C, (**b**) 700 °C, (**c**) 800 °C, (**d**) 850 °C and (**e**) 1000 °C

attributed to filamentous carbon formation. The filamentous carbon can readily react with CO$_2$ [20]. In another study, a Ni/Al$_2$O$_3$ catalyst, calcined to 850 °C for 10 h to increase NiAl$_2$O$_4$ content, was modified with addition of K, Mn, Sn and Ca [21]. Modification with K showed a decrease in coking while modification with other metals showed an increase in carbon deposition [21]. The order of coke formation using different type of modifiers was K < Ni < Ca < Sn < Mn [21]. Although other possibilities exist, it is also likely that these modifiers replace Ni in NiAl$_2$O$_4$ affecting coking characteristics of the catalyst. Proper catalyst characterization might provide additional insight into the possibility of replacement of Ni in NiAl$_2$O$_4$ with these modifiers. Further, Juan et al. serially increased K/Ni ratio from 0 to 0.69 in catalyst calcined to 500 °C for 2 h, and found that while the conversions of CH$_4$ and CO$_2$ decreased by less than 40%, the carbon deposition decreased from 275 mg of **C**/g of catalyst to almost 0 mg of **C**/g of catalyst [22]. Since 2 h may not be enough for completing the aluminate formation, it is likely that the effect of K on coke resistance of Ni/Al$_2$O$_3$ catalyst is more complex and may also involve better dispersion of Ni and enhancement of its electronic properties in the presence of potassium. Similarly, Frusteri et al. found that addition of K in Ni/MgO system decreased carbon deposition markedly [23]. Furthermore, addition of K changed the electronic and geometric property of the catalyst, supporting the above conclusion that the role of potassium on the stability of catalyst may be more complex [23].

4.3 Ceria, Zirconia and Their Combinations Are Useful Supports

Several recent studies have focussed on using ceria, zirconia or their combinations for the dry reforming of methane. In this context, ceria has been shown to improve coking resistance in comparison to Ni/Al_2O_3 system [24, 25]. Ceria provides the lattice oxygen that, through redox reactions, prevents the formation of carbon species from the methane decomposition and Boudard reactions [24]. In the Ni/ CeO_2 system, the addition of zirconia improved the activity of the catalyst, which was attributed to the higher surface density of active sites [26]. Zirconia also improved the resistance to coking [26]. Interestingly, coking resistance was attributed to the formation of filamentous carbon, which was not seen in pure CeO_2-supported catalyst [26]. On the other hand, addition of CeO_2 in Ni/ZrO_2 catalyst reduced the formation of filamentous carbon, improving coking resistance without affecting the activity [27]. Thus, it appears that zirconia improves both coking resistance and activity, and ceria improves the resistance to coking. In contrast, addition of CeO_2 in Ni/SiO_2 system improved both the activity and coking resistance [28]. Further, the effect of ZrO_2 has been studied for two different catalysts (Ni/ Al_2O_3 and Pt/Al_2O_3) [29]. In both systems, adding zirconia reduced carbon deposition, suggesting that zirconia induced gasification of carbon-containing intermediates adsorbed in the catalyst [29].

4.4 Different Supports and Promoters Are Also Used

Different supports and trace additives may also affect carbon deposition on catalyst. Nagaoka et al. studied ruthenium catalyst with different supports (SiO_2, Al_2O_3, MgO, TiO_2) and found that the order of coke deposition is $Al_2O_3 > SiO_2 > MgO > TiO_2$ with TiO_2 having non-detectable amounts of coke deposited [30]. Similarly, Alipour et al. studied the effect of alkaline promoters (MgO, CaO and BaO) on coking in Ni/ Al_2O_3 system. The authors found that the highest amount of carbon deposited was that of filamentous carbon, and concluded that the amount of filamentous carbon decreased with addition of alkaline promoters and was in the order MgO > CaO > BaO, which was the same order as their decreasing basicity [31]. However, no reduction was observed in the case of amorphous carbon, except for CaO, which gave the same amount of amorphous carbon as unpromoted Ni/Al_2O_3 system [31]. Similarly, no reduction was observed in the case of active carbon species, except in the case of MgO [31]. Thus, while filamentous carbon reduces in the order of basicity of alkaline promoters, no clear pattern could be observed in case of amorphous carbon and active carbon species and more studies are needed to classify the effect of alkaline promoters on gasification of these carbonaceous species.

Doping Ni with other elements has also shown varying effects on the coking property of catalysts. For example, adding Ce in case of a modified mineral clay support has shown beneficial effect on activity while reducing the carbon deposition by half [32, 33]. On the other hand, adding Co in alumina-supported Ni catalyst increased the activity, but produced larger amounts of carbon [34]. However, the carbon deposited was of non-deactivating type and did not affect the stability of the catalyst. A similar increase in activity and amount of deactivation were shown by us when Co was added to an alumina-supported Ni catalyst [12]. In contrast, adding Fe to an alumina-supported Ni catalyst improved the stability of the catalyst while maintaining similar conversion levels as the unpromoted alumina-supported Ni catalyst [35]. In these studies, done by us, the amount of carbon deposited was not determined. However, the stability of the catalyst was assumed to be related to the amount of carbon deposited. Adding praseodymium (Pr) in Ni/delaminated clay catalyst reduced the carbon deposition for catalyst calcined at 500 °C [36]. Interestingly, no carbon deposition was found for catalysts calcined at 800 °C [36]. Thus, like alkali metal, adding lanthanides may also improve the coke-resistant property of Ni catalyst. It is important to note that carbon build up in a reactor is detrimental to its continuous operation. Furthermore, analysis of carbon is critical for judging the suitability of a catalyst since carbon formation and stability may not be directly related.

5 Kinetics: Mechanisms and Models

The DRM reaction proceeds in presence of the reverse water gas shift reaction (RWGS) given by the reverse of reaction, i.e.

$$H_2 + CO_2 \rightarrow CO + H_2O$$
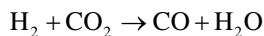
Often, RWGS reaction is at equilibrium under typical operating conditions of the DRM reaction [4]. Wei et al. [4] experimentally determined that kinetics of the forward DRM reaction to be first-order in methane and zero-order in carbon dioxide. The authors proposed the following rate expression for this reaction:

$$r_{CH_4} = k P_{CH_4} \left(1 - \eta\right)$$

where $\eta = \dfrac{P_{CO}^2 P_{H_2}^2}{P_{CH_4} P_{CO_2}} \dfrac{1}{K_{eq}}$ where K_{eq} is the equilibrium constant of the DRM reaction.

Two types of mechanism have been often proposed [37] for the DRM reaction. These are:

1. Eley-Rideal (ER) model
2. Langmuir Hinshelwood–Hougen Watson

Some of the mechanisms describe only the forward reaction and we have included the $(1 - \eta)$ term proposed by Wei et al. to describe the reversible reaction.

5.1 Eley-Rideal Model (ER)

In the ER model, it is assumed that one reactant is adsorbed on the surface while the second reactant remains in the gas phase, reacting with the adsorbed species [37]. The adsorption step is assumed to be fast, while reaction of the second reactant is assumed to be the rate-determining step [37]. There are two kinds of mechanism proposed by Kathiraser et al. [37]. They are characterized as ER-I and ER-II.

For ER I, the reaction steps and rate expression are given below:

$CH_4 + * \leftrightarrow CH_x - *$	Equilibrium constant $= K_{CH_4}$
$CH_4* + CO_2 \leftrightarrow 2CO + 2H_2 + *$	Forward reaction rate constant $= k_{f1}$, and this step is the RDS

$$r_{CH_4} = \frac{k_{f1} K_{CH_4} P_{CH_4} P_{CO_2} \left(1 - \dfrac{P_{CO}^2 P_{H_2}^2}{P_{CH_4} P_{CO_2}} \dfrac{1}{K_{eq}} \right)}{1 + K_{CH_4} P_{CH_4}}$$

For ER-II, the reaction steps and rate expression are given below:

$CO_2 + * \leftrightarrow CO_2*$	Equilibrium constant $= K_{CO_2}$
$CH_4 + CO_2* \leftrightarrow 2CO + 2H_2 + *$	Forward reaction rate constant $= k_{f2}$, and this step is the RDS

$$r_{CH_4} = \frac{k_{f2} K_{CO_2} P_{CH_4} P_{CO_2} \left(1 - \dfrac{P_{CO}^2 P_{H2}^2}{P_{CH_4} P_{CO_2}} \dfrac{1}{K_{eq}} \right)}{1 + K_{CO_2} P_{CO_2}}$$

Akpan et al. [38] studied the DRM reaction on a Ni/CeO_2-ZrO_2 catalyst. The CeO_2-ZrO_2support has a high capacity to store oxygen and is highly reducible. Based on this, Akpan et al. proposed following steps of the DRM reaction:

(i) Adsorption and dissociation of CH_4 into various carbon species:

$CH_4 + * \leftrightarrow C* + 4H*$	Forward rate constant $= k_1$ and backward rate constant $= k_{-1}$

(ii) Reaction of carbon species with lattice oxygen coming from the support

$C* + O_x \leftrightarrow CO + O_{x-1} + *$	Forward rate constant $= k_2$ and backward rate constant $= k_{-2}$

(iii) Reaction of CO_2 with reduced site of the catalyst

$CO_2 + O_{x-1} \leftrightarrow CO + O_x$	Forward rate constant = k_3 and backward rate constant = k_{-3}

(iv) Reaction of adsorbed hydrogen atom

$4H* \leftrightarrow 2H_2 + 4*$	Forward rate constant = k_4 and backward rate constant = k_{-4}

(v) Water is produced by reverse water gas shift reaction

$H_2 + O_x \leftrightarrow H_2O + O_{x-1}$	Forward rate constant = k_5 and backward rate constant = k_{-5}

Authors have assumed each of the first four reactions (i) to (iv) as rate-determining step and have derived following rate expressions (models 1–4, respectively):

Model 1: RDS: equation (i)

$$r_{CH_4} = \frac{k_{01} \exp\left(\frac{-E_1}{RT}\right) N_{CH_4} \left(1 - \frac{N_{CO}^2 N_{H_2}^2}{N_{CH_4} N_{CO_2}} \frac{1}{K_{eq1}}\right)}{\left(1 + K_A \frac{N_{CO}^2}{N_{CO_2}} + K_B N_{H_2}^{1/2}\right)^5}$$

Model 2: RDS: equation (ii)

$$r_{CH_4} = \frac{k_{02} \exp\left(\frac{-E_2}{RT}\right) \frac{N_{CH_4}}{N_{H_2}^2} \left(1 - \frac{N_{CO}^2 N_{H_2}^2}{N_{CH_4} N_{CO_2}} \frac{1}{K_{eq1}}\right)}{\left(1 + K_A \frac{N_{CO}^2}{N_{CO_2}} + K_B N_{H_2}^{1/2}\right)}$$

Model 3: RDS: equation (iii)

$$r_{CH_4} = k_{03} \exp\left(\frac{-E_3}{RT}\right) \frac{N_{CH_4} N_{CO_2}}{N_{CO} N_{H_2}^2} \left(1 - \frac{N_{CO}^2 N_{H_2}^2}{N_{CH_4} N_{CO_2}} \frac{1}{K_{eq1}}\right)$$

Model 4: RDS: equation (iv)
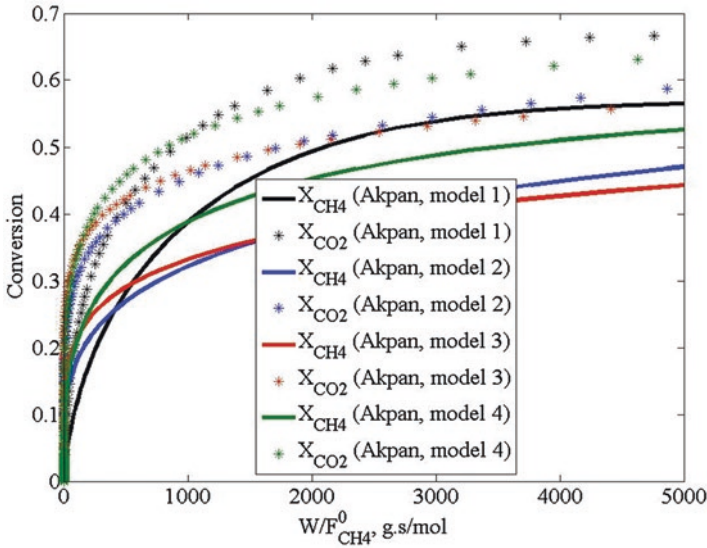
Fig. 18 Comparison of the Eley-Rideal models of Akpan et al.

$$r_{CH_4} = \frac{k_{04} \exp\left(\dfrac{-E_4}{RT}\right) \dfrac{N_{CH_4} N_{CO_2}}{N_{CO}^2} \left(1 - \dfrac{N_{CO}^2 N_{H_2}^2}{N_{CH_4} N_{CO_2}} \dfrac{1}{K_{eq1}}\right)}{\left(1 + K_A \dfrac{N_{CO}^2}{N_{CO_2}} + K_B N_{H_2}^{1/2}\right)^4}$$

In Fig. 18, we modelled the four ER kinetics given by Akpan et al. The figure shows that the initial rate given by the first model is the slowest. However, the rate given by the first model reduces gradually with conversion. On the other hand, for other models, the rate starts off faster but it decreases suddenly, achieving lower conversion than model 1. Akpan et al. [38] compared experimental data with their models and found that model 1 best represents the experimental data followed by model 4. In Fig. 18, we find that models 1 and 4 are close. Similarly models 2 and 3 are close but deviate significantly from models 1 and 4.

5.2 Langmuir Hinshelwood Kinetics

In this model, one or more surface reactions are assumed to be the rate-determining steps while others are at equilibrium. Kinetics is derived using rate-determining steps and substituting intermediate species in terms of the reactants and products. Two representative mechanisms are discussed below.

5.2.1 Bradford Mechanism

After analysing available data on DRM reaction, Bradford et al. [39] propose the following mechanism of this reaction for Ni/MgO and Ni/TiO$_2$catalysts:

(i)	$CH_4 + * \leftrightarrow CH_x * + \left(\dfrac{4-x}{2}\right)H_2$	Rate constants = k_1 and k_{-1}
(ii)	$2[CO_2 + * \leftrightarrow CO_2*]$	Equilibrium constant = K_2
(iii)	$H_2 + 2* \leftrightarrow 2H*$	Equilibrium constant = K_3
(iv)	$2[CO_2* + H* \leftrightarrow CO* + OH*]$	Equilibrium constant = K_4
(v)	$OH* + H* \leftrightarrow H_2O + 2*$	Equilibrium constant = K_5
(vi)	$CH_x* + OH* \leftrightarrow CH_xO* + H*$	Equilibrium constant = K_6
(vii)	$CH_xO* \rightarrow CO* + \left(\dfrac{x}{2}\right)H_2$	Rate constant = k_7
(viii)	$3[CO* \leftrightarrow CO + *]$	Equilibrium constant = $1/K_8$

The first reaction is methane cracking, while reactions (ii) and (iii) are adsorption of CO_2 and dissociative adsorption of H_2 on active sites. Reaction (iv) and (v) are RWGS, while (vi), (vii) and (viii) are product formation from active carbon species. It is assumed that reaction (i) and (vii) are rate-determining steps. Accumulation of active carbon species on the surface gives rise to coking.

The above reaction mechanism has been assumed to be valid if surface carbon formation is at steady state, i.e. the rate of CH_4 dissociation equals the rate of CH_xO decomposition, i.e. rate of reaction (i) = rate of reaction (vii) [39]. Further, it is assumed that the most abundant reaction intermediate is CH_xO [39]. With the above assumptions in place, it can be derived that the rate of CH_4conversion, r_{CH_4} is [39]

$$r_{CH_4} = \frac{\overline{k}_1 P_{CH_4} P_{CO_2}}{\dfrac{\overline{k}_{-1}\overline{K}}{\overline{k}_7} P_{CO} P_{H_2}^{(4-x)/2} + \left(1 + \dfrac{\overline{k}_1}{\overline{k}_7} P_{CH_4}\right) P_{CO_2}} \tag{1}$$

where $\overline{k}_i = k_i L$, L = total number of active sites = $[*] + [CH_xO*]$ and

$$\overline{K} = \frac{K_8}{K_2 K_4 K_6}$$

$$x \leq 6 - 2\left(\frac{r_{CO_2}}{r_{CH_4}}\right)$$

A reasonable value of x is 2 [39].

The proposed kinetic model fits the experimental data very well. It can be seen from the rate expression that for low P_{CO} and P_{H_2} values or high values of P_{CO_2}, the rate is independent of CO_2 concentration.

5.2.2 Tsipouriari Mechanism

On the other hand, Tsipouriari et al. [40] propose a different mechanism for Ni/La_2O_3 catalyst based on the observation that while the rate of reaction decreases with time for reactions over many supports (Al_2O_3, YSZ, SiO_2 and CaO), it shows a reverse trend for La_2O_3, suggesting that La_2O_3 somehow stabilizes the Ni catalyst. It was proposed that LaO_x forms at the catalyst surface which reacts with CO_2 to form carbonates and oxycarbonates. The carbonates and oxycarbonates react with deposited carbon, freeing the active sites [40]. This hypothesis was supported by the observation of $La_2O_2CO_3$ species by Zhang et al. [41]. Further, it was observed that the rate of dissociation of CH_4 is much higher than that of CO_2 and active carbon species consist of carbon only [40]. Furthermore, oxygen for the formation of CO comes from $La_2O_2CO_3$ [42] and methane cracking on Ni/La_2O_3 is a slow step [43]. Based on the above observations, the mechanism proposed by Tsipouriari et al. consists of following steps [40]:

1. Reversible adsorption of methane (fast) followed by its slow cracking:

$CH_4 + * \leftrightarrow CH_4*$	Equilibrium constant $= K_1$
$CH_4* \rightarrow C* + 2H_2$	Rate constant $= k_2$ (RDS)
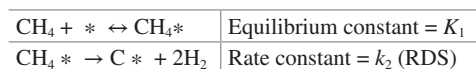
2. Formation of $La_2O_2CO_3$ (fast)

$CO_2 + La_2O_3 \leftrightarrow La_2O_2CO_3$	Equilibrium constant $= K_3$

3. $La_2O_2CO_3$ reacts with carbon deposited on active sites, forming CO and restoring the active site (slow):

$La_2O_2CO_3 + C* \rightarrow La_2O_3 + 2CO + *$	RDS; rate constant $= k_4$

4. H_2 may also get adsorbed at the active sites:

$$H_2 + 2* \leftrightarrow 2H*$$
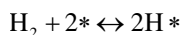
5. $La_2O_2CO_3$ may provide oxygen to adsorbed hydrogen (fast) and carbon (fast)

$$La_2O_2CO_3 + H* \leftrightarrow La_2O_3 + CO + OH*$$

$$OH* + C* \leftrightarrow CO* + H*$$

$$OH* + H* \leftrightarrow H_2O + 2*$$

$$CO* \leftrightarrow CO + *$$
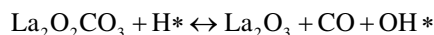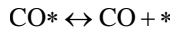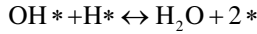
6. Reverse water gas shift reaction also takes places as described by the following steps:

$$CO_2* \leftrightarrow CO_2*$$

$$CO_2* + H* \leftrightarrow CO* + OH* \quad (\text{slow})$$

$$OH* + H* \leftrightarrow H_2O + 2*$$
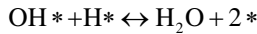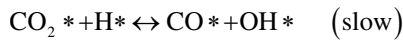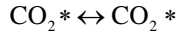
The rate expression [40] developed using above steps is:

$$r_{CH_4} = \frac{K_1 k_2 K_3 k_4 P_{CH_4} P_{CO_2}}{K_1 k_2 K_3 P_{CH_4} P_{CO_2} + K_1 k_2 P_{CH_4} + K_3 k_4 P_{CO}}$$

where,
$$K_1 k_2 = 2.61 \times 10^{-3} \exp\left(-\frac{4300}{T}\right) \text{in} \frac{\text{mol}}{\text{gs}} (KPa)^{-1},$$

$$K_3 = 5.17 \times 10^{-5} \exp\left(\frac{8700}{T}\right) \text{in} (kPa)^{-1}, \text{ and } k_4 = 5.35 \times 10^{-1} \exp\left(-\frac{7500}{T}\right) \text{in} \frac{\text{mol}}{\text{gs}}.$$

In the above rate expression, one can see that for the high value of CO_2 and low CO, the rate of reaction is a constant, predicting that the initial rate of reaction for excess CO_2 is of zero order. Expression by Bradford et al., on the other hand, predicts that the initial rate of reaction will be dependent on CH_4 concentration only and will be of zero-order of very high concentration of CH_4, when active sites get saturated by CH_4. Thus, the two mechanisms presented above show different prediction of the rate far away from equilibrium. Our modelling in an ideal plug flow reactor shows that the initial rate of Bradford kinetics is lower than that of Tsipouriari kinetics (Fig. 19). Comparing steps in the mechanisms described by two studies, we find that while the first study assumes active carbon species of CH_x types, the second study assumes that of only C-containing type. Further, while the first study assumes that CO_2 also gets adsorbed at the active site, the second study assumes that CO_2 not only does not occupy the active site but also frees them through $La_2O_2CO_3$. The difference in two mechanism and rates may be due to the difference in the support used in studies.

6 Process Modelling

DRM reaction causes carbon formation, which is a serious problem towards the development of a process. Carbon can be oxidized with a stronger oxidizer like oxygen. However, oxygen can also oxidize methane-producing CO_2. Formation of CO_2 is undesirable since the net CO_2 converted would be affected. Using equilibrium
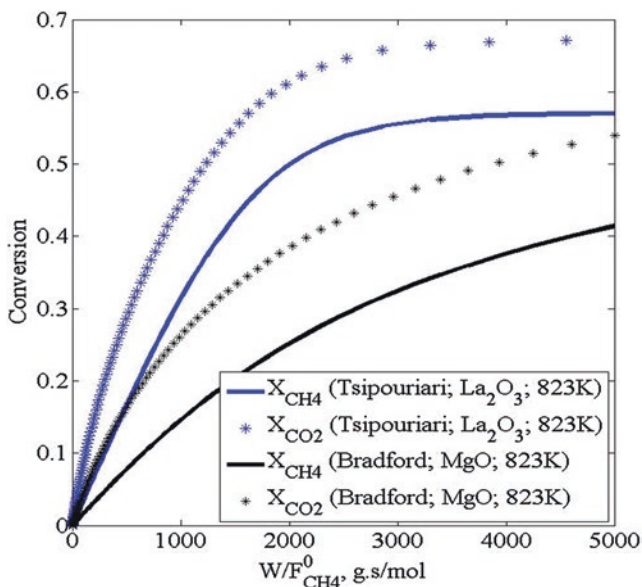
Fig. 19 Comparison of Tsipouriari and Bradford kinetics

calculations, we modelled the oxidative reforming and optimized the reactor temperature and O_2 concentration in the feed. Optimization revealed that at temperatures below 750 °C, no amount of O_2 will eliminate carbon formation (data not shown). At 750 °C, adding O_2 lowers both carbon formation and H_2/CO ratio (Fig. 20). Since the goal is to achieve high H_2/CO along with low or no carbon formation oxidative reforming alone is not sufficient. Thus, equilibrium calculations suggest that we need to modify the process further. By adding H_2O to the feed we found that the H_2/CO ratio increases, while carbon formation decreases (Fig. 21). These results suggest that carbon formation can be eliminated at lower temperatures, for example, 550 °C, with the addition of water and oxygen in the feed. The presence of water and oxygen in the feed corresponds to the tri-reforming reaction. Thus, tri-reforming has the potential to achieve the objective of no carbon formation and a value of H_2/CO ratio that is sufficient for further effective utilization of the syngas.

To achieve carbonless operation and sufficient H_2/CO ratio, Zhang et al. [44], through thermodynamic analysis, found that while excessive H_2O and O_2 amount results in lower H_2 yield, low concentrations of these reactants in feed causes excessive carbon formation. The authors [44] further found an optimum reactant ratio in the feed to have methanol production from syngas, while eliminating carbon formation. Garcia-Vargas et al. experimentally found that H_2O and O_2 have a positive effect on the H_2/CO ratio [45], in agreement with our experimental and theoretical findings above. Song et al. [46] modelled the tri-reforming reaction of methane to achieve high conversion and H_2/CO ratio. They considered various ratios of reactants in the feed and found that a ratio of $CH_4:CO_2:H_2O:O_2 = 1:0.45:$
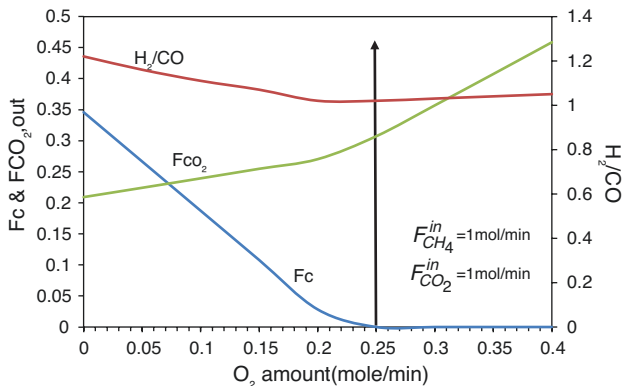
Fig. 20 Effect of O_2addition during DRM at 750 °C (ASPEN PLUS™ modelling)
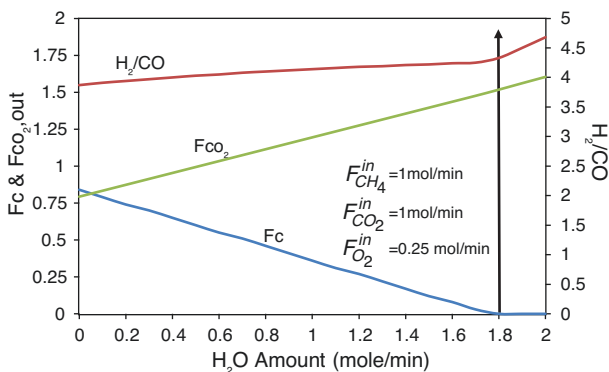
Fig. 21 Effect of H_2O addition during ODRM at 550 °C (ASPEN PLUS™ modelling)

0.45:0.2 gives high conversion of CO_2 at temperature higher than 800 °C with no carbon formation and a H_2/CO ratio close to 1.8. Increasing the amount of water ($CH_4:CO_2:H_2O:O_2 = 1:0.3:0.6:0.2$), increased the H_2/CO ratio and decreased the temperature above which carbon formation was absent. However, the CO_2conversion was significantly lowered. Similarly, increasing oxygen ratio ($CH_4:CO_2:H_2O:O_2 = 1:0.25:0.5:0.5$) worsened the CO_2 conversion. In case of low CO_2 conversion, net CO_2 may not be consumed and the objective of CO_2 utilization may not meet. Net CO_2 conversion analysis is important since some CO_2 will be produced to maintain the reactor at the required temperature since the reactions are mostly endothermic. Thus, the addition of H_2O and O_2 has limitations and further innovation of tri-reforming is warranted.

In this direction, we have added CO_2 separation and recycle to the reactor system as shown in Fig. 22. As the recycle ratio increases, net carbon fixation increases. In contrast, the H_2/CO ratio decreases with increase in recycle ratio. Thus, there lies an optimum recycle ratio at which the objective of CO_2fixation along with sufficient
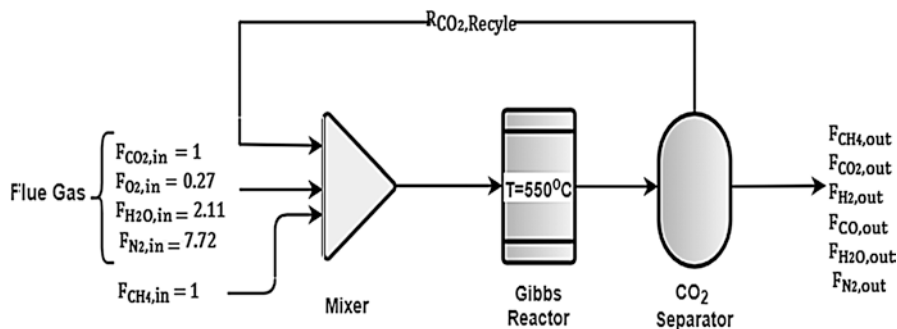
Fig. 22 Schematic diagram of ASPEN PLUS™ Process model
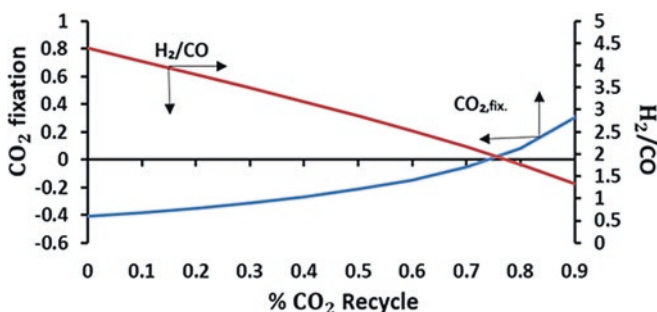
Fig. 23 CO_2 fixation and H_2/CO ratio as a function of percentage recycle of CO_2

H_2/CO can be achieved. Figure 23 shows that at 80% recycle there is a net carbon dioxide fixation, which includes the CO_2 that may be produced to fulfil the energy requirement of the reactor with H_2/CO ratio of 1.8. Further towards innovation in tri-reforming, Noureldin et al. [47] studied various process options, such as combined dry and steam reforming (CDSR), steam reforming (SR), partial oxidation (POX), and autothermal reforming (ATR) and found that the most optimum unit to achieve maximum CO_2 fixation while achieving a specific value of H_2/CO ratio is CDSR. The authors further found an inverse correlation between CO_2 fixation and H_2/CO ratio [47].

6.1 Catalyst Improvement Strategies for Tri-Reforming of Methane

In tri-reforming, besides the process innovation given above to achieve desired syngas parameters, improvement of catalyst can be considered for decreasing the amount of carbon deposited. Towards this end, Kumar et al. [48] studied the effect of different support in Ni-based catalyst and found that while catalyst activity was

in the order: Ni/Al$_2$O$_3$ > Ni/SBA-15 > Ni/ZrO$_2$ > Ni/CeO$_2$-ZrO$_2$ > Ni/TiO$_2$ > Ni/MgO, the stability and the coking resistance of SBA-15 and ZrO$_2$ catalyst was the highest [48]. High coking resistance of Ni/ZrO$_2$ catalyst has also been observed by Singha et al. [49] and Lino et al. [50]. Similarly, it was found that a NiO–YSZ–CeO$_2$ catalyst had better stability than commercial Holder Topsoe and Imperial Chemical Industries catalysts [51]. On the other hand, Pino et al. observed activity enhancement on Ni/CeO$_2$ catalyst which was doped with La [52]. Further, Majewski et al. [53] studied the effect on O$_2$ and H$_2$O over Ni/SiO$_2$ catalyst and found that while oxygen increases methane conversion and reduces coke deposition in agreement with our study, water reduces H$_2$/CO ratio, in contrast to equilibrium predictions. Furthermore, Garcia-Vargas et al. [54] compared the CeO$_2$ support with β-SiC for Ni-based catalyst and observed that lower H$_2$/CO ratio for ceria support was due to more basic sites in a ceria-supported catalyst. Thus, in addition to the feed composition and operating conditions, catalyst design plays an important role in achieving higher methane conversion and H$_2$/CO ratio, while having less carbon deposition on the catalyst, for the tri-reforming reaction.

7 Conclusion

It has been observed that adding oxygen to DRM reaction reduces carbon deposition and does not affect methane conversion significantly. Although theoretically, O$_2$ reduces H$_2$/CO ratio, our experimental results show a marginal increase in this ratio due to O$_2$. Nevertheless, H$_2$/CO ratio is not sufficient and warrants further addition of water to the reaction mixture. Thus, in principle flue gas can be used to reform methane. However, in order to achieve net CO$_2$ consumption further improvement of tri-reforming process is required. In this direction, we modelled the tri-reforming using flue gas as the feed. In the model, we implemented CO$_2$ separation and recycle to the reactor, achieving an H$_2$/CO ratio in the syngas that can be used for the production of petrochemicals while attaining a net CO$_2$ fixation. Thus, components of flue gas help improve properties of syngas and with an innovative process design, and a net CO$_2$ consumption can be attained.

References

1. Song CS, Wei P (2004) Tri-reforming of methane: a novel concept for catalytic production of industrially useful synthesis gas with desired H2/CO ratios. Catal Today 98:463–484
2. IEA (2020), *India 2020*, IEA, Paris https://www.iea.org/reports/india-2020
3. Jacob A, Moulijn MM (2001) Annelies Van Diepen. Wiley, Chemical Process Technology
4. Wei JM, Iglesia E (2004) Isotopic and kinetic assessment of the mechanism of reactions of CH$_4$ with CO$_2$ or H$_2$O to form synthesis gas and carbon on nickel catalysts. J Catal 224:370–383
5. Chein RY, Chen YC, Yu CT, Chung JN (2015) Thermodynamic analysis of dry reforming of CH$_4$ with CO$_2$ at high pressures. J Nat Gas Sci Eng 26:617–629

6. Jang WJ, Jeong DW, Shim JO, Kim HM, Roh HS, Son IH, Lee SJ (2016) Combined steam and carbon dioxide reforming of methane and side reactions: thermodynamic equilibrium analysis and experimental application. Appl Energy 173:80–91

7. Chein RY, Hsu WH (2018) Thermodynamic analysis of syngas production via tri-reforming of methane and carbon gasification using flue gas from coal-fired power plants. J Clean Prod 200:242–258

8. Pakhare D, Spivey J (2014) A review of dry (CO_2) reforming of methane over noble metal catalysts. Chem Soc Rev 43:7813–7837

9. Ginsburg JM, Pina J, El Solh T, de Lasa HI (2005) Coke formation over a nickel catalyst under methane dry reforming conditions: Thermodynamic and kinetic models. Ind Eng Chem Res 44:4846–4854

10. Nikoo MK, Amin NAS (2011) Thermodynamic analysis of carbon dioxide reforming of methane in view of solid carbon formation. Fuel Process Technol 92:678–691

11. Chaudhary PK, Koshta N, Deo G (2020) Effect of O_2 and temperature on the catalytic performance of Ni/Al_2O_3 and $Ni/MgAl_2O_4$ for the dry reforming of methane (DRM). Int J Hydrogen Energy 45(7):4490–4500

12. Sengupta S, Ray K, Deo G (2014) Effects of modifying Ni/Al_2O_3 catalyst with cobalt on the reforming of CH_4 with CO_2 and cracking of CH_4 reactions. Int J Hydrogen Energy 39:11462–11472

13. Ewbank JL, Kovarik L, Diallo FZ, Sievers C (2015) Effect of metal–support interactions in Ni/Al_2O_3 catalysts with low metal loading for methane dry reforming. Appl Catal Gen 494:57–67

14. Long JW, Laskoski M, Peterson GW, Keller TM, Pettigrew KA, Schindler BJ (2011) Metal-catalyzed graphitic nanostructures as sorbents for vapor-phase ammonia. J Mater Chem 21(10):3477–3484

15. Shamskar FR, Rezaei M, Meshkani F (2017) The influence of Ni loading on the activity and coke formation of ultrasound-assisted co-precipitated $Ni-Al_2O_3$ nanocatalyst in dry reforming of methane. Int J Hydrogen Energy 42:4155–4164

16. Boukha Z, Kacimi M, Pereira MFR, Faria JL, Figueiredo JL et al (2007) Methane dry reforming on Ni loaded hydroxyapatite and fluoroapatite. Appl Catal A Gen 317:299–309

17. Son IH, Lee SJ, Song IY, Jeon WS, Jung I et al (2014) Study on coke formation over Ni/gamma-Al_2O_3, Co-Ni/gamma-Al_2O_3, and Mg-Co-Ni/gamma-Al_2O_3 catalysts for carbon dioxide reforming of methane. Fuel 136:194–200

18. Guo JJ, Lou H, Zhao H, Chai DF, Zheng XM (2004) Dry reforming of methane over nickel catalysts supported on magnesium aluminate spinels. Appl Catal A Gen 273:75–82

19. Zhou L, Li LD, Wei NN, Li J, Basset JM (2015) Effect of $NiAl_2O_4$ formation on Ni/Al_2O_3 stability during dry reforming of methane. ChemCatChem 7:2508–2516

20. Pinheiro AL, Pinheiro AN, Valentini A, Mendes J, de Sousa FF et al (2009) Analysis of coke deposition and study of the structural features of MAl_2O_4 catalysts for the dry reforming of methane. Catal Commun 11:11–14

21. Luna AEC, Iriarte ME (2008) Carbon dioxide reforming of methane over a metal modified $Ni-Al_2O_3$ catalyst. Appl Catal A Gen 343:10–15

22. Juan-Juan J, Roman-Martinez MC, Illan-Gomez MJ (2006) Effect of potassium content in the activity of K-promoted Ni/Al_2O_3 catalysts for the dry reforming of methane. Appl Catal A Gen 301:9–15

23. Frusteri F, FA GC, Torre T, Parmaliana A (2001) Potassium-enhanced stability of Ni/MgO catalysts in the dry-reforming of methane. Catal Commun 2:49–56

24. Laosiripojana N, Assabumrungrat S (2005) Catalytic dry reforming of methane over high surface area ceria. Appl Catal B Environ 60:107–116

25. Laosiripojana N, Sutthisripok W, Assabumrungrat S (2005) Synthesis gas production from dry reforming of methane over CeO_2 doped Ni/Al_2O_3: Influence of the doping ceria on the resistance toward carbon formation. Chem Eng J 112:13–22

26. Kambolis A, Matralis H, Trovarelli A, Papadopoulou C (2010) Ni/CeO_3-ZrO_3 catalysts for the dry reforming of methane. Appl Catal A Gen 377:16–26

27. Wolfbeisser A, Sophiphun O, Bernardi J, Wittayakun J, Fottinger K et al (2016) Methane dry reforming over ceria-zirconia supported Ni catalysts. Catal Today 277:234–245
28. Taufiq-Yap YH, Sudarno RU, Zainal Z (2013) CeO_2-SiO_2 supported nickel catalysts for dry reforming of methane toward syngas production. Appl Catal A Gen 468:359–369
29. Pompeo F, Nichio NN, Souza MMVM, Cesar DV, Ferretti OA et al (2007) Study of Ni and Pt catalysts supported on alpha-Al_2O_3 and ZrO_2 applied in methane reforming with CO_2. Appl Catal A Gen 316:175–183
30. Katsutoshi Nagaoka M, Aika K-i (2001) Titania supported ruthenium as a coking-resistant catalyst for high pressure dry reforming of methane. Catal Commun 2:255–260
31. Alipour Z, Rezaei M, Meshkani F (2014) Effect of alkaline earth promoters (MgO, CaO, and BaO) on the activity and coke formation of Ni catalysts supported on nanocrystalline Al_2O_3 in dry reforming of methane. J Ind Eng Chem 20:2858–2863
32. Daza CE, Kiennemann A, Moreno S, Molina R (2009) Dry reforming of methane using Ni-Ce catalysts supported on a modified mineral clay. Appl Catal A Gen 364:65–74
33. Daza C, Kiennemann A, Moreno S, Molina R (2009) Stability of Ni-Ce catalysts supported over Al-PVA modified mineral clay in dry reforming of methane. Energy Fuel 23:3497–3509
34. San-Jose-Alonso D, Juan-Juan J, Illan-Gomez MJ, Roman-Martinez MC (2009) Ni, Co and bimetallic Ni-Co catalysts for the dry reforming of methane. Appl Catal A Gen 371:54–59
35. Ray K, Sengupta S, Deo G (2017) Reforming and cracking of CH_4 over Al_2O_3 supported Ni, Ni-Fe and Ni-Co catalysts. Fuel Process Technol 156:195–203
36. Gamba O, Moreno S, Molina R (2011) Catalytic performance of Ni-Pr supported on delaminated clay in the dry reforming of methane. Int J Hydrogen Energy 36:1540–1550
37. Kathiraser Y, Oernar U, Saw ET, Li ZW, Kawi S (2015) Kinetic and mechanistic aspects for CO_2 reforming of methane over Ni based catalysts. Chem Eng J 278:62–78
38. Akpan E, Sun YP, Kumar P, Ibrahim H, Aboudheir A et al (2007) Kinetics, experimental and reactor modeling studies of the carbon dioxide reforming of methane (CDRM) over a new Ni/CeO_2-ZrO_2 catalyst in a packed bed tubular reactor. Chem Eng Sci 62:4012–4024
39. Bradford MCJ, Vannice MA (1996) Catalytic reforming of methane with carbon dioxide over nickel catalysts .2. Reaction. Appl Catal A Gen 142:97–122
40. Tsipouriari VA, Verykios XE (2001) Kinetic study of the catalytic reforming of methane with carbon dioxide to synthesis gas over Ni/La_2O_3 catalyst. Catal Today 64:83–90
41. Zhang ZL, Verykios XE (1996) Carbon dioxide reforming of methane to synthesis gas over Ni/La_2O_3 catalysts. Appl Catal A Gen 138:109–133
42. Tsipouriari VA, Verykios XE (1999) Carbon and oxygen reaction pathways of CO_2 reforming of methane over Ni/La_2O_3 and Ni/Al_2O_3 catalysts studied by isotopic tracing techniques. J Catal 187:85–94
43. Zhang ZL, Verykios XE (1996) Mechanistic aspects of carbon dioxide reforming of methane to synthesis gas over Ni catalysts. Catal Lett 38:175–179
44. Zhang YS, Zhang SJ, Gossage JL, Lou HH, Benson TJ (2014) Thermodynamic analyses of Tr-reforming reactions to produce syngas. Energy Fuel 28:2717–2726
45. Garcia-Vargas JM, Valverde JL, de Lucas-Consuegra A, Gomez-Monedero B, Dorado F et al (2013) Methane tri-reforming over a Ni/beta-SiC-based catalyst: Optimizing the feedstock composition. Int J Hydrogen Energy 38:4524–4532
46. Song CS, Pan W (2004) Tri-reforming of methane: a novel concept for synthesis of industrially useful syngas with desired H_2/CO ratios using flue gas of power plants without CO_2 pre-separation. Abstr Pap Am Chem Soc 227:U1077–U1077
47. Noureldin MMB, Elbashir NO, Gabriel KJ, El-Halwagi MM (2015) A process integration approach to the assessment of CO_2 fixation through dry reforming. ACS Sustain Chem Eng 3:625–636
48. Kumar R, Kumar K, Choudary NV, Pant KK (2019) Effect of support materials on the performance of Ni-based catalysts in tri-reforming of methane. Fuel Process Technol 186:40–52
49. Singha RK, Shukla A, Yadav A, Adak S, Iqbal Z et al (2016) Energy efficient methane tri-reforming for synthesis gas production over highly coke resistant nanocrystalline Ni-ZrO_2 catalyst. Appl Energy 178:110–125

50. Lino AVP, Calderon YNC, Mastelaro VR, Assaf EM, Assaf JM (2019) Syngas for Fischer-Tropsch synthesis by methane tri-reforming using nickel supported on $MgAl_2O_4$ promoted with Zr, Ce and Ce-Zr. Appl Surf Sci 481:747–760
51. Kang JS, Kim DH, Lee SD, Hong SI, Moon DJ (2007) Nickel-based tri-reforming catalyst for the production of synthesis gas. Appl Catal A Gen 332:153–158
52. Pino L, Vita A, Cipiti F, Lagana M, Recupero V (2011) Hydrogen production by methane tri-reforming process over Ni-ceria catalysts: Effect of La-doping. Appl Catal B Environ 104:64–73
53. Majewski AJ, Wood J (2014) Tri-reforming of methane over $Ni@SiO_2$ catalyst. Int J Hydrogen Energy 39:12578–12585
54. Garcia-Vargas JM, Valverde JL, de Lucas-Consuegra A, Gomez-Monedero B, Sanchez P et al (2012) Precursor influence and catalytic behaviour of Ni/CeO_2 and Ni/SiC catalysts for the tri-reforming process. Appl Catal A Gen 431:49–56

Shifting Trend of Rational Design Heuristics for Methanol-to-Olefins (MTO) Catalysts

Manjesh Kumar

Abstract Invigorated interest from the refiners to simultaneously develop the downstream operations for chemicals along with fuel has catapulted the researchers to investigate new and cheaper feedstocks. Olefins act as primary precursors to multifarious commercial products meeting the demand of modern lifestyle such as polymers, fine chemicals, adhesives, additives, etc. The emergence of shale gas production and new sources of C1 species (syngas) from biomass, coal, and coal bed methane have pushed the need for deriving value-added products commensurate with the upfront demand of petrochemical industries. To this end, the development of methanol-to-hydrocarbon (MTH) gave rise to new chemistry of converting methanol to gasoline-range hydrocarbons, in turn providing pathways for C–C bond formation. With the lapse of time, the process acquired special interest from the research community owing to the efficient conversion of methanol to lighter olefins (MTO) such as ethene, propene, and butenes. Currently, advanced studies are aimed at understanding the reaction mechanism for the first C–C bond formation and propagation thereafter. Major constraints to optimum performance converge to the rational design of the catalyst with enhanced selectivity toward ethene or propene without compromising the lifetime of the catalyst. Here, we will paint the complex blueprint of the MTO process because of the multitude of interacting control parameters determining the desired output. Observations further strengthen the need for symbiotic nature of investigations where the findings must be exchanged continuously among material scientists, simulation experts, and reaction engineers to formulate the holistic picture of the different aspects of the MTO reaction system. Discussion is focused on MTO but not limited to it.

Keywords MTO process · MTH process · MTG process · C–C bond formation · SAPO · Zeolites

M. Kumar (✉)
Department of Chemical Engineering, Indian Institute of Technology Delhi, Delhi, India
e-mail: manjeshkumar@chemical.iitd.ac.in

1 Introduction

The developmental footprint of catalysts and catalysis and their usage trace a long time back in history alleviating the daily experience of life. Among many success stories, sources of energy have been key movers and shakers of modern civilization, and subsequently, the petroleum and petrochemical sectors have been key players. A bird's eye view of the processes involved in these sectors quickly establishes the critical role of catalysts, and subsequently the need for innovation. These quests led to the inception of new chemistry that started in the lab of ExxonMobil in the mid-1970s when a coincidence led to the discovery of new species in reaction product leading to the emergence of methanol to hydrocarbons (commonly known as MTH) chemistry. The novelty of this process emerged from the product distribution which contained aromatics, alkanes, and alkenes providing high octane gasoline from methanol. The advent led to the licensing of methanol-to-gasoline (MTG) processes [1]. Interestingly, these facets of catalysis emerged from the exploratory work of newly found ZSM-5 aluminosilicate catalyst to gauge its potential. While the findings were fascinating, but the questions about different aspects of chemistry pertaining to the mechanism, catalyst role and design, and scale-up were still elusive. In the meantime, it became evident that aromatics in the product pose an environmental challenge; and hence the norms from the regulatory agencies become strict. Additionally, there was a decline in the petrochemical industries in the 1990s. It required the tuning of product selectivity toward more valuable products by re-routing of reaction pathways. Figure 1 demonstrates the economical pathways of chemical transformation by stepwise value addition.

Fig. 1 Life cycle of chemical transformation from sources of C1 (methane/syngas) species to value-products with high commercial viability. Upgraded chemicals feed as precursors to thriving petrochemical industries
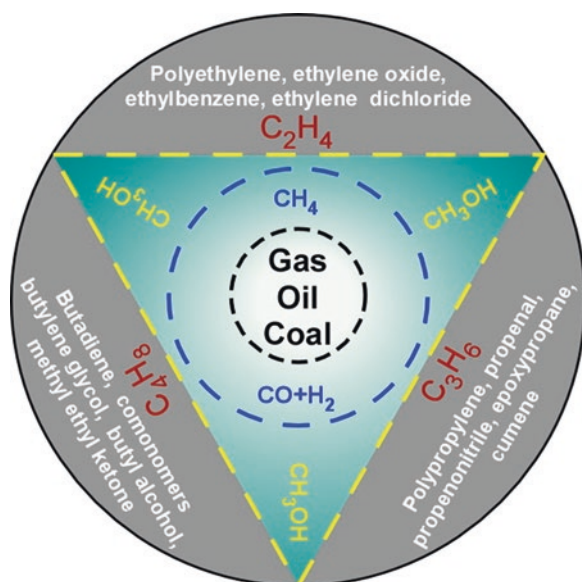
   Over the last two decades, there has been a turnaround in this sector because of a surge in shale gas production [2] along with various other new sources of methane/methanol such as natural gas, coal, coal bed methane, and others. These developments ensured the streamlined production of methanol for which the commercially viable Fischer-Tropsch process exists. The availability of methanol opened the possibility for the huge source of petrochemical feedstocks by making the MTH process efficient for light olefin production. These small molecules act as a major precursor for a wide range of useful products relevant to polymers, petrochemicals, fuels, commodities, fine chemicals, and others [2]. Current trends suggest the huge possibility for ethene ($C_2^=$), polypropylene ($C_3^=$), and 1-butene ($C_4^=$). The global market sizes are 146 billion [Polaris Market research report, 2020–2026], 116 billion [Grand View research, 2020–2027], and 2 billion [Report Buyer, Report ID: 5820653, Feb 2020], respectively, with an anticipated compounded growth rate of 9.8%, 3.1%, and 6.8% for 2019. Current global demands for olefins are met by steam cracking of Naptha or heavier hydrocarbons which might be challenging in the future. It requires an effort to boost the growth of the methanol-to-olefin (MTO) process as another vertical to circumvent the supply-demand gap. This has led to a significant interest in the research community to focus on making the process economically viable by resolving intriguing dynamics of classical catalysis triad, namely, *Structure-Property-Performance.* The commercial feasibility of the MTO process is heavily dependent on the performance which is evaluated by conversion of reactant, selectivity toward the desired product, and a lifetime of the catalyst. Overwhelmingly, nanoporous zeolite catalysts emerged as a material of interest and extensive work is under progress to improve the holistic efficacy of the process. A comprehensive view of the current state-of-art in the MTO process suggests that a synergistic and symbiotic approach by scientists from a varied background such as material design, reaction engineering, and mathematical computation is required to resolve the challenge. Here, we will layout the typical heuristics of exploring design principles involved in the MTO process that are complex and intriguing.

   The catalytic life cycle of the MTO process requires optimization at three different fronts. These include catalyst design, reaction intermediate control, and product distribution. These disparate facets are interconnected and need simultaneous multipronged approach to obtain the best results. However, it pins down to designing a catalyst that controls the intermediates to produce the desired product. For the same, a detailed understanding of the intermediates and products dynamics in relation to catalyst properties becomes an absolute necessity. To this end, we will explore heuristics which impacts MTO reaction and can be tuned to obtain better performance.

2 Catalyst Synthesis and Design

Aluminosilicate molecular sieves have occupied center stage as an MTO catalyst. High thermal stability, shape selectivity owing to the confined space, and tunable acid sites offer attractive opportunities to explore vast design space for

these materials. Typical frameworks such as SAPO-34 [3, 4] and ZSM-5 [5, 6] have been extensively explored due to the inherent advantages of crystalline structure and desired product selectivity. Dalian Institute of Chemical Physics has reached a new height by establishing a commercial MTO plant of 600 kiloton /annum using SAPO-34 [7]. We will explore the challenges and possibilities of MTO catalyst from the prism of catalyst triad.

2.1 Structure

Physical attributes of zeolite crystallites such as pores and channels act as a gateway to the reactants (i.e., methanol), intermediates, and products for MTO reactions during their complete lifecycle. These dynamic species interact differently with different sites of these rigid architectures of catalyst particles. It begins with external surfaces of crystals and pore-mouth of channels within these particles. Subsequently, the path is more tortuous with changing diffusing diameter and chemical environment along the maze of channels. Reactants are screened early on at the crystallite surface. After reaction activates, the shapes and sizes of intermediates and products along the course of diffusion depend strongly on cage topology along with the molecular arrangement of atomic species within these cavities. In this section, we will discuss attributes pertaining to MTO and way forward for new potentials pathways for rational design.

2.1.1 Pore Size
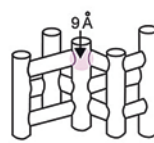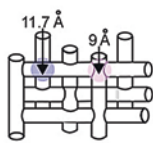
It refers to the size of openings on the terminating crystalline planes or diffusing diameter of channels running through the crystallites. These aluminosilicate frameworks are classified into the small-pore (8-MR), medium-pore (10-MR), and large-pore (12-MR) zeolite that acts as a screening sieve for reactants and products. Methanol has a kinetic diameter of 3.6 Å and faces little barrier while diffusing inside the channel, but the product speciation is significantly impacted by the pore size. Stocker et al [8]. summarized the evolution of different zeolite structures for MTO reaction, promoting different conversion and selectivity of products. The review outlines the preferable use of small-pore zeolite for higher yield of light olefins and medium- and large-pore zeolite for aromatic, and larger alkenes and alkanes. It should be noted that larger pore zeolites have correspondingly larger cages/cavities. Hence, it will be difficult to deconvolute the exact effect of pore size and cage on intermediates and hence products. However, small-pore zeolites suppress the transfer of branched aliphatic and heavy aromatic hydrocarbons, thus impeding the exit of aromatic species and higher alkenes in the product stream and thereby promoting the selectivity of lighter olefins [9]. A dramatic effect of pore size was illustrated by song group [10] where a small variation in pore size by 0.3 Å resulted in no activity for MTO reactions in H-ZSM-22 compared to H-ZSM-12.

Among the small pore zeolite family, silicoaluminophosphate SAPO-34 (CHA framework) [7, 11, 12] (structural analogue SSZ-13) has gained commercial popularity for MTO reactions owing to lighter olefin selectivity. To explore other possibilities, research groups are looking for other small-pore zeolites (RUB, KFI, DNL, etc.) for better efficacy and commercial viability. To this end, the variation of small-pore SAPOs was explored by Hong group [13]. They obtained similar performance for STA-7 (SAV) and poor performance with STA-14 (KFI) attributed to the pore topology and connectivity. Other small-pore zeolites have been studied by various other groups for MTO activity such as Weckhuysen [14], Zheng [15], Corma [16–18], and Davis [19] which might pave a path for a new and more efficient catalyst for MTO. On the other hand, medium- and large-pore zeolites (i.e., ZSM-5, FER, BEA, MOR, Zeolite-Y) [8, 20] provide a conduit to aromatics and higher alkenes which is desirable for MTG or GTL processes. There are extensive studies [20–23] establishing the comparative product speciation for different pore zeolites. We escaped the topology in the discussion, but it is well established that the same pore size zeolite with 1D, 2D, and 3D geometry has a significant impact on the lifetime of catalyst and product distribution. However, it must be noted that a major role in controlling or activating reaction pathways is played by the cage explained in the next section.

2.1.2 Cage/Cavity/Pockets Shape and Size

Cages, cavities, or pockets are the inherent attributes of crystallite which is formed by ordered molecular arrangement along the channels or intersection of multidimensional channels within zeolite structure. Different frameworks with the same pore size can present different shapes and sizes of these cages/cavities [24] as shown in Table 1. Typically, pockets are referred to as regions that are formed by intersecting channels. Extensive investigations [18, 25–27] point toward the primary role of

Table 1 Differentiation of cage architecture with pore size

Descriptor	Small pore zeolite			Medium pore zeolite	
Framework	SAPO-34 (cha)	SAPO-35 (lev)	SAPO-17 (eri)	ZSM-5 (mfi)	ZSM-11 (mel)
Pore size	8-MR	8-MR	8-MR	10-MR	10-MR
Diffusion dia	3.72 Å	3.53 Å	3.42 Å	4.7 Å	5.19 Å
Cage size	1.09 nm 0.67 nm	0.73 nm 0.63 nm	1.30 nm 0.63 nm	9 Å	11.7 Å 9 Å

Frameworks with 8-MR pore size present different cage sizes along the channel. Intersecting channels with similar size and varying topology generate cavities with different shape and size (adapted from reference [24])
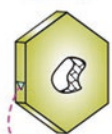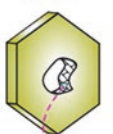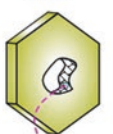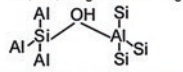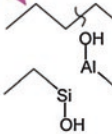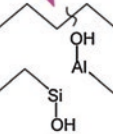
these features compared to other physicochemical properties on the nature of intermediate and correspondingly the selectivity of products and lifetime of the catalyst. Elementary steps in reaction pathways such as alkylation, deprotonation, dealkylation, cracking, etc., depend significantly on the topological arrangement of confined spaces during the initiation, propagation, and termination of typical double-cycle hydrogen pool mechanism. While the reactivity and intermediate will depend on the molecular arrangement of acidic sites as well, however, frameworks with similar acid strength and distribution show varied intermediate depending upon cavity shape and size [28]. To this end, comparative review [20] of product speciation was shown using H-SAPO-34, H-ZSM-5, and H-FER having different cages and topology. Similarly, a study [29] on SSZ-13 and H-UTM-1 shows that MTO reaction cannot activate because of smaller cavity not promoting intermediate such as polymethylbenzene. Supercages in MCM-22 (10-MR) with 2D sinusoidal channels and delaminated ITQ-2 were evaluated for MTO reactions [30]. It was shown that supercage helps with slow deactivation, but sinusoidal channels help with higher propene selectivity compared to ethene. While SAPO-34 has established dominance for high light olefins selectivity, ZSM-58 (DDR Topology, 8-MR pore) [31] has proved to be another candidate with similar selectivity but better thermal stability. Separate studies by Liu et al. have explored disparate 8-MR-SAPO zeolite to assess the effect of pore cavities. Using SAPO-34, SAPO-18, and SAPO-35, group [32] has shown higher selectivity for propene and butenes for former two frameworks while SAPO-35 generated ethene predominantly along with some propene. To ascertain the role of intermediates in product selectivity, they further investigated the SAPO-35, SAPO-34, and DNL-6 [33] with different cavities but the same pore size. These frameworks showed the highest selectivity toward ethene, propene, and butene in order respectively. Commensurate with product distribution, cages of varied size stabilized different intermediates and transition states such as DNL-6 supported carbenium cation with bulkier (butyl) side chain contrary to SAPO-34 with carbenium ion with shorter (methyl and ethyl) side chain due to steric hindrance. SAPO-35 prefers even smaller intermediates such as methylbenzenium (1,2,2,3,5-pentaMB$^+$) and methylcyclopentadienium cations producing ethene. Another interesting study [34] considered three different cavities such as *cha, lta,* and *lev,* and simulated side chain mechanism to estimate energy barriers. Observations complied with prior understanding of depicting minima with *cha* cavities of suitable cage size compared to *lta* and *lev* of being either too small or too big. These observations got further strengthened by experimental studies on an extended list of small pore zeolite (SSZ-13, SAPO-34, SAPO-39, MCM-35, ERS-7, and RUB-37) by Davis group [19, 35]. Framework with CHA topology showed the MTO activation while rest failed to activate due to small-size cavities. Some studies are looking at the preferential diversion of reaction pathways to generate ethene or propene selectively. To this end, two small-pore zeolites, H-RUB-50 [36], and SAPO-14 [37] (AFN topology) have shown higher yield of ethene and propene, respectively. These observations can be reverse engineered where catalysts can be crystallized using organic mimicking reaction intermediates which can promote desired pathways leading to selective products. Recent work from the Corma group

[38] established this principle by synthesizing RTH which favors the paring route of hydrogen pool mechanism, thereby increasing the yield of propylene over conventional CHA framework. Cage size not only impacts the activity of catalysts and selectivity of the product but the deactivation rate as well. Olsbye and coworkers [39] show that the topological maneuvering emerging out of channel intersection for 10 MR-ringed zeolites (i.e., IM-5, TNU-9, ZSM-11, and ZSM-5) has significantly different lifetime owing to complex polyaromatic naphthene intermediates promoted inside the cage. Diffusion pathways were investigated with multi-level and multi-dimensional zeolite frameworks and established the stability order (1L, 2D H-SAPO-35 < 2L, 2D H-SAPO-57 < 3L, 2D H-SAPO-59 < 3D H-SAPO-34) [40] depicting the role of pore dimensionality and cage size. Another study investigated small-pore zeolites frameworks (CHA, DDR, LEV) [14] with large cages interconnected by 8-MR channels for deactivation mechanism during MTO using the nature of reaction intermediates. Observations were interesting not only because there were different aromatic species causing deactivation but their location varied with the framework. In this end, it is quite evident that the cage shape and size play a primary role in activating MTO reaction, generating suitable intermediates, producing desired products, and finally sustaining catalyst activation.

2.1.3   Crystallinity and Defects

Catalyst synthesis is the first portal where major intervention can be introduced to modulate the course of MTO reaction. The understanding of zeolite crystallization is a holy grail to MTO catalysis, but it is still elusive. Limitations emerge from the lack of in situ analytic tools, enough computing power, and siloes in the research community. The overall goal of zeolite synthesis is to tune the physicochemical properties of catalyst amenable to MTO reaction. It involves controlling the crystallinity, external/internal defects, elemental distribution, phase uniformity, surface architecture, and crystal shape and size. Here, we will explore the crystallinity of the zeolite structure and internal/external silanol defects (as shown in Table 2). The presence of a disordered phase in the catalyst particle compromises the stability and integrity of structure which promotes coking and leaching of the ordered phase. Reaction species face extra mass transfer limitations due to the loss of micropore connectivity [41] and intra-crystalline structural defects. A study by Feng group [42] shows that lower crystallinity causes a lower life of the catalyst. A superior catalyst with higher efficiency was synthesized by Yu group [43] using seeds with differing crystallinity. Lower acidity and improved ordered phase ensured a better lifetime compared to convention SAPO-34. Another study used a combination of three organic templates [44] to generate high purity and crystalline particles which showed enhanced light olefin yield. A similar study by Wu group [45] showed high conversion and olefin selectivity (100% and 87.9% respectively) because of small catalyst size and highly crystalline structure. Loss of crystallinity and large pore architecture (such as meso- and macropore) promotes the severe presence of internal isolated and nested silanol (T-OH where T = P, Si, and Al) defects which reduces

Table 2 Nature and molecular arrangement of defect sites and acid sites within the crystallite

the activity and accelerates the catalyst deactivation in MTO reaction. A case in point was presented by the Beato group [46] and others [42, 47, 48] who correlated defects with the lower activity and higher deactivation of the catalyst. A systematic study was presented on ZSM-5 by Gonsiorová [49] and Louis [50] where product selectivity and deactivation were studied. The defective framework results in more of paraffins and C6+ species with shorter lifetime while pure phase promotes propene, ethene, and butenes with slower deactivation. There is an extensive body of work where the defects were healed using secondary growth [51], F⁻ ion treatment [7, 52], NaOH/CTAB treatment [47], resulting in a longer lifetime of the catalyst. At times, these defects were used as precursors for generating the mesopores and thereby creating a better performing catalyst [4].

2.1.4 Crystal Size

Zeolite crystallization is a complex phenomenon. The most pertinent question toward rational design has been aimed at controlling the crystal size. Reduction in the size of catalyst particles results in the increase of effective active sites and a reduction in mass transfer limitation. It has a direct impact on the efficacy by increasing the conversion, selectivity, and lifetime of the catalyst. While this is commonly true, but there is a need to have a relook. A common perception that smaller particles are always better catalysts can be challenged depending upon the reaction system of interest. At times, higher selectivity toward particular product requires longer residence time such as MTH [53], and hence redefinition of the rational design is required which should include developing deterministic pathways of modulating catalyst size based on reaction under consideration. These concepts have been visualized in Fig. 2. Even the catalyst particle produced from the same batch behaves differently [54]. Continuing on the same thought, Holmen group [55]
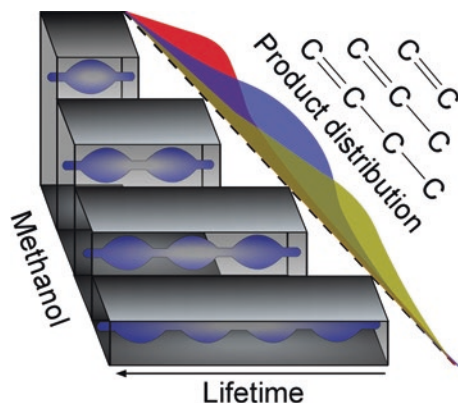
Fig. 2 Product speciation and lifetime control with crystallite size. Depending upon the selectivity toward desired product, crystallite size can be optimized. Optimal size is the function of reaction system under study and product of interest. Different colors refer to different product distribution but not depicting species in any order. However, smaller catalyst particles tend to provide smaller residence for coking phenomena to occur and thereby increasing the lifetime of catalyst

showed that small (0.2μm) and larger (2.5μm) particles were less active and selective but olefin yield increased for medium-size crystallite (0.4–0.5μm) with average activity. It was also observed that the coking rate increased with crystal size. Despite faster coking rate, smaller particles plateau with higher coke content compared to larger particles. Olsbye and coworker [56] showed the same effect using different sized catalyst particles. Interestingly, coke build-up promotes the product selectivity toward lighter ethene or ethane. There is extensive study [57–60] showing the impact of crystal size on an increased lifetime. Among other factors, the short diffusion path length is a key determinant. BET surface area qualitatively corresponds to the size of catalyst particle and hence catalyst lifetime. Lu group [61] showed a similar order by synthesizing zeolite with varied sizes using a different combination of organics. A systematic investigation of size vs. lifetime was presented by Xu and coworker [62]. They synthesized four varied size crystallites (from 20 nm to 8μm) with different morphology (nanoflakes to cubic) and studied deactivation phenomenon using MTO reaction. Nanosized flake showed the longest lifetime compared to cubic 8μm crystals. Particles of an intermediate size such as 80 nm (spheroidal) and 1μm (cubic) fell in between. It should be noted that crystal morphology plays a big role but we will skip the discussion here. To rationally design the catalyst, different synthesis strategies have been explored. It is most common to vary the composition [63], organic phase [44, 64–67], or growth protocol [68] of mother liquor used for synthesis [4]. Hunger group [69] used different structure-directing agents to obtain the three different crystallite sizes referred to as small (S), medium (M), large (L). Catalytic studies showed the anticipated trend as SAPO-34-S > SAPO-34-M > SA PO-34-L because longer residence time promotes higher methylation eventually clogging the cage with polyaromatics and highly branched methylbenzene. Coking does not only reduce the lifetime but decrease the catalyst utilization efficiency.

Varied size shows non-uniform spatial distribution [70] of coke leaving the core of catalyst under-utilized. Collectively, reduced crystallite size is an important determinant for the lifetime of the catalyst.

2.2 Property

The inherent structural features discussed in the earlier section imparts the physico-chemical properties to make an efficient catalyst. These properties control the whole catalytic lifecycle from the entry of reactant to the exit of the product. Physical transport of reactant/intermediate/product species is controlled by pore and cage size distribution and arrangement. Micropore arrangement is determined by the crystalline phase which is inherent in nature. On the other hand, a new set of larger pore systems can be introduced through the invasive method alleviating challenges associated with mass transport limitation. Another critical paradigm is the chemical attributes that are dictated by the elemental arrangement of constituent species. These properties are dependent on the topological arrangement within the crystallite such as confinement effect and spatial distance owing to cage/cavity shape and size. These factors play a significant role in determining the reaction pathways which we will discuss below.

2.2.1 Acid Site Density, Strength, Type, and Distribution

These parameters have been studied to significantly impact the methanol-to-olefin reaction pathways, but details and clear-cut understanding are still elusive. Here, we will explore how they impact the performance and discuss the pathways to tune these properties. Acid density is typically quantified as silicon-to-aluminum ratio (SAR) which is an average value depicting the activity of the catalyst. The density can vary across the crystallite, leading to the phenomenon of "Al zoning." Depending upon the density, the acid strength varies. The isolated bridged hydroxyl group (–Si–OH–Al–) presents the strongest acidity compared to Si(0Al), Si (2Al), Si(3Al), and Si(4Al) [71] as shown in Table 2. Higher acid density gives rise to weaker acid sites. It is well known that a decrease in acid density and site strength reduces the chances of polyaromatics generation and hence slower deactivation [72]. A study by Tatsumi group [73] looks at the lifetime of catalyst as a function of Al content. These acid sites' strength was further manipulated by inserting gallium [74] in the framework resulting in higher stability. Li group [75] looked at four different aluminosilicate frameworks and showed that higher acid sites ensure the higher adsorption of methanol and activation of hydrocarbon pool mechanism. At the same time, high density starts to behave antagonistically by condensing the species from the pool to produce polyaromatic hydrocarbon. Hunger group [76] synthesized low-density isolated acid sites responsible for activating MTO, olefins selectivity, and higher lifetime in AlPO-34. Their study confirms that a low silica framework

produces low coke content. To get lower Brönsted acid sites and defects, Louis group [50] synthesized fluoride-mediated ZSM-5 to selectively increase propene yield. The role of paired Al sites was explored by Davis group [77]. Like earlier observation, increasing SAR value for SSZ-13 helped in obtaining lighter olefins with better lifetime; however, decreasing in SAR led to the pairing of Al sites which promoted selectivity toward propane. Analysis of deactivating species was interesting as the nature varied with Al content. Low SAR resulted in less branched aromatic like naphthalene while high SAR caused highly alkylated species. Framework analogue of SSZ-13, SAPO-34 showed pyrenes as occluded species. Another interesting perspective on acid sites is their locations in the cage and channels. A study by Wang group [78] shows that these locations impact the intermediate species and hence the product selectivity. Al siting in channels promotes olefinic cycle; however, the same species in cages promote aromatic cycle. Accordingly, propene is promoted over ethene by Al in channels compared to cage, resulting in product speciation. More aromatic species are clogged in crystallite having acid sites in a cage compared to channels. They extended the work further to preferentially shift the acid sites by introducing alkali metal in synthesis [79]. By biasing acid sites, they drifted reaction mechanism to yield either ethene or propene. Acid sites are further differentiated in Lewis and Brönsted acid sites. Lercher group [80] studied their mechanistic impact where they ascertained that Lewis sites supported hydride transfer and Brönsted sites led to aromatization. High SAR values also ensure less diffusion limitation due to a lack of active sites. Chemical species can traverse multiple channels without interacting with acid sites and hence creating product selectivities [81]. The synergistic effect of both types of acid sites (Lewis and Brönsted) [82] was illustrated which gives details about first C–C bond formation which is still elusive. However, these attributes are highly dependent on the synthesis mixture composition and protocol. For instance, the silicon-to-aluminum ratio of mother liquor and the presence of stabilizing structure-directing agent among others are some critical parameters which ascertain the final incorporation of elemental species in the framework, thereby controlling the density, strength, type, and distribution. Other invasive techniques [83–87] have been developed using steam and/or alkali solutions to facilitate the altercation in these physicochemical properties of catalysts.

2.2.2 Hydrothermal Stability

Structural integrity of the zeolite structure determine the lifetime of catalyst and usage viability. Deactivated coked catalysts can be regenerated but the loss in the ordered crystalline phase is difficult to recover in the continuous process. The presence of water at high temperatures plays a detrimental role in collapsing the zeolite framework. The interaction of water with the surfaces can be modulated by changing hydrophobicity or hydrophilicity of crystallite. Pure siliceous zeolites are hydrophobic in nature and hence present higher stability. Hydrophilic moieties introduced by the presence of framework or extra-framework aluminum and silanol defects

make them susceptible to attack by water molecules. To this end, SAR and silanol density are used as quantifiable parameters to ascertain the hydrothermal stability of the structure. Higher SAR values ensure a higher resistance to decay under harsh operating conditions. As discussed earlier, usage of OSDA, growth mixture composition, synthesis protocol, and photosynthesis treatment can be used to improve the SAR values [88, 89] and hence the thermal stability. Resasco group [90] and others [91] have performed extensive body of research work studying the impact above mentioned parameter to improve and understand the mechanistic principle of structure loss. In his seminal work, he showed higher resistance to water attack by surface modification of external sites with silanes. Incorporation of metal such as Ni [92] has shown to increase the stability in the harsh condition of higher water content. Corma group [93] improved the resistance to water exposure by steaming the catalyst at 550 °C because of Si migration from isolated place to Si islands without generating any defects. Another interesting synthesis path was developed by Liu group [94] where they synthesized mesopores maintaining hydrothermal stability by the introduction of seed and mesoporogen by reconstructing the disordered channel wall. This attribute makes SAPO-34 a desirable framework for MTO and critical to avoid irreversible damage in general.

2.2.3 Mesoporosity

Pore size and cage/cavity sizes are the inherent property of the crystalline zeolite structure as discussed earlier. However, these features do not facilitate enough mobility to the reaction intermediates or products which lead to final metamorphosis to the coking agent. Broadly, there are two major barriers that restrict the free movement of chemical species through these catalyst particles. Firstly, reactants face challenges at the entry of pore mouth either because of size or blockage due to dangling hydroxyl groups. Later, bulkier intermediates and products find diffusion resistance through the channels. These resistances can be alleviated by introducing mesopores (2–50 nm) within the crystallite. Channel interconnectivity and diffusive transport phenomenon depend on the quality and quantity of mesopores. This helps in increasing the lifetime of catalyst by reducing the coke build-up on the external surface and inside the channel and cage. It contributes to product speciation by allowing better and quick expulsion of desired species. There are detailed reviews [95, 96] elsewhere that have discussed protocol for generating mesopores and their advantages. The research groups have explored various in situ or post-synthesis approaches to introduce mesopores. The general protocol includes the use of soft template [97], hard template [98, 99], additives [100–105], composition [43, 106, 107], chemical treatment [108–110], or synthetic method [111]. While there exist several techniques to generate the mesopores, the quality of the new catalyst varies based on the methodology adopted. One must be mindful of the fact that the generation of mesopores impacts the nature of acid sites, internal/external defects, and orderliness of pore and channel. To this end, assessment pertaining to the

mesoporosity effect must be carefully studied. Overall, these approaches help in increasing catalyst utilization with a better lifetime, and at times better product selectivity.

2.3 Performance

The performance of catalysts in delivering the desired product with a sustainable and economically viable process is the ultimate test for any technology and innovation. For the firsthand feasibility analysis, we look at the conversion of limiting reactants, the selectivity of the desired product, and the lifetime of the catalyst. Under various circumstances, these parameters are antagonistic in nature with each other. The success lies in finding a sweet spot of the optimal structural features and corresponding physicochemical properties of the catalyst which eventually manifests into efficient performance. Figure 3 encapsulates the holistic nature of challenge and demonstrates the complexity of multivariable problem at hand. Notably, commercial process intensification looks at many more critical parameters such as reaction conditions, reactor design, particle mechanical strength, hydrodynamics, among others, that have the potential of making or breaking of a technology.

Zeolites have proved to be a highly active catalyst for MTO/MTH reactions. It attains a 100% conversion in the temperature range of 350–450 °C. In the case of lower conversion or lack of activity, it is easily compensated by an increased amount of catalyst and/or raised reaction temperature incurring a commercial penalty. What becomes critical henceforth is selectivity and lifetime of catalyst for industrial relevance. As discussed in the introduction, the goal post for the desired products has been changing. At the start of MTH studies, high-quality gasoline was of interest. Medium- (ZSM-5, ZSM-11) and large-pore (BEA, MOR, FAU) catalysts [112] played a key role to this end. Increased regulatory norms toward aromatics shifted
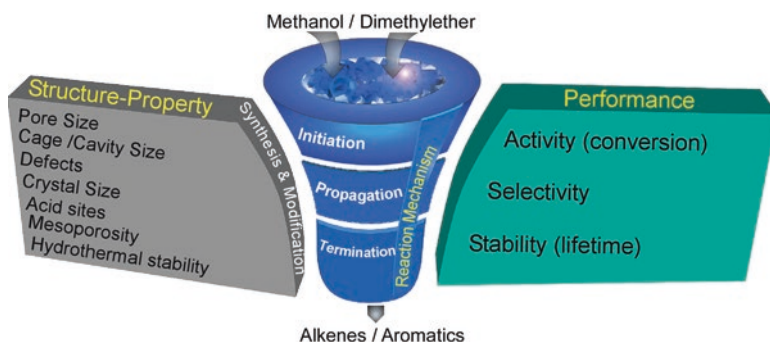
Fig. 3 Scheme depicts life cycle of MTO reaction system. It highlights the interconnectedness among different parameters realizing the multifaceted nature of unanswered questions pertinent to MTO. Moreover, it suggests the need of collaborative research to solve the problem of energy and chemicals for future modern society

the focus toward olefins such as ethene, propene, and butene. While ethene occupies the highest market share, there is thrust to increase the selectivity towards propene [11, 38, 113] and butene placed at the bottom of pyramid. Here, we will refer lighter olefins for the combined amount of ethene and propene as MTO products. Selectivity toward propene compared to ethene is represented by the P/E ratio. Product distribution significantly depends on the physicochemical properties of zeolite discussed earlier. Briefly, small-pore zeolites (8MR) with suitable cage size promote the light olefins. CHA framework zeolite such as SAPO-34 has been very successful in obtaining high C2 and C3 yield along with better hydrothermal stability. Reported yield has varied from 85 to 90%. It suffers from the problem of higher coking rate compared to ZSM-5; but lots of efforts have been made to increase the lifetime by modulating acidity, mesoporosity, crystal size, and crystal defects. Several small-pore zeolites with varied cage sizes have shown promise for olefinic products with different product distribution [18, 114]. Relatively meek acid site density and low-to-medium range acid strength of this framework have been key contributing parameters. Still, there is a need to develop a multifaceted approach for optimal catalyst synthesis which is facile and economical. As we move toward medium-pore zeolites such as ZSM-5 and ZSM-11, we still obtain a higher yield of olefins with products rich in propene compared to ethylene. These catalyst starts forming some aromatics and other higher alkene such as butenes. It should be noted that the overall yield of lighter olefins is less compared to small-pore zeolites. However, mesoporosity development in the medium-pore zeolite, isolating Brönsted acidity, and decreasing crystal size have shown improved selectivity toward commercially attractive propylene [115–118]. Bigger pore size and cage size stabilizes larger intermediates and accelerate reaction pathways via side chain and olefinic reaction pathways leading to aromatics and higher olefins [119]. Moving further to large pore zeolites such as MOR and BEA, they produce more aromatics and higher alkenes. Mechanism pathways show evidence of different intermediates and products. Each framework can further be optimized to tune the selectivity toward given products by promoting desired reaction pathways.

Another critical dimension of performance analysis is the lifetime of the catalyst. It is assessed by studying the mechanism of deactivation and measuring the deactivation rate which plays the key role for industrial application [120, 121]. These investigations in turn determine the reactor types and regeneration process depending upon the nature of deactivation. These processes can be reversible and irreversible. Here, MTO presents coking as a major challenge that can be recovered by high-temperature treatment. The molecular structure of these hydrocarbons resembles polycyclic aromatic rings that get captured within the cage. It is the desired reaction intermediates that transform into larger aromatic structures under suitable conditions, thus blocking the access of active sites. These challenges are alleviated by providing an exit strategy from the cage or modulating the acid strength to control the metamorphosis of the desired intermediate. The comparative study clearly shows that the larger pore size of ZSM-5 sustains for a longer time compared to small pore SAPO-34 [122]. These inherent challenges are being tackled by introducing mesopore suitably to reduce diffusion barriers and thereby increasing the

lifetime. Another approach includes modulating the acid site strength along the diffusing path of intermediates, reactants, and products. Strong acid sites promote cracking and aromatization, leading to the formation of deactivating species. To alleviate this problem, modification procedures such as incorporation, ion-exchange, and impregnation have been proposed [123–125]. Boron incorporation results in smaller [B]-H-ZSM-5 crystal size, reduced strong/mild acid sites ratio, and shows decreased coke formation rates, thus ensuring longer catalytic lifetime [125]. At times, it requires controlling the distribution [7, 126–128] and location [78] of acid density as well. Typically, there is lower acid density on the periphery of crystals which makes stronger acid sites. This results in the higher coking on the external surface and underutilization of catalyst and smaller catalyst lifetime. This can be reduced by avoiding aluminum zoning by making smaller crystallites or controlling the release of aluminum species in the manner that uniformity is maintained. Overall, a quick exit strategy and controlled active sites are the prime drivers of a catalyst lifetime. Recently more mechanistic studies are available that predict the role of formaldehyde in deactivation by Bhan Group [129, 130]. The group [131] has suggested an approach to enhance lifetime by scavenging the coke promoting reagents such as formaldehyde. Overall, control over the structure and physico-chemical properties of zeolite in conjunction with the understanding of reaction mechanism help optimize the performance parameters with higher efficacy.

3   Reaction Mechanism and Intermediates

There is a significant body of work done that explores the underpinnings of MTO reactions. These mechanistic know-hows truly help us to design catalysts and reactions conditions for optimum performance. A detailed review can be found in elsewhere [8, 20, 132–137] but Table 3 shows the major steps and typical chemical species involved during the reaction. For completeness purposes, we will discuss the major understanding of the MTO reaction mechanism. There are two important questions that all researchers are chasing: (I) How does the first C–C bond form? and (II) How does the reaction proceed resulting in different products and deactivation? While the mechanism of C–C bond formation is still intriguing, there is a good understanding of reaction mechanism progression post-induction period. Consensus gravitates toward the hydrogen pool mechanism which encapsulates the dual-aromatic cycle and olefinic cycle. The latter cycle predominantly generates propylene and butenes. It propagates via the multiple methylations of olefins and subsequent cracking. On the other hand, the hydrocarbon pool mechanism has a complex product distribution. It can proceed via either paring mechanism which allows contraction and expansion of ring or side chain mechanism with a fixed ring structure. Major precursors for these pathways can be polymethyl cyclopentadiene or polymethyl benzene which gets protonated to generate cation and start the autocatalytic cycle for hydrogen pool mechanism. Sparsely methylated species generate ethene while the higher density of methyl group promotes propene. The nature and

Table 3 Chemical species during the life cycle of MTO reaction
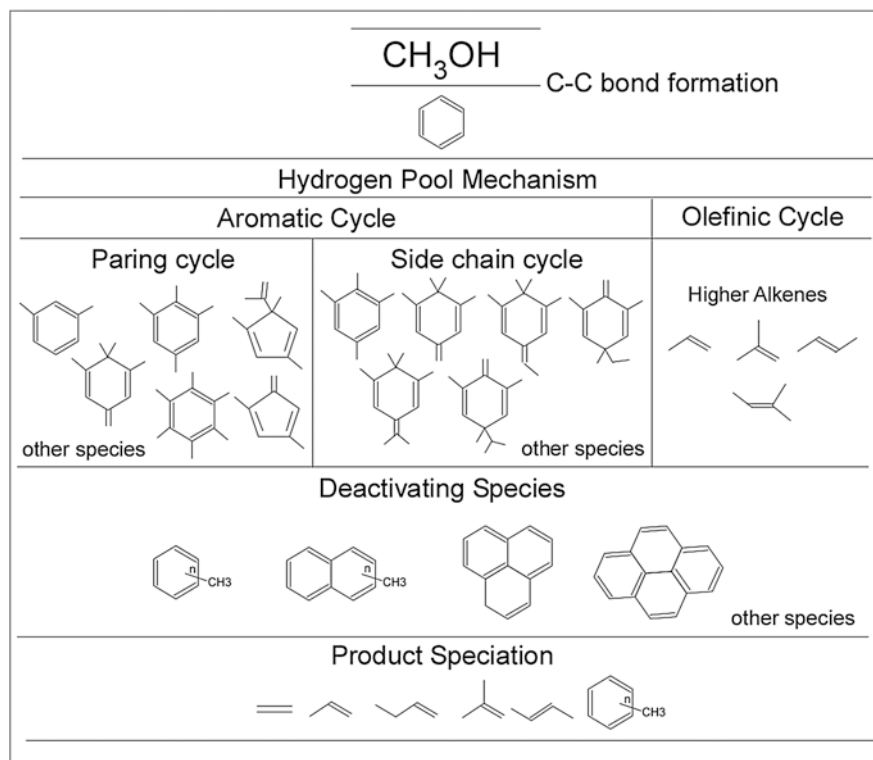
It illustrates the complexity of reaction pathways and need for understanding the mechanism for better catalyst design. Species adapted from references [6, 130, 136, 137]

propagation of intermediates are controlled by the confinement effect of pore and cage structure. These features result in product speciation. For instance, larger side chains on the benzene in a larger cage will allow more of propylene compared to ethene. Similarly, the larger diffusing diameter will allow more aromatics to exit along with higher alkenes and alkanes. Apart from the physical structural effect, acid density and strength play a significant role.

4 Conclusion

The chapter was aimed at developing the general perspective toward design-impact-effect analysis for the methanol-to-olefins reaction system. The rationality of this study emerges from the growing role of petrochemical industries for improving the daily life experience. Keeping the final product speciation in mind, we discussed various facets of control parameters relevant to catalyst design to increase their

efficiency. While process intensification from an industrial point of view needs more efforts to tackle the problems of scaling up among others, but holy grail to the current challenge lies in increasing the lifetime of catalyst and product selectivity by tuning the physicochemical properties of nanoporous zeolite/zeotype frameworks. Surely, the problem is complex owing to many parameters affecting the synthesis and subsequently obtaining details of molecular dynamics occurring within the pores, channels, and cages. It hints toward developing the synergistic approach of research to find a commercially viable catalyst for the problem of interest. To this end, the discussion in the chapter will help readers to gain the perspective necessary for catalyst design for MTO which pervades other reaction systems as well. The aim was to envision the discussion from the prism of catalyst triad—structure-property-performance—and bring a unison in thought process towards the rational design of MTO catalysts.

References

1. Kvisle S et al (2008) Methanol-to-hydrocarbons. In: Handbook of heterogeneous catalysis. Wiley-VCH Verlag GmbH & Co. KGaA https://doi.org/10.1002/9783527610044.hetcat0149
2. (2016) The changing landscape of hydrocarbon feedstocks for chemical production: implications for catalysis. Focus Catal 2016:7. https://doi.org/10.1016/j.focat.2016.08.041
3. Yang M, Fan D, Wei Y, Tian P, Liu Z (2019) Recent progress in methanol-to-olefins (MTO) catalysts. Adv Mater 31:1902181. https://doi.org/10.1002/adma.201902181
4. Sun Q, Xie Z, Yu J (2018) The state-of-the-art synthetic strategies for SAPO-34 zeolite catalysts in methanol-to-olefin conversion. Natl Sci Rev 5:542. https://doi.org/10.1093/nsr/nwx103
5. Chae HJ, Song YH, Jeong KE, Kim CU, Jeong SY (2010) Physicochemical characteristics of ZSM-5/SAPO-34 composite catalyst for MTO reaction. J Phys Chem Solids 71:600. https://doi.org/10.1016/j.jpcs.2009.12.046
6. Xu S et al (2017) Advances in catalysis for methanol-to-olefins conversion. Adv Catal. https://doi.org/10.1016/bs.acat.2017.10.002
7. Tian P, Wei Y, Ye M, Liu Z (2015) Methanol to olefins (MTO): from fundamentals to commercialization. ACS Catal 5:1922. https://doi.org/10.1021/acscatal.5b00007
8. Stöcker M (1999) Methanol-to-hydrocarbons: catalytic materials and their behavior. Microporous Mesoporous Mater 29:3–48
9. Zhu LT, Ma WY, Luo ZH (2018) Influence of distributed pore size and porosity on MTO catalyst particle performance: modeling and simulation. Chem Eng Res Des 137:141. https://doi.org/10.1016/j.cherd.2018.07.005

10. Wang Q, Cui ZM, Cao CY, Song WG (2011) 0.3 Å makes the difference: dramatic changes in methanol-to-olefin activities between H-ZSM-12 and H-ZSM-22 zeolites. J Phys Chem C 115:24987. https://doi.org/10.1021/jp209182u

11. Chen JQ, Bozzano A, Glover B, Fuglerud T, Kvisle S (2005) Recent advancements in ethylene and propylene production using the UOP/hydro MTO process. Catal Today 106:103. https://doi.org/10.1016/j.cattod.2005.07.178

12. Yarulina I, Chowdhury AD, Meirer F, Weckhuysen BM, Gascon J (2018) Recent trends and fundamental insights in the methanol-to-hydrocarbons process. Nat Catal 1:398. https://doi.org/10.1038/s41929-018-0078-5

13. Castro M et al (2009) Silicoaluminophosphate molecular sieves STA-7 and STA-14 and their structure-dependent catalytic performance in the conversion of methanol to olefins. J Phys Chem C 113:15731. https://doi.org/10.1021/jp904623a

14. Goetze J et al (2017) Insights into the activity and deactivation of the methanol-to-olefins process over different small-pore zeolites as studied with operando UV-vis spectroscopy. ACS Catal 7:4033. https://doi.org/10.1021/acscatal.6b03677

15. Li X, Shen W, Zheng A (2019) The influence of acid strength and pore size effect on propene elimination reaction over zeolites: a theoretical study. Microporous Mesoporous Mater. https://doi.org/10.1016/j.micromeso.2018.11.026

16. Boruntea CR, Sastre G, Lundegaard LF, Corma A, Vennestrøm PNR (2019) Synthesis of high-silica erionite driven by computational screening of hypothetical zeolites. Chem Mater 31:9268. https://doi.org/10.1021/acs.chemmater.9b01229

17. Martínez-Franco R, Paris C, Martínez-Triguero J, Moliner M, Corma A (2017) Direct synthesis of the aluminosilicate form of the small pore CDO zeolite with novel OSDAs and the expanded polymorphs. Microporous Mesoporous Mater 246:147. https://doi.org/10.1016/j.micromeso.2017.03.014

18. Ferri P et al (2019) Chemical and structural parameter connecting cavity architecture, confined hydrocarbon Pool species, and MTO product selectivity in small-pore cage-based zeolites. ACS Catal 9:11542. https://doi.org/10.1021/acscatal.9b04588

19. Deimund MA, Schmidt JE, Davis ME (2015) Effect of pore and cage size on the formation of aromatic intermediates during the methanol-to-olefins reaction. Top Catal 58:416. https://doi.org/10.1007/s11244-015-0384-y

20. Haw JF, Song W, Marcus DM, Nicholas JB (2003) The mechanism of methanol to hydrocarbon catalysis. Acc Chem Res 36:317. https://doi.org/10.1021/ar020006o

21. Jing B et al (2017) Comparative study of methanol to olefins over ZSM-5, ZSM-11, ZSM-22 and EU-1: Dependence of catalytic performance on the zeolite framework structure. Journal of Nanoscience and Nanotechnology 17, 3680–3688,https://doi.org/10.1166/jnn.2017.13986

22. Dyballa M et al (2018) Tuning the material and catalytic properties of SUZ-4 zeolites for the conversion of methanol or methane. Microporous Mesoporous Mater. https://doi.org/10.1016/j.micromeso.2018.02.004

23. Teketel S et al (2012) Shape selectivity in the conversion of methanol to hydrocarbons: the catalytic performance of one-dimensional 10-ring zeolites: ZSM-22, ZSM-23, ZSM-48, and EU-1. ACS Catal. https://doi.org/10.1021/cs200517u

24. Wang S et al (2018) Relation of catalytic performance to the aluminum siting of acidic zeolites in the conversion of methanol to olefins, viewed via a comparison between ZSM-5 and ZSM-11. ACS Catal 8:5485. https://doi.org/10.1021/acscatal.8b01054

25. Sastre G (2016) Confinement effects in methanol to olefins catalysed by zeolites: a computational review. Front Chem Sci Eng 10:76. https://doi.org/10.1007/s11705-016-1557-3

26. Li X, Jiang J (2018) Methanol-to-olefin conversion in ABC-6 zeolite cavities: unravelling the role of cavity shape and size from density functional theory calculations. Phys Chem Chem Phys 20:14322. https://doi.org/10.1039/c8cp00572a

27. Bhawe Y et al (2012) Effect of cage size on the selective conversion of methanol to light olefins. ACS Catal 2:2490. https://doi.org/10.1021/cs300558x

28. Park JW, Seo G (2009) IR study on methanol-to-olefin reaction over zeolites with different pore structures and acidities. Appl Catal A Gen 356:180. https://doi.org/10.1016/j.apcata.2009.01.001

29. Zhu Q et al (2007) A comparative study of methanol to olefin over CHA and MTF zeolites. J Phys Chem C 111:5409. https://doi.org/10.1021/jp063172c

30. Min HK, Park MB, Hong SB (2010) Methanol-to-olefin conversion over H-MCM-22 and H-ITQ-2 zeolites. J Catal 271:186. https://doi.org/10.1016/j.jcat.2010.01.012

31. Kumita Y, Gascon J, Stavitski E, Moulijn JA, Kapteijn F (2011) Shape selective methanol to olefins over highly thermostable DDR catalysts. Appl Catal A Gen 391:234. https://doi.org/10.1016/j.apcata.2010.07.023

32. Chen J et al (2014) Spatial confinement effects of cage-type SAPO molecular sieves on product distribution and coke formation in methanol-to-olefin reaction. Catal Commun 46:36. https://doi.org/10.1016/j.catcom.2013.11.016

33. Li J et al (2015) Cavity controls the selectivity: insights of confinement effects on MTO reaction. ACS Catal 5:661. https://doi.org/10.1021/cs501669k

34. Li X et al (2014) Confinement effect of zeolite cavities on methanol-to-olefin conversion: a density functional theory study. J Phys Chem C 118:24935. https://doi.org/10.1021/jp505696m

35. Kang JH, Alshafei FH, Zones SI, Davis ME (2019) Cage-defining ring: a molecular sieve structural Indicator for light olefin product distribution from the methanol-to-olefins reaction. ACS Catal 9:6012. https://doi.org/10.1021/acscatal.9b00746

36. Zhang W et al (2018) Methanol to olefins reaction over cavity-type zeolite: cavity controls the critical intermediates and product selectivity. ACS Catal 8:10950. https://doi.org/10.1021/acscatal.8b02164

37. Yang M et al (2020) High propylene selectivity in methanol conversion over a small-pore SAPO molecular sieve with ultra-small cage. ACS Catal 10:3741. https://doi.org/10.1021/acscatal.9b04703

38. Li C et al (2018) Synthesis of reaction-adapted zeolites as methanol-to-olefins catalysts with mimics of reaction intermediates as organic structure-directing agents. Nat Catal 1:547. https://doi.org/10.1038/s41929-018-0104-7

39. Bleken F et al (2011) Conversion of methanol over 10-ring zeolites with differing volumes at channel intersections: comparison of TNU-9, IM-5, ZSM-11 and ZSM-5. Phys Chem Chem Phys 13:2539. https://doi.org/10.1039/c0cp01982h

40. Ahn NH, Seo S, Hong SB (2016) Small-pore molecular sieves SAPO-57 and SAPO-59: synthesis, characterization, and catalytic properties in methanol-to-olefins conversion. Cat Sci Technol 6:2725. https://doi.org/10.1039/c5cy02103k

41. Rahimi K, Towfighi J, Sedighi M, Masoumi S, Kooshki Z (2016) The effects of SiO2/Al2O3 and H2O/Al2O3 molar ratios on SAPO-34 catalysts in methanol to olefins (MTO) process using experimental design. J Ind Eng Chem 35:123. https://doi.org/10.1016/j.jiec.2015.12.015

42. Izadbakhsh A et al (2009) Effect of SAPO-34's composition on its physico-chemical properties and deactivation in MTO process. Appl Catal A Gen 364:48. https://doi.org/10.1016/j.apcata.2009.05.022

43. Sun Q, Wang N, Bai R, Chen X, Yu J (2016) Seeding induced nano-sized hierarchical SAPO-34 zeolites: cost-effective synthesis and superior MTO performance. J Mater Chem A 4:14978. https://doi.org/10.1039/c6ta06613e

44. Masoumi S, Towfighi J, Mohamadalizadeh A, Kooshki Z, Rahimi K (2015) Tri-templates synthesis of SAPO-34 and its performance in MTO reaction by statistical design of experiments. Appl Catal A Gen 493:103. https://doi.org/10.1016/j.apcata.2014.12.033

45. Li J, Li Z, Han D, Wu J (2014) Facile synthesis of SAPO-34 with small crystal size for conversion of methanol to olefins. Powder Technol 262:177. https://doi.org/10.1016/j.powtec.2014.04.082

46. Barbera K, Bonino F, Bordiga S, Janssens TVW, Beato P (2011) Structure-deactivation relationship for ZSM-5 catalysts governed by framework defects. J Catal 280:196. https://doi.org/10.1016/j.jcat.2011.03.016

47. Yarulina I et al (2016) Methanol-to-olefins process over zeolite catalysts with DDR topology: effect of composition and structural defects on catalytic performance. Cat Sci Technol 6:2663. https://doi.org/10.1039/c5cy02140e

48. Palčić A, Ordomsky VV, Qin Z, Georgieva V, Valtchev V (2018) Tuning zeolite properties for a highly efficient synthesis of propylene from methanol. Chem A Eur J 24:13136. https://doi.org/10.1002/chem.201803136

49. Sazama P et al (2011) FTIR and 27Al MAS NMR analysis of the effect of framework Al- and Si-defects in micro- and micro-mesoporous H-ZSM-5 on conversion of methanol to hydrocarbons. Microporous Mesoporous Mater 143:87. https://doi.org/10.1016/j.micromeso.2011.02.013

50. Bleken FL et al (2012) Conversion of methanol into light olefins over ZSM-5 zeolite: strategy to enhance propene selectivity. Appl Catal A Gen 447–448:178. https://doi.org/10.1016/j.apcata.2012.09.025

51. Liu X et al (2016) Coke suppression in MTO over hierarchical SAPO-34 zeolites. RSC Adv 6:28787. https://doi.org/10.1039/c6ra02282k

52. Chen X et al (2016) The preparation of hierarchical SAPO-34 crystals via post-synthesis fluoride etching. Chem Commun 52:3512. https://doi.org/10.1039/c5cc09498d

53. Khare R, Millar D, Bhan A (2015) A mechanistic basis for the effects of crystallite size on light olefin selectivity in methanol-to-hydrocarbons conversion on MFI. J Catal 321:23. https://doi.org/10.1016/j.jcat.2014.10.016

54. Remi JCS et al (2016) The role of crystal diversity in understanding mass transfer in nanoporous materials. Nat Mater 15:401. https://doi.org/10.1038/nmat4510

55. Chen D, Moljord K, Fuglerud T, Holmen A (1999) The effect of crystal size of SAPO-34 on the selectivity and deactivation of the MTO reaction. Microporous Mesoporous Mater 29:191. https://doi.org/10.1016/S1387-1811(98)00331-X

56. Hereijgers BPC et al (2009) Product shape selectivity dominates the methanol-to-olefins (MTO) reaction over H-SAPO-34 catalysts. J Catal 264:77. https://doi.org/10.1016/j.jcat.2009.03.009

57. Hirota Y, Murata K, Miyamoto M, Egashira Y, Nishiyama N (2010) Light olefins synthesis from methanol and dimethylether over SAPO-34 nanocrystals. Catal Lett 140:22. https://doi.org/10.1007/s10562-010-0421-1

58. Álvaro-Muñoz T, Márquez-Álvarez C, Sastre E (2012) Use of different templates on SAPO-34 synthesis: effect on the acidity and catalytic activity in the MTO reaction. Catal Today 179:27. https://doi.org/10.1016/j.cattod.2011.07.038

59. Lefevere J, Mullens S, Meynen V, Van Noyen J (2014) Structured catalysts for methanol-to-olefins conversion: a review. Chem Pap 68. https://doi.org/10.2478/s11696-014-0568-0

60. Gao M et al (2019) A modeling study on reaction and diffusion in MTO process over SAPO-34 zeolites. Chem Eng J 377:119668. https://doi.org/10.1016/j.cej.2018.08.054

61. Wang P, Lv A, Hu J, Xu J, Lu G (2012) The synthesis of SAPO-34 with mixed template and its catalytic performance for methanol to olefins reaction. Microporous Mesoporous Mater. https://doi.org/10.1016/j.micromeso.2011.11.037

62. Yang G et al (2013) Nanosize-enhanced lifetime of SAPO-34 catalysts in methanol-to-olefin reactions. J Phys Chem C 117:8214. https://doi.org/10.1021/jp312857p

63. Jiang Y et al (2016) Effect of (Si+Al)/CTAB ratio on crystal size of mesoporous ZSM-5 structure over methanol-to-olefin reactions. J. Taiwan Inst Chem Eng 61:234. https://doi.org/10.1016/j.jtice.2015.12.017

64. Martínez-Franco R, Li Z, Martínez-Triguero J, Moliner M, Corma A (2016) Improving the catalytic performance of SAPO-18 for the methanol-to-olefins (MTO) reaction by controlling the Si distribution and crystal size. Cat Sci Technol 6:2796. https://doi.org/10.1039/c5cy02298c

65. Bakhtiar SUH et al (2018) CTAB-assisted size controlled synthesis of SAPO-34 and its contribution toward MTO performance. Dalton Trans 47:9861. https://doi.org/10.1039/c8dt01811a

66. Xu Z et al (2019) Size control of SSZ-13 crystals with APAM and its influence on the coking behaviour during MTO reaction. Cat Sci Technol 9:2888. https://doi.org/10.1039/c9cy00412b

67. Ma M et al (2020) Synthesis of small-sized SAPO-34 assisted by pluronic F127 nonionic surfactant and its catalytic performance for methanol to olefins (MTO). Catal Commun 133:105839. https://doi.org/10.1016/j.catcom.2019.105839

68. Li M et al (2017) Solvent-free synthesis of SAPO-34 nanocrystals with reduced template consumption for methanol-to-olefins process. Appl Catal A Gen 531:203. https://doi.org/10.1016/j.apcata.2016.11.005

69. Dai W, Wu G, Li L, Guan N, Hunger M (2013) Mechanisms of the deactivation of SAPO-34 materials with different crystal sizes applied as MTO catalysts. ACS Catal 3:588. https://doi.org/10.1021/cs400007v

70. Gao S et al (2018) Insight into the deactivation mode of methanol-to-olefins conversion over SAPO-34: coke, diffusion, and acidic site accessibility. J Catal 367:306. https://doi.org/10.1016/j.jcat.2018.09.010

71. Xu B, Bordiga S, Prins R, van Bokhoven JA (2007) Effect of framework Si/Al ratio and extra-framework aluminum on the catalytic activity of Y zeolite. Appl Catal A Gen 333:245. https://doi.org/10.1016/j.apcata.2007.09.018

72. Aguayo AT, Gayubo AG, Vivanco R, Olazar M, Bilbao J (2005) Role of acidity and microporous structure in alternative catalysts for the transformation of methanol into olefins. Appl Catal A Gen 283:197. https://doi.org/10.1016/j.apcata.2005.01.006

73. Zhu Q et al (2008) The study of methanol-to-olefin over proton type aluminosilicate CHA zeolites. Microporous Mesoporous Mater 112:153. https://doi.org/10.1016/j.micromeso.2007.09.026

74. Zhu Q et al (2008) Methanol-to-olefin over gallosilicate analogues of chabazite zeolite. Microporous Mesoporous Mater 116:253. https://doi.org/10.1016/j.micromeso.2008.04.017

75. Dai W et al (2011) Methanol-to-olefin conversion on silicoaluminophosphate catalysts: effect of brønsted acid sites and framework structures. ACS Catal 1:292. https://doi.org/10.1021/cs200016u

76. Dai W et al (2012) Methanol-to-olefin conversion catalyzed by low-silica AlPO-34 with traces of Brønsted acid sites: combined catalytic and spectroscopic investigations. ChemCatChem 4:1428. https://doi.org/10.1002/cctc.201100503

77. Deimund MA et al (2016) Effect of heteroatom concentration in SSZ-13 on the methanol-to-olefins reaction. ACS Catal 6:542. https://doi.org/10.1021/acscatal.5b01450

78. Liang T et al (2016) Conversion of methanol to olefins over H-ZSM-5 zeolite: reaction pathway is related to the framework aluminum siting. ACS Catal 6:7311. https://doi.org/10.1021/acscatal.6b01771

79. Wang S et al (2019) Tuning the siting of aluminum in ZSM-11 zeolite and regulating its catalytic performance in the conversion of methanol to olefins. J Catal 377:81. https://doi.org/10.1016/j.jcat.2019.07.028

80. Müller S et al (2016) Hydrogen transfer pathways during zeolite catalyzed methanol conversion to hydrocarbons. J Am Chem Soc 138:15994. https://doi.org/10.1021/jacs.6b09605

81. Losch P et al (2017) H-ZSM-5 zeolite model crystals: structure-diffusion-activity relationship in methanol-to-olefins catalysis. J Catal 345:11. https://doi.org/10.1016/j.jcat.2016.11.005

82. Chu Y, Yi X, Li C, Sun X, Zheng A (2018) Brønsted/Lewis acid sites synergistically promote the initial C-C bond formation in the MTO reaction. Chem Sci 9:6470. https://doi.org/10.1039/c8sc02302f

83. Wilson S, Barger P (1999) The characteristics of SAPO-34 which influence the conversion of methanol to light olefins. Microporous Mesoporous Mater 29:117–126

84. Mitchell S et al (2015) Aluminum redistribution during the preparation of hierarchical zeolites by Desilication. Chem A Eur J 21:14156. https://doi.org/10.1002/chem.201500992

85. Fjermestad T, Svelle S, Swang O (2013) Mechanistic comparison of the dealumination in SSZ-13 and the desilication in SAPO-34. J Phys Chem C 117:13442. https://doi.org/10.1021/jp4028468

86. Ji Y, Deimund MA, Bhawe Y, Davis ME (2015) Organic-free synthesis of CHA-type zeolite catalysts for the methanol-to-olefins reaction. ACS Catal 5:4456. https://doi.org/10.1021/acscatal.5b00404

87. Ji Y, Birmingham J, Deimund MA, Brand SK, Davis ME (2016) Steam-dealuminated, OSDA-free RHO and KFI-type zeolites as catalysts for the methanol-to-olefins reaction. Microporous Mesoporous Mater. https://doi.org/10.1016/j.micromeso.2016.06.012

88. Dusselier M, Deimund MA, Schmidt JE, Davis ME (2015) Methanol-to-olefins catalysis with hydrothermally treated zeolite SSZ-39. ACS Catal 5:6078. https://doi.org/10.1021/acscatal.5b01577

89. Kong C, Zhu J, Liu S, Wang Y (2017) SAPO-34 with a low acidity outer layer by epitaxial growth and its improved MTO performance. RSC Adv 7:39889. https://doi.org/10.1039/c7ra06488h

90. Zhang L, Chen K, Chen B, White JL, Resasco DE (2015) Factors that determine zeolite stability in hot liquid water. J Am Chem Soc 137:11810. https://doi.org/10.1021/jacs.5b07398

91. Jamil AK et al (2016) Hydrothermal stability of one-dimensional pore ZSM-22 zeolite in hot water. J Phys Chem C 120:22918. https://doi.org/10.1021/acs.jpcc.6b04980

92. Valle B, Alonso A, Atutxa A, Gayubo AG, Bilbao J (2005) Effect of nickel incorporation on the acidity and stability of HZSM-5 zeolite in the MTO process. Catal Today 106:118. https://doi.org/10.1016/j.cattod.2005.07.132

93. Li Z, Martínez-Triguero J, Yu J, Corma A (2015) Conversion of methanol to olefins: stabilization of nanosized SAPO-34 by hydrothermal treatment. J Catal 329:379. https://doi.org/10.1016/j.jcat.2015.05.025

94. Wang C et al (2016) A reconstruction strategy to synthesize mesoporous SAPO molecular sieve single crystals with high MTO catalytic activity. Chem Commun 52:6463. https://doi.org/10.1039/c6cc01834c

95. Lopez-Orozco S, Inayat A, Schwab A, Selvam T, Schwieger W (2011) Zeolitic materials with hierarchical porous structures. Adv Mater 23:2602. https://doi.org/10.1002/adma.201100462

96. Dugkhuntod P, Wattanakit C (2020) A comprehensive review of the applications of hierarchical zeolite nanosheets and nanoparticle assemblies in light olefin production. Catalysts 10:245. https://doi.org/10.3390/catal10020245

97. Wang F et al (2014) Polyethyleneimine templated synthesis of hierarchical SAPO-34 zeolites with uniform mesopores. RSC Adv 4:46093. https://doi.org/10.1039/c4ra08199d

98. Varzaneh AZ, Towfighi J, Sahebdelfar S, Bahrami H (2016) Carbon nanotube templated synthesis of hierarchical SAPO-34 catalysts with different structure directing agents for catalytic conversion of methanol to light olefins. J Anal Appl Pyrolysis 121:11. https://doi.org/10.1016/j.jaap.2016.06.007

99. Wang J et al (2017) Synthesis, characterization, and catalytic application of hierarchical SAPO-34 zeolite with three-dimensionally ordered mesoporous-imprinted structure. Microporous Mesoporous Mater. https://doi.org/10.1016/j.micromeso.2017.06.012

100. Wu L, Degirmenci V, Magusin PCMM, Lousberg NJHGM, Hensen EJM (2013) Mesoporous SSZ-13 zeolite prepared by a dual-template method with improved performance in the methanol-to-olefins reaction. J Catal. https://doi.org/10.1016/j.jcat.2012.10.029

101. Xi D et al (2014) In situ growth-etching approach to the preparation of hierarchically macroporous zeolites with high MTO catalytic activity and selectivity. J Mater Chem A 2:17994. https://doi.org/10.1039/c4ta03030c

102. Wu L, Hensen EJM (2014) Comparison of mesoporous SSZ-13 and SAPO-34 zeolite catalysts for the methanol-to-olefins reaction. Catal Today 235:160. https://doi.org/10.1016/j.cattod.2014.02.057

103. Sharifi Pajaie H, Taghizadeh M (2016) Methanol conversion to light olefins over surfactant-modified nanosized SAPO-34. React Kinet Mech Catal 118:701. https://doi.org/10.1007/s11144-016-1023-8

104. Zhu X et al (2016) Trimodal porous hierarchical SSZ-13 zeolite with improved catalytic performance in the methanol-to-olefins reaction. ACS Catal 6:2163. https://doi.org/10.1021/acscatal.5b02480

105. Chen H et al (2019) Organosilane surfactant-directed synthesis of nanosheet-assembled SAPO-34 zeolites with improved MTO catalytic performance. J Mater Sci 54:8202. https://doi.org/10.1007/s10853-019-03485-w

106. Kang EA et al (2013) Synthesis of mesoporous SAPO-34 zeolite from mesoporous silica materials for methanol to light olefins. J Nanosci Nanotechnol 13:7498. https://doi.org/10.1166/jnn.2013.7905

107. Li Y et al (2014) Hierarchical SAPO-34/18 zeolite with low acid site density for converting methanol to olefins. Catal Today 233:2. https://doi.org/10.1016/j.cattod.2014.03.038

108. Chen X et al (2016) A top-down approach to hierarchical SAPO-34 zeolites with improved selectivity of olefin. Microporous Mesoporous Mater 234:401. https://doi.org/10.1016/j.micromeso.2016.07.045

109. Jin W et al (2018) Selective Desilication, Mesopores formation, and MTO reaction enhancement via citric acid treatment of zeolite SAPO-34. Ind Eng Chem Res 57:4231. https://doi.org/10.1021/acs.iecr.8b00632

110. Liu Z et al (2018) Melting-assisted solvent-free synthesis of hierarchical SAPO-34 with enhanced methanol to olefins (MTO) performance. Cat Sci Technol 8:423. https://doi.org/10.1039/c7cy02283b

111. Yang ST et al (2012) Microwave synthesis of mesoporous SAPO-34 with a hierarchical pore structure. Mater Res Bull 47:3888. https://doi.org/10.1016/j.materresbull.2012.08.041

112. Galadima A, Muraza O (2015) From synthesis gas production to methanol synthesis and potential upgrade to gasoline range hydrocarbons: a review. J Nat Gas Sci Eng 25:303. https://doi.org/10.1016/j.jngse.2015.05.012

113. Jasper S, El-Halwagi MM (2015) A techno-economic comparison between two methanol-to-propylene processes. PRO 3:684. https://doi.org/10.3390/pr3030684

114. Dusselier M, Davis ME (2018) Small-pore zeolites: synthesis and catalysis. Chem Rev 118:5265. https://doi.org/10.1021/acs.chemrev.7b00738

115. Mei C et al (2008) Selective production of propylene from methanol: Mesoporosity development in high silica HZSM-5. J Catal 258:243. https://doi.org/10.1016/j.jcat.2008.06.019

116. Yarulina I et al (2018) Structure–performance descriptors and the role of Lewis acidity in the methanol-to-propylene process. Nat Chem 10:804. https://doi.org/10.1038/s41557-018-0081-0

117. Rownaghi AA, Hedlund J (2011) Methanol to gasoline-range hydrocarbons: influence of nanocrystal size and mesoporosity on catalytic performance and product distribution of ZSM-5. Ind Eng Chem Res 50:11872. https://doi.org/10.1021/ie201549j

118. Jang HG, Min HK, Lee JK, Hong SB, Seo G (2012) SAPO-34 and ZSM-5 nanocrystals' size effects on their catalysis of methanol-to-olefin reactions. Appl Catal A Gen 437-438:120. https://doi.org/10.1016/j.apcata.2012.06.023

119. Wang CM, Wang YD, Du YJ, Yang G, Xie ZK (2016) Computational insights into the reaction mechanism of methanol-to-olefins conversion in H-ZSM-5: nature of hydrocarbon pool. Cat Sci Technol 6:3279. https://doi.org/10.1039/c5cy01419k

120. Müller S et al (2015) Coke formation and deactivation pathways on H-ZSM-5 in the conversion of methanol to olefins. J Catal 325:48. https://doi.org/10.1016/j.jcat.2015.02.013

121. Sun X et al (2014) On reaction pathways in the conversion of methanol to hydrocarbons on HZSM-5. J Catal 317:185. https://doi.org/10.1016/j.jcat.2014.06.017

122. Li J et al (2011) Comparative study of MTO conversion over SAPO-34, H-ZSM-5 and H-ZSM-22: correlating catalytic performance and reaction mechanism to zeolite topology. Catal Today 171:221. https://doi.org/10.1016/j.cattod.2011.02.027

123. Yang Y et al (2012) The synthesis of endurable B-Al-ZSM-5 catalysts with tunable acidity for methanol to propylene reaction. Catal Commun 24:44. https://doi.org/10.1016/j.catcom.2012.03.013

124. Zhang HR et al (2017) A durable and highly selective PbO/HZSM-5 catalyst for methanol to propylene (MTP) conversion. Microporous Mesoporous Mater. https://doi.org/10.1016/j.micromeso.2017.04.031

125. Yaripour F, Shariatinia Z, Sahebdelfar S, Irandoukht A (2015) Effect of boron incorporation on the structure, products selectivities and lifetime of H-ZSM-5 nanocatalyst designed for application in methanol-to-olefins (MTO) reaction. Microporous Mesoporous Mater. https://doi.org/10.1016/j.micromeso.2014.10.024

126. Knott BC et al (2018) Consideration of the aluminum distribution in zeolites in theoretical and experimental catalysis research. ACS Catal 8:770. https://doi.org/10.1021/acscatal.7b03676

127. Dědeček J, Tabor E, Sklenak S (2019) Tuning the aluminum distribution in zeolites to increase their performance in acid-catalyzed reactions. ChemSusChem 12:556. https://doi.org/10.1002/cssc.201801959

128. Nordvang EC, Borodina E, Ruiz-Martínez J, Fehrmann R, Weckhuysen BM (2015) Effects of coke deposits on the catalytic performance of large zeolite H-ZSM-5 crystals during alcohol-to-hydrocarbon reactions as investigated by a combination of optical spectroscopy and microscopy. Chem A Eur J 21:17324. https://doi.org/10.1002/chem.201503136

129. Hwang A, Kumar M, Rimer JD, Bhan A (2017) Implications of methanol disproportionation on catalyst lifetime for methanol-to-olefins conversion by HSSZ-13. J Catal 346:154. https://doi.org/10.1016/j.jcat.2016.12.003

130. Hwang A, Bhan A (2019) Deactivation of zeolites and Zeotypes in methanol-to-hydrocarbons catalysis: mechanisms and circumvention. Acc Chem Res 52:2647. https://doi.org/10.1021/acs.accounts.9b00204

131. Hwang A, Bhan A (2017) Bifunctional strategy coupling Y2O3-catalyzed Alkanal decomposition with methanol-to-olefins catalysis for enhanced lifetime. ACS Catal 7:4417. https://doi.org/10.1021/acscatal.7b00894

132. Olsbye U et al (2012) Conversion of methanol to hydrocarbons: how zeolite cavity and pore size controls product selectivity. Angew Chem Int Ed 51:5810. https://doi.org/10.1002/anie.201103657

133. Svelle S et al (2006) Conversion of methanol into hydrocarbons over zeolite H-ZSM-5: ethene formation is mechanistically separated from the formation of higher alkenes. J Am Chem Soc 128:14770. https://doi.org/10.1021/ja065810a

134. Dahl IM, Kolboe S (1996) On the reaction mechanism for hydrocarbon formation from methanol over SAPO-34: 2. Isotopic labeling studies of the co-reaction of propene and methanol. J Catal 161:304. https://doi.org/10.1006/jcat.1996.0188

135. Schulz H (2010) 'Coking' of zeolites during methanol conversion: basic reactions of the MTO-, MTP- and MTG processes. Catal Today 154:183. https://doi.org/10.1016/j.cattod.2010.05.012

136. Van Speybroeck V et al (2011) First principle kinetic studies of zeolite-catalyzed methylation reactions. J Am Chem Soc 133:888. https://doi.org/10.1021/ja1073992

137. Hemelsoet K, Van Der Mynsbrugge J, De Wispelaere K, Waroquier M, Van Speybroeck V (2013) Unraveling the reaction mechanisms governing methanol-to-olefins catalysis by theory and experiment. ChemPhysChem 14:1526. https://doi.org/10.1002/cphc.201201023

Non-conventional Catalytic Materials for Refining and Petrochemicals

Subhashini and Tarak Mondal

Abstract Over decades, oil refineries have been one of the major energy sources to meet the growing energy demands of world. This extensive dependency will extend for next few decades due to the comprehensive research and development in the evolution of oil refineries. The special achievement of researchers of using zeolites as catalysts in the sector of oil refining and petrochemistry has led to a whole new subdivision in the twentieth century. In this chapter, the introductory part briefly describes about the composition of crude oil and various separation processes involved in its extraction in oil refineries and petrochemical industries. The main body of the chapter focuses on the description of refining processes using various catalysts and later adapting the zeolites as catalysts due to their extraordinary properties and features. The final section contains the brief introduction of MOFs, a new member of crystalline materials, and also the scope of their usage in oil refineries and petrochemical industries.

Keywords Non conventional catalysis · Refining · Petrochemicals · Catalytic cracking · Hydroprocessing · Metal organic frameworks

Petroleum is a complex mixture of hydrocarbons found in vast underground pockets called reservoirs, in various forms of matter such as gaseous, liquid, or solid. Although the word "petroleum" means it is in liquid form, it also appeared in gaseous form (natural gas) and solid form (solid bitumen). Petroleum was formed from the buried ancient marine organisms such as plants, algae, and bacteria underneath sedimentary rocks at high pressure and temperature conditions. Long ago plants and animals lived in shallow seas. The organic material (plants and animals) mixed with other sediments was buried after dying and sinking to the seafloor. In the absence of plentiful oxygen, the aerobic bacteria were not able to decompose the organic

Subhashini · T. Mondal (✉)
Department of Chemical Engineering, Indian Institute of Technology Ropar,
Rupnagar, Punjab, India
e-mail: tarakmondal@iitrpr.ac.in

matter. However, under such conditions of oxygen level, anaerobic bacteria prevail, which reduces the organic matter and transforms it into fossil fuels. Thus, petroleum reservoirs are the locations where ancient seas existed. Petroleum reservoirs can be found beneath land or the ocean floor.

Petroleum is also used as a synonym for crude oil, but it is a widely defined class of hydrocarbon mixtures in liquid state. The components of petroleum are crude oil, lease condensate, unfinished oils, refined products, and natural gas plant liquids. Out of all, crude oil is the most significant component of petroleum which is the origin of energy for the world's human race existence. The crude oil of petroleum reservoirs is extracted with giant drilling machines of the refineries. Naturally occurring crude oil is insignificant to consumers and thereby needs to be converted into useful products. This transformation was carried out through a series of various physical and chemical methods; this process is called *refining*. By refining processes, crude oil is converted into a variety of desired products such as fuels, gases, lube oils, and solvents. These products are obtained from crude oil by applying various process variables such as heat, pressure, catalysts, and chemicals [1]. Crude oil is composed of hydrocarbons (HC) having a wide variety of C/H ratio and molecular structures. It also contains other heteroatoms such as sulfur (S), oxygen (O), nitrogen (N), and heavy metals, e.g., iron, nickel, and vanadium.

Crude oils are classified as follows (Table 1):

- Specific gravity or API gravity—very light, light, medium, heavy, and extra heavy
- Physical appearance—varies from see-through liquids (light) to black solids (heavy crude)
- Chemical composition:

  - *Sour crude* oils having high acidity
  - *Paraffinic* (mostly paraffin)
  - *Naphthenic*
  - *Aromatic* (mostly cyclic or aromatic compounds)

Crude oils go through various separation processes in refining, distillation being the primary operation of separation by boiling crude oil into different fractions or cuts. After the primary separation of crude oil through distillation, each fraction stream is further converted into useful products through:

Table 1 Petroleum products from crude oil [2]

Cut	Carbon chain length	Boiling range (°C)
Petroleum gases	1–4	<5
Naphtha	5–10	20–200
Kerosene	10–16	180–260
Gas oil (diesel oil)	14–20	260–340
Lubricating oil	20–50	370–600
Fuel oil	20–70	330 upwards
Residue	>70	Non-distillable

- *Cracking(FCC)*—conversion of larger molecules into smaller by the cleavage of C−C bonds
- *Reforming*—a combination of reactions leading to the formation of aromatic compounds (e.g., dehydrogenation, isomerization, cyclization, aromatization, etc.)
- *Hydroprocessing*—inducing certain reactions (based on hydrogenation and hydrogenolysis) by addition of hydrogen
- *Isomerization*—molecular conversion from one isomer to another isomer
- *Coking*—conversion of fluid hydrocarbon into coke
- *Alkylation*—reaction between an olefin and a paraffin to produce larger paraffin

All the above processes are various treatment and separation processes used to improve product quality by removing undesirable constituents (Fig. 1).

The operations and processes occurred in petroleum refinery are classified into five basic types:

- *Distillation*—In this process crude oil is separated into different groups of hydrocarbon compounds based on their boiling-point ranges in two separate sections working under atmospheric pressure and vacuum.
- *Conversion processes*—In this process the structure and size of hydrocarbon molecules are changed by:

  - *Decomposition*—large molecules are converted into smaller molecules through cracking and related processes.
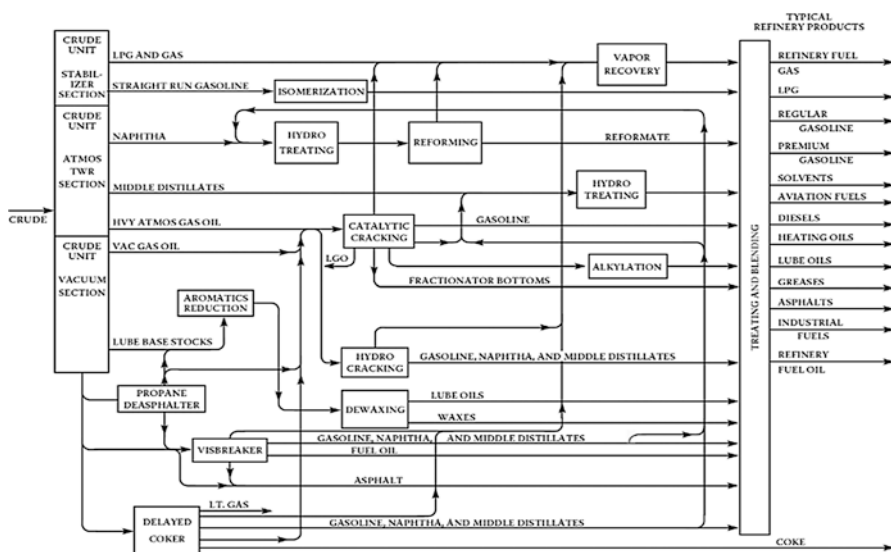
Fig. 1 Refining processes in refinery [1]

- *Unification*—small molecules are converted into larger molecules through alkylation, polymerization, and related processes.
- *Reforming*—molecules are rearranged into different geometric structures by processes like catalytic reforming, isomerization, etc.

- *Treatment processes*—processes such as hydrodesulphurization, desalting, solvent refining, solvent extraction, sweetening, and dewaxing to get finished products.
- *Blending*—to meet the specific performance properties of the finished products by mixing and combining hydrocarbon fractions, additives, and other components.
- *Otherrefining operations*—These include various components water stripping, recovery, product storage and handling, waste treatment, and acid-tail gas treatment [1].

Dynamic market demands and governmental policies and regulations regulate the number and quality of manufactured products from crude oil. Therefore, refining is considered to be a complex dynamic process which requires periodic modernization and revitalizing. Ever since the first oil refinery was opened at Ploiesti, Romania, in 1856, refining technology has evolved from simple distillation technique into a more sophisticated and advanced cascade of processes in order to transform crude oil into various fractions. The number of processes needed to produce any fuel of a given set of specifications depends on the specifications as well as the quality of the oil used as feedstock.

1   Refinery Processes

Since the composition of two crude oils is not identical, the refineries require different separating operations and processes to treat different crude oils. The various processes used in the refineries are:

- Distillation—atmospheric and vacuum distillation
- Catalytic cracking
- Catalytic hydrocracking
- Hydroprocessing and resid processing
- Hydrotreating
- Catalytic reforming and isomerization
- Alkylation and polymerization
- Coking and thermal processes
- Blending
- Supporting processes—gas processing unit, hydrogen production-purification, acid gas removal, sulfur recovery processes, etc.

Let us discuss each of these processes briefly.

1.1 Distillation

It is the foremost process in the refining industry. It fractionates the crude stills into different crude oil cuts which can be used as feedstock in successive refining processes to meet their particular specifications (Fig. 2).

Effective fractionation into simpler cuts with higher efficiencies and lower costs is achieved by performing atmospheric distillation followed by vacuum distillation. Distillation column consists of a set of trays, which collects the vapor at different levels obtained according to their boiling point. Thereafter, lighter components of the crude still, i.e., high volatile vapors, are collected in the upper trays whereas the heavier components or the less volatile compounds are collected in the bottom tray. The high boiling bottom cuts (heavier fractions) are fed into the vacuum tower distillation unit and further are reduced into simpler and smaller cuts. The model fractions obtained from the distillation column in ascending boiling points are as follows:

- *Fuel gas(dry gas)*—it mainly consists of methane and ethane. In certain refineries, propane is also obtained with methane and ethane in the fuel gas stream.
- *Wet gas*—The wet gas stream consists of methane and ethane along with propane and butane. These propane and butane are used for LPG after being separated from methane and ethane. Moreover, butane is used in gasoline admix and alkylation unit feed.
- *LSR naphtha*—The LSR naphtha or LSR gasoline stream is used in gasoline blending after removing sulfur from it. Prior to blending, it is also processed in an isomerization unit to improve its octane number.
- *HSR naphtha* or *HSR gasoline*—HSR naphtha are generally used to produce high-octane reformate for gasoline blending and aromatics.

Fig. 2 Atmospheric distillation tower (open internet source)

- *Gas oils*—The gas oils are used to produce gasoline, diesel, and jet fuels in a hydrocracker/catalytic cracker unit. In addition, the lubricating oils producing processing units use heavier vacuum gas oils as their feedstocks.
- *Residuum*—The lube base stocks and heavy fuel oil are obtained from vacuum still bottoms by further processing them in various units like visbreaker, deasphalting, or coker. The deasphalting unit's product can be further processed to obtain different grades of asphalt crudes. These asphalt crudes can be used in roads and roofing.

The model fraction cut points and their boiling ranges for atmospheric and vacuum distillation are given in the Table 2:

Desalting of the crude oil is required to minimize the scaling and corrosion on the reactor surfaces if the salt content exceeds 10 lb./1000 bbl (expressed as NaCl). In addition to the removal of the salts present in the crude oil, desalting also helps in removing certain metals which causes catalyst deactivation in catalytic processes. Depending on the concentration of salts and metals present in the crude oil, desalting can be done in the two-stage or three-stage method. Desalting process also removes the suspended solids present in the crude oil. Usually these suspended solids act as contaminants like clay, soil and very fine sand particles, iron oxide, sulfides, etc. The various analytical methods used for determining the salt content of crude oils are discussed as follows:

- HACH titration with mercuric nitrate
- Potentiometric titration
- Mohr titration with silver nitrate
- Potentiometric titration in a mixed solvent
- Conductivity

1.2 Coking and Thermal Processes

Due to severe environmental restrictions and regulations, the refineries have to switch to the production of more and more lighter fractions. The bottom products of distillation units are heavier fractions, which usually serve as the feedstock for

Table 2 Boiling ranges of typical crude oil fractions [1]

	Boiling ranges (°C)	
Fraction	ASM	TBP
Butanes and light straight run-naphtha (LSR)	90–220	90–190
Heavy straight-run naphtha (HSR)	180–400	190–380
Kerosine	330–540	380–520
Light gas oil (LGO)	420–640	520–610
Atmospheric gas oil (AGO)	550–830	610–800
Vacuum gas oil (VGO)	750–1050	800–1050
Vacuum-reduced crude (VRC)	1050+	1050+

energy and electric supply for heavy industries. Due to the various limitations of heavier fraction feedstocks, these industries have also initiated to shift towards lighter fraction feedstock such as natural gas. Hence, heavier fractions obtained from distillation are further processed to convert into lighter fractions. This conversion of heavier fractions into lighter fractions is aided by the cooking process. The by-product of the coking process is coke formation that primarily contains carbon. Coking is generally used to pre-treat vacuum residuals to prepare them a suitable feedstock for catalytic crackers and hydrocrackers. There are different types of cokes obtained during delayed coking process:

- *Sponge coke*—it is hard, porous, asymmetrical shaped lumps with particles size ranging from 20 in. to fine dust. Since it looks like a black sponge, it is called sponge coke.
- *Needle coke*—it is obtained from feedstocks with high aromatic content under high pressure (100 psig) and high recycle ratios (1:1). Since it appears to be an elongated crystalline structure, it is called needle coke. Needle coke shows lower electrical resistivity and has a lower thermal expansion coefficient; therefore, it is preferred over sponge coke by electrode manufacturing industries.
- *Shot coke*—it is produced while processing very heavy residuals or during operational upsets. It has a characteristic shape of clusters of shot sized pellets.

The petroleum cokes are mainly used for as follows (Fig. 3):

- Fuel
- Manufacture of electrodes
- Manufacturing elemental calcium carbide, phosphorus, and silicon carbide
- Manufacturing graphite
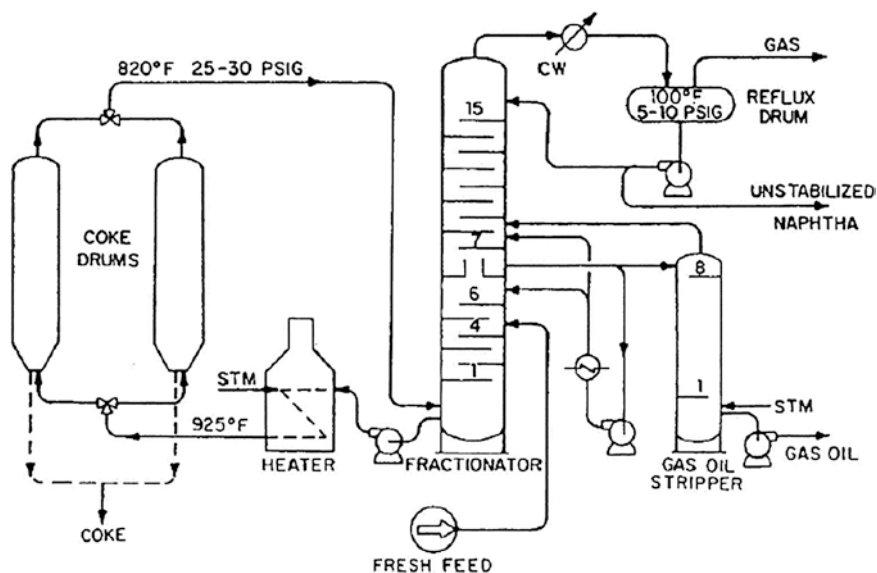
Fig. 3 Delayed coking unit [1]

1.3 Catalytic Cracking

The conversion of heavy oils into valuable and lighter products like gasoline is done by catalytic cracking [3]. The term *cracking* means breaking down the long chain and heavier hydrocarbon molecules into smaller and more useful molecules (Fig. 4).

Earlier thermal cracking was accomplished, but it is being thoroughly replaced by catalytic cracking because catalytic cracking yields more gasoline and light gases. These light gases consist of more olefins in comparison with those obtained from thermal cracking.

Catalytic cracking involves catalyst application for breakdown of the heavier hydrocarbons into lighter. These catalysts do not alter the rate of the reaction. There has been a trend in the development of these catalysts; presently zeolites are the most promising catalysts compared to amorphous catalysts. Zeolites have been used in FCC (fluid catalytic cracking) over 50 years because they have much higher cracking activity, shorter residence times that prevent over cracking of the gasoline to gas and coke. Various advantages of zeolites above natural and synthetic amorphous catalysts are (Table 3):

- Higher activity
- Higher gasoline yields
- Lower coke yield
- Production of gasoline with more paraffinic and aromatic hydrocarbons
- Enhanced isobutene yield
- Perform higher conversion rates without over cracking

1.4 Catalytic Hydrocracking

One of the most historic catalytic processes in petroleum refining is hydrogenation. Since the 1960s it has remarkably matured to a huge extent. Several factors as listed below have engrafted to the significant development of hydrocracking:
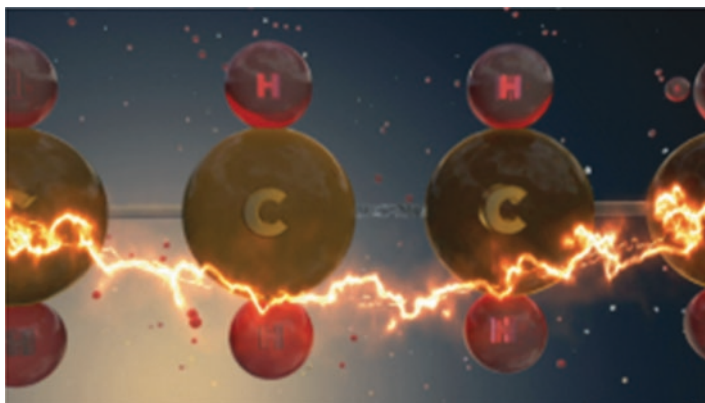
Fig. 4 Catalytic cracking [1]

Table 3 Comparison of amorphous and zeolite catalysts [1]

	Amorphous	Zeolite
Coke, wt.%	4	4
Conversion, vol.%	55	65
C_5+ gasoline, vol.%	38	51
C_3- gas, wt.%	7	6
C_4's, vol.%	17	16

- Higher demand for lighter petroleum products, i.e., gasoline and jet fuel instead of diesel fuel and home heating oils
- Availability of cheaper hydrogen production in large amounts from catalytic reforming
- New environmental regulations demanding lower limits of sulfur and aromatic contents in motor fuels

Various process conditions such as operations at lower pressure, desired product specifications, and catalysts are under continuous evolving stage to bring out the required conversion of higher-boiling fractions.

A few advantages of hydrocracking process are:

- Improved gasoline yield
- Improved octane quality and sensitivity of gasoline pool
- Higher yield of isobutane in butane fraction
- Substitute to the fluid catalytic cracking for upgradation of heavy cracking cuts into valuable gasoline and lighter fuel oils

Catalytic cracking and hydrocracking are considered to be the two sides of a coin in modern refineries. The catalytic cracking uses atmospheric cracked paraffin and vacuum gas oils for their feedstock. However, in case of hydrocracking, the feedstocks are aromatic cycle oils and coking unit distillates. The aromatic cycle oils and coker distillates resist catalytic cracking. But these can be hydrocracked very easily under higher pressures and hydrogen atmosphere (Fig. 5).

1.5 Hydroprocessing and Resid Processing

The atmospheric tower bottoms and vacuum tower bottoms with their initial boiling points as 343 °C and 566 °C respectively are called "resids." The resids contain sulfur, nitrogen, and metals in greater concentrations as compared with that contained in the feedstock crude oil, and contain hydrocarbons in very much lower ratios. The concentrations of sulfur, nitrogen, and metals are even higher in the vacuum-reduced crude (VRC) as compared to atmospheric reduced crude (ARC). Stern environmental regulations and emission norms have made the application of heavy oils for fuels very tough and expensive. Therefore, the heavy oils must be converted into feedstocks for several refining processes that will supplement their
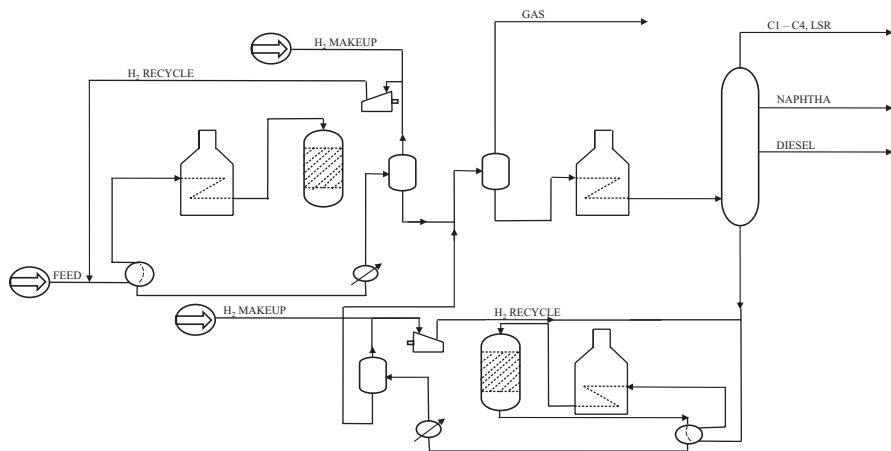
Fig. 5 Two-staged hydrocracker [1]

further conversion into transportation fuel blending stocks. The ARC undergoes extended processing in catalytic cracking units and hydroprocessing units, whereas the delayed coking and solvent extraction (or Flexicoking) are certain thermal cracking processes used for converting VRC feedstocks into more simpler and desired range products (Fig. 6).

1.6 Hydrotreating

The process of treating petroleum products with hydrogen to make them catalytically stable and/or removing the contaminant is known as *hydrotreating*. Petroleum products are stabilized by converting the unstable double bonds (C=C) and triple bonds (C≡C) into stable single (C–C) bonds, for example, converting alkenes and gum-forming unstable diolefins to paraffin. Sulfur, nitrogen, oxygen, halides, and certain trace metals are some of the impurities removed by hydrotreating [16]. A broad domain of feedstocks like from naphtha to reduced crude can be treated by hydrotreating. Employing a hydrotreating process specifically for sulfur removal from crude is known as *hydrodesulphurization*(HDS). Usually the aromatic content present in crude causes environmental pollution; hence their concentration must be controlled. These limitations make it necessary to hydrogenate aromatic rings present in crude oil and thereby reduce the aromatic content of crude oil by converting aromatics to paraffin. Hydrotreating uses different catalysts for catalytically stabilizing the various feedstocks. A few examples of hydrotreating catalysts are oxides of cobalt and molybdenum on alumina, oxide of nickel and vanadium, nickel thiomolybdate, sulfides of tungsten and nickel, and vanadium oxide [4]. The cobalt and molybdenum oxides on alumina catalysts are commonly used hydrotreating
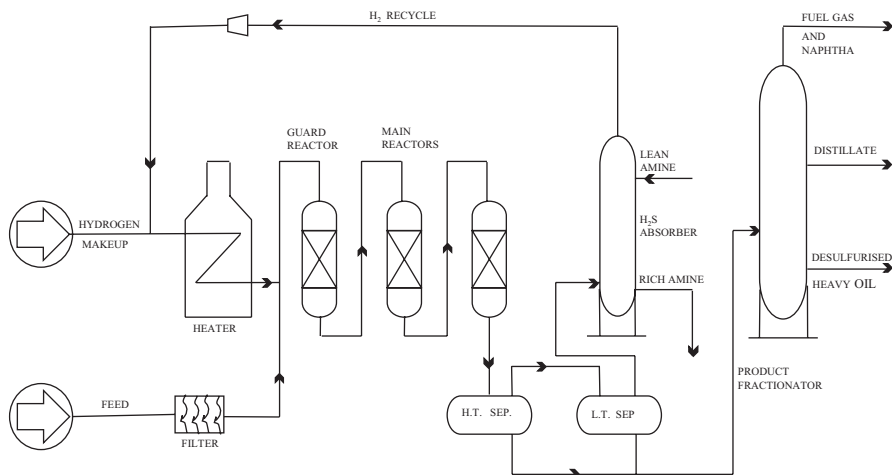
Fig. 6 EXXON RESID fining hydroprocessing unit. (Courtesy Exxon Research and Engineering) [1]

catalysts because they are extremely selective, easily regenerated, and resistant to poisons (Fig. 7).

1.7 Catalytic Reforming and Isomerization

Reforming involves rearranging the naphtha hydrocarbons to manufacture gasoline molecules. This process was developed to increase both the quality and volume of the gasoline produced by refiners. In the reforming process, the substances which have higher octane number than paraffin and naphthenes are converted into aromatics and isomers with the help of catalysts. This conversion is usually accompanied by the hydrogen formation, which can be used in other refining processes like hydrotreating. Reforming produces higher octane reformates which gives cleaner burning fuels (Fig. 8).

A catalytic reformer promotes the formation of aromatics and isoparaffins as via the following desirable reactions:

- Paraffin are isomerized to form naphthenes (to certain extent), then subsequently converted to aromatics.
- Olefins are saturated to form paraffin.
- Naphthenes are converted to aromatics.
- Aromatics remain unchanged.
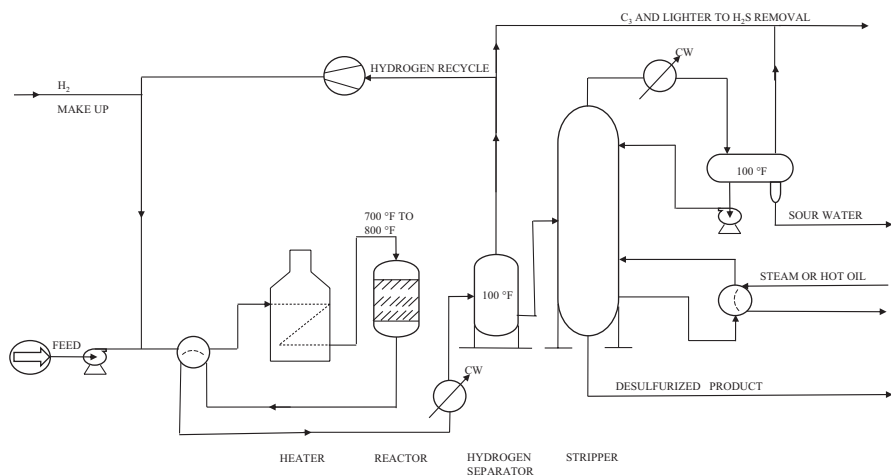
Fig. 7 Catalytic hydrodesulphurization [1]
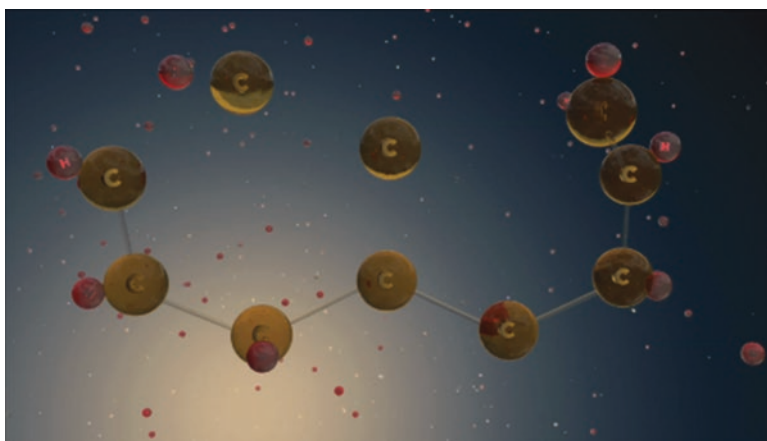
Fig. 8 Catalytic reforming and isomerization (open internet source)

Platinum is the most active material among catalytic reforming catalysts. However, it is deactivated by compounds like hydrogen sulfide, sulfur compounds, ammonia, and organic nitrogen [1]. Therefore pre-treatment of the feedstock by hydrotreating process is required to remove these unwanted materials (Fig. 9).

1.8 *Alkylation and Polymerization*

The reaction to form heavier isoparaffins by reacting low-molecular-weight olefins with isoparaffins is termed as alkylation. Concentrated acids such as sulfuric and hydrofluoric acids are the sole catalysts used for the production of high octane
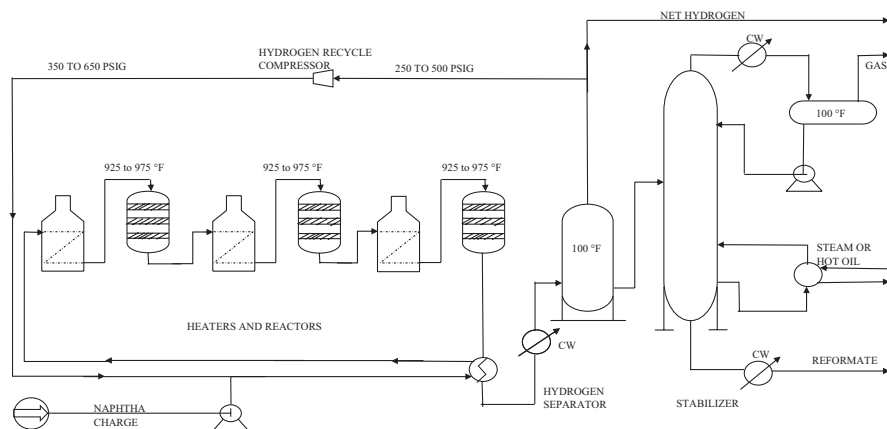
Fig. 9 Catalytic reforming, semiregen generative process [1]

alkylate gasoline commercially. But various other catalysts are employed in the commercial production of ethylbenzene, cumene, and long-chain (C12 to C16) alkylated benzenes.

1.9 Blending

The last major step in the refining process is blending of various streams together to obtain desired finished petroleum products. As an example, reformate, alkylate, and catalytically cracked gasoline are blended into different fractions to produce the various grades of motor fuels. The refineries blend different fractions for meeting the required specifications for acceptable motor fuel performance. Refiners can also mix in the various property-enhancing materials like octane enhancers, anti-oxidants, anti-knock agents, metal deactivators, and rust inhibitors in their hydrocarbon streams.

2 Zeolites

Over 50 years, zeolites are the backbone of the petrochemical and refining industry. These have been exploited prominently as heterogeneous catalysts and separation materials in refineries. But still their applications continue to expand due to their extraordinary flexibility of pore size distribution, shape selectivity, stability, etc [25]. To meet present environmental policy and regulations, the refining and petrochemical industries have focused on the production of cleaner and higher quality oils and lubricants, and cheaper petrochemicals by using new zeolites and mesoporous materials as well as on the improvements of the conventional zeolites. Advancements of the zeolitic materials can be attained by enhancing the

conventional zeolites properties such as the compositional range, matrix-zeolite interactions quality, exterior activity of zeolite, or by focusing on the synthesis, advancement, and commercialization of pristine materials to suit particular selectivity, catalytic activity, and durability. Consequently, industrial research and development are engrossed in developing extremely selective catalysts that can function for longer periods and stand for the presence of trace contaminants.

2.1   Zeolitic Catalysts Used in Various Processes

The advancement of pristine zeolite catalysts have influenced the core catalytic processes of petroleum refining such as FCC, hydrocracking, and hydroprocessing [28].

2.1.1   FCC Catalysts

FCC catalyst like ZSM-5 focuses on bottoms upgrading, light olefin production, yield improvement, and desulfurization. For achieving the main objective of FCC process, associated research continued to focus on the development of ZSM-5 activity and hydrothermal stability by including phosphorus and other elements [5]. Decade's long research have led to synthesis of non-organic forms of ZSM-5 and various improvements in the zeolite, additive matrix, and binder formulations. These optimizations have also reduced cost and improved the effectiveness. FCC catalyst mainly focuses on the production of propylene and butylene with the help of conventional ZSM-5. But none of the alternative catalysts was comparable to ZSM-5 in terms of specific selectivity, activity, and hydrothermally stable (Fig. 10).
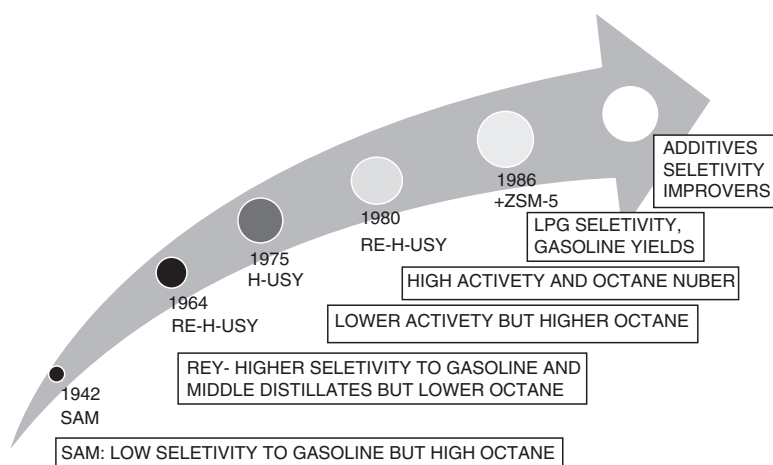
Fig. 10   The evolution of FCC catalysts [5]

Table 4 One-stage hydrocracking of vacuum gas oil over Nimo catalysts supported on MCM-41, USY, and amorphous silica-alumina (ASA) [6]

Catalyst	Conversion at 400 °C	Product distribution at 50% conversion (wt.)		
		Gases	Naphtha	Middle distillates
NiMo/MCM-41	48	16.2	25.8	58.0
NiMo/ASA	35	18.9	23.1	57.9
NiMo/USY	27	19.7	27.3	52.0

2.1.2 Zeolitic Hydrocracking Catalysts

The conventional catalysts used in hydrocracking processes are bifunctional in nature. Since the process demands simultaneous hydrogenation and dehydrogenation the refineries have focused on converting bifunctional catalysts from amorphous to zeolite-based catalysts. The various advantages of zeolite-based hydrocracking catalysts are higher activity, specific selectivity, thermal stability, resistance to poisons and impurities, and lower coking rate [23]. Recently the use of supremely dealuminated USY zeolites and NiMo/MCM-41 has allowed the zeolites to nudge the desired distillate selectivity along with better nitrogen tolerance and cycle lengths as compared with that of the conventional amorphous hydrocracking catalysts [24]. Other catalysts like NiMo- or NiW/dealuminated USY have motivated the refineries to focus on the development of moderate pressure hydrocracking due to their stability under lower hydrogen partial pressures (Table 4).

2.1.3 Fuel Hydroprocessing

Hydroprcessing focuses on distillate dewaxing to improve the flow characteristics of diesel fuel. Earlier hydroprocessing had used supported metal catalysts and bulk metal catalysts for carrying out this process, but recently this has been replaced by the use of zeolites. For instance, a zeolite catalyzed process called Mobil's Isomerization DeWaxing (MIDW) converts vacuum gas oil into diesel (<10 ppm sulfur content) having lower pour point and cloud point [7, 8].

2.1.4 Lubes Hydroprocessing

Lubricating oils are also called lubricants or "Lubes." These are used in machinery and motorized vehicles to reduce friction, heat, and wear between the mechanical components. These have two categories: (1) mineral oils obtained from naturally occurring crude oil and (2) synthetic oils manufactured artificially. In the production of mineral oils from refineries, various conventional catalysts were used but recently the refinery research and development has emphasized on the development of zeolite-based catalysts. Due to the advantageous properties of zeolites, they help in producing better lube yields and products having maintained viscosity over

elongated temperature ranges. Basically the new zeolitic catalysts are an evolutionized form of novel bifunctional shape selective catalysts. These highly engineered zeolites have been successful in replacing the conventional catalyst, i.e., ZSM-5 used in MLDW.

Zeolite catalyst advances continue to improve remarkably the critical petrochemical processes including lighter alkenes production, aromatics isomerization, and alkylation processes. In order to meet new industrial challenges, bureaucratic ordinance, and environmental concern, the development of new eco-friendly materials which can perform better and faster is being focused recently [4].

The classical definition of zeolite is "a crystalline, porous aluminosilicate built of adjacent tetrahedral metal atoms (called T atoms) surrounded by four oxygen anions to form an approximate tetrahedron."[15] Zeolites are microporous in nature. According to The International Union of Pure and Applied Chemistry (IUPAC), porous solids are categorized into following categories: microporous (pore size <2 nm), mesoporous (pore size 2–50 nm), and macroporous (pore size 50–1000 nm). Usually these T atoms are of either Si or Al. The Si/Al ratio varies 1–5 in natural zeolites. This Si/Al ratio was further worked upon and led to the synthetic zeolite formation with greater Silica content in it. The first high silica zeolite was manufactured in the 1960s, and called "Beta." The continuous quest for porous materials resulted in the formation of the all-silica zeolite in the 1970s. Likewise, the dynamic nature of zeolites attracted many researchers' interest which resulted in periodic development of the zeolites. In the 1980s, aluminophosphate molecular sieves were discovered followed by ordered mesoporous materials (OMM). However, all these forms of zeolite came with their own disadvantages and limitations. The major limitations observed with zeolites were their relatively small pore diameter and low acid strength. These limitations could not fulfil the required expectations of refineries to convert the crude oil into desired lighter fractions. Therefore, the investigation of pristine materials in having improved structure variety, morphology and composition of framework is an area to be looked upon.

2.2 Preparation of Zeolites

Zeolites are formed from a hydrogel rich with alkaline aluminosilicate under hydrothermal conditions. In this process, water acts as a reactant as well as reaction medium. The alkaline solution helps in dispersion and transportation of material from the aluminosilicate gel to growing crystals. This dissolution and transportation of aluminosilicate precursors leads to super saturation, causing nucleation in particular zones of the system (Fig. 11, Table 5).

Zeolite nucleation is a spontaneous process. There are various controlling parameters of the zeolite nucleation process, such as: gel composition, reactants purity, aging time, rate of formation of number of nuclei, crystal size, and crystallization temperature. The unit cell formula of zeolites is usually written as:
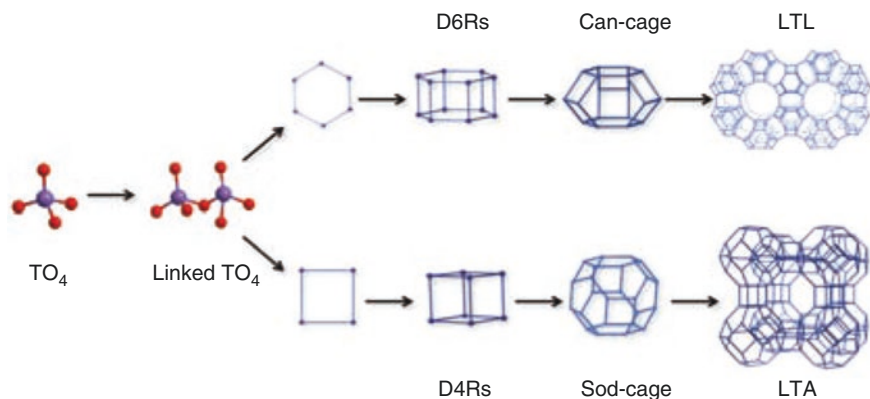
Fig. 11 Schematic representation of the formation of zeolite building units and the resultant zeolite structures [4]

Table 5 Chemical ingredients involved in the zeolite synthesis [9]

Source	Function
SiO_2	Building the primary units of the framework
AlO_2^-	Creating the negative charge
OH^-, F^-	Mineralizer
Alkali cation: Na^+, K^+	Compensating the charge while avoiding Si polymerization
Template: TPA^+, TEA^+	Directing crystallization
Water	Solvent, guest molecule

$$M_x / n \left[\left(AlO_2 \right) x \left(SiO_2 \right) y \right] \bullet z H_2O \tag{1}$$
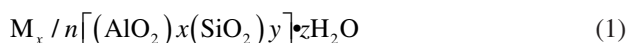
where M represents the cation (alkali or alkaline earth metal), *n* is the charge of the cation, *x, y, and z* represent the number of Al per unit cell, the number of Si, and water molecules entrapped in the channel system, respectively. Here, the cation counterbalances the negative charge correlated to framework aluminium ions.

2.3 Zeolites: Exceptional Heterogeneous Catalysts

The significant traits that make zeolites outstanding heterogeneous catalysts, molecular sieves, and ion exchangers [20] are:

- Crystalline porous structure with varying dimensions, geometry, and pore connectivity.
- Dynamic chemical composition that can be varied in any desired ratio of Si/Al ranging from 1 to infinity. In addition to their vast applications in wide-ranging

chemical processes, lately zeolites are also employed in various other applications, e.g., electronic, optical, and medical.

- Inorganic nature with robust frameworks.
- High stability at elevated temperatures and harsh chemical environments.
- Strong acid/base properties.
- Exceptional selectivity.

Although the zeolites have been considered the backbone of refineries, still they encounter various limitations and disadvantages like smaller pore size, pore volume, and specific surface area. Hence, discovery of new materials to overcome the limitations of zeolites in refineries is very much necessary.

3 MOFs: Metal Organic Frameworks

MOFs are considered as metal-organic hybrid materials imitating classical inorganic zeolites. Since both of them offer flexible synthesis processes and structural diversity, the researchers are engrossed in the development of new zeolites and MOFs. Recently the modifications and development of MOFs are comparatively targeted more due to the ease of tailoring properties for using them in the targeted applications. They differ from zeolites only by their large surface area, higher pore sizes, and higher pore-specific volumes. MOFs are synthetic materials; according to Cambridge Crystal Database, more than 50,000 structures have been reported. The pliability in preparation methods of MOFs offers greater scope of their diversification.

3.1 Structure and Nomenclature

A coordination polymer is an inorganic or organometallic polymer structure containing metal cation centers linked by ligands extending in 1, 2, or 3 dimensions. A subclass of these are the metal-organic frameworks, or MOFs, that are coordination networks with organic ligands containing potential voids [17, 21]. MOFs are hybrid crystalline porous materials in which inorganic building units are connected to organic linkers by coordination bonds of moderate strength. MOFs consist of positively charged metal ions being coordination centers, linked by a diversity of polyatomic organic linking ligands. This kind of structure of MOFs has resulted in 3D cage-like porous materials with high thermal and mechanical stability. Their nomenclature follows the similar format as that of zeolites, i.e., three letters followed by a number, e.g., MIL-47 and MOF-48. The three letters used for representing the new solid can selected accordingly:

- Briefing the geographic origin of new solid
- Kind of solid material component, e.g., MOF-n, COF-n30 (covalent organic framework), RPF-n (rare-earth polymeric framework)

- Structure type, e.g., ZMOF-n (zeolite-like metal organic framework), ZIFn (zeolitic imidazolate framework), or mesoMOF-n (mesoporous metal organic framework)
- Detailing about the group or laboratory or institute where it was synthesized

Whereas, the trailing number roughly represents the chronological order of the preparation of the porous solids in that series. The MOFs display explicit active sites (isolated metal sites), and reactive functional (inorganic or organic) groups, that enhance the feasibility of different types of reactions to occur. Therefore, they have been exclusively studied as heterogeneous catalysts. The examples are: (1) vanadium-based MOFs (MIL-47, MOF-48) are more active and extremely selective in the transformation of CH_4 and CO to acetic acid, (2) ceria-based MOFs help to catalyze water oxidation reactions and gas-phase reactions, etc. These frameworks also offer new materials with a vast degree of crystallinity, chemical nature, and porosity. The building blocks resulting in 3D-skeletons of MOFs are called secondary building units (SBU). A SBU consists of organic linkers bonded covalently to a positively charged metal center. The type and size of the SBU engaged is the dominating parameter which needs to be controlled to obtain the desired porosity with optimum openness of the framework. It is observed that larger organic linkers depress the 3D structure or reduce the porosity through *lattice self-interpenetration*, whereas the stability of MOFs is affected by various factors such as pK_a values of ligands, reduction potential, oxidation state, ionic radius of the metal ions, metal-ligand coordination structure, and its hydrophobicity [11]. However, metal-linker coordination bond is the weakest spot of MOFs. Therefore, in aqueous medium, it hydrolyzed to form a protonated linker and a de-ligated inorganic moiety. Thus, both acidic and basic solutions hasten the disintegration of MOF structures. Modulated synthesis, isoreticular expansion, and topology-governed layout are various kinds of preparation mechanisms for the synthesis of stable MOFs [10]. Thus obtained well-defined crystalline structures of MOFs are characterized by various characterization techniques such as XRD, SEM, TEM, NMR, UV-vis, and Raman spectroscopy. Recently the MOFs crystalline structures are also determined by computational chemistry [11] (Fig. 12).

3.2 Advantages of MOFs

MOFs usually exhibit a number of exceptional properties like higher thermal stability, perpetual porosity, and structural toughness which makes them very promising for future applications. In comparison with zeolites, MOFs allow a proper control of its pore size, shape, and functionalities which makes the more suitable porous materials beyond that of zeolites [18]. For example, the surface area MOF-177 and MIL-101 found to be 5640 and 5900 m^2/g, respectively. Since one of the major advantages of MOFs lies within the diversity of their designing principles which
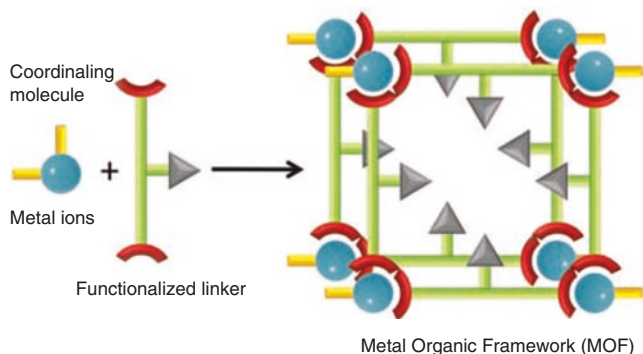
Fig. 12 Schematic representation of the formation of a MOF structure. [12]

includes the judicial selection of metal centere and ligands, a variety of new porous materials can be synthesized endlessly.

3.3 Application of MOFs

Various organic linkers and metal nodes can be combined in a number of ways in order to improve its selectivity and sensitivity toward particular applications. Potential applications of MOFs in various fields are as follows:

- Storage of energy-relevant gases (especially hydrogen)
- Gas separation
- Luminescence
- Chemical sensors
- Adsorbents
- Electrochemistry (coated on positive electrodes as corrosion inhibitors of metal surfaces)
- Biological applications (controlled delivery of drugs)

Porosity of MOFs makes them exceptional adsorbents due to the availability of higher pore volume [19]. Higher porosity of MOFs also favors them to be used as chemical sensors and adsorbents. Recently various membrane separation applications like steam separation, desalination, pervaporation, and wastewater treatment have incorporated water-stable MOFs extensively. Water-stable MOFs are also employed in taking gases under moist conditions. The liberty of tailoring the properties of MOFs to desired level makes them significant catalysts in various important reactions of chemical industries. Mostly, the MOFs are used as oxidizing catalysts with the incorporation of various transition metals like Cr, Mn, Fe, Co, Cu, and Ti into their framework. These MOFs-based oxidizing catalysts support selective oxidation reactions by functionalization of C–C bonds. This selective oxidation reaction can occur in two ways:

- *Homolytic* where oxidation occurs outside the metal coordination sphere via a radical chain mechanism
- *Heterolytic* in which activation of substrate or oxidizing reagent for the nucleophilic attack occurs by coordination to the metal clusters [13]

Recently researchers have been focusing on utilizing the exceptional separation ability of MOFs in petroleum refineries to meet the environmental and governmental policies and regulations. MOFs' tailored topology endures them to execute complex separations far more cheaply than standard oil-refining techniques. More specifically in refineries, the MOFs are used as substances that are capable of separating individual hydrocarbons from various mixtures of organic molecules produced by refining processes. This separation of components from the soup of organic molecules in an energy potent approach is the most challenging task in the petrochemical and chemical industries. Although the refineries constitute various complex operations and complex catalytic reactions, the high energy demand is restraining their advance blooming. It is observed that the separation processes solely account for approximately 40% of the total energy consumed by refineries. Therefore the discovery of using MOFs in separation processes turns out to be a quantum leap for refineries and petrochemical industries [22].

Propylene is one of the most important products obtained from the petrochemical industry. Its production is a very energy-intensive process because it includes separation of propylene from other hydrocarbons. Presently this separation is achieved by cryogenic distillation in which two gases are liquefied at sub-zero temperatures. MOFs which are porous, crystalline polymers have emerged to be a promising alternative to this high energy demanding separation process. The higher surface area and pore volume of MOFs enhances its capturing efficiency of desired molecules. This attracted the interest of researchers toward the evolution of MOFs having various pore shapes and topology and making them the prime candidates in the carbon-capture process. Thus MOFs-based membranes were developed. These are considered to be the best material for separating the molecules with greater efficiency. For example, ZIF-8 MOF allows propylene to diffuse through its pore more potently instead of propane at 30 °C [14].

3.4 Disadvantages of MOFs

There are many disadvantages with MOFs apart from their exceptional properties. The major limitations related with the MOFs are:

- Lower framework density, as low as 0.13 g cm^{-3}
- Lower stability
- Lower selectivity and acid/base properties as compared to zeolites

Due to these limitations the applications of most of the current MOFs are mainly conceptual. Also, the insufficiency of collected data from experiments performed only under ideal conditions restricts them from approving their economically successful application.

4   Conclusion

The present trend of technological and environmental challenges faced by refineries and petrochemical industries was briefly overviewed in this chapter. In order to meet the various governmental regulations and policies regarding the refining products profile, the refineries are stressed to concentrate on the development of either new technologies or improving the conventional processes by incorporating new materials. Since petroleum refining is a well-developed and mature field in itself; hence, researchers have shifted their focus on the improvement of conventional zeolites and development of new porous crystalline materials especially MOFs. MOFs are a resemblance of zeolites with few advantages over them like higher pore size, higher pore specific area, and pore volume, offering better topology and ease in modulating their surface chemistry. Irrespective of their various advantages, the MOFs failed to be suitable for industrial applications because of their limitations like stability, longevity, and higher production cost.

References

1. Gary JH, Handwerk GE, Kaiser MJ (2007) Petroleum refining: technology and economics. CRC Press, Boca Raton
2. Borole AP, Ramirez-Corredores MM (2007) Biocatalysis in oil refining. Oak Ridge National Lab. (ORNL), Oak Ridge
3. O'CONNOR P, Gerritsen LA, Pearce JR, Desai PH, Yanik S (1991) Improve resid processing. Hydrocarbon processing (International ed.), 70(11):76–84
4. Degnan TF Jr (2007) Recent progress in the development of zeolitic catalysts for the petroleum refining and petrochemical manufacturing industries. In: Studies in surface science and catalysis, vol 170. Elsevier, Amsterdam, pp 54–65
5. Blasco T, Corma A, Martínez-Triguero J (2006) Hydrothermal stabilization of ZSM-5 catalytic-cracking additives by phosphorus addition. J Catal 237(2):267–277
6. Corma A, Martínez A (2005) Zeolites in refining and petrochemistry. Stud Surf Sci Catal 157:337–366
7. Kamienski PW, Hilbert TH, Novak WJ, Lewis WE (2006) Technology for producing high quality diesel, including winter diesel. In: Central and Eastern European Refining and Petrochemicals – 9th annual roundtable, Budapest, Hungary, 17–19 Oct 2006
8. Oil and Gas Journal, January 4, (2006)
9. Odriozola JA (2010) 2. Synthesis and identification methods for zeolites and MOFs. Zeolites and Metal-Organic Frameworks 25
10. Chapman KW, Halder GJ, Chupas PJ (2009) Pressure-induced amorphization and porosity modification in a metal− organic framework. J Am Chem Soc 131(48):17546–17547

11. Bai Y, Dou Y, Xie LH, Rutledge W, Li JR, Zhou HC (2016) Zr-based metal–organic frameworks: design, synthesis, structure, and applications. Chem Soc Rev 45(8):2327–2367

12. Colón YJ, Snurr RQ (2014) High-throughput computational screening of metal–organic frameworks. Chem Soc Rev 43(16):5735–5749

13. He G, Dakhchoune M, Zhao J, Huang S, Agrawal KV (2018) Electrophoretic nuclei assembly for crystallization of high-performance membranes on unmodified supports. Adv Funct Mater 28(20):1707427

14. Cirujano FG, Nowacka A. 11. Zeolites and MOFs as catalysts in fine chemical reactions. Zeolites and Metal-Organic Frameworks 289

15. Kubička D, Kikhtyanin O (2015) Opportunities for zeolites in biomass upgrading—lessons from the refining and petrochemical industry. Catal Today 243:10–22

16. Marcilly C (2003) Present status and future trends in catalysis for refining and petrochemicals. J Catal 216(1–2):47–62

17. Mendoza-Cortes JL, Tranchemontagne DJ, Yaghi OM (2009) Secondary building units, nets and bonding in the chemistry of metal-organic frameworks. Chem Soc Rev 38:1257–1283

18. Silva P, Vilela SM, Tomé JP, Paz FAA (2015) Multifunctional metal–organic frameworks: From academia to industrial applications. Chem Soc Rev 44(19):6774–6803

19. Nair S, Gascon J, Lai ZP (2015) Special issue on metal-organic frameworks for emerging chemical technologies. Chem Eng Sci 124:1–2

20. Sousa-Aguiar EF, Arroyo PA, de Barros MASD, de Miranda JL. 12. The future of zeolite and MOF materials. Zeolites and Metal-Organic Frameworks 307

21. Bazer-Bachi D, Assié L, Lecocq V, Harbuzaru B, Falk V (2014) Towards industrial use of metal-organic framework: impact of shaping on the MOF properties. Powder Technol 255:52–59

22. Liu Y, Ban Y, Yang W (2017) Microstructural engineering and architectural design of metal–organic framework membranes. Adv Mater 29(31):1606949

23. Sie ST (1994) Past, present and future role of microporous catalysts in the petroleum industry. Stud Surf Sci Catal 85:587–631. Elsevier.

24. Komvokis V, Xin Lin Tan L, Clough M, Shaun Pan S, Yilmaz B (2016) Zeolites in fluid catalytic cracking (FCC). In: Feng-Shou Xiao FS, Meng X (eds) Zeolites in sustainable chemistry. Springer, New York, p 271

25. Furimsky E (2007) Catalysts for upgrading heavy petroleum feeds. Elsevier. Stud Surf Sci Catal 169:305

Petcoke Gasification: Challenges and Future Prospects

Jyoti Prasad Chakraborty and Rishikesh Kumar Singh

Abstract Gasification is a mature technology to convert carbonaceous materials into valuable chemicals, fuel, or power. The technology of coal gasification is well-established; however, it has some inherent drawbacks like high ash content in Indian coal, slagging, and tar formation. Biomass gasification is a promising area, though sustainable and economic supply of raw material, low calorific value, high moisture content, etc. remain challenging issues. On the other hand, there is a considerable production of petcoke from different refineries, which may be used for different purposes including gasification. Petcoke is rich in carbon; hence, it will yield high concentration of syngas (a mixture of hydrogen and carbon monoxide) in the total gaseous product. This syngas can be used to generate electricity or produce liquid fuels or chemicals. In this chapter, petcoke gasification technology and the associated issues and challenges are discussed. Some novel ideas as well as future prospects are also discussed.

Keywords Petcoke · Gasification · Fixed bed gasification · Entrained flow gasifier · Bubbling fluidized bed gasifiers · Downdraft gasifiers

1 Introduction

Gasification of hydrocarbon materials is a promising thermochemical technology where the carbonaceous material is heated at around 700–1200 °C in the presence of limited supply of air or oxygen. The product consists mainly of hydrogen and carbon monoxide, and this mixture is popularly known as syngas. There may be numerous benefits of using this syngas. The thermal energy of syngas may be utilized to produce electricity by using a turbine. Using Fischer-Tropsch synthesis, this

J. P. Chakraborty (✉)
Department of Chemical Engineering and Technology, Indian Institute of Technology (BHU), Varanasi, India
e-mail: jpc.che@iitbhu.ac.in

R. K. Singh
Department of Mechanical Engineering, Indian Institute of Technology (BHU), Varanasi, India

gas mixture may be converted to gasoline range fuels also. It may be pointed out that the technology of coal gasification is fairly matured. However, coal is slowly being discarded by many countries because of enormous emission of carbon dioxide, a greenhouse gas (GHG) during electricity production in pulverized coal-fired thermal power plants. On the other hand, petcoke is a solid residue obtained mainly from the vacuum distillation tower in a petroleum refinery. With the discovery of shale oil and new discovery of crude petroleum oil, it is logical to corroborate that there will be no supply issue of crude oil in the refinery in near future. However, development of technology for the valorization of petcoke has not matured due to various reasons. One problem is reluctance from the refiners to further process it at their location. It has been easy for them to sell it at a cheaper price to local people, who utilize petcoke for heat requirements during winter seasons and unknowingly suffer from lung infections due to the presence of sulfur in petcoke. Gasification of petcoke at an industrial scale offers many solutions like enhanced production of syngas, waste minimization, and mitigation of atmospheric pollution. Hence, if implemented, the benefits will outweigh the investment in the field of energy and environment. Moreover, there will be low emission of SO_x, NO_x, as well as low solid residue production during gasification which makes it an attractive technology to process carbonaceous materials.

2   Gasification of Carbonaceous Materials

Gasification is defined as the reaction between a carbonaceous material and air or oxygen at elevated temperatures. The amount of air or oxygen should be less than the stoichiometric amount required for complete combustion. The product is syngas as already mentioned. In the absence of oxygen, the reaction is known as pyrolysis or thermal decomposition where the product vapor is condensed and termed as bio-oil or pyrolysis oil. Other products are biochar and non-condensable gases. This bio-oil contains water and, hence, needs upgrading by catalytic hydrodeoxygenation, before it may be used as a drop-in fuel. On the other hand, air-fuel ratio more than the stoichiometric amount will allow combustion where the major product will be carbon dioxide, a greenhouse gas. Hence, the equivalence ratio, defined as the ratio of actual air-fuel ratio and stoichiometric air-fuel ratio, should vary between 0 and 1 so that gasification may occur with the formation of syngas. It is to be noted that the selection of raw material for efficient production of syngas through gasification is a very important step. Hence, the physicochemical characterization of feedstock is of utmost importance. Table 1 presents the proximate analysis of three potential raw materials for gasification, e.g., coal, biomass, and petcoke.

It is important to discuss the influence of compositions of these important carbonaceous feedstocks on the quantity and quality of products from gasification as well as the challenges associated with smooth operation of the process. A low moisture content, preferably below 10 wt% is always preferable for thermochemical operation like pyrolysis and gasification as the energy needed to raise the temperature of

Table 1 Proximate analysis (wt%)

Wt% dry basis constituent	Coal [1]	Biomass [2]	Petcoke [3]
Moisture	11.12	5.43	9.3
Volatile matter	34.99	82.12	9.6
Fixed carbon	44.19	10.96	80.6
Ash	9.70	1.49	0.5

Table 2 Elemental analysis (wt%)

Constituent	Coal [4]	Biomass [2]	Petcoke [5]
C	69.3	46.12	84.1
H	4.9	6.73	3.8
N	1.6	0.73	1.8
S	3.7	–[a]	6.5
O (by difference)	20.5	46.42	3.8

[a]Below detection limit (not a problem as most of the biomass has very low sulfur content which is a very good characteristics of biomass)

moisture is significant. Feedstock with high moisture content may be suitable for liquid phase reactions like fermentation, etc., where there is no need to remove or reduce moisture before actual operation. It has been observed that a high volatile matter generally produces liquid product (bio-oil, etc.) with higher yield. On the contrary, a high fixed carbon will give more syngas at high temperature, or enhanced formation of biochar in case of slow pyrolysis. Hence, from the above table, it may be pointed out that petcoke is a very good candidate for gasification. It is also important, besides the proximate analysis, to know the elemental composition, through ultimate or elemental analysis, so that product composition may be predicted and emission characteristics may be finalized. The ultimate analysis gives, on wt% basis, the composition of carbon, hydrogen, nitrogen, sulfur. The oxygen composition is calculated by difference. Table 2 lists the elemental composition of coal, biomass, and petcoke on wt% basis.

Higher heating value (HHV) or gross calorific value (GCV) of any combustible material is another parameter which indicates the amount of thermal energy that will be released per unit mass when the material is combusted. HHV of fuel grade petcoke is approximately 35 MJ/kg, whereas that of bituminous coal is around 27–30 MJ/kg. For biomass, it varies within 15–20 MJ/kg. Hence, it can be seen that gasification of petcoke is going to be an energetically efficient process.

3 Gasification of Petcoke

Gasification of petcoke has been carried out under different environment and reactor configurations and interesting results were obtained. Nagpal et al. [6] studied the simulation of petcoke gasification in slagging moving bed reactors. The model is

validated using experimental data obtained for a slagging gasifier. The effect of feed oxygen/coke and steam/coke ratios feed coke rates on gasification performance was carried out. High petcoke conversion was achieved and peak gas temperature exceeded 1500 °C. Besides, moving bed gasifier operation in slagging zone with high petcoke flux of over 4000 kg/m²/h was obtained. The moving bed gasifier (MBG) exhibited better performance than an entrained flow gasifier (EFG) while considering energy efficiency and oxygen consumption. Two different empirical molecular formulae were deduced for fixed carbon and volatile carbon, e.g., $CH_xS_{zs}N_{zn}$ and CH_yO_{zo}, respectively; and it worked satisfactorily for the simulation of petcoke gasification. Trommer et al. [7] used concentrated solar power for the production of hydrogen by steam-gasification of petcoke. The benefits with this process are as follows: (1) enhancement of calorific value of feedstock, (2) gaseous products are not contaminated, and (3) discharge of pollutant to the environment is avoided. Two feedstocks were used, e.g., flexicoke and delayed coke. The net process was endothermic by approximately 50% of the lower calorific value of feedstock. An equimolar mixture of H_2 and CO was produced at equilibrium, at above 1300 K. According to a second law analysis, this syngas may be converted to H_2 using water-gas shift reaction followed by H_2/CO_2 separation and then the produced H_2 may be utilized in a fuel cell for power generation, thus doubling the specific electrical output and halving CO_2 emission. Li et al. [8] studied non-isothermal thermogravimetric analysis (TGA) of petcoke gasification. The catalytic effects of $FeCl_3$, $CaCl_2$, KCl, K_2CO_3, K_2SO_4, KAC, and KNO_3 were studied. It was observed that noncatalytic gasification was inefficient below 1000 °C. The rate of gasification, however, increased rapidly upon the addition of catalyst. K_2CO_3 appeared to be a very efficient catalyst as with this catalyst, the gasification reaction was complete within 10 min and at a temperature of 900 °C. The catalytic mechanism was studied in detail by performing Raman spectroscopy and X-ray diffraction (XRD) studies of char samples collected at different conversion levels. XRD analysis suggested that the degree of graphitization decreased with K_2CO_3 addition which was favorable for char gasification. Zou et al. [9] studied gasification of petcoke in the presence of CO_2 using a pressurized TGA, at a temperature range of 1248–1323 K. It was observed that the rate of gasification increased with increasing conversion up to $x = 0.3$, then it decreased. A normal distribution function model was proposed to fit the kinetic data. The rate of reaction followed Arrhenius law. The activation energy obtained during petcoke gasification in the presence of CO_2 was 198 kJ mol⁻¹, and the reaction order was 0.54–0.88. These results were comparable with previously published data. Zou et al. [10] studied the effect of mechanochemical treatment during CO_2 gasification of petroleum coke. A mechanochemical treatment during grinding of petcoke was applied. An additive was derived by drying black liquor obtained from paper industry and it was used in the grinding process. Results showed that grinding improved gasification and wet grinding had more pronounced effect than dry grinding. When wet grinding of petcoke and additive took place together, the active metals in additive were retained in the solid phase, thereby causing a high catalytic reactivity to the coke-CO_2 reaction. It has been observed that long time mechanical grinding is usually responsible for crystalline-amorphous

phase transition. Huo et al. [11] applied TGA to study CO_2 gasification reactivity of biomass, petcoke, and coal chars. Physical structures and chemical components of various chars were examined. The reactivity of char largely depends on crystallinity. Diffusion effects were different for different chars. This was due to difference in intrinsic reactivity and physical properties of chars. Sudiro et al. [12] simulated a process which may be an alternative to conventional coal gasification. They wanted to minimize the use of pure oxygen and also to minimize carbon dioxide emission. They considered simulating an integrated gasification combined cycle (IGCC)plant for power generation. They also considered synfuel production via Fischer-Tropsch (FT) synthesis. They suggested to thermally couple a gasifier fed with coal and steam, and a combustor where coal is burnt with air, which might overcome the need to use pure oxygen, an expensive feedstock. Hence, amount of nitrogen in syngas would be minimal. Besides, the required heat in the gasifier would be supplied from the combustor by means of inert solids. A thermodynamic study of the dual-bed gasification was carried out first; then it was simulated by Aspen Plus. Finally the dual-bed system was coupled with an IGCC process. The simulation results were compared with that of an IGCC system fed with pure oxygen. The global plant efficiency increased by 27.9% and CO_2 emission decreased by 21.8%. In the next part of the study, this dual-bed was integrated with a liquid-to-coal (LTC) process to transform syngas to synthetic fuels by an FT reactor. When compared to a conventional LTC plant, the yield of synthetic fuel increased by 39.4% and energy efficiency improved by about 70%. Sudiro et al. [3] have addressed some of the problems related to modeling the dual-bed system, in their previous study [12]. They have considered both mass transfer and chemical kinetics between char particles and gas phase, to model the coal gasification reactor. The model was validated for both fluid-bed and entrained-flow gasifiers. Sensitivity analysis was performed with regard to a conventional gasifier fed by petcoke. The effect of residence time and oxygen/carbon mass ratio in the feed was studied on process variables like char conversion at gasifier exit, temperature at gasifier exit, and amount of useful syngas produced. Malekshahian and Hill [5] pyrolysis and CO_2 gasification of petcoke.

4 Reactor Configurations

Based on the geometrical configurations and flow geometry, the gasifiers can be mainly divided into three categories as fluidized bed, fixed bed, and entrained flow. However, the fluidized and fixed bed is not suitable for the gasification of petcoke due to the following reasons:

- Both types of gasifiers operate at a relatively lower temperature as compared to entrained flow gasifier which results in a lesser carbon conversion for a low reactive petcoke [13].
- Fixed bed and fluidized bed gasifiers have less efficiency, less syngas production, and lesser carbon conversion as compared to entrained flow gasifier operating on petcoke as a feed.

- While using the petcoke as a feed for the fixed bed gasifier, maintaining the permeability of the bed becomes extremely difficult [14].
- Agglomeration of ash is more prominent in both types of the gasifiers as compared to entrained flow gasifier [15].

In fixed-bed reactors the fuels move either concurrent or countercurrent to the flow of gasification medium (steam, oxygen, or air). Figure 1 represents a fixed bed gasification unit with dry bottom. The operation is not very complicated and erosion in reactor wall is minimum. Important fixed-bed designs include updraft, downdraft, and cross-draft gasifiers. Fuel and gases flow countercurrent to each other in an updraft gasifier. Petcoke is introduced at the top and air or steam is injected at the bottom. Syngas and tar are taken out at the top whereas ash gets deposited at the reactor bottom. Petcoke passes through drying, pyrolysis, reduction, and combustion zones, while experiencing gradual enhancement in temperature. The tar content in syngas is relatively high. Updraft gasifiers generally use steam as reactive agents. If the feed contains high ash, slagging may be severe.

In a downdraft gasifier as presented in Fig.2, feed enters from the top and syngas, tar, etc., are taken out at the bottom. Air or oxygen is introduced through a set of nozzles on the side of the reactor, specifically after the pyrolysis zone. Hence, products from pyrolysis are allowed further decomposition. Moisture evaporated from the feedstock acts as a reactive agent. One big advantage is that the syngas contains considerably less tar. Hence, a downdraft gasifier may be employed in various applications.

Fig. 1 Fixed-bed gasification unit with dry bottom
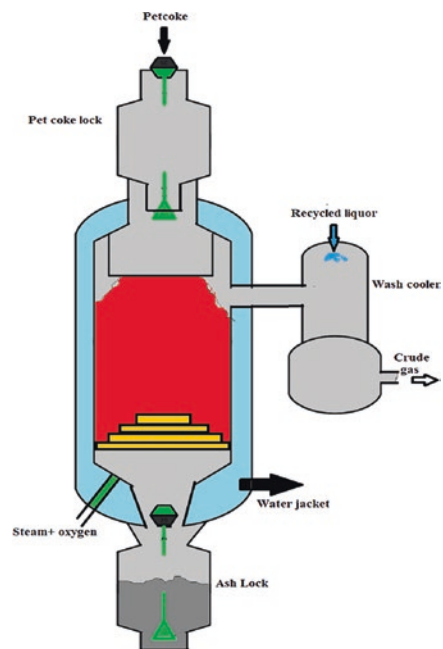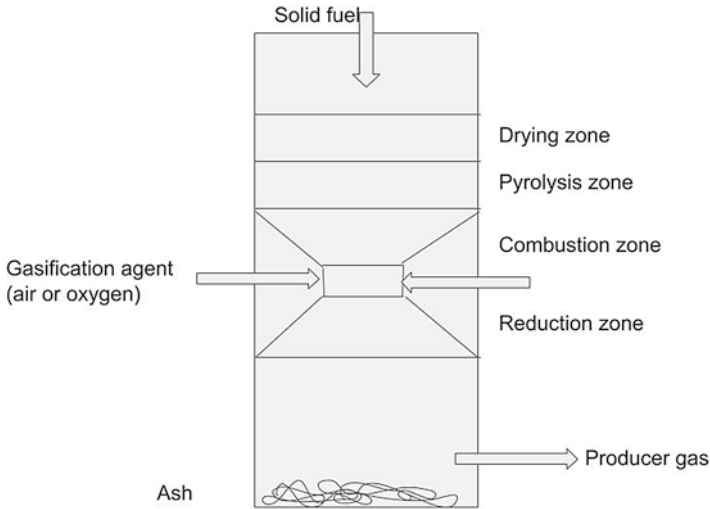
Fig. 2 A sketch of a typical fixed bed downdraft gasifier

The operating characteristics of cross-draft gasifiers are similar to downdraft gasifiers. Air or air/steam mixtures enter through the side of the reactor and syngas is drawn from the opposite side. These types of gasifiers respond rapidly to load changes. The construction is not very complicated and high-quality syngas is produced. Cross-draft gasifiers are sensitive to changes in fuel composition and moisture content.

A typical entrained flow gasifier is represented in Fig. 3. Duchesne et al. [16] used an inorganic element partitioning model to predict the performance of entrained-flow petroleum coke gasification. They concluded that for higher O/C ratio the carbon conversion increased significantly and the CO/CO_2 molar ratio of syngas was sensitive toward O/C molar ratio. However, the CO/H_2 molar ratio of syngas was sensitive toward operating temperature. The study also showed that the ash output for the petroleum coke entrained flow gasification was less as compared to that of coal feed. Zhang et al. [17] performed the statistical analysis and optimization of a entrained flow co-gasification of petcoke with coal. They studied the effect of variation of steam and oxygen concentrations syngas $(CO + H_2)$ and hydrogen production. The study revealed that with an increase in oxygen concentration the average production of hydrogen and syngas increases while for an increase in steam concentration the production of syngas and hydrogen decreases. Also, for the higher oxygen concentration fluctuation in the production of syngas and hydrogen inhibits while for higher steam concentration their fluctuation becomes significant. The optimum condition based on maximum syngas production with minimum fluctuation was obtained at 1.56% oxygen concentration with 50% steam concentration.

Rana et al. [18] performed the supercritical and subcritical water gasification of asphaltene and petcoke in a hydrothermal reactor with varying reaction times

Fig. 3 Basic features of an
entrained flow gasifier
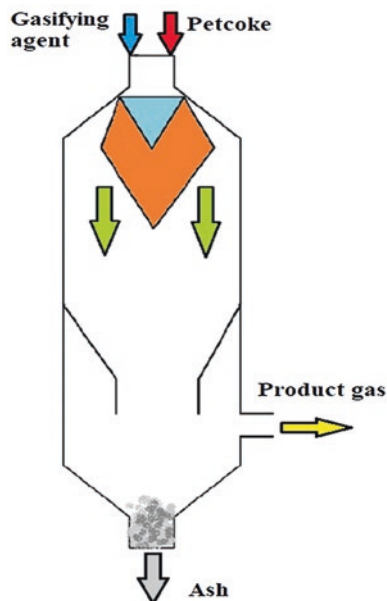
(15–60 min), operating temperatures (350–650 °C), and feed concentrations
(15–30 wt%). They also used nickel-impregnated activated carbon catalyst for the
enhancement of syngas production at the optimum condition (60 min, 650 °C and
15 wt%). The use of catalyst showed an encouraging results in the enhancement of
the syngas production for asphaltene (total syngas yield was 11.97 mmol/g) as com-
pared to that of petcoke (8.04 mmol/g of total syngas yield). The supercritical water
gasification operated at the optimum condition coupled with 5 wt% Ni/AC catalyst
had the total hydrogen yield of 2.98 mmol/g for petcoke while 4.17 mmol/g for
asphaltene. However, the catalytic gasification of petcoke and asphaltene at the
same operating condition had the yield of 1.07 and 2.54 mmol/g, respectively, for
the methane (CH_4) production. Azargohar et al. [19] studied the co-gasification of
petcoke with lignite coal in a fluidized bed reactor. They studied the effect of aver-
age particle size, feed ratio, and equivalence ratio on the production of syngas. The
central composite model (CCD) in response to surface methodology was used to
study the effect of operating parameters on the response. There was a positive syn-
ergistic effect of petcoke with lignite coal on syngas yield with carbon efficiency
reaching up to 70.2% and H_2 + CO yield being 33.2 mol/kg of feed. Improvement
in the gasification performance was observed with an increase in equivalence ratio,
and at the same time reduction in heating value of syngas was observed.

A fluidized bed gasifier has a bed consisting of inert materials like sand, char, etc.
The bed material is used to transport heat to petcoke or other feedstock being gas-
ified. Air or air/steam mixture is blown through a distributor plate at a controlled
rate. In fluidized bed there is no distinct reaction zone; hence drying, pyrolysis, and
reduction occur simultaneously. Some of the advantages of this design are: good

heat transfer characteristics, excellent gas-to-solids contact, better temperature control, high volumetric capacity, etc. They operate at pressure more than atmospheric. They are commercially viable at higher capacities, more than 30 MW, because of the need to have expensive control systems and not-so-simple design. Fluidized bed gasifiers are classified as bubbling, circulating, and spouted beds.

In a bubbling fluidized bed (BFB) gasifier as presented in Fig. 4, air or steam is fed from the bottom and maintains adequate pressure to keep feedstock particles in suspension. Air or steam flows through the bed as bubbles and ultimately burst when they reach the surface of the bed. This type of design is available as either single or dual fluidized beds. The single bed reactor involves simpler design, lower cost, and less maintenance. The energy content of syngas is lower than its counterpart from dual-bed gasifiers. In a dual-bed gasifier, inorganic materials in the feedstock may be separated. Besides, the thermal energy of pyrolysis is evenly distributed. In this design, the construction cost is high and greater maintenance is required.

In a circulating fluidized bed (CFB) gasifier, the design is like a bubbling fluidized bed; however, the solids leaving the reactor are returned through an external collection system. It achieves a better gas-solid contact and the processing capacity is also higher. The cost of a CFB increases with its height.

The third type is a spouted fluidized bed (SFB) gasifier where the bed is partly filled with coarse particles. For gas injection, there is a large opening at the bottom. When the flow rate of gas is sufficiently high, particles within the bed may be made to rise like a fountain in the center of the bed and will develop a circling motion on the bed. This design is mostly used for gasification of coal.

Fig. 4 A typical bubbling fluidized bed (BFB) gasifier
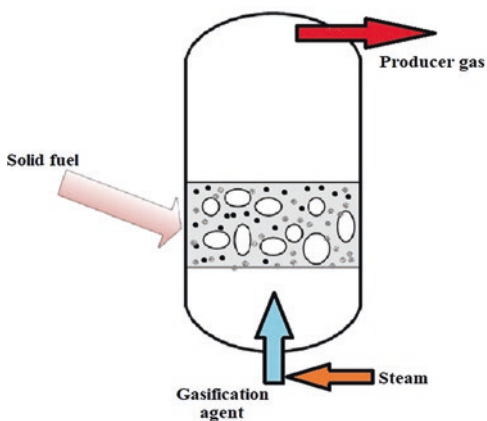
5   Kinetic Analysis

The kinetics of various carbonaceous solid fuels such as biomass, coal, and their char have been extensively studied [20–23]. However, the study of kinetics related to the gasification of petcoke has been limited due to the fact that many reaction models related to the gasification of biomass or coal are not universally acceptable in the case of petcoke gasification [14]. However, in the present section we have tried to cover few studies related to the gasification of the petcoke under various operating conditions.

Zhang et al. [14] studied the kinetics and reactivity of the petcoke steam gasification in a micro-fluidized bed. They used the homogenous model and the shrinking core model for predicting the kinetic parameters related to the petcoke gasification. The shrinking core model showed better results in establishing correlations with the experimental data as compared to the homogeneous model. The activation energy of a 10 wt% blending of black liquor with petcoke had a much lesser value of 77 kJ/mol as compared to that of only petcoke gasification (120 kJ/mol). The activation energy got further decreased to 63 kJ/mol on introducing 5% oxygen with steam suggesting that synergistic effect was present between the black liquor and oxygen. Zou et al. [9] carried out the kinetic modeling of petcoke gasification where CO_2 was used at 0.1 MPa and 1248–1323 K. The activation energy of petcoke CO_2 gasification was 198 kJ/mol with the order of reaction falling between 0.54 and 0.88 within the operated temperature range.

The study of kinetics of co-gasification of petcoke containing high sulfur and biomass (rice husk) were carried by Gajera et al. [24]. They carried out thermogravimetric analysis at three different heating rates (10, 20, and 30 °C/min) and used the TGA data in isoconversional methods such as Flynn-Wall-Ozawa (FWO) and Kissinger-Akahira-Sunose (KAS) for estimating the kinetic parameters. The activation energy for petcoke gasification were 128.3, and 126.75 kJ/mol, for FWO and KAS method, respectively, while it decreased to 87.84, and 86.85 kJ/mol, respectively, for the 1:3 ratio blending of petcoke to biomass. They also stated that during the co-gasification process the reactivity of petcoke increased significantly with presence of rice husk. Wang et al. [25] did the kinetic study of co-gasification for the petcoke and biomass char. They used the TGA data in the three different nth order gas-solid models (unreaction core model (URCM), volume reaction model (VRM), and random pore model (RPM)) to intercept the data of carbon conversion. The activation energy of bio-char (corncob) and petcoke were 243.3 and 203.2 kJ/mol, respectively, while for the co-gasification of petcoke/bio-char ratio of 4:1 was 197.8 kJ/mol.

Edreis et al. [26] studied the kinetic and the synergistic behavior the water co-gasification of petcoke with biomass. There was a significant interaction prevailing between blending ration and H_2O concentration when the value was less than 50%. They also observed only single char gasification stage above 700 °C and at 75% H_2O. The boundary reaction model used for kinetic parameter estimation of

Table 3 Summary of petcoke gasification reported in various studies

Reference	Experimental details	Conclusions
Ren et al. [27]	• Co-gasification of petcoke with coal and coal liquefaction residue • Sample placed in an open quartz reactor ($135 \times 24 \times 10$ mm) kept in a tube reactor • CO_2 was used as a gasifying medium	• Reactivity of petcoke was the leas • Synergistic effect was observed on syngas production • Significant concentration of active ca and Fe in coal and its residue led to high co-gasification reactivity
Nakano et al. [28]	• Entrained bed slagging gasifier was used • Feed consisted of petcoke, coal, or combination of both • Slag flow study	• Addition of petcoke ash to coal ash promoted crystallization in the slag • The mineral impurities which liquefy during gasification interacted with the refractory liner
Fermoso et al. [29]	• Feed as petcoke, coal, biomass or combination of any two • Fixed bed gasifier	• Blending of 10% biomass in 1:1 ratio mixture of petcoke and coal led to increase in syngas production
Shen et al. [30]	• Feed as petcoke and two types of coal • Fixed bed gasifier	• High slag formation due high ash content in bituminous coal during co-gasification with petcoke
Huo et al. [11]	• Petcoke and biomass • Fixed bed gasifier	• During co-gasification heating value of syngas increased to 5.19 MJ/m^3
Watkinson et al. [31]	• Feed as fluid coke and delayed coke from oil • Spouted bed and fluidised bed	• 85% carbon conversion at 1223 K • Producer gas concentration (vol%) was 24% CO, 34% hydrogen, 39% CO_2 and 3% H_2S
Revankar et al. [32]	• Petcoke as a feed • Tubular furnace • Catalytic and non-catalytic gasification • Kinetic analysis of gasification	• Order of reaction increased for all the cases with increase in particle size • However, variation in particle size did not have any appreciable effect on activation energy

pyrolysis and char gasification showed lowest activation energy of 33.65 and 47.15 kJ/mol, respectively, at 25% H_2O; and these values increased with the increase in petcoke and H_2O concentration. Table 3 represents a brief summary of petcoke gasification under different conditions as reported by other investigators.

6 Challenges

The main challenge with petcoke gasification is sulfur content in this raw material, as opposed to coal or biomass. There is a possibility of formation of H_2S, SO_x, etc., which need to be removed from syngas stream so that corrosion may be minimized. Another important aspect is integration of petcoke gasification system with the petroleum refinery and detailed life cycle analysis. The recommendations of these studies should be incorporated to obtain a sustainable solution.

7 Future Prospects

There is availability of huge quantities of high sulfur heavy crude throughout the world. Hence, it is imperative that there will be significant production of petcoke and it should not be wasted. Valuable products should be formed from this petcoke via gasification. Product syngas may be utilized to produce gasoline range fuels, or used to produce electricity in an IGCC system.

References

1. Shelton W, Lyons J (1998) Process Engineering Division, Texaco Gasifier IGCC Base Cases, U.S. Department of Energy (DOE) Report, July 1998: DOE report no. PED-IGCC-98-001
2. Singh RK, Sarkar A, Chakraborty JP (2019) Effect of torrefaction on the physicochemical properties of pigeon pea stalk (Cajanus cajan) and estimation of kinetic parameters. Renew Energy 138:805–819
3. Sudiro M, Zanella C, Bertucco A, Bressan L, Fontana M (2010) Dual-bed gasification of petcoke: model development and validation. Energy Fuel 24(2):1213–1221
4. Ni Q, Williams A (1995) A simulation study on the performance of an entrained-flow coal gasifier. Fuel 74(1):102–110
5. Malekshahian M, Hill JM (2011) Effect of pyrolysis and CO2 gasification pressure on the surface area and pore size distribution of petroleum coke. Energy Fuel 25(11):5250–5256
6. Nagpal S, Sarkar TK, Sen PK (2005) Simulation of petcoke gasification in slagging moving bed reactors. Fuel Process Technol 86(6):617–640
7. Trommer D, Noembrini F, Fasciana M, Rodriguez D, Morales A, Romero M et al (2005) Hydrogen production by steam-gasification of petroleum coke using concentrated solar power—I. Thermodynamic and kinetic analyses. Int J Hydrogen Energy 30(6):605–618
8. Li Y, Yang H, Hu J, Wang X, Chen H (2014) Effect of catalysts on the reactivity and structure evolution of char in petroleum coke steam gasification. Fuel 117:1174–1180
9. Zou JH, Zhou ZJ, Wang FC, Zhang W, Dai ZH, Liu HF et al (2007) Modeling reaction kinetics of petroleum coke gasification with CO2. Chem Eng Process Process Intensif 46(7):630–636
10. Zou J, Yang B, Gong K, Wu S, Zhou Z, Wang F et al (2008) Effect of mechanochemical treatment on petroleum coke–CO2 gasification. Fuel 87(6):622–627
11. Huo W, Zhou Z, Chen X, Dai Z, Yu G (2014) Study on CO2 gasification reactivity and physical characteristics of biomass, petroleum coke and coal chars. Bioresour Technol 159:143–149
12. Sudiro M, Bertucco A, Ruggeri F, Fontana M (2008) Improving process performances in coal gasification for power and synfuel production. Energy Fuel 22(6):3894–3901
13. Murthy BN, Sawarkar AN, Deshmukh NA, Mathew T, Joshi JB (2014) Petroleum coke gasification: a review. Can J Chem Eng 92(3):441–468
14. Zhang Y, Yao M, Gao S, Sun G, Xu G (2015) Reactivity and kinetics for steam gasification of petroleum coke blended with black liquor in a micro fluidized bed. Appl Energy 160:820–828
15. Alibrahim HA, SeedAhmed S, Ahmed U, Zahid U (2019) Comparative analysis of gasification and reforming technologies for the syngas production. In: Kiss AA, Zondervan E, Lakerveld R, Özkan L (eds) Computer aided chemical engineering. Elsevier, Amsterdam, pp 1759–1764
16. Duchesne MA, Champagne S, Hughes RW (2017) Dry petroleum coke gasification in a pilot-scale entrained-flow gasifier and inorganic element partitioning model. Energy Fuel 31(7):6658–6669
17. Zhang J, Hou J, Feng Z, Zeng Q, Song Q, Guan S et al (2020) Robust modeling, analysis and optimization of entrained flow co-gasification of petcoke with coal using combined array design. Int J Hydrogen Energy 45(1):294–308

18. Rana R, Nanda S, Maclennan A, Hu Y, Kozinski JA, Dalai AK (2019) Comparative evaluation for catalytic gasification of petroleum coke and asphaltene in subcritical and supercritical water. J Energy Chem 31:107–118
19. Azargohar R, Gerspacher R, Dalai AK, Peng D-Y (2015) Co-gasification of petroleum coke with lignite coal using fluidized bed gasifier. Fuel Process Technol 134:310–316
20. Gomez A, Mahinpey N (2015) A new model to estimate CO2 coal gasification kinetics based only on parent coal characterization properties. Appl Energy 137:126–133
21. Cortazar M, Lopez G, Alvarez J, Arregi A, Amutio M, Bilbao J et al (2020) Experimental study and modeling of biomass char gasification kinetics in a novel thermogravimetric flow reactor. Chem Eng J 396:125200
22. Irfan MF, Usman MR, Kusakabe K (2011) Coal gasification in CO2 atmosphere and its kinetics since 1948: a brief review. Energy 36(1):12–40
23. Singh RK, Sarkar A, Chakraborty JP (2020) Effect of torrefaction on the physicochemical properties of eucalyptus derived biofuels: estimation of kinetic parameters and optimizing torrefaction using response surface methodology (RSM). Energy 198:117369
24. Gajera ZR, Verma K, Tekade SP, Sawarkar AN (2020) Kinetics of co-gasification of rice husk biomass and high sulphur petroleum coke with oxygen as gasifying medium via TGA. Bioresour Technol Rep 11:100479
25. Wang G, Zhang J, Zhang G, Ning X, Li X, Liu Z et al (2017) Experimental and kinetic studies on co-gasification of petroleum coke and biomass char blends. Energy 131:27–40
26. Edreis EMA, Luo G, Li A, Xu C, Yao H (2014) Synergistic effects and kinetics thermal behaviour of petroleum coke/biomass blends during H2O co-gasification. Energy Convers Manag 79:355–366
27. Ren L, Wei R, Zhu T (2020) Co-gasification reactivity of petroleum coke with coal and coal liquefaction residue. J Energy Inst 93(1):436–441
28. Nakano J, Sridhar S, Moss T, Bennett J, Kwong K-S (2009) Crystallization of synthetic coal−petcoke slag mixtures simulating those encountered in entrained bed slagging gasifiers. Energy Fuel 23(10):4723–4733
29. Fermoso J, Arias B, Plaza MG, Pevida C, Rubiera F, Pis JJ et al (2009) High-pressure co-gasification of coal with biomass and petroleum coke. Fuel Process Technol 90(7):926–932
30. Shen C-H, Chen W-H, Hsu H-W, Sheu J-Y, Hsieh T-H (2012) Co-gasification performance of coal and petroleum coke blends in a pilot-scale pressurized entrained-flow gasifier. Int J Energy Res 36(4):499–508
31. Watkinson AP, Cheng G, Fung DPC (1989) Gasification of oil sand coke. Fuel 68(1):4–10
32. Revankar VVS, Gokarn AN, Doraiswamy LK (1987) Studies in catalytic steam gasification of petroleum coke with special reference to the effect of particle size. Ind Eng Chem Res 26(5):1018–1025

Steam Reforming Catalysts for Membrane Reformer

Rajesh Kumar Upadhyay

Abstract Hydrogen can be used as a clean energy carrier to generate power for both stationary and mobile applications when integrated with the PEM fuel cell. However, the high-purity hydrogen requirement of PEM fuel cell and safety hazard in hydrogen storage and transportation limit the use of the technology. Membrane reformers have the potential to solve these challenges. Generally, alcohols are used as a feed to the membrane reformer, considering their safe storage and easy transportation. However, the membrane reformers are still in the development stage and require numerous systematic studies on different components involved in it to standardize its performance before it can be commercialized. One of the critical components of the membrane reformer is the catalyst used for the steam reforming of alcohol, which is used as a feed to the reformer. In this chapter, different catalysts used for steam reforming of methanol, ethanol, and glycerol are discussed. The advantages and disadvantages of each catalyst concerning their use in membrane reformer are presented. Finally, a broad summary is given regarding the qualities of the catalyst, which are needed for successful integration with high hydrogen-selective membranes in a single unit called membrane reformer.

Keywords Steam reforming · Membrane reformer · PEMFC · Hydrogen generation · Dry reforming · Reforming catalysts

1 Introduction

The continuing rise in energy demands directs the current power scenario of the country, with contributions of coal 55%, hydro 20%, renewables 11%, gas 10%, nuclear 3%, and diesel 1% [1]. This 11% renewable has emerged as one of the major advancements in recent years. In order to narrow the gap between demand and supply of energy, conservation and efficient utilization of resources have been given huge

R. K. Upadhyay (✉)
Department of Chemical Engineering and Technology, Indian Institute of Technology (BHU), Varanasi, Uttar Pradesh, India
e-mail: rku.che@iitbhu.ac.in

recognition. "Hydrogen" yet leads to be a driving force toward a potential replacement to fossil fuels, complemented with high energy content and also as a clean-efficient energy carrier [1]. It can be utilized as a power source (feed) to proton exchange membrane fuel cells (PEMFC), to meet most of the necessary energy needs for the stationary power, automobiles, industrial, and residential sectors. Compared to the conventional internal combustion engine, other benefits of hydrogen utilization in PEMFCs are low noise, no formation of particulate matter, and no NO_x and SO_x emission. Hence, the use of hydrogen as an energy career helps in providing a clean environment that greatly impacts human life and health. However, the "holy grail" of hydrogen usage as an energy carrier lies in its storage and transportation. Traditionally stored in compressed cylinders or as a liquid in cryogenic containers, hydrogen poses a safety threat due to its low volumetric density. Besides, it is highly challenging to compress hydrogen gas from 5000 to 10,000 psi which is required for liquefying it [2]. Hydrogen combustion though does not release any carbon dioxide; but it brings high capital costs, low energy content per unit volume, elevated storage vessel weights, and high storage pressures. To abate these, on-board/on-site generation of hydrogen using lightweight, high energy density alcohols seems to provide a feasible solution to storage problems as well as effective utilization of these alcohols. Negligible dependence on any fossil fuel, these alcohols can be easily produced using any biological matter usually known as fermented wastes "molasses" from sugarcane, corn, wheat straw, etc. The problem with these biofuels is its heavy content of sulfur and other impurities that need to be processed before being used for hydrogen generation. It should be noted that along with increasing hydrogen generation with higher hydrocarbons, the amount of carbon formation also increases in the same proportion. It can also be pointed out that amongst the processes used for hydrogen generation, steam reforming is affected by its strong endothermic nature and its by-product formation [3], while cracking, on the other hand, is highly expensive with the standard by-product distribution as in the case of steam reforming. Coking also forms the bases of unalterable damage to the process and system, thereby causing difficulty to sustain the system as well as auxiliaries such as fuel cells it is connected with. But with all its pros and cons, steam reforming yet remains the only process that can provide high hydrogen yield [3–5]. However, as PEMFC required ultra-pure hydrogen (purity greater than 99.999%) and CO content less than 1 ppm, separation of hydrogen from reformate gases is inevitable.

Separation of hydrogen from the reformate mixture underlines the root of any process in terms of efficiency, yield, and thereby applicability. Talking of higher yield, adsorption-based techniques such as pressure swing adsorption and temperature swing adsorption are widely applied on an industrial scale but show a varying selectivity chart. Besides, it is a highly expensive and bulky process to be handled for on-board applications. Membrane separation nonetheless shows higher selectivity corresponding to the membrane and operating conditions applied. To be precise, dense (non-porous) membranes are the ones with enhanced selectivity to hydrogen over increasing pressure gradients [4–8]. Therefore, balanced synchrony of operating conditions with the catalyst for reforming and membranes for separation purposes is of utmost importance.

Many companies like Daimler AG, General Motors, Hyundai are either already launched their PEMFC-based car or planning to launch it soon. PEMFC is conceptually only an electrochemical device that takes in oxygen and hydrogen which then reacts to produce electric power and water vapor. Although, few companies have come up with a solution to remove water vapor from the system by continuing to run the cell's exhaust for a minute or two but storing gaseous hydrogen on-board persists to be a problem. For liquid hydrogen, the case is even more complex since it would have to be stored at -253 °C in a carefully insulated tank which would increase the weight, design complexity, and expense. Hence, the only solution to the defined issues can hereby be suggested using an on-board ultra-pure hydrogen generator with integrated reforming and separation units.

Membrane reformers are being popular from the last two decades to use as a device to produce the ultra-pure hydrogen for on-site/on-board applications [3–11]. However, it is still far from commercialization due to its low hydrogen recovery. The low hydrogen recovery is mainly caused because of inappropriate integration of hydrogen production catalysts with membrane separation units (dense palladium-based membranes). For better integration with the membranes used in membrane reformer, one needs to modify the traditional steam reforming process to fulfill the requirement of membrane separation unit [6, 12]. Similarly, the membrane separation unit also needs to be modified to accommodate the requirements of the steam reforming reaction.

2 Membrane Reformer

A membrane reformer is a process-intensified reactor in which generation and separation of hydrogen take place in a single unit. Generally, a membrane reformer is comprised of a reforming catalyst for hydrogen generation and palladium-based membranes for selective separation of hydrogen. A typical schematic of membrane reformer is shown in Fig. 1. Continuous transfer of hydrogen moves the equilibrium toward the forward direction which ultimately results in increased conversion as per the Le Chatelier's principle. Hence, through the membrane reformer, thermodynamic limits can be modified and higher hydrogen yield can be obtained [9–12]. This is the major advantage of membrane reformer over the traditional reformer. Further, membrane reformer does not require traditional hydrogen separation units like pressure swing adsorption, cryogenic distillation, etc. Hence, it is very compact and ideal for the production of fuel cell grade ultra-pure hydrogen for on-site/on-board applications [10–13]. However, the contrary requirement of steam reforming reaction and membrane separation makes the integration of these two processes in a single unit more challenging [9, 12]. Steam reforming being an endothermic reaction requires high temperature and low pressure while for high hydrogen recovery membrane requires high pressure and low temperature. There are certain other challenges too which need to be overcome for the successful operation of membrane reformer. These are as follows: (1) production of thin dense membranes having high
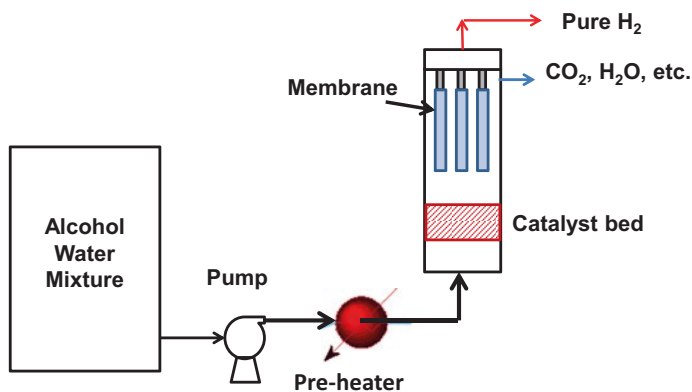
Fig. 1 Schematic of membrane reformer

hydrogen perm selectivities and high hydrogen flux, (2) synthesis of the highly active reforming catalyst with low CO selectivity even at high temperatures, (3) low-temperature reforming catalysts for better integration of membrane reformer with PEMFC, and (4) optimal arrangements of membrane and catalysts inside the membrane reformer to achieve the desired performance. However, even after two decades, most of these challenges are still unresolved and one needs to revisit and modify all these steps for the commercialization of the membrane reformer. In this book chapter, the focus is on required modification in traditional steam reforming catalysts used for steam reforming of alcohols for their application in membrane reformer.

3   Hydrogen Generation

Until the beginning of the renewable revolution, hydrogen has been typically recovered from gas streams where hydrogen presence is more such as gas streams at refineries, petrochemicals plants, and ammonia plants. Normally, energy carriers are not sources. They are produced from a primary energy source (feedstock) using a technology. Hydrogen is a carrier; and its generation is usually accomplished using natural gas, gasoline, methane, methanol, ethanol, and glycerol as feedstock, by processes such as steam reforming, dry reforming, auto-thermal reforming, electrolysis, partial oxidation, cracking, etc. These processes are carried out in their respective operating conditions, depending on their stoichiometry to produce H_2 accompanied with by-products such as CO, CO_2, O_2, C_2H_4, or CH_3CHO, etc. [14]. Electrolysis dates back to the late 1920s when water as feedstock was first electrolyzed to produce hydrogen industrially; later water was replaced with fossil-based feed. This process does not much have commercial impact due to the high electricity consumption (4.5–5 kW/m³H_2) [15] hindering its cost-effectiveness and carbon formation in this process too continues to create a hazard. The reaction of primary fuel with a quantity of oxygen inadequate for the fuel complete oxidation is referred

to as partial oxidation [16]. With waste heat generation, this process is inefficient. Steam reforming combined with oxidation where oxidation reaction provides the energy required for steam reforming, this process is referred to as auto thermal reforming. However, by reacting to a hydrocarbon with a mixture of steam and oxygen/air, careful control of oxygen content is essential to maintain the proper reacting temperatures [16] which may be challenging for on-board applications. Dry (CO_2) reforming results in the formation of either syngas (CO and H_2) or carbon nanofilaments which is a marketable product as "reinforcing fillers" [17]. However, such products can hamper the performance as well as the life of the membrane. Hence, it is not suitable for membrane reformer. In comparison to all these processes, steam reforming is an established technology known for efficient hydrogen generation [3, 18–20].

Steam reforming reactions are endothermic which proceed under increased volume and therefore require high temperature and low pressure for maximum feed conversion. On the other hand, water-gas shift reaction is an exothermic reaction that proceeds simultaneously with most of the alcohol's steam reforming and with no volume change as stated in reaction (1) [20]:

$$CO + H_2O \leftrightarrow CO_2 + H_2, \Delta H_{298K} = -41 \text{ kJ/mol} \tag{1}$$

$$CH_3OH \leftrightarrow CO + 2H_2, \Delta H_{298K} = 90 \text{ kJ/mol} \tag{2}$$

$$CH_3OH + H_2O \leftrightarrow CO_2 + 3H_2, \Delta H_{298K} = 49 \text{ kJ/mol} \tag{3}$$

$$C_2H_5OH \leftrightarrow CO + CH_4 + H_2, \Delta H_{298K} = 33 \text{ kJ/mol} \tag{4}$$

$$C_2H_5OH + H_2O \leftrightarrow 2CO + 4H_2, \Delta H_{298K} = 256 \text{ kJ/mol} \tag{5}$$

$$C_2H_5OH + 3H_2O \rightarrow 2CO_2 + 6H_2, \Delta H_{298K}^0 = 174 \text{ kJ/mol} \tag{6}$$

$$C_3H_8O_3 + H_2O \rightarrow 3CO + 4H_2 \tag{7}$$

$$C_3H_8O_3(g) + 3H_2O \rightarrow 7H_2(g) + 3CO_2 \tag{8}$$

3.1 Partial Oxidation

$$CH_3OH + 1/2O_2 \leftrightarrow 3H_2 + CO_2, \Delta H_{298K} = 49.4 \text{ kJ/mol} \tag{9}$$

3.2 Oxidative SR

$$CH_3OH + (1-p)H_2O + 0.5pO_2 \leftrightarrow (3-p)H_2 + CO_2, \Delta H_{298K}$$
$$= -241.8p + 49.5 \text{ kJ/mol} \tag{10}$$

3.3 Dry Reforming

$$CH_4 + CO_2 \leftrightarrow 2H_2 + 2CO; \Delta H_{298K} = 247.3 \text{ kJ / mol} \qquad (11)$$
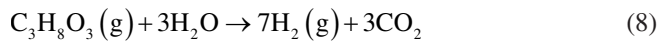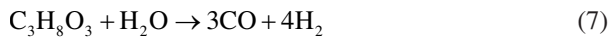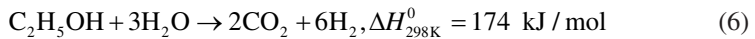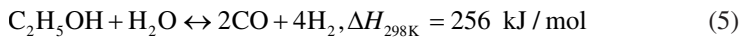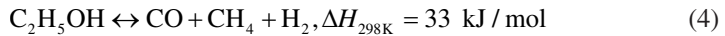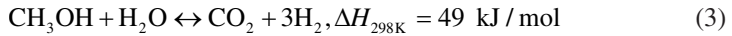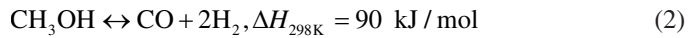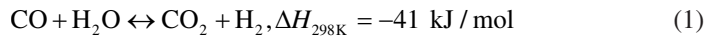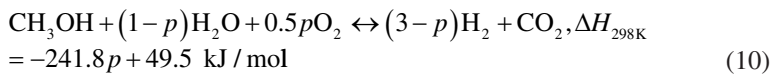
Reactions (2) and (3) state methanol decomposition and methanol steam reforming. This is followed by ethanol decomposition and steam reforming in reactions (4) and (5). The desirable ethanol steam reforming reaction is considered with ethanol: water ratio as 1:3 as presented in reaction (6). Similarly, glycerol steam reforming general reactions are presented by reactions (7) and (8). In these entire reactions, one thing that is prominently observed is the case of hydrocarbons decomposition which will only lead to carbon formation. So, concerning this, excess water is added to remove CO in the form of CO_2 and H_2 by a known mechanism called the "water-gas shift" reaction. Hydrogen generation also includes processes such as partial oxidation (reaction 9), oxidative steam reforming (reaction 10), dry reforming (reaction 11), and steam reforming (reactions 3, 5, 6, and 7). However, steam reforming remains to be the most economic and efficient (maximum H_2 generation up to 75%) [18] mode for a wide range of hydrocarbon feedstocks, e.g., methanol, ethanol, and glycerol. Partial oxidation (reaction 9) is an exothermic reaction revealing rapid start and response times, which makes it suitable for compact reactor design. However, it suffers from the likelihood of the formation of hot spots making it difficult to control the reaction and low H_2 yield [17]. Oxidative or auto-thermal reforming is the simultaneous performing of partial oxidation and steam reforming. It is energetically efficient (adiabatic) and fast process; but this process is also affected by coking. Coking is a function of temperature. Therefore, its formation increases with progressing temperature and contact time [18]. Hence, steam reforming is preferred over all other processes for on-board/on-site generation of hydrogen.

Based on the application, one type of alcohol may dominate over the other, but the steam reforming process for all the alcohols undergoes several simultaneous reactions depending on the operating conditions (temperature, and pressure) and the catalyst used. The reactions mentioned above are just typical reactions that may follow several parallel or series reactions and a differing product distribution based on the operating conditions, active metals, nature of the support, and metal loading. All these affect the performance of MR. Therefore, for MR application a highly selective and efficient catalyst is vital.

4 Reforming Catalysts and Supports for Ethanol, Methanol, and Glycerol

The catalyst's role in augmenting H_2 generation has been studied in depth over the centuries. Its domain includes noble active metal catalysts like Ir, Au, Ru, Pd, Pt, and Rh; non-noble metal catalysts like Cu, Ni and Co; oxide catalysts such as Al_2O_3, MgO, ZnO, CeO_2, V_2O_5, TiO_2, La_2O_3, Sm_2O_3, and mixed oxide catalysts like La_2O_3-Al_2O_3,

CeO_2-Al_2O_3, MgO-Al_2O_3, etc. Here, the oxide catalysts mentioned are majorly used as supports. Supports are thermally more stable and provide high surface area. The metal particles are doped over the support to achieve high mechanical and thermal strength; however, it comes at the cost of reduced metal dispersion and stability. Therefore, the functionality of the catalyst also depends on the interaction mechanism between the metal and the support [21]. Various supports are proposed by researchers depending on their respective properties. For example, Frusteri et al. [22] postulated that CeO_2 or MgO supports should not help the coke formation by ethylene production as dehydrogenation to acetaldehyde or dehydration to ethylene occurs depending on the nature of support. It was also reported that if support has a high basic sites, and high electronic polarizability, it favors dehydrogenation over dehydration.

A few significant features of these supports can be mentioned as the following:

(a) Υ-Al_2O_3 has a high surface area and is widely used due to its thermal and mechanical stability. However, the acidic property of Υ-Al_2O_3 favors dehydration of alcohol to alkene which acts as a precursor to form coke on the catalyst surface. This is completely undesirable and is more harmful to membrane reformer as coke can be deposited on the membranes. This can affect the performance and life of the membrane and hence the overall efficiency of the membrane reformer. To attenuate coking on the catalyst surface incorporation of various alkali metals such as K, Li Ca, and Na is reported [23]. These basic sites not only act to eliminate acidity but also favors the carbon oxidation and reduction in coke deposition by enhancing water adsorption and –OH mobility on the surface [24].

(b) Elias et al. [25] reported an increase in H_2 selectivity for *ethanol steam reforming* with increasing Ca content which leads to decreasing alkenes (like C_2H_4) selectivity and thereby coking. Ca also enhances the stability of the catalysts against the oxidation process. However, the decrease in acidity was more prominent for impregnation-based catalysts.

(c) MgO, ZnO, and CeO_2 too have basic properties that minimize the coke formation on the surface of the catalyst and hence preferred for membrane reformer applications. Llorca et al. [26] proposed that increasing the basicity of the system might also increase the selectivity of acetaldehyde for ethanol steam reforming. Amongst the supports mentioned above, ZnO was reported to be one of the best oxide supports for the Co-based catalyst used for ethanol steam reforming.

(d) The size of cerium oxide crystallites plays a determinant role in increasing the interaction with the noble metals. It promotes CO oxidation and water gas shift (WGS) reaction and promotes the stability of the catalyst due to its higher reducibility and oxygen storage-release capacity [17]. Addition of zirconium enhances the redox property and oxygen adsorption capacity of the CeO_2 [27]. Srinivas et al. [28] have reported that even after several successive cycles of reduction and re-oxidation, the mixed oxides of ceria-zirconia was thermally stable. Such catalysts are preferred; however, the re-oxidation step in the case of membrane reformer is quite challenging.

(e) Y_2O_3 and La_2O_3 have weak acidic and basic properties and exhibit long-term stability to the process.

Along with supports, the preparation method also affects the catalyst performance based on the difference in surface area. The two widely applied techniques for catalyst preparation include co-precipitation and impregnation [29]. Co-precipitation provides high metal dispersion with high attainable metal loading up to 60–80%, because of which catalysts prepared by this method are also termed as bulk catalysts. However, this process creates a lot of problems with its supersaturation conditions above which the product is to be separated from the large quantities of waste salt generation. Impregnation, on the other hand, is a widely applied process not only on a lab scale but also industrially. In impregnation, liquid phase gets adsorbed on the solid phase. However, the contacting of liquid and solid phase is critical to achieve uniform metal dispersion. Dry incipient wetness refers to the impregnation of the previously dried support with a solution containing a precursor of the active phase, i.e., $V=V_{pore}$. The solution gets sucked in the pores by capillary action and no excess solution is left in case of the proper wetness, henceforth called dry or incipient wetness [30].

Either prepared by impregnation or co-precipitation, the specific surface area values for co-precipitation are proposed to be higher than impregnation due to thermal treatment which releases the gases because of the decomposition of the precursor and provides high catalyst porosity [25]. Besides, co-precipitation is a fast precipitation process occurring in super-saturation conditions. Faster nucleation than crystal growth results in an amorphous precipitate with a large disorder prompting a higher surface area. However, reduced acidity of the system was reported for the catalysts synthesized through impregnation method. Active metals, be it noble or non-noble, are normally chosen based on the reaction as well as the basic inherent property it must possess for H_2 generation. These properties comprise C–C bond cleavage, its stability, and activity in the desired reaction conditions, and its resistance to coke, generated during the reaction [21]. Ni shows high selectivity to hydrogen generation. The low cost of Ni and has high C–C bond cleavage activity makes it more attractive. Haryanto et al. [23] compared $Ni/\Upsilon\text{-}Al_2O_3$, Ni/La_2O_3, $Ni/La_2O_3\text{-}Al_2O_3$, Ni/MgO, and found $La_2O_3\text{-}Al_2O_3$ as the best support. Sun et al. [31] proposed that "La" promotes dehydrogenation of alcohols, thereby reducing the formation of alkenes. The order of H_2 selectivity and activity of Ni by Sun et al. [31] was reported as $Ni/La_2O_3 > Ni/Y_2O_3 > Ni/Al_2O_3$ for ethanol steam reforming. Rh and Co-based catalysts are also proposed to be promising in terms of activity and selectivity. Likewise, Pt, Ni, $NiPt/Al_2O_3$ were examined by Sanchez et al. [24] and suggested the reaction pathway over these catalysts by ethanol dehydrogenation and subsequent acetaldehyde decomposition. A complete conversion during 45 h on stream was also reported by Cai et al. [32] using Ir/Ce700 with 59% H_2, 19% CO_2, 17%CO, and 5%CH_4 selectivity. Cavallaro and Freni [33] illustrated the occurrence of intermediates such as acetic acid, ethyl acetate, and acetaldehyde below 325 °C when selectivity of H_2 and CO_2 is very low at 1 atm pressure; water: ethanol 6:1 & 10:1 using catalysts $CuO/ZnO/Al_2O_3$, $NiO/CuO/SiO_2$, Pt/Al_2O_3, etc. It was also identified that selectivity toward H_2, CO, and CO_2 increases with an increase in temperature and that all catalysts shift the system toward equilibrium above 360 °C [34]. Aupretre et al. [35] tested a wide range of active metals (Rh, Pt, Pd, Ru, Ni, Cu,

Zn, Fe) and oxide support (Al_2O_3, 12% CeO_2-Al_2O_3, CeO_2, CeO_2-ZrO_2, ZrO_2) combinations and found Rh, Ni giving the best performance with CeO_2-ZrO_2 support for ethanol steam reforming. They also reported that the degree of mobility of surface OH-groups with ceria-based supports directly affects the steam reforming activity.

Noble metal–based catalysts are believed to be stable catalysts as they are recognized for breaking the C–C bond which results in less carbonaceous deposits. The activity of noble metal catalysts to get a reduction in the C–C bond is of the following order Rh > Co > Ni > Pd [33]. In various oxides supported metal catalysts studied in the literature, Breen et al. [36] proposed that Al_2O_3-supported catalysts promote dehydration of ethanol to ethylene while for CeO_2/ZrO_2-supported catalysts no formation of ethylene was observed. Also the combination of CeO_2/ZrO_2-supported catalysts with alumina will inhibit ethylene, thereby coking in high temperatures. Ru-catalyzed ethanol steam reforming studied in the range of 600–850 °C and found that 5% Ru was comparable to the performance of rhodium with a marked increase in conversion and selectivity to H_2. For low-temperature steam reforming (300–450 °C) Panagiotopoulou et al. [37] found that catalytic performance for better selectivity to H_2 is varied in the order of Pt > Pd > Rh > Ru. The effect of CeO_2, ZrO_2, and Al_2O_3 support conducted on Pt catalyst in the range of 350–450 °C showed the highest performance of Pt/ZrO_2 followed by Pt/Al_2O_3 and lastly Pt/CeO_2 for better selectivity to H_2. Compared with other literature it was also reported that WGS reaction for Pt-supported catalysts occurs with high rates at temperatures above 350 °C. Apart from this, the selectivity of acetaldehyde at 320 °C was reported to decrease in the order ZrO_2 > CeO_2 > Al_2O_3, while the selectivity of CO was affected in the manner CeO_2 > Al_2O_3 > ZrO_2. This unexpected behavior compared to alumina was attributed by low specific surface area which thereby affects reducibility and hence WGS activity [37]. Most of these catalysts tested for ethanol steam reforming are high-temperature catalysts. These catalysts reported low hydrogen yield at a temperature of less than 350 °C. This makes the integration of these catalysts with membrane followed by PEMFC (which operates at around 60–100 °C) very challenging. Further, the CO selectivity is also high at the higher temperature. Hence, a low-temperature catalyst is needed.

The transition metal (member of the group 8–10) is used as a catalyst for *methanol steam reforming*. These metals have multiple oxidation states and can provide a lower activation energy path which makes them attractive and enhances their catalytic active. Similar to ethanol reforming, noble metal catalysts show adequate reforming activity for methanol too for a wide temperature range. However, their high cost limits their use particularly for large-scale implementation. Pd and Ru are considered as active catalysts amongst the noble metal for the methanol steam reforming. However, both show high CO selectivity [38, 39] due to the increased methanol decomposition which is not suitable for membrane reformer application [39]. Cu, Ni, Au, Fe are also used as a non-precious metal catalyst for methanol steam reforming. Among them, copper is a highly abundant low-cost metal which is used for both methanol synthesis and methanol steam reforming. It is mainly preferred because of its high activity at a lower temperature. Further, it can catalyze both oxidation-reduction reactions and shows high hydrogen selectivity. The

addition of zinc on the Cu-Al$_2$O$_3$ catalyst reduces the metal size and increases the metal dispersion [40, 41]. This increases the Cu catalyst activity, hence preferred over the Ni-based catalyst [40]. The addition of ZrO$_2$ on Cu/Zn/Al$_2$O$_3$ catalyst reduces the CO yield [40, 42] which is desirable for membrane reformer application. To reduce the CO selectivity, other supports such as CeO$_2$ [43], ZnO-Al$_2$O$_3$ / CeO$_2$-ZnO [39, 41, 43], ZrO$_2$ [44], and MgO [45] are also studied extensively. As stated earlier it is important to understand the interaction between the impregnated metal and support to determine complete functionality of any catalyst. The physio-chemical property of the combined support and metal significantly affects the surface reaction. It either modifies the electrical property of the metal or promotes the intermediate formation. In Cu and Ni monometallic catalysts with different support, CO formation is observed in the range of 3–18%. The same was around 25–35% for Pd- and Ru-based catalyst supported on Alumina, zirconia, or ceria support. However, Pd supported on In$_2$O$_3$, ZnO, and Ga$_2$O$_3$ shows less than 5% CO selectivity [39]. The alloy formation was mainly responsible for such a vast change in CO selectivity.

Recently, Bimetallic catalysts have gained more attention for methanol steam reforming. Due to the formation of alloy, the bimetallic catalyst shows diverse electrical and chemical properties in comparison to their base metals. Based on the metal properties, temperature, support, and oxidative or reductive environment different structure of bimetallic catalysts can be observed. Mostly hetero-atom and nano-alloys structures are reported in the literature [40] which shows the distinct property. It is reported that the addition of Cu in Ni-based catalysts can reduce the coking and metal sintering [42]. The addition of Fe in Ni-CeO$_2$ catalyst is also studied and found that the addition of Fe reduces the CO formation. Recently, Sharma et al. [46] have shown that the addition of Fe to Cu on Alumina-zinc-zirconia support shows no CO till 400 °C temperature at atmospheric pressure. Such a catalyst is quite suitable for the membrane reformer application. However, the life and performance of such catalyst at high pressure need to be rigorously tested.

The metal-supported catalyst normally used for *glycerol steam reforming* includes Ir [47], Ru [48], Pt [49], Ni [50], and Pd [51]. Zhang et al. [47] obtained the complete conversion of glycerol at 400 °C using Ir/CeO$_2$ with 85% H$_2$ selectivity, while selectivity with Co/CeO$_2$ and Ni/CeO$_2$ were observed 88% and 75% at 425 and 450 °C respectively. They have also verified the presence of a small amount of CH$_4$ at the outlet. For each catalyst, maximum hydrogen selectivity was obtained at the highest temperature of 550 °C. Dave and Pant [52] reported H$_2$ yield 3.7–3.9 with increasing temperatures from 600 to 700 °C by steam reforming at 82% and 100% conversion, respectively, using Ni/CeO$_2$ and Ni-ZrO$_2$/CeO$_2$. Adhikari et al. [53] synthesized the Ni-based catalyst on different supports: MgO, CeO$_2$, and TiO$_2$. They have studied the effect of support on hydrogen selectivity at 600 °C and WGFR of 9. The order for H$_2$ selectivity was observed as follows: CeO$_2$ (70%) > 4MgO (40%) > 4TiO$_2$ (15%). Chiodo et al. [54] compared the performance of Rh- and Ni-based catalyst supported on γ-alumina. It was found that the Rh-based catalyst was more active compared to the Ni-based catalyst. However, for both the catalysts (Rh/Al$_2$O$_3$ and Ni/Al$_2$O$_3$) coke formation was observed at all the

temperature. The thermal decomposition of glycerol to olefins was mainly responsible for the coking which severely affects the performance and is not suitable for membrane reformer application.

Similar to ethanol, for glycerol too hydrogen yield at low temperature is very low. Hence, for better integration, it is desirable to develop a low-temperature catalyst that can provide acceptable hydrogen flux for membrane reformer application.

5 Summary and Future Aspects

The focus of this chapter was mainly on providing an overview of the development of membrane reformer concerning reforming catalyst for ethanol, methanol, and glycerol steam reforming. The membrane reformer has the potential to be commercialized for on-board/on-site production of ultra-pure hydrogen. It can provide clean energy when integrated with PEMFC and can reduce the dependency on fossil fuel. However, the major challenge in commercializing the membrane reformer is its low hydrogen recovery. This is linked to the performance of membrane used for selective hydrogen separation, the catalyst which is used for hydrogen generation, and the way these two are integrated into a single assembly. Hence, it is required to improve all these aspects to make on-board/on-site generation of hydrogen through MR a reality. Here, I have discussed the reforming catalysts for different alcohols which compete with each other based on application. The chapter highlights the different catalysts used or tested for ethanol, methanol, and glycerol steam reforming and their suitability for membrane reformer application. Though several catalysts are available for ethanol steam reforming, mostly ceria-supported catalysts are preferred as they provide low CO selectivity. Ni, Co along with some noble metal like Ru, Rh are preferred as they reduce the coking. However, all these catalysts provide high conversion and high hydrogen production at a higher temperature (>450 °C). Therefore, their integration with the membrane is challenging as such a temperature membrane may develop the leaks at the joints (particularly the ceramic supported membranes). Further, in the case of methanol steam reforming various support and metal combinations are tested. AZZ support and Cu metal are found to be suitable. However, they provide high CO content. A recent study shows that Cu-Fe supported on AZZ supports provide No CO till 450 °C which looks promising. However, the performance and life of this catalyst under high pressure needs to be tested. Further, this catalyst also provides a high hydrogen production rate only above 300 °C. Similarly, for glycerol steam reforming Ni-based catalysts (which have high C–C bond cleavage) supported on alumina or ceria-zirconia support are preferred. However, these catalysts also performed well at a higher temperature and both CO and CH_4 contents are observed in the reformate which is not desirable. Therefore, most of the available catalysts are not suitable for the membrane reformer application. Hence, there is an urgent need to develop a low temperature and high hydrogen-selective catalyst to achieve the desired performance from the membrane reformer.

References

1. Gera RK, Rai HM, Parvej Y, Soni H (2013) Renewable energy scenario in India: opportunities and challenges. Indian J Electr Biomed Eng 1:10–16
2. Gandia ML, Arzamendi G, Dieguez PM (2013) Renewable hydrogen technologies production, purification, storage, application and safety. Elsevier, Amsterdam
3. Gallucci F, Basile A, Tosti S, Iulianelli A, Drioli E (2007) Methanol and ethanol steam reforming in membrane reactors: an experimental study. Int J Hydrogen Energy 32:1201–1210
4. Basille A, Gallucci F (2011) Membranes for membrane reactors: preparation, optimization and selection. Wiley, Chichester
5. Basile A, Iulianelli A, Tong J (2015) Membrane reactors for the conversion of methanol and ethanol to hydrogen. In: Membrane reactors for energy applications and basic chemical production. Woodhead Publishing, Swaston, pp 187–208
6. Sharma R (2018) Production of high purity hydrogen through methanol based membrane reformer. PhD thesis, IIT Guwahati, India
7. Yun S, Oyama ST (2011) Correlations in palladium membranes for hydrogen separation: a review. J Membr Sci 375:28–45
8. Buxbaum R, Lei H (2003) Power output and load following in a fuel cell fueled by membrane reactor hydrogen. J Power Sources 123:43–47
9. Sharma R, Kumar A, Upadhyay RK (2017) Performance comparison of methanol steam reforming integrated to Pd-Ag membrane: membrane reformer vs. membrane separator. Sep Purif Technol 183:194–203
10. Tosti S, Basile A, Bettinali L, Borgognoni F, Gallucci F, Rizzello C (2008) Design and process study of Pd membrane reactors. Int J Hydrogen Energy 33:5098–5105
11. Tosti S, Basile A, Chiappetta G, Rizzello C, Violante V (2003) Pd–Ag membrane reactors for water gas shift reaction. Chem Eng J 93:23–30
12. Sharma R, Kumar A, Upadhyay RK (2018) Characteristic of a multi-pass membrane separator for hydrogen separation through self-supported Pd Ag membranes. Int J Hydrogen Energy 43:5019–5032
13. Marra L, Wolbers PF, Gallucci F, Annaland MVS (2014) Development of a $RhZrO_2$ catalyst for a low temperature autothermal reforming of methane in membrane reactors. Catal Today 236:23–33
14. Hasan AM (2003) Effect of ethanol–unleaded gasoline blends on engine performance and exhaust emission. Energy Conver Manag 44:1547–1561
15. Stojic LD, Marceta MP, Sovilj SP, Miljanic SS (2003) Hydrogen generation from water electrolysis-possibilities of energy saving. J Power Sources 118:315–319
16. Brown FL (2001) A comparative study of fuels for on-board hydrogen production for fuel cell powered automobiles. Int J Hydrogen Energy 26:361–397
17. de Lima MS, Silva AM, da Costa L, Graham UM, Jacobs G, Davis BH, Mattos LV, Noronha FB (2009) Study of catalyst deactivation and reaction mechanism of steam reforming, partial oxidation, and oxidative steam reforming of ethanol over $CO/Ce0_2$ catalyst. J Catal 268:268–281
18. Patel S, Pant KK (2007) Hydrogen production by oxidative steam reforming of methanol using ceria promoted copper–alumina catalysts. Fuel Process Technol 88:825–832
19. Moura SJ, Souza MOG, Bellido JDA, Opportus EMAM, Reyes P, do Carmo Rangel M (2011) Ethanol steam reforming over rhodium and cobalt-based catalysts: effect of the support. Int J Hydrogen Energy 37:3213–3224
20. Gallucci F, de Falco M, Tosti S, Marrelli L, Basille A (2008) Ethanol steam reforming in a dense Pd-Ag membrane reactor: a modeling work. comparison with traditional system. Int J Hydrogen Energy 33:644–651
21. Vaidya DP, Rodrigues AE (2006) Insight into steam reforming of ethanol to produce hydrogen for fuel cells. Chem Eng J 117:39–49

22. Frusteri F, Freni S, Chiodo V, Donato S, Bonura G, Cavallaro S (2006) Steam and auto-thermal reforming of bio-ethanol over MgO and CeO_2 Ni supported catalysts. Int J Hydrogen Energy 31:2193–2199
23. Haryanto A, Fernando S, Murali N, Adhikari S (2005) Current status of hydrogen production techniques by steam reforming of ethanol: a review. Energy Fuel 19:2098–2106
24. Sanchez SMC, Navarro RM, Fierro JLG (2007) Ethanol steam reforming over Ni/M_xO_y-Al_2O_3 (M=Ce, La, Zr and Mg) catalysts: influence of support on the hydrogen production. Int J Hydrogen Energy 32:1462–1471
25. Elias MFK, Lucredio AF, Assaf EM (2013) Effect of CaO addition on acid properties of NieCa/Al_2O_3 catalysts applied to ethanol steam reforming. Int J Hydrogen Energy 38:4407–4417
26. Llorca J, Homs N, Sales J, Piscina PR (2002) Efficient production of hydrogen over supported cobalt catalysts from ethanol steam reforming. J Catal 209:306–317
27. Martinez ML, Araquea TM, Vargas JC, Roger AC (2013) Effect of Ce/Zr ratio in CeZr-Co-Rh catalysts on the hydrogen production by glycerol steam reforming. Appl Catal Environ 132:499–510
28. Srinivas D, Satyanarayana CVV, Potdar HS, Ratnaswamy P (2003) Structural studies on NiO-CeO_2-ZrO_2 catalysts for steam reforming of ethanol. Appl Catal A Gen 246:323–334
29. Ayman MK, Su Y, Sun J, Yang C, Strohm JJ, King YWDL (2010) A comparative study between Co and Rh for steam reforming of ethanol. Appl Catal Environ 96:441–448
30. Jong DPK (2009) Synthesis of solid catalysts. Wiley-VCH, Hoboken
31. Sun J, Qiu XP, Wu F, Zhu WT (2005) Hydrogen from steam reforming of ethanol at low temperature over Ni/Y_2O_3, Ni/La_2O_3 and Ni/Al_2O_3 catalysts for fuel-cell application. Int J Hydrogen Energy 30:437–445
32. Cai W, de la Piscina PR, Gabrowska K, Homs N (2013) Hydrogen production from oxidative steam reforming of bio-butanol over CoIr-based catalysts: Effect of the support. Bioresour Technol 128:467–471
33. Cavallaro S, Freni S (1996) Ethanol steam reforming in a molten carbonate fuel cell. A preliminary kinetic investigation. Int J Hydrogen Energy 21:465–469
34. Montane D, Bolshak E, Abello S (2011) Thermodynamic analysis of fuel processors based on catalytic-wall reactors and membrane systems for ethanol steam reforming. Chem Eng J 175:519–533
35. Aupretre F, Descorme C, Duprez D (2002) Bio-ethanol catalytic steam reforming over supported metal catalysts. Catal Commun 3:263–267
36. Breen PJ, Burch R, Coleman HM (2002) Metal-catalysed steam reforming of ethanol in the production of hydrogen for fuel cell applications. Appl Catal Environ 39:65–74
37. Panagiotopoulou P, Verykios XE (2012) Mechanistic aspects of the low temperature steam reforming of ethanol over supported Pt catalysts. Int J Hydrogen Energy 14:1–13
38. Umile T (2015) Catalysts and sustainability. In: Catalysis for sustainability. CRC Press, Boca Raton, pp 1–22
39. Iwasa N, Takezawa N (2003) New supported Pd and Pt alloy catalysts for steam reforming and dehydrogenation of methanol. Top Catal 22:215–224
40. Dal Santo V, Gallo A, Naldoni A, Guidotti M, Psaro R (2012) Bimetallic heterogeneous catalysts for hydrogen production. Catal Today 197:190–205
41. Yang M, Li S, Chen G (2011) High-temperature steam reforming of methanol over ZnO–Al2O3 catalysts. Appl Catal Environ 101:409–416
42. De Rogatis L, Montini T, Lorenzut B, Fornasiero P (2008) NixCuy/Al2O3 based catalysts for hydrogen production. Energ Environ Sci 1:501–509
43. Hu S, He L, Wang Y, Su S, Jiang L, Chen Q, Liu Q, Chi H, Xiang J, Sun L (2016) Effects of oxygen species from Fe addition on promoting steam reforming of toluene over Fe–Ni/Al2O3 catalysts. Int J Hydrogen Energy 41:17967–17975
44. Patel S, Pant KK (2006) Influence of preparation method on performance of Cu(Zn)(Zr)-alumina catalysts for the hydrogen production via steam reforming of methanol. J Porous Mater 13:373–378

45. Agrell J, Birgersson H, Boutonnet M, Melián-Cabrera I, Navarro RM, Fierro JLG (2003) Production of hydrogen from methanol over cu/ZnO catalysts promoted by ZrO2 and Al2O3. J Catal 219:389–403
46. Sharma R, Kumar A, Upadhyay RK (2019) Bimetallic Fe-promoted catalyst for CO-free hydrogen production in high-temperature-methanol steam reforming. ChemCatChem 11:4568–4580
47. Zhang B, Tang X, Li Y, Xu Y, Shen W (2007) Hydrogen production from steam reforming of ethanol and glycerol over ceria-supported metal catalysts. Int J Hydrogen Energy 32:2367–2373
48. Hirai T, Ikenaga N, Miyake T, Suzuki T (2005) Production of hydrogen by steam reforming of glycerin on ruthenium catalyst. Energy Fuel 19:1761–1762
49. Menezes AO, Rodrigues MT, Zimmaro A, Borges LEP, Fraga MA (2011) Production of renewable hydrogen from aqueous-phase reforming of glycerol over Pt catalysts supported on different oxides. Renew Energy 36:595–599
50. Nichele V, Signoretto M, Menegazzo F, Gallo A, Santo GCVD, Cerrato G (2012) Glycerol steam reforming for hydrogen production: design of Ni supported catalysts. Appl Catal Environ 111:225–232
51. Huber GW, Shabaker WJ, Dumesic AJ (2003) Raney Ni-Sn catalyst for H_2 production from biomass derived hydrocarbons. Science 300:2075–2077
52. Dave DC, Pant KK (2011) Renewable hydrogen generation by steam reforming of glycerol over zirconia promoted ceria supported catalyst. Renew Energy 36:3195–3202
53. Adhikari SD, Fernando SD, Filip To SD, Bricka RM, Steele PH, Haryanto A (2008) Conversion of glycerol to hydrogen via a steam reforming process over nickel catalysts. Energy Fuel 22:1220–1226
54. Chiodo V, Freni S, Galvagno A, Mondello N, Frusteri F (2010) Catalytic features of Rh and Ni supported catalysts in the steam reforming of glycerol to produce hydrogen. Appl Catal A Gen 38:1–7

Fischer-Tropsch Synthesis in Silicon and 3D Printed Stainless Steel Microchannel Microreactors

Nafeezuddin Mohammad, Omar M. Basha, Sujoy Bepari, Richard Y. Abrokwah, Vishwanath Deshmane, Lijun Wang, Shyam Aravamudhan, and Debasish Kuila

Abstract In recent years, environmental challenges have led to a focus on the production of clean synthetic fuels from different carbon sources using Fischer-Tropsch (FT) synthesis. Catalyst development and reactor improvements are the major points of interest to obtain high selectivity toward desired hydrocarbons in FT synthesis. The first part of this chapter summarizes the fundamentals of FT synthesis, catalysts, and possible reaction mechanisms, the drawbacks of present synthesis reactors, and how microchannel microreactor (specified as microreactor in this chapter) technology addresses them with its unique characteristics. Two case studies are presented to describe catalyst screening for FT synthesis in two types of microreactors: Silicon (Si) microreactors are fabricated using conventional microfabrication techniques with dimensions 1.6 cm × 50 μm × 100 μm. Stainless steel (SS) 3D printed microreactors of dimensions 2.4 cm × 500 μm × 500 μm are fabricated by direct metal laser sintering method. The FT studies with Si and SS microreactors coated with different catalysts/supports and temperature-programmed reduction (TPR) experiments with H_2 not only provide insight into metal-support interactions but also catalyst performance in terms of kinetics, selectivity, CO con-

N. Mohammad · S. Aravamudhan
Department of Nanoengineering, Joint School of Nanoscience and Nanoengineering, North Carolina A&T State University, Greensboro, NC, USA

O. M. Basha · L. Wang
Department of Chemical, Biological and Bioengineering, North Carolina A&T State University, Greensboro, NC, USA

S. Bepari · R. Y. Abrokwah · V. Deshmane
Department of Chemistry, North Carolina A&T State University, Greensboro, NC, USA

D. Kuila (✉)
Department of Nanoengineering, Joint School of Nanoscience and Nanoengineering, North Carolina A&T State University, Greensboro, NC, USA

Department of Chemistry, North Carolina A&T State University, Greensboro, NC, USA
e-mail: dkuila@ncat.edu

version, and stability. Conversion of syngas enriched with CO_2 and CO_2 utilization in FT synthesis are the key factors in the production of next-generation biofuels. A case study on the effect of silica and alumina promoters on Co-Fe-K precipitated catalysts in a lab-scale reactor to enhance CO_2 utilization in FT synthesis is also included.

Keywords Fischer-Tropsch synthesis · Syngas conversion · Microreactors fabrication · Microchannel reactors · Microreactor 3D printing

1   Introduction

1.1   *Fischer-Tropsch Synthesis*

Fischer-Tropsch (FT) synthesis enables the conversion of carbon-containing resources, such as coal, biomass, and natural gas into value-added chemicals and fuels. In this process, syngas, which is a mixture of CO and H_2, catalytically reacts to generate primarily linear alkanes and alkenes. Significant details discussing the FT process and economics have been discussed extensively elsewhere [1, 2]. The overall FT process involves three major steps: (1) conversion of hydrocarbon containing resource to generate syngas, (2) syngas conversion into hydrocarbons via the FT process, and (3) upgrading of the generated hydrocarbons to the final products. Figure 1 provides a schematic overview of the process.

Syngas generation is achieved by coal/biomass gasification, steam reforming, CO_2 reforming, or partial oxidation of CH_4 as shown in Eqs. (1)–(3) [3]. The choice of technology depends on the nature of the feedstock, in addition to process and economic parameters, and has been discussed extensively elsewhere [4, 5]:
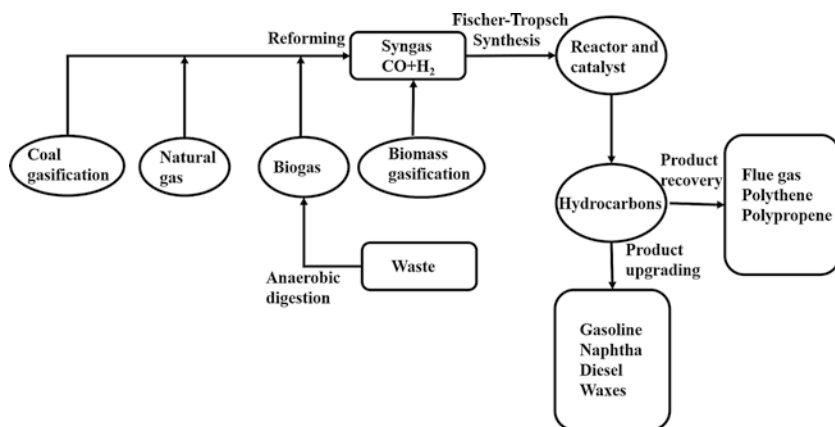
Fig. 1 Overall Fischer-Tropsch process schematic

$$\text{Steam reforming} \quad CH_4 + H_2O \leftrightarrow CO + 3H_2 \tag{1}$$

$$\text{CO}_2 \text{ reforming} \quad CH_4 + CO_2 \leftrightarrow 2CO + 2H_2 \tag{2}$$

$$\text{Partial oxidation} \quad CH_4 + 0.5O_2 \leftrightarrow CO + 2H_2 \tag{3}$$

$$\text{Coal gasification} \quad C + H_2O \leftrightarrow CO + H_2 \tag{4}$$
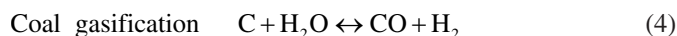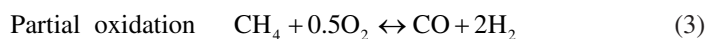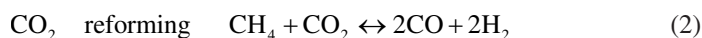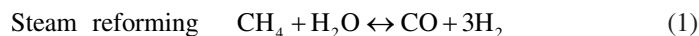
The generated syngas is then passed on to the FT synthesis reactor in which alkanes, alkenes, and alcohols are formed, as shown in Eqs. (5)–(7); and they are highly exothermic. The reaction rates and product compositions are determined by the H_2:CO ratio of the syngas, the catalyst type, in addition to the operating temperature and pressure:

$$\text{Formation of alkanes} \quad (2n+1)H_2 + nCO \rightarrow C_nH_{2n+2} + nH_2O \tag{5}$$

$$\text{Formation of alkenes} \quad (2n)H_2 + nCO \rightarrow C_nH_{2n} + nH_2O \tag{6}$$

$$\text{Formation of alcohols} \quad 2nH_2 + nCO \rightarrow C_nH_{2n+2}O + (n-1)H_2O \tag{7}$$
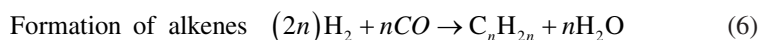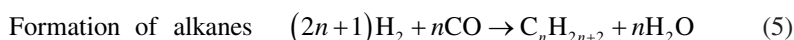
The water gas shift (WGS) reaction, where CO reacts with steam to generate CO_2 and H_2 as shown in Eq. (8), commonly occurs in the presence of a catalyst during FT synthesis. It is typically used to adjust the H_2/CO ratio in the syngas for some FT plant configurations by introducing a Nickel catalyst [6, 7]:

$$\text{Water gas shift (WGS) reaction} \quad CO + H_2O \leftrightarrow CO_2 + H_2 \tag{8}$$
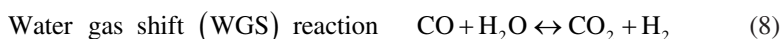
Another common FT side reaction is the Boudouard reaction, in which CO decomposes into carbon dioxide and graphite, as shown in Eq. (9). It leads to the strong chemisorbed coke deposition on the active sites of a catalyst and hinders the catalytic reaction. This is also termed as catalyst poisoning as it deactivates the catalyst during the FT synthesis:

$$\text{Boudouard reaction} \quad 2CO \rightarrow C + CO_2 \tag{9}$$
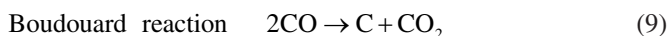
1.2 FT Reaction Mechanisms

The choice of catalyst dictates the mechanisms or reaction pathways governing the Fischer-Tropsch synthesis. It is a surface polymerization reaction to form longer hydrocarbons which typically involves: (1) adsorption of gases on the catalyst, (2) chain initiation by CO dissociation and hydrogenation, (3) chain growth by CO insertion and hydrogenation, (4) chain growth termination, and (5) desorption of hydrocarbon products from the catalyst surface [8]. The three major mechanisms, namely, the carbide mechanism, the CO insertion mechanism, and the hydroxy carbene mechanism [3], are summarized below.

- **Carbide Mechanism:** This mechanism initiates FT reaction by the adsorption of carbon monoxide gas on the surface of the active metal catalyst that results in the formation a metal carbide on the catalyst surface. This chemisorbed carbon monoxide, a C–O bond bridged between metal carbide nodes on the catalyst surface, dissociates into C and O species. In the next step, hydrogen molecules (H–H) dissociate to form H atoms which are used in the hydrogenation of the carbide groups to produce the first C_1 intermediate methyl species (–CH_2–). The methyl species can react with hydrogen atoms to form methane gas or act as alkyl chain extenders (monomeric units) to form the final product. The formation of this intermediate removes oxygen in the form of water and has been assumed to be the suitable mechanism for oxygen removal since the FT synthesis was first demonstrated.
- **CO-Insertion Mechanism:** In this mechanism, a second carbon monoxide molecule inserts between the metal and initially chemisorbed carbon monoxide molecule, i.e., metal-alkyl bond. This step is the key process in forming C–C intermediate which then undergoes hydrogenation and polymerization to form an alkyl chain. This mechanism mostly explains FT synthesis carried out by iron and ruthenium-based catalysts.
- **Hydroxy-Carbene Mechanism:** As the name implies, this mechanism proceeds via a hydroxy carbene (CHOH) intermediate formed during the chain growth process in the reaction. The first chemisorbed CO on the metal will undergo a hydrogenation reaction to form the hydroxy carbene intermediate. Condensation of two intermediates removes oxygen as water in the coupling reaction to form a C–C bond. The surface oxidation of this intermediate propagates chain growth in the reaction. The chain growth termination of this reaction pathway consequently produces mostly oxygenated hydrocarbons such as aldehydes, ketones, ethers, and alcohols.

1.2.1 Adsorption Mechanisms in FT Reaction Kinetics

It is worth noting that different mechanisms have been proposed to predict the possible routes by which the FT reaction could proceed. The desired product selectivity and optimal reactor design require an in-depth understanding of reaction kinetics. However, an understanding of the kinetics of this complex reaction system is fairly difficult, and not much kinetic studies for FT synthesis in microreactors have been reported. The kinetic performance evaluation of the catalyst requires rate expression models that account for the consumption of reactants considering product distribution in the reaction system. The Anderson-Schulz-Flory (ASF) model, which is based on the statistical distribution of the FT products, as governed by the chain growth probability, is typically used to predict the product distribution of the FT reaction. These kinetic models are usually developed by collecting extensive experimentation data by varying conditions like space velocity, temperature, pressure, reactant flowrates, type of catalyst, syngas molar ratio with eliminating heat and mass transfer losses. All the kinetic models based on the chain propagation and

chain termination reactions are presumed to proceed by a solid-surface phenomenon, whereby reactant gases are adsorbed onto the catalyst surface to initiate the reaction. The section below gives a very brief understanding of the adsorption of reactants, i.e., CO, H_2, or both which initiates the FT synthesis [9, 10].

- **H_2 Adsorption:** Most of the supported transition metal catalysts are able to dissociate the molecular hydrogen to more reactive hydrogen atoms on the catalyst surface [10, 11]. This enhances the quick adsorption of hydrogen onto the catalyst surface (S) forming a metal surface-hydrogen (H-S) intermediate/complex as shown below. This is more favored when the metal catalyst is in its pure form (zero oxidation state). However, all the FT synthesis reactions are carried out with unsupported bulk metal or metal oxides immobilized on suitable supports. Derivation of the kinetic rate equations of hydrogen adsorption depends on the type of catalyst, support reaction conditions, and the rate of CO adsorption on the catalyst surface [9].

$$H_2 + 2S \leftrightarrow 2H \cdot S \tag{10}$$

- **CO Adsorption:** CO is adsorbed more strongly than H_2 on transition metals [12, 13], and the type of the adsorption (associative or dissociative) on the catalyst active site is governed by the temperature range and the surface properties of the catalyst used for the FT synthesis.

The adsorption of CO occurs by both associative adsorption on free active catalyst site and dissociative surface interaction between the CO and catalyst active site. This is the most common type of mechanistic consideration while developing kinetic models for the FT synthesis. The equations below show the associative (11) and dissociative (12) schemes of the adsorption mechanism for the CO on the catalyst with support having active sites in the reaction:

$$CO + S \leftrightarrow CO \cdot S \tag{11}$$

$$CO \cdot S \leftrightarrow C \cdot S + O \cdot S \tag{12}$$
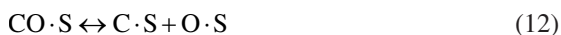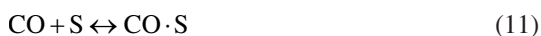
2   Microreactor Technology for FT Synthesis

Recently, more attention has been focused on finding pathways and methods to reduce the physical dimensions of unit operations, such as separators and reactors, which are typically referred to as process modularization or process intensification. Reducing the physical dimensions allows for substantial increases in transport rates, which can be leveraged to significantly reduce overall plant capital cost [14], enhance reliability and response to market and feed fluctuations, facilitate plant deployability, reduce the overall footprint, enable more robust control, [15] and simplify scale-up [16].

Milli- and micro-scale reactors have been a focal interest in process modularization, as they allow better control of the reaction and product distribution by enhancing transport, increasing residence time, and mixing for continuous reactions and allow for inherently safe operations [17, 18]. The fundamental advantage of microreactors is the significant enhancement of heat and mass transfer rates per unit volume when compared to traditional chemical reactors. Typically, microreactor has a minimum feature size in the range of 50–500 μm, which enhances heat transfer coefficients by orders of magnitude, up to 25 kW/m^2 K [19]. Such reactors are typically designed to include parallel arrays of vertical channels that are packed or coated with a catalyst, and cross-flow horizontal cooling channels, which enables the significant reduction of the overall reactor volume and an increase in the overall productivity [20].

From a commercial perspective, a major motivation for utilizing micro-reactor technology for FT synthesis is that it enables the utilization of smaller point sources, without significant commercial or operational risk. The conventional FT technology requires about 50 MMSCF/d of the feed gas over a 30-year period in order to achieve the minimal acceptable production capacity of 50,000 barrels per day, in order to lower the capital cost per barrel to an acceptable level [21].

2.1 Microreactor Fabrication Methods and Materials

Microreactors are typically fabricated using conventional techniques in micro−/nanotechnology and precision engineering. The internal structure of the microreactor, such as channels (referred to as reaction zone), has characteristic dimensions ranging from sub-millimeter to micrometer range. These internal microstructures are constructed hierarchically, usually parallel channels in an array system (reaction or mixing zone) containing an inlet and an outlet. In this chapter, we use the term "microreactor" for all the devices where the characteristic dimension will be in the range of nanometers-sub-micrometer to sub-millimeter.

The design and configuration of microreactors are based on its applications. Structural hierarchy varies based on the type of reactor and unit operation, in addition to the operation mode (continuous flow or batch type processes). Some of the microdevices investigated, previously, are micromixers [22, 23], microreactors [24, 25], micro heat exchangers [26, 27], micro separators [28], and microturbines [29]. The main focus of this chapter is the application of microreactors for FTS.

Microreactors can be fabricated using a variety of materials, the most common of which are silicon, glass, polymer, and metals (316 stainless steel). The selection of the materials depends on the intended application, reaction type, operating conditions, the physical and chemical properties of reactants, reaction complexity, and cost. Table 1 highlights the advantages and disadvantages of common fabrication materials for microreactor applications.

The limitations of polymer and glass materials make them unsuitable to fabricate microreactors for high-temperature and high-pressure reaction systems. The section

Table 1 Advantages and disadvantages of different materials for microreactor fabrication

Material	Advantages	Disadvantages	Dimensions
Silicon	− Production of complex and 3-dimensional microchannel network − Good mechanical strength and temperature control − Good heat and mass transfer − Good chemical compatibility	− Large fabrication infrastructure − Brittle nature of silicon leads to difficult sealing especially for gas-phase high-pressure reactions	Nanometer to sub-micrometer
Polymer	− Easy to manufacture − Low-cost production − Disposable devices for biocompatible reactions	− Limited chemical compatibility − Poor thermal stability	Typically sub-micrometer range
Glass	− Good thermal stability − Favorable for photochemical reactions − Reactions are visible due to reactor transparency − Offers highest chemical compatibility	− Large infrastructure to fabricate dimensions in the nanometer range − Leak tight connections for very high-temperature applications	Nanometer to sub-micrometer
Stainless steel	− No need for large infrastructure (cleanroom) − Easy to design and fabricate, for example, 3D printing technique − Favorable for high-pressure and temperature reaction systems − Good sealing capability for high-pressure gas-phase reactions	− Feature size less than 500 μm is challenging to fabricate − Limited applications	Typically few hundreds of micrometers to sub-millimeter

below explains the fabrication of silicon and 3D printed stainless steel microreactors used for our research to screen catalysts for FT synthesis.

2.2 Fabrication of Silicon Microreactor

The fabrication process of a Si-microreactor has been discussed extensively elsewhere [30, 31]. To fabricate a microdevice on a silicon wafer, a photomask needs to be designed. A photomask is an opaque chromium plate with clear features called transparencies that let light (UV-light) pass through to transfer the pattern onto the photoresist layer. This is generally termed as photolithography. Figure 2 shows two
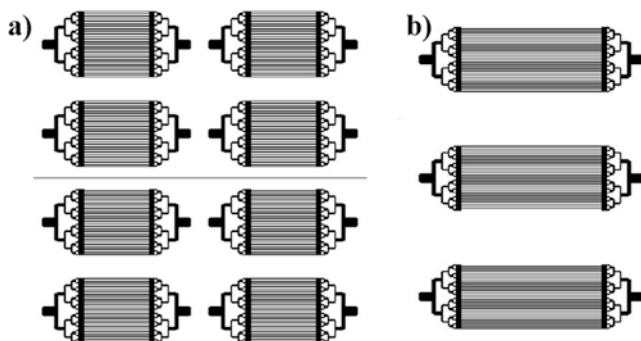
Fig. 2 Types of microreactor design on a 4-in. ch wafer

types of photomasks, Fig. 2a shows the eight microreactor devices that are designed in AutoCAD, and Fig. 2b shows three microreactors devices designed on a 4-in. wafer.

A single microreactor device in Fig. 2a shows inlet, outlet, and the reaction zone. The reaction zone has 118 microchannels of 1.3 cm in length. Each microchannel is 50 μm wide and 100 μm deep. The design of the microreactor is based on the reactant split and product recombination principle. Basically, a typical photomask is fabricated on chromium-deposited glass plate. A 300 nm chromium thin film is deposited on a rectangular glass plate. A photoresist is coated on this chromium-deposited glass plate. The AutoCAD file of the photomask is sent to a laser-assisted mask writing equipment like Heidelberg mask writer. The photoresist is developed in a developer, and the chromium film is wet etched in perchloric acid to transfer the pattern from photoresist to chromium mask.

The fabrication of microreactors shown in Fig. 2a and b is based on the previous research performed at Louisiana Tech University with some modifications in the process flow to gain high aspect ratios. The process flow diagram for the present fabrication process of the microreactor is a little bit different and schematically shown in Fig. 3. In brief, the fabrication of microreactor involves the deposition of titanium (15 nm) and the aluminium thin film of 150 nm using e-beam or magnetron sputtering physical deposition method on a clean 4-in. silicon wafer. Then the wafer is rinsed with acetone, methanol, IPA, water and dried with a nitrogen gun. The wafer is spin-coated with hexamethyldisiloxane and SPR 220 3.0 positive photoresist. The wafer is allowed to soft bake for 115 °C for 90 s and exposed to UV light with a contact gap of 50 μm. A post-baking process is performed in which the wafer is heated to 115 °C for 90 s before developing it in Microposit ® MF® 319 for 2 min. The pattern is transferred from photoresist to metal by wet etching of aluminum and titanium. They are etched to 100 μm deep using Deep Reactive Ion Etching (DRIE) technique. Once the required depth is obtained, the photoresist, aluminum and titanium are stripped off the wafer. Figure 3 shows typical final devices fabricated on the silicon wafer.
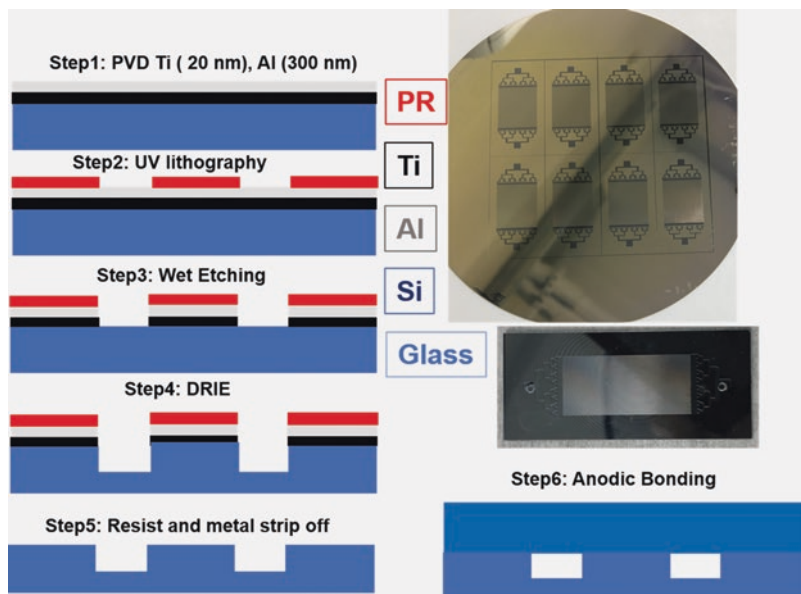
Fig. 3 The process flow diagram of a microreactor fabrication and the final microdevice for FT synthesis

These devices are diced into individual microreactors and are anodically bonded to Pyrex glass plate which is plasma cleaned to remove all the inorganic impurities on the glass plate. The final anodically bonded microreactor, shown in Fig. 3, is used for Fischer-Trospch synthesis, and it is discussed in the later section of this chapter.

The silicon microreactors, well known for excellent heat and mass transfer characteristics, are used for FT synthesis. However, it requires a very huge fabrication infrastructure and optimization of each microfabrication technique like deposition, photolithography, dry etching, etc., with extensive characterization every time to ensure the fabricated device does not have any defects. Another important challenge to use these silicon microreactors for FT synthesis is the extreme difficulty of creating a leak-proof environment for gaseous reactants while assembling into the high-pressure and high-temperature reaction line. Microreactor fabricated with a material with low-cost fabrication techniques in these complex operating conditions can be an interesting research area to address these limitations.

2.3 3D Printed 316 Stainless Steel Microreactors

The second type of microreactors used to evaluate catalyst screening for FT synthesis is a 3D printed 316 stainless steel microreactor. The stainless steel microreactor was procured from Proto Labs Inc. A stainless-steel metal microreactor fabricated
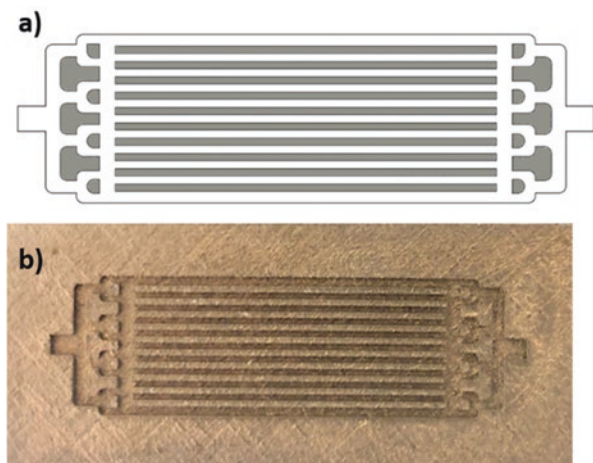
Fig. 4 AutoCAD design of (**a**) microreactor (**b**) final 3D printed SS microreactor

using 3D printing technology having a minimum feature size of 500 μm was designed in AutoCAD and used for catalyst screening in FT synthesis. An example of AutoCAD design of the microreactor is shown in Fig. 4a. The design consists of 11 channels as reaction zones with split and recombination principle. The cover plate has inlet and outlet poles that can fit into the reactor block to handle very high-pressure reaction conditions and maintain a leakage-free environment for reactants. Figure 4b shows the final 3D printed stainless steel microreactor fabricated by a direct metal laser sintering process.

2.3.1 Design Optimization of Microchannel Reactor Using Computational Fluid Dynamics Modeling

A multi-phase CFD model was built and used to optimize the design of the microchannel reactor. The details of the CFD model, closure models, and boundary conditions are similar to those previously developed [32–34]. Preliminary results showing the velocity contour and velocity vector profiles are shown in Fig. 5a and b, respectively. The current design exhibits inefficiency in mixing, with significant velocity gradients and dead zones in several parts of the reactor, which would ultimately reduce the overall reactor efficiency and productivity. Therefore, a design optimization analysis was carried out with the primary objectives of: (1) eliminating dead flow zones in the reactor, while maintaining a free flow area of 57.5% or higher, (2) enhancing mixing throughout the reactor, (3) enhancing heat dissipation, and ultimately (4) maximizing reactor yield. The design analysis focused on two primary aspects, the gas distribution inlet and the channel design. For the inlet design, both T- and V-shaped inlet distributors were investigated, with the objective of breaking the flow at the inlet to prevent zipping and to generate eddies. With
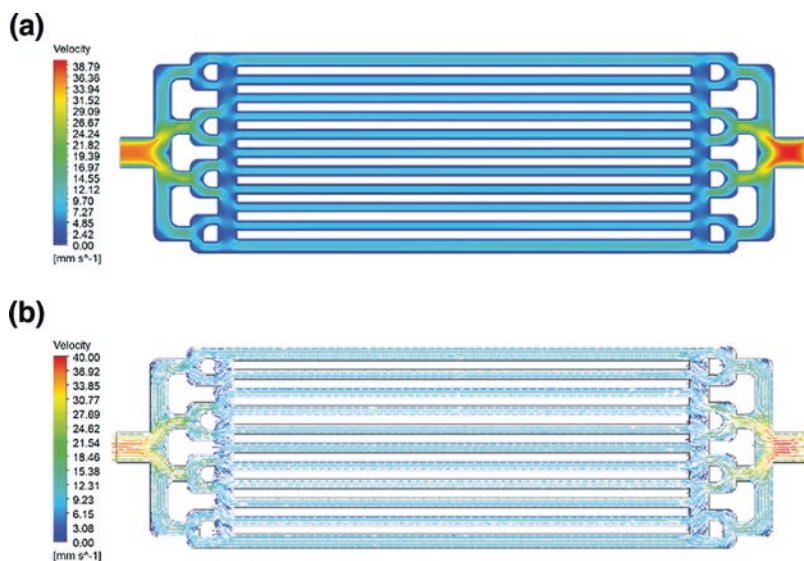
Fig. 5 Velocity contour (**a**) and velocity vector profiles (**b**) of the original microchannel reactor design

regard to the channel design, eight different channel designs were investigated, as shown in Fig. 6. The objective was to maximize mixing, avoid zero-velocity regions, maximize heat dissipation, and enhance mixing quality.

Sample results for the effect of different inlet distributor and channel designs are shown in Figs. 7 and 8, respectively. As can be seen in these figures, changing the inlet to a T or V shape helps enhance feed distribution and reduce feed zipping through the reactors, whereas changing the channel design to a more tortuous path enhances mixing and reduces dead zones, which is intuitive. Therefore, the effects of the different designs on both the flow quality and heat dissipation were quantified. Two main parameters were used to determine the effects of channel design on flow, the dead zone % and the quality index factor, and results are shown in Tables 2 and 3, respectively. A lower dead zone indicates better utilization of the coated catalyst surface, and ultimately a higher reactor efficiency and productivity, whereas a higher quality index factor, as defined in Eq. (13), determines the relative gradient in mass flow rate along the reactor, a lower quality index indicates better mixing throughout the reactor. As can be seen in the results, channel designs 5–9, coupled with T and V inlets, perform significantly better than other configurations, and should be considered for further reactor optimization. Similarly, two main parameters were used to determine the effect of channel design on the heat dissipation within the reactor: cooling requirement (J), and maximum dimensionless temperature increase, and results are shown in Tables 4 and 5, respectively. A higher cooling requirement indicates a higher catalyst utilization rate and subsequently higher reactive productivity, whereas the maximum dimensionless temperature increase, as defined in Eq. (14), is a measure of the temperature gradients throughout the reactor,
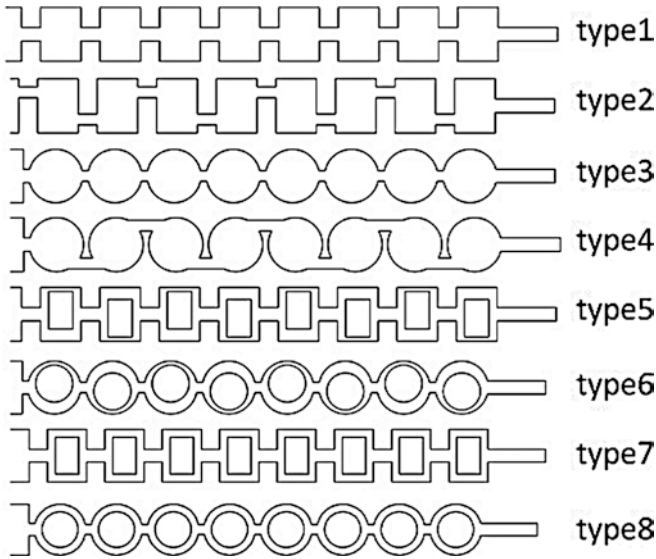
Fig. 6 Micro-reactor channel design investigated in this work. (Adapted from Shaker et al. [35])
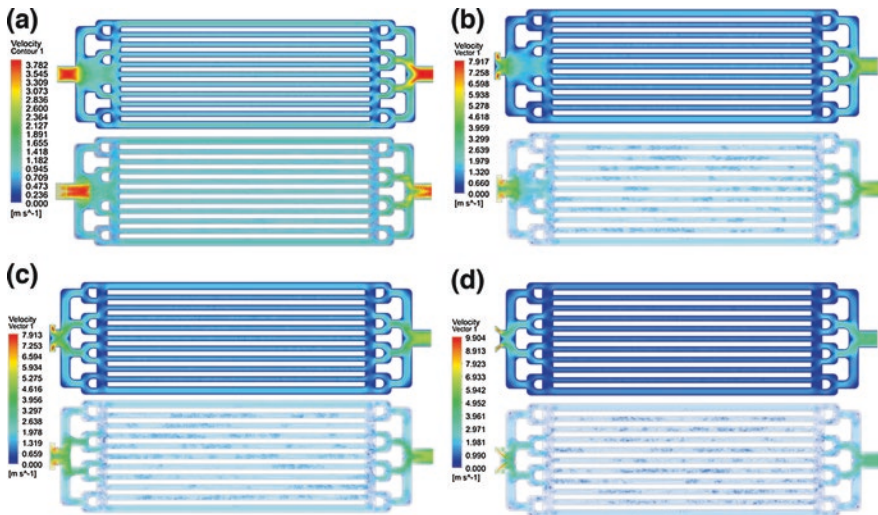
Fig. 7 Preliminary results of the effect of the inlet distributor on the velocity contours and velocity vector profiles in the microchannel reactor

higher temperature gradients typically result in operational challenges and therefore lower values are desired. As can be seen in the results, channel designs 7–9, coupled with T and V inlet, perform better than the other configurations, and will be considered further in future.
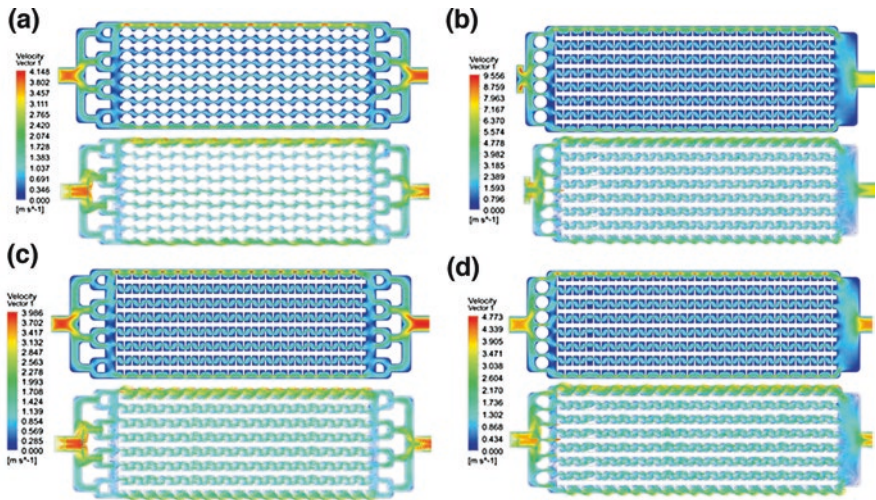
Fig. 8 Preliminary results of the effect of the channel design on the velocity contours and velocity vector profiles in the microchannel reactor

Table 2 Effect of different channel designs on the dead zone % in the reactor

Inlet design	Channel design (%)									
	S	1	2	3	4	5	6	7	8	9
Straight inlet	24.7	16.3	11.9	19.0	9.9	8.4	6.9	8.2	7.4	6.4
T-inlet	22.1	13.7	9.7	17.0	10.6	8.0	6.6	6.2	8.8	8.6
V-inlet	22.8	16.6	11.4	16.4	10.7	8.9	6.2	6.6	9.1	6.8

Table 3 Effect of different channel designs on the quality index factor in the reactor

Inlet design	Channel design									
	S	1	2	3	4	5	6	7	8	9
Straight inlet	0.6	0.48	0.318	0.456	0.288	0.24	0.23	0.16	0.2	0.22
T-inlet	0.35	0.252	0.168	0.294	0.137	0.11	0.09	0.14	0.1	0.1
V-inlet	0.28	0.21	0.101	0.204	0.132	0.12	0.08	0.09	0.12	0.09

Table 4 Effect of different channel designs on the cooling requirement (J) in the reactor

Inlet design	Channel design									
	S	1	2	3	4	5	6	7	8	9
Straight inlet	6.97	7.32	4.36	6.45	5.23	8.19	12.7	8.02	13.4	17.4
T-inlet	4.7	4.7	4.54	4.2	8.23	7.9	11.3	8.9	10.8	16.8
V-inlet	6.2	7.61	4.96	6.2	6.71	6.73	12.2	6.9	12.9	17.7

Table 5 Effect of different channel designs on the maximum dimensionless temperature increase in the reactor

Inlet design	Channel design									
	S	1	2	3	4	5	6	7	8	9
Straight inlet	0.312	0.209	0.144	0.256	0.144	0.13	0.12	0.1	0.1	0.11
T-inlet	0.243	0.175	0.104	0.16	0.092	0.12	0.06	0.06	0.07	0.09
V-inlet	0.271	0.217	0.133	0.23	0.13	0.1	0.11	0.09	0.08	0.08

Future work will investigate flow and heat effects in systems involving multiple microreactors, with the aim of identifying the best overall configuration to number up the microreactors into a standalone FT unit.

$$Q = \frac{m_{max} - m_{min}}{m_{max}} \tag{13}$$

$$\Delta T_{max} = \frac{T - T_w}{T_w} \frac{E_A}{RT_W} \tag{14}$$

3 Catalysts Development for Fischer-Tropsch Synthesis in a Microreactor

3.1 Experimental Setup and Approach

Experiments for FT synthesis are performed in an in-house custom set up with LabVIEW automation and accurate control over a wide range of operating conditions. Figure 9 shows the experimental setup at North Carolina Agricultural and Technical State University. The flow rate of the reactants (hydrogen and carbon monoxide) was monitored and controlled using Cole Palmer mass flow controllers with a range of 0.01–1 sccm. The carrier gas used in this process was nitrogen, which was controlled using an Aalborg mass flow controller (maximum 10 sccm). The upstream and downstream pressures are monitored using Cole-Parmer digital pressure gauges and are fed to the LabVIEW system to control the reaction pressure using a solenoid valve. The products are analyzed by an online GCMS from Agilent Technologies.

The catalyst coating method is different depending on the reactor type. This will be discussed in the catalyst development in later sections. Before experimentation, the coated microreactors are reduced ex-situ under the flow of 10% H_2. To compensate reduction losses while transferring to the reactor line, the reactors are assembled into the reactor block and then again reduced in-situ at 350 °C for 6 h. The FT reactions were performed after the reduction of catalyst, the catalyst performance like selectivity, activity, kinetics, and stability was evaluated by changing operating conditions like temperatures, gas hour space velocities, etc.
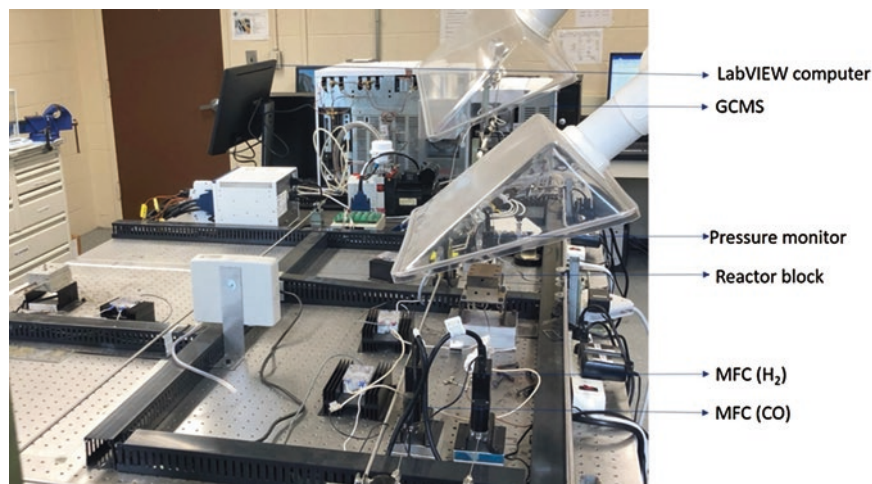
Fig. 9 LabVIEW automated experimental setup showing all the devices on the optical table for FT synthesis in microreactor [24]

3.2 Catalysts for Fischer-Tropsch Studies

The four metals of group 8—ruthenium, iron, cobalt and nickel—possess high activities for Fischer-Tropsch synthesis and are best known catalysts in the industry and research [36]. The use of these transition metals as catalysts for FT synthesis is widely reported in the literature. The activity for ruthenium for carbon monoxide hydrogenation is much higher when compared to the other three metals; due to very high cost, it has limited industrial applications [3]. However, many research studies on both lab-scale and pilot-scale were performed using Ru as a promoter with ab iron- or cobalt-based catalyst for FT synthesis [37–39]. On the other hand, nickel being the more active catalyst for CO hydrogenation favors the formation of methane, i.e., methanation reaction, thereby lacking selectivity toward higher hydrocarbons [40, 41]. In addition, nickel carbonyls are volatile and lead to quick deactivation of the catalyst over the range of FT operating conditions [40]. Thus, cobalt and iron are the best suitable industrial catalysts for FT synthesis and are adopted globally by some of the commercial FT plants. For example, Sasol, a South African based FT plant, uses iron as a catalyst in three of their commercial plants, whereas a Shell-based FT plant in Malaysia produces 12,000 barrels per day using a cobalt catalyst for the hydrocarbon production [42].

Iron- and cobalt-based catalysts are the target for the catalyst design over the times to obtain more selectivity toward the desired products [43]. The optimum performance for Fischer-Tropsch synthesis is obtained by tailoring chemical, mechanical, and physical properties of catalysts during design and synthesis. The optimization of these properties enhances the catalyst performance in terms of activity, stability, and selectivity toward the desired hydrocarbons. The factors like

activity, size, shape, and degree of crystallinity play a major role in overall catalyst design for Fischer-Tropsch synthesis [44]. These factors can be achieved by selecting suitable support materials. The support materials generally improve the catalyst activity by providing mechanical resistance to the catalyst. For example, supports provide porosity with high surface areas and uniform morphology with strong mechanical resistance. As a result, these support materials retain Fe or Co as nanoparticles in its framework and improve the dispersion of metals (Fe, Co or promoters like Ru, K, etc.) that help catalysts to be active and stable during the Fischer-Tropsch synthesis for longer time on stream. Supports such as Al_2O_3, TiO_2, SiO_2, ZrO_2, zeolite, and carbon nanofibers are generally used for heterogeneous catalysis because of their high surface areas and excellent mechanical strength [45].

Metal-support interactions play an important role in catalyst development in terms of activity and selectivity. The study of these interactions is a key factor for the catalyst development for the Fischer-Tropsch synthesis is are presented in two case studies below. Case study-1 describes the catalyst screening in the silicon microreactors fabricated by conventional microfabrication techniques discussed in the previous section. The second case study describes the catalyst screening in the 3D printed stainless steel microreactor.

3.2.1   Case Study-1: Catalyst Screening for FT Synthesis in Silicon Microreactor

The reactions are carried out by aligning the silicon microreactor in the reaction line without breaking and ensuring that the graphite gasket perfectly seals the inlets and outlets in the reactor. The catalyst to be used for FT synthesis is coated into the microchannels. The small microchannel features in the reaction zone play an important and challenging role during experiments for FT synthesis. The methods like dip coating, incineration, and in-situ catalyst growth are few coating techniques that are generally used in FT studies.

Our studies in Si-microreactor published in 2010 [46] covered different methods for the deposition of catalysts in the channels of Si-microreactor. Zhao et al. [30] studied the effect of ruthenium, ~0.4% by weight, as a promoter on silica-supported iron- and cobalt-based catalysts synthesized by sol-gel technique for FT synthesis in silicon microreactor. The addition of Ru to Fe-Co-SiO$_2$ increased the CO conversion by 16% at 200 °C at 1 atm with a syngas ratio of 3:1.

In order to understand how each metal interacts with SiO_2 in terms of CO-conversion and selectivity of hydrocarbons, Mehta et al. [31] used a silica sol-gel-based catalyst coated into the microchannels with a modified closed channel infiltration method called mCCI for FT synthesis. Figure 10 shows the SEM image of the microchannels in the silicon microreactor coated with the FT catalyst. The FT experiments with Fe-SiO$_2$, Co-SiO$_2$, and Ru-SiO$_2$ catalysts, prepared by sol-gel technique (see Table 2 below), were conducted at different temperatures to find the optimum performance of each catalyst with syngas molar ratio (H$_2$:CO) of 2:1 and 3:1 at atmospheric pressure. As shown in Fig. 11, the metal type, temperature, and
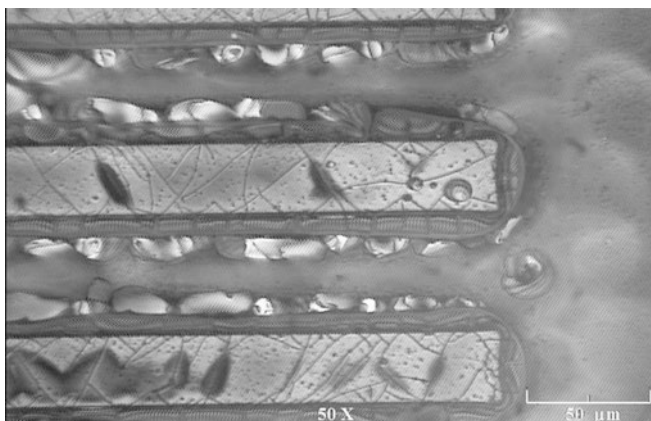
Fig. 10 SEM image of microchannels in silicon microreactor coated with sol-gel FT catalyst

the syngas mole ratio showed a significant effect on the FT reaction. The highest FT reactivity was observed for Ru-SiO$_2$ with 5% selectivity toward butane. A 90% CO conversion was obtained for Co-SiO$_2$ with 44% selectivity toward propane. More significantly, Co-SiO$_2$ showed the highest resistance to stability followed by Fe-SiO$_2$ and Ru-SiO$_2$.

Table 6 shows the surface areas, intended and actual metal loadings from EDX, optimum reaction temperature and conversion of catalysts used for FT synthesis in silicon microreactor.

These results are consistent with that reported in literature. Cobalt is indeed widely used in the industry for FT synthesis. These studies show that the SiO$_2$ support has control over metal, particle size, and the degree of reduction.

In order to investigate the effect of support and metal-support interaction on FT synthesis, silica was replaced with TiO$_2$. Abrokwah et al. [25] prepared TiO$_2$ as support for metals Fe, Co, and Ru and carried out FT synthesis in the range of 150–300 °C at 1 atm in a silicon microreactor. TPR profiles show the reduction profiles with strong metal-support interaction with the Co and Fe than that of Ru. The rutile phase of TiO$_2$ increased the stability of Ru-TiO$_2$ which was not observed in the case of Fe-TiO$_2$ and Co-TiO$_2$, causing quick deactivation of these catalysts. The optimum stability and the selectivity toward hydrocarbons were dependent on the reaction temperature for the different metals in the TiO$_2$ support. Based on deactivation studies, Ru-TiO$_2$ > Fe-TiO$_2$ > Co-TiO$_2$. However, these results from FT studies with TiO$_2$ support are in sharp contrast from that with SiO$_2$. It has been reported in the literature that the rutile phase is important for FT activity of the catalysts. After careful examination of the XRD data, we noticed that Ru-TiO$_2$ also has a rutile phase in contrast to its absence in Co-TiO$_2$ and Fe-TiO$_2$. Our results are consistent that are reported in literature. Thus, the presence of the rutile phase in Ru-TiO$_2$ suggests its higher stability and activity compared to its lower activity observed in silica.
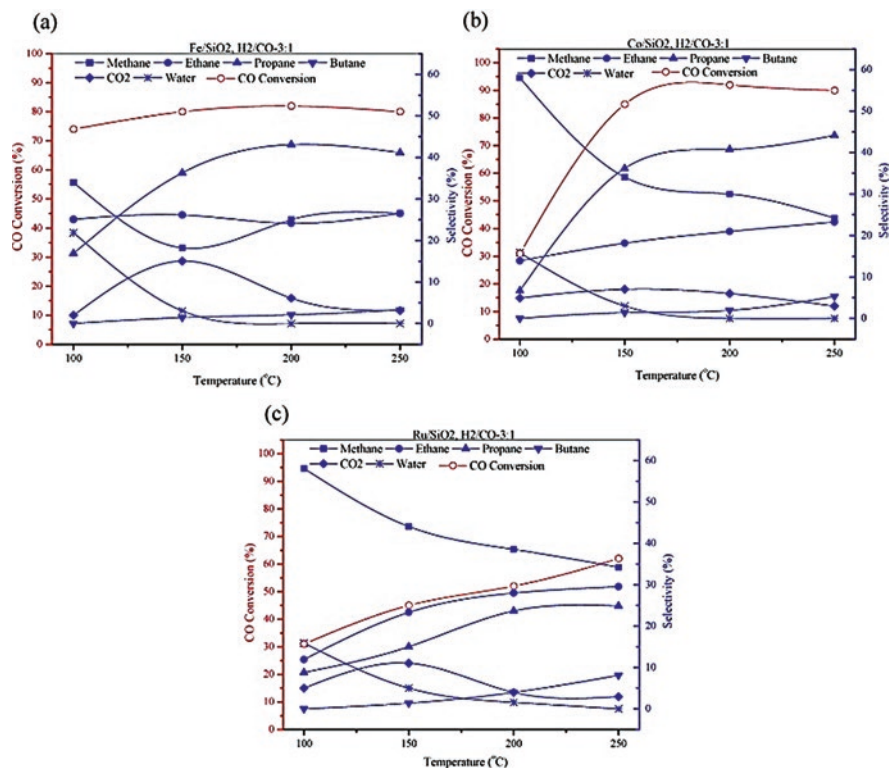
Fig. 11 Effect of temperature on CO conversion and hydrocarbon selectivity of (**a**) Fe-SiO₂ (**b**) Co-SiO₂ (**c**) Ru-SiO₂ during FT synthesis in silicon microreactor at $p = 1$ bar and H₂:CO = 3:1

Table 6 Intended and actual metal loadings, surface areas, optimized reaction conditions of different catalysts used for FT synthesis in silicon microchannel microreactor

Catalyst with intended metal loadings	Surface area (m²/g)	Actual metal loading	Optimum reaction temperature (°C)	CO (%)	Refs
FeCo-SiO₂	325	2.6%Fe 2.7%Co-SiO₂	220	62	[30]
Ru-Fe-Co-SiO₂	325	0.4%Ru-1.9%Fe 2.2%Co-SiO₂	220	77	
12%Fe-SiO₂	53.6	9.8%Fe-SiO₂	200	81	[31]
12%Co-SiO₂	56.3	10.4%Co-SiO₂	250	90	
12%Ru-SiO₂	61.1	4.3%Ru-SiO₂	250	62	
12%Ru-TiO₂	118.4	8.78% Ru-TiO₂	220 and 250	–	[25]
12%Fe-TiO₂	117.	8.34% Fe-TiO₂	300	–	
12%Co-TiO₂	48.1	6.44% Ru-TiO₂	220	–	

3.2.2 Case Study 2: Catalyst Screening for FT Synthesis in 3D Printed SS Microreactor Using Mesoporous Support

One of the problems with Si-microreactors is that it breaks easily and also there is a problem to seal the microreactor with glass to create a leak-proof reaction environment. Also, as indicated in Table 6, the surface areas of sol-gel-coated catalysts are much smaller than the mesoporous supports for heterogeneous catalysts [47, 48]. It was also observed that intended metal wt% did not match with actual metal loadings. To address these problems, mesoporous supports synthesized by one-pot hydrothermal method with very high surface area were used to screen catalysts for FT synthesis in 316 stainless steel (SS) microreactors.

This case study gives a comprehensive understanding of various catalysts functionalized on different types of mesoporous support and the FT studies were carried out in a 3D printed stainless steel microreactor. The kinetics of the catalytic reactions were also investigated. Figure 12 shows the schematic FT process conducted in a microreactor.

Sub-case-1: Cobalt-Based Bimetallic Silica Mesoporous Catalyst for FT Synthesis in 3D Printed Microreactor

Mohammad et al. [45] studied the effect of 5% by weight of Co, Fe, Ru, and Ni incorporated into 10%Co-MCM-41catalyst, which were synthesized using a one-pot hydrothermal process. These powdered catalysts were uniformly coated into the reactor channels using 4% by weight of PVA slurry. The SEM image in Fig. 13 shows the coated microchannels in SS microreactor. The FT experiments were carried out at temperatures between 180 and 325 °C using a syngas molar ratio (H_2:CO) of 3. Results indicated that the inclusion of the second metal into the Co-MCM-41 framework had a significant effect on the CO conversion, C_1-C_4 selectivity toward and the catalyst stability in FT synthesis. The metal loadings calculated by EDX, BET surface area, conversion and selectivity of these catalysts are presented in Table 7.
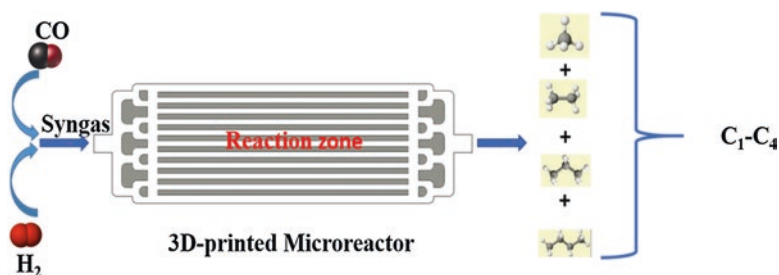
Fig. 12 Schematic FT synthesis in 3D printed stainless steel microreactors
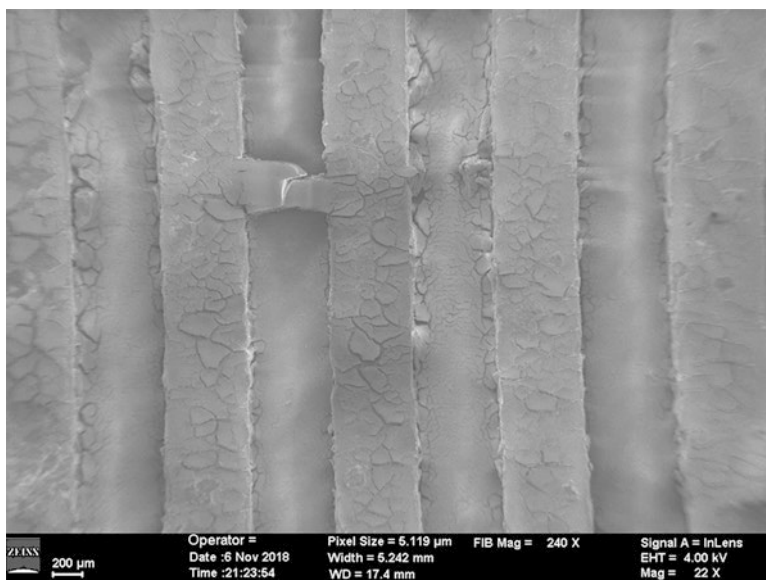
Fig. 13 SEM image of microchannels coated with the catalyst in SS microreactor

Table 7 Metal loadings, surface areas, and optimum reaction temperatures for FT synthesis in 3D printed SS microreactor using MCM-41 supported catalysts

Catalyst	EDX loadings	Surface area (m²/g)	CO (%)	Optimum reaction temperature (°C)	Refs
15%Co MCM-41	14.33% Co-MCM-41	820.5	64	240	[45]
10%Co5%Ru MCM-41	9%Co4%Ru MCM-41	1025.3	77.4	240	
10%Co5%Fe MCM-41	10.2%Co6.8%Fe MCM-41	574	65.5	210	
10%Co5%Ni MCM-41	9.1%Co5.5%Ni MCM-41	434	72	240	

All the catalysts showed significant selectivity toward methane, but the highest selectivity toward butane (11%) and propane (39%) was observed for CoRu-MCM-41 at 240 °C and CoFe-MCM-41 at 210 °C, respectively. Figure 14 shows the effect of temperature on CO conversion and the selectivity to hydrocarbons in FT synthesis using four catalysts in a 3D printed stainless steel microreactor with H_2:CO molar ratio of 3:1. Deactivation studies performed at 240 °C show that CoFe-MCM-41 is more stable and it is followed by Co-MCM-41 and CoNi-MCM-41. CoRu-MCM-41 was found to have the least resistance to catalyst deactivation; however, it showed the highest selectivity towards propane and butane of all the four catalysts. Results show that the selectivity toward hydrocarbons for each catalyst was greatly dependent on metal-support interactions as supported by various characterizations studies such as TPR and XPS.
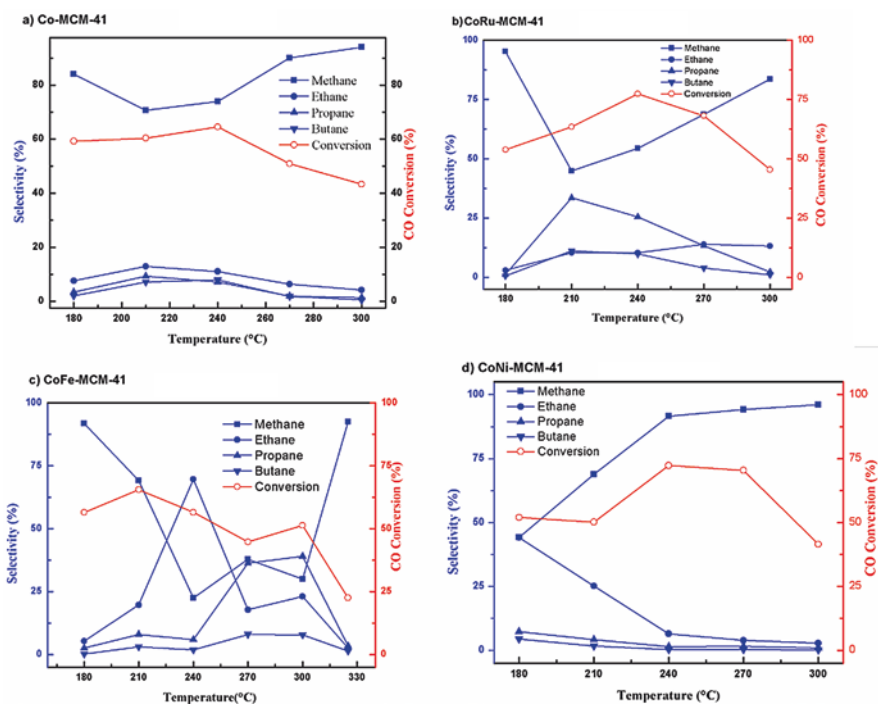
Fig. 14 Effect of temperature on CO conversion and hydrocarbon selectivity in FT synthesis using 3D printed stainless steel microreactor: (**a**) Co-MCM041, (**b**) CoRu-MCM-41, (**c**) CoFe-MCM-41, (**d**) CoNi-MCM-41; $p = 1$ bar and $H_2:CO = 3:1$
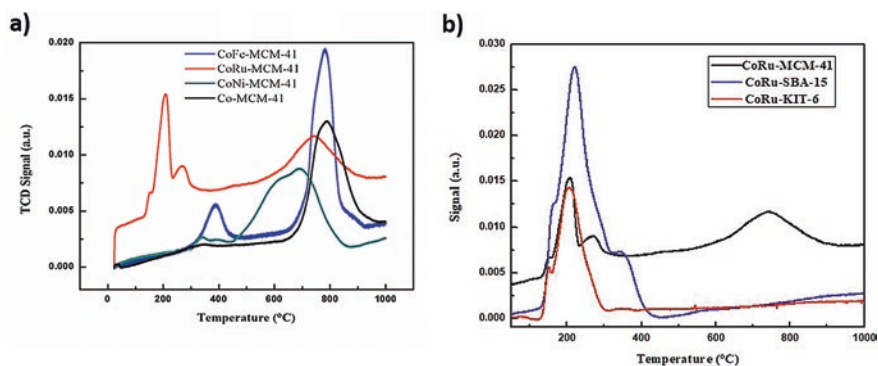
Fig. 15 H_2 TPR (temperature-programmed reduction) profiles of (**a**) MCM-41-based catalysts (**b**) CoRu-S (S = MCM-41, KIT-6 and SBA-15)

For example, the temperature-programmed studies (TPR) shown in Fig. 15a indicate that reduction temperature of cobalt is ~800 °C, forming very stable cobalt silicates and this is consistent with the results from XPS studies [45].

The studies with MCM-41 support resulted in very low selectivity toward higher hydrocarbons despite showing the highest stability over a longer time on stream (TOS). This prompted us to investigate different types of mesoporous silica supports to gain an in-depth understanding of the influence of the structure of mesoporous silica material and its role in the reaction kinetics of FT synthesis.

The kinetic studies for FT synthesis were conducted with three different types of mesoporous silica (MCM-41, SBA-15, and KIT-6) supports having 10% Co and 5% Ru in the support framework [24]. A one-pot hydrothermal process was used to synthesize CoRu-MCM-41, CoRu-KIT-6, and CoRu-SBA-15, in order to study the effect of these long-range ordered mesoporous catalysts on the kinetics of FT reaction. The catalysts were coated in the microchannels of microreactor with 4% PVA catalyst slurry and the kinetic performances were evaluated at three different temperatures based on our previous studies with MCM-41-supported catalysts. The reactions were performed at 210, 240, and 270 °C at different weight hourly space velocities (WHSV = 2.15–25.2 kgcat h/kmol) with 2:1 (H_2:CO) constant syngas ratio. The theoretical kinetic models were proposed based on the Langmuir-Hinshelwood and the Eley-Rideal mechanisms. Table 8 shows the proposed six FT mechanisms, FT 1–6 with elementary reactions, and kinetic eqs. FT-1, FT-2, FT-4, and FT-5 are based on the Eley-Rideal-type mechanism and FT-3 and FT-6 are based on the Langmuir-Hinshelwood mechanism.

All the six FT mechanistic models were fitted against the experimental data to get the best-fitted model for each catalyst. The type of silica support has a significant effect on the kinetic studies. FT-3 was the best kinetic model to fit the data for the CoRu-MCM-41 catalyst, whereas, for CoRu-SBA-15 and CoRu-KIT-6, FT-2 and FT-6 were found to be statistically relevant to the experimental kinetic data. Deactivation studies show that the CoRu-KIT-6 is more stable and active than that of the other two catalysts in terms of CO conversion and activation energy, respectively. The type of mesoporous silica material clearly shows the difference in the kinetic performance of the catalyst which is consistent with the differences shown in extensive characterization of the materials. For example, the TPR studies indicate that the metals Co and Ru on these three supports have different hydrogen consumption temperatures to get active metal into the support framework. Figure 15b shows the TPR profiles of CoRu-MCM-41, CoRu-KIT-6, and CORu-SBA-15. The reduction temperature of cobalt in MCM-41 is around 780 °C, whereas, in Co- KIT-6 and Co-SBA-15, the total hydrogen consumption is observed at much lower temperature.

Sun et al. studied the kinetics of FT synthesis in a reactor having channels of $1 \times 1 \times 40$ mm on 8×8 cm stainless steel metal plate with Co-Ni bimetallic catalyst on SiO_2 support. They investigated FT kinetics over a wide range of operating conditions: $T = 280$–320 °C, 10–50 bar pressure varying syngas (H_2:CO) ratio from 1 to 3 [49]. The comprehensive theoretical kinetic model based on the Langmuir-Hinshelwood-Hougen-Watson carbide mechanism was derived and compared with

Table 8 Elementary reaction steps and the kinetic rate equations of different models proposed for FT synthesis using CoRu-S (S = MCM-41, SBA-15 and KIT-6) in 3D printed SS microreactor [24]

Model	No	Elementary reaction	Kinetic equation
FT-1	1	$CO + S \rightarrow CO \cdot S$	$-r_{CO} = \dfrac{kK_1 p_{CO} p_{H_2}}{\left(1 + K_1 p_{CO}\right)}$
	2	$CO \cdot S + H_2 \rightarrow C + D$	
FT-2	1	$H_2 + S \rightarrow H_2 \cdot S$	$-r_{CO} = \dfrac{kK_1 p_{CO} p_{H_2}}{\left(1 + K_1 p_{H_2}\right)}$
	2	$H_2 \cdot S + CO \rightarrow C + D$	
FT-3	1	$CO + S \rightarrow CO \cdot S$	$-r_{CO} = \dfrac{kK_1 p_{CO} p_{H_2}}{\left(1 + K_1 p_{CO} + K_2 p_{H_2}\right)^2}$
	2	$H_2 + S \rightarrow H_2 \cdot S$	
	3	$CO \cdot S + H_2 \cdot S \rightarrow C + D$	
FT-4	1	$CO + S \rightarrow CO \cdot S$	$-r_{CO} = \dfrac{kK_1 K_2 p_{CO} p_{H_2}}{\left(1 + K_1 K_2 p_{CO} p_{H_2} + K_1 p_{CO}\right)}$
	2	$CO \cdot S + H_2 \rightarrow COH_2 \cdot S$	
	3	$COH_2 \cdot S \rightarrow C + D$	
FT-5	1	$H_2 + S \rightarrow H_2 \cdot S$	$-r_{CO} = \dfrac{kK_1 K_2 p_{CO} p_{H_2}}{\left(1 + K_1 K_2 p_{CO} p_{H_2} + K_1 p_{H_2}\right)}$
	2	$H_2 \cdot S + CO \rightarrow COH_2 \cdot S$	
	3	$COH_2 \cdot S \rightarrow C + D$	
FT-6	1	$CO + S \rightarrow CO \cdot S$	$r = \dfrac{kK_1 K_2 K_3 p_{CO} p_{H_2}}{\left(1 + K_1 K_2 K_3 p_{CO} p_{H_2} + K_1 p_{CO} + K_2 p_{H_2}\right)}$
	2	$H_2 + S \rightarrow H_2 \cdot S$	
	3	$CO \cdot S + H_2 \cdot S \rightarrow COH_2 \cdot S + S$	
	4	$COH_2 \cdot S \rightarrow C + D$	

experimental data obtained in the microreactor using Co-Ni-SiO$_2$ catalyst. They observed that the activation energy of Co-Ni-SiO$_2$ was around 84 kJ mol^{-1} using a tubular reactor. The single support system has disadvantages of the high surface area and lacks catalyst activity and reactivity; therefore the composite support may be an option to enhance the FT activity

Sub-case-2: Composite Oxide Support Catalysts for FT Synthesis in 3D Printed Stainless Steel Microreactor

In order to investigate the effect of mixed-oxide supports on FT synthesis, a binary support with a combination of silica, titania, and alumina was synthesized. Bepari et al. [50] synthesized 10% Fe, 10%Fe 5%Co, 10%Fe 5%Ru impregnated on SiO$_2$-Al$_2$O$_3$ mixed support prepared one-pot hydrothermal method. The H$_2$-TPR studies show much lower reduction temperatures for Co and Fe in binary supports when compared to the catalysts with a single support. The low-angle X-ray diffraction studies showed that the mesoporous structure of impregnated catalysts was conserved after the incorporation of Fe, Co, and Ru metals. The composite oxides mesoporous support have surface areas in the range of 380–650 m^2/g with improved metal dispersion. The surface areas, intended and actual metal loadings and the CO conversion at 300 °C of all the three catalysts, are presented in Table 9. The presence of Co or Ru in Fe-SiO$_2$-Al$_2$O$_3$ improved selectivity toward higher hydrocarbons and also has a remarkable effect on the catalyst activity when compared to that of Fe.

Case-study-3. Iron-Based Catalysts with Various Promoters for the Increase of CO$_2$ Utilization During Fischer-Tropsch Synthesis

One of our goals at the NSF-CREST Bioenergy center is to carry out FT synthesis using syngas enriched with CO$_2$ in microreactors at higher pressure to mimic that done in a lab reactor. In parallel to our research with microreactors, FT synthesis in a tubular reactor was carried out by Wang and his coworkers. The co-precipitated Fe-Cu-K catalysts were further promoted with silica (Si) and alumina (Al) to enhance its catalytic activity for the hydrogenation of CO$_2$ and CO during

Table 9 Metal loading, surface area, and CO conversion of different mixed oxide support for FT synthesis

Catalyst with intended metal loadings	Surface area (m^2/g)	Actual metal loading	CO (%)	Ref
10%Fe-SiO$_2$-Al$_2$O$_3$	479	9.25%Fe-SiO$_2$-Al$_2$O$_3$	96	[50]
10%Fe 5% Co-SiO$_2$-Al$_2$O$_3$	382	8.94%Fe 4.15% Co-SiO$_2$-Al$_2$O$_3$	62	
10%Fe 5%Ru-SiO$_2$-Al$_2$O$_3$	101	10.54%Fe 6.26%Ru-SiO$_2$-Al$_2$O$_3$	71	

Fischer-Tropsch (FT) synthesis. The performance of the catalysts with and without the structural promoters of Al and Si was evaluated in a tubular reactor with 7.8 mm inside diameter and 15.2 mm length. Each catalyst was mixed with SiC at 1:6 volumetric ratio of catalyst to SiC to achieve an isothermal condition along the reaction bed during the experiments. A model syngas at a composition of 54%H_2/10%CO/29%CO_2/7%N_2 was used during the experiments. The model syngas represented typical syngas produced by oxygen/steam gasification of biomass with the composition reported in literature [51]. N_2 was used as an internal standard for the GC analysis and the representative of inert components in the syngas. The feed gas was introduced into the reactor at 30 mL/(h·g-cat) STP. The reaction was carried out at 300 °C and 2 MPa for 72 h [52].

The use of double promoters of Al and Si on the Fe-Cu-K achieved higher conversion efficiencies of CO and CO_2 than the original Fe-Cu-K catalyst and the Fe-Cu-K catalysts promoted by either Al or Si. The doubly promoted catalyst could hydrogenate 89.6% CO and 25.2% CO_2 in the model syngas, compared to 81.8% and 18.5% for the Fe-Cu-K catalyst without the promoters of Al and Si. Potassium is known to improve the catalytic activity of Fe-based catalysts for the reverse water-gas shift (RWGS) reaction. The double structural promoters of Al and Si could improve the dispersion of potassium on a Fe-based catalyst, resulting in the increase of CO_2 hydrogenation via the RWGS reaction. The selectivity to the C_{5+} hydrocarbons for the Fe-Cu-K catalyst doubly promoted with Al and Si was 71.9%, which was slightly lower than 75.5% for the Fe-Cu-K catalyst without the structural promoters [52] (Table 10).

4   Conclusion and Future Work

In this chapter, we have primarily focused on the basic understanding of microreactor research with a goal towards the development of catalysts for effective Fischer-Tropsch synthesis.

Table 10 FT synthesis over iron-based catalysts with biomass-derived syngas [52]

Catalyst	CO conversion (%)	CO_2 conversion (%)	Hydrocarbon selectivity[a] (mole-C %)			Olefin selectivity %	
			CH_4	C_2–C_4	C_{5+}	C_2–C_4	C_5
Fe-Cu-K	81.8	18.5	5.9	18.6	75.5	89.0	81.0
Fe-Cu-K-Al	88.3	12.5	6.9	25.4	67.7	90.0	81.0
Fe-Cu-K-Si-Al	89.6	25.2	7.6	20.5	71.9	81.8	77.3
Fe-Cu-K-Si	67.1	13.2	13.9	18.6	67.4	89.0	82.6

[a]An CO_2-free basis

- This book chapter covers mostly our recent research on the design and application of silicon and stainless steel microreactors for the conversion of syngas and syngas enriched with CO_2 into fuels. The current process intensification challenges in adopting microreactor technology to enable modular reactor models to transfer laboratory research to industry are supported by three case studies.
- The microreactors fabricated using silicon and 3D printed stainless steel offer impressive catalytic performance in terms of CO conversion and hydrocarbon selectivity. Further research is necessary to gain an in-depth knowledge of the reaction mechanism and efficiency to improve the process.
- The choice of FT reactors is usually based on the economics of the entire FT process, not in terms of product selectivity and catalyst performance. Therefore, much research attention in conducting techno-economic analysis of these scale-up of microreactor models will help to understand the FT synthesis in microreactors from the economic viewpoint.
- The study of metal and support interaction is crucial in developing robust catalysts for FT synthesis. The utilization of microreactors consisting of microstructures enables ease of understanding of this metal-metal-support interaction for the effective catalyst development in FT synthesis. Some silica supports like MCM-41, with very high surface area with long-range ordered structures, lack the catalyst activity in terms of selectivity and stability. In contrast, different types of mesoporous supports synthesized from silica have a profound effect on FT synthesis, selectivity, and kinetics of the reaction as evidenced by extensive characterization from TPR and XPS experiments.
- The study of complex reaction kinetics and mechanism is still needed to address the dissociation and addition of reactants on catalyst active surface for chain growth and termination, thereby favoring the desired FT products using modular units.
- Deactivation of the catalyst also depends very much on the metal-support interactions. Therefore, in situ catalyst regeneration during FT synthesis can be a viable option for a longer time on stream in microreactors without losing FT efficiency.

References

1. Maitlis PM, de Klerk A (2013) Greener Fischer-tropsch processes: for fuels and feedstocks. Wiley, Hoboken
2. Basha OM, Sehabiague L, Abdel-Wahab A, Morsi BI (2015) Fischer–Tropsch synthesis in slurry bubble column reactors: experimental investigations and modeling–a review. Int J Chem React Eng 13(3):201–288

3. Jahangiri H, Bennett J, Mahjoubi P, Wilson K, Gu S (2014) A review of advanced catalyst development for Fischer–Tropsch synthesis of hydrocarbons from biomass derived syn-gas. Catal Sci Technol 4(8):2210–2229. https://doi.org/10.1039/C4CY00327F

4. Dry ME (1976) Advances in Fischer-Tropsch chemistry. Ind Eng Chem Process Des Dev 15:282–286

5. Schulz H (1999) Short history and present trends of Fischer-Tropsch synthesis. Appl Catal A Gen 186:3–12

6. Dry ME (1976) Advances in Fishcher-Tropsch chemistry. Ind Eng Chem Prod Res Dev 15(4):282–286

7. Dry M (1990) The Fischer-Tropsch process-commercial aspects. Catal Today 6(3):183–206

8. (2011) Thermochemical processing of biomass conversion into fuels, chemicals and power (Wiley series in renewable resources). Wiley, Hoboken

9. Van Der Laan GP, Beenackers AACM (1999) Kinetics and selectivity of the Fischer–Tropsch synthesis: a literature review. Catal Rev 41(3–4):255–318

10. Rofer-DePoorter CK (1981) A comprehensive mechanism for the Fischer-Tropsch synthesis. Chem Rev 81:447–474

11. Ponec V, van Barneveld WAJI (1979) The role of chemisorption of Fischer-Tropsch synthesis. Ind Eng Chem Prod Res Dev 18(4):268–271

12. Wojciechowski BW (1988) The kinetics of the Fischer-Tropsch synthesis. Catal Rev Sci Eng 30(4):629–702

13. Biloen P, Sachtler W (1981) Mechanism of hydrocarbon synthesis over Fischer-Tropsch catalysts. In: Advances in catalysis, vol 30. Elsevier, Amsterdam, pp 165–216

14. Zennaro R (2013) Fischer–Tropsch process economics. In: Greener Fischer-Tropsch processes for fuels and feedstocks. Wiley-VCH, Chichester, pp 149–169

15. Ehrfeld W, Hessel V, Löwe H (2000) Microreactors: new technology for modern chemistry. Wiley, Weinheim

16. Oroskar A, Van den Bussche K, Abdo S (2001) Intensification in microstructured unit operations performance comparison between mega and micro scale. In: Matlosz M, Ehrfeld W, Baselt J (eds) Microreaction technology. Springer, Berlin, pp 153–163

17. Tonkovich A et al (2008) Improved Fischer-Tropsch Economics Enabled by Microchannel Technology. Velocys Technology, Plain City

18. LeViness S, Tonkovich A, Jarosch K, Fitzgerald S, Yang B, McDaniel J (2011) Improved Fischer-Tropsch Economics Enabled by Microchannel Technology. White Paper generated by Velocys

19. Schubert K, Bier W, Brandner J, Fichtner M, Franz C, Linder G (1998) Realization and testing of microstructure reactors, micro heat exchangers and micro mixers for industrial applications in chemical engineering (in English)

20. Jarosch Kai T, Tonkovich Anna Y Lee T Perry Steven DK, Wang Y (2005) Microchannel reactors for intensifying gas-to-liquid technology. In: Microreactor technology and process intensification, vol 914 (ACS symposium series, no. 914). American Chemical Society, pp 258–272 ISBN13 9780841239234, https://doi.org/10.1021/bk-2005-0914.ch016

21. Tomlinson H, Roth E, Agee K (2004) Movable gas-to-liquid system and process. Google Patents

22. Cai G, Xue L, Zhang H, Lin JJM (2017) A review on micromixers. Micromachines 8(9):274

23. Ehrfeld W, Golbig K, Hessel V, Löwe H, Richter T (1999) Characterization of mixing in micromixers by a test reaction: single mixing units and mixer arrays. Ind Eng Chem Res 38(3):1075–1082

24. Mohammad N, Bepari S, Aravamudhan S, Kuila DJC (2019) Kinetics of Fischer–Tropsch synthesis in a 3-D printed stainless steel microreactor using different mesoporous silica supported Co-Ru catalysts. Catalysts 9(10):872

25. Abrokwah RY, Rahman MM, Deshmane VG, Kuila D (2019) Effect of titania support on Fischer-Tropsch synthesis using cobalt, iron, and ruthenium catalysts in silicon-microchannel microreactor. Mol Catal 478:110566

26. Scotti G, Franssila S (2014) A micro heat exchanger microfabricated from bulk aluminium. J Phys Conf Ser 557:012069
27. Yang C-Y, Yeh C-T, Liu W-C, Yang B-C (2007) Advanced micro-heat exchangers for high heat flux. Heat Transf Eng 28:788–794
28. Roydhouse MD et al (2014) Operating ranges of gas–liquid capillary microseparators: experiments and theory. Chem Eng Sci 114:30–39
29. Breeze P (2016) Chapter 8 - Microturbines. In: Breeze P (ed) Gas-turbine power generation. Academic Press, Boston, pp 77–82
30. Zhao S, Nagineni VS, Seetala NV, Kuila D (2008) Microreactors for syngas conversion to higher alkanes: effect of ruthenium on silica-supported iron−cobalt nanocatalysts. Ind Eng Chem Res 47:1684–1688
31. Mehta S, Deshmane V, Zhao S, Kuila D (2014) Comparative studies of silica-encapsulated iron, cobalt, and ruthenium nanocatalysts for Fischer–Tropsch synthesis in silicon-microchannel microreactors. Ind Eng Chem Res 53:16245–16253
32. Basha O, Gamwo I, Morsi B, Siefert N (2017) Computational fluid dynamics modeling and optimization of absorber design for pre-combustion CO2 capture. In: 34th Annual international pittsburgh coal conference, Pittsburgh
33. Basha OM, Morsi BI (2018) CFD for the design and optimization of slurry bubble column reactors. In: Computational fluid dynamics-basic instruments and applications in science. InTech, Rijeka
34. Basha Omar M, Weng L, Men Z, Badie IM (2016) CFD Modeling with Experimental Validation of the Internal Hydrodynamics in a Pilot-Scale Slurry Bubble Column Reactor. Int J Chem React Eng 14:599
35. Shaker M, Ghaedamini H, Sasmito AP, Kurnia JC, Jangam SV, Mujumdar AS (2012) Numerical investigation of laminar mass transport enhancement in heterogeneous gaseous microreactors. Chem Eng Process Process Intens 54:1–11
36. Perego C, Bortolo R, Zennaro R (2009) Gas to liquids technologies for natural gas reserves valorization: the Eni experience. Catal Today 142:9–16
37. Wang L, Wu B, Li Y (2011) Effects of Ru and cu promoters on Fischer-Tropsch synthesis over Fe-based catalysts. Chin J Catal 32:495–501
38. Taghavi S, Tavasoli A, Asghari A, Signoretto M (2019) Loading and promoter effects on the performance of nitrogen functionalized graphene nanosheets supported cobalt Fischer-Tropsch synthesis catalysts. Int J Hydrogen Energy 44:10604–10615
39. Phienluphon R et al (2014) Ruthenium promoted cobalt catalysts prepared by an autocombustion method directly used for Fischer–Tropsch synthesis without further reduction. Catal Sci Technol 4(9):3099–3107. https://doi.org/10.1039/C4CY00402G
40. Olesen SE, Andersson KJ, Damsgaard CD, Chorkendorff I (2017) Deactivating carbon formation on a Ni/Al2O3 catalyst under methanation conditions. J Phys Chem C 121(29):15556–15564
41. Fajín JLC, Gomes JRB, Cordeiro MNDS (2015) Mechanistic study of carbon monoxide methanation over pure and rhodium- or ruthenium-doped nickel catalysts. J Phys Chem C 119(29):16537–16551
42. Vora BV, Marker T, Arnold EC, Nilsen H, Kvisle S, Fuglerud T (1998) Conversion of natural gas to ethylene and propylene: the most-profitable option. In: Parmaliana A, Sanfilippo D, Frusteri F, Vaccari A, Arena F (eds) Studies in surface science and catalysis, vol 119. Elsevier, Amsterdam, pp 955–960
43. Lappas A, Heracleous E (2016) 18 - Production of biofuels via Fischer–Tropsch synthesis: biomass-to-liquids. In: Luque R, Lin CSK, Wilson K, Clark J (eds) Handbook of biofuels production, 2nd edn. Woodhead Publishing, Sawston, pp 549–593
44. Bartholomew CH, Farrauto RJ (2011) Fundamentals of Industrial Catalytic Processes. Wiley, Chichester

45. Mohammad N, Abrokwah RY, Stevens-Boyd RG, Aravamudhan S, Kuila D (2020) Fischer-Tropsch studies in a 3D-printed stainless steel microchannel microreactor coated with cobalt-based bimetallic-MCM-41 catalysts. Catal Today 303:281–315
46. Zhao S, Kuila D (2010) Nanocatalysis in microreactor for fuels. In: Microfluidic devices in nanotechnology, (John Wiley & Sons, Inc.) pp 281–322. ISBN: 9780470590690, https://doi.org/10.1002/9780470622551
47. Deshmane VG, Owen SL, Abrokwah RY, Kuila D (2015) Mesoporous nanocrystalline TiO2 supported metal (Cu, Co, Ni, Pd, Zn, and Sn) catalysts: effect of metal-support interactions on steam reforming of methanol. J Mol Catal A Chem 408:202–213
48. Abrokwah RY, Deshmane VG, Kuila D (2016) Comparative performance of M-MCM-41 (M: Cu, Co, Ni, Pd, Zn and Sn) catalysts for steam reforming of methanol. J Mol Catal A Chem 425:10–20
49. Sun Y, Yang G, Zhang L, Sun Z (2017) Fischer-Tropsch synthesis in a microchannel reactor using mesoporous silica supported bimetallic Co-Ni catalyst: Process optimization and kinetic modeling. Chem Eng Process Process Intens 119:44–61
50. Bepari S, Stevens-Boyd RG, Mohammad N, Li X, Abrokwah R, Kuila D (2020) Composite mesoporous SiO_2-Al_2O_3 supported Fe, FeCo and FeRu catalysts for Fischer-Tropsch studies in a 3-D printed stainless-steel microreactor. Mater Today, https://doi.org/10.1016/j.matpr.2020.04.582
51. Jun K-W, Roh H-S, Kim K-S, Ryu J-S, Lee K-W (2004) Catalytic investigation for Fischer–Tropsch synthesis from bio-mass derived syngas. Appl Catal A Gen 259(2):221–226
52. Rafati M, Wang L, Shahbazi A (2015) Effect of silica and alumina promoters on co-precipitated Fe–Cu–K based catalysts for the enhancement of CO2 utilization during Fischer–Tropsch synthesis. J CO2 Util 12:34–42

Recent Advancements and Detailed Understanding of Kinetics for Synthesis Gas Conversion into Liquid Fuel

Sonal, Virendra Kumar Saharan, Suja George, Rohidas Bhoi, and K. K. Pant

Abstract Currently, there is a renewed interest in producing liquid fuel from fossil and renewable feedstocks such as coal and biomass via gasification followed by liquefaction, and the processes are CTL (coal to liquid) and BTL (biomass to liquid). Fischer-Tropsch (FT) synthesis has been applied extensively in this process and is considered as the major route for the direct conversion of syngas into liquid fuel employing suitable catalyst systems and conditions. Kinetic study of the syngas conversion process is a prerequisite for the reactor design, optimization, and scale-up study of the process. Therefore, a clear understanding of the kinetics of the process, which includes the rate of feed consumption as well as the rate of product formation, is an ultimate requirement. However, a huge number of simultaneous chain reactions and the complicated reaction network of the FT process make it very stimulating to develop the kinetic model for the system. The detailed mechanistic modeling of FT reactions needs an understanding of complex reaction mechanisms. The knowledge is employed as a bridge to connect the experimental results with a complex mechanistic reaction network to predict the quantitative values of product formation rate and syngas consumption rate. The kinetics of the FT process always remains the topic of debate; however, continuous improvement has been observed in the models and their results. Still, substantial diversity is observed in the developed models. In the present chapter, recent knowledge addition and advancement in the kinetic modeling have been demonstrated. The step-wise development in the

Sonal (✉) · V. K. Saharan · S. George
Department of Chemical Engineering, Malaviya National Institute of Technology Jaipur, Jaipur, Rajasthan, India
e-mail: sonal.chem@mnit.ac.in

R. Bhoi
Department of Chemical Engineering, Malaviya National Institute of Technology Jaipur, Jaipur, Rajasthan, India

Department of Chemical Engineering, Indian Institute of Technology Bombay, Mumbai, Maharashtra, India

K. K. Pant
Department of Chemical Engineering, Indian Institute of Technology Delhi, New Delhi, Delhi, India

kinetic models and improvements in the results have been discussed. Mainly, the chapter presents a detailed review of the current status of FT kinetics and its link to the various prevailing mechanisms responsible for a wide range of FT products.

Keywords Fischer-Tropsch synthesis · Syngas conversion · FTS kinetics · FTS mechanism · Anderson-Schulz-Flory (ASF) model · Non-ASF model

1 Introduction

The rapid growth of population and the demand for liquid transportation fuels necessitates the search for its alternative production routes via non-oil-based processes. Limited oil reserves and their rapid depletion is also a major driving force to turn the research toward the sustainable route to produce liquid fuels. Strong interest has been received to revisit the X (gas to liquid process) to liquid (XTL) process. The XTL process can utilize any available hydrocarbon source material such as coal, natural gas, biomass, and waste material for the production of liquid energy carriers. The two-step XTL process includes feed to syngas conversion and subsequent conversion of syngas into liquid fuel. Fischer-Tropsch (FT) synthesis is a well-known and commercially viable process to convert syngas into a range of gaseous and liquid hydrocarbons. The huge spectrum of products makes the analysis of the process complex and cumbersome. A very simplistic form of a reaction network is shown below, indicating the formation of a range of hydrocarbons:

$$\text{Paraffin}: \quad n\text{CO} + (2n+1)\text{H}_2 \rightarrow \text{C}_n\text{H}_{2n+2} + n\text{H}_2\text{O} \tag{1}$$

$$\text{Olefin}: \quad n\text{CO} + 2n\text{H}_2 \rightarrow \text{C}_n\text{H}_{2n} + n\text{H}_2\text{O} \tag{2}$$

$$\text{Alcohols}: \quad n\text{CO} + 2n\text{H}_2 \rightarrow \text{C}_n\text{H}_{2n+1}\text{OH} + (n-1)\text{H}_2\text{O} \tag{3}$$

$$\text{Aldehydes}: \quad n\text{CO} + (2n-1)\text{H}_2 \rightarrow \text{C}_n\text{H}_{2n}\text{O} + n\text{H}_2\text{O} \tag{4}$$

$$\text{Carboxylic acids}: \quad n\text{CO} + (2n-2)\text{H}_2 \rightarrow \text{C}_n\text{H}_{2n}\text{O}_2 + (n-2)\text{H}_2\text{O} \tag{5}$$

$$\text{Water}-\text{gas shift}: \quad \text{CO} + \text{H}_2\text{O} \rightarrow \text{CO}_2 + \text{H}_2 \tag{6}$$
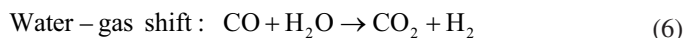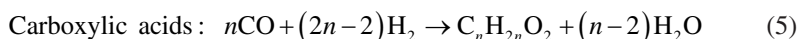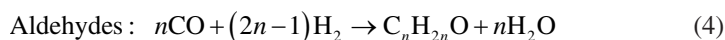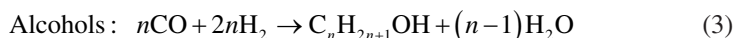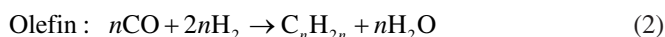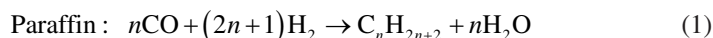
In the FT synthesis, the product selectivity depends on the reaction conditions and the catalyst selection. Immense research has been conducted and various catalysts have been studied on a laboratory scale for syngas conversion under the Fischer-Tropsch synthesis (FTS). However, only iron- and cobalt-based catalysts have qualified to be implemented at the commercial level. Iron-based catalysts are active for FTS as well as water gas shift reaction and hence can be implemented to convert syngas with low H_2/CO ratio. At the same time, iron is significantly cheaper than cobalt but has an attrition problem in the presence of water. On the contrary,

cobalt-based catalysts are highly active toward FTS reaction, and presence of water in the reaction does not strongly inhibit the FTS reaction. However, the cobalt-based catalyst is not active toward water gas shift reaction, hence requiring a stoichiometric ratio of H_2/CO (molar ratio ~ 2.0) for efficient conversion of syngas over the cobalt-based catalysts. The water-gas shift reaction (Eq. 6) is important in FTS synthesis, and the extent of reaction affects the overall distribution of H_2 and CO in the reactor. In the gas-to-liquid process, the molar ratio of H_2/CO of syngas is significant for efficient syngas conversion; therefore, the H_2 produced via water gas shift reaction is undesirable. On the contrary, syngas coming from carbon-rich sources, viz., coal, biomass, have a low H_2/CO ratio, and therefore, a H_2 booster reaction (WGS) is required in the reactor to maintain the required stoichiometric ratio. Thus, many commercial FTS plants based on natural gas (Shell and Sasol in Qatar) are using cobalt-based catalysts and coal-based plants are using iron-based catalysts [1, 2]. The selection of iron and cobalt catalysts also depends on the temperature of the FT reaction. Both iron and cobalt catalysts have been implemented in a low-temperature (180–260 °C) FT (LTFT) process and their major products are long-chain hydrocarbons and wax, whereas the products of a high-temperature (290–360 °C) FT (HTFT) process are short-chain hydrocarbons and gases. Iron is frequently used as a commercial catalyst for HTFT.

Kinetic modeling of the FTS process is an integral part of the analysis, and it is essential for reactor design, scale-up, and catalyst design for the process. Several kinetic models of the FTS reaction on iron and cobalt catalysts have been proposed and gained serious attention. The models were either empirical or based on different proposed mechanisms. However, the ambiguity was always there as the several rate expressions were conflicting and unacceptable. The reason was a multiple proposed mechanism and a complex reaction system. As discussed, the FT process has a large number of products wherein multiple reactions occur simultaneously and are sensitive to the reaction temperature, pressure, H_2/CO ratio, and catalyst selection. The detailed review of the kinetic models of the FTS reaction reported till date is essential to understand the ambiguity and to figure out the root cause of the prevailing conflict in the modeling path. Mainly, two approaches are chosen by various authors while performing FT kinetics. The first approach describes only the rate of consumption of reactants (syngas) either by implementing some empirical model or by applying mechanism derived lumped modeling [3–11]. The other approach aimed at the rate of formation of hydrocarbon or selectivity of products. In that regard, various selectivity models were proposed, and the term "chain growth probability" was introduced [12–19]. However, even though some researchers were able to predict the product distribution successfully, some classical models lacked in the accuracy or quantitative prediction with respect to actual experimental data. Overall, the reaction mechanism plays a vital role in the kinetic modeling of the FTS reaction.

The Fischer-Tropsch synthesis is considered as a polymerization reaction, in which the monomers in the form of CH_x ($x = 1, 2$ or 3) are produced as intermediate species. The proposed reaction pathways as found in literature mainly consisted of three different reactions, i.e., CO activation for the formation of chain initiator, chain growth or propagation, and chain-growth termination or desorption [20]. The

FT synthesis process is a complex reaction system yielding a spectrum of products and is difficult to predict a certain pathway of product formation. It differs along with the catalyst selection, physicochemical properties of the catalyst, and reaction conditions. Therefore, for each of the three steps, various mechanisms have been proposed and are chosen for model derivation based on catalyst selection and reaction condition (Fig. 1). As shown in Fig. 1, the two different approaches for kinetic model development are linked with the reaction mechanism. For example, the CO activation step or initiation step can be ascribed to an enol mechanism or carbide mechanism, wherein adsorbed CO reacts with hydrogen to form a chain initiator and intermediate species. The CO can be adsorbed associatively or dissociatively, and the dissociation can occur with the assistance or without the assistance of hydrogen. Also, the reaction of carbon monoxide with hydrogen occurs on the catalyst surface, wherein CO is in the adsorbed state. The state of hydrogen at the time of interaction with CO remains an open question. Depending on the catalyst and the process conditions, hydrogen may react from both being in the gas phase and adsorbed state on the catalyst surface. Similarly, the chain propagation steps can occur via alkenyl, alkyl, or CO insertion mechanisms.

The chapter presents an extensive review of the various pathways of model development to identify the rationale behind the selection of a particular reaction mechanism. It can also help to understand the link between various reaction mechanisms and the proposed kinetic models, which in turn can provide an opportunity for future research and development in the current field. The chapter will start with the detailed insights of various proposed mechanisms followed by the different approaches of kinetic modeling of FT reaction, viz., rate of consumption of CO, hydrocarbon selectivity models, and comprehensive kinetic models. The focus will also be on the limitation of the models and the approach. The chapter will conclude
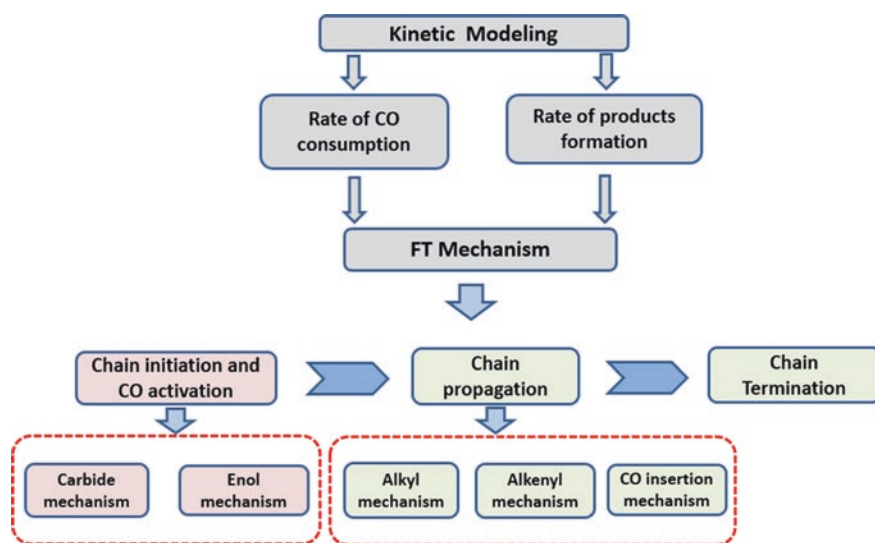
Fig. 1 Reaction mechanism

some recent implications of various model results, the shortcomings, and the advantage of the general mechanistic modeling approach of the Fischer-Tropsch reaction.

2   FTS Mechanism

Over the years, authors have proposed various mechanisms for the FTS process. In 1926, Fischer et al. proposed the carbide mechanism (Fig. 2) wherein the metal carbide was assumed to be intermediate. In this early mechanism, it was proposed that the carbon in the metal carbide phase hydrogenated to form CH_2 species, which further polymerized. Iron-based catalysts form stable carbides under the Fischer-Tropsch synthesis, but other metals active in the FT synthesis, such as cobalt and ruthenium, are not known to form carbides under typical FT synthesis conditions. Furthermore, a study by Kummer et al. [21] showed, using an iron catalyst pre-carbide with radioactively labeled ^{14}CO, that only a small fraction of the products were in the gasoil range (less than 4.2%). This indicates that the carbide phase might be dynamically involved in the FT synthesis, but that carbon in the product compounds does not solely originate from carbide. Hence, this mechanism was subsequently rejected. To justify the alcohol and aldehyde formation, Storch et al. [22] proposed the enol mechanism where hydrogen addition into adsorbed CO forms oxymethylene. In 1970, Pichler and Schulz [23] proposed the CO insertion theory, where CO was inserted to the growing alkyl chain, and $=CH_2$ was the chain growth intermediate. The alkyl theory is an extension of the carbide theory where CH_3 is the chain initiator, and CH_2 is an intermediate that is added to the growing chain successively. The detailed descriptions of the four most discussed mechanisms are explained in the next sections.
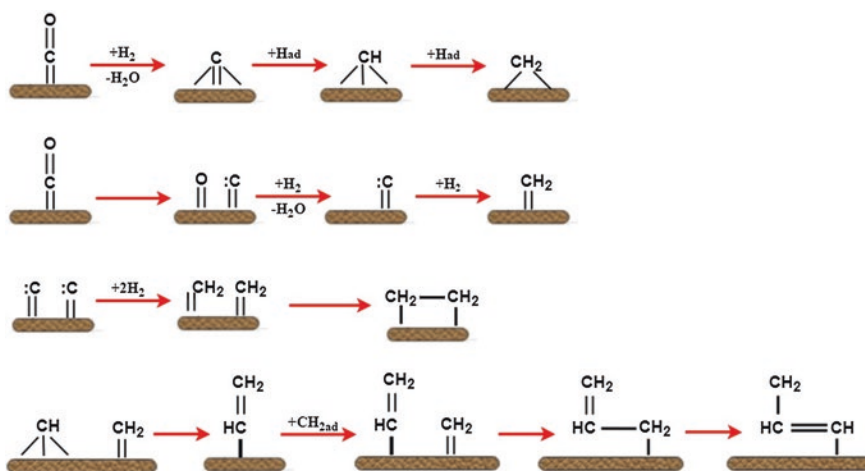
Fig. 2 Carbide mechanism

2.1   Alkyl Mechanism

The Alkyl mechanism is accepted by a large number of the research groups and has been used for deriving rate expressions for FTS reaction. The reaction initiation starts with the dissociative adsorption of CO where the generated surface oxygen is rejected as either water on reacting with hydrogen or CO_2 on reacting with CO. The surface carbon indulges in the formation of the CHX intermediates, viz., CH–, CH_2–, CH_3–, in the consecutive steps. Here –CH_3 is the chain initiator, and –CH_2– is chain propagation monomer. Hydrocarbons form via the successive insertion of these intermediates. In the next step, the growing chain terminates either via β-hydrogen elimination, yielding α-olefins, or hydrogenation producing alkanes [20, 24]. The hydrogen removal is a reversible reaction that enables the olefins to re-adsorb in the growing chain and takes part in the secondary product formation (Fig. 3).

The alkyl mechanism was a continuation of the carbide mechanism, and Brady and Pettit [20] experimentally confirmed the presence of the intermediates of the proposed mechanism. The authors tried to convert diazomethane (CH_2N_2) both in the presence and absence of hydrogen and found that ethene was the only product in case of conversion without hydrogen and that the presence of hydrogen yielded a spectrum of hydrocarbons similar to that of FTS reaction products. This, in turn, confirms that –CH_2– acts as a monomer in the polymerization process and is involved in long-chain hydrocarbon formation. The results also reveal that the hydrogenation step is important to form chain starter species –CH_3. The absence of long-chained hydrocarbons in the earlier case where hydrogen was not in the feed indicates that the CH to –CH_2– formation is an irreversible step; otherwise, the decomposition of adsorbed CH_2 species would yield CH and H, and the adsorbed H could be further used as a hydrogenating agent to facilitate the long change hydrocarbon. However, this was not evident in the product of the first case; hence, the transformation of CH to –CH_2– can be taken as an irreversible step.

The FT synthesis reaction also produces some amount of branched alkane and oxygenates. In the alkyl mechanism, the steps related to the branched alkanes and alcohols formation were not considered. Initially, it was proposed that the branched hydrocarbons result from olefin such as propene reinsertion; however, later, it was concluded that the amount of branched hydrocarbons from experimental results is more than expected from olefin reinsertion [20]. So the modification in the alkyl mechanism was incorporated by Schulz et al. [25] by the addition of some separate pathways. The additional path includes the reaction between surface methyl species (–CH_3) with alkylidene species (R-HC=), which was responsible for branched alkane formation. The probable formation path of alkylidene species is via the reaction of the alkyl group with surface methylidyne ($\equiv$CH). For the oxygenate formation, Johnston and Joyner [26] proposed the involvement of surface hydroxyl groups. They reported that the surface hydroxyl group reacts with an alkyl group to form the alcohols. However, there was a lack of experimental evidence for the same, i.e., the participation of surface hydroxyl groups in the formation of oxygenates.
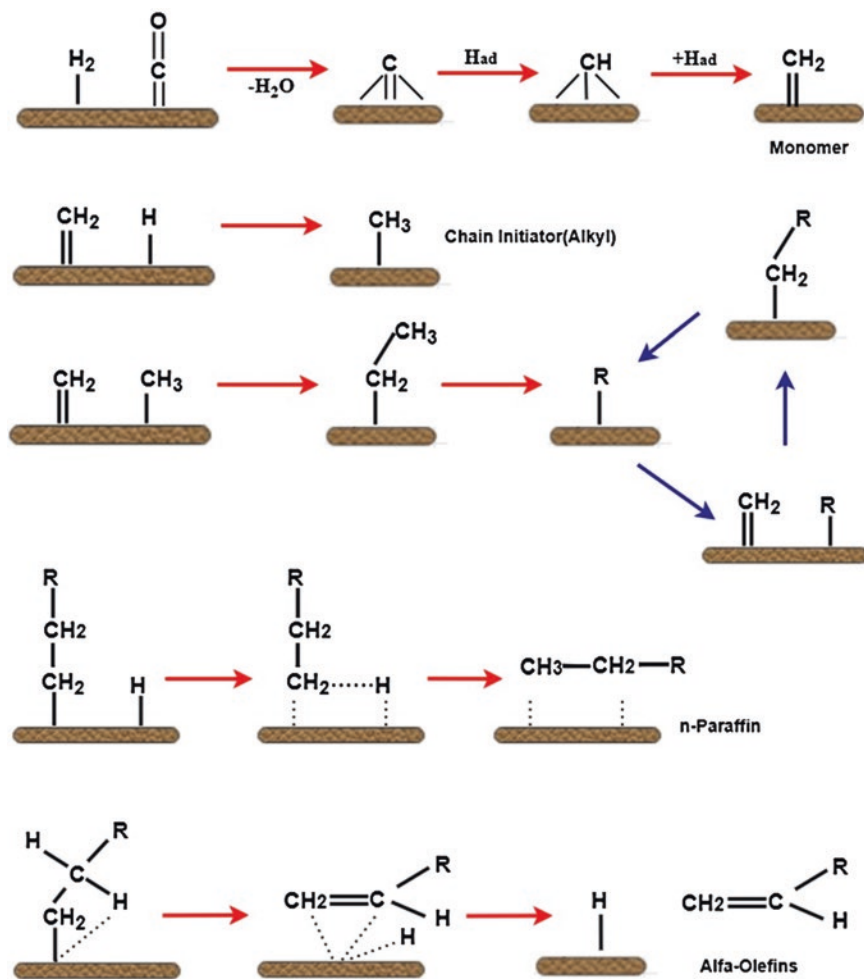
Fig. 3 Alkyl mechanism

2.2 Alkenyl Mechanism

In an alternative pathway to predict the olefin formation in the Fischer-Tropsch synthesis, Maitlis and co-workers [27–29] proposed negating the sp^3–sp^3 coupling of methylene species with methyl species as suggested in the "alkyl"-mechanism. The initial activation of CO is similar to the alkyl mechanism where carbon monoxide transforms into CH– surface species (Fig. 4). The vinyl group (CH=CH$_2$) is considered as a chain initiator, which is assumed to be formed through the connection of methylidyne ($\equiv$CH) and methylene (=CH$_2$). As the chain reaction proceeds, a surface allyl species (–CH$_2$CH=CH$_2$) forms via coupling of a methylene species
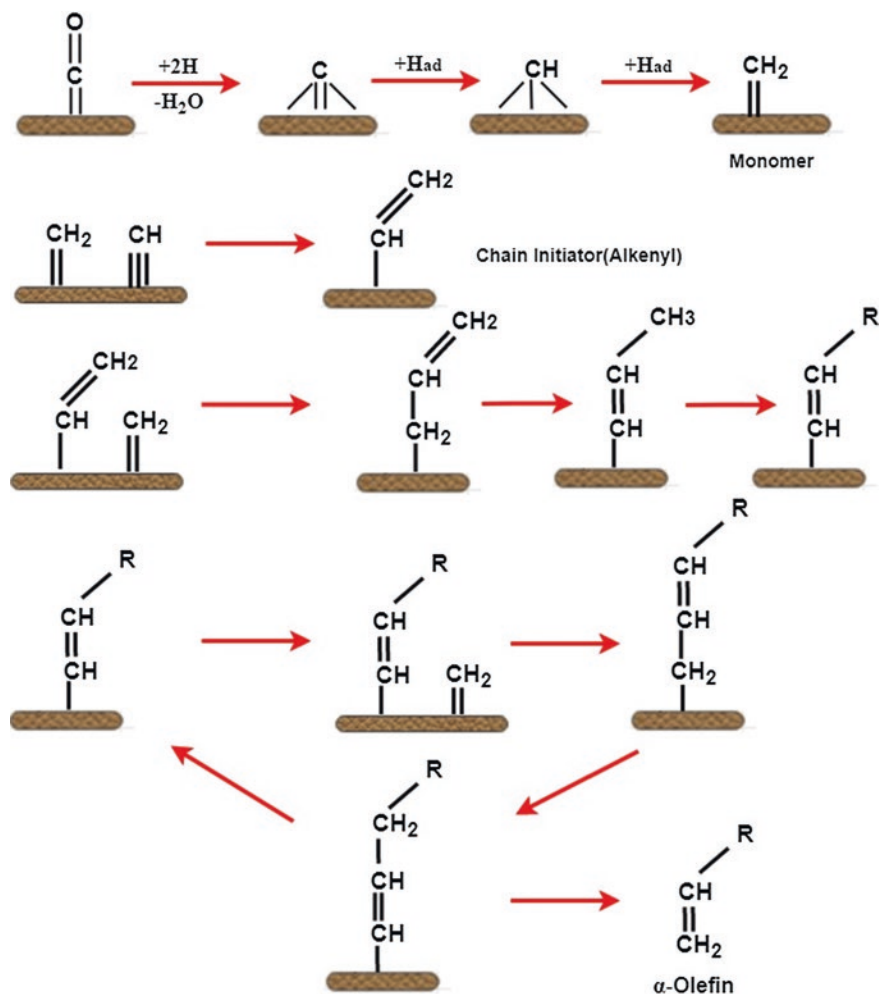
Fig. 4 Alkenyl mechanism

into a surface alkenyl-species (vinyl species). Further, the reaction proceeds by an allyl-vinyl isomerization forming an alkenyl species (–CH=CHCH₃) [30]. The product desorbs through hydrogen addition into an alkenyl, which ultimately forms α-olefins [31]. A very important product *n*-paraffin cannot be explained by this mechanism; therefore, the path for progression of linear chain paraffin is required as an alternative chain growth pathway.

2.3   Enol Mechanism

Storch et al. [32, 33] proposed the enol mechanism as an alternative path for product formation wherein oxygen-containing species called enol were involved in the mechanism. In the proposed mechanism, enol species form through hydrogenation of adsorbed CO. Chain growth occurs through a condensation reaction between oxygen-containing species (=CROH & = CHOH) with the release of a water molecule (Fig. 5). The occurrence of branched hydrocarbons is proposed to form with the involvement of branched alcohol –CHROH surface species [5, 34]. In the final step of chain growth, i.e., termination step, oxygenates (aldehydes and alcohols), and α-olefins are formed through desorption. From the theory of the mechanism, *n*-paraffin is not the primary product; it is a secondary product which forms by the hydrogenation of primarily formed olefins. The primary formation of *n*-paraffin would require an alternative reaction pathway. The mechanism gained strong support from Emmett et al. [35–39] through their results by detailed studies using ^{14}C-labeled alcohol in FT synthesis reaction. The ^{14}C-labeled alcohol was co-fed with syngas, and the distribution of isotopically labeled product confirms that the co-fed alcohol was able to initiate the chain growth.

2.4   CO Insertion Mechanism

The CO insertion mechanism was fully developed by Pichler, and Schulz [23], in which adsorbed CO is proposed to be a monomer of the reaction. The chain initiates through the surface methyl group. The step of oxygen elimination from the surface of oxygen-containing species is the crucial point at which it differentiates the CO insertion mechanism from the alkyl mechanism. The chain propagates via the CO insertion into the metal alkyl bond, yielding a surface acyl species (–C–OR). Oxygen is eliminated from the acyl species in the form of water and enlarged alkyl species (Fig. 6). The products, viz., *n*-paraffin and α-olefins paths are similar to those proposed in the alkyl mechanism, i.e., hydrogenation or β-hydrogen elimination. Oxygen-containing species terminate directly to form alcohols and aldehydes. Hydrogen addition to an acyl species will lead to aldehyde formation. The formation of ketones is proposed to occur through the addition of a surface alky group to the acyl species. Many researchers reported the "CO insertion" mechanism as the particular pathway responsible for the formation of oxygenates [40, 41].

Initiation:
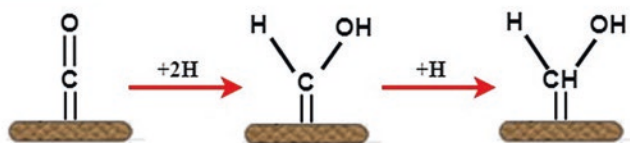
Propagation
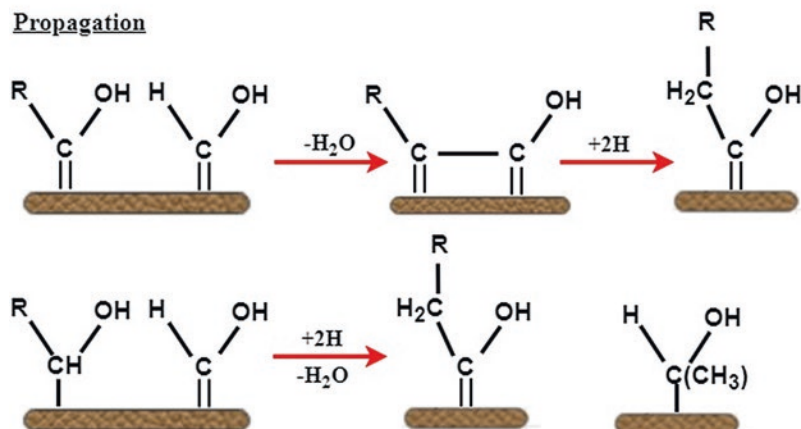
Termination
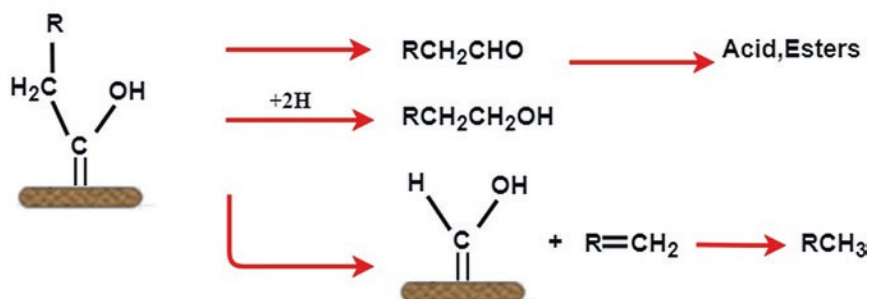
Fig. 5 Enol mechanism

3 FT Synthesis Kinetics

Due to the complex reaction network, various groups of researchers have taken a different approach in describing the kinetic model for the system with decreased intricacy. As discussed earlier, mainly, two approaches were taken for the FT synthesis kinetics, which leads to various empirical, semi-empirical, mechanistic, and semi-mechanistic rate expressions. The mechanistic approach, models, was developed using the LHHW method, and the focus was mainly to predict the rate of consumption of feed gas. FT synthesis mechanism explained in Sect. 2 is selected to derive the model based on the results of best-fitted models. Most of the reported

Initiation:
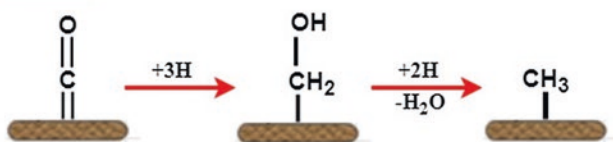
Propagation
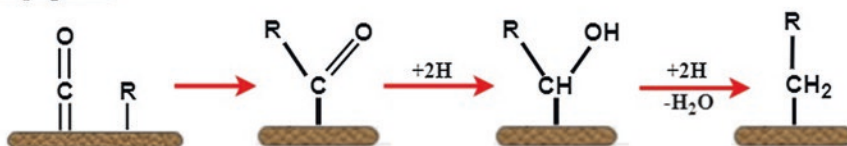
Termination
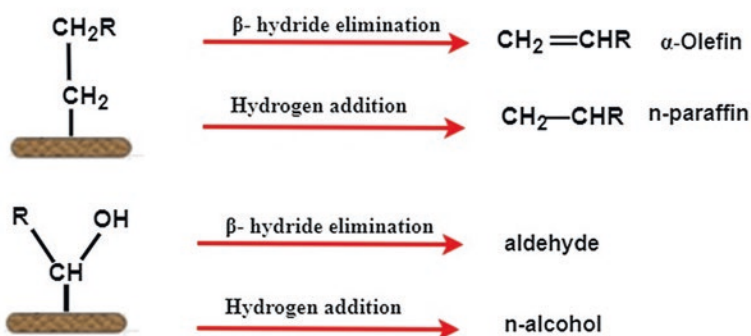
Fig. 6 CO insertion mechanism

mechanistic and semi-mechanistic modeling focuses on the rate of syngas conversion. Moreover, the recently reported studies have a detailed, comprehensive kinetic model that was able to predict the syngas consumption rate as well as the rate of formation of products. The next section will present a detailed insight into both the approaches.

3.1 FT Kinetic for the Rate of Syngas Consumption

Since the 1950s, various studies have been published related to kinetic study over iron [3–5, 7, 28, 42–54] and cobalt [10, 29, 50, 55–64] catalysts. Some proposed mechanisms have been found in literature, and there is a lack of consensus among the authors. In a majority of the kinetics works over iron catalysts, the rate expression is represented as a function of the concentration of CO and H_2. Moreover, the discrepancy related to the inhibition term (H_2O and CO_2) always remained there.

The dissimilarities among the rate expressions existed due to some major reasons, viz., use of the different catalyst systems and a wide range of operating conditions. Also, the selection of catalyst severely affects the rate of CO consumption and the product selectivity, which eventually affects the kinetics of the whole process. For example, iron and cobalt catalysts show a different mechanism for CO activation. In addition to this, a high affinity of iron catalysts for the WGS reaction leads to the inclusion of H_2O and/or CO_2 as an inhibition term in the developed model. In the present chapter, the synergetic effect of the selection of iron, cobalt, or bimetallic catalysts for the kinetics of the FT synthesis reaction is summarized. The objective is to select the prevailing mechanisms through detailed kinetic modeling of the reaction over different catalysts. Table 1 summarizes the current knowledge of kinetic modeling on the Fe, Co catalysts in order to understand the strengths and weaknesses of works, which includes the mechanistic path for CO activation, the effect of CO_2 or H_2O inhibition, and the WGS activity of the catalyst.

3.1.1 CO Activation Path over Iron and Cobalt Catalyst

A series of reactions occur in the FT synthesis process, which follows various routes to produce a series of products. There is a significant role of reaction mechanism in the prediction of a more accurate and reliable rate model. The FT reaction is a structure-sensitive reaction, and it is connected to the structural properties of the catalysts. The FT synthesis reactions and product formation occur via three consecutive steps, viz., CO activation, chain propagation, and chain termination. There are several proposed mechanisms for these steps. However, the selection of more accurate mechanisms over the selected catalysts (Fe-Co) is required to perform the kinetic study. The CO gets consumed in the initial stage of reaction, i.e., activation step wherein CO adsorption, dissociation, and monomer formation occur. Various reported literature confirmed that CO activation is slowest among all steps and hence can be used for the kinetic modeling [80]. The desorption step is liable to control the chain length, i.e., the product distribution [50]. The initiation of reaction is fueled by dissociative or associative CO adsorption over the site. Table 1 represents a collective description of the various developed models and their selected CO activation mechanism for model derivation. The detailed analysis (Table 1) reveals that over the cobalt surface, the CO activation takes place via a dissociative path and then interacts with either molecular hydrogen or adsorbed hydrogen [9, 10, 29, 50, 62, 70, 72, 81], whereas iron [4, 42, 54, 66, 68, 82] favors hydrogen-assisted CO adsorption. A density functional theory (DFT)–based study reported that direct CO dissociation is a favored mechanism at corrugated or stepped cobalt surfaces. And H_2-assisted CO dissociation and adsorption is facilitated over a low reactive site like iron carbide, which is a proven active site for FT synthesis [83, 84]. Van Dijk [85] reported the evidence of the formation of C1 intermediate over cobalt, which polymerizes to form long-chain hydrocarbons. However, there was always some disagreement among the authors over the CO activation path over a similar catalyst (i.e., iron or cobalt based). For example, Okeson et al. [69] revealed in their study that the

Table 1 Published kinetic models on FT synthesis

Model	Catalyst	Reaction conditions	(i) H₂O inhibition	(ii) CO₂ inhibition	(iii) WGS reaction	(iv) Unassisted CO dissociation	(v) H₂-assisted CO dissociation	References
$r_{FT} = aP_{H_2}^{0.6} P_{CO}^{0.4} - fP_{H_2O}^{0.5} r_{FT}^{0.5}$	Reduced nitride Fe	T:225–240 °C P:2.2 MPa H₂/CO: 0.25–2	√				√	Anderson et al. [65]
$r_{FT} = k_{FT} \dfrac{P_{H_2} P_{CO}}{P_{CO} + aP_{H_2O}}$	Precipitated Fe	T:200–340 °C P:0.5–4 MPa H₂/CO:1.7–3.0	√		√		√, adsorbed CO reacts with molecular H2	Dry at al [66].
$r_{FT} = k_{FT} \dfrac{P_{H_2} P_{CO}}{P_{CO} + aP_{H_2O}}$	Nitride fused Fe/K₂O/Al₂O₃/ SiO₂	T:215–315 °C P: 2 MPa H₂/CO: 2	√				√	Atwood et al. [67]
$r_{FT} = \dfrac{kP_{H_2}^2 P_{CO}}{\left(P_{H_2} P_{CO} + bP_{H_2O}\right)}$	Reduced fused Fe/K₂O/CaO/ SiO₂	T:232–263 °C P: 0.4–1.5 MPa H₂/CO: 0.5–1.8	√					Huff and Satterfield [5]
$r_{FT} = \dfrac{kP_{H_2}^{0.5} P_{CO}}{\left(1+ aP_{CO} + bP_{H_2O}\right)^2}$	Fe/Cu/K/SiO₂	T:250 °C P: 1.2–4 MPa H₂/CO: 0.8–4	√		√		√	Vander Laan et al. [19]
$r_{FT} = \dfrac{kP_{H_2} P_{CO}}{\left(1+ aP_{CO} + bP_{H_2O}\right)^2}$	Fe/Cu/K/SiO₂	T:250 °C P: 1.2–4 MPa H₂/CO: 0.8–4	√		√		√	VanderLaan et al. [19]
$r_{FT} = \dfrac{kP_{H_2} P_{CO}}{\left(1+ aP_{CO} + bP_{H_2O}\right)}$	Fe/Cu/K/SiO₂	T:250 °C P: 1.2–4 MPa H₂/CO: 0.8–4	√		√		√, adsorbed CO reacts with molecular H2	VanderLaan at al [19].
$r_{FT} = k_{FT} \dfrac{P_{H_2} P_{CO}}{P_{CO} + aP_{CO_2}}$	Reduced precipitated Fe/K	T:220–260 °C P:1 MPa H₂/CO: 0.5–0.6		√	√		√adsorbed CO reacts with molecular H2	Ledakowicz et al. [4]

(continued)

Table 1 (continued)

Model	Catalyst	Reaction conditions	(i) H2O inhibition	(ii) CO2 inhibition	(iii) WGS reaction	(iv) Unassisted CO dissociation	(v) H2-assisted CO dissociation	References
$r_{FT} = \dfrac{kP_{H_2}^2 P_{CO}}{\left(P_{H_2}P_{CO}+bP_{H_2O}\right)}$	Reduced precipitated Fe/K	T: 220–260 °C P: –H2/CO: 0.5–2	√				√	Deckwer et al. [68]
$r_{FT} = \dfrac{kP_{H_2}^{0.5} P_{CO}}{\left(1+aP_{CO}\right)^2}$	Fe-based catalyst	T: 260 °C P: 1.0–3.0 MPa H2/CO: 0.8–3.2			√		√ adsorbed CO reacts with dissociated H2	Zhou et al. [54]
$r_{FT} = \dfrac{kP_{H_2}P_{CO}}{\left(1+aP_{CO}\right)}$	Fe based catalyst	T: 260 °C P: 1.0–3.0 MPa H2/CO: 0.8–3.2			√		√, adsorbed CO reacts with molecular H2	Zhou et al. [54]
$r_{FT} = \dfrac{kP_{H_2}^{0.5} P_{CO}}{\left(1+aP_{CO}+bP_{H_2O}\right)^2}$	Prec. Fe	T: 220–260 °C P: 0.5–4 H2/CO: 0.5–2	√				√	Botes et al. [42]
$r_{FT} = \dfrac{kP_{CO}^{0.5} P_{H_2}^{0.875}}{\left(1+aP_{CO}^{0.5}\right)^2}$	FeCuK/AlSi	T: 250 °C P_{H_2}: 0.2–0.9 MPa P_{CO}: 0.3–0.89 H2/CO: 0.7–1.5				√		Okeson et al. [69]
$r_{FT} = \dfrac{kP_{CO}^{0.5} P_{H_2}}{\left(1+aP_{CO}^{0.5}+bP_{H_2}^{1.5}\right)}$	Co/alumina	T: 250 °C P: 0.015–0.1 H2/CO: 0.25–5				√		Outi et al. [59]
$r_{FT} = \dfrac{kP_{CO}^{0.5} P_{H_2}^{0.5}}{\left(1+aP_{CO}^{0.5}+bP_{H_2}^{0.5}\right)^2}$	Co/Kieselguhr	T: 190 °C P: 0.2–1.5 H2/CO: 0.5–8.3				√		Sarup and Wojciechowski [70]

Model	Catalyst	Reaction conditions	(i) H₂O inhibition	(ii) CO₂ inhibition	(iii) WGS reaction	(iv) Unassisted CO dissociation	(v) H₂-assisted CO dissociation	References
$r_{FT} = \dfrac{kP_{CO}P_{H_2}^{0.5}}{\left(1+aP_{CO}+bP_{H_2}^{1.5}\right)^2}$	Co/Kieselguhr	T: 190 °C P: 0.2–1.5 H₂/CO: 0.5–8.3				√		Sarup and Wojciechowski [70]
$r_{FT} = \dfrac{kP_{H_2}P_{CO}}{\left(1+aP_{CO}\right)^2}$	Co/MgO/SiO₂	T: 220–240 °C P: 1.5–3.5 H₂/CO: 1.5–3.5				√		Yates and Satterfield [9]
$r_{FT} = \dfrac{kP_{H_2}P_{CO}}{P_{CO}+aP_{H_2O}}$	Prep Co/MnO₃	T: 210–250 °C P: 0.6–2.6 MPa H₂/CO: 1.6–4.1	√		√		√	Keyser et al. [57]
$r_{FT} = \dfrac{kP_{H_2}^{0.74}P_{CO}}{\left(1+aP_{CO}\right)^2}$	Co/TiO₂	T: 180–240 °C P: 2.06 MPa H₂/CO: 1–3.5				√		Zonnero et al. [62]
$r_{FT} = \dfrac{kP_{H_2}^2 P_{CO}}{P_{CO}P_{H_2}+aP_{H_2O}}$	Co/Zr/SiO₂	T: 220–280 °C P: 2.1 MPa H₂/CO: 0.5–2	√			√		Withers et al. [10]
$-r_{FT} = \dfrac{kP_{H_2}P_{CO}}{\left(1+bP_{CO}P_{H_2}^{0.5}\right)^2}$	Co/Ni/Al₂O₃ catalyst	T: 230–270 °C P:0.2–1.2 MPa H₂/CO: 1–3					√, CO dissociates via interaction with H	Fazlollahi et al. [71]
$-r_{FT} = \dfrac{kP_{H_2}^{0.75}P_{CO}^{0.5}}{\left(1+bP_{CO}^{0.5}\right)^2}$	Co/Pt/Al₂O₃	T: 230–270 °C P: 0.5–4 MPa H₂/CO: 1.6–3.2				√		Botes at al [72].
$-r_{FT} = \dfrac{kP_{H_2}^{0.98}P_{CO}^{0.5}}{\left(1+bP_{CO}^{0.5}\right)^2}$	Co–Ru/γ-Al₂O₃	T: 200–240 °C P: 2–3.5 MPa H₂/CO: 1–2.5				√		Sari et al. [29]

(continued)

Table 1 (continued)

Model	Catalyst	Reaction conditions	(i) H₂O inhibition	(ii) CO₂ inhibition	(iii) WGS reaction	(iv) Unassisted CO dissociation	(v) H₂-assisted CO dissociation	References
$r_{FT} = \dfrac{k\left(P_{CO}^{-0.2} P_{H_2}^{0.5}\right)}{\left(1+0.93\left(\dfrac{P_{H_2O}}{P_{H_2}}\right)\right)}$	Co/Al₂O₃	T: 220 °C P: 1.99 MPa H₂/CO: 1–2.4	√					Das et al. [73]
$r_{FT} = \dfrac{k\left(P_{CO} P_{H_2}^{1.5}/P_{H_2O}\right)}{\left(1+a\left(\dfrac{P_{CO}P_{H_2}}{P_{H_2O}}\right)\right)^2}$	Fe, Co	T: 190–310 °C P_{H_2}: 0.01–1.93 P_{CO}: 0.05–2.54	√			√		Van Steen and Schulz [50]
$-r_{CO} = \dfrac{kP_{CO}^a P_{H_2}^b}{\left(1+dP_{CO_2}+cP_{H_2O}\right)}$	Fe, Co	Generalized Model	√	√	√			Ma et al. [74]
$-r_{CO} = \dfrac{kP_{CO}P_{H_2}^{0.75}}{\left(1+aP_{CO}\right)^2}$	Fe, Co	Generalized Model						Mousavi et al. [75]
$-r_{FT} = \dfrac{k*a*b*P_{CO}P_{H_2}}{\left(1+2(aP_{CO})^{0.5}\right)^2}$	Nano-structured Fe-Co-Ce	T:250–330 °C P: 0.2–1.0 MPa H₂/CO:1				√		Eshraghi et al. [76]
$-r_{FT} = \dfrac{k*a*b*P_{CO}P_{H_2}}{\left(1+2(aP_{CO})^{0.5}+bP_{H_2}\right)^3}$	Fe-Co-Mn catalyst	T:220–250 °C P: 0.5–2.0 MPa H₂/CO:0.67–2.0				√		Mirzei et al. [77]
$-r_{FT} = \dfrac{k*a*b*P_{CO}P_{H_2}}{\left(1+aP_{CO}+bP_{H_2}\right)^2}$	Fe-Co-Ni	T:250–270 °C P: 0.1–0.7 MPa H₂/CO: 1–2.5					√	Mirzei et al. [78]
$r_{FT} = \dfrac{kP_{CO}P_{H_2}^{1/2}}{\left(1+aP_{CO}+bP_{H_2}^{1/2}\right)^2}$	Fe-Co/SiO₂	T:200–280 °C P: 1.0–3.0 MPa H₂/CO: 0.5–2.5					√, CO dissociates via interaction with H	Pant et al. [79]

mechanism-based on H_2-unassisted CO activation and adsorption used to develop the rate model and the model gave satisfactory results with the data over iron-based catalyst. On the other hand, Fazlollahi et al. [71] reported an opposite result over a cobalt-based catalyst. According to the author, the model based on hydrogen-assisted CO dissociation significantly fits the experimental data. Various reported rate models based on the Langmuir–Hinshelwood–Hougen–Watson (LHHW) approach and some empirical rate models were validated by Keyser et al. [57]. Their study revealed that the model based on the enolic mechanism was a more significant result and fitted the data more accurately than the models based on the carbide mechanism. Hence, the selection of the CO activation path for model derivation is a crucial step while modeling the development of the rate of CO consumption. Table 1 represents a fair idea of the selected reaction path for model development over iron and cobalt catalysts.

3.1.2 H_2O and CO_2 Inhibition

It is evident in Table 1 that H_2O inhibition is present in almost all the previous models derived for the iron catalyst. However, some authors [4] tried to include the CO_2 inhibition term, and a few models [54, 69] included none of them (neither CO_2 nor H_2O). Anderson et al. [86] related the rate of FT synthesis reaction to a function of PH_2 and PCO with the reasoning that CO and H_2O compete for the active sites and ultimately saturate the catalyst surface. Here H_2 reacts in molecular form. Attwood et al. [67] used their data to illustrate Anderson's model and found that H_2O works as an inhibiting term at a higher temperature. Van Steen et al. [50] also used the H_2O inhibition term and derived a model with a second-order denominator, which indicates the implication of vacant sites in the kinetics. Van der Laan et al. [87] derived some rate equation considering mechanistic insights of adsorption of CO and H_2, and observed that the water and vacant sites are equally important when the catalyst is iron-based (Fe/Cu/K). In their Langmuir–Hinshelwood–Hougen–Watson (LHHW)–type model, the rate was observed to be half or first order in H_2. However, few researchers emphasized the importance of CO_2 inhibition when the catalyst is iron-based [4, 54, 68]. Ledakowicz et al. [4] added the CO_2 inhibition term in the extended model of Huff and Anderson with the reason that over Fe/K catalysts, the water-gas shift (WGS) reaction is so high that the most of the H_2O is converted into CO_2. They concluded that a significant CO_2 inhibition effect was present over K-promoted iron catalysts, and the order of the adsorption coefficient of CO_2 was similar to that of CO ($KCO_2/KCO \sim 1.1$ at 220 °C). Later Deckwer et al. [68] illustrated that the model by Ledakowicz et al. is valid when the H_2O concentration is low or H_2/CO is less than 0.8. Zhou et al. [54] developed the model for the Fe catalyst considering hydrogen-assisted CO dissociation and emphasized the importance of site balance. They tried to incorporate the CO_2 inhibition term along with H_2O. However, they confirmed that the H_2O and CO_2 inhibition terms could be ignored even if the concentration of CO_2 is high, and the concentration of CO and vacant sites are most important parameters while deriving the model. On the same

note, Yates et al. [88] also examined the effect of CO_2 concentration on the kinetics of the FT reaction by adding 20–50% CO_2 in the feed gas and observed that the data is well fitted with a model consisting of the H_2O inhibition term but not for CO_2. Botes et al. [42] also attempted to clarify the ambiguity related to the inhibition term in the kinetic study over the iron catalyst. Their model consists of water, CO, and vacant sites in the squared denominator, which implicated the assumption of a dual site mechanism. However, while validating the model with historical data, the effect of water was observed to be statistically insignificant.

Kinetic studies over cobalt-based catalysts have also received significant attention and are available in the open literature [10, 29, 50, 55–64, 73]. Most of the kinetic rate expressions derived for cobalt came from regression analysis of simple power-law expressions [9, 60, 61]. However, some of them were derived, incorporating the mechanistic pathway with the assumption made regarding the rate-determining step. Unlike Fe catalysts where generally water is accepted as an inhibitor, there is an ambiguity about the role of water over cobalt catalysts. In most of the models (Table 2), the rate of consumption of CO is a function of the partial pressures of CO and H_2 [9, 29, 62, 70–72, 81]. Sari et al. [29] tested five important models (empirical and mechanistic) in which all have incorporated CO inhibition term due to strong CO adsorption on Co–Ru/γ-Al_2O_3 catalysts. The model developed by Sarup and Wojciechowski was found to be a best-fitted model among all the five models and concluded that $-R_{FT} = -R_{co}$ because of the trivial contribution of the WGS reaction. While investigating the kinetics of FT synthesis on commercial cobalt with syngas containing CO, CO_2, H_2, and H_2O, Kaisar et al. [56] observed that CO_2 and H_2O showed negligible or minor influence on the reaction rate. Some authors [10, 57, 73] noted that in the case of cobalt, water also plays an equally important role as CO and H_2. Keyser et al. [57] investigated to establish an integral reactor model involving both the Fischer-Tropsch and the water-gas shift reaction kinetics over Co-MnO catalysts. They claimed that the Co-MnO behaves like a precipitated iron catalyst, and an empirical rate equation for the water-gas shift reaction showed the first-order dependence for CO_2 and H_2O. Das et al. [73] investigated the effects of water on the kinetics of the FT synthesis reaction by adding external water with the feed (<25 vol%) over Co/Al_2O_3 catalysts in a CSTR. Regarding the negative reversible effect of water in the kinetics, their kinetic data was reasonably fitted by a semi-empirical power-law expression with the water inhibition term. Very recently, Ma et al. [74] reviewed the previous kinetic studies done in the last three decades over iron and cobalt catalysts and proposed a generalized model. They argued that the data point at low (<70%) and high conversion level (>70%) was used to fit the models differently and should be treated separately. They tried to fit their 83 sets of data points on the previous as well as this generalized kinetic model and found that the different kinetic parameters were obtained for lower and higher conversion data. Again, their reasoning for this was based on the inhibition effects of CO_2 and H_2O, which are different at two-levels of conversions. Also, the strong water absorption and the presence of CO_2 as the most abundant species cannot be ignored. Other important and contradictory observations were made, and the water inhibition on the FT synthesis rate was insignificant over the entire range of

Table 2 Published comprehensive kinetic models for rate of product formation

Rate expression	Reaction condition	References
$R_{CH_4} = k_{5M} P_{H_2} \sqrt{K_0 P_{H_2}}\, \alpha_1 [*]$ $R_{C_nH_{2n+2}} = k_5 P_{H_2} \sqrt{K_0 P_{H_2}} \sum_n \prod_i^{i=1\ j=1} \alpha_j [*]\quad n \geq 2$ $R_{C_nH_{2n}} = k_6 \sqrt{K_0 P_{H_2}} \sum_n \prod_i^{i=1\ j=1} \alpha_j (1-\beta_n)[*]\quad n \geq 2$ $[*] = \dfrac{1}{1+\sqrt{K_0 P_{H_2}} + \left(1 + \dfrac{P_{H_2O}}{K_3 K_2 K_4 P_{H_2}^2} + 1/K_4 K_4 P_{H_2} + \dfrac{1}{K_4}\right)\sqrt{K_0 P_{H_2}} \sum_{i=1}^n \left(\prod_{j=1}^i \alpha_j\right)}$ $\alpha_1 = \dfrac{k_1 P_{CO}}{k_1 P_{CO} + k_{5M} P_{H_2}}\quad (n=1)$ $\alpha_n = \dfrac{k_1 P_{CO}}{\left(k_1 P_{CO} + k_5 P_{H_2} + k_6 (1-\beta_n)\right)}\quad (n \geq 2)$ $\beta_n = \dfrac{k_6^- P_{C_nH_{2n}}}{k_6\left(\alpha_A^{n-1} \dfrac{k_1 P_{CO}}{k_1 P_{CO} + k_5 P_{H_2}} + \dfrac{k_6^- \sum_{i=2}^n \alpha_A^{i-2} P_{C_{n-i+2}H_{n-i+2}}}{k_1 P_{CO} + k_5 P_{H_2} + k_6}\right)}$ $\alpha_A = \dfrac{k_1 P_{CO}}{\left(k_1 P_{CO} + k_5 P_{H_2} + k_6\right)}$	Fixed bed reactor T—220–270 °C P—1.1–3.1 MPa, H$_2$/CO-1.0–3.0	Wang et al. [51]

Table 2 (continued)

Rate expression	Reaction condition	References
	Reduced Fe-Mn Fixed bed reactor T—267–327 °C P—1.0–3.0 MPa, H_2/CO-1.0–3.0	Yang et al. [53]

$$R_{CH_4} = k_{7M} K_4 K_6 K_3 \left(\frac{P_{H_2}^3 P_{CO}}{P_{H_2O}} \right) [*]^2$$

$$R_{C_nH_{2n+2}} = k_7 K_4 K_6 K_3 \left(\frac{P_{H_2}^3 P_{CO}}{P_{H_2O}} \right) \left(\prod_n^{j=2} \alpha_j \right) [*]^2 \quad n \geq 2$$

$$R_{C_nH_{2n}} = k_8^+ (1-\beta_n) \prod_n^{j=2} \alpha_j [*] \quad n \geq 2$$

$$[*] = \cfrac{1}{1 + \sqrt{K_4 P_{H_2}} + K_1 P_{CO} + K_2 K_1 P_{CO} P_{H_2} + \cfrac{K_3 P_{H_2}^2 P_{CO}}{P_{H_2O}} + \cfrac{K_6 K_4^{0.5} K_3 P_{H_2}^{2.5} P_{CO}}{P_{H_2O}} + \cfrac{K_6 P_{H_2}^2 P_{CO}}{P_{H_2O}} \left(1 + K_6 \sqrt{K_4 P_{H_2}}\right) \sum_n \left(\prod_i^{j=2} \alpha_j \right)}$$

$$\alpha_n = \cfrac{\left(k_5 K_3 P_{CO} P_{H_2}^2 / P_{H_2O}\right)}{\left(k_5 K_3 P_{CO} P_{H_2}^2 / P_{H_2O}\right) + k_7 K_6 K_4 P_{H_2} + k_8^+ (1-\beta_n)/[*]} \quad n \geq 2$$

$$\alpha_A = \cfrac{\left(k_5 K_3 P_{CO} P_{H_2}^2 / P_{H_2O}[*]\right)}{\left(k_5 K_3 P_{CO} P_{H_2}^2 / P_{H_2O}[*]\right) + k_7 K_6 K_4 P_{H_2} [*] + k_8^+} \quad n \geq 2$$

$$\beta_n = \cfrac{k_8^- P_{C_nH_{2n}}}{k_8^+ \alpha_A^{n-1} \cfrac{K_3 P_{CO} P_{H_2}^2}{P_{H_2O}} + \cfrac{k_8^- \sum_{i=2}^n \alpha_A^{i-2} P_{C_{n-i+2}H_{2n-i+2}}}{\left(k_5 K_3 P_{CO} P_{H_2}^2 / P_{H_2O}[*]\right) + k_7 K_6 K_4 P_{H_2} [*] + k_8^+}}$$

Rate expression	Reaction condition	References
$R_{CH_3OH} = k_{9,1} K_1 K_4 K_7 K_8 P_{CO} P_{H_2}^2 [*]^2$ $R_{CH_4} = k_{11,1} K_2 P_{H_2} \alpha_{T,1} [*]^2$ $R_{C_nH_{2n+1}OH} = k_9 K_1 K_4 K_7 K_8 P_{CO} P_{H_2}^2 \prod_{n-1}^{i=1} \alpha_{T,i} [*]^2$ $R_{C_nH_{2n-1}OOH} = \dfrac{k_{10} K_1 K_7 P_{CO} P_{H_2O}}{K_6} \prod_{n-1}^{i=1} \alpha_{T,i} [*]^2$ $R_{C_nH_{2n+2}} = k_{11} K_4 P_{H_2} \prod_{n-1}^{i=1} \alpha_{T,i} [*]^2$ $R_{C_nH_{2n}} = k_{12} \sqrt{K_4 P_{H_2}} \prod_n^{i=1} \alpha_{T,i} (1-\beta_n)][*]$ $\beta_n = \dfrac{k_{10}^- P_{C_nH_{2n}} \sqrt{K_4 P_{H_2}} [*]}{k_{10} \sqrt{K_4 P_{H_2}} \prod_{i=1}^n \alpha_{T,i} [*]}$ $[*] = \dfrac{1}{\left(\begin{array}{c} 1 + + K_1 P_{CO} + \sqrt{K_4 P_{H_2}} + K_1 K_7 P_{CO} \sqrt{K_4 P_{H_2}} + K_1 K_7 K_8 P_{CO} P_{H_2} \sqrt{K_4 P_{H_2}} + \dfrac{K_6 K_4 K_2 K_1 P_{H_2} P_{CO}}{P_{H_2O}} + \dfrac{K_6 K_4 K_3 K_2 K_1 P_{H_2}^2 P_{CO}}{P_{H_2O}} \\[2mm] + \sqrt{K_4 P_{H_2}} \sum_{i=1}^n \prod_{i=1}^i \alpha_{T,i} \left(1 + K_1 K_7 K_8 P_{CO} P_{H_2} \sqrt{K_4 P_{H_2}} + K_1 K_7 P_{CO} \sqrt{K_4 P_{H_2}} + K_1 K_7 P_{CO} \sqrt{K_4 P_{H_2}} \right) \\[2mm] + \dfrac{P_{H_2O}}{K_6 \left(\sqrt{K_4 P_{H_2}} \right)} \end{array}\right)}$	Fe/Mn and Fe/Cu/K Spinning basket reactor T—260–300 °C P—1.1–2.6 MPa, H₂/CO-0.67–2.05	Teng et al. [89]

Table 2 (continued)

Rate expression	Reaction condition	References
(see equations below)	Fe-Co/SiO$_2$ Fixed bed reactor	Pant et al. [90]

$$R_{CH_4} = k_{9Me}\,\alpha_1 K_4 P_{H_2}\,[*]^2$$

$$R_{C_nH_{2n+2}} = k_9 K_4 P_{H_2} \prod_n^{i=3} \alpha_1 \alpha_2 \alpha_i\,[*]^2 \quad n \geq 2$$

$$R_{C_2H_4} = k_{10E}\,e^{2\theta} \sqrt{K_4 P_{H_2}}\,\alpha_1 \alpha_2\,[*]$$

$$R_{C_nH_{2n}} = k_{10}\,e^{n\theta} \sqrt{K_4 P_{H_2}} \prod_n^{i=3} \alpha_1 \alpha_2 \alpha_i\,[*] \quad n \geq 3$$

$$[*] = \frac{1}{\left(1 + \sqrt{K_4 P_{H_2}} + K_1 P_{CO} + K_2 K_1 \sqrt{K_4 P_{H_2}}\,P_{CO} + \dfrac{K_4 K_3 K_2 K_1 P_{H_2} P_{CO}}{K_5 P_{H_2O}} + \dfrac{K_6 K_4^{1.5} K_3 K_2 K_1 P_{H_2}^{1.5} P_{CO}}{K_5 P_{H_2O}} + \dfrac{K_7 K_6 K_4^2 K_3 K_2 K_1 P_{H_2}^2 P_{CO}}{K_5 P_{H_2O}} + \sqrt{K_4 P_{H_2}}\left(\alpha_1 + \alpha_1 \alpha_2 + \sum_{i=3}^n \left(\prod_{j=3}^i \alpha_1 \alpha_2 \alpha_j\right)\right)\right)}$$

$$\alpha_1 = \frac{k_8 \dfrac{K_7 K_6 K_4^2 K_3 K_2 K_1 P_{H_2}^2 P_{CO}}{K_5 P_{H_2O}}}{k_8 K_7 K_6 K_4^2 K_3 K_2 K_1 P_{H_2}^2 P_{CO} \dfrac{}{K_5 P_{H_2O}} + k_{9Me}\sqrt{K_4 P_{H_2}}}$$

$$\alpha_2 = \frac{k_8 K_7 K_6 K_4^2 K_3 K_2 K_1 P_{H_2}^2 P_{CO} \dfrac{}{K_5 P_{H_2O}}}{k_8 K_7 K_6 K_4^2 K_3 K_2 K_1 P_{H_2}^2 P_{CO} \dfrac{}{K_5 P_{H_2O}} + k_{9Me}\sqrt{K_4 P_{H_2}} + k_{10E}\,e^{2\theta}\,[*]}$$

$$\alpha_n = \frac{k_8 K_7 K_6 K_4^2 K_3 K_2 K_1 P_{H_2}^2 P_{CO} \dfrac{}{K_5 P_{H_2O}}}{k_8 K_7 K_6 K_4^2 K_3 K_2 K_1 P_{H_2}^2 P_{CO} \dfrac{}{K_5 P_{H_2O}} + k_{9Me}\sqrt{K_4 P_{H_2}} + k_{10}\,e^{n,\theta}\,/[*]}$$

Rate expression	Reaction condition	References
$$R_{CH_4} = k_7 \dfrac{K_6 K_1 K_2 K_3 K_4 P_{CO}^{2.5} P_{H_2} [*]^2}{P_{H_2O}} \quad (n \geq 2)$$ $$R_{C_n H_{2n+2}} = k_7 \dfrac{K_6 K_1 K_2 K_3 K_4 P_{H_2}^3 P_{CO} \prod_n^{i=2} \alpha_i [*]^2 + P_{H_2} k_h \dfrac{k_8^- P_{C_n H_{2n}}^*}{P_{H_2} k_h + k_8^+} [\sigma]}{P_{H_2O}} \quad (n \geq 2)$$ $$R_{C_n H_{2n}} = k_8^+ \dfrac{K_1 K_2 K_3 P_{H_2}^2 P_{CO}}{P_{H_2O}} (1 - \beta_n) \prod_n^{i=2} \alpha_i [*]^2 - P_{H_2} k_h \dfrac{k_8^- P_{C_n H_{2n}}^*}{P_{H_2} k_h + k_8^+} [\sigma]$$ where $P_{C_n H_{2n}}^* = P_{C_n H_{2n}} \cdot \exp(cn) \quad (n \geq 2)$ $$P_{C_2 H_4}^* = \lambda \cdot P_{C_2 H_4} \cdot \exp(2c)$$ $$[*] = \dfrac{1}{\left(1 + K_1 P_{CO}(1 + K_2 P_{H_2}(1 + K_3\{[(1 + K_6\sqrt{K_4 P_{H_2}})(1 + \sum_{i=2}^{n} \prod_{j=2}^{i} \alpha_j)\} + \sqrt{K_4 P_{H_2}}\right)}$$ $$[\sigma] = \dfrac{1}{1 + K_1 P_{CO} + \sum_{i=2}^{N} \dfrac{k_8^- P_{C_n H_{2n}}^*}{P_{H_2} k_h + k_8^+}}$$ $$\beta_n = \dfrac{k_8^- P_{C_n H_{2n}}^*}{k_8^- \alpha_A^{n-1} \dfrac{K_3 K_2 K_1 P_{H_2}^2 P_{CO}}{P_{H_2O}} + \dfrac{k_8^- \sum_{i=2}^{n} \alpha_A^{i-2} P_{C_{n-i+2} H_{2(n-i+2)}}}{k_5} \dfrac{K_3 K_2 K_1 P_{H_2}^2 P_{CO}}{P_{H_2O}} [*] + k_7 K_6 K_4 P_{H_2} [*] + k_8}$$	Fe/Cu/K/SiO₂ Slurry reactor T—250–290 °C P—1.0–2.5 MPa, H₂/CO-0.67–1.5	Chang et al. [28]

Table 2 (continued)

Rate expression	Reaction condition	References
(see equations below)	Co-Re/Al$_2$O$_3$ Batch reactor T—205, 220, 230 °C P—1.5–2.5 MPa, H$_2$/CO-1.4–2.1	Todic et al. [91]
(see equations below)		Zhang et al. [92]

$$R_{CH_4} = k_{5M} K_7^{0.5} P_{H_2}^{1.5} \alpha_1 [*]$$

$$R_{C_2H_4} = k_{6E,0} e^{2C} \sqrt{K_7 P_{H_2}} \, \alpha_1 \alpha_2 [*]$$

$$R_{C_nH_{2n+2}} = k_5 K_7^{0.5} P_{H_2}^{1.5} \alpha_1 \alpha_2 \prod_n^{i=3} \alpha_i [*] \quad n \geq 2$$

$$R_{C_nH_{2n}} = k_{6,0} e^{C_n} \sqrt{K_7 P_{H_2}} \, \alpha_1 \alpha_2 \prod_n^{i=3} \alpha_i [*] \quad n \geq 3$$

$$[*] = \frac{1}{\left(1 + \sqrt{K_7 P_{H_2}} + K_1 P_{CO} + K_2 K_1 P_{CO} P_{H_2} + \sqrt{K_7 P_{H_2}} \left[\left(1 + \frac{1}{K_4} + \frac{1}{K_3 K_4 P_{H_2}} + \frac{P_{H_2O}}{K_3 K_2 K_4 P_{H_2}^2}\right)\left(\alpha_1 + \alpha_1 \alpha_2 + \alpha_1 \alpha_2 \sum_n^{i=3} \prod_i^{j=3} \alpha_j\right)\right]\right)}$$

$$\alpha_1 = \frac{k_1 P_{CO}}{k_1 P_{CO} + k_{5M} P_{H_2}}$$

$$\alpha_2 = \frac{k_1 P_{CO}}{k_1 P_{CO} + k_5 P_{H_2} + k_{6E} e^{C2}}$$

$$R_{C_nH_{2n+2}} = k_5 K_7^{0.5} P_{H_2}^{0.5} N \alpha^{n-1} [*]^2 \quad (n = 1, 2, \ldots) R_{C_nH_{2n}} = k_6 N \alpha^{n-1} [*]^2 \quad (n = 2, 3, \ldots)$$

$$[*] = \frac{1}{\left(1 + K_7^{0.5} P_{H_2}^{0.5} + N \frac{K_M P_{H_2}^2 P_{CO} / P_{H_2O} + k_5 K_7^{0.5} P_{H_2}^{0.5} + k_6}{k_5 K_7^{0.5} P_{H_2}^{0.5} + k_6}\right)}$$

$$\alpha_1 = \frac{k_{10} P_{C_2H_4}}{k_{10} P_{C_2H_4} + k_5 K_7^{0.5} P_{H_2}^{0.5} + k_6} \quad (n < 7)$$

$$\alpha_2 = \frac{K_M P_{H_2}^2 P_{H_2O}}{\frac{K_M P_{H_2}^2 P_{CO}}{P_{H_2O}} + k_5 K_7^{0.5} P_{H_2}^{0.5} + k_6} \quad (n < 7)$$

where, $N = \alpha K_7^{0.5} P_{H_2}^{0.5}$, $K_M = k_4 M$, $M = K_1 K_2 K_3 K_7^2 K_8 K_9$

Rate expression	Reaction condition	References
$R_{CH_4} = k_{7l}\alpha_1 K_2 P_{H_2} [*]^2$	Co/AC catalyst	Qian et al. [93]
$R_{C_nH_{2n+2}} = k_7 K_2 P_{H_2} \prod_n^{i=1} \alpha_i [*]^2$	Fixed bed reactor	
$R_{CH_3OH} = k_{6l} K_2 \alpha_1 P_{H_2O} [*]^2$	T—220–250 °C	
$R_{C_nH_{2n+1}OH} = k_6 K_2 P_{H_2O} \prod_n^{i=1} \alpha_i [*]^2$	P—2.0–4.0 MPa, H_2/	
$R_{C_nH_{2n}} = k_8 \sqrt{K_2 P_{H_2}} \left(1 - \beta_n\right) \prod_n^{i=1} \alpha_i [*]$	CO-1.0–2.5	
$\beta_n = \dfrac{k_8^- P_{C_nH_{2n}}}{k_8 \prod_{i=1}^n \alpha_i}$		
$\alpha_n = \dfrac{K_1 k_3 P_{CO} [*]}{K_1 k_3 P_{CO} [*] + \dfrac{k_6 P_{H_2O}\sqrt{K_2 P_{H_2}}}{K_5 P_{H_2}} [*] + k_7 \sqrt{K_2 P_{H_2}} [*] + k_8 \left(1 - \beta_n\right)}$		
$[*] = \dfrac{1}{1 + \sqrt{K_2 P_{H_2}} + K_1 P_{CO} + \left(1 + \dfrac{P_{H_2O}}{K_5 P_{H_2}} + \dfrac{P_{H_2O}}{K_4 K_5 P_{H_2}^2}\right) \sqrt{K_2 P_{H_2}} \sum_{i=2}^N \left(\prod_{j=2}^i \alpha_{T,1}\alpha_j\right)}$		

CO conversion (3–91%). However, CO_2 inhibition was significant and different for different conversion levels. Although several studies have been reported over Fe or Co catalysts, very few kinetic studies have been done for Fe-Co bimetallic catalysts till date. A wide range of bimetallic catalysts have been tested in kinetic modeling by Mirzaei and co-workers, viz., Fe-Co-Mn, Fe-Co-Ni, and Co-Ni catalysts [71, 77, 78, 94, 95]. Various routes for monomer formation and carbon chain propagation paths were exercised for FT synthesis kinetic model development. They reported that the different values of the kinetic parameters and activation energies could be attributed to catalyst preparation methods and the formation of active phases of a metal catalyst. However, the detailed explanation and the effect of bimetallic phase formation on kinetics were lacking in their study.

Pant et al. [79] investigated the synergistic effect of Fe-Co bimetallic catalyst on the kinetics of FT synthesis reactions. The rate model for the rate of CO consumption was developed using Langmuir–Hinshelwood–Hougen–Watson (LHHW) approach under the hypothesis that the CO consumption is occurring via enol mechanism/carbide mechanism or combination of both mechanisms. A couple of proposed reaction networks for CO consumption were shown in Fig. 7, wherein the hydrogen-assisted and hydrogen-unassisted CO activation is occurring. The models were validated against experimental data to choose the prevailing mechanism for CO activation over Fe-Co bimetallic catalyst. The model (Eq. 7) based on enol and carbide mechanism wherein CO dissociation occurs with the assistance of hydrogen was found to be best-fitted model. The paths for the $-CH_2-$ formation were different in all cases.
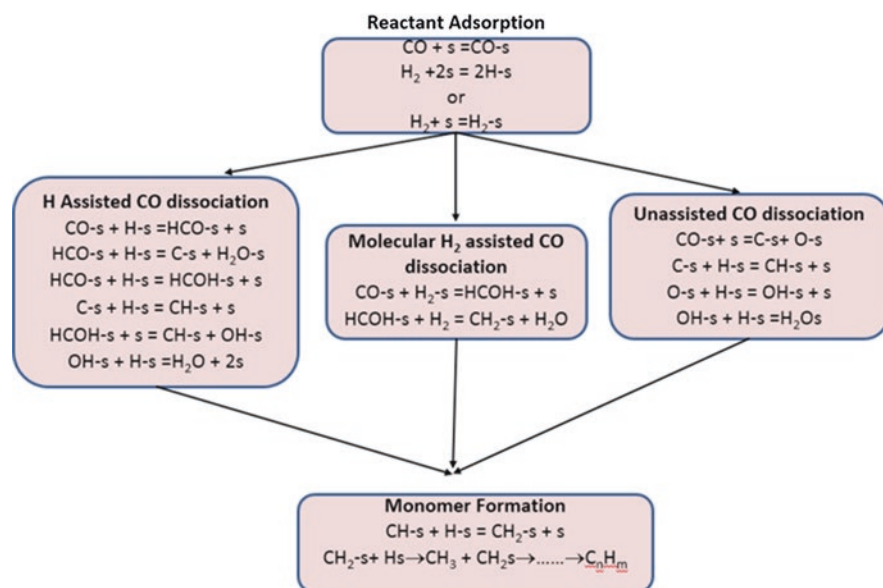
Fig. 7 Elementary reaction for model development

$$r_{\mathrm{FT}} \quad \frac{kP_{\mathrm{CO}}P_{\mathrm{H_2}}^{1/2}}{\left(1+aP_{\mathrm{CO}}+bP_{\mathrm{H_2}}^{1/2}\right)^2} \tag{7}$$

3.2   FT Synthesis Kinetics for the Rate of Product Formation and Product Distribution

The model developed for the prediction of FT synthesis product distribution has been practiced for a very long time. It can be widely categorized into three different approaches, which progressed with time. These phenomenological models are widely reported into three categories: Anderson-Schulz-Flory (ASF) models [33, 65, 86, 96], non-ASF models or hydrocarbon selectivity models [12, 15, 47, 97–101], and Langmuir–Hinshelwood–Hougen–Watson (LHHW) comprehensive kinetic models [28, 51, 53, 89, 91, 92, 102, 103].

3.2.1   Anderson–Schulz–Flory (ASF) Model

Anderson–Schulz–Flory (ASF) distribution model was the first model for the prediction of product distribution in terms of hydrocarbon carbon numbers in the FT synthesis process. This is the oldest hydrocarbon selectivity model and was initially described by Anderson–Schulz and Flory, wherein the distribution of products follows a conventional ASF law [96]. The chain formation is governed by chain growth probability factor α and it is independent of carbon number. The chain growth probability factor is defined as the ratio of the rate of chain propagation to the rate of chain termination plus the rate of chain propagation (Eq. 8):

$$\alpha = \frac{r_{\mathrm{n,p}}}{r_{\mathrm{n,t}}+r_{\mathrm{n,p}}} \tag{8}$$

The relationship between carbon number distribution and chain growth probability α is described on the basis of stepwise polymerization reaction where chain growth takes place via stepwise addition of intermediate. The probability of forming a product with carbon number n (Fig. 8) will be related to the molar fraction of that product as follow (Eq. 9):

$$M_n = \left(1-\alpha\right)\alpha^{(n-1)} \tag{9}$$

where M_n is the molar fraction of the product with the carbon number n. The equation is called Anderson–Schulz–Flory (ASF) distribution and can be used to calculate the chain growth probability factor α for each carbon number through their
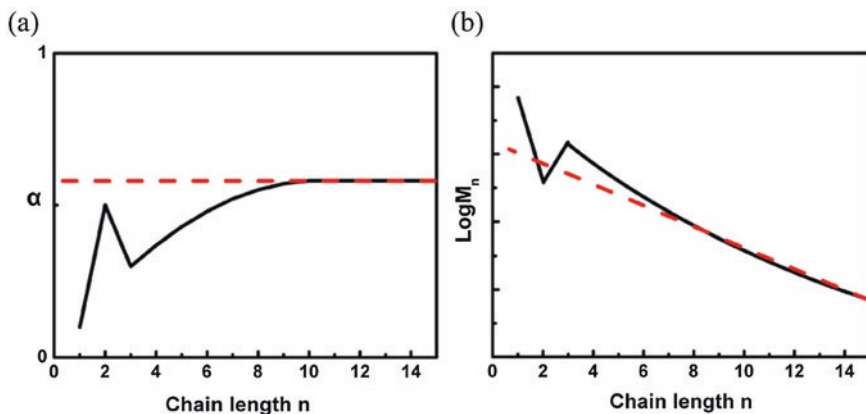
Fig. 8 ASF distribution plots. (■) the deviated ASF distribution, (---) the ideal ASF distribution [104]

molar fraction value. The logarithmic form of Eq. (9) is a more generalized form of the ASF distribution model and as shown below (Eq.10):

$$\log M_n = n \cdot \log \alpha + \log \left[\frac{(1-\alpha)}{\alpha} \right] \tag{10}$$

The value of the chain growth probability factor can also be determined from the ratio of the molar fraction of the two products with different carbon numbers using experimental data (Eq. 11):

$$\frac{M_n}{M_k} = \alpha^{(n-k)} \tag{11}$$

Figure 8a, b (dotted lines) show the variation of α and M_n with carbon number, respectively, and is compared with the experimental trends (solid line). It also reveals that, in ASF distribution model, the value of chain growth probability factor α is independent of carbon number. Despite the fact that the ASF distribution model was based on a well-explained polymerization theory, deviations from the ASF model of product distribution are observed by various researchers [80, 105, 106]. The deviations, such as high C_1 yield, low C_2 production and different slopes in the ASF diagram, i.e., changing chain growth probability with carbon number are evident. Also, a widely observed anomaly is related to higher α-olefin production, which causes a decreasing trend in olefin to paraffin ratio with carbon number.

3.2.2   High C1 Selectivity

The higher yield of methane than the predicted from the ASF law in the FT synthesis product stream has been reported many times and is also evident in Fig. 8 [17, 107, 108]. However, various reasoning has been proposed to explain this anomaly. Schulz et al. [107, 108] suggested some specific sites exist in the FT synthesis reaction environment to promote methane formation only; however, the author could not verify it experimentally. The other theory relates to the presence of secondary reactions such as hydrogenolysis to the excess methane formation [12, 109]. Again, the explanation related to thermodynamics suggests that the heat and mass transfer limitation increase the methane formation, which seems unreasonable as the cases where these limitations were absent the methane yield was still high [110]. The high yield of methane than expected from the ASF model can be explained by using alkyl and carbide mechanism. The chain initiation is more difficult than the chain propagation as the initiation involves two molecules H_2 and CO. Now, the likelihood of desorption step after hydrogenation of M=CH_2 intermediate is higher than the desorption of M=CH_2-R. Henceforth the hydrogenation and desorption of =CH_2 intermediate as methane increases the selectivity of methane as well as decreases the probability of chain growth to adjacently adsorbed intermediate.

3.2.3   Low C2 Selectivity

The C_2 hydrocarbon selectivity is predicted by the ASF distribution model to be much higher than the actual experimental value of C_2 selectivity. Also, the ratio of ethene to ethane yield is lower and does not fit in the trend for the ratio of alkane to alkene for other higher carbon number. The higher adsorption rate of ethylene than other higher olefins can be ascribed to the significantly lower yield of C_2 in the product [13, 15]. On the detailed investigation on the issue, Cheng et al. reported that the significantly high chemisorption energy of ethylene is the cause of the C_2 anomaly [104]. The proposed reaction mechanism (Fig. 2) can be a good explanation for this anomaly. The secondary reaction of ethene can increase when reabsorbed in the form of M-CH_2–CH_2-M. Henceforth, the adsorbed intermediate increases the chain growth probability two times as it has two ends to propagate the chain. The low ratio of ethene to ethane can be attributed to the re-adsorption of ethene and the relative rate of hydrogenation and desorption.

3.2.4   Variation in Value of α with Carbon Number

Several reported experimental results for FT synthesis confirm the variation in the value of α with the carbon number [106, 111–115]. A general trend of α is shown in Fig. 8, wherein the value of α remains almost constant for long-chained hydrocarbon ($n > 10$). The value α decreases with decreasing chain length for carbon number $10 > n > 3$. Also, for lower chain length, the erratic nature of α can be attributed to

a higher yield of methane and lower yield of C_2 fraction. The two models were derived based on the assumption that the entire range of FT products was a combination of two ASF product distribution with two different chain growth factors. The theory was supported by the experimental results where the occurrence of two active sites or two parallel mechanisms were verified [111, 112, 114]. The two α models were not able to explain the relationship between decreasing olefin/paraffin ratio with carbon number and the two different values of α [111, 115]. Also, the two α product distribution model gives the best results for carbon number $n > 3$. The deviation in C_1 and C_2 yields in the distribution cannot be explained using the model. Patzlaff et al. [112, 114] used two α model (Eq. 12) by superimposing two distinct ASF model having two different value of α (α_1 and α_2). As discussed above, the two α distribution model is able to predict the distribution for carbon number higher than two ($n > 2$) (Fig. 9). Figure 9 shows the logarithmic plot for the molar fractions of hydrocarbons formed over a potassium promoted iron catalyst (T = 493 K, pot = 750 kPa, P_{H_2} / P_{CO} = 2) vs. carbon number. For the carbon number $n < 8$, chain growth probability is α_1, and for $n > 12$, the value is α_2. The middle region is a transition region wherein the contribution of both α_1 and α_2 is present in a fraction of A and B, respectively (Eq. 12). The slope of the two different lines fitting to the experimental data provides the value of two chain growth probability α_1 and α_2 in terms of $\ln \alpha_1$ and $\ln \alpha_2$:

$$x_i = A\alpha_1^{i-1} + B\alpha_2^{i-1} \tag{12}$$
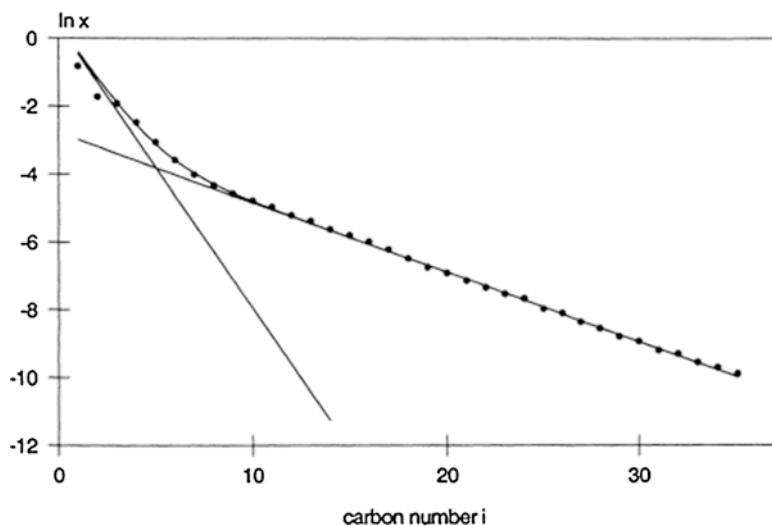
Fig. 9 Carbon number distribution of hydrocarbons formed over a potassium promoted iron catalyst (T = 493 K, p_{tot} = 750 kPa, P_{H_2} / P_{CO} = 2) [112]

3.2.5   Non-ASF Model for Hydrocarbon Selectivity

The deviation from the ASF distribution reported in the literature can be attributed to secondary reactions after chain terminations. Chain terminates via β-hydrogen elimination or α-hydrogenation yielding alkene and alkanes, respectively. Secondary reactions are mainly hydrogenation, hydrogenolysis of the primary product, or the re-insertion into the growing chain. It has been previously reported that the rate of re-insertion and hydrogenation increases with chain length and alter the distributions of higher hydrocarbon [116]. A number of product selectivity models are proposed to describe the varied FT product spectrum [28, 47, 51, 53, 54, 89, 92, 112, 117]. However, the basis of the modeling is divided over the secondary reaction of α-olefin. The first argument is that the primarily formed α-olefins readsorb and hydrogenate to form alkane. Some researcher has observed that the re-adsorbed α-olefin re-inserted in growing chain to form longer chain hydrocarbon. The researchers have presented three different explanations for the enhanced probability of re-insertion of α-olefin with chain length. The increased reinsertion can be attributed to enhanced diffusivity [15, 18, 100, 118, 119] effect, chain length–dependent solubility [120, 121] and/or physisorption effect [12, 99, 122]. The physisorption effect has been reported as a primary reason for the decreased olefin to paraffin ratio with chain length. In order to address the effect, an exponential term has been included in most of the models related to the rate of α-olefin desorption [15, 100, 118]. Various non-ASF product distribution models were developed based on each explanation.

The deviation from ASF distributions was firstly addressed by Van der Laan [47, 122] and co-workers. They introduce the concept of α-olefin re-adsorption during the reaction, and it depends on the chain length. They reported that the olefin readsorption rate increases with the chain length because the strength of the physisorbed molecule on the catalyst active site and solubility in the liquid medium of long-chain molecules increases with chain length, henceforth, their probability of readsorption increases. They proposed the α-olefin re-adsorption product distribution model (ORPDM). In the ORPDM model (Eq. 13), the chain growth probability factor α_n includes an exponential term with a constant c. It was assumed that the decrease of olefin to paraffin ratio with chain length followed an exponential trend and was determined by the introduction of constant c, which is a function of nature of the catalyst and the temperature:

$$\frac{\theta_n}{\theta_{n-1}} = \frac{k_p \theta_m}{k_{t,o}\theta_v / \left(1 + k_R e^{cn}\right) + k_{t,p}\theta_H + k_p\theta_m} = \alpha_n \qquad (13)$$

In Eq. (13), k_p is the reaction rate constant of chain propagation, k_R is the reaction rate constant of re-adsorption of olefins, $k_{t,o}$, and $k_{t,p}$ are the rate constants for chain termination of olefin and paraffin, respectively. The model successfully predicted the selectivity of the entire range of hydrocarbon with marginal deviations.

Kuipers et al. [12, 99] reported from their detailed FT studies that α-olefin hydrogenates at one site and then reinserted into another site the vicinity. Prior to the reinsertion on a particular site, the olefin long-chain breaks the bond from its origin and remains attached to the catalyst surface with the weak van der Waals forces, which increases the probability of re-insertion than the desorption. The rate of reinsertion compared to desorption increases with chain length; however, the small chain length α-olefin prefer to desorb in the vapor phase or can adhere to the next vicinal site for the hydrogenation reaction, which aids to the hydrogenation of these components. Their model (Eq. 14) was used to explain the major influence among the three most probable reactions, olefin reinsertion, hydrogenolysis, and hydrogenation. The model suggested the major influence of olefin re-insertion and hydrogenolysis on the product distribution, which changes with chain length and resulting in a sigmoidal curve of distribution showing a peak at middle range hydrocarbon (carbon number 6–16). On and Pn in the model (Eq. 14) represents the net rate of production of olefin and paraffin per m^2 of catalyst per second:

$$O_n = T_n^{\text{ol}} \cdot I_2 \cdot \prod_{n-1}^{m=2} \left(1 - T^{\text{par}} - T^{\text{ol}}\right) \quad \text{for } n \geq 3$$
$$P_n = T_n^{\text{par}} \cdot I_2 \cdot \prod_{n-1}^{m=2} \left(1 - T^{\text{par}} - T^{\text{ol}}\right) \quad \text{for } n \geq 3 \tag{14}$$

Here I_2 is constant, T_n^{ol} is net termination probability as an α-olefin with chain length n, T_n^{par} is net termination probability as paraffin with chain length n, T^{par} termination probability as paraffin, T^{ol} is termination probability as α-olefin.

Botes [106] argument was in line with the Kuipers [12] findings. He observed that the lower olefins except ethylene do not prefer to readsorb and secondary reaction to such a great extent, which causes an effect on product distributions. The added chain length–dependent α-olefin desorption in their selectivity model (Eq. 15) claims to describe the C$_3$–C$_{10}$ range olefin distribution successfully. The model represents the relation of the chain growth probability factor with olefin and paraffin production rates:

$$\alpha_n = \left[1 + \tau_p + \tau_o \cdot \exp(-k \cdot n)\right]^{-1} \tag{15}$$

where parameter $\tau_p = \dfrac{k_h}{k}$ is the production rate of paraffin, represented as the ratio of the rate of hydrogenation to the rate of chain growth. Similarly, $\tau_o = \dfrac{k_h}{k}$ is the production rate of olefin and is represented as the ratio of the rate of the desorption to ratio of the chain growth. As the chain length increases, olefin's increased interaction with the catalyst surface can be explained by inheriting an exponential term to the rate equation of olefin formation, and this was able to relate the relationship between the rate of desorption of α-olefin and the carbon number even at a higher value of carbon number. The model also predicts the olefin to paraffin ratio for each carbon number (Eq. 16):

$$\left(\frac{\text{Olefin}}{\text{Parafin}}\right)_n = \frac{\tau_o}{\tau_p} \cdot \exp(-k \cdot n) \qquad (16)$$

Iron and cobalt catalyst surfaces show different activities for the α-olefin re-insertion and re-adsorption reactions [115, 120, 123–125]. Schulz [125] found a positive effect of secondary reaction on the product distribution over the cobalt catalyst, which was evident in the form of more fraction of higher hydrocarbon. The alkali-promoted iron catalyst showed the opposite behavior. By alkene co-feeding study, it was suggested by researchers [120, 124] that CO partial pressure plays a crucial role in the occurrence of secondary reaction over iron catalysts. A very less amount of CO has to be present to enhance the secondary hydrogenation or reinsertion to a significant level over alkali-promoted iron catalyst. Other researchers [115, 123] have also concluded that the amount of α-olefins that hydrogenated in the FT synthesis was not significant.

3.2.6   Comprehensive Kinetic Model

Hydrocarbon selectivity models [12, 47, 80, 112, 126–128] were used frequently to interpret the product distribution, and they succeed well; however, they fail to explain the complicated reaction network and related mechanism of product formation. The shortcomings of old approaches have been addressed in the form of comprehensive kinetic models based on Langmuir–Hinshelwood–Hougen–Watson (LHHW) postulating various reaction mechanism one by one. The advantage of taking the detailed mechanistic path for the kinetics of product formation is its more realistic approach regarding the FTS mechanism. The detailed mechanistic modeling has been performed over both iron [28, 51, 53, 89, 92] and cobalt [91, 93, 103, 129] catalysts, including all three key elementary reaction steps, viz., chain initiation (CO dissociation and adsorption), chain propagation by forming monomer, and chain termination. Researchers have proposed various models for product formation rate implementing various reaction mechanisms enol/carbide, alkyl, alkenyl, CO-insertion, etc. However, the importance of secondary reactions such as α-olefin re-adsorption was considered in all the models. The assumptions were made for the effect of physisorption of olefins, the solubility of α-olefin, and the ability of olefin's re-insertion in growing chain. Hydrogenation of α-olefin into paraffin on a separate site does not take part in growing chain. The major discrepancy among the models was observed due to the assumption related to the α-olefin desorption step. Few authors [51, 92, 119, 130] assumed that the α-olefin desorption and re-adsorption is reversible reaction whereas others [90, 91, 103, 106] consider the α-olefin desorption as chain length–dependent irreversible reaction. Figure 10a and b shows the reaction network explaining both the assumption related to the α-olefin desorption step. α-olefin can desorb from the catalyst site without readsorption, and the rate of desorption is the function of hydrocarbon chain length n (Fig. 10a). On the other hand, α-olefin can re-adsorb after desorption in a reversible manner (Fig. 10b).
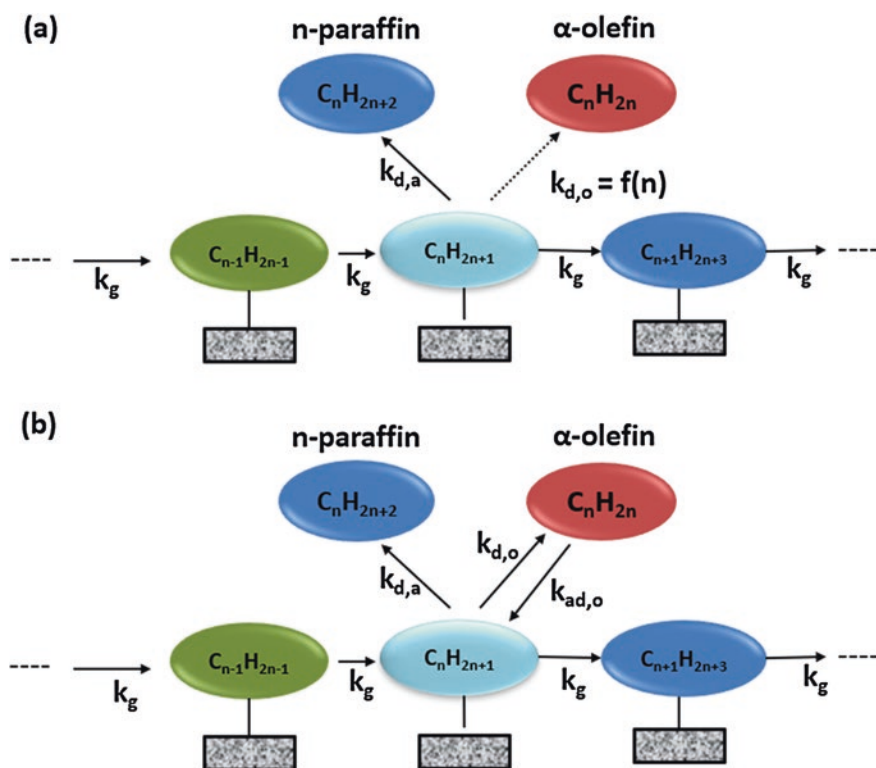
Fig. 10 (**a**) Reaction path for chain growth (k_g), hydrogenation and desorption to paraffin ($k_{d,a}$), olefin desorption ($k_{d,o}$) (**b**)olefin desorption($k_{d,o}$), and re-adsorption($k_{ad,o}$)

Table 2 summarizes the various comprehensive kinetic model developed over iron and cobalt catalysts. The comprehensive model development can be traced from the initial work of Lox and Froment [131], who derived the kinetic model without α-olefin re-adsorption kinetics. Following this, Wang et al. [51] and Yang et al. [53] expanded the work by utilizing the α-olefin re-adsorption steps in the LHHW approach. The model was derived with the addition of the steps such as α-olefin adsorption and desorption in the elementary reaction assuming that these steps are reversible. However, the decreasing trend in olefin to paraffin ratio with increasing chain length was not able to accommodate by the predicted trends from the model. In Addition, Zhang et al. [92] started with the assumption of the presence of two growth intermediate over the catalyst surface, and the developed model gave significant results with experimental data for product distribution over Cu-K promoted iron catalyst. Qian et al. [93] started with the CO insertion mechanism for the derivation of the model. They also added the alkene re-adsorption as the primary secondary reaction and ignored the presence of water gas shift reaction over the Co supported on an activated carbon catalyst. The major products in consideration were paraffin, α-olefin, and alcohol, and olefins. It is important to note that all the above

comprehensive kinetic models have been done either on an cobalt-based or iron-based catalyst. The major similarity among the model was the selection of α-olefin re-adsorption as a secondary reaction. As discussed above and shown in Table 2, although the models are complicated and the model development and validation is a cumbersome task, the results are significantly good.

In a slightly different approach of comprehensive kinetic modeling, Botes et al. [106] introduced the exponential relationship of the rate of formation of olefins with the carbon number. They implemented the theory of physisorption of long-chained olefin on the catalyst surface after the detachment of the catalyst site. And the affinity of olefin with surface increases with the carbon number in the chain, which in turn decreases the probability of its desorption from the surface to the gas phase. The intact olefin re-inserts into another growing chain. The effect of physisorption and the chain length was incorporated through the addition of exponential terms in the models. Based on this assumption, Todic et al. [91] developed the comprehensive kinetic model, combining CO insertion mechanism and chain length–dependent α-olefin desorption over an alumina-based cobalt catalyst. The model successfully addresses the various shortcomings of earlier selectivity models, such as a significant decrease in olefin to paraffin ratio with chain length and changing the value of α. While deriving the model, they did not consider the reversibility of secondary reaction as taken up by others [99, 100, 119]. In a road of extension of this work, Bhatelia and co-worker [103] also applied CO insertion mechanism as CO activation and α-olefin re-adsorption and chain length–dependent desorption mechanism for model derivation over Co–Ru–La/Al$_2$O$_3$. They added an exponential term in the olefin desorption reaction, and the term βn was added to incorporate the re-adsorption of α-olefin. The model described its product distribution well. However, the result does not differ much from the results by the model of Todic et al. [91]. At the same time, simultaneous consideration of both chain length dependency and α-olefin readsorption increase the intricacy of the model, which increased the time for the computation and affected the accuracy of results. In a similar line, Pant et al. [90] performed detailed kinetic study over Fe-Co bimetallic catalyst to determine the product formation rate. The models were developed considering both chain length–dependent α-olefin desorption and α-olefin re-adsorption as a secondary reaction which was coupled with alky or alkenyl mechanism for chain propagation. Both the proposals of secondary reaction were tested and compared with the experimental data over Fe-Co bimetallic catalyst to choose a more suitable model.

4   Conclusion

The complex chain reaction and related mechanism resulted in complexity in the kinetics of the reaction. It always remains debated since several kinetic and mechanistic factors are involved, and the physio-chemical phenomena governing the mechanism is still a topic of debate. The FT synthesis kinetic has been approached by different pathways. In the first one, the simplification was made by using

empirical correlation for the overall rate model. Also, a large number of reported studies have focused on lumped kinetics wherein the rate of CO or syngas consumption was modeled based on chain initiation reaction mechanism. The method neglected the product distribution calculations, which consists of a large number of products. Since the method did not involve long and complex FT reaction networks or, in some cases, the reaction was lumped, the results seem to be more accurate and robust. However, the differences among the rate expressions were evident due to the change in reactor condition viz. present and absence of mass transfer limitation, and the selection of catalyst. In the case of iron catalyst, most of the rate expressions consist of CO_2 and H_2O as inhibition terms due to its good activity toward water gas shift reaction. It also suggests strong competition of CO and H_2O over adsorption on a single site. In the case of cobalt-based FT catalysts, there was no significant role of CO_2 and H_2O in the rate expression as the catalyst was inactive for the water gas shift reactions. The difference between rate expression for iron- and cobalt-based catalysts can also be attributed to the mechanistic approach selected for both. It was observed that a cobalt-based catalyst favors direct dissociation and adsorption of CO before interaction with H_2, whereas iron favors hydrogen-assisted CO dissociation.

In the parallel approach, hydrocarbon selectivity models were proposed, which showed significant deviation from the observed experimental trends due to the presence of secondary reactions. Therefore, the segregation of the syngas conversion model from the product formation rate model gives rise to a significant amount of error in the results. However, this does not signify that the approach is erroneous. Nevertheless, the product distribution models and syngas conversion models were examined over a large number of catalysts by the various researchers. In recent studies, a detailed, comprehensive approach was undertaken to describe the product formation rate considering each elementary reaction. The method was able to explain the syngas conversion rate as well as the product formation rate simultaneously and was more accurate compared to the previous approach of segregated models. Although, the comprehensive modeling is a cumbersome approach wherein the model development is a complicated task, and the solution is time taking, yet the accuracy of the results made the approach more acceptable than the other approaches. Hence, while selecting any of these approaches or the model for kinetic study of FT reaction, one has to take care of the correlation that has been used to develop the model, and the condition should be closest to the condition at which the simulation has been done.

References

1. Liu Z, Shi S, Li Y (2010) Coal liquefaction technologies—development in China and challenges in chemical reaction engineering. Chem Eng Sci 65:12–17. https://doi.org/10.1016/j.ces.2009.05.014
2. Wood DA, Nwaoha C, Towler BF (2012) Gas-to-liquids (GTL): a review of an industry offering several routes for monetizing natural gas. J Nat Gas Sci Eng 9:196–208. https://doi.org/10.1016/j.jngse.2012.07.001

3. Zimmerman WH, Bukur DB (1990) Reaction kinetics over iron catalysts used for the Fischer-Tropsch synthesis. Can J Chem Eng 68:292–301

4. Ledakowicz S, Nettelhoff H, Kokuun R, Deckwer WD (1985) Kinetics of the Fischer-Tropsch synthesis in the slurry phase on a potassium promoted iron catalyst. Ind Eng Chem Process Des Dev 24:1043–1049. https://doi.org/10.1021/i200031a025

5. Huff GA, Satterfield CN (1984) Intrinsic kinetics of the Fischer-Tropsch synthesis on a reduced fused-magnetite catalyst. Ind Eng Chem Process Des Dev 23:696–705. https://doi.org/10.1021/i200027a012

6. Bub G, Bussemeier B, Frohning C (1980) Great Bntam 44. Chem Eng Sci 35:348–355

7. Dry ME, Shingles T, Boshoff LJ (1972) Rate of the Fischer-Tropsch reaction over iron catalysts. J Catal 25:99–104. https://doi.org/10.1016/0021-9517(72)90205-9

8. Anderson RB (1956) Catalysts for the Fischer-Tropsch synthesis, vol 4. Van Nostrand-Reinhold, New York

9. Yates IC, Satterfield CN (1991) Intrinsic kinetics of the Fischer-Tropsch synthesis on a cobalt catalyst. Energy Fuel 5:168–173. https://doi.org/10.1021/ef00025a029

10. Withers HP Jr, Eliezer KF, Mitchell JW (1990) Slurry-phase Fischer-Tropsch synthesis and kinetic studies over supported cobalt carbonyl derived catalysts. Ind Eng Chem Res 29:1807–1814. https://doi.org/10.1021/ie00105a011

11. Satterfield CN (1991) Heterogeneous catalysis in industrial practice, 2nd edn. McGraw Hill, New York, NY

12. Kuipers EW, Scheper C, Wilson JH, Vinkenburg IH, Oosterbeek H (1996) Non-ASF product distributions due to secondary reactions during Fischer–Tropsch synthesis. J Catal 158:288–300. https://doi.org/10.1006/jcat.1996.0028

13. Kuipers EW, Vinkenberg IH, Oosterbeek H (1995) Chain length dependence of α-olefin Readsorption in Fischer-Tropsch synthesis. J Catal 152:137–146. https://doi.org/10.1006/jcat.1995.1068

14. Madon R, Iglesia E (1993) The importance of olefin Readsorption and H_2/CO reactant ratio for hydrocarbon chain growth on ruthenium catalysts. J Catal 139:576–590. https://doi.org/10.1006/jcat.1993.1051

15. Iglesia E, Reyes SC, Madon RJ (1991) Transport-enhanced α-olefin readsorption pathways in Ru-catalyzed hydrocarbon synthesis. J Catal 129:238–256. https://doi.org/10.1016/0021-9517(91)90027-2

16. Chou C-Y, Lobo RF (2019) Direct conversion of CO_2 into methanol over promoted indium-based catalysts. Appl Catal A Gen 583:11714117153. https://doi.org/10.1016/j.apcata.2019.117144

17. Schulz H (1999) Short history and present trends of Fischer–Tropsch synthesis. Appl Catal A Gen 186:3–12

18. Nowicki L, Ledakowicz S, Bukur DB (2001) Hydrocarbon selectivity model for the slurry phase Fischer–Tropsch synthesis on precipitated iron catalysts. Chem Eng Sci 56:1175–1180. https://doi.org/10.1016/S0009-2509(00)00337-7

19. van der Laan GP, Beenackers AACM (2000) Intrinsic kinetics of the gas–solid Fischer–Tropsch and water gas shift reactions over a precipitated iron catalyst. Appl Catal A Gen 193:39–53. https://doi.org/10.1016/S0926-860X(99)00412-3

20. Brady RC, Pettit R (1981) On the mechanism of the Fischer-Tropsch reaction. The Chain Propagation Step. J Am Chem Soc 103:1287–1289. https://doi.org/10.1021/ja00395a081.

21. Kummer JT, DeWitt TW, Emmett PH (1948) Some mechanism studies on the Fischer-Tropsch synthesis using C14. J Am Chem Soc 70:3632–3643. https://doi.org/10.1021/ja01191a029

22. Storch HH (1948) The Fischer-Tropsch and related processes for synthesis of hydrocarbons by hydrogenation of carbon monoxide. In: Frankenburg WG, Komarewsky VI, BT REK (eds) Advances in catalysis, vol 1. Academic, New York, pp 115–156. https://doi.org/10.1016/S0360-0564(08)60674-4

23. Pichler H, Schulz H (1970) Recent findings in the synthesis of hydrocarbons from CO and H_2. Chem Ing Tech 42:1162–1174. https://doi.org/10.1002/cite.330421808.

24. Wang CJ, Ekerdt JG (1984) Evidence for alkyl intermediates during Fischer-Tropsch synthesis and their relation to hydrocarbon products. J Catal 86:239–244. https://doi.org/10.1016/0021-9517(84)90369-5

25. Schulz H, Erich E, Gorre H, van Steen E (1990) Regularities of selectivity as a key for discriminating FT-surface reactions and formation of the dynamic system. Catal Lett 7:157–167. https://doi.org/10.1007/BF00764499

26. Ertl, G. (Gerhard), International Union of Pure and Applied Chemistry., Federation of European Chemical Societies., European Federation of Chemical Engineering., & Dechema. (1984). 8th International Congress on Catalysis, Berlin (West), 2–6 July 1984:proceedings. Verlag Chemie.

27. Maitlis PM (2004) Fischer-Tropsch, organometallics, and other friends. J Organomet Chem 689:4366–4374. https://doi.org/10.1016/j.jorganchem.2004.05.037

28. Chang J, Bai L, Teng B, Zhang R, Yang J, Xu Y et al (2007) Kinetic modeling of Fischer-Tropsch synthesis over Fe – Cu – K – SiO$_2$ catalyst in slurry phase reactor. Chem Eng Sci 62:4983–4991. https://doi.org/10.1016/j.ces.2006.12.031

29. Sari A, Zamani Y, Taheri SA (2009) Intrinsic kinetics of Fischer-Tropsch reactions over an industrial Co-Ru/γ-Al$_2$O$_3$ catalyst in slurry phase reactor. Fuel Process Technol 90:1305–1313. https://doi.org/10.1016/j.fuproc.2009.06.024

30. Turner ML, Long HC, Shenton A, Byers PK, Maitlis PM (1995) The Alkenyl mechanism for Fischer - Tropsch surface methylene polymerisation; the reactions of vinylic probes with CO/H, over rhodium catalysts. Chem Eur J 1:549–556

31. Ndlovu SB, Phala NS, Hearshaw-Timme M, Beagly P, Moss JR, Claeys M et al (2002) Some evidence refuting the alkenyl mechanism for chain growth in iron-based Fischer-Tropsch synthesis. Catal Today 71:343–349. https://doi.org/10.1016/S0920-5861(01)00461-8

32. Storch HH (1951) In: Storch HH, Golumbic N, Anderson RB (eds) In the Fischer-Tropsch and related synthesis. Wiley, New York

33. Anderson RB, Hofer LJE, Storch HH (1958) The reaction mechanism of Fischer-Tropsch synthesis. Chem Ing Tech 30:560–566. https://doi.org/10.1002/cite.330300903.

34. Davis BH (2001) Fischer-Tropsch synthesis: current mechanism and futuristic needs. Fuel Process Technol 71:157–166. https://doi.org/10.1016/S0378-3820(01)00144-8

35. Kokes SJ, Keith Hall W, Emmett PH (1957) Fischer-Tropsch synthesis mechanism studies. The addition of radioactive ethanol to the synthesis gas. Preprints 2:127–138

36. Kummer JT, Emmett PH (1953) Fischer—Tropsch synthesis mechanism studies. The addition of radioactive alcohols to the synthesis gas. J Am Chem Soc 75:5177–5183. https://doi.org/10.1021/ja01117a008

37. Kummer JT, Podgurski HH, Spencer WB, Emmett PH (1951) Mechanism studies of the Fischer—Tropsch synthesis. The addition of radioactive alcohol. J Am Chem Soc 73:564–569. https://doi.org/10.1021/ja01146a018

38. Hall WK, Kokes RJ, Emmett PH (1957) Mechanism studies of the Fischer-Tropsch synthesis. The addition of radioactive methanol, carbon dioxide and gaseous formaldehyde. J Am Chem Soc 79:2983–2989. https://doi.org/10.1021/ja01569a001

39. Hall WK, Kokes RJ, Emmett PH (1960) Mechanism studies of the Fischer-Tropsch synthesis: the incorporation of radioactive ethylene, propionaldehyde and propanol. J Am Chem Soc 82:1027–1037. https://doi.org/10.1021/ja01490a005

40. Dry ME (1990) Fischer-Tropsch process. Commercial aspects. Catal Today 6:183–206. https://doi.org/10.1016/0920-5861(90)85002-6.

41. Anderson KG, Ekerdt JG (1985) Study of Fischer-Tropsch synthesis over Fe SiO2: effect of diethylamine on hydrocarbon and alcohol production. J Catal 95:602–604. https://doi.org/10.1016/0021-9517(85)90138-1

42. Botes FG, Breman BB (2006) Development and testing of a new macro kinetic expression for the iron-based low-temperature Fischer-Tropsch reaction. Ind Eng Chem Res 45:7415–7426. https://doi.org/10.1021/ie060491h

43. Eliason SA, Bartholomew CH (1999) Reaction and deactivation Kinetics for Fischer-Tropsch synthesis on Unpromoted and potassium-promoted iron catalysts. Appl Catal A Gen 186:229–243. https://doi.org/10.1016/S0926-860X(99)00146-5

44. Feimer JL, Silveston PL, Hudgins RR (1981) Steady-state study of the Fischer-Tropsch reaction. Ind Eng Chem Prod Res Dev 20:609–615

45. Jess A, Popp R, Hedden K (1999) Fischer–Tropsch-synthesis with nitrogen-rich syngas. Appl Catal A Gen 186:321–342. https://doi.org/10.1016/S0926-860X(99)00152-0

46. Deckwer WD, Kokuun R, Sanders E, Ledakowicz S (1986) Kinetic studies of Fischer-Tropsch synthesis on suspended Fe/K catalyst-rate inhibition by CO2 and H2O. Ind Eng Chem Process Des Dev 25:643–649. https://doi.org/10.1021/i200034a008.

47. Van Der LGP, Beenackers AACM (1999) Hydrocarbon selectivity model for the gas - solid Fischer - Tropsch synthesis on precipitated iron catalysts. Ind Eng Chem Res 38:1277–1290. https://doi.org/10.1021/IE980561N

48. Liu ZT, Li YW, Zhou JL, Zhang BJ (1995) Intrinsic Kinetics of Fischer-Tropsch synthesis over an Fe-cu-K catalyst. J Chem Soc Trans 91:3255–3261. https://doi.org/10.1039/FT9959103255

49. Markvoort AJ, van Santen RA, Hilbers PAJ, Hensen EJM (2012) Kinetics of the Fischer-Tropsch reaction. Angew Chem Int Ed 51:9015–9019. https://doi.org/10.1002/anie.201203282

50. van Steen E, Schulz H (1999) Polymerisation kinetics of the Fischer–Tropsch CO hydrogenation using iron and cobalt based catalysts. Appl Catal A Gen 186:309–320. https://doi.org/10.1016/S0926-860X(99)00151-9

51. Wang Y-N, Ma W-P, Lu Y-J, Yang J, Xu Y-Y, Xiang H-W et al (2003) Kinetics modelling of Fischer–Tropsch synthesis over an industrial Fe–Cu–K catalyst. Fuel 82:195–213. https://doi.org/10.1016/S0016-2361(02)00154-0

52. Wang Y, Fan W, Liu Y, Zeng Z, Hao X, Chang M et al (2008) Modeling of the Fischer-Tropsch synthesis in slurry bubble column reactors. Chem Eng Process Process Intensif 47:222–228. https://doi.org/10.1016/j.cep.2007.02.011

53. Yang J, Liu Y, Chang J, Wang Y-N, Bai L, Xu Y-Y et al (2003) Detailed Kinetics of Fischer−Tropsch synthesis on an industrial Fe−Mn catalyst. Ind Eng Chem Res 42:5066–5090. https://doi.org/10.1021/ie030135o

54. Zhou LP, Hao X, Gao JH, Yang Y, Wu BS, Xu J et al (2011) Studies and discriminations of the kinetic models for the iron-based Fischer-Tropsch catalytic reaction in a recycle slurry reactor. Energy Fuel 25:52–59. https://doi.org/10.1021/ef101270u

55. Anfray J, Bremaud M, Fongarland P, Khodakov A, Jallais S, Schweich D (2007) Kinetic study and modeling of Fischer-Tropsch reaction over a Co/Al2O3 catalyst in a slurry reactor. Chem Eng Sci 62:5353–5356. https://doi.org/10.1016/j.ces.2006.12.035

56. Kaiser P, Pohlmann F, Jess A (2014) Intrinsic and effective kinetics of cobalt-catalyzed fischer-tropsch synthesis in view of a power-to-liquid process based on renewable energy. Chem Eng Technol 37:964–972. https://doi.org/10.1002/ceat.201300815

57. Keyser MJ, Everson RC, Espinoza RL (2000) Fischer - Tropsch kinetic studies with cobalt - manganese oxide catalysts. Ind Eng Chem Res 39:48–54

58. Li J, Jacobs G, Das T, Zhang Y, Davis B (2002) Fischer – Tropsch synthesis: effect of water on the catalytic properties of a Co/SiO2 catalyst. Appl Catal A Gen 236:67–76. https://doi.org/10.1016/S0926-860X(02)00276-4

59. Outi A, Rautavuoma I, van der Baan HS (1981) Kinetics and mechanism of the Fischer Tropsch hydrocarbon synthesis on a cobalt on alumina catalyst. Appl Catal 1:247–272. https://doi.org/10.1016/0166-9834(81)80031-0

60. Pannell RB, Kibby CL, Kobylinski TP (1981) A steady-state study of Fischer-Tropsch product distributions over cobalt, iron and ruthenium. In: Seivama T, Tanabe K (eds) New horizons in catalysis 7th international congress on catalysis, vol 7. Elsevier, Amsterdam, pp 447–459. https://doi.org/10.1016/S0167-2991(09)60290-1

61. Yang C-H, Massoth FE, Oblad AG (1979) Kinetics of CO + H$_2$ reaction over Co-Cu-Al$_2$O$_3$ catalyst. In: Hydrocarbon synthesis from carbon monoxide hydrogen, vol 178. American Chemical Society, Washington, DC, pp 5–35. https://doi.org/10.1021/ba-1979-0178.ch005

62. Zennaro R, Tagliabue M, Bartholomew CH (2000) Kinetics of Fischer-Tropsch synthesis on titania-supported cobalt. Catal Today 58:309–319. https://doi.org/10.1016/S0920-5861(00)00264-9

63. Mosayebi A, Haghtalab A (2015) The comprehensive kinetic modeling of the Fischer-Tropsch synthesis over Co at Ru/γ-Al$_2$O$_3$ core-shell structure catalyst. Chem Eng J 259:191–204. https://doi.org/10.1016/j.cej.2014.07.040

64. Mirzaei AA, Shirzadi B, Atashi H, Mansouri M (2012) Modeling and operating conditions optimization of Fischer–Tropsch synthesis in a fixed-bed reactor. J Ind Eng Chem 18:1515–1521. https://doi.org/10.1016/j.jiec.2012.02.013

65. Karn FS, Shultz JF Anderson RB(1960) Kinetics of the Fischer—Tropsch synthesis on iron catalysts. Pressure dependence and selectivity of nitrided catalysts. J. Phys. Chem. 64:446–451

66. Dry ME (1996) Practical and theoretical aspects of the catalytic Fischer-Tropsch process. Appl Catal A Gen 138:319–344. https://doi.org/10.1016/0926-860X(95)00306-1

67. Atwood HE, Bennett CO (1979) Kinetics of the Fischer-Tropsch reaction over iron. Ind Eng Chem Process Des Dev 18:163–170. https://doi.org/10.1021/i260069a023

68. Deckwer WD, Kokuun R, Sanders E, Ledakowicz S (1986) Kinetic studies of Fischer-Tropsch synthesis on suspended iron/potassium catalyst - rate inhibition by carbon dioxide and water. Ind Eng Chem Process Des Dev 25:643–649. https://doi.org/10.1021/i200034a008

69. Okeson TJ, Keyvanloo K, Lawson JS, Argyle MD, Hecker WC (2016) On the kinetics and mechanism of Fischer-Tropsch synthesis on a highly active iron catalyst supported on silica-stabilized alumina. Catal Today 261:67–74. https://doi.org/10.1016/j.cattod.2015.08.054

70. Sarup B, Wojciechowski BW (1989) Studies of the fischer-tropsch synthesis on a cobalt catalyst II. Kinetics of carbon monoxide conversion to methane and to higher hydrocarbons. Can J Chem Eng 67:62–74. https://doi.org/10.1002/cjce.5450670110

71. Fazlollahi F, Sarkari M, Zare A, Mirzaei AA, Atashi H (2012) Development of a kinetic model for Fischer–Tropsch synthesis over Co/Ni/Al$_2$O$_3$ catalyst. J Ind Eng Chem 18:1223–1232. https://doi.org/10.1016/j.jiec.2011.10.011

72. Botes FG, Van Dyk B, McGregor C (2009) The development of a macro kinetic model for a commercial Co/Pt/Al$_2$O$_3$ Fischer-Tropsch catalyst. Ind Eng Chem Res 48:10439–10447. https://doi.org/10.1021/ie900119z

73. Das TK, Zhan X, Li J, Jacobs G, Dry ME, Davis BH (2007) Fischer-Tropsch synthesis: kinetics and effect of water for a Co/Al$_2$O$_3$ catalyst. In: Davis BH, Occelli ML (eds) Fischer-Tropsch synthesis in catalysis, vol 163. Elsevier, Amsterdam, pp 289–314. https://doi.org/10.1016/S0167-2991(07)80484-8

74. Ma W, Jacobs G, Sparks DE, Klettlinger JLS, Yen CH, Davis BH (2016) Fischer–Tropsch synthesis and water gas shift kinetics for a precipitated iron catalyst. Catal Today 275:49. https://doi.org/10.1016/j.cattod.2016.01.006

75. Mousavi S, Zamaniyan A, Irani M, Rashidzadeh M (2015) Generalized kinetic model for iron and cobalt based Fischer–Tropsch synthesis catalysts: review and model evaluation. Appl Catal A Gen 506:57–66. https://doi.org/10.1016/j.apcata.2015.08.020

76. Eshraghi A, Mirzaei AA, Atashi H (2015) Kinetics of the Fischer-Tropsch reaction in fixed-bed reactor over a nano-structured Fe-Co-Ce catalyst supported with SiO2. J Nat Gas Sci Eng 26:940–947. https://doi.org/10.1016/j.jngse.2015.06.036.

77. Mirzaei AA, Pourdolat A, Arsalanfar M, Atashi H, Samimi AR (2013) Kinetic study of CO hydrogenation on the MgO supported Fe-Co-Mn sol-gel catalyst. J Ind Eng Chem 19:1144–1152. https://doi.org/10.1016/j.jiec.2012.12.011

78. Mirzaei AA, Sarani R, Azizi HR, Vahid S, Torshizi HO (2015) Kinetics modeling of Fischer-Tropsch synthesis on the unsupported Fe-Co-Ni (ternary) catalyst prepared using co-precipitation procedure. Fuel 140:701–710. https://doi.org/10.1016/j.fuel.2014.09.093

79. Sonal, Pant KK, Upadhyayula S (2017) Synergistic effect of Fe–Co bimetallic catalyst on FTS and WGS activity in the Fischer–Tropsch process: a kinetic study. Ind Eng Chem Res 56:4659–4671. https://doi.org/10.1021/acs.iecr.6b04517

80. van der Laan GP, Beenackers AACM (1999) Kinetics and selectivity of the Fischer-Tropsch synthesis: a literature review. Catal Rev Sci Eng 41:255–318. https://doi.org/10.1016/j.apcata.2013.10.061

81. Rautavuoma AOI, Vanderbaan HS (1981) Kinetics and mechanism of the Fischer-Tropsch hydrocarbon synthesis on a cobalt on alumina catalyst. Appl Catal 1:247–272

82. Satterfield CN, Huff GA, Longwell JP (1982) Product distribution from iron catalysts in Fischer-Tropsch slurry reactors. Ind Eng Chem Process Des Dev 21:465–470. https://doi.org/10.1021/i200018a020

83. Deng L-J, Huo C-F, Liu X-W, Zhao X-H, Li Y-W, Wang J et al (2010) Density functional theory study on surface CxHy formation from CO activation on Fe3C(100). J Phys Chem C 114:21585–21592. https://doi.org/10.1021/jp108480e

84. Gracia JM, Prinsloo FF, Niemantsverdriet JW (2009) Mars-van Krevelen-like mechanism of CO hydrogenation on an iron carbide surface. Catal Lett 133:257–261. https://doi.org/10.1007/s10562-009-0179-5

85. Dijk V (2001) The Fischer-Tropsch synthesis: A mechanistic study using transient isotopic tracing, Eindhoven University of Technology, (Thesis)

86. Anderson RB, Karn FS (1960) A rate equation for the Fischer-Tropsch synthesis on iron catalysts. J Phys Chem 64:805–808. https://doi.org/10.1021/j100835a025

87. van der Laan GP, Beenackers AACM, Krishna R (1999) Multicomponent reaction engineering model for Fe-catalyzed Fischer–Tropsch synthesis in commercial scale slurry bubble column reactors. Chem Eng Sci 54:5013–5019. https://doi.org/10.1016/S0009-2509(99)00225-0

88. Yates IC, Satterfield CN (1989) Effect of carbon dioxide on the kinetics of the Fischer-Tropsch synthesis on iron catalysts. Ind Eng Chem Res 28:9–12. https://doi.org/10.1021/ie00085a003

89. Teng BT, Chang J, Zhang CH, Cao DB, Yang J, Liu Y et al (2006) A comprehensive kinetics model of Fischer-Tropsch synthesis over an industrial Fe-Mn catalyst. Appl Catal A Gen 301:39–50. https://doi.org/10.1016/j.apcata.2005.11.014

90. Sonal, Pant KK, Upadhyayula S (2019) Detailed kinetics of Fischer Tropsch synthesis over Fe-Co bimetallic catalyst considering chain length dependent olefin desorption. Fuel 236:1263. https://doi.org/10.1016/j.fuel.2018.09.087

91. Todic B, Bhatelia T, Froment GF, Ma W, Jacobs G, Davis BH et al (2013) Kinetic model of Fischer–Tropsch synthesis in a slurry reactor on co–re/Al 2 O 3 catalyst. Ind Eng Chem Res 52:669–679. https://doi.org/10.1021/ie3028312

92. Zhang R, Chang J, Xu Y, Cao L, Li Y, Zhou J (2009) Kinetic model of product distribution over fe catalyst for Fischer-Tropsch synthesis. Energy Fuel 23:4740–4747. https://doi.org/10.1021/ef801079u

93. Qian W, Zhang H, Ying W, Fang D (2013) The comprehensive kinetics of Fischer-Tropsch synthesis over a Co/AC catalyst on the basis of CO insertion mechanism. Chem Eng J 228:526–534. https://doi.org/10.1016/j.cej.2013.05.039

94. Arsalanfar M, Mirzaei AA, Atashi H, Bozorgzadeh HR, Vahid S, Zare A (2012) An investigation of the kinetics and mechanism of Fischer–Tropsch synthesis on Fe–Co–Mn supported catalyst. Fuel Process Technol 96:150–159. https://doi.org/10.1016/j.fuproc.2011.12.018.

95. Arsalanfar M, Mirzaei AA, Bozorgzadeh HR (2013) Effect of preparation method on catalytic performance, structure and surface reaction rates of MgO supported Fe–Co–Mn catalyst for CO hydrogenation. J Ind Eng Chem 19:478–487. https://doi.org/10.1016/j.jiec.2012.08.030

96. Anderson RB, Friedel RA, Storch HH (1951) Fischer-Tropsch reaction mechanism involving stepwise growth of carbon chain. J Chem Phys 19:313. https://doi.org/10.1063/1.1748201.

97. Zhan X, Davis BH (2000) Two alpha Fischer-Tropsch product distribution. A role for vapor-liquid equilibrium. Pet Sci Technol 18:1037–1053. https://doi.org/10.1080/10916460008949890

98. Van Santen RA, Markvoort AJ, Ghouri MM, Hilbers PAJ, Hensen EJM (2013) Monomer formation model versus chain growth model of the Fischer-Tropsch reaction. J Phys Chem C 117:4488–4504. https://doi.org/10.1021/jp310245m

99. Kuipers EW, Vinkenburg IH, Oosterbeek H (1995) Chain length dependence of α-olefin readsorption in Fischer-Tropsch synthesis. J Catal 152:137–146. https://doi.org/10.1006/jcat.1995.1068

100. Iglesia E, Reyes SC, Madon RJ, Soled SL (1993) Selectivity control and catalyst design in the Fischer-Tropsch synthesis: sites, pellets, and reactors. In: Eley DD, Herman P, Weisz PB (eds) Advances in catalysis, vol 39. Academic Press, London, pp 221–302. https://doi.org/10.1016/S0360-0564(08)60579-9

101. Fortsch D, Pabst K, Grob-Hardt E (2015) The product distribution in Fischer-Tropsch synthesis: an extension of the ASF model to describe common deviations. Chem Eng Sci 138:333–346. https://doi.org/10.1016/j.ces.2015.07.005

102. Visconti CG, Tronconi E, Lietti L, Forzatti P, Rossini S, Zennaro R (2011) Detailed kinetics of the Fischer-Tropsch synthesis on cobalt catalysts based on H-assisted CO activation. Top Catal 54:786–800. https://doi.org/10.1007/s11244-011-9700-3

103. Bhatelia T, Li C, Sun Y, Hazewinkel P, Burke N, Sage V. Chain length dependent olefin re-adsorption model for Fischer – Tropsch synthesis over Co-Al₂O₃ catalyst Fuel Process Technol 2014;125:277–89.

104. Cheng J, Song T, Hu P, Lok CM, Ellis P, French S (2008) A density functional theory study of the α-olefin selectivity in Fischer–Tropsch synthesis. J Catal 255:20–28. https://doi.org/10.1016/j.jcat.2008.01.027

105. Claeys M, van Steen E (2004) Chapter 8 - Basic studies. In: Steynberg A, Dry ME (eds) Fischer-Tropsch technology, vol 152. Elsevier, Amsterdam, pp 601–680. https://doi.org/10.1016/S0167-2991(04)80465-8

106. Botes FG (2007) Proposal of a new product characterization model for the iron-based low-temperature Fischer-Tropsch synthesis. Energy Fuel 21:1379–1389. https://doi.org/10.1021/ef060483d

107. Schulz H, van Steen E, Claeys M (1995) Specific inhibition as the kinetic principle of the Fischer-Tropsch synthesis. Top Catal 2:223–234. https://doi.org/10.1007/BF01491969

108. Schulz H, Claeys M (1994) Selectivity and mechanism of Fischer-Tropsch synthesis with iron and cobalt catalysts. Stud Surf Sci Catal 81:455–460

109. Komaya T, Bell AT (1994) Estimates of rate coefficients for elementary processes occurring during Fischer-Tropsch synthesis over Ru TiO2. J Catal 146:237–248. https://doi.org/10.1016/0021-9517(94)90027-2

110. Dry ME (1982) Catalytic aspects of industrial Fischer-Tropsch synthesis. J Mol Catal 17:133–144. https://doi.org/10.1016/0304-5102(82)85025-6

111. Tau L-M, Dabbagh H, Bao S, Davis BH (1990) Fischer-Tropsch synthesis. Evidence for two chain growth mechanisms. Catal Lett 7:127–140. https://doi.org/10.1007/BF00764496

112. Patzlaff J, Liu Y, Graffmann C, Gaube J (1999) Studies on product distributions of iron and cobalt catalyzed Fischer–Tropsch synthesis. Appl Catal A Gen 186:109–119. https://doi.org/10.1016/S0926-860X(99)00167-2

113. Filip L, Zámostný P, Rauch R (2019) Mathematical model of Fischer-Tropsch synthesis using variable alpha-parameter to predict product distribution. Fuel 243:603–609. https://doi.org/10.1016/j.fuel.2019.01.121

114. Patzlaff J, Liu Y, Graffmann C, Gaube J (2002) Interpretation and kinetic modeling of product distributions of cobalt catalyzed Fischer–Tropsch synthesis. Catal Today 71:381–394. https://doi.org/10.1016/S0920-5861(01)00465-5

115. Egiebor NO, Cooper WC, Wojciechowski BW (1985) Carbon number distribution of Fischer — Tropsch CO-hydrogenation products from precipitated iron catalysts. Can J Chem Eng 63:826–834. https://doi.org/10.1002/cjce.5450630519

116. Schulz H, Claeys M (1999) Kinetic modelling of Fischer–Tropsch product distributions. Appl Catal A Gen 186:91–107. https://doi.org/10.1016/S0926-860X(99)00166-0

117. Todic B, Olewski T, Nikacevic N, Bukur DB (2013) Modeling of fischer-tropsch product distribution over Fe-based catalyst. Chem Eng Trans 32:793–798. https://doi.org/10.3303/CET1332133

118. Madon RJ, Reyes SC, Iglesia E (1991) Primary and secondary reaction pathways in ruthenium-catalyzed hydrocarbon synthesis. J Phys Chem 95:7795–7804. https://doi.org/10.1021/j100173a046

119. Madon Rostam J, Iglesia E (1993) Importance of olefin readsorption and H_2-CO reactant ratio for hydrocarbon chain growth on Ru catalysts. J Catal 139:576–590

120. Tau LM, Dabbagh HA, Davis BH (1990) Fischer-Tropsch synthesis: carbon-14 tracer study of alkene incorporation. Energy Fuel 4:94–99. https://doi.org/10.1021/ef00019a017

121. Schulz H, Claeys M (1999) Reactions of α-olefins of different chain length added during Fischer–Tropsch synthesis on a cobalt catalyst in a slurry reactor. Appl Catal A Gen 186:71–90. https://doi.org/10.1016/S0926-860X(99)00165-9

122. van der Laan GP (1999) Kinetics, selectivity and scale up of the Fischer-Tropsch synthesis. PhD Thesis. University of Groningen, Groningen, The Netherlands.

123. Huff GA, Satterfield CN (1984) Evidence for two chain growth probabilities on iron catalysts in the Fischer-Tropsch synthesis. J Catal 85:370–379. https://doi.org/10.1016/0021-9517(84)90226-4

124. Hanlon RT, Satterfield CN (1988) Reactions of selected 1-olefins and ethanol added during the Fischer-Tropsch synthesis. Energy Fuel 2:196–204. https://doi.org/10.1021/ef00008a017

125. Schulz H (2007) Comparing Fischer-Tropsch synthesis on iron- and cobalt catalysts: the dynamics of structure and function. In: Davis BH, Occelli ML (eds) Fischer-Tropsch synthesis in catalysis, vol 163. Elsevier, Amsterdam, pp 177–199. https://doi.org/10.1016/S0167-2991(07)80479-4

126. Novak S, Madon RJ, Suhl H (1982) Secondary effects in the Fischer-Tropsch synthesis. J Catal 77:141–151. https://doi.org/10.1016/0021-9517(82)90154-3

127. Raje AP, Davis BH (1996) Effect of vapour-liquid equilibrium on Fischer-Tropsch hydrocarbon selectivity for a deactivating catalyst in a slurry reactor. Energy Fuel 10:552–560. https://doi.org/10.1016/0140-6701(96)89487-2.

128. Sarup B, Wojciechowski BW (1988) Studies of the fischer-tropsch synthesis on a cobalt catalyst I. evaluation of product distribution parameters from experimental data. Can J Chem Eng 66:831–842. https://doi.org/10.1002/cjce.5450660518

129. Mosayebi A, Mehrpouya MA, Abedini R (2016) The development of new comprehensive kinetic modeling for Fischer-Tropsch synthesis process over Co-Ru/gamma-Al2O3 nano-catalyst in a fixed-bed reactor. Chem Eng J 286:416–426. https://doi.org/10.1016/j.cej.2015.10.087

130. Teng B, Chang J, Wan H, Lu J, Zheng S, Liu Y et al (2007) A corrected comprehensive kinetic model of Fischer-Tropsch synthesis. Chin J Catal 28:687–695. https://doi.org/10.1016/S1872-2067(07)60060-6

131. Lox ES, Froment GF (1993) Kinetics of the Fischer-Tropsch reaction on a precipitated promoted iron catalyst. 2. Kinetic modeling. Ind Eng Chem Res 32:71–82. https://doi.org/10.1021/ie00013a011

Recent Developments on Clean Fuels over SAPO-Type Catalysts

Rekha Yadav and Arvind Kumar Singh

Abstract Aluminophosphate (AlPO) materials are analogous to zeolites, and possess wide application in catalysis, sorption, ion-exchange, etc. The advantage of AlPOs over zeolites is that they hold flexible framework and offer different metal ions to be incorporated into their framework. Consequently, their acidity can be tuned or altered. The addition of silica in AlPO framework results in the formation of silicoaluminophosphate (SAPO); the substitution of ions Si^{4+} with P^{5+} leads to the acidic sites in the catalyst. Various types of pore openings ranging from small, medium, to large diameters along with their multidimensional apertures make them unique in catalysis in refineries, petrochemicals, and organic transformations. The most explored SAPO materials for fuel production includes SAPO-11, SAPO-34, SAPO-5, and SAPO-31. Methanol to olefins (MTO) is one of the promising ways to catalytically convert natural gas to lower olefins via methanol. MTO reactions are mostly studied over SAPO-34 molecular sieve. SAPO-34 molecular sieve possesses chabazite (CHA) topology with 3D-8 pore opening. Hydrogenation of CO_2 to light olefins with C_2–C_4 selectivity over bifunctional catalysts is a promising route in checking climate change and meeting fuel demand. The production of diesel is reported over SAPO-11 molecular sieves using soybean oil and palm oil as feed. SAPO-11 molecular sieves possess AEL topology with 1D-10 pore opening. Similarly, SAPO-31 catalyst has been reported for hydro-treating of sunflower oil. The preliminary studies of addition of vegetable oil into petroleum feedstock in small quantities for co-hydro processing showed a promising result by improving fuel product yields.

The current book chapter aims to delineate about the different pathways to produce clean fuel over different SAPO molecular sieves. Highlights have been made on underlying mechanism involved in the catalytic pathways followed during the process. It also encompasses some insights into future significance of the catalysts that could lead to the implementation of a sustainable fuel production.

Keywords Aluminophosphates · Silicoaluminophosphate · SAPO · Molecular sieves · MTO process · Hydroisomerization

R. Yadav
Department of Chemistry, Sri Venkateswara College, University of Delhi, Delhi, India

A. K. Singh (✉)
Department of Chemistry, S.B College, VKSU, Arrah, Bihar, India

1 Introduction

Zeolites are crystalline, caged, tetrahedron framework molecular sieves comprising $(SiO_4)^{4-}$ and $(AlO_4)^{5-}$ units, attached three dimensionally by Si-O-Al linkages. Owing to their high acidic strength, thermal and mechanical stability, they have been one of the most extensively studied and utilized solid acid catalysts till date. Their unique pore apertures (<2 nm) set up a well-defined selectivity rules with provisions of shape as well as size of the reactant and products at a molecular level. Aluminophosphates, a novel class of crystalline microporous materials without silica, were firstly reported by Wilson et al. at Union Carbide [1, 2]. Often termed as AlPO-*n* (*n* refers to a distinct structure type), their framework has alternating AlO_4 and PO_4 tetrahedra, cross-linked via O bridges. They have general formula $[(AlO_2)_x(PO_2)_x] \cdot yH_2O$. Regardless of the structural analogy to zeolites, aluminophosphates differ considerably from aluminosilicates. The first difference is the negatively charged framework of aluminosilicates, compared to the electroneutrality of the AlPO framework. Secondly, Al in aluminosilicate is always T_d coordinated, whereas in the AlPO framework, it may exhibit higher coordination (e.g., penta and hexa-coordination), in addition to tetrahedral coordination. The framework of AlPO is flexible compared to the rigid zeolite framework. Structural flexibility of AlPO results in structural and compositional diversity, as aluminium and/or phosphorous in the lattice framework can be isomorphously substituted by ions of similar charge and size [2–4]. Incorporation of Si or any other metal (M) in the framework leads to formation of silicoaluminophosphate molecular sieves, SAPO-*n*, and metal (M) aluminophosphates MAPO-*n* or MAPSO-*n*, respectively [2–7]. The introduction of hetero-atoms in the aluminophosphates changes its acidic properties without altering the pore shape or size.

In the current book chapter, we summarize some important applications of these silicoaluminophasphate (SAPO) materials for hydrocarbon conversions, and clean fuel production from biomass/vegetable oil, and carbon dioxide.

2 Synthesis Methodology of SAPO-*n*

Conventional hydrothermal synthesis of SAPO involves the presence of inorganic precursors particularly Si, Al, and P. These precursors in the presence of suitable structure directing agents (SDAs) like alkali/ammonium cations and organic amines at different crystallization hours lead to various-sized SAPO frameworks with multiple pore entrances.

Figure 1 illustrates how various factors like molar ratio of inorganic precursors, nature of aluminium/silica source, choice of SDAs, crystallization temperature, duration, etc., may lead to different topological frameworks. The framework topology has been broadly categorized as small (8-membered ring of T atoms (Si, Al, P in case of SAPO), where T atoms are connected to each other via O), medium
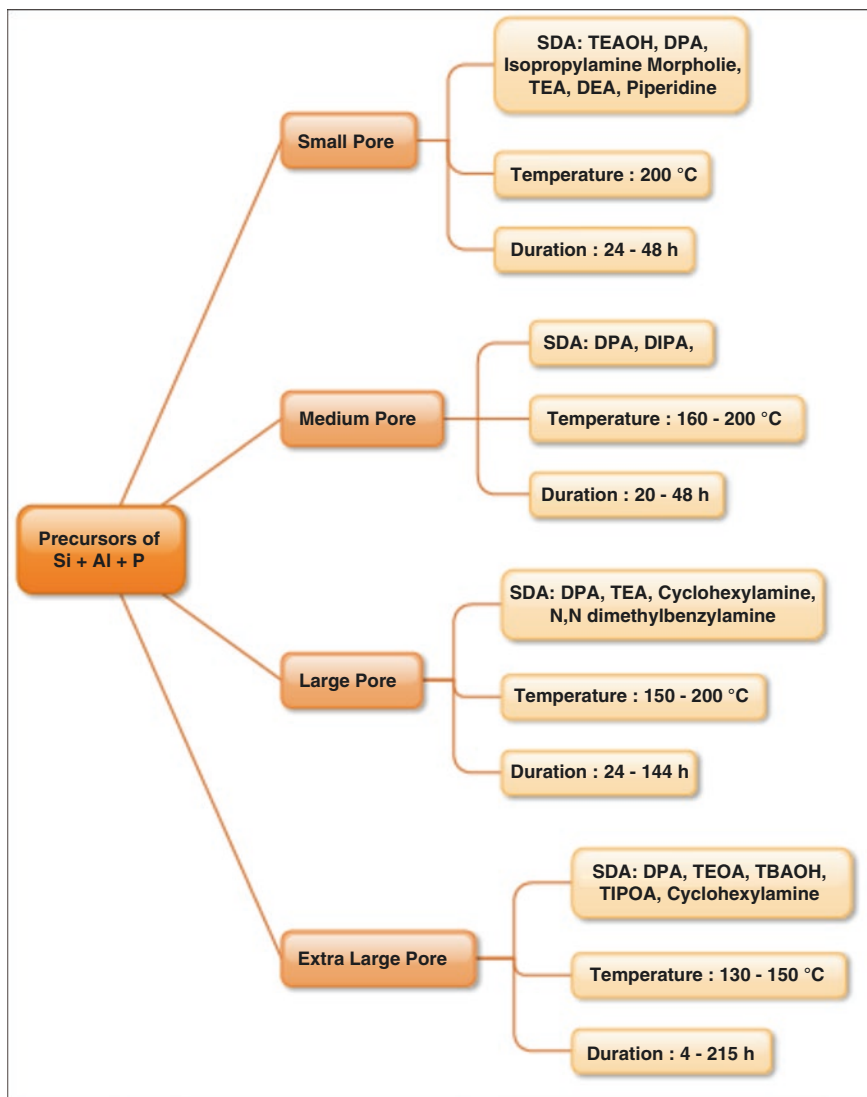
Fig. 1 Synthesis conditions of various framework silicoaluminophosphate molecular sieves

(10-membered ring), and large (12-membered ring) pore systems [8]. Some extra-large pore topology, with more than 12-membered ring (14–18) pore openings, also exists [8]. Among the small-pore SAPO molecular sieves, SAPO-34, possessing chabazite (CHA) topology is most widely explored in methanol-to-olefin (MTO) reaction [9, 10]. It has mild acidic strength, with three-dimensional 8-ring channels having a pore diameter of 0.38 nm and ellipsoidal cages of 0.67 nm × 1 nm [10]. Such kind of CHA topology generally arises at high crystallization temperatures.

Different amines, viz., triethylammonium hydroxide (TEAOH), dipropylamine (DPA) isopropylamine, morpholie, triethylamine (TEA), diethyl amine(DEA), and piperidine [9–14], have been reported for its synthesis. SAPO-11 (medium-pore molecular sieve) is usually synthesized in the presence of DPA and DIPA from the temperature range of 160–220 °C for 20–28 h [15, 16]. It shows structural analogy with AEL-type zeolite having one-dimensional 10-ring pore structure (0.4 × 0.65 nm). It exhibits good thermal stability and surface acidity which makes it a prominent catalyst in alkane isomerization/hydroisomerization and dewaxing processes [15, 16].

SAPO-5 has AFI topology with large-pore (0.73 nm × 0.73 nm) one-dimensional framework. It consists of repetitive connection of double four-membered ring (D4R) and double six-membered ring (D6R) as secondary building units (SBUs) framework with 12-membered pore opening [17, 18]. It is synthesized at various temperatures from 150 to 200 °C for 24–144 h. DPA, TEA, cyclohexylamine, and $N, N,$ dimethylbenzylamine have been successfully employed in its synthesis [19–22]. SAPO-5 finds extensive application in xylene isomerization, benzene alkylation, cumene synthesis, transalkylation of toluene with trimethylbenzene, etc. [23–27]. One template can direct the synthesis of multiple structures and also multiple templates may lead to formation of same framework. For example, dipropyl amine (DPA) has versatile application in the synthesis of almost all types of framework as shown in Fig. 1. The extra-large pore system, VPI-5 (18 rings) can be synthesized in the presence of triple helical periphery created by hydrogen bonded amine with water [28]. Other amines used for its synthesis are tetrabutylammonium hydroxide (TBAOH) [29, 30], di-n-pentylamine (DPeA), triethanolamine (TEOA), triisopropanolamine (TIPOA), cyclopentylamineand cyclohexylamine [31]. The vast variety of organics employed in VPI-5 synthesis not only act as SDAs but also serve the purpose of pH moderators. [31].

The catalytic performance of these solid acid catalysts has been employed in the generation of clean fuels from various sources like hydrocarbons, CO_2 biological feedstocks as well as by increasing the octane count of the petroleum products. The following sections highlight the insights of the various SAPOs in clean fuel production.

3 Catalytic Applications of Molecular Sieves in Clean Fuel Production

3.1 Fuels from Hydrocarbons

Hydrocarbons are ubiquitous in nature. Broadly they have been grouped as aliphatic and aromatic compounds. They range from simplest methane to complex catenated and polymeric sugars with other functionalities. When we talk about the natural sources of hydrocarbons, they are chiefly in the form of coal, petroleum, and natural

gases. However, their crude nature, complex structure, and associated impurities make them less suitable for direct use as fuel sources. The industrial refining and processing makes them ideal fuel with excellent calorific values. In this regard, in the industries several solid acid catalysts with desired pore apertures have been utilized to enhance the fuel quality. The rampant increasing crude oil cost and their depleting resources in coming future compel the researchers to adopt alternative pathways to produce light olefins. Methanol-to-olefin (MTO) reaction established by Mobil researchers in 1977 is the best example in this course [32]. It is the most important process technology to produce light olefins, especially C_2–C_4olefins from nonpetroleum feedstock of coal, natural gas, and biomass [33].

3.1.1   Studies over SAPO-34

Small–pore-sized solid acid catalysts in their H form, i.e., HSAPO-34 and HZSM-5, have been the most explored catalysts in MTO reaction [34]. However, the product selectivity in both differs remarkably. SAPO-34 has exclusive selectivity (>80%) for C_2–C_3olefins on the other hand in ZSM-5, C_4 olefins have higher selectivity [35]. The products are often accompanied with various side products like, H_2O, H_2, CO_X, higher paraffins, aromatics cokes, etc. [34, 35]. The occurrence of these side products imposes barrier in understanding the exact underlying reaction mechanism and rational design of catalyst synthesis for product selectivity [36–38]. The major steps involved in MTO reaction can be divided into following steps:

1. Dehydration of methanol to give equilibrium mixture of methanol and dimethyl ether (DME). This step also involves the formation of electron deficient free radical and carbonation intermediate.
2. Dehydration of resultant DME to give lighter olefin particularly ethylene, the C_2 product.
3. The addition reaction between the carbocation intermediate formed in the first step with the C_2 olefin of the second step to give C_3 olefin.
4. The oligomerization of olefinic products to give C_4 and higher homologues.
5. Dimerization of various cationic species and olefin intermediates to give different paraffin, aromatic products, which ultimately with time on stream get oligomerized, leading to coke formation.

Collectively these steps have been termed as hydrocarbon pool mechanism [33] as shown in Fig. 2. The circular cavity in the figure is analogous to three-dimensional cavity of catalyst where various steps (1–5) involved in MTO reaction take place. More than 20 reaction mechanism pathways have been proposed to describe various possible product formations in the process [33]. Among several mechanistic routes, the oxonium ylide mechanism proposed by Van den Berg et al. [39] is widely accepted. They proposed that dimethyl ether (DME) species obtained by the dehydration of methanol reacts with the methanol attached to the Brönsted acid sites of catalyst. It results in the formation of trimethyl oxonium ion (TMO) intermediate. This TMO species forms trimethyloxonium ylide, which undergoes intramolecular
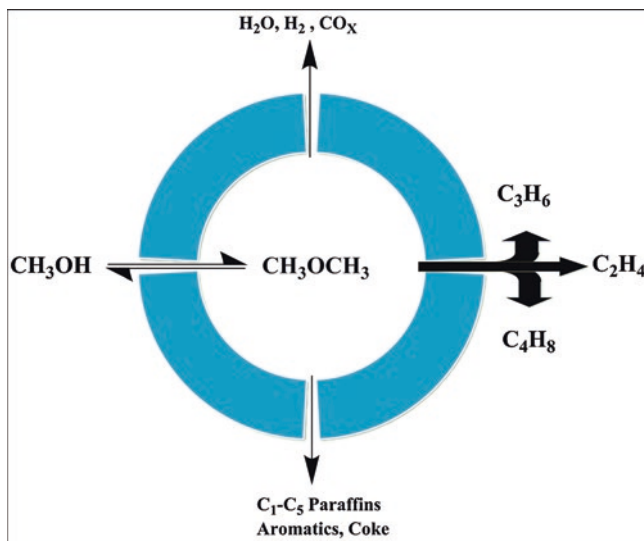
Fig. 2 Hydrocarbon pool mechanism involved in MTO reaction

Stevens rearrangement to form a methylethyl oxonium ion. This intermediate further leads to formation of ethylene and methanol. However, if the resultant ethylene reacts with the methyl carbocation, it results in propylene formation as depicted in Scheme 1.

It is noteworthy to account here that apart from olefins, the aromatics like methyl benzenes are also predominant reactive species in the hydrocarbon pool mechanism [40]. Hence later, based on the evidences of isotopic leveling experimental results, a dual cyclic mechanism in which both methyl benzene (MB route)–based reaction pathway and olefin-based route run parallel has been established [40, 41]. Recently with the help of DFT calculations, certain authors have reported MB-based and olefin-based dual cycle mechanism routes run simultaneously in MTO reaction and formation of ethane occurs through the MB-based route [42]. Rapid coking and exothermic nature of MTO reaction over SAPO-34 catalyst are the major concern for better catalytic performance. Hence the advance technology with efficient heat and mass transfer characteristics is a desirable aspect to attain better quality fuel with excellent selectivity. In this context world's first commercial MTO unit was successfully commissioned in Baotou, China, by DICP (named DMTO technology) in 2010 [43]. The technology involves use of fluidized bed reactors, which permits efficient heat transfer and enables the continuous regeneration of the catalyst [43]. Recently, the synthesis of nanosized SAPO-34 and hierarchical SAPO-34 has attracted attention in MTO reaction [44, 45].

Scheme 1 Oxonium ylide mechanism in MTO reaction

3.1.2 Studies over SAPO-11

SAPO-11 is a medium-pore molecular sieve with AEL topology, and it has been extensively used for fuel production from hydrocarbons (see Table 1). Geng et al. [52] studied different reaction parameters such as temperature, pressure, WHSV, and H_2/HC ratio for hydroisomerization of n-tetradecane over 0.4 wt% Pt-supported SAPO-11 catalyst. The increase in temperature from 593 to 653 K resulted in escalation in conversion from 10 to 80% with (pressure = 3 MPa, WHSV = 1 h^{-1}) with a slight decrease toward isomer selectivity. To study the effect of pressure, the authors varied the pressure from 0.5 to 4.5 MPa at 633 K (WHSV = 2 h^{-1}). The increasing pressure decreased the conversion with almost stable selectivity toward isomerized products. The decrease in the conversion was reported due to negative reaction order with respect to H_2. Variation in WHSV did not show any change toward the selectivity of isomers due to decrease in the contact time of feed with catalyst surface. With decrease in partial pressure of H_2 in H_2/HC ratio from 8.5 to 45, a slight decrease in conversion was reported. Hence optimum temperature, pressure, and WHSV resulted in higher conversion; also very slight or no effect was observed on product distribution. Nieminen et al. [53] studied the effect of source of silica and synthesis time on 1-butene isomerization. Tridymite phase was obtained

Table 1 Reaction conditions used for hydrocarbon conversion over SAPO-11

Reactant	Temperature (K)	WHSV (h^{-1})	Metal	Others	References
85% methyl oleate and 15% methyl stearate	613	2.5	3 wt% Ni	–	Liu et al. [46]
n-hexane, n-octane, and n-hexadecane	548–648	1.0	0.5 wt% Pt	H$_2$/ HC = 5.0	Sinha et al. [47]
n-dodecane	623	2.0	3 wt% Ni & P (different ratio)	H$_2$/ HC = 19	Tian et al. [48]
n-tetradecane	553–613	2.0	0.36 wt% Pt	H$_2$/ HC = 36	Ping et al. [49]
n-pentane	473–673	2.3	0.5 wt% Pt	H$_2$/ HC = 2.75	López et al. [50]
n-heptane	573–653	2.0	0.2 wt% La or Ce and 0.2 wt% Pt	H$_2$/ HC = 36	Liu et al. [51]

when watch glass silica was used whereas with colloidal silica and aluminum oxide SAPO-11 phase was obtained with tridymite as impurity. The increase in the synthesis time resulted in more acidic SAPO-11 phase due to incorporation of more Si in framework. The high selectivity of *iso*-butene was obtained on higher crystalline catalyst which provided more stable catalytic sites. Lee et al. [54] studied the effects of metal loading methods and an optimum amount of platinum on the hydroisomerization of *n*-dodecane.

Different metal loading methods such as incipient wetness (IW), ion exchange (IE), or atomic layer deposition (ALD) were used to load Pt on SAPO-11. The metal distribution was found to be very high in case of ion exchange and atomic layer deposition. However, a catalyst prepared with incipient wetness showed highest conversion as well as selectivity. The low activity in case of IE and ALD samples might be due to the presence of active metals inside the pores of catalyst which are not accessible. Liu et al. [46] applied NiP/SAPO-11 prepared using nickel impregnation on SAPO-11, for catalytic hydrodeoxygenation of fatty acid methyl oleate (85%) and isomerization of consecutive paraffin (15% methyl stearate) on a fixed-bed continuous-flow reactor. The catalyst with 3 wt% Ni loading obtained the high conversion of 97.8% with C$_{15-18}$ yield of 84.5%. The decrease in conversion with an increase in Ni content is attributed to blocking of active sites by high Ni content. The catalyst 3 wt% Ni showed 14% isomerization rate which is low due to steric hindrance of reactants. Without Ni content also, the catalyst showed 5% isomerization rate which is due to the Brönsted acidic sites of the catalyst.

The synthetic conditions can affect its catalytic activities. Sinha et al. [47] reported two different synthesis routes first using aqueous medium (SAPO-11(a)) and other using non-aqueous medium, i.e., ethylene glycol (SAPO (na)). The catalytic activities of the catalysts are compared with SAPO-31 (1D-12) synthesized similar to SAPO-11. The acidity of the materials was reported in the order SAPO-31(na) > SAPO-11(na) > SAPO-31(a) > SAPO-11(a). The high acidity in non-aqueous samples might be due to higher substitution of P^{5+} by Si^{4+}, resulting in less silica

islands. 0.5 wt% Pt loaded samples were utilized for isomerization of *n*-hexane, *n*-octane, and *n*-hexadecane over a temperature range of 548–648 K in presence of H_2. The hydroconversion follows the order Pt-SAPO-31(na) > Pt-SAPO-31(a) > Pt-SAPO-11(na) > Pt-SAPO-11(a). A slight high activity of SAPO-31 was reported which might be due to the large pore of SAPO-31. Among all the hydrocarbons *n*-hexadecane showed highest conversion on all catalysts over the entire temperature range and *n*-hexane showed the least. Also the authors reported more reactions at the pore mouth and the external surface in the case of SAPO-31 compared to SAPO-11. Wu et al. [55] varied the synthetic conditions (including templates) of SAPO-11 and studied for dehydration of ethanol to ethylene. The synthesized SAPO-11 was compared with commercial SAPO-11. Synthesized SAPO-11 showed 99% conversion of ethanol to ethylene at 280 °C, whereas the commercial catalyst needed 300 °C to reach the conversion. The selectivity of products in both the cases remained same. The study showed that tuning the catalyst synthesis conditions and precursors selection can have a huge impact on its catalytic activity. Tian et al. [48] prepared Ni phosphide-supported SAPO-11 and utilize it for hydroisomerization of *n*-dodecane. During the preparation of catalysts, different Ni/P ratios were used with 3 wt% of nominal Ni. The catalytic activity of NiP/SAPO-11was reported higher compared to Ni/SAPO-11 and SAPO-11. Maximum selectivity of *iso*-dodecane was reported with Ni/P ratio of 1; however with increase in Ni/P ratio, increase in conversion was reported. The high conversion and selectivity was reported on the catalyst with medium acidic sites; the synergic effect of acidic sites and Ni sites resulted in high selectivity of the product. At 623 K, 2%NiP (1/1)/SAPO-11 and 3%NiP (1/1)/SAPO-11 are reported to yield above 70% and 65%, respectively. The conversion showed increasing trend with rise in temperature and WHSV (from 1.5 to 6.0 h^{-1}) with lower selectivity toward *iso*-dodecane, whereas H_2 pressure beyond 2.0 MPa was reported unfavorable to alkene intermediate formation.

Not only the synthesis medium, but also the template used in the synthesis can alter catalyst properties. The change in template has an influence on Si distribution, acidity as well as on crystallinity. Ping et al. [49] synthesized SAPO-11 using mixed template of di-*n*-propylamine (DPA) and di-*iso*-propylamine (DIPA) by varying the template content ratio of DPA/DIPA. Catalyst prepared with DPA/DIPA ratio of 1.5 and 0.36% Pt showed the highest number of acidic sites. When applied for *n*-tetradecane isomerization, the catalyst with 1.5 template ratio showed higher conversion of 82% with 94.5% selectivity toward isomerized products at 593 K with WHSV of 2.0 h^{-1}. The higher conversion was reported due to uniform distribution of Si which resulted in small silicon domains and high acidity.

Promoters on a metal-loaded catalyst play a positive role in catalysis by enhancing the synergistic effect between the metal sites and acidic sites of catalysts. Liu et al. [56] studied the effect of Sn as a promotor on the Pt/SAPO-11 catalyst for hydroconversion of *n*-dodecane. The conversion of 91.1% and 90.5% was reported on Sn-Pt/SAPO-11 and Pt/SAPO-11, respectively. The conversion is almost similar in both cases; however, an increase in 10% selectivity toward mono-branched products with a decrease in cracked products was reported. The increased Sn content

(0.5–2 wt%) resulted in decreased conversion from 91.0 to 83.0% with higher iso-mers selectivity from 91.4 to 94.3%. The decrease in the conversion was reported due to masking of active acidic sites whereas an increase in selectivity is due to high metal dispersion.

López et al. [50] studied the hydroisomerization of *n*-pentane over 0.5 wt% Pt/SAPO-11 and compared its catalytic activity with zeolites (0.5 wt% Pt loaded HZSM-5 and acid treated HBEA). Rise in temperature from 523 to 673 K resulted an increase in the conversion for all the catalysts. However, 0.5 wt% Pt/SAPO-11 showed least conversion among all the catalysts. The Pt/HBEA catalyst showed about 95% selectivity toward *iso*-pentane, whereas it is 60–80% in the case of 0.5 wt% Pt/HZSM-5 and nearly 60% for 0.5 wt% Pt/SAPO-11 which is due to higher acidity in the case of zeolite catalysts. Liu et al. [51] studied the effect of addition of rare earth metals (La and Ce) as promoters over 0.2 wt% Pt/SAPO-11 and studied it for hydroisomerization of *n*-heptane. The bimetallic catalysts 0.2 wt% La 0.2 wt% Pt/SAPO-11 and 0.2 wt% Ce 0.2 wt% Pt/SAPO-11 were prepared by the impregnation method. These additive additions could lead to an increase in the amount of Lewis acid. LaPt/SAPO-11 and CePt/SAPO-11 showed good conversion of about 77–78% with i-C$_7$ yield of 67–68% whereas Pt/SAPO-37 showed a conver-sion of 65% with i-C$_7$ yield of 62%. The higher conversion in the case of rare earth metal-–promoted catalyst was reported due to higher Pt dispersion.

Pölczmann et al. [57] compared microporous and mesoporous molecular sieves for the isomerization and hydrocracking of Fischer–Tropsch wax (C$_{20}$–C$_{60}$). The isomerization of wax produces base oil and hydrocracking gives fuel. The authors found that 0.5 wt% Pt/AlSBA-15 catalyst over the temperature range of 548–623 K showed higher isomer content (about 70% at 623 K) compared to 0.5 wt% Pt/SAPO-11 (about 40% at 623 K) which might be due to higher concentration of Brönsted acidic sites on 0.5 wt% Pt/AlSBA-15. Fan et al. [58] reported aluminosili-cate/silicoaluminophosphate composite zeolite ZSM-5/SAPO-11 for fluid catalytic cracking (FCC). The composite was prepared by adding pre-formed ZSM-5 to SAPO-11 synthesis gel followed by hydrothermal treatment. The obtained catalyst was calcined and Ni-Mo was added to it using ion exchange. The obtained catalyst showed better catalytic activity compared to physical mixture of ZSM-5 and SAPO-11 due to the synergic effect between the acidic sites.

3.1.3   Studies over SAPO-5

Different reaction conditions for hydrocarbon conversion over SAPO-5 are sum-marized in Table 2. Hajfarajollah et al. [59] compared SAPO-34 and SAPO-5 and varied the silica source in the catalysts preparation. The SAPO-34 catalyst pos-sessed a high number of strong acidic sites essential for methanol conversion. The crystallite size played the main role in role in the selectivity and conversion. SAPO-34 synthesized using tetraethyl orthosilicate (TEOS) obtained small crystal-lite size compared to catalyst synthesized with fumed silica. The catalyst with small

Table 2 Reaction conditions used for hydrocarbon conversion over SAPO-5

Reactant	Temperature (K)	WHSV (h^{-1})	Metal	Others	References
Methanol	673	7.87	–	Feed = 0.29 mL/min	Hajfarajollah et al. [59]
n-Butane	673–723	1.5–5.5	2 wt% Pt	H$_2$/HC = 4	Kumar et al. [60]
n-C$_7$, n-C$_8$, n-C$_{10}$, n-C$_{12}$, n-C$_{16}$	550–625	–	1 wt% Pd	H$_2$ = 40 mL/min	Wang et al. [61]
Synthesis gas	533	–	–	GHSV = 3000 mL/ g$_{cat}$ H$_2$/CO = 2	Yoo et al. [62]
1-Octene	473–723	8,12, 20	–	H$_2$ = 25 mL/min	Singh at al [63]

crystallite size showed lesser deactivation due to easy diffusion whereas the other catalyst showed hindered diffusion of reactant molecules.

Kumar et al. [60] studied the effect on the alumina source in the synthesis of SAPO-5. The different alumina sources used were aluminium sulphate, sodium aluminate, aluminium oxide, and pseudo-boehmite. The use of aluminium phosphate or sodium aluminate yielded only quartz and berlinite forms whereas the purest structure was obtained with pseudo-boehmite and possessed the highest number of Lewis and Brönsted acidic sites. To study the catalytic activity, i.e., isomerization of n-butane, the catalyst was loaded with 2 wt% Pt using impregnation methods. For temperature from 673 to 723 K, 5% increase in the conversion was reported with a slight decrease in the selectivity towards product. However increased WHSV showed a decrease in the conversion which was due to a decrease in the contact time of reactant with the catalyst surface.

To alter the acidic properties of molecular sieves, the amount of silica in the molecular sieves composition can be adjusted. Wang et al. [61] reported SAPO-5 with Si/Al ratio of 0.25 and 0.42. The catalyst with Si/Al of 0.25 showed higher total acidity of 0.54 mmol/g whereas the other catalyst showed 0.48 mmol/g. The decrease in the acidity with an increase in the molar ratio was reported due to the replacement of P and Al with Si as reported by ^{29}Si MAS NMR spectra. To study the catalytic activity, the catalyst (1 wt% Pd/SAPO-5) was applied to hydroconversion of n-C$_7$, n-C$_8$, n-C$_{10}$, n-C$_{12}$, n-C$_{16}$ over the temperature range of 550–625 K. The catalytic activity increases with an increase in temperature and carbon chain respectively. At 598 K and above 100% conversion and selectivity was recorded for n-C$_{12}$, n-C$_{16}$.

Hulea at al [27] studied the trans-alkylation of toluene with different trimethylbenzenes (TMB). Among all the reactions with 1,2,3-TMB, 1,2,4-TMB, and 1,3,5-TMB as alkylation agents, 1,2,3-TMB showed the highest conversion over SAPO-5 prepared with lower silica content. All different reactions including trans-alkylation, isomerization, and disproportionation were reported; and the catalyst was active with all alkylating agents. Also at 548 K, 1,2,4-TMB was reported with highest yield of xylenes.

Erichsen et al. [64] studied the SAPO-5 for methanol to hydrocarbons and effect of adding benzene as co-reactant. The study showed that most of the products are in C_3–C_5 range. The authors reported that the conversion and selectivity of the reactant depended on the temperature of reaction and not on the feed rate and catalyst deactivation. The authors performed a steady-state isotope transient experiments by switching the $^{12}CH_3OH$ feed to $^{13}CH_3OH$ after 18 minutes on stream, at time of switch, methanol conversion was reported as 75%. The study reported immediate incorporation of ^{13}C in the alkene products, whereas it took time to incorporate ^{13}C in the polymethylated benzenes (polyMBs). Hence polyMBs were not the major reactant intermediates in the formation of alkenes. When benzene was used as co-feed with methanol, product selectivity toward C_2–C_3 products increased. When the co-feeding was added with $^{13}CH_3OH$, C_2–C_3 were reported as predominant products in ^{12}C. On the other hand, *iso*-butene and *iso*-pentene molecules showed larger amounts of ^{13}C, indicating two different mechanisms taking place on the catalysts.

Yoo et al. [62] studied the conversion of synthesis gas to dimethyl ether (DME) over SAPO-5 admixed with $Cu/ZnO/Al_2O_3$ catalyst. The admixed SAPO-5 and SAPO-11 (10% of SAPO composition) showed 55% conversion and 45% stability toward DME, whereas pure SAPO-5 and SAPO-11 showed 36% and 33% of CO conversion at 12 h on time of stream.

Jin et al. [65] compared small-, medium-, or large-pore-sized zeolites and SAPO for methanol to LPG (liquefied petroleum gas) conversions. The catalytic activities were found in the order ZSM-5 > SAPO-5 > SAPO-34 with respective fields of LPG fractions as 54.5%, 10.4%, and 3.9%. The selectivity toward alkene was highest for ZSM-5 (64.3%) compared SAPO-5 (56.2%). The lower activity of SAPO-34 might be due to pore blocking during the course of reaction.

Frietas et al. [66] studied dodecanoic acid decomposed over microporous (SAPO-5) and mesoporous (Al-MCM-41) catalysts. The reaction is important because the pyrolysis or thermal cracking of the oil results in fuel components. The NH_3 TPD studies on both catalysts showed that SAPO-5 contained more number of acidic sites compared to Al-MCM-41. Total conversion of dodecanoic acid was achieved with 78% of aromatics over Al-MCM-41. The high conversion with mesoporous molecular sieve is reported due to accessible pore size and optimum acidity.

Zhang et al. [67] prepared a composite catalyst to utilize the properties of more than one catalyst, the core/shell structure comprised of ZSM-5 core and SAPO-5 shell. The SEM and TEM images of catalyst showed the presence of both phases. The catalytic activity of the material was tested on heavy crude oil cracking. The conversions of heavy oil over ZSM-5, mechanical mixture (SAPO-5 and ZSM-5), and ZSM-5/SAPO-5 was 76.78%, 77.44%, and 80.03%, respectively. Also ZSM-5/SAPO-5 showed high selectivity toward ethene, propene, butane, and LPG, indicating that the pores of ZSM-5 and SAPO-5 were well connected and allowed passage of molecules.

Singh at al [63] prepared composite materials using SAPO-5 secondary building units (SBU) as precursors. The composite materials showed surface area in the mesoporous range, with the distinct acidity pattern compared to SAPO-5. The catalyst was tested for 1-octene hydroisomerization in the vapor phase. Above 673 K, the

Table 3 Reaction conditions used for hydrocarbon conversion over SAPO-11 and SAPO-5

Reactant	Temperature (K)	WHSV (h^{-1})	Metal	Others	References
1-pentene	523–823	–	–	P = 0.1 MPa	Höchtl et al. [68]
n-octene	573–708	–	0.5 wt% Pt	P = 3–5 bar H_2 = 25 mL/min	Campelo et al. [69]
n-hexane	573–708	–	0.5 wt% Pt	P = 3–5 bar H_2 = 25 mL/min	Campelo et al. [70]
Naphthalene: methanol: mesitylene (1: 5: 3.5)	623	0.19	–	–	Wang et al. [71]
n-hexane	498–648	–	0.2 wt% Pt and Ni (0, 0.2, 0.4 and 0.6 wt%)	LHSV = 1.0 h^{-1}	Eswaramoorthi et al. [72]

catalyst showed >90% conversion of 1-octene; however, the product distribution remained same irrespective of the reaction temperature.

3.1.4 Comparison of Activity Between SAPO-5 and SAPO-11

The catalytic activities of medium-pore and large-pore SAPOs for hydrocarbons conversion have been compared (see Table 3); the following section discusses a few of them. Höchtl et al. [68] studied 1-pentene isomerization of 1-pentene over AEL- and AFI-type structure (for both SAPO and CoAPO). The acidic strengths followed the order SAPO-5 < CoAPO-5 < SAPO-11 < CoAPO-11. The equilibrium distribution between the linear and branched products was achieved except at lower temperatures. The SAPO-5 showed higher deactivation due to coking on stronger acidic sites.

The hydroisomerization and hydrocracking of n-Octane was studied by Campelo et al. [69] using 0.5 wt% Pt/SAPO-5 and 0.5 wt% Pt/SAPO-11. Both the catalysts showed good activity in n-octane conversion; the aromatic products obtained over SAPO-5 catalyst were p- and m-xylene which are expected to be formed from cyclization of C_8-isoalkanes. However, over Pt/SAPO-11 ethylbenzene and o-xylene were reported as dominant products which are formed by direct cyclization of n-octane. The selectivity of the products varies due to steric hindrance showed by SAPO-11. The same group studied the hydroisomerization and hydrocracking of n-hexane [70]. The authors reported Pt/SAPO-5 to be more active with high selectivity toward iso-hexane which might be due to its optimum pore and acidity.

Wang et al. [71] studied the shape-selective properties of SAPO-11 and SAPO-5 in methylation of naphthalene using methanol (methylation agent) and mesitylene (solvent). The acidity studies showed that the SAPO-5 possessed only weak acidic sites whereas SAPO-11 possessed both weak acidic sites as well as moderate acidic sites. SAPO-11 and SAPO-5 showed conversion of 55.2 and 26.1%,

respectively. The product mixture shows the presence of ethylnaphthalene (EN), methylnaphthalene (MN), dimethylnaphthalene (DMN), and trimethylnaphthalene (TMN). SAPO-11 showed higher selectivity toward 2,6-dimethylnaphthalene (2,6-DMN) and 2,6−/2,7-DMN ratio than SAPO-5 which was attributed to the pore size of SAPO-11 molecular sieve.

Eswaramoorthi et al. [72] studied 0.2 wt% Pt and a varying amount (0, 0.2, 0.4 and 0.6 wt%) of Ni containing SAPO-11 and SAPO-5 for *n*-hexane isomerization. A decrease in the acidity of catalyst was observed with the addition of Ni. 2-methyl pentane (2MP), 3-methyl pentane (3MP), 2,3-dimethyl butane (23DMB), and 2,2-dimethyl butane (22DMB) were major products obtained in the reaction. 0.2 wt% Pt-0.4 wt% Ni/SAPO-11 showed higher selectivity toward mono and di-branched products.

Bandyopadhyay et al. [73] prepared SAPO-5 and SAPO-11 by the dry-gel conversion (DGC) method. SAPO-5 and SAPO-11 were applied for *iso*-propylation of biphenyl. SAPO-5 was reported more active with higher selectively toward 4,4′-diisopropylbiphenyl.

3.2   Fuel from Vegetable Oils/Biomass

The prevailing worldwide energy crisis, particularly exhausting non-renewable energy sources like coal, petroleum, has shifted the growing interest of researchers toward the development of biofuels. Biodiesel, mixture of mono-alkyl esters of higher fatty acids, is obtained via trans-esterification of triglycerides from vegetable oils with ethanol or methanol. Industries use alkalies (NaOH, KOH) in general practice for biodiesel production. However, the process suffers toxic waste generation, product separation, and purification issues. The use of the heterogeneous catalyst for green materials, biofuels, and sustainable chemicals is growing interest in chemical industries day by day. Different zeolite and zeo-type catalysts blended with active metals like Zn, Ca, Ru, Mg have been successfully used in the transesterification process [74].

3.2.1   Studies over SAPO-34

Abdulkadir et al. [74] have reported transesterification of rambutan seed oil over 15 wt% Mg/SAPO-34 (15 Mg/SAPO-34) catalyst. The catalyst has showed improved catalytic activity at a reaction temperature of 80 °C for 100 min with high fatty acid methyl ester (FAME) yield of 90.7%[74]. Zirconium sulphate (ZS)–supported SAPO-34 has been successfully employed in the esterification process. It was observed that 30wt%ZS/SAPO-34 catalysts display the property of superacid irrespective of calcinations temperature [75]. Ni-supported Ni/SAPO-34 and Ni/SAPO-11 have been used in hydrocracking of palm oil to jet biofuel. The Ni/SAPO-34 catalyst exhibited the highest alkane selectivity (65%) and lowest arene

selectivity (11%), owing to its constraint pore opening suitable for smaller molecular diffusion [76]. The application of SAPOs is not only limited to biofuel production but also in the synthesis of platform chemicals like xylene and furan [77, 78]. Hierarchical SAPO-34 has been used for *p*-xylene production from biomass-derived 2, 5-dimethylfuran (DMF) and ethylene, with a good selectivity (~75%). Similar trends have been reported for SAPO-11, the large-pore system [77].

3.2.2   Studies over SAPO-11

Xing et al. [79] studied the effect of Si/Al ratio of SAPO-11 for isomerization and cracking of *n*-alkanes (castor oil, C_{15}–C_{18}). SAPO-11 with different Si/Al molar ratio of 0.2, 0.4, 0.6 were synthesized and wet impregnated using 15 wt% Ni and 5 wt% Mo. The catalyst Ni-Mo/SAPO-11 with 0.4 Si/Al showed optimum conversion of 97.2% and jet fuel selectivity of 81.6%. The catalyst Ni-Mo/SAPO-11(0.4) was further explored to study the effect of temperature on conversion and selectivity of long-chain *n*-alkanes. It is reported that with an increase in temperature from 583 to 623 K, the conversion and selectivity of C_{15} increases compared to higher hydrocarbon chain.

Yang et al. [80] studied the effect of Ni loading on SAPO-11 for the hydroisomerization of oleic acid to *iso*-alkanes. The acidity of the catalyst was decreased with an increase in Ni loading. Among all the catalysts, catalysts with 7 wt% Ni showed the highest conversion and 67.3 mol% of *iso*-alkanes. The high amount of hydroisomerized products were obtained due to synergic effect between the metal center and Lewis/Brönsted acid sites.

Herskowitz et al. [81] studied conversion of soybean oil to green diesel over 1 wt% Pt/SAPO-11(to increase the surface area the catalyst, catalyst pellets were prepared by combining it with alumina binder). During the catalytic activity, no gas products were recorded only liquid phase products were obtained. The product contained branched paraffins, naphthenes, and mono-aromatics which qualified for diesel fuel blends. Rabaev et al. [82] reported >99% deoxygenation of soybean oil over Pt/ SAPO-11–Al_2O_3.

Rabaev et al. [83] studied 0.5 wt% Pt/SAPO-11 for vegetable oils conversion to diesel and jet fuels. The steady-state performance of the catalyst was studied after 200 h on stream rather than its initial activity. The authors reported three-stage processes to produce drop-in diesel and jet fuel. This stage followed are fractionation, mild hydrocracking on Ni_2P/HY catalyst followed by isomerization on 0.5%Pt/ Al_2O_3/SAPO-11. The fractionation 42–48 wt% of jet fuel with >12% aromatics was obtained with C_{14-16}% monoaromatic and >60% *iso*-paraffinic compounds.

Hancsók et al. [84] studied the oleic acid hydroisomerization over 0.5 wt% Pt/ SAPO-11 in detail and found that the addition of a small amount of oxygenic compounds (0.06–0.5%) yielded high isomer concentration in products. Further the decrease in the catalytic activity was due to structure collapse as a result of water formation during conversion. In a similar study the catalyst was found active for the

isomerization of pre-hydrogenated sunflower oils [85]. Under optimum conditions the yield of biogas oils was >88% with *i-/n*-paraffins ratio of 3.2–6.8.

Pérez et al. [86] studied hydroisomerization of palm oil over Pt/SAPO-11. Before applying palm oil to isomerization its desoxygenated was produced over the sulphided NiMo/Al$_2$O$_3$ catalyst. Under optimum conditions 71% of iso-desoxygenated palm oil (*i*-HDO) and 29% of HDO were reported which possessed cetane index of 92.4.

Liu et al. [87] varied the structure-directing agent (SDA) to prepare nano-sized SAPO-11. The SDA used in synthesis are di-*n*-propylamine (DPA) mixed with *n*-tetradecanoamine–*n*-propanol–H$_2$O medium. Ni/SAPO-11 was tested for hydrodeoxygenation (HDO) of palm oil. Due to large surface of nano-sized SAPO-11, high yield (80%) of liquid hydrocarbons with 80% isomerization selectivity was reported. The same group reported that Ni dispersion on SAPO-11 blocks some of the pores [88]. Also the weak and moderate acidic sites on SAPO-11 are primary reasons for good catalytic activity. Different pathways like hydrodeoxygenation and decarbonylation via the corresponding carboxylic acid intermediates are active on catalyst and the distribution of liquid alkanes depends on it.

Verma et al. [89] studied hydroconversion of non-edible jatropha oil over Ni-W catalyst supported over sulphided NiMo and NiW SAPO-11. About 84 wt% of liquid hydrocarbon with about 40% diesel and about 40% aviation kerosene was obtained. The variation of Si content in a catalyst did not alter the conversion and product distribution.

Kasza et al. [90] studied the application of 0.4 wt%Pt/SAPO-11 in the isomerization of rapeseed oil (C$_{12}$–C$_{20}$ paraffin). Under optimum conditions $T = 623$ K, LHSV 1.0–1.5 h^{-1} high amount of branched products were obtained. Liquid yield of >90% *iso*-paraffin was reported.

Zhao et al. [91] studied bifunctional Ni$_2$P/SAPO-11 for the hydroconversion of methyl laurate. Methyl laurate was reported to have nearly 100% conversion with the highest total selectivity to *iso*-undecane and *iso*-dodecane 36.9%. However, the catalyst deactivated after 10 h of time on stream. The carbon deposits during the course of reaction led to the deactivation.

Chen et al. [92] studied the same reaction on non-sulfide and sulfide NiMo/SAPO-11, reduced NiO/SAPO-11 and MoO$_3$/SAPO-11. On non-sulfide NiMo/SAPO-11 at 648 K, almost 100% conversion was achieved. The selectivity of isomerized products decreased with an increase in reaction temperature. The high activity of the catalyst was attributed to active metal phase Mo^{4+} and Mo^{5+}.

Gong et al. [93] studied the effect of active metal (Pd, Ni, Ru, Pt) on SAPO-11 for the isomerization of hydrodeoxygenated jatropha oil. The catalytic activity of catalysts decreased in the order of Pt/SAPO-11 > Pd/SAPO-11 > Ni/SAPO-11 > Ru/SAPO-11, which might be attributable to the difference of hydrogenation–dehydrogenation activity of these metals. Pt/SAPO-11 catalyst showed high yield of 79.4% toward *iso*-C$_{10–18}$ which might be due to appropriate acidic sites present on the catalyst. The increase in temperature favored multi-branched isomer formation from mono-branched isomers.

Zhang et al. [94] studied the size and acidity of pore in SAPO-11 by introducing surfactant cetyltrimethylammonium bromide (CTAB), nonionic copolymer poly(ethyleneoxide) block poly(propylene oxide)-block-poly(ethylene oxide) (F127), and both in synthesis. 0.5 wt% Pt/SAPO-11 (synthesized with CTAB+F127) was studied for 86.9% with 97.2% selectivity toward C_8isomers. The increase in isomerization yield was due to large pores formed in SAPO-11 (synthesized in presence of both CTAB and F127) which resists cracking of di-branched products and reduces probability of coke formation.

3.2.3 Studies over SAPO-5

Katikaneni et al. [95] studied the performance of aluminophosphate molecular sieve catalysts for the production of hydrocarbons from wood-derived and vegetable oils. The reaction was carried out over temperature range of 330–410 °C, with WHSV of 3.6 h^{-1}. SAPO-5 and SAPO-11 showed highest selectivity toward the aromatic hydrocarbons compared to MgAPO-36. Both the SAPO catalysts were highly selective for benzene formation. SAPO-5 in particular was selective for ethylene and propylene, SAPO-11 for propylene and MgAPO-36 for *iso*-butane.

3.3 Fuels from CO_2

Increasing CO_2concentration causes global rise in atmospheric temperature, ocean acidification, and climate change. Hence the scientific community is making efforts for CO_2 utilization [96]. There are two main reaction paths for the CO_2 hydrogenation to lower olefins: (1) a two-step process, with initial reduction of CO_2 to CO via the reverse water gas shift (RWGS) reaction followed by the conversion of CO to lower olefins via a Fischer-Tropsch; (2) lower olefins production from CO_2 and H_2 by two consecutive processes, viz., methanol synthesis and methanol-to-olefin (MTO) reaction [97, 98]. The use of a bifunctional catalyst (i.e., metal oxides/zeolites) for CO_2 conversion to light olefins is a promising approach to tackle CO_2 emissions [99, 100]. Ramirez et al. [99] have reported the synthesis of coated sulfated zirconia/SAPO-34 (ZrS/SAPO-34) for the direct conversion of CO_2 to light olefins. SAPO-34 causes light olefin selectivity, while ZrS layer allows the cracking of C_5^+ heavy hydrocarbons. Similarly, Li et al. [100] developed bifunctional ZnO-Y_2O_3 oxide and SAPO-34 zeolite, which catalyzes the selective hydrogenation of CO_2 to light olefins with a selectivity of 83.9% and conversion of 27.6% at 390 °C. Several other composite catalysts such as In_2O_3-$ZnZrO_x$/SAPO-34 [101], CuO-ZnO)-kaolin/SAPO-34 [102], $ZnGa_2O_{4,}$ and SAPO-34 [103], ZnO-ZrO_2 and SAPO-34 [104] have been reported in CO_2 to hydrocarbons conversion with high light olefin selectivity.

Not only SAPO-34 but SAPO-5 has also been explored for CO_2 conversion to fuels. Zhu et al. [105] prepared 2-dimensional SAPO-5 nanosheets (3.0 nm in thickness) and applied for photocatalytic reduction of CO_2 into CH_4. The nanosheets showed high CO_2 absorption capacity of 12.9 cm^3g^{-1} with 8.6 μLg^{-1} h^{-1} as rate of production of CH_4. The research can be a milestone considering the high global warming potential of CO_2.

4 Conclusion

Silicoaluminophosphates analogous to zeolites have exhibited paramount applications in petrochemical industries. Their framework can be tailored to unique pore apertures and acidity according to need. Three-dimensional small pores with 8-ring channels having a pore diameter of 0.38 nm, in SAPO-34, serve excellent selectivity for C_2–C_4 alkenes in MTO reactions. The hydrocarbon pool mechanism coupled with methyl benzene (MB route) describes the underlying chemistry in MTO reactions. The olefin conversion and lower olefin selectivity are chiefly controlled by the combined effect of surface acidity and pore size diameter of the catalyst. Consequently, selectivity for C_2–C_4 alkenes follows the trend as small-pore SAPO34 > medium-pore SAPO-11 > large-pore SAPO-5. Active metal loading such as Mg, Zn, Ni, and hierarchical mesoporosity over these systems extends their application in trans-esterification and platform chemical synthesis. The use of bifunctional catalysts like ZrS/SAPO-34, In_2O_3-$ZnZrO_x$/SAPO-34, etc., have been successfully employed in selective hydrogenation of CO_2 to light olefins, serving the dual purpose of checking greenhouse emission and clean fuel production. SAPO-5 is mainly utilized in hydrocarbon isomerization reactions. The absence of very strong acidity makes it good candidate in hydroisomerization reactions. SAPO-11 on other hand possesses potential to be industrial catalyst, most of the vegetable oil/ biomass conversions are successfully studied over it. They possess optimum acidity and active sites for biomass conversion.

References

1. Wilson ST, Lok BM, Messina CA, Cannan TR, Flanigen EM (1982) Aluminophosphate molecular sieves: a new class of microporous crystalline inorganic solids. J Am Chem Soc 104(4):1146–1147
2. Wilson ST, Lok BM, Flanigen EM (1982) US Patent 4,310,440
3. Messina CA, Lok BM, Flanigen EM (1985) US Patent 4,544,143
4. The increase in isomerization was due to large pores formed in SAPO-11(synthesized in presence of both CTAB and F127) which resists cracking of dibranched products and reduces probability of coke formation
5. Wilson ST, Flanigen EM (1989) Zeolite synthesis. In: Occelli MJ, Robson HE (eds) ACS Symposium Series, vol 398. ACS, Washington, DC, pp 329–345

6. Hartmann M, Kevan L (1999) Transition-metal ions in aluminophosphate and silicoalumi-nophosphate molecular sieves: location, interaction with adsorbates and catalytic properties. Chem Rev 99(3):635–664

7. Weckhuysen BM, Rao RR, Martens JA, Schoonheydt RA (1999) Transition metal ions in microporous crystalline aluminophosphates: isomorphous substitution. Eur J Inorg Chem 1999(4):565–577

8. Pastore HO, Coluccia S, Marchese L (2005) Porous aluminophosphates: from molecular sieves to designed acid catalysts. Annu Rev Mat Res 35:351–395

9. Lee YJ, Baek SC, Jun KW (2007) Methanol conversion on SAPO-34 catalysts prepared by mixed template method. Appl Catal Gen 329:130–136

10. Wang P, Lv A, Hu J, Lu G (2012) The synthesis of SAPO-34 with mixed template and its catalytic performance for methanol to olefins reaction. Microporous Mesoporous Mater 152:178–184

11. Najafi N, Askari S, Halladj R (2014) Hydrothermal synthesis of nanosized SAPO-34 molecu-lar sieves by different combinations of multi templates. Powder Technol 254:324–330

12. Parakash AM, Unnikrishnan S (1994) Synthesis of SAPO-34: high silicon incorporation in the presence of morpholine as template. J Chem Soc Faraday Trans 90(15):2291–2296

13. Askari S, Halladj R, Sohrabi M (2012) An overview of the effects of crystallization time, template and silicon sources on hydrothermal synthesis of SAPO-34 molecular sieve with small crystals. Rev Adv Mater Sci 32(2):83–93

14. Dumitriu E, Azzouz A, Hulea V, Lutic D, Kessler H (1997) Synthesis, characterization and catalytic activity of SAPO-34 obtained with piperidine as templating agent. Microporous Mater 10(1–3):1–12

15. Ma Z, Liu Z, Song H, Bai P, Xing W, Yan Z, Zhao L, Zhang Z, Gao X (2014) Synthesis of hierarchical SAPO-11 for hydroisomerization reaction in refinery processes. Appl Petrochem Res 4(4):351–358

16. Blasco T, Chica A, Corma A, Murphy WJ, Agúndez-Rodríguez J, Pérez-Pariente J (2006) Changing the Si distribution in SAPO-11 by synthesis with surfactants improves the hydroi-somerization/dewaxing properties. J Catal 242(1):153–161

17. Meier W, Olson D, Olson DH (1987) Atlas of zeolite structure types. Butterworth-Heinemann, London

18. Sinha AK, Sainkar S, Sivasanker S (1999) An improved method for the synthesis of the silicoaluminophosphate molecular sieves, SAPO-5, SAPO-11 and SAPO-31. Microporous Mesoporous Mater 31(3):321–331

19. Seelan S, Sinha AK (2004) Crystallization and characterization of high silica silicoalumino-phosphate SAPO-5. J Mol Catal A Chem 215(1–2):149–152

20. Young D, Davis ME (1991) Studies on SAPO-5: synthesis with higher silicon contents. Zeolites 11(3):277–281

21. Prakash AM, Unnikrishnan S, Rao KV (1994) Synthesis and characterization of SAPO-5 molecular sieve using N, N-dimethylbenzylamine as template. Microporous Mater 2(2):83–89

22. Elangovan SP, Ogura M, Zhang Y, Chino N, Okubo T (2005) Silicoaluminophosphate molec-ular sieves as a hydrocarbon trap. Appl Catal Environ 57(1):31–36

23. Ivanova II, Dumont N, Gabelica Z, Nagy JB, Derouane EG, Ghigny F (1993) In: von Balmoos R, Higgins JB, Treacy MMJ (eds) Proceedings of the ninth International Zeolite Conference, Montreal, Canada, 1992. Butterwoth-Heinemann, Boston, MA, p 327

24. Pellet RJ, Long GN, Rabo JA, Coughlin PK, Union Carbide Corp (1988) Xylene isomeriza-tion. US Patent 4,740,650

25. Pellet RJ, Long GN, Rabo JA, Union Carbide Corp (1988) Selective production of para-aromatics. US Patent 4,751,340

26. Sridevi U, Pradhan NC, Rao BKB, Satyanarayana CV, Rao BS (2002) Alkylation of ben-zene with isopropyl alcohol over SAPO-5 catalyst in an integral pressure reactor. Catal Lett 79(1–4):69–73

27. Hulea V, Bilba N, Lupascu M, Dumitriu E, Nibou D, Lebaili S, Kessler H (1997) Study of the transalkylation of aromatic hydrocarbons over SAPO-5 catalysts. Microporous Mater 8(5–6):201–206

28. McCusker LB, Baerlocher C, Jahn E, Bülow M (1991) The triple helix inside the large-pore aluminophosphate molecular sieve VPI-5. Zeolites 11(4):308–313

29. Davis ME, Montes C, Hathaway PE, Garces JM (1989) Synthesis of aluminophosphate and element substituted aluminophosphate VPI-5. In: Studies in surface science and catalysis, vol 49. Elsevier, Amsterdam, pp 199–214

30. Davis ME, Montes C, Garces JM (1989) Synthesis of VPI-5. ACS Symp Ser 398(1989):291–304

31. Davis ME, Young D (1991) Further studies on the synthesis of VPI-5. Stud Surf Sci Catal 60:53–64

32. Chang CD, Lang WH, ExxonMobil Oil Corp (1977) Process for manufacturing olefins. US Patent 4,025,576

33. Stöcker M (1999) Methanol-to-hydrocarbons: catalytic materials and their behavior. Microporous Mesoporous Mater 29(1–2):3–48

34. Lok BM, Messina CA, Patton RL, Gajek RT, Cannan TR, Flanigen EM (1984) Silicoaluminophosphate molecular sieves: another new class of microporous crystalline inorganic solids. J Am Chem Soc 106(20):6092–6093

35. Yokoi T, Yoshioka M, Imai H, Tatsumi T (2009) Diversification of RTH-type zeolite and its catalytic application. Angew Chem Int Ed 48(52):9884–9887

36. Teketel S, Skistad W, Benard S, Olsbye U, Lillerud KP, Beato P, Svelle S (2012) Shape selectivity in the conversion of methanol to hydrocarbons: the catalytic performance of one-dimensional 10-ring zeolites: ZSM-22, ZSM-23, ZSM-48, and EU-1. ACS Catal 2(1):26–37

37. Ilias S, Bhan A (2012) Tuning the selectivity of methanol-to-hydrocarbons conversion on H-ZSM-5 by co-processing olefin or aromatic compounds. J Catal 290:186–192

38. Bleken FL, Janssens TV, Svelle S, Olsbye U (2012) Product yield in methanol conversion over ZSM-5 is predominantly independent of coke content. Microporous Mesoporous Mater 164:190–198

39. vanden Berg JP, Wolthuizen JP, van Hooff JHC (1980) Proceedings fifth international zeolite conference (Naples). Heyden, London, p 649

40. Song W, Haw JF, Nicholas JB, Heneghan CS (2000) Methylbenzenes are the organic reaction centers for methanol-to-olefin catalysis on HSAPO-34. J Am Chem Soc 122(43):10726–10727

41. Bjørgen M, Svelle S, Joensen F, Nerlov J, Kolboe S, Bonino F, Palumbo L, Bordiga S, Olsbye U (2007) Conversion of methanol to hydrocarbons over zeolite H-ZSM-5: on the origin of the olefinic species. J Catal 249(2):195–207

42. Wang CM, Wang YD, Xie ZK (2014) Verification of the dual cycle mechanism for methanol-to-olefin conversion in HSAPO-34: a methylbenzene-based cycle from DFT calculations. Cat Sci Technol 4(8):2631–2638

43. Tian P, Wei Y, Ye M, Liu Z (2015) Methanol to olefins (MTO): from fundamentals to commercialization. ACS Catal 5(3):1922–1938

44. Rami MD, Taghizadeh M, Akhoundzadeh H (2019) Synthesis and characterization of nano-sized hierarchical porous AuSAPO-34 catalyst for MTO reaction: special insight on the influence of TX-100 as a cheap and green surfactant. Microporous Mesoporous Mater 285:259–270

45. Aghaei E, Haghighi M, Pazhohniya Z, Aghamohammadi S (2016) One-pot hydrothermal synthesis of nanostructured ZrAPSO-34 powder: effect of Zr-loading on physicochemical properties and catalytic performance in conversion of methanol to ethylene and propylene. Microporous Mesoporous Mater 226:331–343

46. LIU CY, Hao YANG, JING ZY, XI KZ, QIAO CZ (2016) Hydrodeoxygenation of fatty acid methyl esters and isomerization of products over NiP/SAPO-11 catalysts. J Fuel Chem Technol 44(10):1211–1216

47. Sinha AK, Sivasanker S, Ratnasamy P (1998) Hydroisomerization of n-alkanes over Pt– SAPO-11 and Pt– SAPO-31 synthesized from aqueous and nonaqueous media. Ind Eng Chem Res 37(6):2208–2214

48. Tian S, Chen J (2014) Hydroisomerization of n-dodecane on a new kind of bifunctional catalyst: Nickel phosphide supported on SAPO-11 molecular sieve. Fuel Process Technol 122:120–128

49. Ping LIU, Jie REN, SUN YH (2008) Effect of template content on the physicochemical characterization and catalytic performance of SAPO-11 for the hydroisomerization of n-tetradecane. J Fuel Chem Technol 36(5):610–615

50. López CM, Guillén Y, García L, Gómez L, Ramírez Á (2008) n-Pentane hydroisomerization on Pt containing HZSM-5, HBEA and SAPO-11. Catal Lett 122(3–4):267–273

51. Liu WQ, Shang TM, Zhou QF, Liu P, Ren J, Sun YH (2010) Study on the physicochemical and isomerization property of Pt/SAPO-11 catalysts promoted by metallic additive. J Fuel Chem Technol 38(2):212–217

52. Geng CH, Zhang F, Gao ZX, Zhao LF, Zhou JL (2004) Hydroisomerization of n-tetradecane over Pt/SAPO-11 catalyst. Catal Today 93:485–491

53. Nieminen V, Kumar N, Heikkilä T, Laine E, Villegas J, Salmi T, Murzin DY (2004) Isomerization of 1-butene over SAPO-11 catalysts synthesized by varying synthesis time and silica sources. Appl Catal Gen 259(2):227–234

54. Lee E, Yun S, Park YK, Jeong SY, Han J, Jeon JK (2014) Selective hydroisomerization of n-dodecane over platinum supported on SAPO-11. J Ind Eng Chem 20(3):775–780

55. Wu L, Shi X, Cui Q, Wang H, Huang H (2011) Effects of the SAPO-11 synthetic process on dehydration of ethanol to ethylene. Front Chem Sci Eng 5(1):60–66

56. Liu Y, Liu C, Liu C, Tian Z, Lin L (2004) Sn-modified Pt/SAPO-11 catalysts for selective hydroisomerization of n-paraffins. Energy Fuel 18(5):1266–1271

57. Pölczmann G, Valyon J, Szegedi Á, Mihályi RM, Hancsók J (2011) Hydroisomerization of Fischer–Tropsch wax on Pt/AlSBA-15 and Pt/SAPO-11 Catalysts. Top Catal 54(16–18):1079

58. Fan Y, Lei D, Shi G, Bao X (2006) Synthesis of ZSM-5/SAPO-11 composite and its application in FCC gasoline hydro-upgrading catalyst. Catal Today 114(4):388–396

59. Hajfarajollah H, Askari S, Halladj R (2014) Effects of micro and nano-sized SAPO-34 and SAPO-5 catalysts on the conversion of methanol to light olefins. React Kinet Mech Catal 111(2):723–736

60. Kumar N, Villegas JI, Salmi T, Murzin DY, Heikkilä T (2005) Isomerization of n-butane to isobutane over Pt-SAPO-5, SAPO-5, Pt-H-mordenite and H-mordenite catalysts. Catal Today 100(3–4):355–361

61. Wang L, Guo C, Yan S, Huang X, Li Q (2003) High-silica SAPO-5 with preferred orientation: synthesis, characterization and catalytic applications. Microporous Mesoporous Mater 64(1–3):63–68

62. Yoo KS, Kim JH, Park MJ, Kim SJ, Joo OS, Jung KD (2007) Influence of solid acid catalyst on DME production directly from synthesis gas over the admixed catalyst of Cu/ZnO/Al$_2$O$_3$ and various SAPO catalysts. Appl Catal Gen 330:57–62

63. Singh AK, Yadav R, Sudarsan V, Kishore K, Upadhyayula S, Sakthivel A (2014) Mesoporous SAPO-5 (MESO-SAPO-5): a potential catalyst for hydroisomerisation of 1-octene. RSC Adv 4(17):8727–8734

64. Erichsen MW, Svelle S, Olsbye U (2013) H-SAPO-5 as methanol-to-olefins (MTO) model catalyst: towards elucidating the effects of acid strength. J Catal 298:94–101

65. Jin Y, Asaoka S, Li X, Asami K, Fujimoto K (2004) Synthesis of liquefied petroleum gas via methanol/dimethyl ether from natural gas. Fuel Process Technol 85(8–10):1151–1164

66. Freitas C, Pereira M, Souza D, Fonseca N, Sales E, Frety R, Felix C, Azevedo A, Brandao S (2019) Thermal and catalytic pyrolysis of dodecanoic acid on SAPO-5 and Al-MCM-41 catalysts. Catalysts 9(5):418

67. Zhang Q, Li C, Xu S, Shan H, Yang C (2013) Synthesis of a ZSM-5 (core)/SAPO-5 (shell) composite and its application in FCC. J Porous Mater 20(1):171–176

68. Höchtl M, Jentys A, Vinek H (2001) Isomerization of 1-pentene over SAPO, CoAPO (AEL, AFI) molecular sieves and HZSM-5. Appl Catal Gen 207(1–2):397–405

69. Campelo JM, Lafont F, Marinas JM (1995) Pt/SAPO-5 and Pt/SAPO-11 as catalysts for the hydroisomerization and hydrocracking of n-octane. J Chem Soc Faraday Trans 91(10):1551–1555

70. Campelo JM, Lafont F, Marinas JM (1995) Hydroisomerization and hydrocracking of n-hexane on Pt/SAPO-5 and Pt/SAPO-11 catalysts. Zeolites 15(2):97–103

71. Wang X, Liu Z, Wei X, Guo F, Li P, Guo S (2017) Synthesis of 2, 6-dimethylnaphthalene over SAPO-11, SAPO-5 and mordenite molecular sieves. Braz J Chem Eng 34(1):295–306

72. Eswaramoorthi I, Lingappan N (2003) Hydroisomerisation of n-hexane over bimetallic bifunctionalsilicoaluminophosphate based molecular sieves. Appl Catal Gen 245(1):119–135

73. Bandyopadhyay R, Bandyopadhyay M, Kubota Y, Sugi Y (2002) Synthesis of AlPO 4 molecular sieves with AFI and AEL structures by dry-gel conversion method and catalytic application of their SAPO Counterparts on isopropylation of biphenyl. J Porous Mater 9(2):83–95

74. Abdulkadir BA, Ramli A, Lim JW, Uemura Y (2019) Study on the influence of Mg and catalytic activity of SAPO-34 on biodiesel production from rambutan seed oil. Biofuels 438:1–7

75. Li T, Cheng J, Huang R, Zhou J, Cen K (2015) Conversion of waste cooking oil to jet biofuel with nickel-based mesoporous zeolite Y catalyst. Bioresour Technol 197:289–294

76. Li T, Cheng J, Huang R, Yang W, Zhou J, Cen K (2016) Hydrocracking of palm oil to jet biofuel over different zeolites. Int J Hydrogen Energy 41(47):21883–21887

77. Gao Z, Feng Y, Zhang L, Zeng X, Sun Y, Tang X, Lei T, Lin L (2020) Catalytic conversion of biomass-derived 2, 5-dimethylfuran into renewable p-xylene over SAPO-34 catalyst. ChemistrySelect 5(8):2449–2454

78. Romo JE, Wu T, Huang X, Lucero J, Irwin JL, Bond JQ, Carreon MA, Wettstein SG (2018) SAPO-34/5A zeolite bead catalysts for furan production from xylose and glucose. ACS Omega 3(11):16253–16,259

79. Xing G, Liu S, Guan Q, Li W (2019) Investigation on hydroisomerization and hydrocracking of C15–C18 n-alkanes utilizing a hollow tubular Ni-Mo/SAPO-11 catalyst with high selectivity of jet fuel. Catal Today 330:109–116

80. Yang L, Xing S, Sun H, Miao C, Li M, Lv P, Wang Z, Yuan Z (2019) Citric-acid-induced mesoporous SAPO-11 loaded with highly dispersed nickel for enhanced hydroisomerization of oleic acid to iso-alkanes. Fuel Process Technol 187:52–62

81. Herskowitz M, Landau MV, Reizner Y, Berger D (2013) A commercially-viable, one-step process for production of green diesel from soybean oil on Pt/SAPO-11. Fuel 111:157–164

82. Rabaev M, Landau MV, Vidruk-Nehemya R, Goldbourt A, Herskowitz M (2015) Improvement of hydrothermal stability of Pt/SAPO-11 catalyst in hydrodeoxygenation–isomerization–aromatization of vegetable oil. J Catal 332:164–176

83. Rabaev M, Landau MV, Vidruk-Nehemya R, Koukouliev V, Zarchin R, Herskowitz M (2015) Conversion of vegetable oils on Pt/Al2O3/SAPO-11 to diesel and jet fuels containing aromatics. Fuel 161:287–294

84. Hancsók J, Kovács S, Pölczmann G, Kasza T (2011) Investigation the effect of oxygenic compounds on the isomerization of bioparaffins over Pt/SAPO-11. Top Catal 54(16–18):1094

85. Hancsók J, Krár M, Magyar S, Boda L, Holló A, Kalló D (2007) Investigation of the production of high quality biogasoil from pre-hydrogenated vegetable oils over Pt/SAPO-11/Al2O3. In: Studies in surface science and catalysis, vol 170. Elsevier, Amsterdam, pp 1605–1610

86. Pérez W, Marín J, del Río J, Peña J, Rios L (2017) Upgrading of palm oil renewable diesel through hydroisomerization and formulation of an optimal blend. Fuel 209:442–448

87. Liu Q, Zuo H, Wang T, Ma L, Zhang Q (2013) One-step hydrodeoxygenation of palm oil to isomerized hydrocarbon fuels over Ni supported on nano-sized SAPO-11 catalysts. Appl Catal Gen 468:68–74

88. Liu Q, Zuo H, Zhang Q, Wang T, Ma L (2014) Hydrodeoxygenation of palm oil to hydrocarbon fuels over Ni/SAPO-11 catalysts. Chin J Catal 35(5):748–756

89. Verma D, Rana BS, Kumar R, Sibi MG, Sinha AK (2015) Diesel and aviation kerosene with desired aromatics from hydroprocessing of jatropha oil over hydrogenation catalysts supported on hierarchical mesoporous SAPO-11. Appl Catal Gen 490:108–116

90. Kasza T, Holló A, Thernesz A, Hancsók J (2010) Production of bio gas oil from bioparaffins over Pt/SAPO-11. In: 19th international congress of chemical and process engineering, CHISA 2010 and seventh European congress of chemical engineering, ECCE-7

91. Zhao S, Li M, Chu Y, Chen J (2014) Hydroconversion of methyl laurate as a model compound to hydrocarbons on bifunctional Ni2P/SAPO-11: Simultaneous comparison with the performance of Ni/SAPO-11. Energy Fuel 28(11):7122–7132

92. Chen N, Gong S, Qian EW (2015) Effect of reduction temperature of $NiMoO_{3-x}$/SAPO-11 on its catalytic activity in hydrodeoxygenation of methyl laurate. Appl Catal Environ 174:253–263

93. Gong S, Chen N, Nakayama S, Qian EW (2013) Isomerization of n-alkanes derived from jatropha oil over bifunctional catalysts. J Mol Catal A Chem 370:14–21

94. Zhang P, Liu H, Yue Y, Zhu H, Bao X (2018) Direct synthesis of hierarchical SAPO-11 molecular sieve with enhanced hydroisomerization performance. Fuel Process Technol 179:72–85

95. Katikaneni SP, Adjaye JD, Bakhshi NN (1995) Performance of aluminophosphate molecular sieve catalysts for the production of hydrocarbons from wood-derived and vegetable oils. Energy Fuel 9(6):1065–1078

96. Zoundi Z (2017) CO_2 emissions, renewable energy and the Environmental Kuznets Curve, a panel cointegration approach. Renew Sustain Energy Rev 72:1067–1075

97. Jadhav SG, Vaidya PD, Bhanage BM, Joshi JB (2014) Catalytic carbon dioxide hydrogenation to methanol: a review of recent studies. Chem Eng Res Des 92(11):2557–2567

98. Ramirez A, Dutta Chowdhury A, Dokania A, Cnudde P, Caglayan M, Yarulina I, Abou-Hamad E, Gevers L, Ould-Chikh S, De Wispelaere K, Van Speybroeck V (2019) Effect of zeolite topology and reactor configuration on the direct conversion of CO_2 to light olefins and aromatics. ACS Catal 9(7):6320–6334

99. Ramirez A, Chowdhury AD, Caglayan M, Rodriguez-Gomez A, Wehbe N, Abou-Hamad E, Gevers L, Ould-Chikh S, Gascon J (2020) Coated sulfated zirconia/SAPO-34 for the direct conversion of CO_2 to light olefins. Catalysis science & technology

100. Li J, Yu T, Miao D, Pan X, Bao X (2019) Carbon dioxide hydrogenation to light olefins over ZnO-Y2O3 and SAPO-34 bifunctional catalysts. Catal Commun 129:105711

101. Dang S, Li S, Yang C, Chen X, Li X, Zhong L, Gao P, Sun Y (2019) Selective transformation of CO_2 and H_2 into lower olefins over In_2O_3-ZnZrOx/SAPO-34 bifunctional catalysts. ChemSusChem 12(15):3582–3591

102. Ramirez A, Chowdhury AD, Caglayan M, Rodriguez-Gomez A, Wehbe N, Abou-Hamad E, Gevers L, Ould-Chikh S, Gascon J (2020) Coated sulfated zirconia/SAPO-34 for the direct conversion of CO_2 to light olefins. Catalysis Science & Technology 10(5):1507–1517

103. Liu X, Wang M, Zhou C, Zhou W, Cheng K, Kang J, Zhang Q, Deng W, Wang Y (2018) Selective transformation of carbon dioxide into lower olefins with a bifunctional catalyst composed of $ZnGa_2O_4$ and SAPO-34. Chem Commun 54(2):140–143

104. Wang G, Zeng L, Cao J, Liu F, Lin Q, Yi Y, Pan H (2019) Highly selective conversion of CO_2 to hydrocarbons over composite catalysts of ZnO-ZrO_2 and SAPO-34. Microporous Mesoporous Mater 284:133–140

105. Zhu S, Liang S, Wang Y, Zhang X, Li F, Lin H, Zhang Z, Wang X (2016) Ultrathin nanosheets of molecular sieve SAPO-5: a new photocatalyst for efficient photocatalytic reduction of CO_2 with H_2O to methane. Appl Catal Environ 187:11–18

Synthesis of Novel Catalysts for Carbon Dioxide Conversion to Products of Value

Onochie Okonkwo and Pratim Biswas

Abstract This chapter is a description of methodologies for the conversion of carbon dioxide to products of value using catalytic processes. Accumulation of carbon dioxide in the atmosphere is a major problem and an optimal solution is to capture and convert it to useful products. In this chapter, first, the climate challenges due to increasing carbon dioxide emissions, the earth's carbon cycle, sources of carbon dioxide emissions and carbon dioxide capture are discussed. Second, carbon dioxide utilization processes such as enhanced oil recovery, and conversion methodologies including photo-conversion, bio-conversion and catalytic conversion processes are discussed. Third, the importance of scale for carbon dioxide utilization is discussed, and the catalytic conversion pathway is identified as a potential route for utilization in large scales. Wet and gas phase aerosol synthesis methods for catalysts are discussed followed by characterization methods. And finally, a futuristic application on the potential for utilization of carbon dioxide via reforming processes on Mars is presented.

Keywords Carbon cycle · CO_2 emission · CO_2 capture · CO_2 conversion · CO_2 reforming in space · Aerosol catalysts

1 Introduction

Carbon dioxide (CO_2) in the atmosphere is receiving significant attention lately, primarily due to increasing levels in the atmosphere and its impact on global climate change. Anthropogenic sources are a major contributor, and approaches to prevent the release should be explored and implemented. Due to the continued dependence on fossil fuels, a very large volume is released to the atmosphere. While

O. Okonkwo · P. Biswas (✉)

Aerosol and Air Quality Research Laboratory, Department of Energy, Environment and Chemical Engineering, Washington University in St. Louis, St. Louis, MO, USA
e-mail: pbiswas@wustl.edu

sequestration by burying in sub-surface environments is being explored, a better alternative would be to convert the carbon dioxide to value added materials. In theory, carbon dioxide (CO_2) can be converted into several chemicals and fuels. However, the relative unreactivity and very low Gibbs energy of carbon dioxide makes it energetically unfavourable to convert CO_2 into fuel and chemical products of higher value. The large volumes of CO_2 emitted also pose a challenge at doing this at the scales to be dealt with. However, the need to reduce CO_2emissions to the atmosphere demands that CO_2 be treated as a commodity chemical instead of a waste. This perspective will transform CO_2 into an asset as it is considered a primary feedstock to the chemical industry. This chapter provides a background and challenges associated with this proposition. As human exploration of other planets and outer space continues, we also propose the utilization of carbon dioxide by reforming on extra-terrestrial planets, especially Mars.

1.1 Climate Challenges with CO_2

In 2018, the globally averaged carbon dioxide (CO_2) concentration at the earth surface was 407.4 ppm which is a 46% increase of CO_2 levels since pre-industrial times [1]. Over the past decade, CO_2 concentration in the atmosphere increased at the rate of 2 ppm/year, resulting in serious global threats to human life and the environment—global warming and the concomitant effects of climate change [2, 3]. The International Energy Agency's (IEA), global energy and CO_2 status report indicates that there has been a 1 °C increase in global average annual surface temperature above pre-industrial levels [4].

The emissions of CO_2 influence the climate causing global warming via the greenhouse effect. The greenhouse effect is the trapping of solar radiation in the earth's atmosphere as heat by greenhouse gases. Solar radiation, with wavelengths ranging from 0.3 to 5 μm, incident on earth surface is radiated back into space during the night with wavelengths at the infra-red region. The natural frequency of the bonds of the greenhouse gases is within the infra-red frequency of the re-radiated energy, thereby causing resonance in the greenhouse gas molecules. The increased vibration due to resonance heats up the greenhouse gas molecules. Furthermore, the heat is transferred to other gases in the atmosphere, effectively trapping the re-radiated energy as heat in the atmosphere [5].

Major greenhouse gases in the atmosphere include CO_2, water (H_2O) vapour, methane (CH_4), dinitrogen oxide (N_2O) and chlorinated hydrocarbons. Water vapour has been shown to be a more effective greenhouse gas than CO_2, and its concentration in the atmosphere is orders of magnitude higher than carbon dioxide. However, the concentration of water vapour is controlled by temperature. An increase in CO_2 in the atmosphere will increase the atmosphere's temperature slightly which is enough to increase the concentration of water vapour in the atmosphere by evaporation from the oceans. It is this feedback mechanism that has the greatest influence on global temperature. In a sense, paradoxically, the concentration of CO_2 acts as a

regulator for water vapour in the atmosphere and is thus the determining factor in the equilibrium temperature of the earth and therefore global warming [5].

The gradual increase in the overall temperature of the atmosphere (global warming) has led to the following changes in the earth's climate conditions [6]:

- Increase in temperature of the upper layers of the oceans.
- Increase in sea levels.
- Decrease in oxygen (O_2) concentration in the oceans.
- Increased acidification of surface waters.
- Increased loss of ice from glaciers.
- Increased incidence of extreme weather and climate events such as heat waves, flooding, storms.

All these observations and trends emphasize the need to deal with the carbon dioxide being emitted into the atmosphere. We need to understand the earth's carbon cycle and carbon dioxide emission sources. Although eliminating anthropogenic sources of CO_2 emissions by eliminating fossil fuel usage is the best alternative, by all practical estimations the transition to renewable sources of energy will take at least a decade. The carbon cycle and CO_2 emission sources are subsequently discussed.

1.2   Carbon Cycle on Earth

The global carbon cycle can be viewed as a series of reservoirs of carbon in the earth system, which are connected by exchange fluxes of carbon [3]. Figure 1 shows the global carbon cycle in the earth system. The earth system consists of three reservoirs: ocean, land, and atmosphere. CO_2 is the dominant carbon species in the atmosphere. On the land reservoir, carbon is found as organic compounds in vegetation, dead organic matter in soils and fossil fuel reserves in the subsurface. In the ocean, carbon occurs predominantly as dissolved inorganic carbon, dissolved organic carbon and in ocean floor sediments. The marine biota, predominantly phytoplankton, and other microorganisms represent a small organic carbon pool. Carbon is transferred from one reservoir to another through carbon fluxes denoted by arrows in Fig. 1.

Carbon fluxes between the atmosphere and the ocean surface (ocean atmosphere gas exchange) arise by the partial CO_2 pressure difference between the air and the sea while carbon fluxes between the atmosphere and land are mainly due to photosynthesis, respiration, and in the industrial era, fossil fuel combustion and net land use change.

Figure 1 clearly shows that before the industrial era, the carbon fluxes between the atmosphere and the other reservoirs (land and ocean) were essentially in balance such that on the average carbon dioxide concentration in the atmosphere was steady. Before the industrial era, the carbon fluxes were only by natural processes. In the industrial era, new sources of CO_2 emission (fossil fuel combustion and net land use
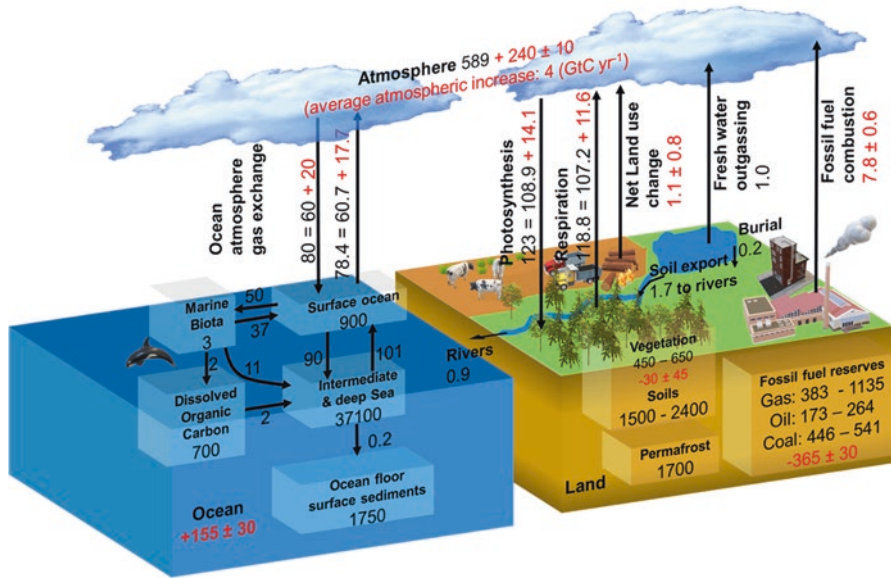
Fig. 1 Illustration of the global carbon cycle with numbers representing reservoir mass or carbon stock, in GtC and annual carbon exchange fluxes (in GtC/year). Reservoir mass and fluxes are denoted by boxes and arrows, respectively. Black numbers denote pre-industrial era reservoir mass and fluxes. Red numbers in the reservoirs denote cumulative changes of anthropogenic carbon over the Industrial Period 1750–2011. Red numbers for the fluxes denote average annual anthropogenic fluxes over the period 2000–2009. CO_2 is the dominant carbon species in the atmosphere. (1GtC equivalent to 3.67 Gt CO_2). Data obtained from Ciais et al. [3]

change) are introduced into the global carbon cycle with no corresponding new CO_2 removal process, leading to a disruption in the pre-existing balance in the global carbon cycle. This disruption leads to the transfer of carbon stocks from the land reservoir to the atmosphere and ocean.

Therefore, the additional CO_2 flux into the atmosphere in the industrial era (fossil fuel combustion, net land use change) has led to increases in the natural CO_2 fluxes (respiration, photosynthesis, and ocean gas exchanges), and subsequently, the accumulation of carbon in the atmosphere and the oceans, and the depletion of carbon in land as depicted in Fig. 1.

1.3 Sources of CO_2 Emissions

CO_2 emissions come from natural and anthropogenic sources as shown in Fig. 1. Natural sources of CO_2 emissions total about 726 Gt/year include mainly respiration from vegetation (59.9%) and ocean outgassing (40%). Other natural sources of CO_2 emissions which account for about 0.1% emissions include volcanic eruptions, forest fires and decomposition of organic matter [3]. Anthropogenic sources of carbon

dioxide emissions, which have become significant from the industrial times, total about 33 Gt/year with contributions from fossil fuel (coal, oil, natural gas) combustion (88%) and net land use change—including deforestation (12%) [3]. Therefore, CO_2 emissions from natural and anthropogenic sources sum up to about 759 Gt/year.

Natural processes remove CO_2 from the atmosphere at a rate of about 745 Gt/year include photosynthesis (60%), dissolution of CO_2 in oceans (39%) and rock weathering (1%) [3]. Presently, no anthropogenic process significantly removes CO_2 from the atmosphere. Consequently, CO_2 accumulates in the atmosphere at the rate of 14 Gt CO_2/year due to the current imbalance between CO_2 emission and removal rates. This accumulation of CO_2 has been linked to anthropogenic CO_2 emissions (mainly fossil fuel combustion) as before pre-industrial times the carbon dioxide emission and removal processes were in balance [2, 3, 7].

Amongst the anthropogenic sources, industrial point sources utilizing fossil fuels contribute 36%, transportation sector 25%, buildings 27% and other sources 12% of the total CO_2 emissions [8]. Industrial point sources emit significant amounts of carbon dioxide at individual emission points unlike highly distributed emissions obtained in transport and building. Table 1 provides a summary listing these industrial point sources and their characteristics. Power plants and various industries produce CO_2 streams with different compositions ranging from a few percent to over 99%. Natural gas processing, ammonia, hydrogen and ethanol production give the highest concentrations of carbon dioxide while conventional power plants yield the least concentrations of CO_2 [9].

As shown in Table 1, carbon dioxide is typically emitted in association with other gases. Even in the air, carbon dioxide is in mixture with oxygen, nitrogen and water vapour. These other gases are undesirable in the CO_2 utilization processes as they often act as a diluent. Hence approaches for CO_2 capture to increase its concentration in flow streams need to be explored.

1.4 Carbon Dioxide Capture

Carbon dioxide capture is a terminology used to describe processes that not only trap but also increase the concentration by separation from other gases in the mixture. Thus, a stream of carbon dioxide with high enough concentration is produced so that effective utilization or conversion processes can be used. Carbon dioxide presently can be captured at scale from air and other industrial point sources.

1.4.1 Direct CO_2 Capture from Air

In 2018, carbon dioxide concentration in the atmosphere was determined to be 407.4 ppm. Plants have successfully captured carbon dioxide from air via photosynthesis. Photosynthesis currently account for the capture and conversion of about 450 Gt CO_2/year. However, CO_2 capture by natural photosynthesis requires

Table 1 Characteristics of industrial CO_2 streams [9]

Industrial CO_2 source	CO_2 content (%)	Process unit	Flue gas component	US CO_2 emission[a] (MMT/year)
Petroleum power plant	3–8	Furnace	CO_2, NO_x, SO_x, O_2, N_2, H_2O	20
Natural gas power plant	3–5	Gas turbine	CO_2, NO_x, SO_x, O_2, N_2, H_2O	589
Coal power plant	10–15	Steam boiler furnace	CO_2, NO_x, SO_x, CO, O_2, N_2, Hg, As, Se	1151
Cement production	30 14–33	Precalciner High T Kiln (calcination)	CO_2, H_2O, N_2, HC, volatiles (K_2O, Na_2O, S, Cl)	65
Petroleum refineries	8–10 3–5 10–20 30–45, 98–100	Process heaters Utilities (steam, electricity) Fluid catalytic cracker (FCC regenerator) H_2 purification	Depends on fuel used Depends on fuel used O_2, CO_2, H_2O, N_2, CO, NO_x, SO_x CO_2, H_2, CO, CH_4	54
Iron and steel manufacturing	20–27 16–42	Blast furnace (high CO_2 if BFG is burned) Basic O_2 furnace (high CO_2 from burning BOF gas)	H_2, N_2, CO, CO_2, H_2S H_2, N_2, CO, CO_2, H_2S	29
Ethylene production	7–12	Steam cracking	H_2O, N_2, CO, CO_2, NO_x, SO_x, O_2	18.8
Ethylene oxide production	~30, 98–100	Absorption unit to purify EO (lower end is air oxidation; higher end is O_2 oxidation)	Mainly CO_2, H_2O, N_2, CH_4, EO	2.6[b]
Ammonia production	98–100	H_2 purification	CO_2, H_2, CH_4	21
Natural gas processing	96–99%	Acid gas removal/CO_2 absorption (low P striper)	96–99% CO_2, 1–4% CH_x (mainly methane), H_2O, N_2	16
Hydrogen production	30–45, 98–100 (15–20% in stream before purification)	H_2 purification (lower end is PSA; higher end is CO_2 specific separation)	CO_2, H_2, CO, CH_4 After chemisorption 100% CO_2	44
Ethanol production	98–99	Fermentation	CO_2, ethanol, methanol, H_2S, acetaldehyde, ethyl acetate	40.1

[a]Data obtained from US GHGRP 2018 FLIGHT database. Process emissions reported for all industry except for the power plants

[b]Ethylene oxide (EO) US CO_2 emission was estimated using an emission factor of 0.88 kg CO_2/kg EO [10]; and the American Chemistry Council estimate of 2.92 MMT US EO production in 2018 [11]

afforestation/reforestation. Natural photosynthesis is a very slow process and afforestation/ reforestation requires conversion of large land mass to forests.

Absorption of CO_2 in alkaline-based solutions such as sodium hydroxide solutions has been proposed and investigated for direct air capture of CO_2. The process involves contacting of air with a sodium hydroxide solution in a tower. The CO_2 is absorbed in the sodium hydroxide solution and is converted to sodium carbonate. The sodium carbonate is regenerated in a closed loop process and converted again into sodium hydroxide, via the causticization process using lime. The CO_2 evolved in the regeneration process is the captured CO_2 from the atmosphere [12, 13].

While this is thermodynamically feasible, the low concentrations in the atmosphere make it impractical for large-scale use.

1.4.2 CO_2 Capture from Industrial Point Sources

Industrial process emissions, on the other hand, have high carbon dioxide concentrations (ethanol production, natural gas processing, ethylene oxide production), and it can be utilized directly. Depending on the composition of CO_2 in the exhaust stream, CO_2 capture may require the use of conventional separation processes such as absorption and adsorption for the capture of carbon dioxide. Most carbon dioxide emissions from industrial sources are from power plants and therefore significant efforts have been expended in carbon dioxide capture from power plants. The main processes for CO_2 capture from power plants include pre-combustion capture processes, post-combustion capture processes and oxy-combustion capture processes [14].

Pre-combustion CO_2 capture involves the conversion of fuels (gasification of coal, reforming of natural gas and liquid fuels) into synthesis gas and further conversion of synthesis gas into hydrogen via the water gas shift reaction. The CO_2 separated from the H_2 is the captured CO_2, while the H_2 is combusted for provide power. Post-combustion capture processes involve the separation of CO_2 from the exhaust gases in a conventional fossil fuel power plant. Oxy-combustion capture process involves the combustion of fuels with high-purity oxygen instead of air to provide an exhaust gas with high-purity carbon dioxide which can be easily separated.

Carbon dioxide capture results in the production of a highly concentrated CO_2 stream. In the next section, we explore various utilization options for captured CO_2.

2   Carbon Dioxide Utilization

Captured carbon dioxide can be either sequestered or utilised. Carbon sequestration involves the long-term storage of captured CO_2 in suitable underground rock formations. While appropriate choice of injection areas will ensure the safety of the sequestration process, it is associated with inherent risks. Furthermore, it represents the conventional method of treating by-products as waste, and no economic gains result from such processes. Carbon dioxide utilization on the other hand describes

processes that transform carbon dioxide from an energy or industrial sector by-product to a useful commodity. When compared to capture and sequestration, CO_2 utilization for chemical synthesis presents several benefits beyond the reduction of emissions. These benefits include the recycle of CO_2 as a feedstock for synthesis, the reduction in the depletion of fossil fuels, possible reduction in other environmental impact categories (eutrophication, terrestrial acidification, photochemical oxidant formation, particulate matter formation) for the process, and increased profitability from synthesised products [15, 16]. Several processes are presently available for the utilization of captured carbon dioxide.

2.1 Enhanced Oil Recovery

Captured CO_2 is compressed and injected into depleted oil and gas reservoirs where they facilitate the recovery of residual oil and gas by providing the driving force for oil and gas recovery. The carbon dioxide displaces the hydrocarbons from the reservoir, and the CO_2 is safely sequestered in the reservoir. Carbon dioxide has been used for enhanced oil recovery for many decades, and several large-scale EOR projects are in operation in North America [14].

2.2 Photo-Catalytic Conversion of CO_2

This process is also referred to as artificial photosynthesis as it has similarities with natural photosynthesis in plants as it is based on using solar energy to reduce CO_2 into various chemical products and fuels. Photocatalytic CO_2 conversion makes use of semi-conductors to promote reactions in the presence of light irradiation. Photocatalytic materials that have been explored as catalysts include metal oxides and metal organic frameworks (MOF). The basic process can be summarized into three steps: (1) generation of charge carriers (electron–hole pairs) upon absorption of photons with suitable energy from light irradiation, (2) charge carrier separation and transportation, (3) chemical reactions between surface species and charge carriers. Photo-catalytic conversion of CO_2 has been shown to yield hydrocarbons such methane, synthesis gas, formaldehyde, formic acid and methanol [17, 18].

2.3 Bio-conversion of CO_2

These processes involve the use of micro-organisms such as algae to convert CO_2 into biofuels. Algae require CO_2 to grow and many algae species produce oil and other bio-refinable products which can be used as bio-fuels. In algae, the fixation of CO_2 occurs due to two separate reaction steps. In the light-dependent set of

reactions, photoexcited electrons are used to reduce the coenzyme NADP+ to NADPH as well as create the high-energy molecule ATP. In the second set of reactions, called the light-independent reactions, these reduced molecules are used to convert CO_2 to organic compounds that can then be used by algae as a source of energy. The oils produced by algae which are used for biofuel production contain the carbon that was fixed in the Calvin cycle. [17].

2.4 Catalytic Conversion of CO_2

Synthesis routes involving CO_2 have been developed for the catalytic conversion to methanol, methane, formaldehyde, formic acid, synthesis gas and polymers [16]. In general, these processes involve the reduction of carbon dioxide at high temperatures over a catalyst. The catalytic conversion mainly involves the conversion into polymers and reduction of carbon dioxide into higher valued products or intermediate (synthesis gas) using hydrogen or methane. Carbon dioxide reduction to synthesis gas or other higher valued products are energy-intensive processes due to the very low energy content and stable nature of CO_2. A significant amount of energy is required to activate carbon dioxide for subsequent reaction. The intermediate, synthesis gas is further used for the synthesis of commodity or fine chemicals. Major routes for CO_2 catalytic conversion involve the hydrogenation of CO_2 and the reforming of methane with CO_2.

Carbon dioxide utilization by conversion into chemicals and fuels has immense potential to transform CO_2 into an important feedstock for the chemical industry. However, this can only be realised if these processes can be implemented in large industrial scales.

3 Importance of Scale for CO_2 Sources and Conversion

Sources of CO_2 include point sources from industrial processes, and distributed sources such as from the transportation sector and agriculture. Distributed sources of carbon dioxide do not provide a continuous, high-volume and reliable supply of carbon dioxide and are not effective sources for large-scale CO_2 utilization projects. Even though the atmosphere is ubiquitous and free, the concentration of CO_2 in the atmosphere is very low (400 ppm) which significantly increases the cost and energy penalty associated with CO_2 capture to obtain concentrated streams. Pilot plant studies have shown that the cost of CO_2 capture from atmospheric air can range from USD94 to USD232 per ton [19]. Industrial sources of CO_2 provide reliable supply of CO_2 at much lower cost (USD14 to USD51 per ton) depending on stream purity [9]. The focus of the rest of this section is therefore on the utilization of CO_2 captured from industrial point sources.

The carbon dioxide utilization technologies that will have an impact by reducing emissions must be done at large scale. A large-scale implementation of CO_2 utilization technologies is necessary because current anthropogenic emissions are at the giga ton scale and it enables the leverage of economies of scale. Table 1 shows the emission rate of CO_2 from various industrial sources in the United States. Requirements for economical large-scale implementation of CO_2 utilization to mitigate carbon dioxide emissions include

- High reaction rates and CO_2 conversion efficiencies
- Net reduction in CO_2 emitted when compared to conventional processes
- Low cost of operation
- High demand for product
- Low-cost and reliable supply of carbon dioxide

High reaction rates and CO_2 conversion efficiencies are required for reasonable sizes of an industrial-scale plant and to reduce energy requirement for separation and recycle of unreacted reactants. To achieve a net reduction in CO_2 emissions, the utilization process should emit less CO_2 per unit of product when compared to the conventional process. Low cost of operation for CO_2 utilization processes is essential to ensure the cost of products is comparable to that of the conventional process. For economic justification of high production rates, typically obtained in industrial scales, there should be at least an equivalently high demand for the product. A low-cost and reliable supply of carbon dioxide is necessary for CO_2 utilization processes to ensure high on-stream time for the process at industrial scales.

Photocatalytic conversion of CO_2 avoids the energy penalty associated with high-temperature catalytic conversion processes, but studies have shown that it is highly kinetically limited with very low photoconversion efficiencies [17, 20–25]. This severely limits the effectiveness of photo-catalytic processes as high reaction rates are required for reasonable sizes for an industrial plant.

Although conversion rates for algae-based processes are marginally more than photocatalytic processes, they are still very low and their cost of operation can be very high. A lot of space and water resources are required to get optimal performance, and frequent tank cleaning will be required to ensure light penetration. Also, algae systems are less robust requiring a narrow range of operating conditions for optimal performance and usually produce a mixture of various products which can add complexity to downstream separations processes [17].

A major route for the catalytic conversion is the hydrogenation of CO_2 to produce fuels and chemical products such as methanol, methane, formaldehyde, formic acid and others [26, 27]. However, hydrogen production via electrolysis or reforming processes is highly energy intensive and can impact negatively on hydrogenation processes [28, 29]. For example, the CAMERE process has not been commercialized despite its development in 1999 and its successful pilot-scale demonstration (100 kg methanol/day) in 2004 [30, 31]. In the CAMERE process, CO_2 is hydrogenated in two steps to produce methanol. In the first reactor, CO_2 and H_2 are converted to CO via the reverse water gas shift reaction using a zinc aluminate-based catalyst at about 60% conversion per pass. By-product water is separated and

the mixture of CO, H_2 and unreacted CO_2 is sent to the methanol reactor where methanol is produced over a Cu/ZnO/ZrO$_2$/Ga$_2$O$_3$ catalyst.

Generally, hydrogenation of CO_2 requires the use of renewable energy for hydrogen production to ensure that the overall process results in a net reduction of carbon dioxide when compared to conventional fossil energy–driven processes. For example, the George Olah renewable methanol plant in Iceland is the first commercial-scale CO_2 hydrogenation plant to methanol with a capacity of about 4000 tons/year of methanol [16]. The process uses industrial CO_2 streams and hydrogen which is generated by electrolysis of water. This process is feasible only in Iceland due to the availability of cheap renewable Icelandic geothermal power [16, 32]. Opportunities also exist for hydrogenation of CO_2 in scale when waste hydrogen from the chlor-alkali industry is used [33].

Industrial-scale CO_2incorporation into polymers has been achieved. The Asahi kasei process [34, 35] incorporates CO_2 into bisphenol A polycarbonate product in three steps. In the first step, CO_2 reacts with ethylene oxide to produce ethylene carbonate. Ethylene carbonate is subsequently reacted with methanol to produce dimethyl carbonate and ethylene glycol. In the third step, dimethyl carbonate is reacted with phenol to produce diphenyl carbonate. In a final polymerisation step, bisphenol A polycarbonate is produced by the reaction of bisphenol A and diphenyl carbonate. A 50,000 ton/year polycarbonate plant based on the Asahi Kasei process has been successfully constructed and commissioned in Taiwan since June 2002.

Another major route for the catalytic conversion of CO_2 is by the reforming of methane with carbon dioxide to produce synthesis gas (a mixture of H_2 and CO). Reforming processes involving CO_2 include dry reforming and tri-reforming. The reaction of methane and carbon dioxide is called dry reforming of methane. When steam and oxygen are added to dry reforming, it is termed tri-reforming. Methane as a raw material is readily sourced from natural gas, bio-gas and land fill gas, and is relatively inexpensive. Synthesis gas is an intermediate which is utilized in several downstream processes depending on its CO to H_2 ratio [36]. Catalyst stability due to coking remains a persistent challenge for dry reforming but tri-reforming minimizes the incidence of coking, making tri-reforming a more practical conversion process at scale [37].

Direct reduction of CO_2 with CH_4 into a variety of gaseous and liquid products via plasma-catalysis has been reported recently [38]. However, this process is still under development in the lab scale and energy requirement for maintaining a plasma may be prohibitive for large-scale implementation of this process.

Among the different approaches for CO_2 conversion into products of value, catalytic conversion has the potential for implementation at scale. Compared to hydrogenation processes that rely on relatively expensive hydrogen, reforming processes with CO_2 have better prospects for industrial-scale implementation. Generally, reforming processes require three major steps for CO_2 conversion into high value products: carbon dioxide capture, reforming, and synthesis gas conversion as shown in Fig. 2.

Carbon dioxide capture has been discussed in Sect. 1.4. Captured CO_2 is mixed with compressed methane, preheated, and sent to the CO_2 reformer where reforming
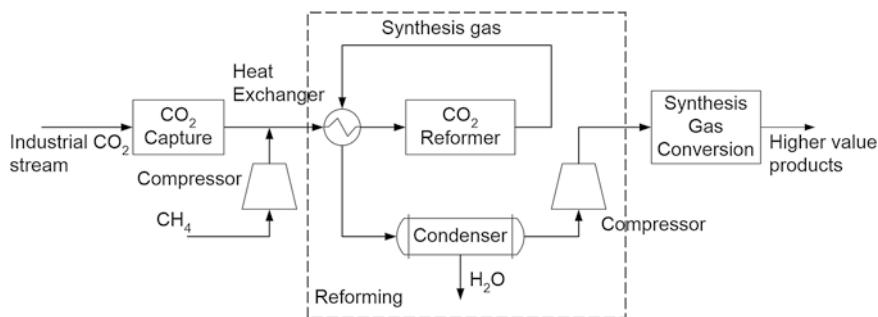
Fig. 2 Schematic diagram for CO_2 conversion into high-value products via reforming processes

reactions occur. Reactions that occur in CO_2 reforming processes are shown in Table 2 [39]. In the overall sense, the reforming reaction is highly endothermic and subsequently reforming is implemented at high temperatures (800–1000 °C) to attain high conversions of CO_2 and CH_4. Also, high temperatures are required to minimize coking [39]. Although the reforming reactions are more efficient at lower pressures, reforming is typically implemented at intermediate pressures to optimize the compression power required to compress synthesis gas for the downstream synthesis gas conversion process. The synthesis gas effluent is cooled, and water is separated by condensation. The synthesis gas is subsequently compressed and sent for further conversion to higher value products. Synthesis gas conversion processes include methanol synthesis for the production of methanol, Fischer-Tropsch synthesis for the production of liquid fuels, hydroformylation with olefins for the production of aldehydes and alcohols, isosynthesis for the production of branched hydrocarbons predominantly isobutane and isobutene, and Syngas to olefins (STO) for the production of C_2–C_4 olefins [36].

Large-scale application of the reforming process with CO_2 has been implemented. Linde AG has developed a licenced technology, Dryref™, which is based on reforming methane with CO_2 and steam after commercial demonstration of the process in an industrial-scale syngas plant with full product utilization in 2018. T2C Energy has developed a proprietary process, TriFTS™, to convert landfill gas to liquid fuels via tri-reforming of landfill gas to synthesis gas and subsequent conversion to liquid hydrocarbon fuels via the Fischer-Tropsch synthesis [40]. A demonstration unit based on TriFTS™ technology capable of converting 25 scfm (1000 m³/day) of crude biogas into diesel fuel has been built in Florida in 2018.

CO_2 reforming reactions are gas phase reactions promoted by heterogeneous catalysts. The nature of the catalyst is critical for reforming reactions. The properties of a catalyst which impact its effectiveness are determined by its synthesis method. The next sections will focus on catalyst synthesis, characterization and performance.

Table 2 CO_2 Reforming reactions

S/N	Reaction	ΔH_{298}[a] (kJ/mole)	Description
1	$CH_4 + CO_2 = 2CO + 2H_2$	+247	Dry reforming
2	$CH_4 + H_2O = CO + 3H_2$	+206	Steam reforming
3	$CH_4 + \frac{1}{2} O_2 = CO + 2H_2$	−36	Partial oxidation
4	$CH_4 + 2O_2 = CO_2 + 2H_2O$	−880	Methane combustion
5	$CO_2 + H_2 = CO + H_2O$	+41.1	Reverse water gas shift
6	$CH_4 = C + 2H_2$	+75	Methane cracking
7	$2CO = C + CO_2$	−172.4	Boudouard reaction
8	$C + H_2O = CO + H_2$	+131.3	Water gas reaction
9	$C + O_2 = CO_2$	−393.5	Coke combustion

[a]ΔH_{298} is the heat of reaction at 298 K

Table 3 Bulk and supported catalyst used in the industry

	Industrial processes
Bulk catalyst	
Al_2O_3	Claus process, dehydration of alcohols to olefins and ethers
Al_2O_3/SiO_2	Fluid catalytic cracking, acid-catalyzed reactions
Fe-Molybdate	Selective oxidation (methanol to formaldehyde)
Bi-Molybdate	Selective oxidation (propene to acrolein)
Vanadyl pyrophosphate	Selective oxidation (butane to maleic anhydride)
Fe_2O_3-Cr_2O_3	High temperature water gas shift
Supported catalyst	
Cu/ZnO-Al_2O_3	Methanol synthesis
Ag/α-Al_2O_3	Selective oxidation (ethylene to ethylene oxide)
Pt-Re/Al_2O_3	Catalytic naphtha reforming
Cr_2O_3/Al_2O_3	Toulene dehydroalkylation
Pt/Al_2O_3	Propane dehydrogenation
Ni/Al_2O_3	Steam methane reforming

3.1 Synthesis of Catalyst: Importance of Aerosol Routes

Heterogeneous catalysts may be broadly divided into bulk catalysts and supported catalysts. Bulk catalysts consist mainly of the active catalytic material (inert binders may be added to aid the forming processes) while supported catalysts consists of active catalytic materials dispersed on the surface of a support material. Table 3 shows bulk and supported catalysts used in industry.

3.1.1 Catalysts Synthesis by Wet Synthesis Methods

Conventionally catalysts are synthesized by wet synthesis methods. These methods include precipitation, co-precipitation, impregnation, sol gel, incipient wetness and hydrothermal synthesis. The precipitation method of catalyst manufacture involves the formation of a new solid phase (catalyst particle precipitate) from a homogeneous liquid solution by nucleation and subsequent agglomeration of particles. The precursor (usually nitrate salts of the active metal) is dissolved in a solvent (usually deionised water) to form a homogeneous solution. The predominant methods employed to create supersaturation conditions necessary to form catalyst particle precipitates include change in pH by addition of acids or bases, addition of complexing agents and solvent evaporation [41, 42]. The co-precipitation method refers to the preparation of multi-component precipitates from a homogeneous solution of several precursors. The precipitate obtained can be a single solid compound consisting of the several metallic components in the precursor solution which may be the active catalyst or the precursor to the active catalyst which is formed by subsequent treatment [41, 42]. Several component precipitates which are highly inter-dispersed in a homogeneous solid phase (solid solution) are also formed by co-precipitation [43].

Impregnation involves the deposition of dissolved aqueous precursors on a preformed support by contacting the preformed support and the active component precursor solution. This can be achieved by immersion of the catalyst support in the precursor solution or spraying of the precursor solution onto the catalyst support. After some contact time, the support is separated from the precursor solution and the excess solvent imbibed by the support is removed by drying. When the volume of the precursor solution contacted with the porous support is equal or less than the pore volume of the porous support, the catalyst preparation method is called incipient wetness method [41, 42].

In contrast with the co-precipitation method, which is a discontinuous transformation, the sol-gel method is a homogeneous process which results in a continuous transformation of a precursor solution into a hydrated porous solid structure. The sol-gel method is based on the controlled hydrolysis and condensation of typically metal alkoxide precursors in an organic medium, usually, by addition of water and carefully controlling pH and temperature to form a sol, and subsequent polymerisation to form a porous solid gel with entrapped solutions of condensation by-products (typically water or alcohol) [41, 44–46]. The gel is further treated to obtain the catalytic material.

The hydrothermal synthesis method involves precipitate or gel formation from a mixture of dissolved precursors with additives such as structure directing agents at elevated temperatures under autogenous pressure in an autoclave for a determined time. This method is successful for the synthesis of metal oxides, mixed metal oxide and zeolite catalysts [47, 48].

Subsequent treatment steps which may include ageing, filtration, washing, drying, forming and calcination are implemented to obtain the catalytic material in its useful form. These final treatment steps also impact useful characteristics to the catalyst. Ageing involves stirring the precipitate or the gel in its mother liquor

(precipitating solution) for a fixed time. Ageing impacts the final morphology of the catalyst as agglomeration and structural changes occur. The precipitate/gel is filtered to separate it from its precipitating solution and typically washed with deionized water to remove unwanted occluded ions. Subsequently it is dried and formed by processes such as palletisation, extrusion or spray drying. And finally, the catalyst is calcined by relatively high temperature treatment. The calcination step improves the physical properties of the catalyst and may impact phase transitions to desirable catalytic phase.

3.1.2   Catalyst Synthesis by Aerosol Synthesis Methods

In general, the wet synthesis method leads to the synthesis of different types of catalytic materials with desirable properties. However, wet synthesis methods are typically multi-step, batch processes with significant waste treatment requirements and present scale-up challenges for continuous catalyst production at industrial scales. The novel catalyst synthesis technique by aerosol processes is an easily scalable, continuous, one-step synthesis method for catalyst synthesis [49–51]. Another advantage of flame synthesis is the manufacture of nano-sized particles with high-purity, well-controlled crystallinity and narrow size distribution [52]. High-purity catalysts obtained from flame synthesis technique may minimize waste generation in reactors from side reactions. The flame synthesis technique has been shown to produce catalysts with well-controlled size, morphology, high dispersion, surface area, strong metal support interaction and therefore good catalytic properties [53–56]. In some cases, flame-made catalysts have been shown to have better catalytic performance compared to conventionally synthesized catalysts by wet methods [57–60].

The aerosol synthesis method describes synthesis methods to produce solid catalyst particles from droplets of liquid precursor solution. Aerosol synthesis methods for catalyst production include flame synthesis and spray pyrolysis. In flame synthesis, the precursor is introduced into a flame while in spray pyrolysis, the precursor is introduced as droplets into a controlled high-temperature tubular reactor.

In aerosol synthesis processes catalyst particle formation mechanism can be either gas to particle conversion mechanism or droplet to particle conversion mechanism. In the gas to particle conversion mechanism, the active component (metal oxide) is first formed in the gaseous phase; and subsequently by nucleation, condensation, coagulation and agglomeration, a solid catalyst material is produced. In the droplet to particle conversion (intraparticle reaction) mechanism, catalyst particles are formed by solvent evaporation, precipitation and thermal decomposition of the precursor to form the active component in the solid phase with subsequent coagulation and agglomeration [52]. A schematic diagram showing the particle formation process in aerosol processes is shown in Fig. 3.

Flame synthesis is further divided based on the method of introduction of the precursor into the flame into vapour-fed flame synthesis and liquid-fed flame synthesis. In vapour-fed flame synthesis, gaseous precursors are fed into typically
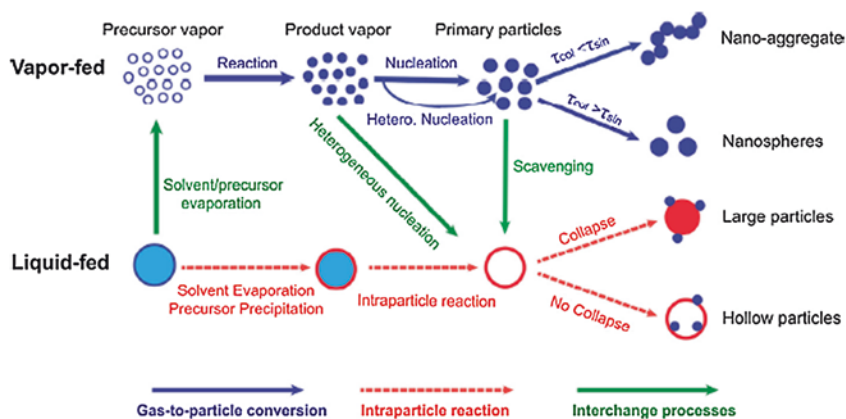
Fig. 3 Schematic of particle formation processes in aerosol processes [52]. Reproduced with permission from Elsevier

hydrocarbon, hydrogen and/ halide flames where combustion, decomposition or hydrolysis of the precursor takes place to produce the catalytic component in the gas phase and subsequent catalyst particle formation is by the gas to particle conversion route. In the liquid-fed flame synthesis, precursor liquid is first aerosolized to form fine liquid droplets and then introduced into the flame. Depending on whether sufficient energy is available in the flame for complete evaporation of the precursor, catalyst particle formation can be either through the gas to particle conversion route or the droplet to particle conversion route [49, 52, 61].

The liquid-fed flame synthesis is divided into flame spray pyrolysis (FSP) and flame-assisted spray pyrolysis (FASP) depending on whether the liquid precursor solution drives the combustion process. In flame spray pyrolysis the precursor is dissolved in a combustible solvent and therefore drives the combustion process [49, 52, 61]. Figure 4 shows different flame aerosol reactors (burner set-up) used in flame synthesis. The coflow diffusion flame and the flame spray pyrolysis aerosol reactors are easily scalable to industrial scales while the others are limited to laboratory scale. The coflow diffusion flame aerosol reactor is typically used for vapour-fed flame synthesis while the flame spray pyrolysis is used for liquid-fed flame synthesis.

In the flame spary pyrolysis burner, the liquid precursor mixture is delivered through the central capillary tube. Oxygen or air used as the dispersion gas is introduced at the annular region around capillary, and it serves to break up the liquid precursor mixture into micron size droplets. The sprayed droplets are ignited by methane flamelets which serve as pilot flames for stabilizing combustion. In the coflow diffusion flame aerosol reactor, the vapourized precursor is introduced at the central nozzle while the oxidant (typically O_2 or air) and fuel are introduced in the annular regions as shown in Fig. 3a. In aerosol reactors, the synthesized catalyst morphology and catalytic properties are determined by the residence time of the catalyst particles in the flame and the temperature profile of the flame.
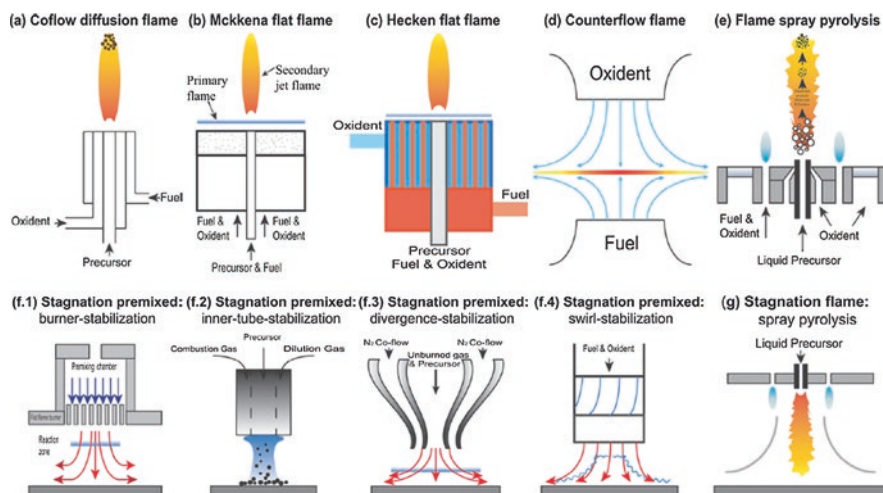
Fig. 4 Burner set-up used in flame synthesis [52]. Reproduced with permission from Elsevier

Precursor solution composition, flow rate and concentration, fuel and oxidant flow rates are process parameters that affect catalyst properties synthesized by flame synthesis. These parameters influence the combustion characteristics, temperature profile and residence time of the catalyst particles in the flame and therefore determine the catalyst particle size, crystallinity, crystal phase and morphology which impact its catalytic activity. For further details the reader is referred to the following papers [51, 61–65]. Table 4 shows various catalysts that have been made by flame synthesis.

Catalyst synthesis methods are optimized using feedback from synthesised catalyst characterisation and performance. Catalyst performance is evaluated in a lab-scale reactor system while catalysts are characterised using several available characterization methods.

3.2 Catalyst Characterization Methods

The three main descriptors for the performance of a catalyst are activity, selectivity and stability. Activity refers to the ability of the catalyst to convert feedstock into products usually measured in terms of conversion and turn over number or frequency. Selectivity is the ability of the catalyst to give a desired product out of all possible product and stability refers to ability of the catalyst to maintain sufficient level of activity and selectivity at the reaction conditions with time [73].

Catalysts are characterized to determine bulk, surface and chemical properties of the catalyst material which influences the performance of a given catalyst for a reaction [74]. The characterization of catalyst also ensures consistent synthesis of the

Table 4 Examples of catalyst synthesised by flame synthesis technique

Catalyst	Reaction	Reaction condition	Optimal performance
Rh/Al$_2$O$_3$ [66]	CH$_4$ steam reforming	600 °C, 100 kPa, H$_2$O/CH$_4$ = 4, GHSV = 60 L CH$_4$/g$_{cat}$h	69% CH$_4$ conversion, TOF = 22/s
Co$_3$O$_4$/CoAl$_2$O$_4$ [67]	CO$_2$ reforming of methane	700 °C, 1 atm, N$_2$:CH$_4$:CO$_2$ = 1:1:1, WHSV = 144 L/g$_{cat}$h	83% CH$_4$ conversion, H$_2$/CO ratio = 1.1
Cu/ZnO/Al$_2$O$_3$ + HZSM-5 [68]	Direct dimethyl ether (DME) synthesis	260 °C, 40 bar, H$_2$:CO:CO$_2$ = 16:8:1, 10% N$_2$, GHSV = 0.9 L/g$_{cat}$h	91% CO conversion, 62% DME selectivity
AuPd/TiO$_2$ [69]	C$_2$H$_2$ hydrogenation	40 °C, 1 atm, 1.5% C$_2$H$_2$, 2% H$_2$ in C$_2$H$_4$; GHSV = 7640/h	46% C$_2$H$_2$ conversion, 96% C$_2$H$_4$ selectivity
Ru/CeO$_2$ [70]	CO$_2$ methanation	300 °C, 1 atm, 22% H$_2$, 4.6% CO$_2$ in Ar, GHSV = 7640/h	83% CO$_2$ conversion, 99% CH$_4$ selectivity
Co/SiO$_2$ [71]	Fischer-Tropsch synthesis	260 °C, 20 bar, H$_2$/CO = 2, GHSV = 3 L/g$_{cat}$h	98% CO conversion, selectivity = 11% CH$_4$, 10% < C$_7$, 73% > C$_7$
Pd/CeO$_2$-TiO$_2$ [72]	Catalytic CH$_4$ combustion	470 °C, 1 atm, 8% O$_2$, 2%CH$_4$ in N$_2$; GHSV = 260 L/g$_{cat}$h	100% CH$_4$ conversion

desirable catalyst material with identical properties and helps to develop new catalytic materials. Catalyst characterisation can also provide insight into the mechanism of reactions taking place at the catalyst surface [75, 76].

Catalysis is a surface phenomenon. The surface area of a catalyst influences the catalyst activity as there are more exposed active sites for the catalytic reaction to occur. Surface area of catalyst is characterized typically by N$_2$ physiosorption using the BET method. The surface species present on the surface of a catalyst influence metal support interactions for supported catalysts and the interaction occurring on the catalyst active sites with reactant molecules. These interactions can affect the activity, selectivity and stability of the catalyst [77]. Available surface species are typically characterised using X-ray photoelectron spectroscopy (XPS). For metal supported catalyst, the fraction of metal atoms on the catalyst surface to the total metal loaded on the catalyst is the metal dispersion. The exposed metal atoms are important for catalysis as catalysis occurs on the surface atoms. The metal dispersion is usually obtained by chemisorption methods such as H$_2$ chemisorption.

Well-controlled pore sizes provide the confinement effect which can stabilize catalyst against sintering [78, 79] and hence affect catalyst stability. Also, pore size distribution in catalysts has been shown to influence selectivity by the shape selectivity effect [80, 81] and metal dispersion [82]. Pore size distribution is typically characterized by N$_2$ physisorption using the BJH method. Temperature-programmed reduction (TPR) of supported metal catalyst is used to characterize the reduction properties of catalyst which is indicative of the strength of the metal support

Table 5 Catalyst characterization methods

Technique	Properties determined
X-ray diffraction	Crystallinity, crystalline phases present, crystallite size
N_2 physiosorption (BET, BJH)	Surface area, pore volume, pore size distribution
Temperature-programmed reduction	Size and temperature ranges of reduction stages
CO_2 temperature-programmed desorption	Basic sites
NH_3 temperature-programmed desorption	Acid sites
H_2 pulse chemisorption	Metal dispersion
Transmission electron microscopy	Particle size, particle size distribution, morphology
Scanning electron microscopy	Morphology, particle size, particle size distribution
Photo electron spectroscopy	Surface elemental concentrations, distribution of active species on catalyst surface
Diffuse reflectance infrared Fourier transform spectroscopy	Chemical nature of surface groups
Energy dispersive X-ray spectroscopy	Elemental composition and spatial distribution
Nuclear magnetic resonance	Chemical environment of elements
Thermo gravimetric analysis	Change in weight of catalyst due to reaction, e.g., carbon deposition, metal oxidation

interaction. Depending on the reaction, concentration of acid sites and basic sites on the catalyst surface can influence the activity of the catalyst as it impacts adsorption and activation of reactant species and coke formation [74]. Concentration of acid and basic sites is characterized using NH_3 and CO_2 temperature-programmed desorption (TPD).

The morphology of synthesized catalyst can be characterized using electron microscopic methods such as transmission electron microscopy (TEM) and scanning electron microscopy (SEM). For more in-depth discussion of catalyst characterisation techniques, the reader is referred to Che and Vedrine [83]. Table 5 gives a brief overview of catalyst characterization techniques.

Considering that tri-reforming is predicted to be the more practical reforming process incorporating CO_2, when compared to other reforming processes, because of lesser severity of catalyst deactivation in tri-reforming, the next section will focus on the performance and kinetics of tri-reforming.

3.3   *Tri-reforming Catalyst Performance and Kinetics*

Generally, the catalysts used for reforming reactions are categorized into two groups; supported noble metals and non-noble transition metals [37]. Significant research has been focussed on the development of non-noble metal-based catalyst (mainly Nickel) for tri-reforming. However, nickel-based catalysts have continued to suffer from severe deactivation [37, 84]. Noble metal-based catalysts, even

though more expensive, have been shown to have high activity and resist deactivation in steam reforming [85, 86], dry reforming [87] and partial oxidation [88] which are the main reforming reactions.

The three main descriptors for the performance of a catalyst are activity, selectivity and stability. Activity refers to the ability of the catalyst to convert feedstock into products usually measured in terms of conversion and turn over number or frequency. Selectivity is the ability of the catalyst to give a desired product out of all possible product, and stability refers to the ability of the catalyst to maintain the sufficient level of activity and selectivity at the reaction conditions with time [73].

For high activity and selectivity, reforming catalysts should absorb and activate CO_2, CH_4, H_2O and O_2 efficiently [74]. Surface acidic and basic sites are essential for CO_2 absorption and activation [74]. Supports for reforming catalyst should have high hydrothermal stability and surface area [74]. Studies have shown that high metal dispersion, stronger metal support interaction, smaller particle size improve catalytic activity [37, 74, 87].

Deactivation mechanisms for reforming catalysts include coking, sintering, metal re-oxidation or irreversible reactions with support [74, 87, 89]. The nature of the catalyst support has been shown to strongly influence catalyst deactivation [74, 89, 90] and hence the stability of the catalyst. Redox, oxygen storage and oxophillic properties of supports have been shown to promote coke gasification and minimize metal oxidation while strong metal support interaction limits sintering [74]. The design of reforming catalysts to ensure stable operation is still an active area of research [91].

Tri-reforming reaction is a complex reaction system which is a combination of several reactions occurring simultaneously. While the kinetics of the individual reactions have been investigated, there are presently few studies that have investigated the kinetics of the combined effects of tri-reforming. In a recent study [92], the kinetics of tri-reforming was developed for a Ni-Mg/β-SiC catalyst, based on the assumption that the relevant reactions are the dry reforming, steam reforming and water gas shift reactions (Table 2, reaction 1, 2 and 5). The rate expressions for the reactions are given as follows:

$$r_{sr} = k_1 P_{CH_4} \left(1 - \frac{P_{CO} P_{H_2}^3}{P_{CH_4} P_{H_2O} K_{sr}} \right) \tag{1}$$

$$r_{dr} = k_2 P_{CH_4} \left(1 - \frac{P_{CO}^2 P_{H_2}^2}{P_{CH_4} P_{CO_2} K_{dr}} \right) \tag{2}$$

$$r_{wgs} = k_3 \left(\frac{P_{CO} P_{H_2O}}{P_{H_2}} - \frac{P_{CO_2}}{K_{wgs}} \right) \tag{3}$$

where r_{sr}, r_{dr}, r_{wgs} are the rate of the steam reforming, dry reforming and the water gas shift reaction (mol/s), respectively. k_1, k_2, k_3 are the apparent forward rate

constants of the steam reforming, dry reforming and the water gas shift reactions (mol/s kPa), respectively. K_{sr}, K_{dr}, K_{wgs} are the equilibrium constants for steam reforming, dry reforming and water gas shift reactions, respectively. $P_{CO}, P_{CH_4}, P_{H_2O}, P_{CO_2}, P_{H_2}$ are the partial pressures of CO, CH$_4$, H$_2$O, CO$_2$ and H$_2$, respectively.

The Arrhenius expression for the forward rate constants is given as follows:

$$k_1 = 85.77 \exp\left(\frac{-74.72}{RT}\right) \tag{4}$$

$$k_2 = 70.99 \exp\left(\frac{-77.82}{RT}\right) \tag{5}$$

$$k_3 = 149.92 \exp\left(\frac{-54.26}{RT}\right) \tag{6}$$

where R is the universal gas constant (kJmol^{-1} K^{-1}) and T is temperature (K).

The equilibrium constants can be estimated as follows:

$$K_{sr} = 1.198 \times 10^{17} \exp\left(\frac{-26830}{T}\right) \tag{7}$$

$$K_{dr} = 6.780 \times 10^{18} \exp\left(\frac{-31230}{RT}\right) \tag{8}$$

$$K_{sr} = 10^{\left(\frac{2078}{T} - 2.029\right)} \tag{9}$$

where T is temperature (K).

Clearly, future research is needed to further elucidate the kinetics of tri-reforming. The oxidation, coke formation and removal reactions should be considered. And a more appropriate Hougen–Watson kinetic model for heterogeneous reactions can be adapted.

Applications for reforming processes for CO$_2$ utilization is not limited to the earth. The Martian atmosphere is predominantly CO$_2$. In the next section, a futuristic potential application for reforming with CO$_2$ in Mars is discussed.

4 Potential for CO$_2$ Reforming in Extra-Terrestrial Space: Mars

The exploration of outer space is now being extended to create habitation on the Moon and other nearby planets such as Mars. In addition to the adventures of exploration, many of these outer space bodies are rich in resources. In addition to sustaining humans in these environments, technological innovations can be used to produce

a range of products. While carbon dioxide has become problematic on Earth, it offers potential as a resource in other planetary systems. This is enhanced by the availability of methane in addition. The prospect for establishing a sustainable human settlement in planets such as Mars requires opportunities for the utilization of extra-planetary resources by the development and deployment of technologies. This is also referred to as in situ resource utilization (ISRU) which is defined as the as the conversion of local resources at a space destination to provide useful infrastructure and commodities [93]. In situ resource utilization was first proposed in 1978 to produce rocket fuel on Mars for refuelling of an empty ascent vehicle for the return flight [94]. Utilization of Martian resources for life support and exploration will significantly reduce the costs of human missions and support for human settlements in Mars by reducing launch mass and cost of storage of consumables (O_2, food, fuel, H_2O). A recent study shows that ISRU for propellant and oxygen production results in about a 95% reduction in mass of the Mars ascent vehicle (MAV) [95]. Also, the availability of Mars-generated consumables could significantly extend the duration and range of crew operations and greatly enhance the science returns of missions to Mars.

The atmosphere of Mars is the most significant natural resource on the planet. It consists about 96% CO_2, 1.9% Ar, 1.9% N_2, 0.014% O_2 and 30 ppm H_2O with an atmospheric pressure of 700 Pa and average temperature of 220 K [93]. The Martian atmosphere will be the principal source of carbon and oxygen. Also, the highest potential sources of water include Martian regolith (hydrated minerals and clays) [96] within the top surface of Mars and ice [97] at the subsurface. Several minerals including oxides, chlorides, perchlorates, sulphates, sulphides, carbonates and silicates of Fe, Mg. Al, Ca, Na, K have been detected in Mars [98].

Oxygen and water are essential for life in Mars. Methane has been identified as an optimal rocket fuel which can be produced in Mars because of its relative ease of production using Martian resources, high specific impulse, low refrigeration power requirement with boiling point similar to oxygen and reduced risk of metal embrittlement in storage [94, 99]. The Sabatier/water electrolysis process has been demonstrated to produce oxygen and methane. In 2011, the Sabatier reactor was integrated into the international space station water recovery system [99].

In the Sabatier/electrolysis process, hydrogen is reacted with compressed CO_2 in a heated chemical reactor to yield methane and water. Ruthenium and Nickel on alumina catalysts have been found very effective for the Sabatier reaction with CO_2 conversion and yield greater than 99% at temperatures between 300 and 400 °C and pressure of 1 atm [100]:

$$CO_2 + 4H_2 = CH_4 + 2H_2O \qquad (10)$$

The methane water mixture is separated in a condenser. While methane is dried and stored for use as a propellant, water is collected, deionized, and electrolyzed in a standard electrolysis cell;

$$2H_2O = 2H_2 + O_2 \qquad (11)$$

The oxygen can be used as a propellant or life support while the hydrogen is recycled back to the Sabatier reactor. An external source of H_2 is required for continuous operation, as only half the amount of H_2 utilised by the Sabatier process is generated by electrolysis. Electrolysis of water obtained from Mars can be used to provide the additional hydrogen required while producing oxygen at the right ratio (3.4:1 O_2/ methane mass ratio) for the combustion of methane as rocket fuel [101].

Dry reforming has the potential to improve space missions and human colonisation of Mars in two distinct ways.

1. In life support systems, based on the Sabatier/electrolysis process, produced methane can be reformed with carbon dioxide to produce hydrogen which will close the loop and potentially eliminate the need for additional hydrogen for the Sabatier reaction

$$CH_4 + CO_2 = 2CO + 2H_2 \tag{12}$$

The combination of reactions (10), (11) and (12) gives the overall reaction:

$$2CO_2 = 2CO + O_2 \tag{13}$$

2. For human colonisation of Mars, reforming of methane produced via the Sabatier process with the Martian atmospheric carbon dioxide will yield synthesis gas which is an important intermediate to produce downstream chemicals and fuels [36]. Dry reforming usually yields a synthesis gas with a H_2/CO ratio close to 1; however preferential separation of CO from the synthesis gas mixture can be used to obtain any desired H_2/CO ratio.

Reforming of methane with carbon dioxide is a feasible process although the heat requirement is significant [39]. Using regenerative heat recuperation where the exit gases from the reactor heat the incoming gases can be used to reduce the heating requirement. High-temperature heating can be potentially provided by radioisotope thermal generators as they operate by converting high-temperature heat (up to 1300 K) emitted by radioactive sources into electricity based on the Seebeck effect [102, 103].

A schematic diagram showing the integration of the dry reforming process to the Sabatier/electrolysis is shown in Fig. 5. CO_2 captured from the Martian atmosphere and H_2 produced from the electrolysis of water obtained from Martian soil or subsurface ice deposits [101] are sent to the Sabatier reactor where they are converted to CH_4 and H_2O. Water is separated from the Sabatier reactor effluent by condensation and sent into the electrolyser where water is decomposed into hydrogen and oxygen by electrolysis. Typically, the water is purified to electrolysis grade water by ion exchange, but this may not be applicable in Mars as large amounts of consumables are required [101]. Membrane processes including forward osmosis can potentially be used instead [101, 104, 105]. Methane is separated from hydrogen and any unreacted CO_2 by a membrane separation process [106]. The H_2 and any unreacted CO_2 are recycled to the Sabatier reactor. The methane is sent to the dry
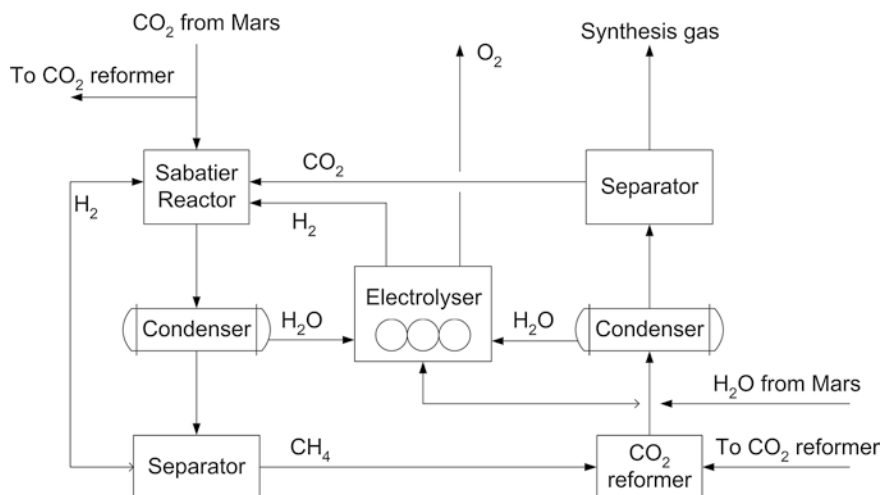
Fig. 5 Schematic diagram of the integration of CO_2 reforming to the Sabatier/electrolysis process

reforming reactor where it reacts with compressed CO_2 to produce synthesis gas. Any water that may exist in the reaction product is separated by condensation. Unreacted CO_2 and H_2 which are recycled to the Sabatier reactor are separated from CO which is vented. When the goal is to produce synthesis gas, which will be further used for downstream chemical/fuels manufacture in Mars, then only unreacted CO_2 is separated from the gas mixture.

5   Conclusions

As sequestered carbon over geological time scales is depleted on land at a faster rate by fossil fuel use via combustion, carbon dioxide is accumulating in the atmosphere and oceans, resulting in its increased concentration. To remediate this, carbon dioxide utilization can transform it from a waste and problematic product to a valuable feedstock for the chemical industry. At industrial scales, catalytic conversion via reforming processes is predicted to be a feasible approach for carbon dioxide utilization. As catalysts are the heart of catalytic processes, synthesis methods are important as they influence properties and therefore their performance. The gas phase aerosol flame synthesis method was described as a viable method for the production of functional catalysts. This is a single-step easily scalable method for catalyst manufacture unlike conventional the wet synthesis methods. Advances in CO_2 utilization technologies such as the Asahi Kasei process, Dryref™, TriFTS™ and the Camere process were discussed. With human interest in exploration and human settlement of planets such as Mars, there is a potential for extending reforming technologies for future production of chemicals in outer space.

References

1. Blunden J, Arndt DS (2019) State of the climate in 2018. Bull Am Meteorol Soc 101:Si-S306
2. Inamuddin AM, Asiri E (2019) Lichtfouse, sustainable agriculture reviews 37: carbon sequestration, vol 1 Introduction and biochemical methods, 1st edn. Springer, New York
3. Ciais P, Sabine C, Bala G, Bopp L, Brovkin V, Canadell J, Chhabra A, DeFries R, Galloway J, Heimann M, Jones C, Quéré CL, Myneni RB, Piao S, Thornton P (2013) Carbon and other biogeochemical cycles. In: Stocker TF, Qin D, Plattner G-K, Tignor M, Allen SK, Boschung J, Nauels A, Xia Y, Bex V, Midgley PM (eds) Climate change 2013: the physical science basis. Contribution of Working Group I to the Fifth Assessment Report of the Intergovernmental Panel on Climate Change, Cambridge, pp 33–118
4. IEA (2019) Global energy and CO_2 status report 2019. IEA, Paris
5. Letcher TM (2019) Why do we have global warming? In: Managing global warming. Elsevier, Amsterdam, pp 3–15
6. Stocker TF, Qin D, Plattner G-K, Tignor M, Allen SK, Boschung J, Nauels A, Xia Y, Bex V, Midgley PM (2013) Climate change 2013: The physical science basis. Contribution of working group I to the fifth assessment report of the Intergovernmental Panel on Climate Change, Cambridge, p 1535
7. Houghton RA (2014) The comtemplary carbon cycle. In: Turekian KK (ed) Treatise on geochemistry. Elsevier, Oxford, pp 399–435
8. Edenhofer O, Pichs-Madruga R, Sokona Y, Farahani E, Kadner KS, Seyboth AA, Baum I, Brunner S, Eickemeier P, Kriemann B, Savolainen J, Schlömer S, von Stechow C, Zwickel T, Minx JC (eds) (2015) Climate change 2014: mitigation of climate change. Contribution of Working Group III to the Fifth Assessment Report of the Intergovernmental Panel on Climate Change, in, Intergovenmental Panel on Climate Change (IPCC), Cambridge
9. Bains P, Psarras P, Wilcox J (2017) CO_2 capture from the industry sector. Prog Energy Combust Sci 63:146–172
10. Farla JC, Hendriks CA, Blok K (1995) Carbon dioxide recovery from industrial processes. Clim Change 29:439–461
11. Swift T, Moore G (2019) The economic benefits of ethylene oxide and the potential cost of deselection in, Economics and Statistics Department, American Chemistry Council
12. Koytsoumpa EI, Bergins C, Kakaras E (2018) The CO_2 economy: review of CO_2 capture and reuse technologies. J Supercri Fluids 132:3–16
13. Stolaroff JK, Keith DW, Lowry GV (2008) Carbon dioxide capture from atmospheric air using sodium hydroxide spray. Environ Sci Technol 42:2728–2735
14. Leung DY, Caramanna G, Maroto-Valer MM (2014) An overview of current status of carbon dioxide capture and storage technologies. Renew Sustain Energy Rev 39:426–443
15. Armstrong K, Styring P (2015) Assessing the potential of utilization and storage strategies for post-combustion CO2 emissions reduction. Front Energy Res 3:8
16. Artz J, Müller TE, Thenert K, Kleinekorte J, Meys R, Sternberg A, Bardow A, Leitner W (2018) Sustainable conversion of carbon dioxide: an integrated review of catalysis and life cycle assessment. Chem Rev 118:434–504
17. Wang W-N, Soulis J, Yang YJ, Biswas P (2014) Comparison of CO_2 photoreduction systems: a review. Aerosol Air Qual Res 14:533–549
18. Tu W, Zhou Y, Zou Z (2014) Photocatalytic conversion of CO_2 into renewable hydrocarbon fuels: state-of-the-art accomplishment, challenges, and prospects. Adv Mater 26:4607–4626
19. Keith DW, Holmes G, Angelo DS, Heidel K (2018) A process for capturing CO_2 from the atmosphere. Joule 2:1573–1594
20. Li Y, Wang W-N, Zhan Z, Woo M-H, Wu C-Y, Biswas P (2010) Photocatalytic reduction of CO_2 with H_2O on mesoporous silica supported Cu/TiO_2 catalysts. Appl Catal Environ 100:386–392
21. Lin LY, Kavadiya S, He X, Wang W-N, Karakocak BB, Lin Y-C, Berezin MY, Biswas P (2019) Engineering stable Pt nanoparticles and oxygen vacancies on defective TiO_2 via

introducing strong electronic metal-support interaction for efficient CO_2 photoreduction. Chem Eng J 389:123450

22. Lin L-Y, Kavadiya S, Karakocak BB, Nie Y, Raliya R, Wang ST, Berezin MY, Biswas P (2018) ZnO1− x/carbon dots composite hollow spheres: facile aerosol synthesis and superior CO_2 photoreduction under UV, visible and near-infrared irradiation. Appl Catal Environ 230:36–48

23. Nie Y, Wang W-N, Jiang Y, Fortner J, Biswas P (2016) Crumpled reduced graphene oxide–amine–titanium dioxide nanocomposites for simultaneous carbon dioxide adsorption and photoreduction. Cat Sci Technol 6:6187–6196

24. Wang W-N, An W-J, Ramalingam B, Mukherjee S, Niedzwiedzki DM, Gangopadhyay S, Biswas P (2012) Size and structure matter: enhanced CO_2 photoreduction efficiency by size-resolved ultrafine Pt nanoparticles on TiO_2 single crystals. J Am Chem Soc 134:11276–11281

25. Wang W-N, Park J, Biswas P (2011) Rapid synthesis of nanostructured $Cu–TiO_2–SiO_2$ composites for CO_2 photoreduction by evaporation driven self-assembly. Cat Sci Technol 1:593–600

26. Dwivedi A, Gudi R, Biswas P (2017) An improved tri-reforming based methanol production process for enhanced CO_2 valorization. Int J Hydrogen Energy 42:23227–23241

27. Dwivedi A, Gudi R, Biswas P (2020) An oxy-fuel combustion based tri-reforming coupled methanol production process with improved hydrogen utilization. Int J Greenhouse Gas Control 93:102905

28. Artz J, Müller TE, Thenert K, Kleinekorte J, Meys R, Sternberg A, Bardow A, Leitner W (2017) Sustainable conversion of carbon dioxide: an integrated review of catalysis and life cycle assessment. Chem Rev 118:434–504

29. Sternberg A, Jens CM, Bardow A (2017) Life cycle assessment of CO_2-based C1-chemicals. Green Chem 19:2244–2259

30. Park S, Chang J, Lee K, Joo O, Jung K, Jung Y (2004) CAMERE process for methanol synthesis from CO_2 hydrogenation. Stud Surf Sci Catal 153:67–72

31. Joo OS, Jung K-D, Moon I, Rozovskii AY, Lin GI, Han S-H, Uhm S-J (1999) Carbon dioxide hydrogenation to form methanol via a reverse-water-gas-shift reaction (the CAMERE process). Ind Eng Chem Res 38:1808–1812

32. Quadrelli EA, Centi G, Duplan JL, Perathoner S (2011) Carbon dioxide recycling: emerging large-scale technologies with industrial potential. ChemSusChem 4:1194–1215

33. Lee D-Y, Elgowainy A, Dai Q (2018) Life cycle greenhouse gas emissions of hydrogen fuel production from chlor-alkali processes in the United States. Appl Energy 217:467–479

34. Fukuoka S, Tojo M, Hachiya H, Aminaka M, Hasegawa K (2007) Green and sustainable chemistry in practice: development and industrialization of a novel process for polycarbonate production from CO 2 without using phosgene. Polym J 39:91–114

35. Fukuoka S, Kawamura M, Komiya K, Tojo M, Hachiya H, Hasegawa K, Aminaka M, Okamoto H, Fukawa I, Konno S (2003) A novel non-phosgene polycarbonate production process using by-product CO 2 as starting material. Green Chem 5:497–507

36. Wender I (1996) Reactions of synthesis gas. Fuel Process Technol 48:189–297

37. Schmal M, Toniolo FS, Kozonoe CE (2018) Perspective of catalysts for (Tri) reforming of natural gas and flue gas rich in CO_2. Appl Catal Gen 568:23–42

38. Wang L, Yi Y, Wu C, Guo H, Tu X (2017) One-step reforming of CO2 and CH4 into high-value liquid chemicals and fuels at room temperature by plasma-driven catalysis. Angew Chem Int Ed 56:13679–13683

39. Okonkwo O, Yablonsky G, Biswas P (2020) Thermodynamic analysis of tri-reforming of oxy-fuel combustion exhaust gas. J CO2 Utili 39:101156

40. Zhao X, Naqi A, Walker DM, Roberge T, Kastelic M, Joseph B, Kuhn JN (2019) Conversion of landfill gas to liquid fuels through a TriFTS (tri-reforming and Fischer–Tropsch synthesis) process: a feasibility study. Sustain Energy Fuels 3:539–549

41. Schwarz JA, Contescu C, Contescu A (1995) Methods for preparation of catalytic materials. Chem Rev 95:477–510

42. Munnik P, de Jongh PE, de Jong KP (2015) Recent developments in the synthesis of supported catalysts. Chem Rev 115:6687–6718

43. Behrens M (2015) Coprecipitation: An excellent tool for the synthesis of supported metal catalysts–From the understanding of the well known recipes to new materials. Catal Today 246:46–54

44. Kung HH, Ko EI (1996) Preparation of oxide catalysts and catalyst supports—a review of recent advances. Chem Eng J Biochem Eng J 64:203–214

45. Gonzalez RD, Lopez T, Gomez R (1997) Sol—gel preparation of supported metal catalysts. Catal Today 35:293–317

46. Esposito S (2019) "Traditional" sol-gel chemistry as a powerful tool for the preparation of supported metal and metal oxide catalysts. Materials 12:668

47. Duan C, Zhang X, Zhou R, Hua Y, Zhang L, Chen J (2013) Comparative studies of ethanol to propylene over HZSM-5/SAPO-34 catalysts prepared by hydrothermal synthesis and physical mixture. Fuel Process Technol 108:31–40

48. Fu H, Zhang L, Yao W, Zhu Y (2006) Photocatalytic properties of nanosized Bi_2WO_6 catalysts synthesized via a hydrothermal process. Appl Catal Environ 66:100–110

49. Strobel R, Baiker A, Pratsinis SE (2006) Aerosol flame synthesis of catalysts. Adv Powder Technol 17:457–480

50. Sheng Y, Kraft M, Xu R (2018) Emerging applications of nanocatalysts synthesized by flame aerosol processes. Curr Opin Chem Eng 20:39–49

51. Schimmoeller B, Pratsinis SE, Baiker A (2011) Flame aerosol synthesis of metal oxide catalysts with unprecedented structural and catalytic properties. ChemCatChem 3:1234–1256

52. Li S, Ren Y, Biswas P, Stephen DT (2016) Flame aerosol synthesis of nanostructured materials and functional devices: Processing, modeling, and diagnostics. Prog Energy Combust Sci 55:1–59

53. Boningari T, Koirala R, Smirniotis PG (2013) Low-temperature catalytic reduction of NO by NH_3 over vanadia-based nanoparticles prepared by flame-assisted spray pyrolysis: Influence of various supports. Appl Catal Environ 140:289–298

54. Schubert M, Pokhrel S, Thomé A, Zielasek V, Gesing TM, Roessner F, Mädler L, Bäumer M (2016) Highly active Co–Al_2O_3-based catalysts for CO_2 methanation with very low platinum promotion prepared by double flame spray pyrolysis. Cat Sci Technol 6:7449–7460

55. Lovell EC, Horlyck J, Scott J, Amal R (2017) Flame spray pyrolysis-designed silica/ceria-zirconia supports for the carbon dioxide reforming of methane. Appl Catal Gen 546:47–57

56. Schimmoeller B, Hoxha F, Mallat T, Krumeich F, Pratsinis SE, Baiker A (2010) Fine tuning the surface acid/base properties of single step flame-made Pt/alumina. Appl Catal Gen 374:48–57

57. Campagnoli E, Tavares A, Fabbrini L, Rossetti I, Dubitsky YA, Zaopo A, Forni L (2005) Effect of preparation method on activity and stability of $LaMnO_3$ and $LaCoO_3$ catalysts for the flameless combustion of methane. Appl Catal Environ 55:133–139

58. Niu F, Li S, Zong Y, Yao Q (2014) Catalytic behavior of flame-made Pd/TiO_2 nanoparticles in methane oxidation at low temperatures. J Phys Chem C 118:19165–19171

59. Strobel R, Krumeich F, Stark WJ, Pratsinis SE, Baiker A (2004) Flame spray synthesis of Pd/Al_2O_3 catalysts and their behavior in enantioselective hydrogenation. J Catal 222:307–314

60. Pisduangdaw S, Panpranot J, Methastidsook C, Chaisuk C, Faungnawakij K, Praserthdam P, Mekasuwandumrong O (2009) Characteristics and catalytic properties of Pt–Sn/Al_2O_3 nanoparticles synthesized by one-step flame spray pyrolysis in the dehydrogenation of propane. Appl Catal Gen 370:1–6

61. Koirala R, Pratsinis SE, Baiker A (2016) Synthesis of catalytic materials in flames: opportunities and challenges. Chem Soc Rev 45:3053–3068

62. Mädler L, Stark WJ, Pratsinis SE (2002) Flame-made ceria nanoparticles. J Mater Res 17:1356–1362

63. Mädler L, Kammler H, Mueller R, Pratsinis SE (2002) Controlled synthesis of nanostructured particles by flame spray pyrolysis. J Aerosol Sci 33:369–389

64. Schulz H, Mädler L, Strobel R, Jossen R, Pratsinis SE, Johannessen T (2005) Independent control of metal cluster and ceramic particle characteristics during one-step synthesis of Pt/TiO₂. J Mater Res 20:2568–2577

65. Tiwari V, Jiang J, Sethi V, Biswas P (2008) One-step synthesis of noble metal–titanium dioxide nanocomposites in a flame aerosol reactor. Appl Catal Gen 345:241–246

66. Yu J, Zhang Z, Dallmann F, Zhang J, Miao D, Xu H, Goldbach A, Dittmeyer R (2016) Facile synthesis of highly active Rh/Al₂O₃ steam reforming catalysts with preformed support by flame spray pyrolysis. Appl Catal Environ 198:171–179

67. Horlyck J, Sara M, Lovell EC, Amal R, Scott J (2019) Effect of metal-support interactions in mixed Co/Al catalysts for dry reforming of methane. ChemCatChem 11:3432–3440

68. Lee S, Schneider K, Schumann J, Mogalicherla AK, Pfeifer P, Dittmeyer R (2015) Effect of metal precursor on Cu/ZnO/Al₂O₃ synthesized by flame spray pyrolysis for direct DME production. Chem Eng Sci 138:194–202

69. Pongthawornsakun B, Mekasuwandumrong O, Aires FJCS, Büchel R, Baiker A, Pratsinis SE, Panpranot J (2018) Variability of particle configurations achievable by 2-nozzle flame syntheses of the Au-Pd-TiO₂ system and their catalytic behaviors in the selective hydrogenation of acetylene. Appl Catal Gen 549:1–7

70. Dreyer JA, Li P, Zhang L, Beh GK, Zhang R, Sit PH-L, Teoh WY (2017) Influence of the oxide support reducibility on the CO₂ methanation over Ru-based catalysts. Appl Catal Environ 219:715–726

71. Comazzi A, Pirola C, Di Michele A, Compagnoni M, Galli F, Rossetti I, Manenti F, Bianchi C (2016) Flame spray pyrolysis as fine preparation technique for stable Co and Co/Ru based catalysts for FT process. Appl Catal Gen 520:92–98

72. Wang N, Li S, Zong Y, Yao Q, Zhang Y (2017) Flame synthesis of novel ternary nanocatalysts Pd/CeO₂TiO₂ with promotional low-temperature catalytic oxidation properties. Proc Combust Inst 36:1029–1036

73. Spencer MS (1996) Fundamental principles. In: Twigg MV (ed) Catalyst handbook. CRC Press, Boca Raton

74. Kumar R, Kumar K, Choudary N, Pant K (2019) Effect of support materials on the performance of Ni-based catalysts in tri-reforming of methane. Fuel Process Technol 186:40–52

75. Lee SM, Lee YH, Moon DH, Ahn JY, Nguyen DD, Chang SW, Kim SS (2019) Reaction mechanism and catalytic impact of Ni/CeO₂₋ₓ catalyst for low-temperature CO₂ methanation. Ind Eng Chem Res 58:8656–8662

76. Wang F, He S, Chen H, Wang B, Zheng L, Wei M, Evans DG, Duan X (2016) Active site dependent reaction mechanism over Ru/CeO₂ catalyst toward CO₂ methanation. J Am Chem Soc 138:6298–6305

77. Yentekakis IV, Goula G, Hatzisymeon M, Betsi-Argyropoulou I, Botzolaki G, Kousi K, Kondarides DI, Taylor MJ, Parlett CM, Osatiashtiani A (2019) Effect of support oxygen storage capacity on the catalytic performance of Rh nanoparticles for CO₂ reforming of methane. Appl Catal Environ 243:490–501

78. Xu L, Zhao H, Song H, Chou L (2012) Ordered mesoporous alumina supported nickel based catalysts for carbon dioxide reforming of methane. Int J Hydrogen Energy 37:7497–7511

79. Zhang D, Liu W-Q, Liu Y-A, Etim U, Liu X-M, Yan Z-F (2017) Pore confinement effect of MoO3/Al2O3 catalyst for deep hydrodesulfurization. Chem Eng J 330:706–717

80. Hu X, Foo ML, Chuah GK, Jaenicke S (2000) Pore size engineering on MCM-41: selectivity tuning of heterogenized AlCl3 for the synthesis of linear alkyl benzenes. J Catal 195:412–415

81. Olsbye U, Svelle S, Bjørgen M, Beato P, Janssens TV, Joensen F, Bordiga S, Lillerud KP (2012) Conversion of methanol to hydrocarbons: how zeolite cavity and pore size controls product selectivity. Angew Chem Int Ed 51:5810–5831

82. Sharma L, Kumar M, Saxena A, Chand M, Gupta J (2002) Influence of pore size distribution on Pt dispersion in Pt-Sn/Al₂O₃ reforming catalyst. J Mol Catal A Chem 185:135–141

83. Che M, Védrine JC (2012) Characterization of solid materials and heterogeneous catalysts: From structure to surface reactivity. Wiley, Chichester

84. Sehested J (2006) Four challenges for nickel steam-reforming catalysts. Catal Today 111:103–110
85. Amjad UES, Quintero CWM, Ercolino G, Italiano C, Vita A, Specchia S (2019) Methane steam reforming on the Pt/CeO₂ catalyst: effect of daily start-up and shut-down on long-term stability of the catalyst. Ind Eng Chem Res 58:16395–16406
86. Jones G, Jakobsen JG, Shim SS, Kleis J, Andersson MP, Rossmeisl J, Abild-Pedersen F, Bligaard T, Helveg S, Hinnemann B (2008) First principles calculations and experimental insight into methane steam reforming over transition metal catalysts. J Catal 259:147–160
87. Pakhare D, Spivey J (2014) A review of dry (CO₂) reforming of methane over noble metal catalysts. Chem Soc Rev 43:7813–7837
88. López-Fonseca R, Jiménez-González C, de Rivas B, Gutiérrez-Ortiz JI (2012) Partial oxidation of methane to syngas on bulk NiAl₂O₄ catalyst. Comparison with alumina supported nickel, platinum and rhodium catalysts. Appl Catal A Gen 437:53–62
89. Nagaoka K, Seshan K, Lercher JA, Aika K-i (2000) Activation mechanism of methane-derived coke (CHx) by CO₂ during dry reforming of methane–comparison for Pt/Al₂O₃ and Pt/ZrO₂. Catal Lett 70:109–116
90. García-Vargas JM, Valverde JL, Dorado F, Sánchez P (2014) Influence of the support on the catalytic behaviour of Ni catalysts for the dry reforming reaction and the tri-reforming process. J Mol Catal A Chem 395:108–116
91. Kumar R, Kumar K, Pant K, Choudary N (2020) Tuning the metal-support interaction of methane tri-reforming catalysts for industrial flue gas utilization. Int J Hydrogen Energy 45:1911–1929
92. García-Vargas JM, Valverde JL, Díez J, Dorado F, Sánchez P (2015) Catalytic and kinetic analysis of the methane tri-reforming over a Ni–Mg/β-SiC catalyst. Int J Hydrogen Energy 40:8677–8687
93. Starr SO, Muscatello AC (2020) Mars in situ resource utilization: a review. Planet Space Sci 104824
94. Ash R, Dowler W, Varsi G (1978) Feasibility of rocket propellant production on Mars. Acta Astronaut 5:705–724
95. Kleinhenz JE, Paz A (2017) An ISRU propellant production system for a fully fueled mars ascent vehicle. In: Tenth symposium on space resource utilization, 2017, p 0423
96. Leshin L, Mahaffy P, Webster C, Cabane M, Coll P, Conrad P, Archer P, Atreya S, Brunner A, Buch A (2013) Volatile, isotope, and organic analysis of martian fines with the Mars Curiosity rover. Science 341:1238937
97. Plaut JJ, Safaeinili A, Holt JW, Phillips RJ, Head JW, Seu R, Putzig NE, Frigeri A (2009) Radar evidence for ice in lobate debris aprons in the mid-northern latitudes of Mars. Geophys Res Lett 36:L02203
98. Ehlmann BL, Edwards CS (2014) Mineralogy of the Martian surface. Annu Rev Earth Planet Sci 42:291–315
99. Vogt C, Monai M, Kramer GJ, Weckhuysen BM (2019) The renaissance of the Sabatier reaction and its applications on Earth and in space. Nat Catal 2:188–197
100. Rapp D (2013) Use of extraterrestrial resources for human space missions to moon or mars. Springer, New York
101. Muscatello A, Santiago-Maldonado E (2012) Mars in situ resource utilization technology evaluation. In: 50th AIAA Aerospace sciences meeting including the New Horizons Forum and Aerospace Exposition, 2012, p 360
102. Bennett GL, Lombardo JJ, Hemler RJ, Silverman G, Whitmore C, Amos WR, Johnson E, Zocher RW, Hagan JC, Englehart RW (2008) The general-purpose heat source radioisotope thermoelectric generator: a truly general-purpose space RTG. In: AIP conference proceedings. American Institute of Physics, pp 663–671
103. O'Brien R, Ambrosi R, Bannister N, Howe S, Atkinson HV (2008) Safe radioisotope thermoelectric generators and heat sources for space applications. J Nucl Mater 377:506–521

104. Pickett MT, Roberson LB, Calabria JL, Bullard TJ, Turner G, Yeh DH (2020) Regenerative water purification for space applications: needs, challenges, and technologies towards 'closing the loop'. Life Sci Space Res 24:64–82
105. Flynn MT (2013) Microgravity testing of the Forward Osmosis Bag (FOB), a personal water purification device. In: 43rd International conference on environmental systems, 2013, p 3472
106. Muscatello AC, Hintze PE, Meier AJ, Bayliss J, Formoso R, Shah M, Vu B, Lee R, Captain J (2017) Testing and modeling of the Mars Atmospheric Processing Module. In: AIAA SPACE and Astronautics Forum and Exposition, 2017, p 5149

Perspectives in Carbon Oxides Conversion to Methanol/Dimethyl Ether: Distinctive Contribution of Heterogeneous and Photocatalysis

Komal Tripathi, Rajan Singh*, Shreya Singh*, Sonal Asthana*, and K. K. Pant

Abstract This book chapter reveals the recent advancements in the synthesis of methanol/dimethyl ether (DME) synthesis via carbon oxides hydrogenation using heterogeneous as well as photocatalysis approach. This gas-phase process could be well thought out as a promising alternative for carbon oxides recycling towards a fuel such as DME/methanol. The conversion of these oxides (CO/CO_2) into value-added chemicals has been considered as one of the top most research priorities all over the world to mitigate the level of these gases in the atmosphere. In this view, the production of methanol/DME from catalytic hydrogenation (heterogeneous as well as photocatalysis) of carbon oxides appears as a technology able to countenance also the ever-escalating demand for alternative, environmentally benign fuels and energy carriers.

Fundamental considerations upon thermodynamic aspects controlling methanol/DME production from CO/CO_2 are presented in the chapter along with an assessment of the most pioneering catalytic systems developed in this field. The effect of the catalytic properties, reaction mechanism, nature of the active sites, and the types of the reactors used for this particular process has been discussed in details. Novel catalytic approaches adopted for the hydrogenation of especially CO_2 has been fore fronted in the separate section of this chapter. Special emphasis has also been given to the photocatalytic approach adopted for the conversion of the carbon oxides into methanol/DME. All these aspects are discussed in details, summarizing modern achievements in the related research field.

Keywords Carbon oxide conversion · Heterogeneous · Photocatalysis · Methanol · Dimethyl ether

---

*Rajan Singh, Shreya Singh and Sonal Asthana contributed equally.

K. Tripathi · R. Singh · S. Singh · S. Asthana · K. K. Pant (✉)
Department of Chemical Engineering, Indian Institute of Technology Delhi, New Delhi, Delhi, India
e-mail: kkpant@chemical.iitd.ac.in

1 Introduction

The current human activities depend largely on energy, and their annual consumption of crude oil is expected to be 68% higher by 2030. The recent IEA (International Energy Agency) reported the worldwide oil demand averaged 96.9 million barrels a day previous year and will hike to 105.4 million a day in 2030 as projected. Demand will reach 106.4 million barrels a day in 2040 [1]. Steady energy supply from numerous energy sources and moves to renewable energies are essential to sustain the activities of mankind. Concurrently, solutions to global environmental problems are needed. With mounting concerns on energy safety, environmental pollution, and potential oil supplies, the universal community is in quest of nonpetroleum-based alternative fuels, along with more sophisticated energy technologies (e.g., fuel cells) to increase the competence of energy usage. The most promising alternative fuel will be having the supreme impact on the society. The major affected areas comprise well-to-wheel greenhouse gas emissions, fuel versatility, non-petroleum feedstocks, infrastructure, economics, safety, and availability.

The energy demand is rapidly increasing on the global platform because of the fast economic growth. In order to pacify this growing demand, a plentiful quantity of fossil fuel (coal, natural gas, and oil) is needed. India, with its abundant coal reserves, projects a substantial potential to meet this energy demand. However, combustion of coal poses a significant problem of NOx, SOx, and particulate matter emissions [2]. Also, the high ash content (35–40% of the total weight) of Indian coal affects the thermal power plants efficiency [3]. Moreover, CO_2 emission from direct coal combustion is a major challenge for sustainability of coal-fired power plants [4]. Thus, there is an immediate need for development of alternative technologies for electricity generation from the coal. The history of synthetic fuel is long, beginning in the 1930s with the creation of artificial petroleum from coal and continuing into the present day as GTL (gas to liquid)/CTL (coal to liquid) technology. Recently, coal gasification to syngas (a mixture of CO, CO_2, and H_2) has drawn significant attention over coal combustion of research community worldwide by suppressing pollutant emissions [5, 6].

Research on conversion of syngas to value-added fuels and chemicals secures the ability of future generations to meet their energy demands. The use of syngas as an intermediate in the production of many compounds is presented in the Fig. 1. Among these products, methanol has potential to replace fossil fuels (diesel, petrol) for transportation use and thus plays a prominent role in our future economy [7, 8].

Over the past several years, enormous efforts have been put into the improvement of stable and active heterogeneous catalysts for carbon oxides hydrogenation to methanol. A number of prominent publications have reviewed the technical aspects related to the catalysis for methanol [9]. Apart from heterogeneous catalysis, many other approaches such as homogeneous catalysis, thermocatalytic, photocatalytic, biocatalytic, electrocatalytic, and photo-electrocatalytic have been used for carbon oxide conversion to value-added product. However, the challenge in each approach is the activation of linear CO/CO_2 molecule due to its very high stability.
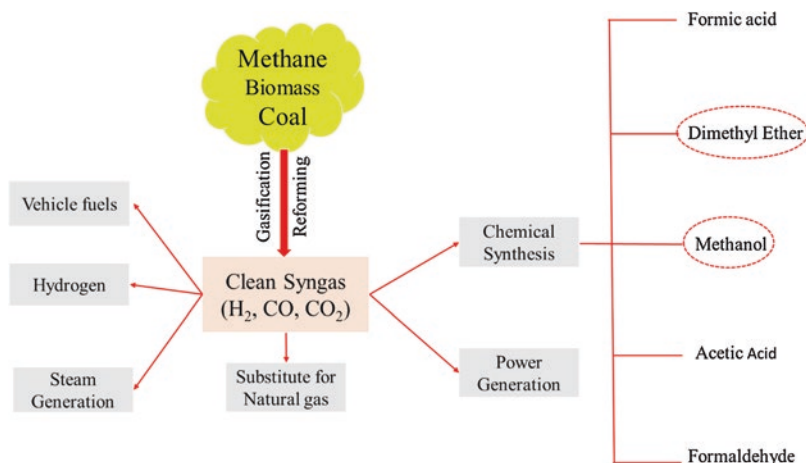
Fig. 1 Syngas as an intermediate for various applications

These processes require high energy for carbon oxide reduction; hence, utilization of nonrenewable sources of energy such as sunlight can be considered as one of the alternative approaches for carbon oxide conversion process. There exist a lot of other reduction techniques that could be implemented on various scales [10]. However, the main aim of all these techniques should focus on reducing the carbon footprints in the environment. Conversion of these carbon oxides follows "two flies with one flap" approach so that energy scarcity and environmental security can be tackled at the same platform.

In view of this, the subsequent sections of this chapter provides a brief overview about all the technical aspects related to the synthesis process of methanol and DME from the carbon-rich source gases, viz., CO and CO_2 together known as carbon oxides. Also, a small description of methanol history is included.

1.1 Methanol: Historical Background

Many processes have been established in the past decades for production of methanol from different carbon source feedstocks such as natural gas, coal, biomass, catalytic hydrogenation of carbon oxides, etc. During the growing industrial era before the 1600s, methanol was discovered as "wood spirit." This was synthesized by heating of wood in the lack of free oxygen atoms, a process called wood distillation. Wood spirit consisted of many impurities along with the methanol. In the 1660s, Sir Robert Boyle attempted to separate methanol from the impurities, and pure methanol was known as "wood vinegar." However, wood vinegar was not known in the market for about two centuries; until in the 1800sss, methanol was identified by Liebig and J.B.A. Dumas. During the same time, chemical name of methanol "methyl alcohol" was recognized.

A fundamental approach for the catalytic synthesis of methanol was given by Paul Sabatier in the 1920s. According to Sabatier and group, methanol was synthesized over Ni-based catalyst by hydrogenation of functional groups [11]. Thereafter, breakthrough catalyst was developed, and first industrial process for methanol production was established by BASF in Germany [12]. Catalyst used in the same process was of zinc oxide and chromate based. This catalyst was not that active and thus required a very high temperature (300–400 °C). This is a high-pressure favorable reaction due to exothermic and compressing volume nature of reaction. Pressure required was 250–350 bar along with high temperature of 300–400 °C [13–16]. This breakthrough technology was dominated in the market over 50 years, and exportation of process was started by DuPont and commercial solvents corporation in the United States. Besides, improvements in the operating conditions (temperature, pressure) have sought the attention of research community worldwide. In the 1940s, the Swiss Lonza Company started the methanol formation from electrolytic hydrogen and carbon oxides. Following this, Prof. Natta suggested catalytic hydrogenation of purified syngas over ZnO-based catalyst. Feedstocks (CO, CO_2, and H_2) were purified by vapors of calcium nitrates to increase the production and selectivity of methanol [17].

In the 1966s, important discovery was found in imperial chemical industries. According to this, drastic change was observed in the catalyst formulation, operating conditions, and quality of syngas. Catalyst was copper based and was found more efficient than ZnO-based catalyst but even more prone to deactivation by sulfur impurities present in the coal-gasified syngas. Operating conditions were reduced up to 300 °C and 100 bar, and purer syngas was obtained from the steam reforming of methane or from natural gas and naphtha feedstocks. Since then, the so-called low-temperature, low-pressure ICI process was applied for methanol synthesis in industries [10]. On this basis, in the 1970s, many plants such as Lurgi, Haldor Topsoe, and Linde have been established for methanol production from purified syngas. A lot of investigations and efforts have been done for developing even lower temperature and pressure process. All the abovementioned plants are currently running at 250–300 °C and 50 bar over Cu-/ZnO-based catalyst [18] (Fig. 2). A consolidated quick description of how methanol synthesis has evolved over a period of time has been given in Table 1.

1.2   Primary Reactions for Methanol Synthesis

Methanol is one of the utmost essential commodities and building block chemicals in today's world. Since 1960, more than 90 production plants with production capacity of 110 metric tons (MTs) have been established to meet the rise in global demand of 70 MTs [10]. Apart from being used as a fuel, methanol can also be used as a raw material for the production of olefins and paraffins and serves as a key intermediate for production of many other industrially relevant chemicals like formaldehyde, methyl *tert*-butyl ether, and acetic acid [19]. It also finds application as a
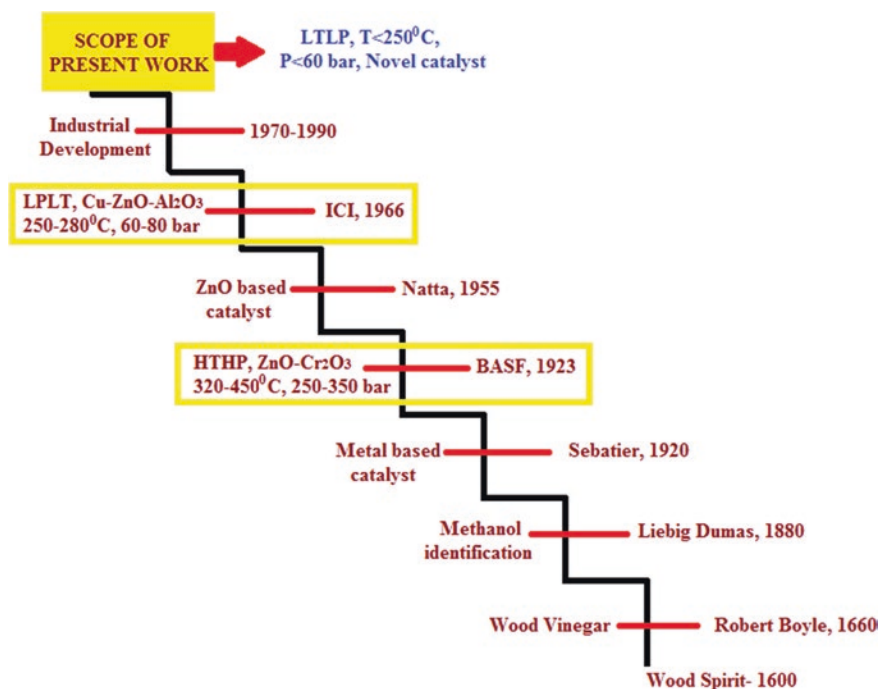
Fig. 2 Evolution of methanol synthesis process over a period of 400 years

blender in gasoline, methanol-based fuel cells, and many household purposes. Methanol synthesis reaction is an exothermic and equilibrium-restricted reaction [20, 21]. To circumvent the accumulation of large amount of reaction heat, per pass conversion of the reactant is limited to 15–25%. The following reactions occur in overall methanol synthesis process:

$$CO + 2H_2 \leftrightarrow CH_3OH \quad \Delta H^\circ = -91 \ kJ/mol \tag{1}$$

$$CO + H_2O \leftrightarrow CO_2 + H_2 \quad \Delta H^\circ = -41 \ kJ/mol \tag{2}$$

$$CO_2 + 3H_2 \leftrightarrow CH_3OH + H_2O \quad \Delta H^\circ = -49 \ kJ/mol \tag{3}$$
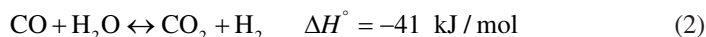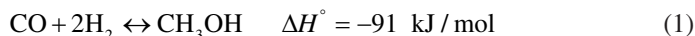
Reaction (3) of methanol synthesis from CO_2 hydrogenation takes place with the combination of the above two reactions, which are methanol synthesis reaction (1) from CO hydrogenation and water gas shift reaction (2). In the instance when water gas shift reaction does not occur, reactions (1) and (3) propagate independently when both CO and CO_2 are in the same feed stream. Both of the reactions (1) and (3) involve compression in moles of the products as compared to that of the reactants, increasing the process pressure and decrease in the overall entropy of the reaction. This leads to higher conversion, thereby making the reaction favorable at

Table 1 Historical reconstruction of methanol synthesis [18]

Time period	Description	Source/conditions	Key features
Before the 1600s	Known as wood spirit/ wood distillation process	Wood heating in anaerobic conditions	The wood distillates extract contained many impurities besides methyl alcohol
1660s	Termed as wood vinegar, developed by sir Robert Boyle	Distillation of buxus (boxwood), the obtained extract was subjected to purification by reacting it with milk of lime	• Identification of methanol was attempted for the first time • However, the technology was not marketed for about two centuries
1800s	Exact composition of wood vinegar remained unknown; J. V. Liebig and J. B. A dumas attempted to isolate methanol molecule	Dry distillation of wood	• Elemental composition of methanol was determined • Term "methyl" was formally introduced into chemistry • In the same period, methanol began to be commercialized
1920s	Paul Sabatier tried to hydrogenate large variety of functional groups by metal-based catalysis	Dry distillation of wood, high pressure/ high temperature	• Numerous metal compounds were studied • Ni-based catalyst allowed CO hydrogenation to obtain methyl alcohol
First breakthrough			
1923s	German company BASF developed metal-based catalytic hydrogenation over ZnO/Cr_2O_3 catalyst	High pressure-high temperature (300–400 °C, 250–350 bar)	• First catalyst-based HTHP process for methanol synthesis • Remained dominant technology for the next 45 years • Introduced by both DuPont and commercial solvents Corporation in the United States
Reduction in operating parameters			
1940s	Industrial methanol synthesis was carried out by Swiss Lonza Company from electrolytic H_2 and CO_2 (derived from $Ca(NO_3)_2$). ZnO-based catalyst was used which was developed by Prof. Giulio Natta in Italy	–	• Gases were purified from nitrous vapors for the first time • Industrial methanol synthesis was carried out

Table 1 (continued)

Time period	Description	Source/conditions	Key features
Another breakthrough			
1966s	Hydrogenation of purified syngas over Cu/ZnO catalyst was carried out by ICI industries	300 °C, 100 bar	• For the first time, methanol synthesis was carried out at such low operating conditions • Many new industrial plants adapted the technology like Lurgi, Haldor Topsoe, Linde
1970s–2000s	Improvements and development of novel catalysts		
2000s–till date	Nanocatalysts and liquid methanol production in slurry reactors		

high pressure and low temperature. As far as water gas shift reaction (2) is considered, it is independent of the pressure variation and also becomes independent of temperature variation above 200°C. Since methanol synthesis process is conducted in the temperature range of 250–300°C, water gas shift reaction becomes inevitable. However, it helps in maintaining the desired H_2/CO ratio; therefore, it is partially beneficial for the synthesis process.

1.3 Thermodynamics

Activation of carbon oxides (CO/CO_2) is challenging because of the stability of the molecules. Out of these two, CO_2 is a more stable ($\Delta G^0_f = -394.0$ kJ/mol) linear molecule. The oxidation state of carbon is +4 which is the most stable configuration; in contrast, carbon in methanol has oxidation state −2. Since, methanol synthesis is an energy-driven process and requires 228 KJ of energy and six electrons to reduce the oxidation state of carbon (−2) for conversion of one mole of CO_2 to methanol. The linear and small bond length (116.3 pm) of carbon oxygen bond in CO_2 makes it highly inert and is a barrier for economic conversion to different products [22]. The major reactions that took in methanol synthesis are mentioned in the previous section.

Maximum conversion is limited in these types of reactions because desired direction of the reaction is thermodynamically not favored. Overall rate of reaction is controlled chemically due to which net reaction rate becomes low because of high kinetic resistances or low kinetic driving forces at operating conditions. Maximum possible conversion of the reactants is limited and equivalent to equilibrium conversion. Enthalpies and Gibbs free energies [23] of the various products from carbon oxide conversions are described here (Eqs. 4–9). Feasibilities of the product formation are decided according to the free energy values. Enthalpy values of same

product obtained from CO and CO_2 conversions are comparable, while Gibbs free energy values show that CO hydrogenation is more spontaneous than CO_2.

$$CO_2 + 4H_2 \leftrightarrow CH_4 + 2H_2O \quad \Delta H^\circ = -259.9 \text{ kJ/mol } \Delta G^\circ = -132.4 \text{ kJ/mol}$$
(4)

$$CO + 3H_2 \leftrightarrow CH_4 + H_2O \quad \Delta H^\circ = -205.9 \text{ kJ/mol } \Delta G^\circ = -141.9 \text{ kJ/mol}$$
(5)

$$2CO_2 + 6H_2 \leftrightarrow C_2H_5OH + 3H_2O \quad \Delta H^\circ = -173.8 \text{ kJ/mol } \Delta G^\circ = -65.7 \text{ kJ/mol}$$
(6)

$$2CO + 4H_2 \leftrightarrow C_2H_5OH + H_2O \quad \Delta H^\circ = -256.1 \text{ kJ/mol } \Delta G^\circ = -122.7 \text{ kJ/mol}$$
(7)

$$CO_2 + H_2 + CH_3OH \leftrightarrow CH_3COOH + H_2O \quad \Delta H^\circ = -135.4 \text{ kJ/mol } \Delta G^\circ$$
$$= -63.6 \text{ kJ/mol} \quad (8)$$

$$CO + CH_3OH \leftrightarrow CH_3COOH \quad \Delta H^\circ = -129.2 \text{ kJ/mol } \Delta G^\circ = -82.8 \text{ kJ/mol}$$
(9)
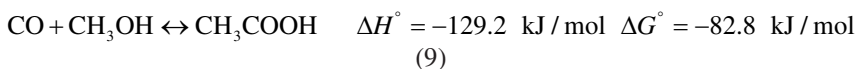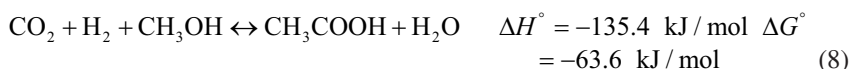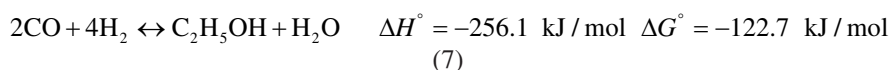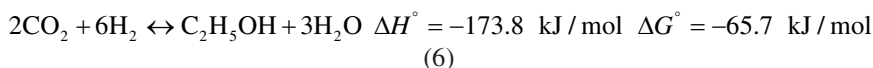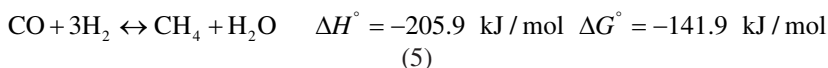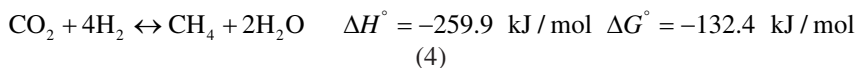
Graaf et al. [24] measured and modelled equilibrium of methanol synthesis reaction (1–8 Mpa, 473–543 K) using Soave-Redlich-Kwong (SRK)equation of state (EOS). Skrzypek et al. [25] modelled equilibrium for high-pressure methanol synthesis (5–30 Mpa, 425–675 K) without considering condensation. The use of Peng Robinson and SRK EOS for equilibrium modelling of methanol synthesis reaction does not provide results at 473 K and 30 Mpa. The probable reason for this deviation was condensation [26]. Many models with Gibbs free energy minimization approach and tangent plane criterion for checking phase stability has been reported.

Heeres and co-workers suggested thermodynamic model for methanol synthesis at elevated pressure (20 Mpa, 190–280 °C) with modified SRK EOS. The use of modified SRK EOS allows the calculation of chemical and phase equilibria throughout high-pressure methanol synthesis. The dew point was formulated as function of temperature and conversion [27]. Later theoretical results were confirmed by the experimental results that condensation of methanol and water improved methanol synthesis with higher carbon dioxide conversion in comparison with single gasphase chemical equilibrium [28].

DME is formed over solid acid catalyst by dehydration of methanol. The reaction is mildly exothermic. The one pot DME synthesis reaction is closely related to methanol synthesis as methanol is an intermediate to the DME synthesis (Eqs. 10 and 11).

$$2CH_3OH \leftrightarrow CH_3OCH_3 + H_2O \quad \Delta H^\circ = -23.4 \text{ kJ/mol} \quad (10)$$

$$2CO_2 + 6H_2 \leftrightarrow CH_3OCH_3 + 3H_2O \quad \Delta H^\circ = -123.0 \ kJ/mol \quad (11)$$

Shen et al. [29] reported higher CO_2 equilibrium conversion for single step CO_2 conversion to DME than CO_2 conversion to methanol. The equilibrium DME yield decreased with temperature and increased with pressure in accordance to Le Chatelier's principle. Aguayo et al. [30] proposed a kinetic model for single pot DME synthesis using conventional Cu-ZnO-Al_2O_3/γ-Al_2O_3 hybrid bifunctional catalyst with CO/H_2 and CO_2/H_2 as feed. In their proposed model, the main reactions that were considered are methanol synthesis, its subsequent dehydration, hydrocarbon synthesis, and water gas shift reaction. Similar results were also reported for Cu–Fe_2O_3–ZrO_2/H-ZSM-5 catalyst using intrinsic kinetic model for single step CO_2 hydrogenation to DME [31]. The above studies show that single step DME synthesis has the thermodynamic advantages in terms of CO_2 conversion, methanol, and DME yield.

1.4 Methanol Chemistry

1.4.1 Catalysts

In the early 1920s and 1930s, more active copper-based catalysts were studied and described. Copper was identified as a quite active metal for synthesis of methanol in these early studies. The activity was found to be increased when it was used along with the ZnO and stabilized with Al_2O_3. Workers at ICI pioneered the efforts in the area of methanol synthesis [32, 33], and by now, the Cu/ZnO/Al_2O_3 catalyst is almost exclusively used. Few formulations for state of the art/commercial methanol synthesis catalyst are briefly described in the following Table 2.

The catalyst for methanol synthesis is combined with solid acid (for methanol dehydration) for making the hybrid bifunctional catalyst for DME synthesis by various methods, viz., physical mixing, ball milling, impregnation, etc. The prevailing combination method is physical mixing of powder or granules of each component. The catalytic entity for DME synthesis contains dual active sites, one for methanol

Table 2 Commercial methanol synthesis catalyst formulations [10]

Manufacturer→ Description↓	BASF	DuPont	Haldor Topsoe	ICI
Copper	38.5	50	>55	20–35
Zinc	48.8	19	21–25	15–50
Aluminium	12.9	17	8–10	4–20
Others	Rare earth oxides	–	–	Mg
Feedstock	Syngas	Syngas	Syngas	Carbonaceous
Yield (tons/year)	28.82	41.61	87.6×10^4	91.25×10^4
Patent date	1978	–	–	1965

synthesis and other for methanol dehydration. Coprecipitation of Cu and Zn salts using sodium carbonate was reported to yield active catalysts. Solid acids such as γ-Al$_2$O$_3$ and HZSM-5 were used as they are or often modified by basic oxides in order to optimize the acidity and to attain high selectivity for DME [34].

1.4.2 Promoters

Since methanol synthesis is a structural sensitive reaction, many associated problems come along in realistic operating conditions such as agglomeration of the metal particles, sintering, rapid deactivation, etc. To handle these problems, the role of promoters comes into existence. Many promoters can be used along with Cu and ZnO to modify the methanol synthesis component, viz., divalent cations Mg^{2+}, Mn^{2+}, and Ca^{2+}; trivalent cations Al^{3+}, Cr^{3+}, La^{3+} and Ga^{3+}; and tetravalent cations Ce^{4+} and Zr^{4+}. Alkali metals such as K and Cs can also be used to promote the catalyst. These promoters can be used to modify the physicochemical characteristics of the catalyst like acidity, basicity, surface area, uniform dispersion of the active metal, etc. Also, the synergy between the Cu and ZnO can be enhanced using different promoters.

Out of all these promoters, Al$_2$O$_3$ is the most popular and industrially relevant component that is used as a promoter for methanol synthesis reaction. It is a trivalent refractory oxide that can induce monovalent cationic defects in the catalytic entity because of its dissimilar trivalent cationic charge (with Cu^{2+}, Zn^{2+}). Al$_2$O$_3$ forms a spinel with ZnO known as zinc aluminate (ZnAl$_2$O$_4$) which accelerates the adsorption as well as activation of CO molecule. These defective sites may serve as the sites for adsorption of the intermediate species produced during the reaction and can be converted into the product.

1.4.3 Carbon Source

It is still debated intensively whether the carbon of methanol is derived from CO or CO$_2$ and what is the reaction mechanism corridor through which the reaction propagates [35–39]. Copper based which are used for methanol synthesis are also active for the water gas shift (WGS) and reverse water gas shift reactions [35] (RWGS).

$$CO + H_2O \rightarrow CO_2 + H_2 \quad (WGS)$$

$$CO_2 + H_2 \rightarrow CO + H_2O \quad (RWGS)$$
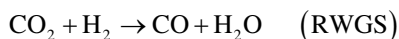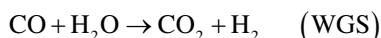
Since both CO and CO$_2$ are present as reactants as well as products, they created a perplexed inference about the major carbon source for methanol. At present, it is acknowledged that methanol is mainly formed through CO$_2$ hydrogenation at the typical operating industrial process [40, 41]. However, CO hydrogenation was

assumed to be the main reaction pathway for methanol synthesis [42, 43], whereas CO_2 modulates the surface composition, oxidation state of metal, and dispersion of Cu as a passive reactant [43]. This was considered as the main mechanism until the isotopic labelling experiments were performed first time by Chinchen et al. [44], where CO_2 was found to be the main source of methanol as per the reaction.

$$CO_2 + 3H_2 \rightarrow CH_3OH + H_2O$$
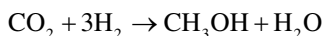
In another study conducted by Zhang et al., different feed components CO/H_2, CO_2/H_2, and $CO/CO_2/H_2$ were used to investigate the primary carbon source. It was found that MeOH formation rate was highest in case of $CO/CO_2/H_2$ feed. Also, higher methanol formation was observed in CO_2/H_2 feed as compared to CO/H_2. It signifies that the CO_2 hydrogenation was the dominant reaction, whereas presence of CO facilitates the adsorption phenomenon of the reactant feed.

However, many studies conducted in the recent past indicated that the major carbon source for methanol synthesis is dependent upon the reaction conditions [45] used. Even after four decades of debate on carbon source, still a disagreement exists in the literature about the most reliable kinetic track for methanol synthesis. However, a majority of the research groups are in agreement that methanol synthesis via CO_2 hydrogenation is the main reaction which provides the carbon of methanol.

1.4.4 Reaction Mechanism Pathways

Methanol synthesis reaction is accomplished by the propagation of three reactions which are CO hydrogenation, CO_2 hydrogenation, and water gas shift. All these reactions proceed through particular pathways. Many mechanism pathways are devised in the literature by various research groups using rigorous DFT studies [35, 45, 46]. All the engaged reactions involve the formation of various reaction intermediates which can also get converted into various by-products like formaldehyde, formic acid, methyl formate, etc.

Methanol Synthesis via CO Hydrogenation

Considering the methanol synthesis from CO hydrogenation, the mechanism can follow two competitive pathways depending upon the reaction barrier (activation energy [E_a]) of the initial step. The mechanism of CO hydrogenation to methanol is depicted in Fig. 3. As it can be observed, after adsorbing and activating on the surface, CO reacts with H^+ ions to form aldehyde isomers (one binding through C end and other through O end). The pathway (left) involving intermediates formed by binding through C end is more spontaneous as compared to the other route (right). This can be explained on the basis of the activation energy which is lower for the former route as compared to the latter. Furthermore, the concentration of the
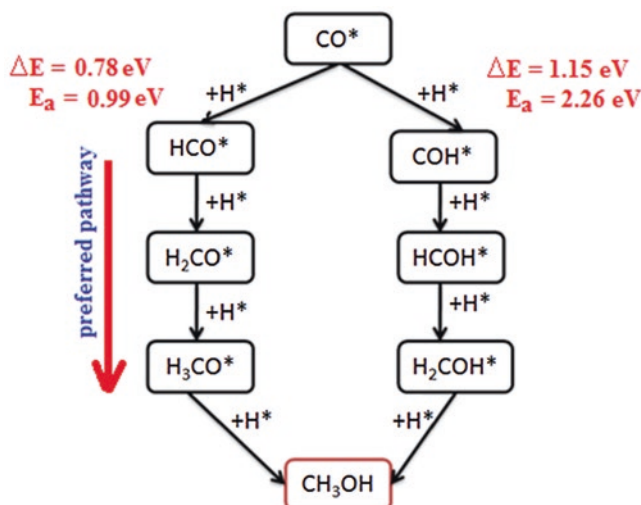
Fig. 3 Mechanistic view of competitive pathways of CO hydrogenation of methanol [35]

adsorbed HCO* species is mainly responsible for the methanol yield, and the conversion of H_3CO^* species to CH_3OH is the rate-determining step.

Methanol Synthesis via CO_2 Hydrogenation

The catalytic hydrogenation of CO_2 to methanol/DME is accepted to be the most promising route for CO_2 fixation and reducing its atmospheric concentration. The process of CO_2 conversion to methanol/DME can proceed directly or indirectly. According to the key surface intermediates formed during the reaction, two different mechanistic approaches are being proposed: the hydrocarboxylic (COOH*) pathway and the formate (HCOO*) pathway. Many studies have proposed the methanol synthesis process via HCOO-mediated mechanism because of the lower activation energy for HCOO* formation as compared to that of the COOH*. Also, HCOO* is a highly stable surface intermediate which is found on the catalyst surface in abundance. Also TOFs for methanol synthesis are found to be linearly proportional to the surface coverage of the catalyst Zn/Cu (111) by HCOO* species as observed in the micro kinetic model developed by Grabow et al. [35] using DFT studies. In further steps, hydrogenation of HCOO* species to form $H_2CO_2^*$ or HCOOH* at either C atom or O atom, respectively, takes place. The hydrogenation through O atom end possesses low activation barrier thereby is more thermodynamically stable [35]. The reverse of this is applicable for CO hydrogenation in which C atom end possesses lower activation barrier. The subsequent CO_2 hydrogenation steps yield intermediates $CH_3O_2^*$, CH_2O^*, CH_3O^*, and CH_3OH^*. A brief comparison of the reaction pathways of CO and CO_2 hydrogenation is presented in Fig. 4 [45–60].
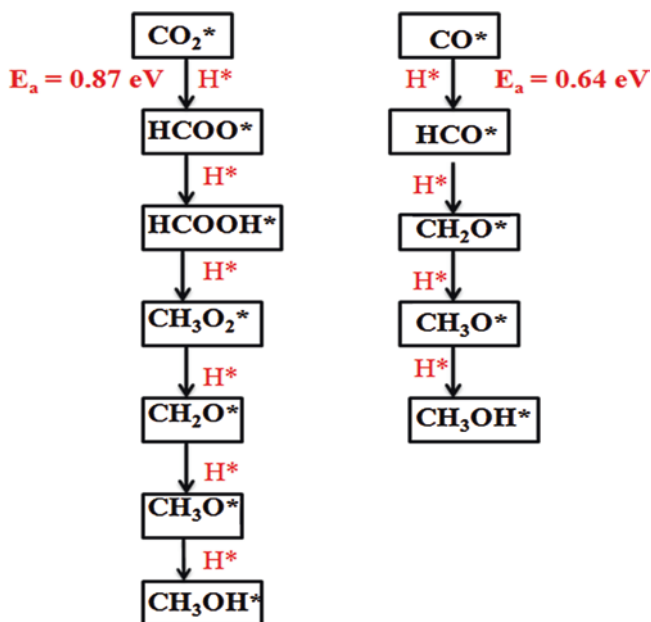
Fig. 4 Comparison between the hydrogenation pathways of CO and CO_2 [45]

Table 3 A comparative analysis of CO_2 vs. CO/CO_2 feed in relation to the activation energy of different mechanism steps [35]

Surface reaction steps	Activation energy (E_a) for only CO_2 as a feed	Activation energy (E_a) for CO/CO_2 as a feed
$CO^* \rightarrow HCO^*$	0.99	0.99
$O^* \rightarrow OH^*$	0.96	Spontaneous
$OH^* \rightarrow H_2O^*$	1.18	0.30
$HCOO^* \rightarrow HCOOH^*$	0.91	0.60
$HCOO^* \rightarrow H_2CO_2^*$	1.59	0.80
$HCOOH^* \rightarrow CH_3O_2^*$	1.04	0.42
$CH_2O^* \rightarrow CH_3O^*$	0.24	Spontaneous
$CH_3O^* \rightarrow CH_3OH^*$	1.17	0.38

Although higher activation barrier was found when the reaction proceeds through CO_2 hydrogenation individually as compared to CO hydrogenation, co-feeding CO_2 with CO (even in small amount) results in lowering down of this activation barrier [43]. This demonstrates the promotional effect of using CO in the CO_2-rich feed. A brief comparison of CO_2 vs. CO_2/CO feed related to the activation energy of the surface reaction steps has been provided in Table 3 [35].

Water Gas Shift Reaction

The description of mechanism for methanol synthesis is incomplete without mentioning the mechanism for inevitable water gas shift reaction. WGS is an essential part of methanol synthesis process which involves consumption of water produced during hydrogenation reaction. The combination of WGS and hydrogenation reaction provides a strong driving force, thereby increasing the syngas conversion dramatically. Water gas shift reaction proceeds through carboxylic path which can undergo three main reactions as follows [45, 61–66].

As depicted in the Fig. 5, WGS reaction can follow the three paths which are surface adsorption of CO* and OH* species to form *trans-* and *cis*-COOH* carboxylic group intermediates and HCOO* formate group intermediate. Out of these three, the preferential pathway for WGS reaction to occur is through *cis*-COOH* intermediate. This may be because of the low activation energy needed for this pathway at Cu+surface.

1.4.5   Active Sites

Although methanol synthesis has been a subject of research for hundreds of years, the views regarding the commanding active site for the methanol synthesis are still controversial [67–69]. Some studies conducted by the researchers in the past have suggested Cu+ ions to be the active centers for the reaction [43, 70], whereas some experimental evidences support the linear relation between the amount of surface metallic copper (Cu^0) and catalytic activity [71]. Further experiments [35] on single crystal Cu (100) [72, 73], Cu (110) [74], and polycrystalline Cu films with exposed Cu (111) facet suggested that the reaction is facilitated by metallic Cu [75]. Most of the kinetic models are developed considering the Cu (111) facet because it is the most thermodynamically stable phase and under reducing conditions (like methanol synthesis) this phase is predominantly exposed to the reactants. Also, the observed kinetic reaction rates on polycrystalline Cu exposing mostly Cu (111) are found in line with the reaction rates derived from realistic experimental data performed under kinetic regime using Cu/ZnO catalyst [35]. On the other hand, Chen et al. reported that the coexistence of Cu^0/Cu^+ on the catalyst surface can also serve as the active site for the reaction to occur. Apart from this, a variety of views regarding the nature of active sites exist in the literature. The major thoughts can be divided as follows [51, 52]:
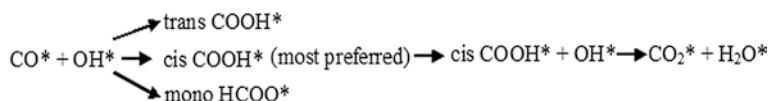
Fig. 5 Water gas shift (WGS) reaction pathways

Cu-Zn alloy on Zn/Cu (111) surface

- Existence of Cu^+ monovalent cations in ZnO matrix
- Stabilized Cu ions in morphologically active ZnO
- Formation of Cu-ZnO interface through oxygen (Cu-O-Zn)

1.4.6   Importance of ZnO

The significance of ZnO in methanol synthesis catalyst could be realized by the fact that Cu metal alone is not able to provide active centers for the reaction to occur. In fact, a study conducted by Herman et al. signifies the co-existence of ZnO in the catalyst as the activity of the binary catalyst (Cu/ZnO) increased by three orders of magnitude as compared to that of pure Cu metal. From the early findings of the methanol synthesis catalysts to the present stage of the catalytic platform, the role of ZnO to facilitate the easy reaction propagation has remained contrasting. A few important roles of ZnO, as identified from literature, are as follows:

- ZnO is reported to enhance Cu dispersion, thereby elucidating a synergistic effect with Cu species [76].
- Promotes the stability of active Cu^+ sites in the catalyst by allowing the incorporation of Cu^+ into the crystal lattice of ZnO [74].
- The main function of ZnO was identified to facilitate heterogeneous H_2 splitting ($H^{\delta+}/H^{\delta-}$) and spillover which involves the migration of H^+/OH^- species over the catalyst surface.
- Incorporation of ZnO in the catalyst matrix induces the shape changes in Cu particles impregnated on the support depending upon the redox potential of surrounding gas phase as identified by atom-resolved TEM [77]. These changes in shape of the particle results in irregularities on the surface which enhances the catalytic activity.

Table 4 demonstrates the exemplary behavior of ZnO when exposed to different feed streams. On the other hand, some studies demonstrated the negative or neutral effect of ZnO addition into the Cu-based catalytic system. Chinchen et al. emphasized that there does not exist any significant difference in catalytic activity between the Cu-supported catalyst on SiO_2 and MgO as compared to that supported on ZnO, thereby totally denying the well-known Cu-ZnO synergy. Another controversial discussion related to Cu-ZnO interaction exists in the explanation of the Schottky junction effect existing between these two. The effect is known to increase the oxygen vacancies in ZnO thrice when used alone, but no reaction intermediates were observed when Cu is present along with ZnO. This suggests that the theory fails to explain the increased activity of Cu-ZnO catalyst [78].

Table 4 Promotional effect of ZnO for different feedstock [46]

Feed stream	Cu	Industrial catalyst (Cu/ZnO)
CO	• Low overall energy barrier • Fast CO hydrogenation	• Zn addition increases the energy barrier of first few reaction intermediates • Slow CO hydrogenation
CO + CO$_2$	• Significant formate coverage • CO hydrogenation blocked • CO$_2$ major carbon source • CO$_2$ hydrogenation has high barrier, overall reaction rate slow	• High formate coverage • CO hydrogenation blocked • CO$_2$ major carbon source • CO$_2$ hydrogenation fast, overall reaction rate fast

1.5 Deactivation and Remedies

There are a variety of deactivation factors towards which Cu-based methanol catalysts are sensitive enough. Since Cu is the second last metal (above Ag only) in the list of thermal stability, exposure to high temperature (>300 °C) can lead to drastic irreversible effects on its properties [79]. The major problems faced by these catalysts are easy sintering, swift agglomeration, and rapid deactivation. Hence, in order to make catalyst resistant towards these factors and to increase the shelf life of the catalyst, it is essential to add a suitable promoter to enhance its thermal stability. Some of the major reasons of catalyst deactivation are:

• Non-uniform distribution of Cu metal particles on the catalyst surface resulting in metal sintering [80].
• Presence of poisonous compounds like sulfur and chlorine in the feed stream.
• Conducting the reaction at higher pressure that aids in increasing deactivation rate.
• Deposition of carbon and other species on the catalyst surface as a result of side reactions like boudouard reaction and methanation reaction.
• Formation of water resulting from the unavoidable water gas shift reaction.

After identifying the primary causes for the catalyst deactivation, it has been observed that there does not exist any guaranteed solution that can prevent the catalyst from getting deactivated. However, the deactivation phenomenon can be delayed or controlled up to some extent. The major remedies that can be executed to increase the shelf life of the catalyst are as follows:

• Incorporate co-promoters like ZnO and Al$_2$O$_3$ in the catalyst so as to increase the active metal dispersion and to stabilize dispersed Cu crystals, thereby making it reluctant to sintering and agglomeration.
• ZnO reacts with sulfur poison present in the feed gas to form ZnS and Zn(SO$_4$) (favorable thermodynamic reaction in methanol synthesis conditions), thus inhibiting sulfur to react with active Cu metal.

- Addition of metal oxide in the form spinel or doping it with other non-refractory oxide can permit the catalyst to get operated at higher pressures without compromising its activity for a longer duration of time.
- Use of hydrophobic oxide promoters so that the accumulation of water at the catalyst surface can be avoided.

2   Novel Catalyst Approaches for CO_2 Hydrogenation

After the discovery of $Cu/ZnO/Al_2O_3$catalyst, low-pressure methanol synthesis units are established all around the globe as the operating cost was significantly reduced by low-pressure process. The research paradigm shifted to development of Cu-based catalyst with suitable metal oxide (ZnO, ZrO_2, CeO_2, MgO) and structural promoters (ternary metal oxide) like Al_2O_3, ZrO_2, and CeO_2. The novel catalyst synthesis approaches and parameters like pH, temperature, and composition are the prime focus for catalyst development. Jadhav et al. [81] and Álvarez et al. [82] complied literature on Cu-based catalytic system. Besides, Pd is the second most reported metal for methanol synthesis via CO_2hydrogenation. The bimetallic sites of Pd with Ga, In, and Zn formed on catalyst reduction were explored for the reaction. Li et al. [83] complied the literature reports on bimetallic catalyst used for the reaction system. Here we elaborate application of In_2O_3-based catalyst, metal carbides, and MOF for the hydrogenation of CO_2.

The DFT calculations on defective [84] and non-defective [85] $In_2O_3(110)$ revealed that oxygen vacancy on the In_2O_3 surface is helpful for methanol synthesis. The methanol synthesis mechanism over In_2O_3 comprises of cyclic creation and annihilation of oxygen vacancies. The main challenge for methanol synthesis from CO_2 hydrogenation is selective dissociation one of the C=O bonds. The C=O bonds in reported Cu-based catalytic systems break only by dissociation of intermediates formed during reaction [84], whereas, for In_2O_3, one oxygen atom of the intermediate fills the vacancy on the surface, and cleavage of C=O occurs. The DFT results were experimentally verified with application of commercial In_2O_3 as catalyst. Methanol selectivity of 54.9% with methanol production rate 3.69 mol h^{-1} kgcat^{-1} at 330 °C and 4 MPa [86]. Martin et al. [87] reported 99.8% methanol selectivity at 573 K and 50 bar over ZrO_2 supported In_2O_3 catalyst. The interaction ZrO_2 with In_2O_3 increased number of the active sites on the surface. The supported In_2O_3/ZrO_2catalyst was stable for run time of 1000 h [87]. The existence of ZrO_2 under the In_2O_3 overlayer obstructs CO_2 dissociation to CO and improved the concentration of oxygen vacancies on In_2O_3 catalytic surface [88]. Moreover, incorporation of Ga ions into the lattice of In_2O_3 improved the physicochemical properties and desorption temperature of CO_2 for Ga_x/In_xO_{n-2} catalyst. However, strong adsorption of CO_2 results to CH_4 synthesis, and significant reduction in CO yield was noticed over Ga_x/In_xO_{n-2} catalyst [89]. Additionally, Chou [90] et al. reported lanthanum and yttrium promoted In_2O_3 catalyst by wet impregnation method. Improved CO_2 adsorption sites and methanol selectivity were witnessed for La, and Y promoted In_2O_3 catalyst

in comparison with bare In_2O_3 due to the strong basic sites present on the catalyst surface. Moreover, hexagonal-phase In_2O_3 (H-In_2O_3) structured onto thin-felt Al_2O_3/Al-fiber matrixes via the mix-solvothermal preparation method has been used for CO_2 hydrogenation to methanol. The H-In_2O_3/Al_2O_3/Al-fiber catalyst showed positive results in terms of CO_2 conversion and methanol selectivity of 4.4% and 67.6%, respectively, at 325 °C and 40 bars. The In_2O_3/Al_2O_3/Al-fiber catalyst was stable for 200 h of run time without deactivation. Men [91] et al. synthesized Pt/In_2O_3 hybrid films by cold-plasma/peptide-assembly (CPPA) method and showed appreciable results for CO_2 conversion.

DFT study revealed that formation of Pd-In bimetallic site improved (compared to In_2O_3) the catalytic performance by providing metal (Pd) sites generation of atomic H_2 and interfacial sites for CO_2 adsorption and hydrogenation. However, poor methanol yield was observed in experimental studies. The H_2 chemisorption results revealed that the Pd-In bimetallic interface has fewer active sites for adsorption of atomic hydrogen compared to Pd; therefore, the rate of hydrogenation decreased in the experiments [92]. To increase the methanol yield over the Pd/In_2O_3 catalyst, one must minimize formation of Pd-In bimetallic during the catalyst synthesis. Thus Qingfeng et al. [93] research groups synthesized highly dispersed Pd NPs (3.6 nm) on In_2O_3 using peptide template. The Pd-In bimetallic sites formed appreciably enhanced dissociative adsorption of hydrogen, with preserving the density of the oxygen vacancies. The CO_2 conversion >20% with methanol selectivity >70% was observed for the catalyst (STY 0.89 g MeOH h^{-1} gcat^{-1} at 300 °C and 5 MPa).

Metal organic frameworks (MOFs) also termed as "porous coordination polymers" (PCP) are three-dimensional porous crystalline materials. MOF consists of regular arrangement of a metal cation or cluster (secondary building units (SBUs)) and a polydentate organic ligand with coordination-type connections. MOFs have attracted attention for their application in catalysis due to their metal center, highly ordered porous structure, uniform pore size, and functional organic linkers. Therefore, Rungtaweevoranit et al. [94] synthesized Cu nanoparticles encapsulated within framework of UiO-66 and reported 100% methanol selectivity (175 °C and 10 bar). The variable oxidation state of Cu and increased interfacial contact between Cu NCs and Zr oxide SBUs enhanced TOF for methanol formation (>20×10^3 s^{-1} at 200 °C). The degree of charge transfer from Cu nanoparticle to the Zr^{4+} at the interface of Cu-UiO66 is linearly related to the activity of MOF-based catalyst for methanol synthesis reaction [95]. An et al. [96] reported Cu/ZnO_x supported on UiO-bpy (synthesized by solvothermal process 2,2′-bipyridine-5,5′-dicarboxylate (bpydc) bridging ligand and $Zr_6(\mu_3$-O$)_4(\mu_3$-OH$)_4$ SBUs) MOF, owing to the high thermal stability (>250 °C). The well-mixed Cu, ZnO_x, and Zr SBUs surface/interfacial sites contributed to the adsorption and activation of H_2 and CO_2 in the CuZn@UiO-bpy catalyst. The Cu/ZnOx@MOF catalysts show very high activity with STY of up to 2.59 g MeOH kg Cu^{-1} h^{-1}, 100% methanol selectivity at 180 °C, and high stability for about 100 h.

The surface chemistry of transition metal carbides (TMCs) is alike to that of Pt group metals like Pd, Rh, or Ru during the transformation of hydrocarbons. Thus,

TMCs are reported as catalyst in hydrogenation and hydro-treatment (oil-derived feedstock) process. In addition, TMCs act as a suitable support to get high metal dispersion catalyst. Also (001) surface of TMCs of Ti, Zr, Hf, Nb,Ta, and Mo has been found appropriate for CO_2 adsorption and activation [97]. The TMCs of Ti and Mo are reported methanol synthesis via CO_2 hydrogenation. The incorporation of small amount of Cu and Au over TiC (001) causes charge polarization and makes CO_2 activation easy and also enhances methanol selectivity. The apparent activation energy for methanol synthesis decreases to 11.6 kcal/mol on Cu/TiC (001) from 25.4 kcal/mol on Cu (111). The TOFs for methanol production on Cu/TiC (001) were 170–500 times higher than on Cu (111) [98]. The interfacial sites of Cu and Au adsorbed atoms to TiC (001) were more active than bare Cu (111) and Au (111) [99]. The metal-to-carbon ratio in metal carbide catalyst plays a crucial role in selective hydrogenation of CO_2 to methanol. The CO_2 hydrogenation over β-Mo_2C (001) having metal-to-carbon ratio of 2 results to hydrogenation of formate to CH_4 through cleavage of both C–O bond rather than CH_3OH. Further, the orthorhombic β-MoC (001) with polar Mo-terminated surface promotes CO_2 activation by breakage of one C–O bond and then leads to CO formation, whereas for C-terminated non-polar orthorhombic β-MoC (001) surface, CO_2 activation occurs but without C–O bond cleavage [100]. Geng et al. [101] used protic ionic liquid (*N*-butylimidazolium molybdophosphate and *N*-butylimidazolium *p*-toluenesulfonate) as a precursor and synthesized N,P,S co-doped C@nano-Mo_2C catalyst by direct carbonization. At 200 °C and 30 bar, CO_2 conversion of 19% and MeOH selectivity of 85.4% were observed for N,P,S co-doped C@nano-Mo_2C carburized at 1023 K. Similar synthesis approach was used by Wei et al. [102] for synthesis of N,S co-doped C@Mo_2C and reported CO_2 conversion of 16% and MeOH selectivity of 90.5% with STY of methanol 0.405 g_{MeOH}/g_{cat}/h (30 bar, 220 °C, and 7500 mL/g/h).

3   Reactors

Conventionally, there are mainly two types of reactors available for gas-phase methanol synthesis: adiabatic and isothermal reactors (Fig. 6). Recently, for liquid phase synthesis of methanol, slurry reactors are coming into role along with overcoming the problems associated with gas-phase reactors. Adiabatic reactors comprise fixed bed reactors in series with cooling medium connected in the downstream of each reactor for removal of heat. Fixed bed reactor systems lead to low installation cost and high production capacity. Due to no exchange of heat between system and surroundings (adiabatic nature), temperature rises as reaction approaches to equilibrium state, and this high temperature is responsible for low single per pass conversion. Accordingly, high recycle ratio, more dilution of reagents, and more amount of catalyst are used to improve the efficiency. Design of isothermal reactors is similar to the heat exchanger in which water/gas is continuously circulated through the mantle of the tube to maintain the temperature inside the reaction zone.
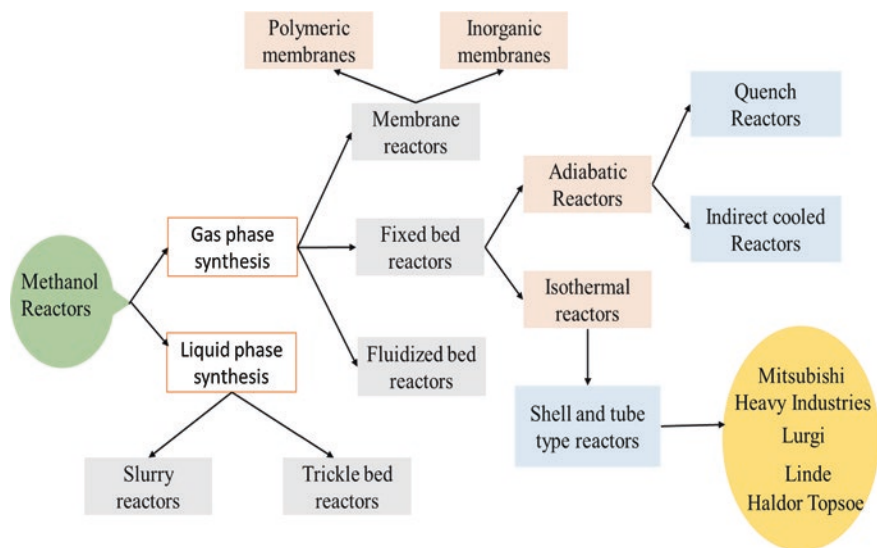
Fig. 6 State of the art of conventional reactors for methanol synthesis

Homogeneity of temperature leads to high per pass conversion for lower volume of catalyst than adiabatic reactors. However, for achieving higher reaction rate and increasing selectivity of methanol, reaction should be carried out at temperature range of 240–260 °C with high recycle ratio. Application of these reactors is limited owing to its high installation cost than adiabatic system and size constraints due to multiple tubes type arrangement [33].

3.1 Fixed Bed Reactors

Conventionally, fixed bed reactors are used for methanol synthesis in gas phase, and these are categorized into isothermal and adiabatic reactors. Isothermal reactors are designed similar to shell and tube heat exchanger where catalyst is placed in shell or tube side and coolant is circulated in other side to maintain the temperature uniformity, thereby increasing the reluctance towards local hot spot generation. The adiabatic reactors, used for methanol synthesis, composed of a series of fixed bed reactors, each of which is connected to a cooling sink for effective heat removal. Adiabatic conditions (no heat transfer between system and surroundings) and exothermicity result in a low degree of per pass conversion due to increase in temperature as reaction approaches towards steady state. Enhancements in conversion have been made by recycling of more amount of unreacted gases and catalyst. Constant temperature in isothermal reactors leads to more per pass conversion than adiabatic reactors, but it has some disadvantages such as size constraints, methanol productivity limited to 2000 tonnes/day due to shell- and tube-type arrangements, and higher

installation cost than adiabatic reactors. Owing to low-temperature range of 240–260 °C for increasing reaction rates and selectivity in isothermal reactors, these reactors have limited applications. Various industries like Mitsubishi Heavy Industries, Linde, Lurgi, and Haldor Topsoe are using these shell- and tube-type reactors with higher recycle ratio and lower catalyst volume due to ease of operation [10].

3.1.1 Adiabatic Reactors: On the Basis of Design, These Adiabatic Reactors Are Generally Classified in Two Types

Quench Reactors

A fraction of feedstock is heated before being fed upstream of the reactor. The fed reactants react with the catalyst surface, and conversion of these reactants increase the temperature of the process stream due to exothermic nature of the reaction. Remaining feedstock along with catalyst fed cold in the reactor, which decreases the temperature and increases the methanol yield. Despite the ease of process, this scheme leads to non-uniform utilization of catalyst volume as upstream reacts with higher catalyst volume as compared to the downstream. Haldor Topsoe's multiple bed reactor is a quench-type reactor.

Indirect Cooled Reactors

Adiabatic reactors are displaced in series with cooling devices connected between the reactors. The reaction temperature is lowered due to these coolers and, thus, enhanced per pass conversion and selectivity of methanol. As the complete feedstock directly enters into the reactor, it reduces the utilized catalyst volume than quench-type reactors.

Examples of such reactors are (1) Kellog, Brown, and Root's adiabatic reactors and (2) Toyo Engineering Corporation's MRF-Z reactors.

3.2 Liquid Phase Reactors

Single pass conversion in fixed bed reactors is limited owing to equilibrium nature of this methanol synthesis reaction. Significant recycling of unreacted synthesis gas can diminish this conversion limitation which is the main problem associated with conventional fixed bed reactors. Many studies have been carried out in reactor design to improve the methanol productivity for gas phase using multifunctional reactor systems (coupling of exothermic and endothermic reaction systems for better heat utilization) and shell-tube-type heat exchangers. However, these reactors also have some limitations like pressure drops, hot spots formation during reaction

due to exothermicity of reaction, high investment, and operating costs due to multiple recycling. Also, these traditional reactors are not preferable for coal-gasified synthesis gas as stoichiometric number S ((moles H_2-moles CO_2)/(moles CO_2 + moles CO)) is found to be less than two indicating hydrogen deficiency which promotes catalyst deactivation because of coking. To deal with these problems, three phase (gas-solid-liquid) slurry and trickle bed reactors stand out to be one of the major solutions and represent future of the methanol industry [33].

3.2.1   Trickle Bed Reactors

Catalyst synthesis and loading in trickle bed reactors has been proposed in similar fashion as fixed bed reactors. The feed gas and solvent/liquid enters into the reactor in a co-current manner. Inert solvents with high heat capacity like mineral oil/hydrocarbons are used for suspension of catalyst, and these solvents facilitate good heat transfer that ensures homogeneity in temperature during reaction. Removal of product during reaction reduces recycling costs and striking the thermodynamic limitations [10].

3.3   Membrane Reactors

The thermodynamic limitations of methanol synthesis reaction reduce the overall yield of conventional fixed bed reactor systems. The overall yield of methanol can be increased either by recycling of the unreacted feed or by in situ removal of products. Membrane reactors can be used for selective adsorption of methanol or water or both for in situ removal of products. The in situ separation of methanol is helpful to achieve high purity of product, whereas in situ separation of water shifts the equilibrium towards methanol synthesis reaction (Le Chatelier's principle). In addition, water removal avoids secondary reaction like methanol reforming and catalyst deactivation via sintering in Cu/ZnO catalyst.

Struis et al. [103] reported lithiated Nafion membrane (polymeric membrane) for in situ methanol separation. The removal of methanol enhanced the performance of membrane reactors over the conventional fixed bed reactor system. The same group developed a mathematical model combining methanol synthesis and permeation. The model predicted an improved single pass reactor yield by 40% at 200 °C, GHSV = 5000 h^{-1}, and ΔP = 39 bar with 10μm lithiated Nafion membrane [104]. However, low thermal stability of membrane (150 °C) limited the industrial application of membrane reactors. The industrial methanol synthesis is at around 240–300 °C; thus, the application of polymeric membrane is difficult; thus, the research focus has been synthesis and application of inorganic membrane in the context of methanol synthesis membrane reactors.

Zeolite can separate molecules based on their size because of their well-structured narrow pore size distribution. In addition, thermal, mechanical, and chemical

stability of the zeolites makes them suitable for application as membrane. When the size of molecule and the pore size of material are comparable, the molecular diffusivity decreases exponentially. Thus, synthesis of zeolites is challenging as the zeolite pores are usually 0.3–1.3 nm in size and a small crystal spacing (2–3 nm) can degrade the separation quality. Nevertheless, zeolites have been used for separation of organic isomers, close boiling point mixture, and at high temperature and pressure reaction. Barbieri et al. [105] performed thermodynamic analysis of methanol synthesis via CO_2 hydrogenation in zeolite membrane reactor. They proposed a mathematical model for non-isothermal, microporous zeolites with different permeation value of methanol and water. The membrane reactors can operate at lower pressure and higher temperature as compared to the conventional fixed bed reactor system with 40–50% conversion and nearly 100% selectivity. The per pass methanol yield in membrane reactor (8.9%) was more than two times than in fixed bed reactor (2.4%). The proposed modelling approach was heavily dependent on the methanol and water permeation rates. Gallucci et al. [106] reported the application of A-type zeolite for methanol synthesis reaction in a packed bed membrane reactor (PBMR). The higher methanol yield at lower operating conditions in membrane reactors compare to fixed bed reactor system suggests that operating conditions are energy saving. They reported CO_2 conversion of 11.6% with 75% methanol selectivity at 206 °C and 20 bar pressure. The STY of 343 $g_{methanol}$ kgcat^{-1} h^{-1} with 84% of methanol selectivity (240 °C, 7 bars, and GHSV = 18,000 L kgcat^{-1} h^{-1}) obtained by using NaA membrane [107]. Zebarjad et al. [108] used 1-ethyl-3-methylimidazolium tetrafluoroborate (ionic liquid) on the tube side in membrane reactor and syngas on the shell side of the reactor. They used commercial methanol synthesis catalyst and modified mesoporous alumina (hydrophobic) membrane.

Rahimpour and co-workers reported a reactor configuration with shell and tube Pd membrane (H_2 permeable) reactor. The feed flow from the tube side and pure hydrogen was on the shell side. The unique membrane configuration allows diffusion of H_2 from the shell to the tube to maintain a desired ratio of H_2/CO_2 along the reactor length. Methanol yield was enhanced with decrease in membrane thickness and increasing the shell side flow rate [109]. Further, the same research group have performed comparative study between conventional methanol synthesis reactor and dual membrane reactors with similar shell and tube arrangement. The first reactor in dual configuration was cooled by cooling water, and second reactor was cooled by feed syngas. The application of H_2 permeable palladium-silver (Pd-Ag) membrane on the tube side of second reactor configuration improved methanol yield by H_2 diffusion through the tube side of the reactor [110]. The dual membrane reactor with two different membranes in each reactor configuration has been also reported; one membrane was used for feeding H_2 and other for removal of water. The objective function used to determine the optimal operating condition was a function of outlet molar flow rate of methanol. The optimal operating conditions were determined using genetic algorithm. The optimized dual membrane reactor provides higher CO_2 conversion and methanol yield [111].

Increasing CO_2 concentration problem can be solved by utilizing it to convert in valuable products in order to mitigate the global warming and its associated effects

by simultaneously meeting the increasing energy demands. Many approaches such as thermocatalytic, photocatalytic, biocatalytic, electrocatalytic, and photoelectrocatalytic have been used for conversion of CO_2 to value-added product [112]. However, the challenge in each approach is the activation of linear CO_2 molecule due to its high stability (dissociation energy of 750 kJ mol^{-1} of C=O bond) [113]. Several value-added products like formic acid, formaldehyde, methane, and methanol are possible from CO_2 reduction reaction. CO_2 reduction process requires energy input; hence, utilization of renewable sources of energy such as sunlight is a sustainable means. In photocatalytic processes, solar energy is utilized to carry out the chemical reaction. Therefore, heterogeneous and homogeneous photocatalytic CO_2 reduction could be a promising way to tackle the dual problem of global warming and meeting the increasing energy demand.

4 Advantages of Photocatalytic Conversion Process over Thermocatalytic Conversion

The CO_2 conversion process takes place at moderate reaction conditions, i.e., at atmospheric pressure and temperature, unlike in case of thermocatalytic process where high temperature and pressures are required. Energy source in case of photocatalytic process is solar light which is present in enormous amount. In photocatalytic route, the hydrogen source is water, while in the case of thermocatalytic conversion process, the source of hydrogen is H_2 gas. Hence, cost of water as a hydrogen source in photocatalytic process is lesser compared to hydrogen gas. The total energy input cost in case of photocatalytic is far less compared to that in case of thermocatalytic conversion process. The photocatalysts used in case of photoconversion processes possess the quality of recyclability. As the conversion process takes place at low temperature and pressure in case of photocatalytic conversion, the number of cycles for which catalysts can be used are more in case of photocatalyst when compared to the recyclability of the thermocatalyst. With lesser initial investment and higher duration of use, the photocatalytic process is a promising means to utilize CO_2 for conversion to value-added chemicals.

The photocatalysts are majorly semiconductors, possessing band structure with conduction and valance bands. The highest occupied energy band that is completely occupied is the valance band, and the energy band from top that is unoccupied is the conduction band. The difference between the valance and conduction band is the band gap, and through thermal interactions, the electrons can move from valance to conduction band and vice versa. Conduction band energy is higher compared to that of the valance band. The population density of the charge carriers, i.e., electron (negative charge carrier) and holes (positive charge carriers), can change upon interaction with light. For the activation of stable CO_2 molecules, the energy input is desired; in photocatalytic process, this energy is provided by the high-energy electrons. The high-energy electrons are the electrons that are present in the conduction

band of the photocatalyst. The holes generated are present in the valance band of the photocatalyst. These charge carriers contribute in the reduction of CO_2 reduction process by different interaction mechanism with adsorbed species.

4.1 Photocatalytic Reduction

The photocatalytic CO_2 reduction process consists of the following steps (shown in Fig. 7):

1. The first step is the photoexcitation of electrons in photocatalyst from valence band to conduction band by absorption of photon having energy more than the material band gap. In this step, generation of charge carriers, i.e., electrons and holes, in equal concentration in conduction band and valance band, respectively, takes place.
2. The second step is the diffusion of charge carriers from bulk to the catalyst surface where these participate in redox reactions. This step proceeds competitively with electron-hole charge recombination depending upon timescale for carriers to reach the catalyst surface and lifetime of the charge carrier before they combine with their counterpart to generate heat which depends on material properties and modifications of the surface.
3. The third step is reduction reaction of the adsorbed CO_2 on the conduction band via reduction pathway to form products like CO, CH_3OH, CH_4, and HCOOH depending on thermodynamic potential. The CO_2 reduction reaction proceeds competitively with the reduction of water to form hydrogen, i.e., hydrogen evo-
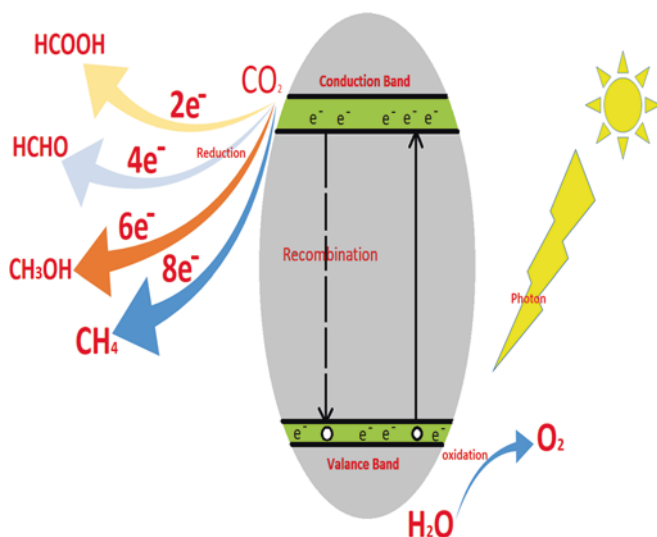
Fig. 7 Photocatalytic reduction of CO_2 to various possible products

lution reaction (HER), whereas on the valance band, the oxidation of H_2O takes place to form O_2, i.e., oxygen evolution reaction (OER).

4. Final step after the photocatalytic reaction is the desorption of products. It is essential that the formed products are timely released from catalyst surface or else the catalyst sites are blocked for further substrate adsorption, or further back oxidation/reduction could take place.

4.2 Thermodynamics of Photocatalytic Reduction of Carbon Dioxide

Due to the high stability of CO_2, its reduction is thermodynamically not feasible without external energy supply. In photocatalytic process, this extra energy is provided by high-energy electrons generated via photoexcitation. However, the reduction reaction feasibility is governed by thermodynamic driving force which is the potential of the conduction band edge relative to the reaction reduction potential [114]. Reactions with less negative reduction potential than the conduction band edge potential are thermodynamically feasible, whereas reactions with more negative reduction potential are not favored. Similarly, for oxidation reactions which occur via electron transfer to valence band holes, reaction with reduction potential less positive than the valence band edge potential is thermodynamically feasible. The substrate with more positive reduction potential is a better oxidant and tends to reduce those with lower reduction potential values. Hence, if the reduction potential of donor is less positive than valance band edge and reduction potential of acceptor is less negative than the conduction band edge, electron transfer will be thermodynamically feasible. Table 5 enlists the reactions stoichiometry with redox potential

Table 5 Standard redox potential for CO_2 reduction reactions ($P = 1.0$ atm and $T = 25\ °C$)

Reactions	Redox potential w.r.t NHE at pH = 7
$CO_2 + e^- \rightarrow CO_2^-$	$\left(E^0_{redox} = -1.9\ \text{eV}\right)$
$CO_2 + 2H^+ + 2e^- \rightarrow HCOOH$	$\left(E^0_{redox} = -0.61\ \text{eV}\right)$
$CO_2 + 2H^+ + 2e^- \rightarrow CO + H_2O$	$\left(E^0_{redox} = -0.53\ \text{eV}\right)$
$CO_2 + 4H^+ + 4e^- \rightarrow HCHO + H_2O$	$\left(E^0_{redox} = -0.48\ \text{eV}\right)$
$CO_2 + 6H^+ + 6e^- \rightarrow CH_3OH + H_2O$	$\left(E^0_{redox} = -0.38\ \text{eV}\right)$
$CO_2 + 8H^+ + 8e^- \rightarrow CH_4 + 2H_2O$	$\left(E^0_{redox} = -0.24\ \text{eV}\right)$
$2H_2O + 4H^+ \rightarrow 4H^+ + O_2$	$\left(E^0_{redox} = +.82\ \text{eV}\right)$
$2H^+ + 2e^- \rightarrow H_2$	$\left(E^0_{redox} = -0.41\ \text{eV}\right)$
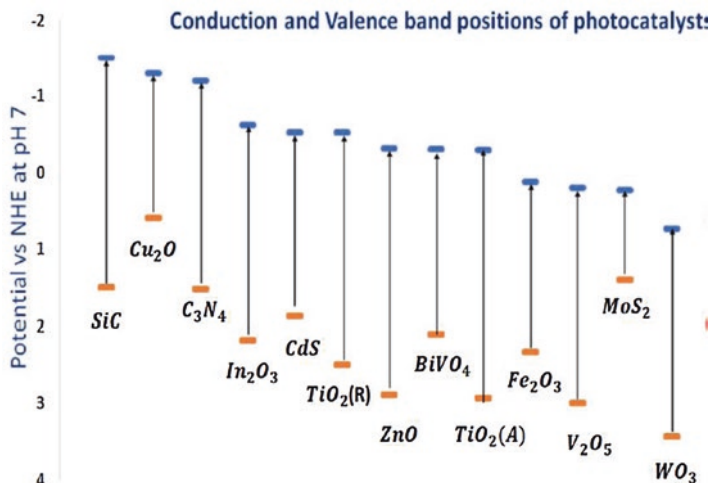
Fig. 8 Band gap energies of different semiconductors with their respective band edges

(vs. SHE) which could occur while reducing CO_2, and Fig. 8 shows different photocatalyst band edges potential w.r.t SHE. Therefore, if reduction potential of reduction reactions is less negative than the conduction band edges potential, the reduction reaction would be favored on to that photocatalyst. Similarly, if oxidation reaction potential is less positive than the valance band edge potential, the oxidation reaction is favored on the photocatalyst. Other than the thermodynamic feasibility of reaction, several factors play important role in driving the CO_2 photoconversion process.

4.3 Mechanism of Photoreduction of CO_2

The CO_2 photoconversion is a complicated process in which the photoexcitation of the catalyst provides the electrons. The transfer of the electrons takes place competitively on the adsorbed CO_2 and protons over the catalyst surface [115]. Transfer of electron to the stable linear structure of CO_2 (first elementary reaction) is typically the rate-controlling step in most of the proposed pathways. Reaction medium, i.e., water, primarily acts as the proton and electron donor. The transfer of protons and electrons governs the type of intermediate formed and its rate. Based on the product formation, many possible reduction pathways are proposed. In 1979, Innoue et al. [114] proposed two electrons and two protons formaldehyde pathway in an aqueous medium.

$$\text{catalyst} + h\vartheta \rightarrow \text{catalyst} * \left(e_{\text{cond}}^{-} + p_{\text{val}}^{+} \right)$$

Oxidation reactions

$$H_2O + 2p_{\text{val}}^{+} \rightarrow \frac{1}{2}O_2 + 2H^{+}$$

Reduction reactions

$$CO_2\left(aq\right) + 2H^{+} + 2e_{\text{cond}}^{-} \rightarrow HCOOH$$

$$HCOOH + 2H^{+} + 2e_{\text{cond}}^{-} \rightarrow HCHO + H_2O$$

$$HCHO + 2H^{+} + 2e_{\text{cond}}^{-} \rightarrow CH_3OH$$

$$CH_3OH + 2H^{+} + 2e_{\text{cond}}^{-} \rightarrow CH_4 + H_2O$$
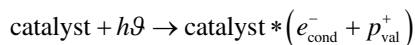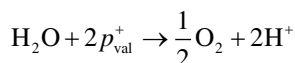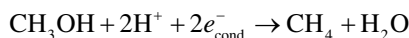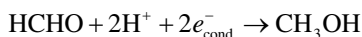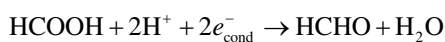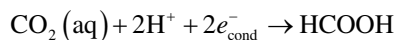
Their research proposed that the formation of C1 products like formic acid, methanol, methane, and formaldehyde formation is well explained based on reaction potential. However, this pathway was unable to explain the formation of intermediate free radical species, which were observed in ESR experiments. Therefore, Subrahmanyam et al. proposed carbene radical mechanism that explained the formation of the hydrocarbons via radical pathway [116].

$$CO_2 \rightarrow CO_2^{''-} \rightarrow HCO_2^{''} \rightarrow HCO_2H \rightarrow H_3CO_2^{''} \rightarrow HCOOH + H_2O \rightarrow H_2CO^{-}$$
$$\rightarrow H_3CO^{''} \rightarrow CH_3OH \rightarrow CH_3^{''} + H_2O \rightarrow CH_4$$
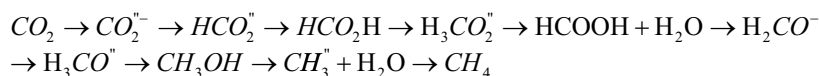
Apart from C1 hydrocarbon and alcohol formation of different products like formate and methyl formate, formaldehyde was explained by glyoxal pathway proposed by Shkrob et al. [117]. In this pathway, initially formaldehyde intermediate is formed, which gets converted to glyoxal intermediate and then to final products.

4.4 Catalyst Modifications in CO₂ Reduction

The photoreduction of CO_2 takes place via photoexcitation of electrons under light illumination. At a larger band gap, the UV radiations would be able to excite the electrons. The sunlight contains approximately 40% radiations in the visible light range. Therefore, to enhance the photoresponse range, several techniques have been

adopted. Metal and non-metal doping, sensitization, and coupling semiconductors are few commonly known strategies. Each method has its advantage and disadvantage, and the adopted process can vary depending on application and conditions.

4.4.1   Metal and Non-metal Doping

Doping is the intentional introduction of the metal or non-metal in semiconductor lattice for tuning the optical and electrical properties. In the case of doping in crystalline structures, less amount of species is introduced in the crystal lattice. Norskov et al. [118] found that upon doping, introduction of new d states near the Fermi level can take place. Due to the new state, there is variation in electrical and optical properties, which affects the activity and light absorption. Koci et al. [119] found silver doping on TiO_2 for range of 1–7% and found the shift in the absorption band edge of TiO_2 from 2.98 to 2.74 eV for 7%Ag-TiO_2. The product yield has increased with increased doping content due to the formation of a Schottky barrier at the contact region of the metal and semiconductor, which prevents charge recombination, thereby enhancing the activity. Nogueira et al. [120] found that methanol formation was enhanced due to Nb doping via not modified sputtering technique compared to that modified by sputtering primarily due to metallic Nb particles promoting the transportation of electrons. Li et al. [121] studied the effect of various metal dopant for varied loading amount and found that methane formation is maximum for 0.2 wt% loading of Pt compared to Ag and Au. In the same study, N doping were found to enhance visible light absorption. The optical properties and synergism with noble metal determined the overall catalytic performance. From metal and non-metal doping, the restructuring of the band structure happens which alters the reactivity trends.

4.4.2   Semiconductor Coupling Via *z*-Scheme or Heterojunction formation

To enhance the activity of semiconductor photocatalyst, coupling with another semiconductor of an appropriate valance band potential is a promising strategy. The coupling of two semiconductors can be of two types, either a type II heterojunction contact formation takes place, or they could form a *z*-scheme-type of arrangement. Contact type depends on the relative positions of band edges, Fermi level, and work functions of parental semiconductors. When *z*-scheme type arrangement is formed, it tends to promote spatial charge separations and utilize the benefits of two-component semiconductors [122]. Yu et al. [123] found the binary system of ZnO-C_3N_4 enhanced the selective methanol formation by 2.5 times due to the extended light absorption range because of direct *z*-scheme construction. Tahir et al. [124] found that the combination of ZnV_2O_6/C_3N_4 gives better selectivity for methanol formation due to 2D–2D nanosheets heterojunction with faster charge separation. Several other combinations for coupling are possible, which can enhance the activity. However, the activity depends on environmental and operating conditions;

therefore, to qualitatively select a catalyst uniform scale to quantify, the activity is required.

Efficiency Measurement

The photocatalytic reaction rate can be measured as product yield expressed in $\mu molg^{-1}h^{-1}$ or pm $g^{-1}h^{-1}$. Another factor that controls the efficiency of product formation is incident photon rate which is dependent on light intensity, irradiation area, and time, which can be measured by quantum efficiency [125].

$$\text{Overall quantum efficiency}(\%) = \frac{\text{Number of reacted electrons}}{\text{Number of absorbed photons}} * 100$$

The apparent quantum yield is expressed in terms of ratio of the reacted photons to the incident photons.

$$\text{Apparent quantum efficiency}(\%) = \frac{\text{Number of reacted electrons}}{\text{Number of incident photons}} * 100$$

$$\text{Apparent quantum efficiency of } CO(\%)$$
$$= \frac{2 * \text{Number of } CO \text{ molecules formed}}{\text{Number of incident photons}} * 100$$

$$\text{Apparent quantum efficiency of } HCOOH(\%)$$
$$= \frac{2 * \text{Number of } HCOOH \text{ molecules formed}}{\text{Number of incident photons}} * 100$$

$$\text{Apparent quantum efficiency of } HCHO(\%)$$
$$= \frac{6 * \text{Number of } HCHO \text{ molecules formed}}{\text{Number of incident photons}} * 100$$

$$\text{Apparent quantum efficiency of } CH_3OH(\%)$$
$$= \frac{2 * \text{Number of } CH_3OH \text{ molecules formed}}{\text{Number of incident photons}} * 100$$

$$\text{Apparent quantum efficiency of } CH_4(\%)$$
$$= \frac{2 * \text{Number of } CH_4 \text{ molecules formed}}{\text{Number of incident photons}} * 100$$

Turnover number (TON) is another quantification parameter for measuring the performance of CO_2 reduction, expressed as:

$$TOF = \frac{Number\ of\ molecules\ reacted}{Number\ of\ active\ sites(Unit\ time)}$$

TCEN, i.e., total consumed electron number, per unit time and per unit photocatalyst mass can also be used for estimating the efficiency of CO_2 reduction. It is given as a function of product amount and the incident photon number [126] given by following relation:

$$TCEN = \frac{\sum\left(C_{product} * n_{electrons}\right)V_{reactor}}{m_{cat} * t_{irr}}$$

where $V_{reactor}$ denotes reactor volume, t_{irr} is time of irradiation, m_{cat} is mass of catalyst, $C_{product}$ is product concentration, and $n_{electrons}$ is electrons number for conversion to product. The efficiency of process is dependent on incident photons, which is governed by light distribution inside the reactor. Therefore, reactor system considered is an important factor which governs the efficiency.

4.5   Reactor Systems for Photocatalytic CO_2 Reduction

The photocatalytic reactor design influences performance due to variation in geometrical configuration, light source, and degree of mixing. The critical parameters for the type of photoreactor are phases involved. In two-phase systems, the phases can be either gas-catalyst or liquid-catalyst. In three phase system, catalysts are in solid phase, while reactants and products are in liquid or gaseous phases depending on mode of operation (batch, semi-batch, or continuous). Catalyst distribution/loading is another criterion to group photoreactor system into two categories: fluidized and slurry bed photoreactors and fixed bed photoreactor [127]. Briefly, some commonly used photoreactor systems are discussed below.

4.5.1   Fluidized and Slurry Bed Reactors

Solid catalyst powder is dispersed in a liquid medium with CO_2 in the gas phase. Reductants in these reactor configurations can be $H_2O(l)$ and $H_2(g)$. The advantages of the slurry photoreactors are:

- The particles suspension is over the entire volume; hence, they can offer high surface area.
- Heat and mass transfer rates increase considerably due to the high mixing of solid particles in the fluid.
- Initial investment is low, and the construction is simple to design a reactor at large scale.

The operation mode of the photoreactor can be either batch or continuous. CO_2 bubbling takes place initially, and then the reactor is sealed for carrying out the reaction by irradiating the lamp. On the other hand, continued injection of CO_2 is required into the irradiated reactor for the continuous photoreactor's configuration. The liquid products (e.g., CH_3OH, $HCOOH$) and gaseous products (e.g., CH_4, CO, H_2) are collected continuously in specific time intervals for analyzing quantitatively and qualitatively by chromatographic or titration techniques. The limitations of the slurry photoreactors in either configurations are:

- After reaction, it is challenging to separate the catalyst from the reaction mixture.
- As the reaction proceeds in the liquid medium suspended with catalyst, due to the light scattering and absorption, there is a decrement in light utilization efficiency.

4.5.2 Fixed Bed Photoreactors

Fixed bed reactor configuration came into the picture to overcome product separation limitations in the slurry reactor system. In this system, the catalysts are usually set up over fixed support, say beads, monoliths, etc. The photocatalyst can be coated on support or kept directly over the photoreactor wall. The advantages of fixed over slurry reactors are [127]:

- As the catalysts are immobilized on a fixed support, the process can be operated continuously avoiding the cost of catalyst separation.
- The reaction completes faster in the fixed bed photoreactor system. Larger grain size catalysts can be utilized, providing the advantage of better external mass transfer and lower pressure drop.
- Higher surface volume ratio and lesser pressure drop enable achieving a higher flow rate, which leads to more straightforward modification.
- Flow regime relatively closer to plug flow can be obtained leading to higher conversion rate per unit mass of catalyst.
- Photons in this system configuration directly reach the exposed catalyst surface avoiding any light scattering or absorption.

The downsides of fixed bed reactors are:

- The problem of the temperature gradient between gas and solid surface arises.
- Maximum usage of optical fixed bed reactors is difficult to achieve.
- Due to the heat buildup, it can lead to deactivating the catalyst rapidly.

However, both the reactor systems have their advantage, and the choice of the system configuration depends on the product requirement and application.

4.6 Challenges Associated with Carbon Dioxide Reduction

The generation of charge carriers limits CO_2 photoreduction process. It is a reversible process and is accompanied by bulk or surface recombination of electrons and holes to generate heat energy, thereby decreasing the efficiency of the conversion process. Even if the reduction process is feasible, the conversion of CO_2 to $CO_2^{\bullet -}$ requires higher energy due to its more reduction potential and therefore becomes the rate-controlling step in most of the proposed pathways for CO_2 reduction. Controlling the selectivity of the final product is an essential factor due to several possible products, and re-oxidation of the formed products is also a crucial parameter. The quantum efficiency depends on irradiations and reactor design. Designing a reactor to uniformly distribute the catalyst and illuminate the larger area for high activity also plays a crucial role. Separation of formed products is also a critical factor that would govern the scale-up of the process.

5 DME: A Valuable Methanol Derivative

Synthetic fuels from non-conventional and renewable resources are going to replace the lion-share petroleum-derived fuels in the transportation sector. Steady energy supply from various energy sources and shifts to renewable energies are required to sustain the activities of mankind. Along with bioethanol and biodiesel, dimethyl ether (an important derivative of methanol) is also gaining importance as an alternative synthetic fuel. DME can be used as a cleaner highly efficient fuel with reduced SO*x*, NO*x*, and particulate matter. It does not possess any large toxicity issues and can be proficiently reformed to H_2 at lower temperatures. DME can be produced from natural gas, coal, biomass, and also from heavy oil. Currently, almost all DME is produced through dehydration of methanol with well-established infrastructure for production.

There are two methods under development: the two-step process (indirect method) of adding a dehydration step to the latter part on industrial methanol processing and the one-step (direct method) of synthesizing DME directly from syngas (mixture of H_2 and CO). Methanol dehydration reaction occurs over solid acid catalysts such as γ-alumina, zeolites, and aluminum silicates. For direct synthesis of DME from syngas, catalysts with two active centers, one for methanol synthesis and one for methanol dehydration, are required. The direct method of DME synthesis from syngas is considered to be more feasible as compared to the indirect process. The main reasons are as follows:

- Thermodynamic thresholds associated with CO conversion to methanol could be surmounted by the synergistic effect between methanol synthesis and its dehydration catalyst components.

- As methanol is formed in situ and converts to DME within the same reactor, methanol purification can be eliminated which increases the cost-effectiveness of the process.

The zeolite-based catalysts are preferred over other solid acid catalysts, due to stability and easy tuning of acidic sites. The combination of various methanol synthesis components like $Cu/ZnO/Al_2O_3$, $Cu/ZnO/ZrO_2$, and $Cu/ZnO/Ga_2O_3$ with zeolites is reported in literature for single-step DME synthesis. The water produced using DME synthesis deactivates conventional $Cu/ZnO/Al_2O_3$ catalyst. Thus, Zr-modified $Cu/ZnO/Al_2O_3$ hybridized with HZSM 5; DME yield of 18.3% was obtained at 220 °C and 27.6 bar [128]. Frusteri et al. [129] reported Cu-Zn-Zr/FER catalyst prepared by gel oxalate coprecipitation of Cu/Zn/Zr precursors in FER slurry. The CO_2 conversion of 26% with 55.7% DME selectivity was observed at 260 °C and 50 bar. The specific features of zeolites alter surface chemistry of the Cu-Zn-Zr catalyst. In addition, the acidity of the Cu-Zn-Zr/zeolites is also altered [130]. Temvuttirjon et al. [131] reported Cu-Zn-Zr catalyst admixed with solid SO_4^{2-}-ZrO_2 catalyst. The solid SO_4^{2-}-ZrO_2 was synthesized by impregnation of ZrO_2 with H_2SO_4. The sulfur loading influences the physicochemical properties of sulfated ZrO_2 catalyst and DME synthesis. At monolayer coverage of S (3.63 wt%), the DME yield was highest (4.54% at 260 °C and 20 bar).

Parallel to the process development, catalytic design of DME synthesis catalysts remains important. Special aspects are the improvement of activity, selectivity, and resistance to sintering and deactivation. Most recent research deals with exclusively copper-based catalysts.

The focus will be on the detailed study of the physicochemical foundations of direct DME synthesis from syngas, resulting in the development of the appropriate catalyst and process technology. Development of the rigorous catalytic system which can work at lower pressures and temperatures (lower than that of the current industrial processes) is aimed in near future.

6 Conclusions and Future Trends

Despite several amendments in the catalytic technologies for conversion of carbon oxides, there is still a scope for improvement. More research in process system engineering in particular for heat integration is the main avenue towards overcoming the economic limitation. Since the main drawback of the methanol synthesis process is the thermodynamic limitation, the use of membrane reactors finds a potential to separate the reaction products, thereby shifting the equilibrium in the forward direction and increasing the conversion. The future research should focus on scaling up these membrane reactors so that they can be applied industrially. From catalyst point of view, the major shortcomings are the early deactivation, formation of water, easy metal sintering, hot spot formation, etc. which results in the degraded efficiency of the process. Use of reproducible water permeable membranes seems to

be an effective solution to remove the produced water from the system. This will help in protecting the active metal from the water corrosive environment and increasing shelf life of the catalyst. On the other hand, structured catalyst motifs (like honeycomb monoliths) are the new class of catalysts identified by some of the researchers which may facilitate the solutions to the catalyst-related problems encountered during the methanol synthesis process.

As far as photocatalysis is considered, use of solar energy for carbon oxide conversion appears to be economically promising route. However, poor product selectivity and low conversion efficiency are the major challenges associated with this phenomenon. New photocatalytic materials with high quantum yields and innovation in the reactor design and configuration are the need of the hour.

Carbon oxide conversion is presenting challenges as well as opportunities to the research community worldwide for protecting the energy and environment. A lot of measures can be expected in near future to achieve stable economic process, efficient catalytic systems, and simple innovative reactor designs which will prove to be fruitful in enhancing the CO/CO_2 utilization via greener means.

References

1. World oil.com/news/2019/11/13ieaprediction
2. Kumar R, Kumar K, Pant KK, Choudary NV (2020) "Tuning the metal-support interaction of methane tri-reforming catalysts for industrial flue gas utilization"Int J Hydrogen Energy 45(3):1911–1929
3. Tiewsoh LS, Sivek M, Jirásek J (2017) "Traditional energy resources in India (coal, crude oil, natural gas): A review" Energy Sour B Econ Plann Policy 12(2):110–118
4. Sonal EA, Upadhyayula S, Pant KK (2019) "Biomass-derived CO_2 rich syngas conversion to higher hydrocarbon via fischer-tropsch process over Fe-Co bimetallic catalyst" Int J Hydrogen Energy 44(51):27741–27748
5. Das SK, Mohanty P, Majhi S, Pant KK (2013) "CO-hydrogenation over silica supported iron based catalysts: Influence of potassium loading"Appl Energy 111:267–276
6. Sonal, Pant KK, Upadhyayula S (2020) "An insight into the promotional effect on Fe-Co bimetallic catalyst in the fischer tropsch reaction: A drifts study" Fuel 276:118044–118068
7. Kumar R, Pant KK (2020) "Promotional effects of Cu and Zn in hydrotalcite-derived methane tri-reforming catalyst"Appl Surf Sci 515:146010–146022
8. Olah GA, Goeppert A, Prakash GKS (2006) "Beyond oil and gas: the methanol economy" Wiley-VCH, Weinheim
9. Ganesh I (2014) "Conversion of carbon dioxide into methanol – a potential liquid fuel: Fundamental challenges and opportunities (a review)" Renew Sustain Energy Rev 31:221–257
10. Bozzano G, Manenti F (2016) "Efficient methanol synthesis: Perspectives, technologies and optimization strategies" Prog Energy Combust Sci 56:71–105
11. Sebatiar P (2016) "How I have been led to the direct hydrogenation method by metallic catalysts 1926" Ind Eng Chem 18(10):1005–1008
12. Tijm PJA, Waller FJ, Brown DM (2001) "Methanol technology developments for the new millennium" Appl Catal A Gen 221(1–2):275–282
13. Khadzhiev SN, Kolesnichenko NV, Ezhova NN (2016) "Slurry technology in methanol synthesis" Pet Chem 56(2):77–95
14. Alwin M, Mathias P (1926) "Synthetic manufacture of ethanol", US1569775

15. Alwin M, Mathias P, Karl W (1925) "Production of oxygenated organic compounds", US1558559
16. Goeppert A, Czaun M, Jones JP, Surya Prakash GK, Olah GA (2014) "Recycling of carbon dioxide to methanol and derived products – closing the loop" Chem Soc Rev 43:7995–8048
17. Natta G (1953) P.H. Emmet (Ed.) Catalysis,Vol. III . Reinhold Publishing, New York
18. Basile A, Dalena F (2017) "Methanol production and applications: An overview" Methanol: science and engineering. Elsevier, Amsterdam
19. Olah GA (2013) "Towards oil independence through renewable methanol chemistry" Angew Chem Int Ed 52:104–107
20. Asthana S, Samanta C, Bhaumik A, Banerjee B, Voolapalli RK, Saha B (2016) "Direct synthesis of dimethyl ether from syngas over Cu-based catalysts: Enhanced selectivity in the presence of MgO"J Catal 334:89–101
21. Zhen X, Wang Y (2015) "An overview of methanol as an internal combustion engine fuel" Renew Sustain Energy Rev 52:477–493
22. Li K, Chen JG (2019) "CO_2 hydrogenation to methanol over ZrO_2-containing catalysts: Insights into ZrO_2 induced synergy" ACS Catal 9(9):7840–7861
23. Lee S (1989) "Methanol synthesis technology" CRC press, Boca Raton
24. Graaf GH, Sijtsema PJJM, Stamhuis EJ, Joosten GEH (1986) "Chemical equilibria in methanol synthesis" Chem Eng Sci 41:2883–2890
25. Skrzypek J, Lachowska M, Serafin D (1990) "Methanol synthesis from CO_2 and H_2: dependence of equilibrium conversions and exit equilibrium concentrations of components on the main process variables" Chem Eng Sci 45:89–96
26. Chang T, Rousseau RW, Kilpatrick PK (1986) "Methanol synthesis reactions: calculations of equilibrium conversions using equations of state" Ind Eng Chem Process Des Dev 25:477–481
27. Van Bennekom JG, Winkelman JGM, Venderbosch RH, Nieland SDGB, Heeres HJ (2012) "Modeling and experimental studies on phase and chemical equilibria in high-pressure methanol synthesis" Ind Eng Chem Res 51:12233–12243
28. Van Bennekom JG, Venderbosch RH, Winkelman JGM, Wilbers E, Assink D, Lemmens KPJ, Heeres HJ (2013) "Methanol synthesis beyond chemical equilibrium" Chem Eng Sci 87:204–208
29. Shen JW, Jun WK, Choi SH, Lee WK (2000) "Thermodynamic investigation of methanol and dimethyl ether synthesis from CO_2 hydrogenation" Korean J Chem Eng 17:210–216
30. Aguayo TA (2007) "Kinetic modeling of dimethyl ether synthesis in a single step on a CuO−ZnO−Al_2O_3/γ-Al_2O_3 catalyst" Ind Eng Chem Res 46:5522–5530
31. Qin Z, Su T, Ji H, Chen J (2015) "Experimental and theoretical study of the intrinsic kinetics for dimethyl ether synthesis from CO_2 over Cu–Fe–Zr/HZSM-5" AICHE J 61:857–866
32. Bowker M (2019) "Methanol Synthesis from CO_2 hydrogenation" ChemCatChem 11:4238–4246
33. Palma V, Meloni E, Ruocco C, Martino M, Ricca A (2017) " Chapter 2 " State of the art of conventional reactors for methanol production" Methanol: science and engineering. Elsevier, Amsterdam
34. Spath PL, Dayton DC (2003) "Preliminary screening – technical and economic assessment of synthesis gas to fuels and chemicals with emphasis on the potential for biomass-derived syngas" NREL is a US department of energy laboratory
35. Grabow LC, Mavrikakis M (2011) "Mechanism of methanol synthesis on Cu through CO_2 and CO hydrogenation" ACS Catal 1:365–384
36. Liu G, Willcox D, Garland M, Kung HH (1985) "The role of CO_2 in methanol synthesis on CuZn oxide: An isotope labeling study" J Catal 96:251–260
37. Yang Y, Mims CA, Mei DH, Peden CHF, Campbell CT (2013) "Mechanistic studies of methanol synthesis over Cu from CO/CO_2/H_2/H_2O mixtures: The source of C in methanol and the role of water" J Catal 298:10–17

38. Studt F, Behrens M, Kunkes EL, Thomas N, Zander S, Tarasov A, Schumann J, Frei E, Varley JB, Abild-Pedersen F, Nørskov JK, Schlögl R (2015) "The Mechanism of CO and CO_2 hydrogenation to methanol over Cu-based catalysts" ChemCatChem 7(7):1105–1111
39. Kandemir T, Friedrich M, Parker SF, Studt F, Lennon D, Schlogl R, Behrens M (2016) "Different routes to methanol: inelastic neutron scattering spectroscopy of adsorbates on supported copper catalysts" Phys Chem Chem Phys 18:17253–17258
40. Waugh KC (1992) "Methanol synthesis" Catal Today 15(1):51–75
41. Frenzel J, Marx D (2014) "Methanol synthesis on $ZnO(000\bar{1})$. IV. reaction mechanisms and electronic structure" J Chem Phys 141:124710
42. Behrens M, Studt F, Kasatkin I, Kühl S, Hävecker M, Abild-pedersen F, Zander S, Girgsdies F, Kurr P, Kniep B, Tovar M, Fischer RW, Nørskov JK, Schlögl R (2012) "The active site of methanol synthesis over $Cu/ZnO/Al_2O_3$ industrial catalysts" Science 759:893–897
43. Klier K (1982) "Methanol synthesis" Adv Catal 31:243–313
44. Chinchen GC, Denny PJ, Parker DG, Spencer MS, Whan DA (1987) "Mechanism of methanol synthesis from $CO_2/CO/H_2$ mixtures over copper/zinc oxide/alumina catalysts: Use of ^{14}C-labelled reactants" Appl Catal 30(2):333–338
45. Liu YM, Liu JT, Liu SZ, Li J, Gao ZH, Zuo ZJ, Huang W (2017) "Reaction mechanisms of methanol synthesis from CO/CO_2 hydrogenation on Cu_2O (111): Comparison with Cu (111)" J CO_2 Util 20:59–65
46. Kunkes EL, Studt F, Abild-pedersen F, Schlögl R, Behrens M (2015) "Hydrogenation of CO_2 to methanol and CO on $Cu/ZnO/Al_2O_3$: Is there a common intermediate or not?" J Catal 328:43–48
47. Taylor PA, Rasmussen PB, Chorkendorff IJ (1995) "Is the observed hydrogenation of formate the rate-limiting step in methanol synthesis?" J Chem Soc Faraday Trans 91:1267–1269
48. Yatsu T, Nishimura H, Fujitani T, Nakamura J (2000) "Synthesis and decomposition of formate on a Cu/SiO_2 catalyst: Comparison to Cu (111)" J Catal 191(2):423–429
49. Kattel S, Chen JG, Liu P (2017) "Active sites for CO_2 hydrogenation to methanol on Cu/ZnO catalysts" Science 355:1296–1299
50. Edwards JF (1984) "In situ characterization of adsorbed species on methanol synthesis catalysts by FT-IR spectroscopy" Ph.D. thesis, Iowa State University, Ames
51. Fujitani T, Choi Y, Sano M, Kushida Y, Nakamura J (2000) "Scanning tunneling microscopy study of formate species synthesized from CO_2 hydrogenation and prepared by adsorption of formic acid over Cu (111)" J Phys Chem B 104(6):1235–1240
52. Fujitani T, Nakamura I, Ueno S, Uchijima T, Nakamura J (1997) "Methanol synthesis by hydrogenation of CO_2 over a Zn-deposited Cu (111): formate intermediate" Appl Surf Sci 121-122:583–586
53. Millar GJ, Rochester CH, Howe C, Waugh KC (1992) "Vapour liquid equilibria of the lennard-jones fluid from the NpT plus test particle method" Mol Phys 76(4):833–849
54. Nakano H, Nakamura I, Fujitani T, Nakamura J (2001) "Structure-dependent kinetics for synthesis and decomposition of formate species over Cu (111) and Cu (110) model catalysts" J Phys Chem B 105(7):1355–1365
55. Nishimura H, Yatsu T, Fujitani T, Uchijima T, Nakamura JJ (2000) "Synthesis and decomposition of formate on a Cu (111) surface- kinetic analysis" J Mol Catal A Chem 155(1–2):3–11
56. Taylor PA, Rasmussen PB, Ovesen CV, Stoltze P, Chorkendorff I (1992) "Formate synthesis on Cu (100)" Surf Sci 261(1–3):191–206
57. Youngs TGA, Haq S, Bowker M (2008) "Formic acid adsorption and oxidation on Cu (110)" Surf Sci 602(10):1775–1782
58. Sotiropoulos A, Milligan PK, Cowie BCC, Kadodwala M (2000) "A structural study of formate on Cu (111)" Surf Sci 444:52–60
59. Ying DHS, Madix RJ (1980) "Thermal desorption study of formic acid decomposition on a clean Cu (110) Surface" J Catal 61(1):48–56

60. Gao HW, Yan TX, Zhang CB, He HJ (2008) "Theoretical and experimental analysis on vibrational spectra of formate species adsorbed on Cu–Al$_2$O$_3$ catalyst" J Mol Struct THEOCHEM 857(1–3):38–43

61. Campbell CT, Daube KA (1987) "A surface science investigation of the water-gas shift reaction on Cu (111)" J Catal 104(1):109–119

62. Zhao Y, Yang Y, Mims C, Peden CHF, Li J, Mei D (2011) "Insight into methanol synthesis from CO$_2$ hydrogenation on Cu (1 1 1): complex reaction network and the effects of H$_2$O" J Catal 281:199–211

63. Van Herwijnen T, Guczalski RT, Jong WAD (1980) "Kinetics and mechanism of the CO shift on Cu/ZnO II. kinetics of the decomposition of formic Acid" J Catal 63(1):94–101

64. Van Herwijnen T, Jong WAD (1980) "Kinetics and mechanism of the CO shift on Cu/ZnO I. kinetics of the forward and reverse CO shift reactions" J Catal 63:83–93

65. Grabow LC, Gokhale AA, Evans ST, Dumesic JA, Mavrikakis M (2008) "Mechanism of the water gas shift reaction on Pt: first principles, experiments, and microkinetic modeling" J Phys Chem C 112(12):4608–4617

66. Gokhale AA, Dumesic JA, Mavrikakis M (2008) "On the mechanism of low-temperature water gas shift reaction on copper" J Am Chem Soc 130(4):1402–1414

67. MartI L, Siemer N, Frenzel J, Marx D (2015) "Reaction network of methanol synthesis over Cu/ZnO nanocatalysts" ACS Catal 5(7):4201–4218

68. Suh YW, Moon SH, Rhee HK (2000) "Active sites in Cu/ZnO/ZrO$_2$ catalysts for methanol synthesis from CO/H$_2$" Catal Today 63(2–4):447–452

69. Fujitani T, Nakamura J (2000) "The chemical modification seen in the Cu/ZnO methanol synthesis catalysts" Appl Catal A Gen 191(1–2):111–129

70. Szanyi J, Goodman DW (1991) "Methanol synthesis on a Cu (100) catalyst" Catal Lett 10:383–390

71. Chinchen GC, Waugh KC, Whan DA (1986) "The activity and state of the copper surface in methanol synthesis catalysts" Appl Catal 25:101–107

72. Rasmussen PB, Kazuta M, Chorkendorff I (1994) "Synthesis of methanol from a mixture of H$_2$ and CO$_2$ on Cu (100)" Surf Sci 318(3):267–280

73. Rasmussen PB, Holmblad PM, Askgaard T, Ovesen CV, Stoltze P, Nørskov JK, Chorkendorff I (1994) "Methanol synthesis on Cu (100) from a binary gas mixture of CO$_2$ and H$_2$" Catal Lett 26:373–381

74. Yoshihara J, Campbell CT (1996) "Methanol synthesis and reverse water–gas shift kinetics over Cu (110) model catalysts: structural sensitivity" J Catal 161(2):776–782

75. Yoshihara J, Parker SC, Schafer A, Campbell CT (1995) "Methanol synthesis and reverse water-gas shift kinetics over clean polycrystalline copper" Catal Lett 31:313–324

76. Chen HY, Lau SP, Chen L, Lin J, Huan CHA, Tan KL, Pan JS (1999) "Synergism between Cu and Zn sites in Cu/Zn catalysts for methanol synthesis" Appl Surf Sci 152(3–4):193–199

77. Hansen PL, Wagner JB, Helveg S, Rostrup-Nielsen JR, Clausen BS, Topsøe H (2002) "Atom-resolved imaging of dynamic shape changes in supported copper nanocrystals" Science 295(5562):2053–2055

78. Ovesen CV, Clausen BS, Schiotz J, Stoltze P, Topsøe H, Nørskov JK (1997) "Kinetic implications of dynamical changes in catalyst morphology during methanol synthesis over Cu/ZnO catalysts" J Catal 168(2):133–142

79. Liu X, Lu GQ, Yan Z, Beltramini J (2003) "Recent advances in catalysts for methanol synthesis via hydrogenation of CO and CO$_2$" Ind Eng Chem Res 42(25):6518–6530

80. Twigg MV, Spencer MS (2001) "Deactivation of supported copper metal catalysts for hydrogenation reactions" Appl Catal A Gen 212(1–2):161–174

81. Jadhav SG, Vaidya PD, Bhanage BM, Joshi JB (2014) "Catalytic carbon dioxide hydrogenation to methanol: A review of recent studies" Chem Eng Res Des 92(11):2557–2567

82. Álvarez A, Bansode A, Urakawa A, Bavykina AV, Wezendonk TA, Makkee M, Gascon J, Kapteijn F (2017) "Challenges in the greener production of formates/formic acid, metha-

nol, and DME by heterogeneously catalyzed CO_2 hydrogenation processes" Chem Rev 117(14):9804–9838

83. Li MMJ, Tsang SCE (2018) "Bimetallic catalysts for green methanol production via CO_2 and renewable hydrogen: a mini-review and prospects" Cat Sci Technol 8:3450–3464

84. Ye J, Liu C, Mei D, Ge Q (2013) "Active oxygen vacancy site for methanol synthesis from CO_2 hydrogenation on In_2O_3(110): A DFT study" ACS Catal 3(6):1296–1306

85. Ye J, Liu C, Ge Q (2012) "DFT study of CO_2 adsorption and hydrogenation on the In_2O_3 surface" J Phys Chem C 116(14):7817–7825

86. Sun K, Fan Z, Ye J, Yan J, Ge Q, Li Y, He W, Yang W, Liu CJ (2015) "Hydrogenation of CO_2 to methanol over In_2O_3 catalyst" J CO_2 Util 12:1–6

87. Martin O, Martin AJ, Mondelli C, Mitchell S, Segawa TF, Hauert R, Drouilly C, Curulla-Ferré D, Pérez-Ramírez J (2016) "Indium oxide as a superior catalyst for methanol synthesis by CO_2 hydrogenation" Angew Chem Int Ed 55:6261–6265

88. Dou M, Zhang M, Chen Y, Yu Y (2018) "Theoretical study of methanol synthesis from CO_2 and CO hydrogenation on the surface of ZrO_2 supported In_2O_3 catalyst" Surf Sci 672-673:7–12

89. Akkharaphatthawon N, Chanlek N, Cheng CK, Chareonpanich M, limtrakul J, Witoon T (2019) "Tuning adsorption properties of $Ga_xIn_{2-x}O_3$ catalysts for enhancement of methanol synthesis activity from CO_2 hydrogenation at high reaction temperature" Appl Surf Sci 489(30):278–286

90. Chou CY, Lobo RF (2019) "Direct conversion of CO_2 into methanol over promoted indium oxide-based catalysts" Appl Catal A Gen 583:117144

91. Men YL, Liu Y, Wang Q, Luo Z, Shao S, Li Y, Pan Y (2019) "Highly dispersed Pt-based catalysts for selective CO_2 hydrogenation to methanol at atmospheric pressure" Chem Eng Sci 200:167–175

92. Ye J, Liu CJ, Mei D, Ge Q (2014) "Methanol synthesis from CO_2 hydrogenation over a Pd_4/In_2O_3 model catalyst: A combined DFT and kinetic study" J Catal 317:44–53

93. Ye J, Ge Q, Liu C (2015) "Effect of PdIn bimetallic particle formation on CO_2 reduction over the Pd–In/SiO_2 catalyst" Chem Eng Sci 135(2):193–201

94. Rungtaweevoranit B, Baek J, Araujo JR, Archanjo BS, Choi KM, Yaghi OM, Somorjai GA (2016) "Copper nanocrystals encapsulated in Zr-based metal organic frameworks for highly selective CO_2 hydrogenation to methanol" Nano Lett 16(12):7645–7649

95. Kobayashi H, Taylor JM, Mitsuka Y, Ogiwara N, Yamamoto T, Toriyama T, Matsumura S, Kitagawa H (2019) "Charge transfer dependence on CO_2 hydrogenation activity to methanol in Cu nanoparticles covered with metal–organic framework systems" Chem Sci 10(11):3289–3294

96. An B, Zhang J, Cheng K, Ji P, Wang C, Lin W (2017) "Confinement of ultrasmall Cu/ZnOx nanoparticles in metal organic frameworks for selective methanol synthesis from catalytic hydrogenation of CO_2" J Am Chem Soc 139(10):3834–3840

97. Kunkel C, Vin F (2016) "Transition metal carbides as novel materials for CO_2 capture, storage, and activation" Energ Environ Sci 9:141–144

98. Vidal AB, Feria L, Evans J, Takahashi Y, Liu P, Nakamura K, Illas F, Rodriguez JA (2012) "CO_2 activation and methanol synthesis on novel Au/TiC and Cu/TiC catalysts" J Phys Chem Lett 3(16):2275–2280

99. Rodriguez JA, Evans J, Feria L, Vidal AB, Liu P, Nakamura K (2013) "CO_2 hydrogenation on Au/TiC, Cu/TiC, and Ni/TiC catalysts: Production of CO, methanol, and methane" J Catal 307:162–169

100. Posada-Pérez S, Ramírez PJ, Gutiérrez RA, Stacchiola DJ, Viñes F, Liu P, Llas F, Rodriguez JA (2016) "The conversion of CO_2 to methanol on orthorhombic β-Mo_2C and Cu/β-Mo_2C catalysts: mechanism for admetal induced change in the selectivity and activity" Cat Sci Technol 6:6766–6777

101. Geng W, Han H, Liu F, Liu X, Xiao L, Wu W (2017) "N,P,S-codoped C@nano-Mo_2C as an efficient catalyst for high selective synthesis of methanol from CO_2 hydrogenation" J CO_2 Util 21:64–71

102. Han H, Geng W, Xiao L, Wu W (2019) "Modeling and assessment of novel configurations to enhance methanol production in industrial mega-methanol synthesis plant" J Taiwan Inst Chem Eng 95:112–118

103. Struis RPWJ, Stucki S, Wiedorn M (1996) "A membrane reactor for methanol synthesis" J Membr Sci 113(1):93–110

104. Struis RPWJ, Stucki S (2001) "Verification of the membrane reactor concept for the methanol synthesis" Appl Catal A Gen 216(1–2):117–129

105. Barbieri G, Marigliano G, Golemme G, Drioli E (2002) "Simulation of CO_2 hydrogenation with CH_3OH removal in a zeolite membrane reactor" Chem Eng J 85(1):53–59

106. Gallucci F, Paturzo L, Basile A (2004) "An experimental study of CO_2 hydrogenation into methanol involving a zeolite membrane reactor" Chem Eng Process 43(8):1029–1036

107. Van Tran T, Le-Phuc N, Nguyen TH, Dang TT, Ngo PT, Nguyen DA (2018) "Application of NaA membrane reactor for methanol synthesis in CO_2 hydrogenation at low pressure" Int J Chem React Eng 16(4):1–7

108. Zebarjad FS, Hu S, Li Z, Tsotsis TT (2019) "Experimental investigation of the application of ionic liquids to methanol synthesis in membrane reactors" Ind Eng Chem Res 58(27):11811–11820

109. Rahimpour MR, Ghader S (2003) "Theoretical investigation of a Pd-membrane reactor for methanol synthesis" Chem Eng Technol 26(8):902–907

110. Rahimpour MR, Lotfinejad M (2007) "Enhancement of methanol production in a membrane dual-type reactor" Chem Eng Technol 30(8):1062–1076

111. Farsi M, Jahanmiri A (2011) "Methanol production in an optimized dual-membrane fixed-bed reactor" Chem Eng Process Process Intensif 50(11–12):1177–1185

112. Yaashikaa PR, Senthil Kumar P, Varjani SJ, Saravanan A (2019) "A review on photochemical, biochemical and electrochemical transformation of CO_2 into value-added products" J CO_2 Util 33:131–147

113. Chang X, Wang T, Gong J (2016) "Insights into CO_2 activation and reaction on surfaces of photocatalysts" Energ Environ Sci 9:2177–2196

114. Inoue T, Fujishima A, Konishi S, Honda K (1979) "Photoelectrocatalytic reduction of carbon dioxide in aqueous suspensions of semiconductor powders" Nature 277:637–638

115. Ma Y, Wang X, Jia Y, Chen X, Han H, Li C (2014) "Titanium dioxide-based nanomaterials for photocatalytic fuel generations" Chem Rev 114(19):9987–10043

116. Subrahmanyam M, Kaneco S, Alonso-Vante N (1999) "A screening for the photo reduction of carbon dioxide supported on metal oxide catalysts for C_1-C_3 selectivity" Appl Catal Environ 23(2–3):169–174

117. Dimitrijevic NM, Shkrob IA, Gosztola DJ, Rajh T (2012) "Dynamics of interfacial charge transfer to formic acid, formaldehyde, and methanol on the surface of TiO_2 nanoparticles and its role in methane production" J Phys Chem C 116(1):878–885

118. García-Mota M, Vojvodic A, Abild-Pedersen F, Nørskov JK (2013) "Electronic origin of the surface reactivity of transition-metal-doped TiO_2 (110)" J Phys Chem C 117(1):460–465

119. Kočí K, Matějů K, Obalová L, Krejčíková S, Lacný Z, Plachá D, Čapek L, Hospodková A, Šolcová O (2010) "Effect of Silver Doping on the TiO_2 for Photocatalytic Reduction of CO_2" Appl Catal Environ 96(3–4):239–244

120. Nogueira MV, Lustosa GMMM, Kobayakawa Y, Kogler W, Ruiz M, Monteiro Filho ES, Zaghete MA, Perazolli LA (2018) "Nb-doped TiO_2 photocatalysts used to reduction of CO_2 to methanol" Adv Mater Sci Eng 2018:1–8

121. Li X, Zhuang Z, Li v, Pan H (2012) "Photocatalytic reduction of CO_2 over noble metal-loaded and nitrogen-doped mesoporous TiO_2" Appl Catal A Gen 429–430:31–38

122. Xu Q, Zhang L, Yu J, Wageh S, Al-Ghamdi AA, Jaroniec M (2018) "Direct Z-Scheme photocatalysts: principles, synthesis, and applications" Mater Today 21(10):1042–1063

123. Yu W, Xu D, Peng T (2015) "Enhanced photocatalytic activity of G-C_3N_4 for selective CO_2 reduction to CH_3OH via facile coupling of ZnO: A direct Z-scheme mechanism" J Mater Chem A 3(39):19936–19947

124. Bafaqeer A, Tahir M, Amin NAS (2019) "Well-designed ZnV_2O_6/g-C_3N_4 2D/2D nanosheets heterojunction with faster charges separation via PCN as mediator towards enhanced photocatalytic reduction of CO_2 to fuels" Appl Catal Environ 242:312–326

125. Nahar S, Zain MFM, Kadhum AAH, Hasan HA, Hasan MR (2017) "Advances in photocatalytic CO_2 reduction with water: A review" Materials 10(6):626

126. Li K, Peng B, Peng T (2016) "Recent advances in heterogeneous photocatalytic CO_2 conversion to solar fuels" ACS Catal 6(11):7485–7527

127. Ola O, Maroto-valer MM (2015) "Review of material design and reactor engineering on TiO_2 photocatalysis for CO_2 reduction" J Photochem Photobiol C Photchem Rev 24:16–42

128. Ren S, Fan X, Shang Z, Shoemaker WR, Ma L, Wu T, Li S, Klinghoffer NB, Yu M, Xinhua L (2020) "Enhanced catalytic performance of Zr modified CuO-ZnO-Al_2O_3 catalyst for methanol and DME synthesis via CO_2 hydrogenation" J CO_2 Util 36:82–95

129. Frusteri F, Migliori M, Cannilla C, Frusteri L, Catizzone E, Aloise A, Giordano G, Bonura G (2017) "Direct CO_2-to-DME hydrogenation reaction: New evidences of a superior behaviour of FER-based hybrid systems to obtain high DME yield" J CO_2 Util 18:353–361

130. Bonura G, Cannilla C, Frusteri L, Catizzone E, Todaro S, Migliori M, Giordano G, Frusteri F (2019) "Methanol production in an optimized dual-membrane fixed-bed reactor" Catal Today 345:175–182

131. Temvuttirojn C, Chuasomboon N, Numpilai T, Faungnawakij K, Chareonpanich M, Limtrakul J, Witoon T (2019) "Development of $SO4^{2-}$–ZrO_2 acid catalysts admixed with a CuO-ZnO-ZrO_2 catalyst for CO_2 hydrogenation to dimethyl ether" Fuel 241:695–703

Efficient Homogeneous Catalysts for Conversion of CO₂ to Fine Chemicals

Rajendran Arunachalam, Eswaran Chinnaraja, and Palani S. Subramanian

Abstract Fossil fuel combustion is often considered as one of the major threats to the environment, because of the carbon dioxide (CO_2) release in the atmosphere. Such an accumulation of CO_2 in the atmosphere leads to drastic climate change in the environment. The control in the discharge of CO_2 into the atmosphere and the effective utilization of CO_2 are great global challenges behind us. The recent research works show there are reasonable technologies developed on the CO_2 capture, and utilization leaves us to relieve little. The recent progresses in the organometallic chemistry and catalysis afford the effective chemical transformation of CO_2 and its incorporation into synthetic organic molecules under mild reaction conditions. The catalytic conversion of CO_2 into small and beneficial molecules such as carbonates, methylamines, methanol, formic acid, etc., by molecular catalysts, is an interesting topic that has significantly developed in recent years. The aim of this chapter is to reveal the recent advancement in the CO_2 capture and its utilization in the synthesis of commodity chemicals. In addition, this also converses various homogenous metal complexes, catalyzed fine chemicals synthesis, and their challenges.

Keywords Carbon dioxide · Trapping technologies · Homogenous catalysis · Fine chemicals · Energy materials

1 Introduction

The CO_2 is the most essential gas molecule required for the survival of the living organism in the environment. The photosynthetic process which involves the conversion of CO_2 to glucose via the chlorophyll is the natural process. The CO_2 intake and oxygen release during photosynthesis deserve everlasting importance due to its connectivity on the survival of all living organism in the atmosphere. Due to modern civilization and industrialization, a huge volume of CO_2 is discharged into the

R. Arunachalam · E. Chinnaraja · P. S. Subramanian (✉)
Inorganic Materials and Catalysis Division, CSIR-Central Salt and Marine Chemicals Research Institute, Bhavnagar, Gujarat, India
e-mail: siva@csmcri.res.in

atmosphere and becomes a hazardous pollutant [1–4]. The CO_2 is an eco-friendly, stable, and renewable carbon resource; hence, it is considered as a very attractive feedstock for the synthesis of fine chemicals, fuels, materials, etc. Thus, the CO_2 is not only an eco-friendly feedstock, but it also replaces the phosgene and carbon monoxide in many industrial processes [5]. The usages of fossil fuels can be reduced when the fuels are derived from CO_2. Hence, the technology on the CO_2 capture from an industrial source, atmosphere, and utilization to make "fine and specialty chemicals" is highly essential [6]. The concept, development, and deployment of a green, high-efficiency and cost-effective CO_2 capture and conversion technology not only help the society to become cleaner, safer, and more sustainable but also offer the development of a more sustainable energy economy [7].

1.1 Carbon Dioxide Activation

The CO_2 molecules exist in the gaseous state at atmospheric temperature and pressure. It becomes solid which is well-known as dry ice at the temperature below -78.5 °C. In addition, the molecules can be liquified by compression and removing the heat which is known as supercritical CO_2 (scCO_2), at temperature (>31.1 °C) and pressure (>73.9 bar) [8]. The CO_2 is a bifunctional molecule with Lewis acidity at carbon and Lewis basicity at the oxygen atom. Overall, CO_2 is a weak electrophile [9].

CO$_2$ possesses the lowest free energy ($\Delta G_f^\circ = -396$ kJ/mol) among all carbon-containing binary neutral species, due to its fully oxidized state of carbon [10]. Hence, CO_2 requires high amount of energy for its activation and conversion to fine chemicals. Hence, the usage of energy-rich substrates such as hydrogen, unsaturated molecules, cyclic organic molecules, and organometallics is usually required to activate the CO_2 molecule. In some reactions, it is essential to remove the product or by-product in order to shift the equilibrium towards the selective product formation (Fig. 1) [11].

Since the carbon atom in CO_2 is electrophilic, it will be prone to interact with the nucleophile. Therefore, the CO_2 is activated upon interaction with Lewis base, e.g., the molecule containing hydroxyl group [12], DBU (1,8-diazabicyclo[5.4.0]undec-7-ene), NHC (N-heterocyclic carbene) [13], N-heterocyclic olefin, and so on [14]. In addition, the CO_2 can be activated using metal centers through its four different modes η^1-C, η^1-O, η^2-(C-O), and η^2(O,O) depicted in Fig. 1. All these four different modes for the interaction of CO_2 are well established [15]. The first well-characterized side-on metal–CO_2 complex $(PCy_3)_2Ni(CO_2)$[where Cy =cyclohexyl] is reported in the literature. Here the Ni coordinating to two phosphine ligands the CO_2 exists in planar environment. Here the Ni is coordinated in η^2-(C,O) fashion which is confirmed by crystallography [15].
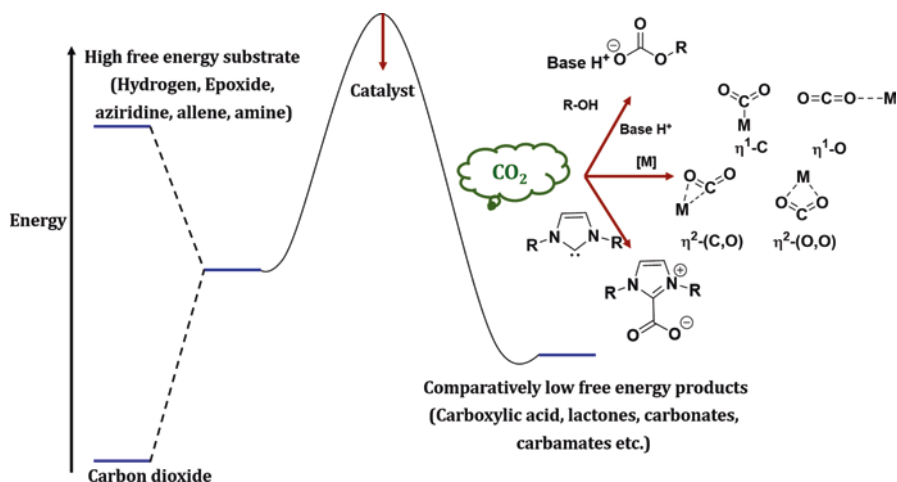
Fig. 1 Energy profile diagram and activation of carbon dioxide
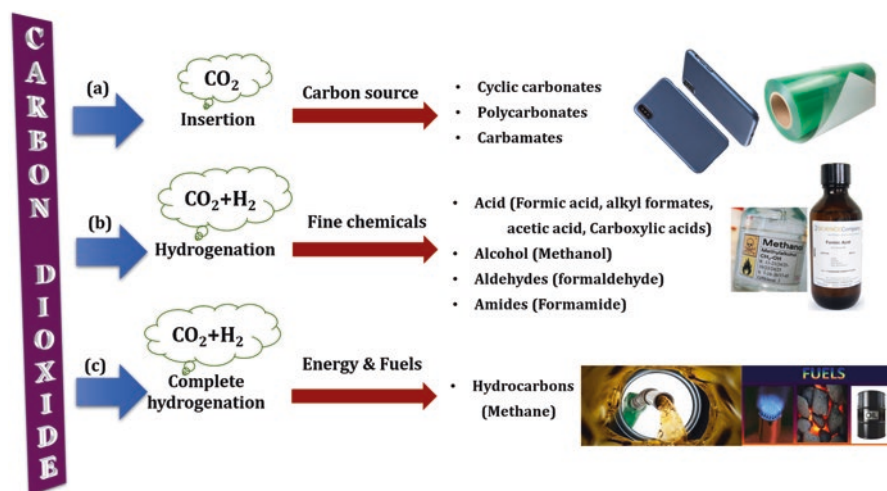
Fig. 2 (**a–c**) Fine chemicals and fuel synthesis from CO$_2$

1.2 Chemical Fixation of CO$_2$ to Value-Added Products

The catalytic reactions for CO$_2$ conversion [16] are broadly classified into three different categories (Fig. 2). In first, the CO$_2$ is incorporated (or fixation) into the substrates without breaking the molecule, i.e., the oxidation state at the carbon remains the same. The carbonates material or organic scaffolds are achieved in presence of suitable substrate (Fig. 2a). The polycarbonates are most extensively used as

plastic materials, solvents, and commercially important intermediates. The present annual production of polycarbonate production was around 2 million tons worldwide [17]. The second scenario is the partial hydrogenation of CO_2 by using the stoichiometric ratio of reactants especially CO_2 and H_2. The selective synthesis of formic acid, methanol, formaldehyde, amide derivatives, urea, salicylic acid, and so on can be achieved (Fig. 2b) [18]. The complete reduction of CO_2 using an excess of H_2 or other hydrogen sources produces hydrocarbons such as methane, light olefin, and so on using suitable catalysts (Fig. 2). The hydrogenation of CO_2 to liquid hydrocarbon is converted using the process of reverse water gas shift (RWGS) reaction and Fischer-Tropsch synthesis (FTS). This process is also known as "power-to-gas," i.e., the electrical energy achieved using CO_2, without the consumption of fossil fuels [19, 20].

The reactions of CO_2 with organic molecules such as amines or olefins, etc. are exothermic, which doesn't require high-energy input. This is because the CO_2 is encapsulated into the organic molecules without changing its oxidation state. The organic scaffolds like carboxylates, lactones, carbamates, urea derivatives, isocyanates, carbonates, etc. fall in this category [21]. The products obtained by reducing the CO_2 are the endothermic processes which require high energy (heat) due to breaking of CO_2. Hence, the synthesis of commercial chemicals like formic acid, oxalate, formaldehyde, carbon monoxide, methanol, dimethyl ether, methane, etc. requires high energy in combination with suitable catalysts (Fig. 3) [22].

To achieve the selective fine chemicals, fuels, and intermediate compounds (Fig. 3) from CO_2, various catalysts are explored, and some are involved in the commercial process [23]. The material catalysts such as metal oxides are extensively applied and reviewed. But the homogeneous catalyst which includes various metal complexes, organocatalysts, etc. are rarely explored for commercial purpose because of their non-cyclability and non-suitablity for continuous batch process [24, 25].

2   Carbon Dioxide Capture and Separation from Various Sources

CO_2 capture aims to remove selectively CO_2 from the mixture of air and industrial source and from other sources of emissions. This methodology involves the capture of CO_2 to produce huge volume, which can be compressed, transported, and used as carbon source [26, 27]. The CO_2 capture technology developed is based on the amount of CO_2 emits from the source, i.e., from the stationary point (e.g., the industrial source where huge amount of CO_2 is dumped into the atmosphere), and the second from the atmosphere, i.e., the ambient air which is having less concentration of CO_2 (Fig. 4). CO_2 capture from industries like coal power plants contains CO_2/N_2, the emission from natural gas wells contains the mixture of CO_2/CH_4, and the
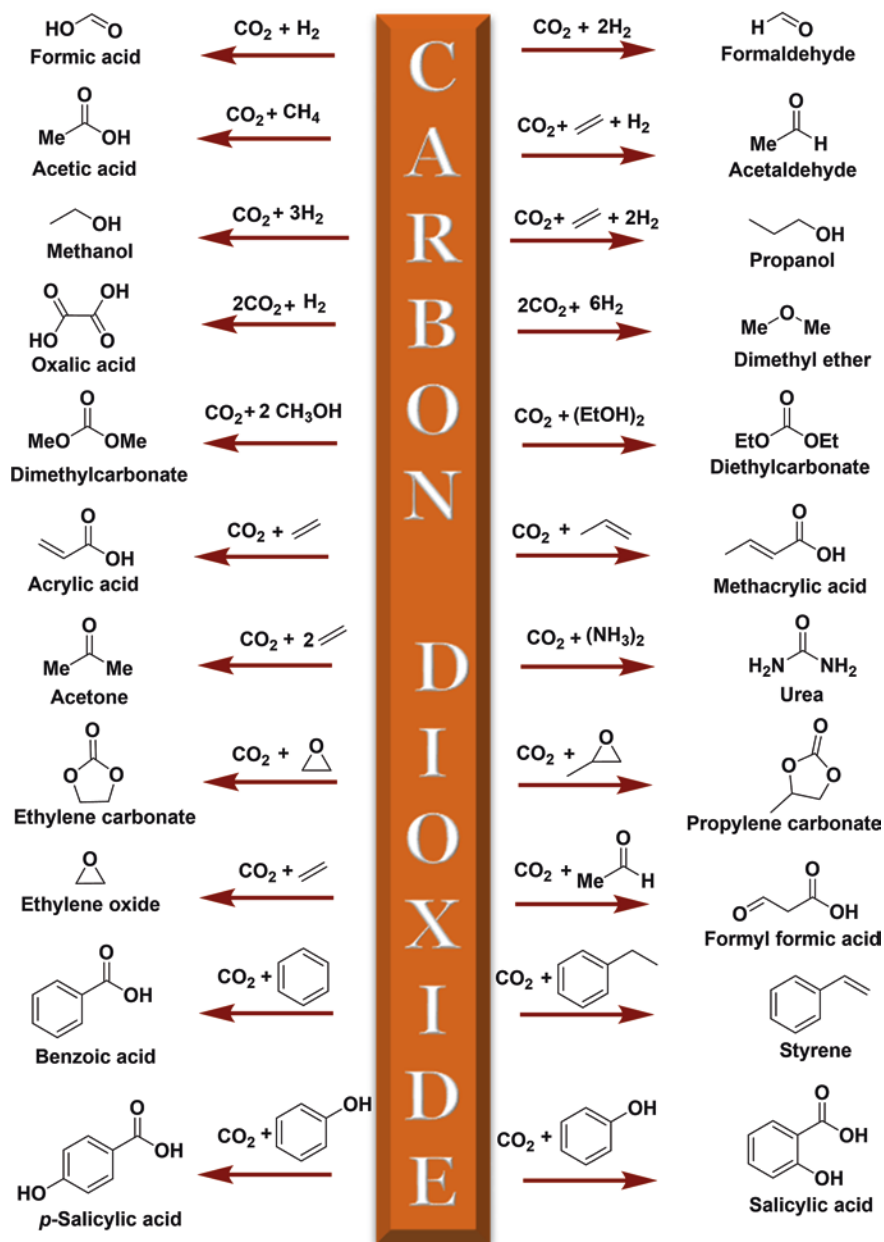
Fig. 3 List of fine chemicals obtained by catalytic fixation of carbon dioxide
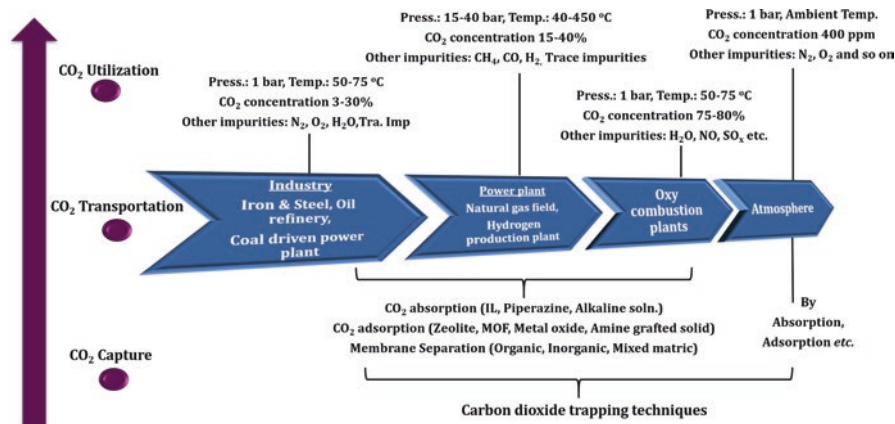
Fig. 4 CO₂ capture from various sources using efficient techniques

gasification plant's emission contains large amount of CO_2/H_2 gases. In addition to the mixture of gases from industrial emission, the CO_2 concentration in iron-steel industry plant contains 3–30%, the power plant emission contains 15–40% CO_2, whereas in the case of oxy-combustion plants, it exists with high concentration, i.e., 75–80% along with additional impurities (Fig. 4). Capturing the low ppm level of CO_2 from atmosphere still remains to have challenges. However, a significant success has been achieved in the case of stationary point sources [28].

In addition to the various sources of CO_2 emission, the selective capture of CO_2 from the atmosphere is still a challenge due to low concentration (400 ppm) at atmospheric temperature, when compared to the stationary point source from industry [29]. In general various absorbents, adsorbents, and membranes are used for CO_2 capture from a stationary source and atmosphere.

Pre-combustion capture refers to the removal of CO_2 before the complete combustion of fossil fuels. The post-combustion capture refers to capturing of CO_2 from the flue gas after complete combustion of the fossil fuels. The pre-combustion process emits a high concentration of CO_2 when compared to post-combustion. Hence, the suitable adsorbents with desired functionality for selective CO_2 capture are essential which should be stable at high temperature and pressure.

There are successful techniques employed for the CO_2 capture from various sources. However, the CO_2 capture materials are broadly classified into three types as follows: (1) the absorption of CO_2 using the amines, alkaline, ionic liquids, etc.; (2) the adsorption of CO_2 using porous solid material such as zeolite, MOF, and so on; and (3) the separation using membrane such as organic, inorganic, and matric membranes. Hence the materials for CO_2 capture needs to be efficient at specific pressure and temperature with excellent selectivity [29].

2.1 Chemical Absorption

The CO_2 is separated from the flue gas by passing through a continuous scrubbing system that contains an absorber and a desorber. The absorption processes utilize the reversible chemical reaction of CO_2 with an aqueous alkaline solvent, usually an amine [26]. In the desorber, the absorbed CO_2 is stripped, and a pure stream of CO_2 is sent for compression. The technique is suitable for post-combustion CO_2 capture, and this process was initially established in 1930 to capture the CO_2 from ammonia plant. They mostly used ammonia, aqueous amines, and alkali for CO_2 capture from flue gases [30].

The CO_2 absorption mostly occurs in an aqueous medium [26, 31]. Among the alkali, monoethanolamine (MEA) was mainly adopted for the removal of CO_2 from natural gas and hydrogen. In view of amine, the piperazine in aqueous solution exhibits better performance in the CO_2 capture. Moreover, the amount of CO_2 absorbed on piperazine is more than twice compared to MEA [32, 33]. There are three amine-based technologies (such as Fluor Econamine FG Plus^SM (EFG+) technology, KM-CDR, and the Kerr-McGee/AGG Lummus Crest (KMALC) technology) for the absorption of CO_2, under moderate working conditions. All these amines are efficient at ambient pressure for CO_2 capture [31, 34, 35]. In addition to organic amines, the aqueous ammonia can also be employed for chemisorption of CO_2 from flue gas and natural gas streams. This process relies upon a temperature swing to cycle between ammonium carbonate and ammonium bicarbonate. The major drawbacks include their low CO_2 adsorption capacity and the associated high cost as major challenges to commercialize. The drawbacks may be possible to overcome using the amine-grafted and amine-impregnated materials by enriching the amine or nitrogen groups [34, 35].

2.2 Chemical Adsorbents: Amine-Impregnated and Amine-Grafted Material

To enhance the adsorption capacity, the amines are generally loaded on solid material. Among the various amines tested, polyethyleneimine (PEI)-impregnated mesoporous silica, MCM-41, etc. are showing well adsorption capacity. A higher PEI loading significantly enhanced CO_2 adsorption capacity together with the decreases of surface area, pore size, and pore volume of the PEI-impregnated supports. The highest CO_2 adsorption capacity of 3.02 mmol/g was achieved for the PEI-impregnated MCM-41 (PEI/MCM-41) with 75 wt% of PEI loading [36].

Although high CO_2 adsorption capacity was observed in amine-impregnated materials, the lack of thermal stability in desorption needs to be overcome. The amine-impregnated materials are further improved as amine-grafted solids in which the amine is covalently impregnated to the intra-channel surface of mesoporous silica. There are various amine-functionalized silica materials used for the

Fig. 5 The structure of 3N APS amine grafted on SBA-15 for CO_2 adsorption
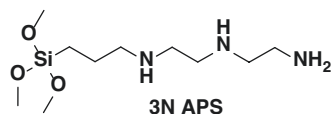
3N APS

post-combustion and capture of CO_2 from ambient air [37, 38]. Among the amine-grafted materials, the N-[(3-trimethoxysilyl)propyl]diethylene-triamine (3N-APS) grafted (Fig. 5) on SBA-15 exhibits a better adsorption capacity of 3.06 mmol/g.

2.3 Solid Adsorbents

Adsorbents are mainly classified into two types depending upon their interaction with the gaseous molecules: (1) physisorption and (2) chemisorption. The physical adsorption through physisorption involves the van der Waals interaction, whereas in the case of chemisorption, the covalent bonding type interaction mediates between the gas molecules. In the case of physical absorption, the ionic liquids (ILs) include a broad category of salts used to trap gaseous CO_2 and are stable even at high temperatures [39, 40] and pressure.

The solid sorbent materials can remove CO_2 selectively from gaseous streams by adsorbing on its solid surface. The CO_2 uptake capacity, selectivity, stability, and regenerability are few main adsorption properties of solid adsorbents [41]. The surface-adsorbed CO_2 can be regenerated through a vacuum swing system to liberate CO_2 at suitable temperature and pressure. The solid sorbent materials used for CO_2 capture include activated carbon, metal oxides, zeolites, alkaline, amine-enriched solids, lithium zirconates, MOFs, COFs, etc.

The CO_2 capture using physical adsorbent material on solid state deserves several advantages when compared to chemisorption materials. The activated carbon materials are abundant; the zeolite materials along with abundance possess high crystalline structure, high surface area, ability to alter their composition structure and ratio, etc. In addition, the mesoporous silica exhibits high volume, surface area and tunable pore size, and thermal and mechanical stability. The metal-organic frameworks (MOFs) exhibit advantages of very high surface area, adjustable pore spaces, pore surface properties, and exceptional adsorption capacity for CO_2 [42].

Similarly, the zeolites, a crystalline aluminosilicate, are known for their well-defined porous structures. The crystalline materials stack into regular arrays with the appropriate channels, making them potential for CO_2 capture. In general, the gaseous stream when pass through such porous materials needs to be cooled below 100 °C. The main drawback of using such zeolites is its poor adsorption capacity and stability in the presence of moisture and other impurities. Hence, the impurities in the zeolites need to be removed before utilizing them for CO_2 capture [42, 43].

Similar to zeolite, another category of emerging porous material is MOF. The metal-organic frameworks (MOFs) are well-known for their porosity and gas

adsorption studies. The MOF with desired porosity and cavity is considered to be more suitable for selective gas adsorption. The materials can be designed with desired pore size, active sites, polar functional groups and also with alkali metal cations that are essential for selective adsorption. MOFs are suitable for capturing CO_2 under elevated pressure sceneries such as natural gas purification and coal gasification. At low CO_2 partial pressures, zeolites and activated carbons perform better than MOFs. However, the MOF with excellent adsorption capacity under mild reaction conditions is rare in the literature [44, 45].

2.4 Separation Through Membrane

Membranes, another kind of fascinating separation material, are generally applied for gas separation. In general, the membrane-type materials are fabricated using the permeable or semipermeable materials, and such permeable and semipermeable membranes showed better selectivity towards CO_2. The major advantage for the membrane separation includes (1) simple operational techniques with minimum energy, (2) compactness in their design with suitable concentration of adsorbent material, and (3) simple installation of modules into existing infrastructures without any movable parts.

The zeolite membranes are most explored for the pre- and post-combustion CO_2 capture, when compared to other inorganic membranes [46, 47]. The highlighted advantages of zeolite membrane [48] include (1) outstanding mechanical properties, (2) thermal stability, (3) least fabrication costs, etc. Such properties made zeolites as efficient materials for post- [49] and pre-combustion CO_2 capture [50]. The MOF membrane with extremely high porosity and surface areas is found efficient for selective trapping of CO_2 [51].

Mixed matrix membranes [52] include a bulk and uniform polymer phase in combination with a homogeneously assembled inorganic distinct phase. Both of them are promising, because they enable synergistic enhancements in CO_2 permeability and selectivity with desirable mechanical and thermal stability.

2.5 CO₂ Capture from Atmosphere

The industrial process for capturing CO_2 from ambient air is one of an emerging set of technologies for making clean environment. This CO_2 capture is having great impact on geological storage of biotic carbon as well as the acceleration of geochemical weathering [53, 54]. In order to address this global climate change problem, the capture of atmospheric CO_2 is very crucial in addition to the CO_2 capture from the industrial stationary points. The CO_2 removal from atmospheric air has become a very critical area of research [55, 56], alternatively avoiding CO_2 to mix with the air and capturing them at the mixing point from industry/vehicles, etc.

The CO_2 capture from air is very challenging because of thermodynamic limitations resulting from the awfully low CO_2 concentrations and the energy cost for driving large volumes of air through a capturing process. Hence the CO_2 separation processes like cryogenic distillation and membrane separation are not economically viable. During the past several years, enormous contributions have been devoted through different approaches for CO_2 capture from the ambient air [57].

Alkaline solution-based technologies are well investigated and incorporating the chemisorption approach via. $LiOH/NaOH/KOH/Ca(OH)_2$ scrubbing to produce metal carbonates with CO_2. The produced metal carbonate solution is recycled back to the hydroxide-based solution to establish a cyclic process. The captured CO_2 can be further sequestered or utilized as C1 chemical feedstocks [58].

Traditional solid sorbent materials were also attempted to capture CO_2 from ambient air. Among the solid adsorbents, the activated carbon and zeolite materials which are well-known for post-combustion/pre-combustion CO_2 capture are not found efficient for capture from ambient air. This is due moisture existing in atmosphere leading to poor selectivity towards CO_2 in air [59]. Hence, the emerging technologies for CO_2 capture from stationary point source are economically more worthwhile when compared to atmospheric carbon capture [60].

2.6 Technologies on Carbon Dioxide Conversion to Chemicals and Fuels from Various Sources

The CO_2 technologies have the great impact on the reduced usage of fossil fuels towards energy materials. Although this is the eco-friendly carbon source existing in the atmosphere, the suitable methodology will be useful to achieve the value-added materials. The Table 1 describes the diverse value-added chemicals that are derived on industrial scale using thermo-, electro-, and photochemical and biological methods. The commercially existing technologies on CO_2 utilization will be described in this section in brief [61–63].

2.6.1 Polycarbonate

The Asahi Kasei Corporation (Japan) has established the synthetic methodology for aromatic polycarbonate using CO_2 for the first time. In the earlier days, the usage of phosgene or diphenyl carbonate is used for the synthesis of polyaromatic carbonate. The carbonate in polycarbonate links directly to the residual aromatic rings of the bisphenol. This process being clean technology does not require any purification process and produces no waste or by-products. Followed by this, several plants are built with license agreement in South Korea, Russia, and Saudi Arabia. A total of around six companies are involved in the production of polycarbonate using this technology with 1.07 million tons/year by consuming 0.185 million tons of CO_2 per annum [62, 63].

Table 1 List of industries using CO_2 as feedstock to synthesize fine chemicals

Ent.	Company	CO_2 source	Method	Product	Trade name
1	Novomer	Waste CO_2	TC	Acrylic acid/ butanediol	Converge® polyols
2	Liquid Light	–	EC	Ethylene glycol	–
3	Newlight	Emission from industry	BC	Plastic	Polyhydroxyalkanoates
4	Skyonic	Industry[a]	BC	Hydrochloric acid	–
5	Dioxide Materials	–	EC	Gasoline/diesel/ chemicals	–
6	LanzaTech	Exhaust gas from industry	BC	Liquid fuels/ plastics	–
7	Bayer Material Science	CO_2 from lignite power plant	Zinc Cat.	Polyurethane plastic	Polyether polycarbonate polyols
8	Brain	–	M	Fine and specialized chemicals	–
9	Joule	Ambient air	BC	Diesel/jet fuel	Sunflow-D (diesel)
					Sunflow-E (EtOH)
10	Geely Group/CRI	Fossil fuel source	TC	Methanol	Vulcanol (TM)
11	Audi/Global Bioenergies	From combustion champers	BC	Bio-isooctane	e-Gasoline
12	Audi/Joule	Waste CO_2 emissions	BC	Ethanol/diesel	Liquid fuel
13	Audi/Sunfire	–	TC	Diesel	–
14	Krajete GmbH	Industrial source	M	Methane	Sabatier process
15	Panasonic	–	PC	Formic acid	–
16	Green Earth	–	SD	Syngas	–
17	Solar Fuel	–	TC	Syngas	–
18	Sunfire GmbH	Steam + CO_2	TC	Diesel/kerosene	Blue crude
19	Proterro	–	BC	Sugars	–
20	Elcriton	–	MC	Biofuel	–
21	Renewable Energy Institute International	–	TC	Liquid fuels	–

[a]Removes CO_2 selectively from acid gas
TC thermochemical, *BC* biochemical, *EC* electrochemical, *MC* microbial catalyst, *SD* solar dissociation, *M* microorganism, *PC* photochemical method

The leading company **Covestro** in **Germany** produces polyether-polycarbonate polyols using the CO_2 as the feedstock. The product is commercially known as cardyon™ polyols. The polyols are used for the flexible polyurethane foams for use in mattresses and furniture using this clean technology [62, 63].

Another company, **Novomer Inc.**, in the USA is involved in the production of polypropylene carbonate polyols. This several thousand tons commercial scale company in Houston markets in the trade name Converge® polyols contain 50% wt of CO_2. The polyols are used enormously in polyurethane production for having wide applications [62, 63].

Nanyang Zhongju Tianguan Low Carbon Technology in China established the methodology for the production of biodegradable polypropylene carbonate with efficient catalysts [62, 63]. The CO_2 from the ethanol synthesis process is used efficiently for polycarbonate synthesis.

2.6.2 Biopolymers

A company named **Newlight Technologies** in the **USA** is involved actively in the production of biodegradable polymers in the commercial name "AirCarbon." This polymer contains ≈40 wt% of oxygen from air and 60 wt% carbon and hydrogen from captured emissions. This process involves three steps: the first stage involves the insertion of the concentrated methane or carbon dioxide to the reactor. Secondly, the catalyst pulls out the carbon from the CO_2, which is combined with oxygen and hydrogen to form a biodegradable long-chain polymer. This high-performance thermoplastic can be used as a substitute for oil-derived plastics [62, 63].

2.6.3 Methanol

The industry named **Carbon Recycling International (CRI)** has involved in the process of methanol synthesis using CO_2 from the geothermal power plant, with a capacity of 5 million L/year methanol production and 5500 tons CO_2/year recycling capacity which is otherwise released into the atmosphere. The methanol is distributed in the commercial name Vulcanol™ which is used as a blend component of gasoline and for further conversion into a diesel substitute. In this process, the H_2 and CO_2 are mixed at 3:1 ratio at optimized temperature and pressure [62, 63].

2.6.4 Hydrocarbon

The hydrocarbon technology of CO_2 captured from atmosphere is established by **Carbon Engineering**, an industry in Canada. The industry establishes the air-to-fuel systems (A2F) using the CO_2 in atmosphere by direct air capture (DAC) technology. Following three major steps involved in the hydrocarbon synthesis (1) the CO_2 trapped from air is purified and compressed, (2) water electrolysis using the

solar photovoltaic electrolyzer to produce hydrogen and (3) third step involves the hydrogenation adopting thermochemical methods to produce syngas followed by hydrocarbon synthesis. The hydrocarbon is having applications on diesel alternative and jet fuel [62, 63].

BSE Engineering (Germany) explored the commercial technology on methanol synthesis from CO$_2$. The hydrogen is produced by alkaline electrolyzer process, and the captured CO$_2$ is inserted into reactor in a stoichiometric ratio. The crude product contains methanol-water mixture, and by distillation, the methanol was achieved with 99% purity [62, 63].

Sunfire GmbH in Germany has established the methodology for hydrocarbon synthesis from syngas in the commercial name of blue crude by FTS process. The syngas is produced by electrolysis of water and CO$_2$ using solid electrolysis cell. The heat generated during the process is used to evaporate water for steam electrolysis. Thus, the efficiency of this process is increased by 70% [62, 63].

3 Homogenous Catalysts for Carbon Dioxide Conversion

One of the major advancements in the organometallic chemistry is the functional application of the metal complexes as homogeneous catalysts [64, 65]. Metal complexes are found efficient for many catalytic reactions when compared to heterogeneous catalysts, but they lack in their recyclability. In addition, the catalyst removal from the reaction is challenging sometimes. Among the diverse metal complexes, the pincer-type catalysts are extensively applied for hydrogenation of CO$_2$, whereas the salen and other metal complexes are used for CO$_2$ fixation reactions. Follow-up to the importance of CO$_2$, their application in fine chemical synthesis, capture, and utilization process is essential. The heterogeneous catalyst is also widely used for the conversion of CO$_2$; the review focuses selectively on homogenous catalysts. This content discusses the efficient and selective homogenous catalysts for the conversion. The reactions are broadly classified into carbon dioxide insertion and reduction of carbon dioxide to value-added products [66–68].

3.1 Carbon Dioxide Insertion Reaction

3.1.1 Cyclic Carbonate

The addition of CO$_2$ into organic substrates such as epoxide, diol, etc. is demonstrated to form cyclic carbonates. The conversion of CO$_2$ to cyclic carbonate is an atom economy process in nature. The cyclic carbonates are highly potential intermediates in organic synthesis [69], excellent building blocks for synthesizing

Scheme 1 Cyclic carbonates synthesis from various organic substrates and CO$_2$
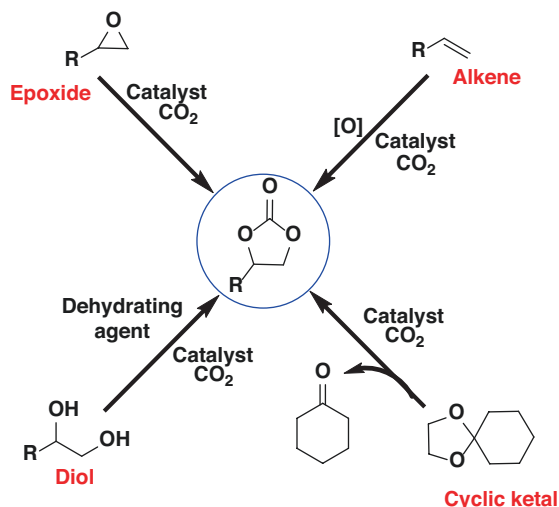
polycarbonates [70], and isocyanate-free polyurethanes [71], polar aprotic solvents [72, 73], alkylating agents, electrolyte components, and scaffolds for biologically active pharmaceutical agents [74–81]. In addition to the epoxide and diols, the cyclic carbonate can also be achieved from alkene via oxidative carboxylation and from ketals in presence of a suitable catalyst (Scheme 1). The catalytic conversion of epoxide to cyclic carbonate is feasible, whereas the conversion of diol to cyclic carbonate is challenging. The synthesis of cyclic carbonates from epoxides is an established industrial reaction that is used in the synthesis of aromatic polycarbonates [70]. The cycloaddition of CO$_2$ to internal epoxides has received increasing attention in recent years as these compounds can be used as synthons for isocyanate-free polyurethane synthesis. In addition, there are few reports available on the asymmetric cyclic carbonate.

3.1.2 Metal Complexes as Catalysts

The homogenous catalytic system incorporating salen, salphen, and porphyrin-based metal complexes with a wide choice of Lewis acids has been investigated for the efficient synthesis of cyclic carbonate utilizing CO$_2$ [82, 83]. Among the several metal ions, the aluminum and magnesium complexes are well explored when compared to other metal complexes. In addition to the catalyst, the tetrabutylammonium salts are used for the epoxide ring opening and carbon dioxide activation. Very few catalysts are working under ambient conditions either atmospheric temperature or pressure.

   M. North and co-workers have reported a series of μ-oxo-bridged bimetallic aluminum-salen complexes (Scheme 2) which are working as catalysts under minimum pressure (1 bar CO$_2$) in RT. The bimetallic aluminum catalysts (**1–6**) are

R₁ = R₂ = -(CH₂)₄- R₃ = Bn (2a)
R₁ = R₂ = -(CH₂)₄- R₃ = -CH₂-polystyrene (2b)
R₁ = R₂ = -H, R₃ = -(CH₂)₃ silica (2c)

R = -CH₃
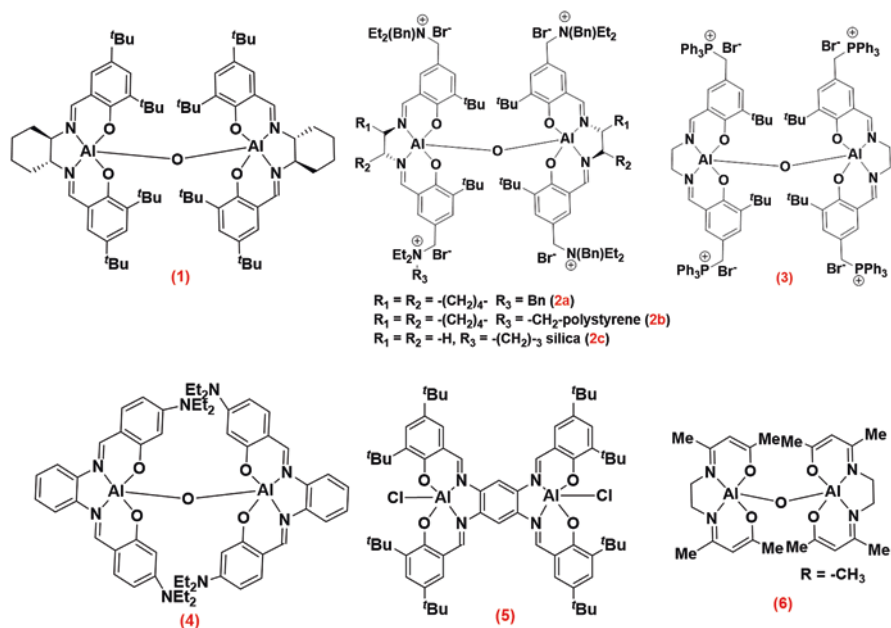
Scheme 2 Binuclear aluminum catalysts for the synthesis of cyclic carbonates from epoxide

reported to be efficient at ambient conditions (Scheme 2). All these catalysts are giving better conversion in atmospheric pressure at 25 °C, with high catalytic conversion along with TBAB (0.5–1.5 mol%) as additive. The catalyst (**1**), without any co-catalyst, requires high pressure (50 bar CO_2) to attain 50% conversion in 24 h [84, 85]. The binuclear aluminum complexes (**2a–2c**), with substituted ammonium bromide moiety on the ligand, improved the efficiency of the catalyst [86, 87] by enhancing the yield to 89% in 6 h at atmospheric pressure and temperature [86]. Further, a similar catalyst supported on polystyrene (**2b**) and silica (**2c**) [87] also gave better conversion in absence of a co-catalyst but long reaction time (24 h). A similar bimetallic catalyst with covalently attached quaternary phosphonium group (**3**) on the aromatic moiety of the ligand was also attempted [88]. The similar results were achieved in 24 h, suggesting that there is no drastic change due to the phosphonium group. The amine-functionalized complex (**4**) exhibits better activity than the tertiary butyl group in (**1**) under the same reaction conditions with 1.5 mol% catalyst [89]. The usages of the enantiopure ligand system and long reaction time in this reaction remain to be explored although there are advantages proven for their catalytic system.

3.1.3 Metal Catalysts with Maximum TOF for Cyclic Carbonate Synthesis

Efficiency of the catalyst is described in terms of turnover frequency (TOF). Followed by salen complexes, the amino triphenolate complexes have gained significant attention for their efficient conversion (Scheme 3). A. W. Kleij and co-workers have developed the amino triphenolate ligands, and their complexes incorporating with various metal ions are adopted as catalyst. As a homogenous catalyst, this system has shown high activity with wide substrate scope and functional group tolerance.

The iron(III) amino triphenolate complex (**7**) in combination with tetrabutylammonium iodide (TBAI) gave the maximum conversion of 74% with propylene oxide (reaction condition 25 °C, 2 bar in 18 h). As the temperature increased to 85 °C, the conversion is also found to increase [90]. Kleij replaced the Fe(III) with Al(III) in (**8**) with minor modification in the ligand system and demonstrated an excellent activity, adopting epoxy hexane as substrate (reaction condition 0.05 mol%, catalyst 0.25 mol%, TBAI 90 °C, 10 bar in 2 h). The addition of TBAI is found to enhance the efficiency of the catalyst, by raising the TOF from 960 to 36,000 h^{-1} [91]. In addition, the catalyst (**8**) was found effective in converting various functionalized internal epoxides and oxetanes. Further, the catalyst is found to give high selectivity towards the formation of *cis*-carbonates. However, upon hydrolysis, the *cis*-carbonates provides *cis*-diol is also established. A similar but modified bimetallic aminophenolate
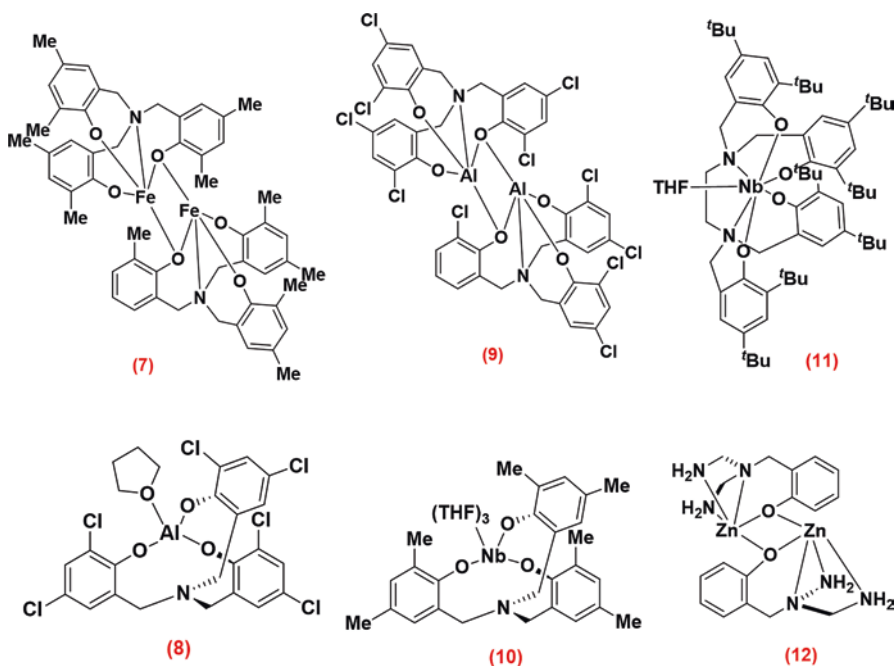
Scheme 3 Amino triphenolate metal complexes for cyclic carbonate synthesis

aluminum complex (**9**) as catalyst and TBAI as addictive gives better conversion at atmospheric pressure, but with long reaction time (24 h) at 85 °C [92].

Yuan and Yao have reported the Nb amino triphenolate complex (**10**) and TBAB for CO$_2$ fixation to cyclic carbonates [93]. In this case, the maximum TOF up to 4000 h^{-1} was obtained. Similarly, the bimetallic amino triphenolate complex (**11**) is found to give better conversion with terminal and internal epoxides (85 °C, 1 bar, 25 h) in the presence of TBAB [94]. The Cu, Zn, and Cd complexes of amine-functionalized triphenolate ligand were also employed as a catalyst. Among them, the Zn-triphenolate complex (**12**) was found catalytically active. Even though atmospheric pressure is sufficient, the temperature 100 °C is required to achieve a maximum of 79% conversion [95].

In this series in 2013, Deng and co-workers have reported the coordination polymer (CPs) with aluminum and cobalt (**13, 14**) able to capture CO$_2$ and demonstrated them for their catalytic conversion (Scheme 4). The CPs are capable for CO$_2$ storage, similar to zeolites or MOF. The captured CO$_2$ is used for propylene carbonate synthesis at room temperature, in 48 h. The maximum of 80% conversion was achieved with **14**, and 78% conversion was achieved with **13** at ambient condition [96]. In 2014, the same group reported a similar CPs with zinc (**15**) for the same reaction, but it requires harsh reaction condition (120 °C, 3 MPa CO$_2$, 3.6 mol% TBAB, in 1 h). The maximum TOF up to 11,600 h^{-1} was achieved, and the catalyst is reported to be recyclable [97].

Among the various catalysts reported for cyclic carbonate synthesis, very few catalysts are efficient under additive-free conditions. In this series, the catalyst with inbuilt anions doesn't require any additional co-catalyst. Arunachalam et al. have adopted the Zn-CP (**16**) for CO$_2$ fixation to cyclic carbonates in solvent- and additive-free conditions with ambient pressure of 1 MPa CO$_2$ at 100 °C in 4 h
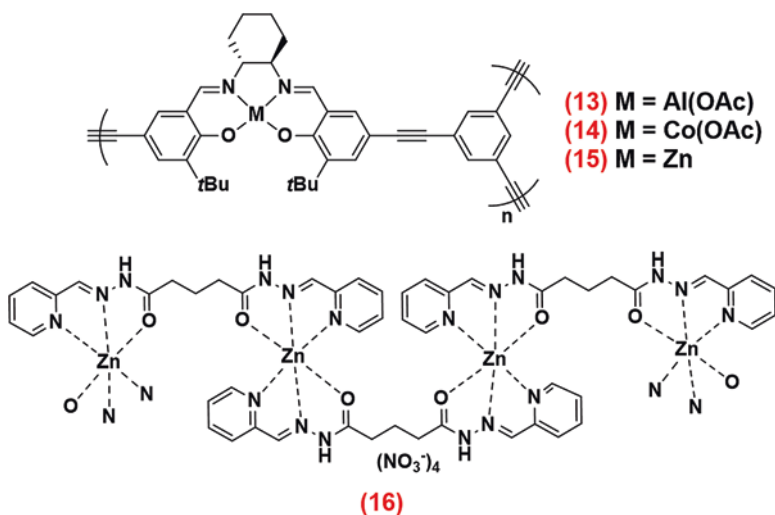
Scheme 4 Coordination polymer for cyclic carbonate synthesis

(Scheme 4) [98]. The alkyl-substituted terminal epoxides are giving better conversion when compared to internal epoxide. The path of the reaction is established with kinetic experiments [98].

3.1.4   Porphyrin Complexes

Porphyrin is one of the important molecules; the respective complexes have been extensively studied by Ema and workers. This group has developed a bifunctional molecular catalyst (**17–22**) with embedded co-catalysts for better activity (Scheme 5). In this case, if the ratio of the co-catalyst increased, then the activity was also found to increase. The initial TOF of the catalyst with 1:4 (LA/co-catalyst, where LA = Lewis acidic center) ratio is found to be 12,000; when the ratio raised to 1:8 (LA/co-catalyst), TOF is found to further enhance up to 19,000 h^{-1} [99].

Further, the metal centers and porphyrin ratio were varied systematically into bimetallic and trimetallic as shown in Scheme 5. The TOF of the monometallic complex (**17**) is 2500 h^{-1}, and for bimetallic catalyst (**18**), the TOF was enhanced to 5100 h^{-1}, and in the case of trimetallic (**19**), up to 6500 h^{-1} (reaction condition 1.7 MPa CO_2, 120 °C in 24 h) were reported. In this series, initial TOF up to 46,000 h^{-1} was obtained at 0.002 mol% trimetallic complex catalyst (**19**) at 160 °C in 1 h. The Zn-porphyrin catalysts developed by the same group are being highly stable; they are less efficient when compared to magnesium under similar reaction condition. The respective TOF of the zinc catalytic systems includes 2580 h^{-1} for monometallic (**20**), 5700 h^{-1} for bimetallic (**21**), and 8500 h^{-1} for trimetallic catalysts (**22**) [100]. The Zn-porphyrin complex is heterogenized on SBA-15 silica by Yang et al., adopted for the cycloaddition (reaction condition propylene oxide, 120 °C, 6 h) reaction. The solid catalysts are more efficient (TOF 1686 h^{-1}) when compared to the plain catalyst (TOF 370 h^{-1}) [101].

R = -[O(CH$_2$)$_6$NBu$_3$]Br

(17): M = Mg
(20): M = Zn

(18): M = Mg
(21): M = Zn

(19): M = Mg
(22): M = Zn
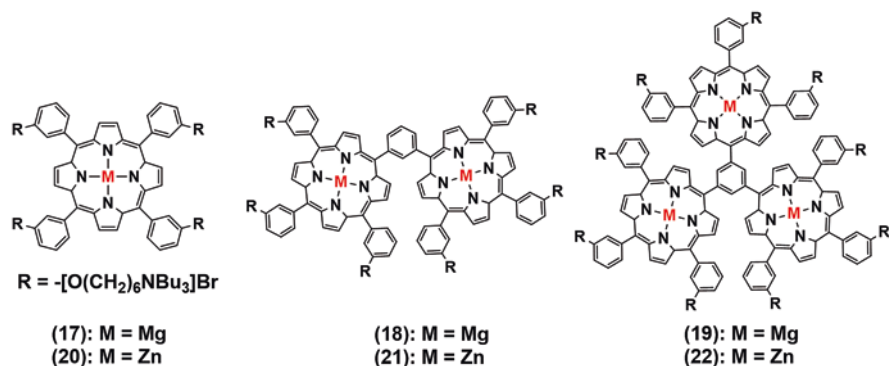
Scheme 5   Mono, bis, and tris metal porphyrin complexes of Mg and Zn [99]

3.1.5 Kinetic Resolution of Epoxide to Cyclic Carbonate

Following up this synthesis of achiral version of cyclic carbonates, the kinetic resolution of epoxide in presence of CO$_2$ leads to chiral epoxide and cyclic carbonate (Scheme 6). The Al-, Co-, and Cr-based chiral catalysts are employed, and most of the reactions are established at ambient temperature with high CO$_2$ pressure [102].

In 2004, the first report on the kinetic resolution of propylene oxide using chiral Co catalyst (**23**) was performed by Nugen and co-workers [103]. The ee up to 68% was obtained in combination with [(R)-(+)-4-dimethyl-aminopyridinyl (pentaphenylcyclopentadienyl)iron] as co-catalyst, under 2 MPa CO$_2$ in 50 h [103]. The modified cobalt catalyst (**24**) for the kinetic resolution of epoxide, with the 97% enantiomeric propylene carbonate, was achieved (Scheme 6). In combination with the catalyst (**24**), the [(bis(triphenylphosphoranylidene)ammonium, 2,4-dinitrophenoxide)] is used as an additive. At −25 °C in 12 h reaction time, the conversion is found low, i.e., less than 20% [104].

3.1.6 Cyclic Carbonate from Diol

As stated above, the catalytic conversion of diol to cyclic carbonate is quite challenging when compared to epoxide because the epoxide is less stable than the cyclic carbonates (Scheme 7). In addition, the reactions are slightly thermodynamically favorable due to the lower reactivity of the hydroxyl group. Water being the by-product formed during such reaction interferes with the product formation and alters the reaction path. Hence, the requirement of a suitable dehydrating agent was
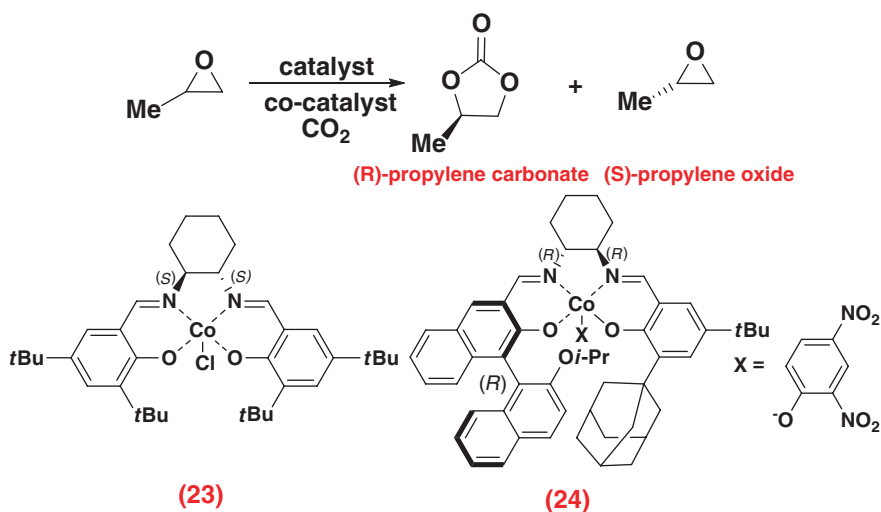
Scheme 6 Kinetic resolution of epoxide to enantiopure epoxide and cyclic carbonate

Scheme 7 Conversion of diol to cyclic carbonate
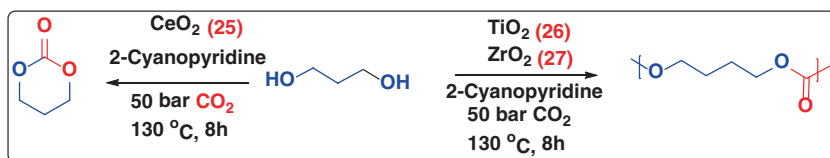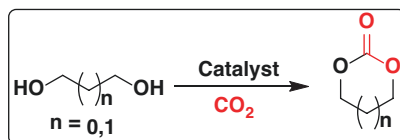
Scheme 8 Synthesis of cyclic carbonate and polycarbonates from the diol

considered essential to promote the equilibrium towards the cyclic carbonate product. There are very few reports available on such reactions.

In 2014, K. Tomishige has adopted CeO_2 (cerium oxide) as the catalyst for synthesizing the propylene carbonates from the 1,2-propanediol (Scheme 8). The 2-cyanopyridine adopted as a dehydrating agent was hydrated to 2-aminopyridine under the same reaction condition and thus promotes the forward reaction. The maximum conversion was obtained using 1:10 to substrate/2-cyanopyridine ratio using 5 MPa CO_2 at 150 °C with reaction time up to 48 h. This is the first biphasic reaction performed on cyclic carbonate [105]. In 2016, the same group has reported the polycarbonate from diol in the presence of other metal oxides. The similar reaction condition with ZnO, TiO_2, γ-Al_2O_3, Nb_2O_5, and ZrO_2 leads to the formation of polycarbonate [106].

3.1.7 Polycarbonates

Polycarbonates (PCs) represent another challenging molecule which can be achieved in green pathway by treating CO_2 and epoxide. In producing polycarbonates via CO_2, water is generated as the only by-product and makes this reaction route more environmentally friendly. The carbonate materials are having excellent mechanical properties such as low rigidity, brittleness, and high thermal stability. Among them, the excellent material is bisphenol-based polycarbonates used as engineering plastics having applications in optical component and electronic devices as construction material (Scheme 9) [107].

In general, most of the polycarbonate synthesis requires high temperature and pressure, when compared to cyclic carbonates. There are few reports with the ambient conditions (Scheme 10) [108]. In 2003, Coates reported [109] catalysts (**28**) for polycarbonate synthesis with high molecular weight. The ambient condition of 0.7 MPa CO_2, 50 °C is adopted for the conversion with a TON of 354. The stereoselective synthesis of carbon dioxide co-polymer with cyclohexene oxide with chiral diol was first reported in 2003 [109]. The bimetallic zinc catalyst (**29**) regulates the
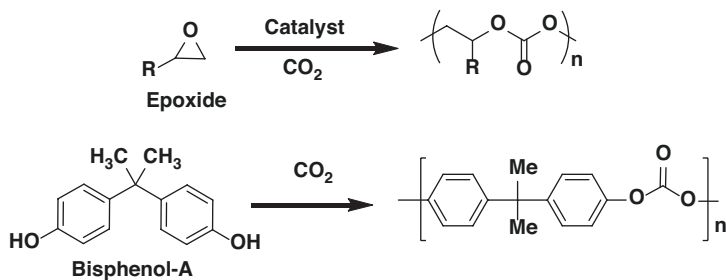
Scheme 9 Polycarbonate for epoxide and bisphenol-A using CO_2
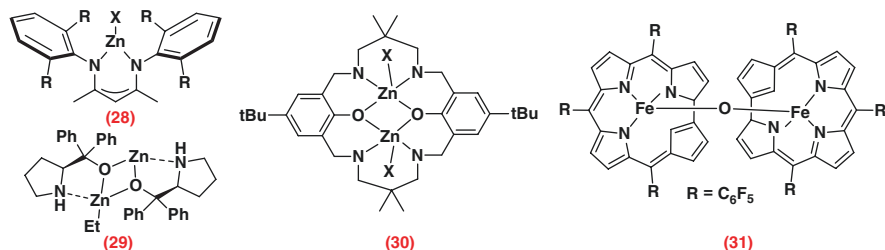
Scheme 10 The homogeneous catalyst for copolymerization of epoxide and CO_2

polymer as highly isotactic with enantioselectivity up to 70% using 3 MPa CO_2. In 2009, Williams [110] established another bimetallic Zn complex (**30**) for polycarbonate synthesis at atmospheric CO_2 pressure and 100 °C. The copolymerization of propylene oxide (PO-CO_2) and glycidyl phenyl ether (GPE-CO_2) was catalyzed by iron complex (**31**) [111]. In particular, the GPE-CO_2 copolymers were found to be crystalline materials because of the existence of isotactic poly(GPE) units.

3.1.8 Dialkyl Carbonates

Follow-up to the cyclic/poly carbonates, another class of carbonates includes the dialkyl carbonates. This included the dimethyl carbonate (DMC), diethyl carbonate (DEC), and so on, having wide applications on reagents in chemical synthesis as well as fuel materials. The direct synthesis of DMC from methanol and CO_2 is challenging because interference of the by-product water molecules disturbs the reaction equilibrium. In the DMC synthesis from methanol in the presence of catalyst and methyl iodide as an additive (base), the formation of salt impurities takes place generally. Such formation of salt makes the separation process difficult. These hurdles can be removed by (1) increasing the CO_2 concentration by using supercritical CO_2 (scCO_2) and (2) removing the byproduct water using appropriate dehydrating agents [112].

An alternative process for DMC proceeds via cyclic carbonates and subsequent transesterification (Scheme 11). Here, CO_2 reacts initially with epoxides to form cyclic carbonates. Ester exchange with alcohol followed later leading to the linear carbonate as the end product. The main advantage of using this method is that the dehydrating reagents are not essential. The disadvantage, however, is the large excess of alcohol required for ester exchange [113, 114].

3.2 Hydrogenation of CO_2 to Fine Chemicals

3.2.1 To Methanol

Methanol is a commercially important chemical having a wide range of applications. It is used for the production of various other large-scale chemicals such as acetic acid (Monsanto process), formaldehyde, methyl *tert*-butyl ether (MTBE), etc. It has excellent combustion characteristics and can be used in fuel cells to produce energy. Dimethyl ether (DME), which is easily synthesized from methanol by dehydration over acidic catalysts, has also been proposed as a diesel substitute [115–117]. The $Cu/ZnO/Al_2O_3$ is an industrially explored catalyst for methanol synthesis from CO_2. The pressure ≈ 6 MPa and 250 °C has been widely used for methanol synthesis over 40 years in industries (Scheme 12) [118].

3.2.2 Hydrogenation Using Molecular Hydrogen

In the view of homogenous catalysts, the carbonyl complexes of ruthenium, rhodium, nickel, etc. are adopted initially for methanol synthesis [119]. Sasaki [120] has reported the metal carbonyl complexes in combination with potassium iodide to produce methanol for the first time. The selectivity of methanol is found low because of the by-product formation such as CO, CH_4, and trace amount of ethane. Among the carbonyl complexes as catalysts, the better catalytic result was achieved with the $Ru_3(CO)_{12}$-KI system [121]. In follow-up, various modified complexes especially the pincer complexes are found efficient for CO_2 hydrogenation.
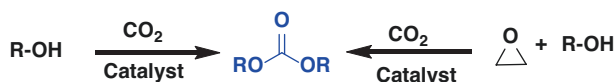
Scheme 11 Synthesis of dialkyl carbonate from carbon dioxide

$$CO_2 + 2\,H_2 \longrightarrow CH_3OH \quad \Delta H_{298\,K} = -49.4\ kJ\ mol^{-1}$$
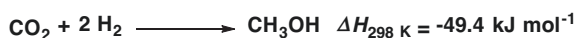
Scheme 12 Hydrogenation of CO_2 to methanol

In 2011, Sanford established a cascade ruthenium pincer complexes (**32a, 32c**) and scandium triflate (**32b**) for the reduction of CO_2 to methanol (Scheme 13). The conversion follows three steps; the first is the hydrogenation of CO_2 to formic acid using (**32a**), followed by esterification of formic acid to methyl formate by $Sc(OTf)_3$ (**32b**), and reduction to methanol using (**32c**) [122].

In 2015, Leitner reported the Ru-triphos catalyst (**33**) for the hydrogenation of CO_2 to methanol at 140 °C with a TON of 603 (Scheme 14). The reactions are performed on biphasic solvent system, i.e., water-2-MTHF (2-methyl tetrahydrofuran)
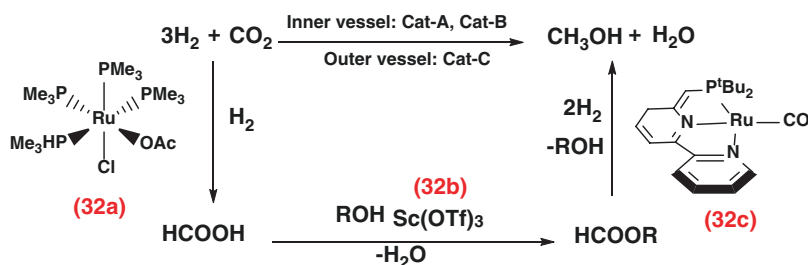
Scheme 13 Catalytic hydrogenation of CO_2 to methanol
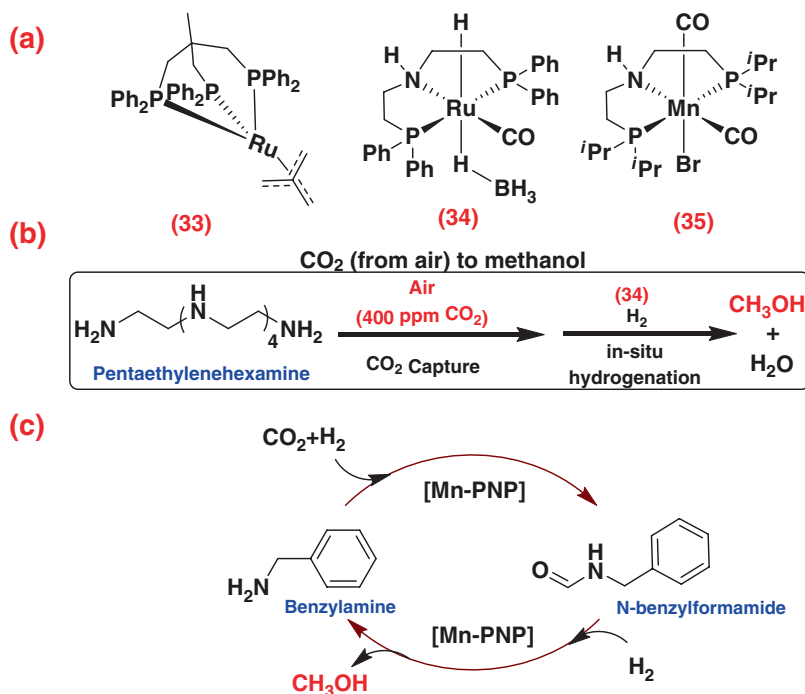
Scheme 14 (**a**) Pincer complexes for hydrogenation of CO_2 to methanol; (**b**) CO_2 capture from air and conversion to methanol using Ru-PNP catalyst; (**c**) Mn-PNP-catalyzed synthesis of methanol via formamide route
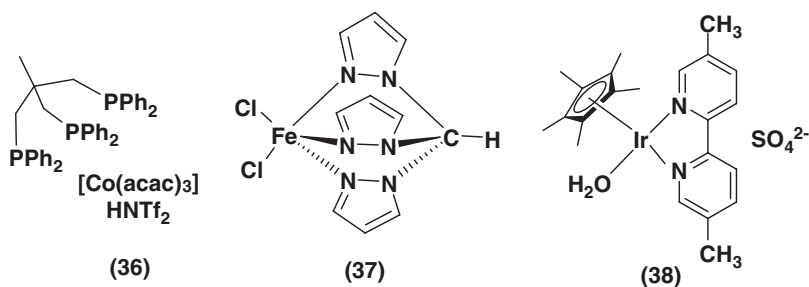
Scheme 15 Co, Fe, and Ir complexes for hydrogenation of CO_2

in which the catalyst is separated on 2-MTHF layer and methanol residing in aqueous layer [123]. In 2016, Prakash and co-workers have reported the methanol synthesis using CO_2 captured from the air. Here the Ru-PNP complex (**34**) effectively converts the CO_2 and H_2 to methanol, in the presence of polyamine at 125–165 °C using an ethereal solvent. The methanol and water are separated by distillation, and the catalyst is reused. The polyamine is replaced with pentaethylenehexamine having the capacity to capture CO_2 from the air, used for direct conversion to methanol adapting a Ru-PNP complex (**34**). The maximum of 79% CO_2 captured from the air was converted to CH_3OH [124]. In 2017, a manganese PNP complex (**35**) was adopted for the CO_2 hydrogenation in the presence of amines (such as benzylamine and morpholine) for methanol synthesis. The catalytic mechanism follows the formamide pathway, i.e., when benzylamine is treated with CO_2/H_2, the *N*-benzyl formamide is formed initially. The formamide will undergo hydrogenation to produce methanol in presence of catalyst. Eighty-four percent of methanol yield is obtained with benzylamine, and 71% methanol was obtained when morpholine is used [125].

The in situ Co-triphos catalyst (**36**) prepared from cobalt acetate in the presence of bis(trifluoromethylsulfonyl)amide additive produced methanol at 100 °C with TON up to 78 (Scheme 15) [126]. Iron(II) scorpionate catalyst (**37**) was reported by Pomberio and co-workers for methanol synthesis at 80 °C and 7.5 MPa of total pressure. The maximum of 46% methanol is obtained in the presence of pentaethylenehexamine as co-catalyst with the TON of 2283. Replacing pentaethylenehexamine by 1,1,3,3-tetramethyl guanidine (TMG) proved the former is better by its catalytic conversion because of the superior absorption capacity [127]. Himeda and co-workers in 2017 adopted the iridium half-sandwich complex (**38**) for hydrogenation of formic acid to methanol with 47% selectivity, at ambient temperature of 50–60 °C and a hydrogen pressure of 5.2 MPa [128].

3.2.3 Methanol Synthesis from CO_2 and Hydrosilane

Molecular hydrogen is being used as a reducing agent; attempts were given to explore hydrosilane or alkylsilanes as H_2 source. The end-product obtained as silyl derivatives of methanol, which upon hydrolysis give methanol. The pincer catalysts presented in Scheme 16 are found efficient for such hydrogenation.
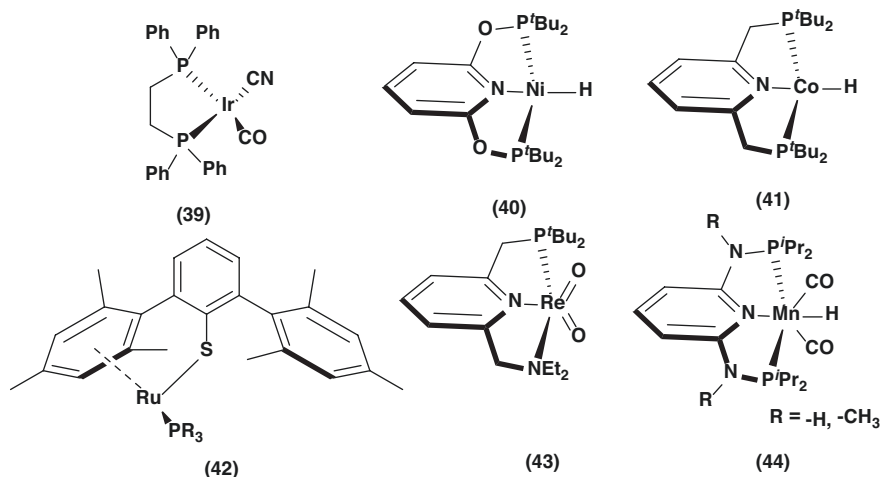
Scheme 16 Homogeneous catalyst for methanol synthesis from CO_2 and hydrosilane

The first report on methanol synthesis using hydrosilane as a reducing agent was reported by Eisenberg et al. The iridium pincer carbonyl complexes (**39**) are efficient at ambient temperature (40 °C) with low TON [129]. In 2010, Guan adopted the Ni PNP hydride complex (**40**) for the hydrogenation reaction in the presence of organoboranes [130, 131]. The cobalt PNP hydride complex (**41**) promoted the hydrosilylation of CO_2 using $PhSiH_3$ leading to the mixture of silyl formate, bis(silyl)acetals, and methoxysilyl derivatives [132]. The ruthenium catalyst (**42**) in the presence of monohydrosilanes, with selectivity towards bis(silyl)acetals or methoxysilyl products at high temperature (150 °C), takes long reaction time with better selectivity [133]. Mazzota et al. have reported an oxorhenium PNN pincer complex (**43**) in the presence of $PhMe_2SiH$, and $PhSiH_3$ reduces the CO_2 to methoxysilyl [134, 135]. Mn(I)-PNP complex (**44**) catalyzed CO_2 hydrosilylation to silyl derivative of methanol under mild reaction conditions (80 °C, 1 bar CO_2). The mechanistic pathway suggesting the reaction proceeds via formato complexes by hydride transfer to CO_2 followed by hydrogenation of silyl formate to silyl acetal species [136].

3.2.4 Formic Acid

As we know formic acid is the most widely used fine chemicals in various industries. Formic acid having an excellent application as hydrogen source contains 4.4 wt% of H_2 with volume capacity of 53.4 g/L at STP. The hydrogen can be released by decomposing the formic acid; hence, it is used as energy material [137, 138]. As formic acid is being recognized as best storage material, varieties of homogeneous and heterogeneous catalysts have been explored for the hydrogen production. Similarly, formic acid production from CO_2 can also be possible; various

heterogeneous and homogeneous approaches have been reported intensively in the literature [139, 140].

3.2.5 Homogenous Catalysts

Inoue in 1976 established the first homogeneous catalyst hydrogenation of CO_2 to formic acid [141]. After carrying out a series of experiments, this group has identified that the trace amount of water enhances the catalytic activity. Most of the pincer complexes established for hydrogenation reactions are insoluble in water; hence, the reactions are performed in DMSO with trace water molecules. In 1993, Leitner and co-workers have reported [142] a rhodium catalysts that soluble in water and reactive under mild reaction conditions such as 4 MPa pressure and room temperature (Scheme 17) produced turnover number (TON) 3440.

In 2004, Fukuzumi and co-workers reported the ruthenium catalyst (**45**) for formic acid synthesis under acidic reaction conditions. The better conversion was achieved in acidic conditions with pH ranging 2.5–5.0, at 40 °C, in 70 h using H_2 (5.5 MPa) and CO_2 (2.5 MPa). It is found that as the pressure increases, the TON was also found to increase [143]. In the follow-up detailed investigation by G. Laurenczy and co-workers, the role of solvent in the catalytic hydrogenation using the Ru-PTA (1,3,5-triaza-7-phosphaadamantane) complex (**46**) has been extensively investigated. The direct hydrogenation of CO_2 to formic acid in an additive-free condition using aqueous and DMSO as solvents was conducted independently. In water, at 40 °C, 0.2 M formic acid has been obtained under 20 MPa, whereas under similar conditions with DMSO, the catalyst produced 1.9 M formic
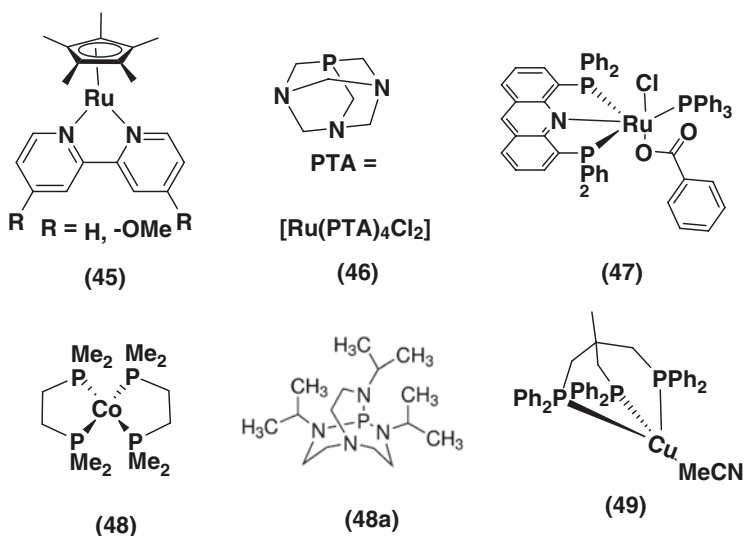
Scheme 17 Homogeneous catalyst for hydrogenation of CO_2 to formic acid

acid [144]. In 2016, W. Leitner again reported another Ru-catalyst (**47**) for the hydrogenation of CO$_2$ to give formic acid using DMSO and DMSO/H$_2$O without treating amine bases as co-reagents. Thus, the catalyst (**47**) is identified as one of the active catalysts under the additive-free condition with TON 4200 and TOF 260 h^{-1}. Leitner and coworker produced 0.3 mol of formic acid at 60 °C, in DMSO-water (95:05), using 8 MPa H$_2$, 4 MPa CO$_2$ in reaction time of 16 h. Interestingly upon using acetate buffer, this group has identified that the TOF enhanced further to 1019 h^{-1} for this catalyst [145].

Followed by the Ru and Rh complexes, there are reports incorporating varieties of transition metal complexes (Scheme 17). Among them, the Co-diphos complex (**48**) in combination with (**48a**) can effectively convert CO$_2$ to formic acid at ambient conditions (room temperature) in THF. At the atmospheric pressure, the TOF being 3400 h^{-1}, the TOF has enhanced to 74,000 h^{-1} suggesting the gas-liquid mixing rate is efficient at high catalyst concentration [146]. In 2015, Aaron M. Appel adopted the Cu-Tripos catalyst (**49**) for the hydrogenation of CO$_2$. In presence of 50 mmol of DBU as a base, 140 °C, 4 MPa pressure (1:1), the TON 500 was achieved in 20 h [147].

3.2.6   Iridium Catalysts

The iridium catalysts exhibit superior activity when compared to Ru and Rh complexes as discussed above. The wide variety of iridium complexes with PTA (1,3,5-triaza-7-phosphaadamantane), sandwich, pincer, and NHC complexes (**50–57**) is found efficient for the hydrogenation of CO$_2$ to formic acid (Scheme 18). In 2008, Gonsalvi et al. have reported a half-sandwich iridium complex (**50**), composed of a water-soluble phosphine ligand PTA. The catalyst (**50**) in additive-free conditions, at 100 °C and 1 MPa pressure, gives maximum TOF (23 h^{-1}) with moderate activity [148].

The half-sandwich iridium complexes (**51–52**) with 4,4′-dihydroxy-2,2′-bipyridine (DHBP) and 4,7-dihydroxy1,10-phenanthroline (DHPT) are adopted for formate synthesis [149]. The catalyst (**51**) produces a moderate yield in the presence of KOH as a base, at 120 °C, 57 h, using 6 MPa total pressure. The initial TOF of 42,000 h^{-1} was obtained whereas the same catalyst under ambient reaction condition (60 °C, 0.1 MPa, 50 h), the initial TOF as 33 h^{-1} is achieved, suggesting that they are efficient at moderate condition. This also suggests that the corresponding hydride complexes can easily be generated as an active species at atmospheric pressure. Followed by this, in the catalyst (**52**) under similar reaction condition (120 °C, 6 MPa pressure), the maximum TON of 222,000 was obtained with 0.4 M formate. A similar catalyst with ruthenium metal center exhibits better activity by forming formate up to 1.25–1.5 M using long reaction time (165 h), high temperature, and pressure [149].

In 2010, Beller and co-workers designed a PNP-Ir trihydride complex (**53**) in which alkyl-phosphine-based pincer ligands were employed as efficient electron donors. These complexes were used for the hydrogenation of CO$_2$ in H$_2$O/THF [150].
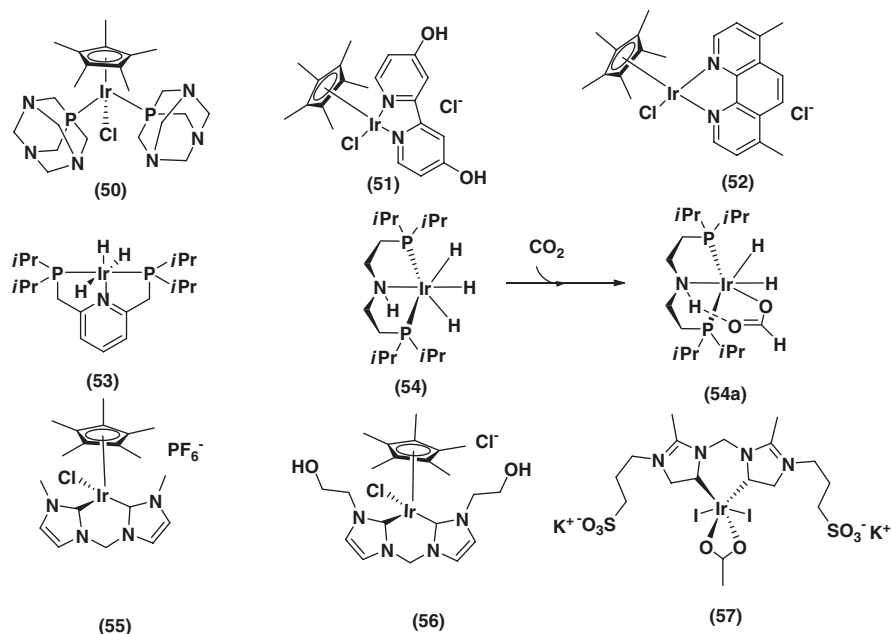
Scheme 18 Iridium complexes for hydrogenation of CO_2 to formic acid

In 2011, Hazari and co-workers using DFT calculations investigated CO_2 insertion into iridium(III) trihydride PNP ligand (**54–54a**) [151]. In 2015, the same group has demonstrated the catalyst (**54**) for the electrochemical conversion of CO_2 to formate. The catalyst is found to give moderate conversion in water-acetonitrile medium, at the ambient condition with 99% faradaic efficiency [152].

Followed by the pincer complexes, the N-heterocyclic carbene complexes (NHC) of iridium (**55–57**) are found to be better catalysts [153, 154]. These NHC ligands showing better stability, electron-donating nature, and better solubility in water medium are considered as added advantages of NHC ligand compared to pincer ligand. Peris and co-workers reported a series of NHC-iridium complexes (**55–57**) for the synthesis of formate. The catalyst (**55**) exhibits moderate activity, with a TON of 1600 in aqueous medium when using KOH as a base. To enhance the solubility of the NHC complex in an aqueous medium, the hydroxyl group is introduced in the ligand incorporated to (**56**). Upon using this (**56**) as catalyst, the TOF is enhanced to 9500 in aqueous medium under optimized conditions [153]. Further, substituting methyl on imidazole ligand in (**57**) gains higher electron-donating ability. In addition, the introduction of sulfonate groups in (**57**) further increased its water-soluble nature. Upon these modifications, this catalyst was found to enhance the maximum TON to 190,000 with complex **57** [154].

3.2.7 Acetic Acid

Acetic acid, the commercially well-known fine chemical, is generally produced through Monsanto process. This involves the carbonylation of methanol using carbon monoxide with appropriate choice of catalyst (Scheme 19). However, the eco-friendly method in acetic acid synthesis involves the CO_2 and methane which is thermodynamically unfavorable and requires high temperatures [155]. Most of the reported catalyst produces low yield of acetic acid [156, 157], and in presence of iodomethane, the selectivity of acetic acid was obtained up to 10.7% [158].

The formation of propanoic acid by treating olefin and CO_2 in the presence of complex **59 [Rh(PPh$_3$)$_3$Cl]** was achieved (Scheme 20). The 92% ethylene conversions were achieved with the formation of propanoic acid (38%) and ethanol (15%) at 14 MPa CO_2 [6].

B. Han and co-workers have reported the acetic acid synthesis by reduction of CO_2 in the presence of methanol and molecular hydrogen. The ruthenium carbonyl-rhodium acetate salts **60** in combination with imidazole as a ligand and lithium iodide as the promoter using 1,3-dimethyl-2-imidazolidinone (DMI) solvent are found more efficient (Scheme 21). The conversion increases when the reactions are adopted at a temperature above 180 °C, and the role of imidazole is considered significant [159]. Recently, the modified zeolite catalysts were synthesized and used for the oxidation of methane to acetic acid [157].

Scheme 19 Synthesis of acetic acid from CO_2
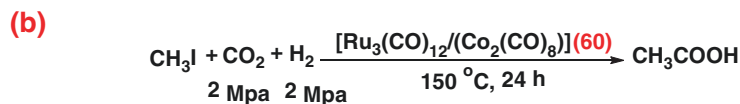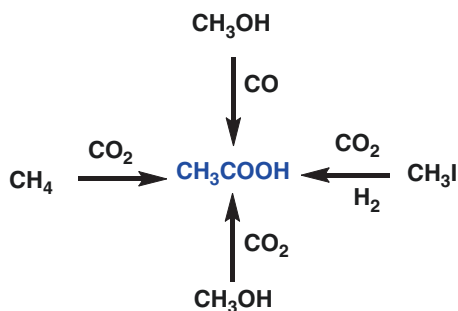
Scheme 20 Synthesis of (**a**) propanoic acid and (**b**) acetic acid from carbon dioxide

$$CH_3OH + CO_2 + H_2 \xrightarrow[\substack{Imidazole\ LiI \\ 200\ ^oC,\ 12\ h}]{Ru_3(CO)_{12}/Rh_2(OAc)_4\ (60)} \begin{array}{l} CH_3COOH \\ Yield\ 77\% \\ TOF:\ 22.5 \end{array}$$

4 MPa
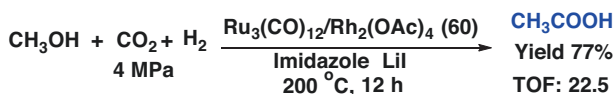
Scheme 21 Synthesis of acetic acid catalyzed by Ru/Rh carbonyl complex
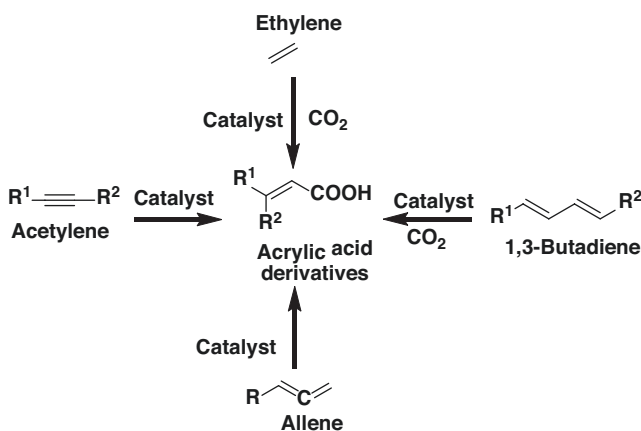
Scheme 22 Carboxylation of alkenes and alkynes to acrylic acid derivatives using CO_2

3.2.8 Acrylic Acid

In the catalytic reduction of olefin to carboxylic acid, the saturated carboxylic acid is more preferred, when compared to unsaturated acids. In such attempt, the acrylic acid is the most important and challenging conversion. Further, the acrylic acid derivatives are important building blocks for synthesizing various industrial products, such as plastics, textiles, coatings, elastomers, adhesives, paints, etc. [160].

Generally, the acrylic acid derivatives are synthesized in a two-step process, i.e., oxidation of propene with O_2 via a transient acrolein intermediate over heterogeneous catalysts at high temperature. The alternate process includes carboxylation of unsaturated hydrocarbon using C1 feedstock. The most popular processes utilize CO and H_2O as the C1 source with nickel or palladium complexes as active catalysts. The alternate and eco-friendly pathway includes the synthesis from CO_2 and ethylene which is highly challenging [161].

In addition to the acrylic acid, the carboxylation of various unsaturated organic substrates provides varieties of fine chemicals such as acrylic acid derivatives as shown in Scheme 22.

The Ni-(COD)$_2$ [Bis(1,5-cyclooctadiene)nickel(0)] complex (**61**) in which the nickel existing in 0 oxidation state found more reactive and well explored for carboxylation of alkene derivatives (Scheme 23). In many of the reactions, the DBU (1,8-diazabicyclo[5.4.0]undec-7-ene) as a base enhances the rate of reaction even at atmospheric pressure [162, 163].

(A)

Carboxylic acid derivatives
Carboxylation of Conjugated Enynes

DBU
Ni(0)
CO_2

Carboxylation of Diynes

J. Org. Chem. 1999, 64, 3975-3978

(B)

Dicarboxylation of 1,3-Dienes

Ni(0) $CO2$
DBU THF

JACS, 2001, 123,
2895-2896

Ni(COD)$_2$
(61)

(C)

Addition of CO_2 and aldehyde
to Allenes

Ni(COD)$_2$ PhCHO
DBU

Org. Lett., 2003, 5,
2599

(D)

Coupling of CO_2 with allenes
CO_2
Ni(COD)
L

Coupling of CO_2 with various alkynes

Ni(COD)
L
CO_2

Bu Bu

L = (59a)

Chem. Commun., 2004, 2568 – 2569

Scheme 23 Synthesis of carboxylic acid from alkenes (**B–D**) and alkynes (**A–D**) catalyzed by Ni(0)

In 1999, the carboxylation of conjugated enynes and diynes (Scheme 23a) to the carboxylic acid at the atmospheric pressure and temperature were reported. Ni-(COD)$_2$ in combination with DBU, the reactions proceed in the selective pathway of terminal alkynes as shown in Scheme 23a [164]. Followed by this, the dicarboxylation of 1,3-dienes with Ni-(COD)$_2$ catalyst in the presence of dimethyl zinc is reported under mild condition (Scheme 23b). The reaction proceeds in the stereoselective pathway with the retention of geometrical isomer [165].

The methodology for the synthesis of R-methylene-γ-lactones by the addition of aryl aldehydes and CO_2 to terminal allenes was achieved using Ni-$(COD)_2$ catalyst (Scheme 23c). The R-methylene-γ-lactones are obtained with excellent regio- and stereoselectivity [166]. The conversion of allenes and alkenes to the carboxylic acid derivatives using carbon dioxide (Scheme 23d) was reported by N. Iwasawa group. The Ni-COD in combination with 2,2′-(dibutylated methylene) bis(imidazoline) ligand is suitable for carboxylation of aryl-substituted internal alkynes [167].

3.2.9   Dimethyl Formamide

A. J. Vorholt and co-workers established a process for the DMF synthesis using CO_2 and dimethylamine where CO_2 itself acts as formylating agent [168]. The ruthenium chloride with pincer ligand as catalyst (**62**) is used. The process is mainly depending upon the CO_2 concentration, i.e., when CO_2 is in excess, the 14% DMF is achieved, while the stoichiometric CO_2 concentration provides 43% DMF and is achieved in 3.5 h (Scheme 24). The carbon monoxide as the only by-product formed in small ppm level was observed [168].

Following this study, more concentrated $scCO_2$ was used. Accordingly, there are few reports available using the $scCO_2$ for the conversion of dimethylamine to DMF (Scheme 25). The reaction follows the formic acid pathway, i.e., the reduction of $scCO_2$ to formic acid. Further the thermal condensation of dimethylamine with formic acid at a temperature ranging 80–100 °C, which leads to DMF. The ruthenium pincer complexes (**63–66**) in the Scheme 25 are efficient for the catalytic conversion. The production of formamides in less basic amines, e.g., aniline, requires the additional base [169].

R. Noyori and co-workers adopted the $RuCl_2[P(CH_3)_3]_4$ (**63**) for the hydrogenation of CO_2 to formic acid at 50 °C, and the respective TON was achieved as 420,000. The catalyst can effectively convert CO_2 to DMF in the presence of dimethylamine at 8 MPa H_2 and at 13 MPa CO_2 at 100 °C in 22 h reaction time [170]. In 2007, T. Ikariya and co-workers have reported a similar conversion of dimethylamine to DMF using the ruthenium catalyst (**64**). This catalyst with a minimum quantity of 0.005 mmol at 100 °C, with total initial pressure 22 MPa, the respective TON achieved is 4800. Changing the catalysts to Cp-Ru complex (**65**), the respective TON is calculated as 3300 in a reaction time of 15 h [171]. The solvent-free synthesis of DMF using the ruthenium complex (**66**) bidentate phosphine ligand
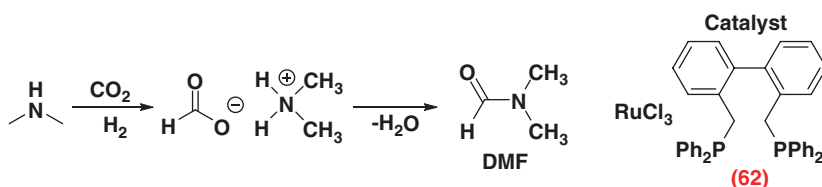
Scheme 24   Process for the synthesis of DMF from CO_2 catalyzed by ruthenium (**62**)
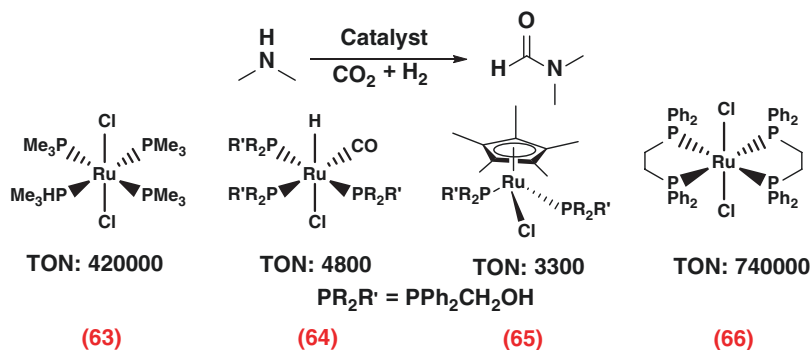
Scheme 25 Homogenous catalyst for synthesizing DMF using scCO_2

requires high pressure CO_2 (13 MPa) and H_2 (8.5 MPa). The TOF obtained as 360,000 h^{-1} (TON 740,000) at 353 K in 2 h is suggested as a superior catalyst when compared to others [172].

3.2.10 Oxalate

It is known that two molecules of CO_2 combining with one molecule of H_2 can produce one molecule of oxalic acid. However, such reactions are certainly the most demanding in view of the atom economy approach.

In this direction, recently in 2014, the conversion of CO_2 to oxalate catalyzed by copper complexes is reported by Maverick and co-workers [173]. The Cu-complex (**67**) when treated with sodium ascorbate in DMF, under nitrogen, gives the reduced complex as yellow solid, which is stable (Scheme 26). This reduced complex reacts with CO_2 and produces the oxalate-bridged Cu(II) dimer. The oxalate is released upon treating with acid. When the complex is allowed to evaporate slowly in the air, the complex traps selectively CO_2 and leads to form oxalate with a yield of up to 96% as shown in Scheme 26 [173]. In addition, there are few reports existing on oxalic acid synthesis via electrochemical methods [174].

3.2.11 Hydrocarbon

The third category is the complete reduction of CO_2 to hydrocarbons using the stoichiometric or excess of hydrogen. The methane is the major hydrocarbon generally obtained upon the process of CO_2 hydrogenation. The other hydrocarbon derivatives such as higher or α-olefin are known to have wide applications such as lubricants, detergents, and polyolefins. In addition, hydrocarbons are used as fuels and energy materials [175]. The direct route of converting CO_2 into hydrocarbons has been developed based on Fischer-Tropsch synthesis (FTS). The FTS involves a two-step process: (1) the reduction of inert CO_2 to active CO by reverse water gas shift
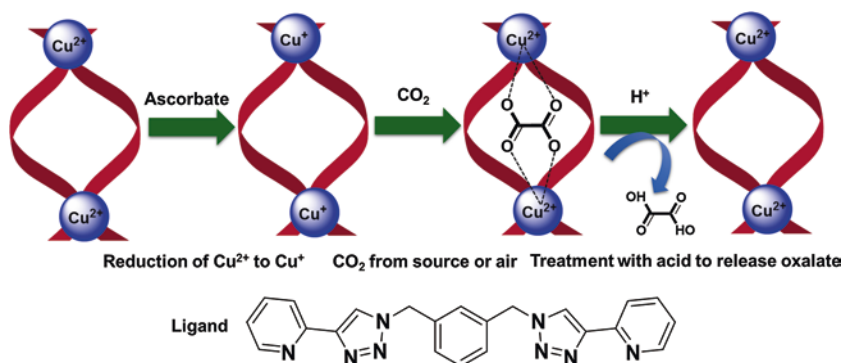
Scheme 26 Synthesis of oxalate using copper catalysts and CO_2 from atmosphere catalyzed by $[Cu_2L_2]$ (**67**)

Scheme 27 Zr complex (**68**) for methane synthesis
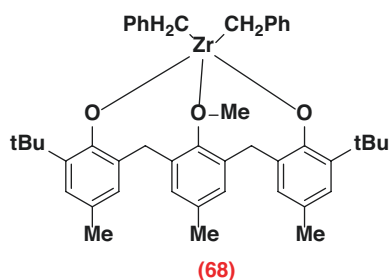
(RWGS) reaction and (2) the hydrogenation of CO to hydrocarbons using molecular hydrogen. The catalyst used should be active in both RWGS and FTS. The indirect route for hydrocarbon synthesis is enrouted via methanol, i.e., the conversion of CO_2 into methanol and subsequent transformation into hydrocarbons such as olefins, LPG, gasoline, aromatics, and so on [17].

In 2006, H. Kawaguchi has reported a zirconium benzyl phenoxide complex (**68**) for the synthesis of methane from CO_2 and hydrosilane (Scheme 27). In the presence of $B(C_6F_5)_3$, the effective conversion was achieved at ambient conditions [176].

Recently, Chen established the conversion of CO_2 to methane using the boron-aluminum catalytic system (Scheme 28). Here, the $HSiEt_3$ is used as the hydrogen source, and the respective yield was observed up to 94%. The mixed catalytic system (**69a**, **69b**) combinedly plays the role of selective reduction process. The catalyst **69a** initially converts CO_2 into $HCOOSiEt_3$, followed by the consecutive reduction of intermediate ($HCOOSiEt_3$) which is catalyzed by **69b** as shown in Scheme 28. The mechanistic investigations established as the reaction proceed through formaldehyde intermediate [177].
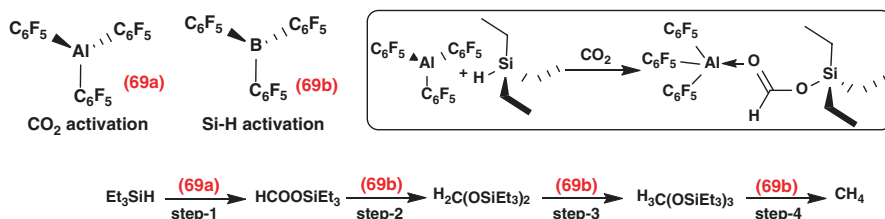
Scheme 28 Synthesis of methane using aluminum and boron catalysts

4 Summary

Carbon dioxide conversion to fine chemicals, fuels, etc. is attractive and fascinating in the area of catalysis with wide opportunities and enormous challenges. A reasonably significant number of technologies are already developed for the CO$_2$ capture, transport, sequestration, and utilization. Several industrial methods have already been developed and promoted to mitigate atmospheric CO$_2$ so that they need not simply be stored. In addition, there are various commodity chemicals derived from CO$_2$, and many excellent catalysts are developed for the conversion of CO$_2$ in atmospheric condition.

The artificial photosynthesis process, i.e., synthesis of carbohydrates using CO$_2$ and water with efficient catalyst, is a challenging reaction and yet needs to be addressed. However, there are few points to consider. (1) The process involves the conversion of CO$_2$ to chemicals/fuels and requires huge energy which releases CO$_2$. (2) The industries that utilize the CO$_2$ would be very trace when compared to the amount of CO$_2$ dumped into the atmosphere by fossil fuel combustion. (3) In addition, the molecules or fine chemicals obtained by CO$_2$ fixation will also emit CO$_2$ when disposed. Hence, the controlled emission of CO$_2$ into the atmosphere and the effective utilization of CO$_2$ are great global challenges.

References

1. Monastersky R (2013) Global carbon dioxide levels near worrisome milestone. Nature 497:13
2. Aresta M (2010) Carbon dioxide: utilization options to reduce its accumulation in the atmosphere. Wiley-VCH, Weinheim
3. Kätelhön A, Meys R, Deutz S, Suh S, Bardow A (2019) Climate change mitigation potential of carbon capture and utilization in the chemical industry. Proc Natl Acad Sci U S A 116(23):11187–11194
4. Hansen J, Ruedy R, Sato M, Lo K (2010) Global surface temperature change. Rev Geophys 48:RG4004

5. Rayner CM (2007) The potential of carbon dioxide in synthetic organic chemistry. Org Process Res Dev 11:121–132
6. Sakakura T, Choi J-C, Yasuda H (2007) Transformation of carbon dioxide. Chem Rev 107:2365–2387
7. Yang Y, Lee J-W (2019) Toward ideal carbon dioxide functionalization. Chem Sci 10:3905
8. Darensbourg DJ (2010) Chemistry of carbon dioxide relevant to its utilization: a personal perspective. Inorg Chem 49:10765–10780
9. Paparo A, Okuda J (2017) Carbon dioxide complexes: bonding modes and synthetic methods. Coord Chem Rev 334:136–149
10. Yu B, He L-N (2015) Upgrading carbon dioxide by incorporation into heterocycles. ChemSusChem 8:52–62
11. Müller TE, Leitner W (2015) CO_2 chemistry. Beilstein J Org Chem 2015(11):675–677
12. Yang Z-Z, He L-N, Zhao Y-N, Li B, Yu B (2011) CO_2 capture and activation by superbase/polyethylene glycol and its subsequent conversion. Energy Environ Sci 4:3971–3975
13. Kayaki Y, Yamamoto M, Ikariya T (2009) N-heterocyclic carbenes as efficient organocatalysts for CO_2 fixation reactions. Angew Chem Int Ed 48:4194–4197
14. Wang Y-B, Wang Y-M, Zhang W-Z, Lu X-B (2013) Fast CO_2 sequestration, activation, and catalytic transformation using N-heterocyclic olefins. J Am Chem Soc 135:11996–12003
15. Aresta M, Nobile CF, Albano VG, Forni E, Manassero M (1975) New nickel–carbon dioxide complex: synthesis, properties, and crystallographic characterization of (carbon dioxide)-bis(tricyclohexylphosphine)nickel. J Chem Soc Chem Commun:636–637
16. Song Q-W, Zhou Z-H, He L-N (2017) Efficient, selective and sustainable catalysis of carbon dioxide. Green Chem 19:3707–3728
17. Centi G, Quadrelli EA, Perathoner S (2013) Catalysis for CO_2 conversion: a key technology for rapid introduction of renewable energy in the value chain of chemical industries. Energy Environ Sci 6:1711–1731
18. Burke MJ, Stephens JC (2018) Political power and renewable energy futures: a critical review. Energy Res Soc Sci 35:78–93
19. Ansari MB, Park S-E (2012) Carbon dioxide utilization as a soft oxidant and promoter in catalysis. Energy Environ Sci 5:9419
20. Artz J, Müller TE, Thenert K, Kleinekorte J, Meys R, Sternberg A, Bardow A, Leitner W (2018) Sustainable conversion of carbon dioxide: an integrated review of catalysis and life cycle assessment. Chem Rev 118:434–504
21. Banerjee A, Dick GR, Yoshino T, Kanan MW (2016) Carbon dioxide utilization via carbonate-promoted C–H carboxylation. Nature 531:215
22. Liu Q, Wu L, Jackstell R, Beller M (2015) Using carbon dioxide as a building block in organic synthesis. Nat Commun 6:5933–5948
23. Klankermayer J, Leitner W (2015) Love at second sight for CO_2 and H_2 in organic synthesis. Science 350:629–630
24. Grim RG, Huang Z, Guarnieri MT, Ferrell JR III, Tao L, Schaidle JA (2020) Transforming the carbon economy: challenges and opportunities in the convergence of low-cost electricity and reductive CO_2 utilization. Energy Environ Sci 13:472. https://doi.org/10.1039/C9EE02410G
25. Aresta M, Dibenedetto A, Quaranta E (2016) State of the art and perspectives in catalytic processes for CO_2 conversion into chemicals and fuels: the distinctive contribution of chemical catalysis and biotechnology. J Catal 343:2–45
26. Rochelle GT (2009) Amine scrubbing for CO_2 capture. Science 325:1652–1654
27. Keith DW (2009) Why capture CO_2 from the atmosphere? Science 2009(325):1654–1655
28. D'Alessandro DM, Smit B, Long JR (2010) Carbon dioxide capture: prospects for new materials. Angew Chem Int Ed 49:6058–6082
29. Spigarelli BP, Kawatra SK (2013) Opportunities and challenges in carbon dioxide capture. J CO2 Util 1:69–87
30. MacDowell N, Florin N, Buchard A, Hallett J, Galindo A, Jackson G, Adjiman CS, Williams CK, Shah N, Fennell P (2010) An overview of CO_2 capture technologies. Energy Environ Sci 3:1645–1669

31. Markewitz P, Kuckshinrichs W, Leitner W, Linssen J, Zapp P, Bongartz R, Schreiber A, Müller TE (2012) Worldwide innovations in the development of carbon capture technologies and the utilization of CO$_2$. Energy Environ Sci 5:7281–7305

32. Qi G, Fu L, Giannelis EP (2014) Sponges with covalently tethered amines for high-efficiency carbon capture. Nat Commun 5:5796

33. Freeman SA, Dugas R, van Wagener DH, Nguyen T, Rochelle GT (2010) Carbon dioxide capture with concentrated, aqueous piperazine. Int J Greenh Gas Control 4:119–124

34. Goeppert A, Zhang H, Czaun M, May RB, Prakash GKS, Olah GA, Narayanan SR (2014) Easily regenerable solid adsorbents based on polyamines for carbon dioxide capture from the air. ChemSusChem 7:1386–1397

35. Otto A, Grube T, Schiebahn S, Stolten D (2015) Closing the loop: captured CO$_2$ as a feedstock in the chemical industry. Energy Environ Sci 8:3283–3297

36. Chaikittisilp W, Khunsupat R, Chen TT, Jones CW (2011) Poly(allylamine)–mesoporous silica composite materials for CO$_2$ capture from simulated flue gas or ambient air. Ind Eng Chem Res 50:14203–14210

37. Serna-Guerrero R, Da'na E, Sayari A (2008) New insights into the interactions of CO$_2$ with amine-functionalized silica. Ind Eng Chem Res 47:9406–9412

38. Xu XC, Song CS, Andresen JM, Miller BG, Scaroni AW (2002) Novel polyethylenimine-modified mesoporous molecular sieve of MCM-41 type as high-capacity adsorbent for CO$_2$ capture. Energy Fuel 16:1463–1469

39. Gurkan BE, de la Fuente JC, Mindrup EM, Ficke LE, Goodrich BF, Price EA, Schneider WF, Brennecke JF (2010) Equimolar CO$_2$ absorption by anion-functionalized ionic liquids. J Am Chem Soc 132:2116–2117

40. Karadas F, Atilhan M, Aparicio S (2010) Review on the use of ionic liquids (ILs) as alternative fluids for CO$_2$ capture and natural gas sweetening. Energy Fuel 24:5817–5828

41. Kim J, Lin LC, Swisher JA, Haranczyk M, Smit B (2012) Predicting large CO$_2$ adsorption in aluminosilicate zeolites for post combustion carbon dioxide capture. J Am Chem Soc 134:18940–18943

42. Remy T, Peter SA, Van Tendeloo L, Van der Perre S, Lorgouilloux Y, Kirschhock C, Baron GV, Denayer JFM (2013) Adsorption and separation of CO$_2$ on KFI zeolites: effect of cation type and Si/Al ratio on equilibrium and kinetic properties. Langmuir 29:4998–5012

43. Li JR (2011) Carbon dioxide capture-related gas adsorption and separation in metal-organic frameworks. Coord Chem Rev 255:1791–1823

44. Millward AR, Yaghi OM (2005) Metal–organic frameworks with exceptionally high capacity for storage of carbon dioxide at room temperature. J Am Chem Soc 127:17998–17999

45. Li JR, Sculley J, Zhou HC (2012) Metal–organic frameworks for separations. Chem Rev 112:869–932

46. Tsapatsis M (2011) Toward high-throughput zeolite membranes. Science 334:767–768

47. Sublet J, Pera-Titus M, Guilhaume N, Farrusseng D, Schrive L, Chanaud P, Siret B, Durécu S (2011) Technico-economical assessment of MFI-type zeolite membranes for CO$_2$ capture from post combustion flue gases. AICHE J 58:3183–3194

48. Yampolskii Y (2012) Polymeric gas separation membranes. Macromolecules 45:3298–3311

49. Merkel TC, Lin H, Wei X, Baker R (2010) Power plant post-combustion carbon dioxide capture: an opportunity for membranes. J Membr Sci 359:126–139

50. Merkel TC, Zhou M, Baker RW (2012) Carbon dioxide capture with membranes at an IGCC power plant. J Membr Sci 389:441–450

51. Qiu S, Xue M, Zhu G (2014) Metal–organic framework membranes: from synthesis to separation application. Chem Soc Rev 43:6116–6140

52. Vinh-Thang H, Kaliaguine S (2013) Predictive models for mixed matrix membrane performance: a review. Chem Rev 113:4980–5028

53. Sanz-Pérez ES, Murdock CR, Didas SA, Jones CW (2016) Direct capture of CO$_2$ from ambient air. Chem Rev 116:11840–11876

54. Major CJ, Sollami BJ, Kammermeyer K (1965) Carbon dioxide removal from air by adsorbents. Ind Eng Chem Process Des Dev 4:327–333

55. Wurzbacher JA, Gebald C, Piatkowski N, Steinfeld A (2012) Concurrent separation of CO_2 and H_2O from air by a temperature vacuum swing adsorption/desorption cycle. Environ Sci Technol 46:9191–9198
56. Goeppert A, Czaun M, Prakash GKS, Olah GA (2012) Air as the renewable carbon source of the future: an overview of CO_2 capture from the atmosphere. Energy Environ Sci 5:7853–7833
57. The American Physical Society (2011) Direct air capture of CO_2 with chemicals; A technology assessment for the APS panel on public affairs. The American Physical Society, College Park, MD
58. Mazzotti M, Baciocchi R, Desmond MJ, Socolow RH (2013) Direct air capture of CO_2 with chemicals: optimization of a two-loop hydroxide carbonate system using a counter current air-liquid contactor. Clim Chang 118:119–135
59. Lackner KS, Grimes P, Ziock H (1999) Carbon dioxide extraction from air? LAUR-99-5113. Los Alamos National Laboratory, Los Alamos, NM
60. Gebald C, Wurzbacher JA, Tingaut P, Zimmermann T, Steinfeld A (2011) Amine-based nano-fibrillated cellulose as adsorbent for CO_2 capture from air. Environ Sci Technol 45:9101–9108
61. Zhu Q (2019) Developments on CO_2-utilization technologies. Clean Energ 3:85–100
62. Yuan Z, Eden MR (2016) Toward the development and deployment of large-scale carbon dioxide capture and conversion processes. Ind Eng Chem Res 55:3383–3419
63. Alper E, Yuksel-Orhan O (2017) CO_2 utilization: developments in conversion processes. Petroleum 3:109–126
64. Ma J, Sun N, Zhang X, Zhao N, Xiao F, Wei W, Sun Y (2009) A short review of catalysis for CO_2 conversion. Catal Today 148:221–231
65. Pérez-Fortes M, Schöneberger JC, Boulamanti A, Tzimas E (2016) Methanol synthesis using captured CO_2 as raw material: techno-economic and environmental assessment. Appl Energy 161:718–732
66. Rosas-Hernandez A, Steinlechner C, Junge H, Beller M (2018) Photo- and electrochemical valorization of carbon dioxide using earth-abundant molecular catalysts. Top Curr Chem 376:1
67. Leung C-F, Ho P-Y (2019) Molecular catalysis for utilizing CO_2 in fuel electro-generation and in chemical feedstock. Catalysts 9:760
68. Quadrelli EA, Centi G, Duplan J-L, Perathoner S (2011) Carbon dioxide recycling: emerging large-scale technologies with industrial potential. ChemSusChem 4:1194–1215
69. Guo W, Gónzalez-Fabra J, Bandeira NAG, Bo C, Kleij AW (2015) A metal-free synthesis of N-aryl carbamates under ambient conditions. Angew Chem Int Ed 54:11686–11690
70. Fukuoka S, Kawamura M, Komiya K, Tojo M, Hachiya H, Hasegawa K, Aminaka M, Okamoto H, Fukawa I, Konno S (2003) A novel non-phosgene polycarbonate production process using by-product CO_2 as starting material. Green Chem 5:497–507
71. Maisonneuve L, Lamarzelle O, Rix E, Grau E, Cramail H (2015) Isocyanate-free routes to polyurethanes and poly(hydroxy urethane)s. Chem Rev 115:12407–12439
72. Schäffner B, Schäffner F, Verevkin SP, Börner A (2010) Organic carbonates as solvents in synthesis and catalysis. Chem Rev 110:4554–4581
73. Lawrenson SB, Arav R, North M (2017) The greening of peptide synthesis. Green Chem 19:1685–1691
74. Sakakura T, Kohno K (2009) The synthesis of organic carbonates from carbon dioxide. Chem Commun:1312–1330
75. Guo W, Kuniyil R, Gómez JE, Maseras F, Kleij AW (2018) A domino process toward functionally dense quaternary carbons through Pd-catalyzed decarboxylative C(sp^3)–C(sp^3) bond formation. J Am Chem Soc 140:3981–3987
76. Han L, Park M-S, Choi S-J, Kim Y-J, Lee S-M, Park D-W (2012) Incorporation of metal ions into silica-grafted imidazolium-based ionic liquids to efficiently catalyze cycloaddition reactions of CO_2 and epoxides. Catal Lett 142:259–265
77. Chen F, Dong T, Chi Y, Xu Y, Hu C (2010) Transition-metal-substituted Keggin-type germanotungstates for catalytic conversion of carbon dioxide to cyclic carbonate. Catal Lett 139:38–41

78. Felder SE, Redding MJ, Noel A, Grayson SM, Wooley KL (2018) Organocatalyzed ROP of a glucopyranoside derived five-membered cyclic carbonate. Macromolecules 51:1787–1797

79. Scrosati B, Hassoun J, Sun Y-K (2011) Lithium-ion batteries. A look into the future. Energy Environ Sci 4:3287–3295

80. Guerin W, Diallo AK, Kirilov E, Helou M, Slawinski M, Brusson J-M, Carpentier J-F, Guillaume SM (2014) Enantiopure isotactic PCHC synthesized by ring-opening polymerization of cyclohexene carbonate. Macromolecules 47:4230–4235

81. Parker HL, Sherwood J, Hunt AJ, Clark JH (2014) Cyclic carbonates as green alternative solvents for the Heck reaction. ACS Sustain Chem Eng 2:1739–1742

82. Buttner H, Longwitz L, Steinbauer J, Wulf C, Werner T (2017) Recent developments in the synthesis of cyclic carbonates from epoxides and CO_2. Top Curr Chem 375:50

83. Maeda C, Miyazaki Y, Ema T (2014) Recent progress in catalytic conversions of carbon dioxide. Catal Sci Technol 4:1482–1497

84. Melendez J, North M, Pasquale R (2007) Synthesis of cyclic carbonates from atmospheric pressure carbon dioxide using exceptionally active aluminium (salen) complexes as catalysts. Eur J Inorg Chem 21:3323–3326

85. Castro-Osma JA, North M, Wu X (2014) Development of a halide-free aluminium-based catalyst for the synthesis of cyclic carbonates from epoxides and carbon dioxide. Chem Eur J 20:15005–15008

86. Melendez J, North M, Villuendas P (2009) One-component catalysts for cyclic carbonate synthesis. Chem Commun 45:2577–2579

87. Melendez J, North M, Villuendas P, Young C (2011) One-component bimetallic aluminium(salen)-based catalysts for cyclic carbonate synthesis and their immobilization. Dalton Trans 40:3885–3902

88. North M, Villuendas P, Young C (2012) Inter- and intramolecular phosphonium salt cocatalysis in cyclic carbonate synthesis catalysed by a bimetallic aluminium(salen) complex. Tetrahedron Lett 53:2736–2740

89. Castro-Osma JA, North M, Wu X (2016) Synthesis of cyclic carbonates catalysed by chromium and aluminium salphen complexes. Chem Eur J 22:2100–2107

90. Whiteoak CJ, Martin E, Belmonte MM, Benet-Buchholz J, Kleij AW (2012) An efficient iron catalyst for the synthesis of five- and six-membered organic carbonates under mild conditions. Adv Synth Catal 354:469–476

91. Whiteoak CJ, Kielland N, Laserna V, Escudero-Adan EC, Martin E, Kleij AW (2013) A powerful aluminum catalyst for the synthesis of highly functional organic carbonates. J Am Chem Soc 135:1228–1231

92. Xu B, Wang P, Lv M, Yuan D, Yao Y (2016) Transformation of carbon dioxide into oxazolidinones and cyclic carbonates catalyzed by rare-earth-metal phenolates. ChemCatChem 8:2466–2471

93. Qin J, Wang P, Li Q, Zhang Y, Yuan D, Yao Y (2014) Catalytic production of cyclic carbonates mediated by lanthanide phenolates under mild conditions. Chem Commun 50:10952–10955

94. Gao P, Zhao Z, Chen L, Yuan D, Yao Y (2016) Dinuclear aluminum poly(phenolate) complexes as efficient catalysts for cyclic carbonate synthesis. Organometallics 35:1707–1712

95. Zhao D, Liu X-H, Shi Z-Z, Zhu C-D, Zhao Y, Wang P, Sun W-Y (2016) Three powerful dinuclear metal–organic catalysts for converting CO_2 into organic carbonates. Dalton Trans 45:14184–14190

96. Xie Y, Wang T-T, Liu X-H, Zou K, Deng W-Q (2013) Capture and conversion of CO_2 at ambient conditions by a conjugated microporous polymer. Nat Commun 4:1960

97. Xie Y, Wang T-T, Yang R-X, Huang N-Y, Zou K, Deng W-Q (2014) Efficient fixation of CO_2 by a zinc-coordinated conjugated microporous polymer. ChemSusChem 7:2110–2114

98. Arunachalam R, Chinnaraja E, Valkonen A, Rissanen K, Subramanian PS (2019) Bifunctional coordination polymers as efficient catalyst for carbon dioxide conversion. Appl Organomet Chem 33:e5202

99. Maeda C, Taniguchi T, Ogawa K, Ema T (2015) Bifunctional catalysts based on *m*-phenylene-bridged porphyrin dimer and trimer platforms: synthesis of cyclic carbonates from carbon dioxide and epoxides. Angew Chem Int Ed 54:134–138

100. Ema T, Miyazaki Y, Shimonishi J, Maeda C, Hasegawa J (2014) Bifunctional porphyrin catalysts for the synthesis of cyclic carbonates from epoxides and CO_2: structural optimization and mechanistic study. J Am Chem Soc 136:15270–15279

101. Jayakumar S, Li H, Tao L, Li C, Liu L, Chen J, Yang Q (2018) Cationic Zn-porphyrin immobilized in mesoporous silicas as bifunctional catalyst for CO_2 cycloaddition reaction under cocatalyst free conditions. ACS Sustain Chem Eng 6:9237–9245

102. Wu X, Castro-Osma JA, North M (2016) Synthesis of chiral cyclic carbonates via kinetic resolution of racemic epoxides and carbon dioxide. Symmetry 8:4

103. Paddock RL, Nguyen ST (2004) Chiral(salen) Co^{III} catalyst for the synthesis of cyclic carbonates. Chem Commun:1622–1623

104. Ren WM, Wu GP, Lin F, Jiang JY, Liu C, Luo Y, Lu XB (2012) Role of the co-catalyst in the asymmetric coupling of racemic epoxides with CO_2 using multi chiral Co(III) complexes: product selectivity and enantioselectivity. Chem Sci 3:2094–2102

105. Honda M, Tamura M, Nakao K, Suzuki K, Nakagawa Y, Tomishige K (2014) Direct cyclic carbonate synthesis from CO_2 and diol over carboxylation/hydration cascade catalyst of CeO_2 with 2-Cyanopyridine. ACS Catal 4:1893–1896

106. Tamura M, Ito K, Honda M, Nakagawa Y, Sugimoto H, Tomishige K (2016) Direct copolymerization of CO_2 and Diols. Sci Rep 6:24038

107. Cheng M, Lobkovsky EB, Coates GW (1998) Catalytic reactions involving C1 feedstocks: new high-activity Zn(II)-based catalysts for the alternating copolymerization of carbon dioxide and epoxides. J Am Chem Soc 120:11018–11019

108. Nozaki K, Nakano K, Hiyama T (1999) Optically active polycarbonates: asymmetric alternating copolymerization of cyclohexene oxide and carbon dioxide. J Am Chem Soc 121:11008–11009

109. Moore DR, Cheng M, Lobkovsky EB, Coates GW (2003) Mechanism of the alternating copolymerization of epoxides and CO_2 using β-diiminate zinc catalysts: evidence for a bimetallic epoxide enchainment. J Am Chem Soc 125:11911–11924

110. Kember MR, Knight PD, Reung PTR, Williams CK (2009) Highly active dizinc catalyst for the copolymerization of carbon dioxide and cyclohexene oxide at one atmosphere pressure. Angew Chem Int Ed 48:931–933

111. Nakano K, Kobayashi K, Ohkawara T, Imoto H, Nozaki K (2013) Copolymerization of epoxides with carbon dioxide catalyzed by iron–corrole complexes: synthesis of a crystalline copolymer. J Am Chem Soc 135:8456–8459

112. Chaemchuen S, Semyonov OV, Dingemans J, Xu W, Zhuiykov S, Khan A, Verpoort F (2019) Progress on catalyst development for direct synthesis of dimethyl carbonate from CO_2 and methanol. Chem Afr 2:533. https://doi.org/10.1007/s42250-019-00082-x

113. Gong J, Ma X, Wang S (2007) Phosgene-free approaches to catalytic synthesis of diphenyl carbonate and its intermediates. Appl Catal A Gen 316:1–21

114. Pacheco MA, Marshall CL (1997) Review of dimethyl carbonate (DMC) manufacture and its characteristics as a fuel additive. Energy Fuel 11:2–29

115. Saeidi S, Amin NAS, Rahimpour MR (2014) Hydrogenation of CO_2 to value added products—a review and potential future developments. J CO2 Util 5:66–81

116. Wang W, Wang S, Ma X, Gong J (2011) Recent advances in catalytic hydrogenation of carbon dioxide. Chem Soc Rev 40:3703–3727

117. Ganesh I (2014) Conversion of carbon dioxide into methanol—a potential liquid fuel: fundamental challenges and opportunities (a review). Renew Sust Energ Rev 31:221–257

118. Behrens M, Zander S, Kurr P, Jacobsen N, Senker J, Koch G, Ressler T, Fischer RW, Schlogl R (2013) Performance improvement of nanocatalysts by promoter-induced defects in the support material: methanol synthesis over Cu/ZnO:Al. J Am Chem Soc 135:6061–6068

119. Li Y-N, Ma R, He L-N, Diao Z-F (2014) Homogeneous hydrogenation of carbon dioxide to methanol. Catal Sci Technol 4:1498–1512

120. Tominaga KI, Sasaki Y, Kawai M, Watanabe T, Saito M (1993) Ruthenium complex catalysed hydrogenation of carbon dioxide to carbon monoxide, methanol and methane. J Chem Soc Chem Commun:629–631

121. Tominaga K, Sasaki Y, Watanabe T, Saito M (1995) Homogeneous hydrogenation of carbon dioxide to methanol catalyzed by ruthenium cluster anions in the presence of halide anions. Bull Chem Soc Jpn 68:2837–2842

122. Huff CA, Sanford MS (2011) Cascade catalysis for the homogeneous hydrogenation of CO₂ to methanol. J Am Chem Soc 133:18122–18125

123. Wesselbaum S, Moha V, Meuresch M, Brosinski S, Thenert KM, Kothe J, vom Stein T, Englert U, Hölscher M, Klankermayer J, Leitner W (2015) Hydrogenation of carbon dioxide to methanol using a homogeneous ruthenium–triphos catalyst: from mechanistic investigations to multiphase catalysis. Chem Sci 6:693–704

124. Kothandaraman J, Goeppert A, Czaun M, Olah GA, Prakash GKS (2016) Conversion of CO₂ from air into methanol using a polyamine and a homogeneous ruthenium catalyst. J Am Chem Soc 138:778–781

125. Kar S, Goeppert A, Kothandaraman J, Prakash GKS (2017) Manganese catalyzed sequential hydrogenation of CO₂ to methanol via formamide. ACS Catal 7:6347–6351

126. Schneidewind J, Adam R, Baumann W, Jackstell R, Beller M (2017) Low-temperature hydrogenation of carbon dioxide to methanol with a homogeneous cobalt catalyst. Angew Chem Int Ed 56:1890–1893

127. Ribeiro APC, Martins LMDRS, Pombeiro AJL (2017) Carbon dioxide-to-methanol single-pot conversion using a cscorpionate iron(II) catalyst. Green Chem 19:4811–4815

128. Tsurusaki A, Murata K, Onishi N, Sordakis K, Laurenczy G, Himeda Y (2017) Investigation of hydrogenation of formic acid to methanol using H₂ or formic acid as a hydrogen source. ACS Catal 7:1123–1131

129. Eisenschmid TG, Eisenberg R (1989) The iridium complex catalyzed reduction of carbon dioxide to methoxide by alkylsilanes. Organometallics 8:1822–1824

130. Huang F, Zhang CG, Jiang JL, Wang ZX, Guan HR (2011) How does the nickel pincer complex catalyze the conversion of CO₂ to a methanol derivative? A computational mechanistic study. Inorg Chem 50:3816–3825

131. Chakraborty S, Zhang J, Krause JA, Guan H (2010) An efficient nickel catalyst for the reduction of carbon dioxide with a borane. J Am Chem Soc 132:8872–8873

132. Scheuermann ML, Semproni SP, Pappas I, Chirik PJ (2014) Carbon dioxide hydrosilylation promoted by cobalt pincer complexes. Inorg Chem 53:9463–9465

133. Metsanen TT, Oestreich M (2015) Temperature-dependent chemoselective hydrosilylation of carbon dioxide to formaldehyde or methanol oxidation state. Organometallics 2015(34):543–546

134. Mazzotta MG, Xiong M, Abu-Omar MM (2017) Carbon dioxide reduction to silyl-protected methanol catalyzed by an oxorhenium pincer PNN complex. Organometallics 36:1688–1691

135. Morris DS, Weetman C, Wennmacher JTC, Cokoja M, Drees M, Kühn FE, Love JB (2017) Reduction of carbon dioxide and organic carbonyls by hydrosilanes catalysed by the perrhenate anion. Catal Sci Technol 7:2838–2845

136. Bertini F, Glatz M, Stöger B, Peruzzini M, Veiros LF, Kirchner K, Gonsalvi L (2019) Carbon dioxide reduction to methanol catalyzed by Mn(I) PNP pincer complexes under mild reaction conditions. ACS Catal 9:632–639

137. Enthaler S, von Langermann J, Schmidt T (2010) Carbon dioxide and formic acid-the couple for environmental-friendly hydrogen storage? Energy Environ Sci 3:1207–1217

138. Joo F (2008) Breakthroughs in hydrogen storage-formic acid as a sustainable storage material for hydrogen. ChemSusChem 1:805–808

139. Grasemann M, Laurenczy G (2012) Formic acid as a hydrogen source recent developments and future trends. Energy Environ Sci 5:8171–8181

140. Barnard JH, Wang C, Berry NG, Xiao JL (2013) Long-range metal-ligand bifunctional catalysis: cyclometallated iridium catalysts for the mild and rapid dehydrogenation of formic acid. Chem Sci 4:1234–1244

141. Inoue Y, Izumida H, Sasaki Y, Hashimoto H (1976) Catalytic fixation of carbon dioxide to formic acid by transition-metal complexes under mild conditions. Chem Lett 863-864

142. Gassner F, Leitner W (1993) CO_2 Activation 3. Hydrogenation of carbon dioxide to formic acid using water-soluble rhodium catalysts. J Chem Soc Chem Commun 19:1465–1466

143. Hayashi H, Ogo S, Fukuzumi S (2004) Aqueous hydrogenation of carbon dioxide catalysed by water-soluble ruthenium aqua complexes under acidic conditions. Chem Commun:2714–2715

144. Moret S, Dyson PJ, Laurenczy G (2014) Direct synthesis of formic acid from carbon dioxide by hydrogenation in acidic media. Nat Commun 5:4017

145. Rohmann K, Kothe J, Haenel MW, Englert U, Hçlscher M, Leitner W (2016) Hydrogenation of CO_2 to formic acid with a highly active ruthenium acriphos complex in DMSO and DMSO/Water. Angew Chem Int Ed 55:8966–8969

146. Jeletic MS, Mock MT, Appel AM, Linehan JC (2013) A cobalt-based catalyst for the hydrogenation of CO_2 under ambient conditions. J Am Chem Soc 135:11533–11536

147. Zall CM, Linehan JC, Appel AM (2015) A molecular copper catalyst for hydrogenation of CO_2 to formate. ACS Catal 5:5301–5305

148. Eckenhoff WT, Garrity ST, Pintauer T (2008) Highly efficient copper-mediated atom-transfer radical addition (ATRA) in the presence of reducing agent. Eur J Inorg Chem 4:620–627

149. Himeda Y, Onozawa-Komatsuzaki N, Sugihara H, Kasuga K (2007) Simultaneous tuning of activity and water solubility of complex catalysts by acid–base equilibrium of ligands for conversion of carbon dioxide. Organometallics 26:702–712

150. Federsel C, Jackstell R, Beller M (2010) State-of-the-art catalysts for hydrogenation of carbon dioxide. Angew Chem Int Ed 49:6254–6257

151. Schmeier TJ, Dobereiner GE, Crabtree RH, Hazari N (2011) Secondary coordination sphere interactions facilitate the insertion step in an iridium(III) CO_2 reduction catalyst. J Am Chem Soc 133:9274–9277

152. Ahn ST, Bielinski EA, Lane EM, Chen Y, Bernskoetter WH, Hazari N, Palmore GTR (2015) Enhanced CO_2 electroreduction efficiency through secondary coordination effects on a pincer iridium catalyst. Chem Commun 51:5947–5950

153. Sanz S, Benitez M, Peris E (2010) A new approach to the reduction of carbon dioxide: CO_2 reduction to formate by transfer hydrogenation in iPrOH. Organometallics 29:275–277

154. Azua A, Sanz S, Peris E (2011) Water-soluble Ir(III) N-heterocyclic carbene based catalysts for the reduction of CO_2 to formate by transfer hydrogenation and the deuteration of aryl amines in water. Chemistry 17:3963–3967

155. Jones JH (2000) The Cativa™ process for the manufacture of acetic acid. Platin Met Rev 44:94–105

156. Huang W, Xie KC, Wang JP, Gao ZH, Yin LH, Zhu QM (2001) Possibility of direct conversion of CH_4 and CO_2 to high-value products. J Catal 201:100–104

157. Wu JF, Yu SM, Wang WD, Fan YX, Bai S, Zhang CW, Gao Q, Huang J, Wang W (2013) Mechanistic insight into the formation of acetic acid from the direct conversion of methane and carbon dioxide on zinc-modified H-ZSM-5 zeolite. J Am Chem Soc 135:13567–13573

158. Fukuoka A, Gotoh N, Kobayashi N, Hirano M, Komiya S (1995) Homogeneous bimetallic catalysts for production of carboxylic acids from carbon dioxide, hydrogenation, and organic iodides. Chem Lett 24:567–568

159. Qian Q, Zhang J, Cui M, Han B (2016) Synthesis of acetic acid via methanol hydrocarboxylation with CO_2 and H_2. Nat Commun 7:11481

160. Wang X, Wang H, Sun Y (2017) Synthesis of acrylic acid derivatives from CO_2 and ethylene. Chemistry 2:211–228

161. Limbach M (2015) Chapter Four: Acrylates from alkenes and CO_2, the stuff that dreams are made of. In: Pérez PJ (ed) Advances in organometallic chemistry. Academic Press, New York, NY, pp 175–202

162. Weissermel K, Arpe HJ (1997) Industrial organic chemistry. VCH ver-lagsgesellschaft, Weinheim
163. Lejkowski ML, Lindner R, Kageyama T, Bdizs G, Plessow PN, Muller IB, Schafer A, Rominger F, Hofmann P, Futter C, Schunk SA, Limbach M (2012) The first catalytic synthesis of an acrylate from CO_2 and an alkene-A rational approach. Chem Eur J 18:14017–14025
164. Saito S, Nakagawa S, Koizumi T, Hirayama K, Yamamoto YJ (1999) Nickel-mediated regio- and chemoselective carboxylation of alkynes in the presence of carbon dioxide. Org Chem 64:3975–3978
165. Takimoto M, Mori M (2001) Cross-coupling reaction of oxo-π-allylnickel complex generated from 1,3-Diene under an atmosphere of carbon dioxide. J Am Chem Soc 123:2895–2896
166. Takimoto M, Kawamura M, Mori M (2003) Nickel (0)-mediated sequential addition of carbon dioxide and aryl aldehydes into terminal allenes. Org Lett 5:2599–2601
167. Aoki M, Kaneko M, Izumi S, Ukai K, Iwasawa N (2004) Bidentate amidine ligands for nickel(0)-mediated coupling of carbon dioxide with unsaturated hydrocarbons. Chem Commun:2568–2569
168. Kuhlmann R, Prüllage A, Künnemann K, Behr A, Vorholt AJ (2017) Process development of the continuously operated synthesis of N, N-dimethylformamide based on carbon dioxide. J CO2 Util 22:184–190
169. Olmos A, Asensio G, Pérez PJ (2016) Homogeneous metal-based catalysis in supercritical carbon dioxide as reaction medium. ACS Catal 6:4265–4280
170. Jessop PG, Hsiao Y, Ikariya T, Noyori R (1996) Homogeneous catalysis in supercritical fluids: hydrogenation of supercritical carbon dioxide to formic acid, alkyl formates, and formamides. J Am Chem Soc 118:344–355
171. Kayaki Y, Shimokawatoko Y, Ikariya T (2007) Synthesis of ruthenium(II) complexes containing hydroxymethylphosphines and their catalytic activities for hydrogenation of supercritical carbon dioxide. Inorg Chem 46:5791–5797
172. Kröcher O, Köppel RA, Baiker A (1997) Highly active ruthenium complexes with bidentate phosphine ligands for the solvent-free catalytic synthesis of N,N-dimethylformamide and methyl formate. Chem Commun:453–454
173. Pokharel UR, Fronczek FR, Maverick AW (2014) Reduction of carbon dioxide to oxalate by a binuclear copper complex. Nat Commun 5:5883
174. Angamuthu R, Byers P, Lutz M, Spek AL, Bouwman E (2010) Electrocatalytic CO_2 conversion to oxalate by a copper complex. Science 327:313–315
175. Zhou W, Cheng K, Kang J, Zhou C, Subramanian V, Zhang Q, Wang Y (2019) New horizon in C1 chemistry: breaking the selectivity limitation in transformation of syngas and hydrogenation of CO_2 into hydrocarbon chemicals and fuels. Chem Soc Rev 48:3193–3228
176. Matsuo T, Kawaguchi H (2006) From carbon dioxide to methane: homogeneous reduction of carbon dioxide with hydrosilanes catalyzed by zirconium-borane complexes. J Am Chem Soc 128:12362–12363
177. Chen J, Falivene L, Caporaso L, Cavallo L, Chen EYX (2016) Selective reduction of CO_2 to CH_4 by tandem hydrosilylation with mixed Al/B catalysts. J Am Chem Soc 138:5321–5333

Potential Application of Ionic Liquids and Deep Eutectic Solvents in Reduction of Industrial CO$_2$ Emissions

Mohd Belal Haider, Mata Mani Tripathi, Zakir Hussain, and Rakesh Kumar

Abstract Global warming is attributed to CO$_2$ emissions which are responsible for climate change. Various industries such as cement manufacturing plants, power plants, petrochemical industries, iron, and steel are the major contributors of CO$_2$ emissions. Carbon capture and storage has been considered as an essential technology to reduce CO$_2$ emissions into the atmosphere. Conventionally, amine-based solvents are used for the CO$_2$ capture in the industry. These conventional processes suffer from numerous problems such as high vapor pressure, corrosion, degradation of the solvents, and requirement of high regeneration energy. Ionic liquids (ILs) are widely accepted as the solvents of next generation having capability to replace the amine solvents for the CO$_2$ absorption. The non-volatility, superior thermal stability, non-corrosiveness, and low regeneration energy make them ideal for future perspective. However, ionic liquids have significantly lower CO$_2$ solubility as compared to conventional solvents and requires complex purification step which adds to its cost. Deep eutectic solvents (DESs) are believed to be IL-analogues having similar property and have shown ability for CO$_2$ absorption. The potential application of ionic liquids and deep eutectic solvents as alternatives to amine solvents has been discussed in this chapter.

Keywords Carbon dioxide capture · Ionic liquid · Deep eutectic solvents · Absorption

1 Introduction

Energy plays a pivotal role in the growth and sustainable development of any country. Mostly, fossil fuels are used for meeting the world's energy demand. Developing countries, like India and China, are heavily dependent on the fossil fuels for meeting their

M. B. Haider · M. M. Tripathi · R. Kumar (✉)
Department of Chemical Engineering and Engineering Sciences,
Rajiv Gandhi Institute of Petroleum Technology, Amethi, India
e-mail: rkumar@rgipt.ac.in

Z. Hussain
Department of Chemical Technology, Loyola Academy, Secunderabad, Telangana, India

energy requirements which is increasing day by day. The increase in energy demand is associated with carbon dioxide (CO_2) emissions generated by fossil fuels combustion. The burning of fossil fuels for heat and power and chemical process used in various industries such as cement, iron, and steel are the major contributors of CO_2 emissions. Global warming is attributed to CO_2 emissions which is responsible for climate change. The impact of the climate changes are rise in sea level and extreme weather conditions such as droughts and floods. To mitigate the adverse effect of CO_2 emissions, carbon capture utilization and storage (CCUS) has been considered as an essential technology.

International Energy Agency (IEA) reported that to limit the global temperature rise by 2 °C, there is a need to cut down 50% of the global carbon dioxide emissions. The cost of mitigating the climate change issue without considering the CO_2 emission would be 70% higher [1]. According to the report by the IEA, the energy sector alone will contribute to more than 130% in CO_2 emissions by 2050 due to increased usage of fossil fuels. Approximately 70% of the carbon dioxide emissions is contributed by power and industry sector. The type of process and feed used in various industries also affects the concentration of CO_2 emission into the atmosphere [2, 3]. With the growth and development of India, CO_2 emissions are also increased from 1.14 emission per capita in 2000 to 1.67 emission per capita in 2012 [4–6].

CCUS is considered to be a vital technology to lower the greenhouse gas (GHG) emissions and meet the environmental norms [4]. The fossil fuel-based power plants have major share in the CO_2 emissions, and it is crucial to diminish these emissions by employing proper carbon capture technology in these plants along with focus on increasing the shares of renewables and nuclear power [4–6]. Apart from those power plants, fertilizer plants, cement manufacturing plant, and natural gas processing terminals contribute highly in total carbon dioxide emissions [6]. CCS is the process of capturing CO_2 released from various industrial processes followed by drying and compression (~15 MPa). Thereafter, it is shipped through pipeline to a storage site. It is stored underneath the ocean, saline aquifers, and depleted oil and natural gas fields by various mechanisms. The captured CO_2 is utilized in "enhanced oil recovery," where CO_2 is injected into an oil field to extract the remaining oil. Alternatively, the CO_2 can be converted into various chemicals such as carboxylates, carbonates, carbamates, formic acid, methanol, and fuels [7].

1.1 CO₂ Capture Technology

In general, there are three ways of CO_2 capture methods, namely, post-combustion, pre-combustion, and oxy-fuel combustion.

1.1.1 Post-combustion

In post-combustion carbon absorption method, CO_2 is absorbed after the combustion of fossil fuels. In this process, concentration of CO_2 produced is significantly higher. Since air is used as the oxidant for the combustion, therefore flue gas
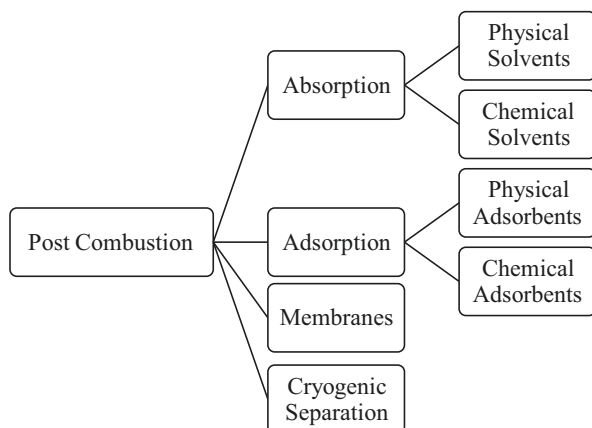
Fig. 1 Post-combustion CO_2 capture methods

contains significant amounts of NO_2. Post-combustion offers flexibility in the operation of a power plant. That is, if CO_2 capture plant is shut down, the power plant can still be operated [5]. This process can be retrofitted potentially to the existing industry; therefore, it is the most celebrated technology to reduce greenhouse gases [5, 8].

There are various methods available for CO_2 capture such as absorption using chemical and physical solvents, adsorption, membranes, and cryogenic separation as shown in Fig. 1. However, CO_2 absorption by amine solvent is the most preferred method because of higher CO_2 loadings and greater selectivity of amines towards CO_2 over other gases [9]. Besides these advantages, this process suffers from several problems like equipment corrosion and high-energy requirement for solvent regeneration.

1.1.2 Pre-combustion

It refers to the CO_2 removal before the combustion of fossil fuels. This process is mainly pertinent to an integrated gasification combined cycle (IGCC) in which coal is partially oxidized in the presence of steam and oxygen at high temperature and pressure resulting into synthesis gas [10]. Synthesis gas produced is then converted into H_2 and CO_2 using water gas shift reaction, and subsequently, CO_2 is captured and stored. Pre-combustion CO_2 removal is more efficient as compared to the post-combustion because of rich concentration of CO_2 at higher pressure which results in the easier removal [10]. Compared to post-combustion capture, pre-combustion technologies are not mature enough and can be employed only to the new plants as integrated part of the combustion process [11].

1.1.3 Oxy-Fuel Combustion

In this process, oxygen is used instead of air. Air is used as the source of oxygen and is used for combustion of the fuel in oxygen-rich atmosphere. So the absence of N_2 and the simultaneous oxygen-rich atmosphere produces the flue gases consisting

mainly concentrated CO_2 stream along with water which can be purified easily [11]. Oxy-fuel combustion does not require separate equipment for NOx elimination due to the absence of NOx emissions. In addition, complete combustion of fuel occurs in this process; therefore, almost pure CO_2 is formed which can be stored without requiring a CO_2 separator. The boiler size is also reduced because combustion occurs in the presence of pure oxygen [12]. The main drawback associated with oxy-fuel technology is the high capital investment for air separation unit compared to post-combustion technology [11].

Among all three technologies, post-combustion is commonly employed in the industry because of flexibility in the operation. Pre-combustion processes are restricted only to new industries. The energy requirement is less in the pre-combustion as compared to the post-combustion CO_2 capture, whereas high capital required for oxy-fuel combustion limits its industrial application.

2 Amine-Based Solvents for CO_2 Capture

The amine-based solvents are most widely used in the industry. Amines have been extensively used for the CO_2 absorption with the alkanolamines being the most popular solvent. Depending on the degree of substitution of alkanol group to the nitrogen, amines can be classified as primary, secondary, or tertiary. The CO_2 is absorbed in alkanolamines by chemical absorption, and the product after absorption largely depends on the nature of amine solvents [13]. For example, CO_2 rapidly react with primary and secondary amines to form carbamate, but tertiary alkanol-amines are devoid of hydrogen atom and therefore only facilitate the bicarbonate formation through hydrolysis. Further, the tertiary amine can be easily regenerated because the heat of formation of carbamate is higher than the heat of reaction to form bicarbonate [14].

2.1 Reaction Mechanism

The reaction mechanism for the primary and secondary amines occur through the zwitterion formation resulting into the carbamate product [15]

Zwitterion formation:

Zwitterion formation:
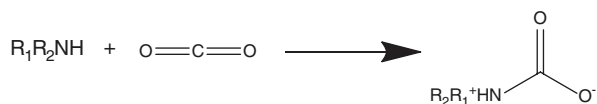
$$R_1R_2NH \ + \ O{=}C{=}O \ \longrightarrow \ \underset{R_2R_1{}^+HN}{\overset{O}{\parallel}}{\diagup}{C}{\diagdown}{O^-} \qquad 1$$

Carbamate formation:

Carbamate formation:

$$2$$
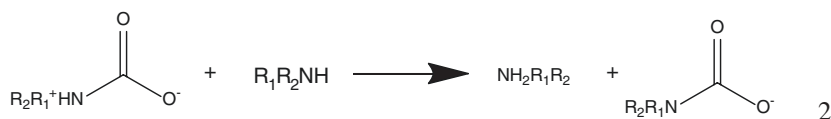
In the termolecular mechanism [16], reaction proceeds in single step by the formation of the loosely bound complex as an intermediate in the presence of base(X) and simultaneously reacts with CO_2.

$$3$$

Methyldiethanolamine (MDEA) being tertiary amine is believed not to participate in the reaction due to absence of a proton attached to nitrogen. However, it was proposed that they do behave as the base promoter for the reaction to occur [17].

2.2 Industrial Process for CO_2 Absorption

The process flow diagram for the CO_2 absorption using aqueous alkanolamine solution (30 wt% of amine) is shown in Fig. 2. The process mainly comprises of a stripper column and an absorber column. The flue gas is contacted with the solvent counter currently in the absorber column leaving the essential pure gas from the absorber column and the CO_2-rich solvent from the absorber column bottom. The CO_2-rich solvent is then heated to a desired temperature and sent to the stripper column. The CO_2 is removed from the stripper column at the top, and almost pure solvent is obtained at the stripper column bottom. The regenerated solvent is recycled to the absorber column after cooling in a heat exchanger.

The monoethanolamine (MEA) is the most celebrated solvent for CO_2 absorption having CO_2 uptake of ~0.5 mol of CO_2/mol of MEA [18]. Besides MEA, other amines such as methyldiethanolamine (MDEA) [19–21] and sterically hindered amines such as 2-amino-2-methyl-1-propanol have also been studied [22–24]. The sterically hindered amines have been observed to perform better at higher CO_2 partial pressure (8–15% CO_2) [25]. The typical CO_2 loadings in MDEA and AMP have been found to be ~1 mol of CO_2/mol of amine and ~0.7 mol of CO_2/mol of amine, respectively. In order to take advantages of both primary and tertiary amines, solvents are often mixed for CO_2 capture [26–28]. The blended solvents have high CO_2 loading capacity with low absorption heat due to tertiary amines and the fast reaction rate due to primary amines. This helps in the reduction of solvent circulation rate and stripper heat duty [21, 29]. The pilot plant studies have been done using MEA/MDEA and MEA/AMP blends [30–32]. The cyclic diamine additive such as piperazine was also added to these blends to enhance the absorption rate.
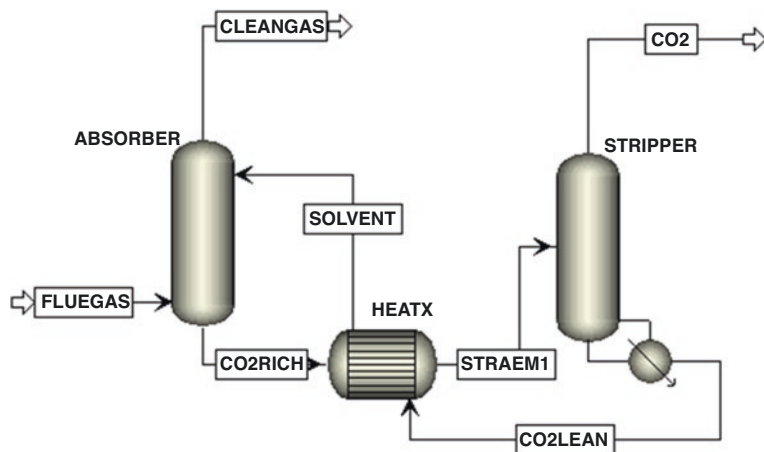
Fig. 2 Process flow diagram for carbon capture using aqueous amine solvents

2.3 Need of Green Novel Solvents

In conventional CO_2 capture process, aqueous alkanolamines solution such as MEA or MDEA or mixture of these solvents is used as the sorbent medium. This method is energy intensive because high energy is required in the regeneration or recovery of solvent. Also, amines being volatile in nature result in the solvent loss during regeneration. Besides the high energy consumption, corrosion of equipment and degradation of the amine solvent are other major drawbacks associated with amine-based process.

In general use of organic solvents is of great concern because of their higher volatility and higher regeneration cost. The problem gets worse if the solvent is hazardous and sometime can increase the carbon footprint. In Paris Agreement 2015, India vows to reduce the carbon footprint by 2030 [33]. It means there is a need to implement greener and sustainable solutions for reduction of CO_2 emissions.

To reduce the environmental hazards and to minimize the negative economic, social, and environmental impacts, Anastas and Warner put forward 12 principle of green chemistry in the book *Green Chemistry: Theory and Practice* [34]. Based on similar principle, Gu et al. redefine the principle to attain sustainable green solvents [35].

1. **Availability:** A green solvent should be constantly and readily available on a large scale.
2. **Price:** To ensure chemical process sustainability, the price of solvents should be competitive.
3. **Recyclability:** Solvents should be recyclable.
4. **Grade:** To avoid complex purification step, technical grade solvents are favored.

5. **Synthesis:** Green solvents synthesis should have high atom economy. It means the waste produced during the synthesis should be minimum and the reactant used should be completely converted into the product.
6. **Toxicity:** The solvents should exhibit negligible toxicity.
7. **Biodegradability:** Solvent should be biodegradable and also should not produce toxic products or by-products.
8. **Performance:** A green solvent should have same or superior performances to replace conventional solvents.
9. **Stability:** A green solvent should have high thermal and chemical stability.
10. **Flammability:** It should be inflammable.
11. **Storage:** Easy to store and should fulfill all criteria for safe and easy transportation.
12. **Renewability:** Raw materials should be renewable for the green solvents production to avoid carbon footprint.

Researchers are therefore focused on the development of environmental-friendly novel green solvents to replace the conventional solvents. In recent years, active research has been performed on ionic liquids and deep eutectic solvents.

3   Ionic Liquids

These solvents are mainly composed of cations and anions, and they exist in a liquid state at room temperature and atmospheric pressure. Ionic liquid is also called the molten salts, liquid organic salt, or fused salt because of their existence in the liquid form below the room temperature [36]. The conventional salt remains in a solid state at normal room temperature and has a high melting point which limits their use as solvent. In salts, there are large attractive forces between cation and anion which lock them together. These attractive forces can be weakened by increasing temperature, making them into bulkier group or by enduring asymmetry. In case of ionic liquids, attractive forces between anions and cation are weak because of their irregular shapes. Paul Walden in 1914 first described about the ionic liquid which was ethylammonium nitrate which is known as first room temperature ionic liquid [37]. A comparison between the ionic liquids and common salts has been given in Table 1.

The list of different cation and anion combination used to make ILs is shown in Fig. 3. Their physical as well as chemical properties can be controlled by the appropriate choice of anion and cation. Therefore, these are also known as designer solvent. Ionic liquids have found its application in different fields such as acid gas removal, catalysis, chemical synthesis, electrochemistry, etc. [38]. Till date, the use of ionic liquid is limited to laboratory scale only, and efforts are made for its commercialization. ILs are commonly referred as green solvents because of negligible vapor pressure and low flammability which make them environmental friendly. However, in recent year, the term "green" for ILs has become dubious since their synthesis results in by-product and waste generation [39]. In addition, the synthesis of ILs requires complex purification steps which add cost to the solvent.

Table 1 Comparison between the ionic liquids and salts

Ionic liquid	Salts
van der Waals force is prevalent	Ionic bonds are prevalent
Melting point is below 100 °C	Melting point is usually above 500 °C
They are electrolytes and itself a solvent	They form electrolytes when mixed with solvents
Generally, liquid at room temperature	They are solid at room temperature
Ionic liquid has lower symmetry	Highly symmetrical in nature
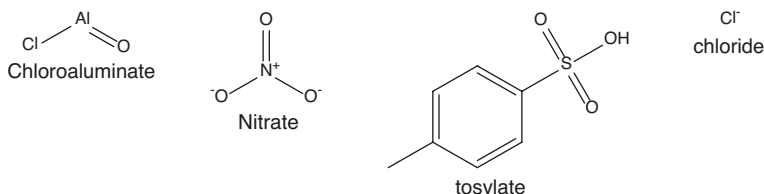
Fig. 3 Common types of cations and anion for ionic liquids

3.1 Properties of Ionic Liquids

The understanding of thermophysical properties of ILs is essential for their industrial application and greatly depends on the choice of cation and anion. Here, the important IL characteristics are discussed.

Thermal Stability: ILs are thermally stable at high temperature range. This can be further changed depending on the choice of anion and cation. Generally, for same cation with increase in the anion size, the stability of ILs generally increases and decreases with increase in the size of cation [40, 41].

Melting Point: The ILs melting point is one of the most important characteristics. The melting point of ILs is normally below 100 °C. Room temperature ILs have their melting point below room temperature and hence the name. The low melting point of ILs arises from the asymmetry of anion and cation which decrease the lattice energy and prevent their crystallization.

Volatility: The most celebrated property is its negligible vapor pressure compared to conventional organic solvents. According to Brennecke et al., ionic liquids do not evaporate [42]. Here, strong ionic bond between anion and cation reduces the volatility of ILs.

Viscosity: Ionic liquids, in general, have more viscosity compared to conventional organic solvents. There enhanced viscous nature arises from ionic bond between anion and cation. This is one of the major factors affecting their use in the industry. Viscosity in turn is a strong function of the nature of anions and cation [42]. For example, higher alkyl chain length ILs have more viscosity compared to lower alkyl chain length ILs [43]. Viscosity of ILs in general decreases with the increase in the temperature [44].

Toxicity: Even though ILs are regarded as green solvent, they are not actually eco-friendly because of their ecotoxicity [45]. Researchers even have shown the acute toxicity of ILs [46]. The toxicity of ILs depends on the type of anion and cation [47].

Biodegradability: Another cause of concern is the biodegradability of ILs. The most of ionic liquids are not biodegradable and have serious concerns [48]. The biodegradability depends mostly on the type of cation and the functional group attached [49].

3.2   CO₂ Capture with Ionic Liquids

The following properties of ILs make them advantageous for CO_2 capture as compared to conventional solvents [61–64]:

- The lesser energy requirement for their regeneration compared to conventional solvents due to the physical absorption mechanism.
- Low vapor pressure provides little or no loss of solvent into the gas stream.
- High thermal and chemical stability.
- Favorable physicochemical properties like heat capacities, thermal decomposition temperature, non-corrosiveness, and non-toxicity make ionic liquids as green solvent.

3.2.1   Room Temperature Ionic Liquids (RTILs)

The ability of ionic liquids for CO_2 uptake was first reported in 1-butyl-3-methylimidazolium hexafluorophosphate ([bmim][PF_6]). The ([bmim][PF_6]) has ability to absorb the CO_2, and at 8 MPa, the mole fraction of CO_2 solubility can reach up to 0.6 [50]. After this, Blanchard et al. investigated several ionic liquids 1-n-octyl-3-methylimidazolium tetrafluoroborate ([C_8mim][BF_4]), 1-n-octyl-3-methylimidazolium hexafluorophosphate([C_8mim][PF_6]), 1-ethyl-3-methylimidazolium ethyl sulfate ([C_2mim][$EtSO_4$]), 1-n-butyl-3-methylimidazolium nitrate([C_4mim][NO_3]), and N-butylpyridinium tetrafluoroborate ([N-bupy][BF_4]) at high pressure and concluded that these ionic liquids have varying degree of CO_2 capture ability [51]. The maximum CO_2 uptake (~0.3 mol of CO_2/mol of ILs) was found in bmim[PF_6] among all the above listed ILs. The CO_2 absorption in different imidazolium-based ionic liquid was explored, and it was observed that CO_2 loadings increase by increasing the imidazolium alkyl side chain length. Also, CO_2 loadings in ionic liquid having Tf_2N anion were higher compared to ILs having PF_6 anions. The impact of cation fluorination on the CO_2 was also investigated, and it was deduced that the CO_2 solubility increases as the number of fluorine atoms in the alkyl chain increases [52]. The similar study was carried out by several other researches, and it was observed that with increasing fluorine atom number in the anion increases the affinity for CO_2.

However, increasing the number of fluorine atoms on cation does not significantly affect the CO_2 solubility [53]. The CO_2 absorption increases due to strong columbic interaction suggesting that the effect of anion-IL interaction is more dominant as compared to the cation-IL [54].

The 1-n-butyl-3-methylimidazolium acetate [bmim][Ac] has been found to be RTIL which can absorb CO_2 through chemical reaction. Similarly, Yokozeki et al. performed experiments for CO_2 solubility in 18 RTIL, eight of which showed chemisorption [55]. The imidazolium-based ILs have been widely studied for CO_2 solubility as well as for their interaction. The most acidic protonic carbon atom of the imidazolium is considered to be responsible for CO_2-IL interaction [56]. Similar experiments by Kanakubo et al. asserted that there is preferentially CO_2 absorption in PF_6 anion [57]. The selectivity of the conventional ionic liquid (bmim[PF_6]) was highest for CO_2 compared to other gases. CO_2 selectivity of the ionic liquids was further enhanced by using amine moieties such as [MDEA][Cl]-ionic liquids [58–60]. IL consisting of guanidinium lactate anion has shown the higher CO_2 solubility than [bmim][PF_6] [60]. Similar to lactate anion, CO_2 solubility can also be increased by increasing the number of potential sites for CO_2-IL interaction [61]. The CO_2 capture abilities of various RTILs have been presented in Table 2.

CO_2 selectivity of ILs was quite large as compared to other gases [62, 63]. The CO_2 solubility and selectivity can be further enhanced by proper selection of cation and anion [64, 65]. In general, it has been investigated that CO_2 solubility in ionic liquids is still low in comparison with conventional alkanolamines or polyethylene glycol of dimethyl ethers which therefore requires further research on ionic liquids for better CO_2 solubility [66].

Table 2 CO_2 absorption in RTIL

Ionic liquid	P (bar)	T (K)	CO_2 mole fraction	Reference
bmim[PF_6]	15.17	313.15	0.231	[58]
C_8mim[PF_6]	17.83	313.15	0.234	[58]
bmim[NO_3]	15.47	313.15	0.196	[58]
C_8mim[BF_4]	17.26	313.15	0.197	[58]
n-bupy[BF_4]	15.47	313.15	0.144	[58]
emim[EtSO$_4$]	16.43	313.15	0.100	[58]
bmim[BF_4]	12.74	313.15	0.137	[62]
bmim[dca]	14.16	313.15	0.158	[62]
bmim[TfO]	20.94	313.15	0.217	[62]
bmim[methide]	18.75	313.15	0.315	[62]
bmim[Tf$_2$N]	17.21	313.15	0.269	[62]
hmmim[Tf$_2$N]	15.37	313.15	0.298	[62]
omim[Tf$_2$N]	18.33	313.15	0.292	[62]
emim[Tf$_2$N]	12.12	312.10	0.212	[63]
[$C_6H_4F_9$mim][Tf$_2$N]	17.30	313.15	0.394	[68]
[$C_8H_4F1_3$mim][Tf$_2$N]	13.10	298.15	0.351	[68]
[Et_3NBH_2mim][Tf$_2$N]	15.00	298.15	0.043	[68]
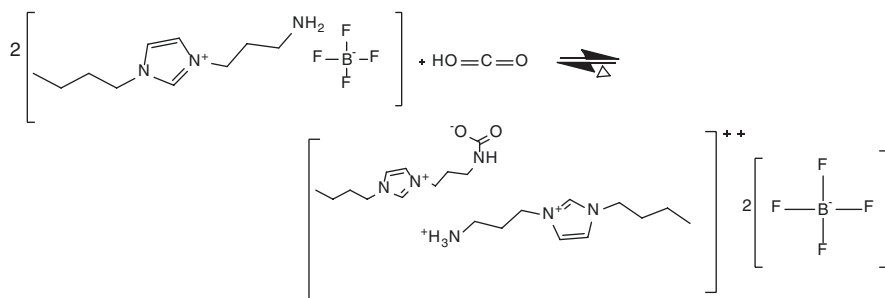
Fig. 4 CO_2 reaction with functionalized ionic liquids [78]

3.2.2 Task-Specific Ionic Liquids

The carbon dioxide solubility in the room temperature ionic liquids is very less; therefore, further research has been focused to enhance the CO_2 solubility in ILs by adding the functional groups. The task-specific ionic liquids (TSILs), also referred as functionalized ionic liquids, are tailor-made for specific task to be executed. The designer aspects of the ionic liquids are utilized in a sense that various functional groups can be incorporated to the ionic liquid. The first TSIL was synthesized by Bates et al. in which imidazolium was covalently bonded with the primary amine [67]. The synthesized TSIL showed 0.5 mol of CO_2 solubility/mol of ionic liquid which is similar to the CO_2 solubility of alkanolamine. Due to the presence of amine, CO_2 reacts with ionic liquids as shown in Fig. 4.

Functionalized ionic liquids containing amino acid group were prepared by Gurkan et al. [68]. Amino acid-based functional ILs have both amine and carboxyl functional groups. The rate of CO_2 absorption in TSIL was significantly higher than the RTIL such as [bmim][BF_4] [69, 70]. However, the chemical reaction increases the viscosity of ionic liquid which can be controlled by reducing the number of hydrogen atoms from anion to prevent hydrogen bonding [70–72]. The solubility of CO_2 in tetraethyl-ammonium prolinate ([N2222] [Pro]) and tetramethylammonium glycinate ([N1111] [Gly]) was analyzed by ^{13}C-NMR under wet conditions. In these ILs, anions are amine functionalized which react with the CO_2 to form carbamate. The ionic liquids with dual functionalization, i.e., functionalizing both the cation and anion of the ILs by amino phosphonium group, were also synthesized for investigating their effect on CO_2 uptake [70, 73]. These ILs showed the chemical absorption of CO_2 having loadings of 1 mol CO_2/mol IL. Higher viscosity due to hydrogen bonding of these functionalized ionic liquids is the main problem which needs to be overcome by further research.

3.2.3 Supported Ionic Liquid Membrane

Supported ionic liquid membranes (SILMs) have been also explored for CO_2 capture. SILMs are porous membranes whose pores are saturated with ionic liquids. In SILMs, the ionic liquid contributes towards the liquid phase of the membrane.

High viscosity and non-volatility of ionic liquid prevent the membrane solvent from flowing out of the porous membrane [74]. Four water stable anions bis(trifluoromethanesulfonyl)amide [Tf_2N]$^-$, trifluoromethanesulfone [CF_3SO_3]$^-$, dicyanamide [DCA]$^-$, and chloride [Cl]$^-$, supported on the hydrophilic polyethersulfone (PES), were studied for CO_2 absorption [75]. Results showed that higher permeability along with greater selectivity of CO_2 can be achieved. These permeability and selectivity were even better than the polymeric membranes. Nerves et al. found that the nature of ionic liquid affects the CO_2 absorption behavior [76]. The hydrophobic ionic liquids are more stable and have high capacity for CO_2 absorption as compared to hydrophilic ionic liquids. Presence of water vapor in the gas stream increases the permeability but results in the lower CO_2 selectivity due to the water cluster formation. It was also investigated that increasing the temperature increases the permeability of these membranes which in turn decreases the CO_2 selectivity. The selectivity and permeability of SILM largely depend on the nature of porous material. The CO_2 absorption in SILM can be increased by increasing the van der Waals intermolecular interaction of CO_2 and ionic liquid [77].

3.2.4 CO_2 Capture with Polymeric Ionic Liquid

The polymerized ionic liquids (PILs) have also shown the capability to absorb the CO_2. Tang et al. first made the ionic liquid into polymeric form [78]. These polymerized ionic liquids have greater CO_2 absorption capacity than the conventional ionic liquids. Tetraalkylammonium-based polymeric ionic liquid has 7.6 times larger CO_2 solubility as compared to conventional ionic liquid [C_4mim][BF_4] [79]. CO_2 absorption capacity in PILs depends on the cation, and the highest CO_2 absorption was observed in ammonium-based PILs. Imidazolium-based PILs show relatively lower CO_2 solubility [80, 81]. Similarly, anions of the PILs significantly affect the CO_2 solubility and follow the trend as $BF_4^- > PF_6 > Tf_2N$.

3.3   *Ionic Liquid Blends*

The viscosity of conventional ionic liquid is approximately 40 times higher than that of aqueous alkanol amine (30 wt%) which causes huge difference in the CO_2 solubility [82]. Amine-functionalized ionic liquid showed better CO_2 solubility than the conventional ionic liquids. However, the functionalized ionic liquids synthesis requires complex procedure and subsequent purification steps [83]. Therefore, in addition to modifying the structural and functional group, mixing with other solvent is an alternative way to improve the CO_2 absorption ability of these ionic liquids.

3.3.1 IL-Water

The water addition into ionic liquids greatly decreases the ionic liquid viscosity; however, it also affects the CO_2 solubility. The presence of 1% water in the amino-functionalized ionic liquid could absorb equimolar amount of CO_2, and the obtained product so formed is different from the products obtained by pure ionic liquids [73]. Experiments conducted by Ventura et al. suggest that though the viscosity of ionic liquid decreases with the addition of water, at the same time, CO_2 absorption capacity also decreases [84]. The CO_2 absorption capacity of ILs-water blends largely vary with the choice of ionic liquid and the amount of water present. Additionally, the energy required for regeneration of these blends is lesser than that required for the aqueous amine (30%) solution. The enthalpy of CO_2 absorption was measured for the ILs-water (60 wt% IL) system which was found to be significantly lower $(41.1 \pm 3.2$ kJ/mol IL) as compared to the aqueous MEA-based solvent (82 kJ/mol MEA) [85]. This suggests that addition of water reduces the regeneration energy of the ionic liquids.

3.3.2 IL-Amine

Further improvement for the CO_2 solubility can be achieved by addition of alkanolamine to ionic liquid. Partly replacing the water from the aqueous alkanolamine solution by ionic liquid can diminish the solvent regeneration energy and also limits the loss of alkanolamine. Industrial CO_2 capture process uses solvents with 60 wt% water; therefore, a large volume of water is also lost during solvent regeneration. Ionic liquid $[C_6mim][Tf_2N]$ with MEA blend showed significant increase in CO_2 absorption [86]. Four ionic liquids with tetramethylammonium and tetraethylammonium as cations and glycinate and lysinate as anions, e.g., ([N1111][Gly]), ([N2222][Gly]), ([N1111][Lys]), and ([N2222][Lys]), were blended with the MDEA aqueous solution to study the CO_2 absorption capacity. All these blends were found to have high CO_2 solubility capacities than the conventional ILs [87]. The experimental results of amines-IL-H_2O, amines-H_2O, and IL-H_2O blends in the temperature range of 30–70 °C suggest that amines-IL-H_2O blends are better for CO_2 absorption as compared to IL-H_2O and amines-H_2O [88]. Baj et al. reported that CO_2 absorption follows physisorption process in [EMIM][OcSO$_4$]-MEA-water system [89], whereas pure ionic liquid like [bmim][OAc] absorbs the CO_2 by chemical absorption process. The experiments conducted by Murugesan et al. showed that the CO_2 uptake is more in [bmim][BF$_4$] as compared to bis(2-hydroxyethyl) ammonium acetate (bheaa), whereas aqueous blend of bheaa-MEA showed higher CO_2 solubility than the aqueous mixture of MEA-[bmim][BF$_4$] [90].

The MEA-based blend with three ILs [bmim][DCA], ([Bpy][BF$_4$]), and ([bmim][BF$_4$]) was explored for CO_2 absorption process. It was found that [Bpy][BF$_4$]-MEA blends can reduce energy consumption by 15% as compared to conventional amine process [91]. The techno-economical aspect for the CO_2 capture was also investigated for water-MEA-[bmim][BF$_4$] blends. The results show that solvent
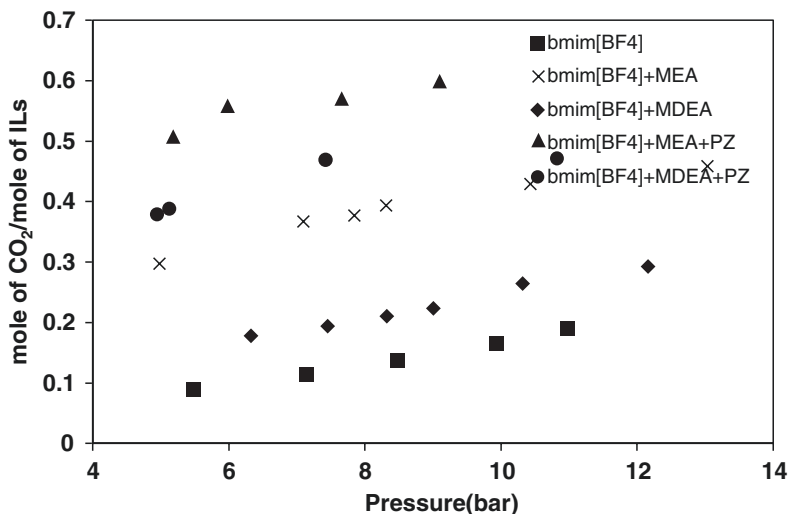
Fig. 5 Effect of amine and piperazine on CO_2 solubility in [bmim][BF_4]

Fig. 6 (**a**) 70%
[Bmim]$^+$[BF_4]$^-$—10%
PZ–20% MDEA before
CO_2 absorption; (**b**) and (**c**)
70% [Bmim]$^+$[BF_4]$^-$—10%
PZ–20% MDEA after CO_2
absorption
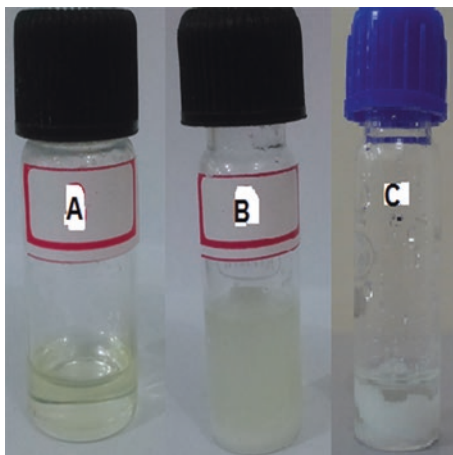
regeneration for blended solution requires 37.2% lower energy than aqueous amine
solution [92]. Haider et al. measured CO_2 uptake in various IL-amine blends as
shown in Fig. 5. The highest CO_2 solubility and the reaction rate were observed by
the [bmim][BF_4]-MEA-piperazine blend [93]. The amine addition in ionic liquid
significantly increases the CO_2 uptake.

The CO_2 solubility was further enhanced using piperazine owing to its chemi-
sorption behavior. Addition of piperazine results into the solid phase separation as
shown in Fig. 6. In general, IL-amine blends have shown significantly high CO_2
loadings, and in some cases, CO_2 loadings are more than the aqueous alkanolamine
solution [87, 94].

A comparison of CO_2 uptake in ionic liquids and aqueous amine solution has been
given in Table 3. It was found that most of the ionic liquids have lower CO_2 solubility

Table 3 Comparison of CO_2 solubility in ionic liquids and aqueous amine solution

Solvents	T (K)	P (bar)	Mole fraction CO_2	Mass fraction CO_2	Reference
[bmim][PF$_6$]	303.15	10.17	0.186	0.029	[54]
[bmim][BF$_4$]	303.15	09.96	0.166	0.032	[93]
[bmim][Tf$_2$N]	313.15	22.00	0.667	0.070	[54]
[emim][BF$_4$]	298.15	8.80	0.119	0.026	[101]
[emim][TF$_2$N]	298.15	10.07	0.293	0.033	[100]
[P$_{66614}$][Pyr]	296.15	1.00	1.020	0.082	[83]
[bmim][DCA]	313.15	14.20	0.188	0.040	[54]
[C$_6$mim][PF$_6$]	313.15	25.70	0.427	0.060	[102]
[P$_{66614}$][Pro]	295.15	1.00	~0.900	0.066	[68]
[P$_{66614}$][Met]	295.15	1.00	~0.900	0.063	[68]
30 wt% aqueous MEA	313.15	12.56	0.763	0.550	[103]
30 wt% aqueous MDEA	313.15	12.41	1.065	0.393	[103]

than the aqueous amine solution. Ionic liquids are intensively studied solvents with exceptional properties such as negligible volatility, excellent chemical and thermal stability, and high heat capacity [95, 96]. However, ILs require complex purification steps which add to the cost of these solvents [37, 97]. Moreover, their high viscosity and environmental acceptability further limit their application for CO_2 capture [98, 99].

4   Deep Eutectic Solvents

Abbott and co-workers synthesized a new kind of solvents known as deep eutectic solvents (DESs) which are believed as a substitute to ILs. These are formed by mixing suitable molar ratio of hydrogen bond donor (HBD) and hydrogen bond acceptor (HBA) [104, 105]. Due to hydrogen bonding, these mixtures are homogeneous liquids as room temperature. DESs contain large asymmetric ions having low lattice energy resulting into the lower melting point. Charge delocalization through hydrogen bonding produces lower melting point of these mixtures. Common types of the hydrogen bond donor (HBD) and hydrogen bond acceptor (HBA) used for deep eutectic mixtures are shown in Fig. 7.

The first DES was synthesized by Abbot et al. using choline chloride (ChCl) as HBA and urea as HBD [104]. The DES formed at HBA/HBD molar ratio of 1:2 showed significantly lower melting point (12 °C) than the pure HBA and pure HBD. It should be interesting to note that mixing of HBD and HBA does not always produce lower melting point, but instead a glass transition temperature may be observed [106]. These kinds of solvents are regarded as low transition temperature mixtures [97, 106]. DESs are easy to synthesize and do not require complex purification steps. A schematic of ChCl and ethylene glycol-based DES synthesis has been shown in Fig. 8.

However, DESs are considered to be IL analogues sharing similar physicochemical properties. It should be noted that DESs are fundamentally different from the ILs. DESs are formed by simple mixing of the HBDs and HBAs in fixed molar ratio,
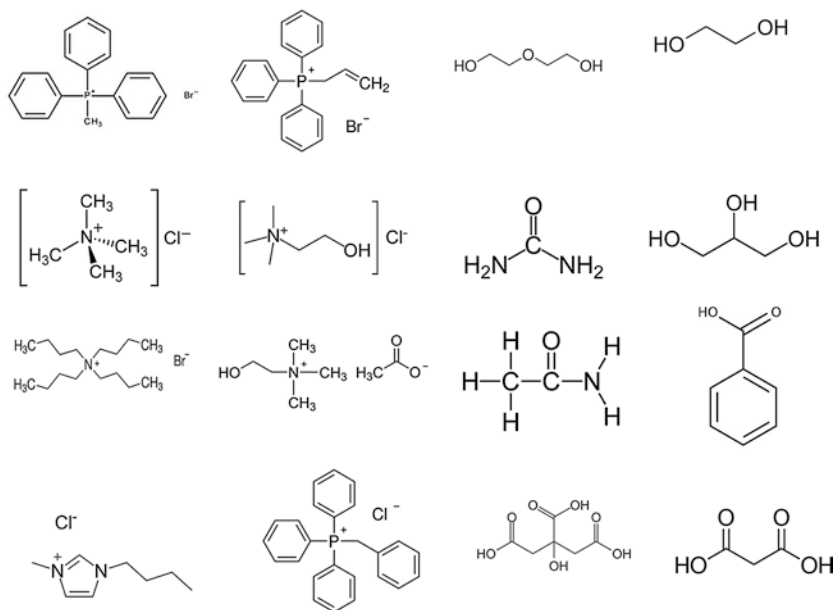
Fig. 7 Common hydrogen bond acceptor and hydrogen bond donor

Choline Cholride   Ethylene Glycol   Deep Eutectic Solvent
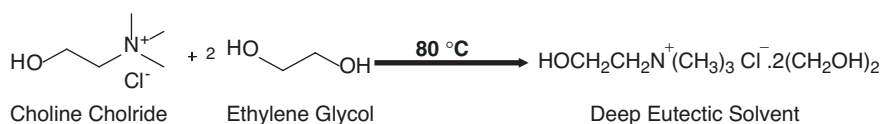
Fig. 8 Synthesis of reline (deep eutectic solvents formed by ChCL/EG)

whereas ionic liquids are synthesized by combination of protonation and complexation reaction. Therefore, ILs require purification step which makes ILs costly.

Abbott et al. described the DESs by a general formula AP^+B^-zC, where AP^+ is in principle any phosphonium- or ammonium-based salt having Lewis base (commonly halide) "B" [107, 108]. The z number of Lewis or Bronsted acid C molecule forms the complex anionic species with B^-. Most of the current research concerning DES is based on quaternary ammonium salts.

4.1 Physicochemical Properties of DESs

Deep eutectic solvents have physicochemical properties similar to that of ionic liquids (ILs). These solvents are non-volatile in nature having high thermal stability [107, 109]. Their properties can be further altered based on the proper selection of

the HBA and HBD. DESs have find their application in various fields including gas separation because of their green physiochemical properties [110, 111]. Garcia et al. presented a comprehensive review on the DESs application in gas separation highlighting the properties which need to be focused while selecting the solvent [112].

Like ionic liquids, one of the most important aspects of DESs is their ability to be tailored for the particular application. However, DESs have edge over ILs when compared in terms of stoichiometry. This means different HBD/HBA molar ratio can be used for the synthesis of DESs. However, reaction in a fixed stoichiometry is done for the synthesis of ILs. Combination of various HBD and HBA as well as different HBD/HBA molar ratio helps in designing a desired DES for a particular application. Therefore, DESs have found their application in many fields such as extractive desulfurization, gas separation, extraction of target compounds, biodiesel production, biocatalysis, polysaccharides processing, nanotechnology, and others [108, 112–119]. Some of the important physicochemical properties of DESs have been discussed here.

4.1.1 Phase Behavior

Phase diagram of DESs is important to identify the physical state of the mixture under different pressure and temperature conditions. The phase diagrams of choline chloride, glycol and choline chloride, and urea have been shown in Fig. 9. Generally, these DESs formed at different HBD/HBA molar ratios have lower melting point than the individual compounds. The higher the interaction among compounds, the more the depression in the melting point. At a particular HBD/HBA molar ratio, the melting point of DES may approach to the lowest value which is called as the eutectic point. According to Kroon et al., DESs are not ionic, and most of the DES properties arise from hydrogen bonding and van der Waals interaction [106].
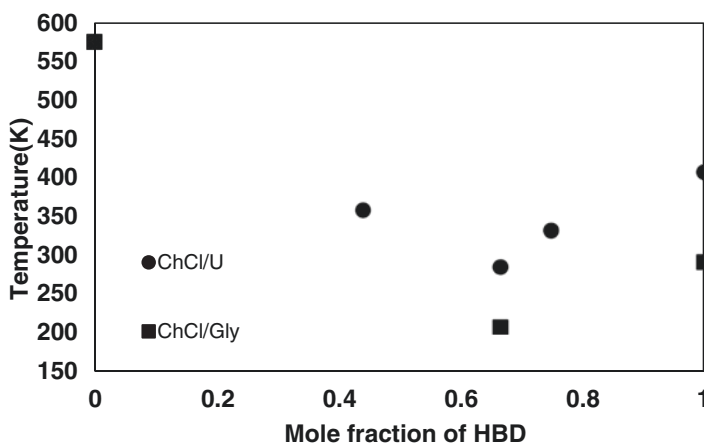
Fig. 9 Phase diagram of DESs with different hydrogen bond donor

4.1.2 Density

Density is an important property for the chemical processing. DESs have density more than water but less than ILs. Density usually changes with type of HBD and HBA and their molar ratio. In general, density is significantly affected by the HBA/HBD molar ratio and decreases with increase in temperature. Like ionic liquids, the density effects in DESs are explained based on the hole theory or free volume [120]. The density (ρ) of DESs can be modelled using a quadratic equation as given below:

$$\rho = \rho_0 + aT + bT^2 \tag{1}$$

where "a," "b," and ρ_0 are constant and temperature T is in K.

4.1.3 Viscosity

The viscosity represents the resistance to flow which indirectly indicates the strength of intermolecular interaction among the DESs' precursor compounds. Most of the DESs show high viscosity at room temperature which is due to extensive hydrogen bond network between the DES precursors [113]. Viscosity of DESs depends on the nature of precursor compounds, water content, and temperature. The viscosity behavior of DESs can be also explained through hole theory. The viscosity of DES is high if the empty vacancies are less due to higher structuring effect. At higher temperature, the empty vacancies in DESs increase, and therefore viscosity decreases. The effect of temperature (T) on the viscosity (μ) of DESs can be described using Arrhenius equation as given below:

$$\ln\left(\mu / \mu_\infty\right) = \frac{E_\mu}{RT} \tag{2}$$

where μ_∞ is the empirical constant, E_μ is the activation energy for viscous flow, and R is the gas constant.

4.1.4 Volatility

In the synthesis of DESs, one of the precursors is a salt, and other is volatile compounds. This makes DESs partially volatile as compared to non-volatile ILs. Moreover, volatility of the DESs depends on the individual precursor. For example, DESs formed by mixing two solid have low volatility compared to DESs formed by mixing one volatile and one solid compound [112]. However, all the DESs have sufficiently low volatility to categorize them under green solvent.

4.1.5 Thermal Stability

Thermal stability of DESs largely depends on the type of precursor compounds and their molar ratio. Strong intermolecular interaction among precursor compounds results in high thermal stability of DESs. Some of the DESs are having higher thermal stability than those of hydrogen bond donors and ionic liquids [121].

4.1.6 Toxicity

Hayyan et al. investigated the toxicity of various DESs [122, 123] and found that DESs are more toxic as compared to their individual compounds. The toxicity of DESs varies with the type of salt and hydrogen bond donor. Natural DESs are less toxic compared to the DESs precursors [124, 125]. Therefore, the toxicity of the DESs can be tailored based on the choice of hydrogen bond donor and acceptor.

4.2 DESs for CO_2 Capture

Along the line of ILs, DESs have been considered to be a green solvent having advantageous properties owing to biodegradability, non-flammability, simple synthesis, and high chemical as well as thermal stability. Li et al. first studied the CO_2 uptake in the DESs synthesized from urea and choline chloride having molar ratio of 1.5:1, 2:1, and 2.5:1 in the temperature range from 40 to 60 °C up to a pressure of 13 MPa [126]. Their results revealed that for a fixed pressure and temperature, CO_2 solubility depends upon the DESs molar ratio and the highest CO_2 solubility was observed for 1:2 molar ratio of choline chloride and urea. Much of the later work was focused on CO_2 solubility in DESs; however, some studies were also done for other gases such as CO, N_2, CH_4, and SO_2.

4.2.1 CO_2 Solubility in Ammonium-Based DESs

Since the first synthesized DES by Abbott et al. was based on ammonium salt, therefore much of the later work was focused on the ammonium-based salt only. An extensive study was done for investigation of CO_2 solubility in DESs having ammonium salts. The most commonly used ammonium salt was choline chloride and later work extended to tetrabutylammonium bromide, tetrabutylammonium chloride, and other ammonium salts.

4.2.2   HBDs with OH Moiety

Solubility of CO_2 in ethaline (ChCl:2ethylene glycol) and glycine (ChCl:2glycerol) DESs was investigated by Leron et al. [127, 128]. Their results suggest that CO_2 capture in the ethaline DESs was comparable to the ionic liquids [BMIM][PF$_6$] and [BMIM][BF$_4$] [51, 52]. Li et al. compared the CO_2 dissolution in the ChCl:diethylene glycol and ChCl:triethylene glycol DESs having molar ratios of 1:3 and 1:4, respectively [129]. The CO_2 solubility of ChCl:glycol-based DESs at different molar ratio has been shown in Fig. 10. It was observed that with increase in the ChCl:glycol molar ratio, there was only little increment in the CO_2 solubility. The effect of molar ratio was more pronounced in ChCl:TEG-based DESs. Further, CO_2 solubility in the glycine(ChCl:2glycerol) DES was found to be higher than glycol-based DESs.

Lu et al. used levulinic acid and furfuryl alcohol as HBAs and ChCl as HBD for CO_2 capture [130]. The ChCl:levulinic-based DESs showed maximum CO_2 solubility which increases with increase in the molar ratio of HBD/HBA. The solubility of CO_2 in ChCl:levulinic-based DESs was comparable to ChCl:triethylene glycol-based DESs but lower than the glycine. The CO_2 absorption in DESs composed of ChCl and dihydric alcohol was measured by Chen et al. [131]. In their study, highest CO_2 solubility was shown by the ChCl:3(1,4-butanediol)-based DES, and the lowest CO_2 solubility was observed in ChCl:4(1,2-propanediol). This suggests that the chain length of HBDs affects the CO_2 solubility and longer chain length produces higher CO_2 solubility. However, as compared to ethaline (ChCl:2ethylene glycol), dihydric alcohol-based DESs show lesser CO_2 capture ability.
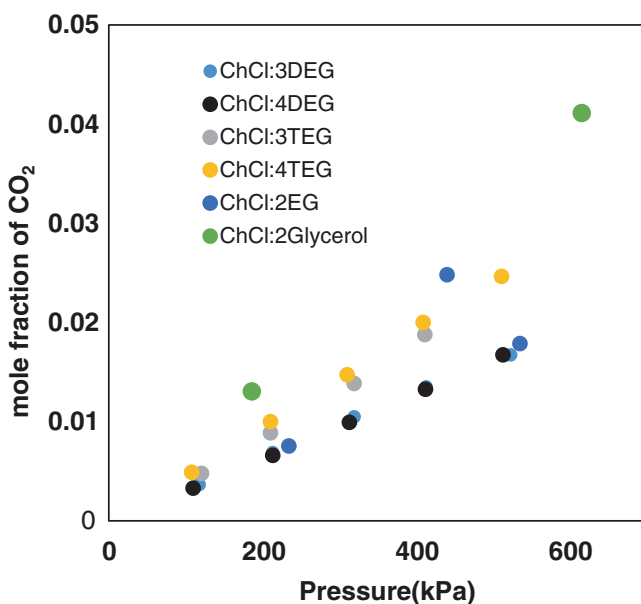
Fig. 10 CO_2 solubility in ChCl:glycol-based DESs at 303 K
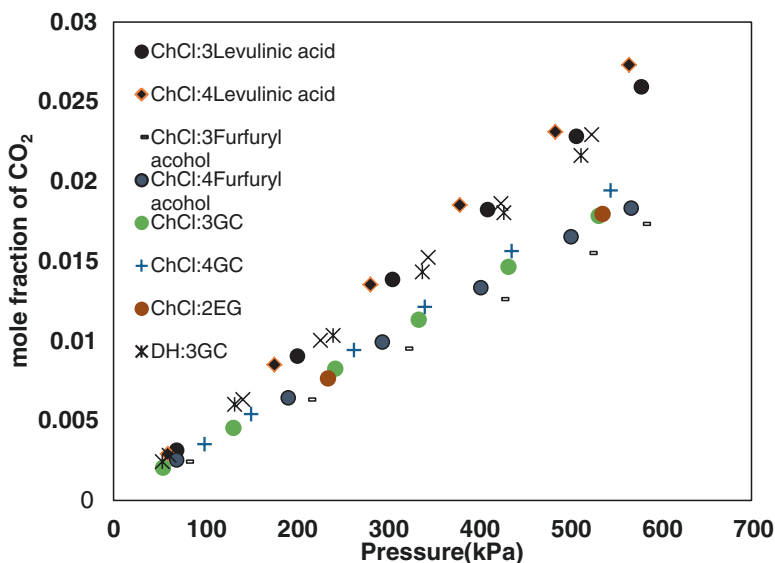
Fig. 11 CO_2 solubility in ChCl-based DESs with different HBDs at 303.15 K

The CO_2 uptake in different type guaiacol (GC)-based DESs was investigated by the Liu et al. [132]. The DES composed of diethylamine hydrochloride as HBA and GC as HBD (1:5) has the highest CO_2 loading capacity. However, the observed CO_2 solubility was lesser than the glycine DES. A comparison of CO_2 solubility in ChCl-based DESs with different HBD has been presented in Fig. 11. The results show that changing the HBDs has significant effect on the CO_2 uptake of DESs. Haider et al. have synthesized 15 different DESs using ChCl and TBAB as HBA for investigating CO_2 solubility [133]. The results show that increase in the chain length of HBA increases CO_2 solubility. The effect of HBA on CO_2 solubility for a fixed HBD (levulinic acid) has been shown in Fig. 12. It was observed that changing the HBA significantly affects the CO_2 solubility. The DESs containing tetrabutylammonium bromide (TBAB) have higher CO_2 capture ability than the other HBDs.

4.2.3   HBDs with NH Moiety

Further studies were focused on DESs consisting of HBDs with -NH moieties. ChCl:urea (reline) DESs having molar ratios of 1:1.5, 1:2, and 1:2.5 were synthesized by Li et al. and Leron et al. [129, 134]. Highest CO_2 uptake was observed in the DES having ChCl:urea molar ratio of 1:2. The amount of CO_2 absorb was comparable to imidazolium-based ILs and found to be higher than ethaline and glycine. Effect of water addition in the DESs was also explored for CO_2 capture. The results demonstrate that presence of water in reline reduces the CO_2 solubility [135]. Similar findings were also described by Maheswari et al. for alkanolamine-based
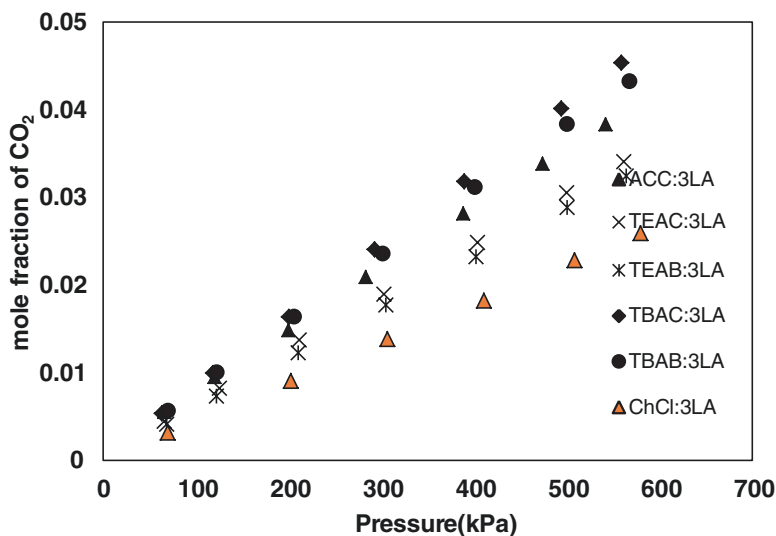
Fig. 12 CO_2 solubility in ammonium:3LA-based DESs at 303.15 K

DESs [136]. Ali et al. synthesized 17 different DESs and found that amine-based DESs have higher CO_2 solubility as compared to glycol-based DESs [137].

4.2.4 Task-Specific DESs

The task-specific DESs were also explored for CO_2 capture, and the first task-specific DES was synthesized by Sze et al. by combining deep eutectic solvents (ChCl:glycerol) with the superbases [138].

The increased CO_2 absorption was observed due to the formation of alkyl carbonate in the presence of superbase. Similarly, Bhawna et al. investigated the CO_2 uptake in ethaline and reline in the presence and absence of three superbases 1,5,7-triazabicyclo[4.4.0]-dec-5-ene, 1,5-diazabicyclo[4.3.0]-non-5-ene, and 1,8-diazabicyclo[5.4.0]undec-7-ene [139]. It was observed that CO_2 uptake of the ethaline and reline significantly enhances due to addition of superbase. Also, DES made of monoethanolamine hydrochloride/ethylenediamine shows very good CO_2 uptake of 33.7 wt% via carbamate formation upon the interaction with CO_2 [140].

4.2.5 CO_2 Solubility in Phosphonium-Based DESs

Very few research has been conducted on the CO_2 solubility of phosphonium-based DESs. Ghaedi et al. first studied CO_2 absorption in different phosphonium-based deep eutectic solvents. Their results show that phosphonium-based DESs have significantly higher CO_2 solubility as shown in Fig. 13 [141, 142]. It is evident from the figure that
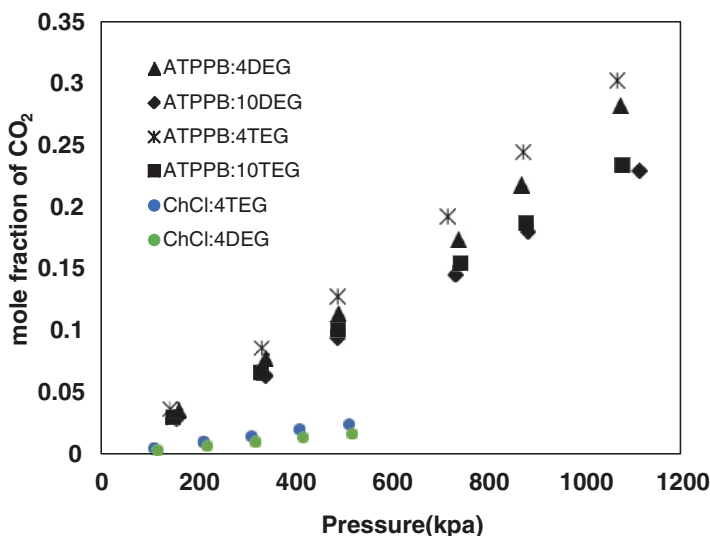
Fig. 13 CO_2 solubility in phosphonium-based DESs at 303.15 K

Table 4 Comparison of CO_2 solubility in different DESs

Solvents (HBD/HBA)	T (K)	P (bar)	CO_2 loading (mol CO_2/ mol solvent)	CO_2 loading (g CO_2/g solvent)	Reference
4MAE/TBAB	303.15	10.46	0.30	0.106	[145]
3TEA/TBAB	298.15	10.00	0.08	0.021	[137]
4EAE/TBAB	303.15	09.93	0.22	0.071	[145]
6DEA/TBAB	303.15	10.11	0.11	0.036	[146]
6EA/TBAB	298.15	10.00	0.12	0.059	[137]
6EA/MTPPhBr	298.15	10.00	0.14	0.072	[137]
GUA/2EA	298.15	11.29	1.36 (mol/kg)	0.060	[147]
6EA/TPAC	298.15	10.57	0.94 (mol/kg)	0.041	[147]
4MAE/BTEACl	303.15	10.07	0.24	0.100	[145]
6DEA/ChCl	303.15	09.71	0.09	0.036	[146]

for same HBDs, DESs with phosphonium as HBAs have significantly higher CO_2 uptake. Also, DESs with higher HBD chain length show higher CO_2 solubility.

The solubility in the hydrophobic solvents was also investigated. Zubeir et al. synthesized six different DESs and investigated the CO_2 solubility from 298 to 323 K [143, 144]. Their results indicate that the CO_2 absorption in the prepared DESs was similar to renowned fluorinated ILs. These solvents could be helpful where the water content is more and can affect the CO_2 solubility of hydrophilic solvents. Table 4 presents the comparison of different DESs for the ability to capture CO_2.

5 Conclusions

Ionic liquids being non-corrosive and having negligible vapor pressure are the emerging solvents for CO_2 capture and considered to be the green solvent. The low cost of the solvent regeneration is the major advantage over conventional amine systems. The limited solubility and high viscosity of the ILs are the major issues. The ionic liquids (bmim[BF_4], bmim[PF_6]) have shown good CO_2 solubility as compared to other ionic liquids. However, the rate of absorption was slow due to physical absorption. To exploit the reactivity of aqueous amine with CO_2 for higher loading and negligible vapor pressure of ILs for easier regeneration, IL-amine blends were explored. These blends have shown higher CO_2 capture ability along with faster rate of absorption. Therefore, a lot is to be investigated for these systems to make them economically feasible for CO_2 absorption. The limited CO_2 solubility and high viscosity of the ILs are the major issues for their commercial applications.

To overcome the drawbacks associated with ionic liquids, deep eutectic solvents (DESs) which are considered as an alternatives to ionic liquids were explored for CO_2 capture. These mixtures are formed by mixing suitable molar ratio of hydrogen bond donor and hydrogen bond acceptor. The DESs are easy to synthesize and do not require complex purification steps. These solvents are cheaper than ionic liquids. The CO_2 solubility in these solvents depends on the type of hydrogen bond donor and hydrogen bond acceptor. Even though DESs have shown good CO_2 capture ability, there is a lot of further research required to use these solvents in the industry.

References

1. IEA (2010) Energy technology perspectives scenarios & strategies to 2050. IEA, Paris
2. Core Writing Team, Pachauri RK, Reisinger A (2007) Climate Change 2007: An assessment of the intergovernmental panel on climate change. IPCC, Geneva
3. Mackay A (2008) Climate Change (2007) Impacts, adaptation and vulnerability. Contribution of working group II to the fourth assessment report of the intergovernmental panel on climate change. J Environ Qual 37:2407–2407
4. Washington W M (2010) Advancing the science of climate change. The National Academies Press, Washington, DC
5. Raynal L, Bouillon PA, Gomez A, Broutin P (2011) From MEA to demixing solvents and future steps, a roadmap for lowering the cost of post-combustion carbon capture. Chem Eng J 171:742–752
6. Parry ML, Canziani OF, Palutik JP, Van der Linden PJ, Hanson C (2007) Climate change 2007: impacts, adaptation and vulnerability; contribution of working group II to the fourth assessment report of the IPCC. Cambridge University Press, Cambridge
7. Aresta M, Dibenedetto A (2007) Utilisation of CO_2 as a chemical feedstock: opportunities and challenges. J Chem Soc Dalton Trans:2975–2992
8. Samanta A, Zhao A, Shimizu GKH, Sarkar P, Gupta R (2012) Post-combustion CO_2 capture using solid sorbents: a review. Ind Eng Chem Res 51:1438–1463

9. Bhown AS, Freeman BC (2011) Analysis and status of post-combustion carbon dioxide capture technologies. Environ Sci Technol 45:458624–458632

10. Pardemann R, Meyer B (2015) Pre-combustion carbon capture. In: Handbook of clean energy systems. John Wiley & Sons, New York, NY

11. Buhre BJP, Elliott LK, Sheng CD, Gupta RP, Wall TF (2005) Oxy-fuel combustion technology for coal-fired power generation. Prog Energy Combust Sci 31:283–307

12. Kanniche M, Gros-Bonnivard R, Jaud P, Valle-Marcos J, Amann JM, Bouallou C (2010) Pre-combustion, post-combustion and oxy-combustion in thermal power plant for CO_2 capture. Appl Therm Eng 30:53–62

13. Wang M, Lawal A, Stephenson P, Sidders J, Ramshaw C (2011) Post-combustion CO_2 capture with chemical absorption: a state-of-the-art review. Chem Eng Res Des 89:1609–1624

14. Mazari SA, Si Ali B, Jan BM, Saeed IM, Nizamuddin S (2015) An overview of solvent management and emissions of amine-based CO_2 capture technology. Int J Greenh Gas Control 34:129–140

15. Versteeg GF, van Swaaij WPM (1988) On the kinetics between CO_2 and alkanolamines both in aqueous and non-aqueous solutions-I. Primary and secondary amines. Chem Eng Sci 43:573–585

16. Crooks JE, Donnellan JP (1989) Kinetics and mechanism of the reaction between carbon dioxide and amines in aqueous solution. J Chem Soc Perkin Trans 2:331–333

17. Versteeg GF, van Swaaij WPM (1988) On the kinetics between CO_2 and alkanolamines both in aqueous and non-aqueous solutions-II. Tertiary amines. Chem Eng Sci 43:587–591

18. Abu-Zahra MRM, Schneiders LHJ, Niederer JPM, Feron PHM, Versteeg GF (2007) $CO2$capture from power plants. Part I. A parametric study of the technical performance based on monoethanolamine. Int J Greenh Gas Control 1:37–46

19. Lu J, Wang L, Sun X, Li J, Liu X (2005) Absorption of CO_2 into aqueous solutions of methyldiethanolamine and activated methyldiethanolamine from a gas mixture in a hollow fiber contactor. Ind Eng Chem Res 44:9230–9238

20. McCann N, Maeder M, Attalla M (2008) Simulation of enthalpy and capacity of CO_2 absorption by aqueous amine systems. Ind Eng Chem Res 47:2002–2009

21. Idem R, Wilson M, Tontiwachwuthikul P, Chakma A, Veawab A, Aroonwilas A, Gelowitz D (2006) Pilot plant studies of the CO_2 capture performance of aqueous MEA and mixed MEA/MDEA solvents at the University of Regina CO_2 capture technology development plant and the boundary dam CO_2 capture demonstration plant. Ind Eng Chem Res 45:2414–2420

22. Sartori G, Savage DW (1983) Sterically hindered amines for CO_2, removal from gases. Ind Eng Chem Fundam 22:239–249

23. Bosch H, Versteeg GF, Van Swaaij WPM (1990) Kinetics of the reaction of CO_2 with the sterically hindered amine 2-Amino-2-methylpropanol at 298 K. Chem Eng Sci 45:1167–1173

24. Haider HAM, Yusoff R, Aroua MK (2011) Equilibrium solubility of carbon dioxide in 2(methylamino)ethanol. Fluid Phase Equilib 303:162–167

25. Hook RJ (1997) An investigation of some sterically hindered amines as potential carbon dioxide scrubbing compounds. Ind Eng Chem Res 36:1779–1790

26. Conway W, Beyad Y, Feron P, Richner G, Puxty G (2014) CO_2 absorption into aqueous amine blends containing benzylamine (BZA), monoethanolamine (MEA), and sterically hindered/tertiary amines. Energy Procedia 63:1835–1841

27. Dubois L, Thomas D (2009) CO_2 absorption into aqueous solutions of monoethanolamine, methyldiethanolamine, piperazine and their blends. Chem Eng Technol 32:710–718

28. Hagewiesche DP, Ashour SS, Al-Ghawas HA, Sandall OC (1995) Absorption of carbon dioxide into aqueous blends of monoethanolamine and N-methyldiethanolamine. Chem Eng Sci 50:1071–1079

29. Aroonwilas A, Veawab A (2004) Characterization and comparison of the CO_2 absorption column. Ind Eng Chem Res 43:2228–2237

30. Nwaoha C, Idem R, Supap T, Saiwan C, Tontiwachwuthikul P, Rongwong W, Al-Marri MJ, Benamor A (2017) Heat duty, heat of absorption, sensible heat and heat of vaporization of

2–Amino–2–Methyl–1–Propanol (AMP), Piperazine (PZ) and Monoethanolamine (MEA) tri–solvent blend for carbon dioxide capture. Chem Eng Sci 170:26–35

31. Nwaoha C, Saiwan C, Tontiwachwuthikul P, Supap T, Rongwong W, Idem R, Al-Marri MJ, Benamor A (2016) Carbon dioxide capture: absorption-desorption capabilities of 2-amino-2-methyl-1-propanol (AMP), piperazine (PZ) and monoethanolamine (MEA) tri-solvent blends. J Nat Gas Sci Eng 33:742–750

32. Lv B, Guo B, Zhou Z, Jing G (2015) Mechanisms of CO_2 capture into monoethanolamine solution with different CO_2 loading during the absorption/desorption processes. Environ Sci Technol 49:10728–10735

33. UNFCCC (United Nations Framework Convention on Climate, Change) (2015) The Paris agreement. Climate Focus summary; Briefing note on the Paris Agreement III. Climate Focus, Amsterdam

34. Anastas PT, Warner JC (1998) Green analytical chemistry. Oxford University Press, Oxford

35. Gu Y, Jérôme F (2013) Bio-based solvents: an emerging generation of fluids for the design of eco-efficient processes in catalysis and organic chemistry. Chem Soc Rev 42:9550–9570

36. Wilkes JS (2002) A short history of ionic liquids - from molten salts to neoteric solvents. Green Chem 4:73–80

37. Plechkova NV, Seddon KR (2008) Applications of ionic liquids in the chemical industry. Chem Soc Rev 37:123–150

38. Kokorin A (2012) Ionic liquids: applications and perspectives. InTech, Rijeka

39. Lei Z, Chen B, Koo YM, Macfarlane DR (2017) Introduction: ionic liquids. Chem Rev 117:6633–6635

40. Maton C, De Vos N, Stevens CV (2013) Ionic liquid thermal stabilities: decomposition mechanisms and analysis tools. Chem Soc Rev 42:5963–5977

41. Villanueva M, Coronas A, García J, Salgado J (2013) Thermal stability of ionic liquids for their application as new absorbents. Ind Eng Chem Res 52:15718–15727

42. Brennecke JF, Maginn EJ (2001) Ionic liquids: innovative fluids for chemical processing. AICHE J 47:2384–2389

43. Singh VV, Nigam AK, Batra A, Boopathi M, Singh B, Vijayaraghavan R (2012) Applications of ionic liquids in electrochemical sensors and biosensors. Int J Electrochem 2012:1–19

44. Okoturo OO, VanderNoot TJ (2004) Temperature dependence of viscosity for room temperature ionic liquids. J Electroanal Chem 568:167–181

45. Zhao D, Liao Y, Zhang ZD (2007) Toxicity of ionic liquids. Clean Soil Air Water 35:42–48

46. Pretti C, Chiappe C, Pieraccini D, Gregori M, Abramo F, Monni G, Intorre L (2006) Acute toxicity of ionic liquids to the zebrafish (Danio rerio). Green Chem 8:238–240

47. Stolte S, Matzke M, Arning J, Böschen A, Pitner WR, Welz-Biermann U, Jastorff B, Ranke J (2007) Effects of different head groups and functionalised side chains on the aquatic toxicity of ionic liquids. Green Chem 9:1170–1179

48. Garcia MT, Gathergood N, Scammells PJ (2005) Biodegradable ionic liquids Part II. Effect of the anion and toxicology. Green Chem 7:9–14

49. Romero A, Santos A, Tojo J, Rodríguez A (2008) Toxicity and biodegradability of imidazolium ionic liquids. J Hazard Mater 151:268–273

50. Blanchard LA, Hancu D (1999) Green processing using ionic liquids and CO_2. Nature 399:28–29

51. Blanchard LA, Gu Z, Brennecke JF (2001) High-pressure phase behavior of ionic liquid/CO_2 systems. J Phys Chem B 105:2437–2444

52. Zhang S, Yuan X, Chen Y, Zhang X (2005) Solubilities of CO_2 in 1-butyl-3-methylimidazolium hexafluorophosphate and 1,1,3,3-tetramethylguanidium lactate at elevated pressures. J Chem Eng Data 50:1582–1585

53. Karadas F, Atilhan M, Aparicio S (2010) Review on the use of ionic liquids (ILs) as alternative fluids for CO_2 capture and natural gas sweetening. Energy Fuel 24:5817–5828

54. Aki SNVK, Mellein BR, Saurer EM, Brennecke JF (2004) High-pressure phase behavior of carbon dioxide with imidazolium-based ionic liquids. J Phys Chem B 108:20355–20365

55. Yokozeki A, Shiflett MB, Junk CP, Grieco LM, Foo T (2008) Physical and chemical absorptions of carbon dioxide in room-temperature ionic liquids. J Phys Chem B 112:16654–16663

56. Anthony JL, Maginn EJ, Brennecke JF (2002) Solubilities and thermodynamic properties of gases in the ionic liquid 1-n-butyl-3-methylimidazolium hexafluorophosphate. J Phys Chem B 106:7315–7320

57. Kanakubo M, Umecky T, Hiejima Y, Aizawa T, Nanjo H, Kameda Y (2005) Solution structures of 1-butyl-3-methylimidazolium hexafluorophosphate ionic liquid saturated with CO_2: experimental evidence of specific anion-CO_2 interaction. J Phys Chem B 109:13847–13850

58. Bara JE, Gabriel CJ, Carlisle TK, Camper DE, Finotello A, Gin DL, Noble RD (2009) Gas separations in fluoroalkyl-functionalized room-temperature ionic liquids using supported liquid membranes. Chem Eng J 147:43–50

59. Muldoon MJ, Aki SNVK, Anderson JL, Dixon JK, Brennecke JF (2007) Improving carbon dioxide solubility in ionic liquids. J Phys Chem B 111:9001–9009

60. Aparicio S, Atilhan M (2010) Computational study of hexamethylguanidinium lactate ionic liquid: a candidate for natural gas sweetening. Energy Fuel 24:4989–5001

61. Yuan X, Zhang S, Liu J, Lu X (2007) Solubilities of CO_2 in hydroxyl ammonium ionic liquids at elevated pressures. Fluid Phase Equilib 257:195–200

62. Palgunadi J, Kang JE, Nguyen DQ, Kim JH, Min BK, Lee SD, Kim H, Kim HS (2009) Solubility of CO_2 in dialkylimidazolium dialkylphosphate ionic liquids. Thermochim Acta 494:94–98

63. Revelli AL, Mutelet F, Jaubert JN (2010) High carbon dioxide solubilities in imidazolium-based ionic liquids and in poly(ethylene glycol) dimethyl ether. J Phys Chem B 114:12908–12913

64. Kurnia KA, Harris F, Wilfred CD, Abdul Mutalib MI, Murugesan T (2009) Thermodynamic properties of CO_2 absorption in hydroxyl ammonium ionic liquids at pressures of (100-1600) kPa. J Chem Thermodyn 41:1069–1073

65. Camper D, Scovazzo P, Koval C, Noble R (2004) Gas solubilities in room-temperature ionic liquids. Ind Eng Chem Res 43:3049–3054

66. Akanksha, Pant KK, Srivastava VK (2008) Mass transport correlation for CO_2 absorption in aqueous monoethanolamine in a continuous film contactor. Chem Eng Process Process Intensif 47:920–928

67. Bates ED, Mayton RD, Ntai I, Davis JH Jr, Tong KH, Wong KY, Chan TH (2002) CO_2 capture by a task specific ionic liquid. J Am Chem Soc 124:3423–3425

68. Gurkan BE, De Fuente JC, Mindrup EM, Ficke LE, Goodrich BF, Price EA, Schneider WF, Brennecke JF (2010) Equimolar CO_2 absorption by anion-functionalized ionic liquids. J Am Chem Soc 132:2116–2117

69. Goodrich BF, De La Fuente JC, Gurkan BE, Zadigian DJ, Price EA, Huang Y, Brennecke JF (2011) Experimental measurements of amine-functionalized anion-tethered ionic liquids with carbon dioxide. Ind Eng Chem Res 50:111–118

70. Gutowski KE, Maginn EJ (2008) Amine-functionalized task-specific ionic liquids: a mechanistic explanation for the dramatic increase in viscosity upon complexation with CO_2 from molecular simulation. J Am Chem Soc 130:14690–14704

71. McDonald JL, Sykora RE, Hixon P, Mirjafari A, Davis JH (2014) Impact of water on CO_2 capture by amino acid ionic liquids. Environ Chem Lett 12:201–208

72. Goodrich BF, De Fuente JC, Gurkan BE, Lopez ZK, Price EA, Huang Y, Brennecke JF (2011) Effect of water and temperature on absorption of CO_2 by amine-functionalized anion-tethered ionic liquids. J Phys Chem B 115:9140–9150

73. Zhang Y, Zhang S, Lu X, Zhou Q, Fan W, Zhang XP (2009) Dual amino-functionalised phosphonium ionic liquids for CO_2 capture. Chemistry 15:3003–3011

74. Cserjési P, Nemestóthy N, Bélafi-Bakó K (2010) Gas separation properties of supported liquid membranes prepared with unconventional ionic liquids. J Membr Sci 349:6–11

75. Scovazzo P, Kieft J, Finan DA, Koval C, DuBois D, Noble R (2004) Gas separations using non-hexafluorophosphate [PF$_6$]⁻ anion supported ionic liquid membranes. J Membr Sci 238:57–63

76. Neves LA, Crespo JG, Coelhoso IM (2010) Gas permeation studies in supported ionic liquid membranes. J Membr Sci 357:160–170
77. Gonzalez-Miquel M, Palomar J, Omar S, Rodriguez F (2011) CO_2/N_2 selectivity prediction in supported ionic liquid membranes (SILMs) by COSMO-RS. Ind Eng Chem Res 50:5739–5748
78. Tang J, Tang H, Sun W, Plancher H, Radosz M, Shen Y (2005) Poly(ionic liquid)s: a new material with enhanced and fast CO_2 absorption. Chem Commun:3325–3327
79. Tang J, Sun W, Tang H, Radosz M, Shen Y (2005) Enhanced CO_2 absorption of poly(ionic liquid)s. Macromolecules 38:2037–2039
80. Hu X, Tang J, Blasig A, Shen Y, Radosz M (2006) CO_2 permeability, diffusivity and solubility in polyethylene glycol-grafted polyionic membranes and their CO_2 selectivity relative to methane and nitrogen. J Membr Sci 281:130–138
81. Blasig A, Tang J, Hu X, Tan SP, Youqing Shen A, Radosz M (2007) Carbon dioxide solubility in polymerized ionic liquids containing ammonium and imidazolium cations from magnetic suspension balance: P[VBTMA][BF$_4$] and P[VBMI][BF$_4$]. Ind Eng Chem Res 46:5542–5547
82. Zhao Z, Dong H, Zhang X (2012) The research progress of CO_2 capture with ionic liquids. Chin J Chem Eng 20:120–129
83. Wang C, Luo X, Luo H, Jiang D, Li H, Dai S (2011) Tuning the basicity of ionic liquids for equimolar CO_2 capture. Angew Chem Int Ed 50:4918–4922
84. Ventura SPM, Pauly J, Daridon JL, Lopes da Silva JA, Marrucho IM, Dias AMA, Coutinho JAP (2008) High pressure solubility data of carbon dioxide in (tri-iso-butyl(methyl)phosphonium tosylate + water) systems. J Chem Thermodyn 40:1187–1192
85. Wappel D, Gronald G, Kalb R, Draxler J (2010) Ionic liquids for post-combustion CO_2 absorption. Int J Greenh Gas Control 4:486–494
86. Camper D, Bara JE, Gin DL, Noble RD (2008) RTIL–Amine solutions tunable solvents for efficient and reversible capture of CO_2. Ind Eng Chem Res 47:8496–8498
87. Feng Z, Cheng-Gang F, You-Ting W, Yuan-Tao W, Ai-Min L, Zhi-Bing Z (2010) Absorption of CO_2 in the aqueous solutions of functionalized ionic liquids and MDEA. Chem Eng J 160:691–697
88. Zhao Y, Zhang X, Zeng S, Zhou Q, Dong H, Tian X, Zhang S (2010) Density, viscosity, and performances of carbon dioxide capture in 16 absorbents of amine + ionic liquid + H_2O, ionic liquid + H_2O, and Amine + H_2O systems. J Chem Eng Data 55:3513–3519
89. Baj S, Siewniak A, Chrobok A, Krawczyk T, Sobolewski A (2013) Monoethanolamine and ionic liquid aqueous solutions as effective systems for CO_2 capture. J Chem Technol Biotechnol 88:1220–1227
90. Taib MM, Murugesan T (2012) Solubilities of CO_2 in aqueous solutions of ionic liquids (ILs) and monoethanolamine (MEA) at pressures from 100 to 1600kPa. Chem Eng J 181–182:56–62
91. Huang Y, Zhang X, Zhang X, Dong H, Zhang S (2014) Thermodynamic modeling and assessment of ionic liquid-based CO_2 capture processes. Ind Eng Chem Res 53:11805–11817
92. Yang J, Yu X, Yan J, Tu ST (2014) CO_2 capture using amine solution mixed with ionic liquid. Ind Eng Chem Res 53:2790–2799
93. Haider MB, Hussain Z, Kumar R (2016) CO_2 absorption and kinetic study in ionic liquid amine blends. J Mol Liq 224:1025–1031
94. Conway W, Bruggink S, Beyad Y, Luo W, Melián-Cabrera I, Puxty G, Feron P (2015) CO_2 absorption into aqueous amine blended solutions containing monoethanolamine (MEA), N,N-dimethylethanolamine (DMEA), N,N-diethylethanolamine (DEEA) and 2-amino-2-methyl-1-propanol (AMP) for post-combustion capture processes. Chem Eng Sci 126:446–454
95. Maase M, Massonne K (2005) Biphasic acid scavenging utilizing ionic liquids: the first commercial process with ionic liquids. ACS Symp Ser 902:126–132

96. Vekariya RL (2017) A review of ionic liquids: applications towards catalytic organic transformations. J Mol Liq 227:44–60

97. Rodríguez NR, González ASB, Tijssen PMA, Kroon MC (2015) Low transition temperature mixtures (LTTMs) as novel entrainers in extractive distillation. Fluid Phase Equilib 385:72–78

98. Petkovic M, Seddon KR, Rebelo LPN, Pereira CS (2011) Ionic liquids: a pathway to environmental acceptability. Chem Soc Rev 40:1383–1403

99. Wells AS, Coombe VT (2006) On the freshwater ecotoxicity and biodegradation properties of some common ionic liquids. Org Process Res Dev 10:794–798

100. Cadena C, Anthony JL, Shah JK, Morrow TI, Brennecke JF, Maginn EJ (2004) Why is CO_2 so soluble in imidazolium-based ionic liquids? J Am Chem Soc 126:5300–5308

101. Kim YS, Choi WY, Jang JH, Yoo KP, Lee CS (2005) Solubility measurement and prediction of carbon dioxide in ionic liquids. Fluid Phase Equilib 228–229:439–445

102. Shariati A, Peters CJ (2004) High-pressure phase behavior of systems with ionic liquids: Part III. The binary system carbon dioxide + 1-hexyl-3-methylimidazolium hexafluorophosphate. J Supercrit Fluids 30:139–144

103. Shen KP, Li MH (1992) Solubility of carbon dioxide in aqueous mixtures of monoethanolamine with methyldiethanolamine. J Chem Eng Data 37:96–100

104. Abbott AP, Boothby D, Capper G, Davies DL, Rasheed RK (2004) Deep eutectic solvents formed between choline chloride and carboxylic acids. J Am Chem Soc 126:9142

105. Abbott AP, Capper G, Davies DL, Rasheed RK, Tambyrajah V (2003) Novel solvent properties of choline chloride/urea mixtures. Chem Commun:70–71

106. Francisco M, Van Den Bruinhorst A, Kroon MC (2013) Low-transition-temperature mixtures (LTTMs): a new generation of designer solvents. Angew Chem Int Ed 52:3074–3085

107. Smith EL, Abbott AP, Ryder KS (2014) Deep eutectic solvents (DESs) and their applications. Chem Rev 114:11060–11082

108. Tang B, Row KH (2013) Recent developments in deep eutectic solvents in chemical sciences. Monatshefte Fur Chemie 144:1427–1454

109. Paiva A, Craveiro R, Aroso I, Martins M, Reis RL, Duarte ARC (2014) Natural deep eutectic solvents - solvents for the 21st century. ACS Sustain Chem Eng 2:1063–1071

110. Abo-hamad A, Hayyan M, Abdulhakim M, Ali M, Cui X, Zhang S, Shi F, Zhang Q, Ma X, Lu L, Deng Y, Earle MJ, Seddon KR, Medycznego U, Maria A, Cieczy ZAS, Nowych JO, Zlotin SG, Makhova NN (2010) Potential applications of deep eutectic solvents in nanotechnology. Chem Eng J 273:551–567

111. Liu P, Hao J-W, Mo L-P, Zhang Z-H (2015) Recent advances in the application of deep eutectic solvents as sustainable media as well as catalysts in organic reactions. RSC Adv 5:48675–48704

112. Garcia G, Aparicio S, Ullah R, Atilhan M (2015) Deep eutectic solvents: physicochemical properties and gas separation applications. Energy Fuel 29:2616–2644

113. Zhang Q, De Oliveira Vigier K, Royer S, Jérôme F (2012) Deep eutectic solvents: syntheses, properties and applications. Chem Soc Rev 41:7108–7146

114. Chandran D, Khalid M, Walvekar R, Mubarak NM, Dharaskar S, Wong WY, Gupta TCSM (2019) Deep eutectic solvents for extraction-desulphurization: a review. J Mol Liq 275:312–322

115. Tang B, Zhang H, Row KH (2015) Application of deep eutectic solvents in the extraction and separation of target compounds from various samples. J Sep Sci 38:1053–1064

116. Troter DZ, Todorović ZB, Dokić-Stojanović DR, Stamenković OS, Veljković VB (2016) Application of ionic liquids and deep eutectic solvents in biodiesel production: a review. Renew Sust Energ Rev 61:473–500

117. Wazeer I, Hadj-kali MK (2017) Deep eutectic solvents: designer fluids for chemical processes. J Chem Tech & Biotech 93:945–958

118. Xu P, Zheng GW, Zong MH, Li N, Lou WY (2017) Recent progress on deep eutectic solvents in biocatalysis. Bioresour Bioprocess 4:34

119. Zdanowicz M, Wilpiszewska K, Spychaj T (2018) Deep eutectic solvents for polysaccharides processing. A review. Carbohydr Polym 200:361–380
120. Abbott AP (2004) Application of hole theory to the viscosity of ionic and molecular liquids. ChemPhysChem 5:1242–1246
121. Rengstl D, Fischer V, Kunz W (2014) Low-melting mixtures based on choline ionic liquids. Phys Chem Chem Phys 16:22815–22822
122. Hayyan M, Hashim MA, Al-Saadi MA, Hayyan A, AlNashef IM, Mirghani MES (2013) Assessment of cytotoxicity and toxicity for phosphonium-based deep eutectic solvents. Chemosphere 93:455–459
123. Hayyan M, Hashim MA, Hayyan A, Al-Saadi MA, AlNashef IM, Mirghani MES, Saheed OK (2013) Are deep eutectic solvents benign or toxic? Chemosphere 90:2193–2195
124. Juneidi I, Hayyan M, Mohd Ali O (2016) Toxicity profile of choline chloride-based deep eutectic solvents for fungi and Cyprinus carpio fish. Environ Sci Pollut Res 23:7648–7659
125. Mbous YP, Hayyan M, Hayyan A, Wong WF, Hashim MA, Looi CY (2017) Applications of deep eutectic solvents in biotechnology and bioengineering—promises and challenges. Biotechnol Adv 35:105–134
126. Li X, Hou M, Han B, Wang X, Zou L (2008) Solubility of CO_2 in a choline chloride + urea eutectic mixture. J Chem Eng Data 53:548–550
127. Leron RB, Li MH (2013) Solubility of carbon dioxide in a choline chloride-ethylene glycol based deep eutectic solvent. Thermochim Acta 551:14–19
128. Leron RB, Li MH (2013) Solubility of carbon dioxide in a eutectic mixture of choline chloride and glycerol at moderate pressures. J Chem Thermodyn 57:131–136
129. Li G, Deng D, Chen Y, Shan H, Ai N (2014) Solubilities and thermodynamic properties of CO2 in choline-chloride based deep eutectic solvents. J Chem Thermodyn 75:58–62
130. Lu M, Han G, Jiang Y, Zhang X, Deng D, Ai N (2015) Solubilities of carbon dioxide in the eutectic mixture of levulinic acid (or furfuryl alcohol) and choline chloride. J Chem Thermodyn 88:72–77
131. Chen Y, Ai N, Li G, Shan H, Cui Y, Deng D (2014) Solubilities of carbon dioxide in eutectic mixtures of choline chloride and dihydric alcohols. J Chem Eng Data 59:1247–1253
132. Liu X, Gao B, Jiang Y, Deng D (2017) Solubilities and thermodynamic properties of carbon dioxide in guaiacol-based deep eutectic solvents. J Chem Eng Data 62:1448–1455
133. Haider MB, Jha D, Sivagnanam BM, Kumar R (2018) Thermodynamic and kinetic studies of CO_2 capture by glycol and 2 amine-based deep eutectic solvents. J Chem Eng Data 63:2671–2680
134. Leron RB, Caparanga A, Li MH (2013) Carbon dioxide solubility in a deep eutectic solvent based on choline chloride and urea at T = 303.15-343.15K and moderate pressures. J Taiwan Inst Chem Eng 44:879–885
135. Su WC, Wong DSH, Li MH (2009) Effect of water on solubility of carbon dioxide in (Aminomethanamide + 2-Hydroxy-N,N,N-trimethylethanaminium chloride). J Chem Eng Data 54:1951–1955
136. Uma Maheswari A, Palanivelu K (2015) Carbon dioxide capture and utilization by alkanolamines in deep eutectic solvent medium. Ind Eng Chem Res 54:11383–11392
137. Ali E, Hadj-Kali MK, Mulyono S, Alnashef I, Fakeeha A, Mjalli F, Hayyan A (2014) Solubility of CO_2 in deep eutectic solvents: experiments and modelling using the Peng-Robinson equation of state. Chem Eng Res Des 92:1898–1906
138. Sze LL, Pandey S, Ravula S, Pandey S, Zhao H, Baker GA, Baker SN (2014) Ternary deep eutectic solvents tasked for carbon dioxide capture. ACS Sustain Chem Eng 2:2117–2123
139. Bhawna A, Pandey S (2017) Superbase-added choline chloride-based deep eutectic solvents for CO_2 capture and sequestration. Chem Select 2:11422–11430
140. Trivedi TJ, Lee JH, Lee HJ, Jeong YK, Choi JW (2014) Deep eutectic solvents as attractive media for CO_2 capture. Green Chem 18:2834–2842
141. Ghaedi H, Ayoub M, Sufian S, Shariff AM, Hailegiorgis SM, Khan SN (2017) CO_2 capture with the help of phosphonium-based deep eutectic solvents. J Mol Liq 243:564–571

142. Ghaedi H, Ayoub M, Sufian S, Murshid G, Farrukh S, Shariff AM (2017) Investigation of various process parameters on the solubility of carbon dioxide in phosphonium-based deep eutectic solvents and their aqueous mixtures: experimental and modeling. Int J Greenh Gas Control 66:147–158

143. Haider MB, Jha D, Kumar R, Marriyappan Sivagnanam B (2020) Ternary hydrophobic deep eutectic solvents for carbon dioxide absorption. Int J Greenh Gas Control 92:102839

144. Zubeir LF, Van Osch DJGP, Rocha MAA, Banat F, Kroon MC (2018) Carbon dioxide solubilities in decanoic acid-based hydrophobic deep eutectic solvents. J Chem Eng Data 63:913–919

145. Haider MB, Jha D, Marriyappan Sivagnanam B, Kumar R (2019) Modelling and simulation of CO_2 removal from shale gas using deep eutectic solvents. J Environ Chem Eng 7:102747

146. Haider MB, Kumar R (2020) Solubility of CO_2 and CH_4 in sterically hindered amine-based deep eutectic solvents. Sep Purif Technol 248:117055

147. Sarmad S, Xie Y, Mikkola J-P, Ji X (2017) Screening of deep eutectic solvents (DESs) as green CO_2 sorbents: from solubility to viscosity. New J Chem 41:290–301

Evolution of Ziegler-Natta Catalysts for Polymerization of Olefins

Akhoury Sudhir Kumar Sinha and Umaprasana Ojha

Abstract This chapter provides a brief account of the discovery and gradual evolution of Ziegler-Natta catalysts for polymerization of various olefins, α-olefins, and functional olefins. The structure of first and second generation catalysts is introduced, and the different mechanisms proposed by the scientists for the polymerization of ethylene using this catalyst is discussed. Subsequently, the control of branching and mechanism to produce stereospecific poly-α-olefins is elaborated. Development of catalysts for synthesis of stereo-controlled polyolefins is discussed along with methods to determine the stereospecificity of the polymers. The evolution of metallocene-based Ziegler-Natta catalysts and the mechanism of polymerization based on these catalysts are briefed. The following section discusses about the catalyst compositions useful for polymerization of functional olefin monomers and their copolymerization with propylene. Development of catalyst compositions based on Pd, Ni, Cu, and Fe is discussed, and subsequent polymerization mechanism is included. A series of catalysts synthesized using vanadium and various chelated ligands are discussed in context of their catalytic activity and the structure of polymer formed. The last chapter unveils some of the recent advances in these categories of catalysts and future scope of the catalyst.

Keywords Ziegler-Natta catalysts · Polymerization mechanism · Stereospecific polyolefins · Tridentate ligands · Vanadium-based complexes · Polyolefins synthesis

1 Introduction

Polyethylene (PE) was a serendipitous invention by Reginald O. Gibson and Eric W. Fawcett of Imperial Chemical Industries (ICI) in 1933. The above two organic chemists, while performing a reaction between ethylene and benzaldehyde in an

A. S. K. Sinha (✉)
Department of Chemical Engineering and Engineering Sciences,
Rajiv Gandhi Institute of Petroleum Technology, Amethi, UP, India
e-mail: asksinha@rgipt.ac.in

U. Ojha
Department of Basic Sciences & Humanities,
Rajiv Gandhi Institute of Petroleum Technology, Amethi, UP, India

Table 1 Mechanical and thermal properties of HDPE, MDPE, LLDPE, and LDPE

Properties	HDPE	MDPE	LLDPE	LDPE
UTS (psi)	2200–6530	1810–5080	1150–6600	1500–2600
Young's modulus (10^5 psi)	0.90–2.10	1.16	0.20–2.27	0.28–0.75
Ultimate elongation (%)	3–1900	50–1100	8–1100	100–850
Melting point (°C)	130–140	126–128	75–128	108–121
Flexural modulus (10^5 psi)	0.7–7.0	0.86–1.74	0.02–1.10	0.22–3.20
Density (g/cm³)	0.93–1.27	0.93–1.05	0.87–0.96	0.91–0.95

The properties were collected from matweb.com
UTS ultimate tensile strength
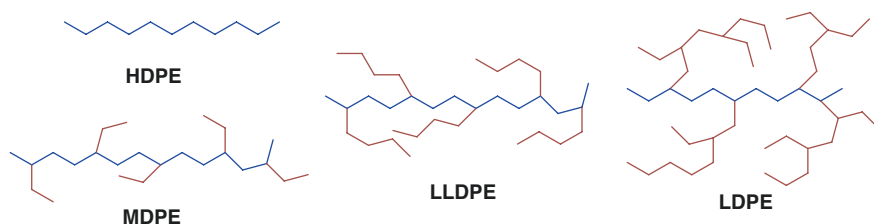
Fig. 1 Schematic representation of the polymer chains of high-density PE (HDPE), medium-density PE (MDPE), linear LDPE (LLDPE), and LDPE

autoclave, observed formation of a white, waxy, and light substance. Apparently, a drop in pressure due to an inadvertent leak and presence of trace amount of oxygen facilitated the polymerization and formation of this plastic material. This revolutionary plastic substance was later termed as PE. Soon PE found its first commercial application, and a patent on this polymer was filed by ICI in 1936. In 1944, the real commercial implementation of PE commenced. Both DuPont and Bakelite Corporation obtained the license from ICI to start large-scale commercial production of PE. PE possessing excellent commercial value owing to its moisture and chemical and electrical resistance is one of the major petrochemical products. Currently, PE is synthesized in a large scale in several countries all over the world with around 90 million metric tons of production per year. The C2 and C3 olefin side products emanating from the fluid catalytic cracking units have promoted the large-scale production of PE.

However, the PE synthesized under free radical condition was low-density PE (LDPE) and exhibited inferior mechanical properties with low tensile strength and Young's modulus along with low melting point and low crystallinity (Table 1). In presence of a free radical initiator such as peroxides and azobisisobutyronitrile (AIBN) and under high pressure and temperature conditions, inter- and intramolecular chain transfer to polymer chain resulted in long- and short-chain branching (Fig. 1). Occurrence of these chain transfer reactions increased the polydispersity index (PDI), broadened the molecular weight distribution, and lowered the packing efficiency and density of the samples. As a result, the mechanical properties of LDPE were compromised to certain extend.

2 Zeigler-Natta Catalyst

The commercial viability of PE took a revolutionary leap in 1953 after the momentous invention of a versatile organometallic catalyst for polymerization of ethylene by Karl Waldemar Ziegler of the Kaiser Wilhelm Institute and Erhard Holzkamp. Ziegler utilized a binary mixture of transition metal halides of group IV and metal alkyls of group I to III, typically $TiCl_4$ and $AlEt_3$ to polymerize ethylene under normal pressure and room temperature conditions [1]. The procedure was able to minimize the branching and produced high-density polyethylene (HDPE). Soon after this invention, Giulio Natta and coworkers further demonstrated the versatility of this catalyst and trivalent titanium chloride-based system to polymerize different α-olefins such as propylene and butylene to produce stereoregular isotactic polymers [2]. This path-breaking invention led to development of commercial plastics and elastomers, and living cationic, anionic, and radical polymerizations evolved with time, expanding the research and development on synthetic high polymers. The income earned from his patents ensured financial independence and further expansion of the Institute of which he was the Director.

Since 1955, the scientific literature exploded especially with several thousands of reports on utilization of these catalysts for polymerization of a range of olefins and dienes and further modification of the catalyst to improve the versatility and efficiency. This chemistry associated with the name of Karl Ziegler is considered as one of the "historical landmarks in chemistry," and in recognition to their efforts, both Professor K. Ziegler and G. Natta were honored with the prestigious Nobel Prize in Chemistry in 1963. In general, though the number of variations in transition and alkyl metals is large, the number of useful combinations for efficient catalysis is limited. Titanium and vanadium have so far displayed excellent activity, and zirconium, hafnium, and tungsten have shown promise for future development. Similarly, in case of alkyl metals, aluminum have been outstanding and utilized in a number of catalyst compositions followed by magnesium and zinc in selective cases. The versatility of this Ziegler-Natta catalyst is ascertained to the number of monomers these catalyst systems can efficiently polymerize and the number of different products those can be obtained from each monomer.

2.1 Mechanism of Polymerization

Several mechanistic pathways are proposed in the literature towards the polymerization of olefins in presence of Ziegler-Natta catalyst. Most of the reports agree to one general aspect of the polymerization, i.e., the polymerization occurs through insertion of olefin monomer between the metal atom and one of the alkyl groups of

the organometallic compound. However, some disagreement still exists regarding the nature of active center, i.e., the growing polymer chain is attached to the transition metal or the non-transition metal.

2.2 Mechanism Based on Bimetallic Complex

Natta and Mazzanti proposed a bimetallic mechanism while studying the ethylene polymerization using a soluble complex of titanium chloride and aluminum alkyl (Fig. 2a) [3]. Similarly, Furukawa and Tsuruta also supported the bimetallic mechanism, and the complex of AlR_3-$TiCl_3$ was proposed to be responsible for polymerization (Fig. 2b) [4]. In a later stage, several other researchers including Huggins, Boor, and Patat supported the above bimetallic mechanism.

As per the mechanism proposed by Rodriguez et al., since the Ziegler-Natta polymerization is stereospecific, a bimetallic complex is involved as shown in Scheme 1 [5]. The vacant t_{2g} orbital on the Ti atom is forming a π-complex with the olefin monomer as a part of the initiation step. Subsequently, insertion of the olefin occurs between Ti-C bond and simultaneous rupture of Al-C bond. The alkyl group migrates to the olefin carbon, and the CH_2 of olefin replaces the alkyl group originally placed between Ti and Al. The active center is restored now after insertion of one olefin moiety. The propagation occurs via repetition of the above olefin insertion steps, and polyolefin possessing the alkyl group at the chain end is obtained after the polymerization.

2.3 Mechanism Based on Monometallic Complex

Cossee proposed that a monometallic complex is involved in the polymerization and the active center is an alkylated Ti-ion [6]. As per the detailed study by Arlman and Cossee, a penta-coordinated alkyl titanium complex is formed by exchange reaction of titanium chloride with alkyl aluminum (Scheme 2). The vacant site on the alkyl titanium complex formed π-complex with the olefin monomer. Subsequently, insertion of olefin occurred between the Ti and alkyl group, and the vacant site on Ti surface was restored for addition of next monomer. Involvement of alkyl titanium

Fig. 2 Bimetallic complexes used by (**a**) Natta et al. and (**b**) proposed by Furukawa et al. responsible for polymerization of olefin
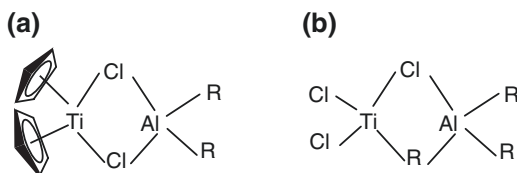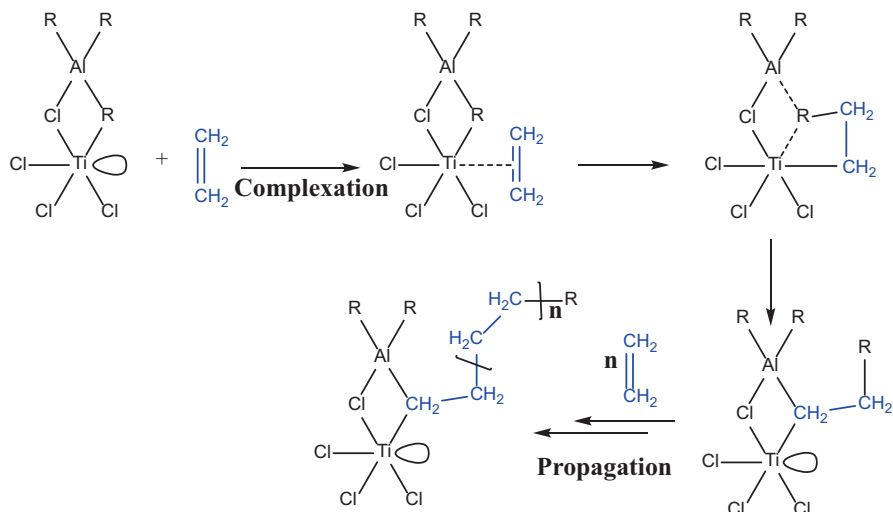
Scheme 1 Olefin polymerization mechanism based on bimetallic complex by Rodriguez

Scheme 2 The monometallic mechanism for Ziegler-Natta polymerization proposed by Arlman and Cossee
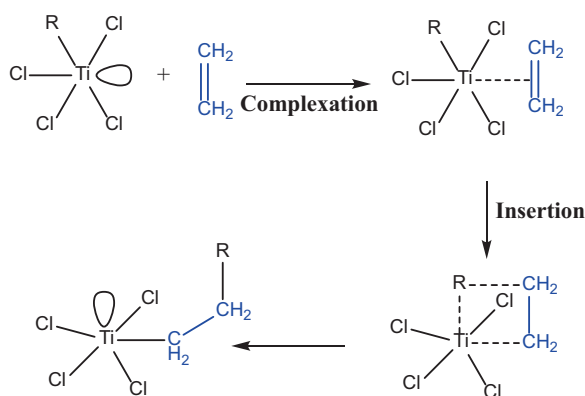
complex in the polymerization mechanism was already supported by Ludlum and Ziegler [7, 8]. The role of alkyl aluminum is primarily to serve as the alkylating agent. Cossee further reasoned that for formation of π-complex between metal and olefin, the d orbital of metal atom must be sufficiently large to efficiently overlap with the anti-bonding orbital of the olefin. This particular case is suitable with metal possessing low effective nuclear charge. In fact, Natta had already proposed that the metals with ionization potential less than 7 eV are suitable for such π-complex formation.

The most intriguing aspect of the mechanism is carbon-carbon bond formation. In this regard, Rooney and Green proposed that the mechanism involves 1,2-hydrogen shift from the α-carbon to the metal surface followed by the formation of metallo-cyclobutane (Scheme 3) [9]. As per this mechanism, the metathesis involving
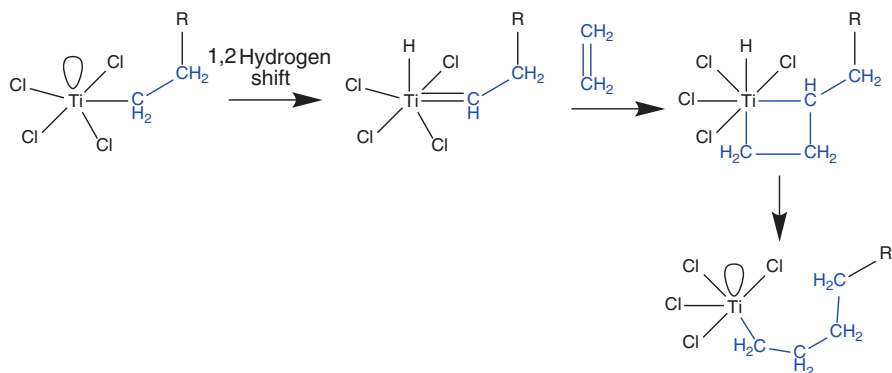
Scheme 3 The polymerization mechanism based on hydrogen shift proposed by Rooney and Green

metallocyclobutane and metal-olefin-carbene interconversion guided the polymerization. The kinetics of the polymerization was anticipated to be strongly dependent on the isotopic effect if the hydrogel shift was part of the mechanism. However, Grubbs soon reported that the isotopic effect on the polymerization is absent or negligible that tilted the mechanism in favor of Arlman and Cossee theory [10]. Corradini et al. further studied the Cossee model via computation of non-bonded interactions at the catalyst surface. They proposed that the olefin coordinates in an inward position to minimize the steric hindrance on the catalyst surface. This strongly restricts the orientation of the first carbon-carbon bond, which may explain the stereospecificity of the polymer chain [11]. This allowed the synthesis of stereoregular polyhydrocarbons (Scheme 3).

3   Synthesis of Stereospecific Polyolefins

Stereoselective poly-α-olefins are especially important, since the thermal and mechanical properties of isotactic poly-α-olefins are strongly dependent on the number of carbons in the side chain of the monomer. For example, the melting temperature (T_m) of the poly-α-olefins decreases from 176 to -50 °C by changing the number of carbons in side chain from one to six (Fig. 3). The T_m further increases to 80 °C on increasing the number of carbons in the side chain to 17 [12]. Over the period of time since discovery of Ziegler-Natta catalyst, the catalyst composition was varied to produce stereoselective polyolefins. A substantial research was devoted to achieve technological advances with the existing catalyst system. In 1970, matrix-supported catalyst system was reported in which the titanium chloride was supported on crystalline $MgCl_2$ matrix. Soon, research on development of homogeneous catalyst gained momentum. Especially, the homogeneous catalyst systems were suitable to synthesize polyolefins with syndiotactic polypropylene.
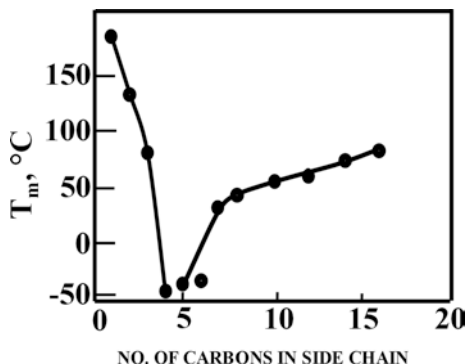
Bis(cyclopentadienyl)titanium chloride and trialkyl aluminum-based catalyst compositions were studied as possible homogeneous system for polymerization of ethylene.

The catalytic activity of these systems was dependent on the chloride content of these catalysts [13]. Interestingly, Vollmer and coworkers showed that in presence of trace amount of water, these catalyst systems even in absence of chloride content efficiently polymerized ethylene [14]. Furthermore, the molecular weight of resulting polymer was dependent on the polymerization temperature. For example, a tri(cyclopentadienyl)zirconium- and trialkylaluminum-based catalyst system effectively polymerized ethylene, and the molecular weight increased from 40,000 to 1.5×10^6 g/mol on decreasing the temperature from 90 to 50 °C. Controlled synthesis of methylalumoxanes from trialkylaluminum in presence of water was proposed to be the key factor in improving the efficiency of these systems [15]. Soon the potential of Cp_2MX_2-AlR_3 systems as efficient polymerization catalyst was realized, and systems based on other group 4 metals such as Zr or Hf were studied. However, the polymerization of propylene in presence of bis(cyclopentadienyl)M(IV), where M is Ti or Zr, and methylalumoxanes produced atactic structures (Fig. 4) [16].

Catalysts and conditions were optimized to produce isotactic and syndiotactic polypropylene. Ewen synthesized a polypropylene with mmmmmrmmmmmr stereo sequence using bis(cyclopentadienyl)bis(phenyl)titanium catalyst system (Fig. 5) [17]. Two successive methyl groups on same plane were assigned as a meso (m)-diad, whereas two successive methyl groups in opposite plane are assigned as racemic (r)-diad.

Nuclear magnetic resonance (NMR) spectroscopy was utilized to estimate the population of stereospecific segments and corresponding configuration in the polypropylene samples. The relative intensities of pentads mostly followed a Bernoullian statistical distribution of a chain-end controlled stereospecific polymerization (Table 2). The ^{13}C NMR spectroscopic data revealed that under low temperature conditions, the steric factor predominated the stereochemistry of monomer insertion reaction. The ^{13}C resonances in the range of 19–23 ppm were studied to understand the presence and population isotactic (m) type sequences in the polypropylene chains. The m sequences were observed at higher chemical shift region (~21.5 ppm).
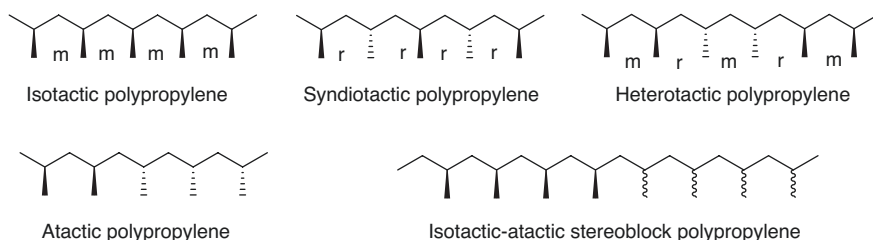
Fig. 4 Schematic representation of stereo-controlled polypropylene chain
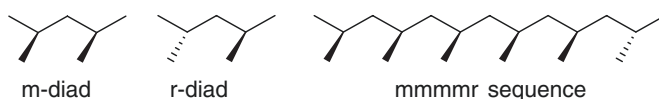
Fig. 5 The schematic representation of m-diad, r-diad, and mmmm pentad configuration of polypropylene chain segment

Table 2 The Bernoullian probability distribution of stereochemical sequences, especially diads and pentads in polypropylene chains [20]

Sequence	m	r	mm	mr	rr	mmmm	mmmr	rmmr	mmrr
Bernoullian	P	$(1-P)$	P^2	$2P(1-P)$	$(1-P)^2$	P^4	$2P^3(1-P)$	$2P^2(1-P)^2$	$2P^3(1-P)$

mrmm	rmrm	rrrr	rrrm	mrrm
$P^2(1-P)^2$	$2P^2(1-P)^2$	$2P(1-P)^3$	$P^2(1-P)^2$	$(1-P)^4$

Similarly, the methylene (CH_2) carbons resonated in between 44 and 46 ppm [18]. The polymerization data revealed that the polypropylenes synthesized at low temperature ($-45\ ^\circ$C) conditions possessed mmmm pentads with small amounts of mmmr and mmrm pentads [17]. The stereoregularity of the polymer increased up to 85% on decreasing the polymerization temperature to $-60\ ^\circ$C. Similarly, the VC1$_4$-Al(C_2H_5)$_2$Cl catalyst system produced syndiotactic polypropylene with similar stereoregularity [19]. Furthermore, the syndio-regulating ability is reinforced in presence of cyclohexene, oxygen, or *tert*-butyl perbenzoate.

The bulkiness of R group in alkyl aluminum halide and the nature of halide (when halide is chloride only) controlled the syndio-regularity of polymer. The reaction conditions such as low temperature ($-40\ ^\circ$C) and shorter polymerization period favored the above stereospecificity of polypropylene. Addition of anisole as donor with donor:V ratio as one under low conversion scenario and a non-polar solvent like heptane complemented the yield of syndiotactic polypropylene. Boor et al. proposed the mechanism to be coordination-anionic type with an alkylated vanadium species acting as the active site. The initiation occurred with complexation of propylene to the V empty orbital (Scheme 4).

Subsequently, the CH_2 and CH of the monomer formed bond with V and R, respectively, through a concerted four-membered ring pathway. During the course
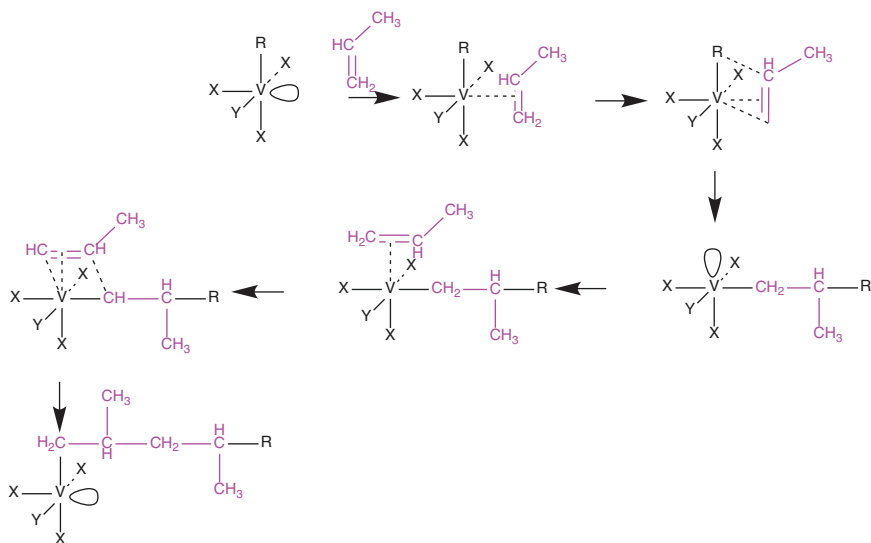
Scheme 4 Mechanism for the formation of syndiotactic polypropylene in presence of VCl$_4$-Al(C$_2$H$_5$)$_2$Cl catalyst system

of polymerization, development of partial +ve charge on CH and −ve charge on CH$_2$ moieties of the monomer guided the cis opening and head-to-tail arrangement of the monomers in the polymer chain. The opposite complexation mode is less preferable since this required opposite polarization of the charge in the double bond. The formation of isotactic chains was only possible if free rotation of V-R bond was possible in the active site. However, such rotation was restricted due to the presence of halide further favoring the above complexation mode. This also suggested that the size of central atom and nature of ligand have significant roles to play to obtain syndio-specific chains as rotational barrier is key to the above stereospecificity.

4   Catalysts for Isotactic and Syndiotactic Poly-α-olefins

Both isotactic and syndiotactic poly-α-olefins possessed contrasting properties and were important from the prospective of application. A comparative tensile properties data of the polypropylenes with different tacticity is summarized in Table 3. The syndiotactic polypropylene is soluble in ether and hydrocarbon solvents unlike the isotactic ones. The T_m of syndiotactic polypropylene is ~40 °C lower compared to that of the isotactic analog possessing similar crystallinity. Similarly, the isotactic polypropylene has a higher unit cell density (0.94 g/cm^3) and much higher heat of fusion (2350 cal/unit) compared to that of the syndiotactic polypropylene (unit cell density = 0.90 g/cm^3, heat of fusion = 450 cal/unit). Owing to this, specialized catalyst compositions to synthesize stereospecific polypropylenes rich with isotactic or

Table 3 Properties of isotactic, syndiotactic, and atactic polypropylene (PP) [22]

Properties	PP	Isotactic PP	Syndiotactic PP
UTS (MPa)	40	600	330
Elongation at break (%)	100	130	230
Young's modulus (GPa)	1.9	20.0	3.0
Density (g/cm^3)	0.89–0.92	0.91–0.94	–
Melting point (°C)	–	171	130

syndiotactic chains are desirable. Typically, the isotactic and syndiotactic character is defined by the amount of m and r-diads present in the polymer. In an isotactic polypropylene, the extent of m-diad can be more than 99%, whereas the amount of r-diad in a syndiotactic polypropylene can extend up to 85% [21].

Collette et al. developed a series of metal oxide-supported group IVB metal-based R_4M (M = Ti, Zr, and Hf; R = benzyl, neophyl, and neopentyl) type catalyst systems [23]. These R_4M catalysts supported on Al_2O_3 exhibited high efficiency with 600 g of polymer/nM R_4M, and the resulting polymers were of high molecular weight. The isotactic content in the polypropylene reached up to 70%. The stereoregulation was strongly dependent on the M:Al_2O_3 ratio and the amount of M on the surface. Presence of H_2 further improved the yield but compromised the crystallinity. The Table 4 below summarizes the yield, molecular weight, and thermal properties of the polypropylene obtained based on different catalyst. The T_m (147 °C) of the polypropylene obtained using Al_2O_3-supported catalyst was observed closed to that of the $TiCl_4$/$MgCl_2$/$AlEt_3$-based system (T_m = 159 °C). However, the polydispersity indices (M_w/M_n) of the former (8.0) were compared to that of the $TiCl_4$/$MgCl_2$-based system (5.6). Presence of H_2 marginally increased the T_m of the samples to 151.8 °C, though the M_w/M_n further increased to 10.0. The major concern in these solid supported systems was the yield. The value (47.7 g/mmol of metal) was much inferior compared to that of the $TiCl_4$/$MgCl_2$-based system (2680 g/mmol of metal). Importantly, the molecular weight (M_n = 75,500 g/mol) of the polypropylene based on solid-supported catalyst was much higher compared to that of the $TiCl_4$/$MgCl_2$-based system (22,400 g/mol) suggesting the polymerization is faster in case of the former.

Ewen et al. showed that catalyst systems may be developed by selecting suitable ligands to predominantly synthesize either isotactic or syndiotactic polypropylene. A C_2-symmetric metallocene catalyst based on indene produced isotactic polypropylene (Fig. 6a). A stereorigid C_5-symmetric prochiral catalyst based on cyclopentene and fluorene produced syndiotactic polymer predominantly (Fig. 6b). The mechanism of syndiotactic polymer formation was attributed to the chain migratory insertion of monomer as shown in Scheme 5. The two accessible sites on the catalytic sites are for the growing chain and the incoming monomer. If the growing chain shifts between these two sites at each monomer addition, then a syndiotactic polypropylene is the preferred product. However, several authors also hypothesized that the steric repulsion between the methyl group of the complexed monomer and last unit of the growing chain guided the above stereoselectivity of the polymer [24].

Table 4 Properties of polypropylene obtained using different catalyst compositions [23]

Catalyst	Yield[a]	Fraction	%	η_{inh} (dL/g)	T_g (°C)	T_m (°C)	ΔH_f (J/g)	$M_n \times 10^3$	$M_w \times 10^3$
TNZ-Al$_2$O$_3$	47.7	Total	100	10.2	−10.1	147.1	13.1	75.5	600
		Ether Sol.	28.2	3.81	−8.0	52.0	1.6	80.8	604
		Hept. Sol.	17.9	4.78	−7.8	130.2	27.7	39.3	934
		Hept. Insol.	50.0	15.3	−7.4	147.7	49.0	455	2626
TNZ/Al$_2$O$_3$ + H$_2$ (5 psi)	92.7	Total	100	4.08	−11.5	151.8	5.0	34	370
		Ether Sol.	49.0	2.54	−8.8	53.0	1.8	22.3	261
		Hept. Sol.	33.0	3.28	−10.1	137.0	29.2	22	478
		Hept. Insol.	24.0	8.04	−7.5	149.9	68.7	108	3460
MgCl$_2$/TiCl$_4$/ AlEt$_3$	2680	Total	100	2.11	−394	159.6	62.5	22.4	128
		Ether Sol.	21.0	0.82	−3.6	nd	nd	19.1	66.8
		Hept. Sol.	19.3	0.78	−1.6	140.1	63.0	28	110
		Hept. Insol.	53.0	3.45	nd	166.3	102.0	160	531
MgCl$_2$/TiCl$_4$/ AlEt$_3$ + H$_2$ (5 psi)	2140	Total	100	0.53	−9.8	159.0	78.2	12.1	42.3
		Ether Sol.	26.6	0.31	−10.4	Nd	nd	6.7	16.5
		Hept. Sol.	24.5	0.28	−1.8	156.4	63.5	10	26.7
		Hept. Insol.	45.7	0.83	nd	161.3	105.0	26.8	110

The polymerization was carried out in heptane at 60–65 °C for 1 h

TNZ tetraneophylzirconium

[a]g/mmol of metal
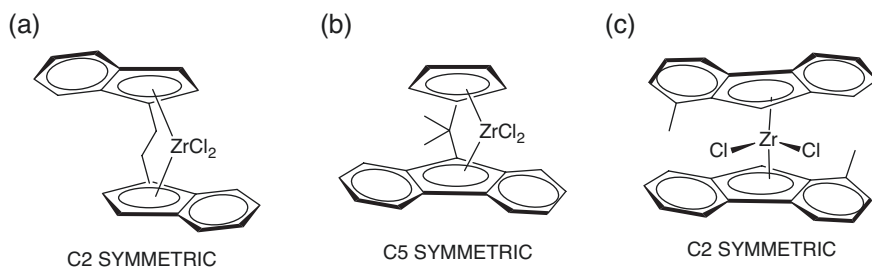
Fig. 6 Structures of the stereorigid (**a**) C$_2$-symmetric, (**b**) C$_5$-symmetric, and (**c**) unbridged C$_2$-symmetric metallocene catalysts
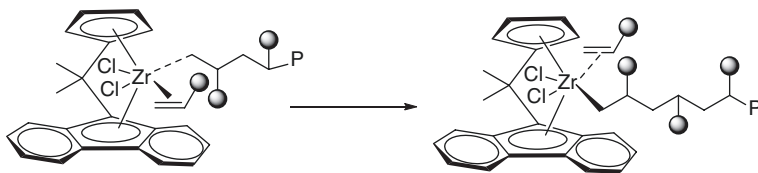
Scheme 5 The mechanism for syndiotactic propagation of the polymer chain as proposed by Ewen et al.

Table 5 Properties of polypropylene synthesized using metallocene-based catalyst

Properties	Polypropylene from metallocene-based catalyst	Polypropylene from first-generation metallocene-based catalyst
Melting point (°C)	161	162
M_w/M_n	2.5	5.8
Tensile strength (N/mm²)	1620	1190
Hardness	86	76

These metallocene-based systems revolutionized the synthesis of stereo-controlled poly-α-olefin using a homogenous catalyst. These catalyst systems rendered a better control over the distribution of molecular weight and ratio of monomers in a copolymer. The properties of polypropylene synthesized using metallocene-based catalyst system also improved compared to that of first-generation Ziegler-Natta catalyst system (Table 5) [25, 26].

The geometry around the metal center of these metallocene catalysts were presumed to be pseudotetrahedral. Subsequently, catalyst based on octahedral complex possessing C_2 symmetry and a N-C-C-N bridge was developed that produced isotactic poly-α-olefin with mmmm-pentad content up to 80% [27]. Interestingly, when the bridging from the above catalyst was removed, the catalyst efficiently produced syndiotactic poly-α-olefin with rrrr-pentad amount of 96%. A close analysis of the origin of stereoregularity in these systems revealed that the insertion of monomer is a key parameter in regulating the stereospecificity of the resulting polymer. The monomer either inserts in primary (the primary carbon is bonded to the metal atom) or secondary (the secondary carbon is bonded to the metal center) manner (Scheme 6). The primary insertion is dominant in the bridged systems, whereas the secondary insertion mostly occurs in case of the unbridged catalysts with octahedral geometry similar to that of the homogeneous vanadium-based catalyst.

Presence of chiral active species in catalyst is necessary to guide the stereoselection between two monomer enantiofaces during insertion in the following two ways. Firstly, the coordination of ligands to the metals is responsible for the chirality of the active sites. For example, the relative orientation of the two bidentate ligands in the catalysts shown in Fig. 8 is interchangeable if the bridging is absent. However, in presence of bridged chemical linkage, the system becomes stereorigid, and no interchange is possible. Secondly, the chirality of the tertiary carbon of the last inserted
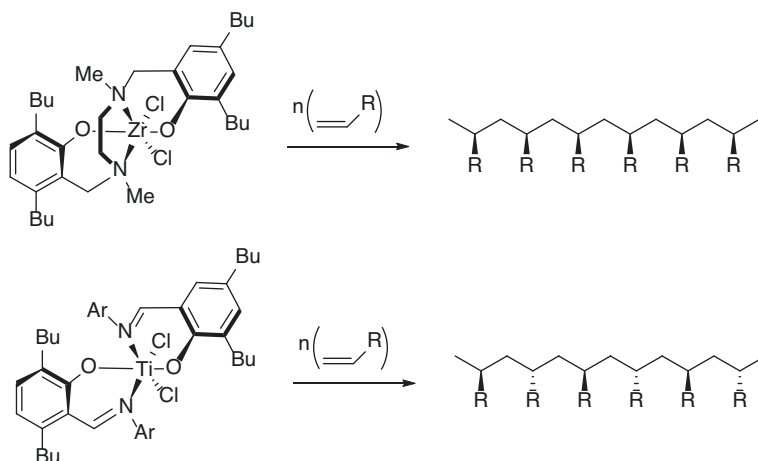
Scheme 6 Bridged and unbridged C_2-symmetric octahedral catalysts for poly-α-olefin synthesis

monomer in the growing polymer chain regulates the incoming enantioface of the incoming monomer. If the insertion of prochiral monomer is guided by the chirality of the catalytic site, then the phenomena is termed as chiral-site stereocontrol. If the chirality is guided by the conformation of the last inserted monomer, then chain-end stereocontrol occurs. The chain-end stereocontrol follows the Bernoullian statistics of the r or m stereochemical sequences, whereas non-Bernoullian statistics originates from chiral-site stereocontrol. A stereo mistake if occurs during polymerization gets propagated for chain-end stereocontrol, whereas the same stereo mistake under chiral-site stereocontrol remains isolated having little effect on the site chirality.

These metallocene catalysts are especially useful for polymerization of cyclic olefins (cyclopentene, norbornene, and substituted compounds) and synthesis of copolymers (Fig. 7). The copolymer of ethylene and propylene exhibits elastomeric properties. At low temperature, selectivity of monomer addition is observed with metallocene catalysts leading to block copolymer. More specifically, the polymerization catalyzed by hafnocenes polymerizes propene first followed by ethylene. The polymerization of cyclopentene follows 1,3-enchainment, whereas the polymerization of norbornene proceeds through 1,2-addition. The processing temperature of polycyclic olefins may be decreased by copolymerizing with ethylene.

5 Catalysts for Polymerization of Functional Olefins

Polymers based on functionalizable olefin monomer such as methyl acrylate, vinyl ethers, acrylamides, and acrylic acid are important from commercial point of view with potential applications in the areas of anticorrosive coatings, food packaging, and antioxidants. These functional monomers were initially polymerized under free

Cyclopentene   Norborene   Substituted Norborene

Fig. 7 Cyclic olefin monomers polymerizable using metallocene catalyst
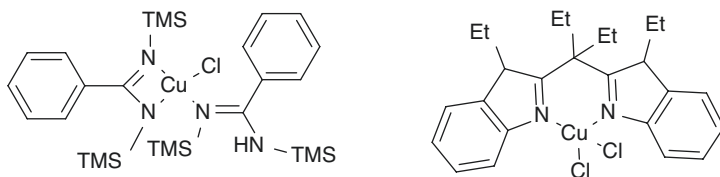
Fig. 8 Copper(II)-based catalyst systems for polymerization of olefins

[CpSi(Me)₂N-t-Bu]TiCl₂   (Benzind)₂ZrCl₂
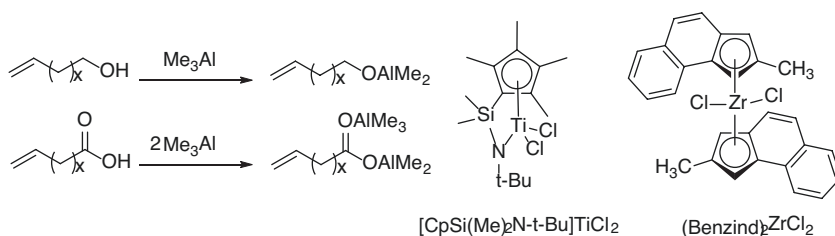
Scheme 7 Protection of functional groups with trimethyl aluminum and the catalysts used for polymerization of functional monomers

radical conditions. Recently, efforts were made to develop Ziegler-Natta catalysts for polymerization of these monomers. However, early transition metals were oxophilic, and the titanium-, zirconium-, and chromium-based catalysts were easily poisoned by these functional olefins possessing oxygen-based functional groups. Late transition metals though less oxophilic possess weak catalytic efficiency and produce oligomers of olefin. One of the approaches to circumvent this issue was to protect the polar functional group present in the monomer during polymerization. For examples, trimethyl aluminum was utilized to protect the –OH and –COOH functional groups present in the polymerizable monomer [28]. The protected monomers were polymerized using zirconium-based metallocene catalysts (Benzind)$_2$ZrCl$_2$, [CpSi(Me)$_2$N-t-Bu]TiCl$_2$, and [Et(Ind)$_2$]ZrCl$_2$ (Scheme 7). The resulting polymers displayed molecular weight up to 197,000 g/mol with polydispersity index value in the range of 1.9–2.9. The functionalities were regenerated by hydrolyzing the protected groups, subsequent to the polymerization. However, during copolymerization, the incorporation of these protected monomers was lower compared to that of the ethylene and propylene due to the steric factor associated with these systems. Less than ~10 mol% of the functional monomers were incorporated in a copolymerization of ethylene and 10-undecen-1-oic acid.

5.1   Palladium- and Nickel-Based Catalyst Systems

With the evolution of cationic Pd(II) and Ni(II) α-diimine catalysts, the olefin polymerization received a further boost. DuPont also commercialized this catalyst with trade name Versipol. These catalyst systems polymerized olefin and α-olefin and also copolymerized olefin with a range of functional olefins. The important features of these catalyst systems were the highly electrophilic and cationic Ni or Pd metal centers, use of bulky α-diimine ligands, and non-coordinating counterions. The electrophilicity of the metal centers improved the rate of olefin insertion, whereas the bulkiness of the ligands facilitated insertion in comparison with chain transfer. The non-coordinating counterions provided site for the olefin coordination. Easy and high-yield synthetic routes to α-diimine ligands allowed development a range of catalyst based on Ni(II) and Pd(II). The cationic form of the catalyst is essential for the catalytic activity. The catalyst precursor possessing a halide group was treated with salts of non-coordinating anions to synthesize the cationic species. For example, the α-diimine-Pd-chloride was reacted with NaBAF and stabilized with acetonitrile to synthesize a cationic catalyst (Scheme 8). However, attempts to use ether in place of acetonitrile resulted in the chloride-bridged dimers {[(N-N) PdMe]2-μ-Cl}BAF. Alternative routes were utilized to synthesize the cationic Pd and Ni ether complexes by opting for Pd or Ni dimethyl precursors (Scheme 8).

Subsequently, phosphine-sulfonate-based catalyst systems possessing broad functional group tolerance were developed by Brookhart to insert vinyl ethers [29], acrylonitrile [30], vinyl chloride [31], and vinyl acetate [32] in polyethylene chain. These active Ni(II)- and Pd(II)-based ligands of general formula [(ArN=C(R) C(R)=NAr)M(CH$_3$)(OEt$_2$)]$^+$BAr$'_4$$^-$] copolymerized ethylene and functional ethylene [33]. The polymerization initiation step via formation of the active species was much slower compared to that of the chain propagation favoring the polymerization. The aryl groups of the diimine ligand possessed bulky substituents that blocked associative olefin exchange and effectively minimized chain transfer. As per the proposed mechanism, a six-membered chelate formed after insertion of functional monomer via chelation of the carbonyl group that opened up on subsequent insertion of ethylene monomer, and the copolymerization occurred via repetition of the
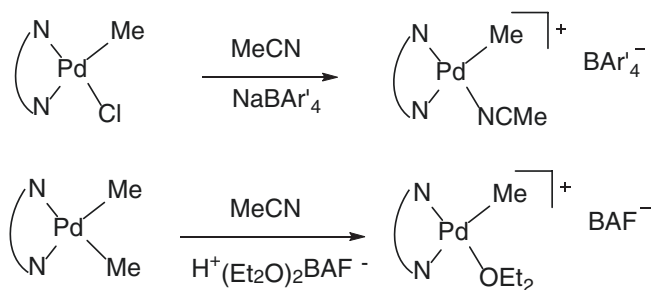
Scheme 8 Synthesis of cationic catalysts for polymerization of functional olefins
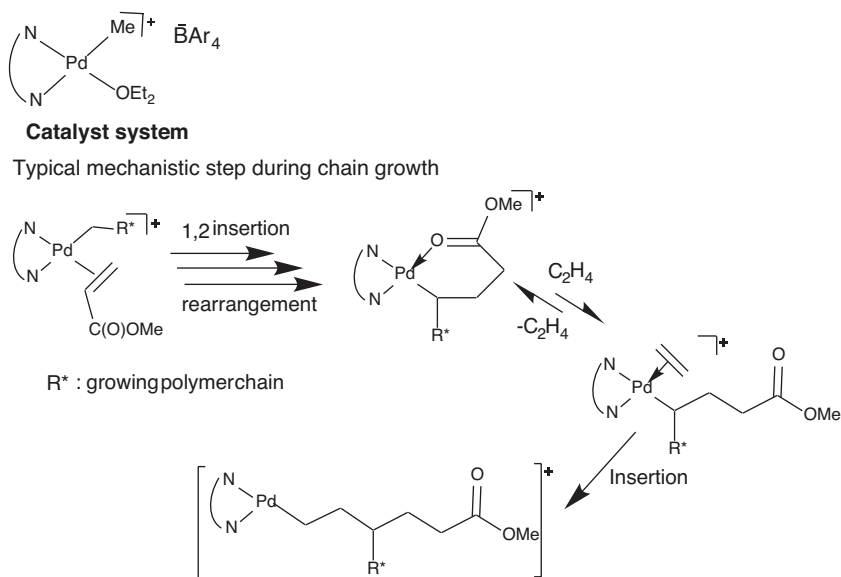
Scheme 9 The catalyst system used for copolymerization and a mechanistic step showing the insertion of monomers in the polymer chain

above steps (Scheme 9). However, the resulting copolymers were highly branched in nature due to extensive chain walking during polymerization.

Analogous Ni(II)-based catalyst and phosphine-sulfonate-based Pd(II) neutral catalyst systems produced linear copolymers. However, the neutral Pd(II) phosphine-sulfonate complexes were less reactive compared to the Pd(II) diimine-based catalyst system. The polymerization rate in case of the neutral Pd(II)-based system was improved by raising the polymerization temperature, and the higher temperature stability of the catalyst allowed higher polymerization. Subsequently, single-component catalyst systems based on P-O-chelated (PΛO) Pd(II) systems ligated with pyridine, lutidine, PPh$_3$, Me$_2$NCH$_2$CH$_2$NMe$_2$, and dimethyl sulfoxide were utilized to polymerize functional olefin monomers. The above studies revealed that the dimethyl sulfoxide (DMSO) binds less strongly to the metal center and gets readily displaced by olefin monomer facilitating the insertion process. This catalyst system allowed up to 50 mol% of acrylate insertion.

Further modification in catalyst structure allowed insertion of 1,1-bisfunctional vinyl monomers in the polyethylene chain. For example, Chikkali and coworkers synthesized an acetonitrile-ligated Pd-phosphine sulfonate complex that successfully incorporated up to ~9.6 mol% of ethyl-2-cyanocryalate monomer in the polyethylene chain possessing a molecular weight value of ~3100 g/mol and a narrow polydispersity index value of 1.3 [34]. Subsequently, a range of NΛN-type ligands were developed and utilized to synthesize catalysts for this purpose (Table 6). Comparatively, the Pd-based catalyst systems produced high molecular weight polyolefin compared to that of the Ni-based catalyst system. The ethylene produced

Table 6 List of NAN-type ligands utilized for development of Pd- and Ni-based catalyst systems

PPID–N   N–DIPP

An   N   Am

Ph   Ph
Ph–N   N–Ph

Cy–NH   HN–Cy

NH₂   NH₂

Ph–N   N–Ph
Et   Et

PPID–NH   HN–DIPP

PPID–NH   HN–DIPP

R₃   R₂
R₁

Ph   Ph
Ph

iPr   iPr

R = H, TMS, Et
R   R

O   HN   NH

O   NH   HN–DIPP
PPID–NH

SMe   S

R   R

from the Pd-based catalyst systems is amorphous and highly branched in nature with density value up to 0.85. This allowed the researchers to produce blended polyethylene by using mixed catalyst systems. For example, combining a palladium α-diimine-based catalyst with a metallocene catalyst in a specific ratio, the crystallinity of resulting polyethylene may be controlled.

Mecking provided mechanistic insight into the acrylate insertion by studying the PΛO chelation-based system (Scheme 10) [35]. The relative binding strength of DMSO versus ethylene at 80 °C and 10 bar was determined to be 1.1×10^{-3}. He proposed that delayed displacement of the chelating carbonyl ligand via π-coordination of incoming monomer (equilibrium constant = 2×10^{-3} L/mol) substantially retards but allows polymerization. Importantly, the nature of ligand in the chelate has strong impact on the reaction entropy. The study further revealed that the second insertion of the acrylate or ethylene monomer is subjected to the dissociation of O-coordinated carbonyl moiety from the Pd center. The acrylate insertion was less favorable by 35 kJ/mol, whereas the insertion of ethylene moiety was favored by 41 kJ/mol. The overall study suggested the efficiency of the catalyst system towards copolymerization of the functional and non-functional olefin
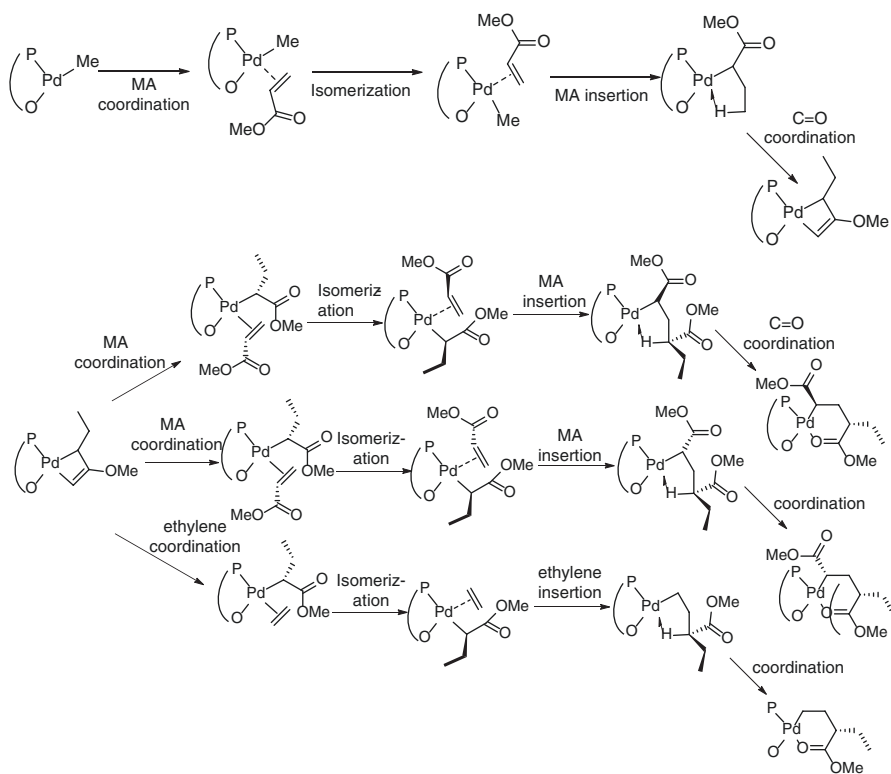
Scheme 10 Initiation of the active site and possible pathways for the insertion of methyl acrylate (MA) or ethylene in the copolymerization process on (PΛO)Pd-based catalysts

monomer. Furthermore, the migratory insertion involves a cis-trans isomerization with the monomer remaining cis to P donor, which proceeded through a concerted step without dissociation. This also made the second acrylate insertion less favorable compared to that of the ethylene owing to steric factors.

These Pd- and Ni-based cationic catalyst systems were effective in polymerizing cyclo-olefins to produce crystalline polymers with molecular weight up to 251,000 g/mol. These polymers exhibited a broad melting temperature ranging from 241 to 330 °C. This is in contrast to the polymers derived using metallocene catalyst, which were not melt-processable. The chain growth in cyclopentene proceeded via insertion at the secondary alkyls. However, chain walking to methyl unit was noticed during polymerization of substituted cyclopentene. The diamine chemistry was extended to other metals such as Fe and Co, though these catalyst systems displayed low-to-moderate activity. Similarly, N,N'-ditrimethylsilylbenzamidinato, an amidinate ligand, is known to support Cu-catalyzed polymerization of ethylene [36]. A cupper chloride complex synthesized from hexamethyldisilazane, benzonitrile, and trimethylsilyl chloride and activated with methylaluminoxane-polymerized ethylene and the molecular weight was found to be 820,000 g/mol with melt temperature of 138 °C (Fig. 8) [37]. However, the 2,2′-bis[2-(1-ethyl benzimidazol-2-yl)biphenyl]copper-based system produced polyethylene of low molecular weight (M_n = 4900 g/mol) [36]. Subsequently, other polymerization techniques such as atom transfer radical polymerization were discovered for polymerization of active olefin monomers including acrylates and styrene.

5.2   Catalysts Based on Tridentate Ligands

The use of tridentate ligands was useful as the catalyst systems based on several tridentate ligands including pyridine bis(imine) (PBI), furan bis(imine), pyrrole bis(imine), and anionic amine and phosphine polymerized ethylene at fast rates to form linear high-density polyethylene (Fig. 9). Even at low ethylene pressures of 1 atm, the polymerization was highly exothermic, and the crystalline polyethylene swiftly precipitated from solution. As per the proposed mechanism, low barrier to insertion in these systems facilitated the polymerization process. A comparative analysis between Co- and Fe-based systems revealed that the activity of the cobalt PBI systems is independent of the ethylene pressure in the reactor (Table 7). Interestingly, the activity of the Fe-PBI-based system increased with the ethylene pressure [38]. Even the "R" group in the PBI affected the activity of the catalyst. These catalyst systems exhibited adequate thermal stability with reasonable lifetimes at 100 °C.

The bulkiness around the metal center in PBI-based Co and Fe complexes is a key parameter to retard the chain transfer process during polymerization and produce high molecular weight polymers. Reduction in ligand size by decreasing the size of ortho-substituents on the imine aryl group inhibits the polymer growth and causes a drop in the molecular weight of the resulting polymer. Overall, the Fe-based
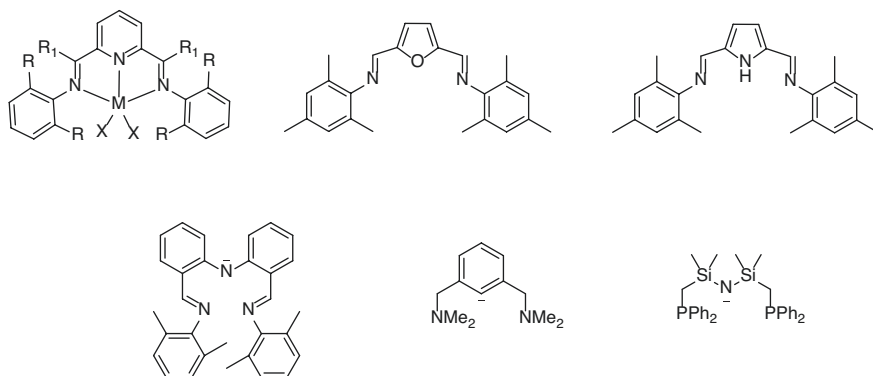
Fig. 9 Different tridentate and anionic tridentate ligands used for synthesis of Co- and Fe-based complexes

Table 7 Effect of ethylene pressure on the polymerization activity [39]

Metal	Ethylene pressure (atm)	Activity (kg of polyethylene/g of M/h)
Co	7	140
	41	140
Fe	7	1860
	41	4220
	340	11,900

complexes produce higher molecular weight polyethylene compared to that of the Co-based systems. Longer polymerization times and use of methylaluminoxane in low concentrations produced monomodal, narrow dispersity, and really high molecular weight polyethylene. The copolymerization of ethylene and propylene is sluggish in Fe-PBI-based systems. During homopolymerization of polypropylene, the regioregularity of polymer decreases with the decrease in steric bulk of ligands in the catalyst. These are the first reports on isotactic polypropylene synthesis via 2,1-insertion using late metal systems [40]. The PBI catalysts synthesized using small-size ligands, preferably possessing a single ortho-substituent on the imine aryl group, are known to produce high-quality polymers in absence of chain walking. The PBI oligomerization catalysts also exhibit high turnover frequencies (100,000 kg/g of Fe/h) [41]. Advantageously, these oligomerizations can be carried out over a large range of temperature and pressure and at a lower pressure compared to the previously utilized 11–200 atm. Use of similar tridentate ligands in Ru system exhibited low activity. For example, the complex based on pyridylbis (oxazoline) pyridine (pybox) and Ru produced 0.28–2.14 kg of polyethylene/mol of Ru/h at 25–60 °C and 6–12 atm [42]. This low activity was attributed to limited participation of Ru in the polymerization process.

6 Vanadium-Based Complexes for Precise Polyolefin Synthesis

It is well-known that in case of classical Ziegler-type catalyst system, the vanadium-based catalyst produced high molecular weight polyolefin with narrow molecular weight distribution at high activity (1000 kg PE/mol V h) [43]. The M_w/M_n value (1.5) of the polymer obtained from V-based catalyst was much lower compared to that of the Ti-based catalyst (15–30). This fact strongly suggested the formation of a single catalytically active species in this catalysis [44]. The V-based catalyst also allowed copolymerization of ethylene and propylene to produce high molecular weight amorphous polymers [45]. The catalyst system was subsequently extended to synthesis of ethylene/propylene/diene copolymers (EPDM), which were commercialized as synthetic rubbers [46]. The ethylene-cyclic olefin copolymers (COC) synthesized using V-based catalyst systems were commercialized as lenses for DVD recorders and camera phones by Mitsui Chemical, Inc. (APEL). The V(acetylacetonato)$_3$-Et$_2$AlCl catalyst system polymerized propylene to produce syndiotactic "living" polymer with low M_w/M_n value of 1.05–1.20 [47]. The breakthrough in functional polymer synthesis was achieved with the copolymerization of propylene with methyl methacrylate, although the catalytic activity was low (~4 kg of polymer/mol V h) (Scheme 11) [48].

Trivalent and tetravalent complexes based on V(III) are mainly utilized for the olefin polymerization processes. However, the V(III) is unstable and gets readily reduced to V(II) in presence of aluminum species. Therefore, the research mainly concentrated on stabilizing the V(III) form using suitable ligand system. For example, suitable modification of the β-diketonate (acac) ligand altered the catalytic activity of complexes during ethylene/propylene copolymerization (Table 8) [49].
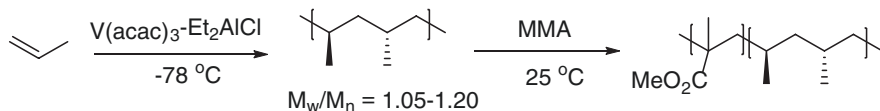
Scheme 11 Syndio-specific propylene followed by diblock copolymer with methyl methacrylate synthesis using V(acac)$_3$-Et$_2$AlCl system

Table 8 Ethylene-propylene copolymer synthesis in presence of V(β-diketonate)$_3$-Et$_2$AlCl/Et$_3$Al$_2$Cl$_3$ catalyst system [50]

V cat.	V(acac)$_3$		V(Cy-acac)$_3$		V(tBu-acac)$_3$		V(CF$_3$-acac)$_3$	
Al cocat.	Et$_2$AlCl	Et$_3$Al$_2$Cl$_3$	Et$_2$AlCl	Et$_3$Al$_2$Cl$_3$	Et$_2$AlCl	Et$_3$Al$_2$Cl$_3$	Et$_2$AlCl	Et$_3$Al$_2$Cl$_3$
Activity	1988	1960	2336	1980	1492	1244	1524	1600
$M_w \times 10^{-5}$	2.19	7.02	2.18	7.16	2.90	12.65	2.77	8.01
M_w/M_n	2.3	2.5	2.3	2.2	2.2	2.4	2.2	2.3
% ethylene	62	52	59	53	65	57	63	54

Reaction condition: vanadium 5 µmol, Al 0.2 mmol (Al/V = 40, molar ratio), Cl$_3$CCO$_2$ET 20 µmol, 200 mL of cyclohexane, ethylene/propylene = 2 bar, 22 °C, 30 min, activity (kg polymer/mol V h)

(a)   **(b)**   **(c)**

V(acac)$_3$ V(Cy-acac)$_3$ V(tBu-acac)$_3$ V(CF$_3$-acac)$_3$
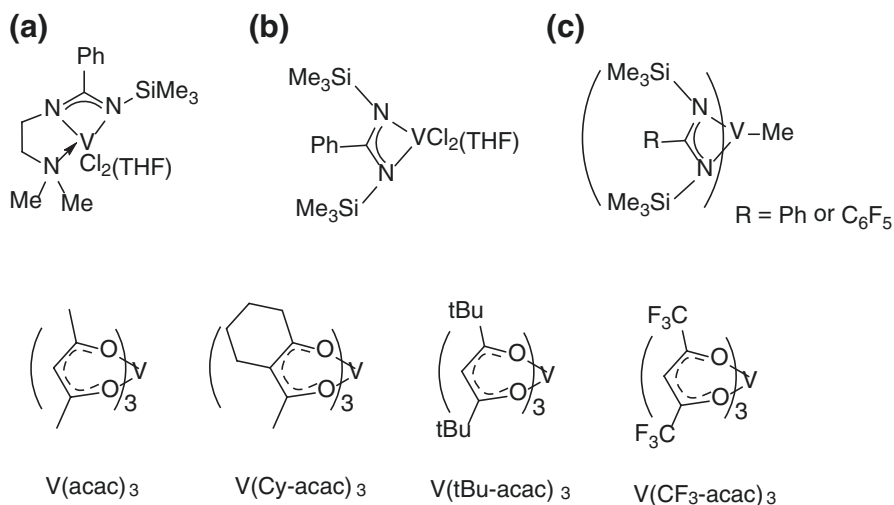
Fig. 10 (**a–c**) V(III)-based complexes utilized for olefin polymerization

However, use of β-diiminato ligands, such as [ArNC(R)CHC(R)NAr]-[R = Me, *t*Bu; Ar = Ph, 2,6-iPr$_2$C$_6$H$_3$, 2,4,6-Me$_3$C$_6$H$_2$], displayed insignificant catalytic activities.

The catalyst systems based on V(III) possessing (dimethylamino)ethyl-functionalized benzamidinate ligand (Fig. 10a) along with Et$_2$AlCl displayed modest catalytic activity for polymerization of ethylene. The activity for above polymerization at 30 °C was 447 kg polymer/mol V h bar for ethylene loading of 6 bar. The activity (447 kg polymer/mol V h bar) of the complex based on {[PhC(NSiMe$_3$)$_2$]VCl$_2$(THF)}$_2$ (Fig. 10b) was somewhat lower under the same conditions [50]. On increasing the temperature, the activity of **10b** increased, whereas **10a** exhibited a decrease in catalytic activity. The V(III) complex based on **10b** and **10a** when placed on MgCl$_2$/AlEt$_n$(OEt)$_{3-n}$ support exhibited exceptional catalytic activity of 1490 kg polymer/mol V h bar and 3120 kg polymer/mol V h bar, respectively. V(III) methyl bis(amidinate) complex oligomerized ethylene (M_n = 1780, M_w/M_n = 2.3) without any additional co-catalyst. Replacing the Ph group with C$_6$F$_5$ further improved the catalytic activity (8.1 kg oligomer/(mol V h)) [51].

Subsequently, dinuclear catalyst systems were developed and analyzed. A dinuclear vanadium(III) chloride complex possessing a bis(amido)amine [(Me$_3$Si) NCH$_2$CH$_2$]$_2$N(SiMe$_3$) in presence of Me$_2$AlCl (activity = 660 kg polymer/(mol V h)) or methylaluminoxane (activity = 237 kg polymer/(mol V h) exhibited strong catalytic activity for ethylene polymerization at 50 °C [52]. However, the lifetime of the catalyst was limited to 20–30 min only; this may be attributed to the conversion of V(III) to inactive V(II) species (Scheme 12). Similarly, other complexes based on V(III) species were synthesized and utilized for polymerization of ethylene (Fig. 11). For example, dithiolate ligand (**11a**, **11b**, and **11c**)-based complexes displayed catalytic activity up to 1990 kg PE/mol V h in presence of Et$_2$AlCl and MgCl$_2$ as
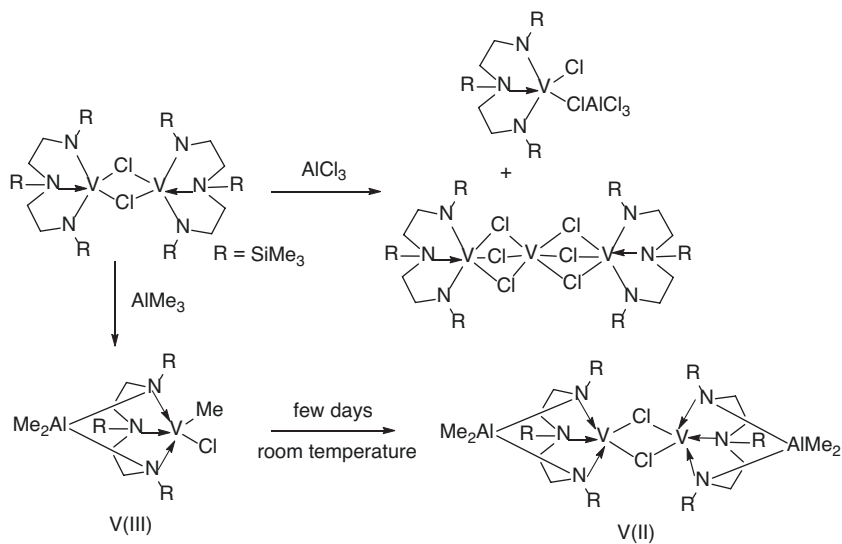
Scheme 12 The dinuclear V(III)-based complex and conversion to the V(II) species
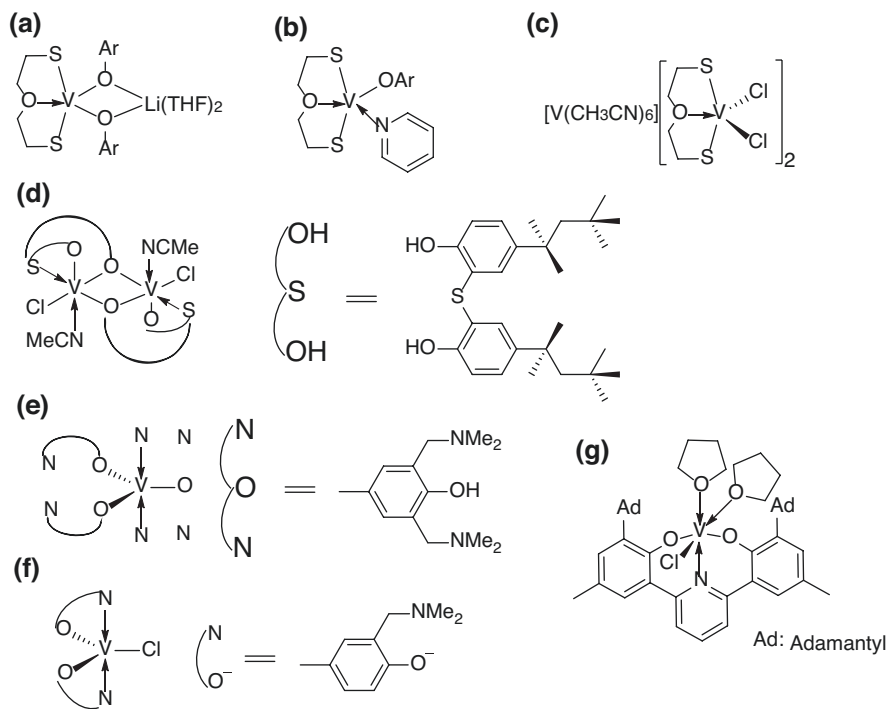
Fig. 11 (**a–g**) Chelated V(III) complexes utilized for polymerization of olefin

co-catalyst at ethylene pressure of 6 atm at 50 °C. The mixed-valence complex system (**11c**) exhibited lower activity (254 kg PE/mol V h) compared to that of the **11a** and **11b**. Replacement of dithiolato ligand with thiobis(phenoxy) moiety (**11d**) vastly improved the catalytic activity. The catalyst in presence of Al*t*Bu$_3$ as the co-catalyst exhibited a catalytic activity of 11,708 kg PE/(mol V h) for polymerization of ethylene [53].

V(III) complexes possessing O,N-chelating aminophenolate ligands (**11e** and **11f**) were tested as catalysts for ethylene polymerization. These systems in presence of Et$_2$AlCl and EtAlCl$_2$ co-catalysts exhibited moderate activity (27–159 kg PE/mol V h), and the molecular weight of the resulting polymer was relatively high ($M_w = 6.7 \times 10^5$) [54]. Bis(phenoxy)pyridine ligand-based V(III) complex (**11g**) along with methylaluminoxane co-catalyst was suitable for polymerization of propylene with activity value of 803 kg polymer/(mol V h) [55]. The polypropylene produced under 5 atm propylene pressure and 0 °C exhibited M_w value of 1.17×10^6 with $M_w/M_n = 2.03$. Complexes based on V(IV) and V(V) states were later synthesized and utilized as the catalyst for ethylene polymerization along with co-catalysts. The (arylimido)-V(IV)Cl$_2$ complexes in combination with Et$_2$AlCl exhibited adequate activity for polymerization of ethylene, and the resulting polymers displayed uniform distribution of molecular weight (Fig. 12a) [56].

A bis(amide)-based V(IV) complex was effective for copolymerization of ethylene and propylene (Fig. 12b). The nature and amount of aluminum-based co-catalyst controlled the activity of the system [57]. Use of Et$_2$AlCl and EtAlCl$_2$ exhibited maximum activity (860 kg polymer/mol V h) compared to that of the individual ones (80–330 kg polymer/mol V h). Complexes were also synthesized using salen-type tetradentate ligands (Fig. 12c). However, the polyolefins obtained using the catalyst system displayed broad molecular weight distribution in the range of 7.3–10.4 [58]. The V(V) complexes were synthesized using VOCl$_3$ as the precursor.
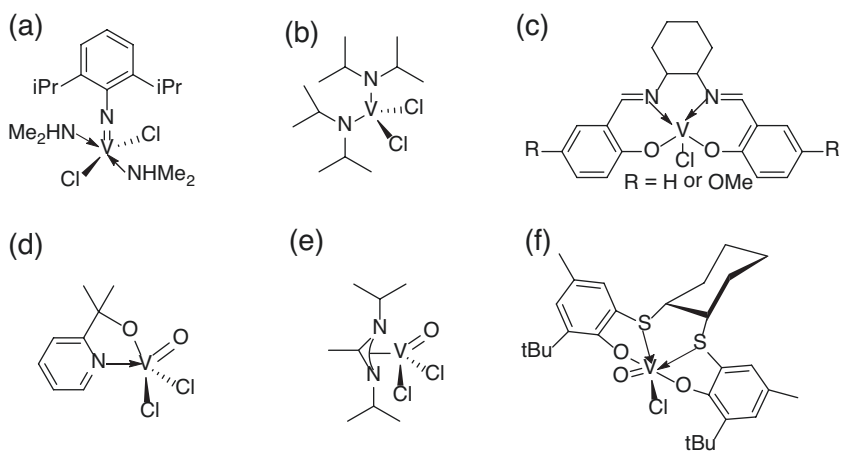
Fig. 12 (**a–f**) Catalyst systems based on vanadium(IV) and vanadium(V) species for olefin polymerization

Among several complexes studied, the complex based on O,N chelate exhibited high activity (642 kg polymer/mol V h) towards ethylene polymerization in presence of Et_2AlCl (Fig. 12d) [59]. However, conversion of the V=O group in the complex to V-N-Ph-Me compromised the activity of the system. Amidinate-based V(V) Cl_2 complexes were studied for copolymerization of propylene and 1,3-butadiene (Fig. 12e). The polymerization was effective at −60 °C and produced syndiotactic-rich polymer in presence of Et_2AlCl co-catalyst and atactic polymer in presence of methylaluminoxane co-catalyst [60]. An oxovanadium complex based on O,S,S,O chelation exhibited high activity for ethylene polymerization (Fig. 12f) [61]. Similar studies supported that aromatic-O- and aromatic-N-based ligands stabilized the vanadium-based complexes in presence of Al-based co-catalyst. $VO(OR_3)$ complexes based on tetradentate ligands possessing phenolic moieties exhibited extremely high activity (96,500 kg polymer/(mol h bar)) towards ethylene polymerization to produce polyethylene with very high molecular weight ($M_w = 5.18$–8.67×10^6 g/mol) (Fig. 13a). A dimeric complex of $[VO(OR_3)]_2$ type also displayed high activity (123,000 kg of polymer/mol h bar) for ethylene polymerization in presence of Me_2AlCl and Cl_3CCO_2Et at 80 °C (Fig. 13b). Oxo complexes based on calyx-[3]arenes were synthesized from the vanadium alkoxide precursors (Fig. 13c).

The resulting catalysts produced polyethylenes of very high molecular weight under ambient temperature conditions [62]. Vanadium(V) complexes possessing a combination of arylimido and aryloxo ligands were synthesized and utilized for polymerization of ethylene in presence of methylaluminoxane as the co-catalyst by
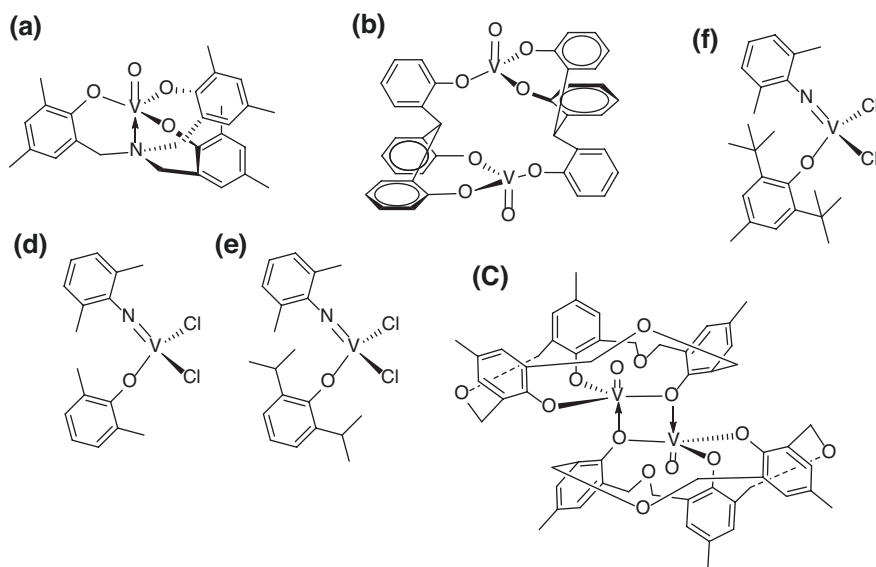
Fig. 13 (**a–f**) The range of catalysts based on vanadium(V) for polymerization of ethylene and copolymerization of olefins

Table 9 Ethylene polymerization data using 13d–f as the catalyst and methylaluminoxane as the co-catalyst in toluene solvent [64]

Complex	Temperature (°C)	Activity (kg/mol V h)	$M_w \times 10^{-5}$ (g/mol)	M_w/M_n
13d	25	1770	2.73	4.65
13d	25	2930	17.5	1.64
13e	25	1050	2.38	4.92
13e	0	576	60.9	2.61
13e	25	967	20.3	2.73
13e	40	348	–	–
13f	25	242	–	–
13f	60	486	7.84	2.07

Nomura and coworkers (Fig. 13d–f) [63, 64] The complex systems produced polyethylenes with molecular weight in the range of 2.38–60.9 × 10⁵ g/mol and relatively narrow polydispersity index values in between 1.64 and 4.65 (Table 9). The activities of the above complexes were observed in the range of 242–2930 kg of polymer/mol h bar.

7 Recent Advances

The Ziegler-Natta catalyst has undergone extensive transformation since inception, and a range of ligand and metal combinations along with co-catalysts have been investigated in detail. The catalyst systems have been developed to precisely control the stereoselectivity of the resulting polymer. The advancement in catalyst structure has rendered the synthesis of poly-α-olefins with precise tacticity. The $MgCl_2$-supported Ti-based catalyst composition has reached up to the sixth generation via modification of internal and external donor species (Table 10). Catalysts are available to synthesize random and block copolymers of olefins and selectively polymerize a particular olefin in a mixture of olefin monomers. Especially, the role of metallocenes in the catalysis and chelated complex systems can be considered as landmark innovations in the area. The research area is still attracting a substantial attention of researchers, and a large number of publications are emanating from the research conducted in the area. Involvement of advanced spectroscopic and microscopic characterization tools has made this possible to characterize the catalyst systems and resulting polymers. This has facilitated to draw the structure-property relationship of the synthesized catalyst systems. The origin of stereoselectivity is unraveled by using a set of sterically related external donors and correlating the amount of a particular stereo block in the resulting polymers via high-throughput screening. The internal structure of the catalyst system is determined with the help of machine learning by using a genetic algorithm and density functional calculations [65]. High-throughput experimentation is also utilized to understand the hydrogen response of propylene polymerization [66].

The number of active sites in the catalyst plays a crucial role in controlling the molecular weight distribution and tacticity of the polymers. Recently, methyl

Table 10 MgCl$_2$-supported Ti-based Ziegler-Natta catalyst system and resulting polymer properties [66]

Generation	Internal donor	External donor	Productivity × 10^{-3} (kg of polymer/g of Ti)	M_w/M_n
Third	Ethyl benzoate	Aromatic monoester	0.5–0.8	6–9
Fourth	Diethyl phthalate	Alkoxysilane	1–2	6–8
Fifth	2,2′-Dialkyl-1,3-dimethoxypropane	None or alkoxysilane	>2	4–6
Sixth	Dialkyl succinate	Alkoxysilane	1–2	>8
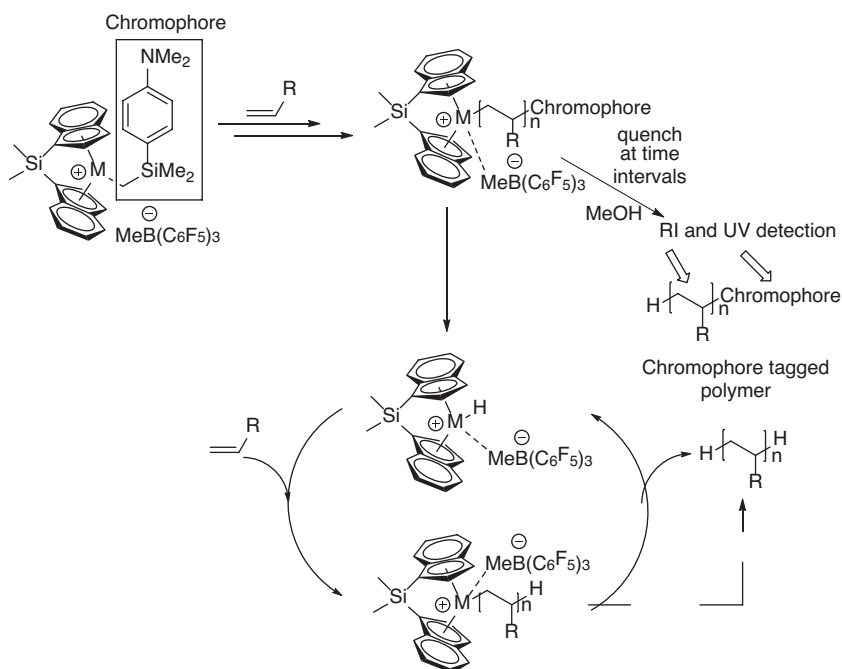
Scheme 13 Chromophore labeling technique to estimate the molecular weight of growing polymer chain at regular intervals

propargyl ether possessing ~100% labeling efficiency was used as a labeling agent via a coordination-insertion reaction to count the number of active sites in the catalyst [67]. Lately, single-site group four metal-based catalysts are developed to control the polymerization and stereochemistry of the product. Kinetic modeling is currently carried out to understand the polymerization pathway and possible intermediates formed during the course of reaction [68]. Chromophore labeling technique is utilized to understand the polymer growth rate using size exclusion chromatography (SEC). Presence of chromophore at the chain end enabled the polymer chain to be detected using UV detector in the SEC analysis (Scheme 13) [69]. Other techniques such as quench labeling with radioactive element such as tritium, MeOD, ^{14}CO, etc. are utilized to understand the growth rate of the polymer chain.

Advanced techniques such as 3D X-ray ptychography and X-ray fluorescence tomography are recently utilized to understand the fragmentation behavior of catalyst and radial distribution of metal in the catalyst-polymer particles and continuous bisection of the catalyst particles during polymerization [70]. A combination of two homogeneous catalysts is utilized as an approach to synthesize disentangled ultrahigh molecular weight polyethylene. The synergy between Ti^{3+} and Al^{3+} is established using a set of physicochemical and spectroscopic techniques to further understand the chain growth during polymerization [71]. Overall, the field of Ziegler-Natta catalysis is unraveling exciting avenues to contribute towards the quality of polyolefins produced in terms of thermos-mechanical properties and exhibit sufficient promise of being extended to synthesis of other polymeric systems in future.

References

 1. Ziegler K, Holzkamp E, Breil H, Martin H (1955) Polymerization of ethylene and other olefins. Angew Chem 67(16):426
 2. Natta N, Pino P, Corradini P, Danusso F, Mantica E, Mazzanti G, Moraglio G (1955) Crystalline high polymers of α-olefins. J Am Chem Soc 77(6):1708–1710
 3. Natta G, Pino P, Mazzanti G, Giannini U, Mantica E, Peraldo M (1957) The nature of some soluble catalysts for low pressure ethylene polymerization. J Polym Sci 26(112):120–123
 4. Furukawa J, Tsuruta T (1959) Catalytic reactivity and stereospecificity of organometallic compounds in olefin polymerization. J Polym Sci 36(130):275–186
 5. Rodriguez LAM, van Looy HM (1966) Studies on Ziegler-Natta catalysts. Part V. Stereospecificity of the active center. J Polym Sci A Polym Chem 4(8):1971–1992
 6. Cossee P (1960) On the reaction mechanism of the ethylene polymerization with heterogeneous Ziegler-Natta catalysts. Tetrahedron Lett 38(1):12–16
 7. Ludlum DB, Anderson AW, Ashby CE (1958) The polymerization of ethylene by lower valent compounds of titanium. J Am Chem Soc 80(6):1380–1384
 8. Ziegler K (1959) International Conference on Co-ordination Chemistry, London. The Chem Soc Spec Publ 12(1). Chemistry Society, London
 9. Ivin KJ, Rooney JJ, Stewart CD, Green MLH, Mahtab R (1978) Mechanism for the stereospecific polymerization of olefins by Ziegler–Natta catalysts. J Chem Soc Chem Commun 14:604–606
10. Soto J, Steigerwald ML, Grubbs RH (1982) Concerning the mechanism of Ziegler-Natta polymerization: isotope effects on propagation rates. J Am Chem Soc 104(16):4479–4480
11. Corradini P, Barone V, Fusco R, Guerra G (1979) Analysis of models for the Ziegler-Natta stereospecific polymerization on the basis of non-bonded interactions at the catalytic site—I. The Cossee model. Eur Polym J 15(12):1133–1141
12. Langer AW Jr (1977) Base effects on selected Ziegler-type catalysts. Ann N Y Acad Sci 295(1):110–126
13. Breslow DS, Newburg NR (1959) Bis-(cyclopentadienyl)-titanium dichloride-alkylaluminum complexes as soluble catalysts for the polymerization of ethylene[1,2]. J Am Chem Soc 81(1):81–86
14. Andresen A, Cordes HG, Herwig J, Kaminsky W, Merck A, Mottweiler R, Pein J, Sinn H, Vollmer HJ (1976) Halogen-free soluble Ziegler catalysts for the polymerization of ethylene. Control of molecular weight by choice of temperature. Angew Chem 15(10):630–632

15. Kaminsky W, Külper K, Niedoba S (1986) Olefin polymerization with highly active soluble zirconium compounds using aluminoxane as co-catalyst. Macromol Chem 3(1):377–387

16. Pino P, Mulhaupt R (1980) Stereospecific polymerization of propylene: an outlook 25 years after its discovery. Angew Chem 19(11):857–875

17. Ewen JA (1984) Mechanisms of stereochemical control in propylene polymerizations with soluble Group 4B metallocene/methylalumoxane catalysts. J Am Chem Soc 106(21):6355–6364

18. Zambelli A, Locatelli P, Provasoli A, Ferro DR (1980) Correlation between ^{13}C NMR chemical shifts and conformation of polymers. 3. Hexad sequence assignments of methylene. Spec Polyprop 13(2):267–270

19. Boor J Jr, Youngman EA (1966) Preparation and characterization of syndiotactic polypropylene. J Polym Sci A Polym Chem 4(7):1861–1884

20. Bovey FA, Tiers GVD (1960) Polymer NSR spectroscopy. II. The high resolution spectra of methyl methacrylate polymers prepared with free radical and anionic initiators. J Polym Sci 44(143):173–182

21. Moore EPJ (1996) Polypropylene handbook: polymerization, characterization, properties, applications. Hanser Publishers, Munich

22. Uehara H, Yamazaki Y, Kanamoto T (1996) Tensile properties of highly syndiotactic polypropylene. Polymer 37(1):57–64

23. Collette JW, Tullock CW, MacDonald RN, Buck WH, Su ACL, Harrell JR, Mulhaupt R, Anderson BR (1989) Elastomeric polypropylenes from alumina-supported tetraalkyl Group IVB catalysts. 1. Synthesis and properties of high molecular weight stereoblock homopolymers. Macromolecules 22(10):3851–3858

24. Corradini P, Guerra G, Pucciariello R (1985) New model of the origin of the stereospecificity in the synthesis of syndiotactic polypropylene. Macromolecules 18(10):2030–2034

25. Kaminsky W (1998) Highly active metallocene catalysts for olefin polymerization. J Chem Soc Dalton Trans 9:1413–1418

26. Wild FRWP, Zsolnai L, Huttner G, Brintzinger HH (1982) ansa-Metallocene derivatives IV. Synthesis and molecular structures of chiral ansa-titanocene derivatives with bridged tetrahydroindenyl ligands. J Organomet Chem 232(1):233–147

27. Tshuva EY, Goldberg I, Kol M (2000) Isospecific living polymerization of 1-hexene by a readily available nonmetallocene C2-symmetrical zirconium catalyst. J Am Chem Soc 122(43):10706–10707

28. Marques MM, Correia SG, Ascenso JR, Ribeiro AFG, Gomes PT, Dias AR, Foster P, Rausch MD, Chien JCW (1999) Polymerization with TMA-protected polar vinyl comonomers. I. Catalyzed by group 4 metal complexes with η5-type ligands. J Polym Sci A Polym Chem 37(14):2457–2469

29. Luo S, Vela J, Lief GR, Jordan RF (2007) Copolymerization of ethylene and alkyl vinyl ethers by a (phosphine- sulfonate)PdMe catalyst. J Am Chem Soc 129(29):8946–8947

30. Nozaki K, Kusumoto S, Noda S, Kochi T, Chung LW, Morokuma K (2010) Why did incorporation of acrylonitrile to a linear polyethylene become possible? Comparison of phosphine–sulfonate ligand with diphosphine and imine–phenolate ligands in the Pd-catalyzed ethylene/acrylonitrile copolymerization. J Am Chem Soc 132(45):16030–16042

31. Leicht H, Gottker-Schnetmann I, Mecking S (2013) Incorporation of vinyl chloride in insertion polymerization. Angew Chem 52(14):3963–3966

32. Ito S, Munakata K, Nakamura A, Nozaki K (2009) Copolymerization of vinyl acetate with ethylene by palladium/alkylphosphine–sulfonate catalysts. J Am Chem Soc 131(41):14606–14607

33. Johnson LK, Mecking S, Brookhart M (1996) Copolymerization of ethylene and propylene with functionalized vinyl monomers by palladium(II) catalysts. J Am Chem Soc 118(1):267–268

34. Gaikwad SR, Deshmukh SS, Gonnade RG, Rajamohanan PR, Chikkali SH (2015) Insertion copolymerization of difunctional polar vinyl monomers with ethylene. ACS Macro Lett 4(9):933–937

35. Guironnet D, Caporaso L, Neuwald B, Göttker-Schnetmann I, Cavallo L, Mecking S (2010) Mechanistic insights on acrylate insertion polymerization. J Am Chem Soc 132(12):4418–4426

36. Suzuki Y, Hayashi T (1997) JP Patent 10298231 to Mitsui Chemicals Inc., Japan
37. Stibrany RT, Schulz DN, Kacker S, Patil AO (1997) WO Patent Application 9930822 to Exxon Research and Engineering Company
38. Britovsek GJP, Bruce M, Gibson VC, Kimberley BS, Maddox PJ, Mastroianni S, McTavish SJ, Redshaw C, Solan GA, Stromberg S, White AJP, Williams DJ (1999) Iron and cobalt ethylene polymerization catalysts bearing 2,6-bis(imino)pyridyl ligands: synthesis, structures, and polymerization studies. J Am Chem Soc 121(38):8728–8740
39. Ittel SD, Johnson LK, Brookhart M (2000) Late-metal catalysts for ethylene homo- and copolymerization. Chem Rev 100(4):1169–1204
40. Small BL, Brookhart M (1999) Polymerization of propylene by a new generation of iron catalysts: mechanisms of chain initiation, propagation, and termination. Macromolecules 32(7):2120–2130
41. Small BL, Brookhart M (1998) Iron-based catalysts with exceptionally high activities and selectivities for oligomerization of ethylene to linear α-olefins. J Am Chem Soc 120(28):7143–7144
42. Nomura K, Warit S, Imanishi Y (1999) Olefin polymerization by the (Pybox)RuX2(ethylene)–MAO catalyst system. Macromolecules 32(14):4732–4734
43. Carrick WL, Kluiber RW, Bonner EF, Wartman LH, Rugg FM, Smyth JJ (1960) Transition metal catalysts. I. Ethylene polymerization with a soluble catalyst formed from an aluminum halide, tetraphenyltin and a vanadium halide. J Am Chem Soc 82(15):3883–3887
44. Nomura K, Zhang S (2011) Design of vanadium complex catalysts for precise olefin polymerization. Chem Rev 111(3):2342–2362
45. Junghanns E, Gumboldt O, Bier G (1962) Polymerization of ethylene and propylene to amorphous copolymers with catalysts made from vanadium oxychloride and aluminum haloalkylene. Makromol Chem 58(1):18–42
46. Christman DL, Keim GI (1968) Reactivities of nonconjugated dienes used in preparation of terpolymers in homogeneous systems. Macromolecules 1(4):358–363
47. Doi Y, Ueki S, Keii T (1978) "Living" coordination polymerization of propene initiated by the soluble V(acac)3-Al(C2H5)2Cl system. Macromolecules 12(5):814–819
48. Doi Y, Koyama T, Soga K (1985) Synthesis of a propene—methyl methacrylate diblock copolymer via "living" coordination polymerization. Makromol Chem 186(1):11–15
49. Ma Y, Reardon D, Gambarotta S, Yap G, Zahalka H, Lemay C (1999) Vanadium-catalyzed ethylene–propylene copolymerization: the question of the metal oxidation state in Ziegler–Natta polymerization promoted by (β-diketonate)₃V. Organometallics 18(15):2773–2781
50. Brandsma MJR, Brussee EAC, Meetsma A, Hessen B, Teuben JH (1998) An amidinate ligand with a pendant amine functionality; synthesis of a vanadium(III) complex and ethene polymerization catalysis. Eur J Inorg Chem 1998(12):1867–1870
51. Brussee EAC, Meetsma A, Hessen B, Teuben JH (1998) Electron-deficient vanadium(III) alkyl and allyl complexes with amidinate ancillary ligands. Organometallics 17(18):4090–4095
52. Feghali K, Harding DJ, Reardon D, Gambarotta S, Yap G, Wang Q (2002) Stability of metal–carbon bond versus metal reduction during ethylene polymerization promoted by a vanadium complex: the role of the aluminum cocatalyst. Organometallics 21(5):968–976
53. Janas Z, Wiśniewska D, Jerzykiewicz LB, Sobota P, Drabenta K, Szczegot K (2007) Synthesis, structural studies and reactivity of vanadium complexes with tridentate (OSO) ligand. Dalton Trans:2065–2069
54. Hagen H, Boersma J, Lutz M, Spek AL, van Koten G (2001) Vanadium(III) and -(IV) complexes with O,N-chelating aminophenolate ligands: synthesis, characterization and activity in ethene/propene copolymerization. Eur J Inorg Chem 2001(1):117–123
55. Golisz SR, Bercaw JE (2009) Synthesis of early transition metal bisphenolate complexes and their use as olefin polymerization catalysts. Macromolecules 42(22):8751–8762
56. Lorber C, Donnadieu B, Choukroun R (2000) Synthesis and X-ray characterization of a monomeric Cp-free d1-imido–vanadium(IV) complex. Dalton Trans (24):4497–4498
57. Desmangles N, Gambarotta S, Bensimon C, Davis S, Zahalka HJ (1998) Preparation and characterization of (R2N)2VCl2 [R=Cy, i-Pr] and its activity as olefin polymerization catalyst. Organomet Chem 562(1):53–60

58. Biazek M, Czaja K (2008) Dichlorovanadium (IV) complexes with salen-type ligands for ethylene polymerization. J Polym Sci A Polym Chem 46(20):6940–6949
59. Hagen H, Bezemer C, Boersma J, Kooijman H, Lutz M, Spek AL, van Koten G (2000) Vanadium(IV) and -(V) complexes with O,N-chelating aminophenolate and pyridylalkoxide ligands. Inorg Chem 39(18):3970–2977
60. Liguori D, Centore R, Csok Z, Tuzi A (2004) Polymerization of propene and 1,3-butadiene with vanadyl(V) monoamidinate precatalysts and MAO or dialkylaluminum chloride cocatalysts. Macromol Chem Phys 205(8):1058–1063
61. Meppelder GM, Halbach TS, Spaniol TP, Mülhaupt R, Okuda J (2009) A vanadium(V) complex with a tetradentate [OSSO]-type bis(phenolato) ligand: synthesis, structure, and ethylene polymerization activity. J Organomet Chem 694(7):1235–1237
62. Redshaw C, Rowan MA, Warford L, Homden DM, Arbaoui A, Elsegood MRJ, Dale SH, Yamato T, Casas CP, Matsui S, Matsuura S (2007) Oxo- and Imidovanadium complexes incorporating methylene- and dimethyleneoxa-bridged calix[3]- and -[4]arenes: synthesis, structures and ethylene polymerisation catalysis. Chem Eur J 13(4):1090–1107
63. Nomura K, Sagara A, Imanishi Y (2002) Olefin polymerization and ring-opening metathesis polymerization of norbornene by (arylimido)(aryloxo)vanadium(v) complexes of the type VX2(NAr)(OAr'). Remarkable effect of aluminum cocatalyst for the coordination and insertion and ring-opening metathesis polymerization. Macromolecules 35(5):1583–1590
64. Wang W, Nomura K (2005) Remarkable effects of aluminum cocatalyst and comonomer in ethylene copolymerizations catalyzed by (Arylimido)(aryloxo)vanadium complexes: efficient synthesis of high molecular weight ethylene/norbornene copolymer. Macromolecules 38(14):5905–5913
65. Takasao G, Wada T, Thakur A, Chammingkwan P, Terano M, Taniike T (2019) Machine learning-aided structure determination for TiCl4–capped MgCl2 nanoplate of heterogeneous Ziegler–Natta catalyst. ACS Catal 9(3):2599–2609
66. Vittoria A, Meppelder A, Friederichs N, Busico V, Cipullo R (2020) Ziegler–Natta catalysts: regioselectivity and "hydrogen response". ACS Catal 10(1):644–651
67. Yu Y, Cipullo R, Boisson C (2019) Alkynyl ether labeling: a selective and efficient approach to count active sites of olefin polymerization catalysts. ACS Catal 9(4):3098–3103
68. Desert X, Carpentier JF, Kirillov E (2019) Quantification of active sites in single-site group 4 metal olefin polymerization catalysis. Coord Chem Rev 386(1):50–68
69. Moscato BM, Zhu B, Landis CR (2010) GPC and ESI-MS analysis of labeled poly(1-hexene): rapid determination of initiated site counts during catalytic alkene polymerization reactions. J Am Chem Soc 132(41):14352–14354
70. Bossers KW, Valadian R, Zanoni S, Smeets R, Friederichs N, Garrevoet J, Meirer F, Weckhuysen BM (2020) Correlated X-ray ptychography and fluorescence nano-tomography on the fragmentation behavior of an individual catalyst particle during the early stages of olefin polymerization. J Am Chem Soc 142(8):3691–3695
71. Piovano A, Thushara KS, Morra E, Chiesa M, Groppo E (2016) Unraveling the catalytic synergy between Ti3+ and Al3+ sites on a chlorinated Al2O3: a tandem approach to branched polyethylene. Angew Chem 128(37):11369–11372

Stability and Destabilization of Water-in-Crude Oil Emulsion

Vikky Anand and Rochish M. Thaokar

Abstract The crude oil explored from oil wells is in the form of a water-in-oil emulsion. To process the oil for refining into different useful products, the water needs to be separated from the water-in-oil emulsion. There are several procedures reported for breaking the water-in-oil emulsion. Generally, the water present in crude oil is in the form of brine droplets, and the salt concentration may vary from a few hundred to several thousand ppm. The salts present in the crude oil create severe problems in the downstream processing in refineries such as deactivation or poisoning of the catalyst. Therefore, the removal of water from the emulsion is typically the first unit operation in a crude oil refinery. The overall process of separation of water (brine) from crude oil is generally known as desalting. In this chapter, we give a brief discussion on the stability as well as destabilization of the water-in-oil emulsion system. The mechanism of demulsification and the method of breaking water-in-oil emulsion are also discussed in detail.

Keywords Water-in-oil emulsion · Electrocoalescence · Desalting

1 Introduction

Petroleum is one of the most important products that form the backbone of the economy as well as of the society. It is a major raw material for a variety of fuels which provides energy for heating and transportation and is essential to the industry. "The word petroleum, derived from the Latin *petra* (rock) and *oleum* (oil), refers to hydrocarbons that occur widely in the sedimentary rocks in the form of gases,

V. Anand (✉)
Department of Chemical Engineering, Indian Institute of Technology Jodhpur, Jodhpur, Rajasthan, India
e-mail: vikky@iitj.ac.in

R. M. Thaokar
Department of Chemical Engineering, Indian Institute of Technology Bombay, Mumbai, India
e-mail: rochish@che.iitb.ac.in

liquids, semisolids, or solids" [1]. The crude oil, generally brownish green to black liquid substance, is found throughout the world at different depths of earth's crust. The location of petroleum inside the earth crust is generally discovered by oil drilling after a geological survey of the land or seabed. The crude oil drilled from the earth's crust is in the form of a water-in-oil emulsion. The crude oil also has a very high concentration of salts due to brine droplets emulsified in the oil. The salt concentration may vary from a few hundred ppm to several thousand ppm. The water content in emulsion varies typically from 5% to 10% and can go up to 50%, depending upon the source of the oil [2, 3].

The water or brine water (salted water) present in crude oil can cause severe problems in the downstream processing of refineries such as deactivation and poisoning of the catalyst [2, 4]. The salts present in the crude oils are also responsible for corrosion in the processing equipment, thereby leading to high maintenance costs in the refineries. Petroleum consists of hydrocarbons of different molecular weights and chemical structure and is refined and separated based on demands in various applications. The separation is on account of their boiling points and is most easily done in distillation columns. The different fractions are kerosene, gasoline (petrol), and chemical reagents (polymers) and are used for making plastics and in various applications in pharmaceutical and petrochemical industries. To achieve all these fractions during refineries, several downstream reactions are performed in the presence of a catalyst. The performance of the catalyst can be adversely affected by the salts present in crude oil. Therefore, for safe and efficient refineries operation, it is critical to remove the brine from the crude oil. The overall procedure of separation of water (brine) from crude oil is generally known as desalting.

The size of water droplets in the water-in-oil crude oil emulsions may vary from 0.1 to 100 μm [2–5]. The ease of separation of water and oil in the emulsion depends on the stability of the emulsion. Several parameters that can directly or indirectly affect the stability of the emulsion can be listed as % water content, pH of wash water, interfacial tension, the nature of asphaltene and naphthenic acids, nature of brine (such as $NaCl$, $CaCl_2$), the conductivity of emulsion phase, demulsifier dosage, API value of crude oil, processing temperature, and electrical and physical properties of an emulsion [6–13]. Various techniques such as gravity separation, chemical treatment, membrane separation, centrifugation, and electrocoalescence are available for breaking the water-in-oil emulsion [2, 14–21]. All the individual methods have their advantages and disadvantages and are discussed in detail in this chapter.

The chapter is organized as follows: the nature of crude oil, classification, and their properties are discussed, followed by the factors affecting the stability of the water-in-oil emulsion. Breaking of water-in-oil emulsion, also known as oil demulsification, is discussed next. This is followed by the mechanism and method of demulsification. The chapter concludes with a detail procedure and mechanism of breaking of the water-in-oil emulsion by using electrocoalescence technique.

1.1 Crude Oil: Elemental Composition and Classification

Crude oil composition obtained from wells and offshore varies from region to region and also depends on the life of the well and the reservoir. The stability of the crude oil may also depend on the life of wells and the individual composition of crude oil. The main elemental compositions (percentage) of crude oil are given in Table 1, and these are hydrogen, carbon, oxygen, nitrogen, sulfur, and metals like vanadium and nickel [1]. Four major types of hydrocarbon molecules present in crude oil are given in Table 2 [22]. The relative percentage of each molecule may vary from oil to oil. However, small changes of any of the element may significantly change the properties of crude.

The classification based on solubility and polarity of crude oil is mainly divided into four major classes named as saturates, aromatics, resins, and asphaltenes (SARA) shown in Fig. 1 [22]. For the separation of the SARA classes, high-performance liquid chromatography (HPLC) is used because of the speed and simplicity of analysis as compared to the American Society for Testing and Materials (ASTM) procedure which is based on liquid chromatography (LC) [23]. Saturates (aliphatics) are non-double bond and non-polar compounds and include both cycloalkanes and alkanes. Waxes are a subclass of saturates. The aromatics contain one or more than one ring compounds and may be attached to naphthenes [22]. Resins are polar molecules which contain heteroatoms such as oxygen, sulfur, or nitrogen and naphthenic acids which is also part of this fraction. Resins are likely to be soluble in light alkanes, such as heptane and pentane, but insoluble in propane [24]. Asphaltenes are also polar but have higher molecular weight generally in the range of 500–1500 g/mol. It also contains heteroatoms such as oxygen, sulfur, or nitrogen, along with the small fraction of organometallic constituents (V, Ni, and Fe) [25]. Because of the polar nature of resins and asphaltenes, they behave as surface-active compounds. Asphaltenes and resins in crude oil, therefore, stabilize the water-in-oil emulsion.

Table 1 Elemental compositions of crude oil

Element	Weight %; mg/L
Carbon	83–87%
Hydrogen	0.1–1.5%
Oxygen	0.1–1.5%
Nitrogen	0.05–2%
Sulfur	0.05–6%
Metals (V and Ni)	1000 mg/L

Table 2 Classifications of hydrocarbons in crude oil

Hydrocarbon	Weight % (average)
Paraffins (alkanes)	30%
Naphthenes	49%
Aromatics	15%
Asphaltics	6%
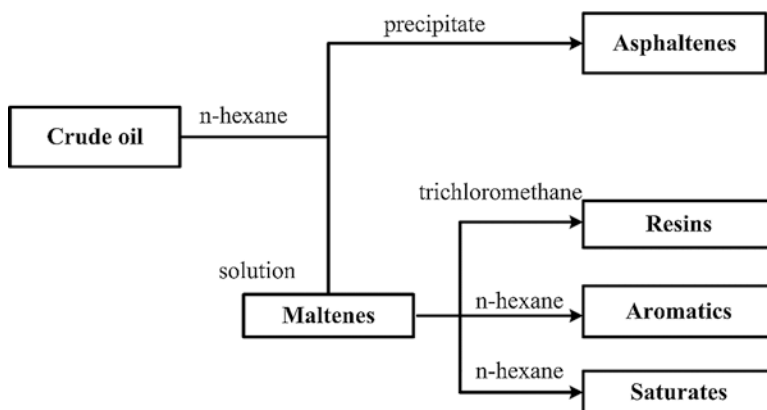
Fig. 1 SARA-separation scheme

1.2 Crude Oil Characteristics and Properties

Crude oil characterization is of primary importance in the refinery (industry). As discussed in the previous section, crude oil is a complex mixture of an organic compound. Therefore, there is a need to understand the physical and chemical characteristics of crude before further processing. There exist many such properties and characteristics, but here a few are discussed in brief.

1.2.1 API Gravity

American Petroleum Institute (API) gravity and specific gravity (S_g) are a standard in trading of crude oil. Specific gravity (density) with respect to water is one of the important properties widely used in industry for preliminary assessment of crude oil quality and character. API gravity of crude is calculated by the Eq. (1) given below:

$$\mathrm{Degree\,API} = \frac{141.5}{S_g} - 131.5 \tag{1}$$

According to API gravity grade, the crudes are further classified as light, medium, and heavy crude oil. API gravity greater than 31.1° ($S_g < 0.867$ g/cm³) is called light crude, API value in between 22.3° and 31.1° ($S_g = 0.917 - 0.867$ g/cm³) is called medium crude, while API value below 22.3° ($S_g > 0.917$ g/cm³) is termed as heavy

crude oil. A crude oil-specific gravity equal to 1 (API value is 10) is known as an extra heavy oil.

1.2.2 Viscosity

Viscosity (η) measures the internal resistance to the flow of crude oil, and the dynamic viscosity is generally expressed in Pa s. The viscosity of crude varies in a wide range (10–1000 Pa s). Highly viscous crudes create problems in the refinery in transportation and operations. Generally, light and heavy crudes also have low and high viscosities, respectively. This is attributed to the presence of high molecular weight asphaltenes or suspended particles. The crude oil viscosity mainly depends upon temperature, pressure, and amount of emulsified water.

1.2.3 Interfacial Tension

Interfacial tension (IFT) and surface tension originate in the presence of two phases (oil/water, gas/oil, or gas/water) having a difference in attractive intermolecular force. Crude oil contains surface-active compounds such as asphaltenes which affect static or dynamic tension. The interfacial films formed by asphaltenes and resins are highly sensitive to the pH of the aqueous phase [12]. IFT is generally expressed in dynes/cm (or mN/m) and has typical values in range 1–30 mN/m. Interfacial tension strongly depends upon surfactant concentration, temperature, pressure, pH, and the composition of each phase.

1.2.4 Crude Oil Conductivity

Electrical conductivity in crude oil can be attributed to the motion of polar organic (predominantly asphaltenes), conductive solids, and inorganic constituents, apart from dissolved water [26]. The conductivity of crude depends upon temperature, pressure, soluble, and insoluble water in the crude oil, the composition of crude oil, and conductive metallic species [27]. Conductivity is generally measured in Siemens per centimeter (or Siemens per meter) and is usually in a range of 10^{-10} to 10^{-7} S/m. The conductivity of crude oil increases with temperature [27].

2 Crude Oil-Water Emulsion

The crude oil recovered from oil wells is in the form of a water-in-oil emulsion. Approximately two-thirds of the world's crude is found in emulsion form that must be treated before being marketed [28]. Emulsions generally consist of two immiscible liquids: one acts as a continuous phase and the other as a dispersed phase
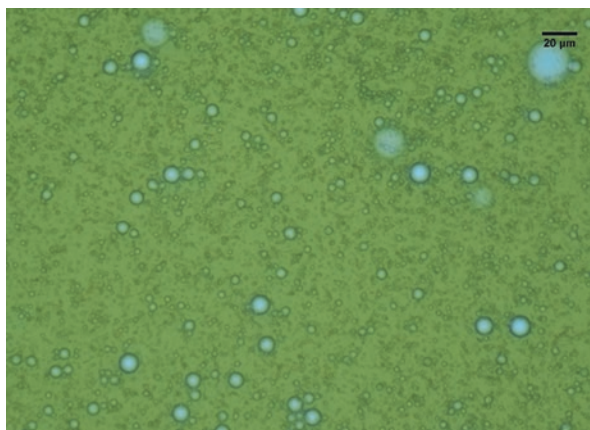
Fig. 2 Microscopic view of water-in-crude oil emulsion (10 v/v%). Scale bar is 20 μm

which is stabilized by surface-active agent present in an emulsion. This is discussed in brief in the next section. The water percentage in the water-in-oil emulsion varies in a broad range from 1% to 50%. A microscopy image of the crude oil-in-water emulsion is shown in Fig. 2.

2.1 Stability of Water-in-Crude Oil Emulsions

Emulsions are unstable from a thermodynamic point of view (water and hydrocarbon system) and are highly sensitive to temperature and pressure. In general, there is a natural tendency for a liquid-liquid system to separate. Therefore, emulsions are kinetically stable only for a finite time. The emulsions can be simply classified as follows: (1) loose emulsions wherein water separates within a few minutes; (2) medium emulsions wherein water separates in tens of minutes; and (3) tight emulsions where water separates in hours sometimes a day [29]. For easy separation of tight emulsions, the surfactant is typically added.

The water-in-oil crude oil emulsions are stable because of a film formed by some surface-active molecule (high molecular weight polar molecules) around the water droplets at the water-oil interface. The interfacial films increase the interfacial viscosity, which retards the rate of separation of water. The properties of an interfacial film depend upon the crude type (amount of asphaltenes, paraffinic, etc.), pH of water, the temperature of emulsion system, and time of contact or aging time [30]. The interfacial films are divided into two types on the basis of mobility, namely, rigid films and mobile films [12]. Rigid (solid) films are unlike soluble, solid films at the water-oil interface that lead to high interfacial viscosity. These films are stabilized by the presence of very fine solid particulate. This provides a strong barrier to droplets for agglomeration or coalescence. Mobile (liquid) films have low

interfacial viscosity. When a demulsifier is added into the emulsion, the films change into liquid films. The liquid films are slightly soluble as compared to solid films, and the coalescence of droplets is enhanced.

The emulsion stability primarily depends upon the type of interfacial films. Therefore, it is important to understand the factors which affect the stability of these films. Some factors that are briefly discussed herein [31, 32] are:

- Polar surface-active molecules (e.g., asphaltenes, resins)
- Solids including waxes and inorganic salts (cause of corrosion)
- Droplet size distribution in the emulsion
- Temperature
- Brine concentration
- pH of brine

Heavy polar fractions such as resins, asphaltenes, organic acids (carboxylic, naphthenic), and bases are present in varying quantities and forms in crude oil and contribute to the stabilization of the crude oil emulsion to a varying degree. Asphaltenes are very complex polyaromatic molecules attached with some hetero-atoms or metals (N, O, S, V, Ni) such as shown in Fig. 3 [33]. These are soluble in benzene or ethyl acetate but insoluble in low molecular weight n-alkanes.

The diffusion of fine solid particles present in the crude to the oil-water interface can stabilize water-in-oil emulsions. Solid particles can also get electrically charged at the interface, thereby enhancing the stability of an emulsion. Typically the diameter of particles is in the range of submicron to a few microns [34]. Wettability of particles is defined as the degree of solids that is wetted by water or oil (when the emulsion is present). Wettability also enhances the stability of an emulsion. The oil-wet solids are waxes and asphaltenes, whereas water-wet solids are clays, sand, $CaCO_3$, $CaSO_4$, etc. [35]. Binks and Lumsdon [36] report that the emulsion may be stabilized by the presence of colloidal silica particles. These particles are charged and appear at the interface but are destabilized at higher pH. The charge on the particles is due to modification of pH (e.g., silica has zero charge at pH 2, but it becomes negatively charged at pH more than 2) and addition of electrolyte.

Temperature significantly affects the stability of an interface and also the solubility of surfactant. With an increase of temperature, the viscosity of the system reduces significantly, which helps to reduce the stability of an emulsion. Jones et al. [37] studied the effect of temperature on the interfacial film stability and found that it gradually decreases with an increase in temperature.

Strassner et al. [12] studied the effect of pH on interfacial film stability. The author found that there are two types of stable films found in the oil-water emulsion, namely, rigid and mobile. Solid (rigid) films are mainly formed by the presence of polar molecules such as asphaltene, whereas liquid (mobile) films are formed because of resins. According to Strassner et al. [12], the amount of demulsifier used for coalescence may be reduced by adjusting to a proper pH. The author gives an idea about how in low pH range (acidic region) solid films are formed by asphaltenes which are highly stable. However, with an increase in the pH of emulsion, the rigid films change into liquid films which are less stable. The author suggested that film
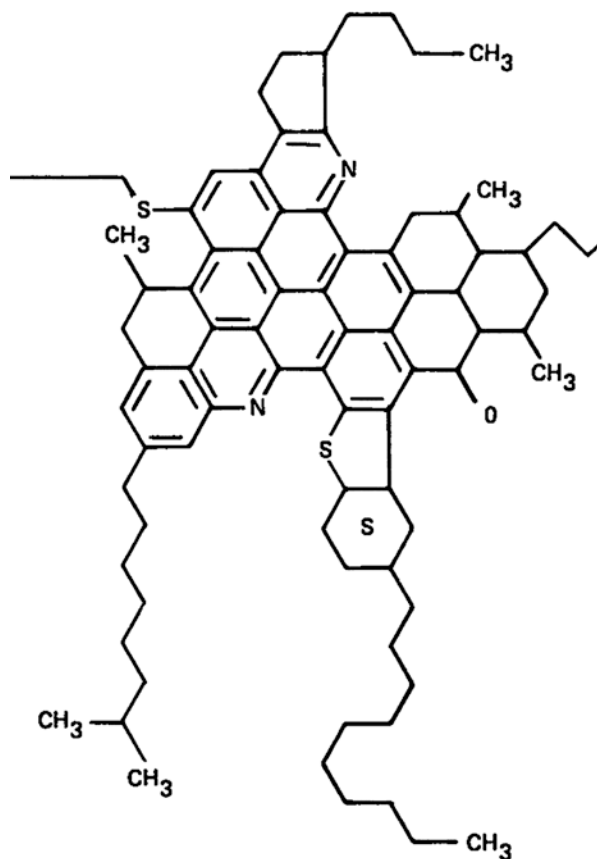
Fig. 3 Molecular structure of asphaltenes proposed by Speight and Moschopedis [33]. (Copyright 1982 American Chemical Society Publishing. Figure is adapted with permission from ref. [33])

stability could reduce if one operates under basic condition because of the reduction in interfacial tension. In the presence of brine, better separation of water is reported to be achieved in the pH 6–7. An increase in water and demulsifier concentration in the emulsion also leads to better separation. The author also suggested some limitation such as controlled supervision is required to maintain pH since the change in pH may lead to lower efficiency of separation and corrosion.

Specific ions in the brine composition can also influence the film stability. Strassner et al. [12] have studied the effect of constituent ions in the brine present in crude emulsions and investigated the optimum pH and demulsifier concentration for better separation of water. According to Strassner et al. [12], optimum pH for getting better separation of water, when brine is contained in the crude, is low (pH 6–8) as compared to non-brine crude pH which is higher (pH 9–10). This may be because the interfacial pH of brine may be higher as compared to bulk concentration. The brine which contains high Ca^{2+} ions or high Ca^{2+}/Mg^{2+} ratio makes a rigid (solid)

film with the interface of the oil-water emulsion which leads to stability of the emulsion [37].

In the crude oil analysis, typically the total acid number (TAN) is measured, which corresponds to the mass of *KOH* in milligrams necessary to neutralize the acids contained in 1 g of oil. The acidity of crude oil can be attributed to the presence of naphthenic acids. The pK_a value for naphthenic acids in crude oil was found to be ~4.9, which depends upon the number of carbon chains and presence of one, two, or three saturated rings [38].

2.2 Skin Formation

It is very often reported that the water-in-oil emulsion is stabilized by asphaltenes or high molecular surface-active compound [39, 40]. Crude oil contains various natural surfactants such as high molecular weight surface-active compounds (asphaltenes and resins) and low molecular surface-active compounds (sodium naphthenate, calcium naphthenate). Czarnecki and Moran [41] studied the contribution of low molecular weight surface-active compounds such as sodium naphthenate (SN), etc. Czarnecki and Moran [41] explained the competitive nature in making of a skin (layer) on the oil-water interface in Fig. 4. Figure 4 shows that the high asphaltenic (high molecular weight) compounds have lower surface activity and slow and irreversible rate, whereas surfactants such as sodium naphthenates are highly active and have a fast adsorption rate.

Czarnecki and Moran [41] also studied the interfacial tension with respect to SN concentration. With an increase in the concentration of SN, the surface and interfacial tension (γ) is reduced. At low concentration, SN makes a rigid interface, but at higher concentration, the interface becomes flexible and shows a low interfacial
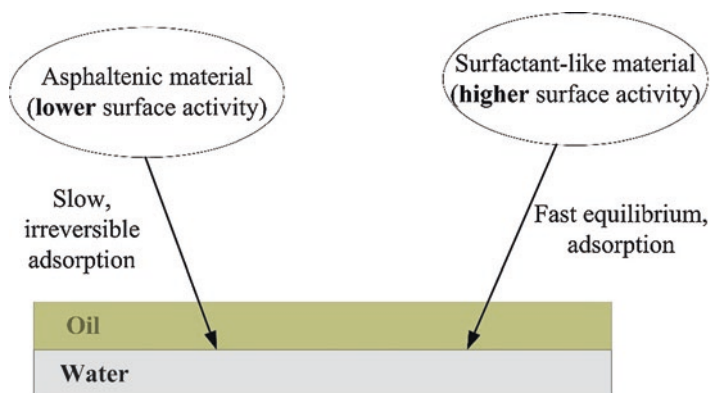
Fig. 4 Schematic of the model depicting the competition between subfractions of asphaltenes and low molecular weight surfactants at the oil/water interface. (Copyright 2005 American Chemical Society publishing. The figure is adapted with permission from ref. [41])
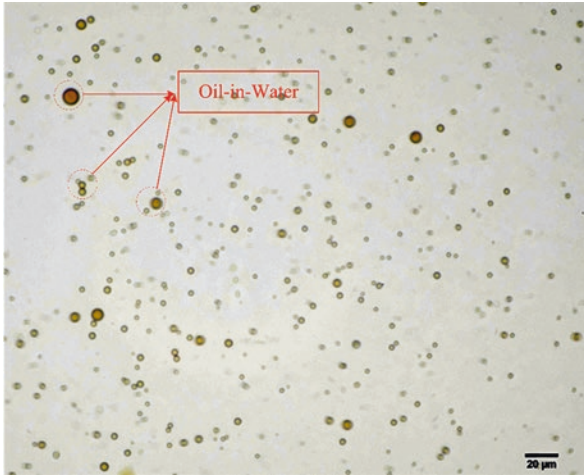
Fig. 5 Microscopic image of unresolved brine at pH 10 using NaOH. Carryover oil droplets can be clearly seen in the image. Scale bar is 20 μm. (Copyright 2018 Elsevier publishing. The figure is adapted with permission from ref. [14])
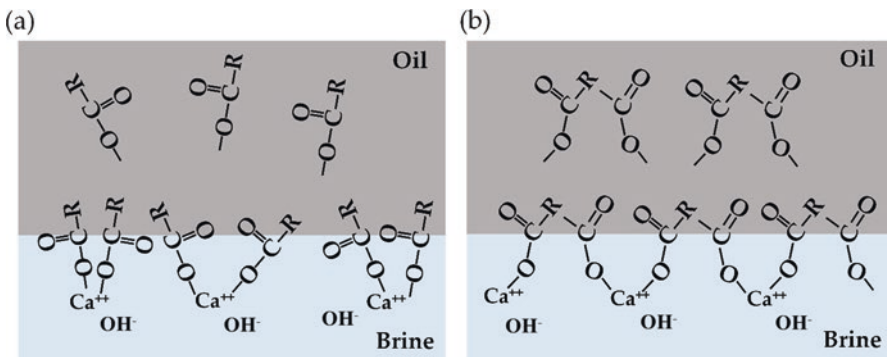
Fig. 6 Schematic diagram of carboxylate and calcium ion interaction at the interface. (**a**) Monocarboxylate interacted with calcium ions. (**b**) Dicarboxylate interacts with calcium ions and formed cross-link at the interface. (Copyright 2018 Elsevier publishing. The figure is adapted with permission from ref. [14])

tension. Because of low interfacial tension, water drops may be picked up by oil resulting in an unresolved (rag) layer formation, as shown in Fig. 5 [2]. The skin formation around the droplets also depends upon the nature of carboxylates such as monocarboxylate or dicarboxylate. The mechanism of the skin formation due to mono- and dicarboxylate in the presence of Ca^{2+} at the water-oil interface is shown in Fig. 6.

The stability of an emulsion can be determined, from the practical point of view, by performing an important test named as the bottle test. It determines the ease of

separation of the water-in-oil emulsion system. The separation of water data recorded as a function of time and the relative stability can be compared under different experimental condition.

3 Desalting

Desalting of crude oils is a process of removing brine from crude oil emulsions. The crude oil contains brine which can cause various problems in the downstream processes such as deactivation of the catalyst and corrosion, thereby reducing the plant efficiency and increasing the operational costs. To avoid this problem, a two-stage desalting is done at the crude oil production site followed by another at the refinery site to get crude specifications corresponding to the industry regulation. In desalting process (Fig. 7), 5–10% (v/v) of fresh (wash) water is added to heated crude oil and mixed by static mixers to ensure appropriate contact of crude oil and water, and the emulsion is then sent to a desalter (electrocoalescer) for separating oil or aqueous phases [4, 15]. The desalting becomes difficult because the oil contains surface-active compounds such as asphaltenes or resins that make a film on a water droplet, thereby making a stable emulsion. Because of the presence of asphaltenes, waxes, resins, and small solid particles (impurity), the oil-water interface becomes highly viscous [42]. In order to reduce this problem, a chemical called demulsifier is added, which helps to rupture the asphaltic layer and make coalescence easier [43, 44].

The recent technology for oil desalting in refineries uses a combination of methods such as thermal, mechanical, chemical, and electrical for improving the efficiency of dewatering. Electrostatic destabilization has emerged as a promising
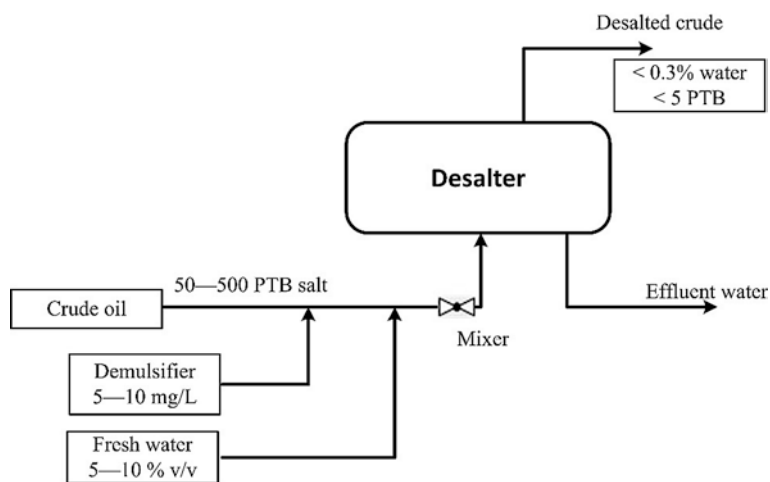
Fig. 7 Process flow diagram of desalting

method to separate oil-in-water emulsion and was first demonstrated by Cottrel century ago [45].

3.1 Oil Demulsification

Demulsification is a process of breaking of the water-oil emulsion into water and oil phase. From an industrial point of view, the refineries are more concerned about three aspects:

- Rate of separation of phases (oil and water)
- Amount of water remaining in oil after separation
- Quality of separated water for disposal

A number of techniques can be applied for demulsification process. The final water concentration in crude should not exceed 0.3% (v/v), and total dissolved salts are about 0.7–1.0 lb per thousand barrels (PTB) which are sent to refinery units [3, 4]. Factors affecting the demulsification are temperature, agitation or shear, residence time, and demulsifier concentration.

Increasing the temperature of an emulsion increases the mobility and reduces the viscosity of the oil, such that the collision efficiency of droplets increases and the rate of coalescence enhances which results in an increase in the settling rate of water drops. However, crude conductivity increases with temperature. The other disadvantage of higher temperature is high heating costs and loss of light ends. High agitation decreases the separation efficiency, because at high agitation, the drops may break into small drops. So a gentle (or low) agitation is required for assuring the mixing of chemical demulsifier. Increasing residence time increases the separation efficiency, but high residence time increases the cost of operation. The optimum amount of demulsifier is required to break the emulsion, and higher demulsifier concentration makes the oil in water emulsion stable.

3.2 Mechanism of Demulsification

Demulsification or separation of both water and oil phase for oil-water emulsion system is a two-stage process. The first step is an aggregation (flocculation) of water droplets, and the second step is the coalescence of drops to make bigger drop which settles down by gravity. Anyone out of two steps may be the rate-determining step.

In flocculation, the dispersed phase (water droplets) in an emulsion accumulates together, forming aggregates. Sometimes, the water droplets are close enough, but they do not coalesce. Coalescence happens when emulsion film stability is low. The factors that enhance the rate of flocculation are [29]:

- Water concentration (v/v) of emulsion and high water cut increase the rate of flocculation.
- At higher temperature, the thermal energy of droplets increases, and the rate of collision increases which leads to flocculation.
- The high-density difference leads to settling of the drop so that the flocculation at the bottom is higher.
- By applying an electrostatic field, the droplets move towards the electrode, and the droplets aggregate towards the electrode.

Coalescence is a phenomenon in which two drops fuse or merge together and form large drops [8]. Generally, this is an irreversible process (no breakage of large drop), drops become bigger, and gravitational forces acting on drops help in settling the drops. With an increase in the rate of flocculation, an increase in the rate of coalescence is observed in an emulsion having films with low interfacial viscosity. Solid interfacial films reduce coalescence, and addition of demulsifier helps to modify solid films to mobile films such that the film can be ruptured easily [46]. The coalescence rate can depend on three simple steps [47]: first, the applied external force, such as gravity in which the droplets (particles) approach each other; second, film formation and drainage, the rate of film thinning may be the rate-determining step for coalescence [48, 49]; and, finally, the critical film can rupture (break) by any significant mechanical (low mixing) or thermal disturbance which may cause coalescence [49]. The mechanism (Fig. 8) and the rate of film rupture may be enhanced by the addition of demulsifiers [43].

Sedimentation and creaming are caused by the density difference in sedimentation of the high-density droplet. The reverse is creaming of a low-density phase (oil) wherein oil moves upwards. Sometimes there is no clear separation of both phases, and a layer called unresolved (rag/pad layer) emulsion accumulates in between water and oil interface which creates a lot of problems in the desalters. It reduces the efficiency of coalescence, increases the basic sediments and water in the treated oil, and occupies the tank space. The unresolved layer forms because of the use of
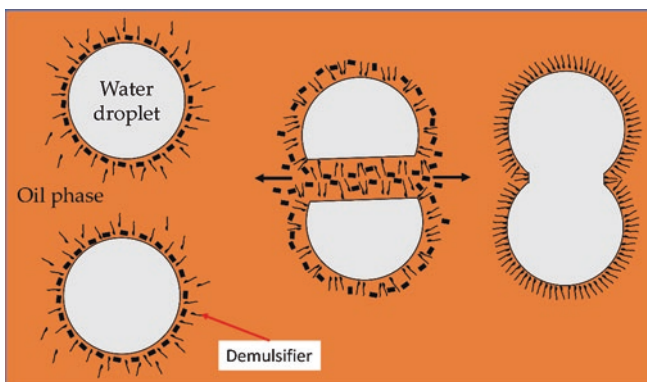
Fig. 8 Mechanism of demulsification

ineffective or low concentration of demulsifier. This is assisted by the presence of solid particles and when the system is operated at low temperature.

3.3 Method of Demulsification

The demulsification of crude is required for further transportation and processing, and in a refinery, demulsification is done by several methods [29]:

- Thermal method
- Mechanical method
- Electrical method
- Chemical method

Anyone or any combination of methods may be useful for demulsification in industry. The choice of a method depends upon the crude properties and product specification with proper consideration of economics. The most common method in small scale is thermal along with proper chemical demulsifier, which assists the destabilization of the emulsions. This is followed by mechanical and, finally, the electrical method. In most of the refineries, a combination of all the techniques such as chemical and the electrostatic field is used for enhancing the coalescence at a high temperature that helps to increase the collision frequency.

3.3.1 Thermal Method

Higher temperatures reduce the interfacial viscosity and oil viscosity and therefore increase the separation of a water-in-oil emulsion. The thermal energy of the water droplet increases, and collision frequency also increases at high temperature, although the heating cost also increases. Moreover, there is a loss of light ends so that API of the crude reduces and the tendency of corrosion in a vessel also increases.

3.3.2 Mechanical Method

A wide variety of mechanical equipment (desalters, settling tank, and two- and three-phase separators) are used in demulsification of crude emulsions. Most commonly, electro-desalters are used in the refineries. The oil from the separator generally contains an unacceptable level of water, solids, and salts (less than 10 PTB). Therefore, one needs to treat the crude further to match the final specifications in the refinery. Sometimes freshwater (5–10 v/v%) is added to remove salts in a process known as desalting. In industry, mainly single or multistage desalters are used. Demulsifier is added, and the crude, freshwater, and the demulsifier are passed through a mixer in a single-stage desalter as shown in Fig. 7. Aryafard et al. [9] studied the water and salts removal efficiency by using a single-stage desalter

model. The author found that the dehydration and desalting efficiency of simulated results were 98.48% and 96.06%, respectively, which is very close to the experimental result of 96.77% and 94.15%, respectively, in their study. They also observed that by increasing the pressure of mixing valve from 20 to 30 psi, the efficiency of dehydration does not change significantly. Aryafard et al. [50] studied the drop size distribution, desalting, and dehydration efficiency by using a two-stage desalter model. Aryafard et al.'s [50] simulation results show that by increasing the addition of freshwater from 3% to 6%, the salts content in treated crude can be reduced from 2.06 to 0.71 PTB.

3.3.3 Electrical Method

Electrostatic fields are applied for the emulsion treatment and separating water from the oil-water emulsion. When non-conductive continuous phase (oil) that contains a small fraction of conductive dispersed phase (water) is subjected to an electrostatic field, the water drops coalesce by following one of the three physical phenomena [8, 29].

- Under the electric field, the water drops polarize and align along the electric field lines so that positive-negative poles are developed on the water droplets leading to their attraction and coalescence.
- In case of direct electric (DC) field, the charges are induced on the water drops; the drops aggregate and attract towards the electrode or bounce in between the electrodes until the drops become large and settle by gravity.
- Application of electric field disturbs or weakens the interfacial film of original droplets. Under the application of sinusoidal alternating current (AC), the line of forces is higher in the first half of the cycle. The drops elongate or make elliptical shape, but because of surface tension, they try to retain their original shape. This process is repeated again and again so that the interfacial film becomes weak and it leads to coalescence.

However, it may be theorized that water droplets have a net charge and under the electrostatic field, collision probability increases and coalescence increases. The electrical field is generally measured in kV/cm, and with an increase in the field, the rate of coalescence increases. However, at some point, it reaches a non-coalescence regime when other factors also contribute to the interaction significantly such as salt concentration and cone angle formed in between the drops discussed in detailed in Sect. 4.

3.3.4 Chemical Method

Chemical method is one of the most common techniques for emulsion breaking. In this method, a chemical called demulsifier is added, which neutralize the emulsifying agent. Some common demulsifiers such as epoxy resins, polyamines,

polyethyleneimines, polyols, di-epoxides, and phenol-formaldehyde resins are often used. The demulsifiers have two parts: one is a head group that generally is a surface-active molecule which is hydrophilic, while the other is a linear hydrocarbon lipophilic group. When a demulsifier is added into the emulsion, it migrates towards the oil-water interface, which weakens or ruptures the rigid film and helps it to coalesce. Figure 8 shows the basic mechanism of demulsification in which a demulsifier comes at the surface of an emulsion and replaces the film formed by rigid materials (asphaltenes or resins) thereby assisting coalescence [43]. The type of demulsifier or optimum amount of demulsifier varies from crude to crude and mainly depends upon the crude properties or SARA analysis (percentage of asphaltenes).

Aveyard et al. [51] studied the effect of changing the hydrophilic-lipophilic balance (HLB) value. They used sodium bis(2-ethylhexyl) sulfosuccinate and octylphenyl-polyethoxylates as demulsifiers, and the HLB value was controlled by changing the number of ethoxy groups. They found that with an increase of surfactant concentration, the rate of demulsification increased. The higher concentration of surfactant may decrease the rate of demulsification because of overdosing that can stabilize the emulsion.

Sjöblom et al. [44] studied the destabilization of the water-in-crude oil emulsion. Crude from Norwegian continental shelf was used and 1-butanol and benzyl alcohol and amines for demulsification. They observed that the alcohol groups modify the solid film by diffusion/partitioning process, whereas amines strongly affect the interfacial film by hydrophilizing the whole film. The authors also observed that the interfacial tension trends depend upon the addition of alcohols and amines.

The typical experimental condition in the industry is the emulsion enters the desalter which has typical residence time between 10 and 30 min, depending on the API of the crude being desalted, and temperatures vary from around 110–145 °C. The desalter is a huge vessel, typically horizontal, around 3 m in diameter and 15–20 m in length. The crude with water emulsion is introduced from the bottom and is separated into a brine that leaves at the bottom of the desalter and desalted crude, which is drawn out from the top. Table 3 gives a summary of the method used, desalting, and dewatering efficiency for the treatment of water-in-crude oil emulsions.

4 Electrocoalescence of Water-in-Oil Emulsion

The water droplets in water-in-oil emulsion move under gravitational force which is resisted by the viscous drag. In the presence of an electric field, the droplet in addition experiences electrostatic forces, which can affect the motion of the droplets [15, 54]. Under an electrostatic force, a conducting droplet (particles) experiences a dipolar force that can align the droplets in the direction of the applied electric field, simultaneously getting attracted to each other and coalescing, resulting in what is known as electrocoalescence. This technique was first introduced by Cottrell and Speed [55].

Table 3 Literature on method used, desalting, and dewatering efficiency for the treatment of water-in-crude oil emulsions

Method used	Crude oil (API gravity)	Brine conc. (mg/L)	% Water	Desalting efficiency (%)	Dewatering efficiency (%)	Reference
Electrical and thermal	27	–	10.8	96.8	93.9	Less and Vilagines [3]
Chemical	13.2	4440	50	–	90.0	Strassner et al. [12]
Thermal	19.1	–	45	–	94.2	Fortuny et al. [31]
Thermal, mechanical, and chemical	16.6	32,400	9.3	99.8	97.3	Sad et al. [52]
Chemical	27.4	–	10	–	90	Atta [53]
Electrical and chemical	21.4	–	10	–	99	Anand et al. [2]
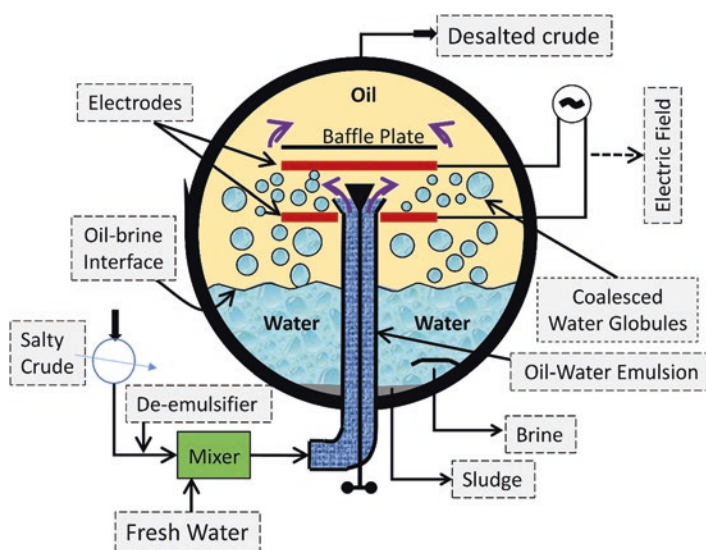
Fig. 9 Schematic flow diagram of the desalting process (cross-sectional view)

Figure 9 shows the typical cross-sectional view of electrodesalter practiced in oil refineries. The overall desalting operation can be understood as follows: the crude oil (continuous phase) is mixed with water (dispersed phase) and demulsifier by using a static mixer, and the emulsion with an average size of 10 μm is produced and fed into the desalter unit as shown in Fig. 9. The emulsion is distributed throughout the vessel using a distributor between the regions of the electrodes. The electrodes are connected to the transformer to apply an appropriate electric field. The droplets under electric field region grow by electrocoalescence and settle due to gravity. At a

result, the water phase is separated at the bottom and oil phase at the top. Further, the aqueous phase is sent to the second stage of desalting or an effluent treatment plant, and the crude oil is sent for downstream processes.

To understand the mechanism of droplets coalescence of emulsion under an applied electric field, the droplets can interact in two ways, drop-drop interaction (Fig. 10c) and drop-interface interaction (Fig. 10e) as shown in Fig. 10. In the case of drop-drop interaction, droplets may show coalescence or non-coalescence, on the other hand, for drop-interface interaction, droplets may show coalescence, partial coalescence, or non-coalescence (Fig. 10d, f) [6, 56]. In electrocoalescence, coalescence is the desired phenomena. On the other hand, partial coalescence and non-coalescence are undesired and may slow the rate of separation or deteriorate the efficiency of coalescence.

Several parameters that can influence the coalescence, partial coalescence, and non-coalescence of droplet interaction are the strength of the electric field, frequency of electric field, the conductivity of droplets phase, the conductivity of oil phase, electrode configuration, the volume fraction of water in the emulsion, the quality (purity) of oils, the viscosity of the oil, the concentration of asphaltenes, total acid number, and interfacial rheology of the water-oil system [10, 12, 13, 19, 57, 58].

The coalescence under electric field is generally believed to follow three steps: (1) drops approach each other, assisted by an electric field, (2) film drainage of the continuous phase in the liquid film separating the droplets, and (3) film rupture and coalescence [54]. The drops are attracted to each other due to dipolar force, following which they may coalesce or non-coalesce. This outcome depends upon the strength of the electric field. The migration of droplets depends upon the nature of the electric field, such as uniform or non-uniform fields [59]. When an electric field is applied to a pair of drops, it leads to their deformation due to the resulting Maxwell stress that depends upon the electrocapillary number. Figure 11 shows the
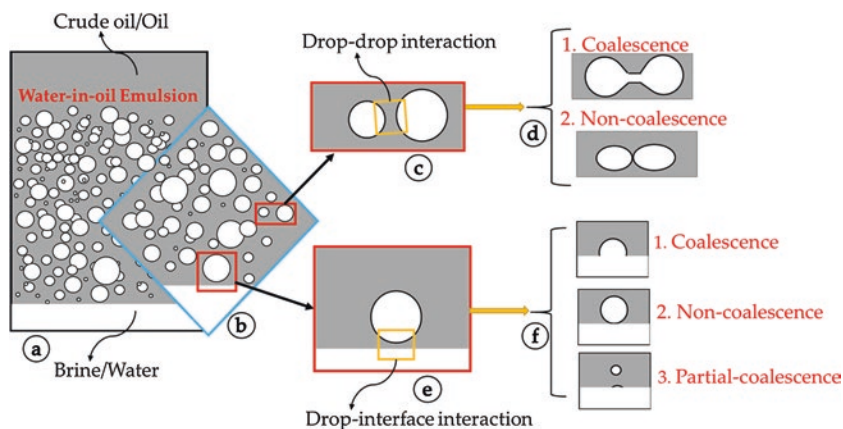
Fig. 10 Type of interaction and phenomena of droplets under an electric field
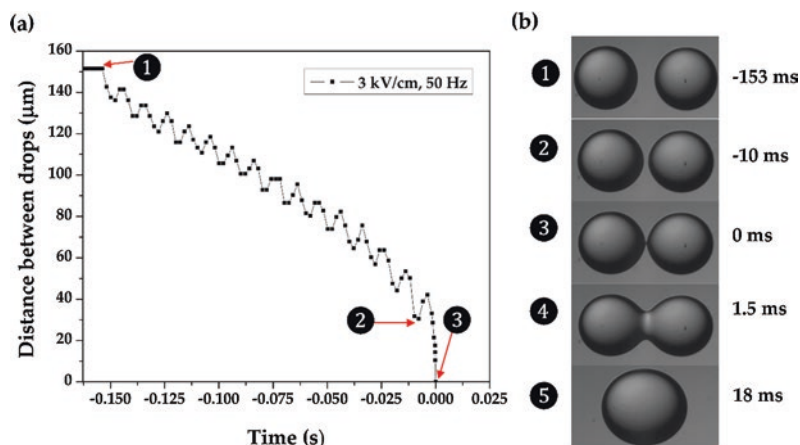
Fig. 11 Interaction of droplets under electric field. (**a**) Distance between the droplets vs. time. (**b**) Sequence of images of drop-drop coalescence. Electric field 3 kV/cm at frequency 50 Hz
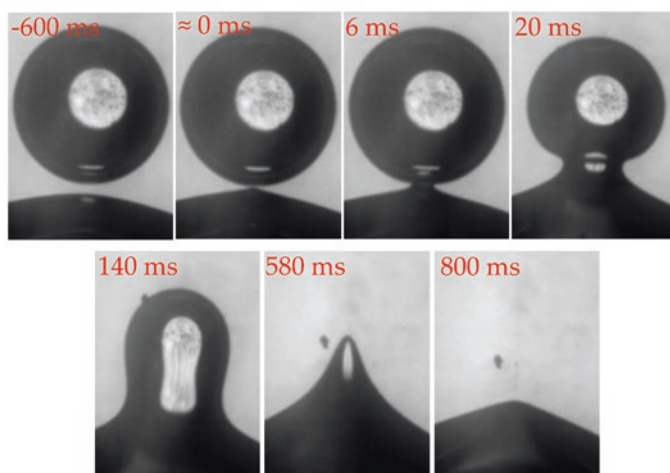
Fig. 12 Sequence of images of drop-interface coalescence under an electric field = 0.5 kV/cm

experimental images of approach and coalescence phenomena of drop-drop coalescence under an electrical field. Figure 12 shows the sequence of the image of drop-interface coalescence under an electric field. The detailed discussion regarding the mechanism of coalescence and non-coalescence under an electric field is not part of this chapter. The overall discussion on droplet coalescence presented in this chapter will help to understand the destabilization mechanism of the water-in-oil system.

5 Summary

In this chapter, we have given a brief introduction to elemental composition, classification, crude oil characteristics, and stabilization of the crude oil-water emulsion. We also discussed the destabilization of the emulsion, factors affecting the demulsification, and various methods and parameters affecting the separation of water from the water-in-oil emulsions. The stability of water-in-oil emulsion primarily depends upon the nature and the source of the oil. The high molecular weight asphaltenes because of their surface-active nature form a skin around the droplets. Because of the skin, even under an electric field, the droplets approach to each other but can resist coalescence. Therefore, a small molecular weight demulsifier is often added that helps to replace the skin layer and make coalescence possible. An overall procedure to separate the water (brine) from the oil helps removal of salts from crude oil which is responsible for the deactivation and poisoning of the catalyst in the downstream process of refineries.

References

1. Speight JG (2006) The chemistry and technology of petroleum. CRC Press, Boca Raton, FL
2. Anand V, Vashishtha M, Shown B, Patidar P, Malhotra A, Ghosh S, Jaguste S, Naik VM, Thaokar RM, Juvekar VA (2018b) Interrelationship between electrocoalescence and interfacial tension in a high acidity crude: effect of pH and nature of alkalinity. Colloids Surf A Physicochem Eng Asp 555:728–735
3. Less S, Vilagines R (2012) The electrocoalescers' technology: advances, strengths and limitations for crude oil separation. J Pet Sci Eng 81:57–63
4. Pereira J, Velasquez I, Blanco R, Sanchez M, Pernalete C, Canelon C (2015) Crude oil desalting process. In: Advances in petrochemicals, pp 67–84
5. Lashkarbolooki M, Ayatollahi S, Riazi M (2014) Effect of salinity, resin, and asphaltene on the surface properties of acidic crude oil/smart water/rock system. Energy Fuel 28(11):6820–6829
6. Anand V, Juvekar VA, Thaokar RM (2019a) An experimental study on the effect of conductivity, frequency and droplets separation on the coalescence of two aqueous drops under an electric field. Chem Eng Res Des 152:216–225
7. Anand V, Juvekar VA, Thaokar RM (2019b) Modes of coalescence of aqueous anchored drops in insulating oils under an electric field. Colloids Surf A Physicochem Eng Asp 568:294–300
8. Anand V, Roy S, Naik VM, Juvekar VA, Thaokar RM (2019d) Electrocoalescence of a pair of conducting drops in an insulating oil. J Fluid Mech 859:839–850
9. Aryafard E, Farsi M, Rahimpour M (2015) Modeling and simulation of crude oil desalting in an industrial plant considering mixing valve and electrostatic drum. Chem Eng Process Process Intensif 95:383–389
10. Chiesa M, Ingebrigtsen S, Melheim JA, Hemmingsen PV, Hansen EB, Hestad Ø (2006) Investigation of the role of viscosity on electrocoalescence of water droplets in oil. Sep Purif Technol 50(2):267–277
11. Eow JS, Ghadiri M (2003) Drop-drop coalescence in an electric field: the effects of applied electric field and electrode geometry. Colloids Surf A Physicochem Eng Asp 219(1):253–279

12. Strassner J et al (1968) Effect of pH on interfacial films and stability of crude oil-water emulsions. J Pet Technol 20(03):303–312
13. Vafajoo L, Ganjian K, Fattahi M (2012) Influence of key parameters on crude oil desalting: an experimental and theoretical study. J Pet Sci Eng 90:107–111
14. Anand V, Juvekar V, Thaokar R (2018a) Coalescence and noncoalescence of two aqueous drops in insulating oil under an electric field. Bull Am Phys Soc 63
15. Anand V, Patel R, Naik VM, Juvekar VA, Thaokar RM (2019c) Modelling and particle based simulation of electro-coalescence of a water-in-oil emulsion. Comput Chem Eng 121:608–617
16. Gupta AKS (1977) Process for refining crude glyceride oils by membrane filtration. US Patent 4,062,882
17. Mohammed R, Bailey A, Luckham P, Taylor S (1994) Dewatering of crude oil emulsions 3. Emulsion resolution by chemical means. Colloids Surf A Physicochem Eng Asp 83(3):261–271
18. Noik C, Chen J, Dalmazzone C (2006) Electrostatic demulsification on crude oil: a state-of-the-art review. In: International Oil & Gas Conference and Exhibition in China. Society of Petroleum Engineers, Richardson, TX
19. Ristenpart W, Bird J, Belmonte A, Dollar F, Stone H (2009) Noncoalescence of oppositely charged drops. Nature 461(7262):377
20. Roy S, Anand V, Thaokar RM (2019) Breakup and non-coalescence mechanism of aqueous droplets suspended in castor oil under electric field. J Fluid Mech 878:820–833
21. Staiss F, Roland B, Kupfer R (1991) Improved demulsifier chemistry: a novel approach in the dehydration of crude oil. SPE Prod Eng 6(03):334–338
22. Sjöblom J, Aske N, Auflem IH, Brandal Q, Havre TE, Saether Q, Westvik A, Johnsen EE, Kallevik H (2003) Our current understanding of water-in-crude oil emulsions: recent characterization techniques and high pressure performance. Adv Colloid Interf Sci 100:399–473
23. ASTM-D4124-09, 2009. Standard test method for separation of asphalt into four fractions. ASTM International, West Conshohocken, PA, 04.03, 1-8.
24. Sheu E, Storm D (1995) Asphaltenes: fundamentals and applications, vol 245. Plenum Press, New York, NY
25. Kilpatrick PK (2012) Water-in-crude oil emulsion stabilization: review and unanswered questions. Energy Fuel 26(7):4017–4026
26. Lesaint C, Spets Ø, Glomm WR, Simon S, Sjöblom J (2010) Dielectric response as a function of viscosity for two crude oils with different conductivities. Colloids Surf A Physicochem Eng Asp 369(1):20–26
27. Cametti C, Codastefano P, Tartaglia P, Rouch J, Chen S-H (1990) Theory and experiment of electrical conductivity and percolation locus in water-in-oil microemulsions. Phys Rev Lett 64(12):1461
28. Steinhau F (1962) Modern oil field demulsification. Part I. Petroleum 25:294–296
29. PetroWiki (2014) Stability of oil emulsions. https://petrowiki.org/Stability_of_oil_emulsions. Accessed 9 Apr 2016
30. Schramm LL (1992b) Fundamentals and applications in the petroleum industry. American Chemical Society, Washington DC, pp 1–49
31. Fortuny M, Oliveira CB, Melo RL, Nele M, Coutinho RC, Santos AF (2007) Effect of salinity, temperature, water content, and pH on the microwave demulsification of crude oil emulsions. Energy Fuel 21(3):1358–1364
32. Hajivand P, Vaziri A (2015) Optimization of demulsifier formulation for separation of water from crude oil emulsions. Braz J Chem Eng 32(1):107–118
33. Speight JG, Moschopedis SE (1981) On the molecular nature of petroleum asphaltenes. ACS Publications, Washington DC, pp 1–15
34. Tambe DE, Sharma MM (1993) Factors controlling the stability of colloid-stabilized emulsions: I. An experimental investigation. J Colloid Interface Sci 157(1):244–253
35. Kokal S, Al-Juraid J et al (1998) Reducing emulsion problems by controlling asphaltene solubility and precipitation. In: SPE Annual Technical Conference and Exhibition. Society of Petroleum Engineers, Richardson TX

36. Binks BP, Lumsdon SO (1999) Stability of oil-in-water emulsions stabilised by silica particles. Phys Chem Chem Phys 1(12):3007–3016
37. Jones T, Neustadter E, Whittingham K et al (1978) Water-in-crude oil emulsion stability and emulsion destabilization by chemical demulsifiers. J Can Pet Technol 17(02):100–108
38. Havre TE, Sjöblom J, Vindstad JE (2003) Oil/water-partitioning and interfacial behavior of naphthenic acids. J Dispers Sci Technol 24(6):789–801
39. Kilpatrick PK, Spiecker PM (2001) Asphaltene emulsions. in encyclopedic handbook of emulsion technology. Basel, New York, NY, p 207
40. McLean JD, Kilpatrick PK (1997) Effects of asphaltene solvency on stability of water-in-crude-oil emulsions. J Colloid Interface Sci 189(2):242–253
41. Czarnecki J, Moran K (2005) On the stabilization mechanism of water-in-oil emulsions in petroleum systems. Energy Fuel 19(5):2074–2079
42. Kang W, Xu B, Wang Y, Li Y, Shan X, An F, Liu J (2011) Stability mechanism of w/o crude oil emulsion stabilized by polymer and surfactant. Colloids Surf A Physicochem Eng Asp 384(1):555–560
43. Ramalho JBV, Lechuga FC, Lucas EF (2010) Effect of the structure of commercial poly (ethylene oxide-b-propylene oxide) demulsifier bases on the demulsification of water-in-crude oil emulsions: elucidation of the demulsification mechanism. Quim Nova 33(8):1664–1670
44. Sjöblom J, Söderlund H, Lindblad S, Johansen E, Skjarvo I (1990) Water-in-crude oil emulsions from the Norwegian continental shelf. Colloid Polym Sci 268(4):389–398
45. Cottrell FG (1911) Process for separating and collecting particles of one liquid suspended in another liquid. US Patent 987114
46. Schramm LL (1992a) Emulsions (fundamentals and applications in the petroleum industry). Advances in chemistry series. American Chemical Society, Washington DC
47. Zdravkov A, Peters G, Meijer H (2003) Film drainage between two captive drops: peo-water in silicon oil. J Colloid Interface Sci 266(1):195–201
48. Jain RK, Ivanov IB (1980) Thinning and rupture of ring-shaped films. J Chem Soc Far Trans 2 Mol Chem Physi 76:250–266
49. Stein H (1993) The drainage of free liquid films. Colloids Surf A Physicochem Eng Asp 79(1):71–80
50. Aryafard E, Farsi M, Rahimpour M, Raeissi S (2016) Modeling electrostatic separation for dehydration and desalination of crude oil in an industrial two-stage desalting plant. J Taiwan Inst Chem Eng 58:141–147
51. Aveyard R, Binks B, Fletcher P, Lu J (1990) The resolution of water-in-crude oil emulsions by the addition of low molar mass demulsifiers. J Colloid Interface Sci 139(1):128–138
52. Sad CM, Santana IL, Morigaki MK, Medeiros EF, Castro EV, Santos MF, Filgueiras PR (2015) New methodology for heavy oil desalination. Fuel 150:705–710
53. Atta AM (2013) Electric desalting and dewatering of crude oil emulsion based on Schiff base polymers as demulsifier. Int J Electrochem Sci 8:9474–9498
54. Atten P (1993) Electrocoalescence of water droplets in an insulating liquid. J Electrost 30:259–269
55. Cottrell F, Speed J (1911) Separating and collecting particles of one liquid suspended in another liquid. US Patent 987,115
56. Anand V, Juvekar VA, Thaokar RM (2020) Coalescence, partial coalescence and non-coalescence of an aqueous drop at an oil-water interface under an electric field. Langmuir 36:6051
57. Atten P (2013) Electrohydrodynamics of dispersed drops of conducting liquid: from drops deformation and interaction to emulsion evolution. Int J Plas Environ Sci Technol 7:2–12
58. Mhatre S, Deshmukh S, Thaokar RM (2015) Electrocoalescence of a drop pair. Phys Fluids 27(9):092106
59. Mhatre S, Thaokar R (2015) Electrocoalescence in non-uniform electric fields: an experimental study. Chem Eng Process Process Intensif 96:28–38

Index